Flow Processes in Composite Materials

FPCM - 11

Auckland, New Zealand, 9-12th July 2012

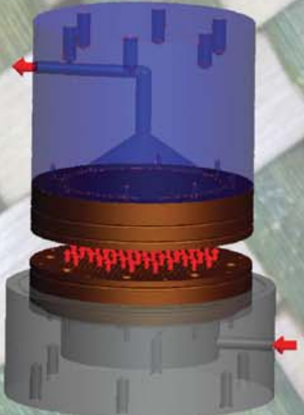

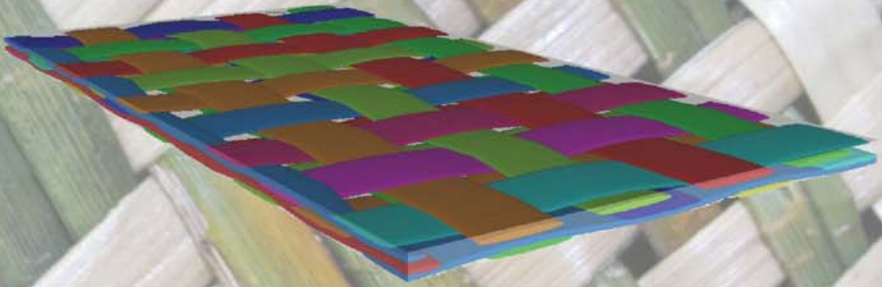

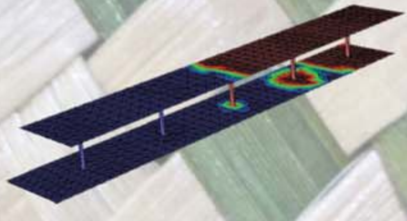

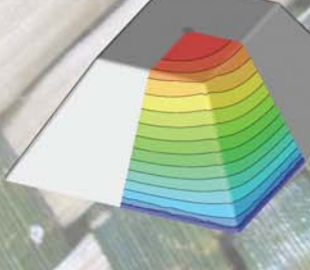

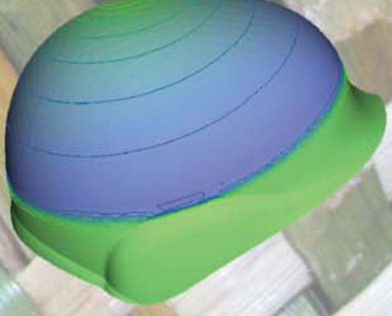

Proceedings

Preface

These volumes contain the papers presented at the ***Eleventh International Conference on Flow Processes in Composite Materials (FPCM-11)*** held in Auckland, New Zealand. The Centre for Advanced Composite Materials, housed within the Faculty of Engineering at the University of Auckland (Auckland, New Zealand), was the principal organiser of this international event held during the period July 9th-12th, 2012. The FPCM series of conferences aims to represent a forum for scientists, engineers and designers, both in Academia and Industry, for exchanging ideas, proposing new solutions and promoting international collaboration. FPCM-11 has attracted original papers on the science and engineering of composites manufacturing, specifically in the following areas:

- Permeability
- Voids, Dual-scale and Capillary Flows
- Processing
- Measurement, Monitoring and Control
- Process Modelling and Simulation
- Thermoplastics
- Natural Fibres and Green Composites
- Applications and Industry

This conference is a collection of papers from 17 countries. Over 100 abstracts that include both invited and contributed papers, were received and reviewed for oral presentations. A total of 70 manuscripts were reviewed and finally accepted for inclusion in the proceedings. On behalf of the Local Organising Committee, we extend our warmest thanks and appreciation to the authors of the manuscripts, and the session chairs for their interest, enthusiasm and support. Sincere thanks are also due to the technical editors, and the members of the International Advisory Committee.

P. A. Kelly S. Bickerton	P. Lescher Q. Govignon
Editors	***Technical Editors***

Local Organising Committee

Member	Affiliation
Simon Bickerton	**The University of Auckland**
Piaras Kelly	**The University of Auckland**
Sheeja Chidambaram	**The University of Auckland**
Mark Battley	**The University of Auckland**
Debes Bhattacharyya	**The University of Auckland**
Raj Das	**The University of Auckland**
Quentin Govignon	**The University of Auckland**
Krishnan Jayaraman	**The University of Auckland**
Richard Lin	**The University of Auckland**
Kim Pickering	**University of Waikato**
Mark Staiger	**University of Canterbury**
Xiaowen Yuan	**The University of Auckland**

Technical Editors

Member	Affiliation
Peter Lescher	**The University of Auckland**
Quentin Govignon	**The University of Auckland**

International Scientific Committee

Member	Affiliation	Country
S. G. Advani	**University of Delaware**	**USA**
S. Bickerton	**The University of Auckland**	**New Zealand**
C. Binétruy	**École Centrale de Nantes**	**France**
P. Ermanni	**ETH Zurich**	**Switzerland**
H. Hamada	**Kyoto Institute of Technology**	**Japan**
A. C. Loos	**Michigan State University**	**USA**
T. S. Lundström	**Luleå University of Technology**	**Sweden**
V. Michaud	**Ecole Polytechnique Fédérale de Lausanne**	**Switzerland**
C. M. O'Bradaigh	**National University of Ireland, Galway**	**Ireland**
R. B. Pipes	**Purdue University**	**USA**
J. Summerscales	**University of Plymouth**	**UK**
F. Trochu	**Ecole Polytechnique de Montréal**	**Canada**
Peter Mitschang	**Universität Kaiserslautern**	**Germany**
Remko Akkermann	**University of Twente**	**The Netherlands**
Joel Breard	**Université du Havre**	**France**
Juan Garcia	**Universitat Politècnica de València**	**Spain**
Stepan Lomov	**Katholieke Universiteit Leuven**	**Belgium**
Andrew Long	**The University of Nottingham**	**United Kingdom**
Krishna Pillai	**University of Wisconsin-Milwaukee**	**USA**
Gerhard Ziegman	**Clausthal University of Technology**	**Germany**

Contents

7 Natural Fibres and Green Composites 386

8 Applications and Industry 487

Section 1

Permeability

NUMERICAL PREDICTION OF PERMEABILITY OF TEXTILES FOR THE INTERNATIONAL BENCHMARK EXERCISE

Xuesen Zeng, Andrew C. Long, Andreas Endruweit

Faculty of Engineering – Division of Materials, Mechanics & Structures,
University of Nottingham, University Park, Nottingham, NG7 2RD, U.K.
Corresponding author's e-mail: xuesen.zeng@nottingham.ac.uk

ABSTRACT: A recent international benchmark exercise compared in-plane permeability data for two woven reinforcement fabrics and determined experimentally using 16 different procedures. The results showed a scatter of one order of magnitude in principal permeability values, which was attributed to the difference in procedures implemented by the participants in the study and to operator induced effects, in particular related to specimen preparation and execution of the experiments. A second round of the benchmark exercise is under way, aiming at standardisation of experimental methods. Numerical permeability prediction can provide complementary validation data to the new benchmark exercise. A unit cell based Computational Fluid Dynamics (CFD) model for permeability prediction is presented in this study. The first step was to scan the fabrics at the same compression state as for permeability measurement using micro-Computed Tomography (μ-CT). The obtained 3D image data were then evaluated to characterise the actual fabric geometry. The second step was more predictive in that the geometric model was generated based on a set of approximate rules as defined in the textile scheme, TexGen. Comparison of the CFD results from TexGen models with those from experiments indicates the level of idealisation that is acceptable for permeability modelling.

KEYWORDS: *Liquid Composite Moulding, resin flow, numerical analysis, permeability, textile modelling*

INTRODUCTION

A recent international benchmark exercise [1] gave an overview of the methods for permeability measurement in practical use and the range of results obtained implementing these methods. For two materials, a 2×2 twill weave carbon fibre fabric and a 2×2 twill weave E-glass fibre fabric, in-plane permeability data, determined experimentally using 16 different procedures, were compared. The results showed a scatter of one order of magnitude in principal permeability values. The ratio of the principal permeability values, which determines the mould filling pattern and thus is of high relevance for design of tools for Liquid Composite Moulding processes, varies by factors of up to 2. The significant observed variability in results was attributed to the difference in procedures implemented by the participants in the study and to operator induced effects, in particular related to specimen preparation and execution of the experiments.

Aiming at standardisation of experimental methods, a second round of the benchmark exercise is currently under way. For measurement of the permeability of a 2×2 twill weave carbon fibre fabric in unsaturated flow experiments with linear injection at constant pressure, experimental conditions (number of layers in specimen, cavity height, injection pressure, test fluid viscosity, number of repeats) are prescribed, thus allowing quantitative comparison between results.

This study aims at geometrical analysis and numerical permeability prediction for the fabric used in the second permeability benchmark exercise in order to provide complementary validation data.

GEOMETRY ANALYSIS

The fabric for the second permeability benchmark exercise is the 2×2 twill weave carbon fibre fabric Hexcel G0986 D1200, made from 6K yarns at a nominal spacing of 3.5 yarns/cm in warp and weft direction. The nominal superficial density of the fabric is 285 g/m^2.

For analysis of the fabric lay-up, a composite plaque was moulded from 9 fabric layers at a cavity height of 3.5 mm. All fabric layers had identical orientation. No attempts were made to control nesting, e.g. by through-thickness fixation of layers relative to each other. The fabric was impregnated by vacuum-driven infusion (along the fabric warp direction) of an epoxy resin system into a stiff rectangular tool with a linear injection gate. After resin cure, the produced plaque was cut into brick-shaped specimens with dimensions 20 mm × 12 mm × 3.5 mm. Thus, at least one fabric unit cell (4 × 4 yarns) was included in each layer. The specimens were scanned using x-ray micro-Computed Tomography (μ-CT), which allowed the shape and arrangement of yarns and inter-yarn channels to be identified in detail (Fig. 1).

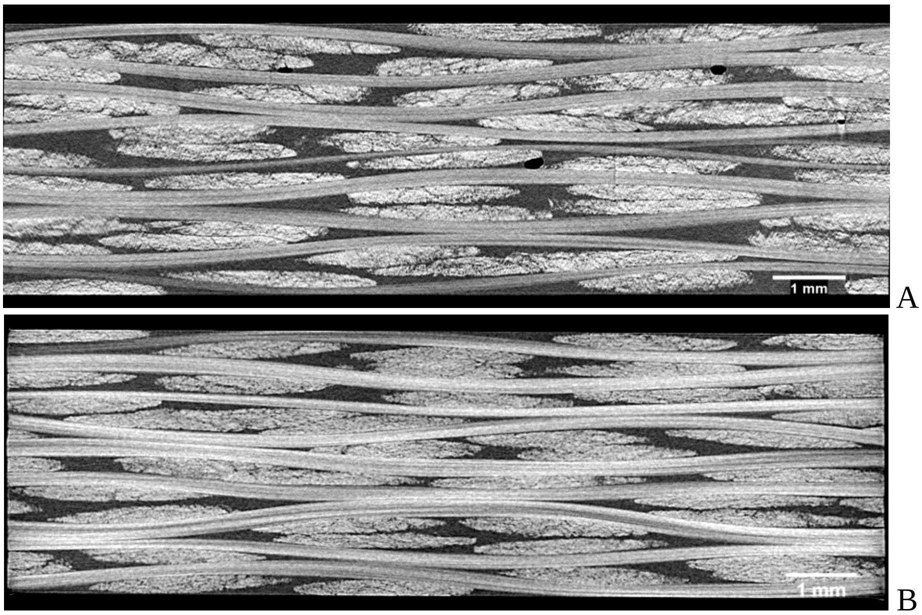

Fig. 1: Selected slices from 3D μ-CT data set: A, warp yarn cross-section; B, weft yarn cross-section. The scan resolution is 6.75 μm

Each scan captures 1800 image slices in warp- and weft-direction. To reduce the number of slices for geometry characterisation of the laminate, new images are created by averaging pixel intensities over stacks of originally acquired slices. Thus, the scan is reduced to stacks of 45 images in both fabric directions, each representing 40 slices corresponding to a distance of 0.27 mm. The employed averaging procedure effectively enhances the image quality, resulting in improved contrast between resin and yarns. Based on the processed data, the basic four input parameters for TexGen modelling, laminate thickness, yarn height, yarn width and yarn spacing (Table 1), were determined. While, here, the geometry was evaluated manually, there are continuous efforts to make more comprehensive and accurate measurements, such as using a power-ellipse to fit yarn cross-section deformations, in an automated manner. More details on representing the complex geometry variations observed in the laminate are given in the following section on geometrical modelling.

Table 1: Geometry parameters from μ-CT scan of the laminate (average values and standard deviations are given)

Laminate thickness (mm)	*Yarn spacing (mm)*	*Yarn width – weft (mm)*	*Yarn height – weft (mm)*	*Yarn width-warp (mm)*	*Yarn height-warp (mm)*
3.51 ± 0.00	2.83 ± 0.02	2.69 ± 0.16	0.21 ± 0.03	2.73 ± 0.26	0.23 ± 0.03

NUMERICAL PERMEABILITY ANALYSIS

The data in Table 1 were used as input parameters to create a single ply in TexGen [2]. First, an idealised model with constant elliptical yarn cross-sections and regular yarn paths was created according to the specified input. Then, a yarn surface mesh was used to correct yarn intersections within the unit cell. Yarn cross-sections and yarn paths were re-generated by interpolating the modified surface mesh. Fig. 2 illustrates how the geometry was improved by the refinement. In Fig. 2B, the yarn cross-sections are no longer elliptical and vary along the yarn paths with some degree of rotation. The refined model is physically closer to the actual laminate shown in Fig. 1. The fibre volume of TexGen model was also used to assess the geometry model.

$$V_f = v_f \frac{V_Y}{V_U} \tag{1}$$

Where yarns in TexGen model are treated as porous media with an assumed fibre volume fraction v_f, typically 0.60; V_Y and V_U are the volume of yarn and unit cell in a TexGen model. For comparison, the calculated fibre volume fraction for an idealised model with yarn intersections in Fig. 2A is 0.45 while a refined model in Fig. 2B has V_f of 0.40. The theoretical V_f for the actual laminates is 0.41.

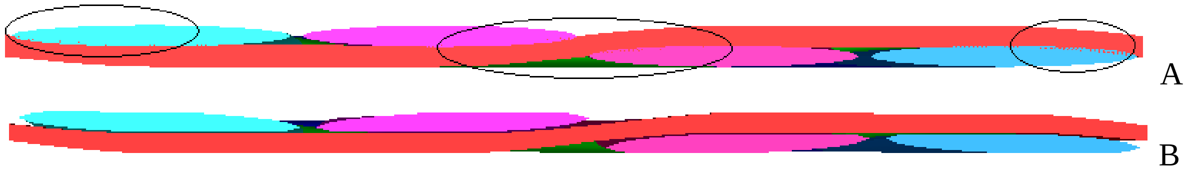

Fig. 2: Ply geometry refinement in TexGen. A: Idealised geometry with constant cross-section, where yarn intersections are highlighted; B: Refined geometry with no yarn intersection

So far, the geometry within a single ply is represented by variable yarn cross-sections and yarn paths. Other sources of variability which need to be considered for the laminate include nesting and ply geometry deviation. To account for the random nature of nesting and inter-ply variability while keeping a minimum number of simulations, Latin hypercube sampling [3] was employed to generate variation vectors. Unlike Monte Carlo sampling, Latin hypercube sampling produces more evenly distributed samples from the entire ranges of the variables, thus allowing to fully explore multi-dimensional inputs based on limited numbers of simulations. Fig. 3 shows a sample of three normalised parameters for weft yarn nesting, warp yarn nesting and ply thickness for the 9-layer laminate. The three variables are sampled from the whole range and combined by random permutation. Nesting is modelled as relative in-plane displacement to a reference model shown in Fig. 1B, and it is normalised over the full length of one unit cell in weft- and warp-direction. Ply thickness variation is normalised to obtain thicknesses deviating by up to ± 5 % from the nominal ply thickness, while the total thickness of the laminate is ensured to be constant. Yarn width and yarn height variations are related to ply thickness variations based on the assumption that the yarn cross-sectional area is conserved.

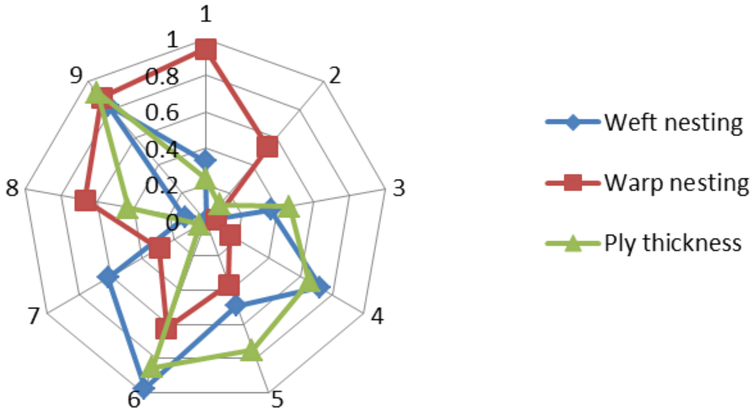

Fig. 3: A sample of the laminate variation by Latin hypercube sampling: Layers are numbered from 1 to 9, and the normalised variation ranges from 0 to 1

Three TexGen models were generated, incorporating incrementally increasing levels of geometrical detail. The description of each model is listed in Table 2. For the results reported in this paper, one random sample was generated by Latin hypercube sampling for each model. More samples will be modelled for each model and the standard deviation of permeability can be obtained from the sampled predictions. A unit cell of Model II is shown in Fig. 4. It gives a very accurate geometrical representation of the actual laminate, featuring variable yarn cross-sections and ply nesting. It is worth emphasising that the fibre volume fraction of the model is 0.402, which is remarkably close to the fibre volume fraction of the actual material (0.41). The high level of detail in the geometry model is expected to allow relatively accurate permeability prediction based on Computational Fluid Dynamics (CFD) simulations.

Since yarns are treated as porous media, the intra-yarn permeability can be calculated by the analytical models proposed by Gebart [4]. The resulting yarn permeabilities are 3.3×10^{-13} m^2 (along the yarn axis) and 7.1×10^{-14} m^2 (perpendicular to yarn axis). The values are so low compared to the overall laminate permeability that the yarn can be assumed to be impermeable in order to reduce computational cost for CFD simulations. Inter-yarn channels were meshed with uniform hexahedral voxels, and steady-state flow through these pore spaces was simulated using the commercial CFD package Ansys CFX^{TM} (Fig. 5). From the applied pressure gradients along different fabric directions and the calculated flow velocities, in-plane permeabilities were determined. The flow velocity distribution in the laminate is visualised in Fig. 5, where the influence of randomness of flow channels due to nesting and ply geometric variation is evident. The predictions from the three TexGen models are listed in Table 2 together with the experimental measurement obtained at University of Nottingham.

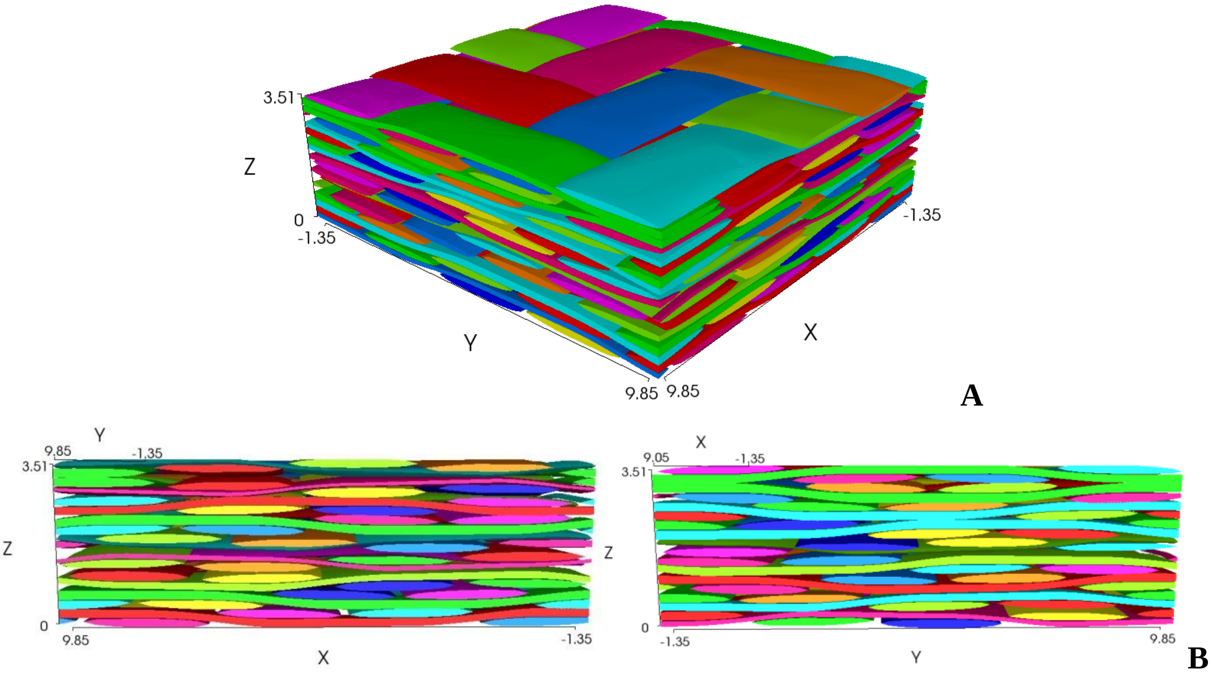

Fig. 4: TexGen model of the laminate composites includes nesting factor and laminate variations. A: 3D view of unit cell; B: Cross-sections of weft and warp yarns

Table 2: Specimen thickness, *h*, number of fabric layers, *n*, fibre volume fraction, V_f, permeabilities in fabric warp- and weft-direction, K_{warp} and K_{weft}, and ratio K_{weft}/K_{warp}

TexGen model	*Model description*	*h* / mm	*N*	V_f	K_{warp} / 10^{-10} m^2	K_{weft} / 10^{-10} m^2	K_{weft} / K_{warp}
Model I	warp yarn identical to weft yarn	3.51	9	0.402	3.24	3.39	1.05
	identical plies						
	randomly varied ply nesting						
Model II	warp yarn identical to weft yarn	3.51	9	0.402	3.71	4.00	1.08
	varied ply thickness, yarn width and yarn height						
	randomly varied ply nesting						
Model III	varied weft and warp yarn dimensions according to Table 1	3.51	9	0.38	4.33	5.21	1.20
	varied ply thickness, yarn width and yarn height						
	randomly varied ply nesting						
Experiment		3.5	9	0.40	2.237	3.645	1.650

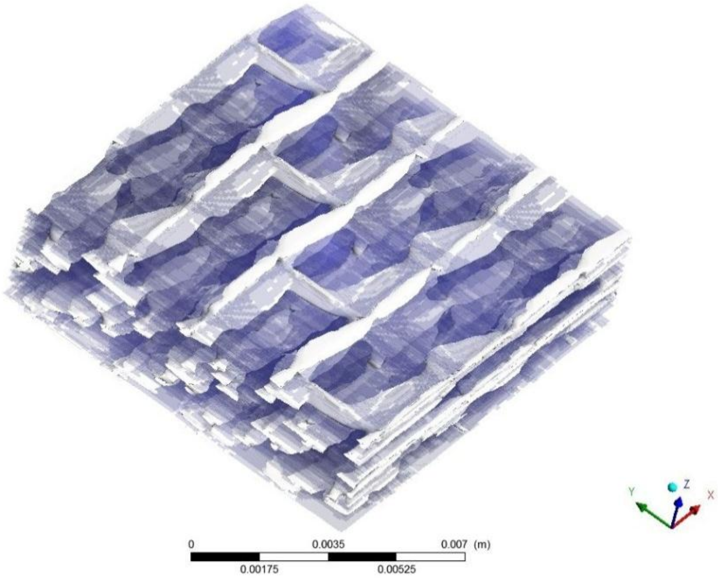

Fig. 5: CFD visualisation for flow velocity field in the laminate under a pressure drop in warp direction: Flow velocity iso-surface in white while fibre tows in semi-transparent blue

DISCUSSION

The results listed in Table 2 indicate that, for the same fibre volume fraction, the predicted permeability values in weft-direction are close to the experimental data, differing by -5 % (Model I) and 10 % (Model II), while the predictions in warp-direction are significantly higher than the experimental measurement. The permeability is slightly higher along the fabric weft-direction than along the warp direction for Model I and II. As warp yarns in Model I and II were assumed to have identical cross-sections as weft yarns, the difference of permeability in weft- and warp-direction is not as significant as suggested by experiment results. In Model III, warp yarns are thicker and wider than weft yarns as observed in the μ-CT measurement. It resulted in a higher ratio of permeability in weft over warp, which is consistent with the experimental data. The permeability from Model III increased by 30 % compared to Model II as its fibre volume fraction (0.38) was lower than that of Model II (0.402) and the actual material (0.40). Overall, the permeability predictions are in good agreement with experimental data in weft-direction. For the discrepancy in warp-direction, further geometric characterisation is required. Even though the manufacturer's data and the μ-CT data suggest that the fabric is a balanced weave, uneven crimp and inter-layer interaction may be considered for the geometric model. Although the three models incorporated different levels of material variability, the limited number of simulations suggests that the scatter of permeability due to material non-uniformity is ~ 15 % - 30 % around a fixed fibre volume fraction.

Experimental values for K_1, K_2 and the ratio K_1/K_2, determined in the first run of the permeability benchmark exercise [1], are plotted in Figs. 6 to 8. Different experimental procedures are not considered here. While the diagrams illustrate the significant scatter in results obtained by different participants in the benchmark study, all data sets indicate that the main flow direction is oriented along the fabric weft direction. For comparison, the numerically determined values are indicated in the figures together with the recent experimental measurement at Nottingham for the same fibre volume fraction. The numerical prediction will be valuable in the context of more experimental data at the same fibre volume fraction to be gathered from the second round of the benchmark.

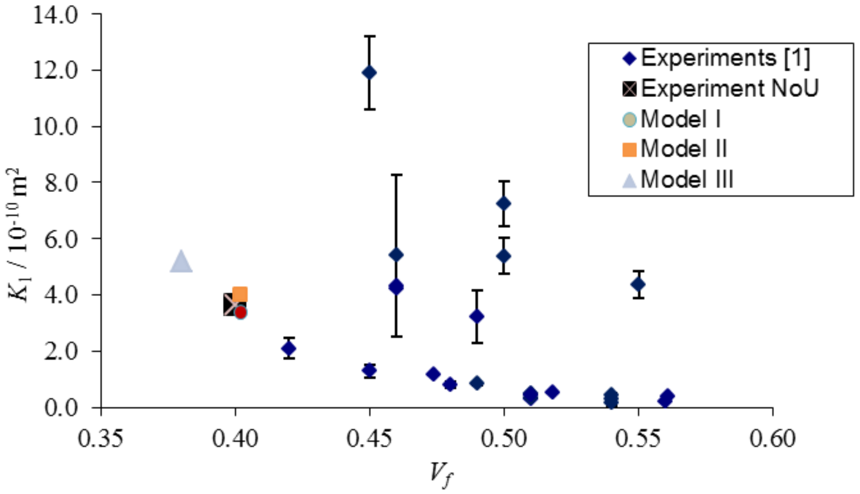

Fig. 6: Values for K_1 at different fibre volume fractions, V_f, measured employing different experimental procedures

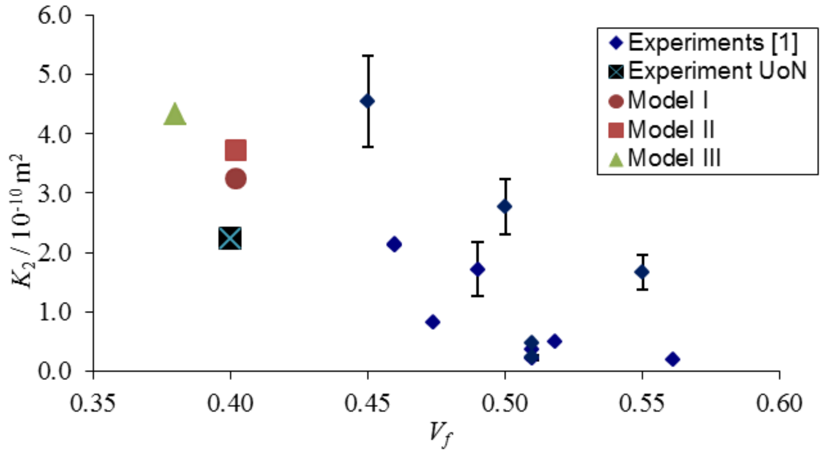

Fig. 7: Values for K_2 at different fibre volume fractions, V_f, measured employing different experimental procedures

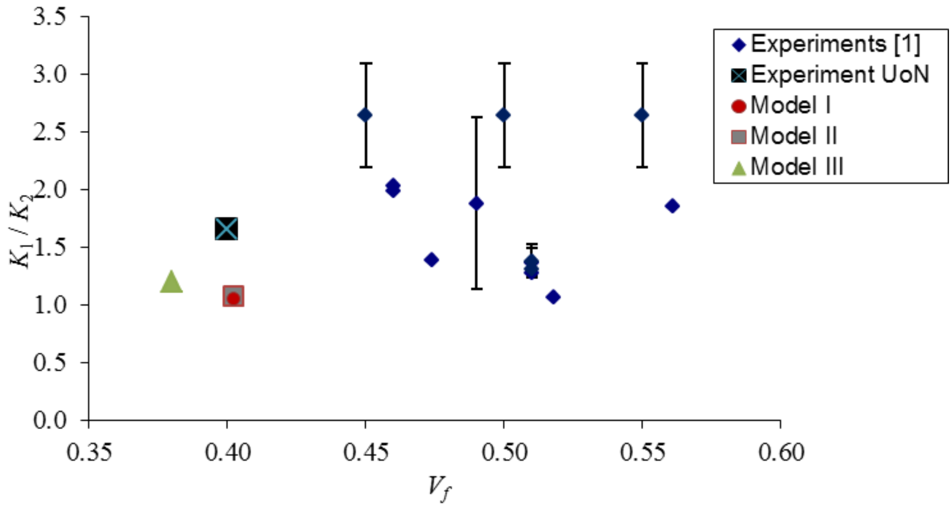

Fig. 8: Ratio of K_1 and K_2 at different fibre volume fractions, V_f, measured employing different experimental procedures

CONCLUSIONS

Given accurate geometry data, statistical sampling of material variability, appropriate boundary conditions and setting of the fluid properties, numerical permeability values deduced from results of flow simulations can be predictive, and more reliable than experimental data, since the numerical solution is not affected by operator effects. The geometric model incorporates two levels of material variability to represent the laminate material. The first level is fibre tow shape variation due to geometric constraints imposed by the weaving process, which is captured by geometric refinement for each single layer. The second level is the statistical variability in ply stacking and intra-ply deformation due to material handling. Here, a random distribution modelled by Latin hypercube sampling is used, a more efficient sampling technique than the pure Monte Carlo method to minimise the number of simulations for statistical assessment. Based on the geometric model, good agreement of permeability prediction in weft direction by CFD analysis validates the approach for modelling the material variability. In warp direction, further geometric characterisation may improve the prediction of permeability.

ACKNOWLEDGEMENTS: This work was partially funded by the Engineering and Physical Science Research Council as part of Centre for Innovative Manufacturing in Composites. The authors wish to thank to Dr. Craig Sturrock for scanning of the specimens. Material was provided by Hexcel.

REFERENCES

1. Arbter R, Beraud JM, Binetruy C, Bizet L, Bréard J, Comas-Cardona S, Demaria C, Endruweit A, Ermanni P, Gommer F, Hasanovic S, Henrat P, Klunker F, Laine B, Lavanchy S, Lomov SV, Long A, Michaud V, Morren G, Ruiz E, Sol H, Trochu F, Verleye B, Wietgrefe M, Wu W and Ziegmann G (2011). 'Experimental determination of the permeability of textiles: A benchmark exercise', *Compos Part A-Appl S*, 42(9), 1157-1168.

2. TexGen (Version 3.5.0). University of Nottingham (2011). http://texgen.sourceforge.net (Viewed 31 January 2012).

3. McKay MD, Beckman RJ and Conover WJ (1979), 'Comparison of Three Methods for Selecting Values of Input Variables in the Analysis of Output from a Computer Code', *Technometrics*, 21(2), 239–245.

4. Gebart BR (1992), 'Permeability of unidirectional reinforments for RTM', *J Compos Mater*, 26(8), 1100-1133.

INFLUENCE OF BINDER ACTIVATION AND FABRIC DESIGN ON THE PERMEABILITY OF NON-CRIMP CARBON FABRICS

Matthias Dickert, David C. Berg and Gerhard Ziegmann

TU Clausthal, Agricolastrasse 6, 38678 Clausthal-Zellerfeld, Germany
Corresponding author's e-mail: matthias.dickert@tu-clausthal.de

ABSTRACT: In this study we present results of permeability measurements. Different binder types (epoxy-based powder, acrylate-styrene co-polymer powder and co-polyamide-based veils) were applied to non-crimp carbon fiber fabrics in varying amounts. Depending on the activation parameters used, different modes of interaction of binder and fabric could be observed. High press temperatures and long pressing times lead to capillary flow of the binder. In this study lower temperatures and shorter pressing times are used to solely deform the binder particles by compaction forces, leaving them on the roving surface. In one fabric we find both a permeability increase as well as a decrease depending on the binder types. A second type of fabric only yields permeability decrease for increasing binder amounts. From these observations we conclude that in addition to binder type and activation parameters fabric parameters also impact the binder's influence on permeability.

KEYWORDS: *Permeability, Binder, Tackifier, Preform , Non-Crimp Fabric.*

INTRODUCTION

Binders or tackifiers are thermoplastic or thermoset materials that typically are used to bond individual fabric layers to each other thus producing a preform of a desired geometry. To do this, binder usually is applied as powder, solution, hotmelt, or web. While the weight fraction can be individually chosen for the first three types, in the latter case, the amount is fixed to multiples of the veils' areal weight. Through the use of binder, tool time is reduced and production processes can be accelerated or even automated. Preform properties such as thickness, springback, or peel strength can be controlled using binder [1, 2]. Furthermore, binder may affect mechanical properties of the part. For inadequate binder amounts or binder/resin combinations it is found that T_g, ILSS, or G_{1c} are reduced [1-5] and porosity in the final part is increased [3, 4]. Compatible binder-resin systems, on the other hand, may increase composite toughness [6], G_{Ic} [2], or G_{IIc} [5, 7] find an increase in T_g when adding binder to a resin. Viscosity changes from solving binder in resin are also reported [7, 8]. The present study, however, focusses on another effect binder has on the production cycle: it changes permeability. The complex nature of the interactions of binder and permeability is addressed in [1, 4]. There, preforming conditions are found to influence the resulting permeability towards higher or lower values which will be further analyzed in this work.

MATERIALS AND METHODS

Two types of fabric and three types of binder have been used in this study and several lay-ups are made from them. Their properties are listed in tables 1–3. Non-crimp fabrics have been chosen because of their reproducible quality and ease of handling. Two powder binders were chosen to be tested versus one veil binder to show their differences. Lay-ups 1, 2, and 5 in their non-symmetrical lay-up serve purely academic purposes, whereas Lay-ups 3 and 4 have more practical relevance.

After cutting the fabrics (240 mm x 140 mm), binder was applied to them. Binder veils have been placed between each fabric layer by hand while powder binder was applied using a sieve and a scale. Binder is applied to one side of each layer except the top layer; Lay-ups 1, 2, and 5 consist of six layers of fabric with five layers of binder in between. Binder content is calculated referring to the layer the binder is applied to. Hence the finished preform has got a lower binder content since the top layer is not bindered. Lay-ups 3 and 4 are prepared the same way with the exception that the glass mats were bindered with the same amount as the carbon fiber layers. Due to their low areal weight, the relative binder content is high. The lay-ups were then hot pressed at the given preforming parameters (press duration, press temperature, preform height). Press movement was controlled by distance plates.

Table 1: Used fabrics

#	Used for orientation	Type	Manufacturer	Areal weight	Fiber
1	+16/-74	S37CX	Saertex, Saerbeck, Germany	308 g/m² (of which 6 g/m² stitching)	Toray T 700 24K 50C
2	0/90	HexForce NLT00 HR1270 0200 UGZ0F	Hexcel, DE, USA	200 g/m²	ZOLTEK PANEX 35 50K

Table 2: Used binders

#	Type	Manufacturer	Polymer	Spacing Sieve	D_{50} (Q_3)	Tg
1	EPR5390	Momentive	Epoxy	100 µm	106 µm	61 °C
2	PA1401	Spunfab	Co-Polyamid	n/a	n/a	95 °C
3	Vinnex LL2319 A9133	Wacker	Acrylate Styrene Co-Polymer	63 µm	82 µm	63 °C

Table 3: Used lay-ups

Description	Fabric	Orientation	Binder type	Binder areal weight per layer	Preforming parameters	Fiber volume content
Lay-up 1	1	$[+16/-74]_6$	1	0, 6, 12, 18 g/m²	1 min, 90 °C, 3.0 mm	40.7 %
Lay-up 2	1	$[+16/-74]_6$	2	0, 6 g/m²	1 min, 120 °C, 3.0 mm	40.7 %
Lay-up 3	2	$[\text{Glass}/0/90/+45/-45]_S$	2	0, 3, 6, 12 g/m²	5 min, 105 °C, 1 mm	47.1 %
Lay-up 4	2	$[\text{Glass}/0/90/+45/-45]_S$	1	0, 3, 6, 12 g/m²	5 min, 70 °C, 1 mm	47.1 %
Lay-up 5	1	$[+16/-74]_6$	3	0, 6 g/m²	1 min, 160 °C, 3.0 mm	40.7 %

Microscope pictures were taken using a VHX-500F digital microscope (Keyence Corporation, Osaka, Japan). Permeability measurements were conducted on a testing apparatus devised by the authors, which allows for an optical tracking of the flow front. The textile is placed between a glass plate and a steel plate. To avoid deflection of the cavity, the steel plate and the glass plate are both supported by a block of cross beams. These blocks are bolted together to achieve the compaction of the textile. The height of the cavity is determined by a set of distance plates, which are placed on the circumference of the textile. However, cavity height is also measured ex-post using waxen pellets that are compacted along with the textile and whose height can be measured after the experiment has finished. Possible deflections of the cavity can thus be detected. In order to prevent race tracking, the textile is sealed along its edges after it has been compacted to its final thickness.

The injection fluid is a vegetable oil of a known, temperature-dependent viscosity of about 100 mPas. Injection pressure is kept constant at 1 bar using a pressure control valve. Flow front advancement is captured using a camera operating in series pictures mode. The obtained images are then evaluated using a semi-automated Matlab script. Permeability is calculated on the basis of Darcy's law.

RESULTS AND DISCUSSION

Higher press temperatures as well as longer pressing times result in capillary flow of binder (Fig. 1). Binder location can thus be controlled by preforming parameters. Preform cohesion is lost when binder migrates completely from the interlayer into the rovings (Fig. 1, 160 °C). To prevent this, binder activation is conducted at low temperatures and short pressing times.

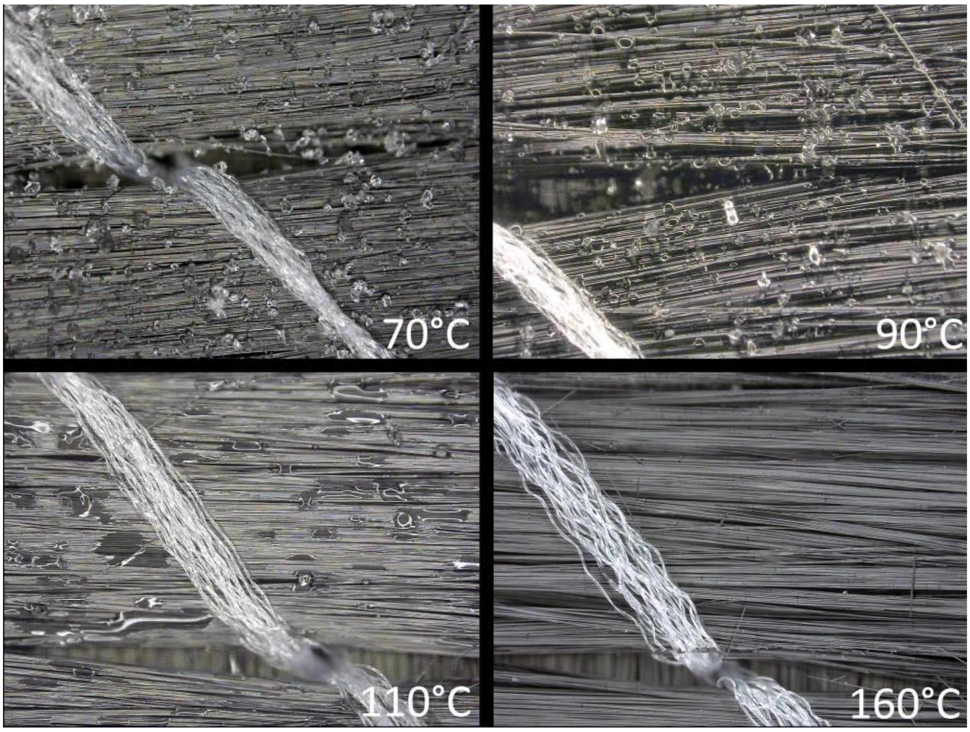

Fig. 1: Different press temperatures applied for 1 min to 2 wt% EPR5390 on the S37CX fabric

In the case of Lay-up 1 and 2, the permeability of unbindered preforms (base permeability) is at 2.7E-11 m². For 2 wt% binder content a permeability increase of 65 % can be observed for Lay-up 1. Permeability values for 4 wt% and 6 wt% are above the base value, but slightly decrease compared to 2 wt%. Lay-up 2 also exhibits an increase in permeability for 2 wt%

binder content, its magnitude however is lower (20 %). Lay-up 5 on the other hand shows an almost constant permeability whose average at 2.65E-11 m² is marginally lower than the base permeability (Fig. 2).

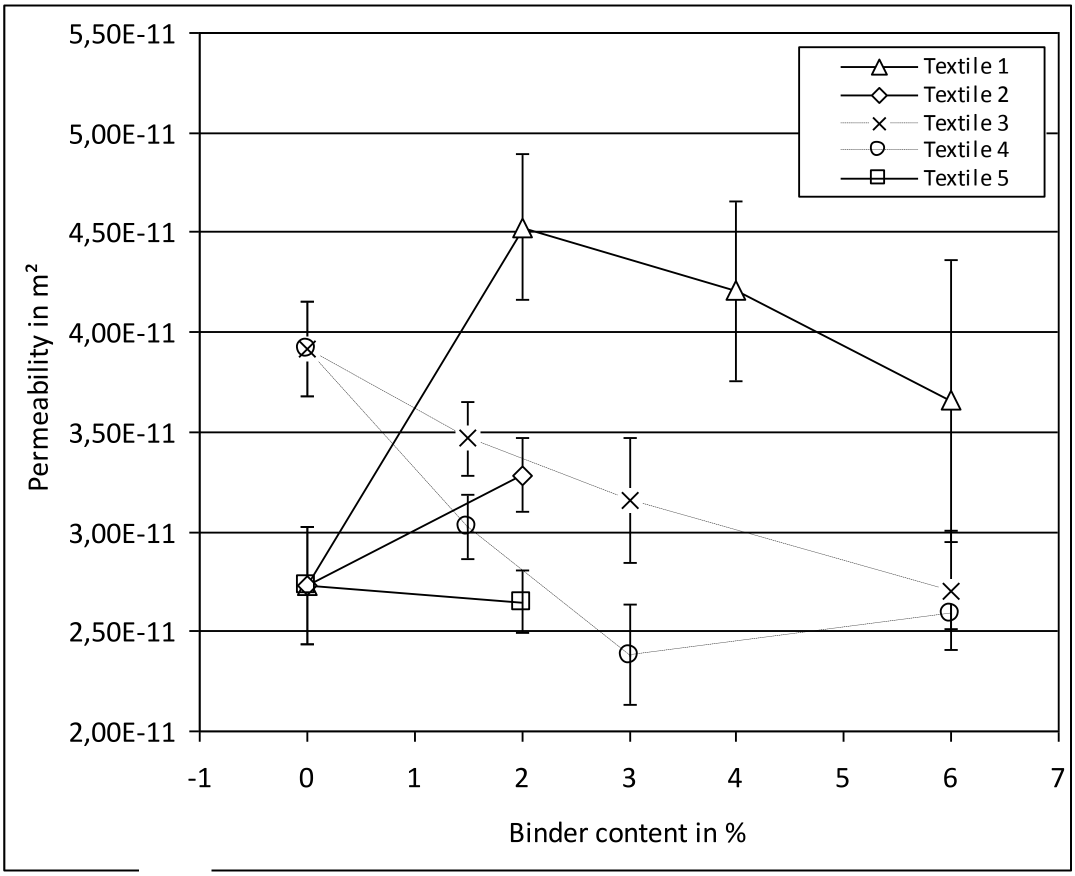

Fig. 2: Results of permeability measurements for different lay-ups

[1] and [4] observe a continuously decreasing permeability for increasing binder contents when preforming at conditions where the binder stays on the roving surface. When applying the binder in a solvent or preforming at high temperatures such that it enters the rovings, they find a higher permeability. In the first case, they conclude that blockage of large gaps between rovings causes the decrease whereas in the second case, the solvent shrinks the rovings through capillary forces creating more large gaps between them for fluid flow.

The findings in this study partially differ from those results. Micrographs (Fig. 3) of the preformed textile show a distinct interlayer forming with the addition of binder. Imprints of filaments in binder particles are clearly visible (Fig. 4), i.e. at least in the vicinity of a binder particle, the two fabric layers bonded by this particle are kept at a distance. The binder acts as a spacer between them. Moreover, at the given preforming conditions for Lay-up 1 the binder does not enter the inter-filament spaces. Preforming with these parameters thus can be seen as deformation of binder particles rather than binder flow. Assuming that binder particles are not placed on top of each other (no indication to the contrary could be found) this distance should be in the order of a particle diameter or less considering its deformation. The binder is evenly distributed (Fig. 5), hence the separation of layers should span over the entire area of each interlayer. The spacing widens flow channels between two layers and permeability increases as a consequence instead of decreasing. Adding more binder fills the newly created void volume until the entire ply surface is covered (Fig. 3, 10 wt%). This leads to the permeability decrease for higher binder amounts apparent in Lay-up 1.

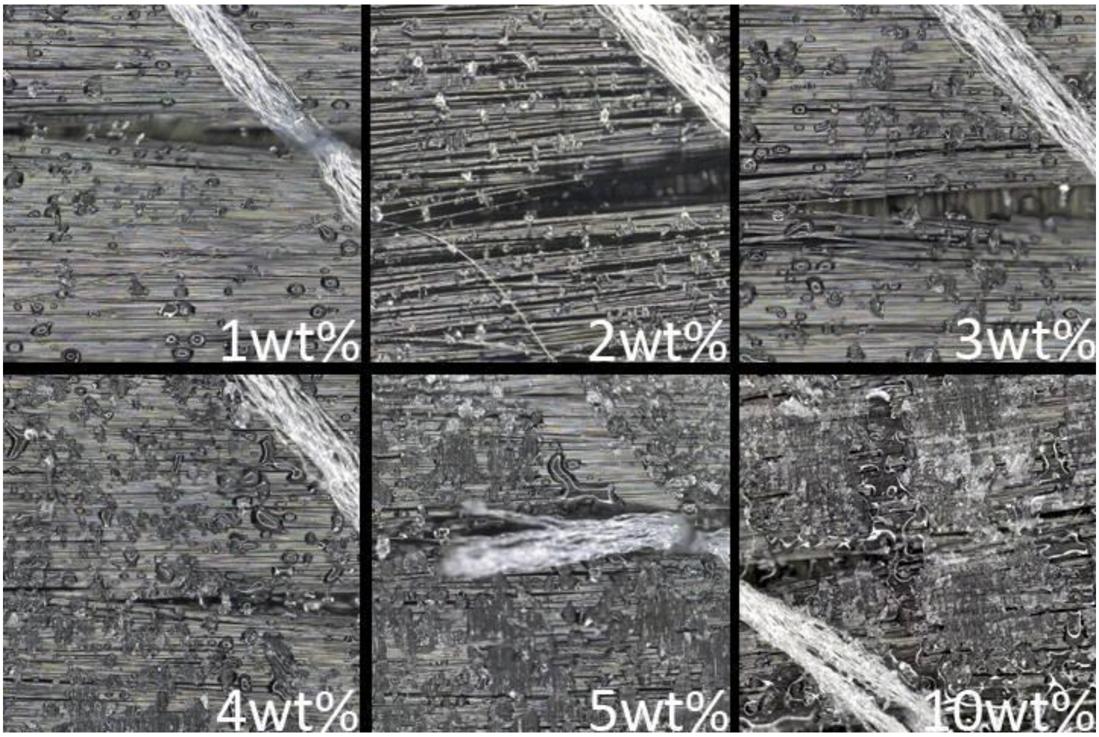

Fig. 3: Different amounts by weight of EPR5390 applied to S37CX and pressed for 1min at 90°C; note how for increasing binder amounts a distinct binder layer is forming and how the porous space between particles is not connected anymore

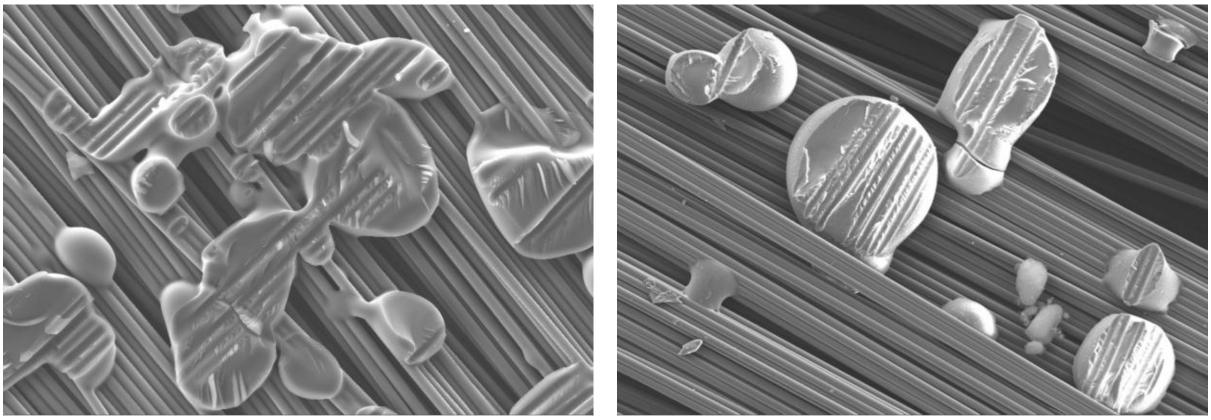

Fig. 4: EPR5390 (left, magnification 300x) and Vinnex LL2319 9133 (right, magnification 250x) applied to S37CX textile after binder activation and removal of top layer

A slight increase in permeability can be seen in Lay-up 2. Although the same areal weight of binder has been applied as in Lay-up 1, the increase is much smaller. This is explained by the binder distribution in the interlayer. In contrast to the powder binder used in Lay-up 1, the interlayer created by the binder veil in Lay-up 2 is much more porous. Its height has been determined to be around 260 µm as compared to Binder 1 which has been sieved using a spacing of 100 µm. Accordingly, the mean free path between two binder particles in Lay-up 1 is much smaller than in Lay-up 2. As a result, fiber filaments can ondulate around the binder filaments and occupy the space initially opened up by the binder (Fig. 7). The additional cross section available for macroscopic flow is lower in this case and thus the permeability increase is also lower.

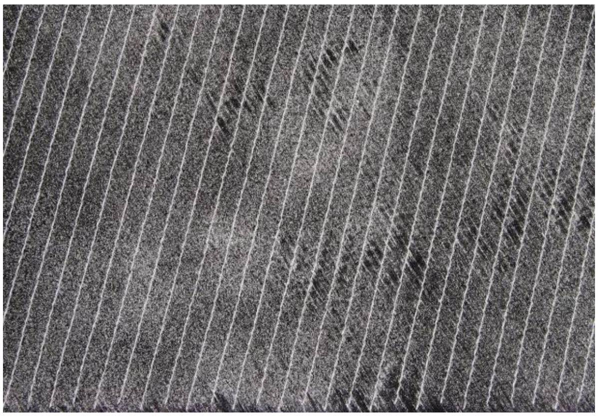

Fig. 5: One layer of S37CX with 6 g/m² (2 wt%) EPR5390 applied to it

The powder binder particles used in Lay-up 5 are spherically shaped compared to Binder 1 whose particles are irregularly shaped (Fig. 6). Additionally the D_{50} differs (Table 2). For these reasons, a homogenous sieve application of Binder 3 is only possible with smaller sieve spacing than used for Binder 1. Accordingly the spacing effect of Binder 3 will be lower, firstly because of its lesser diameter and secondly because of its embedding between filaments. Binder 1 gets entangled between the filaments due to its irregular shape and thus remains on the roving surface when applying it. As a result, the binder in Lay-up 5 occupies space with only small flow channels being created thus the permeability sinks.

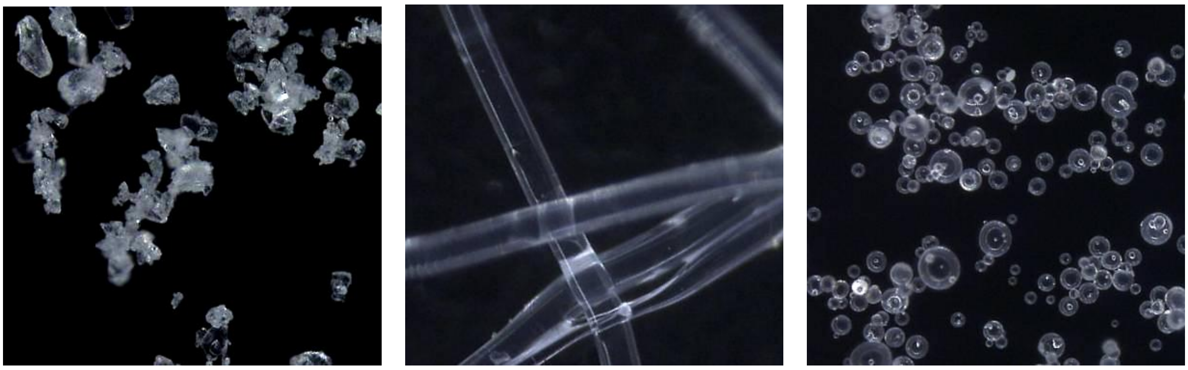

Fig. 6: Binder particle shape before activation (Binder 1 left, Binder 2 middle, Binder 3 right)

Permeability measurements of Lay-up 3 and 4 yield a permeability of 3.9E-11 m² in non-bindered state. A decrease can be observed for 1.5 wt%, 3 wt% and 6 wt% of binder. This decrease is apparent for both binder types. Lay-up 3 shows an almost linear relation whereas the decrease for Lay-up 4 is greater but not linear. A minimum permeability occurs for 3 wt% binder content (Fig. 2).

Both lay-ups (3 and 4) are built in the same lay-up sequence. Glass mats (28 g/m²) with random fiber orientation on the top and bottom function as high permeable layer and enhance flow. Given the optical nature of flow front tracking in this study, the permeability measured on the surface of the lay-up is a mixed value of the glass mat permeability and the sink effect of flow into the carbon fiber. The glass mats dominate the flow behaviour; therefore, reduced porosity in this layer has a large impact on the flow regime. Powder binder nests in the voids between glass filaments resulting in a large drop of permeability. Binder veil cannot nest as well which is why the reduction in permeability is smaller.

It is difficult to determine whether the binder between the carbon fiber layers has got a significant impact on the overall permeability. One possible explanation is that the size of flow channels created is too small for a permeability increase because the carbon fiber plies are too stiff in thickness direction and ply spacing is possible only on small areas around a particle. At the same time, the already low roving porosity is further reduced through local compaction induced by added binder particles. This would lead to a permeability decrease in the carbon fiber plies and an even greater drainage from the glass mats.

Another explanation is that the permeability increase is not high enough to be visible on the surface. In this case the reduced glass mat permeability would still be higher than the increased carbon fiber permeability. In fact, the permeability reduction from introducing binder into the glass mats would have to be even higher than visible because the fluid sink into the carbon fiber plies now is smaller.

CONCLUSIONS

Binder affects the flow behavior of a fluid through a porous medium in a complex way. Previously decreasing permeabilities were observed when adding binder and activating it such that it stayed on the outside of the rovings. In this study with activation parameters chosen to reach the same binder location, an increase of permeability for small amounts of binder with subsequent decrease with more binder added was found for one lay-up. Micrographs suggest that binder particles separate fabric layers (probably due to local compaction of rovings) thus creating macroscopic flow channels. With further increasing binder amounts these flow channels are blocked and permeability decreases again. Binder geometry (size and shape) influences this behavior and may even cause a permeability decrease (Fig. 7).

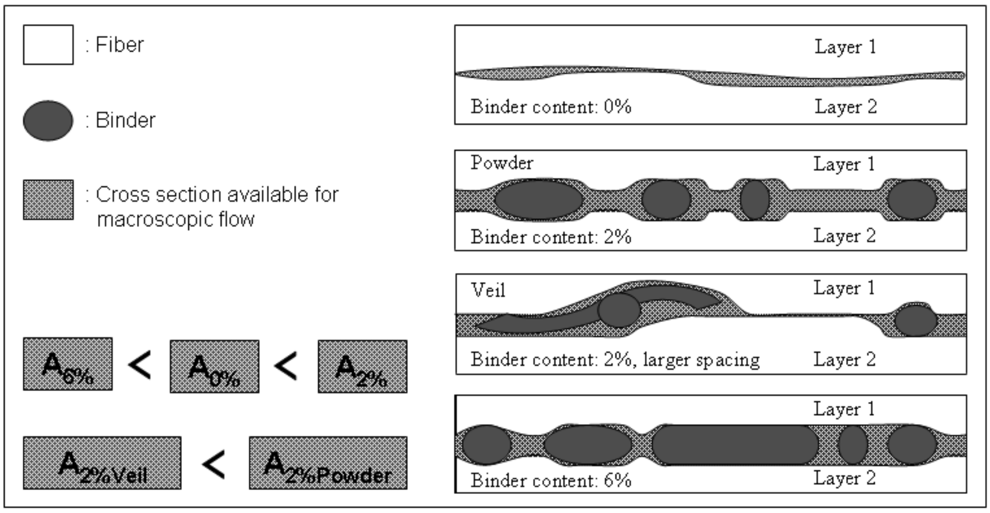

Fig. 7: Schematic of fiber/roving ondulation around binder particles and thus varying cross section available for macroscopic flow of fluid.

Essentially, the nesting behavior of binder in the fiber structure causes the permeability changes apparent in this study. If void space is filled with binder (e.g. bindered glass mat), permeability decreases. If, on the other hand, filaments deform because of the addition of binder, permeability may be increased due to a spacer effect.

ACKNOWLEDGMENTS: The authors would like to thank the German Research Foundation (DFG) for their financial support. Momentive Performance Materials and Wacker Chemie AG have contributed to this study through their material donation and support in preparing SEM pictures.

REFERENCES

1. Rohatgi V, Lee LJ (1997), ‘Moldability of Tackified Fiber Preforms in Liquid Composite Molding’, Journal of Composite Materials, 31(7), 720-744

2. Brody JC, Gillespie JW (2005), ‘Reactive and Non-reactive Binders in Glass/Vinyl Ester Composites’, Polymer Composites, 26(3), 377-387

3. Shih CH, Liu Q, Lee LJ (2001), ‘Vacuum-Assisted Resin Transfer Molding Using Tackified Fiber Preforms’, Polymer Composites, 22(6), 721-729

4. Shih CH, Lee LJ (2001), ‘Tackification of Textile Fiber Preforms in Resin Transfer Molding’, Journal of Composite Materials, 35(21), 1954-1981

5. Hillermeier RW, Seferis JC (2001), ‘Interlayer toughening of resin transfer molding composites’, Composites Part A, 32(5), 721-729

6. Depase EP, Hayes BS, Seferis JC (2001), ‘Interlayer toughened VARTM composites using preformed particle toughened tackifiers’, Proc. of The 33rd International SAMPE Technical Conference (ISTC)

7. Brody JC, Gillespie JW (2005), ‘The Effect of a Thermoplastic Polyester Preform Binder on Vinyl Ester Resin’, Journal of Thermoplastic Composite Materials, 18(3), 157-179

8. Chen J, Backes D, Jayaraman K (1996), ‘Dynamics of Binder Displacement in Liquid Molding’, Polymer Composites, 17(1), 23-33

OPTIMIZATION OF 3D WETTING PERMEABILITY MEASUREMENTS

Andrew George [1], Anthony Pickett [2], Justas Sirtautas [2] and Klaus Drechsler [2]

[1] *Swerea SICOMP AB, PO Box 271, SE-94126, Piteå, Sweden.*
[2] *Institute of Aircraft Design, University of Stuttgart, Pfaffenwaldring 13, DE-75069 Stuttgart, Germany. Corresponding author's e-mail: andy.george@swerea.se*

ABSTRACT: The simplest method for through-thickness permeability characterization is by point-infusion into the top of a stack of material. Nedanov and Advani presented a solution for the flow geometry at the point the resin reaches the bottom of the mold in point-infusion. The three unknown fabric permeability components can be difficult to solve, however. A ratio simplification method is proposed to greatly simplify the calculation of the permeability components. The effects of binders, the compressibility under a vacuum bag, and capillary pressure are also discussed. The robustness of this test method is evaluated in light of measurements from a selection of different fabrics.

KEYWORDS: *transverse permeability measurement, capillary pressure, compressibility.*

INTRODUCTION

Flow simulation of liquid composite molding (LCM) processes in composites manufacturing allows less prototyping and faster/less expensive process optimization. As the composites industry and LCM application continues to grow, the demand for simulation tools grows ever larger. LCM flow simulation is commonly based on Darcy's Law, which requires the permeability (K) of the reinforcement material to be characterized. Some LCM variant processes such as resin transfer molding (RTM) are dominated by in-plane flow which only required in-plane (K_{xx}, K_{yy}) characterization. But in other LCM variants using flow distribution media, such as vacuum infusion (VI, analogous to vacuum assisted resin infusion), the vacuum assisted process (VAP), resin film infusion (RFI), or pre-preg consolidation, the through-thickness flow is the most time-consuming path. Accurate simulation for these processes therefore requires through-thickness (K_{zz}) data.

Some advances have been made in flow simulation of VI such as coupling it with compressibility [1,2] and accounting for capillary forces [1]. But K_{zz} measurement remains a more significant problem because of the lack of a standardized measurement method, the high scatter in results, as well as the high sensitivity of the flow velocity to K_{zz} variation. Many reported measurement methods force 1D flow through the thickness. Some involve 1D flow in a compression cell, enabling continuous measurement of K_{zz} and compressibility at a range of fiber contents (v_F) [3]. The often-discussed problem of racetracking is the greatest weakness of 1D K_{zz} methods. In addition, the saturated flow and high pressures usually applied can cause flow phenomena inaccurate to industrial VI.

Single point infusion through a stack of dry plies gives a simple test setup for K_{zz} measurement that is most representative of actual processing. All three major K components can be determined from the flow dimensions of one experiment and race-tracking is not an issue. The unique challenge with such a K_{zz} measurement in unsaturated flow is that the flow front is not so easily observed as with in-plane measurements, as the fabric itself, impedes observation. Flow perturbation often occurs from embedded sensors, and other methods (ultrasound, mass flow measurement, etc.) require expensive equipment and calibration work. By using a transparent mold base, the time at which the flow reaches the bottom of the mold (t_F) can be measured. The resulting K calculation has been shown to be sufficiently accurate when based on only this one data point [4].

Another drawback of this method is the inlet complications. Flow disturbances near the inlet are common for all K measurement methods, and require sufficient test length to minimize them. As with 2D radial testing, the shape of the flow-front is constricted by the tube and needs some flow length to develop into the correct geometry [5]. Related to this is the point singularity phenomena; tow-based fabrics will have different initial flow patterns based on the x/y location of the inlet tube, e.g. how many channels or stitches the inlet covers. But this error is also assumed to be mitigated far from the inlet. Therefore, the sample needs to be sufficiently thick to achieve developed flow.

The low pressures and wetting flow of such a test ensure that the capillary effects are similar to typical industrial processing. But this also complicates the data analysis as K must be evaluated independent of these. Infusion under a vacuum bag is the simplest implementation of this test, but adds the complication of variable mold thickness (compressibility).

EXPERIMENTATION

Test samples (150 mm x 150 mm) of various reinforcement materials were prepared for point infusion testing. A bindered uni-directional (UD) weave (272 g/m2) was used as the baseline material. This was tested in two different orientations: first, with all tows in parallel (UD) and second as a quasi-isotropic, QI layup (0/+45/90/-45). Three different preforming treatments were tested with the QI stacks: untreated, heated to 130°C, and heated to 130°C while under a bag and 1 bar vacuum. “NCF1,” a biax bindered NCF of 548 gsm was also tested (untreated, UD). Other non-crimp fabrics (NCF), braids, and tailored fiber placement (TFP) fabrics were also included in this study and are described in [6]. All of the tested materials consist of HTS40 carbon fiber tows. All materials were stacked with sufficient layers to achieve a compressed thickness of approximately 10 mm.

VI point infusion tests were performed on the weave using paraffin oil, with a few select tests of QI stacks being infused at 120°C with Hexcel RTM 6. The other materials were all infused with Hexion RIM235. Most samples were compressed to 1 bar vacuum for the infusion. Some select weave samples were infused at 0.5 bar vacuum. For some of the materials from [6], only one test was performed on each. For all other materials and treatments, three to seven replicates were performed and the results averaged.

The in-plane major axis radii (r_x, r_y) and t_F were recorded at the moment the fluid first appeared at the bottom of the sample. Measuring the wetted experimental thickness (r_z) under a vacuum bag is not straightforward. Considering the ellipsoid flow shape at t_F, r_z should be the thickness of the sample directly under the inlet. But this is difficult to measure as the inlet tube is in the way. An estimate was made by waiting some minutes after t_F and then measuring the thickness at a point away from the center where the flow front along the bottom has just past. This gives a minimum r_z as the measurement represents a fully lubricated material at a minimal resin pressure (P_R). P_R on the top of the sample would be slightly higher directly under the tube. But as P_R drops quickly through the thickness in a 3D infusion, and v_F changes little for all but the highest P_R, this difference was neglected.

Early attempts at point infusion testing occasionally resulted in very low / negligible flow-rates due to tacky-tape, which seals the inlet tube to the bag, as it was drawn by vacuum into the tube. This problem was solved by using thin adhesive tape between the tacky-tape and the tube-to-bag connection. All tests were confirmed to have unrestricted flow by inspection of the inlet after the test.

Data analysis

Both inverse estimation methods (IEM) and analytical solutions were applied to the data in this study. A constant v_F is assumed in both cases (neglecting the compressibility). IEM consists of iterations of flow simulation by guessing K values until the flow front geometry and times match the experiment. PAM-OPT was used to repeatedly call PAM-RTM (both from ESI-group) and optimize all three K values to achieve the same flow geometry at the experimental time. Both classical gradient search (adaptive response surface) and evolutionary (genetic) methods were tried. Optimization was only partially successful, with computed K values giving times close to the target in two flow directions, but not the third.

The data analysis for point-infusion is a difficult task, as modeling Darcy’s law for three principle directions and the three unknowns (K_{xx}, K_{yy}, and K_{zz}) is mathematically taxing. Nedanov and Advani [4] presented a mathematical model based on isotropic transformation, as was previously done for 2D radial testing [5]. The flow rates for the inlet tube, expanding hemisphere in an isotropic medium, and Darcy flow in an isotropic medium were set equal to each other to result in a system of three non-linear equations to solve for the K tensor. Although data presented in [4] converges to a solution, attempts at solving the data from many of the tests in this study did not converge, despite trying various functions and tolerance levels in Mathcad, Matlab, and Maple. The few materials where data did converge to a solution were the highest K and least anisotropic of the materials. A tight local minimum solution was observed in subsequent analysis of the residual error [6].

Ratio simplification

A simplification is proposed that approximates the solution and only requires solving for a single variable. For any instantaneous time t during filling, if a point is considered on each of the three axes, (x,0,0), (0,y,0), (0,0,z) such that the normalized positions with respect to the flow front positions (r_x, r_y, r_z) are equal:

$$x/r_x = y/r_y = z/r_z = \alpha \tag{1}$$

then P_R as well as the pressure gradient at each of those three points should be equal, assuming constant v_F and viscosity (μ). This considers the 3D flow as three different “effective” 1D flows in each of the principle directions. In the integrated 1D Darcy solution the permeability is proportional to the square of the flow front length. This assumes a constant pressure gradient, v_F and μ. The pressure gradient decreases along any flow path in 3D flow. But it is equal at any set of three points at a given α along each of the flow axes (Eqn. 1). If these assumptions are again applied to the three effective 1D flows in a 3D point infusion, then:

$$K_{xx} / K_{zz} = r_x^2 / r_z^2 \; ; K_{yy} / K_{zz} = r_y^2 / r_z^2 \; ; K_{xx} / K_{yy} = r_x^2 / r_y^2 \tag{2}$$

The same relationship has already been applied to simplify data analysis for 2D testing [7]. The isotropic permeability (Equation 4.5) then reduces to a function of the ellipsoid shape:

$$K = K_{zz} \cdot (r_x \cdot r_y / r_z^2)^{2/3} \tag{3}$$

The dimensionless hemispherical flow radius then reduces to 1. All other variables are evaluated as in [4]. This reduces the optimization problem to a single variable, which is mathematically straightforward to solve. This method was verified by comparing results to those from the full 3-variable isotropic transformation solution. The data used for comparison included results from [4] as well as any converging results from this study. In all cases, the ratio simplification produced the same values for K_{xx}, K_{yy}, and K_{zz}.

This numerical solution assumes constant pressure gradients and porosity. In reality, P_{cap} causes the pressure gradients along the axes to vary. Also, compressibility changes the porosity along the filled regime under a vacuum bag, which causes further changes in the pressure gradients. These effects are highly coupled with each other and the Darcian flow.

Compressibility

Z-direction strain results from the combination of lubrication (compression) and P_R (relaxation). In the case of 3D point infusion the lubrication effect will slowly continue to cause negative *z* displacement for any point (*x*,*y*) as the elliptical flow continues to wet to a lower depth in the sample. This negative displacement will be offset by positive displacement caused by accumulation of P_R at a given point as the flow front moves farther beyond that point. In a 1D infusion this effect is most pronounced close to the resin inlet as it takes a high P_R to cause a significant change in the sample thickness (exponential function of the pressure). Due to the characteristic low pressures for 3D infusion, any significant effects will be limited to an even closer range around the inlet. A plot of the *z* displacement along a line across the top of the sample shows a downward curve due to the elliptical lubrication. Resin pressure eventually causes the curve to flatten at the bottom and eventually a peak shows up in the middle around the inlet. This was confirmed with Digital image Correlation (DIC, ARAMIS).

In [2] filling times were compared for a model with no compressibility, and a compressibility-coupled model. The ratio between the two in 1D flow varied from 1.14 for a non-compliant fabric to 1.44 for a compliant one, with the ratio dropping to 1.13 and 1.38 respectively for 2D flow. No 3D solution for compressibility-coupled filling simulation currently exists. But this decrease in effect from 1D to 2D, along with the lower strain measurements for 3D infusions suggests that neglecting 3D compressibility is more justified than 2D or 1D. The long range of high thicknesses due to P_R away from the inlet in 1D infusions is responsible for the higher filling velocities in VI compared to RTM. DIC scanning of 2 of the weave point-infusion tests showed that the *z*-thickness never reached above the initial dry thickness outside of the 10 mm around the inlet (measurements closer to the inlet were prohibited by the inlet tube and tacky-tape). This confirms that high P_R is only found close to the inlet, and that it is extends less far from the inlet than in 1D infusions. 3D compressibility is therefore deemed insignificant, at least for the UD weave studied here, as it is sufficiently rigid to prevent significant effects from coupling compressibility to 1D simulation, and should have even less of an effect in 3D.

Capillary Effects

Both capillary effects and compressibility have been coupled to flow for 1D flow prediction [1]. This model for capillary effects has yet to be fully characterized, or proven, but it seems to accurately portray micro-phenomena in that study. Therefore it was applied again to couple P_{cap} to the 3D flow solution. The full details of the P_{cap} model and implementation in the point infusion solution are presented in [6]. This model entails a dynamic contact angle, dependent on the instantaneous velocity (v). But filling times for 1D infusions at similar μ and lengths result in little change when using a dynamic or a constant contact angle. This is due to the low v during the majority of the infusion. As 3D infusions involve even lower velocities, a static constant angle of 30° was assumed for all these test fluids. This implies a constant P_{cap} modification throughout the infusion, of 12 to 24 kPa depending on the v_F and surface tension. Therefore the mechanically applied pressure gradient (ΔP) in the closed form solution need only be modified by this P_{cap}. Again. due to low v the inter-tow flow is assumed to be slow enough that capillary forces increase the bulk flow, allowing P_{cap} to be added to ΔP.

A related dual-scale flow issue is which flow front to record. In each of these fabrics, the tow organization causes a different flow in between the fibers (micro) compared to the bulk flow front (macro). For these fabrics, the micro flow front usually extends a maximum of ~ 3 mm beyond the bulk front. This lag seems to dissipate with filling time. As t_F is recorded as the moment the fluid first reaches the bottom, this is most likely the micro flow front.

Binders

The binder applied to the weave softens at about 100°C. 1D infusions with RTM 6 at 120°C showed a lower K_{xx}. A layer of inactivated powder binder is thought to cause little difference to the permeability. But if activated by heat, the binder flows into many inter-tow and intra-tow gaps by capillary forces. This reduces the architecture porosity which inhibits flow. The K for a typical industrial bindered preform must therefore be evaluated with the binder in a state similar to the infusion to be simulated.

The typical design of a binder calls for it to dissolve in the passing resin and be washed out during infusion. When the resin first reaches the bindered fabric, the fabric will still be in the less-porous bindered state. But behind the flow front, where the binder is dissolved, a reverse effect on the fabric architecture should be seen where the fabric has returned to the original unbindered K. This is assumed to have an effect on the pressure gradient similar to the thickness gradient under a vacuum bag as this involves a similar higher K behind the flow front. Therefore the pressure gradient would be even more curved upwards and the filling time would decrease. However, dissolution of the binder also increases μ of the resin. Models such as the Einstein relation (kinetic theory) may be used to predict the rise in μ due to dissolution of particles. The difficult part is modeling the local concentration of binder particles in the filled regime. At the flow front, μ is unmodified by the dissolved binder. But just behind the flow front the majority of dissolved particles should be located assuming free motion with the flowing resin. Particle dispersion models could theoretically model this. It is assumed that the magnitude of this phenomenon's effect on the pressure gradient behind the flow front would be roughly equal to the change in fabric architecture due to binder dissolution. As these two phenomena have opposing effects on v, they are assumed to cancel out.

RESULTS

The resulting r_x, r_y and t_F were used to calculate the K tensor using the ratio-simplified model. To evaluate the effects of the lag in bulk flow, K_{zz} for all tests was calculated a 2nd time with both x and y flow fronts reduced by 3 mm. To evaluate the effects of P_{cap}, the calculations were made a 3rd time with ΔP increased by the estimate for P_{cap}. The results for all tests with the UD-weave are presented in Fig. 1, normalized to 60% v_F by the Kozeny-Carman equation. The differences between the modelling methods are small. Subtracting the 3 mm from r_x and r_y only decreases the resulting K_{zz} by ~ 5% which is deemed insignificant in comparison to the scatter in results. The farthest flow front is therefore assumed, as this agrees with the practice of measuring t_F at the farthest z flow length. As P_{cap} is thought to be significant at low v in these experiments the P_{cap} model is used throughout the rest of this paper.

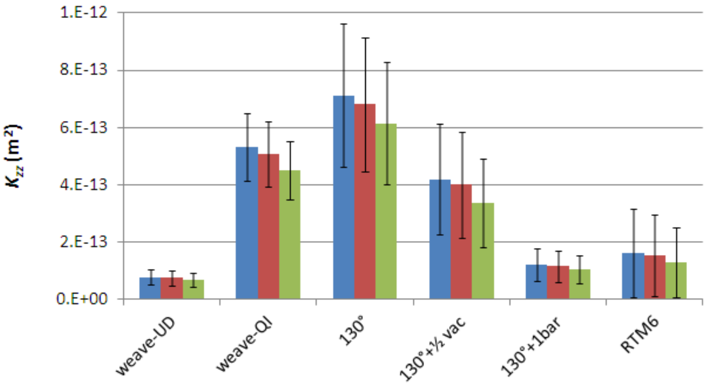

Fig. 1: K_{zz} (60% v_F) by model and test: blue = simple; red = 3mm lag; green = P_{cap} modified.

Preforming at 130°C did not cause significantly different results from no preforming. Adding 1 bar of vacuum to the heat during preforming however results in a K_{zz} very close to that of an RTM6 test. This suggests that only with pressurized consolidation can heated binder seal a fabric similar to high temperature infusion. This also suggests that a room temperature test can mimic a high temperature infusion with proper preforming. This is especially advantageous if high temperature testing is significantly more difficult than at room temperature.

The half vacuum tests (at 0.5 bar) were run to see if a relationship between K and v_F could be determined similar to practice in 1D K_{zz} testing [3] by simply changing the sample thickness. Lowering v_F should result in a higher K, but results showed no significant difference from full vacuum (actually slightly lower K). Under a vacuum bag, it is hard to achieve significantly different thicknesses, as the thickness changes little from 0.5 bar to 1 bar compaction. Furthermore, it is suspected that capillary pressure forces will modify the flow with increasing severity as the mechanically applied pressure is significantly decreased in this way.

Fig. 2 compares all three resultant permeability components, normalized to 55% v_F. Since only one point-infusion test was performed for the five right-most materials in Fig. 2, a standard deviation (σ) of 100% was assumed. The weave tests with RTM6 also resulted in σ ~ 100% over three replicates, indicative of the challenges of implementing this test in an oven. Otherwise, σ ranged from 8 to 55% for the other tests. The in-plane K proved to be 5 to 100x K_{zz} for these materials; TFP-UD being the lowest ratio (high stitching content) and the bindered weave being the highest ratio (combination of binder plugging channels and no *z*-direction stitching). The QI layup of the weave resulted in a 5x higher K_{zz} than the UD layup. This is attributed to the greater inter-tow *z*-direction channelling in the QI lay-up.

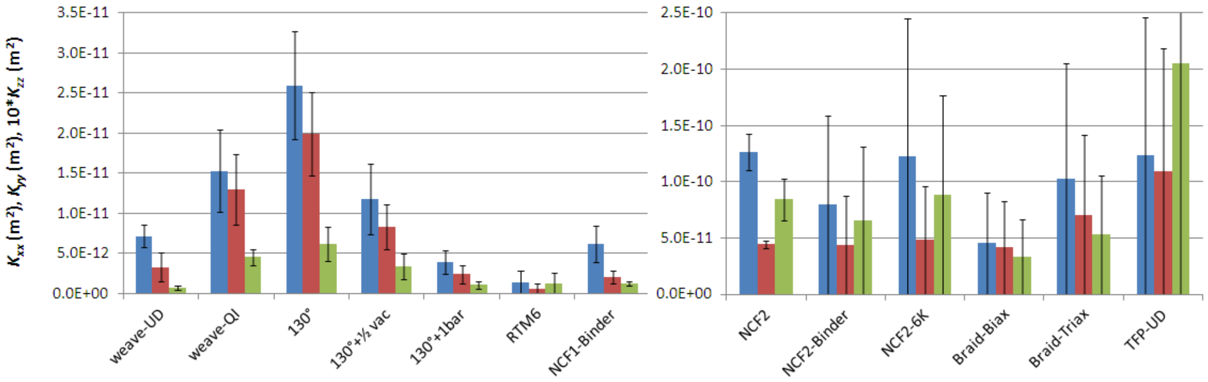

Fig. 2: K (55% v_F) by point infusion testing: blue = K_{xx}, red = K_{yy}, green = 10* K_{zz}.

Validation

Fig. 3 compares the resulting K_{xx} from point-infusions to that from dedicated 1D testing. All results are again normalized to 55% v_F. The weaves and NCF1 were tested in 1D with rapeseed oil and RIM 235, respectively. The 1D data for all other materials is detailed in [6].

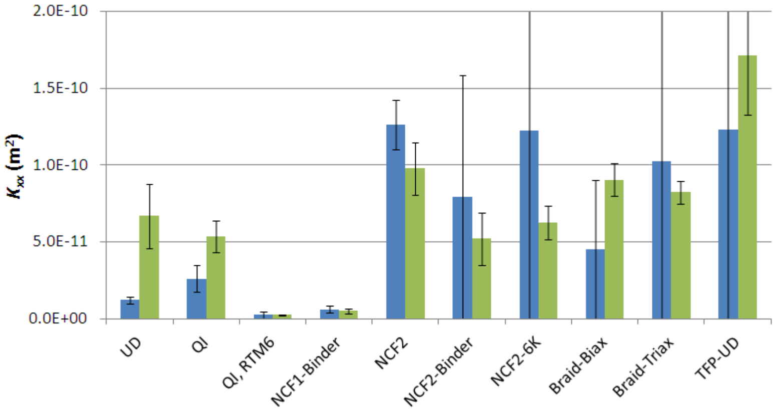

Fig. 3: K_{xx} (55% v_F) from 3D point infusion testing (blue), and 1D testing (green)

The weave samples were measured in 1D under a vacuum bag as the fabric was too stiff to conform to the rigid mold cavity used in in-plane testing. The 1D K_{xx} results for the weaves are significantly higher for the room temperature tests (left-most two samples in Fig. 3) compared to 3D. This is attributed to bag lift-off by the resin close to the inlet for these experiments, a phenomenon common to VI infusions at very slow v. Besides these two cases, all the other tests resulted in K_{xx} within each others' σ. This is deemed satisfactory agreement given the difference in test methods, and verifies that point-infusion testing can achieve satisfactory in-plane results as well.

Measurements of the experimental P_R by the inlet have recently been reported in which it is lower than predicted by modeling [2]. With time, the pressure rises to meet predicted gradients. A related observation is that pressure driven flow results in higher speeds than under a vacuum bag [6]. It has been suggested [2] that this is due to a loss of the applied pressure, either due to the inlet tubing geometry, or the evacuation of air from the tube as the resin fills it. This air must pass through the fabric and has a non-zero pressure loss associated with it. Another possible explanation is local fabric compaction by the inlet due to the initially high P_R shifting the cut fibers along the edges ("washout"). This would be mitigated as the pressure gradient moves farther out into the mold. In any case, if this initial low pressure gradient could be incorporated in the 3D K solution, the lower total gradient and the same v would result in slightly higher K calculations.

CONCLUSIONS

The point-infusion method for simultaneous measurement of K_{xx}, K_{yy}, and K_{zz} was evaluated. A simplified numerical solution for data analysis was presented. This method was shown to achieve good agreement between K_{xx} for these tests and separate dedicated 1D tests.

ACKNOWLEDGMENTS: This study was funded by Sweden's NFFP5-KOMPLETT and EU's FP-7 INFUCOMP.

REFERENCES

1. George A, Ahlborn H, ElGhareeb M, Drechsler K and Heider D (2011), 'Compressibility Modeling and Validation for Coupled Flow Simulation', Proc. of the 18th International Conference on Composite Materials (ICCM18).

2. Modi D (2008), Modeling and Active Control of the Vacuum Infusion Process for Composites Manufacture, PhD. thesis, University of Nottingham.

3. Comas-Cardona S, Binetruy C and Krawczak P (2007), 'Unidirectional compression of fibre reinforcements. Part 2: A continuous permeability tensor measurement', *Composites Science and Technology*, 67, 638–645.

4. Nedanov PB and Advani SG (2002), 'A Method to Determine 3D Permeability of Fibrous Reinforcements', *Journal of Composite Materials*, 36(2), 241–254.

5. Weitzenböck JR, Shenoi RA and Wilson PA (1999), 'Radial flow permeability measurement. Part A: Theory', *Composites: Part A*, 30, 781-796.

6. George A (2011), Optimization of Resin Infusion Processing for Composite Materials, PhD. thesis, University of Stuttgart.

7. Liu Q, Parnas RS and Giffard HS (2007), 'New set-up for in-plane permeability measurement', *Composites: Part A*, 38, 954–962.

INFLUENCE OF TEXTILE PARAMETERS ON THE IN-PLANE PERMEABILITY OF WOVEN TEXTILES

Gunnar Rieber[1], Jinhua Jiang[2], Carsten Deter[1], Nanliang Chen[2], Peter Mitschang[1]

[1]*Institut fuer Verbundwerkstoffe GmbH, Erwin-Schroedinger-Strasse, Geb. 58, 67663 Kaiserslautern, Germany. Corresponding author´s e-mail: peter.mitschang@ivw.uni-kl.de*
[2]*College of Textiles, Donghua University, China Engineering Research Center of Technical Textiles, College Building 3, No.2999, North Renmin Road, Shanghai, China*

ABSTRACT: Product parameters of woven textiles like weave, linear density, yarn density and crimp determine the permeability, infiltration, and use as reinforcement textile in a polymer composite structure. Nevertheless, attempts to link these parameters to the permeability of woven textiles are rare. In the empirical part of this study, 19 woven glass fiber textiles were selected to determine the effect of the weave, linear density, yarn density, and crimp on in-plane permeability. Further influencing parameters, like the finish and the filament diameter, have been left constant. The measurements have been conducted on a stiff two-sided aluminum tool with eight linear capacitive sensors. The anisotropic flow behavior of isotropically built up textiles is explained by using the crimp in the warp and weft yarns. It was observed that a higher difference between the crimp in the warp and weft yarns resulted in a higher difference between the K1- and K2-permeability data. A pattern was found to divide textiles into dense and open weave textiles to characterize the permeability behaviour. A generally valid relationship was found between the weaving density (defined as the product of linear density and yarn density) of a textile and the slope of the permeability-fiber volume fraction curve. In a comparison of three identically built up twill and satin weave textiles, it was found that the K2 permeability of twill weave textiles is significantly lower compared to the K1 permeability, meaning that twill weave textiles are more anisotropic. The results of this study allow the selection and tailoring of woven textiles with specific, for example very low or isotropic, permeabilities.

KEYWORDS: *Permeability, RTM, woven textiles, yarn density, linear density*

INTRODUCTION

To manufacture continuous fiber reinforced composites the fibers have to be impregnated with polymer matrix. The resistance of the textiles to the impregnation process is described by the permeability of the specific textile. Knowledge about the permeability allows to set up a fast and reliable injection process. Based on the textile permeability the resin flow direction, flow velocities, and pressure distributions can be predicted to reduce the production time and the number of rejections. There is very little stringently certain and generally valid information available about the influence of textile parameters on permeability. In 1996 Shafi compared the permeability of two plain weave and two satin weave textiles in an optical (PMMA) permeability measurement cell [1]. He detected higher permeability values and a higher decrease of the permeability with increasing fiber volume fraction for plain weave textiles. Pearce, Guild, and Summerscales determined as well a higher permeability for textiles with more warp and weft weaving points [2] – twill weave higher permeability than 5-harness satin. Pearce et al. showed that the amount of big flow channels is lower in twill weave textiles in comparison to plain weave textiles. Pore sizes have been measured by light microscopy and image analysis software and cumulatively plotted. This supports the hypothesis that more warp and weft weaving points result in bigger pore sizes. The permeability in through-the-thickness direction seems to follow other rules. Lu, Tung, and Hwang [3] determined for the permeability in through-the-thickness direction an opposite weave-permeability order - satin has higher permeability than twill and plain weave.

Besides empirical models physical models have been used. Summerscales [4] determined that the permeability of a fiber network is higher if fibers are clustered in comparison to a homogeneous distribution by application of the hydraulic radius model.

Geometrical textile models have become much more precise in the past years and offer the adjustment of a lot of parameters [5-8]. Lomov, Verpoest, Peeters, et al. showed that only by changing the degree of nesting permeability values may vary significantly [9]. This is in agreement with a study of Nedanov and Summerscales who determined, that it is insufficient only to model one textile layer [10].

The prediction of the permeability by geometrical textile models is not yet possible. Lomov, Huysmans, Luo, et al. took into account 29 different parameters of the single filament, the yarn, and of woven textiles. Nevertheless the permeability values especially at higher fiber volume fractions did not agree with experimental results [11].

The goal of this study is to correlate the textile parameters of woven textiles (weave, linear density, yarn density, and crimp) with permeability. This is achieved by measuring the in-plane permeability of 19 woven textiles. As the crimp is not given in the technical data sheet it is measured as well. Permeability measurements are conducted in radial injection in the unsaturated state.

Materials

Woven textiles

The fiber finish can change the permeability of a textile significantly. As the woven textiles have been obtained from 4 different weaving companies the finishes of the companies had to be compared. The reason for this is not a change of the contact angle and thereby capillary pressures, but a change of the yarn stiffness influenced by the fiber finish. The yarn stiffness influences the architecture and nesting behavior of the textile. Lomov showed the influence of nesting on the permeability [9]. Different nesting results in different permeabilities.

In Table 2 the textile parameters of all 19 glass fiber woven textiles used in this study are shown. As there is evidence in the literature that the single filament diameter of multifilament textiles has a significant influence on the permeability [4] all plain and twill weave textiles selected for this study have a single filament diameter of 9 µm. 14 of the 19 measured woven textiles are commercially available.

No.	Manufacturer and notation	Finish	Weaving type	Yarn-density in warp-direction [filament/cm]	Yarn-density in weft-direction [filament/cm]	Linear density in warp-direction [g/km]	Linear density in weft-direction [g/km]	Areal weight (measured) [g/m²]	Filament (warp– /weft-direction)	K1 (fvc[%]) results from [13]	K2 (fvc[%]) results from [13]
1	**PGTex #1**	**A**	**twill 2/2**	**7,45**	**7,45**	**272**	**272**	**408,54**	**EC9-34x2**	**2.42E-11(49.2)**	**2.26E-11(49.2)**
2	**PGTex #2**	**A**	**twill 2/2**	**7,45**	**7,45**	**136**	**136**	**202,83**	**EC9-34x2**	**3.10E-11(49.6)**	**3.65E-11(49.6)**
3	**PGTex #3**	**A**	**twill 2/2**	**7,45**	**7,45**	**272**	**136**	**305,73**	**EC9-34x2**	**3.78E-11(49.1)**	**2.63E-11(49.1)**
4	**PGTex #4**	**A**	**twill 2/2**	**7,45**	**7,45**	**136**	**272**	**303,45**	**EC9-34x2**	**2.47E-11(48.8)**	**2.02E-11(48.8)**
5	**PGTex #5**	**A**	**twill 2/2**	**7,45**	**7**	**204**	**204**	**291,76**	**EC9-34x2**	**2.38E-11(50.8)**	**1.70E-11(50.8)**
6	**P-D Interglas Tech. 92105**	**B**	**plain**	**12**	**11,5**	**68**	**68**	**161,02**	**EC9-68**	**2.89E-11(49.3)**	**1.67E-11(49.3)**
7	**P-D Interglas Tech. 92110**	**B**	**twill 2/2**	**12**	**11,5**	**68**	**68**	**160,13**	**EC9-68**	**2.82E-11(49.6)**	**3.81E-12(49.6)**
8	**P-D Interglas Tech. 92626**	**B**	**8-harness satin**	**22**	**21**	**68**	**68**	**286,4**	**EC6-68**	**1.05E-11(51.3)**	**9.53E-12(51.3)**
9	**Schlösser& Cramer 3106**	**B**	**twill 2/2**	**6**	**6,7**	**340**	**272**	**386,4**	**EC9-68x5**	**3.76E-11(48.0)**	**1.80E-11(48.0)**
10	**Hexcel 1102**	**C**	**twill 2/2**	**7**	**7**	**204**	**204**	**284,79**	**EC9-68x3**	**3.38E-11(51.3)**	**6.74E-12(51.3)**
11	**Hexcel 7781**	**C**	**8-harness satin**	**23**	**21**	**68**	**68**	**296,13**	**EC6-68**	**1.20E-11(51.5)**	**9.92E-12(51.5)**
12	**Hexcel 7581**	**C**	**8-harness satin**	**22**	**21**	**68**	**68**	**295,7**	**EC9-68**	**1.89E-11(51.5)**	**1.54E-11(51.5)**
13	**P-D Interglas Tech. 92125**	**B**	**twill 2/2**	**7**	**6,5**	**204**	**204**	**280,48**	**EC9-68x3/EC9-204**	**2.63E-11(51.4)**	**5.51E-12(51.4)**
14	**Hexcel 1113**	**C**	**twill 2/2**	**5,9**	**6,6**	**340**	**272**	**385,22**	**EC9-68x5/EC9-**	**4.54E-11(50.4)**	**8.19E-12(50.4)**
15	**Hexcel 1265**	**C**	**plain**	**5,9**	**6,6**	**340**	**272**	**389,46**	**EC9-68x5/EC9-**	**5.17E-11(51.0)**	**3.31E-11(51.0)**
16	**Hexcel 1103**	**C**	**plain**	**7**	**7**	**204**	**204**	**285,68**	**EC9-68x3**	**4.24E-11(51.4)**	**2.83E-11(51.4)**
17	**Hexcel 1035**	**C**	**twill 2/2**	**14,7**	**14,7**	**68**	**68**	**202,81**	**EC9-68**	**3.39E-11(50.1)**	**7.63E-12(50.1)**
18	**Hexcel 1039**	**C**	**twill 2/2**	**11,8**	**11,5**	**68**	**68**	**159,55**	**EC9-68**	**4.55E-11(48.1)**	**4.55E-12(48.1)**
19	**Hexcel 1038**	**C**	**twill 2/2**	**7,35**	**7,35**	**408**	**408**	**612,3**	**EC9-136x3**	**1.34E-10(48.7)**	**5.90E-11(48.7)**

Table 1: Textile parameters of the evaluated woven textiles taken from the technical data sheet. (Remarks: PD: P-D Interglas Technologies; SCC: Schlösser & Cramer)

Methods

Measurement of crimp

The crimp is the degree of undulation (or waviness) of the yarns inside woven textiles. According to DIN 53 852 “Determination of yarn length percentages in woven textiles” [12] crimp is defined by formula 1.

$$A = \frac{(l_f - l_w)}{l_w} \qquad (1)$$

The relation between warp and weft yarn tension during textile production affects the yarn crimp. This allows to use the crimp of warp and weft yarn to determine the influence of the unknown yarn tension during production. This parameter has an influence on the permeability.

To define an average crimp each warp and weft yarn has been measured four times.

Measurement of permeability

The measurement fluid is filtered rapeseed oil with a temperature dependent viscosity $\eta = -0.0026T^3 + 0.2997T^2 - 12.403T + 221.56$ where T is the oil temperature.

The measurement cell is described in detail by Kissinger [13, 14]. The flow front is tracked by 8 capacitive linear sensors. The patented [15] procedure is based on the linear correlation

of the sensor length that is covered with oil and the output signal of the sensors (change of dielectric). Measurements have been conducted with constant pressure. Upper and lower mold half consist of 160 mm thick aluminum. The FEM simulation showed that this results in a stiffness that is required to guaranty a deflection-free measurement and plane-parallelism of less than 10 µm even at high fiber volume fractions and injection pressure up to 10 bar. The textiles are cut computer controlled to 465 mm x 465 mm. Fiber volume fractions were adjusted by 15 interchangeable aluminum spacer frames (1 mm – 7 mm). The calculation of K1- and K2- permeability data follows the publication of Adams and Rebenfeld as well as Russel [16, 17]. Furthermore, the difference of opposed sensor signals are calculated. This value (given in the appendix) shows the homogeneity of the flow front ellipse. If the difference of opposed sensor signals is higher than 15 % the permeability data should be questioned as the ellipse is not symmetrical to the injection point and the requirement for the used calculation procedure is invalid. In this study the difference is less than 6 % and all measurements fulfill the given requirements. This procedure is very useful to determine inhomogenities of textiles.
Each textile was measured three times at three different fiber volume fractions. A hole was punched into the center of the preform with a radius of 6 mm. The number of layers depending on the given fiber volume fraction varied from 5 to 20. Within this range the number of layers has no influence on permeability as shown by Rieber and Mitschang in [18]. All layers were oriented in warp direction. The permeability data were averaged and plotted versus the fiber volume fraction. For better clarity the permeability axis is plotted logarithmically [19-24] and the three data sets are approximated by a linear regression line. If the three points are approximated well they are all close to the regression line [21-24].

RESULTS

Influence of the linear density and the yarn density on permeability

The linear density and the yarn density have to be considered jointly. It is not possible to investigate them independently. As it is the combination of yarn density and linear density that is of importance for each textile, the averaged warp and weft yarn density is plotted versus the averaged warp and weft yarn linear density as shown in Figure 9.

The so called ´Density Boundary Curve´ is not a regression curve but has been calculated with the assumption, that a woven textile can be classified as ‘dense’ as soon as neighboring yarns are just touching each other. The curve is based on a yarn height to width ratio of 1:9 (in uncompacted state). This ratio has been determined by µCT pictures and leads to the curve equation $f(x) = 110.5*x^{-0,5}$. A classification into dense and open textiles is of importance as this determines the intensity by which the permeability decreases with increasing fiber volume fraction (presented in Figure 10 and 11). The permeability of dense woven textiles declines much faster with increasing fiber volume fraction as the permeability of open woven textiles. An example for this is shown in Figure 10. Textile No. 19 is much more dense in comparison to textile No. 2 and therefore, the K1- and K2-permeability declines much faster.

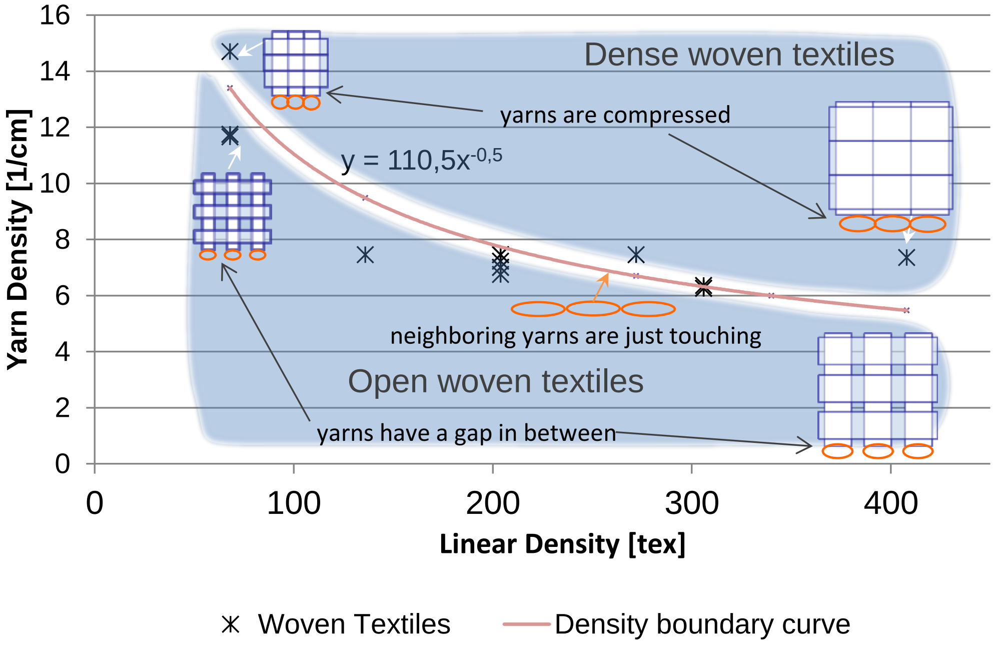

Figure 9: Averaged warp and weft yarn densities of all 19 textiles plotted versus the averaged warp and weft yarn linear densities. The continuous line classifies the woven textiles into dense and open weave textiles; this is the “Density Boundary Curve”.

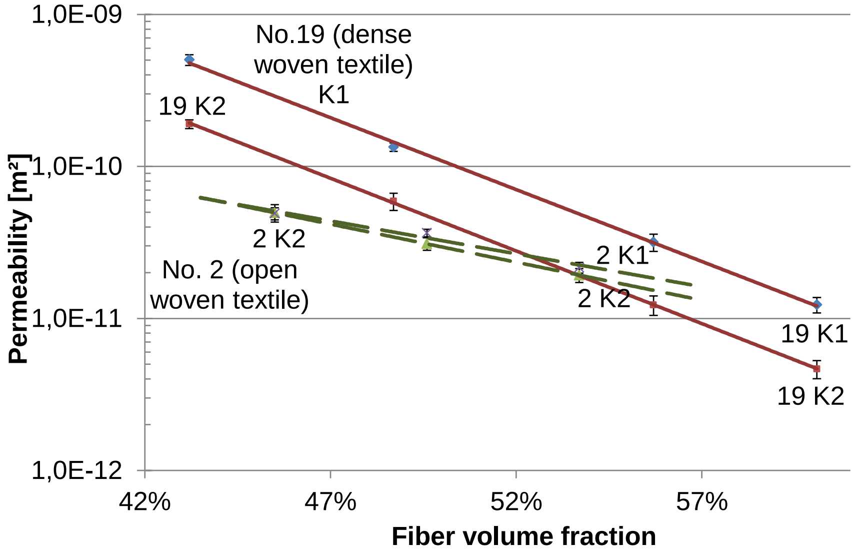

Figure 10: Comparison of the permeability-fiber volume fraction gradient of textile No. 19 and No. 2

Figure 11 shows the slope of the permeability-fiber volume fraction-curve for all measured textiles versus the deviation (shortest distance) of the textiles from the density boundary curve shown in Figure 9. The deviation, d, is calculated by the formula

$$d = \sqrt{\frac{\left(\frac{1}{yd} - \sqrt{ld} \times m\right)^2}{1+m^2}} \tag{3}$$

where m is the linear slope of the density boundary curve that can be obtained by plotting the reciprocal of the yarn density, yd, versus the square root of the linear density, ld.
Even though there is some scatter a general trend can be seen.

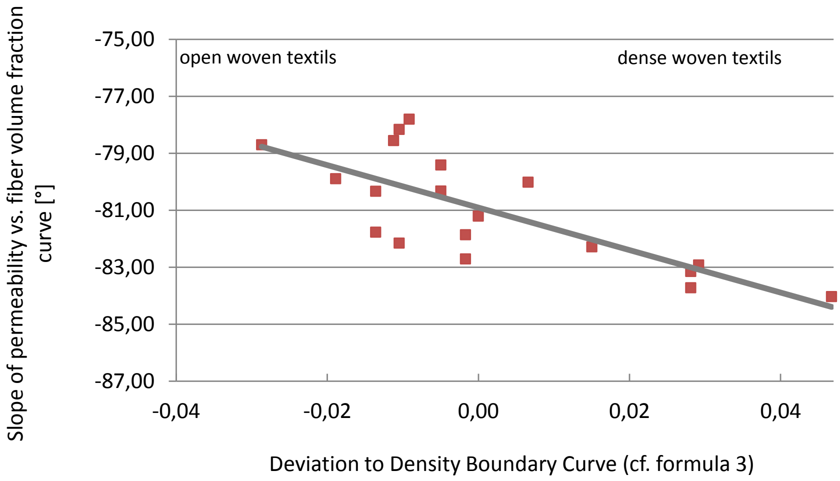

Figure 11: Slope of the permeability-fiber volume fraction curves (in degrees) of all textiles plotted versus the deviation of the textiles from the Density Boundary Curve (for boundary curve cf. Figure 9)

Influence of the crimp on permeability

The relation between the two in-plane permeability data, K2 divided by K1, is described as anisotropy. For this study the 15 textiles where the K1-permeability was in warp direction were selected. As described the crimp is dependent on the warp yarn tension during manufacturing, the linear density and the yarn density in warp and weft. The measured crimp of all textiles is shown in Table 4.

Table 4: Measured crimp data of 19 woven textiles

Material No.	1	2	3	4	5	6	7	8	9	10	11	12	13	14	15	16	17	18	19
Company description	PGTex #1	PGTex #2	PGTex #3	PGTex #4	PGTex #5	PD 92105	PD 92110	PD 92626	SCC 3106	Hexcel 1102	Hexcel 7781	Hexcel 7581	PD 92125	Hexcel 1113	Hexcel 1265	Hexcel 1103	Hexcel 1035	Hexcel 1039	Hexcel 1038
Crimp in weft [%]	1.01	0.89	1.27	0.54	0.84	1.08	0.76	1.04	1.18	0.83	0.83	0.67	0.94	0.94	2.37	1.47	1.14	1.0	1.33
Crimp in warp [%]	0.89	0.85	0.42	1.04	0.51	0.39	0.26	0.5	0.38	0.33	0.44	0.67	0.44	0.43	0.57	0.57	0.57	0.4	0.5

The crimp in warp direction is in the range of 0.26 % - 1.04 % and the crimp in weft direction is in the range of 0.54 % - 2.37 %. If the textile is built up with the same yarn density and linear density in warp and weft, the difference in crimp only results from the warp yarn tension during production. Higher warp yarn tension results in a higher weft yarn crimp. The higher weft yarn tension leads to a higher permeability in warp direction compared to the permeability in weft direction. In Figure 12 the K1- and K2-permeability data of four textiles that have each equal yarn density and linear density in warp and weft are plotted.

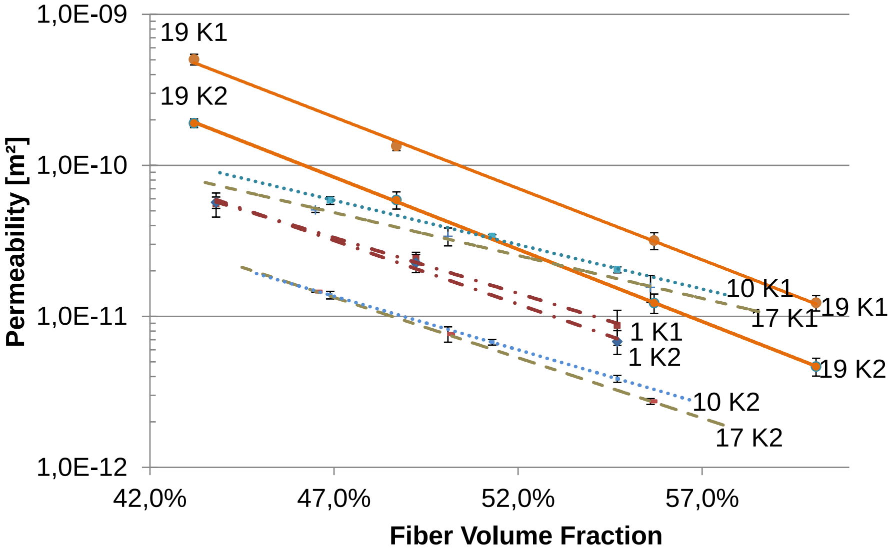

Figure 12: K1- and K2-permeability plotted versus fiber volume fraction of all textiles that have each equal yarn density and linear density (No. 1, 10, 17, and 19)

Even though all textiles have each the same yarn density and linear density in warp and weft only textile No. 1 shows isotropic flow behavior (K1=K2; circular flow front). For textile No. 10 and 17, in comparison, the K1-permeability is higher than the K2-permeability by a factor of 9.

The correlation between the anisotropy data of the textiles and their relation of weft to warp crimp becomes apparent in Figure 13. Plotted are the anisotropy data (K2/K1) of all twill weave textiles (No. 7, 10, 13, 14, 17 and 18).

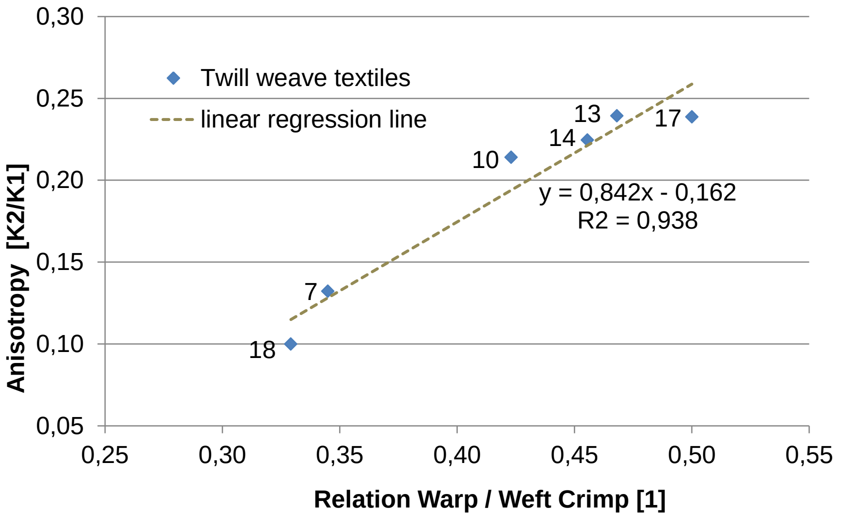

Figure 13: Anisotropy data (at 50 % Vf) of twill weave textiles No. 7, 13, 10, 14, 17, and 18 plotted versus the relation of warp to weft yarn crimp

Figure 13 allows drawing the conclusion: the higher the warp yarn tension (less crimp) the higher the permeability in warp direction. If the textiles are grouped, related to the manufacturer of the textile it can been seen, that company C is using a higher warp yarn tension than company A (Figure 14). Less crimp in the warp yarn results in a higher permeability in warp direction in comparison to weft direction.

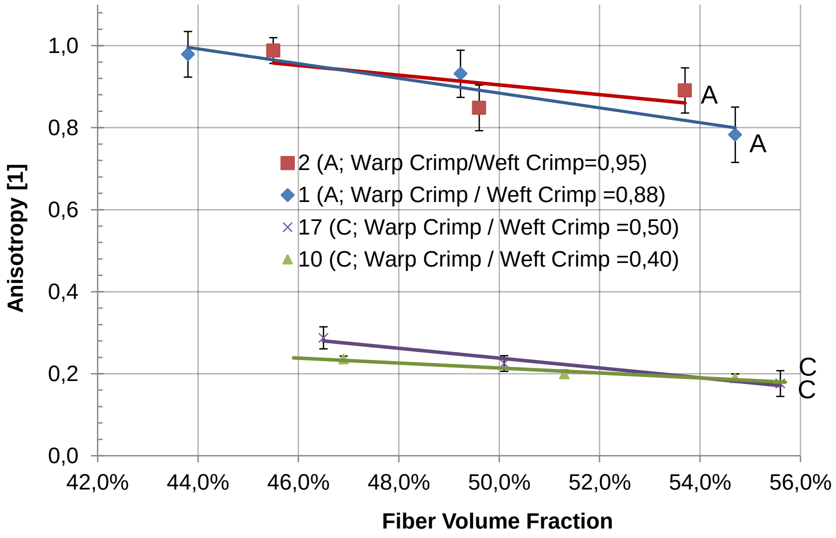

Figure 14: Anisotropy of two twill weave textiles manufactured from different companies plotted versus fiber volume fraction. Note the warp to weft yarn crimp relation is written in the caption

It can be seen if the warp to weft yarn crimp relation is low the woven textile shows anisotropic flow behavior (anisotropy values of about 0.2).

CONCLUSIONS

In the empirical part of this study, 19 woven glass fiber textiles covering a specific variety of weave, linear density, yarn density, and crimp were selected in order to determine their effects on in-plane permeability. The additionally influencing parameters, namely finish and filament diameter, have been left constant. In total 180 permeability measurements have been conducted on a radial in-plane permeability measurement cell. A density-boundary-curve has been found to separate close (dense) woven textiles from open woven textiles.

The results can be summarized as follows:

- The K2-permeability of twill weave textiles is lower in comparison to plain weave textiles.
- The slope of the permeability-fiber volume fraction curve can be predicted if linear density and yarn density are known. The more dense a textile the more the permeability decreases with increasing fiber volume fraction.
- The crimp has a big influence on the permeability. The anisotropy of woven textiles can be predicted by the relation of warp to weft yarn crimp.

Figure 15 summarizes the findings of this study.

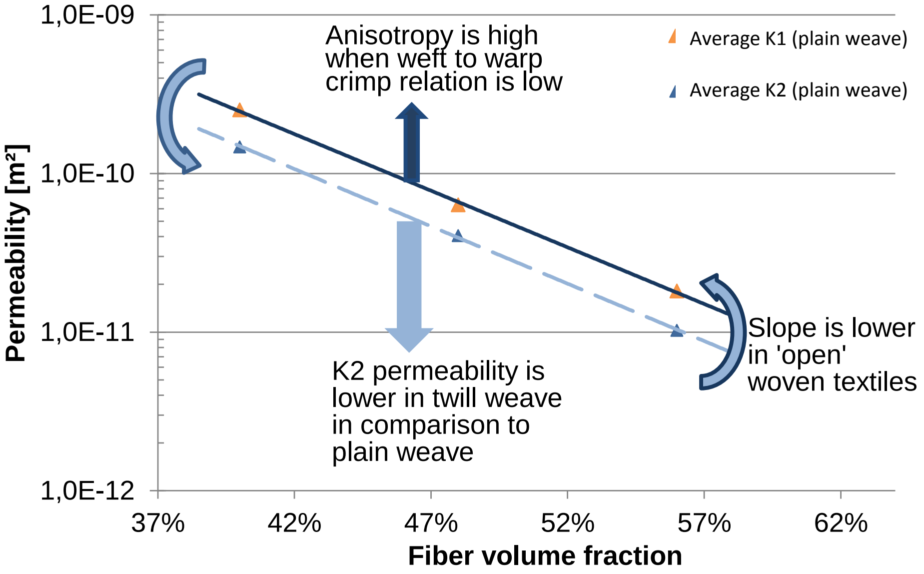

Figure 15: Overview of the main influences of textile parameters on the permeability of woven textiles based on an averaged plain weave curve

With the knowledge of these interrelations specifically designed woven textiles can be defined to allow a very fast injection process. At the same fiber volume fraction textiles differed in their K1 and K2 permeabililty by up to a factor of 27.

ACKNOWLEDGMENTS: Thank you to PGTex Shanghai for their inestimable support by manufacturing 5 woven textiles specifically for this study. Thank you to PDInterglas for providing textiles free of charge. The authors would like to thank the DFG (German Research Foundation) for the financial support (Mi647/15-2: “Influence of preforming on the permeability in liquid composite moulding”).

REFERENCES

1. Shafi V. ‘Beitrag zur Charakterisierung der Permeabilität flächiger Verstärkungsmaterialien’. Ph.D. Thesis TU Kaiserslautern: IVW GmbH; 1996.

2. Pearce NRL, Guild FJ, Summerscales J. ‘An investigation into the effects of fabric architecture on the processing and properties of fibre reinforced composites produced by resin transfer moulding’. *Composites Part A: Applied Science and Manufacturing.* 1998;29(1-2):19-27.

3. Lu WM, Tung KL, Hwang KJ. ‘Fluid flow through basic weaves of monofilament filter cloth’. *Textile Research Journal.* 1996;66(5):311-323.

4. Summerscales J. ‘A model for the effect of fibre clustering on the flow rate in resin transfer moulding’. *Composites manufacturing.* 1993;4(1):27-31.

5. Lomov SV, Chi TT, Verpoest I, Peeters T, Roose D, Boisse P, et al. ‘Mathematical modelling of internal geometry and deformability of woven preforms’. *International Journal of Forming Processes.* 2003;6:413-442.

6. Robitaille F, Clayton BR, Long AC, Souter BJ, Rudd CD. ‘Geometric modelling of industrial preforms: woven and braided textiles’. *Proceedings of the Institution of Mechanical Engineers Part L-Journal of Materials-Design and Applications*. 1999;213(L2):69-83.

7. Verleye B, Morren G, Lomov SV, Sol H, Roose D. ‘Userfriendly permeability predicting software for technical textiles’. *5th Industrial Simulation Conference*, 2007. p. 455-458.

8. Verpoest I, Lomov SV. ‘Virtual textile composites software WiseTex: Integration with micro-mechanical, permeability and structural analysis’. *Composites Science and Technology*. 2005;65(15-16):2563-2574.

9. Lomov SV, Verpoest I, Peeters T, Roose D, Zako M. ‘Nesting in textile laminates: geometrical modelling of the laminate’. *Composites Science and Technology*. 2003;63(7):993-1007.

10. Nedanov PB, Advani SG. ‘Numerical computation of the fiber preform permeability tensor by the homogenization method’. *Polymer Composites*. 2002;23(5):758-770.

11. Lomov SV, Huysmans G, Luo Y, Parnas RS, Prodromou A, Verpoest I, et al. ‘Textile composites: modelling strategies’. *Composites Part A: Applied Science and Manufacturing*. 2001;32(10):1379-1394.

12. DIN 53 852: September 1991. ‘Bestimmung von Garnlängenverhältnissen in Geweben und Maschenwaren’.

13. Kissinger C. ‘Ganzheitliche Betrachtung der Harzinjektionstechnik’. Ph.D. Thesis TU Kaiserslautern: IVW GmbH; 2001.

14. Kissinger C, Mitschang P, Neitzel M, Roder G, Haberland R. ‘Continuous on-line permeability measurement of textile structures’. *Bridging the Centuries with Sampe's Materials and Processes Technology*, Vol 45, Books 1 and 2, 2000. p. 2089-2096.

15. Daniel P, Kissinger C, Röder G. ‘Anordnung zur Vermessung der Ausbreitung eines Matrixmaterials in elektrisch leitfähigen Verstärkungsmaterialien’. Patent: DE 100 04 146 C 22000.

16. Adams KL, Rebenfeld L. ‘In-Plane Flow of Fluids in Fabrics - Structure/Flow Characterization’. *Textile Research Journal*. 1987;57(11):647-654.

17. Adams KL, Russel WB, Rebenfeld L. ‘Radial Penetration of a Viscous-Liquid into a Planar Anisotropic Porous-Medium’. *International Journal of Multiphase Flow*. 1988;14(2):203-215.

18. Rieber G, Mitschang P. ‘2D-Permeability changes due to stitching seams’. *Composites Part A: Applied Science and Manufacturing*. 2010;41(1):2-7.

19. Gauvin R, Kerachni A, Fisa B. ‘Variation of Mat Surface Density and Its Effect on Permeability Evaluation for RTM Modelling’. *Journal of Reinforced Plastics and*

Composites. 1994;13(4):371.

20. Trevino L, Rupel K, Young WB, Liou MJ, Lee LJ. ‘Analysis of resin injection molding in molds with preplaced fiber mats. I: Permeability and compressibility measurements’. *Polymer Composites*. 1991;12(1):20-29.

21. Ouagne P, Breard J. ‘Continuous transverse permeability of fibrous media’. *Composites Part A: Applied Science and Manufacturing*. 2010;41(1):22-28.

22. Ahn SH, Lee WI, Springer GS. ‘Measurement of the 3-Dimensional Permeability of Fiber Preforms Using Embedded Fiber Optic Sensors’. *Journal of Composite Materials*. 1995;29(6):714-733.

23. Hoes K, Dinescu D, Sol H, Vanheule M, Parnas RS, Luo YW, et al. ‘New set-up for measurement of permeability properties of fibrous reinforcements for RTM’. *Composites Part A: Applied Science and Manufacturing*. 2002;33(7):959-969.

24. Endruweit A, Harper LT, Turner TA, Warrior NA, Long AC. ‘Random discontinuous carbon fibre preforms: Permeability modelling and resin injection simulation’. *Composites Part A: Applied Science and Manufacturing*. 2008;39(10):1660-1669.

INFLUENCE OF TEXTILE PARAMETERS ON THE THROUGH-THE-THICKNESS PERMEABILITY OF WOVEN TEXTILES

P. Mitschang, M. Glawe, D. Kreutz, G. Rieber, D. Becker

Institut fuer Verbundwerkstoffe GmbH, Erwin-Schroedinger-Strasse, Geb. 58, 67663 Kaiserslautern, Germany. Corresponding author´s e-mail: peter.mitschang@ivw.uni-kl.de

ABSTRACT: The impregnation of the textile with matrix is characterized by the permeability. Knowledge about the permeability allows the design of a fast and reliable process by permitting the prediction of the flow directions, velocities, and pressures. There is no consistent information available about the influence of textile parameters on permeability. In this study, 19 woven glass fibre textiles are selected to determine the effect of the weave, linear density, yarn density and filament diameter on the through-the-thickness permeability. The finish of all textiles has been left constant. The measurements have been conducted on an unsaturated z-permeability measurement device consisting of a small central injection port and an ultrasound sender and receiver that track the flow front height. The overall injected fluid mass is measured by a scale. There is a linear dependency of the time of flight of the ultrasound signal and the height of the flow front in z-direction. It was observed that a higher number of textile layers leads to lower permeability values at the same fibre volume fraction. A systematic pattern was developed to characterize textiles as dense and open weave textiles by the linear density and yarn density. The more open a textile is the higher is the influence of the fibre volume content on the through-the-thickness permeability. Further influences of the weaving have been observed. The results of this study allow the selection and tailoring of woven textiles with specific, permeabilities for different applications.

KEYWORDS: *permeability, through-the-thickness, impregnation, Resin Transfer Moulding (RTM), Liquid Composite Moulding (LCM), flow front prediction.*

INTRODUCTION

Manufacturing methods for fibre-reinforced polymers have continuously advanced, aiming at an efficient production and increased mechanical properties. Hereby, the group of liquid composite moulding (LCM) processes has been recognized as a cost-effective and promising approach [1]. The members of the group of LCM processes share the principle of injecting a liquid monomer into a cavity wherein a reinforcing fibre preform is placed. This procedure offers several advantages compared to open mould processes, like better component quality and properties [2]. But the quality and the efficiency of the process strongly depend on the wetting of the fibre preform. To overcome the time-consuming and economic prohibitive trial-and error methods, numerical mold-filling simulations have been developed [3]. One of the most important inputs of these simulations is the permeability of the fabric. According to Darcy´s law, the flow rate of a liquid inside a porous medium is proportional to the pressure gradient $\vec{\nabla} p$ and the invert of the fluid viscosity η. The permeability is the constant of this proportionality. For the three-dimensional case Darcy´s law can be expressed as

$$\vec{v} = -\frac{K}{\eta}\vec{\nabla} p \tag{1}$$

with K being the permeability tensor and $\vec{v}$ being the flow front velocity. If the material axes coincide with the axes of the flow geometry, the second order tensor K is fully described by the highest in-plane permeability K1, the lowest in-plane permeability K2 and the through-the-thickness permeability K3 [4]. Because of its importance for the process, the permeability of fabrics has to be accurately measured, in order to achieve realistic models for numerical simulation, an advanced tool design and an optimized process control. In doing so an essential fact to be considered, is that the permeability of a fabric depends on the direction of the liquid flow relative to the fabric. Particularly K3 often differs significantly from K1 and K2. Even if composite components are often rather flat, K3 is an important factor especially when impregnating thick sectioned parts or using specific RTM-related processes, like resin film infusion or Compression RTM [5, 6].

The first work known in the field of K3-measuring for reinforcement textiles was done by Stedile [7], who measured the pressure drop of a liquid floating through a fibre stack. Apart from such saturated measurements several unsaturated approaches were developed, based on the monitoring of the flow front through different technologies. For example through the usage of thermistors [8] or optical fibres [9] inside the fabric stack, through video caption using transparent tools [10, 11], through flow arrival detection sensors on the upper and lower tool [12] or like in this study through ultrasonic technique [5].

The wide and cost-efficient usage of LCM-processes requires preferably general statements, about the suitability of a fabric for a certain application. The results from measurements of the through-the-thickness permeability will help to support an application-related selection of fabrics. Since fabrics are classified through a row of textile parameters it is obvious, that the best way hereby is to examine the influence of these parameters on the permeability. Expanding former studies concerning woven textiles and their in-plane permeability depending on several parameters from Rieber [13], this study deals with the influence of textile parameters on the through-the thickness permeability.

EXPERIMENTAL

Approach

The experiments were executed with an apparatus enabling the continuous monitoring of the flow front of a liquid medium, which is point-injected (circular shaped, diameter: 1.18 mm, according to experimental results from [14]). into a stack of unsaturated fabrics. The height of the flow front in the out-of-plane direction can be measured through an ultrasonic sender and an ultrasonic receiver, which are coupled and arranged oppositely on the z-axis, on both sides of the stack, as illustrated in Fig. 1.

While the flow front proceeds the time for an acoustic wave, sent out by the ultrasonic sender, to reach the receiver (time-of-flight, TOF, t_R) decreases. This is caused by the higher sound speed in the saturated fabric (c_2) compared to the unsaturated fabric (c_1). As can be derived from the diagram in Fig. 1, the TOF, decreases proportional to the height of the flow front in z-direction (z_f = flow front height; z_R = cavity height). With T_0 being a test rig dependent time offset the correlation can be mathematically expressed as (symbols illustrated in Fig. 1):

$$t_R = \frac{z_f}{c_2} + \frac{z_R - z_f}{c_1} + T_0 \tag{2}$$

Besides the flow front progression there is also a continuous measurement of the injected liquid mass which has a known density and viscosity, so that at any time during the injection a statement can be made about the height of the flow front and the volume of the liquid in the fabric. Using this data the out-of-plane permeability can be calculated through a mathematical model which correlates the measured data and the constant injection pressure with the three-dimensional geometrical shape of the flow front. The approach was verified through a number of experiments and simulations, with the most important ones described in [5]. Based thereon a standardized measurement process was developed, including a computer-based calculation-tool. Hereby a high consistency of the results at a minimum effort could be ensured.

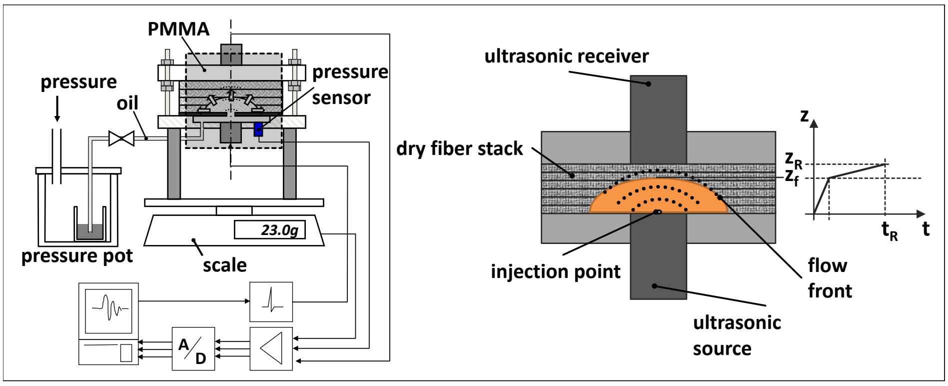

Fig. 1: Measuring apparatus

Materials

The study comprised nineteen different glass fibre fabrics covering a wide range concerning weave, yarn density and linear density. The materials and their textile parameters are listed in Table 1. The filament notation is set together, i.e. EC9-68 indicates a continuous fibre made of E-glass (EC), with a monofilament diameter of 9µm and a linear yarn density of 68 tex. Samples of the materials were cut into a circle-shape with a diameter of 100 mm and stacked in order to reach the intended fibre volume content (fvc), which also depends on the fixed cavity height (8 mm) of the measuring apparatus. The woven fabrics are two-dimensional structures comprising orthogonally crossed multifilament yarns. The manner in which the yarns cross is expressed through the weaving type. Yarns in direction of production are referred to as warp yarns. Yarns in a perpendicular direction are referred to as weft yarns. Concerning the permeability, the weaving types especially differ in the geometry of the flow spaces, which are not filled through yarn. Further textile parameters are pictured in Fig. 2.

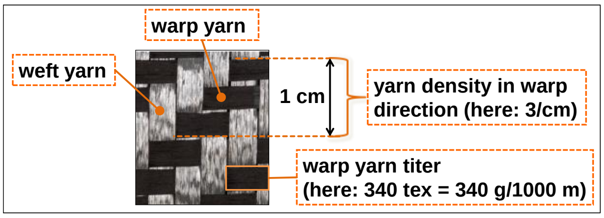

Fig. 2: Illustration of warp, weft, filament density and titer

Table 1: Textile parameters of the examined fabrics

No.	Manufacturer and notation	Finish	Weaving type	yarn-density in warp-direction [filament/cm]	yarn-density in weft-direction [filament/cm]	Titer in warp-direction [g/km]	Titer in weft-direction [g/km]	areal weight (measured) [g/m²]	Filament (warp– /weft-direction)	K1 (fvc[%]) results from [13]	K2 (fvc[%]) results from [13]	K3 (fvc [%]) results from this study
1	PGTex #1	A	twill 2/2	7.45	7.45	272	272	408.54	EC9-34x2	2.42E-11(49.2)	2.26E-11(49.2)	1.72E-12(50.1)
2	PGTex #2	A	twill 2/2	7.45	7.45	136	136	202.83	EC9-34x2	3.10E-11(49.6)	3.65E-11(49.6)	1.41E-12(50.7)
3	PGTex #3	A	twill 2/2	7.45	7.45	272	136	305.73	EC9-34x2	3.78E-11(49.1)	2.63E-11(49.1)	2.37E-12(49.5)
4	PGTex #4	A	twill 2/2	7.45	7.45	136	272	303.45	EC9-34x2	2.47E-11(48.8)	2.02E-11(48.8)	1.47E-12(50.6)
5	PGTex #5	A	twill 2/2	7.45	7	204	204	291.76	EC9-34x2	2.38E-11(50.8)	1.70E-11(50.8)	1.68E-12(48.6)
6	P-D Interglas Tech. 92105	B	plain	12	11.5	68	68	161.02	EC9-68	2.89E-11(49.3)	1.67E-11(49.3)	7.54E-13(48.9)
7	P-D Interglas Tech. 92110	B	twill 2/2	12	11.5	68	68	160.13	EC9-68	2.82E-11(49.6)	3.81E-12(49.6)	5.32E-13(48.7)
8	P-D Interglas Tech. 92626	B	8-harness satin	22	21	68	68	286.4	EC6-68	1.05E-11(51.3)	9.53E-12(51.3)	6.78E-13(49.1)
9	Schlösser& Cramer 3106	B	twill 2/2	6	6.7	340	272	386.4	EC9-68x5	3.76E-11(48.0)	1.80E-11(48.0)	1.34E-12(49.2)
10	Hexcel 1102	C	twill 2/2	7	7	204	204	284.79	EC9-68x3	3.38E-11(51.3)	6.74E-12(51.3)	1.16E-12(48.9)
11	Hexcel 7781	C	8-harness satin	23	21	68	68	296.13	EC6-68	1.20E-11(51.5)	9.92E-12(51.5)	9.50E-13(49.4)
12	Hexcel 7581	C	8-harness satin	22	21	68	68	295.7	EC9-68	1.89E-11(51.5)	1.54E-11(51.5)	1.15E-12(49.3)
13	P-D Interglas Tech. 92125	B	twill 2/2	7	6.5	204	204	280.48	EC9-68x3/EC9-204	2.63E-11(51.4)	5.51E-12(51.4)	7.58E-13(49.5)
14	Hexcel 1113	C	twill 2/2	5.9	6.6	340	272	385.22	EC9-68x5/EC9-	4.54E-11(50.4)	8.19E-12(50.4)	1.89E-12(49.1)
15	Hexcel 1265	C	plain	5.9	6.6	340	272	389.46	EC9-68x5/EC9-	5.17E-11(51.0)	3.31E-11(51.0)	2.29E-12(49.6)
16	Hexcel 1103	C	plain	7	7	204	204	285.68	EC9-68x3	4.24E-11(51.4)	2.83E-11(51.4)	2.07E-12(49.0)
17	Hexcel 1035	C	twill 2/2	14.7	14.7	68	68	202.81	EC9-68	3.39E-11(50.1)	7.63E-12(50.1)	1.42E-12(48.7)
18	Hexcel 1039	C	twill 2/2	11.8	11.5	68	68	159.55	EC9-68	4.55E-11(48.1)	4.55E-12(48.1)	8.09E-13(48.5)
19	Hexcel 1038	C	twill 2/2	7.35	7.35	408	408	612.3	EC9-136x3	1.34E-10(48.7)	5.90E-11(48.7)	5.93E-12(51.0)

The permeability was measured with plant oil (rapeseed) as injection fluid, since it is comparable to resin concerning the viscosity and surface tension. Furthermore the oil is non-reactive, follows the Newtonian law and is easy to dispose. The viscosity of the oil depending on the temperature was measured for a range between +10 °C and +35 °C, using a spindle rheometer DV-II+ Pro from Brookfield with an LV1 spindle, steered with the software rheocalc. The correlation between temperature and viscosity could be very accurately approximated with a third grade regression curve. The viscosity of the oil at 20 °C is 73 mPas. The oils average surface tension at 20 °C is 33.67 mN/m ± 0.61, examined with the hanging drop method. All in all the plant oil can be seen as an adequate measuring liquid.

Procedure

The permeability of all materials was measured with the described apparatus. Since some materials share certain properties while they differ in others, statements about the influence of various parameters on the permeability could be made. In order to receive an integrated overview of the several correlations, the permeability of each material sample was measured at three different values of the fibre volume content. Furthermore every constellation was

measured three times. To secure the results Dixon`s Q-test is used for the identification and rejection of outliers. All together the test series comprised 237 measuring operations.
During the measurement the injection pressure was held constant. The determination of the pressure value was based on experiments examining the correlation between the value of the fibre volume content and the compaction-pressure necessary to reach this value. Only if the pressure value is lower than the compaction-pressure an additionally augmentation of the fibre volume content can be avoided. Since on the other side a too low pressure leads to a rising influence of capillary pressure, which falsifies the permeability measurements, the lowest injection pressure in the test series was 50 kPa, with the highest being 250 kPa.

RESULTS

An obvious result was that the differences of the materials, concerning the textile parameters, have led to a wide range of measured injection masses (3.7 g to 14.4 g) and time spans between the beginning of the injection and the arrival of the flow front at the cavity top (18 s to 611 s). One of the most important parameters was found to be the weaving type. Among others the weaving type directly affects the through-the-thickness permeability (K3). All other parameters being equal, fabrics with plain weave showed a K3 that was between 31% and 112 % higher than K3 of twill weaved fabric, which is shown in Fig. 3. Similar results were found by Rieber [13] for K2, while the influence of the weaving type on K1 is extremely slight.

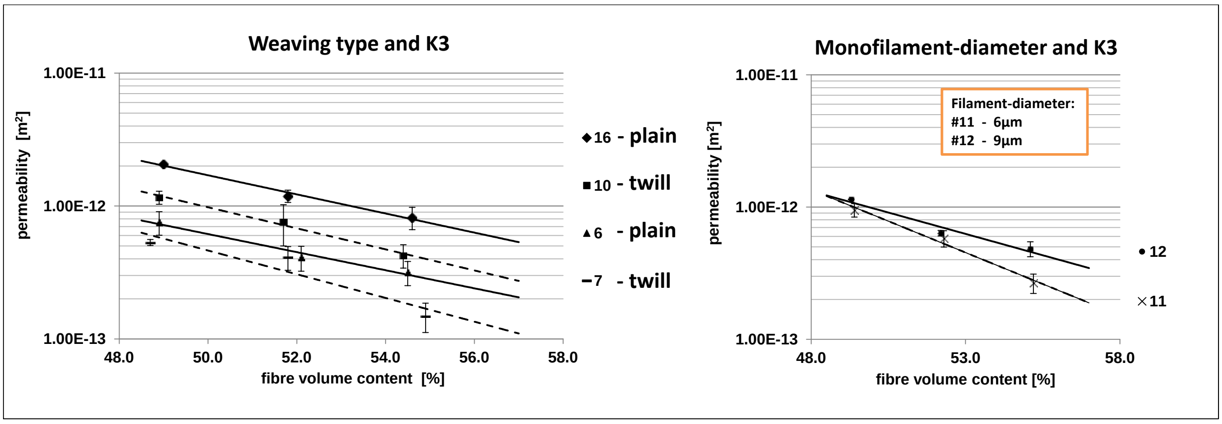

Fig. 3: Influence of weaving type on K3

Apart from the macro structure, also the micro structure influences the through-the-thickness permeability. A higher diameter of the monofilaments causes a higher permeability. Thereby the difference between two fabrics, only distinguishing in this parameter, increases with increasing fibre volume contents. As can be seen in Fig. 3 the measurements showed a maximum enhancement of K3 of 77 % at a fibre volume content of about 55 %. The results of Rieber [13] for K1 and K2 are similar.

The linear density and the yarn density were also part of the studies. As shown in Fig. 4 it was found, that a smaller yarn density causes a lower permeability, if the linear density is similar. For material #18 the average yarn density, which is the mean value of the yarn density in weft and warp direction, is 22 % lower. The average linear density, which is the mean value of the linear density in weft and warp direction, is equal for both materials. This leads to a remarkably lower permeability. On the other side the permeability of material #9, which has an average yarn density that is 57 % lower than that of material #17, is almost identical. However this does not lead to a lower K3. The only other parameter distinguishing the two materials is the linear density, which is five times as large as that of #18 and #17. This leads to the conclusion, that there is interdependence between linear and yarn density. A fact already experienced by Rieber [13] for K1 and K2. For that reason it is necessary to examine the influence of both parameters simultaneously. In this study a parameter called openness respectively density is used for this purpose. The openness of a fabric is not a value which can be calculated out of the yarn and the linear density, but it is determined by the position of a fabric in a two-dimensional space, spanned by yarn and linear density. In this space a border curve can be defined according to reasonable assumptions. The distance of the position of a fabric to this curve can then be used as a value for the openness. In Fig. 4 a border curve is illustrated, which is based on the definition, that a fabric is dense, as soon as neighbouring yarns are just touching. All points on this openness-curve mark a linear to yarn density ratio, where yarns with a height to width ratio of 1:9 (in uncompacted state) just touch each other. The ratio of 1:9 has been a result of an examination of corresponding µCT-pictures by Rieber [13].

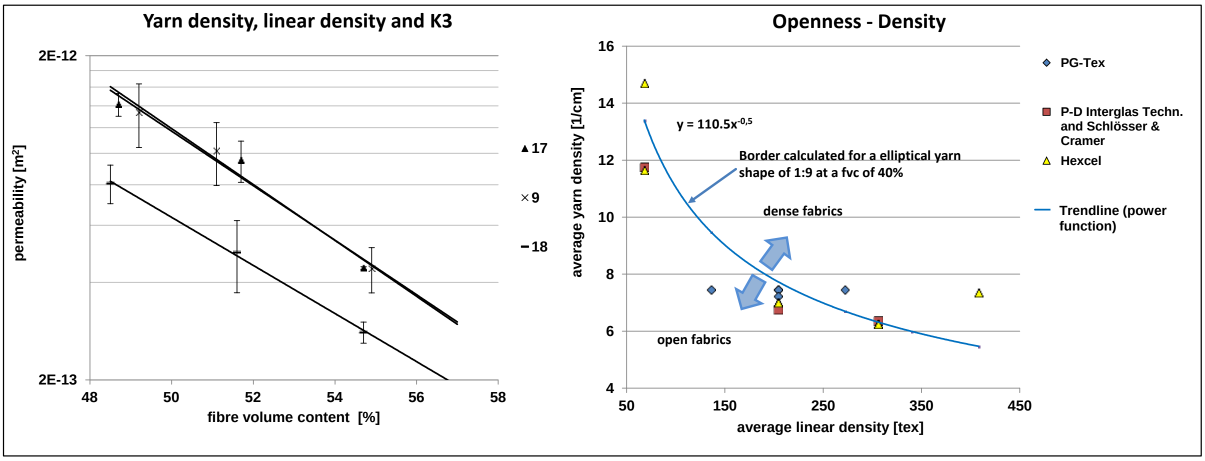

Fig. 4: Classification of open and closed fabrics

The distance of a fabric to the openness curve can then be calculated through:

$$d = \sqrt{\frac{\left(\frac{1}{yd} - \sqrt{ld} \times m\right)^2}{1+m^2}} \tag{3}$$

Thereby yd and ld are the yarn respectively the linear density of a fabric and m is the steepness of the openness-curve when it is transferred into a diagram with the invert yarn density as vertical axis and the square root of the linear density as the horizontal axis (in that case the openness-curve is a straight line). Results from Rieber [13] have shown that the logarithmic regression curve illustrating the dependence of the K1 and K2 permeability on the fibre volume content gets steeper, for fabrics with increasing density. This also suits with the measurements of this study for plain and twill fabrics which are shown in Fig. 5. The influence of the fibre volume content on K3 increases for a higher fabric density. This leads to a higher gradient angle of the regression curve. The satin weaved fabrics are not shown in the diagram, since they do not follow the found tendency.

A tendency between the density of a fabric and K3 could not be shown. Hereby a problem which had to be faced was an effect of the number of fabric layers used while measuring the permeability on the measured permeability. This effect was already examined by [13] and [15] for the in-plane permeability. According to their results a higher number of layers can decrease the measured K1 respectively K2. Since the cavity height of the measurement apparatus used for this study was constant and the fibre volume content was adjusted through the number of layers, more layers had to be stapled to a stack if the areal weight is relatively low, in order to reach the same fibre volume content. This can falsify the measurements.
Because of the importance of a statement concerning possible correlations between the openness and K3 for the RTM-process, further research has to be done. For that the influence of the number of layers has to be excluded.

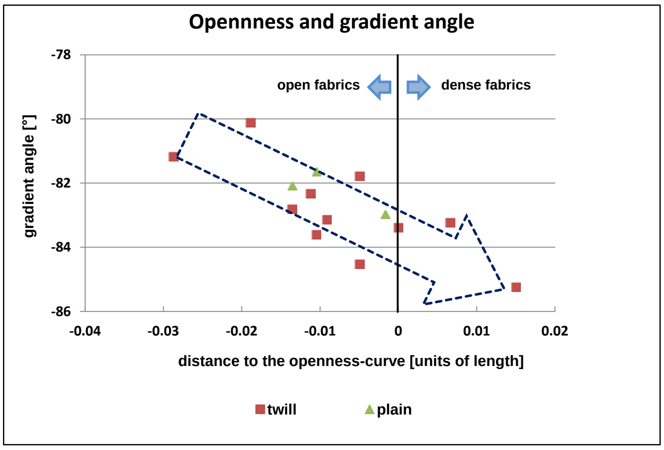

Fig. 5: Influence of openness on gradient angle and K3

CONCLUSIONS

The through-the-thickness permeability of nineteen materials, covering a wide range of textile parameters, was examined. It was observed, that the weaving type influences the through-the-thickness permeability. Plain weave leads to a higher permeability than twill weave. Also raising diameters of the monofilaments in a fabric cause a higher permeability. Furthermore it was found, that linear density and yarn density have to be examined simultaneously, since they are interdependent. This is why the openness respectively the density of a fabric was calculated as the distance of a fabric to a determined border-curve in a two-dimensional diagram with the invert yarn and the square root linear density as axes. An increasing openness was found to increase influence of the fibre volume content on the through-the-thickness permeability. Further research is needed to investigate the correlation between the openness and the through-the-thickness permeability. Thereby the possible influence of the number of layers used in the measurement and the measured through-the-thickness permeability has to be excluded. All in all the studies show the importance of taking into account the influence of textile parameters on the in and out-of-plane permeabilites when constructing a component for which the usage of resin injection technologies is planned.

ACKNOWLEDGMENTS: The authors would like to thank the Deutsche Forschungsgemeinschaft, DFG, for their support within the Project “Einfluss der Preformtechnik auf die 3-D-Permeabilität bei Flüssigimprägnierverfahren” (engl.: “Influence

of the preform-technique on the 3D-permeability at Liquid Compression Moulding processes“).

REFERENCES

1. Gutowski*, TG (1997), Ed.,* 'Advanced Composites Manufacturing',1st ed.*,* Wiley*,* New York.

2. Walbran WA, Verleye B, Bickerton S, Kelly PA (2012), 'Prediction and experimental verification of normal stress distributions on mould tools during Liquid Composite Moulding', *Composites Part A: Applied Science and Manufacturing*, 43(1), 138-149.
3. Tan H, Pillai KM (2012), 'Multiscale Modeling of unsaturated flow in dual-scale fiber preforms of liquid composite molding I: Isothermal flows', *Composites Part A: Applied Science and Manufacturing*, 43(1), 1-13.

4. Luthy T (2003), 'Three-Dimensional Permeability Measurements based on Direct Current and Ultrasound Monitoring Techniques', Dissertation, University of Neuchâtel.

5. Stöven T, Weyrauch F, Mitschang P and Neitzel M (2003), 'Continous monitoring of a three-dimensional resin flow through a fibre preform', *Composites Part A: Applied Science and Manufacturing*, 34(6), 475-480.

6. Simacek P, Advani SG, Iobst S (2008), 'Modeling Flow in Compressio Resin Transfer Molding for Manufacturing of Complex Lightweigth High-Performance Automotive Parts', *Journal of Composite Materials, 42(23),* 2523-2545.

7. Stedile U (1971), Felt Permeability testing apparatus, US Patent No. 3,577,767.

8. Weitzenböck JR, Shenoi A and Wilson PA (1998), 'Measurement of three-dimensional permeability', *Composites Part A: Applied Science and Manufacturing*, 29(1-2), 159-169.

9. Ahn SH, Lee WI and Springer, GS (1995), 'Measurement of the Three-Dimensional Permeability of Fiber Preforms Using Embedded Fiber Optic Sensors', *Journal of Composite Materials* 6, Vol. 29, 714-733.

10. Nedanov, P and Advani, SA (2002), 'Method do Determine 3D Permeability of Fibrous Reinforcements', *Journal of Composite Materials 2, Vol.* 36, 241-254.

11. Wu X, Li J and Shenoi, RA (2007), 'A New Method to Determine Fiber Transverse Permeability', *Journal of Composite Materials* 6, Vol. 41, 747-755.

12. Okonkwo K, Simacek P, Advani SG, Parnas RS (2011), 'Characterization of 3D fiber preform permeability tensor in radial flow using an inverse algorithm based on sensors and simulation', *Composites Part A: Applied Science and Manufacturing*, 42(10), 475-480.

13. Rieber G (2011), 'Einfluss von textilen Parametern auf die Permeabilität von Multifilamentgeweben für Faserverbundwerkstoffe', Dissertation, TU Kaiserslautern, Institut für Verbundwerkstoffe GmbH.

14. Stöven T (2004), ‘Beitrag zur Ermittlung der Permeabilität von flächigen Halbzeugen’, Dissertation, TU Kaiserslautern, Institut für Verbundwerkstoffe GmbH.

15. Lekakou C, Johari M and Bader MG (1996), ‘Compressibility and flow permeability of two dimensional woven reinforcements in the processing of composites’, *Polymer Composites,* 17(5), 666-672.

VALUE CORRECTION IN THE DETERMINATION OF TRANSVERSE PERMEABILITY VALUES BY USING FLOW SIMULATION IN DEFORMABLE POROUS MEDIA

F. Klunker [1], M.Danzi [1], T. Lämmlein [1], B. Louis [1], P. Ermanni [1]

[1] *Centre of Structure Technologies, ETH Zürich, Leonhardstrasse 27, 8092 Zurich, Switzerland. Corresponding author's e-mail: fklunker@ethz.ch*

ABSTRACT: The determination of through thickness permeability is usually performed by a "black box"- principle: An inflow is generated by applying pressure boundary conditions or volume rate boundary conditions, e.g. with a 1D-flow; with Darcy's Law the permeability is evaluated, assuming a constant fiber volume fraction in the cavity. It is well known that in the through thickness direction textiles can be compacted. Due to the flow, the pressure loss in the fluid induces stress on the fibers, so that they are deformed. This has a strong implication in the determination of through thickness permeability, as the fiber volume content is not homogeneous. In this paper, numerical simulation is applied to predict the deformation behavior in the textile as a result of the fluid pressure. Based on the results of the simulation a procedure to measure the through thickness permeability in saturated state, which takes the change of fiber volume content into account, is presented and discussed. The conclusions concerning the method to determine the saturated through thickness permeabilities are: (1) permeability measurements in through thickness direction cannot be reliable without the knowledge of the compaction behavior, (2) it is not possible to measure the through thickness permeability at a single fiber volume fraction if the fiber volume fraction is low with respect to the relations of pressure gradient and compaction behavior.

KEYWORDS: Through thickness permeability, textile deformation, fluid structure interaction, flow simulation.

INTRODUCTION

Flow simulation gives the opportunity to gain valuable insight about the complex interactions occurring during the filling and the post filling stage of LCM-processes with regards to wet out, fiber compaction and cure of the resin system. This paper is a contribution about the relationship of flow and its impact on fiber compaction.

The interaction of fiber deformation and resulting flow is finding application in vacuum infusion processes (filling [1, 2] and post filling [1, 3, 4]), processes with a rigid tool like gap impregnation process [5], as well as combined rigid mold/flexible membrane processes like flexible injection [6].

Ouagne and Bréard [7] determined the through thickness permeability measurement with a device performing continuous measurements and found, that the permeability depends on compaction velocity of the device. Endruweit et al. were investigating this effect in detail by applying different injection pressures in a device for through thickness permeability [8] preparing a pressure dependent permeability model and showing that permeability decreases with increasing injection pressure.
There are various techniques of how to determine through thickness permeabilities. Nevertheless, even in recent literature, the effect of flow on textile deformation has so far been neglected [9-11].

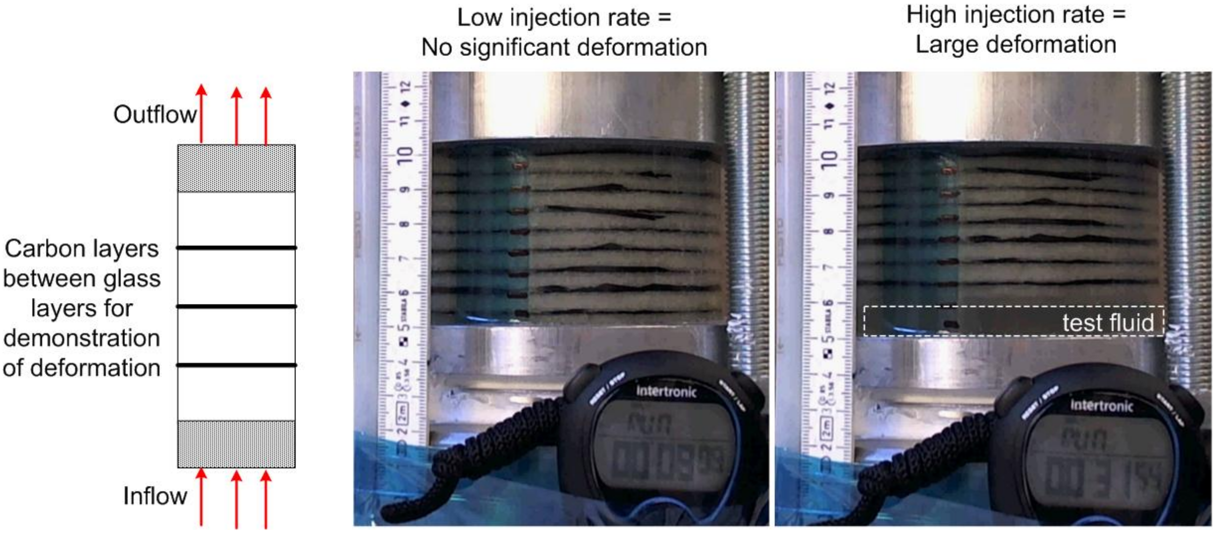

Fig. 1: Demonstration of textile deformation as a result of through thickness fluid flow

In order to demonstrate the effect of fiber deformation as a result of through thickness fluid flow, an existing cavity has been modified, as it is shown in

Fig. 1: Here a stack of layers mixed with carbon and glass fiber sheets are placed in a cavity, a fluid was injected from the bottom. The position of the carbon layers where marked on the blue stripe next to the ruler. At low injection rates, no significant deformation was visible. At high injection rates (here an injection pressure of 2.5 bars), the fiber stack was compacted so much, that even pure test fluid was visible, as it is marked in the figure.

In this paper, the behavior demonstrated in
Fig. **1** will be modeled and taken into account in the determination for through thickness permeability. A first approach to simulate the fluid structure interaction in through thickness flows can be found in Merotte et al. [12], where the compaction behavior of the textile was measured and coupled in the simulation with the pressure field in order to calculate the deformation of the wetted textile.

This paper extends the ideas presented in [12] by modeling the textile as a solid material with a specific Young’s modulus and embedding the flow analysis in a structural mechanical simulation. This approach is applied for the proposal of a procedure to determine the through thickness permeability in saturated state.

EQUATIONS AND MODELLING

The flow in textiles is modeled as flow in porous media. An important relationship to describe the flow in porous media is Darcy's Law:

$$v = -\frac{K}{\eta}\nabla p, \tag{1}$$

where v is the volume averaged fluid velocity, K the permeability tensor, η the resin viscosity and p the pressure field in the fluid.
Darcy's Law has to be combined with the mass balance. In case of incompressible fluids it can be written as:

$$\nabla \cdot v = -\dot{\varepsilon} = -\frac{\dot{V}}{V} \underbrace{=}_{stat.} 0, \tag{2}$$

where $\dot{\varepsilon}$ is the volumetric linear strain rate which can also be expressed as the relative change of an elementary volume V. As this paper is focused on saturated flow (stationary) with constant pressure boundary conditions, it is $\dot{\varepsilon} = 0$. The combination of (1) and (2) results in:

$$\nabla\left(-\frac{K}{\eta}\nabla p\right) = 0. \tag{3}$$

The pressure loss in the fluid is acting as a stress σ on the textile. This is modeled by

$$-\nabla\sigma = \nabla p. \tag{4}$$

As the flow has an influence on the compaction of the textile, the compaction behavior is experimentally characterized. There are different models available in literature for describing the compaction behavior [1,12,13]. Nevertheless, independent from analytical descriptions, for mechanical simulations a specific Young's modulus E can directly be derived from the compaction experiments by:

$$E = \frac{\sigma}{\varepsilon}, \tag{5}$$

where σ describes the stress exerted on the textile and ε the linear strain. Viscoelastic effects, as they are e.g. reported in [14], are not considered in this paper.

EXPERIMENTAL SETUP AND RESULTS

Materials

In this paper, the textile Sigmatex TCS 516, twill weave carbon fiber textile with 284 gsm and as the test fluid the silicon oil Rhodorsil huile 47 V 100 HT with a viscosity of 0.1 Pas were used.

Compaction experiments

The compaction experiments were performed with a compression test performed on a testing machine (Zwick 1474): 20 wetted plies of the textile were inserted between two parallel plates. The space between these plates is decreased by a velocity of 0.1mm/min. The resulting force is measured. In Fig. 2 the compaction stress and the resulting Young's modulus as a function of fiber volume content are shown.

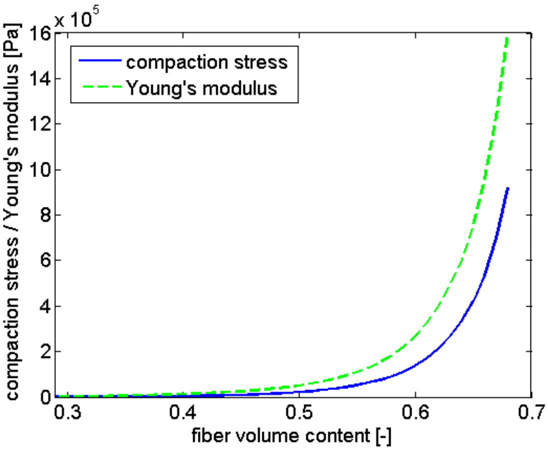

Fig. 2: Compaction stress and Young's modulus as a function of fiber volume content

Procedure and results of the flow experiments

Similar to the setup shown in Fig. 1, dry textile plies were inserted into the mold with a cavity height of 10 mm. High viscosity grease was used for sealing the fiber edge boundary in order to prevent runners, while guaranteeing a free motion of the textiles. After that, the textiles were impregnated by a low fluid pressure in the range of 1e4 Pa. After full impregnation the measurements were started:

The injection pressure was raised in steps to certain injection pressure levels (5e4, 7.5e4, 1e5, 1.5e5, 2e5 Pa) and kept constant over a period of 90s. The outflow was measured by a balance (Mettler-Toledo SB16001). These measurements have been conducted for four different fiber volume contents (0.42, 0.5, 0.565, 0.597).

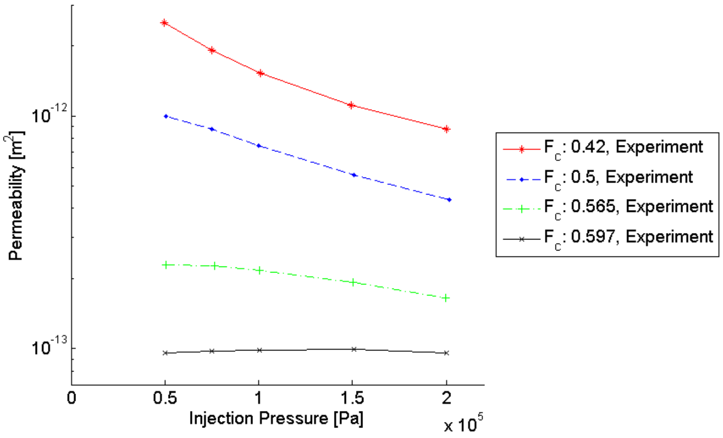

Fig. 3: Measured “apparent through thickness permeabilities”

Fig. 3 shows that the permeability is decreasing with higher injection pressure. The effect of permeability reduction is lower for higher fiber volume fractions, as higher compaction pressures are needed to increase the fiber volume content.

PROCEDURE FOR THROUGH THICKNESS PERMEABILITY DETERMINATION

In Fig. 4 (left) an exemplary result of the simulation can be seen. The upper boundary is kinematically constraint, having no displacement, while the lower boundary can be moved in z-direction as a result of a kinematic constraint (compression) or a force constraint (wash out effects due to high injection pressures). In the flow simulation the lower boundary is the injection area (x=0), the upper boundary is the vent (x=L). The colored area shows the local fiber volume content.

Fig. 4 (center and right) shows numerical results for the local distribution (variable normalized position within the sample: $\alpha = x/L$, where L is the compacted preform height) of the fiber volume fraction for two different initial fiber volume contents (F_{init}: 0.5 and 0.597) at different levels for the injection pressure. It can be seen, that

- the fibre volume content is higher in the upper area, the outlet area, than in the injection area,
- with increasing injection pressure, and therefore increasing pressure gradient, the range of local fiber volume contents is increasing.

In conclusion, the pressure gradient cannot be assumed to be linear as it can only be used to describe an “apparent through thickness permeability” which is changing with injection pressure.

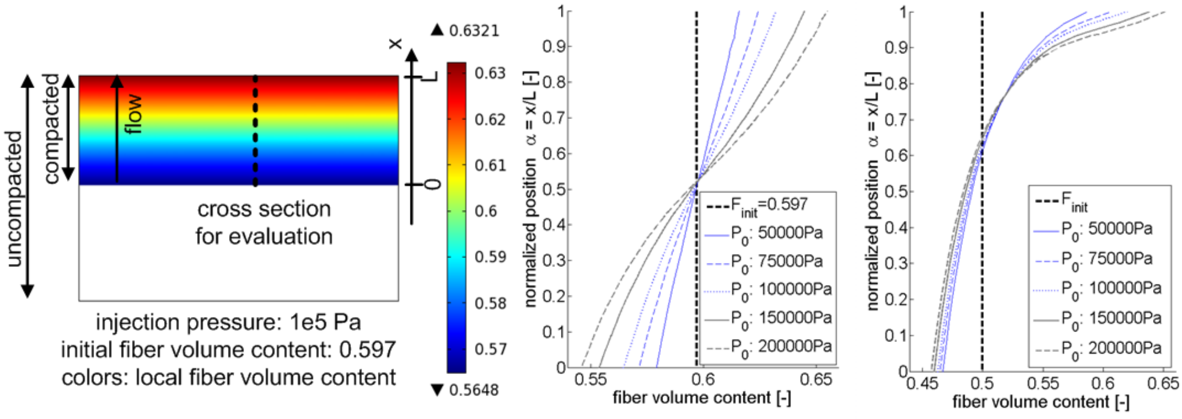

Fig. 4: Local variation in fiber volume fraction as a result of flow induced compaction

As high compaction forces are required to compact the textile to an initial fiber volume content of 0.597 (1.29e5 Pa, compare also Fig. 2), the change of the range of fiber volume contents with increasing injection pressure is lower than for low initial fiber volume contents (here 0.5 with a necessary compaction pressure of 2.12e4 Pa).

This effect has to be taken into account in the determination of the through thickness permeability. In the following text, a procedure to determine through thickness permeability is proposed.

The procedure for the determination of through thickness permeability in saturated state is based under following assumptions:

- for a defined fiber volume fraction there is one unique permeability, i.e. nesting of tows or tow compaction is not considered,

- for an injection pressure "close to zero", the deformation of the textile can be neglected, therefore the apparent through thickness permeability equals the real permeability.

As in experimental practice there are limitations concerning these assumptions, an iterative approach to determine through thickness permeability is proposed:

- The apparent permeability has to be experimentally determined for different fiber volume fractions,
- the results of the experiments can be fitted by simulation results:
    - Initial step:
      The highest fiber volume fraction has the lowest sensitivity of the local fiber volume fraction with respect to the pressure gradient. The apparent through thickness permeability is an average result caused by the local fiber volume contents. For a defined injection pressure levels the related band of fiber volume fractions has to be taken into account during the fitting (e.g. 0.5648-0.6321 for an initial fiber volume content of 0.597 at 1 bar injection pressure as seen in Fig. 4 (left)).
      The fitting procedure aims to an averaged permeability value, therefore it should be noticed that there is no unique solution: Increasing permeability values for fiber volume contents lower than the average can be compensated by decreasing permeability values for higher fiber volume contents.
      In order to avoid this problem, regularities of the permeability function have to be introduced. In this paper, following regularities are used:
        - The permeability is strictly monotonic decreasing with increasing fiber volume content ,
        - the slope of the permeability function should be as low as possible,
        - the permeabilities are defined sectionwise as an exponential function.
    - Further steps: The fitting procedure of the initial step is applied for the other fiber volume fractions as well with the constraint that the permeability values already defined in the previous steps are not changed.

Fig. 5 (left) shows a logarithmic plot of the simulated apparent through thickness permeability as a function of injection pressure as a result of the fitting procedure described above. For this paper, the fitting was conducted manually. In future, it is planned to implement an automated fitting scheme.

As expected, for the highest fiber volume content there is almost a perfect match of the permeability curves. For lower fiber volume contents the deviation from simulation results to experimental results is increasing, as the biggest part of the permeability range is already fixed in the iteration steps before. Nevertheless, as the apparent permeability is an average of a wide range of permeability with a maximum error of 17.5 % (at the low pressure values of 0.5e5 Pa for a fiber volume content of 0.565 and 0.5), a good result could be achieved.

In Fig. 5 (right) the fitted permeability model is shown in comparison with the apparent permeabilities for 1e5 Pa injection pressure. The sections of the different steps of fitting with the related fibre volume contents are marked. It has to be denoted that these do not necessarily match with the sections for the piecewise defined exponential function in the procedure described above.

Generally it can be observed, that for high volume contents, the two curves in Fig. 5 (left) are in the same range. For low fiber volume contents in the range of 42%, the model predicts a permeability which is of a factor six higher than the apparent permeability for 1 bar injection pressure. This points out, that not taking into account the deformation due to the flow could lead to a large error.

It has to be noticed that these results still have to be validated with a different approach, independent from the compaction related deformation due to flow. Nevertheless, as the fitting showed quite consistent results, the major trend of permeability behavior seems to be clear: For this textile between 54% an 60% fiber volume content, a strong decrease of permeability with increasing fiber volume content is observed; below 54% and higher than 60% the decrease is much lower. Therefore it can be concluded that permeability models in through thickness direction have to represent this changes of slopes as well.

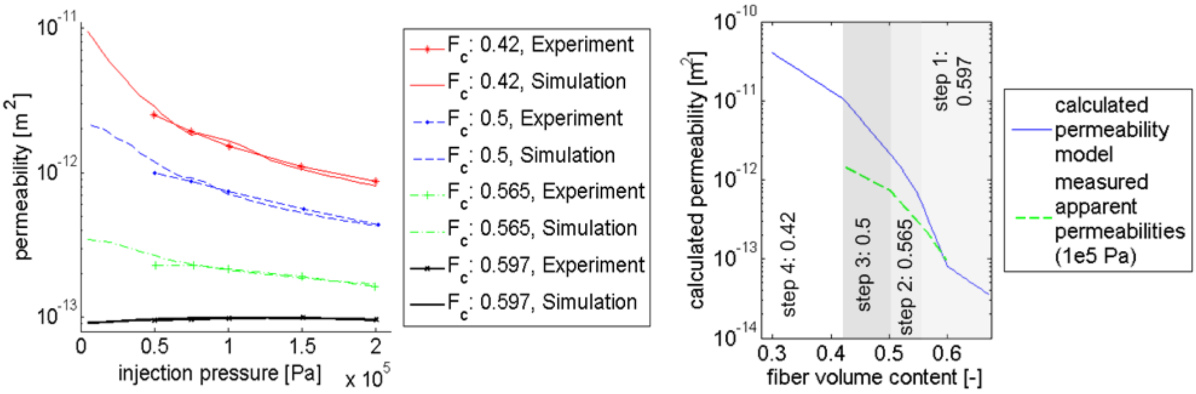

Fig. 3: Apparent permeabilities in experiment and simulation (left) and the calculated permeabilities as a result of manual variation in comparison with measured apparent permeabilities (right)

CONCLUSION AND OUTLOOK

A methodology to determine the through thickness permeability was derived, taking into account the compaction properties of the fibers and their influence in the permeability measurement. It could be shown, that the measured permeability and the permeability determined by the methodology can differ a lot, even up to an order of magnitude for the textile investigated in this paper.

The procedure for permeability determination in general showed good results, especially for higher fiber volume fractions. For low fiber volume fractions the compaction during the through thickness flow is significant. Therefore, permeability measurements in through thickness direction cannot be reliable without the knowledge of the compaction behavior.

As within one measurement the fiber volume fraction is inhomogeneously distributed, it is not possible to measure the through thickness permeability at a single fiber volume fraction if the fiber volume fraction is low with respect to the relations of pressure gradient and compaction behavior.

Nevertheless, there are still open issues, which have to be clarified for future work. In detail these are:

- Validation of the found permeability values for low fiber volume content with a methodology which is not influenced by the compaction
- Influence of viscoelastic effects during the measurement of compaction and permeability
- Applying the models to the wetting stage of a textile

REFERENCES

1. Govignon Q, Bickerton S and Kelly PA (2010), ‘Simulation of the reinforcement compaction and resin flow during the complete resin infusion process,’ *Composites Part A: Applied Science and Manufacturing*, 41, 45-57.
2. Park CH and Saouab A (2009), ‘Analytical Modeling of Composite Molding by Resin Infusion with Flexible Tooling: VARI and RFI processes,’ *Journal of Composite Materials*, 43, 1877-1900.
3. Simacek P, Eksik Ö, Heider D, Gillespie Jr. JW and Advani S (2012), ‘Experimental validation of post-filling flow in vacuum assisted resin transfer molding processes,’ *Composites Part A: Applied Science and Manufacturing*, 43, 370-380.
4. Simacek P, Heider D, Gillespie Jr. JW and Advani S (2009), ‘Post-filling flow in vacuum assisted resin transfer molding processes: Theoretical analysis,’ *Composites Part A: Applied Science and Manufacturing*, 40, 913-924.
5. Michaeli W and Fischer K (2008), ‘Untersuchungen zur Fertigung von flächigen Bauteilen aus faserverstärkten Kunststoffen mithilfe des Spaltimprägnierverfahrens ,‘ *Journal of Plastics Technology*, 4, 1-29.
6. Ruiz E, Briones L, Allardand E and Trochu F (2008), ‘Flexible injection: a novel LCM technology for low cost manufacturing of high performance composites. Part I – experimental investigation,’ *Proc. of FPCM 9*, Montreal.
7. Ouagne P and Bréard J (2010), ‘Continuous transverse permeability of fibrous media,’ *Composites Part A: Applied Science and Manufacturing*, 41, 22-28.
8. Endruweit A, Luthy T and Ermanni P (2002), ‘Investigation of the influence of textile compression on the out-of-plane permeability of a bidirectional glass fiber fabric,’ *Polymer Composites*, 23, 538-554.
9. Jiang J, Wang Z and Chen N (2012), ‘Measurement of Transverse Permeability of Fabric Preforms Using Ultrasound Monitoring Technique in LCM Processes,’ *Advanced Materials Research*, 311-313, p.214-217.
10. Okonkwo K, Simacek P, Advani SG and Parnas RS (2011), ‘Characterization of 3D fiber preform permeability tensor in radial flow using an inverse algorithm based on sensors and simulation,’ *Composites Part A: Applied Science and Manufacturing*, 42, 1283-1292.
11. Lee SH, Yang M, Song YS, Kim SY and Youn JR (2009), ‘Three-dimensional flow simulation of resin transfer molding utilizing multilayered fiber preform,’ *Journal of Applied Polymer Science*, 114, 1803-1812.
12. Merotte J, Simacek P and Advani SG (2010), ‘Resin flow analysis with fiber preform deformation in through thickness direction during Compression Resin Transfer Molding,’ *Composites Part A: Applied Science and Manufacturing*, 41, 881-887.
13. Klunker F, Ziegmann G, Aranda S, Baisch P, Fideu P and Herrmann A (2008), ‘Permeability and Compaction Models for Non Crimped Fabrics to perform a 3D-filling simulation of Vacuum Assisted Resin Infusion,’ *Proc. of FPCM 9*, Montréal.
14. Kelly PA, Umer R and Bickerton S, ‘Viscoelastic response of dry and wet fibrous materials during infusion processes,’ *Composites Part A: Applied Science and Manufacturing*, 37, 868-873, 2006.

IN-PLANE PERMEABILITY CHARACTERIZATION OF FIBER METAL LAMINATES MADE BY RTM PROCESS

Iñigo Ortiz de Mendibil [1], René Hoto [2], Juan A. García[2], Javier Andrés[3], Mariasun Sarrionandia[1] and Jon Aurrekoetxea[1]

[1] Department of Mechanics and Industrial Production, Mondragon Unibertsitatea,
Loramendi 4, 20500 Mondragon, Spain.
[2] Universitat Politécnica de Valencia. Camino de Vera s/n, 46022, Valencia, Spain.
[3]Universidad Jaume I. Vicent Sos Baynat, s/n, 17071 Castellón, Spain.

ABSTRACT: Fiber metal laminates (FMLs) consist of alternate thin layers of metal and fiber-reinforced polymer–matrix composite. The FMLs are usually manufactured using autoclave processing. These processes are well established and offering excellent reliability and part quality but they are expensive to produce and dimensional restrictions apply. LCM processes seems to be a good candidate to replace the autoclave process. In order to carry out accurate numerical simulations, the permeability of the FMLs must be measured. In this research work the effective permeability of a FML stack has been measured as well as the permeability of the single porous phase.

KEYWORDS: *Fiber Metal Laminate (FML), Liquid Composites Molding (LCM), Resin Transfer Molding (RTM), Permeability Measurement*

INTRODUCTION

Fiber metal laminates (FML) are hybrid materials based on stacked arrangements of alternate thin layers of metal and fiber/reinforced polymer/matrix composite. The first generation of FMLs was basically destined for aerospace industries, concretely for fatigue prone areas of modern aircrafts [1]. Most of the scientific investigation on these composites has been held at Delft University of Technology early in the 80s and nowadays FMLs are commercially available under the trade name of ARALL (aramid fiber/aluminum) or GLARE (glass fiber/aluminum)[1]. The combination of metals and composites results in an ability to impede and arrest crack growth caused by cyclic loading, with both excellent impact and damage tolerance characteristics and low density.

Combining all the above mentioned properties with a good machinability, they usually need long and expensive processing cycles such as autoclave processing or compression molding. Although well established, the high cost of these manufacturing processes is an obstacle for a wider adoption of FML, and their main application field has been restricted to the aeronautic and military industries.

In order to increase the competitiveness of FMLs; that is, to potentially reduce cost, minimizing materials waste and reducing capital investment, an alternative manufacturing technique must be developed. Such a new, alternative manufacturing technique among other seem to be LCM (Liquid Composites Molding) processes. One of the first attempts to use LCM processes to manufacture FML parts has been proposed by the NASA Langley Research Center (LaRC) [2] by means of Vacuum Assisted Resin Transfer Molding (VARTM) processes the metallic foils need to be perforated in order to infiltrate the resin. The major problem with this approach is the fact that these holes act as crack initiators [3]. So as to overcome this weak point, this work proposes to locate the holes only in the inner sheets of the FML, leaving the outer ones exempt of any holes. This configuration also allows to perform a conventional Resin Transfer Molding (RTM). During LCM processes the resin impregnates the reinforcing fibers placed inside in the mold cavity. The motion of the resin is induced by an applied pressure gradient. In order to optimize manufacturing processes, many mold filling codes have been developed (LIMS, PAM-RTM, etc). These tools are based on Darcy’s Law [4].

Darcy’s Law shows that it is essential to know the permeability value to compute the filling time and the filling patterns. The full characterization of the preform imply the knowledge of the three principal permeability values. Since the parts obtained through LCM processes are usually thin shells, the through-thickness permeability is usually neglected and only planar permeabilities need to be obtained. Various theoretical expressions based on the perform architecture have been developed to predict the values the permeability for LCM processes, but they can only be applied in some specific cases. As permeability is an intrinsic property of a fibrous material, it ought to be evaluated experimentally. Hence, methods to experimentally measure the permeability value have been developed. In the case of the unidirectional in-plane unsaturated permeability measurement method one must perform injection in a rectangular mold along three directions in order to obtain the effective permeability values. Then the principal permeability values can be easily computed [5]. Performing an injection to create a flow in the in-plane direction of the FML stack, the unidirectional method for permeability measurement may become applicable to obtain an averaged effective permeability of the overall stack.

IN PLANE FLOW VISUALIZATION TEST

A RTM equipment to measure unidirectional permeability designed and constructed by the Universitat Politécnica de Valencia has been employed to execute the tests. The mold consists of a removable aluminum bottom plate and a fixed methacrylate top counter mold stiffened with a metallic frame. A picture of this permeability measuring equipment is shown in figure 1a. The mould is closed with a flexible silicone sealant and the preform thickness is set by modular frame made of spacers alongside the mold. The clamping force is provided by two hydraulic pistons. The maximum dimensions of the preform inside mold are 900×200 mm^2; however the samples to measure have been cut to 700×200 mm^2 to avoid any out of plane flow at the injection inlet. The injected fluid is a calibrated silicone oil of viscosity 0.1 Pa.s (Dow Corning® XT.PMX-200). A constant 1.5 bar manometric pressure is applied at the inlet port, injection pressure has been measured at the inlet tube with a pressure transducer. The flow front position can be observed through the transparent top part (figure 1b), transversal marks have been plotted on the transparent surface every 40 mm and the flow front speed has been calculated by recording the time to fill each mark.

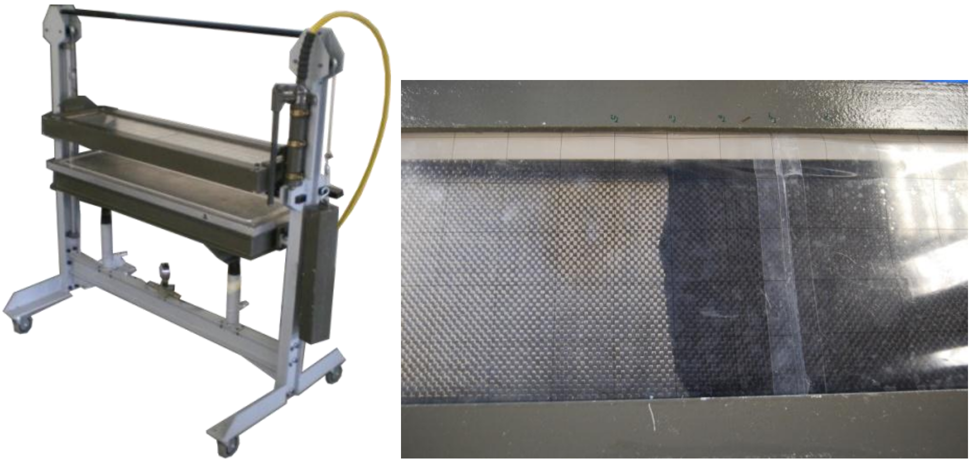

Fig. 1: a) Permeability measurement equipment; b) Flow front progression

In order obtain and understand the effective permeability in the warp direction of the FML three different tests have been carried out:

- ✓ First, the permeability of the porous media has been measured according to the benchmark proposed by Arbter *et al* [5]. The used preform consists on a 3 mm thick pile of 9 plies of woven basalt fabric (Reference TBR-400 kindly supplied by Kamenny Vek) with a total areal weight of 3600 $g \cdot m^{-2}$. The porosity of the sample is calculated to be approximately 55%.

- ✓ In a second step the tests have been repeated with a thinner sample as the final FML is composed by a sequence of thin permeable phases separated by non-porous metallic sheets. Three layers of the same woven basalt fabric have been stack, with a total areal weight of 1200 $g \cdot m^{-2}$. The thickness of the spacers has been reduced to 1mm, keeping the porosity of the media unaltered to 55%.

- ✓ Finally the permeability of a FML construction like the exposed in the figure 2 has been measured. A 3/2 construction has been chosen for the exercise, consisting of two metallic skin and another sheet in the core. Two porous reinforcement phases have been placed among the metallic layers. Each reinforcement phase comprises three basalt woven fabric layers. The original Aluminum sheets have been replaced with 0.5 mm thick transparent polycarbonate sheets in order to make the flow visualization possible. The total thickness of the FML is set to 3.5 mm. The thickness and porosity of the permeable phases are then kept invariable to 1 mm and 55% respectively.

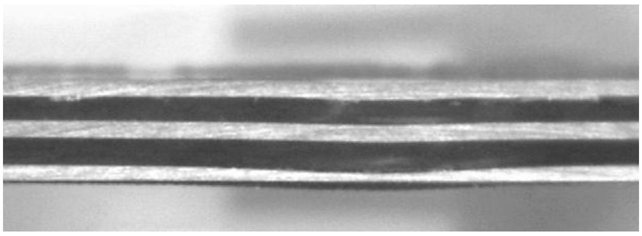

Fig. 2: FML construction.

Although the present work does not study any out of plane permeability between two porous phases, the polycarbonate sheets have been drilled so the resin transference between the two porous phases can take place and the flow front of both phases can be balanced. The drilling pattern follows the same strategy as the research carried out by Cano *et al* [2]. With a flow path diameter of 0.75 mm and spacing between holes of 21 mm, the transversal permeability is estimated to be 1.76×10^{-11} m^2.

Permeability Estimation

The flow front position is observed and the time to fill each differential length of the preform is registered and plotted. In figure 3a the evolution of the flow front of one FML injection is shown. The curves of every different configuration have a square root function shape as it is predicted by Darcy's permeability Law. Thus, if the flow front position is squared and plotted versus time, a straight line is obtained as shown in figure 3b. The slope is determined by least squares fitting.

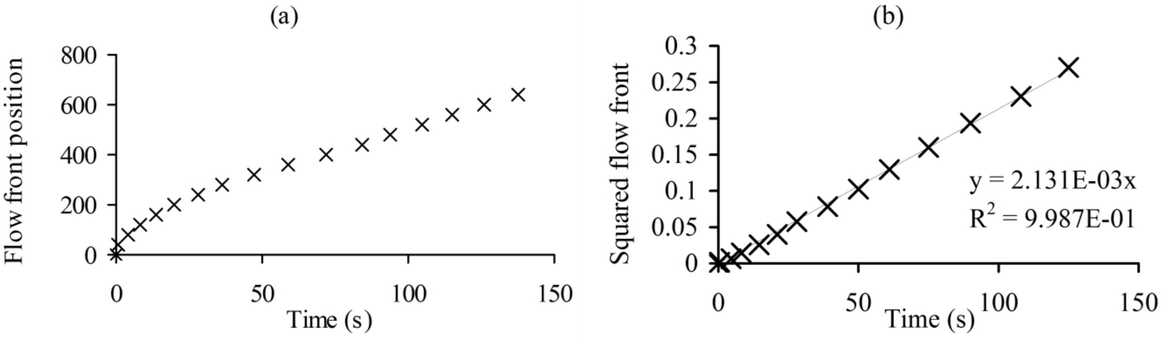

Fig. 3: FML flow front (a) and squared flow front (b) *vs*. time.

The experimental permeability value can be obtained as defined in Eqn. 1. Where m is the value of the slope from the figure 3b, P_{inj} is calculated as the mean value of pressure measured at the inlet gate during the test and μ is the viscosity of the fluid.

$$\mathrm{K}_{\exp} = \frac{m}{2 \cdot P_{inj}} \mu \tag{1}$$

The permeability is also calculated by the least square fit approach. Table 1 shows the calculated permeability of the three different configurations. Although the fiber volume fraction of the porous phase is kept constant, the overall porosity of the FML is smaller as the polycarbonate plies are supposed to have porosity. In order to compare the permeability of the fiber reinforced stage, the permeability the porosity is not considered when the permeability the permeability values are calculated.

Table 1: Measured Permeability

Test type	Construction	Thickness (mm)	Porous Phase porosity	Overall Porosity	Permeability Squared Flow Front (m^2)	Permeability Least Square Fit (m^2)
Bulk	9 ply Thick Porous Media	3	55%	55%	8.57E-10	9.03E-10
Phase	3 ply Thin Porous Media	1	55%	55%	2.97E-10	2.86E-10
FML	3/2, 3 Ply per Porous Phase	3.5 (3x0.5+2x1)	55%	31%	9.06E-10	9.22E-10

The hybrid preform provides a permeability value that is similar to the composite preform with comparable thickness. The amount of plies of the FML construction is fewer than in the bulk, the geometry of the flow channels at the interface with the non porous part is different, modifying the effective permeability. No apparent relationship can be found between the permeability of the layer and the permeability of the FML as it was the aim of the present research work. Further research may be done to relate these permeability values. Some discrepancies between the permeability value of the phase and those of the bulk have been observed.

Finally, the permeability calculated by both methods (Squared Flow Front and Least Square Fit) gives similar results. The calculated Two in plane filling models have been applied and both fit to the behavior of the tests as it can be seen in the figure 4. Darcy's permeability model can be implemented to simulate in plane filling of Fiber Metal Laminates.

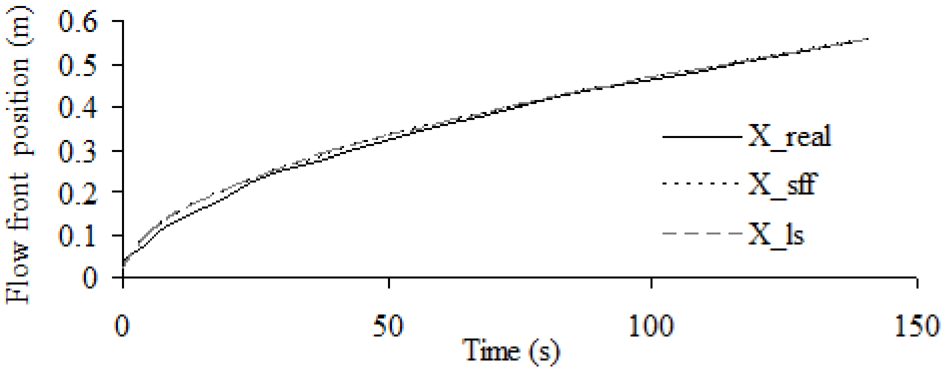

Fig. 4: FML filling curves

CONCLUSIONS

In this work it has been shown that the measurement of permeability in the case of FMLs is possible to perform using a set-up designed for unidirectional measurements of LCM reinforcements. An effort to relate the permeabilities of the composite phase and the FML construction has been done. However during the evaluation of the permeability of thinner preform, thickness influence has been spotted. These contradictions have to be tackled in order to achieve a better understanding of the filling process of these hybrid materials.

ACKNOWLEDGMENTS: Iñigo Ortiz de Mendibil would like to thank the Department of Education University and Research of Basque Country for the pre-doctoral grant (BFI 2010.47). The authors also thank the Basque Government (PI2012-35) and the Spanish Government (DPI2011-25067 and DPI2010-20333) for providing financial support for this study.

REFERENCES

1. Ad Vlot and Jan Willem Gunnink (2001), 'Fiber Metal Laminates: An introduction', Kluwer Academic Publishers.

2. Cano R.J.; Loos A. C; Jensen B. J *et al* (2011), 'Epoxy/Glass and polyimide (LaRC ™ PETI-8/Carbon Fiber Metal Laminates Made by the VARTM Process', *Sampe Journal* 47(2) , 50-58

3. Baumert E. K; Johnson W.S; Cano J. R *et al* (2011), 'Fatigue damage development in new fibre metal laminates made by the VARTM' *Fatigue & Fracture of Engineering Materials & Structures*, 34(4), 240-249

4. Suresh G. Advani and E. Murat Sozer (2003), 'Process Modeling in Composites Manufacturing' Marcel Dekker, Inc., New York

5. Arbter R.; Beraud et *al* (2011) 'Experimental determination of the permeability of textiles: A benchmark exercise' *Composites Part A: Applied Science and Manufacturing,* 42(9), 1157-1168.

EFFICIENT GENERATION OF THE VOXEL DESCRIPTION OF TEXTILE GEOMETRIES FOR THE COMPUTATION OF THE PERMEABILITY

Jonas De Greef[1], Yichen Shen[2], Christoph Hahn[2], Stepan V. Lomov[3], Dirk Roose[1],
Bart Verleye[1], and Ignaas Verpoest[3]

[1] *KU Leuven, Dept. Computer Science,*
Celestijnenlaan 200A, B-3001 Leuven, Belgium.
[2] *TU München, Lehrstuhl für Carbon Composites,*
Boltzmanstr. 15 85748 Garching, Germany.
[3] *KU Leuven, Dept. of Metallurgy and Materials Engineering,*
Kasteelpark Arenberg 44 B-3001 Leuven, Belgium.

Corresponding author's e-mail: bart.verleye@cs.kuleuven.be

ABSTRACT: For the accurate simulation of Liquid Composite Moulding processes, the input of the permeability of the preform is required. The permeability of a textile can be obtained experimentally, or can be computed. To compute the permeability, the software FlowTex was developed at the KU Leuven, as part of the textile modelling software package WiseTex. FlowTex transforms the vector description of the textile models into a voxel description, which is input for the finite difference flow solver. In this paper we present the implementation of the flooding algorithm to make this transformation more efficient. Validation and convergence studies, both for the voxelisation as for the permeability computation are presented.

KEYWORDS: *Flooding, Non-crimp fabrics, Permeability, Voxel*

INTRODUCTION

The permeability of a technical textile is a key input parameter for simulation of Liquid Composite Moulding processes like Resin Transfer Moulding. In previous work, we have shown that the combination of the WiseTex modelling software [3,9], and the permeability computation module FlowTex [7,8], results in an accurate prediction of the permeability. Extensive experimental validation has been presented, however, mainly for woven textiles.

Although for Non-Crimp Fabrics (NCFs), results were presented, not many computations were done for this kind of textiles. The reason being that the creation of a voxel description of the NCF textile model [3,4,5], required as input for FlowTex, was computationally too expensive. In this paper we present a voxelisation method based on the flooding technique, that speeds up the creation of voxel files significantly. The technique does not only for the NCFs but for all textiles that can be modelled with WiseTex. We also present validation results and permeability convergence studies.

MODELLING OF NON-CRIMP FABRICS

For the modelling of textiles, WiseTex internally employs a textile model that allows for a complete description of the fabric's structure and properties at any point in the object space. In the following, we explain this internal model, but omit details that are not required for the voxelization. Textiles are modelled in a unit cell, the smallest parallelepiped of the fabric that uniquely defines the entire fabric. That is, by periodically repeating the unit cell in space the entire fabric can be reconstructed. Two structures are modelled for NCFs, namely the stitched mats and the stitching yarns. Due to the definition of the unit cell being periodical in space, each mat spans the entire unit cell in x- and y-direction. They can be structurally modelled by the z-coordinate of their centre and their thickness in that direction. The mats contain either stitching holes or channels which also need to be considered. To take stitching holes into account, it suffices to note that they are always periodical and identical in shape. They can be modelled by retaining the periodicity in x- and y-direction and their initial width. Channels can be modelled in a similar manner.

Yarns, however, can take various more complex shapes throughout the entire unit cell. In the model, a linear approximation of these shapes is employed: The yarn is divided into several smaller yarn sections by taking cross sections over the entire length of the yarn. The yarn sections are then linear interpolations of those cross sections. The cross sections are therefore chosen in such a way that their resulting linear approximations remain accurate over the entire yarn. For the interpolation of these cross sections, an additional axis is defined, called the s-axis. The s-axis is the 3D-curve that connects the centres of the entire yarn. This axis can then be used to interpolate between cross sections and construct the yarn sections (as illustrated in Fig. 1). Several values are retained for each cross section which allow it to be reconstructed, namely its location, tangent, shape and dimensions.

To indicate the location, the 3D-coordinates of the centre and its position on the s-axis (denoted by an S-coordinate, or S-value) are stored. The tangent of the s-axis at the centre of each cross section is also stored, which can be interpreted as a vector pointing in the direction of the yarn flow. Using this tangent, the S-value of any point in space, given two cross sections, can be defined as its projection upon the s-axis between those two cross sections. The two cross sections are important in this definition, as a yarn can flow throughout the entire fabric and therefore multiple S-values might exist for a single point, but not more than one when given two cross sections. The shape of a yarn is either elliptic, lenticular or rectangular. Each of these shapes can be described using two vectors perpendicular to the tangent, indicating the two major axis of the cross section. Their lengths of these vectors are also stored to indicate the dimensions.

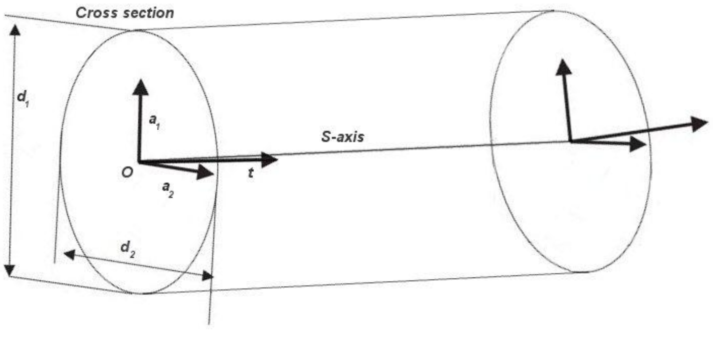

Fig. 1: Model of a yarn section [3].

FAST GENERATION OF A VOXEL DESCRIPTION

A voxel description is necessary to study the flow and permeability of a given fabric with FlowTex. This description (or voxelization) is the discretization of the geometry into a grid of points in the 3D-space, so-called voxels. Each point contains the fabric's local properties. The old algorithm used a top-down approach. This approach would inspect the fabric for each voxel in the grid to determine whether or not it is located inside a yarn of the fabric. This was accomplished by investigating all yarns and mats and determining possible membership of the voxel. Even though this seems a natural way to accomplish the task, a lot of redundant work was done. To be more precise, voxels that were located in the free space between the yarns, would investigate all yarns in vain. A single voxel would also often query many yarns before finding the correct one. This takes an unnecessarily large amount of time as it scaled particularly poor with an increasing number of yarns.

The new algorithm also had to be robust against the arbitrary complexity and structure of fabrics. Ideally, the algorithm's scaling is independent of the fabric's complexity and only dependent on the amount of voxels that need to be modelled. For this reason, the new algorithm for voxel description generation employs a technique called flooding (also called flood fill or tint fill [6]) which assures that the generation is independent of the above factors, such as an increasing number of yarns.

In general, the flooding algorithm starts by queuing a single voxel known to be part of the geometric shape as the starting point of the iterative flood that will follow. The technique will then iteratively investigate a queued voxel and determine whether it is part of the geometry, based on the local properties of the object. If this is the case, it adds all neighbouring voxels to the queue as well (the flood); if it is not the case, it simply ignores the voxel and removes it from the queue. Flooding continues as such until all voxels in the queue have been investigated. By the above proceeding, the queue now contains all the voxels part of the geometry and not a single more. A significant advantage of this technique is that by remembering which voxels have already been checked, the algorithm not only assures its termination but also avoids revisiting the same voxel and thereby doing redundant work. It is clear that as long as it is easy to determine whether a voxel is contained inside the local shape of the geometry, this technique is both efficient and complete. For the local shapes of the yarn, this can indeed be expressed rather trivial and lightweight.

This technique is a straightforward solution to voxelizing large geometric shapes that are quite complex as a whole but have clearly defined local shapes as borders. In the case of fabrics, a yarn is considered as a sequence of ellipses, lenses or rectangles of varying width and orientation (the aforementioned cross sections). This yarn is quite often complex as a whole but has a very specific definition at a local level, namely an ellipse, lens or rectangle. Flooding is therefore especially suited for textile models.

The following algorithm is employed to flood the yarns of a fabric:

```
For each yarn in fabric do
  Create voxel queue containing starting voxel
  Create index queue containing the corresponding yarn section index
  While queue is not empty do
        Pop voxel and index from queues
        Determine S-value of voxel by trigonometry
        If s < smallest s then
              Push voxel back on voxel queue
              Push index-1 on index queue unless index = 0
```

```
(10)        Else if s > largest s then
(11)              Push voxel back on voxel queue
(12)              Push index+1 on index queue unless index = N
(13)        Else
(14)              If voxel is within local yarn-dimensions then
(15)                    Store data in voxel
(16)                    Push neighbours of voxel on queues
```

As is quite clear from the presented algorithm, some deviations were made from standard flooding to accommodate some domain-specific elements of flooding a yarn.

Queuing as in (2) and (3)

Two queues are used: one to store the voxels and one to keep track of the index of the yarn section that the voxel is most likely in. While standard flooding is deterministic in its decision whether a voxel is either within the shape or not, this is not as trivial for yarns due to the definition of a yarn section. That is, a yarn exists of several discrete yarn sections and therefore an easy global membership check does not exist for a yarn. An exact calculation of which yarn section a voxel belongs to is also a hard problem. This is however unnecessary because the algorithm can take advantage of the locality of each iteration. If a voxel is added to the queue, it can be expected to lie within the same yarn section as the neighbour that spawned it. For this reason, an additional queue is used to store the index of the expected yarn section.

Determining the correct section index in (7), (10) and (13)

The above expectation is not always correct. If a voxel lies at the other side of the cross section (the border of two yarn sections), its neighbour will give it the wrong index. However, in that case it will become clear from the calculations made in (6) that the voxel is indeed not part of the yarn section because its S-value is outside the interval defined by that yarn section. The voxel is then added to the queue again with the rectified index. This means that each voxel can be investigated twice (instead of only once) during the flood, but due to the lightweight calculations and the rarity of such voxels near the borders of yarn sections, this has only a negligible effect.

Queuing continued

There is another reason why queues are employed. A naive implementation of flooding has a voxel call the *flood()*-method on each neighbouring voxel. The main reason to use this naive approach is that it requires less memory compared to storing all queued neighbours. However, especially for large discretizations that contain a lot of voxels, this means a lot of calls will be put on the stack. As the stack is significantly smaller than the working memory, this quickly poses a worse problem than a minor memory and performance disadvantage. For this reason, a queue is mandatory to tackle large problems.

Also note that using naive calls automatically results in a depth-first algorithm. Using a queue leaves the freedom to choose between depth-first and breadth-first.

Determining the S-value (6)

The old approach of voxelization relied on iterative dichotomy (also called bisection) to determine the S-value for a voxel. Of course, there were two major downsides concerning such a choice: it was iterative and therefore inherently slow, and it was only an approximation. An alternative method is now employed using only simple trigonometry to avoid both of these downsides. The rationale will be given before presenting the actual algorithm:

The goal remains to find the S-value of the voxel. This S-value is defined as the coordinate of the voxel on the yarn-axis, which is found by projecting the voxel coordinate $\overrightarrow{voxel}$ perpendicular onto that yarn-axis. The tangent $\vec{T}$ to the yarn-axis can also be linearly interpolated between two cross sections. If an auxiliary vector is defined which has the same origin $\vec{\mathrm{O}}$ as the tangent, reaches to the given voxel, and is also perpendicular to the tangent, then the following expression is derived:

$$(\overrightarrow{voxel} - \vec{O}) \times \vec{T} = 0$$

This expression is of notable interest as both $\vec{\mathrm{O}}$ and $\vec{T}$ are linearly dependent of the sought S-value for this given voxel because of the above definitions. From this expression and the properties of the dot product, a quadratic equation for the required S-value is obtained. Moreover, the following observation often simplifies the equation: the second order term of the equation is close to zero. This is the direct result of the fact that the second order term most closely resembles the dot product of the differences between the $\vec{\mathrm{O}}$ and $\vec{T}$ of the two cross sections. These differences are nearly perpendicular and the dot product close to zero because the cross sections to model a yarn are chosen to keep the error of the linear interpolation small. The better the interpolation is, the more perpendicular these differences are.

It should be clear that this approach is constant in time if the cross sections are known. Moreover, it can approximate the S-value of voxels that are not between the given cross sections accurately, a property which was already used to determine the correct section index.

Complexity

The complexity of the algorithm can be determined as O(#Voxels). During a single flood each voxel is at most investigated twice due to condition *(7)* and *(10)*: A voxel can be part of maximally two yarns, so it can only be called four times. This result is independent of increasingly difficult fabrics with more yarns and their vastly more complex paths throughout the fabric. This is of particular importance for non-crimp fabrics, where the stitching yarn follows a complex path.

Complexity of the whole algorithm

As stated above, including the revised mat algorithm will not change the complexity as yarns and mats will only check very few colliding voxels on their borders and both only scale with the number of voxels. Therefore the complexity remains O(#Voxels).

VALIDATION

Natte

To validate the new algorithm, the Natte 2115 fabric will be used. It is a basket woven fabric that is engineered specifically for permeability validations because of its useful properties [2]. This validation is necessary because the voxelization results differ slightly between the old and new version, mainly due to the different approach in calculating the S-value. This should however not influence the accuracy of the permeability calculations. Fig. 2 shows the computed permeability values of the Natte textile, as function of the number of discretisation points. Only for a unreal coarse discretisation, the computed permeability values differ significantly. Table 1 illustrates the difference in runtime for the Natte fabric. The discretizations are the same as those in Fig. 2 and the given timings are the average runtimes over 100 runs.

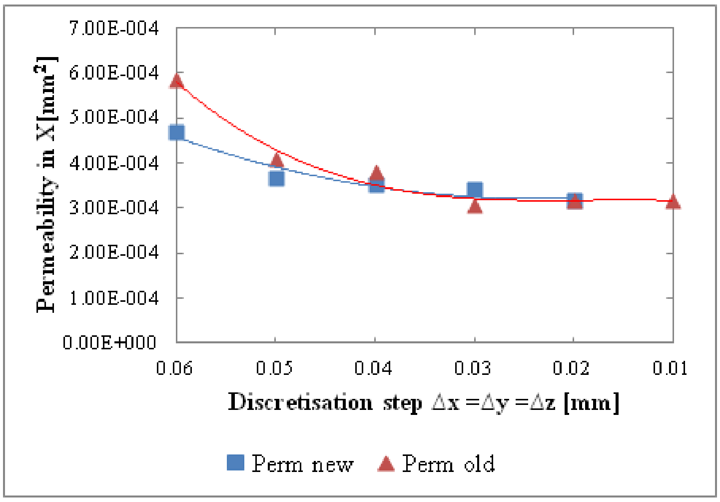

Fig. 2: Computed permeability of the Natte textile, as a function of voxel number, and for voxel files created with the new and old method.

Table 1: Computation times of the voxel description of the Natte 2115

dx = dy = dz (mm)	0.06	0.05	0.04	0.03	0.02
Time new (s)	0.07	0.36	0.51	1.17	3.16
Time old (s)	0.69	1.38	2.89	5.58	20.31

Non-Crimp Fabric

For a NCF example, we create a stitched mat model of 52.6% fiber volume fraction (Vf) with a unit cell size of 3.250x5.167x0.580(mm) (Fig. 3).

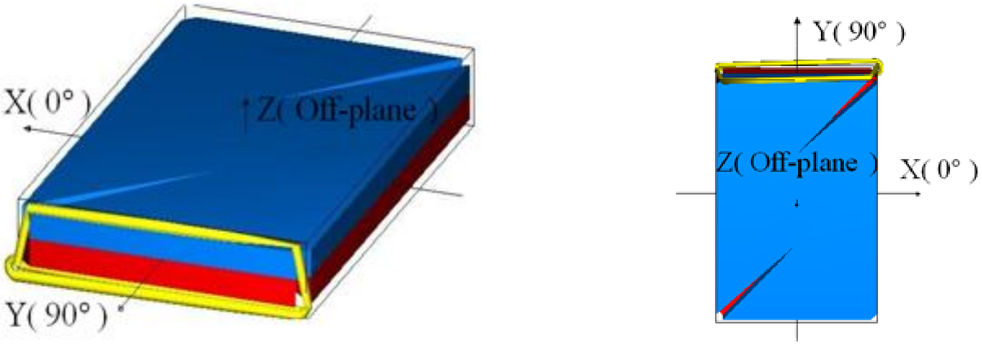

a) Full view

b) Top view

Fig. 3: Stitched mat model created in WiseTex

The model refers to a Saertex bi-diagonal NCF with fiber orientation +45°/-45°, aerial weight of 540g/m^2 and franse stitch. More details of the fabric can be found in [1]. Most of the parameters were taken from the data sheet. The crack width of fiber bundle was calibrated by microscope and the Vf was determined by the acid digestion method. Finally the computed areal density was crosschecked with data sheet to verify the physical correctness of our model. We use the finite difference Stokes solver with a 1E-04 precision.

In Fig. 4, we can see that with a fine discretization step of $\Delta x = \Delta y = \Delta z = 0.0365$mm, a converged numerical result is reached. Fig. 5 shows that for such a mesh the time for dicretization and the permeability computation are 39s and 102s respectively. The performance comparison of old and new voxelizer is unavailable, as for the old version it was unfeasible to generate such a voxel file. Note that the time for dicretization and the permeability computation of the new technique increases linearly with the number of voxels. In general, the voxelization and computational time required is within a reasonable range. Moreover, the new voxelizer produces voxel files with a stable estimated Vf regardless of variant voxel numbers, which is an advantage compared with the last version.

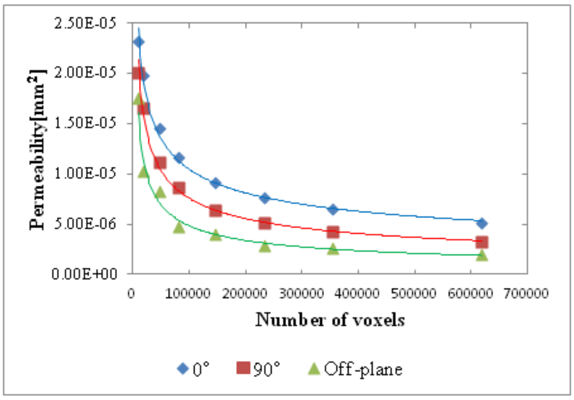

Fig. 4: Computed permeability as a function of the number of voxels.

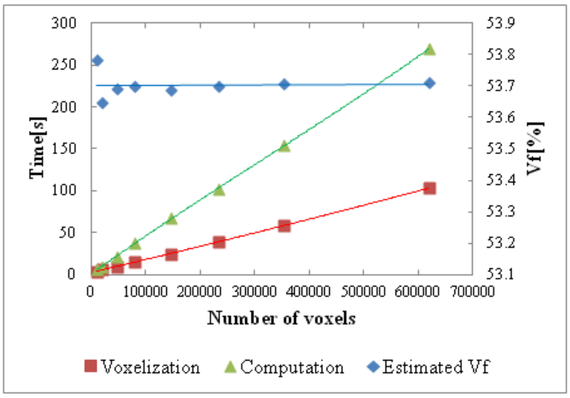

Fig. 5: The fibre volume fraction (Vf), voxelization computation time and computational time of the permeability as function of the number of voxels.

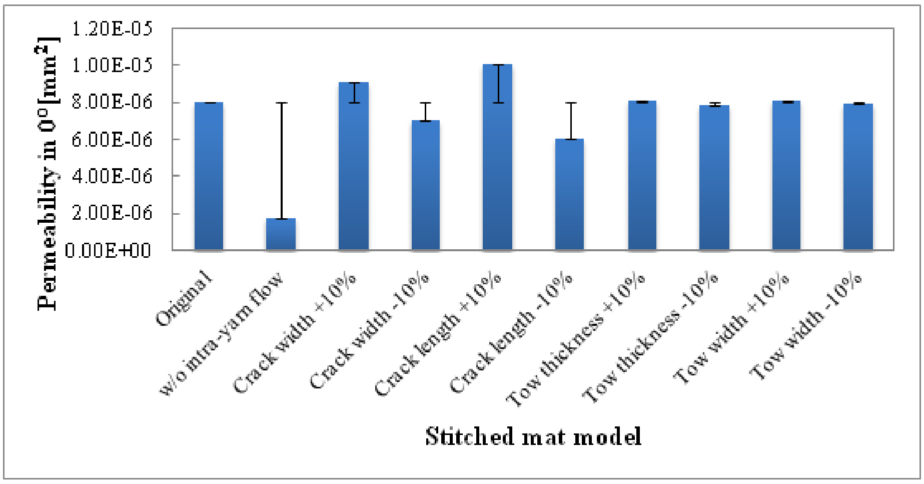

Fig. 6: Parameter study for crucial parameters defined in stitched mat model.

A parametric study has been performed on the NCF model, to estimate the influence of different properties on the permeability. The results are presented in Fig. 6, where the NCF model described above is called *original*. From Fig. 6 it is clear that the intra-yarn flow has the largest influence: The computed permeability is 78% lower when intra-yarn flow is neglected. A 10% crack width and length deviation leads to 12% and 25% vibration of computed permeability respectively. The computed permeability in 90° and off-plane direction has a similar behaviour as that in 0° direction and is omitted here.

CONCLUSIONS

In this paper, we presented a new algorithm to create a voxel description of textile models. It is shown that by using an adapted flooding technique, voxel files can be created very efficiently. The new technique is applied to create accurate voxel descriptions of non-crimp fabrics, which was previously not feasible. The results of a permeability study and a parametric study are also presented.

ACKNOWLEDGMENTS: This research is sponsored by the INFUCOMP FP7 project.

REFERENCES

1. Hahn C, Binetruy C, Hinterhölzl R, Drechsler K (2012), ‘A Numerical Method of Permeability Determination for RTM Process Simulation’, *Proc. of the 11th International Conference on Flow Processing in Composite Materials (FPCM-11),* to be published.

2. Hoes K, ‘Development of a new sensor-based setup for experimental permeability identification of fibrous media’, *PhD thesis,* Vrije Universiteit, Brussel, 2003.

3. Lomov SV, Mikolanda T, Kosek M and Verpoest I (2006), ‘Model of internal geometry of textile fabrics: Data structure and virtual reality implementation’, *Journal of the textile institute,* 98(1), 1-13.

4. Lomov SV, Belov EB, Bischoff T, Ghosh SB, Truong Chi T and Verpoest I (2002), ‘Carbon composites based on multiaxial multiply stitched preforms. Part 1: Geometry of the preform’, *Composites part A,* 33(9), 1171-1183.

5. Lomov SV (2011), ‘Understanding and modelling the effects of stitching on the geometry of non-crimp fabrics’, in: Lomov, S.V. (Ed.), *Non-crimp fabric composites: manufacturing, properties and applications*, Woodhead Publishing, Oxford, 84-102.

6. Smith AR (1979), Tint Fill, *SIGGRAPH 79 Conference Proceedings*, 276-282.

7. Verleye B, Lomov S, Long A, Verpoest I and Roose D (2010), ‘Permeability prediction for the meso-macro coupling in the simulation of the impregnation stage of Resin Transfer Moulding’, *Composites A, Applied Science and Manufacturing*, 41(1),29-35.

8. Verleye B, Croce R, Griebel M, Klitz M, Lomov S, Morren G, Sol H, Verpoest I and Roose D (2008) ‘Permeability of textile reinforcements: simulation, influence of shear, validation’, *Composites Science and Technology,* 68(13),2804-2810.

9. Verpoest I and Lomov SV (2005), ‘Virtual textile composites software Wisetex: integration with micro-mechanical, permeability and structural analysis’, *Composites Science and Technology*, 65(15-16),2563–2574.

ANALYTIC METHOD TO ESTIMATE MULTIPLE PERMEABILITY COMPONENTS FROM A SINGLE RECTILINEAR EXPERIMENT IN LIQUID MOLDING PROCESSES

J. Lugo, S.G. Advani and P. Simacek

Department of Mechanical Engineering and Center for Composite Materials
University of Delaware, Newark, DE 19711, USA

ABSTRACT: One of the important issues in Liquid Composite Molding modeling and simulation is the evaluation of permeability of individual system components such as flow enhancement media (distribution media) and multiple preform layups. Extensive work has been devoted to various methods of this evaluation. Majority of the work has focused on characterization of single type of fabric characterization. The experiment if conducted in radial set up can characterize permeability usually in the in-plane directions, under different compaction loads and evaluate its statistical variation. There is, however, a need for a simple experimental setup to provide distribution media permeability along with the permeability of fabric underneath it in the in-plane and through the thickness direction from a single experiment, albeit lower accuracy. In addition to providing an input to the model, it is an easy way to check new batch of materials, since the flow related properties are rarely checked by the manufacturer. Also, for realistic manufacturing, the permeability values depend on the combined effect of individual components. The number and orientation of preform plies may also influence the permeability values. Bag and peel ply materials, and even the de-bulking process, may interfere with flow enhancement media and this may require one to measure an effective permeability for combination of these materials. This paper will present a new approach for determining in plane permeability of the preform , the distribution media and the effective permeability of preform and the distribution in the flow direction and the transverse permeability in the through thickness direction from a single rectilinear experiment, which models the VARTM infusion. The approach is based on tracking the resin flow-front during linear infusion along the top and the bottom surface over a sample representing several material layups (a segment of which includes the flow enhancement media). Analytic solution of flow progression is used to derive estimates for permeability of all components/layups. The solution, the error due to the assumptions and approximations made and its limits of applicability are presented. Numerical techniques using flow simulation can be further utilized to improve the permeability estimate.

INTRODUCTION

The determination of permeability of various preforms and distribution media systems is important for infusion design, be it by well-established LCM process modeling [1-7] or by some simple formulas [8]. The complication arises from the effects of layering on the determination of the permeability value. This makes the utilization of individual component properties to “assemble” the effective property set inaccurate. Thus, it may be necessary to measure the effective preform properties directly, in a particular layup. The properties of distribution media and other discardable plies then should be determined along with the particular preform and the bagging system.

This issue poses a few challenges. First, one needs a fast way to experimentally estimate the "system" (as opposed to "component") properties and compare them with those obtained by some combination of component properties. Should the numbers be close, there is no need to do more characterization and combined values can be used. The difference may provide some error estimate and hence bounds on the results obtained from numerical simulations in which these properties are provided as input.

Second, it would be beneficial to measure the "system" properties rapidly and efficiently, even at a cost of lower accuracy. For usual characterization, at least three values are to be determined: two components of preform permeability (in plane in the direction of flow and through thickness) and one of distribution media permeability also in the infusion direction. Note that the respective preform permeability is assumed to be one value in which the internal preform variations are averaged. This should be accomplished within a single experiment. Note that if the part is more complex, additional experiment would need to be repeated in the other principal direction as well.

Despite the fact that the flow patterns during such experiment will be more complex than usual one- or two-dimensional flow data, the experimental data should be converted into the approximate permeability component using guidance from analytic model which is based on certain assumptions and approximations and will introduce substantial error under conditions when the assumptions are no longer valid. This error should be bound by some estimate. If its magnitude is admissible, there is no need for additional analysis. If higher accuracy is needed, the numerical iterations can be employed just as in the case of multi-dimensional flow in a single material [9].

In this paper we will first outline the experimental layout and the analytic solution used to extract the permeability values from the flow front location data recorded from the experiment. We will then analyze the error introduced due to the assumptions in the analytic solution by comparing the analytical results with a set of numerically performed experiments with known permeability values in order to establish the limitations of its applicability.

EXPERIMENTAL LAYUP

The experiment represents typical VARTM (VIP) infusion, with one modification that the distribution media spans only a part of the total preform length (L_{DM}) and the reminder of the preform (of length L_{NDM}) length is infused without the distribution media. This results in two segments with different flow characteristics. The relation of the lengths of these segments, preform thickness h and permeability ratios necessary for reasonable results will be discussed later. The distribution media thickness is h_{DM}. The layup is infused from left to right and the flow-front position at top and bottom (T and B) is recorded hence the experiment needs to be carried on a transparent tool surface such as plexiglass. After a transition zone, the T and B value in the second segment should be the same as there is no distribution media in the second segment.

The flow advancement within the first segment serves to evaluate the "effective" permeability of preform/distribution media/peel-ply combination. The flow advancement in the second segment evaluates the in-plane permeability of the preform only. After that is accomplished, the distribution media permeability value can be isolated from the effective permeability and, finally, the transverse preform permeability can be evaluated from the difference between the top and the bottom flow-front positions recorded during the flow in the first segment.

The layout, relevant dimensions and coordinate system are depicted in Fig. 1.

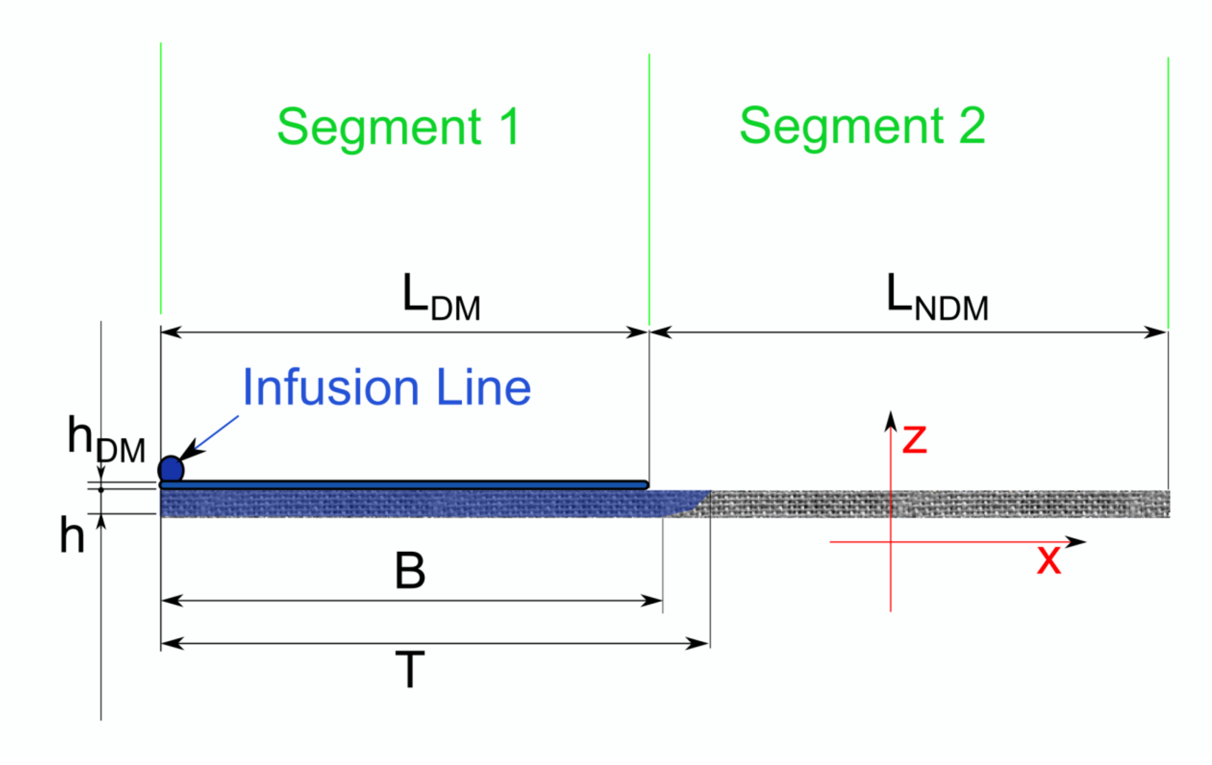

Fig. 1: Schematic of the experiment layup. Infusion Line is placed on top of the distribution media (DM)

PERMEABILITY EVALUATION FROM EXPERIMENTAL DATA

In-plane permeability in the flow direction is evaluated in both segments: In the first segment in which it represents the effective permeability of the preform covered with distribution media whereas in the second segment it represents the permeability of the preform only. The averaged progress of the position of the top (T) and bottom (B) flow front allows one to calculate the “effective” permeability value. In the second segment, the in-plane permeability value of the preform in the flow direction is determined. It is consequently used to determine the distribution media permeability from the first segment. Finally, the difference between the top and the bottom flow-front in the first segment is used to estimate the through-the thickness preform permeability.

Determination of in-plane effective permeability of preform with distribution media

For multi-layered system with i layers, the effective values for thickness h_{eff}, porosity ϕ_{eff} and in-plane permeability K_{eff} of layered system is usually evaluated using rule of mixtures as follows:

$$h_{eff} = \sum_i h_i$$
$$\phi_{eff} = \frac{\sum_i \phi_i . h_i}{h_{eff}} \tag{1}$$
$$K_{eff} = \frac{\sum_i K_i . h_i}{h_{eff}}$$

Thus, K_{eff} is the weighted average of the individual component permeabilities in the lay-up. The validity of this expression is generally assumed to be limited to similar values, but it should be reasonable as long as the three-dimensional effects are limited – i.e., lead length are small compared to overall dimensions (difference between T and B positions is called lead length). The error in applying this relation to the system of preform and distribution media layers will be examined later.

In our case, in the segment 1 with the distribution media we will assume two layers: preform and distribution media. Note that the preform value may be effective property as the preform may be non-homogenous through the thickness. Hence Eqn. (1) can be written as:

$$h_{eff} = h_{DM} + h$$
$$\phi_{eff} = \frac{\phi_{DM} . h_{DM} + \phi . h}{h_{eff}} \tag{2}$$
$$K_{eff} = \frac{K_{DM} . h_{DM} + K_{xx} . h}{h_{eff}}$$

The first two values should be know from preform and distribution media data, the last one is obtained from measurements of T and B positions in the first segment from the experiment. In the first segment, the experimental infusion is basically a one-dimensional (linear) infusion experiment [10] and can be processed accordingly. The distance travelled by the flow front at each recorded time along the top and bottom is averaged, and the slope of the line that plots the square of the averaged flow front position L against time t is used to determine the effective permeability value in the flow direction from the following relation

$$L^2(t) = \left(\frac{T(t) + B(t)}{2} \right)^2 = \frac{2 . K_{eff} \cdot p_{\text{in}}}{\eta . \phi_{eff}} . t \tag{3}$$

where t is the time. With K_{eff} extracted from Eqn. (3), one can determine K_{DM} from Eqn. (2) once we find K_{xx} (preform permeability) from flow front movement in the second segment as a function of time.

Determination of in-plane preform permeability

Once the flow is in the second segment, the top and bottom positions of the flow front eventually equalize, the experiment simplifies to a linear one dimensional flow experiment. Nevertheless, as the resin has to flow first through the first segment, the effective permeability necessitates some modifications of the *L*-*t* relation in Eqn. (3).

Under the quasi-steady solution approach, the instantaneous governing equations for 1D flow in *x* direction through a thin plate of variable, but pressure independent permeability K_{xx} and thickness *h* according to Darcy's Law is:

$$\langle v \rangle = -\frac{K_{xx}(x)}{\eta} \cdot \frac{dp}{dx} \tag{4}$$

and a simple, one-dimensional mass conservation equation is

$$\langle v \rangle . h(x) = Q = Const. \tag{5}$$

Combining them, we obtain

$$\frac{dp}{dx} = -Q . \frac{\eta}{K_{xx}(x) . h(x)} \tag{6}$$

Following pressure from inlet (p_{in}) to flow-front position (*L*), this equation can be integrated over *x* going from 0 to the flow-front position *L*:

$$p_{\text{in}} = Q . \eta . \int_0^L \frac{dx}{K_{xx}(x) . h(x)} \tag{7}$$

This provides relation for the flow rate *Q* as

$$Q = \frac{p_{\text{in}}}{\eta} \cdot \frac{1}{\int_0^L \frac{dx}{K_{xx}(x) . h(x)}} \tag{8}$$

and, finally, for the progress of the flow front (*dL/dt*):

$$\frac{dL}{dt} = \dot{L} = \frac{p_{\text{in}}}{\eta . h(L) . \; \phi(L)} \cdot \frac{1}{\int_0^L \frac{dx}{K_{xx}(x) . h(x)}} \tag{9}$$

This equation can be integrated in all generality (including transient inlet pressure) with time to obtain the transient description of *L(t)*:

$$\int_0^L \left(h(\psi).\ \phi(\psi).\int_0^\psi \frac{dx}{K_{xx}(x).h(x)} \right) d\psi \;=\; \int_0^t \left(\frac{p_{\text{in}}(\chi)}{\eta} \right) d\chi \tag{10}$$

The solution may be obtained for continuous change in thickness and permeability – which is not too practical in our case – as well as for a step change(s) which has a number of applications in production and experimental characterization. The current experimental technique with DM and no DM regions falls under that category.

In the current case, we have to obtain the relation for two domains and constant infusion pressure: for flow front distance, x less than L_{DM} the thickness is heff, porosity is ϕ_{eff} and permeability is K_{eff}. For r $x > L_{DM}$ the thickness due to the absence of DM is h, porosity is ϕ and permeability of the preform is K_{xx}. In the first segment, integrating time and distance from 0, the governing equation simplifies to well known:

$$L^2(t) \;=\; \frac{2.K_{eff}.p_{\text{in}}}{\eta.\ \phi_{eff}}.t \tag{11}$$

This equation provides K_{eff} as a slope between t and L^2 and is well suitable for acquiring this value from experimental data, as stated in the previous section.

In the second segment we integrate from L_{DM} and t_{DM} (time to reach L_{DM}) as follows:

$$\int_{L_{DM}}^{L} \left(h.\phi.\left(\frac{L_{DM}}{K_{eff}.h_{eff}} + \frac{\psi}{K_{xx}.h} \right) \right) d\psi \;=\; \int_{t_{DM}}^{t} \left(\frac{p_{\text{in}}}{\eta} \right) d\chi \tag{12}$$

which results in a closed form solution as

$$\left(\frac{L_{DM}.K_x}{K_{eff}.h_{eff}}.(L - L_{DM}) + \frac{1}{2.h}\left(L^2 - L_{DM}{}^2\right) \right) \;=\; \left(\frac{p_{\text{in}}.K_{xx}}{\eta.h.\ \phi} \right).(t - t_{DM}) \tag{13}$$

By re-arranging it as shown below, we obtain K_{xx} as the slope between two experimentally observed functions of L and t:

$$\frac{1}{2.h}\left(L^2 - L_{DM}{}^2\right) \;=\; K_{xx.}\left(\left(\frac{p_{\text{in}}}{\eta.h.\phi} \right).(t - t_{DM}) \;-\; \frac{L_{DM}}{K_{eff}.h_{eff}}.(L - L_{DM}) \right) \tag{14}$$

and thus, after obtaining K_{eff} from the first segment of the flow, K_{xx} can be obtained from the recorded time-position data from the second segment with some confidence. Once K_{eff} and K_{xx} are known, one can determine K_{DM} from Eqn. (2).

Approximate solution for flow in the lead-length region and determination of through the thickness permeability (K_{zz})

Top and bottom positions of the flow-front in the first segment are denoted as T and B, respectively. It is assumed that their difference eventually reaches a steady state and settles to a constant value [8]. The flow in the preform between T and B is assumed to be one dimensional from top to bottom.

If one can approximate the resin pressure distribution in the distribution media between these points, one can compute the penetration of resin through the preform (which must reach the bottom in the available time) to evaluate the unknown K_{zz}.

$$\int_0^h (\psi) d\psi = \frac{K_{zz}}{\eta . \phi} . \int_0^{t_F} (p(\chi)) d\chi \qquad (15)$$

Here, t_F represents the time needed for the flow to reach the bottom and $p(\chi)$ is the transient pressure distribution between T and B. The pressure distribution and time should scale inversely to each other [8].

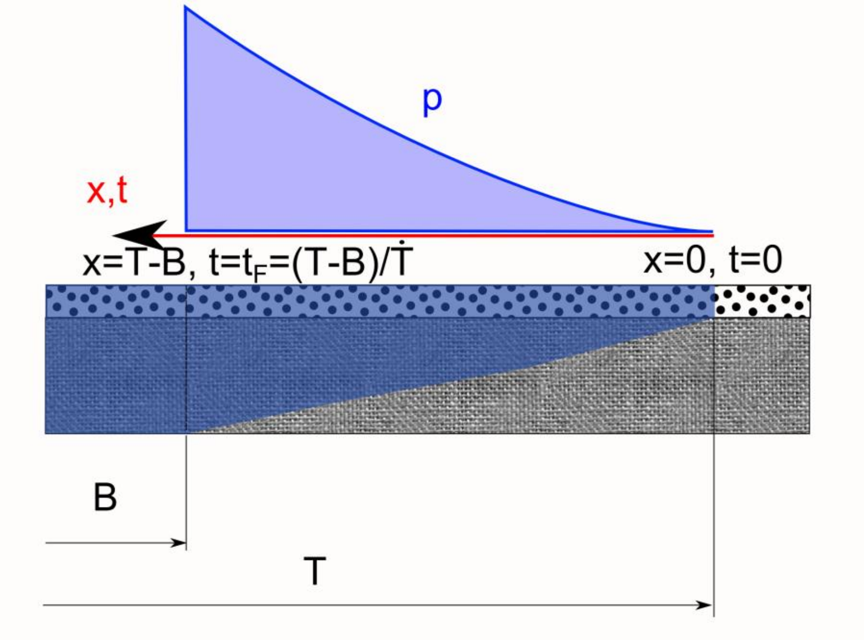

Fig. 2: Assumed pressure distribution in the resin over the lead-length (T-B).

The task is thus to find a suitable approximate pressure distribution over the lead-length segment. This is shown in Fig. 2, together with the local coordinate system in spatial/temporal coordinates. The mapping between time and position is assumed to be linear, i.e., the flow-front speed $\dot{T} = \dot{B}$ is considered constant in the lead-length region and the mapping from x to t is simply $t = x / \dot{T}$. The linear distribution of pressure along distribution media comes to mind as a first approximation. This approximation was tested and failed to yield reasonable transverse permeability value. This is understandable, as it violates the basic continuity principles as the flow through the distribution media never changes. Thus, one needs to build a better approximation.

Three conditions for the pressure field would be:

1. Pressure at the flow-front (t=0) is zero.

2. The pressure gradient at the flow-front delivers resin to advance the flow in the distribution media through the distribution media.
3. The pressure gradient at $t=t_F$ delivers resin to advance flow in the distribution media and the preform through the distribution media only. This condition is approximate.

These three conditions can be formulated (in coordinate system of Figure 2) as follows

$$\begin{aligned} p(0) &= 0 \\ \frac{dp(0)}{dx} &= \dot{T}.\frac{\eta.\ \phi_{DM}}{K_{DM}} \\ \frac{dp(T-B)}{dx} &= \dot{T}.\frac{\eta}{K_{DM}}.\left(\phi_{DM}+\frac{h.\phi}{h_{DM}}\right) \end{aligned} \tag{16}$$

These conditions can be satisfied by a simple parabolic function of x (resp. t):

$$p(t) = \frac{\eta.(\dot{T})^2}{K_{DM}}.\left(\phi_{DM}.t+\frac{h}{2.h_{DM}}.\ \phi.\dot{T}.\frac{t^2}{T-B}\right) \tag{17}$$

Substituting (17) into (15) and integrating, we obtain:

$$h^2 = \frac{K_{zz}}{K_{DM}}.\left(\frac{\phi_{DM}}{\phi}.(T-B)^2 + \frac{h}{3.h_{DM}}.(T-B)^2\right) \tag{18}$$

which can be re-arranged as follows

$$\frac{K_{zz}}{K_{DM}} = \frac{h^2}{(T-B)^2}.\frac{\phi}{\phi_{DM}}.\frac{1}{1+\frac{h.\phi}{3.h_{DM}.\ \phi_{DM}}} \tag{19}$$

In the Eqn. (16) and (17), a dot with respect to the variable denotes the time derivative. As the lead-length (T-B) will converge to a constant value, so will the estimate of through-the thickness permeability provided by Eqn. (19).

Procedure to evaluate preform and distribution media permeability values

The following approach is used to estimate the transverse permeability of the preform and the distribution media permeability

1. Measure length, thickness and porosity values of the preform and the distribution media to be used.
2. Establish time t_{DM} when flow reaches the end of the distribution media on top and when it arrives at the same location (L_{DM} t_l) at the bottom.
3. Establish effective permeability for distribution media/preform from Eqn. (3) using the average of the top and bottom positions to obtain the average flow-front position L.
4. Establish in-plane preform permeability value from plotting the Eqn. (14) for times above t_1. Evaluate distribution media permeability from Eqn.(2). Evaluate through the thickness preform permeability from Eqn. (19).

THE PERMEABILITY EVALUATION ERROR

The approach introduced above is based on several assumptions which may become inaccurate for certain dimensional and material property relations. For, example, the application of Eqn. (2) to evaluate the effective permeability or several assumptions concerning the flow-front in the lead-length area Eqn. (15) may have only limited applicability. Thus, the next challenge to overcome is to (i) identify the independent relations that may influence the accuracy of the assumptions and (ii) map the accuracy of the above described routine for these parameters.

Non-dimensional parameters to evaluate error in permeability estimation

The flow in our system (Fig. 1) is relatively simple, and the non-dimensional numbers necessary to map this flow should serve very well as our independent parameters. The flow in the preform in the first segment is governed by a simple two-dimensional equation

$$K_{xx} \frac{\partial^2 p}{\partial x^2} + K_{zz} \frac{\partial^2 p}{\partial z^2} = 0 \tag{20}$$

The flow in distribution media can be condensed into a rather complex boundary condition

$$h_{DM} . K_{DM} . \frac{\partial^2 p}{\partial x^2} - K_{zz.} \frac{\partial p}{\partial z} = 0 \tag{21}$$

With straightforward non-dimensionalization of the involved parameters as

$$\tilde{x} = x / L_{DM} \quad \tilde{z} = z / h \quad \tilde{p} = p / p_{inlet} \tag{22}$$

both Eqns. (21) and (22) will yield two non-dimensional parameters:

$$\psi_1 = \frac{K_{zz}}{K_{xx}} . \left(\frac{L_{DM}}{h} \right)^2 \tag{23}$$

$$\psi_2 = \frac{K_{zz}}{K_{DM}} . \frac{(L_{DM})^2}{h . h_{DM}} \tag{24}$$

The flow in the second segment is governed only by Eqn. (20), which yields an additional non-dimensional parameter

$$\psi_3 = \frac{K_{zz}}{K_{xx}} . \left(\frac{L_{NDM}}{h} \right)^2 \tag{25}$$

the last dimensionless number in Eqn. (24) can be compared to the one in Eqn. (23) and replaced by a simpler similarity number

$$\psi_3' = \left(\frac{L_{NDM}}{L_{DM}}\right) \tag{26}$$

Thus, the accuracy of the described experimental evaluation will be examined in relation with these three non-dimensional parameters. It should be noted that the permeability ratios are needed for their evaluation. Thus, one needs to process the experimental data by a given algorithm before the accuracy of the algorithm can be established.

Limitations of the Analytic Model

To study the effects that the experimental layup and material properties have on the accuracy of the experimental evaluation, experiments were performed numerically, processed by the above methodology and the error was determined. The numerical analysis was performed using software known as Liquid Injection Molding Simulation (LIMS) [11]. LIMS User Interface is a graphical user interface tool that uses finite element analysis to simulate Resin Transfer Mold filling processes. The interface allows one to display fully customizable finite element meshes, modify relevant material properties and run the simulation directly. A benefit to using this interface is that it allows one to create 1D or 2D edge of plane coverings of the mesh to represent race-tracking channels or presence of the distribution media.

For this error analysis, a 2D rectangular mesh was defined with preset in-plane and through-thickness permeability, as well as a 1D element covering to represent the distribution media. Figs. 3(a) and (b) below show a sample mesh, before and after fill:

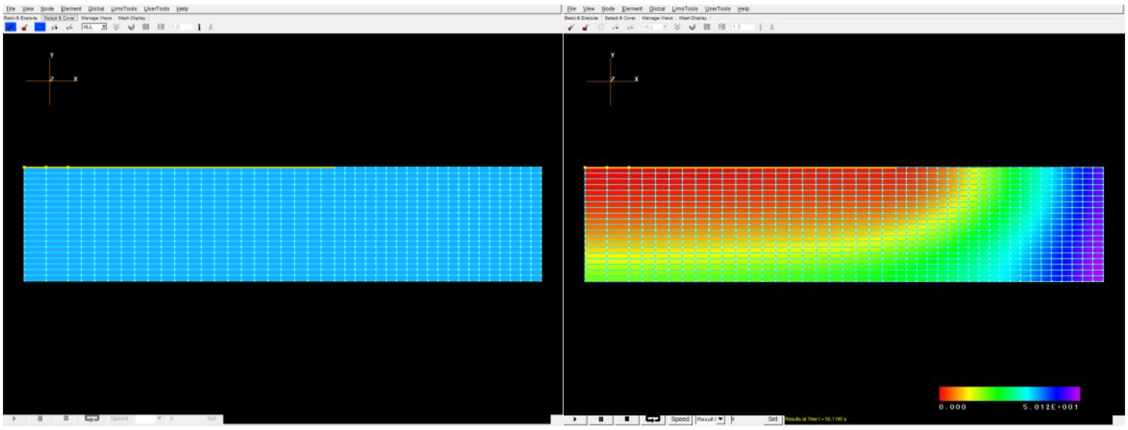

Fig. 3: (a) Sample mesh displayed in LIMS User Interface. (b) Completed simulation. Colors show arrival of resin at various location (Red= early times, Blue =last region to fill)

LIMS outputs a result file containing fill times at each node. This allows for simple calculation of the desired permeabilities using the procedure described in section 3.4) . Knowing the pre-established preform permeabilities, error analysis can be fully performed by comparing the expected values with values found using the experimental evaluation procedure outlined in section 3.4. For various values of the dimensionless numbers expressed by Eqns. (23) to (25), simulations were run keeping certain geometric and input permeability ratios constant, thus checking the validity of the experimental evaluations derived. It is important to find for what range of preform property values these equations are valid, and how much error one can expect if the parameters are not in this range.

Figs. 4(a) and (b) below show the error in the calculated in-plane permeability (K_{xx}) found as a relation to the non-dimensionalised numbers Ψ_1 and Ψ_2 expressed by Eqns (23) and (24). The plots show that for a wide range of values, the error one could expect in K_{xx} tends to be very low, with a highest error percentage of roughly 20% occurring when Ψ_1 and Ψ_2 are both very small. Following the trend shown in Figs. 4(a) and (b), it would be recommended to use larger ratios of Ψ_1 and Ψ_2 to obtain low error. This could be easily achieved by using sufficient sample length and only a moderate thickness. The physical explanation is rather obvious: for very thick samples the flow in the second zone does not really reach the uniform one-dimensional flow state before the sample ends.

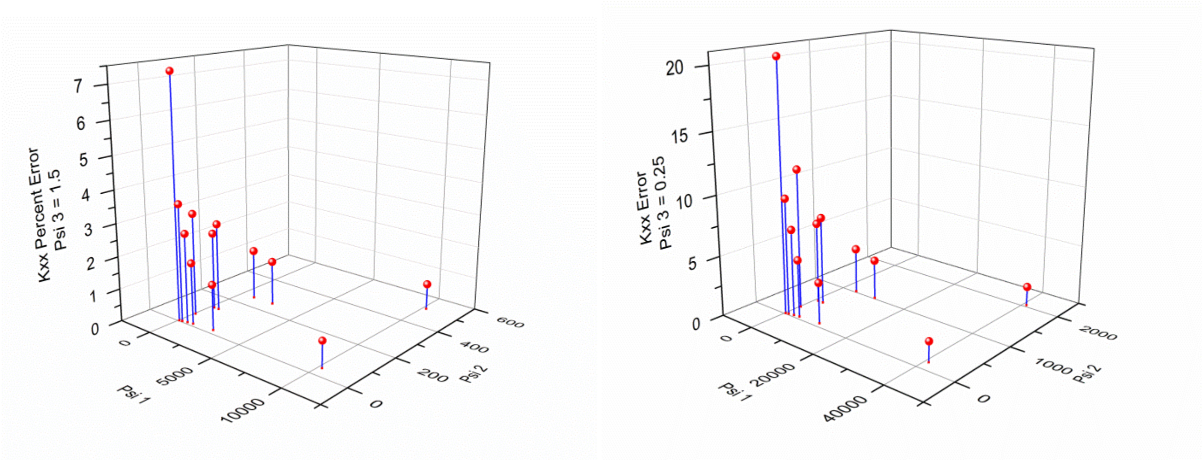

Fig. 4: Percent error found in K_{xx} as a relation to Ψ_1 and Ψ_2 for (a) $\Psi_3 = 1.5$ (b) $\Psi_3 = 0.25$

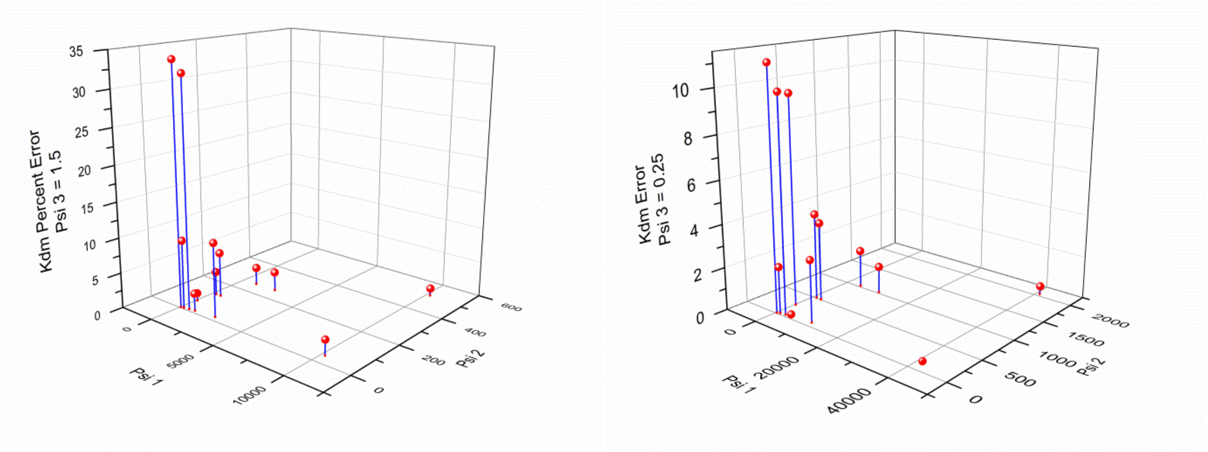

Fig 5: Percent error found in K_{DM} as a relation to Ψ_1 and Ψ_2, for (a) $\Psi_3 = 1.5$ and (b) $\Psi_3 = 0.25$

Generally one can also see that for larger Ψ_3, K_{xx} error decreases. This makes physical sense, since the experimental evaluation assumes that there is sufficient time/preform length for the top and bottom flow front to match up, and flow uniformly.

Similarly, plotting the error found in distribution permeability also displays a trend. For larger values of Ψ_3 (that is, L_{NDM} greater than L_{DM}), the error found in distribution media permeability is generally greater. This is evidently seen when comparing Figs. 5(a) to 5(b) below, where the Ψ_3 values are 1.5 and 0.25, respectively. Within the range of constant Ψ_3, one notes that error seems to increase with lower values of Ψ_1 and Ψ_2, which directly coincides with the results found from K_{xx} analysis. This is noteworthy since a range of values is desired to accommodate the experimental evaluations for all three permeability values. Physically, this is inevitable as the distribution media permeability is computed *using* the K_{xx}.

It is more challenging to define a set range of values that will definitely expect low error in through-thickness permeability (K_{zz}). Again, error percentages from the simulations are shown for varying Ψ_1 and Ψ_2 in Figs. 6(a) and (b):

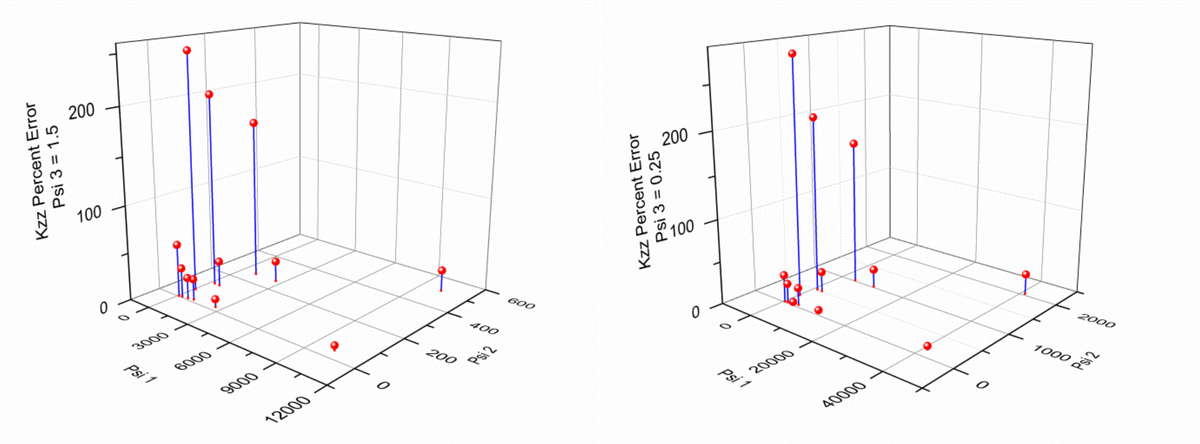

Fig. 6: Percent error found in K_{zz} as a function of $\Psi 1$ and $\Psi 2$, for (a) $\Psi 3 = 1.5$ and (b) $\Psi 3 = 0.25$

The one clear relation made from these results is that K_{zz} error is dramatically reduced for larger values of Ψ_1. Recalling equation (23), Ψ_1 depends on the ratio between K_{zz} to K_{xx} and L_{DM} to h. The latter is physically important, as without sufficient length, the constant lead-length flow assumed in the derivation of Eqn. (19) cannot hold. The physical interpretation suggests that the dependence on Ψ_2 should be similar. The data essentially supports this but more points are needed to establish this.

Although specific numerical ranges were not clearly established yet, the trends found from these results will be very helpful in future work to determine a set range for the assumptions made in the evaluations.

CONCLUSIONS

Based on a number of assumptions, equations were developed to estimate the system permeability and component permeability of fibrous preform and distribution media. The evaluation is based on simple flow front tracking and should provide equivalent values covering most of the phenomena that complicate the permeability evaluation from individual components data, such as non-homogenous layups, nesting, bag and peel ply penetration into the distribution media.

The error in the estimate depends on how well the assumptions hold. It was shown that the actual flow and consequently its deviations from simplified one should depend on limited number of non-dimensional parameters. Using comparison with the “numerical experiments” in which two-dimensional numerical flow modeling was used to provide "experimental" values, the error was established for a number of cases.

The experimental evaluations used to calculate in-plane permeability (K_{xx}) and distribution media permeability (K_{DM}) proved reliable, showing overall low error differences for a wide range of geometric and material property ratios. To ensure that the experiment falls into this range, one has to ensure the length aspect ratios are sufficiently large or small as the permeability values are unknown before the experiment. Essentially, sufficient length of both zones and moderate thickness is imperative.

Physical interpretation of these results is fairly important and in most cases straightforward. For example, in the case of the in-plane permeability, a larger Ψ3 yields better results since it allows time for the top and bottom flow front to flow uniformly. For the case of the through-thickness permeability, it was found that larger K_{zz}/K_{xx} values tend to show more accurate results. Physically, this may represent the fact that the K_{zz} evaluation assumes a fully-developed flow front, with a constant difference between top and bottom flow front location. Having this K_{zz}/K_{xx} ratio larger allows the resin to flow down and reach the bottom of the preform thickness sooner, thereby establishing a fully-developed flow earlier during the experiment. This would produce more accurate results.

Some effects are at this point still under investigation. For example, more data and analysis is needed to describe the error of the through-the-thickness permeability based on the non-dimensional parameters. Comparison with the actual experimental data is also pending.
It should be realized that the experimental error estimate as outlined herein depends on the experimental results. In that case, one may use the resulting estimates as starting values and iterate the recorded flow fronts against the numerical model to improve the values without additional experiments.

ACKNOWLEDGEMENTS: The funding for this project was provided by the NSF under grant number 0856399 and by Greater Philadelphia Region LSAMP Bridge to the Doctorate (BTD) Cohort IX Program.

REFERENCES

1. C.A. Hieber, S.F. Shen, "A finite element/finite difference simulation of the injection mold filling process," J. Non-Newtonian Fluid Mech. 7, pp. 1-31, (1980).

2. T.A. Osswald, C.L. Tucker, C.L., Polymer Eng. & Sci. 28, pp. 413-420, (1988).

3. M. Bruschke, S.G.Advani, " Finite Element/Control Volume Approach to Mold Filling in Anisotropic Porous Media," Polymer. Composites 11, pp. 398-405, (1990).

4. R.W. Lewis, A.S. Usmani, J.T. Cross, "Finite Element Modeling of Mold Filling," Finite Elements in the 90's, ed.by E. Onate, J. Periaux and A. Samuelsson, Springer-Verlag/CIMNE, Barcelona, (1991).

5. V.R. Voller, Y.F. Chen, "Prediction of Filling Times of Porous Cavities," International Journal Numerical Methods 10, (1995).

6. N.D. Ngo, R.V. Mohan, P.W. Chung, K.K. Tamma, "Recent Developments Encompassing Non-Isothermal/Isothermal Liquid Composite Molding Process

Modeling/Analysis: Physically Accurate, Computationally Effective, and Affordable Simulations and Validations," Journal of Thermoplastic Composite Materials 6, pp. 493-532, (1998).

7. F. Trochu, R. Gauvin, D.-M. Gao, "Numerical Analysis of the Resin Transfer Molding Process by the Finite Element Method." Advances in Polymer Technology 12(4), pp. 329-342, (1993).

8. R. Mathuw, S.G. Advani, D. Heider, C. Hoffmann, J.W. Gillespie Jr., B.K. Fink, "Flow front measurements and model validation in the vacuum assisted resin transfer molding process" Polymer Composites, v 22, n 4, p 477-490, (2001).

9. K. Okonkwo, P.Simacek, S.G. Advani, R.S. Parnas, "Characterization of 3D fiber preform permeability tensor in radial flow using an inverse algorithm based on sensors and simulation," Composites Part A: Applied Science and Manufacturing, v 42, n 10, p 1283-1292, (2011).

10. B.R. Gebart and P. Lidstrom, "Measurement of in-plane permeability of anisotropic fiber reinforcements," Polymer Composites, 17, p. 43–51, (1996).

11. P. Simacek, S.G. Advani, "Desirable Features in Mold Filling Simulations for Liquid Composite Molding Processes," Polymer Composites, Volume 25, 4 , p 355-367, (2004).

A Numerical Method of Permeability Determination for RTM Process Simulation

Christoph Hahn [1], Christophe Binetruy [2], Roland Hinterhölzl[1] and Klaus Drechsler [1]

[1] *Lehrstuhl für Carbon Composites, Technische Universität München (TUM),*
Boltzmannstraße 15, 85748 Garching, Germany.
[2] *Institut de Recherche en Génie Civil et Mécanique (GeM), Ecole Centrale de Nantes, 1 Rue de la Noë, 44321 Nantes, France.*
Corresponding author's e-mail: hahn@lcc.mw.tum.de

ABSTRACT: Resin injection such as resin transfer molding (RTM) is commonly applied in industry for serial production of composite components. RTM process simulation enables prediction of process parameters that are essential for component and tool design. As for all simulations where material behavior is modeled, validated material properties are indispensable for realistic simulations. Currently, material properties have to be determined experimentally which is costly and time consuming. Furthermore, standardized methods for permeability testing are not yet available. This paper presents an approach to determine permeability numerically for carbon fiber fabrics. The most important benefit is the speed-up compared to experimental testing. With fast material characterization, process simulation can be employed in the early design phase of a component. An optimal trade-off between component quality and producibility can be reached without extensive prototyping and testing. The approach is exemplarily applied for a biaxial non-crimped fabric. The way forward is as follows: Information that is inherent in digital images of scanned fabrics is extracted using image analysis. The results are taken as input data for textile modeling with WiseTex. Then, FlowTex is employed in order to determine permeability. A self-developed Matlab® routine performs the image analysis, interacts with the abovementioned tools and finally writes a material card for direct use in RTM simulation. In the paper, numerical results are correlated to experimental results in order to show the quality in predicting material behavior.

KEYWORDS: *Numerical permeability determination, image processing, textile modeling, software interface, flow simulation.*

INTRODUCTION

Manufacturing of complex composite components using RTM requires knowledge about the interactions between geometry, material and the manufacturing method. Therefore, RTM simulation is applied to capture these interactions and give predictions about the process robustness and part quality. As for all simulations where material behavior is modeled, validated material properties are indispensable for realistic simulations. Currently, one major drawback is the great effort in cost and time to determine material parameters like permeability and viscosity. Additionally standardized methods for permeability testing are not yet available and the expenditure of time will remain high for full characterization of textile fabrics. This paper presents a fast and automated numerical procedure for the determination of permeability.

The approach is restricted to lay-ups of uni- or biaxial carbon fiber (CF) non-crimped fabrics (NCF) and also for thin components with equal lay-up over its dimensions. Following Darcy's law, which is commonly used for resin flow simulations, the permeability is the only parameter describing the fibrous preform. Furthermore, it is assumed that resin impregnation does not alter the textile structure. Hence, it cannot be accounted for varying lay-up thickness during impregnation as it happens during resin infusion with flexible tooling (RIFT) and phenomena like fiber washing are neglected. This assumption is necessary since important parameters for textile modeling are obtained from digital images of dry fabrics in a glass mold by image analysis.

Fig. 1 illustrates the presented method beginning with digital images and familiar parameters providing information on the fabric, its lay-up and the desired fiber volume fraction (FVF). A self-programmed Matlab® tool performs the following steps: (I) image analysis, (II) textile modeling (interface to WiseTex), (III) permeability calculation (interface to FlowTex) and (IV) the export of a permeability look-up table for a desired range of FVF and shear angle. In addition to other information, this data is applied to RTM process simulation.

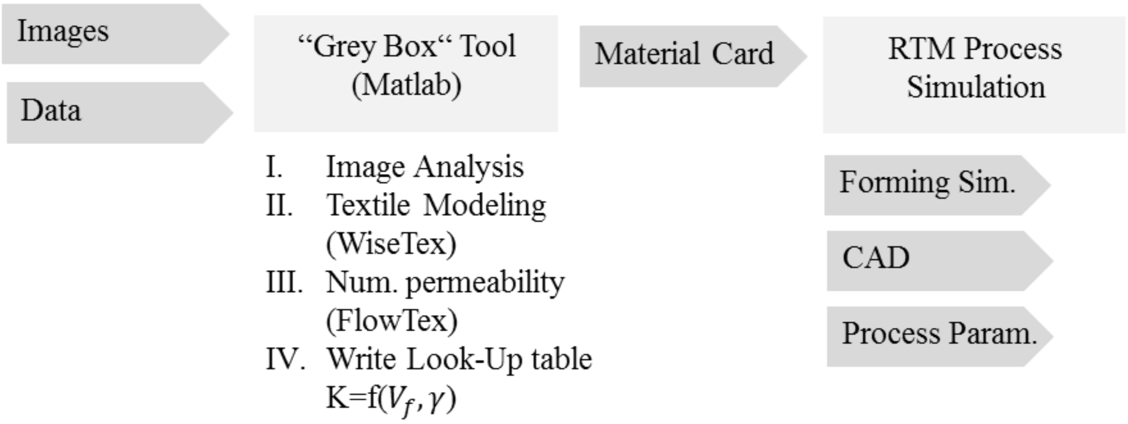

Fig. 1: Flow chart of the method for numerical permeability prediction

The studies presented in that paper have been conducted with a Saertex biaxial NCF (+45°/-45°, 540g/m^2, franse stitched). For following considerations the direction of the stitching seam is defined as 0° direction.

IMAGE ACQUISITION

Light transmission characteristics of glass fiber fabrics can help to determine fabric quantities of a multilayer stack. However, this technique cannot be applied to CF fabrics because they absorb most of the light. For image acquisition, therefore, both sides of a textile must be analyzed.

To investigate the textile preform in the in-situ state (inside a RTM tool with fixed cavity geometry), a fabric layer is put into a glass mold where spacer disks are used to adjust thickness. Fig. 2 shows the mold, consisting of two 10mm-thick glass plates. Between the two plates, shim washers set the distance and with it the FVF.

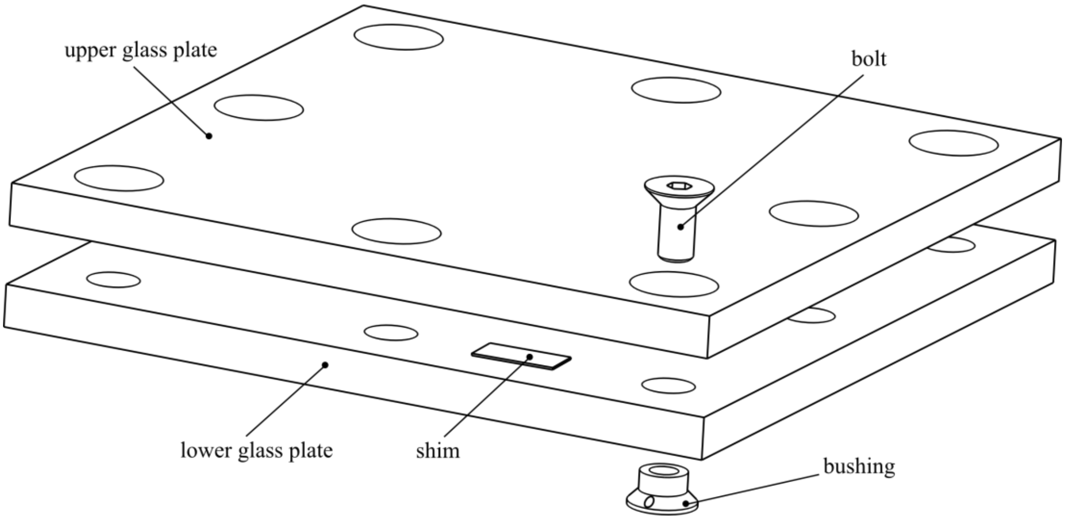

Fig. 2: Glass mold

The diagonal dimension of the mold is 246mm enabling it to rotate on a A3-format scanner and accounting for image differences due to the light's direction. Maximum patch size for the textile is 115mm x 115mm. This corresponds to image dimensions of about 10 000 pixels in width and height (100 megapixels), using the scanner's 2200 dpi resolution (here: Epson 10000 XL).

DIGITAL IMAGE ANALYSIS

Fig. 3 (left) shows the original input image for image processing; the actual image size is approx. one square centimeter. The initial image is segmented by a gray-level thresholding. Main areas to be segmented are fiber bundles, gaps and stitchings. Binary morphological operations are incorporated to further improve the segmentation results. A marker based watershed algorithm is applied to cut the connected stitching line into separated stitches. Then, morphological blob analysis is used to determine information about orientation, length, width and area of gaps and separated stitches. Data concerning fiber angles is provided by Fourier analysis with the help of an edge image generated by a 'canny' edge-finding algorithm. The distances between stitching lines are gathered by applying the first order polynoms, which are created using curve fitting by calculating the mean of the y-axis differences on the left and right fringes of the initial image. The complete image analysis is conducted using Matlab [1].

Fig. 3 (right) illustrates the fabric after segmentation and the extracted properties:

a. (Projected) fiber bundle width
b. Segmented stitching area and area centroid
c. Fiber angle
d. Distance between stitching lines
e. Crack length
f. Watershed ridges, separating the stitchings from one another.

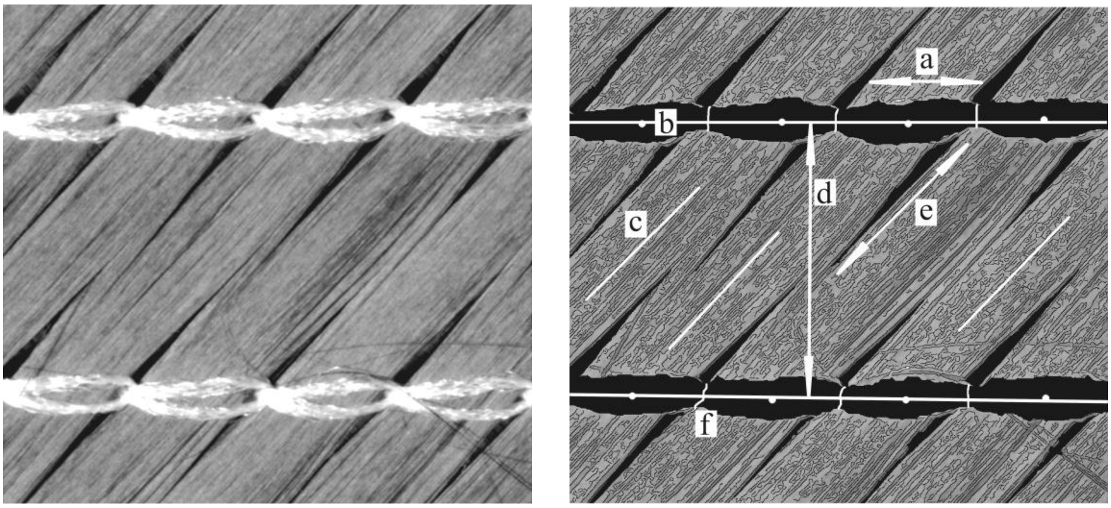

Fig. 3: Original image of bottom side (left) and analysis results (right)

TEXTILE MODELING AND PERMEABILITY PREDICTION

Modeling approach and permeability predictions for unsheared fabrics

A geometrical representation of the fabric is created using the textile modeler WiseTex [2], and the computation of permeability is conducted using the meso-level CFD solver FlowTex [3]. Both tools have been developed at the KU Leuven by Prof. S. Lomov et al.

The geometrical description of the textile model is based on the smallest repetitive volume of the preform, often denoted as representative volume element (RVE). FlowTex distinguishes between solid and fluid domain of a fabric. The Stokes equations are the underlying governing equations for the fluid domain. In case intra-yarn flow is taken into account, which is strongly recommended for NCFs, Brinkmann equation is used to model flow within the yarns. The RVE is discretized with a collocated grid and the system equations are solved with a finite difference solver. Boundaries between adjacent cells are taken to be spatially periodic, to account for the real dimensions of the preform. Computations are carried out for three orientations (here 0°, 45°, 90°) giving the effective permeabilities and from these the principal permeability tensor will be derived. Bear [4] has demonstrated that the square root of the effective permeabilities follows an ellipse and furthermore that the square roots of the principal permeabilities are the major and minor axes of the ellipse. Thus, the principal in-plane permeability tensor is deduced using a least squares ellipse fit algorithm (cf. Fig. 5 and Fig.8).

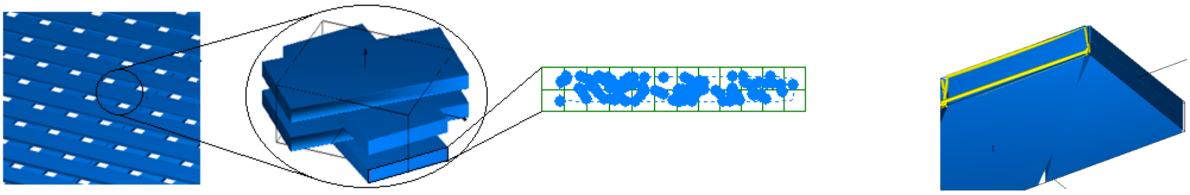

Fig. 4: Unit cell model of UD preform (left) and stitched mat (right)

For the numerical permeability determination two modeling strategies have been used, a UD preform model (udp model, cf. Fig. 4, left) and a stitched mat model (stm model, cf. Fig. 4,

right) proposed by Lomov et al. [5]. Stm models give a better geometry description of the preform, because stitching and its influence on permeability is taken into consideration.
The permeability experiments for the results depicted in Fig. 5 have been performed with a self-developed test-setup at the Lehrstuhl für Carbon Composites (TUM).
In the following, results from the numerical and experimental tests are presented and compared. In Table 1, the entries of the principal in-plane permeability tensor (K1, K2 and rotation angle β with respect to) are denoted for fiber volume content 46.1%, 52.6% and 61.4%.

Table 1: Principal in-plane permeability data for FVF of 46.1%, 52.6% and 61.4%

FVF[%]	46.1			52.6			61.4		
	Exp	Udp	Stm	Exp	Udp	Stm	Exp	Udp	Stm
K1[x10^{-11}m^2]	19.96	15.71	9.95	7.08	5.04	0.87	4.79	2.04	0.21
K2[x10^{-11}m^2]	13.60	15.10	2.18	5.02	4.69	0.52	2.54	1.90	0.19
Angle[°]	24.48	45.00	24.22	155.40	45.00	21.09	68.01	40.80	157.5

In Fig. 5, the (square rooted) results from experiments as well as numerical analyses for 0°, 45° and 90° direction are plotted together with the fitted principal permeability ellipses.

To increase the accuracy of the ellipse fit algorithm, the results have been extended to the inverse direction assuming equal permeability in back and forth direction.

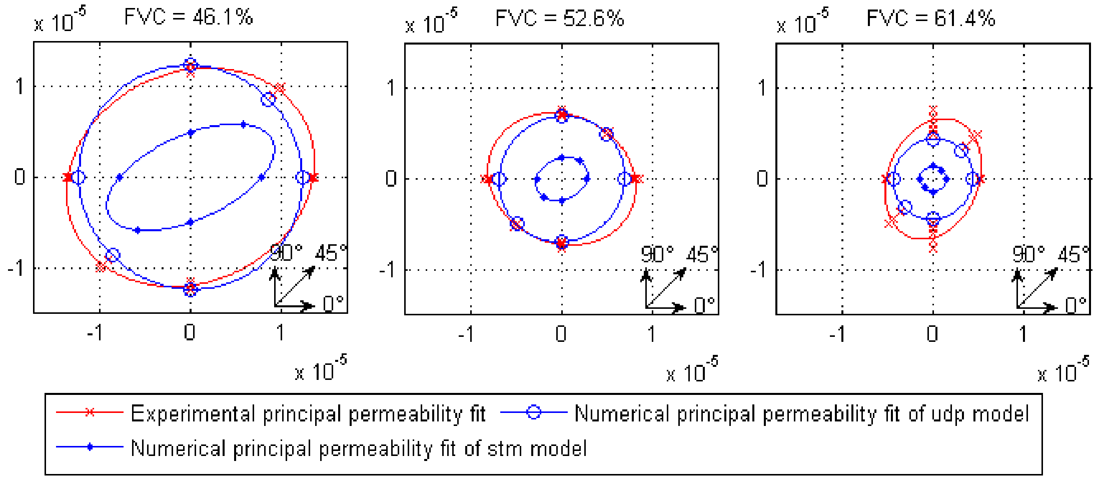

Fig. 5: Fitted experimental and numerical effective permeability results (square-rooted) for FVF of 46.1%, 52.6% and 61.4% (from left to right)

Experimental and numerical results in Fig. 5 show a strong correlation. Udp and stm models, both, capture the decrease of permeability with increasing fiber volume content nicely. Numerical results from the stm model are generally lower as those from udp models and experimental results.
Since the experimental results are not based on a standardized test method for testing it cannot be confirmed at that point which models gives more correct results. Therefore the method has to be validated in realistic test cases.

Permeability results taking into account fabric shear deformation

In order to capture the behavior of permeability under shear, adaptions of the udp model are proposed. The FVF of a fabric undergoing shear is increasing with increasing shear angle following the relation (cf. Fig. 6)

$$V_f(\gamma) = \frac{V_f(\gamma = 0°)}{\cos\gamma}. \tag{1}$$

Hence, the edge length of the unit cell S and the yarn width d_2 are adapted to shear with

$$S(\gamma) = S(\gamma = 0°) \cdot \cos\gamma \tag{2}$$
$$d_2(\gamma) = d_2(\gamma = 0°) \cdot \cos\gamma, \tag{3}$$

so that the FVF follows the relation depicted in (1). With the proposed adaptions, the model is able to correlate nicely the increase of FVF in the udp model due to increasing shear angle up to 35° as depicted in Fig. 7.

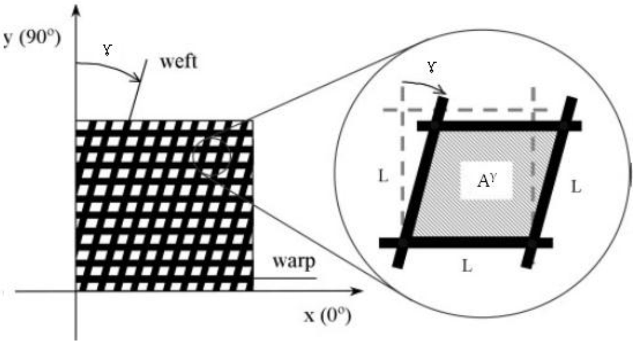

Fig. 6: Shear deformation of a fabric [6]

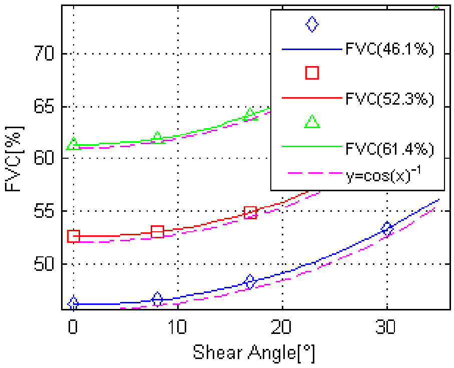

Fig. 7: Correlation of FVF and shear angle γ

Analogously to unsheared fabrics, permeability of fabrics undergoing shear deformation was determined experimentally. The maximum value for the shear angle (17°) was chosen, because for higher shear angles the fabric would relax after shear deformation. A fixation (e.g. thermoplastic binder powder) was not used to keep the textile structure for permeability testing unchanged. The scatter of experimental results for sheared permeability is considerably higher than for the unsheared results. This is mainly because the cavity size of the test-setup for the sheared tests had to be reduced due to the size of the shear frame. The fitting algorithm for the determination of principal permeability is sensitive to results with a high scatter, as can be seen in Fig. 8 (right).

Table 2: Principal in-plane permeability data for shear angles 0°, 8° and 17°

Shear angle[°]	0		8		17	
	Exp	Udp	Exp	Udp	Exp	Udp
K1[x10^{-11}m^2]	9.29	5.04	7.08	6.45	42.10	6.58
K2[x10^{-11}m^2]	3.76	4.69	3.75	4.92	3.77	3.58
Angle[°]	143.74	45.00	138.20	169.61	133.26	13.46

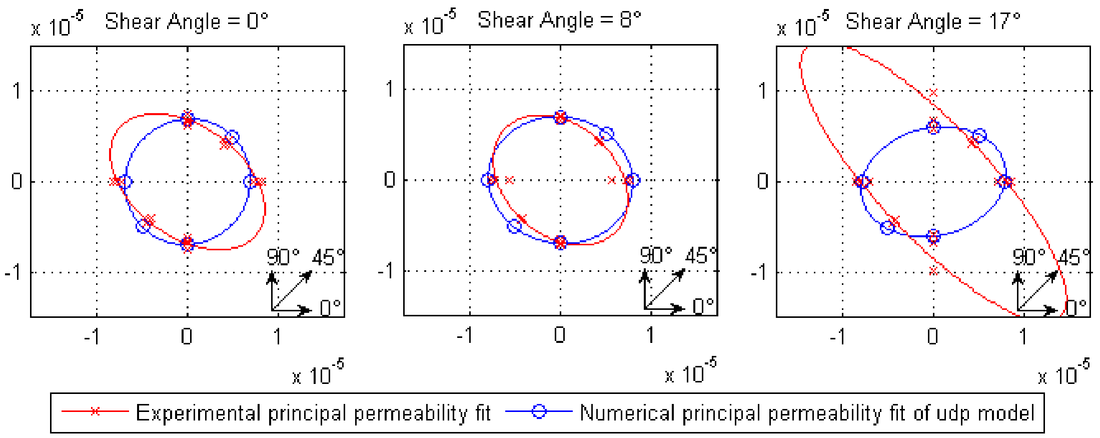

Fig. 8: Fitted experimental and numerical effective permeability results (square-rooted) for shear angles 0°, 8° and 17° (from left to right)

Analogously to the unsheared fabric (cf. Table 1 and Fig. 5), the results are plotted in Table 2 and Fig. 8 using the abovementioned model. The results indicate that the numerical model can estimate permeability reasonably well.

Comparing unsheared results and sheared results for different FVF, it can be concluded that the influence of varying FVF on permeability is much higher than the influence of pure shear. This statement is supported by extending the sheared numerical model to values of FVF from 46% and 61% which are not presented here.

Software interface

Within this study a Matlab tool was developed that, apart from the image analysis, is used as a software wrapper for textile modeling and permeability calculation, i.e. it is embedding WiseTex and FlowTex.

With the XML interface implemented in WiseTex and the compatibility of WiseTex and FlowTex to MS-DOS command line, Matlab is able to interact with them.

The results from image analysis are written to XML-files representing the WiseTex models. After completion of permeability calculation Matlab collects all the data from the result files. Depending on the software tool employed for RTM simulation (e.g. PAM-RTM by ESI Group), a compatible material card is written.

CONCLUSIONS

This paper proposes an automated numerical scheme for permeability characterization of textile fabrics. The main advantage of this method is fast determination of material parameters that are essential for process simulation. A complete run of the tool can be performed in less than 6 min (cf. Table 3) which enables the creation of a look-up table within hours. Table 3 shows exemplarily the CPU times for processing a typical model.

Table 3: Overview of CPU times for processing a typical model

Process step	**CPU time [s]**	**Remarks**
Image analysis	~ 60	Depending on image size and analysis amount
Voxelisation:	10 / 60	Udp / Stm model with 100 000 / 350 000voxels
FlowTex	~ 200	Depending on discretization, consideration of intra yarn flow (Yes / No) and stitching

Assistance can be provided for the industry’s challenge of ensuring high quality and process robustness for composite components. A faster material characterization will allow process simulation in a component’s early design phase. An optimal trade-off between component quality and producibility will then be possible without extensive prototyping and testing. Furthermore, automated material characterization will help quality assurance to investigate variations within fabrics and their influence in the following production steps.

ACKNOWLEDGMENTS: The author would like to thank Prof. K. Drechsler for providing a powerful and positive research environment. Gratitude is granted to Prof. C. Binetruy for his support and the fruitful discussions. Thanks to Prof. S. Lomov and Dr. B. Verleye for their cooperation and support with the software tools WiseTex and FlowTex. Finally thanks to all involved persons at the Institute for Carbon Composites, especially Johannes and Yichen.

REFERENCES

1. Gonzales RC and Woods RE (2008), Digital Image Processing, 3rd ed, New Jersey: Pearson Prentice Hall.
2. S. V. Lomov, G. Huysmans, Y. Luo, R. S. Parnas, A. Prodromou, I. Verpoest, F. R. Phelan (2001), ‘Textile composites: modelling strategies’, *Composites Part A: Applied Science and Manufacturing*, 32(10), 1379-1394.
3. B. Verleye, S.V. Lomov, A. Long, I. Verpoest, D. Roose (2010), ‘Permeability prediction for the meso–macro coupling in the simulation of the impregnation stage of Resin Transfer Moulding’, *Composite Part A: Applied Science and Manufacturing*, 41(1), 29–35.
4. Bear J. (1972), Dynamics of fluids in porous media, New York: American Elsevier Publishing Company.
5. Lomov SV, Belov EB, Bischoff T, Ghosh SB, Truong Chi T, Verpoest I (2002), ‘Carbon composites based on multiaxial multiply stitched preforms. Part I: Geometry of the preform’, *Composite Part A: Applied Science and Manufacturing*, 33(9), 1171–1183.
6. C. Demaria, Edu Ruiz, F. Trochu. In-Plane Anisotropic Permeability Characterization of Deformed Woven Fabrics by Unidirectional Injection. *Polymer Composites*, Volume 28, Issue 6, pages 812–827, December 2007.

AIR TRANSPORT THROUGH POROUS MEDIA AND APPLICATIONS TO IN-PLANE PERMEABILITY MEASUREMENT

Yi Hou[1,2] , Sebastien Comas-Cardona[3], Sylvain Drapier[2], Christophe Binetruy[3] *

[1] *Polymers and Composites Technology & Mechanical Engineering Department, Ecole des Mines de Douai, 941 rue Charles Bourseul BP 10838, 59508 Douai, France.*
[2] *Mechanics and Materials Processing Department, LCG UMR CNRS 5146, Ecole Nationale Superieure des Mines, 158 cours Fauriel, 42023 St Etienne cedex 2, France.*
[3] *Research Institute in Civil Engineering and Mechanics (GeM), UMR CNRS 6183, Ecole Centrale de Nantes, 1 rue de la Noe, BP 92101, 44321 Nantes Cedex 3, France.*
Corresponding author's e-mail: christophe.binetruy@ec-nantes.fr

ABSTRACT: Permeability of a fibrous reinforcement is an important physical parameter in Liquid Composite Molding (LCM). A great amount of effort has been spent on measuring such material property. Most of the techniques employed rely on liquid injection experiments. However permeability measurement using air instead of a liquid can provide a cleaner and faster measurement with reusable fabrics. This paper introduces a methodology to measure in-plane permeability of fibrous media using a transient one dimensional air flow. The method, based on the measurement of gas pressure at the boundaries throughout the transient flow, avoids usage of a gas flow meter and offers a way to study the gas transport within fibrous media. The permeability, only depending on the porous structure, is determined by inverse method, fitting the simulation results to the experimental data. Several models are built to describe air transport in different flow regimes. Results obtained by liquid injection and transient air flow match well in Darcy's regime. The deviation from Darcy's law caused by air sliding effect is analyzed.

KEYWORDS: *Air permeability, Klinkenberg sliding, Transient measure, Fabric*

INTRODUCTION

Permeability of a fibrous reinforcement is an important physical parameter in Liquid Composite Molding (LCM). A great amount of effort has been spent on measuring such material property. Most of the techniques employed rely on liquid injection experiments. However permeability measurement using air instead of a liquid can provide a cleaner and faster measurement with reusable fabrics [1-3]. To analyse the pressure drop along unfilled fabrics and the actual boundary condition at the flow front, it is necessary to understand how air flows through fabrics.

DARCIAN MODEL

Considering air as a Newtonian fluid, the momentum conservation for the air flow across a porous medium may be described using Darcy's law, which is the simplest assumption in the form of a linear relationship between a flux and a driving force [4, 5],

$$\mathbf{q} = -\frac{\mathbf{K}}{\mu}(\nabla P - \rho \mathbf{g}) \tag{1}$$

where q is the filtration velocity or Darcy flux (discharge per unit area related to the pore fluid velocity v by porosity ϕ : $\mathbf{q} = \mathbf{v}\phi$), g the gravity acceleration, and ∇P the pressure gradient vector.

Combining Equation (1) with the ideal gas law and mass conservation equation, considering one dimensional flow in a homogeneous medium and neglecting gravity (term $\rho\mathbf{g}$ = 0) leads to the fundamental equation [6],

$$\frac{\partial P}{\partial t} = -\nabla \cdot \frac{\mathbf{K}}{\phi\mu} \cdot P\nabla P \tag{2}$$

The fundamental equation provides a fast method to back-calculate air permeability from measured pressure data.

SLIDING MODEL

The Klinkenberg's sliding effect is observed and promoted on gas transport through fine-grained low-permeability porous media, such as soils, with small pore size. Klinkenberg used nitrogen and brine as fluids in a mini-permeameter device [8]. When high flow rates can be maintained, the results are comparable. At low flow rates, the effective permeability measured with N_2 gas will be higher than the viscous permeability measured with brine. Klinkenberg explains changes of gas permeability under different pressures by the slippage of gases along the pore walls, since gas does not adhere to the pore walls as liquid does. The effective gas permeability K_g (or apparent permeability) depending on gas pressure is given by

$$K_g = K_\infty (1 + \frac{b}{P}) \tag{3}$$

where K_∞ is the intrinsic permeability, which is considered to be the absolute gas permeability under very large gas pressure at which condition the Klinkenberg effect is negligible. The Klinkenberg factor b depends on the mean free path of the gas molecules which also depends on the micro-structure of the porous medium.

EXPERIMENTAL METHODS

Experimental set-up and measurement

The experimental set-up to measure air permeability of the fibrous preform by one dimensional flow is shown in Fig. 1. A preform is inserted between a set of top and bottom platens, sealed with an o-ring seal. The outlet and inlet are respectively connected to a vacuum pump and the atmosphere, and controlled by valves. Pressures P_1 and P_2 are monitored by pressure gauges and recorded by a data acquisition system.

For one-dimensional transient flow, the experiment begins by setting the initial pressure, corresponding to $t < 0$ in Eq.4. This is obtained by closing valve 2 and opening valve 1 until the values of P_1 and P_2 equilibrate exactly atmospheric pressure within the fabric. Then, a dropping pressure at the boundary 2 is applied while closing valve 1 and opening valve 2 to let the vacuum in, corresponding to $t > 0$ in Eq.4. During all the steps, $P_1(\mathrm{t})$ and $P_2(\mathrm{t})$ are recorded for further analysis. In conclusion, the boundary conditions are,

$$\begin{cases} P_1 = P_{atm}, \nabla P_2 = 0 & & \mathrm{t} < 0, \\ P_1 = P_2 = P_{atm} & \text{when} & \mathrm{t} = 0, \\ \nabla P_1 = 0, P_2 = P_{vac} & & \mathrm{t} > 0. \end{cases} \tag{4}$$

where P_{vac} is a vacuum pressure around 2000 Pa. The method is referred to as dropping pressure method (DPM). Simulation is based on solving Eq.2 for P_1, with boundary and initial conditions associated. $P_1(t)$ and $P_2(t)$ are recorded during experiments, and other parameters are determined: viscosity μ is calculated from environmental temperature T, and porosity of sample ϕ is provided by the sample thickness and areal weight. Then permeability K is estimated by minimizing the difference between experimental and simulated results obtained for $P_1(\mathrm{t})$, under the prescribed experimental pressure $P_2(\mathrm{t})$.

The experiment could also begin with vacuum initial pressure and then a raised pressure is applied as one boundary condition,

$$\begin{cases} P_1 = P_{vac}, \nabla P_2 = 0 & & \mathrm{t} < 0, \\ P_1 = P_2 = P_{vac} & \text{when} & \mathrm{t} = 0, \\ \nabla P_1 = 0, P_2 = P_{atm} & & \mathrm{t} > 0. \end{cases} \tag{5}$$

which is referred to as raised pressure method, or RPM.

Boundary condition modification

The boundary condition is considered to be zero flux when the corresponding valve is closed. Since air is compressible, the air trapped between the valve and the side of fabric, shown in Fig. 1, may cause a slight flux at the boundary when pressure is changing. Assuming a quasi-static flow, the trapped air shares same values of pressure, density and temperature. For the location of pressure sensors at points x = 0 and x = L, mass conservation gives,

$$\begin{cases} \dfrac{\partial \rho}{\partial t} V + \rho A v = 0 & x = 0 \\ \dfrac{\partial \rho}{\partial t} V - \rho A v = 0 & x = L \end{cases} \tag{6}$$

where *V* is the volume of air trapped, *A* is the cross sectional area for air flow, and L is the length of the fabric sample. Combining ideal gas law and Darcy's law, boundary conditions can be obtained in terms of *P*,

$$\begin{cases} \dfrac{K}{\phi\mu} P \dfrac{\partial P}{\partial x} - \dfrac{\partial P}{\partial t} \dfrac{V}{A} = 0 & x = 0 \\ \dfrac{K}{\phi\mu} P \dfrac{\partial P}{\partial x} + \dfrac{\partial P}{\partial t} \dfrac{V}{A} = 0 & x = L \end{cases} \tag{7}$$

where the volume area ratio *V/A* is the dominant parameter. For a set of experimental P_1 and P_2 , the permeability obtained by back-calculation could change remarkably with different volume area ratio. The variation of calculated permeability can be estimated as,

$$\frac{K}{K_0} = 1 + 2\frac{V}{AL} \tag{8}$$

where K_0 is the permeability obtained from back-calculation with unmodified boundary conditions. This empirical relationship is confirmed by sets of experiments on different materials, shown in Fig. 2, where K_g is obtained by back-calculation accounting for different volume area ratio which equals to 0 to calculate K_0 without considering trapped air. The results are based on experimental pressures for three types of fabrics and the slope of best fitting line varies slightly for different procedures, but shows independence on the samples.

Since *V/A* is close to 0.1 in these experiments, leading to 100% difference in permeability, it's important to apply the real boundary condition considering the air trapped in the setup.

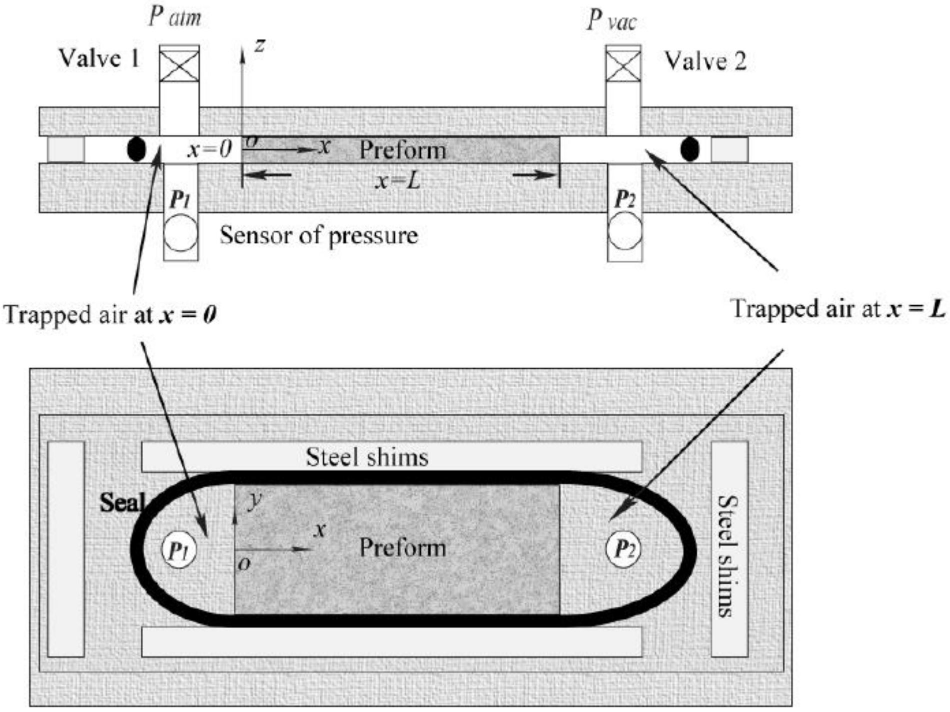

Fig. 1. Experimental set-up showing air trapped between valve, platens and preform

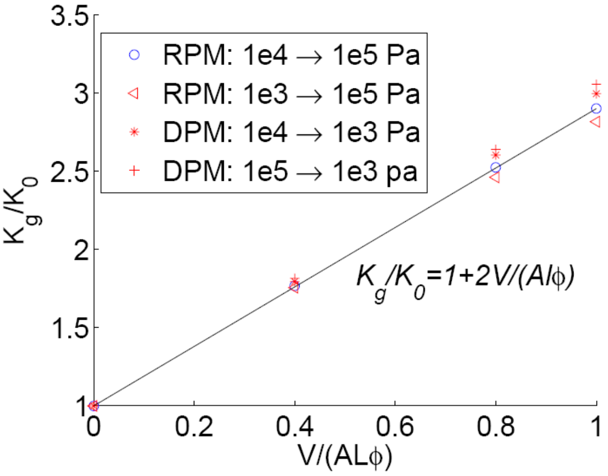

Fig. 2. Variation of permeability K_g/K_0 vs. volume to area ratios

MATERIALS AND RESULTS

Carbon twill-weave fabric

Raised and dropping pressure measurements are carried out on Carbon G986 twill weave (Hexcel, France), 6 plies at 0° orientation, with volume fraction of 44%, 49% and 55%. Permeabilities (with a standard-deviation lower than 10% for 8 sets of experiments with flow rates) obtained by transient air flow measurement are compared with liquid compression measurements [7]. The differences are close to the error of measurements, shown in Fig. 3. Simulations of flow based on Darcy's law fits well with experimental data, shown in Fig. 4.

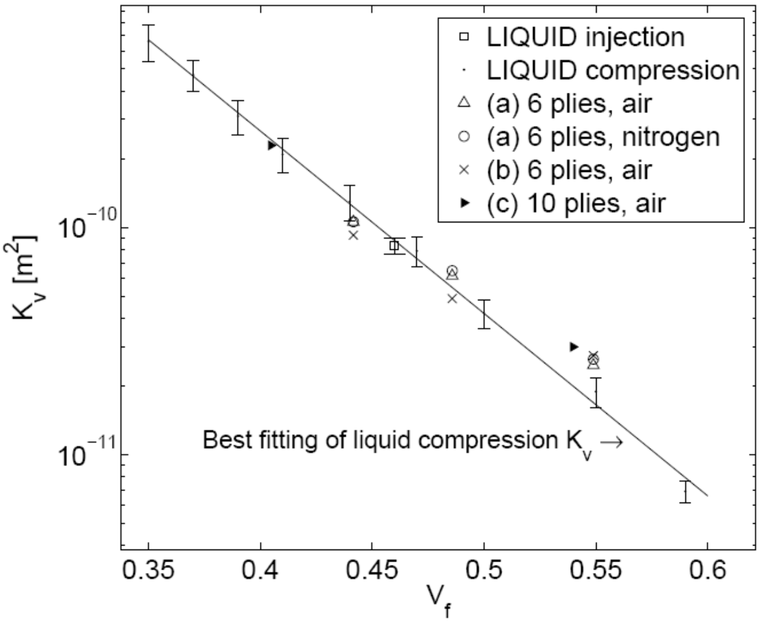

Fig. 3. Comparison of permeability K obtained by transient air flow measurement and liquid compression measurement on G986 carbon woven fabric of different volume fraction V_f [7] .

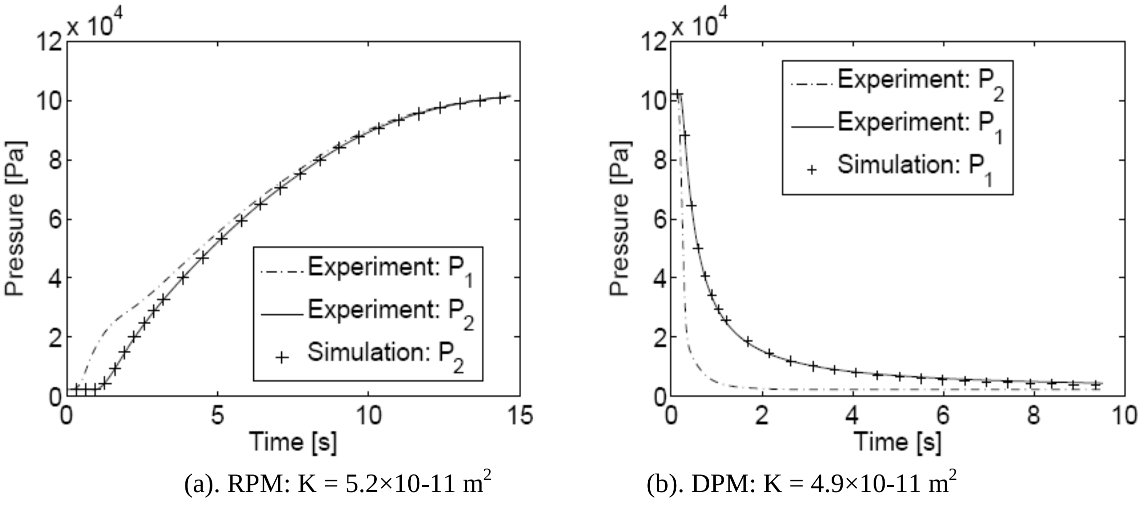

(a). RPM: K = 5.2×10-11 m^2 (b). DPM: K = 4.9×10-11 m^2

Fig. 4. Comparison between experimental and computed P_1 in raised pressure measurement for carbon G986 twill-weave perform at 48.6 % fibre volume fraction.

Carbon unidirectional fabric (CUD)

As shown in Eq. (3), the apparent permeability K_g increases while the local pressure decreases. The carbon unidirectional fabric, where the porous structures can be viewed as an unidirectional allay of parallel tubes, shows some sliding effect in the initial stage where pressure is around 2000 Pa , and Darcian model shows a difference between simulated and experimental curves (Fig. 5 (a)). The sliding effect has significant effect on the apparent permeability when Klinkenberg parameter *b* is comparable with the loading pressure, e.g., *b* and P_a have the same order of magnititude, leading to a 70% difference between K_g and K (in the case shown in Fig. 5). Hence raising loading pressure can reduce the sliding effect.

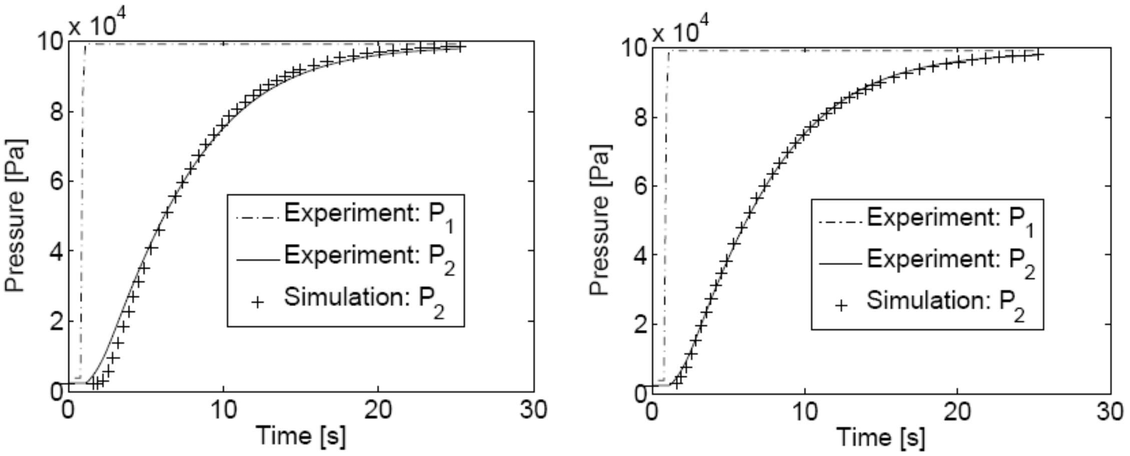

(a) Darcian model (b) Sliding model,

Fig. 5. Comparison between experimental and predicted pressures P_2 using Darcy's law (a): $K_g = 1.7\times10^{-12}\,\mathrm{m}^2$ and sliding model (b): $K = 9.3\times10^{-13}\,\mathrm{m}^2$, $b = 0.5\times10^5$ Pa, in RPM for CUD preforms at 61% fibre volume fraction.

CONCLUSIONS

A methodology to measure fabric in-plane permeability using a transient air flow has been described. The results match well the permeability measured with liquid compression and injection techniques. The method, based on the simple measurement of gas pressure throughout the transient flow, is convenient, clean and fast, avoids usage of a gas flow meter and offers a way to further study the air transport within porous media.

Darcy's law (viscous flow) can be applied to gas flow through fabric with large pore size and high pore pressure. While for smaller pore size and lower pore pressure, gas molecules slide on pore walls. The sliding effect, also called Klinkenberg effect, reveals a dependence of apparent permeability on pressure in porous media. For fibrous media, the sliding effect is observed on carbon unidirectional fabric with a high fiber volume fraction. Sliding model is recommended for such cases and also raising the maximum pressure in measurements can also avoid sliding effect.

ACKNOWLEDGMENTS: The authors would like to thank the European Union for funding this study through the INFUCOMP project.

REFERENCES

1. Tavares, S. Sequeira, V. Michaud, and J.A.E. Manson (2009). ‘Through thickness air permeability of prepregs during cure’. *Composites Part A: Applied Science and Manufacturing.*, 40(10), 1587–1596.

2. J. Feser, A. Prasad, and S. Advani (2006). ‘Experimental characterization of in-plane permeability of gas diffusion layers’, *Journal of Power Sources*, 162(2), 1226–1231.

3. R. Pomeroy, S. Grove, J. Summerscales, Y. Wang, and A. Harper (2007), ‘Measurement of permeability of continuous filament mat glass-fibre reinforcements by saturated radial airflow’, *Composites Part A: Applied Science and Manufacturing*, 38(5), , 1439–1443.

4. J. Bear (1998), Dynamics of Fluids in Porous Media. Courier Dover Publications.

5. H. Darcy (1956), ‘Les Fontaines Publiques de la Ville de Dijon’, *Victor Dalmont*, Paris, 590-594.

6. A. E. Scheidegger (1958), ‘The Physics of Flow Through Porous Media’, *Soil Science*.

7. S. Comas-Cardona, C. Binetruy and P. Krawczak (2006), ‘Unidirectional compression of fibre reinforcements. Part 2: A continuous permeability tensor measurement’, *Compos. Sci. Technol.* 67(3-4), 638-645.

8. L. Klinkenberg (1941). ‘The permeability of porous media to liquids and gases, ‘In Drilling and Production Practice’, *American Petroleum Inst.*, 200-213.

ANALYSIS OF HYSTERESIS PHENOMENON FOR SATURATED FLOW IN LCM PROCESS

Sung Ha Kim[1], Sung Woong Choi[1], Mei Xian Li[1], Chung Hae Park[2] and Woo Il Lee[1]

[1]*Department of Mechanical and Aerospace Engineering, Seoul National University, Seoul, Korea*
[2]*Laboratoire d'Ondes et Milieux Complexes, UMR 6294 CNRS, University of Le Havre, Le Havre, France*
Corresponding author's e-mail: wilee@snu.ac.kr

ABSTRACT: Liquid Composite Molding (LCM) such as Resin Transfer Molding (RTM) is becoming one of the promising processes in the composite manufacturing process due to their versatility, economic advantages among other merits. To understand the flow behavior in LCM process, it is important to observe the permeability characteristics. Tow deformation and pressure gradient behavior through the flow were observed with different volume flow rates and fluid viscosities to characterize the relation between the volume flow and permeability regarded to tow deformation. Permeability was varied with the volume flow, and it showed hysteresis when increasing and decreasing the volume flow rate due to tow deformation. The intensity of hysteresis was changed by fluid viscosity which affects tow deformation.

KEYWORD: *permeability, saturated flow, hysteresis, liquid composite molding*

INTRODUCTION

Recently, there has been much research of composite material manufacturing processes because of increasing interest for environmental issues and needs for the high functional materials. Among these manufacturing processes, liquid composite molding (LCM) processes are becoming more and more popular in the composite manufacturing industries due to their versatility and economical merits. In the LCM process, porous preforms impregnated by polymeric resin are mainly used. We can regard this impregnation as a porous media flow in order to predict the resin flow and analyze the process including void formation.

When analyzing the flow behavior of the porous media flow, it is reasonable to approach with the Darcy's law. Flow pattern and filling time of the impregnation can be predicted by using Darcy's law for practical calculation and simulation of LCM process [1-4]. When applying the Darcy's law, permeability is the key parameter to analyze the resin impregnation. In order to obtain the reasonable result, appropriate value of permeability need to be provided, especially when the process and mold geometry are complicated. However, it is difficult to determine the value of the permeability because of the various flow behaviors appeared in the mold flow [5].

The permeability reflects the microstructure of the porous medium so that it is expected to remain unchanged by measurement methods and flow conditions. However, resin flow itself might cause the changes of the microscopic geometry of the preform depending on the flow conditions such as flow rate. Moreover, voids which were formed during the impregnation caused by velocity difference between tow area and channel area might also affect the microscopic structure of the porous media [6].

To investigate the influence of the flow conditions on the saturate permeability, void inside the saturated flow and tow deformation should be considered. Channel void can be formed when low flow rate impregnation is saturated. As the flow rate increases, it can be observed that the void swept away through the porous media so that we can consider saturated flow with high flow rate contains fewer voids inside the flow. Tow deformation can be regarded to depend on the pressure gradient of the flow which is proportional to fluid viscosity. In this study, saturated permeability was investigated by measuring the pressure gradient through the mold, changing the flow rate continuously with the different fluid viscosities to analyze the effect of the microscopic geometry change due to void and tow deformation.

EXPERIMENTAL

Experimental setup

Three different viscosities of silicone fluid (KF-96, Shin Etsu) were used as fluid of the experiment. The specification of the fluid is on Table 1. The fluid was injected from a resin injection pump which can control the flow rate.

Table 1: Specification of the silicone fluid

Model No.	Specific gravity 25℃	Viscosity 25℃ (Pa s)	Surface tension (mN/m)
KF-96-30cs	0.955	0.02865	20.7
KF-96-100cs	0.965	0.0965	20.9
KF-96-350cs	0.97	0.3395	21.1

Non-crimped unidirectional glass fiber mat used in this work was manufactured by Owens Coring. Density of the fiber mat was 2.6g/cm^3. Diameter of the single fiber was 16.5μm, and one tow bundle was 2mm and the thickness was 0.43mm.

The size of the mold was 500 mm x 55 mm x 3.5 mm. The upper mold was made of 25mm-thick tempered glass to observe the flow inside during the experiment. The bottom mold was made of SUS403 stainless steel coated in blue color to observe easily. A spacer which made of the same material as bottom mold was placed between the upper and bottom molds to make the mold cavity gap of 3.5mm. The mold cavity was clamped with a hydraulic press which enables the constant closure condition through the experiment.

Pressure transducers were installed to monitor the pressure during the flow. The measureable pressure range of the transducer was 0 to 10^5 Pa. The accuracy of the transducer was 0.030%. Seven pressure transducers were installed along the flow direction. Each pressure transducers were installed 100, 160, 220, 280, 340, 400, and 460mm distance from the inlet.

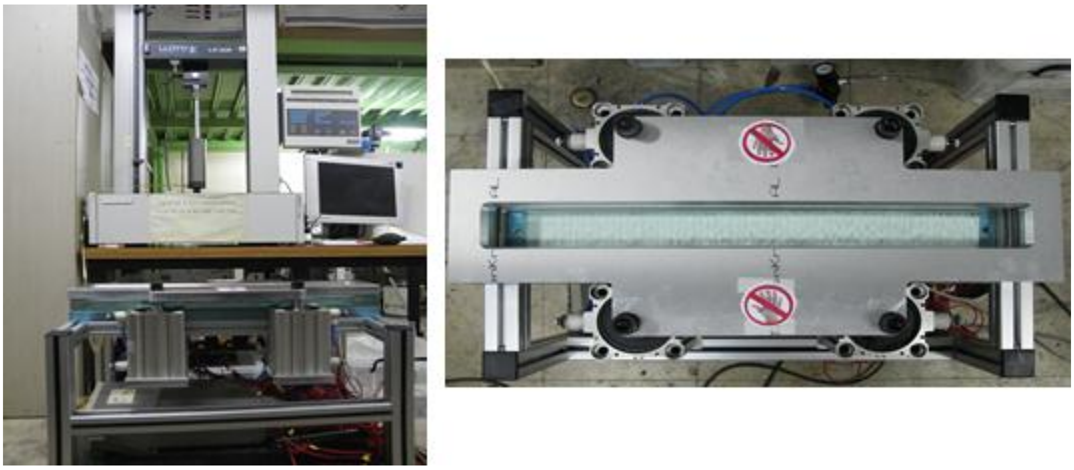

Fig. 1: Experimental setup

Experimental procedure

First of all, glass fiber mats which were arranged in a perpendicular direction to the flow direction were placed on the bottom mold. After that, spacer and upper mold were placed to close the mold by hydraulic press clamping. Silicone fluid was injected by resin injection pump into the cavity while recording the pressure by pressure transducers continuously.

Injections were carried out with the different viscosities, and the flow rate was changed continuously for each injection. Flow rate of 25mm^3/s silicone fluid was injected until flow was fully saturated, and then flow rated was doubled until 800, 1200, and 1600mm^3/s for silicone fluid of 30, 100, and 350cs respectively.

RESULTS AND DISCUSSTION

Dependence of saturated permeability on flow rate

To obtain the saturated permeability which depends on the different flow rates, experiments were conducted with the injection flow rates varying sequentially from 25 to 50, 100, 200, 400, and 800mm^3/s for 350cs silicone fluid. Flow rate of 1200 and 1600mm^3/s were additionally conducted for 100cs and 30cs silicone fluid respectively, since the pressure gradient of the low viscosity fluid is relatively low compared to that of 350cs silicone fluid at the same flow rate.

Fig. 2 shows the overall pressure behavior of the experiment which was conducted with 100cs silicone fluid. Sensor 1 is the nearest transducer from the inlet, and sensor 8 is the nearest transducer from the outlet of the mold. Before the saturation, pressure of each sensor rises as the fluid propagates and maintains constant value when the flow is saturated. Pressure increases as the flow rated increases and it reaches another saturation state. Saturated permeability of the flow can be obtained from these pressure gradients by Darcy’s law.

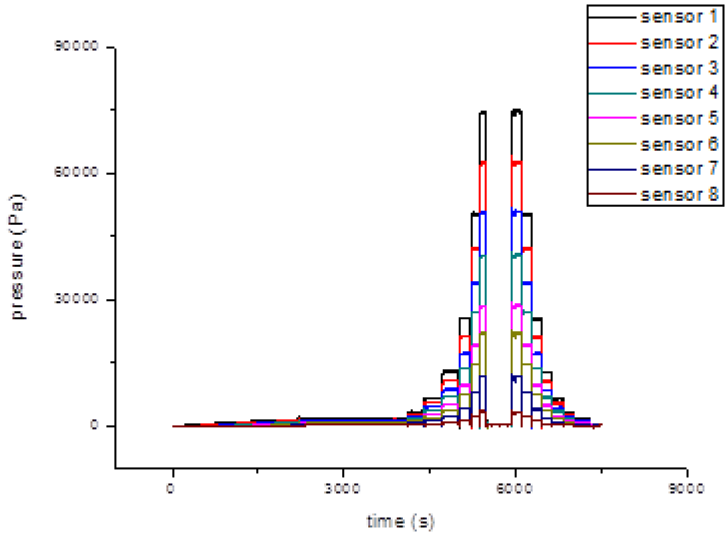

Fig. 2: Pressure profile from flow rate 25 to 50, 100, 200, 400, 800, and 1600 mm^3/s (100cs)

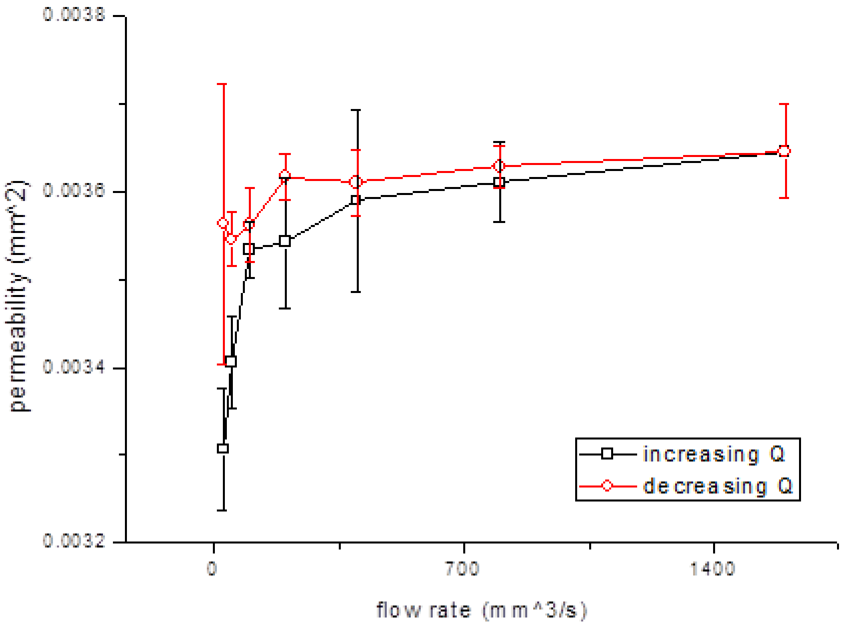

Fig. 3: Permeability behavior of 30cs silicone fluid depending on flow rate

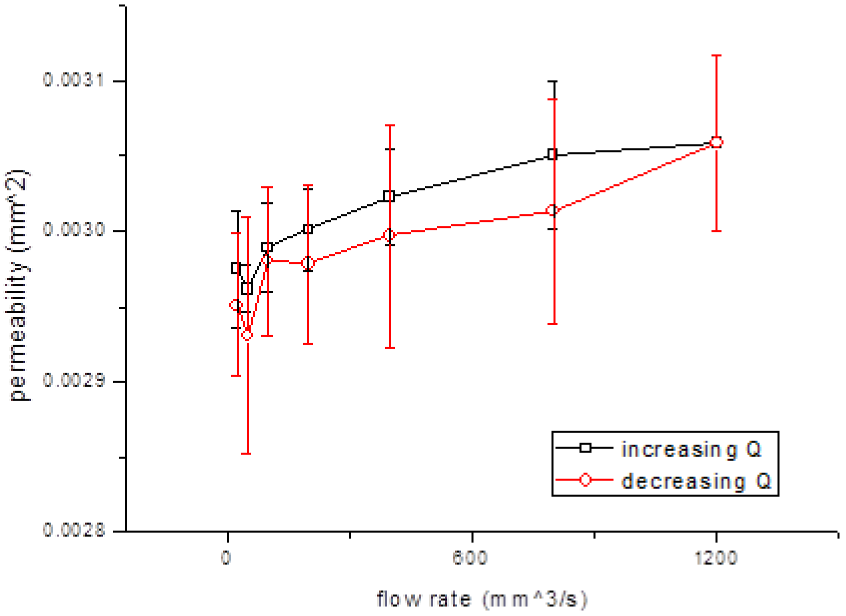

Fig. 4: Permeability behavior of 100cs silicone fluid depending on flow rate

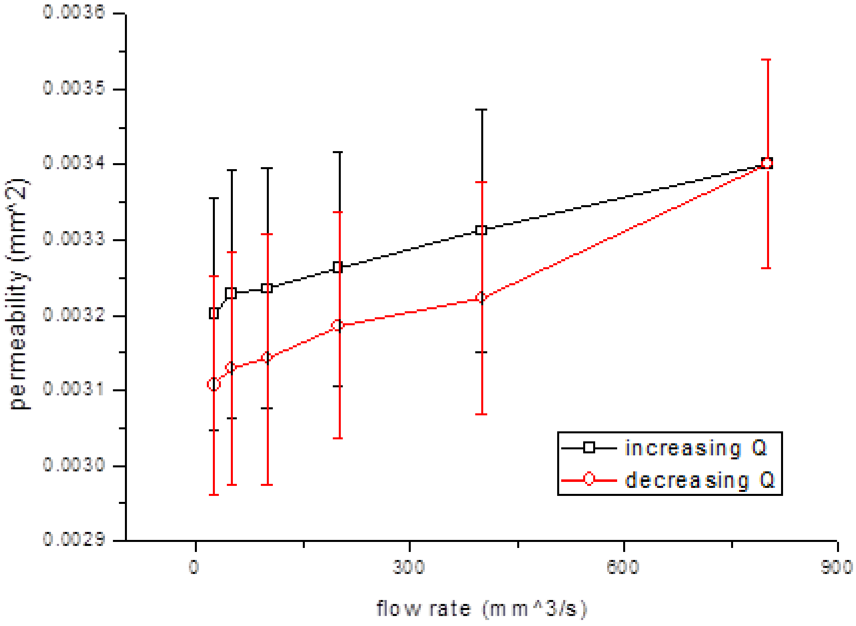

Fig. 5: Permeability behavior of 350cs silicone fluid depending on flow rate

Fig. 3, Fig 4, and Fig. 5 shows the permeability behavior of the 30, 100, and 350cs silicone fluid during the experiment. It can be observed that as the flow rate increases permeability also increases. When the flow rate decreases, permeability change is differed with the viscosities. Silicone fluid of 30cs for decreasing case shows that permeability remains higher value compared to increasing case. In contrast, Silicone fluid of 100cs shows that permeability decreases as flow rate decreases with the lower value compared to increasing case, and this is more obvious in the 350cs case. All three cases show the hysteresis between increasing and decreasing the flow rates.

Observation of void formation and migration in saturated flow

Since the flow rate of all three cases of silicone fluids begin with the low flow rated (25mm^3/s), capillary driven tow area flow will be faster than channel area flow. Because of this velocity difference between two areas, voids are formed in the flow. It can be observed that voids formed at the low flow rate migrate and swipe out through the out let when the flow rate increases (Fig.6). Therefore, we can infer that voids affect the pressure gradient of the saturated flow causing the permeability change in increasing flow rate case.

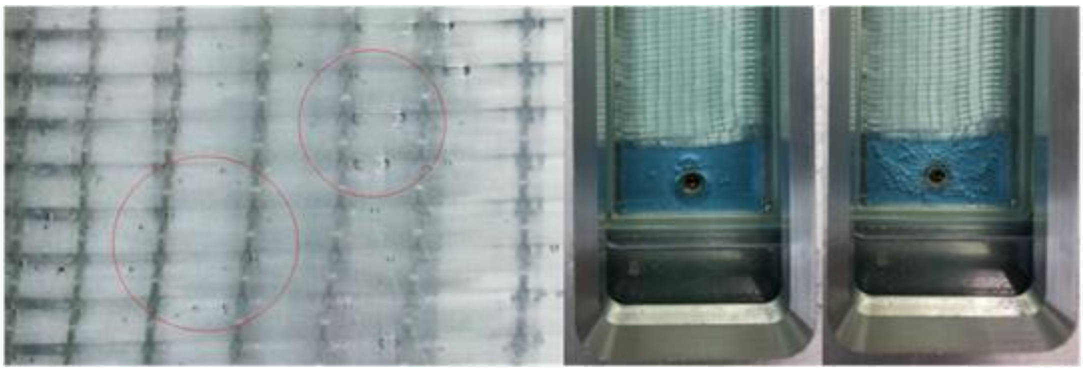

Fig. 6: Void in the saturated flow and void migration when increasing the flow rate

Since the voids are minimized by increasing the flow rate, migration of the voids cannot be observed when decreasing the flow rate. Therefore, difference of the void content in the saturated flow merely affects the permeability change in case of the decreasing flow rate.

In spite of constant void content, there is permeability change in decreasing case of high viscosity fluid. This can be explained by tow deformation caused by resin flow. When flow rate is increased, pressure difference between channel area and tow area increase and shear stress caused by fluid brings about the tow deformation. Shear stress of the fluid is proportional to the viscosity so that we can observe the highest change of permeability in the decreasing flow rate of 350cs silicone fluid case.

CONCLUSIONS

In this work, experimental studies were conducted in unidirectional glass fiber performs to analyze the hysteresis behaviors of saturated permeability depending on flow rate and viscosity in the LCM manufacturing process.

In 30cs silicone fluid case, saturated permeability increases as the flow rate increases. In contrast, it merely changes when decreasing the flow rate. In the 100cs and 350cs silicone fluid cases, saturated permeability increases when the flow rate increases as same as the 30cs case, but it decreased when the flow rate decreases. The decreasing value of the permeability is lower than that of increasing cases, and this is observed more clearly in the 350cs case.

Since we can observe the void formation and migration in the increasing flow rate cases, void might affect the saturated permeability change in the increasing cases. Since there was no void migration in the deceasing cases, the saturated permeability change of the decreasing case can be explained by tow deformation.

Dependence of the saturated permeability on flow rate is affected by combined effect of voids and tow deformations. Separate experiments and mechanisms which can explain the effects of each factor are expected to analyze the hysteresis of saturated permeability.

ACKNOWLEDGMENTS: This research was supported by WCU(World Class University) program through the National Research Foundation funded by the Ministry of Education, Science and Technology (R31-2008-000-10083-0).

REFERENCES

1. N. Patel, V.Rohatgi, and L. James Lee (1995), ‘Micro Scale flow behavior and void formation mechanism during impregnation throug a unidirectional stitched fiberglass mat’, *Polymer Engineering and Science,* 35(10), 837

2. C. Lekakou and M.G. Bader (1998), ‘Mathematical modelling of macro- and micro-infiltration in resin transfer moulding (RTM)’, *Composite Part A*, 29A, 32

3. Joël Breard, Yann Henzel, Francois Trochu and Raymond Gauvin (2003), ‘Analysis of dynamic flows through porous media. Part I: Comparison between saturated and unsaturated flows in fibrous reinforcements’, *Polymer composites*, 24(3), 391-408

4. Pillai, K.M. (2004), ‘Experimental investigation of the effect of fiber-mat architecture on the unsaturated flow in liquid composite molding’, *Journal of Composite Materials*, 38(23), 2097-2118

5. Dungan FD and Sastry AM (2002), ‘Saturated and unsaturated polymer flows: Microphenomena and modeling’, *Journal of Composite Materials*, 36(13), 1581-1603

6. Chung Hae Park, Aurelie Lebel, Abdelghani Saouab, Joel Breard, Woo Il Lee (2011), ‘Modeling and simulation of voids and saturation in liquid composite molding processes’, Composites part A-applied science and manufacturing, 42(6), 658-668

PERMEABILITY PREDICTION OF FIBROUS POROUS MEDIA WITH COMPLEX 3D ARCHITECTURES

Hai Long Liu and Wook Ryol Hwang

School of Mechanical Engineering, Research Center for Aircraft Parts Technology (ReCAPT), Gyeongsang National University, Gajwa-dong 900, Jinju, Korea, 660-701 Corresponding author's e-mail: wrhwang@gnu.ac.kr

ABSTRACT: We present a new three-dimensional finite element technique to solve flows in a representative porous volume with fibrous microstructures, which employs a fictitious domain method to deal with immersed microstructures and a mortar-element method to satisfy rigorously the tri-periodic boundary condition for the representative volume element. Through the extensive numerical simulations for various fiber and fabric architectures, we investigate the relationship between the permeability and fiber architectures in order to seek a reasonable approximation method in estimating the permeability of complex architectures. Specifically we discuss the applicability and limitation of a macroscopic permeability averaging rule in estimating those of complex microstructures, using the information of simple structural building blocks. We then investigate the Kozeny constants of various microstructures for a wide range of the fiber volume fraction, which may facilitate simple permeability estimation of complex 3D porous structures using the Kozeny-Carman model.

KEYWORDS: *Computational modeling, Microstructures, Resin transfer moulding (RTM)*

INTRODUCTION

A wide variety of environmental and technological processes involve problems of a viscous flow through porous media, such as filtration, spreading of contaminants in soil, enhanced oil recovery, and composites manufacturing. Among them, we are interested in composite manufacturing, specifically the liquid composite molding (LCM) processes (e.g., RTM, VARTM, SRIM), which have been considered attractive techniques to produce large-scale structural parts or products with good surface at a relatively low tooling cost [1]. In these processes, a fabric reinforcement, which is either an assembly of unidirectional fiber filaments or of stitched fiber strands, is placed in a closed mold and then uncured resin is infused by an assigned pressure or vacuum to infiltrate the fabric reinforcements. Therefore the accurate prediction of the resin permeability is of great significance in setting up process parameters for successful processing and to avoid unsaturated parts. A proper estimation method based on physical understanding of the micro-scale flow that could bridge the permeability and the complex porous microstructure is particularly necessary especially for thick composite parts or 3D textile reinforcements.

In this work. We investigated the relationship between the permeability and fiber architectures to establish a proper approximation method in estimating the permeability of complex architectures for a wide range of the solid volume fraction. Specifically, we discuss the applicability and limitation of the macroscopic permeability averaging rule in predicting those of micro-structured systems using the permeability of simple structural building blocks. Finally, we investigate the Kozeny constant of various microstructures for a wide range of the fiber volume fraction, which might facilitate simple permeability estimation for complex structured systems using the Kozeny-Carman model, a commonly employed method to account for the permeability dependence on the solid fraction.

MODELING AND NUMERICAL METHODS

The macroscopic Darcy's equation is commonly employed to model slow resin flows through the fibrous reinforcement:

$$\bar{\boldsymbol{u}} = -\frac{\boldsymbol{K}}{\eta}\cdot\nabla p \tag{1}$$

Where $\bar{\boldsymbol{u}}$, $\boldsymbol{K}$, η and p are the averaged superficial fluid velocity, the permeability tensor, the fluid viscosity and the pressure, respectively. The permeability tensor is a measure of the fluid conductance capability in porous media. In the Cartesian coordinate system when the coordinate axis coincides with the principal direction of a porous body, the second-order permeability tensor reduces to a diagonal matrix as $\boldsymbol{K} = \mathrm{diag}\left(K_{xx}, K_{yy}, K_{zz}\right)$. In the LCM process with thin composite parts, two principal values of the permeability tensor in larger dimensions are often referred to as the in-plane permeability and the remaining one as the transverse (through-thickness) permeability. From Eq. (1), the permeability tensor can be obtained by solving the flow problem and measuring the flow rate for a given pressure drop in the model porous system.

Equations for the momentum balance of a Newtonian fluid and the continuity over the entire domain, including the interior of the solid body, are

$$\eta\,\nabla^2\boldsymbol{u} = \nabla p, \tag{2}$$

$$\nabla\cdot\boldsymbol{u} = 0, \tag{3}$$

the symbols $\boldsymbol{u}$, p, and η are the velocity , the pressure and the viscosity, respectively. We remark that the balance equations are satisfied even in the interior of the solid body due to the rigid shell description, with which the solid body is identified by the zero velocity condition on its boundary. For the boundary condition, the periodicity is assigned in all the three directions and it can be expressed in terms of the velocity continuity over the periodic boundary. In addition to the periodicity, we assign a uniform pressure difference, the driving force of the flow along one principal direction.

In terms of numerical technique, this work is a 3D extension of the authors' previous works, Wang and Hwang [2,3] for the permeability prediction in a bi-periodic domain. Following their approach, one can derive a weak form of the Stokes flow around immersed solid bodies in a tri-periodic domain. For the discretization of the weak form, we use a regular cubic element over the entire computational domain. We employ a tri-quadratic interpolation for the velocity, and a linear discontinuous interpolation for the pressure. In implementing the discretization methods discussed above, an equation with a large symmetric sparse matrix is obtained. We employ a sparse massively parallel multi-frontal direct solver (MUMPS) with the message passing interface (MPI) to solve the matrix system

RESULTS AND DISCUSSIONS

Permeability of 3D architectures

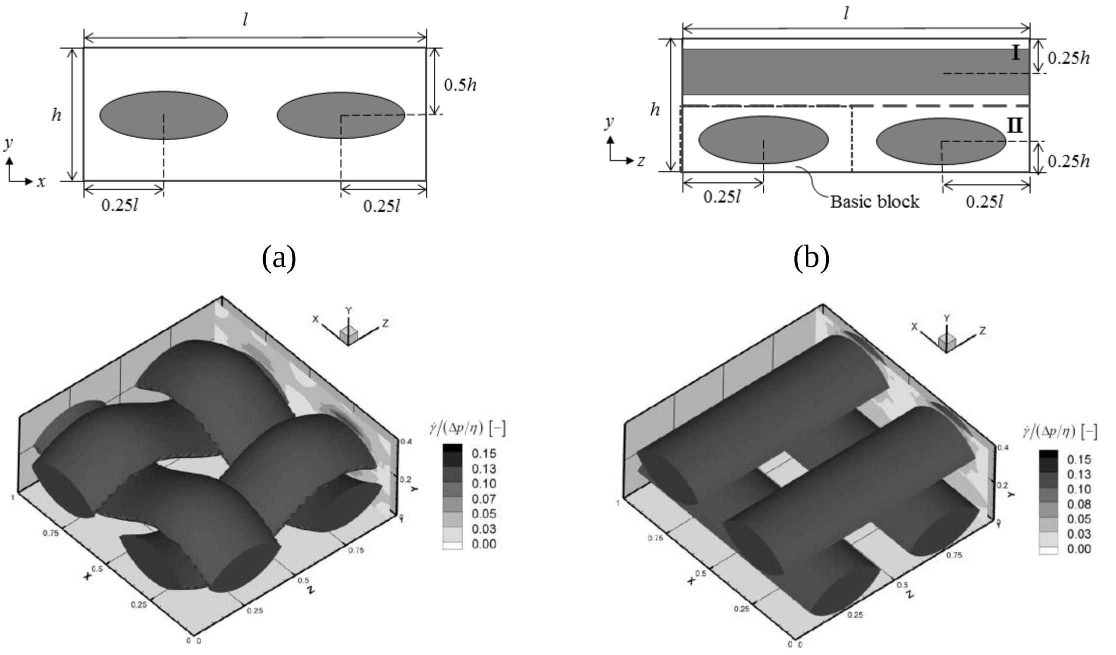

(a) (b)

(c) (d)

Fig. 1: The spatial configuration of (a) plain woven fiber tows and (b) cross-ply fiber tows; (c) the plain woven fiber tow geometry with shear rate distribution; (d) the non-woven cross-ply fiber tows with shear-rate distribution.

The plain woven fabrics with wavy solid tows (Fig. 1(c)) and the cross-ply fiber tows (Fig. 1(d)) in the RVE are investigated. Figs. 1(a) and 1(b) show the cross-sectional configurations of solid fiber tows in each case. The dimensions of RVE in both cases are $l = 10\,[mm]$ and $h = 4\,[mm]$. Plotted in Fig. 2 are the normalized in-plane and transverse (through-thickness) permeability for both structures, as a function of the fiber fraction. In case of the woven fabrics, the in-plane permeability appears consistently higher than the transverse component, up to approximately 250% when highly packed. For the cross-ply fiber tow structure, however, the difference between transverse and in-plane components is very minor: the in-plane permeability is at most 15% larger than the transverse component at high volume fractions.

Furthermore, we tested the averaging rule for the cross-ply fiber tow geometry as well in predicting the in-plane permeability. As shown in Fig. 2(b), the cross-ply tows are decomposed into the subdomain I with two elliptic tows parallel to the flow and the subdomain II with two elliptic tows transverse to the flow. Each subdomain can be considered again as a composite system consisting of an elliptic tow in a rectangular box, which is identified as the basic building block in this case. The in-plane transversal permeability $K_{\perp}$

and the in-plane longitudinal permeability $K_{\parallel}$ of the basic building block are plotted as well in Fig. 2 for a wide volume fraction. The permeability in the subdomain I is $K_I = K_{\parallel}$ and the permeability in the subdomain 2 is estimated as $K_2 \approx K_{\perp}$. Therefore, the effective in-plane permeability of the total cross-ply tows becomes $K_{xx} \approx \left(K_{\perp} + K_{\parallel}\right)/2$. The in-plane permeability from this simple estimation shows a good agreement with direct numerical simulations in this case.

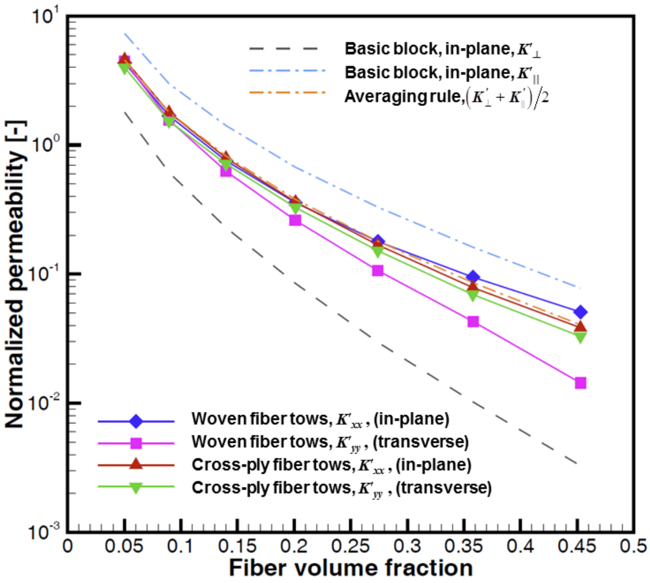

Fig. 2: Permeability of the woven and the non-woven cross-ply fiber tows as a function of the fiber fraction. The estimated in-plane permeability by the macroscopic permeability rule is $K_{xx} \approx \left(K_{\perp} + K_{\parallel}\right)/2$.

Dependence of Kozeny constants on fibrous architecture and fiber fractions

The Kozeny-Carman model is widely used to characterize the relationship between the permeability and the fiber volume fraction. This model can be expressed in the simplest form as [1]:

$$K = A\frac{\left(1-V_f\right)^3}{V_f^{\,2}}, \tag{4}$$

where V_f is the fiber volume fraction and K is the permeability. The parameter A is the Kozeny constant that accounts for all the complexities of microstructures. Although it was developed for granular beds for the isotropic permeability, the Kozeny-Carman model has turned out very useful for its simplicity. As for the last section, it would be worthwhile to present the normolized Kozeny constants from our simulations for all the porous architectures investigated in this work as a function of the fiber fraction. Fig. 3 shows that all the Kozeny constants of the 3D architectures are valued between two limiting cases of the transversal and in-plane permeability of the regular square packing fibers and they increases gradually with the fiber volume fraction, except for the cases of the transverse (through thickness) permeability in cross-ply fibers and in woven fiber tows architectures. The Kozeny constant varies significantly with the fiber fraction, which implies that care should be exercised in employing the Kozeny-Carman model for the prediction of the permeability. The only exception is the permeability of the transverse permeability of the woven fiber tow geometry which is almost on a plateau for a wide range of solid volume fraction.

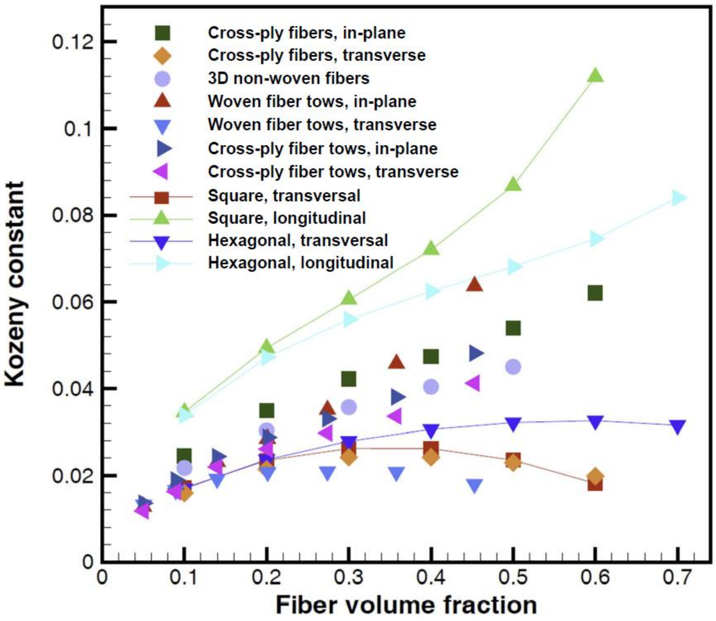

Fig. 3: The Kozeny constant with respect to the fiber fraction for the various 3D fiber and fiber tow architectures.

CONCLUSIONS

In this work, we presented an efficient finite-element scheme for flows in 3D micro-structured porous media which is particularly well suited with the unit cell flow simulations in a tri-periodic RVE. Extensive numerical simulation results for various fiber and fiber tow geometries, including unidirectional, cross-ply, 3D orthogonal fibers and non-woven and woven fiber tows, for their permeability with the dependence on the fiber fraction, have been studied and the variations of the Kozeny constant for all the porous architectures in this work on the fiber architectures and fiber fractions have been investigated.

ACKNOWLEDGMENTS: This work was supported by the National Research Foundation of Korea (NRF) funded by the Ministry of Education, Science and Technology (2011-0031383 and 2010-0021614).

REFERENCES

1. Advani SG, Sozer EM (2002). Process modeling in composite manufacturing, New York: Marcel Dekker Inc.

2. Wang JF, Hwang WR (2008). Permeability prediction of fibrous porous media in a bi-periodic domain, *Journal of Composite Materials*, 42(9), 909-929.

3. Wang JF, Hwang WR (2011). Transverse mobility prediction of non-Newtonian fluids across fibrous porous media, *Journal of Composite Materials*, 45(8), 883-893.

Section 2

Voids, Dual-scale and Capillary Flows

EXPERIMENTAL DETERMINATION OF VOID FORMATION AND TRANSPORT IN THE RTM PROCESS

Sébastien Guéroult [1], Laurent Bizet [1] and Joël Bréard [1]

[1] *LOMC, CNRS UMR 6294, Université du Havre, 53 rue de Prony, 76600, Le Havre, France*
Corresponding author's e-mail: sebastien.gueroult@univ-lehavre.fr

ABSTRACT: The RTM (Resin Transfer Molding) process is a technological solution that enables the production of high quality structural composites. Defects in the form of voids are formed during the injection process. These defects are detrimental to the final mechanical properties of the composite materials. Thus, it is important to control their formation and transport. Depending on their relative size and location within the preform, these voids can be classified in two categories and they are named microvoids and macrovoids. In this study, all the injections were carried out longitudinally in an experimental device designed to replicate the conditions of an RTM process. Two model liquids were chosen to replace the thermosetting resins that are traditionally used in the injection processes. A network of sensors dynamically measured the evolution of the saturation in the mould. A homemade conductivity sensor was used for conductive liquids in combination with insulating material such as glass fibre preforms. Alternatively, a homemade permittivity sensor was developed for insulating materials such as unidirectional glass fibres and silicone oil. The evolution of the saturation profiles as a function of time and place was measured at constant pressure and flow rate. Both techniques generate data describing the saturation and the void formation and transportation. The results are consistent with models from the literature that describe the macrovoids for low capillary numbers, the microvoids for high capillary numbers and a minimum of voids for an optimal capillary number.

KEYWORDS: Resin Transfer Molding, Void, Saturation, Sensor.

INTRODUCTION

RTM (Resin Transfer Molding) is an elaboration process for composite materials. The resin mixed with the catalyst is injected into a closed mold containing the fiber preform. The main problems of this type of process are the formation of dry areas due to poor filling strategy and the creation of voids. The latter ones weaken the mechanical properties of the final product [1]. These voids are of two sizes according to their location and may be appointed as macrovoids and microvoids. This bubble formation comes from the dual scale of porosity in fibres media [2-3]. Macropores correspond to the spaces between tows and micropores, the intra-tows spaces. The empty spaces present in the macropores in the final composite will be appointed as macrovoids and those present in the micropores will be called microvoids.

Imposed injection pressure or imposed flow rate leads to a difference of permeability between tows and inside tows. In the macropores, the resin flows more easily and thus the permeability is higher. At the opposite, in the micropores, the permeability is lower and capillary effects become more important. The RTM injection parameters will primarily condition the presence of microvoids or macrovoids in the material [3-4]. In the case of low fluid velocity, capillary effects will participate in the flow inside the tow and macrovoids should appear. Otherwise, there will be presence of microvoids.

Instead of connecting directly the rate of microvoids and macrovoids during their transport to flow parameters such as fluid velocity, various authors [5-6] proposed a dimensionless number called capillary number (Ca) which takes into account the forces due to fluid viscosity and surface tension:

$$\mathrm{Ca} = \frac{\mu v}{\gamma} \tag{1}$$

where μ represents the dynamic viscosity of the fluid, ν its velocity and γ its surface tension. Macrovoids and microvoids content are usually represented as a function of capillary number. Then an optimal capillary number appears for a minimum void content. This modified adimensional number highlights the importance of the wettability parameters in the RTM process. It has been found experimental laws that give the void content as a logarithm function of this modified capillary number. The measurement of the void rate usually consists in using a destructive control of composite samples [5]. The empirical laws of void rate as a function of Ca have then been used in the implementation of numerical models predicting the void content in RTM.

This work proposes a network of saturation sensors inside the mold in order to measure the void formation and transport during RTM injection. This paper describes the two types of used sensors and the first results obtained with them.

MATERIAL AND METHODS

Experimental device

The experiment device allows to model an RTM injection and consists of a lower plate in steel and an upper mold made of glass for the visualization of the flow. The lower part of the mold is adjustable between two experiments in order to define the thickness of the preform. This thickness was set to 0.0026 m for the presented experiments. The other dimensions for the cavity of the mold are a length 0.550 m and a width of 0.140 m. The sealing all around the preform is ensured by a compressible silicone sheet. The bottom steel plate is marked by several pressure transducers. Four saturation sensors described in detail in the following paragraph are placed in the mould at the positions 0.04 m, 0.160 m, 0.280 m and 0.390 m from the beginning of the preform.The injections are unidirectional through the length of the preform. The liquid flow is obtained either by a constant injection pressure system where injection pressure can be adjusted in a range from 0 to 3.10^5 Pa or at constant flow rate where the maximum allowed pressure in the mould is 3.10^5 Pa.

Materials

All experiments are performed with preforms of unidirectional glass fabrics and model liquid whose characteristics are summarized in Tab. 1. The fluid models used are either silicone oil or a mixture of water, glycerol and surfactant in order to approach the characteristics of conventional resins.

Table 1: Liquid and preform characteristics

Model liquid	Permittivity	Viscosity (mPa.s)	Surface tension (mN.m^{-1})	Contact angle (°)	**Preform**	Unidirectional glass fabrics
Water	80	1	72	~ 0	Areal weight	646g.m^{-2}
Glycerol	--	1490	63	80	Volume fraction of fibres	50,4 %
Water/glycerol/ surfactant	--	132	46,96	45	Density	2,6
Silicone oil	4.71	100	20.9	15	Saturated permeability at Vf=50.4%	8.61.10^{-10} m²

Saturation sensors

Theory

Saturation sensors are based on the electrical properties of the materials such as conductivity and dielectric properties [7-8]. The sensors are formed by two electrodes whose dimensions are 60mm*5mm*0.05mm and glued on the upper and lower parts of the mould. One electrode is linked to a power generator and the other, to a reference. Depending of the electrical properties of the model liquid, two types of sensors are used. They are both based on the electrical system described Fig. 1.

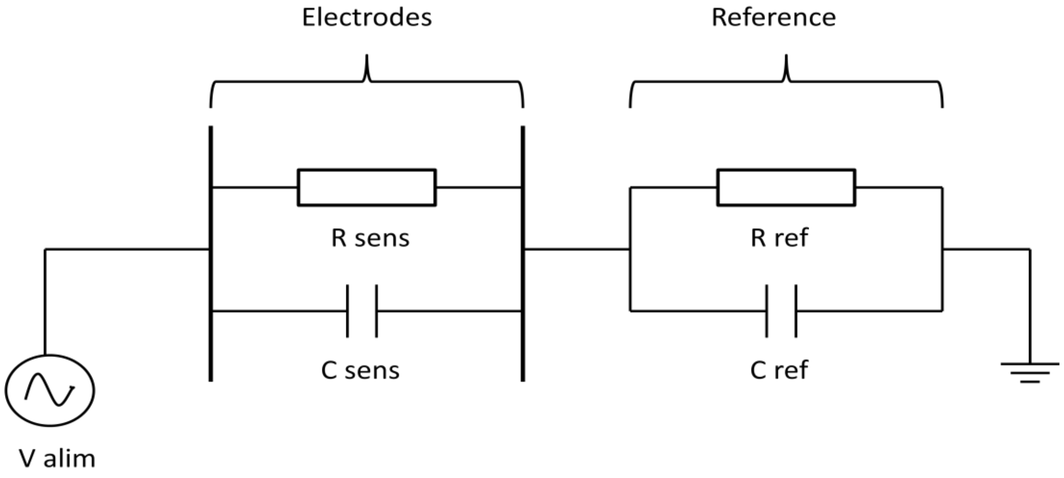

Fig. 1: Electrical system

As it appears on Fig. 1, the reference is made of a resistor and a capacitor in parallel. The tested materials between the electrodes are also represented by a resistor and a capacitor in parallel. The sensor and reference impedances are:

$$Z_{sens}(t) = \frac{1}{\frac{1}{R_{sens}}+i\omega C_{sens}} \quad Z_{ref}(t) = \frac{1}{\frac{1}{R_{ref}}+i\omega C_{ref}} \tag{2}$$

where C_{sens} and R_{sens} are respectively the capacity and the resistivity between the two plates of the sensor and C_{ref} and R_{ref} , the capacity and the resistivity of the reference. In the case of a low frequency, the capacitive part is negligible compared to the resistive part leading to a conductivity sensor:

$$R_{sens} = R_{ref} \frac{V_{meas}}{V_{alim} - V_{meas}} \tag{3}$$

where V_{alim} is the alimentation voltage and V_{meas}, the voltage measured by the acquisition system over the reference. At high frequency, the resistive part is neglected in front of the capacitive part:

$$C_{sens} = C_{ref} \frac{V_{alim} - V_{meas}}{V_{meas}} \tag{4}$$

Knowing the length A and width d of the sensor plates, the permittivity measured by the sensor is described as:

$$C_{sens} = \frac{\varepsilon_r \varepsilon_0 A}{d} \tag{5}$$

where ε_r and ε_0 are respectively the relative and void permittivity. The sensor works as a dielectric sensor. Depending of the electrical properties of both the model liquid and the preform, the sensor can be used either as a conductivity sensor for conductive model liquid and insulating fibers or as a dielectric sensor for any other combination.

Link between conductivity sensor and saturation

If a conductivity sensor is used in a conductive liquid with insulating fibers, then the conductivity decreases with the void ratio. As proposed by [7], there is a linear relationship between the measured voltage and the void ratio therefore with the saturation of the fibrous preform S:

$$S = a * \ V_{meas} \tag{6}$$

Saturation is then available as the ratio between voltage measured at time t and voltage V_{max} obtained when the fiber preform is fully saturated:

$$S = \frac{V_{meas}}{V_{max}} \tag{7}$$

The maximal voltage is determined before each experiment with a calibration curve because fiber content and maximum voltage are proportionally related.

Link between permittivity sensor and saturation

For the dielectric sensor, the objective is to link the permittivity with the void fraction. Many studies concern the physical behavior of heterogeneous materials or mixtures and especially their permittivity. Most studies details the permittivity of each component separately and the structural properties of the mixture itself (percentage of each component, form of the components, etc). A formula for dielectric mixtures where inclusions are contained in a media

[9] is used for fiber preform and model liquid with air bubble leading to the calibration curve given in Fig. 2.

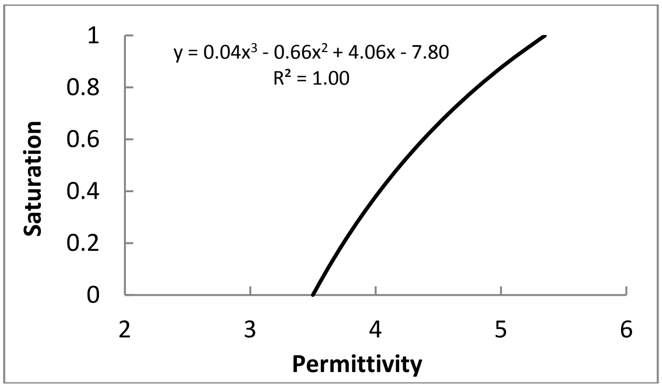

Fig. 2: Calibration curve for the dielectric sensor with silicone oil

This calibration curve depends on the permittivity and geometry of the different materials. Fibres are considered as infinitely thin cylinders and air bubble as perfect sphere

EXPERIMENTAL RESULTS

Saturation curves

The first series of experiments was performed with a mixture of water, glycerol and surfactant in a preform of unidirectional glass fabrics at V_f=50.4% with the following dimensions: length of 0.430 m and width of 0.100 m. In the case of injections at constant pressure, the pressure values range between $0.6.10^5$ and 2.10^5 Pa. In case of injection at constant flow rate, the flow rate is chosen between 1.7 cm³/min and 5.3 cm³/min. The conductivity sensor is used to measure the saturation. The second series of experiments only change by the use of silicone oil. The permittivity sensor is used to measure the saturation. Fig. 3 presents two sets of curves chosen among all experiments. Both graphs give the saturation as a function of time for the four conductivity or permittivity sensors at the different locations inside the preform.

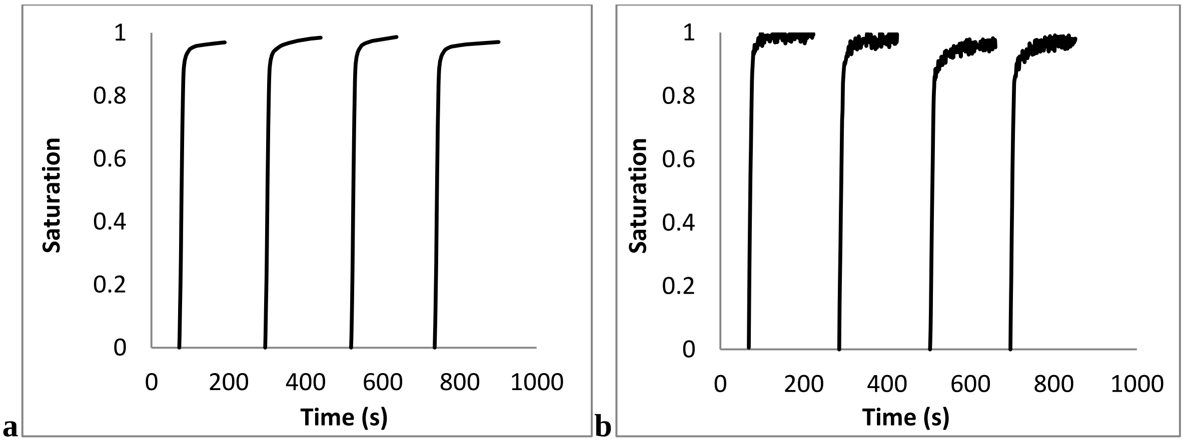

Fig. 3: Saturation profiles for water/glycerol mixture at constant flow rate (conductivity) (a) and silicone oil (permittivity) (b)

Each experimental profile of saturation can be divided in three steps. The first step corresponds to the filling of the electrode volume and ends when the liquid front leaves the volume between the sensor electrodes. During this step, the delay between flows within and between tows will generate a different evolution of the saturation. Bubbles are created because the liquid passes the sensor leaving unfilled pores. Then the curve presents an inflection point which corresponds to the apparition of both bubble compression and transport. The third step corresponds to a steady state where the saturation will not evolve anymore. All bubbles able to move have already been transported out of the preform.

Knowing the fluid velocity during the experiment and considering that the variation of permeability is negligible, then the saturation curves as a function of time can be transformed in saturation curves as a function of the position for each sensor. The reference position is chosen as the sensor position and the reference time is chosen when the front has passed the saturation sensor (Fig. 4).

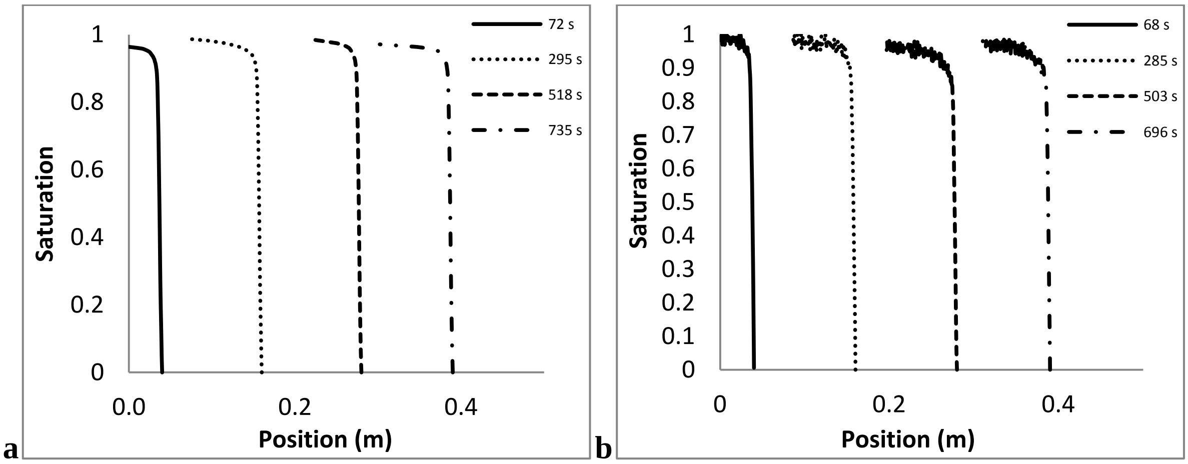

Fig. 4: Saturation profiles for water/glycerol mixture at constant flow rate (conductivity) (a) and silicone oil (permittivity) (b) as a function of the position

Each curve gives information on the distribution of saturation as a function of the position at a given time. This time correspond to the model liquid leaving the sensor location.

Void formation

Voids are formed during the first part of the saturation curve. When the front has passed the saturation sensor, the saturation curve presents the inflexion described earlier and the maximum void content can be extracted at this point. Each void content, whether obtained at constant pressure or constant flow rate, is plotted against the corresponding capillary number (Fig. 3). The capillary number is obtained from the position of the front as a function of the fluid velocity and the characteristics of the model liquid. The advantage of injection at constant pressure lies in the fluid velocity variation during one experiment. With four sensor locations, one can obtain four points on the Fig. 5 during one experiment with different void contents and types of voids. With constant flow rate there is only one point which is the average of the four sensors.

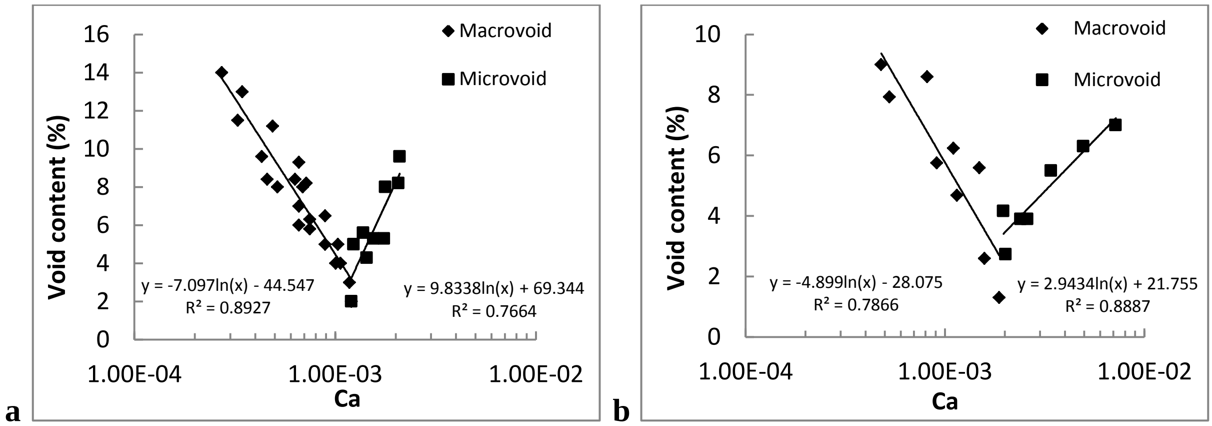

Fig. 5: Maximum void content as a function of capillary number for water/glycerol mixture (a) and silicone oil (b)

Curves are consistent with the bibliography [5,7]. There is an optimal capillary number at the order of $1.23.10^{-3}$ for water/glycerol and 2.10^{-3} for silicone oil. At this optimal capillary number, the minimal void fraction is different from zero. This difference may be explained by imperfections of the preform: imperfect weaving, compression of tows, etc. resulting in a slightly different distribution of macro and micropores and leading to the creation of voids. By adding the experimental errors, one can explain the dispersion of the results.

Void transport

Transport of voids can be evaluated by the comparison between the voids created and the voids at the end of the experiment at the same position when saturation does not evolve anymore. Results are given for different injection pressures on Fig. 6. Low pressure value ($0.6.10^5$ Pa) corresponds to the formation of macrovoids whereas high pressure value ($1.6.10^5$ Pa) relies to the formation of microvoids.

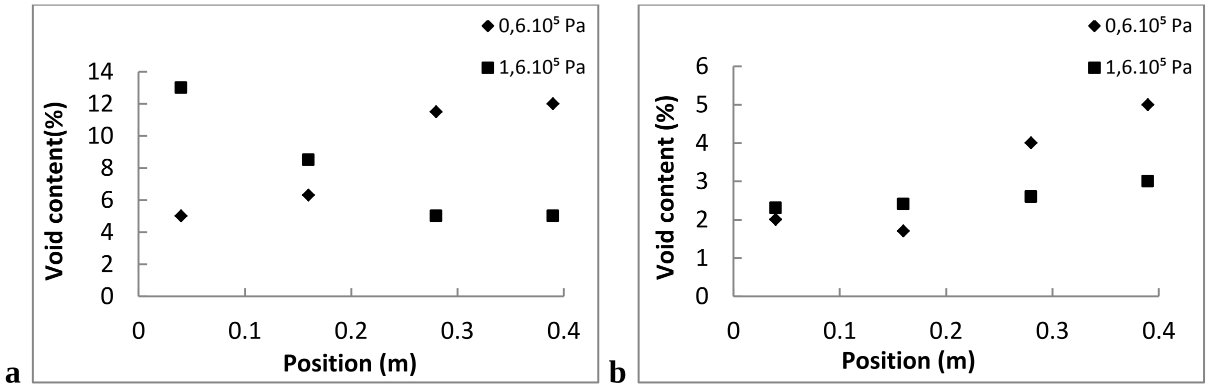

Fig. 6: Void content as a function of position for water/glycerol mixture: created voids (a) and final voids (b)

According to the literature [3-4], bubbles should be compressed and moved to the vent by the increase of the local pressure during the experiment. It is therefore quite normal to observe a greater saturation at the end of the experiment than at the beginning. The final void distribution varies with the injection pressure. At low pressure, the void content is a step function with a highest value in the second part of the preform. For higher pressure, the final void distribution is almost constant. These void evolutions are also observed with silicone oil experiments. These results suggest different transport phenomena for microvoids and macrovoids.

CONCLUSION

The aim of the study was to provide new technical solution and new results for the measurement of saturation in RTM processes. With a network of electrical sensors, information is obtained on saturation at given time and position. The sensors can be used a broad range of liquids and preforms. The conductivity sensor can be used for conductive liquid and insulating preform and the dielectric sensor can be used for other combinations of materials. Results obtained with sensors are consistent with literature. Experimental void content as a function of capillary number is similar to previous numerical results. The experimental optimal capillary number around 10^{-3} falls within the range of values proposed in the literature.

REFERENCES

1. Varna J et al (1995), ‘Effects of voids on failure mechanisms in RTM laminates’ *Composites Science and Technology,* 53(2), 241-9

2. Patel N, Lee LJ (1995), ‘Effects of fiber architecture on void formation and removal in LCM’, *Polymer Composites,* 16 (5), 386-399.

3. Breard J et al (2003), ‘Analysis of dynamic flows through porous media. Part I: Comparison between saturated and unsaturated flows in fibrous reinforcements’, *Polymer Composites,* 24(3), 391-408

4. Patel N, Rohatgi V, Lee LJ (1995), ‘Micro scale flow behavior and void formation mechanism during impregnation through a unidirectional stitched fibreglass mat’, *Polym Eng Sci,* 35(10), 837-851

5. Leclerc J. S., Ruiz D, (2008), ‘Porosity reduction using optimized flow velocity in Resin Transfer Molding’ *Composites: Part A,* 39, 1859-1868

6. Lee D. H., Lee W. I., Kang M. K. (2006), ‘Analysis and minimisation of void formation during Resin Transfer Molding process’ *Composites Science and Technology*, 66, 3281-3289

7. Labat L., Bréard J., Pillut-Lesavre S., Bouquet G (2001), ‘Void fraction prevision in LCM parts’ *The European Physical Journal Applied Physics,* 16, 157-164

8. Yenilmez B, Sozer E.M, (2009), ‘A grid of dielectric sensors tom monitor mold filling and resin cure in resin transfer molding’ *Composites: Part A,* 476-489

9. Sihvola A, (1988), ‘Effective permittivity of dielectric mixtures’ *IEEE Geosciences and remote sensing*, 26(4), 420-429

THEORETICAL AND EXPERIMENTAL MODELLING OF BUBBLE FORMATION WITH CONNECTED CAPILLARIES IN LIQUID COMPOSITE MOULDING PROCESSES

Yanneck Wielhorski, Amine Ben Abdelwahed, Laurent Bizet and Joël Bréard

Laboratoire Ondes et Milieux Complexes, LOMC, UMR 6294 CNRS, 53 rue de Prony, BP 540, 76058 Le Havre, France
Corresponding author's e-mail: yanneck.wielhorski@univ-lehavre.fr

ABSTRACT: The void prediction in LCM processes sparks off interest within the composite material industry because it is a significant issue to keep the expected mechanical properties. The liquid properties, the preform geometry and the flow conditions impact the quantity of void entrapped inside the final product. The complex geometry of the reinforcement due to the arrangement of the bundles and the fibres is a key point to understand and quantify this phenomenon. This paper deals with both simple model networks which can occur inside a fabric representing connected capillaries, so-called "Pore Doublet Model (PDM)". A first is considering two capillaries converging on a node (T-junction) and a second is representing two capillaries interconnected with a supplying principle. These configurations can affect locally the evolution of flow fronts. First, experiments of bubble formed in a T-junction device have been performed and studied. Then a theoretical approach was proposed to forecast microvoid and macrovoid formation, by taking into account a supplying principle and arranged Washburn equation in forced filling.

KEYWORDS: *LCM, Void, Imbibition, Pore Doublet Model, Supplying principle, Filling*

INTRODUCTION

The well-known LCM processes refers to composite manufacturing techniques where a resin is injected through a fibrous preform. During this process, the void formation can occur and gas (air) bubbles are also entrapped (Fig. 1.*i*), decreasing therefore the mechanical properties of the final composite material. The origins of this phenomenon stem mainly, on a one hand, from the complex geometry of the reinforcement and, on the other hand, the wetting properties between liquid and solid. The fibrous preform is often represented with mainly two pore scales: a macroscale between the bundles and a microscale within the bundles and then the flows are governed differently according to the scale, either by the Laplace pressure inside the tow or by the viscous force between the tows. Hence, the bubble formation can be explained by the competition between the capillary and the viscous forces that are compared inside the capillary number *Ca*. Indeed, these both kinds of flow induce locally a difference between the front positions leading consequently to the bubble formation that can be summarized as follows: the intra-tow void, so-called microvoid, which is located inside the bundle and the inter-tow void, also called macrovoid, between two consecutive bundles. More precisely, the microvoids occur at high capillary number *Ca* because the viscous flow overcomes the capillary forces whereas the macrovoids are obtained at lower *Ca* because the capillary pressure dominates the viscous pressure.

To quantify the void and attempt to minimize its rate inside composite materials, many experimental studies have been carried out [1-4]. However, it is often difficult to visualize bubble formation and transport during the LCM process. Therefore, to determine the final saturation, numerical works [5], experimental and theoretical studies in porous Pore-Doublet Model [4, 6] are ways to get round this difficulty. The latter is a widely used modelling to understand the dynamic of immiscible fluids in porous media [7, 8].

In this paper, we attempt to underline the influence the wetting effect and geometrical configuration on capillary flow on the bubble formation by using two “Pore Doublet Models”: a T-junction device (Fig. 1.*ii*) and two parallel capillaries first continuously interconnected over a variable distance then connected by nodes (Fig. 4).

First, to study the wetting influence on bubble shape and length, we performed experiments by using T-junctions devices [6, 9-11] based on the physical mechanism of cross-flowing streams. Moreover, this is widely used as well in microchemical engineering as in microbiology so that obtain, for instance, calibrated and controlled amounts of liquids (reagents, polymer, etc.). This kind of device allows to study interactions between two immiscible fluids (liquid/liquid or liquid/gas) by converging a dispersed phase (break-up stream) with a continuous phase (shear stream). Two main regimes can be distinguished: the squeezing and the dripping regimes respectively based on confined and unconfined breakup mechanisms. The squeezing regime, occurring at low *Ca*, in which the interfacial force overcomes the viscous shear stress and thus the bubble is usually quite longer than the channel width (slug bubbles), will be showed here.

Secondly, we emphasise the supplying principle arising from the bulk provided by the macrochannel, which plays the role of a tank, to the microchannel [4, 6, 12]. A theoretical model will be presented by taking into account supplying principle within interconnected capillaries.

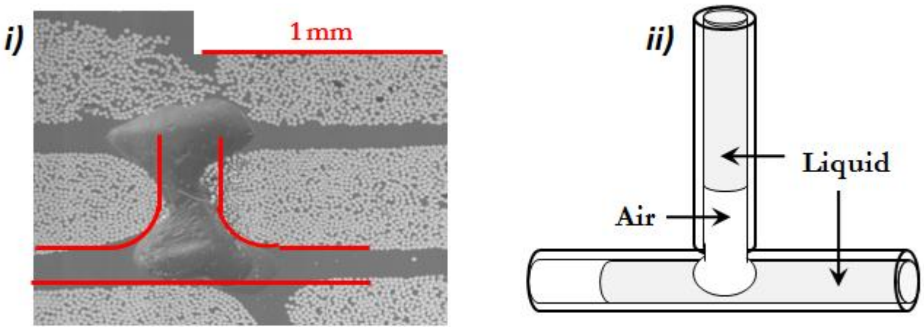

Fig. 1: *i)* Transversal view of a composite material with an entrapped air bubble and *ii)* its equivalent model sketch.

BUBBLE FORMATION WITHIN PORE DOUBLET MODELS

T-junction device

In order to investigate the advance-delay effect involved in bubble production phenomenon in LCM processes, we have carried out experiments converging two immiscible fluids in a cylindrical T-shaped junction device (Fig. 2a) with inner radius of R_c = 0.5mm and 1.0mm.

The injections are controlled by two syringe pumps and we name the flow rates of the continuous phase (either silicone oils or a glycerol/water mixture) and the dispersed phase (gaseous phase) respectively Q_1 and Q_2 (Fig. 2a). This simple device allows to create a steady train of calibrated bubbles by controlling both injection flow rates. An example of a confined breakup mechanism is showed in Fig. 1b for silicone oil 47V100 with a relatively low cross flow rate about 0.83µL.s^{-1}. A bubble emerges at the T-junction and grows as far as the opposite wall (Fig. 2b.*i*). The bubble neck is then pinched (Fig. 2b.*ii*) and breaks up (Fig. 2b.*iii*). The created bubble is then carried away by the cross flow.

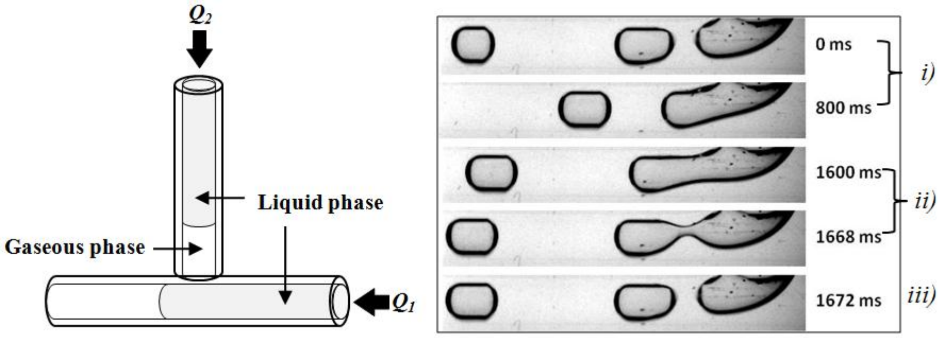

a) **b)**

Fig. 2: (a) Sketch of the gas entrapped at the T-junction; (b) Bubble formation mechanism: *i)* filling phase, *ii)* squeezing phase and *iii)* break-up.

Garstecki et al. [9], who gave an empirical law for lengths of water droplets in oil, relate the coefficient α to the ratio of the both channel widths. In their approach, the authors use a coefficient β, which is equal to 1, meaning independent of flow conditions and the geometry. Recently, van Steijn et al. [11] made an extension to Garstecki's scaling rule in considering that the coefficient β is linked to the volume of the bubble or the droplet at the filling time but yet independent from the flow conditions. They calculated both coefficients and concluded that they are fully characterized by the shape of the T-junction. These both analyses [9, 11] show that the bubble and droplet shapes are independent from the fluid properties.

For the squeezing regime, the experimental trends (Fig.3) show a normalized bubble length evolution depending linearly on the flow rate ratio with fitted coefficients α and β (Eq. 1).

$$\frac{L}{2R_c} = \alpha\frac{Q_2}{Q_1} + \beta \tag{1}$$

Note that measurements for both silicone oils are consistent with the linear model proposed by Garstecki et al. with $\alpha = 1$ (capillary radius ratio) and $\beta = 1$. However, for the glycerol/water mixture, experimental values are quite far from the Garstecki's model. Indeed, we obtain coefficients almost equal and close to $\alpha \approx \beta \approx 3$. Consequently, the coefficients (α and β) obtained are higher than those predicted by Garstecki et al. So the particular case where $\alpha = \beta = 1$ is also a relevant approximation for wetting liquids [9].

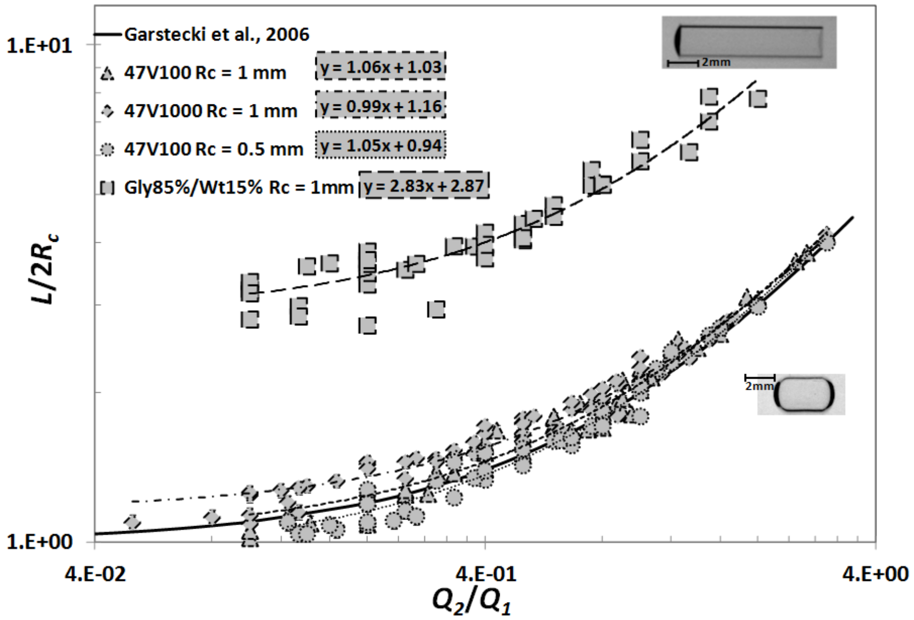

Fig. 3: Normalized bubble length as a function of flow rate ratio for the squeezing regime. Experimental fit: short dashed line for 47V100 (R_c = 1mm); dotted line for 47V100 (R_c = 0.5mm); dash dotted line for 47V1000 (R_c = 1mm) and large dashed line for glycerol 85% - water 15% (R_c = 1mm).

Interconnected capillaries: supplying principle

The pore doublet model studied in this part is composed of two circular capillaries with different radii: R_M, for the larger capillary, called "macrochannel" and R_m for the smaller one, named "microchannel". The PDM capillaries are divided into two parts over the length: a first part where the capillaries are continuously interconnected on over a distance l, so-called "continuous interconnectivity", subsequently followed by a second part of length L, wherein the capillaries are interconnected at both ends forming nodes, so-named "node interconnectivity" (see Fig. 3a). Note that the void entrapped in the macrochannel and in the microchannel will be respectively called macrovoid (see Fig. 3b) and microvoid (see Fig. 3c). The filling of the PDM can be divided into two phases according to the position $x(t)$ of the both menisci into the two parts. The first phase, which is defined for the time range $[0, t_{fl}]$, occurs when one of the both menisci reaches first the end of the first part ($x(t_{fl}) = l$). The second phase, defined for $t \epsilon [t_{fl}, t_{fL}]$, is when one of the both streams completely fills the second part ($x(t_{fL}) = l + L$). In order to simplify the following analytical development, the void is assumed to be incompressible and the liquid as Newtonian. Furthermore, we will neglect the gravity and the inertial effects and consider that the advanced contact angle at the intersection between the liquid-gas interface and the solid surface is supposed to be approximately equal to the apparent equilibrium contact angle (wetting liquids). To lighten the notations, we will use the subscripts m and M, respectively for the microchannel and the macrochannel and the continuous interconnectivity and the node interconnectivity parts are noted with respectively the exponents ci and ni. The governing flow equations describing the forces filling of the PDM is given below.

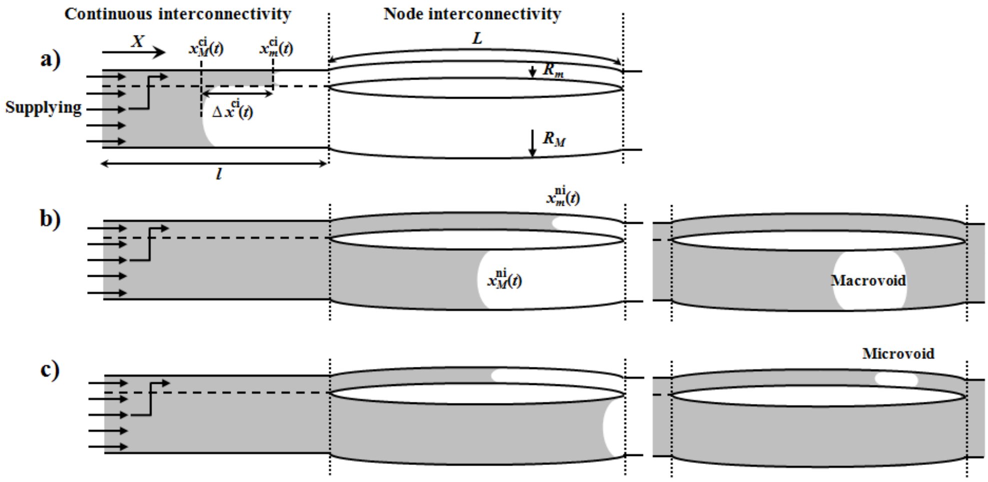

Fig.4: Sketch of void formation inside a PDM formed by a continuous interconnectivity and a node interconnectivity parts: a) Supplying principle, b) macrovoid and c) microvoid creations.

We consider the supplying principle [12] that consists in supplying mass to the microchannel from the macrochannel which plays the role of a tank. Consequently, the meniscus inside the microchannel is always ahead. Then, the difference between the both menisci $\Delta x^{ci}(t)$, given by balancing the viscous pressure drop with the capillary pressure between the both menisci, is as follows:

$$\Delta x(t) = \left(\frac{(R_M - R_m)^2 R_m^2}{R_M^3} \frac{\gamma_L \cos\theta_e}{2\eta}\right)^{1/2} t^{1/2} \qquad (2)$$

For the first part of the macrochannel and for the second part of the both capillaries, the motion equation is deduced from balancing the pressures, with the addition of an injection pressure P_i to the Lucas-Washburn equation [13, 14]:

$$\frac{8\eta}{R_{m,M}^2} x\dot{x} = P_i + \frac{2\gamma_L cos\theta_e}{R_{m,M}} \qquad (3)$$

Besides, we define a pressure P^*, for which the both menisci arrive at the same time t_{fl} at the node $x = l$, expressed as follows:

$$P^* = \frac{2\gamma_L cos\theta_e}{R_M}\left[\frac{\alpha(2+\alpha-\alpha^2)}{1+\alpha}\right] \qquad (4)$$

Where $\alpha\epsilon[0,1]$ representing the ratio of capillary radii R_m/R_M. In the following, we set β the part length ratio L/l.

- For $P_i < P^*$, we assume that the meniscus in the small capillary reaches first the node of the first part $x_m^{ci}(t_{fl}) = l$. From this configuration, two possibilities can occur: either *i)* the meniscus inside the macrochannel reaches first the second node $x_M^{ni}(t_{fL}) = l + L$, creating therefore the microvoid; or *ii)* the stream inside the microchannel remains in advance and reaches first the second node $x_m^{ni}(t_{fL}) = l + L$, hence the macrovoid is created.
    - *i.* the difference between the both fronts at t_{fL} can be expressed as follows:

$$\Delta x_m^{ni}(t_{fL}) = l\left(\beta - \alpha\left(\frac{P_iR_m+2\gamma_L cos\theta_e}{P_iR_m+2\alpha\gamma_L cos\theta_e}\right)^{1/2}\left(1+\beta-\frac{x_M^{ci}(t_{fl})}{l}\right)\right) \tag{5}$$

ii. the difference between the both menisci at t_{fL} is given by:

$$\Delta x_M^{ni}(t_{fL}) = l\left(1+\beta-\frac{\beta}{\alpha}\left(\frac{P_iR_m+2\alpha\gamma_L cos\theta_e}{P_iR_m+2\gamma_L cos\theta_e}\right)^{1/2}-\frac{x_M^{ci}(t_{fl})}{l}\right) \tag{6}$$

- For $P_i > P^*$, we suppose that the flow inside the macrochannel reaches first the node at $x_M^{ci}(t_{fl}) = l$. In this configuration, we have only one possibility because in the one hand, the flow in the macrochannel fills first the first part and in the other hand, as the flow in the largest capillary is the fastest of the both, the stream in the small capillary couldn't catch up the other. Thus, the meniscus in the macrochannel will reach first the node at $x_M^{ni}(t_{fL}) = l+L$, so the microvoid is formed and the difference between the both front positions at t_{fL} is given by:

$$\Delta x_m^{ni}(t_{fL}) = l\left(1+\beta-\alpha\beta\left(\frac{P_iR_m+2\gamma_L cos\theta_e}{P_iR_m+2\alpha\gamma_L cos\theta_e}\right)^{1/2}-\frac{x_m^{ci}(t_{fl})}{l}\right) \tag{7}$$

Curves plotted in Fig. 5 are given for $\alpha = 0.1$ and by varying the parameter β. We observe that for each value of β and for $P_i < P^*$, the macrovoid rate decreases with the increase of the pressure P_i because the stream inside the macrochannel is flowing increasingly quickly. Besides, for a given P_i, the macrovoid rate grows with the decrease of the parameter β. Moreover, one observes that when $P_i > P^*$, the microvoid rate is almost independent from β and increases with P_i until a limit value (about 1\%) corresponding to the volume rate of the microchannel in whole of the PDM.

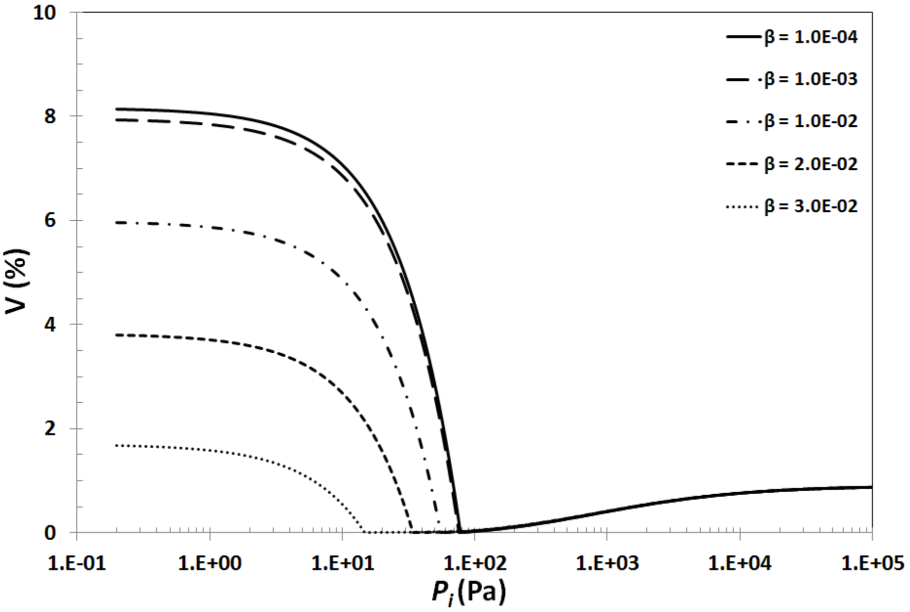

Fig. 5: Void rate evolution as a function of the imposed pressure P_i for different values of β with α = 0.1, l = 500mm and R_m = 10µm.

Curves presented in Fig. 6 are obtained for $\beta = 2 \times 10^{-3}$ and different values of α. First, at a given α, the macrovoid rate decreases when P_i increases for $P_i < P^*$ and the microvoid rate increases with P_i when $P_i > P^*$. Secondly, at constant P_i, the void rate grows when α raises. This can be explained by the reduction of the total volume of the PDM when α increases (decrease of R_M). However, the values of P_i relatively to P^*, influence more or less significantly this evolution. Actually, in the case of $P_i < P^*$, the decrease of the macrovoid with α is also notably due to a faster flow inside the macrochannel, reducing therefore the difference between the both meniscus positions at the end of the PDM. Moreover, the microvoid rate evolution is negligible compared to the macrovoid one. For $P_i > P^*$, the raise of the microvoid rate with α is mainly due to the decrease of the whole volume of the PDM.

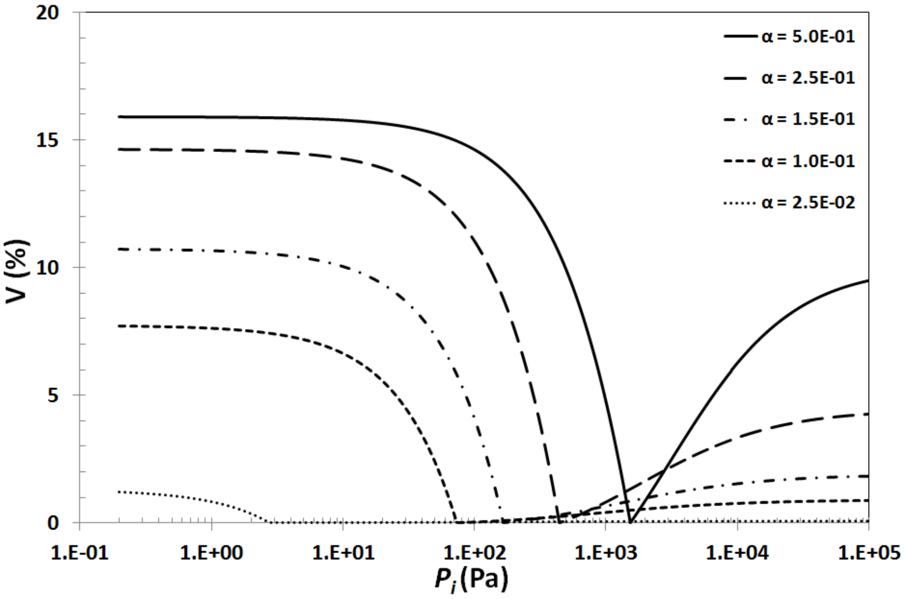

Fig. 6: Void rate evolution as a function of the imposed pressure for different values of α with β = 0.002, l = 500mm and R_m = 10μm.

CONCLUSIONS

To conclude, in this paper, we have proposed issues to quantify the void created and entrapped in LCM processes. The measurements performed in the T-junction device emphasize the behaviour of non-wetting liquids (glycerol solution) which is quite different from wetting liquids (silicone oils). We showed that the Garstecki et al.'s model was well validated for wetting liquids but there is a discrepancy for the non-wetting liquid which has a higher value of the static contact angle. For instance, the chemical characterization of the polyester, vinylester and epoxy resins, that are partially wetting liquids, is a significant way to enhance LCM processes by improving the knowledge of the adhesion fibre/resin and notably the quantification of the void rate entrapped. Furthermore, we have proposed an analytic approach of void prediction based on both the Lucas-Washburn equation and the supplying principle for the imbibition case through an original PDM combining continuous and node interconnectivities.

REFERENCES

1. Lundström TS and Gebart BR (1994), 'Influence from process parameters on void formation in resin transfer molding', *Polymer Composites,* 15(1), 25-33.

2. Patel N, Rohatgi V and Lee LJ (1996), 'Modeling of void formation and removal in liquid composite molding, part II: model development', *Polymer Composites,* 17(1), 104-114.

3. Verrey J, Michaud V and Mansön JAE (2006), 'Dynamic capillary effects in liquid composite moulding with non-crimp fabrics', *Composite Part A,* 37, 92-102.

4. Lundström TS, Gustavsoon LH, Jëkabsons N and Jakovics A (2008), 'Wetting dynamics in multiscale porous media. Porous Pore-Doublet Model, experiment and theory', *AIChE Journal*, 54(2), 372-380.

5. Gourichon B, Deléglise M, Binetruy C and Krawczak P (2008), 'Dynamic void content prediction during radial injection in liquid composite molding', *Composite Part A*, 39, 46–45.

6. Ben Abdelwahed MA (2011), 'Mécanismes d'imprégnation en milieux fibreux : modélisation et application à la mise en œuvre des composites à fibres longues', *Phd Thesis, Université du Havre*.

7. Chatzis I and Dullien F A L (1983), 'Dynamic Immiscible Displacement Mechanisms in Pore Doublets: Theory versus Experiment', *Journal of Colloid and Interface Science*, 91, 199-222.

8. Sorbie KS, Wu YZ and McDougall SR (1995), 'The extended Washburn Equation and Its Application to the Oil/Water Pore Doublet Problem', *Journal of Colloid and Interface Science*, 174, 289-301.

9. Garstecki P, Fuerstman MJ, Stone HA and Whitesides GM (2006), 'Formation of droplets and bubbles in a microfluidic T-junction-scaling and mechanism of break-up', *Lab on a Chip,* 6, 437-446.

10. de Menech M, Garstecki P, Jousse F and Stone HA (2008), 'Transition for squeezing to dripping in a microfluidic T-shaped junction', *Journal of Fluid Mechanics,* 595, 141-161.

11. van Steijn V, Kleijn CR and Kreutzer MT (2010), 'Predictive model for the size of bubbles and droplets created in microfluidic T-junctions', *Lab on a Chip,* 10, 2513-2518.

12. Bico J (2000), 'Mécanismes d'imprégnations: Surfaces Texturées, Bigouttes, Poreux' *Phd Thesis, Paris VI.*

13. Lucas R (1918), 'Ueber das Zeitgesetz des Kapillaren Ausfstiegs von Flussigkeiten', *Kolloid-Z,* 23, 15-22.

14. Washburn EW (1921), 'The Dynamics of Capillary Flow', *Phys. Rev.,* 17(3), 273-283.

SIMULATION AND EXPERIMENTAL VALIDATION OF THE SATURATION IN LCM PROCESSES

García J.A.[1], Gascón Ll.[1], Ruiz E.[2], Lebel F.[2], Trochu F.[2]

[1] *Universidad Politécnica de Valencia. Camino Vera s/n, 46022, Valencia (Spain).*
[2] *Chair on High Performance Composites (CCHP), Département de Génie Mécanique, École Polytechnique de Montréal, Montréal, Canada, H3C 3A7*
Corresponding author's e-mail jugarcia@mcm.upv.es

ABSTRACT: In a previous work, equations that describe the LCM filling process with void formation were introduced. These equations are based on a two phase flow model and lead to a coupled system of a nonlinear advection-diffusion equation for saturation and an elliptic equation for pressure and velocity. This model introduces the relative permeability as a function of saturation and a modified equation for the saturation as a non-linear advection-diffusion equation including viscous and capillary phenomena. The hyperbolic nature of the saturation equation and its strong coupling through relative permeability represent a challenging numerical issue. Many numerical methods used to solve hyperbolic equations suffer from nonphysical oscillations and numerical dispersion. Usually, two terms contribute to smooth the numerical flow front position: one is related to the source term, and the other is a purely mathematical term introduced by the discretization scheme. The last effect can be reduced by using higher order numerical scheme to solve the nonlinear equation. The technique used in this paper for solving the saturation equation is based on an essentially non-oscillatory fixed mesh FEM approach. A detailed analysis for different relative permeability models combined with saturation equation is performed to assess the saturation profiles. To validate the proposed model, FEM predictions were compared with experimental data obtained on a glass RTM mold under controlled manufacturing conditions. Injections were carried out at different flow rates and saturation and saturation as measured as a function of time during impregnation. Measured saturation profiles in time were then compared to those numerically predicted.

KEYWORDS: *Liquid Composite Molding, Saturation, Void, Essentially Non-Oscillatory Techniques.*

INTRODUCTION

In the manufacturing of composite parts by Liquid Composite Molding process (LCM), complete saturation of the fibrous reinforcement is key. Incomplete saturation leads to voids within the fibers which cause failure of the final product. Thus, understanding of the formation of voids is necessary for proper molding of composite parts. In order to analyze the formation of voids during the resin impregnation process, a one-dimensional solution based on two-phase flow through a porous medium, is proposed. This model leads to a coupled system of a nonlinear advection-diffusion equation for saturation and an elliptic equation for pressure and velocity. The permeability is assumed to be a function of saturation, and then the continuity equation that governs the pressure distribution, includes a source term which depends on the saturation. A key part of our work is the relative permeability model and the mathematical formulation for saturation equation we proposed to determine the saturation curves.

Essential to the optimum process design in LCM is the mathematical model and the numerical simulation of the modified saturation equation. In general, the saturation equation is a non-linear advection-diffusion equation which includes the capillary pressure effect and it reduces to a purely advection transport equation when capillary effects are neglected. The hyperbolic nature of the saturation equation and its strong coupling through relative permeability represent a challenging numerical issue. Common numerical methods used to solve these equations suffer from nonphysical oscillations, numerical dispersion or a combination of both. The technique here used for solving the equation which governs the evolution of the degree of saturation of porous media is based on an essentially non-oscillatory fixed mesh strategy and was described in [1]. For the ENO schemes, interpolation polynomials of one order less than the order of accuracy required in the solution are computed and these polynomials are a good approximation to the values of the numerical flux function at the cell walls. The key idea in the *r*th-order ENO schemes is to use the “smoothest” stencil among *r* possible candidates to approximate the fluxes at cell boundaries to high-order accuracy and at the same time to avoid spurious oscillations near shocks.

A description of relative permeability in LCM is essential to describing fluid flow. The approach presented here combines relative permeability models with the saturation equation in order to find an optimal mathematical model to simulate the saturation in LCM process. Some preliminary numerical results are presented and compared with experimental results in order to validate the proposed mathematical model and the numerical scheme.

GOVERNING EQUATIONS

The mathematical formulation of the saturation in LCM takes into account the interaction between resin and air as it occurs in a two phase flow. Combining equations that describe mass conservation and Darcy’s laws for resin and air phases as described in [1, 2], the resulting equation for the saturation in its most general form gives

$$\phi\,\frac{\partial S}{\partial t}+\nabla\cdot\left(vf(S)\right)=-\,\nabla\cdot\left(D_{cf}(S)\nabla S\right) \tag{1}$$

where

$$f(S)=\frac{\lambda_R\left(S\right)}{\lambda_R\left(S\right)+\lambda_A\left(S\right)}\qquad,\qquad D_{cf}(S)=f(S)\lambda_A\left(S\right)\frac{\partial P_c}{\partial S} \tag{2}$$

Here $D_{cf}(S)$ is the nonlinear diffusivity coefficient due to capillary pressure P_c, defined as $P_c=P_A-P_R$; v is the total velocity, S is the degree of saturation of the reinforcement by the liquid resin, $\lambda_j(S) = K_{Rj}(S) \cdot K / \mu_j$ is the phase mobility, with $K_{Rj}(S)$ the relative permeability of the phase j, μ_j the viscosity of phase j and K the permeability tensor.

Replacing the total velocity v by $v_R + v_A$ and simplifying, Eqn. 1 can be rewritten as follows

$$\phi \frac{\partial S}{\partial t} + \nabla \cdot \left(v_R f(S) \right) = \nabla \cdot \left(\left(1 - f(S)\right) \lambda_R(S) \frac{\partial P_R}{\partial S} \nabla S \right) \tag{3}$$

In what follows we consider the following equation for the saturation,

$$\phi \frac{\partial S}{\partial t} + \nabla \cdot \left(v_R f(S) \right) = 0 \tag{4}$$

The treatment of the diffusivity coefficient will be more widely investigated in the future. To simulate the flow of the resin phase, we can derive the governing equations combining, for the resin phase, Darcy's law (the subscript R for v and p has been omitted),

$$v = -\frac{K_R(S) K_{sat}}{\mu} \nabla p \tag{5}$$

with mass conservation

$$\nabla \cdot v = -\phi \frac{\partial S}{\partial t} \tag{6}$$

The simulation of the filling process involves the following operations at each time step:

1. Calculate the pressure distribution by applying a standard finite element discretization to Equation

$$\nabla \cdot \left(K_R(S) \nabla p \right) = \frac{\phi \mu}{K_{sat}} \frac{\partial S}{\partial t} \tag{7}$$

where the relative permeability and the term on the right side depend on the saturation degree. The modelling of the relative permeability is very essential for two phase flow models. In this work we use the power law model for relative permeability considered in [2], which is a particular case of the often called the Corey model, even though it is not the same as the model originally presented in [3]

$$K_R(S) = \left[(1 - R_s^{1/m}) S + R_s^{1/m} \right]^m \tag{8}$$

Standard choices for K_R are linear (m=1) and quadratic (m=2). Other model, based on the soil science literature, the Van Genuchten permeability model [4], has been considered in this paper

$$K_R(S) = \sqrt{S} \left[1 - (1 - S^{1/m})^m \right]^2 \tag{9}$$

2. Calculate the velocity field from Darcy's law for the resin.
3. Update the saturation distribution by integrating Eqn. 4 using a fourth-order ENO technique described in [1]. In the general case, the saturation equation depends on the phase mobility, and therefore, we use

$$\phi \, \frac{\partial S}{\partial t} + \nabla \cdot \left(v \frac{S^m}{S^m + M\left(1-S\right)^m} \right) = 0 \tag{10}$$

   where M denotes the resin-air viscosity ratio. We take S for the saturation of the resin phase and (1-S) for the air phase. When m=1 in Eqns. 8 and 10 we consider a linear model and if m =2 we have a quadratic model. The best results in this work have been obtained using the Van Genuchten permeability model (Eqns. 9 and 10) with m=2.

The boundary conditions are given by: a) the pressure gradient in the normal direction to the mold walls vanishes, b) the flow rate is specified on the inflow boundary and c) the pressure is zero in the empty part of mold.

NUMERICAL RESULTS

In order to test and evaluate the ability of commonly used relations for two phase flow predictions in RTM, results of saturation simulation are compared to experimental data. Three experiments were compared. The geometry considered in the current study consists of a mold cavity RTM with 36mm of length, 105mm of width and 3.175mm of thickness. The analyzed area has been composed by 21 long representative elementary volume (REV) by 5 wide REV, which have been used to analyze the saturation. The saturation value has been calculated in the centre of each REV and an average value has been performed in the width of the piece. Each REV has a dimension of 15 mm by 15 mm, so after the port before injection and before the vent port, there are two small bands of 22.5 mm long by 105 mm wide which are not analyzed for the saturation. Three injections were performed by changing only the injection rate: 0.025 ml/s, 0.1 ml/s and 0.3 ml/s. The saturated permeability *Ksat*, resin viscosity and the porosity have been set to $7.9\mathrm{x}10^{-10}$ m^2, 0.4788 Pa.s and 0.614, respectively.

Figs. 1, 2 and 3 show experimental saturation results in function of time for three REV (V3, V10 and V19) compared with the numerical solution. Injections in Figs. 1, 2 and 3 were carried out to constant flow rates of 0.025 ml/s, 0.1 ml/s and 0.3 ml/s, respectively. For each Figure, graphics illustrated at the left are based on a linear model of Corey permeability with linear saturation (m=1 in Eqns. 8-10), graphics at the right column are based on a quadratic model of Corey permeability with a quadratic saturation (m=2 in Eqns. 8-10). The last graph (at the right) shows the results obtained with the permeability of van Genuchten with a quadratic saturation model (m=2 in Eqns. 9-10). In linear and quadratic cases, results depend on the value of R_s. For large values of R_s ($0 < R_s < 1$) the solution is more diffusive and yield predictions that closely matched the experimental data at the beginning of the filling, but for small values of R_s, the solution is closer to that obtained in the last iterations. In the numerical simulations, the linear and quadratic models for two constant values R_s=0.1 and R_s=0.8 have been represented and we tested a relative permeability model with R_s linearly variable with the time for both models. For each injection at constant flow rate, we have analyzed seven cases.

We use the following notation for the pictures: the first letter indicates linear (L) or quadratic (Q) model, followed by the injection velocity and then it indicates the value of R_s, which has been replaced by VARIA if R_s is linearly variable with the time.

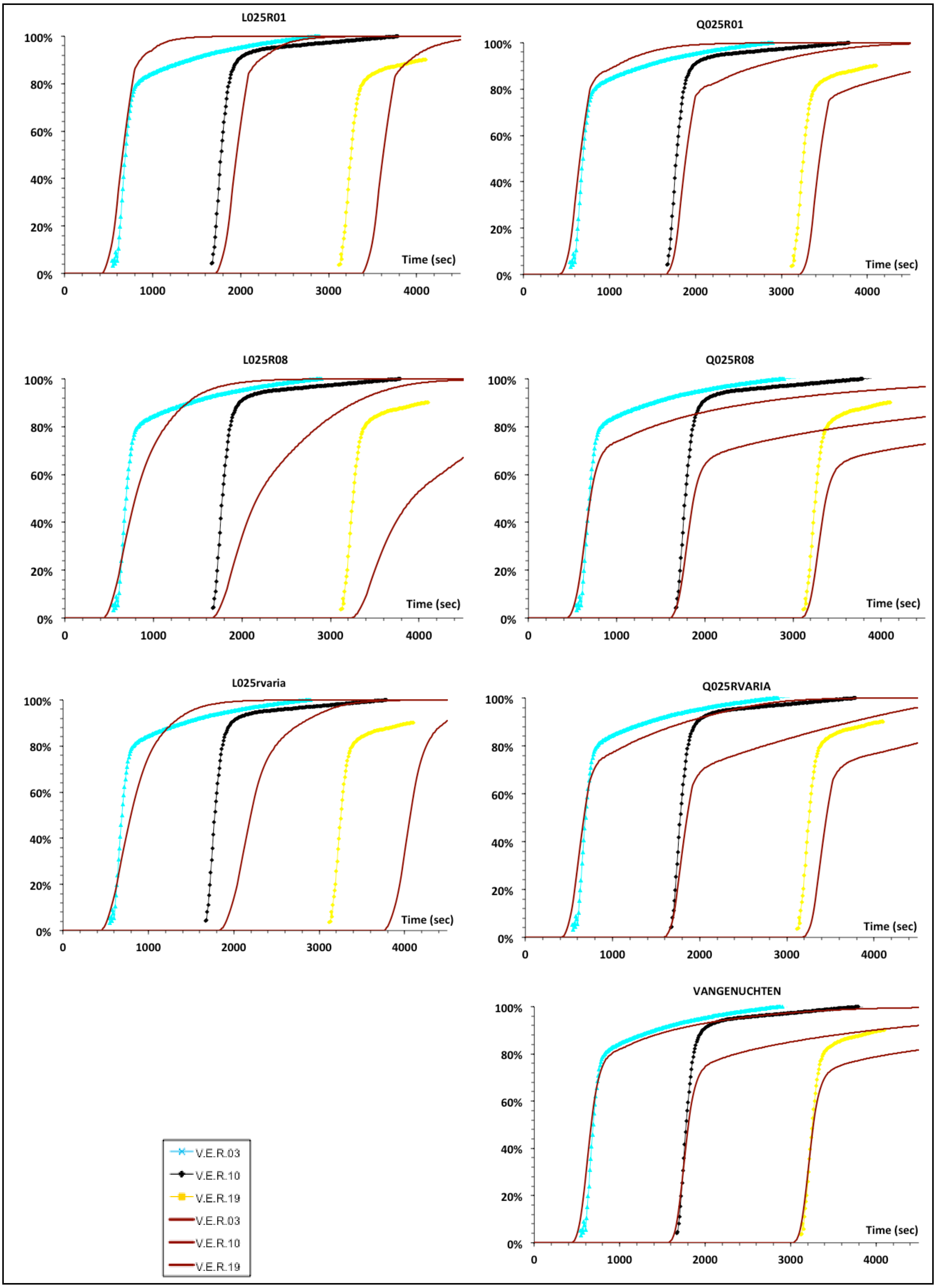

Fig. 1: Curves of saturation as a function of time for three REV (V3, V10 and V19) for the injection at constant flow of 0.025 ml/s (numerical solution is represented by straight lines)

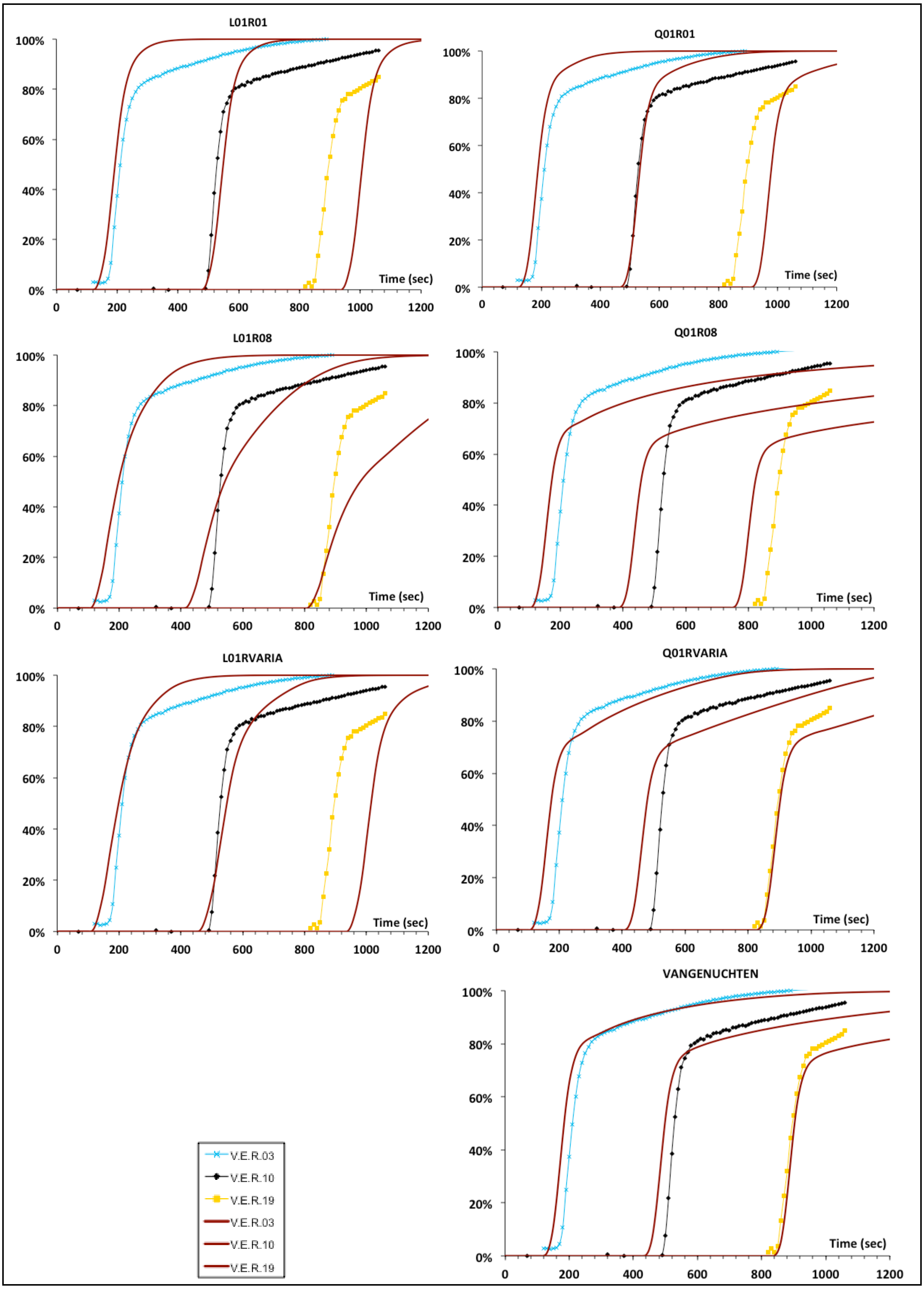

Fig. 2: Curves of saturation as a function of time for three REV (V3, V10 and V19) for the injection at constant flow of 0.1 ml/s (numerical solution is represented by straight lines)

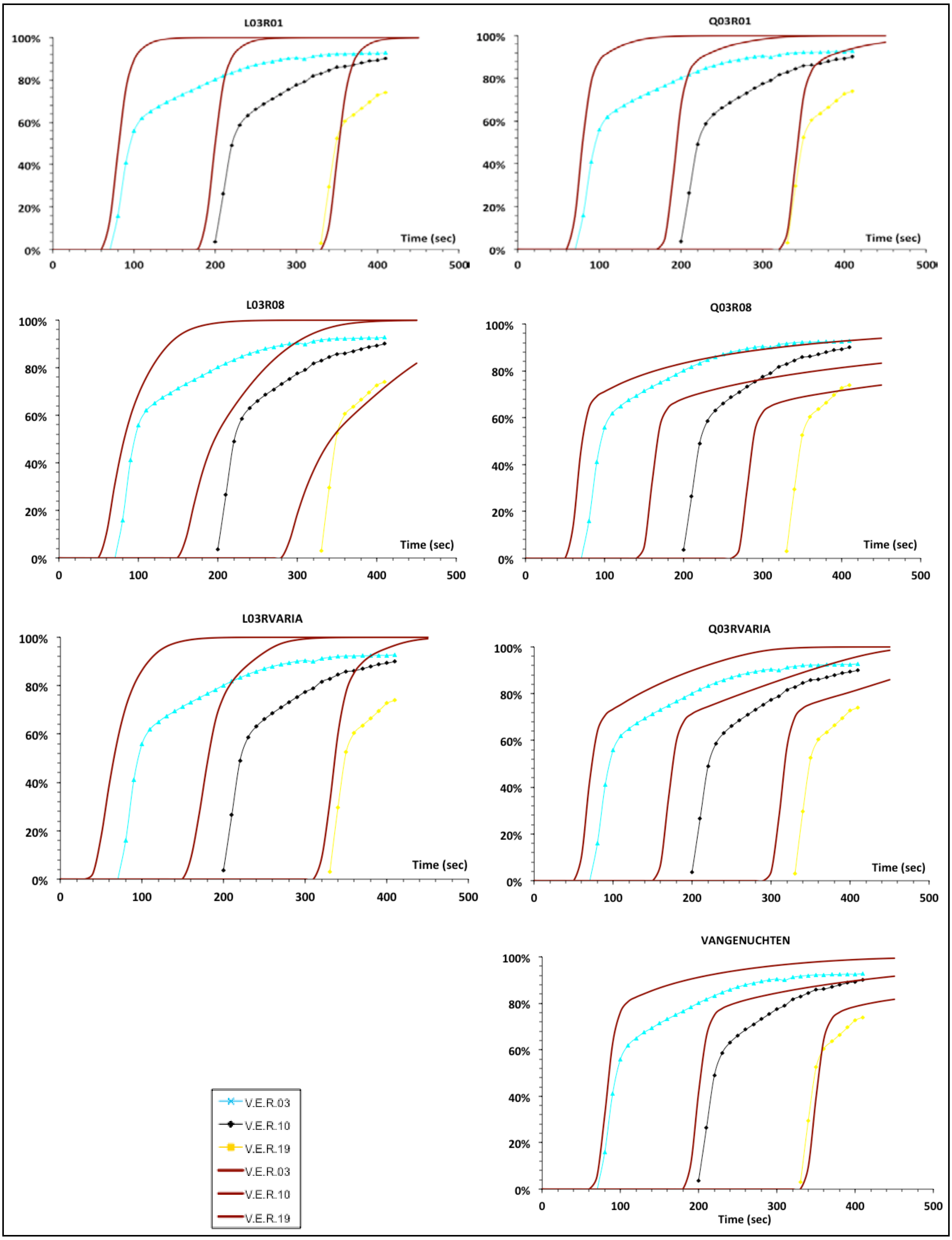

Fig. 3: Curves of saturation as a function of time for three REV (V3, V10 and V19) for the injection at constant flow of 0.3 ml/s (numerical solution is represented by straight lines)

In general, numerical results show that quadratic models for the relative permeability and the saturation equation provide solutions closest to the experimental. However, linear models for relative permeability and the saturation equation do not seem to match with experimental observations. The model based on the van Genuchten relative permeability for the resin with a quadratic model for the saturation equation shows trends that are in good agreement with experimental results.

CONCLUSIONS

A detailed analysis for different relative permeability models combined with the saturation equation is performed to assess the saturation profiles in LCM. Numerical results using a FEM code have been compared with measured saturation profiles in time for three experiments at different injection flow rates. In order to numerically solve the saturation equation for the LCM process a high order essentially non-oscillatory (ENO) technique proposed in [1] has been used. Models based on the linear Corey relative permeability with linear saturation equation did not agree as well with the experimental data as those obtained with the quadratic model for the relative permeability with quadratic saturation equation. The relative permeability based on the van Genuchten for the resin with a quadratic model for the saturation equation yielded predictions that closely matched the experimental data in the experiments. This formulation opens up new opportunities to improve LCM flow simulations and optimize injection molds.

ACKNOWLEDGMENTS: The authors agree the financial support provided by the Spanish Government (Project DPI2010-20333).

REFERENCES

1. Gascón L, García JA, Chinesta F, Ruiz E, Trochu F (2010), “Analysis of the Saturation in Liquid Composite Molding Processes using an Essentially non-oscillatory (ENO) Technique”, *Proc. of the 10th International Conference on Flow Processes in Composite Materials: (FPCM-10),* 63.

2. Breard J, Saouab A and Bouquet G (2003), "Numerical simulation of void formation in LCM", *Composites Part A: Applied Science and Manufacturing,* 34, 517- 523.

3. Corey AT (1954), "The Interrelation Between Gas and Oil Relative Permeabilities", *Prod. Montly* 19 (1): 38–41.

4. Van Genuchten M Th (1980), “Closed-form equation for predicting the hydraulic conductivity of unsaturated soils”, *Soil Science Soc. Am. J.*, 44(5), 892-898.

EXPERIMENTAL STUDY OF CAPILLARY FLOWS, VOIDS FORMATION AND VOID MIGRATION IN LCM MANUFACTURING

E. Ruiz, F. LeBel, F. Trochu

Chaire sur les Composites à Haute Performance (CCHP), École Polytechnique de Montréal,
C.P. 6079, Station Centre-ville, Montréal (Québec), H3C 3A7, Canada
Corresponding author: edu.ruiz@polymtl.ca

ABSTRACT: Engineered fibrous reinforcements commonly used in LCM processes behave as a dual scale porous media with a macroscopic porosity defined between the tows and a microscopic porosity between the filaments inside the fiber tows. This dual scale porosity is a result of the stitching/weaving process of the fabric. On a microscopic scale, capillary flows developed during impregnation of fiber tows play a major role on the quality of composites made by resin injection through fibrous reinforcements. In this work, a study of dual scale fabric saturation was carried out in order to understand the mechanisms that govern the impregnation of fibrous reinforcements and the formation of porosities in LCM manufacturing. The experimental approaches of this research are based on a new visible light transmission (VLT) method and on RTM injections in a glass mold. This VLT method was based on fundamentals of optics and it allows a better understanding of the mechanisms of void formation and transport in dual scale fibrous reinforcements. The result of this advanced monitoring tool for fibrous reinforcement saturation was to propose an impregnation model linking the formation of the macroscopic and microscopic porosities to the capillary number. Finally, a thermosetting resin was used to carry out RTM injections at constant flow rate in order to validate the proposed impregnation model as well as the predictions of optimal injection conditions obtained by the capillary rise experiments with the same resin and the same fibrous reinforcement.

KEYWORDS: capillary flow, voids formation, porosities, composites manufacturing, imbibition.

INTRODUCTION

One key issue in composites manufacturing by resin injection is related to the impregnation of the fibrous reinforcement by the reactive liquid resin [1]. In order to produce high performance composites, fibers must be completely saturated prior to resin gelation [2]. Indeed, impregnation defects such as microscopic and macroscopic voids have a detrimental impact on the mechanical properties of composite parts [3, 4]. It has also a substantial effect on crack initiation and fatigue life and on moisture absorption and surface finish. Hence developing practical strategies to produce composite parts of high impregnation quality becomes a critical industrial goal. In order to minimize final void content in composite parts manufactured by LCM processes, the study of unsaturated flows in dual scale fibrous reinforcements at the macroscopic level is becoming increasingly necessary. In this regard, a new monitoring technique of fibers saturation has been developed in the current work. This non-intrusive monitoring technique is based on the optical principle of 2D tomographic reconstruction by visible light transmission (VLT) method.

This work presents the studies carried out on an RTM mold instrumented with the VLT technique. Injection experiments were carried out to study the key parameters that govern void formation by air entrapment and void transport during part filling. This VLT technique was also validated using a standard characterization method of void content based on ASTM D2734 standard. This research aims a better understanding on the saturation phenomena that take place during Liquid Composites Molding and on the process parameters that have a key impact on voids formation and transport.

Void formation by air entrapment in LCM processes

Researchers have noticed that smaller scale defects such as microscopic and macroscopic voids in composite parts have detrimental impact on their mechanical. These voids may be generated by air entrapment at the flow front, by gases from chemical reaction during impregnation and polymerization, by volume change during cure as a result of resin shrinkage and increase in temperature, by bubble nucleation from dissolved air or water vapor in the liquid resin or by bubble creation following the in-line mixing with curing agents. However, for many researchers, the main reason for void formation in LCM processes is air mechanical entrapment rather than gas nucleation. This latter phenomenon is an important source of voids in autoclave processed laminates.

The dual scale architecture of woven fabrics is mainly responsible for air entrapment between the fiber tows (spherical macroscopic voids) and inside the tows (cylindrical microscopic voids) [5]. The fingering behavior of resin during impregnation is considered as a risk factor of void formation because the leading resin front can entrap air by over passing the microscopic flow front in crosswise tows of low permeability. These microscopic voids are difficult to predict because they can result from intrinsic tow variability, fiber beds randomly packed, heterogeneous pore size distribution and local defects of the reinforcement. Moreover, in infusion processes with low viscosity resins or for the injection of large parts, capillary fingering inside tows can entrap air and generate macroscopic voids as shown by Patel et al. [6].

Several authors have found that air entrapment mechanisms in LCM can be mainly related to the impregnation velocity of the reinforcement by the liquid resin [4]. During impregnation at low velocities, capillary forces are leading viscous forces. Consequently, the resin impregnates more rapidly the fiber bundles than the open space between them. This flow scenario represents a risk of macroscopic void formation between the fiber tows. On the other hand, for high impregnation velocities the viscous forces become more important than capillary forces making the resin to surround fiber tows creating microvoids inside the tows. Therefore, an optimal impregnation velocity exists that minimize the formation of voids in fibrous reinforcements [7]. In a recent publication [8], the authors proposed a predictive model to calculate the optimal capillary number Ca^*_{opt} that minimizes void formation by air entrapment in RTM. This model is based on the properties of the fibrous reinforcement and was defined as follows:

$$Ca^*_{opt} = \frac{f_{geo}}{2k_o} \cdot \frac{d_f \ \phi_m}{\tau^2 \ L_c \left(1-\phi_m\right)} \qquad (1)$$

where d_f , ϕ_m, τ and L_c are respectively the diameter of fiber tow filaments, the microscopic porosity of fiber tows, their tortuosity and the characteristic distance of the fabric weaving/stitching *unit cell*. f_{geo} and k_o are geometrical constants which depend on pore size distribution, on the flow direction with respect to the fiber tows and on the filament packing configuration of fiber tows. For the selected bidirectional glass fabric, the estimated range of optimal capillary numbers Ca^*_{opt} using Eqn. (1) was about [1.2 to 2.4] × 10^{-3}. On the other hand, the observed range of optimal capillary number Ca^*_{opt} using the capillary rise method developed elsewhere was about [0.8 to 2.8] × 10^{-3}. Note that this *a priori* estimation of optimal impregnation conditions was obtained without having to perform expensive and time-consuming manufacturing tests or carrying out complex numerical modeling of dual scale flows in fibrous reinforcements. This *a priori* estimation of optimal impregnation conditions will be validated in the current study.

Saturation observation based on Visible Light Transmission (VLT)

An experimental setup was conceived in this work to study the saturation of fibrous reinforcements during RTM injections (see Fig. 4). The setup consists of a closed mold made of tempered glass plates specially conceived for this application, a white light source set over the mold, monochromatic filters inserted between the light source and the mold and a digital camera (CCD). A high resolution digital camera from *Nikon* (*D80*) with optical lens and PC control software was implemented. The setup was installed on a covered black painted box to protect from any external light source.

A computer-assisted injection system was also developed to carry out this study under controlled manufacturing conditions. This unit is able to perform precise injections at constant pressure or constant flow rate. The injection equipment uses double-acting pistons from *Magnum Venus Plastech* to inject a vinylester resin and catalyst at desired mixing ratios. High accuracy pressure transmitters were installed at the mold inlet, between a pneumatically controlled *CPC-1200-A* injection gun and a *MAS-1000* autosprue from *Magnum Venus Plastech*. Finally, an *Ohaus® Adventurer ARC120* scale was installed at the mold vent to measure the fluid mass exiting the mold. This hybrid injection unit provides the flexibility and reliability needed to perform this saturation study with an error on in flow rates below 1%.

The analysis of dynamic saturation in fibrous reinforcement developed in the current work is based on 2D tomographic reconstruction using VLT as shown in Fig. 1(a). This optical phenomenon is modeled by the *Beer-Lambert* and *Fresnel* laws. The *Beer-Lambert*'s law relates the light transmission to the properties of the medium through which the light is travelling. Note that fiber saturation is not directly proportional the transmitted light through the partially impregnated fiber bed. A mathematical relationship can be found from these laws to estimate the saturation of fibers from transmitted light through the glass mold. This optical mapping of fiber saturation can be expressed as follows [9]:

$$S_r = \frac{\ln\left(\left[\frac{I_{unsat} - \left(\frac{I_{unsat}^{ref}}{I_{dry}^{ref}}\right)\cdot I_{dry}}{I_{sat} - \left(\frac{I_{sat}^{ref}}{I_{dry}^{ref}}\right)\cdot I_{dry}}\right]\cdot\left[\left(\frac{I_{sat} - B}{I_{dry} - B}\right) - \left(\frac{I_{sat}^{ref}}{I_{dry}^{ref}}\right)\right] + \frac{I_{unsat}^{ref}}{I_{dry}^{ref}}\right)}{\ln\left(\frac{I_{sat} - B}{I_{dry} - B}\right)} \qquad (2)$$

where I_{dry}, I_{unsat} and I_{sat} are respectively the transmitted light intensities through the reinforcement at the dry, partially and totally saturated states. I_{dry}^{ref}, I_{unsat}^{ref} and I_{sat}^{ref} are respectively the light source intensities at these three states. B is a corrective parameter that represents the background intensity (i.e. intensity when no light is transmitted). Light intensities were obtained from digital images acquired with a CCD camera as shown in Fig. 1(b). Two *Matlab* subroutines were developed for post-processed of images to analyze saturation of the fabric and flow front progression respectively.

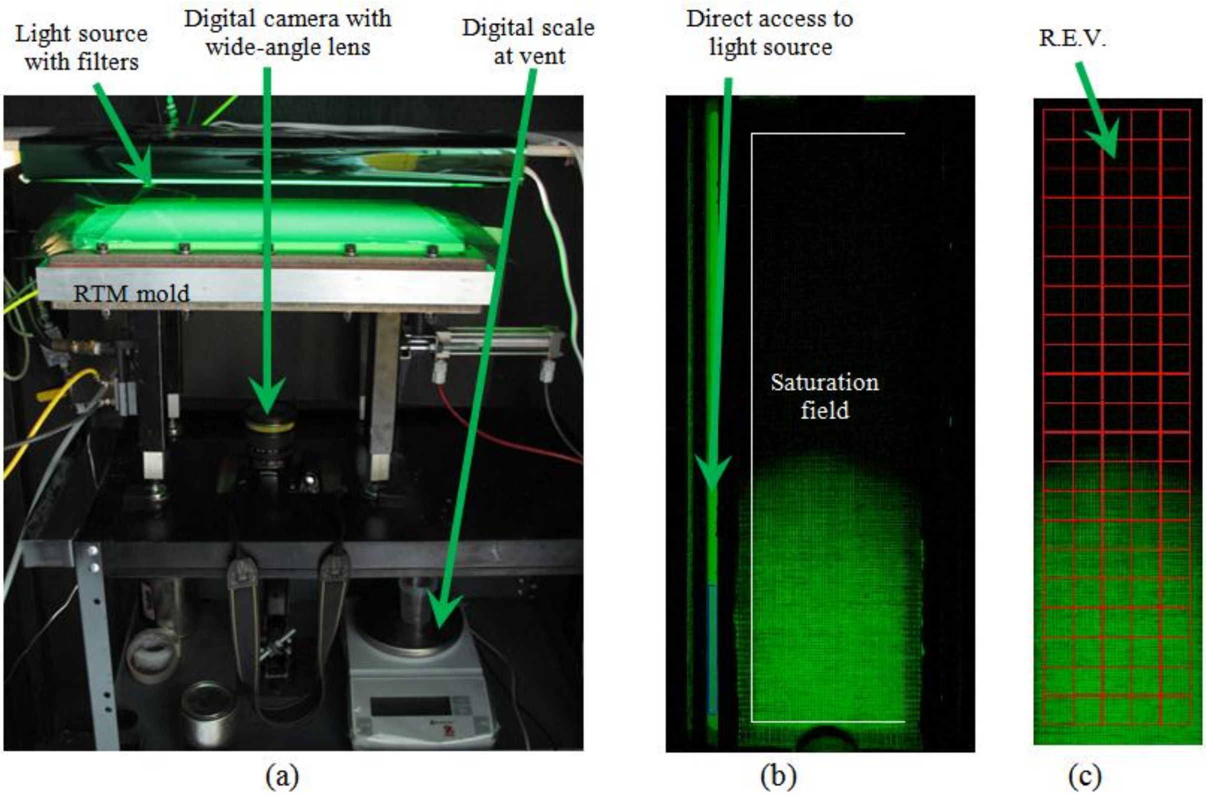

Fig. 1: RTM injection setup for VLT evaluation of fabric saturation:
(a) RTM mold with digital camera and filtered light source;
(b) Image acquisition of dynamic saturation of a glass fabric with vinylester resin;
(c) Division of the studied region in R.E.V.

EXPERIMENTAL RESULTS

RTM injections were performed at room temperature and atmospheric pressure in order to study the phenomena of air entrapment. Resin was degassed under vacuum and using bubble nucleation elements prior to injection. Two sets of experiments were carried out to investigate the phenomena of void formation and transport during RTM injections at constant pressures and constant flow rates as well as during post-filling and curing.

RTM injections at constant pressure

Five RTM injections were performed at four different pressures (1, 2.4, 4.1 and 5.2 bars). The void content of these glass/vinylester plates was measured using ASTM D2734 standard. The plates were cut in square samples as shown in Fig. 1(c) for void content characterization. For each sample, the average modified capillary number was estimated with a *Matlab* subroutine from the flow front evolution in time. Fig. 2 shows the results of void formation as a function of modified capillary number for the four RTM injections carried out at constant pressure. Voids are localized near the vent position while at the injection gate near fully saturation is observed. A fiber washout phenomenon was initiated above a modified capillary number Ca^*_{ff} of 5.4×10^{-2} as reported in Fig. 2. Moreover, no matter what injection pressure was used, there was a clear change in trend of void content evolution around Ca^*_{ff} of 1.8×10^{-2} indicating the existence of an optimal impregnation speed that minimize the presence of voids by minimization of air entrapment or by void mobilization (transport).

RTM injections at constant flow rate

The second study of this work focus on saturation analyses using the VLT technique and the relationship proposed in Eqn. (2). For this study, a total of 21 RTM injections were carried out at constant flow rates varying from 0.025 to 0.5 ml/s. The lower injection speed corresponds to a modified capillary number of 2×10^{-3}, which was predicted as the optimal injection condition from Eqn. (1).

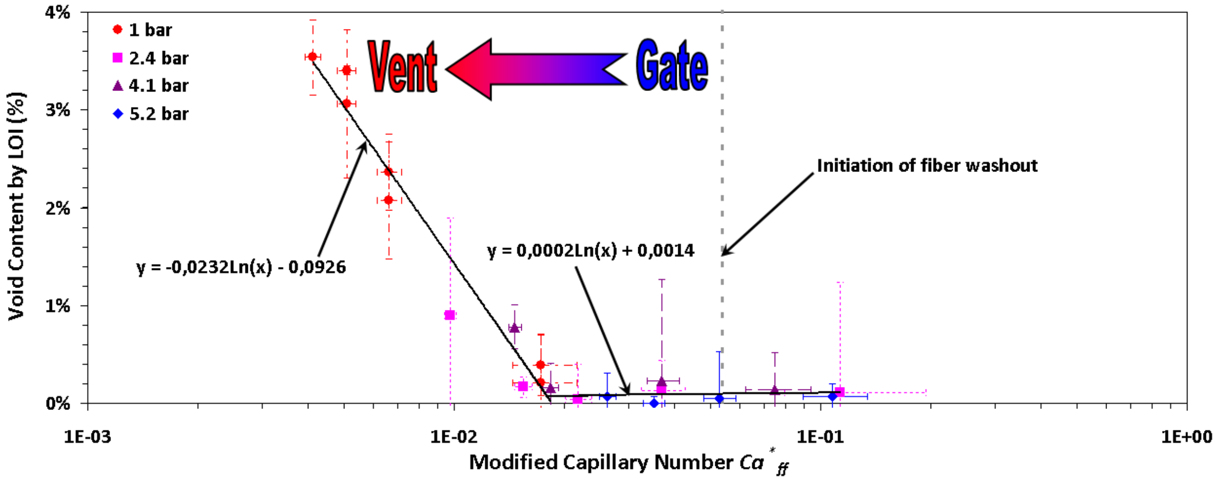

Fig. 2: Void content analyses of 5 RTM injections at 4 different constant pressures.

Results of the VLT analysis of these injections at constant flow rates are presented in Fig. 3 for three flow front positions at 85, 180 and 275 mm. It can be observed that the shape of saturation profiles varies according to the modified capillary number. Indeed, the saturation fronts show a step-like profile that is more or less diffuse according to Ca^*_{ff}. These results indicate that higher is the flow front velocity, lower is the fibers saturation at the flow front. Moreover, for injections carried out at the optimal impregnation conditions minimizing void formation ($Ca^*_{ff} = 2\times10^{-3}$), the saturation profiles are clearly more steep than other injections at higher flow rates. These experimental results demonstrate that the *a priori* estimation of optimal impregnation conditions (see Eqn. (1)), are appropriate to predict the ideal injection conditions with minimal labour.

The impact of fluid pressure on fiber saturation can also be observed in Fig. 3. In fact, during injections at constant flow rates the pressure at injection gates increases proportionally to the flow front position as described by Darcy’s law for saturated flows. At each time step, the pressure varies linearly from injection gate towards the flow front position. It can be seen from profiles at different time steps (see Fig. 3), that saturation slowly evolves towards higher levels as a result of local pressure increments in time. This demonstrates the complexity of the saturation phenomena that take place in dual scale porous media.

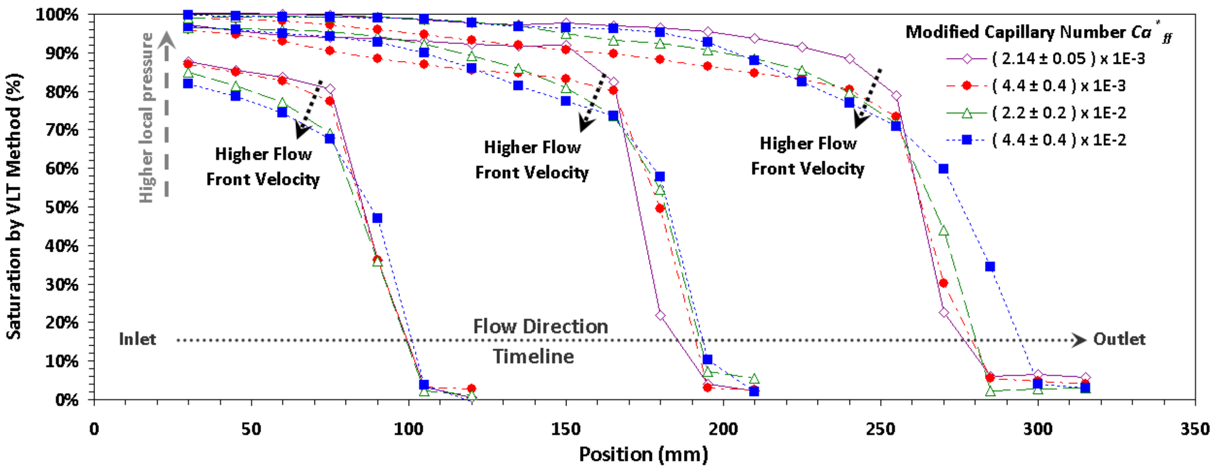

Fig. 3. Saturation profiles from mold inlet to outlet at different flow rates.

Finally in this study, a qualitative validation of fibers saturation carried out with the optical setup was presented in Fig. 4. This validation was based on an RTM injection at constant flow rate of 0.1 ml/s. During injection, the resin delivery into the mold was sequentially paused three times and then continued afterwards. Each time the injection system was stopped, the resin flow front was spontaneously progressing by capillarity inside the fiber tows. This results in an increased saturation level at the flow front position. After the injection was restarted, the saturated flow front position remained highlighted even after the resin reached the vent port. These contrasted areas resulted from the lower air entrapment by the resin front in fiber tows at slow impregnation velocities. This visual contrast of localized zones shown in Fig. 4 emphasized the role of the impregnation velocity as a key parameter in the air entrapment at the flow front. Finally, it is interesting to point out that Fig. 4 shows a gradual increase of light transmission from the mold inlet to the outlet such as the spatial distribution of void contents. This phenomenon can be related to wicking action inward fiber tows as well as the compression and the dissolution of voids into the flowing resin. Therefore, this observation highlighted the need to also consider the pressure distribution as a key parameter in void transport phenomena.

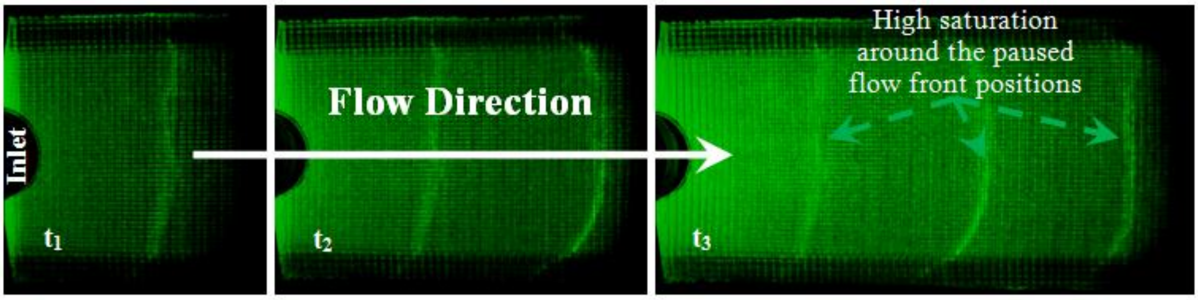

Fig. 4: Capture frames of a sequential RTM injection, namely t1, t2 and t3, in which the flow front progression was stopped three times, leaving behind three areas of high saturation.

CONCLUSION

This paper presents a new approach to monitor the dynamic saturation of fibrous reinforcements that take place during LCM manufacturing. This setup is based on filtered visible light transmission (VLT) through the fibrous reinforcement allowing evaluation of the partial saturation of the fabric. Two set of experiments were carried out to evaluate the saturation of a glass/vinylester composite subject to different manufacturing conditions. RTM injections at constant pressures and constant flow rates were performed at room temperature and void content measured from ASTM D2734 standard. Results indicate that voids are formed near the vent region while nearly fully saturation occurs at injection gate. Moreover, these results show the existence of an optimal injection condition that minimizes the formation of voids by air entrapment. Injections carried out at constant flow rate were evaluated with the new LVT setup. Results from the VLT analysis indicate that fiber saturation increases with local fluid pressure and decreases while increasing impregnation velocity. Finally, the numerically estimated optimal injection conditions were demonstrated to be experimentally appropriate to minimize the formation of voids by air entrapment. This is a key validation that opens the door for simple characterization of fiber impregnation to compute optimal manufacturing conditions with minimal labour.

REFERENCES

1. Rudd, C.D., Liquid moulding technologies resin transfer moulding, structural reaction injection moulding and related processing techniques. 1997, Cambridge, England, Warrendale, PA: Woodhead Publishing Limited. Society of Automotive Engineers.

2. Ruiz, E., et al., Modeling of resin cure kinetics for molding cycle optimization, Int. Conf. in Flow Processes in Composite Materials. 2006: Ecole des Mines de Douai, Douai, France.

3. Ghiorse, S.R., Effect of void content on the mechanical-properties of carbon epoxy laminates. Quarterly-Society for the Advancement of Material and Process Eng., 1993. 24(2): p. 54-59.

4. Leclerc, J.S. and E. Ruiz, Porosity reduction using optimized flow velocity in Resin Transfer Molding. Composites Part A: Applied Science and Manufacturing, 2008. 39(12): p. 1859-1868.

5. Lundstrom, T.S., B.R. Gebart, and C.Y. Lundemo, Void Formation in RTM. Journal of Reinforced Plastics and Composites, 1993. 12(12): p. 1339-1349.

6. Patel, N., V. Rohatgi, and L.J. Lee, Micro scale flow behavior and void formation mechanism during impregnation through a unidirectional stitched fiberglass mat. Polymer Engineering and Science, 1995. 35(10): p. 837-851.

7. Ruiz, E., et al., Optimization of injection flow rate to minimize micro/macro-voids formation in resin transfer molded composites. Composites Sci. and Technology, 2006. 66(3-4): p. 475-486.

8. Lebel, F., et al., Prediction of optimal flow front velocity to minimize void formation in dual scale fibrous reinforcements. Composites Part A, 2011. Article in review (2012).

9. Lebel, F., et al., Dynamic study of void formation and saturation in dual scale reinforcement by 2d tomographic reconstruction. Composites Sci. and Technology. Article in review (2012).

Section 3

Processing

COMPARISON BETWEEN THE NUMERICAL SIMULATION PROGRAM PAM-RTM AND RTM-MEASUREMENTS ON A FLAT PLATE

M. Arnold[1], G. Rieber[1], M. Wahl[2] and P. Mitschang[1]

[1] Institut für Verbundwerkstoffe, Erwin-Schrödinger-Str. Geb. 58, D-67663 Kaiserslautern,
Germany. Corresponding author’s e-mail: matthias.arnold@ivw.uni-kl.de
[2] Audi AG, Innovation und IT, Werkzeugbau, D-85045 Ingolstadt, Germany

ABSTRACT: In this study, the calculated flow fronts of the Resin Transfer Molding (RTM) simulation program PAM-RTM are compared to RTM experiments. Using experimental data (2D-permeability measurements of a wide variety of reinforcement material) recorded by IVW´s permeability measurement cell 2D-Capa-Perm. Oil is used as the flow medium as its viscosity is well known as a function of temperature. During the experiments, radial flow of the oil is detected by eight linear capacitive sensors making it possible to visualize the flow front position of every sensor with respect to time. The experiments are simulated with the program PAM-RTM which enables the user to record the flow front position with respect to time at every node in the finite element mesh. The flow front positions of the associated experiments were afterwards compared with those of the simulation. The comparisons are performed for three glass fiber fabrics (plain, twill 2/2 and satin1/7) utilizing different injection pressures and fiber volume contents. Results of the comparisons show, that the correlations between experiments and simulations match very well. However, with increasing anisotropic flow behavior the correlation between the simulated flow front and the sensor signals in experiment at 45 degree orientation to the K1 and K2 directions becomes worse.

KEYWORDS*: RTM, filling simulation, permeability, viscosity.*

INTRODUCTION

Resin Transfer Molding (RTM) has become an important process for the production of automobile, aeronautic and engineering components, because of the production time and cost savings that can be made compared to prepreg production [1]. The prediction of the flow behavior of the matrix system in complex parts manufactured by the RTM-process is quite complicated, but necessary to achieve a high quality process. Therefore several numerical simulation programs (LIMS, PAM-RTM, RTM-Worx, SimLCM, etc.) have been developed in order to help visualize the flow behavior of matrix systems in dry reinforced textiles [2-4]. With the resultant information about the flow behavior, tool geometry, gate and vent locations, filling time and selection of the reinforcement material can be optimized.

The literature depicts a lot of investigations of filling simulations which are compared to experiments. Trochu et al. compared numerical simulations to experiments for a rectangular mold and a mold with obstacles. The resin is injected by a point and the mold is closed by a

PMMA plate to allow visual recording of the flow front position [5]. Kang et al. found close agreement between experiments and numerical simulation on a flat plate with obstacles injected by a point central on the laminate. The experiments were carried out in a steel tool covered with a transparent PMMA top plate to visualize the fill behavior [6]. Walbran et al. compared filling simulations to experiments on a truncated pyramid, which also had a transparent PMMA upper mold half to allow flow front monitoring [7]. All these experiments were carried out with a transparent upper mold half to allow recording of the flow front progression so that the flow behavior of the simulations can be compared optically.

In this study the flow fronts are calculated in the simulation program PAM-RTM and compared to RTM-measurements on a flat plate. Therefore experiments are realized in a closed square aluminum tool. The measurement fluid is injected by a central point and the flow front is detected by linear capacitive sensors, which are positioned radially around the injection point. Thus, it is possible to record the flow front position on every sensor with respect to time. These curves are compared to computerized curves of the simulation and the deviation between the measurements and the simulation is shown. A good correlation between experiments and simulation was found. Moreover, the influence on the results of the filling simulation due to permeability values with a standard deviation is shown.

MATERIAL AND METHODS

For the validation, six different experiments were compared to the filling simulations. Table 1 shows the material data used for the experiments.

Table 1: Material data of the experiments

Test number	**Material**	**Weave**	**Number of layers**	**Areal weight [m²/g]**	**Fiber volume fraction [%]**	**Measurement fluid**
1	Glass fiber	2/2 Twill	6	289	46.9	rapeseed oil
2	Glass fiber	2/2 Twill	7	289	54.7	rapeseed oil
3	Glass fiber	8H Satin	8	300	48.3	rapeseed oil
4	Glass fiber	8H Satin	13	300	51.5	rapeseed oil
5	Glass fiber	Plain	11	289	51.3	rapeseed oil
6	Glass fiber	Plain	7	289	54.7	rapeseed oil

In Table 2 the parameters used for the measurements and the determined values of each permeability experiment are shown. The permeability values and the orientation angle were determined separately for each experiment. Figure 1 depicts the measurement method of the six experiments and how the orientation angle α is defined.

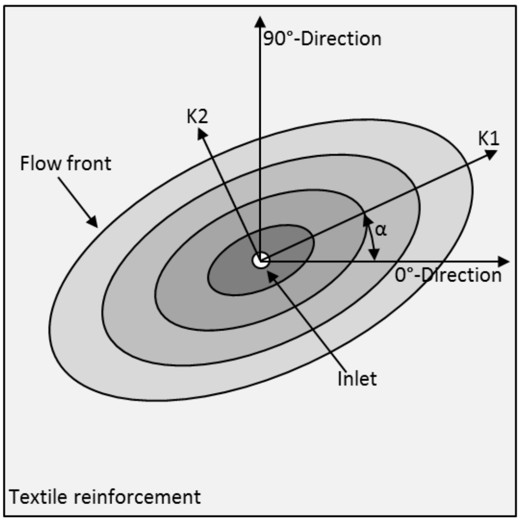

Figure 1: 2D-Measurement method to determine the permeability of textile reinforcement

Table 2: Specification of the parameters used for the tests and input data for the simulation

Test number	**Injection pressure [bar]**	**Temperature measurement fluid [°C]**	**Permeability K1 [m²]**	**Permeability K2 [m²]**	**Orientation angle α [°]**
1	2	21.9	$5.5 \cdot 10^{-11}$	$1.4 \cdot 10^{-11}$	1.6
2	6	21.9	$2.1 \cdot 10^{-11}$	$0.41 \cdot 10^{-11}$	-1.3
3	2	21.6	$2.1 \cdot 10^{-11}$	$1.7 \cdot 10^{-11}$	24.3
4	3	21.9	$1.2 \cdot 10^{-11}$	$1.0 \cdot 10^{-11}$	18.3
5	4.5	21.0	$4.5 \cdot 10^{-11}$	$2.0 \cdot 10^{-11}$	0.3
6	5.5	20.9	$2.2 \cdot 10^{-11}$	$1.6 \cdot 10^{-11}$	0.5

The viscosity of the used rapeseed oil does not have an influence on the experiments or simulation, because the viscosity is very well known with respect to temperature (see Figure 2). It was measured using a Brookfield spindle rheometer DV-II+ Pro in the temperature range +10 °C to +35 °C. The hanging drop method was used to measure the surface tension of the oil (33.67 mN/m ±0.61 at room temperature).

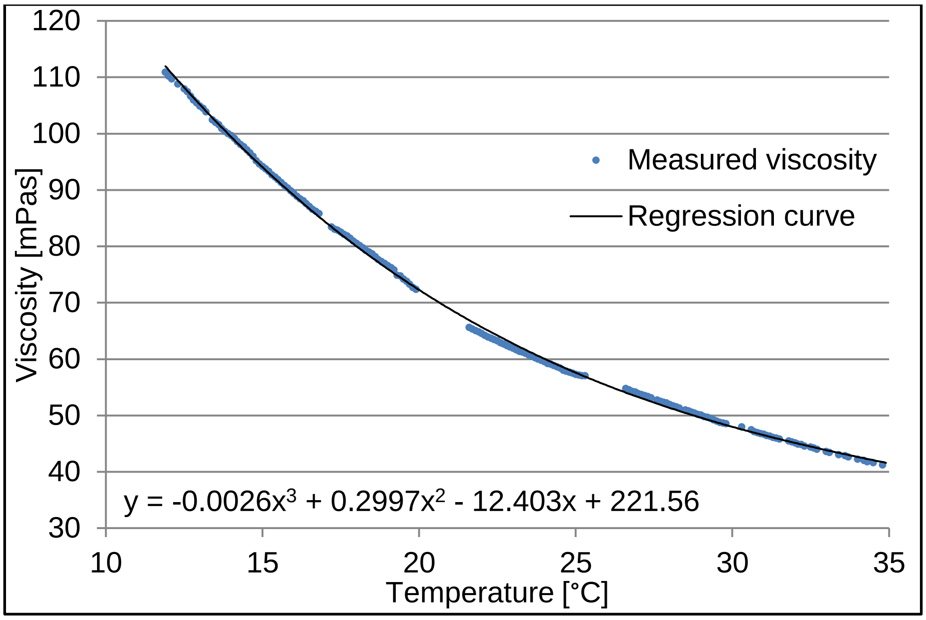

Figure 2: Viscosity measurement data of rapeseed oil and polynomial regression curve

The tests were conducted with the permeability measurement cell 2D-Capa-Perm (see Figure 3), which is described in detail in [8, 9]. The rapeseed oil is injected in the center of the measurement cell using a constant injection pressure between 1-6 bar. To ensure 2D-flow, a hole (Ø 12 mm) is punched through the middle of the 465 mm by 465 mm sized preform. The flow of the measurement oil changes the dielectric properties of the eight sensors allowing the flow front position to be tracked with time. The radially positioned sensors are named like the cardinal directions (north; north-east; east; south-east; south; south-west; west; north-west). The fiber volume fraction can be adjusted with the help of 15 different cavity height frames and the number of layers of the preform. For the tests all layers are orientated in warp direction. The point injection in the middle of the textile ensures that there is no race tracking during the experiments, which is very important for the comparison to the simulation. Moreover, Finite Element Method (FEM) simulation of the tooling equipment showed that there is no significant bending and that the cavity height remains parallel to within 10 µm up to an injection pressure of 10 bar, due to the applied upper and lower mold thickness of 160 mm.

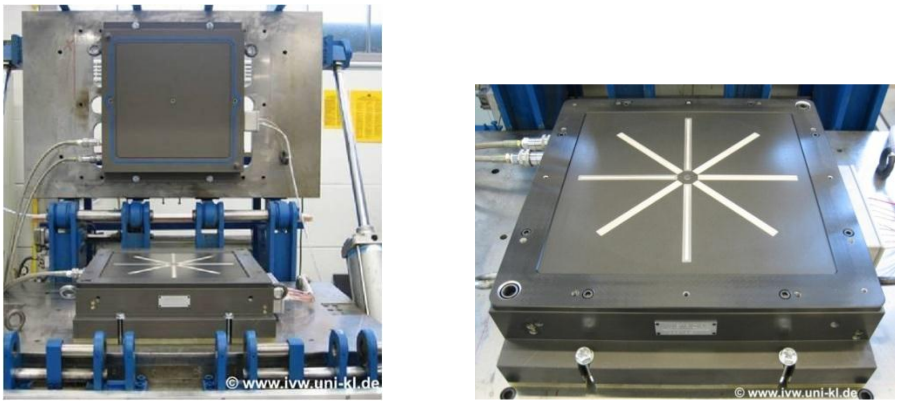

Figure 3: Permeability measurement cell 2D-Capa-Perm (left) and closeup shot of the lower mold half with the sensors

The permeability is measured as a function of the fiber volume fraction at three different fiber volume fractions, three times. Because of material inhomogeneity the measured permeability values of reinforced textiles can have a standard deviation of up to 10 % and more [10]. The accuracy of the measurement cell is high. With a high quality textile reinforcement (glass fiber, 8H Satin, 48% fiber volume fraction, 68 tex in warp and weft, 23 and 21 yarn density per cm) a coefficient of variation less 1.6 % was determined. For the validation of the filling simulation the permeability measurement of one experiment was used as input parameter for the simulation. Thus it is possible to compare the flow behavior in the measurement cell for exact one test number to the flow behavior in simulation.

The calculation of the permeability and the orientation angle is described in the publication of Adams and Rebenfeld as well as Russel [11, 12]. Figure 4 shows the principles of the evaluation. Mathematically a point symmetric ellipse is described by three points on the ellipse. The 2D-Capa-Perm records 8 points on the ellipse and so it is possible to calculate the permeability values for one measurement several times. At the IVW the first fitted flow ellipse is calculated with the average measurements of the sensors north and south, north-east and south-west and east and west (see figure 4 left) and the second fitted flow ellipse is calculated with the average measurements of the sensors north and south, north-west and south-east and east and west (see figure 4 right). To calculate the permeability values and the orientation angle the values of these two fitted flow ellipses are averaged. Because of material inhomogeneities the recorded flow front on the sensor is not exactly point symmetric and thus there is a very small deviation between the fitted flow ellipse and the recorded data.

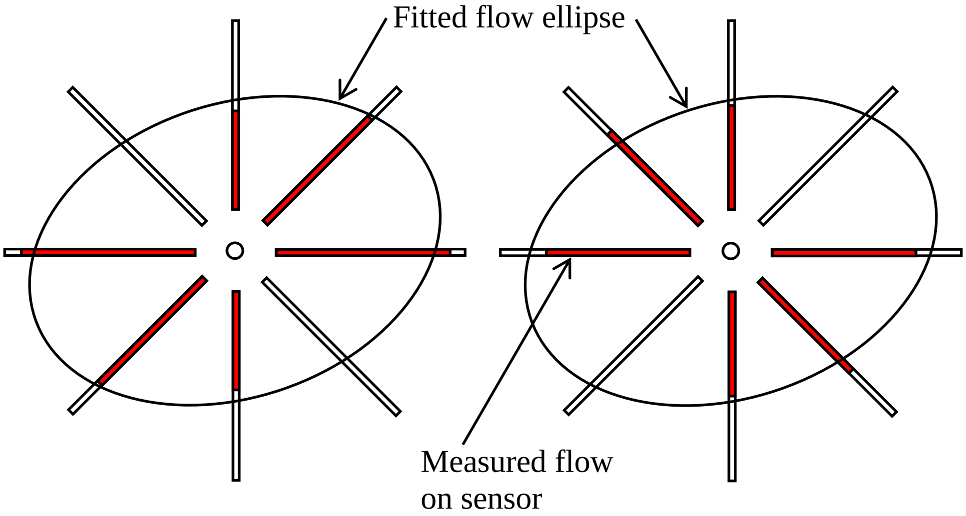

Figure 4: Evaluation of the permeability values and the orientation angle at the IVW

The model which was used for the validation of the filling simulation is shown in Figure 5. The radially positioned linear sensors can be identified by Numbers 2-9 (see Figure 5) and correspond to the dimensions of the lower mold half. The mesh on the sensors is constructed with squares with an element side length of 2.5 mm and afterwards split into triangles. Thus there is a node every 2.5 mm in the centerline of each sensor. The inlet is described by the boundary nodes of the inner circle and the vent is defined by the boundary nodes of the outer edges of the model.

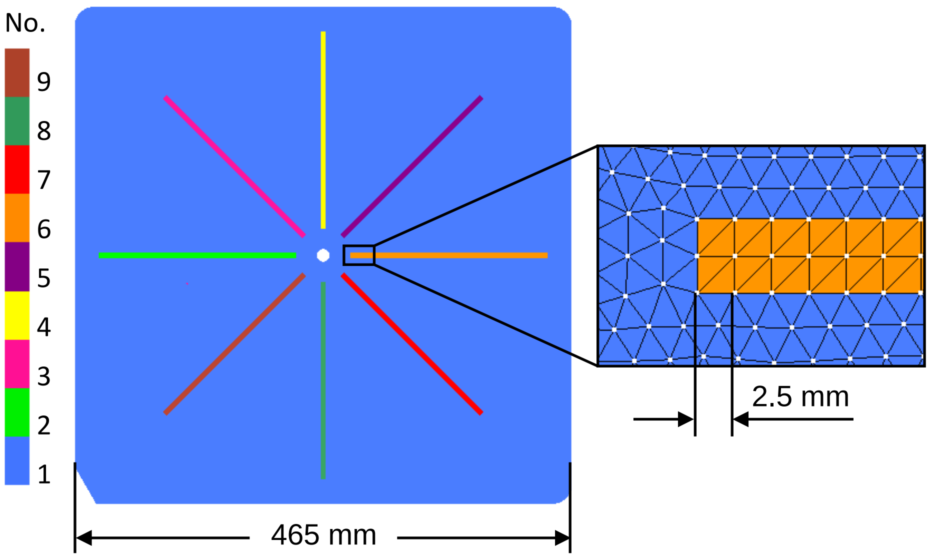

Figure 5: Model used for the filling simulations

The simulation was run with the simulation program PAM-RTM 2010 (64-bit) and the dmp-solver (parallel solver) was used with 4 cores. In the post processing the pressure was plotted at every node along the centerline of each sensor. The time step when the first pressure value was detected at each point was defined as the point of time when the flow front reaches this node. Consequently every node of the sensor has an exact position and a point of time when the flow front reaches the node. Thus it is possible to illustrate the flow front movement on every sensor with respect to time as recorded in the experiments.

RESULTS

For comparison the recorded data of four sensors is compared, because the shape of the flow front ellipse is symmetric to the injection point, meaning that the sensor values are the same for diametral sensors. In Figure 6 the flow front progression of the experiments and the filling simulation are shown for test number 1 from Table 1. A twill 2/2 glass fiber weave at a fiber volume fraction of 46.9 % was used. The average of the sensors west and east and south and north of the experiment and the simulation show excellent agreement. For the average of the sensors south-west and north-east and south-east and north-west the simulation is still very good but there is a small difference between simulation and experiments. The maximum deviation between the simulation and the experiment (test number 1) is measured at the last tracked point of the sensor line No. 7 (see figure 5) to 7.3 mm (see figure 7). If all influences causing variations in the experiments are considered, this is still a very good prediction of the resin flow by the filling simulation.

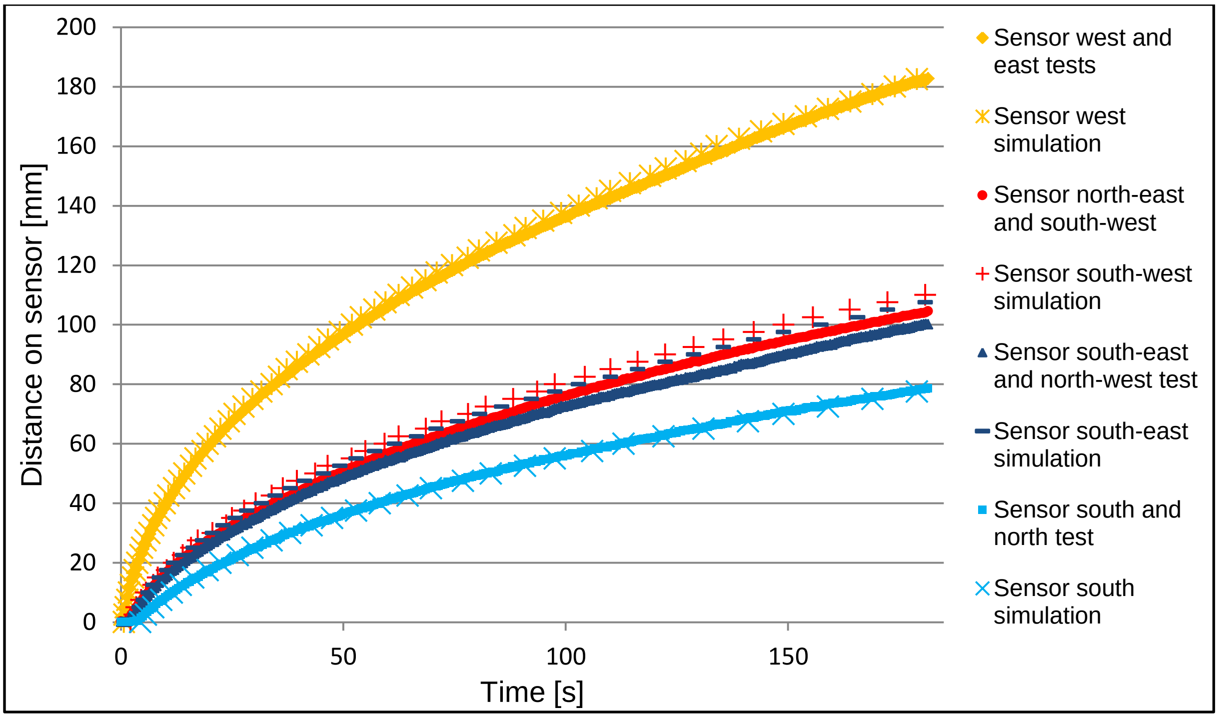

Figure 6: Flow front progressions on the sensors of the experiment and the filling simulation for the material Hexcel 1102 and a fiber volume fraction of 46.9%

The deviation of the measurements and the simulation for each test number is shown in figure 7. The results of test number 2 also show the maximum deviation at the Sensor line No. 7 (figure 5). The correlations of materials with an isotropic flow behavior are better than the results of the materials with an anisotropic flow behavior. For example the permeability values of the tests 3 and 4 are quite isotropic and show very good agreement (see figure 7). The maximum deviation at the end of the measurement of the experiments 5 and 6 to the simulations were found on sensor line No. 9 (figure 5) to be about 4 %.

One reason for the deviation between measurements and filling simulation can be seen in the inhomogeneity of the reinforced textiles. During the measurements the difference of diametral sensors are tracked which is an indicator for local fabric defaults. If there is a difference between two diametrical sensors the flow front is not exactly symmetric to the injection point, but this is a requirement for the calculation of the permeability values and in the simulation afterwards (see figure 4). In this study the deviation of diametral sensors during measurements was less than 4.5 % for all tests. The test number 3 had the lowest deviation during the experiments between the diametral sensors of 0.7 %, which means it was the most homogeneous material. This can be seen in the results between simulation and measurement (see figure 7, test number 3) which shows the lowest deviation in the study. Another reason for the deviation can be seen in the model of the simulation. In several investigations it was found that the mesh size and the element shape also influence the filling simulation results. Overall the maximum deviation between the measurements and the simulation is smaller than 8 mm, which is a very good value if the inhomogeneity of the Material is considered.

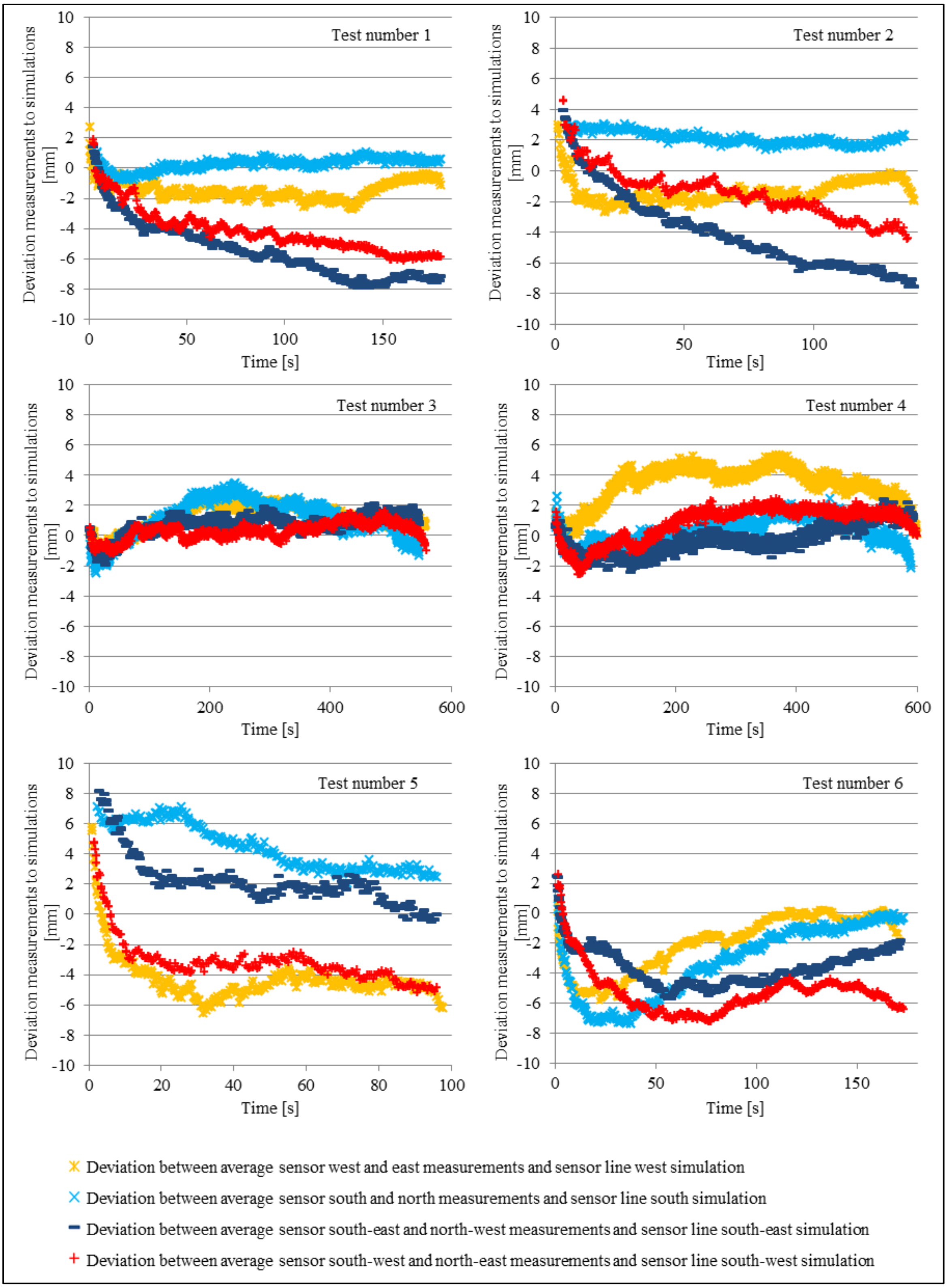

Figure 7: Deviation of the flow front progression of the measurements and the simulation

For industrial applications it is not possible to measure the permeability value during the impregnation of a part, as done for the validation above. Therefore the standard deviation of permeability values has to be considered during the parameter setting of the simulation.

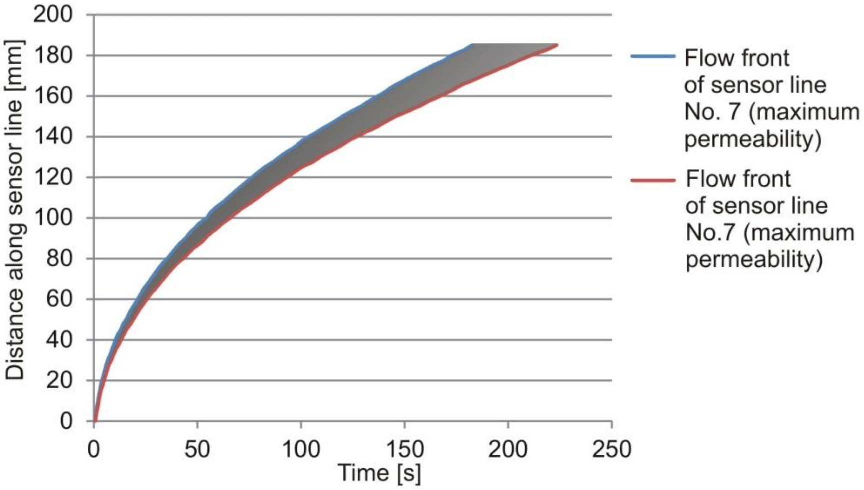

Figure 8: Progression of the flow front on the sensor line Number 7 in the filling simulation for a material with a permeability value of $K1=5\cdot10^{-11}$ m² ± 10% and $K2=3\cdot10^{-11}$ m² ± 10%. The upper curve of the area describes the progression along the sensor line for the highest permeability value ($K1_1=5.5\cdot10^{-11}$ and $K2_1=3.3\cdot10^{-11}$) and the lower curve of the area for the lowest permeability value ($K1_2=4.5\cdot10^{-11}$ and $K2_2=2.7\cdot10^{-11}$).

Figure 8 shows the progression of the flow front at the sensor line No. 7 (Figure 5) described with an input permeability value with a coefficient of variation of 10 %. The upper curve (Figure 8) of the area describes the progression of the flow front on the sensor line for the highest permeability value ($K1_1=5.5\cdot10^{-11}$ and $K2_1=3.3\cdot10^{-11}$) and the lower curve for the lowest permeability value ($K1_2=4.5\cdot10^{-11}$ and $K2_2=2.7\cdot10^{-11}$). The area between the two curves describes at what time which distance along the sensor line can be overflown by the flow front. The deviation at the end position of the sensor line No. 7 at 185 mm is 17.5 mm. To set up a robust process the standard deviation of the permeability has to be considered also in the filling simulation. The filling simulation have to show the complete filling of the component for the highest and lowest permeability values, otherwise the process will not be stable due to material variation.

CONCLUSION

In this study the flow behavior of the filling simulation with the program PAM-RTM (2D simulation) is compared to RTM-measurements on a flat plate. The experiments were conducted using IVW´s permeability measurement cell 2D-Capa-Perm, where the position of the flow front can be tracked with respect to time. The simulation results were compared to the experiments and the deviation of both were small for all six tested materials. This shows that the simulation software PAM-RTM is a valid tool for RTM filling simulation and that the permeability values measured at the IVW´s permeability measurement cell 2D-Capa-Perm are useable in such simulations. Moreover the need of accurate measured permeabilities is shown and the influences of permeability values with a standard deviation on the RTM-process are discussed.

ACKNOWLEDGEMENTS: Thanks to Audi AG for supporting this study and especially the innovation and IT section of the tool shop.

REFERENCES

1. Herrmann AS, Papsch A and Kleinberg M (2001), 'SLI-RTM Fairings for Fairchild Dornier DO 328 Jet', *22nd SAMPE Europe International Conference*.

2. Trochu F and Gauvin R (1994), 'RTMFLOT - An integrated software environment for the computer simulation of the resin transfer molding process', *Journal of reinforced plastics and composites*, 13(3), 262-270.

3. Koorevaar A (2002), 'Simulation of Liquid Injection Molding', *23rd SAMPE Europe Conference*.

4. Simacek P, Advani SG and Binetruy C (2004), 'LIMS: a comprehensive tool', *JEC - Composites*, 143-146.

5. Trochu F, Gauvin R and Gao DM (1993), 'Numerical analysis of the resin transfer molding process by the finite element method', *Advances in Polymer Technology*, 12(4), 329-342.

6. Kang MK, Il Lee W and Jung JJ (2000), 'Analysis of resin transfer molding process with controlled multiple gates resin injection', *Composites Part A: Applied Science and Manufacturing*, 31, 407-422.

7. Walbran WA, Verleye B, Bickerton S and Kelly PA (2011), 'RTM and CRTM Simulation for Complex Parts', *Processing and Fabrication of Advanced Materials XIX*, 1302-1313.

8. Kissinger C, Mitschang P, Neitzel M, Roder G and Haberland R (2000), 'Continuous on-line permeability measurement of textile structures', *45th International SAMPE Symposium and Exhibition*, 2089-2096.

9. Rieber G and Mitschang P (2010), '2D Permeability changes due to stitching seams', *Composites Part A: Applied Science and Manufacturing*, 41(1), 2-7.

10. Rieber G (2011), 'Einfluss von textilen Parametern auf die Permeabilität von Multifilamentgeweben für Faserverbundkunststoffe', Dissertation, TU Kaiserslautern.

11. Adams KL and Rebenfeld L (1987), 'In-Plane Flow of Fluids in Fabrics - Structure/Flow Characterization', *Textile Research Journal*, 57(11), 647-654.

12. Adams KL, Russel WB and Rebenfeld L (1988), 'Radial Penetration of a Viscous-Liquid into a Planar Anisotropic Porous-Medium', *International Journal of Multiphase Flow*, 14(2), 203-215.

PREPARATION AND OPTIMISATION OF MODIFIED DGEBA-BASED EPOXY RESIN AS A SELF-HEALING COMPOSITE MATRIX

E.H. Lim and K.L. Pickering

School of Engineering, Faculty of Science and Engineering, University of Waikato, Private Bag 3105, Hamilton, New Zealand.
Corresponding author's email: ehl7Qwaikato.ac.nz

ABSTRACT: This paper presents an optimisation study of a modified epoxy resin, consisting of thermoplastic poly(bisphenol-A-co-epichlorohydrin) dissolved in diglycidyl ether of bisphenol A epoxy resin (DGEBA), and cured with nadic methyl anhydride and an accelerator. The purpose of the modification was to produce a polymer capable of self-repair. Thermoplastic beads as the main element of the healing system were stirred in heated epoxy resin for at least 24 hours until fully dissolved in the solution. The viscosity of the blends before cure with varying concentrations of thermoplastics in weight percentage was measured for use as one of the performance indices of the composite matrix. In conjunction with the concentration of thermoplastic, the highest healing efficiency without significant deterioration of matrix properties was also targeted in obtaining the optimum matrix. The polymer was found exhibiting highest mechanical properties when cured at 80˚C for 4 hours and further post-cured at 130˚C for 3 hours. It was also found that the modified epoxy resin not only facilitated the cured matrix to self-repair, but also improved the mechanical properties. Overall, therefore, it has been shown that addition of thermoplastic does not have to disadvantage matrix properties. Most importantly, test results also show a promising healing efficiency.

KEYWORDS: *Optimisation, modified epoxy resin, self-repair*

INTRODUCTION

Evolution of composite use in the aircraft industry up to 53% by weight onboard a plane reflects high market demand for composites these days [1]. With lightweight composites, aircraft manufacturers can offer changes to the design of aircraft components and assembly practices. For instance, multiple parts can be integrated into large single piece components and mechanical fastening can be replaced by adhesive bonding that will eliminate stress concentration. Composites, however, can easily contain damage that is invisible to naked eyes; they may have hidden damage from impact such as delamination and matrix cracking [2] but leave no sign of exterior damage to be noticed. The incidents of the Delta II Launch Vehicle [3] and the Airbus AA-587 [4] are two examples of how hidden damage can be fatal if left unrepaired. Effective repair methods, therefore, must be facilitated for composite materials. One of the most promising new strategies of repairing composites is the use of autonomic healing polymeric matrices.

Autonomic healing polymeric matrices are materials designed to have capacity of self-repairing damage at the very beginning level without the need of prior detection of damage. Unlike conventional practices where early formation of damage would eventually nucleate to critical damage that requires major repair or replacement, these autonomic healing materials can manage damage itself, where early damage will be repaired by repair mechanism integrated within the material, hence preventing damage progression such that the lifetime of the composite component is appreciably extended. One of the milestones in the development of autonomous healing materials applicable to composites came from Hayes [5, 6]. The approach is to include thermoplastic additives into thermosetting polymer matrices. Different from liquid-phase healing [7, 8, 9] that requires vessels containing healing agents, Hayes used thermoplastic beads to act as healing agents which melt upon being heated and flow into cracks bonding the crack surfaces upon solidification; the healing agents then remain solid in the matrix, available for further future repair; therefore, thermoplastic-included polymeric matrices are capable of undergoing repeated healings. Also, with heat-stimulated healing characteristic, repair can be initiated whenever required. Hidden damage may indeed occur during the manufacturing stage of composites. Theoretically, an overall heating of composite components will allow the repair of the hidden damage. Another benefit worth-mentioning is that this approach fits well with readily available thermoset resins without complex modification. The main challenge in this research is to find out the optimal content of healing agents to incorporate in polymeric matrices for the achieving highest autonomous repair efficiency without affecting the mechanical performance of original materials.

EXPERIMENTAL

Materials

Epoxy resin employed as the matrix polymer in this experimental work was diglycidyl ether of bisphenol A (*Epikote-828*) purchased from Fraser Brown & Stratmore Limited (Lower Hutt, New Zealand). Characteristics of this material are presented in Table 1 [10]. The selected thermoplastic acting as healing agent was poly(bisphenol A-co-epichlorohydrin), *PBE*, purchased from Sigma-Aldrich (Auckland, New Zealand). Other constituents involved were curing agent nadic methylene anhydride (*NMA*) and accelerator Cognis Capcure 3-800, purchased from Hunstman Advance Materials (Deer Park, Australia) and Fraser Brown & Stratmore Limited (Lower Hutt, New Zealand), respectively. All materials were used as received.

Processing

Neat matrix

Neat matrix without addition of healing agent was prepared for reference purposes. Epikote-828 was heated to 80°C, to mimic the procedure used when healing agent was also incorporated, before curing with NMA and Capcure 3-800. Capcure 3-800 acts as an accelerator for the anhydride curing agent to reduce the curing time and the curing temperature [10]. The proportions of Epikote-828 : NMA : Capcure 3-800 are in the ratio of 5 : 4 : 1. Once blended, the mixture was subjected to deaeration in vacuum oven under pressure of 95kPa for 30 minutes at the temperature of 80°C to remove air bubbles captured during stirring. Subsequently the mixture was poured into pre-heated silicone rubber moulds of 4 mm thick Type I dumbbell-shape [11] for tensile testing samples and of 7 x 14 x 62 mm^3

rectangular column [12] for single-edge notched bending (SENB) samples. Then the resins were cured at 80°C for 4 hours followed by a post-cure at 130°C for 3 hours. After curing, tensile samples were used as moulded, with the edges slightly polished to remove any possible stress concentrators. For SENB samples, columns obtained from mouldings were polished and notched by milling machine with V-shape thread milling cutter to a depth of approximately 2.5 mm. All notched samples were conditioned at room temperature before subjected for testing.

Healable matrix

Production of healable matrix followed a similar route to that taken to produce neat matrix. Initially PBE healing agent pellets were dissolved in Epikote-828 in temperature range 80-100°C. Magnetic stirring was continued until there was no sign of pellets in the mixture. This could take up to more than 24 hours depending on the content of healing agent and mixture temperature. The rest of the procedure was similar to the neat matrix preparation with the exception of temperature for deaeration varied in the range of 80-100°C following the mixing temperature.

Table 1: Characteristics of Epikote-828 and poly(bisphenol A-co-epichlorohydrin)

Typical properties	Epikote828	PBE
Form	Viscous liquid	Pellets
Density, g/mL	1.17	1.18
Flash point, °C	> 150	-
Viscosity, Pa.s		
20°C	32	-
30°C	6.0	-
40°C	1.5	-
50°C	0.55	-
60°C	0.24	-
70°C	0.12	-

Viscosity measurement

Addition of fillers into polymer materials affects rheological properties of filled polymers. An important rheological property of fluids is viscosity. Assessment of the influence of thermoplastic healing agent on the viscosity of epoxy resins containing 5%wt, 10%wt, 15%wt, 20%wt, 25%wt and 30%wt of healing agent at three different temperatures was conducted; viscosity of neat epoxy resin was also measured for reference. The used device was a Brookfield DV-II Digital Viscometer, a rotational apparatus which measures the torque required to rotate a spindle at constant speed immersed in the resin and gives the viscosity values in Poise (equivalent to 0.1 Pascal second, Pa.s). It is important to note that mixtures must be poured into beaker sufficiently high to immerse the indicated portion of the measuring spindle to obtain an accurate viscosity measurement.

Mechanical testing

The effect of healing agent on polymer matrices was assessed using tensile and fracture toughness testing according to ASTM D638-03 [11] and ASTM D5045-99 [12], respectively. Samples were produced from resin mixtures containing healing agent up to 20%wt. in 5%wt. intervals. Mixtures containing a higher content of healing agent were too high in viscosity resulting in deaeration difficulty and poor flowability of mixture to pour into silicone mould. Samples made of pure epoxy resin were also produced for reference purposes.

Tensile testing

An Instron 4204 universal testing machine was used for tensile testing. Samples were mounted by means of wedge grips prefixed to the crossheads. Grip surfaces of samples were too flat causing slippage during testing; this problem was overcome by adding sand paper wrap around the sample the grip areas. As the grips were not the self-aligning type, caution to align sample with center line of machine crossheads was necessary to assure slippage was prevented insofar as possible. A 5 kN load cell was used and the speed of test was set at 5 mm/min given testing time of about 1 minute. A 50mm extensometer was clipped at the full gauge length of the sample for measurement of loads applied and the corresponding displacements. Only samples fractured within the gauge length were accepted for measurement of required tensile properties. An average value calculated from 5 measurements was obtained, according to standard requirements.

Single-edge notched bending (SENB) test

Upon testing, a natural (sharp) crack was initiated by sliding a new razor blade across the notch tip of each sample. The test samples were fractured in a three-point flexure jig with a 56 mm span in an Instron 4204 universal testing machine where test time for sample was within 1 – 3 s. Peak fracture forces were determined. After testing, the lengths of precracks at both ends of the notch were measured using a microscope and the dimensions were added to the prior measured notch depth to obtain the total crack length. Only samples that fulfilled the test conditions in accordance with the standard [12] were considered valid for calculations of the plane-strain fracture toughness, K_{IC}. An average value calculated from 3 measurements was obtained.

Assessment of healing efficiency

All *SENB* samples subjected to three-point bending testing were broken into two pieces. The two halves were brought together and clamped by a simple clamping device. The samples were then heated in an oven at 130°C for 6 hours. Upon cooling, the samples were retested to assess the recovery efficiency for both the neat matrix and the healable matrices. The procedures were repeated for healing at 160°C for 1 hour.

RESULTS AND DISCUSSION

Effect of healing agent on viscosity of resin mixture

Results of viscosity measurements for pure epoxy resin as a function of temperature are presented in Table 3. Viscosity at higher temperature possessed a slightly higher percentage of difference in comparison with the data obtained from manufacturer data sheet. The viscosity values in the range of 80 – 100°C served as reference for viscosity measurements of epoxy/thermoplastic healing agent mixture. These results are shown in Figure 1. As can be seen in the figure, a higher temperature resulted in lower values of viscosity for all mixtures while higher concentration of thermoplastic healing agent increased viscosity.

Table 3: Viscosity of pure Epikote-828 at different temperatures

Mixture temperature, °C	Viscosity, Pa.s	% difference (in comparison to data sheet)
20°C	31.3	2.19
30°C	5.97	0.50
40°C	1.57	4.67
50°C	0.64	16.36
60°C	0.30	25.00
70°C	0.14	16.67
80°C	0.07	-
90°C	0.06	-
100°C	0.04	-

During preparation of resins containing 5%wt. and 10%wt. of healing agent, stirring at 80°C was smooth from the moment healing agent pellets were added until all were dissolved in the resin; the entire process was completed within 24 hours. At 15%wt. healing agent, it was observed that stirring at 80°C became slower after several hours; all healing agent eventually dissolved, but the entire process took up to about 36 hours. This time was effectively shortened to within 24 hours when the temperature was increased to 90°C. At 20%wt., the healing agent was yet to completely dissolve after 48 hours of blending at 80°C. Even when the temperature was increased to 100°C, blending was completed only after 32 hours. Though increase of temperature higher than 100°C can shorten the dissolution time, the attempt was proven not practical because addition of curing agent at temperatures higher than 100°C resulted in a gel almost instantly. For mixtures with more than 20%wt. healing agent, the viscosity was too high for sufficient workability.

The reason of the viscosity measurement was to find out the limits for concentration of healing agent to be added to epoxy resin in a range of temperature from 80 - 100°C. From Figure 1 and the viscosity values tabulated in Table 3, mixtures at 80°C with viscosity lower than 3.90 Pa.s was manageable for dissolving healing agent in epoxy within 24 hours. Beyond that, longer blending time was required. For mixtures containing 25%wt. and 30%wt. of healing agent, with viscosity measured at approximately 10 Pa.s and higher, the blending was simply not workable at temperatures less than 100 °C.

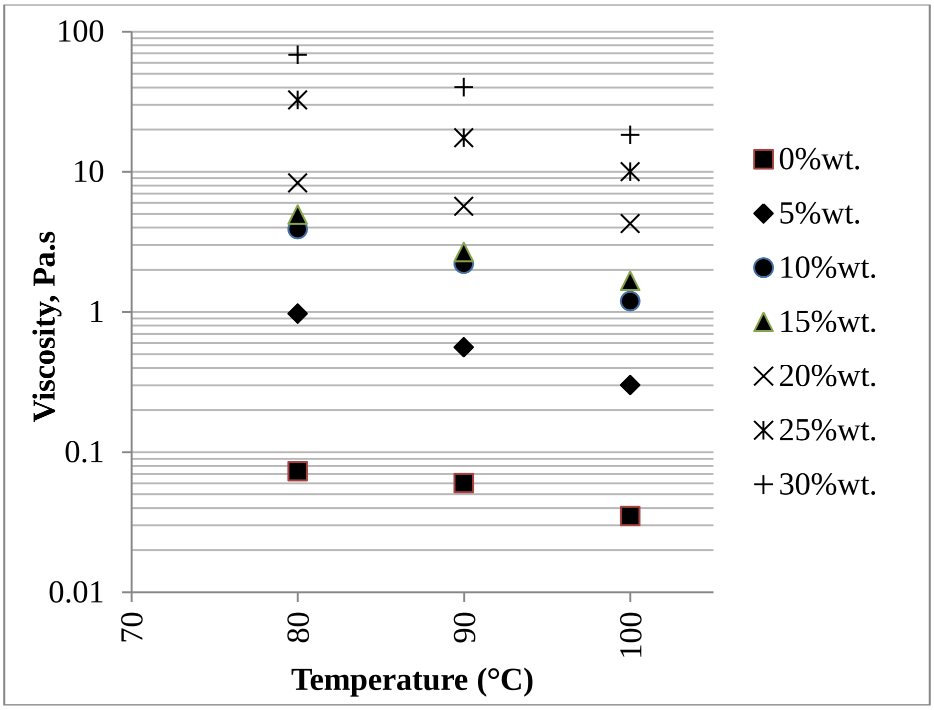

Fig. 1: Viscosity of resin mixtures containing different concentration of healing agent in a function of time

Table 3: Viscosity of mixtures with different concentrations of healing agent

Temperature of mixture	Mean values of viscosity in Pa.s						
	0%wt.	5%wt.	10%wt.	15%wt.	20%wt.	25%wt.	30%wt.
80	0.07	0.97	3.90	4.95	8.32	32.44	68.18
90	0.06	0.56	2.21	2.67	5.67	17.44	40.02
100	0.04	0.30	1.19	1.66	4.27	9.97	18.32

The effect of healing agent on original matrix performance

Three different mechanical properties for neat matrix and healable matrices containing up to 20%wt. of thermoplastic healing agent in 5%wt. intervals were determined from tensile and single-edge notched bending tests. The results are presented in Figure 2. The mean value for maximum tensile stress, Young's modulus and fracture toughness for the neat matrix were the values of 54.67 MPa, 650.13 MPa and 1.41 MPa.m$^{1/2}$, respectively. As can be seen in the figure, increases of about 8% and 13% were achieved in maximum tensile stress and Young's modulus for healable matrices. The increase was even more significant for fracture toughness; the matrix containing 20%wt. healing agent increased by 60%. These increases were attributed to an increased concentration of included healing agent in epoxy matrix. The trendlines in the figure indicate that higher concentration of healing agent resulted in higher improvement of mechanical properties.

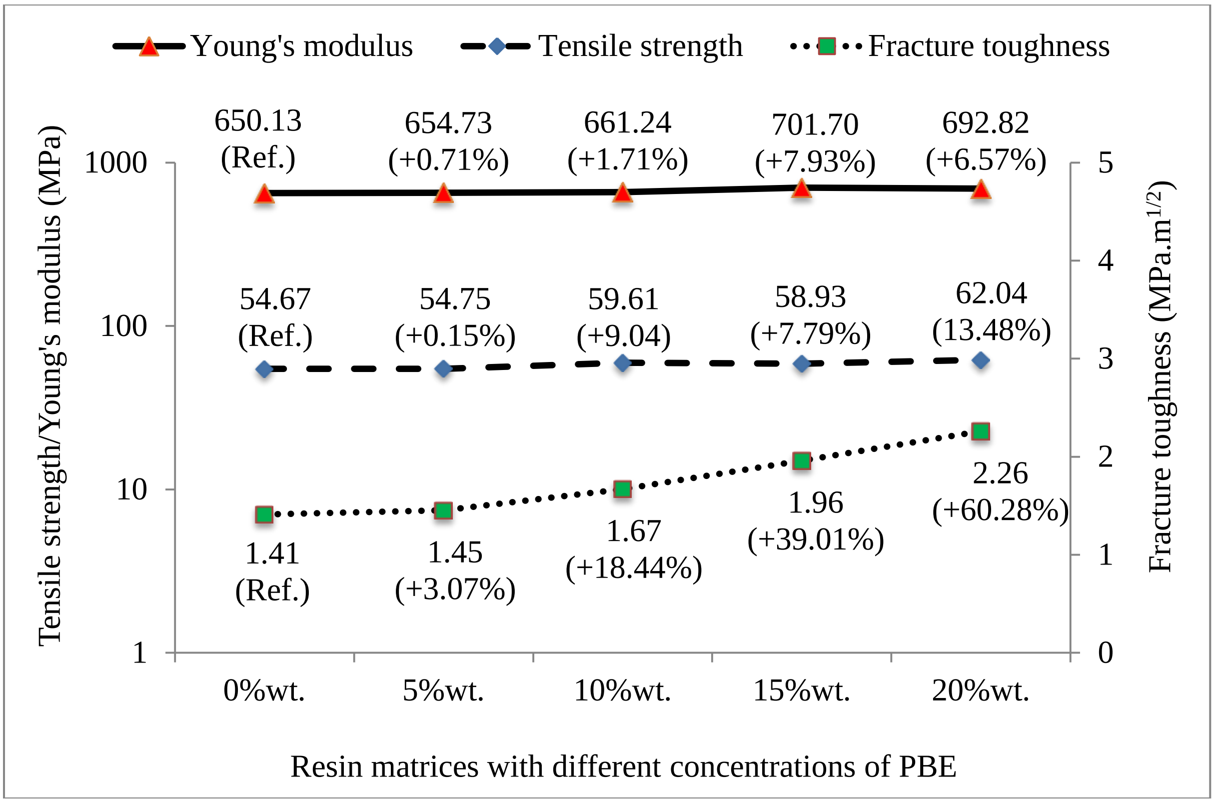

Fig. 2: Tensile strength, Young's modulus and plane-strain fracture toughness of matrices with different concentrations of PBE

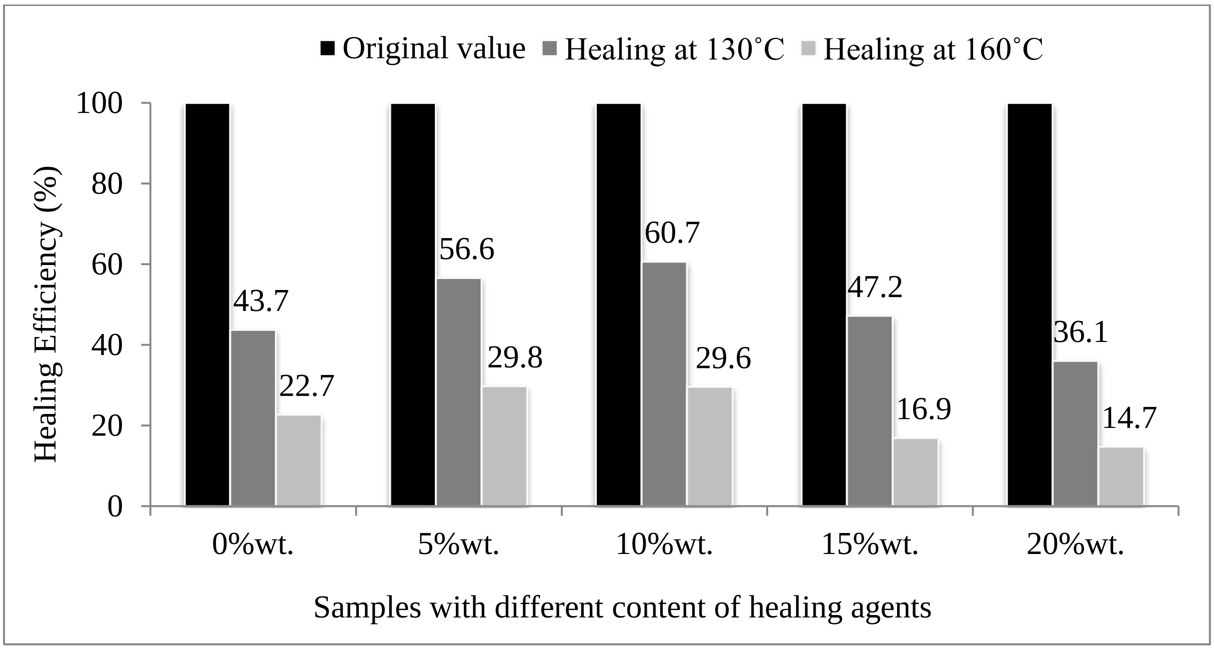

Fig. 3: Healing efficiencies of matrices at healing condition (a) 130°C for 6 hours and (b) 160°C for 1 hour

The effect of healing agent on matrix healing efficiency

Results of the self-healing assessment are shown in Figure 3. Healing at 130°C for 6 hours generally had a greater healing efficiency than healing at 160°C for 1 hour, for all matrices. The highest healing efficiency of 60.7% was achieved for 10%wt. healing agent. Surprisingly the neat matrix also possessed a relatively high recovery in fracture toughness. A recovery of up to 43.7% was achieved under healing at 130°C for 6 hours and 22.7% under healing at 160°C for 1 hour. These healing efficiencies were comparable to matrices containing 15%wt. and 20%wt. healing agent.

CONCLUSIONS

The results found that the polymers made of an epoxy/thermoplastic blend not only facilitated cured matrices to self-repair, but also improved their mechanical properties. This makes them obvious candidates for an autonomous repair composite matrix. In future work, experiments will be carried out to assess the healing efficiency of composites made of the healable matrix. The influence of healing agent on original composite properties will also be evaluated.

ACKNOWLEDGEMENTS: The authors wish to express their sincere appreciation to the Faculty of Science and Engineering (FSEN), University of Waikato, for their support in this research.

REFERENCES

1. McConnell VP (2011), ‘Past is Prologue for Composite Repair’, *Reinforced Plastics,* November/December, 17-21.

2. Talreja R (1989), ‘Damage Development in Composites: Mechanism and Modeling’, *Journal of Strain Analysis,* 24, 215-222.

3. Gunn LC (2000), ‘Operational Experience with Health Monitoring on the Delta II Program’, *In Proc. of the 2nd Int. Workshop on Structural Health Monitoring (Ed. Chang FC),* Florida: CRC Press.

4. Alfonso-Zaldivar R (2001), ‘NASA to Study Tail Fin from Jet Crash’, *In Los Angeles Time,* November 20, Home Edition A37.

5. Hayes SA, Zhang W, Branthwaite and Jones FR (2007), ‘Self-Healing of Damage in Fibre-reinforced Polymer Matrix Composites’, *Journal of the Royal Society Interface,* 4(13), 381-387.

6. Hayes SA, Jones FR, Marshiya K and Zhang W (2007), ‘A Self-Healing Thermosetting Composites’, *Composite Part A: Applied Science and Manufacturing*, 38, 1116-1120.

7. Dry CM (1996), ‘Procedures Developed for Self-Repair of Polymer Matrix Composite Materials’, *Composite Structure,* 35, 2763-2771.

8. Pang JWC and Bond IP (2005), ‘A Hollow Fibre Reinforced Polymer Composite Encompassing Self-Healing and Enhanced Damage Visibility’, *Compos Sci. Tech.*, 65, 1791-1799.

9. Brown EN, Kessler MR, Sottos NR and White SR (2003), ‘In Situ Poly (Urea-Formaldehyde) Microencapsulation of Dicyclopentadiene’, *J Microencapsul*, 20, 719-730.

10. Technical data sheet (2005, September), Retrieved from *http://www.momentive.com /products/technicaldatasheet.aspx?id=4364*

11. ASTM D638-03 (2004), ‘Standard Test Methods for Tensile Properties of Plastics’, *Annual Book of ASTM Standards*, 1-15.

12. ASTM D5045-99 (1999), ‘Standard Test Methods for Plane-Strain Fracture Toughness and Strain Energy Release Rate of Plastic Materials’, *Annual Book of ASTM Standards*, 1-9.

VARTM PROCESSING OF GLASS FABRIC REINFORCEMENTS COATED WITH GRAPHITE NANOPLATELETS

Rehan Umer [1], Eric Waggy [2] and Alfred C. Loos [2]

[1] *Khalifa University of Science, Technology & Research, P.O. Box127788, Abu Dhabi, UAE*
[2] *Department of Mechanical Engineering and Composite Vehicle Research Center, Michigan State University, East Lansing, MI 48824-1226, USA Corresponding author's e-mail: aloos@egr.msu.edu*

ABSTRACT: The processing characteristics of glass fabric reinforcements coated with graphite nanoparticles were investigated. Exfoliated graphite nanoplatelets (xGnP) were mixed in a solvent. Controlled amounts of xGnP solution were coated on to either one surface only or both surfaces of plain weave glass fabric and the solvent evaporated. Experiments were conducted to measure compaction response and permeabilities of the xGnP coated fabrics. It was found that xGnP coated glass reinforcements were stiffer than the pure glass reinforcements which reduced the final fiber volume fraction that could be obtained during VARTM processing. The in-plane permeability measurement results show that the xGnP coated reinforcements filled faster compared with the pure glass samples. This was mainly attributed to high porosity due to greater resistance to compaction during infusion. The transverse permeability of the xGnP coated glass fabrics did not show much change compared with the uncoated glass. xGnP coated glass fabric preforms were infused using SC-15 epoxy resin by the VARTM process and cured. Micrographs show that xGnP was uniformly dispersed in the glass fabric with negligible washout.

KEYWORDS: LCM, VARTM, Permeability, Compaction Response, Exfoliated Graphite, Nanoplatelets.

INTRODUCTION

The addition of exfoliated graphite nanoplatelets to the polymer matrix has been shown to produce nanocomposites that are multifunctional with improvements in mechanical properties [1-3]. However, the use of exfoliated graphite nanoplatelets as a secondary reinforcement in glass fiber composite laminates has not been studied extensively. In this study the effects of exfoliated graphite nanoplatelets on the processing characteristics of glass fabric composites fabricated by the VARTM process were investigated. Recent studies on the effects of nanoparticles on resin infiltration during manufacture of composites by VARTM have focused primarily on carbon nanotubes [4] and carbon nanofibers [5]. Little information has been published on VARTM processing effects using graphite nanoplatlets.

There are two primary methods used to introduce nano-particles into composite materials. One method involves dispersing the nano-particles in the resin [4-9]. However, the high surface area and aspect ratio of the nanoparticles can result in an increase in resin viscosity [4]. Further, during resin infiltration, aggregation of the nanoparticles can occur within the fiber tows. A second technique is to coat the nanoparticles directly onto the fibers [5] which eliminate the problems observed with the first technique.

In this investigation exfoliated graphite dispersions were coated onto the surface of glass fabric reinforcements. The compaction characteristics and permeabilities of the nano-particle coated glass fabrics were measured to determine the impact of nanoplatelets on the reinforcement flow properties.

EXPERIMENTAL

Materials

The materials used in the study were as follows. Owens Corning ShieldStrandS, S2-glass plain weave fabric with areal weight of 818 g/m^2 was used as reinforcement. The resin was Applied Polyramic SC-15 two-phase epoxy cycloaliphatic amine with an ambient viscosity of 0.35 Pa.s.

The nano-reinforcement was untreated exfoliated graphite nanoplatelet (xGnP) prepared at Michigan State University. The diameter of the nanoplatelet was 5μm and the thickness was ~7nm.

xGnP Coating Process

Solutions of 2% xGnP by weight in 2-propanol solvent were prepared. The solutions were mixed using both a mechanical stirring device and a sonicator. The S-2 glass fabrics were cut to the desired dimensions and weighed. Measured amounts of the xGnP 2-propanol solution was then poured onto the surface of the glass fabric and brushed until it was evenly distributed. The coated fabrics were placed beneath a fume hood until the 2-proponal was evaporated. Samples were prepared with 0.5 wt% and 1.0 wt% xGnP coated on one surface of the glass fabric and with 0.5 wt% coated on both sides of the glass fabric. Samples were also prepared by coating the surface of the glass fabric with 2-proponal to assess the effect of the solvent. These samples are referred to as 0 wt% xGnP. The results were also compared to “As Received” pure glass samples.

Compaction Characterization

The reinforcement compaction experiments are conducted under dry conditions to measure the compaction response of the glass preforms at pressures experienced during VARTM processing. The compaction test fixture is composed of two flat plates used to compact the samples. The upper plate has dimensions of 15.2 cm x 15.2 cm, and the lower plate has dimensions of 15.2 cm x 35.6 cm. A laser displacement sensor (L-Gage) and a digital dial indicator were used to monitor the crosshead displacement and thus the thickness of the sample being tested. A schematic of the compaction test setup is shown in Fig. 1.

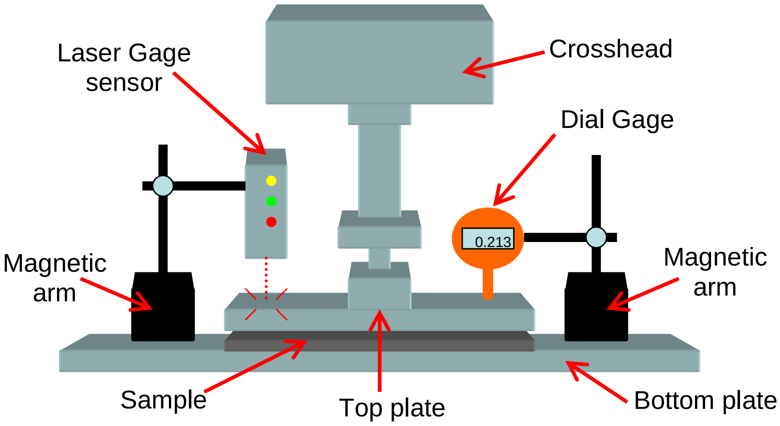

Fig. 1: Schematic diagram for the compaction test setup.

The fixture was mounted between upper and lower platens of an MTS Insight 100 kN Material Testing Machine. The MTS machine is controlled by the software "Testworks 4". The software allows the user to create custom programs to control the machine.

In compaction characterization experiments, a compressive load was applied up to a set high load limit and then releasing this load down to a set low load limit. The test cycle was decomposed into two cycles*: Loading* and *Unloading*. Both cycles were performed with a constant crosshead speed of 0.127 mm/min. Glass preform specimens were compacted to 101.5 kPa which corresponds to the maximum VARTM compaction pressure. Once the maximum load limit was reached, the crosshead begins unloading the specimen until the load drops to zero.

Permeability Characterization

Separate fixtures were used to measure the in-plane (S_{xx} and S_{yy}) and the transverse (S_{zz}) permeabilities. The transverse or through-thickness permeability test fixture was designed to establish one-dimensional saturated flow of fluid through the preform and is shown in Fig. 2. This fixture was designed to accommodate 5.08 cm x 5.08 cm preform specimens. The fluid was injected through the thickness of the specimen by rigid distribution plates mounted in the plunger and in the bottom of the cavity. The plates were machined with 0.50 cm holes drilled every 0.64 cm. A single linear voltage differential transducer (LVDT) was used to measure the thickness of the preform specimen. Two pressure transducers were located at the inlet and outlet to measure the pressure gradient in the transverse direction.

The preform specimens were placed inside the cavity of the permeability fixture. Once the crosshead was lowered to the desired starting thickness or fiber volume fraction, a constant flow rate pump was used to inject the test fluid into the mold cavity. A mass balance Mettler-Toledo® model (SB16001) was used to measure the flow rate of the test fluid at the outlet. Once steady-state flow conditions were established, the inlet and outlet pressures were measured. At each fiber volume fraction, the difference between inlet and outlet pressures over a range of different flow rates was measured and the data was used to construct a curve of volumetric flow rate versus the pressure drop. Measuring the slope of the curve gives the average permeability for the preform at the specified fiber volume fraction.

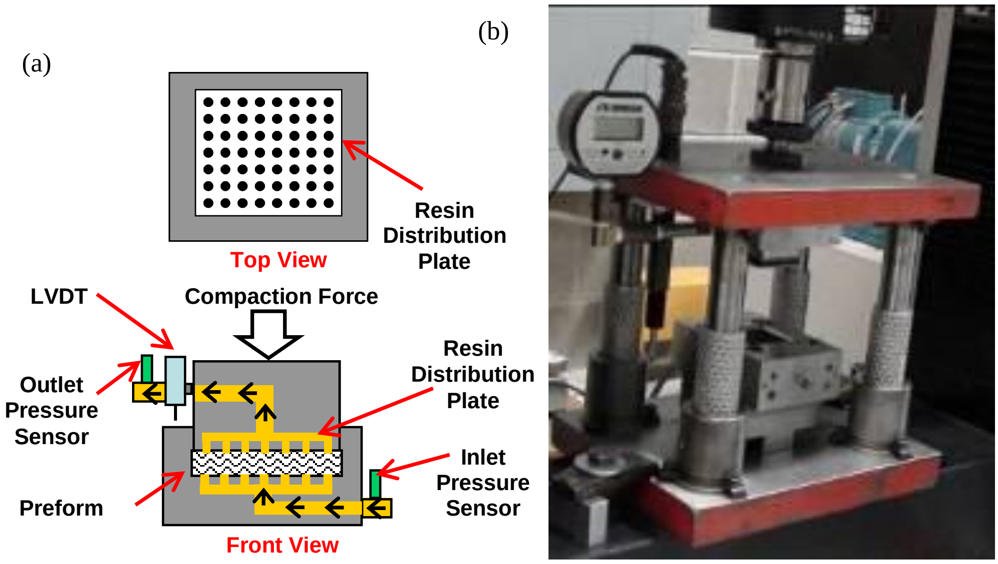

Fig. 2: (a) Schematic diagram of Transverse Permeability Fixture, and (b) Photograph of the fixture

The in-plane permeabilities of the xGnP coated glass fabrics could not be measured using a one-dimensional flow of fluid through a saturated preform due to significant washout of the nanoparticles observed during the measurements. Hence, a transient advancing front measurement technique was used where the flow front positions are recorded as a function of time. The flow visualization fixture shown in Fig. 3 was used to obtain the measurements and includes a polycarbonate tool plate 0.914 m long by 0.508 m wide. The resin inlet tube is shown on the right and the vacuum outlet tube is shown on the left.

Mounted below the polycarbonate tool was a mirror which was used to observe the resin flow along the bottom surface of the preform. Use of the mirror allows the video camera to simultaneously record the flow fronts on both the top and bottom surfaces of the preform.

Flow visualization tests were performed for samples having different wt % of xGnP coatings. Four layers of 7.6 x 15.2 cm S2-glass fabric samples were placed on the tool. Three layers of 31.7 x 381 cm distribution media were placed at the injection side before the sample to facilitate a uniform flow front pattern before the fluid reaches the preform boundary as shown in Fig. 3. A 2.54 cm square grid was placed both at the top and bottom half of preform samples. The flow fronts on the top and bottom surfaces of the preform were measured using a video camera throughout the experiments.

Composite Manufacture

Glass fabric preforms coated with xGnP nanoparticles with dimensions 20.32 cm long x 20.32 cm wide by 4 layers thick were infused with SC-15 epoxy by the VARTM process. The specimens were fabricated on a 60.96cm x 91.44cm steel mold with a single injection port and a single vacuum port. Two layers of Resinflow 60 LDPE/HDPE fabric was used as the distribution medium. After the materials were placed, the mold was sealed using a vacuum bag and sealant tape. The mold was then infused under vacuum with a pressure of 1 atm. The resin infused preform was cured in a convection oven at 60°C for two hours and post cured at 94°C for four hours.

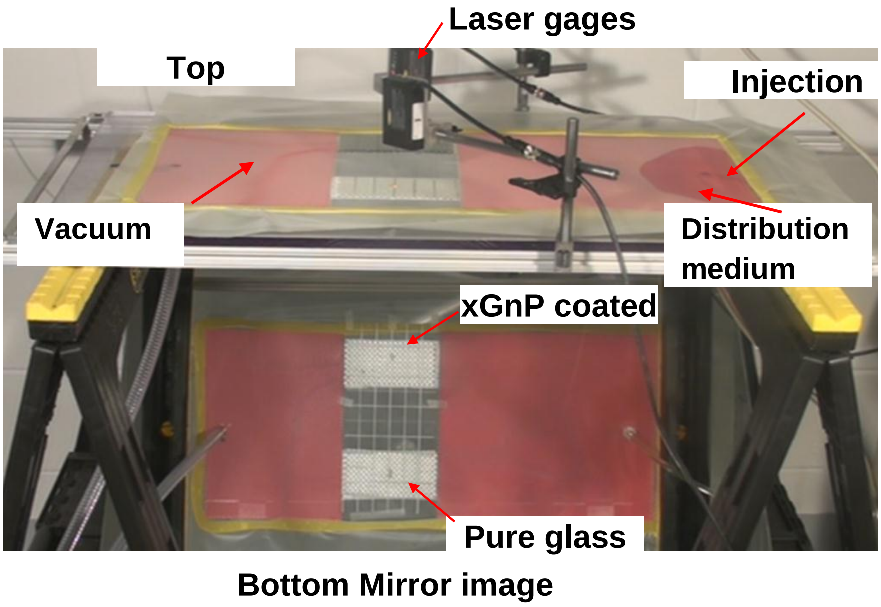

Fig. 3: Flow visualization fixture

RESULTS AND DISCUSSION

Compaction

Fig. 4 presents thickness change as a function of compaction pressure of S2 glass fiber reinforcements coated with different wt % of xGnP. The figure presents both loading and unloading curves for all samples tested. The results were also compared with “As Received” S2 glass reinforcement. The figure shows a clear trend of thickness variation at a set maximum pressure (corresponding to full vacuum condition). As the xGnP amount increases, the resistance to compaction of the S2 glass reinforcement increases. It is suspected that solvent affected the properties of the sizing present on glass fibers, causing it to become stiffer. Also, the nano particles fill the voids between the glass tows and hence causing resistance to slipping of fibers under compaction loads. This implies that a glass fiber reinforcement coated with higher wt % of xGnP will have higher resistance to compaction and hence the final product will be thicker compared to a product manufactured using “As Received” glass reinforcements.

Permeability

Permeability characterization tests were performed in the transverse (Szz) direction. The test results for S2 glass reinforcements coated with different wt % of xGnP are presented in Fig. 5. Two sets of tests were done and the exponential equation was fit to the average data points. The transverse permeability values for S2 glass fabric with xGnP were very similar. The only difference was found in the solvent treated sample, where the permeability was found to be higher as compared to other samples. It is suspected that due to the use of solvent, the sizing on the glass fibers may have dissolved as a result leaving behind channels for the fluid to flow through the thickness direction without much resistance.

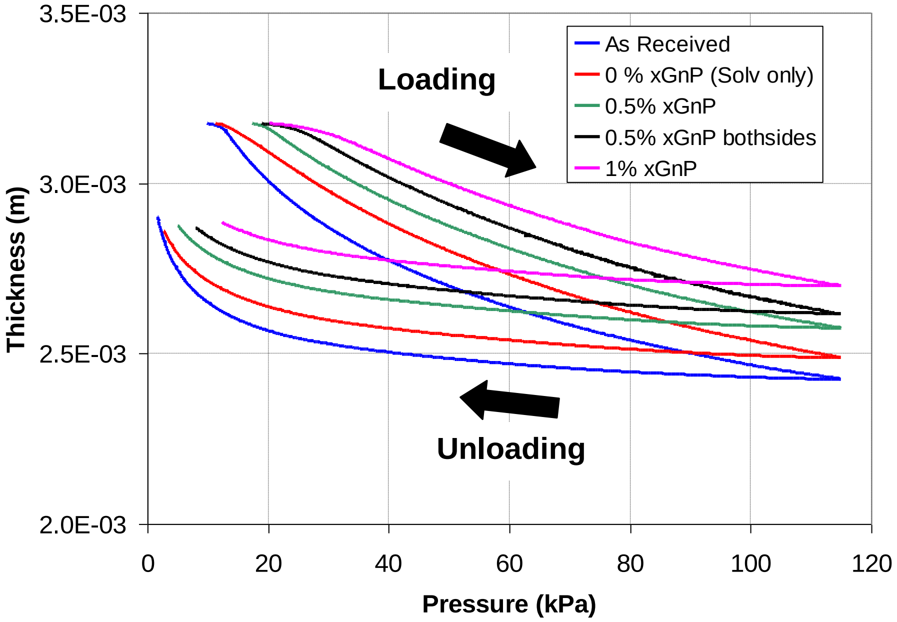

Fig. 4: Compaction response of different percentages of xGnP coated S2 glass fiber reinforcement

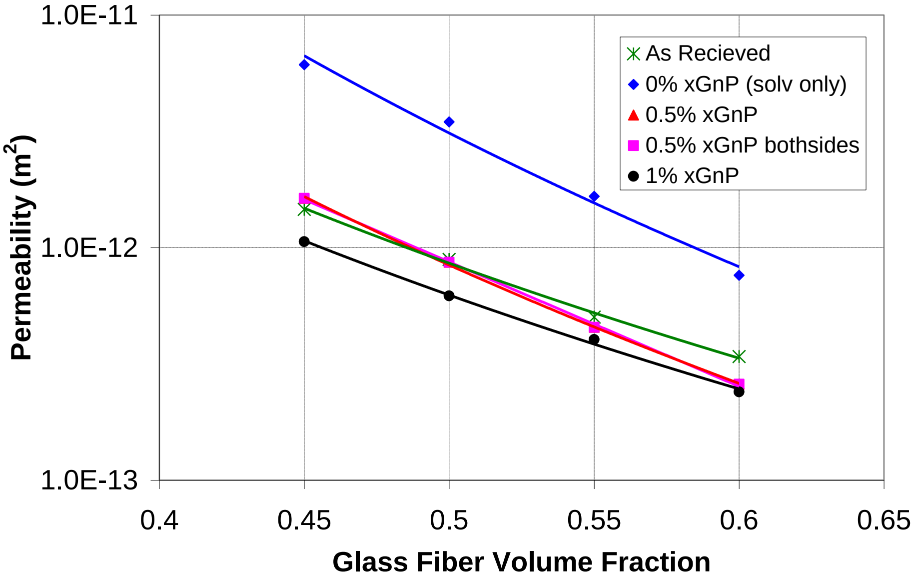

Fig. 5: Transverse permeability results of different percentages of xGnP coated S2 glass fiber reinforcement

To measure the in-plane transient permeability, the flow front positions for all xGnP coated and "As Received" samples were continuously monitored and recorded using a video camera. The transient permeability was estimated using the Darcy's law. It was observed that the flow fronts for all xGnP coated samples were faster compared to samples without any xGnP coating.

Fig. 6 presents estimated permeability results based on flow front positions. The permeability increases with increase in xGnP content. This is mainly attributed to greater cavity thickness due to higher resistance to compaction under full vacuum conditions (see Fig. 4).

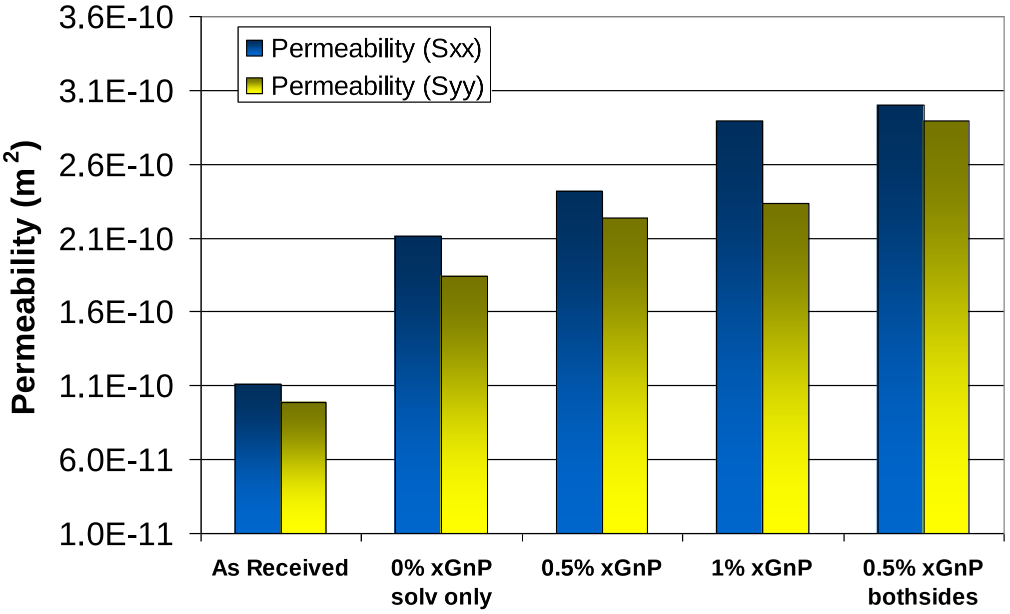

Fig. 6: Transient permeability results of different percentages of xGnP coated S2 glass fiber reinforcement

CONCLUSIONS

The VARTM processing characteristics of S2 glass reinforcements coated with graphite nanoparticles were investigated in this study. Controlled amounts of xGnP were coated onto either one surface only or both surfaces of the reinforcements using a brush coating technique. Solution coating is a viable method for introducing xGnP into a reinforcing fabric for the liquid composite molding process. The compaction response results show that as the xGnP wt % increased, the resistance to compaction also increased. The transverse permeability of xGnP coated samples did not change much except for the solvent treated samples, where the permeability was found to be higher due to possible removal or dissolution of the sizing in the solvent. The advancing front or transient permeability increased with an increase in xGnP wt % which was mainly due to an increase in compaction resistance under full vacuum conditions. Micrographs obtained from sections of the composite panels fabricated by VARTM show that xGnP dispersed well in the glass fabric with a very small amount of washout. Over all, no significant impact of xGnP on the flow characteristics was observed.

ACKNOWLEDGMENTS: This research was sponsored by the Army Research Laboratory and was accomplished under Cooperative Agreement Number W911NF-11-2-0017. The views and conclusions contained in this document are those of the authors and should not be interpreted as representing the official policies, either expressed or implied, of the Army Research Laboratory or the U.S. Government. The U.S. Government is authorized to reproduce and distribute reprints for Government purposes notwithstanding any copyright notation herein.

REFERENCES

1. Kim S and Drzal LT (2009), 'Thermal stability and dynamic mechanical behavior of exfoliated graphite nanoplatelets–LLDPE composites', *Polymer Composites,* 31, 755–761.

2. Jiang X and Drzal LT (2010), 'Multifunctional high density polyethylene nanocomposites produced by incorporation of exfoliated graphite nanoplatelets 1: morphology and mechanical properties', *Polymer Composites,* 31(6), 1091-1098.

3. Biswas S, Fukushima H and Drzal LT (2011), 'Mechanical and electrical property enhancement in exfoliated graphene nanoplatelet/liquid crystalline polymer nanocomposites', *Composites Part-A,* 42(4), 371-375.

4. Fan Z, Hsiao KT and Advani SG (2004), 'Experimental investigation of dispersion during flow of multi-walled carbon nanotube/polymer suspension in fibrous porous media', *Carbon.* 42, 871-876.

5. Movva S, Zhou G, Guerra D and Lee LJ (2009), 'Effect of Carbon nano fibres on mold filling in a vacuum assisted resin transfer molding system', *Journal of Composite Materials,* 43(6), 611-620.

6. Zhou Y, Pervin F, Rangari VK and Jeelani, S (2006), 'Fabrication and evaluation of carbon nano fiber filled carbon/epoxy composite', *Materials Science and Engineering A,* 426, 221-228.

7. Peila R, Seferis JC, Karaki T and Parker G (2009), 'Effects of nanoclay on the thermal and rheological properties of a VARTM Epoxy Resin', *Journal of Thermal Analysis and Calorimetry,* 96(2), 587–592.

8. Mahrholz T, Stängle J and Sinapius M (2009), 'Quantification of the reinforcement effect of silica nanoparticles in epoxy resins used in liquid composite molding processes', *Composites: Part A,* 40, 235–243.

9. Lin LY, Lee JH, Hong CE, Yoo, GH and Advani, SG (2006), 'Preparation and characterization of layered silicate/glass fiber/epoxy hybrid nanocomposites via vacuum-assisted resin transfer molding (VARTM)', *Composite Science and Technology.* 66, 2116-2125.

REACTIVE FLOW OF THERMOSETTING RESINS: IMPLICATIONS TO LCM PROCESSING

Jesús Maldonado[1], Bryan Louis[1], Florian Klunker[1], Paolo Ermanni[1]

[1] Centre of Structure Technologies, Swiss Federal Institute of Technology Zurich,
Leonhardstrasse 27, 8092, Zürich, Switzerland. Corresponding author's email:
fklunker@ethz.ch

ABSTRACT: The flow in textiles can be described by Darcy's Law, which states a relationship of fluid flux and pressure gradient, depending on the viscosity of the fluid and the permeability of the medium. For liquid composite molding processes, the viscosity and the permeability are usually assumed to be independent, only related to fluid (viscosity) and textile (permeability). This paper shows that for reactive flows, i.e. when the thermoset matrix is significantly curing during the injection, the permeability depends on cure progression and injection velocity. This is due to the laminar nature of the flow which is often present in LCM processes: Assuming the flow channels to be capillary tubes, the laminar streamlines at the wall are much slower, and therefore have a longer residence time within the tube than the central streamlines. This leads to a build-up of gelled resin at the walls, decreasing the diameter of the pore, and therefore the representative permeability. This behavior is simulated within capillary tubes and verified by experiments. The accuracy of the predictions can be improved, but the effect is evident and should be considered in the forthcoming simulations of highly reactive flows.

KEYWORDS: *Liquid composite molding, Reactive flow, Permeability, Thermosetting resin, Cure behavior, Finite element analysis, Flow simulations.*

INTRODUCTION

Fluid flow simulations for composites manufacturing have been used for approximately 25 years. An essential simulation parameter is permeability, the ability of a porous material to allow fluid transport. The flow of a liquid through a porous material is governed by Darcy's Law [1]:

$$\mathbf{v} = -\frac{\mathbf{K}}{\mu}\nabla\mathbf{p} \tag{1}$$

Eqn. 1 considers a constant permeability K. For a fiber preform, this value is assumed to be dependent solely on fiber architecture and fiber volume content. A higher permeability allows more fluid flow through the porous material for a steady state condition. Pressure gradient is $\nabla\mathbf{p}$, volumetric fluid flow per unit area is **v**, and viscosity is μ.

A thermosetting resin is a liquid polymer that cures irreversibly into a solid, changing its properties [2]. This transformation is characterized by a cure kinetics model. The injection of an actively curing thermosetting polymer will be further denoted as reactive flow. In LCM, this kind of flow is common through the textile. There are diverse studies about textile permeability in general [3- 5], i.e. not taking reactive flow into account. Considering the cure in flow simulations requires modeling of cure kinetics of the resin [6-8] and its effect on the viscosity [9-11]. These models have been used in flow simulation for simulating the reactive flow [10-13]. The simulations were done on macroscopic level, i.e. viscosities and degrees of cure and their effect on the flow where calculated by volume averaging methods. The microscopic structure and a wall build up of the resin in the flow channels were not considered.

Interconnected capillary tubes are used as simple representations of the flow paths inside a complex textile. Figure 1 shows two stages of the laminar reactive flow in a capillary tube, completely filled with resin, where uncured resin is injected from the left side. Figure 1a shows the initial state when the fluid is free to flow through the cylinder. When the injection time equals the gelation time of the first resin injected, the slow laminar layers will reach its gelation. A time-dependent, increasing wall build-up will be created due to the gelation point of the liquid resin still inside. The expected wall build-up after this gelation time is shown in the diagonal pattern in figure 1b. Recalling the relationship between the capillary pores and the textile, in this context, the reactive flow is expected to cause a local permeability decrease.

1a: Flow before gelation time ($t < t_{gelation}$)   1b: Flow after gelation time ($t > t_{gelation}$)

Figure 1: Stages of reactive laminar flow, before and after gelation time.

The focus of this work is to investigate the effects of reactive flow. Instead of real textile architectures, capillary tubes are used as simple representations of flow paths. A numerical model is developed to analyze the reactive flow in a capillary pore. Experimental tests are used as validation and comparison.

GOVERNING EQUATIONS

The laminar flow models are governed by the Navier-Stokes equation [3]:

$$\rho\left(\frac{\partial \mathbf{u}}{\partial t} + \mathbf{u}\cdot\nabla\mathbf{u}\right) = -\nabla\mathbf{p} + \mathrm{div}(\mu\cdot\nabla\mathbf{u}) - \rho\mathbf{g} \tag{2}$$

Equation (2) defines the balance between momentum, stress and body forces within a fluid system. Here, the velocity vector is $\mathbf{u}$, viscosity is μ, pressure is p, density is ρ and gravity vector is $\mathbf{g}$. The laminar flow in saturated porous media can be modeled by Darcy’s Law (see Eqn. (1)). The flow paths inside a complex textile can be simplified as interconnected capillary pores for ease of analysis. With this simplification of the flow through porous media, by the use of a cylindrical capillary pore in Fig. 1a, the velocity for constant viscosity in the pore of radius R can be defined depending on the radial coordinate r, showing that there is a significant volumetric rate reduction, if the radius R is decreased:

$$\mathbf{v}(\mathrm{r}) = (-\nabla\mathbf{p} + \rho \mathrm{g}_{\mathbf{z}})\frac{(R^2 - r^2)}{4\mu} \tag{3}$$

The curing of epoxy resin is characterized by cure kinetics models, in the form of a differential equation [6-8]. The differential form characterizes the increase of degree of cure (DoC) from zero to one, where zero defines a freshly mixed resin without chemical bindings, and one is a fully cured solid system. The cure kinetics equation is applied to moving fluids by addition of a convective term on the left hand side. Studies have also seen fit to include a diffusion term **c** [7]. The final application to moving fluid systems can be summarized as:

$$\frac{\partial\alpha}{\partial t} + \mathbf{u}\cdot\nabla\alpha + \nabla(-\mathbf{c}\cdot\nabla\alpha) = f(\alpha,T) \tag{4}$$

For this paper, a specific cure kinetics model was established, and fitted with DSC measurements. The warm-curing transparent epoxy resin used in this study was an Araldite LY 564 with XB 3486 hardener [Huntsman]. The corresponding cure kinetics model is:

$$\begin{gathered} f(\alpha,T) = [(k_1 + k_2\alpha^m)(1-\alpha)^n]F_1 \\ k_i(T) = A_i\cdot\exp\left(-\frac{E_i}{RT}\right) \qquad i = 1{,}2 \\ n = q_1 + q_2\cdot\ln(1-\alpha) \\ F_1 = 2\left[1 + exp\left(\frac{\alpha - \alpha_{max}}{b}\right)\right]^{-1} - 1 \\ \alpha_{max} = 0.086[1 + exp(c_1 + d_1\cdot T)]^{-1} + 0.914 \end{gathered} \tag{5}$$

with A_i, E_i and b as fitting parameters, T as temperature, and R as the ideal gas constant. Exponents n_1 and m are adjustable, while n_2 is a variable order exponent [5]. A Fournier diffusion factor F_1 [6] is also included. The value of α_{max} is the final DoC at the isothermal temperature. The list of the parameters can be found in table 1. The root mean square deviation of the fitted model is RMSD=0.0079. For values of $\alpha = [0{,}1]$, this represents a good model agreement.

Table 1: Summary of physical properties as used in the calculations.

Cure kinetics parameters		*Physical properties*	*Rheological parameters*
A_1 = 707,382 [1/s]	q_1 = 2.822	Density ρ = 1125 [Kg/m^3]	A_μ = 1.2685e-07 [Pa·s]
A_2 = 230,673 [1/s]	q_2 = 0.34	Conductivity k = 0.15 [W/m·K]	E_μ = 35,324.48 [J/mol]
E_1 = 63,068 [J/mol]	b = 0.008	Specific heat cp = 1310 [J/kg·K]	C = 1.676
E_2 = 53,065 [J/mol]	c_1= 72.299	Enthalpy = 440 [J/g]	D = 1.396
m_1 = 1.241	d_1= -0.189		

A typical exponential model [8] is adopted and a variable order term is added to account for the highly non-linear viscosity increase:

$$\mu = A_\mu\cdot\exp\left(\frac{E_\mu}{RT}\right)\cdot\left(\frac{\alpha_{max}}{\alpha_{max} - \alpha}\right)^{C - D\cdot\log\left((\alpha_{max}-\alpha)^D\right)} \tag{6}$$

where A_μ, E_μ, C and D are fitting parameters. The viscosity parameters are listed in table 1.

NUMERICAL MODEL AND EXPERIMENTAL VALIDATION

The reactive resin flow was investigated with a numerical model, and compared to experiments. In reactive flow, it is relevant to state the limitations of a statically determined gelation time: it is a material property obtained from a still sample of resin. But in a fully developed laminar flow system, the distribution of the DoC can be affected by velocity. The stagnation time, i.e. the time when the flow stops, is a system property, which may require more considerations than what a material property can provide.

The reactive flow is modeled and investigated with the finite element software Comsol. Laminar flow is coupled with the curing differential equation. An axisymmetric geometry and time-dependent solver are used. The resulting model is shown in figure 2, along with the experimental schematic setup. The flow is tested with FEM software to investigate the deviation between the helix and a straight geometry. The variation between both is under 1‰ and therefore neglectable.

A liquid of known viscosity (silicon oil Baysilone M-20) is selected for comparing numerical and experimental flow. The numerical mass flow is 2% larger than the average experimental value, which is within the standard deviation. The weight of the output resin is registered with a Mettler-Toledo SB16001 balance. A transparent resin is infused by vacuum, followed by a resin, which is colored with a compatible red agent for epoxy [R&G GmbH], added to the mixing pots (0.5% weight). The coloring provides a boundary for determining the area reduction from gelled resin. After curing, sample cuts are taken from the tube at different lengths. These cross-section cuts are examined using a Leica DMRXA microscope, and a Leica DC480 digital camera accessory.

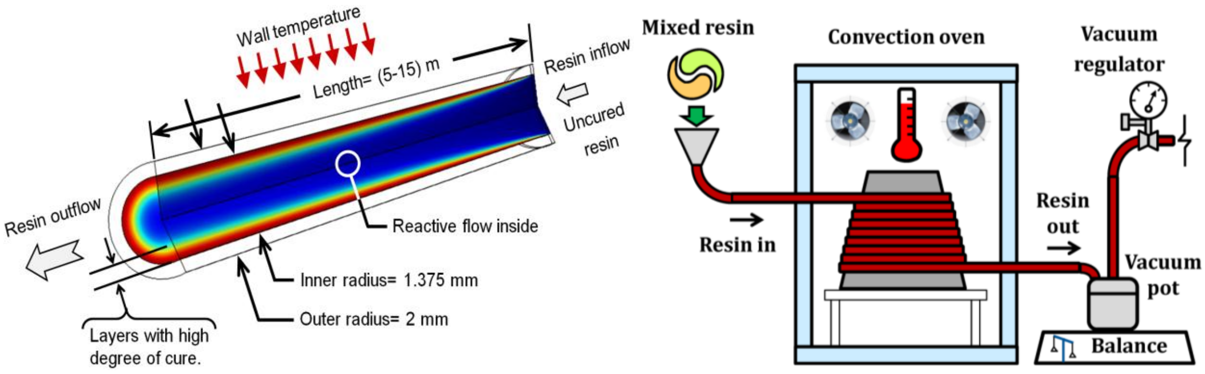

Figure 2: Finite element model (left) and schematic of the experimental method (right).

Figure 3 shows the relationship between the cross-sectional DoC and the corresponding velocity in time. A cross-section cut is taken at 99% of the length of the tube geometry in figure 2. The horizontal axis is the inner radius of the tube. Velocity is represented by the solid lines, and DoC by the dashed lines. The gelation point is also marked with the horizontal line. The markers indicate the normalized time t_n. This is defined by a quotient of the injection time t_{inj} over the gelation time t_{α_g} of the first resin injected, i.e. different points in time.

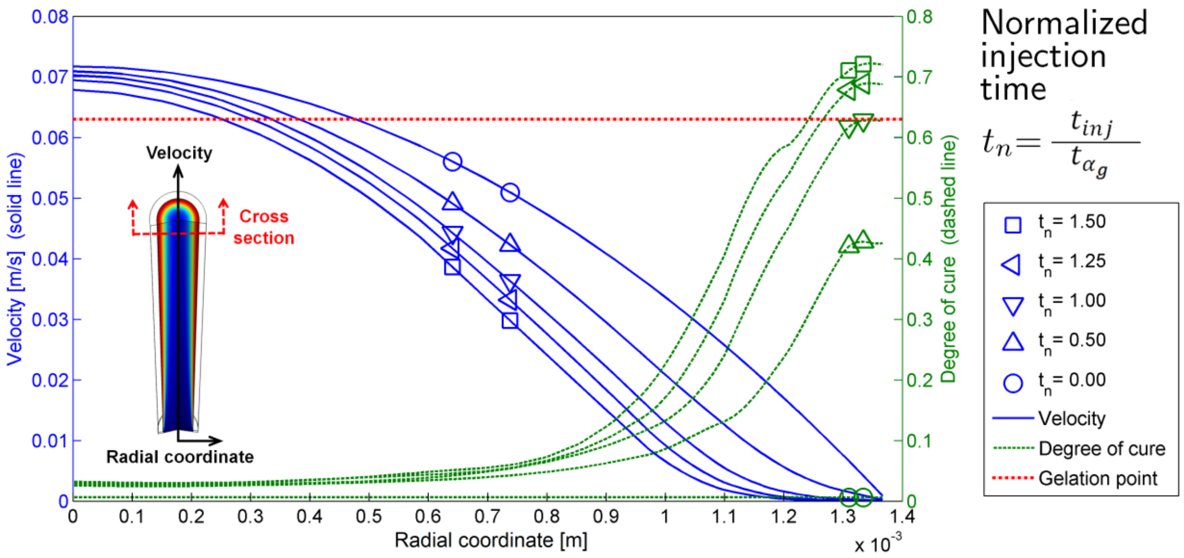

Figure 3: Comparison plot between transient states of velocity and cure near the end of the simulated tube with reactive flow. Length: 5m, temperature: 80°C, vacuum: 20kPa.

As time progresses, the slow layers remain longer and reach higher levels of cure. A gelation point is defined at a DoC of $\alpha_g = 63\%$. At this DoC, with viscosity of $\mu \geq 10\ Pa \cdot s$, and solidification occurring, there are no significant contributions to flow. The rheological effects from α_g are more significant to this assumption than the strict chemical definitions. At the normalized injection time of 1, the velocity in the profile is practically zero in any radial coordinate that has a DoC equal to the assumed α_g. The overall velocity will continue to decrease until α_g is reached all over the radial coordinate, and flow will then completely stop. The limit in time when no more significant flow can occur, denoted as stagnation time t_s, may be different than t_{α_g}, as seen in figure 3.

In the simulations and experiments, the stagnation time was usually longer than the gelation time ($t_s > t_{\propto_g}$). Layers with a high DoC remain close to the walls, and faster layers introduce fresh resin. Therefore, a resin transport was still possible past the gelation time of the initially injected resin.

From the numerical simulations, the following statements can be made:

- **A.** A wall build-up can be expected in highly reactive flows, creating a flow constriction, and reducing velocity.
- **B.** The representative permeability is decreasing continuously with time, even in fully saturated media in which freshly mixed resin is continuously injected.
- **C.** The stagnation time is a system property, while the gelation time is a material property. The limitations defined by a material property do not necessarily apply to a larger, flowing system.

RESULTS AND DISCUSSION

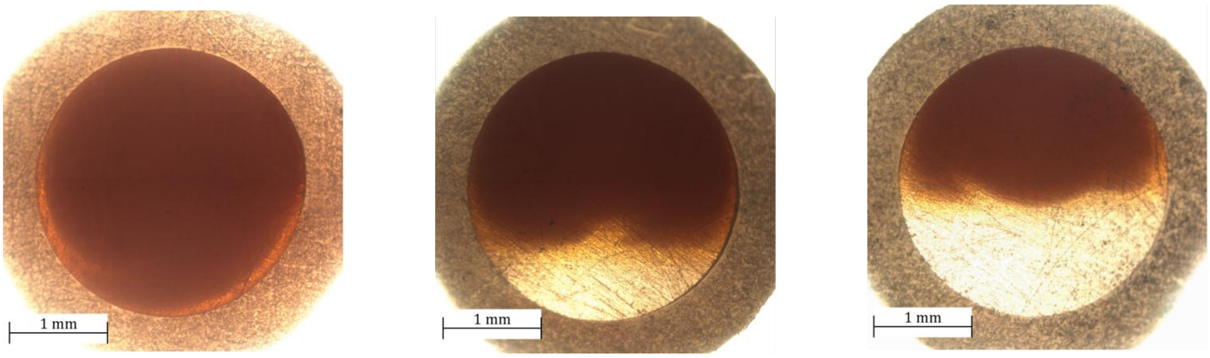

Figure (4a): Section cut at 5% of the tube length

Figure (4b): Gelled resin wall build-up at 50% of the length.

Figure (4c): Increase of build-up at 95% of the tube length.

Figure 4: Cross-section cuts from tubes with reactive resin flow.
Length: 10 meters, oven temperature: 80°C, vacuum differential: 20 kPa.

Fig. 4 shows cross-section samples at different lengths of the tube, as analyzed by a Leica DMRXA microscope. The tube was 10 meters long, with 20 kPa vacuum differential, inside the convection oven at 80°C. The transparent resin at the inlet was initially injected, followed by red colored resin, introduced at a normalized injection time of $t_n = 1.1$. The clear boundary between both resins reveals how the second batch of red resin had already a reduction of the available area for flow. Subfigure (4a) shows the small wall build-up at the beginning of the tube. A very thin transparent layer can be confirmed by the microscope image, even this close to the inlet. Subfigure (4b) shows that a large amount of resin has settled to the lower wall. Subfigure (4c) illustrates the increase of wall build-up at 95% of the tube length. Thin layers still adhere to the vertical walls of the tube, but most of the gelled resin remains in the bottom, probably due to gravity as the resin density rises with increasing degree of cure [2]. All the experiments show the same effect, and since the simulation considers constant density, deviations from the ideal axisymmetric model are expected.

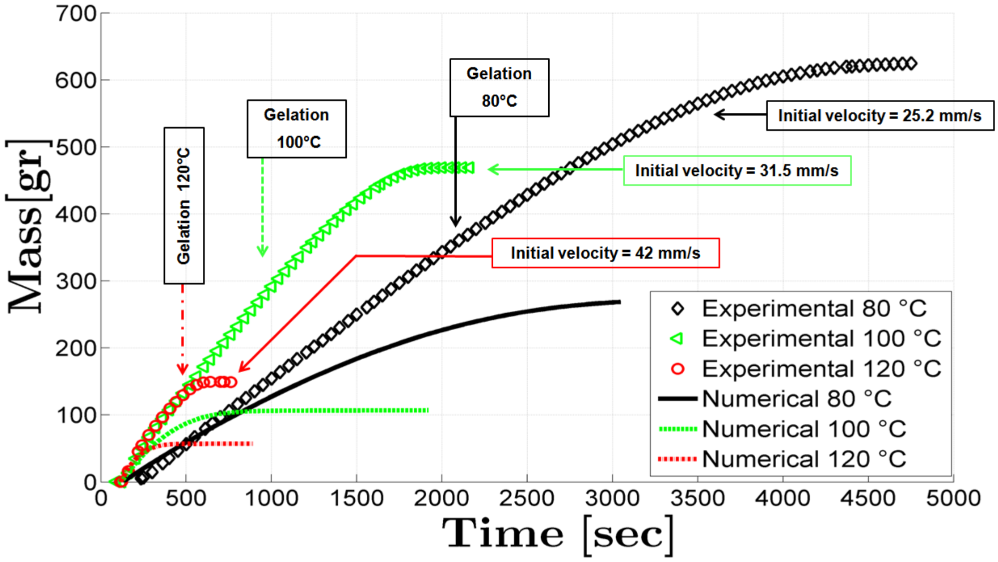

Figure 5: Comparison of experimental and numerical data for different temperatures.
Tube length: 7.5m, vacuum differential: 20kPa, tube inner radius: 1.375 mm.

Figures 5 and 6 show the comparison between experimental and numerical simulations with a changing parameter, the former with temperature, the latter with length. The flow parameters are listed in the caption of the figures. There is still flow in the tube although α_g of the initial resin is reached, which is another indicator that within a cross-section, the distribution of DoC is not homogeneous. When the "statically determined" gelation point is reached, and the wall build-up appears, the mass rate starts to significantly decrease with time. The data suggest that the higher the injection velocity, the longer the flow is able to continue beyond the gelation time.

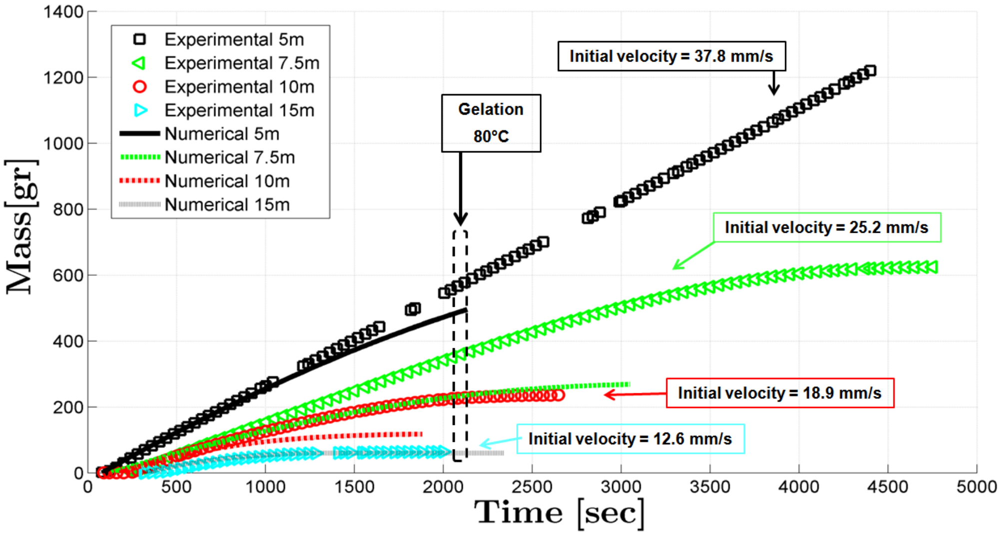

Figure 6: Comparison of experimental and numerical data for different lengths. Temperature: 80°C, vacuum differential: 20kPa, tube inner radius: 1.375 mm.

Different reasons cause deviations between the numerical and experimental data. The wall build-up has noticeable settling effects that change the expected geometry of the channel, which is not a circle anymore. A strong influence on the predicted mass transfer can be attributed to the assumption of constant density in the simulations, ignoring the settling of gelled resin to the bottom, deviating from the experimental observations. Surface tension effects may also prevent adhesion to the top wall. The convection oven might also provide local heat variations. Heat transfer was included for smaller models, resulting in a uniform isothermal temperature over 90% of the length. There might also be variations from the fitting of the highly non-linear viscosity behavior of the resin. Nevertheless, the effect of mass flow decrease in reactive flow is represented. The cease of flow is also fully developed. Further inclusion of realistic physical conditions can improve the accuracy of the reactive flow model. Studies of the cured resin wall build-up provide further insight, necessary to fully understand and predict the effects in reactive resin flow.

CONCLUSIONS

Experiments and numerical simulations show that in reactive flows, a link between the permeability of the textile and the progression of degree of cure for thermosetting polymers exists. Several interconnected capillary tubes are used as simple representations of the flow paths inside a complex textile. For typical LCM processing, laminar flow is expected. New resin can be constantly introduced, but slow laminar layers remain attached to the surfaces.

These layers will reach a higher degree of cure, and will have an increased viscosity and become solid layers after their gelation. The mass flow will be directly affected by this gelled resin constriction. Therefore, the flow behavior can change due to the inhomogeneous distribution of degree of cure in highly reactive flows. Experimental results have shown these statements to be true. Numerical predictions are able to consider these effects. The data suggest that the reactive flow is able to continue beyond the "statically determined" gelation time when the injection velocity is high enough. The stagnation time is a system property, but the gelation time is a material property. The limitations defined by a material property do not necessarily apply to a larger reactive flow system. Further complexity in the numerical models is necessary to improve accuracy.

REFERENCES

1. Bear J (2007), Hydraulics of Groundwater, McGraw Hill.
2. Ersoy N, Garstka, Potter, Wisnom, Porter, Clegg and Stringer, (2010), "Development of the properties of a carbon fibre reinforced thermosetting composite through cure", *Composites: Part A,* (41), 401-409.
3. Ding L, Shih C, Liang Z, Zhang C and Wang B, (2003) "In situ measurement and monitoring of whole-field permeability profile of fiber preform for liquid composite molding processes", *Composites: Part A*, (34), 779-789.
4. Verleye B, Lomov S, Long, Verpoest I and Roose D, (2010) "Permeability prediction for the meso-macro coupling in the simulation of the impregnation stage of Resin Transfer Moulding", *Composites: Part A*, (41), 29-35.
5. Okonkwo K, Simacek P, Advani S and Parnas R, (2011) "Characterization of 3D fiber preform permeability tensor in radial flow using an inverse algorithm based on sensors and simulation", *Composites: Part A,* (42), 1283-1292.
6. Karkanas PI, Partridge IK and Attwood, (1996) "Modelling the Cure of a Commercial Epoxy Resin for Applications in Resin Transfer Moulding", *Polymer International,* (41), 183-191.
7. Zhao L and Hu X, (2007) "A variable reaction order model for prediction of curing kinetics of thermosetting polymers", *J. of Polymer,* (48), 6125-6133.
8. Fournier J, Williams G, Duch C and Aldridge GA, (1996) "Changes in Molecular Dynamics during Bulk Polymerization of an Epoxide-Amine System As Studied by Dielectric Relaxation Spectroscopy", *Macromolecules,* (29), 7097-7107.
9. Castro JM and Macosko CW, (1982) "Studies of Mold Filling and Curing in the Reaction Injection Molding Process", *AlChE*, (28), 250-260.
10. Deléglise M, Grognec PL, Binetruy C, Krawczak P and Claude B, (2011) "Modeling of high speed RTM injection with highly reactive resin with on-line mixing", *Composites: Part A,* (42), 1390–1397.
11. Tan H and Pillai KM, (2012) "Multiscale modeling of unsaturated flow in dual-scale fiber preforms of liquid composite molding III: reactive flows", *Composites: Part A,* (43), 29-44.
12. Kim SK and Daniel IM, (2007) "Observation of Permeability Dependence on Flow Rate and Implications for Liquid Composite Molding", *Journal of Composite Materials,* (17), 837-849.
13. Pillai KM and Jadhav RS, (2005) "A numerical study of nonisothermal reactive flow in a dual-scale porous medium under partial saturation", *Numerical Heat Transfer, Part A,* (47), 109-136.
14. Versteeg HK and Malalasekera W, (2007) An Introduction to Computational Fluid Dynamics, 2nd. ed, Pearson Prentice Hall.

CHARACTERISATION OF AN INORGANIC BASED RESIN FOR THE LIQUID MOULDING PROCESSING OF COMPOSITES FOR INTERMEDIATE TEMPERATURE APPLICATIONS

Pascal Beneditti [1,2], Gilles Dusserre [1], Thierry Cutard [1], Julitte Huez [3]

[1] Université de Toulouse ; Mines Albi, INSA, UPS, ISAE, ICA (Institut Clément ADER) ;
Campus Jarlard, F-81013 Albi cedex 09, France.
[2] Nexeya Systèmes 14 avenue Didier Daurat – Z.I. de Montaudran, 31400 Toulouse, France.
[3] CIRIMAT-ENSIACET, bâtiment ENSIACET, 4 allée Emile Monso - BP44362, 31030
Toulouse cedex 4 – France.
Corresponding author's e-mail: gilles.dusserre@mines-albi.fr

ABSTRACT: The weight decrease of the aeronautical structures has been made possible in the past decades by the development of composite materials. Significant progresses have been achieved for various parts of the aircraft primary structure by replacing most of aluminium alloys by composites. A next step requires the development of new materials with functional properties, without impacting the mechanical properties. In particular a significant lightening would be possible if composite materials are able to work at intermediate temperatures. This aim is mainly related to the existence of matrix materials bearing temperatures up to 400°C. The properties of an inorganic matrix precursor are investigated in order to assess the compatibility of this polysilazane resin with LCM (Liquid Composite Moulding) processes. At the liquid state, the resin is characterized by rheometry. The thermomechanical behavior of the matrix (issued from this resin) is characterized by Dynamic Mechanical Thermal Analysis (DTMA) on composite samples and SEM (Scanning Electron Microscopy) observations of post-mortem samples help to point out the main difficulty to process the resin.

KEYWORDS: *Liquid Composite Molding, Ceramic Matrix Composites, Inorganic Resin, Intermediate Temperature Applications, Rheology, Dynamic Mechanical Thermal Analysis.*

INTRODUCTION

The aeronautical industry focuses its research and development activity on the elaboration of new functionalized materials in order to reduce the weight of different parts of the airplane. A major challenge is now the introduction of composite materials in parts located in the vicinity of the engines and so exposed to higher temperature. Structural materials such as composites exhibiting excellent long term mechanical properties up to 400 °C appear to concurrence metals in various parts of the engine nacelle. Organic matrix composites are the most relevant materials for structures undergoing temperatures lower than 180 °C. Many processes are available to manufacture small or large parts, at acceptable production rate. However their use at higher temperature is yet impossible because of matrix degradation. Long fiber ceramic matrix composites were developed for high temperature applications. The associated processes are expensive and often optimized for small size parts. The framework of this paper is the development of ceramic matrix composites obtained from a liquid precursor. The aim is the combination of the advantages of both material families mentioned above, in order to manufacture composite parts bearing temperatures of 400 °C by LCM. One important objective is to ensure a relevant production rate for civil aeronautic industry. This paper deals with the rheological properties of a polysilazane resin used as ceramic precursor [1] and with its variation with time and temperature. The thermomechanical behavior of the composite is also investigated by DMTA experiments and some SEM observations are performed to evaluate the damage of the composite under DMTA tests.

MATERIALS AND EXPERIMENTS

Materials

Polysilazane resin

The considered resin is a Clariant® HTT 1800 polysilazane. It is a low viscosity liquid that can be used as a thermosetting resin: when heated above 175 °C [2], silicon and nitrogen atoms are bonded alternatively according to a 3D network [3] leading to a solid state polymeric material. This material is likely used as a precursor for ceramic coatings (silicon carbide or silicon nitride) after pyrolysis. In the present work, the material in its liquid state is studied by rheometry. The thermosetting of the resin can be achieved at lower temperature by adding a free radical initiator [2]. The effect on the resin rheokinetic of an addition of 0.275 wt.% of dicumyl peroxide was investigated by rheological characterization. In this work, this mixture was studied by DMTA at the polymeric state as a matrix of the composite.

Carbon fibers and reinforcement

The carbon fiber used in this study is manufactured by Toho Tenax® from PAN precursors. It is a 7 µm diameter fiber with an epoxy size. The 400 tex yarns (HTA 5131) are made of 6000 fibers. They are woven by Hexcel® according to a 2/2 twill weave. The 285 $g.m^{-2}$ resulting reinforcement is 0.29 mm thick (reference HexForce™ G0986 D 1200).

Composite processing

The composite materials characterized in this study are processed by the compression under 12 bars of 22 plies. Each ply consists of reinforcements impregnated manually with the polysilazane resin catalyzed with 0.275 wt.% of dicumyl peroxide. Heating plates permitted to cure the composite at 250 °C for 5 h under the press in order to apply a constant pressure. The tools were coated with a polysilazane releasing agent Clariant® CAG 37.

Characterization methods

Rheometry

A rheological characterization of the resin was performed using a Haake MARS® oscillation rheometer fitted out with parallel 35 mm diameter plates. The 1 mm thick liquid sample is heated in an oven. The tests are controlled by a 0.5 Hz frequency sinusoidal rotation with a maximal shear strain of 10 %. Complex viscosities between 0.1 and 5000 Pa.s are measured using this setup. 3 °C.min^{-1} heating ramps were applied for the anisothermal tests. Isothermal tests were performed between 150 °C and 200 °C, a response time of about 300 s was necessary to achieve the set point.

Dynamic Mechanical Thermal Analysis (DMTA)

DMTA experiments were carried out using a DMA8000 Perkin Elmer® apparatus. A dual cantilever setup was used to clamp the samples in its stationary extremities and in the middle on the oscillatory actuator. The setup is located in an oven allowing to perform characterization up to 600 °C. The composite samples length is of 50 mm and its cross section is a 5 mm edge square. The characterizations were carried out between room temperature and 580 °C using different thermal paths involving 5 °C.min^{-1} temperature ramps and dwell times at different temperatures. An oscillatory displacement of 5 µm was applied in the middle of the sample at a frequency of 1 Hz and 10 Hz. Only 1 Hz results will be discussed here.

Scanning Electron Microscopy

Some DMTA composite samples were broken in flexion. The fracture pattern was observed after metallization using a FEI-ESEM-FEG-XL30 scanning electron microscope in the aim to study the effect of the temperature on the fracture mechanism of the composite.

EXPERIMENTAL RESULTS

Rheology of the resin

The resin under study undergoes a reticulation mechanism when heated above 175 °C [2]. The rheokinetic of this reaction is very sensitive to the temperature. On Fig. 1.a, the complex viscosity of the resin is plotted against time for different temperatures. These results show that the reaction starts at 150 °C and its kinetic accelerates when the temperature increases. At 150 °C, the rheokinetic of the resin catalyzed with an addition of 0.275 wt.% of dicumyl peroxide is significantly accelerated as shown on Fig. 1.b. The reaction starts after 300 s (before the temperature set point) with the peroxide, corresponding to a temperature of 143 °C, whereas it begins after 535 s without peroxide (temperature set point almost achieved: 149 °C). The same trend is noticed during anisothermal tests. Fig. 1.c shows an inset of viscosity increase respectively at 141 °C and 148 °C with and without peroxide. Moreover the viscosity still increases very quickly above 3000 Pa.s whereas the reaction of the non catalyzed resin begins to slow down when the viscosity reaches this value, even at 200 °C. This behavior indicates that the degree of conversion could be higher with peroxide, which is confirmed by the higher mechanical properties measured by tensile tests carried out in this study (not reported in this paper): higher failure stress is obtained with peroxide addition.

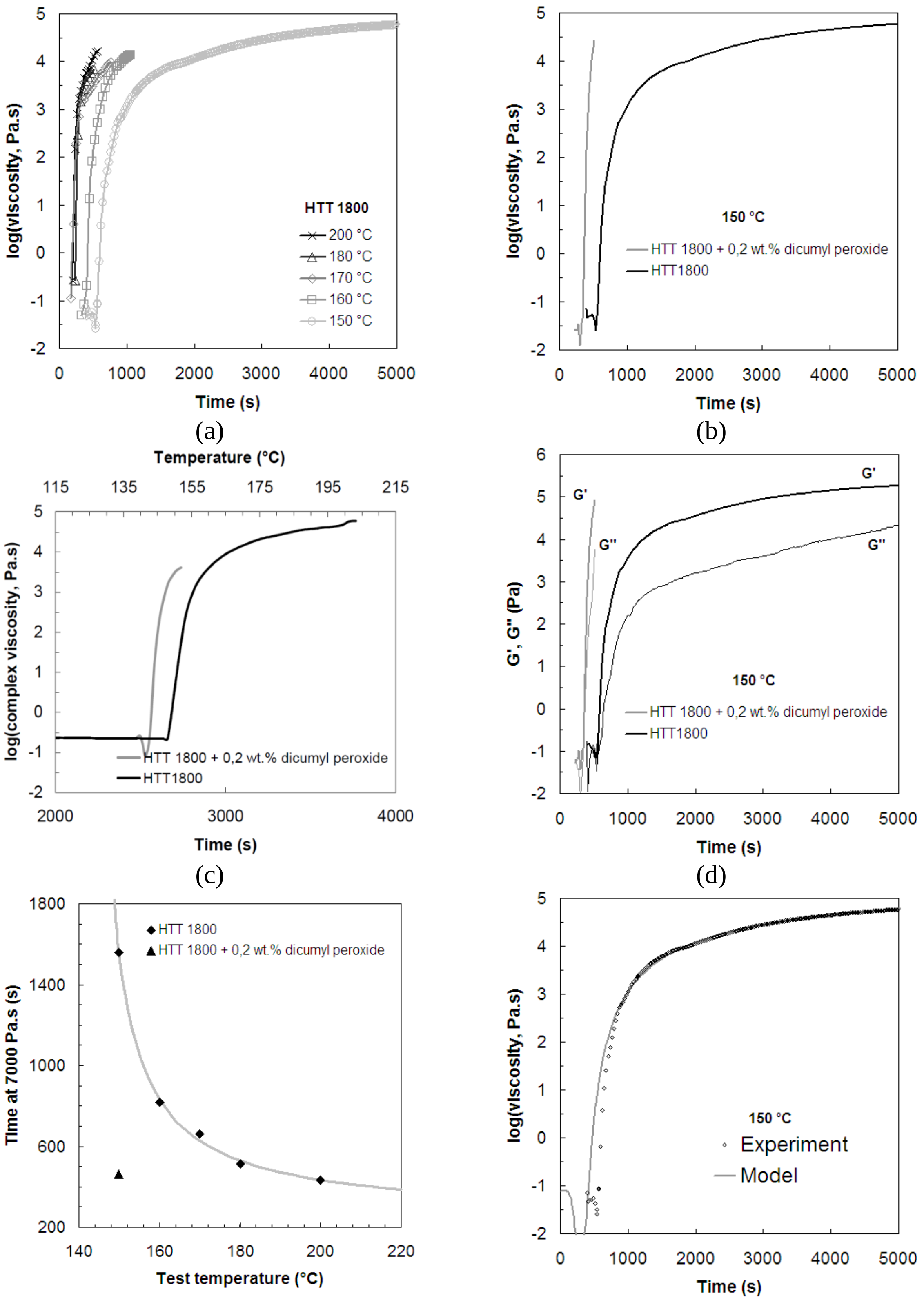

(a) (b)

(c) (d)

(e) (f)

Fig. 1: Influence of temperature (a), and of the addition of dicumyl peroxide (b, c, d) on the rheokinetic of the polysilazane resin under isothermal conditions (a, b, d) and 3 °C.min^{-1} temperature ramp (c): complex viscosity (a, b, c) and complex moduli, G’ and G” (d). Hyperbolic evolution with temperature of the time to reach a complex viscosity of 7000 Pa.s (e) and modeling of an isothermal viscosity variation (f)

Fig. 1.d, where the two parts of the complex modulus, *G'* and *G"* are presented, points out that the real part of the complex modulus, *G'*, is higher than the imaginary part, *G"*, immediately after the inset of viscosity increase. This can be interpreted as the result of a gelation that already occurred in the sample [4]. The rheokinetic has to be further studied with higher diameter plates in order to obtain reliable results in the low viscosity range and accurately assess the gelation time.

However, to compare the viscosity variation obtained in the different isothermal conditions investigated, the time to reach an arbitrary viscosity is plotted against temperature for both resin with and without dicumyl peroxide, Fig. 1.e. The effect of the peroxide addition is highlighted: at 150 °C, the time to reach a viscosity of 7000 Pa.s is three times lower than without peroxide, it corresponds to a curing temperature of 200 °C without peroxide. In order to assess the curing time as a function of the curing temperature, the evolution of the time to reach 7000 Pa.s without peroxide was properly fitted using a hyperbolic function, Eqn. 1. The asymptotical value of 142 °C could be interpreted as the reaction starting temperature.

$$t_{\eta^*=7000Pa.s} = 253 + \frac{10500}{T°C - 142} \tag{1}$$

An attempt to model the viscosity evolution during curing with the models classically used for thermosetting resins is presented. Fig. 1.f compares the complex viscosity variation at 150 °C without peroxide to the response of an isothermal simulation using a Kamal-Sourour [5] model to estimate the degree of conversion, correlated to the viscosity using a Castro and Macosko model. All parameters were identified using the displayed experimental curve. This preliminary study validates the use of these models in the present case.

Thermomechanical behavior of the composite

The thermomechanical behavior of the composite was studied by DMTA analysis between room temperature and 580 °C. The results plotted on Fig. 2 and Fig. 3 show the evolution of the storage modulus, *E'*, divided by its initial value E'_0 in order to compare the trend of each experiment. The values of the initial storage modulus E'_0 are between 18 and 22 GPa depending on the sample. A very good reproducibility is then obtained.

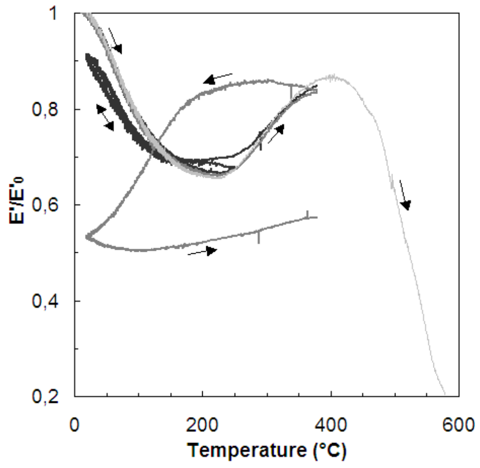

Fig. 2: Composite storage modulus relative variation at 5 °C.min^{-1} (—: 25 °C→250 °C→25 °C→380 °C ; —: 25 °C→380 °C→25 °C→380 °C; —: 25 °C→580 °C)

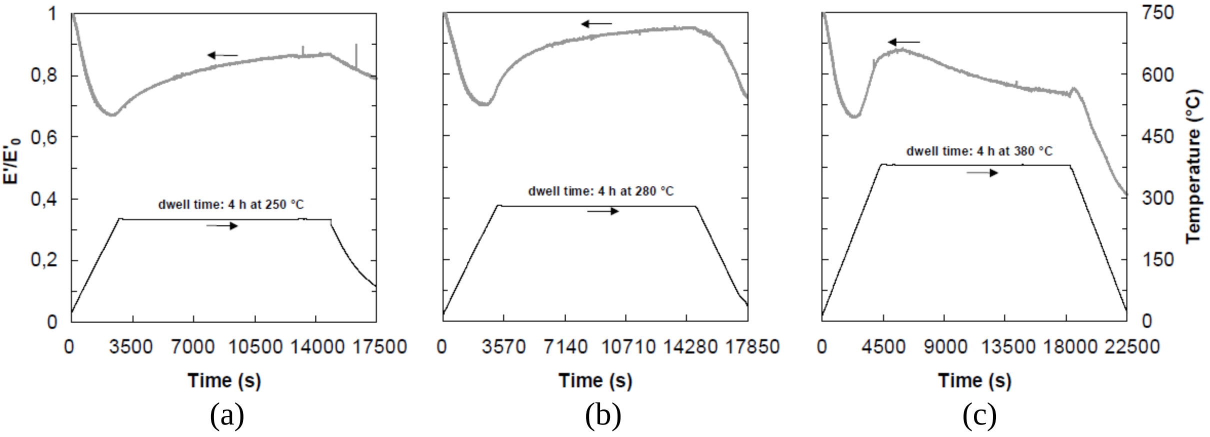

Fig. 3: Composite storage modulus relative variation during 3.5 hours dwell times at 250 °C (a), 280 °C (b) and 380 °C (c)

The results presented in Fig. 2 show a first non linear decrease of 30 % of the storage modulus up to 250 °C. This variation is due to a reversible phenomenon since the modulus increases when the sample is cooled to room temperature and decreases again along the same curve when the sample is heated again (black curve of Fig. 2). This phenomenon, also observed on samples without fibers could be a glass transition since the point of inflexion of the curve corresponds to a *tan δ* peak. After 250 °C, the storage modulus increases in a non linear way up to 400 °C. The phenomenon involved during this step is irreversible. This could be related to the mineralization reaction whose starting is observed at 300 °C by Gonon et al. [3]. When the sample is cooled down to room temperature from 380 °C (dark grey curve of Fig. 2), the first trend is a conservation of the maximum modulus arisen, and then a rapid decrease below 200 °C. The most probable behavior interpretation is that the mineralized matrix has a modulus very weakly sensitive to temperature but damages under thermomechanical stresses when the temperature decreases. This is confirmed by an almost constant modulus about 50 % of the initial value when the sample is again heated up to 380 °C. After 380 °C (light grey curve of Fig. 2), the storage modulus begins to decrease quickly and the sample is then fully damaged. This damage is probably due to matrix cracking under thermomechanical stresses, degradation of the epoxy size and/or of the carbon fibers.

In order to better understand what happens above 250 °C, DMA experiment were performed with 3.5 hours dwell times at 250 °C (Fig. 3.a), 280 °C (Fig. 3.b) and 380 °C (Fig. 3.c). The results show that the modulus increase attributed to material mineralization starts occurring at 250 °C, and that its kinetic is sensitive to temperature. At 280 °C, a full conversion can not be completed during the test, but a modulus of 95 % of the initial value is reached and is still increasing. At 380 °C, the modulus increase due to mineralization is compensated by a damage mechanism (due to matrix cracking, size and/or fiber degradation) that leads to a rapid decrease of the modulus. In each case, the cooling to room temperature results in a modulus decrease due to damaging under thermomechanical stresses.

Fracture surface observations

In order to investigate the damage mechanisms involved during cooling, the fracture surface of composite samples were observed (Fig. 4) to characterize the fiber/matrix interface as manufactured and after a dwell time at different temperatures (3 h at 280 °C and 380 °C).

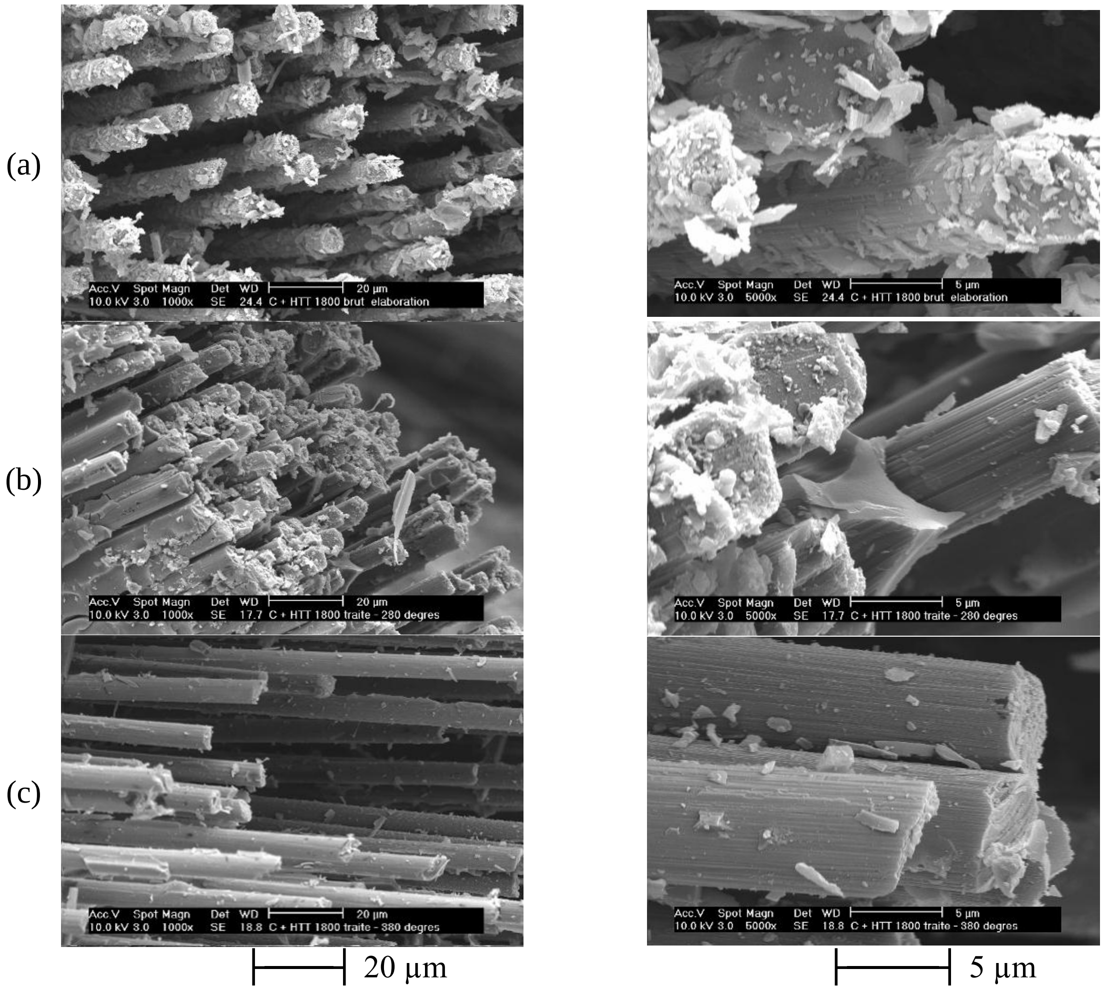

Fig. 4: Fracture surface observations of composite samples broken after composite processing (a), after dwell time of 3 h at 280 °C (b) and dwell time of 3 h at 380 °C (c)

Fig. 4 focuses on the fibers extracted out of the matrix in the fracture area of a sample as manufactured (Fig. 4.a), and after a dwell time of 3 h at 280 °C (Fig. 4.b) and 380 °C (Fig. 4.c). These temperatures were chosen to obtain two different mechanisms:
-at 280 °C, any size degradation is undergone [6] and no modulus decrease is observed during mineralization (Fig. 3.b), but only during cooling, whereas
-at 380 °C a modulus decrease takes place under isothermal conditions during mineralization (Fig. 3.c).
The fracture surface of the sample as manufactured shows a large number of small matrix aggregates (less than 1 µm) covering the fibers. The interface strength seems to be higher than the matrix resistance, what is consistent with the previous results since the matrix has not been mineralized and is not in a true solid state but in a gel state. After a thermal loading at 280 °C, the fracture surface (Fig. 4.b) shows larger matrix aggregates (5 to 10 µm). The matrix has been partially mineralized and its strength is significantly higher. The fibers are not covered of matrix but the presence of large matrix aggregates on the fibers is consistent with a thermomechanical damage during cooling resulting of shear stresses at the interface due to the difference of thermal expansion between the matrix and the fiber. Finally the fracture surface of the sample subjected to a temperature of 380 °C does not show any cohesion between fiber and matrix. This observation is consistent with a thermal degradation of the size that continuously damages all the interfaces.

CONCLUSIONS

An experimental study of a polysilazane resin rheology and of the resulting composite thermomechanical behavior was carried out in order to assess the feasibility of inorganic matrix composites by Liquid Composite Molding processes. The rheology study has highlighted the usefulness of an addition of dicumyl peroxide in order to accelerate the rheokinetic during the curing cycle. A dynamic mechanical analysis was performed between room temperature and 580 °C in order to characterize the composite thermomechanical behavior. In conjunction with fracture surface observations, some assumption can be made on the damage mechanisms in the composite subjected to thermomechanical loads. A reversible storage modulus decrease occurs between room temperature and 250 °C and could be attributed to a glass transition in a semi-solid state material. Above 250 °C the trend is reversed and the modulus increases probably as a result of a mineralization mechanism. However this new matrix seems to be very brittle and damages when the sample is cooled down under 200 °C. Above 300 °C the degradation of the fibers size starts and it results in an irreversible modulus decrease up to a fully disintegrated sample at 580 °C. A composite plate was successfully processed by Resin Transfer Molding of the polysilazane resin. The main difficulty was the ammoniac produced during the curing cycle. Interesting mechanical properties were achieved at room temperature. Nevertheless significant progresses have to be done in order to keep these properties up to 400 °C (curing cycle optimization in order to obtain a stable matrix, improvement of the fiber/matrix cohesion).

ACKNOWLEDGMENTS: this work was carried out with the financial support of the french Region Midi-Pyrénées in the framework of the project “Recherche et Transfert de Technologies” “Fonctionnalisation de l’Interface Renfort carbone/Matrice Inorganique”.

REFERENCES

1. Kroke E, Li YL, Konetschny Ch, Lecomte E, Fasel C and Riedel R (2000), ‘Silazane derived ceramics and related materials’, *Materials Science and Engineering: Reports,* 26(4-6), 97-199

2. HTT 1800 Heat curable, high temperature coating resin, Product and test information, Product datasheet, KiON® Specialty Polymers, http://www.kioncorp.com/datasheets/HTT%201800%20Product%20Bulletin.pdf

3. Gonon MF, Hampshire S, Disson JP and Fantozzi G (1995), ‘A polysilazane precursor for Si-C-N-O matrix composites’, *Journal of the European Ceramic Society,* 15(7), 683-688.

4. Tung CYM and Dynes PJ (1982), ‘Relationship between viscoelastic properties and gelation in thermosetting systems’, *Journal of Applied Polymer Science,* 27(2), 569-574.

5. Kamal MR, Sourour S (1973), ‘Kinetics and thermal characterization of thermoset cure’, *Polymer Engineering and Science,* 13(1), 59-64.

6. Margueritat-Regenet C (2002), Elaboration et caractérisation de fils composites C/Al. Infiltration spontanée et continue par activation chimique du mouillage, PhD Thesis, Ecole des Mines de Paris, France, in french.

FLOW AND HEAT TRANSFER INSIDE AN AUTOCLAVE

N.E. Jimmy Olsson [1], T. Staffan Lundström [1], L-G Westerberg [1] and Tonny Nyman [2]

[1] *Division of Fluid and Experimental Mechanics, Luleå University of Technology, SE-941 87 Luleå, Sweden. Corresponding author's e-mail: jimmy.olsson@ltu.se*
[2] *Saab Aeronautics, SE-582 54 Linköping, Sweden*

ABSTRACT: This work, that involves both experiments and numerical simulations, concerns autoclave molding. An autoclave is basically a pressure vessel, where the entrapped and often highly compressed gas is heated and circulated in order to heat the components that have been placed inside the vessel. In the autoclave process, the desirable state would be that an even and optimal temperature existed in the whole part that is manufactured. Unfortunately, this is not always the case. All in all we need to get a better understanding of the flow inside an autoclave and the convective heat transfer from the heated gas to the composite components. In this work we have therefore investigated the flow behavior by performing qualitative measurements with particle image velocimetry inside an autoclave. The concept is to dope the gas within the autoclave with smoke and illuminate the smoke with a thin sheet of laser light. Captured images of the moving smoke are then cross correlated to give velocity fields. We have also investigated the heat transfer to the tool by measuring the temperature at multiple locations during heating. The obtained velocity field is used to produce inlet condition for the simulations, performed with Computational Fluid Dynamics, which subsequently are compared with the experimentally obtained tool temperature. The simulation technique may then be used to optimize both the tools, and the actual location of the tools inside the autoclave in order to improve quality and reduce costs.

KEYWORDS: *Autoclave, CFD, Convection, Conduction*

INTRODUCTION

Background

In the context of composites manufacturing an autoclave is basically a pressure vessel, where entrapped and often highly compressed gas is heated and circulated. This is done to heat and densify molded pre-impregnated composite fibers (pre-pregs) that have been placed inside the vessel. The size of these vessels can be very large, even so that moldings of a whole aircraft wing sections can be placed within them. The manufacturing technique is especially associated with the air-craft industry where a large amount of composite products are used and very high quality composites are required. In the autoclave process, manufacturers achieve to maintain the temperature differences within reasonable limits in order to attain a uniform solidification of the material. Traditionally the research on the autoclave process has been focused on the flow of resin, the temperature distribution and the curing of the resin within the mold, e.g. [1-3]. In the models developed the temperature within the autoclave is allowed to vary as a function of time but the temperature is usually assumed to be constant as a function of spatial coordinate meaning that only spatial variations within the mold are accounted for. One way to refine the models is to account for temperature variations on the surface of the molds and thus model convective heat transfer from the gas within the autoclave to the mold surface. To exemplify, the front side of the mold is generally, seen from the gas stream, hotter than the back side and it is likely that the detailed flow field on a single surface creates variation in its temperature. Moreover and as another example, if several molds are placed inside the autoclave, the average temperature during the manufacturing cycle can be lower for a mold that is placed behind another one. Thickness differences in the parts also create temperature differences. All in all we need to get a better understanding of the gas flow inside an autoclave and the convective heat transfer from the heated gas to the composite components.

Heat transfer

When dealing with heat transfer, four mechanisms are generally dealt with, conduction, convection, phase change and radiation [4]. We will consider conduction and convection although the other two may be of importance at very special conditions. If the temperature within the autoclave is low enough the heat release during curing may affect the results while if the temperature is very high radiation may influence the results. Conduction is heat transfer mechanism within solids or a stationary fluid [4]. Hence, for the autoclave process, this mechanism is important within the molding tool. Convection occurs when heat is transferred by the flow of a fluid where, for instance, the fluid handles the transport of energy to, or from, a solid wall. The rate, of which heat transfer occurs between the fluid and the wall, is greatly affected by the flow behavior since for example with a higher velocity, the energy transport occurs more rapidly. Another characteristic that affect the effectiveness is the turbulence level [5]. As a consequence, forced convection, which is the case in autoclave technology since gas is circulated by a fan, is much more efficient than natural convection. The temperature difference between the solid wall and he fluid far away from the wall is regulated in a boundary layer, where the velocity in an infinitesimally thin layer next to the surface is zero. Hence, the heat transfer is simple conduction between the wall and this infinitesimally thin layer. The heat transfer coefficient may be derived from the following expression:

$$h = -\frac{k}{T_w - T_\infty}\left(\frac{\partial T}{\partial y}\right)_{y=0^+} \tag{1}$$

where k is the conductivity of the fluid, T_w is the temperature at the wall, and T_∞ is the temperature of the free stream. The heat transfer coefficient can hence be measured experimentally, but if the flow is known it can also be predicted with for example Computational Fluid Dynamics (CFD), see [6, 7]

EXPERIMENTS

Experiments were performed within a production autoclave, 11 m long, 3.0 m in diameter and the height from the floor to the roof inside of the autoclave was 2.2 m.

Measurement of flow field

From the manufacturer of the autoclave, an average velocity inside the autoclave is given. However, since the autoclave utilized in these experiments was old and since it is of highest interest to investigate how the flow field actually behaves, the flow field was captured in single planes with Particle Image Velocimetry (PIV), [8]. The planes were located at the end of an autoclave up-stream the manufacturing tool.

The concept is to dope the gas within the autoclave with smoke and illuminate the smoke with a thin sheet of laser light. Captured images of the moving smoke are then cross correlated to give velocity fields with the analysis software DaVis. The thin sheet was illuminated by a 150 mW industrial red laser line generator. The smoke was generated with a Safex nebelgerät F2010 device, using a smoke liquid that generated a dense smoke. The principle in the analysis is that patterns of the smoke are identified at two occasions separated with a suitable time rather than that individual smoke particles are followed. Since the smoke quickly became homogeneously distributed inside the autoclave the smoke had to be portioned manually by filling large plastic bags with smoke, and then release it in the end of the autoclave which gave measurable smoke patterns for a shorter period of time. These runs were performed at room temperature (24 °C) and without applied pressure. Focus was set on measurements in front of the molding tool and the height of the camera was adjusted between a low and high position between runs in order to capture the whole area from the floor to the roof of the autoclave. The camera in use was a Canon EOS 550D, capturing a 720p video at 50Hz. The images from the video was then extracted and used in the correlation process. The correlation method adds the results from multiple image pairs into one, which gives an average velocity field over the whole area. A correlation between only two images would only have given the velocity in the spots where smoke was in translocation at that time.

Pressure and temperature measurements

The pressure and temperature within the autoclave and the temperature of the molding tool, made of steel, was measured to compare the results with the posterior simulations. The runs were not performed as ordinary industrial runs were the temperature inside the autoclave is adjusted in order to retain the molding tool temperature within certain limits. Instead, the temperature was increased as fast as possible so that temperature differences on the molding tool should become apparent. The relative pressure, in its turn, was increased to 610kPa.

The built in measurement equipment of the autoclave was used to monitor the pressure and the temperature of the air inside the autoclave as well as the temperature on the molding tool. The molding tool had a total of 48 measurement locations out of which 4 were built in on the molding tool in order to monitor the process during manufacturing. The others were mounted with joint sealant and tape. A selection of these locations will be presented here, see Fig. 1b and 3 for a description of the locations.

SIMULATION

For all parts in the simulation, the commercial code StarCCM+ 7.02.008 was used. The whole usable volume inside the autoclave was modeled with the mold placed in the centre of the autoclave, mimicking the experiments, see Fig. 1. Two domains have been initialized, one for the flow that essentially is the usable volume inside the autoclave minus the volume of the molding tool, and one domain for the solid molding tool. The geometry of the molding tool was slightly simplified and in order to obtain a closed volume which is necessary for meshing, the StarCCM+ surface wrapper tool was applied. Hexahedral cells have been used in the flow domain in order to minimize the number of cells which still counted to 2.7 million. The volume of the molding tool have been meshed with thin polyhedral cells, consisting of 5 layers, since it is built out of plates that can be considered as thin.

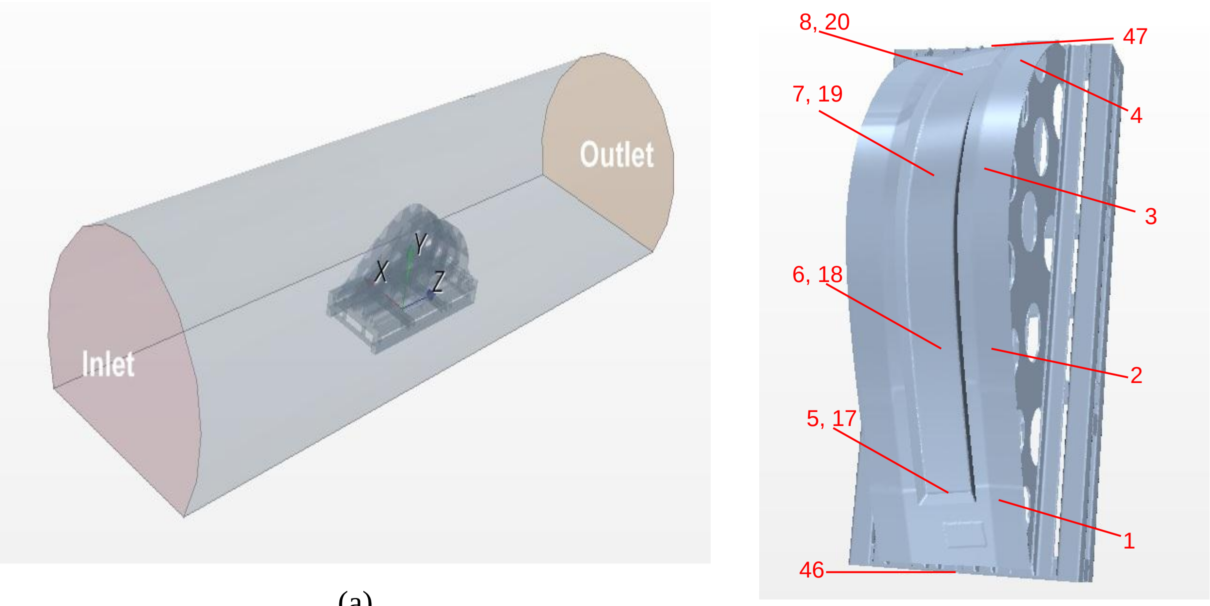

(a)

(b)

Fig. 1: The geometry of the virtual model. The length of the autoclave is approximately 11.1m (a). Close-up of the mold with some of the measurement locations marked (b). Locations 17-20 in placed beneath 5-8 on the opposite side if the mold surface.

The problem was simulated with a two coupled simulation approach, one for the gas flow inside the autoclave that surrounds the molding tool, and another case for the solid steel molding tool. The inlet velocity is derived from the experiment, and is only allowed to vary as a function of the height inside the autoclave. A more realistic description would have been that it is also dependent on the radius. From the fluid simulation solution, the local heat transfer coefficients and reference temperatures are mapped to the solid domain where convective and conductive heat transfer is solved for. The new obtained surface temperature is then mapped to the fluid domain where also the gas temperature and pressure is updated from the experimental values, and a new fluid simulation is initiated. This process continues until the whole experimental run was simulated. See Fig. 2 for a schematic view of the simulation process.

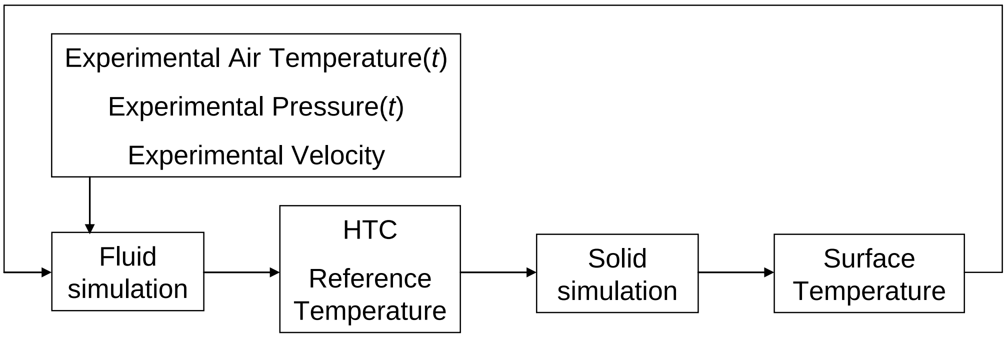

Fig. 2: Outline of the process for the simulations. First, the fluid flow inside the autoclave is derived where the inlet velocity, air temperature and pressure is obtained from the experiments. Then, the calculated heat transfer coefficient and reference temperature is mapped to the solid domain where a new surface temperature is computed. This new temperature is then mapped to the fluid domain where a new air temperature and pressure is used as well from the experiments.

The simulation process is performed automatically by a simple macro, which furthermore is written so that the number of time steps in the solid simulation before updating the fluid simulation depends on how large the experimental temperature steps are. See Table 1. So, for 0-1 degrees difference, the experimentally obtained values are used in the simulations. If the difference is larger, linearized values from the experimental values are applied.

Table 1: Time-steps applied for different experimental temperature differences which were updated every 60th second.

ΔT	0-1	2-3	4-6	7-8	≥ 9
Time-steps (s)	60	30	20	10	5

The gas (air) was simulated as an ideal gas, using Sutherland’s law for the dynamic viscosity and the thermal conductivity. To model the turbulence the *k*-ε turbulence model was employed in these initial simulations. The heat transfer coefficient may be obtained in several ways and in the present case it is the local heat transfer coefficient that was used and the corresponding local reference temperature. Local means here that it is the value in the centroid in the cell next to the boundary that is used for calculations. The local heat transfer coefficient is given by

$$h_{local} = \frac{\rho_f(y_c) C_{p,f}(y_c) u^*}{T^+\left(y^+(y_c)\right)} . \tag{2}$$

In this equation ρ_f is the density of the fluid, $C_{p,f}$ is the specific heat of the fluid, u^* is the reference velocity and T^+ is the non-dimensional temperature. The corresponding local reference temperature is given by the following equation where $\dot{q}''_w$ is the surface heat flux:

$$T_{local} = T_w + \frac{\dot{q}''_w}{h} . \tag{3}$$

RESULTS

The velocity profile from the experiment is visualized in the simulation model in Fig. 3. As seen, the velocity is much higher near the floor than what it is near the roof of the autoclave authorizing the experiments performed.

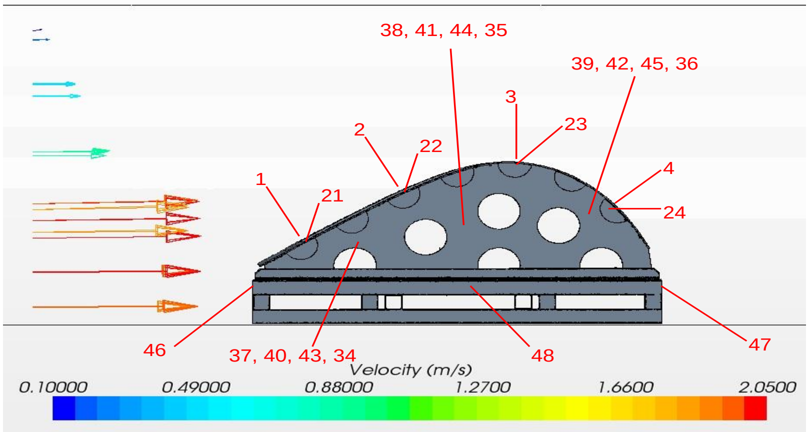

Fig. 3: The inlet velocity from the experiment visualized in the virtual model where also the measurement locations can be seen on the mold. Multiple values mean multiple locations, but placed further into the mold.

With knowledge of the inlet velocity field the flow can be simulated and temperatures from the simulations can be compared to experiments. For all results presented in Fig. 4-7, the vertical scale show the temperature in °C and the horizontal scale is the time given in seconds. The locations of the measurement points can be seen in Fig. 1b and 3.

As seen in Fig. 4 the computed temperature is in better agreement with the experimental data for location 1-4 than 5-8 where the geometry is more complex (see Fig. 1b). Moreover, in Fig. 4a it can be seen that the accordance is very good for location 1 and 2, while it gets a little worse for location 3 and 4 on the back side if the mold. Fig. 5 presents the corresponding results to the results presented in Fig. 4, that is, the locations placed on the other side of the metal sheet, and as seen, the results behave similarly. The temperatures in the middle section can be seen in Fig. 6 where locations 37-39 in Fig. 6a is placed on the outside on the outermost plate, 40-42 in Fig. 6b is placed on opposite side of 37-39 on the outermost plate. The temperatures on the plate inside of the outermost plate can be seen in Fig. 6c and 6d where 43-35 in Fig. 6c are placed on the outer side of the plate, and 40-42 (Fig. 6d) are placed on the opposite inner side of that plate in Fig. 6c. It can be seen that the agreement is best for the outermost plate, and then the agreement become worse the further inside the mold the measurements are performed. Fig. 7 presents the front (location 46) and rear (location 47) temperature of the mold as well as the temperature on the side of the framework (location 48). As seen, the computed values in all of these locations are in very good agreement with the experimental.

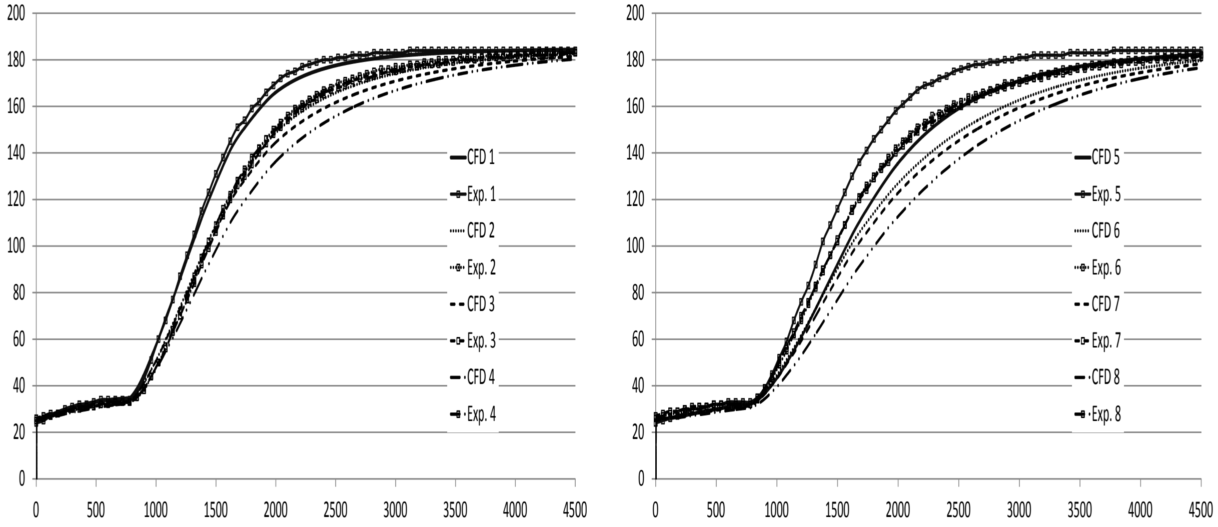

(a) (b)

Fig. 4: The temperature for location 1-4 (a) and 5-8 (b).

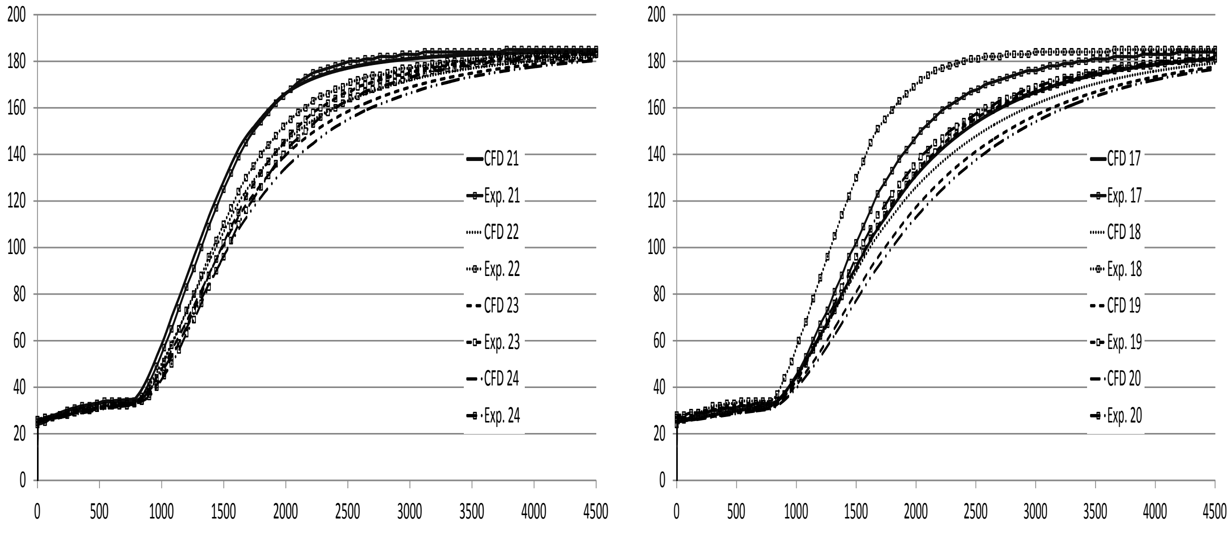

(a) (b)

Fig. 5: The temperature for location 21-24 (a) and 17-20 (b).

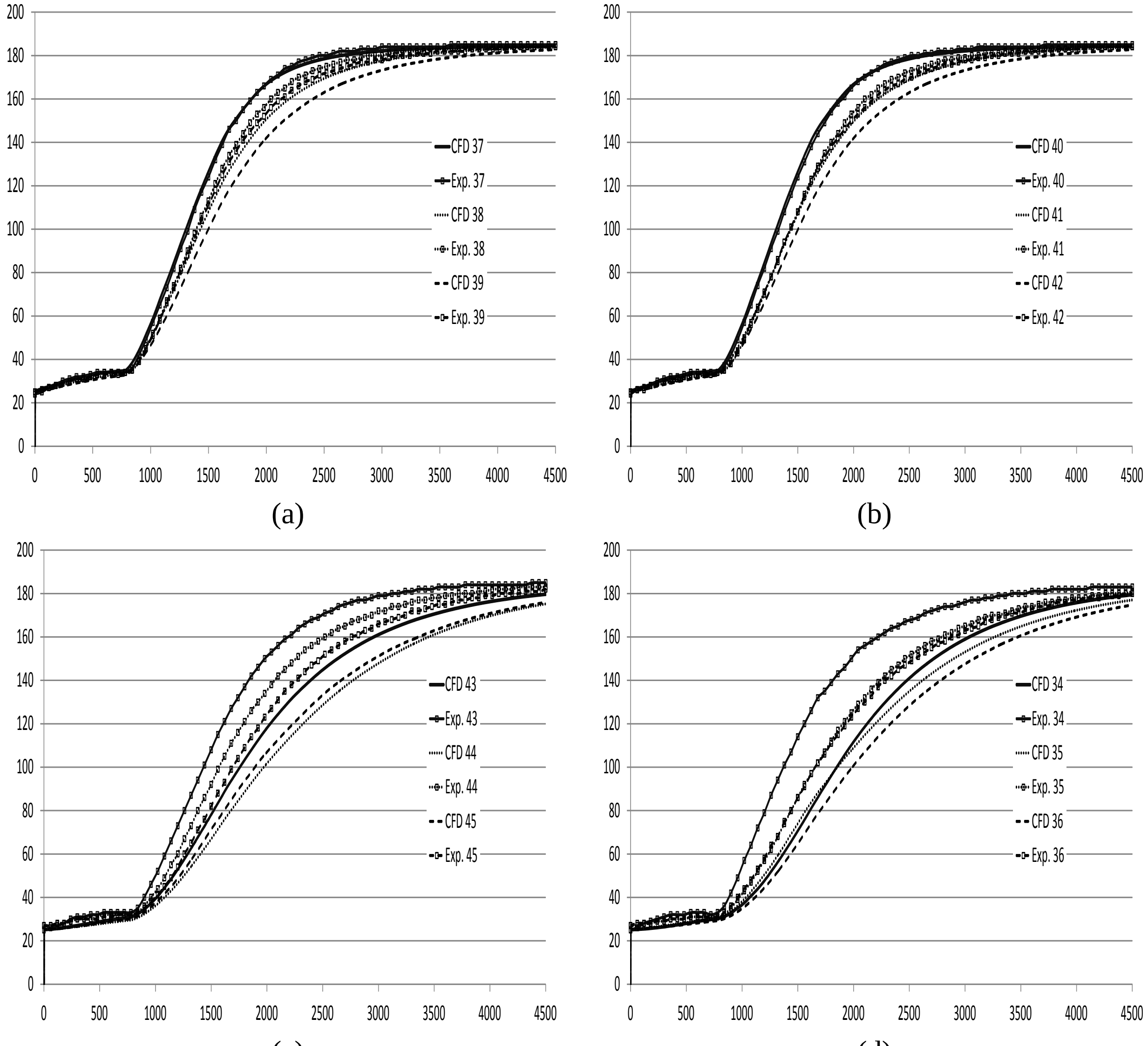

(a) (b)

(c) (d)

Fig. 6: The temperature in the middle section for locations 37-39 (a), 40-42 (b), 43-35 (c), and 34-36 (d).

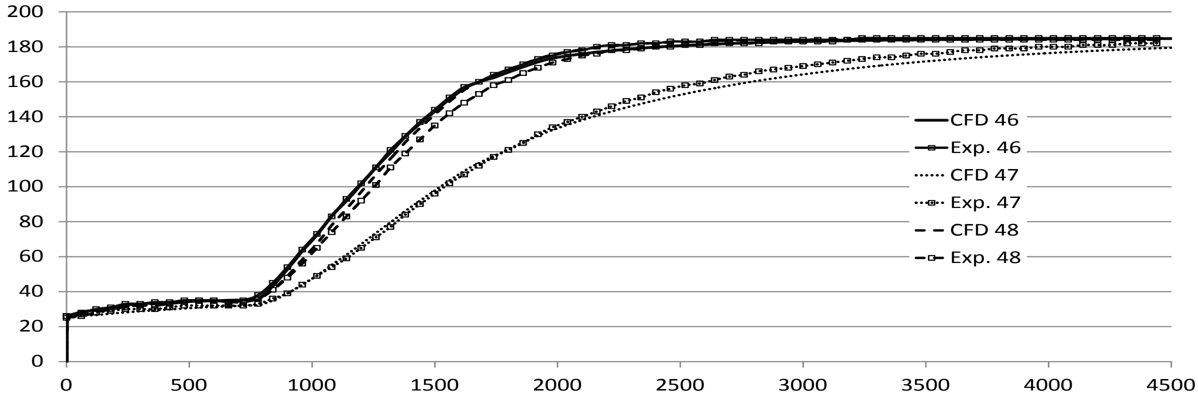

Fig. 7: The temperature for the hottest spot on the mold (46), the corresponding point on the rear (47), and a measurement on the side of the framework (48).

CONCLUSIONS

With simple means, the velocity field within the autoclave was successfully measured. For the simulations, it seems like the temperature can be accurately predicted with this method at least at locations involving simple geometries and flow. Further work needs to be done to also compute the temperature distribution inside the mold accurately.

ACKNOWLEDGMENTS:

Everyone involved in the project for their valuable help and expert knowledge that they enthusiastically share, and especially Staffan Nilsson and Roland Andersson at Saab Aerostructures for running the autoclave during the experiments.

REFERENCES

1. White and H. T. Hahn: 'PROCESS MODELING OF COMPOSITE-MATERIALS - RESIDUAL-STRESS DEVELOPMENT DURING CURE .2. EXPERIMENTAL VALIDATION', *Journal of composite materials*, 1992, **26**(16), 2423-2453.
2. L. Skartsis, B. Khomami, and J. L. Kardos: 'RESIN FLOW THROUGH FIBER BEDS DURING COMPOSITE MANUFACTURING PROCESSES .2. NUMERICAL AND EXPERIMENTAL STUDIES OF NEWTONIAN FLOW THROUGH IDEAL AND ACTUAL FIBER BEDS', *Polymer engineering and science*, 1992, **32**(4), 231-239.
3. C. Kim, H. Teng, C. L. Tucker, and S. R. White: 'THE CONTINUOUS CURING PROCESS FOR THERMOSET POLYMER COMPOSITES .1. MODELING AND DEMONSTRATION', *Journal of composite materials*, 1995, **29**(9), 1222-1253.
4. A. Bejan and A. D. Kraus: 'Heat transfer handbook'; 2003, Hoboken, New Jersey, John Wiley & sons, Inc.
5. A. Bejan: 'Heat transfer'; 1993, John Wiley & Sons, Inc.
6. A.-L. Ljung, T. S. Lundstrom, B. D. Marjavaara, and K. Tano: 'Convective drying of an individual iron ore pellet - Analysis with CFD', *International journal of heat and mass transfer*, **54**(17-18), 3882-3890.
7. A.-L. Ljung, T. S. Lundstrom, B. D. Marjavaara, and K. Tano: 'Influence of Air Humidity on Drying of Individual Iron Ore Pellets', *Drying technology*, **29**(9), 1101-1111.
8. T. M. Green, E. M. Lindmark, T. S. Lundstrom, and L. H. Gustavsson: 'Flow characterization of an attraction channel as entrance to fishways', *River research and applications*, **27**(10), 1290-1297.

COMPACTION RESPONSE AND AIR PERMEABILITY CHARACTERISATION OF OUT-OF-AUTOCLAVE PREPREG MATERIALS

Christopher M.D Hickey, Jamie. G. Timms, Simon Bickerton

Centre for Advanced Composite Materials, Department of Mechanical Engineering, School of Engineering, University of Auckland, Private Bag 92019, Auckland 1142, New Zealand.
Corresponding author's e-mail: chic014@aucklanduni.ac.nz

ABSTRACT: Out-of-autoclave prepreg materials offer the ability to produce high quality laminates without the size and cost constraints of traditional autoclave prepreg manufacture. Because of the lower pressures involved, the complete removal of air from the laminate before cure is critical to ensuring a void-free laminate is produced, and maximum mechanical performance is achieved. The rate and direction of air removal from the laminate can vary widely between materials, so an accurate understanding of the air permeability of the prepreg, both in-plane and through thickness, is critical for optimal process design for laminates of varying size, thickness and material. This paper presents the development of an experimental method to measure the decoupled compaction response and in-plane air permeability of out-of-autoclave prepreg materials using a radial air flow technique. Decoupling the compaction response and permeability allows for the implementation of an air removal simulation, including the effects of spatially and time varying thickness and permeability. Initial experiments on unidirectional tape and plain weave cloth materials have shown the cloth exhibits higher porosity under 1 atmosphere of pressure, resulting in higher in-plane permeabilities over each material's achievable volume fraction range, by approximately three orders of magnitude, as compared to the unidirectional material.

KEYWORDS: *Out-of-Autoclave prepreg, air permeability, compaction*

INTRODUCTION

Composite materials manufactured using prepreg and cured under pressure in an autoclave offer repeatable, high performance laminates, and hence are the performance benchmark in composites manufacturing , particularly the aerospace industry. In recent years new prepregs have become available, that can be cured under vacuum alone within an oven, without the use of an autoclave. These out-of-autoclave prepregs offer the excellent mechanical properties of traditional prepreg laminates, without the expense and size constraints imposed by the use of an autoclave.

Of critical importance in out-of-autoclave prepreg processing is the removal of entrapped air from the laminate, as with the absence of autoclave pressure (~6 bar) any entrapped air is not compressed, and will result in significant void content in the laminate. Voids in the laminate have a significant detrimental impact on the mechanical performance of the part, particularly strength properties. A widely cited paper in this area by Judd[1] showed that inter-laminar shear strength decreased by approximately 7% for every 1% of void content, up to a void content of 4%. Such results indicate the significant potential benefit of producing void free laminates.

Manufacturers of out-of-autoclave prepreg materials are aware of this issue, and have developed a variety of methodologies to improve the rate at which air can be removed from the prepreg stack. These include only partially impregnating the reinforcement with resin, or applying the resin in films or stripes, all in an effort to create air evacuation pathways.

PREVIOUS RESEARCH

Research in this area has primarily sought to quantify air removal rates, in order to determine the duration and choice of consumable layouts for the debulk stage, where entrapped air is removed from the laminate, prior to cure.

For monolithic laminates, a large series of work by Seferis [2-5] quantified the air permeability of prepreg materials. The experimental technique comprised a laminate placed under a vacuum bag, with consumables arranged to ensure in-plane flow. One end of the laminate was connected to vacuum, and the other open to the atmosphere via an air flow meter. The entire apparatus was placed in an autoclave. Experiments varying the applied autoclave pressure and the applied vacuum were performed. It was found that increasing the autoclave pressure decreased the flowrate through the laminate, indicating the strong relationship between applied stress, thickness and permeability. It was also found that increasing the level of vacuum applied decreased the flowrate through the laminate, showing that the increased pressure gradient was outweighed by the reduction in permeability. In this experimental technique there exists a pressure drop between the applied vacuum and atmospheric conditions. Assuming the pressure drop through the flowmeter and associated tubes is negligible, a pressure gradient must exist across the length of the laminate. Although this work showed the strong dependence on flowrate of the applied compaction stress, the effect of this pressure gradient and hence permeability gradient was ignored. Permeability measurements using a similar technique to that by Seferis have also been more recently performed by Louis [6].

In studies of the liquid permeability of dry reinforcement the permeability has been shown to be a strong nonlinear function of fibre volume fraction, indicating that methods assuming an average thickness and average permeability may be erroneous.

Grunenfelder [7] used a technique where a prepreg laminate under a vacuum bag was evacuated, and then vented to atmosphere. The rate at which the pressure rose was used to infer the permeability. This method has deficiencies as per the Seferis method, but also measures the permeability in an unloading situation, rather than the loading situation that occurs in reality. Any hysteresis in the compaction response of the prepreg will therefore have an influence on the relevance of any measured permeability obtained.

There has also been a significant quantity of work, with a particular focus on honeycomb cored sandwich panels, where prepreg permeability becomes even more significant, due to the large quantity of air in the honeycomb that is trapped by the prepreg skins. A range of studies by Tavares [8-10], and subsequently Kratz [11], investigated the through thickness permeability, using a falling pressure technique, where the transient measured pressure in a cavity underneath the skin can be used to calculate the through-thickness permeability of the skin.

In these through-thickness experiments, a constant laminate thickness is assumed, which does not take into account the changing thickness, porosity and hence permeability with increasing compaction stress. Any porosity or permeability gradient through the thickness, similar to that described previously for in-plane flow, is also ignored.

Recently Xin [12] quantified the in-plane and through thickness permeability of prepreg under varying compaction stresses, where the compaction stress was applied externally by a loading bar to a metal plate, ensuring the sample was held at uniform thickness. It was found that over the compaction range of 0-10 bar, the permeability changed by approximately a factor of 3. It was also found that the in-plane permeability was approximately 2 orders of magnitude higher than the through-thickness permeability and that increasing temperature decreased the permeability due to resin flow. However this method has deficiencies, in that the force from the air pressure field is not removed from the total applied force to infer the true compaction stress on the laminate.

Recommended debulk times based on measured air permeability have been limited to constant laminate thickness models with constant permeability. Such models do not take into account the compaction response of the prepreg, and hence ignore spatially and time varying thickness, porosity and permeability, that will occur as air is removed from the laminate and the internal pressure decreases. The calculated air removal times for laminates of varying length and/or thickness are therefore put into doubt, as the permeability measurement experiments and associated implementation into a model do not take into account any thickness profile and hence permeability distribution in the experiment.

Through the current work the authors seek to decouple the relationship between applied stress, porosity and permeability of out-of-autoclave prepreg materials. This will allow the development of much improved material compaction and permeability models for input into an air removal simulation that takes into account spatially and time varying laminate thickness, porosity and permeability.

EXPERIMENTAL SETUP

Figure 1 presents a schematic of the permeability measurement rig. It is comprised of two platens mounted in an Instron 1186 Universal Testing Machine. The upper platen is fixed and is aligned relative to the lower pattern using a spherical alignment unit and strain-gauged compression specimen, to ensure parallelism and uniform cavity thickness to a tolerance of 0.01mm. The lower platen position is controlled by the Instron machine, enabling a range of cavity thicknesses to be achieved. Two thickness gauges are used to accurately measure the cavity thickness, removing the effect of compliance in the testing machine and fixture.

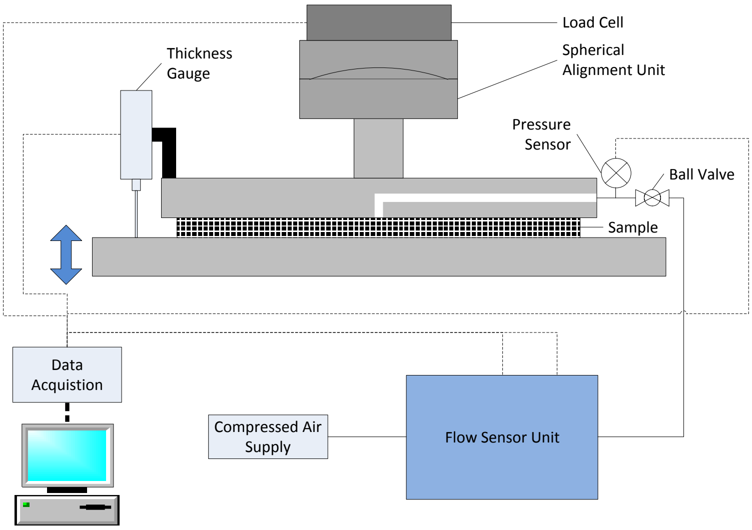

Figure 1: Air permeability measurement equipment

For compaction testing, the ball valve is closed and as the cavity thickness decreases, any pressure rise due to squeeze flow can be measured by the pressure sensor. The component of force, due to this squeeze flow pressure distribution can then be removed to find the true compaction response of the material.

For permeability measurements, compressed air flows from a laboratory compressed air supply, through a flow sensor measurement unit containing two Brooks Thermal Mass Flow Meters (Model SLA5860), past a pressure sensor (Impress IMP1000) and into the centre of the circular sample, where it flows radially to the edge of the sample. The flow rate range of the flow sensors was selected based on a literature review of past prepreg air permeability research, the flow geometry and the pressure range available from the laboratory air supply.

Experimental Procedure

Materials

The compaction and air permeability characteristics of two carbon fibre prepreg materials with different fibre architectures were investigated, both supplied by SP High Modulus. Their specifications are shown in Table 1.

Table 1: Material Specifications

	Cloth	***Unidirectional***
Fibre Areal Weight(g/m^2)	300	150
Fibre Architecture	Plain Weave	Unidirectional
Resin System	SE70	SE70
Resin Weight (%)	42	37
Fibre Density(kg/m^3)	1808	1800
Uncured Resin Density(kg/m^3)	1160	1160

Samples were cut into 130mm diameter circular discs using a hydraulic click press, to ensure dimensional accuracy, with the unidirectional laid up 0/90 to achieve quasi-isotropy. A 15mm diameter hole was punched in the centre of the sample to ensure purely two-dimensional flow was obtained.

Compaction

During the compaction tests, the mould cavity was closed at a prescribed force ramp rate until 1atm of compaction pressure was reached, followed by a 15 minute hold at 1atm. The sample was then unloaded to zero stress at the same force ramp rate as for loading, to investigate any potential hysteresis effects.

Permeability

For the permeability measurement experiments, the mould cavity was closed at 0.05mm/min, until the target thickness was reached. This thickness was then held constant for 5 minutes, while the air flow rate and inlet pressure were recorded at an acquisition frequency of 2 Hz. The mould cavity was then closed to the next target thickness and the process repeated until all target thicknesses were measured. Target thicknesses were chosen based on the results of the compaction tests. An advantage of the described technique is that it allows the measurement of air permeability, at a range of thicknesses and porosities from the same sample. Permeability was calculated using Darcy's law including a correction for the compressibility of air:

$$K = \frac{Q_{high}\mu \ln\left(\frac{r_o}{r_i}\right)}{\pi h\left(P_{high} - \frac{P_{low}{}^2}{P_{high}}\right)} \tag{1}$$

where K is the quasi-isotropic in-plane air permeability, Q_{high} is the volumetric flowrate at the high pressure side, μ is the air viscosity, r_o is the outer radius of the sample, r_i is the inner radius of the sample, h is the sample thickness, P_{high} is the absolute pressure at the high pressure side, and P_{low} is the absolute pressure at the low pressure side, in this case atmospheric pressure.

Experimental Results

Compaction

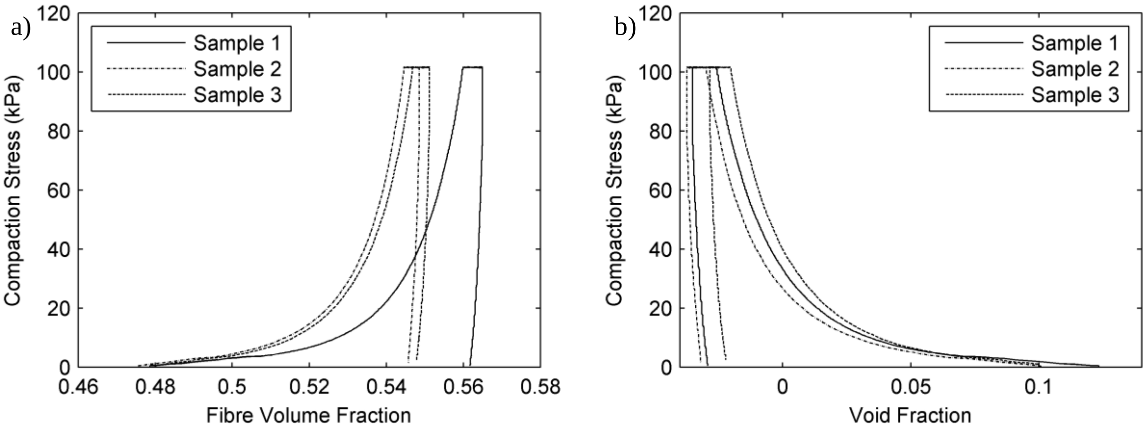

Figure 2: Compaction response of three 16-layer samples of unidirectional material vs. a) fibre volume fraction and b) void fraction

Figure 2 presents a plot of the compaction response of three 16-layer samples of unidirectional material. The loading phase shows a typical highly non-linear compaction response with increasing fibre volume fraction, as is typically seen in the compaction of dry reinforcements. During the hold at a pressure of 1atm for 15 minutes, there is noticeable creep, seen as an increase in fibre volume fraction and decrease in void fraction at constant stress. In the unloading phase, the curve does not follow the loading curve, indicating significant permanent deformation has occurred. All samples start at a similar free fibre volume fraction, yet sample 1 reaches a higher fibre volume fraction than samples 2 and 3. This can be attributed to the variation in mass of the samples. Figure 2b presents a plot of compaction stress vs. void fraction (or porosity), which was calculated using:

$$\phi = 1 - \frac{n}{t}\left(\frac{A_f}{\rho_f} + \frac{A_r}{\rho_r}\right), A_r = \frac{m_{sample}}{na} - A_f \tag{2}$$

where ϕ is porosity, n is the number of layers, t is thickness, A_f and A_r areal weights of fibre and resin respectively, and ρ_f and ρ_r the densities of fibre and resin respectively. The true resin areal weight was calculated based on the measured sample mass, m_{sample}, the sample area a, the number of layers n, and the nominal fibre areal weight A_f.

Figure 2b shows a more repeatable compaction response when the effect of variation in resin mass is taken into account. Of note are porosities that are lower than zero. This was unexpected and is assumed to be a result of the compressibility of the uncured resin, and is the subject of further investigations. In all tests, no pressure increase was seen at the centre; therefore no correction for the component of force due to squeeze flow was required.

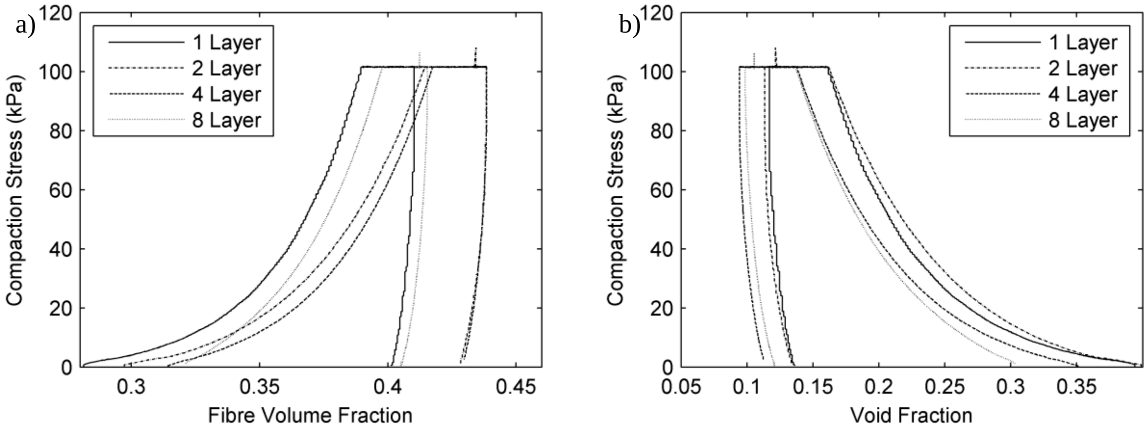

Figure 3: Compaction response of cloth samples at varying layers vs. a) fibre volume fraction and b) void fraction

Figure 3 presents the compaction response of the cloth material at varying number of layers. Compared to the unidirectional material, the maximum fibre volume fractions reached are lower by approximately 10%. There also appears to be a greater magnitude of creep than for the unidirectional material. The cloth material exhibits a greater range of fibre volume fraction for the same pressure range. The free fibre volume fraction is seen to increase with increasing number of layers, indicating some nesting of the sample occurring during initial layup. The variation in the peak fibre volume fraction shows no relationship with number of layers, which could be due to the variation in sample mass.

Figure 3b presents the same data against void fraction, using the same calculation as described for the unidirectional material. In these tests only positive values of porosity are observed, up to a maximum of 0.10. This may be due to the lower fibre packing density of the cloth material, compared to the unidirectional material which is more optimally packed.

Permeability

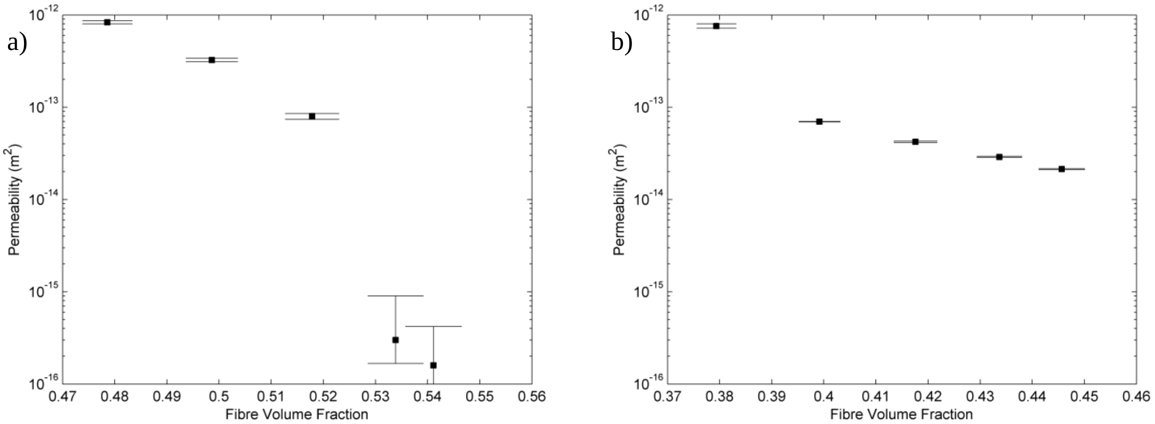

Figure 4: Permeability vs. fibre volume fraction for a) unidirectional 16 layers and b) cloth 8 layers

Figure 4 presents the air permeability of a 16-layer sample of unidirectional material and 8 layers of cloth material, both with a total fibre areal weight 2400g/m^2 as an example of the data output from these tests. The fibre volume fraction ranges are different for each material, representing the fibre volume fraction range obtained from the compaction tests. Both materials exhibited a decreasing permeability with increasing fibre volume fraction, with the unidirectional material exhibiting a higher decrease over the relevant compaction range. Generally the cloth material was significantly more permeable than the unidirectional material. This may be attributed to the woven nature of the cloth, resulting in higher porosities and hence permeability under the same compaction levels. The resin application on the cloth was also noticeably more irregular than for the unidirectional material, where a uniform application of resin is required to bind the fibres together, unlike the cloth where the fibres are held together by the weave.

The unidirectional exhibited a linear trend when plotted on a log scale versus volume fraction, until a fibre volume fraction of 0.52 which corresponded to 0.0 calculated porosity. Below this level, measured permeability deviated from the linear trend, and was unsteady over time. For the cloth material, the lowest fibre volume fraction deviated from the linear trend, exhibiting higher permeability. This may be due to a ‘racetracking’ effect as the sample is not in uniform contact with the mould platen, so preferential low resistance paths exist for air flow, giving a higher measured permeability.

CONCLUSIONS

An experimental technique has been developed that enables the decoupled compaction response and permeability of out-of-autoclave prepreg materials to be measured accurately. Preliminary investigations on cloth and unidirectional material showed that the unidirectional material reached lower levels of porosity than the cloth under 1 atmosphere of pressure, resulting in significantly lower air permeability.

FUTURE WORK

The development of this experimental fixture enables a vast array of further investigations to be conducted. This may include investigation of loading rate effects, layup orientation, compaction history and time dependent behaviour on compaction response and permeability. Future work will also involve the measurement of through-thickness air permeability using similar methodologies as for in-plane permeability, but with a custom manufactured through-thickness permeability rig.

REFERENCES

1. Judd, N.C.W. and W.W. Wright, *Voids and their effects on the mechanical properties of composites - an appraisal.* SAMPE Journal, 1978. **14**(1): p. 10-14.
2. Nam, J.-D., J.C. Seferis, S.-W. Kim, and K.-J. Lee, *Gas permeation and viscoelastic deformation of prepregs in composite manufacturing processes.* Polymer Composites, 1995. **16**(5): p. 370-377.
3. Putnam, J.W., Seferis J.C., *Prepreg gas permeation as a function of fiber orientation and aging time.* Journal of Advanced Materials, 1995. **26**(3): p. 35-41.
4. Shim, S.-B. and J.C. Seferis, *Thermal and air permeation properties of a carbon fiber/toughened epoxy based prepreg system.* Journal of Applied Polymer Science, 1997. **65**(1): p. 5-16.
5. Stark, E.B., A.M. Ibrahim, T.E. Munns, and J.C. Seferis, *Moisture effects during cure of high-performance epoxy matrices.* Journal of Applied Polymer Science, 1985. **30**(4): p. 1717-1731.
6. Louis, B.M., *Gas Transport in Out-of-Autoclave Prepreg Laminates*, 2007, The University of British Columbia.
7. Grunenfelder, N., *Air Removal in Vbo Prepreg Laminates: Effects of Breathe-Out Distance and Direction*, 2011.
8. Tavares, S.S., N. Caillet-Bois, V. Michaud, and J.-A.E. Månson, *Non-autoclave processing of honeycomb sandwich structures: Skin through thickness air permeability during cure.* Composites Part A: Applied Science and Manufacturing, 2010. **41**(5): p. 646 - 652.
9. Tavares, S.S., V. Michaud, and J.A.E. Månson, *Assessment of semi-impregnated fabrics in honeycomb sandwich structures.* Composites Part A: Applied Science and Manufacturing, 2010. **41**(1): p. 8-15.
10. Tavares, S.S., V. Michaud, and J.A.E. Månson, *Through thickness air permeability of prepregs during cure.* Composites Part A: Applied Science and Manufacturing, 2009. **40**(10): p. 1587-1596.
11. Kratz, J., *Processing Composite Sandwich Structures using Out-of-Autoclave Technology*, 2009, McGill University.
12. Xin, C., M. Li, Y. Gu, Y. Li, and Z. Zhang, *Measurement and Analysis on in-Plane and Through-Thickness air Permeation of Fiber/Resin Prepreg.* Journal of Reinforced Plastics and Composites, 2011.

Section 4

Measurement, Monitoring and Control

INNOVATIVE APPROACH TO TRACK FLOW-FRONT IN LCM-PROCESSES THROUGH PRESSURE SENSORS FOR IN-LINE QUALITY CONTROL

Claudio Di Fratta, Florian Klunker and Paolo Ermanni

Center of Structure Technologies, ETH Zürich, 27 Leonhardstrasse, 8092 Zurich, Switzerland. Corresponding author's e-mail: claudiodifratta@mavt.ethz.ch

ABSTRACT: Quality of laminates made by Liquid Composite Molding (LCM) processes is closely related to resin system impregnation. Problems like void or dry spot formation often result in flaws and defects, which are usually recognized only after the final part is manufactured, through standard conformity verification. In this work, an innovative approach to track flow-front progression has been developed, which can allow early quality control during impregnation stage. The system relies on using a minimum number of pressure sensors, strategically located in the cavity, which alone give enough information for flow-front estimation over the time. This estimation is done by comparing pressure values from sensors with the pressure distributions obtained by flow simulations in an optimization loop. A big effort has been done to set up a numerical code that in a fast way follows fluid progression along its flow paths. Tests show that, with this approach, the introduction of just three sensors provides a sufficient resolution of flow-front position.

KEYWORDS: *Liquid Composite Molding, Process Monitoring, Resin Flow, Computational Modeling, Sensing Techniques, RTM.*

INTRODUCTION

Liquid Composite Molding (LCM) processes, like Resin Transfer Molding (RTM) and its variants, are widely used techniques for manufacturing composite structures, especially in transportation industries [1, 2]. However, laminates fabricated through resin flow technologies present a significant variability in their final quality, which is threatened by small, often unavoidable, variations in material properties (e.g. fabric permeability) and process arrangements [3]; that can lead to unpredictable flow patterns with possible formation of defective parts.

Improving the robustness of LCM-processes is an on-going issue that research is tackling in diverse ways, including, for instance, stochastic modeling of permeability changes [4] or combined experimental/numerical methods [5-9]. In general, since part quality is related to the success of designed resin injection, early identification of flow irregularities by a suitable monitoring system is necessary to recognize potential defects and flaws and, thus, carry out a quality assessment already during the impregnation phase. Literature in this field has proposed several solutions for process monitoring, based on various sensing techniques [5-13]; anyhow, it has to be stated that most of the sensor systems are actually not suitable for a generic LCM-process, because of technical reasons (inapplicability at manufacturing conditions or intrusiveness/incompatibility with materials used) or economical implications (complex and expensive implementation).

In this work a new approach for process monitoring has been investigated; it makes use of only few pressure sensors, which can be easily embedded in a mold without affecting the final composite materials and are applicable at typical process conditions. Placed in selected locations of the mold cavity, the sensors provide discrete pressure values that are analyzed and input into a numerical code, which is able to reconstruct the flow-front profile at every impregnation time, as a result of an optimization loop. The procedure to evaluate the flow-front position from fluid pressure information is based on a recursive comparison between data sensed by the transducers and values computed through steady flow simulations. Adaptive moving of flow-front coordinates in the simulations allows calculation of pressure values closer and closer to the real ones at every iteration step, until an adequate match is found. In addition, a feature for detecting flow paths has been introduced in the numerical algorithm; in this way the flow-front points are moved along the actual fluid trajectories, enabling an effective front estimation in cavity with geometrical complexities. Full details on the flow-front estimation procedure are given in the next section, together with examples of application in a virtual environment. Successively, results of real tests, validating the proposed approach, are shown and discussed, and, finally, conclusions are drawn.

FLOW-FRONT ESTIMATION METHODOLOGY

In LCM-processes, the resin pressure p field in the mold cavity can be determined by solving the following equation:

$$\nabla \cdot (\mathbf{K}/\eta \cdot \nabla p) = 0, \tag{1}$$

where $\mathbf{K}$ is the preform permeability and η the fluid viscosity. Since air viscosity is significantly lower than resin’s one, the pressure drop from the flow-front to the outlet can be neglected and the pressure distribution can be easily calculated from Eqn. 1, by applying vent condition at the flow-front. As a consequence, assuming a homogeneous permeability, in one-dimensional cases, the pressure decreases linearly from the inlet value p_i to the front value p_f at every considered impregnation time. Thus, knowing the pressure p_{sens} at a fixed sensor location, it is trivial to identify the unknown front position at any time.

In all the other cases, the flow-front detection is not so straightforward; nevertheless it is possible to estimate it by applying an iterative scheme, taking always advantage of pressure information from sensors in known position:

1. A flow-front position is guessed (possible initial guesses can be the sensor or the vent locations);
2. The pressure distribution is computed though Eqn. 1, by means of a steady flow simulation;
3. The pressures measured by sensors are compared with the calculated pressures at corresponding locations;

4. If calculated and sensed pressures do not coincide (or not fall within an interval equal to the measurement uncertainties), a new estimation for the flow-front is made, based on the results of the comparison;
5. A new pressure distribution is computed and a comparison with reference sensed values is performed; this cycle continues until the calculated pressures are sufficiently close to the measured ones, thus so a satisfactory approximation for the flow-front position is found.

An explanatory example of working principle of the methodology is given in Fig. 1. Here a virtual wet-out of a rectangular cavity is considered and the figure shows the filling status at a certain impregnation time, with filled zones in red and unfilled ones in blues (in the virtual impregnation, two runners have been set along the sides, so to introduce irregularities in the flow advancement). As it is noticeable in Fig. 1, five sensors have been located in the cavity, to each of them corresponds a control point for flow-front estimation. During the above mentioned iterative scheme, those control points are moved along lines connecting inlet and outlet and passing though the related sensor points, until an acceptable front estimation is found. The flow-front shape is then obtained by spline interpolation of the control points.

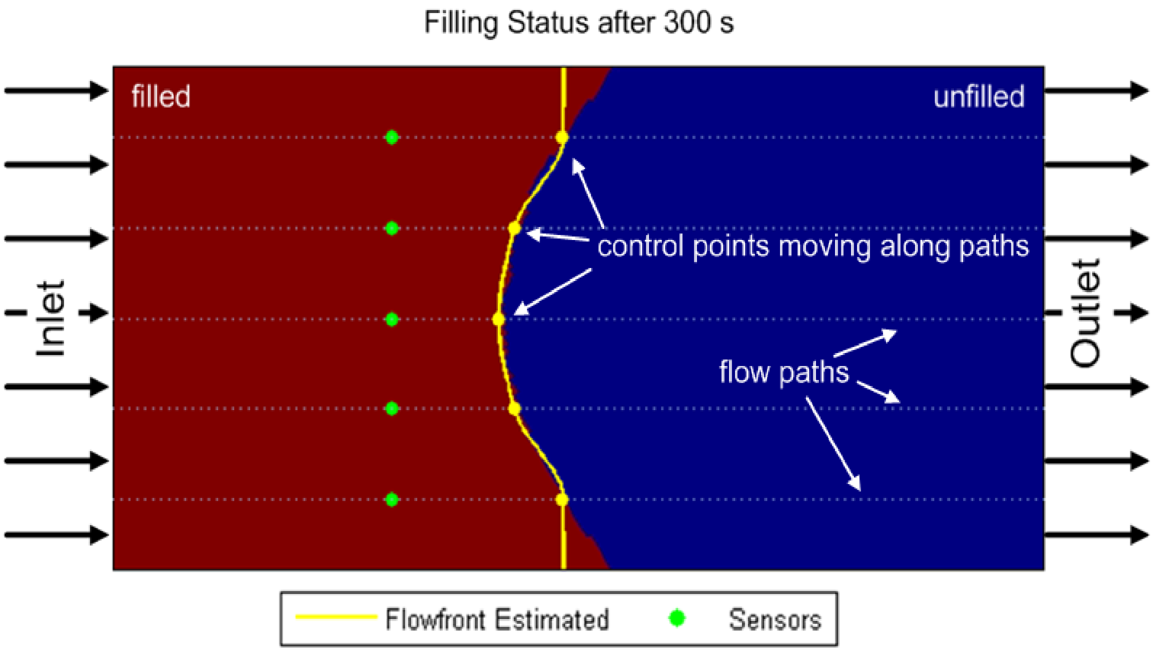

Figure 1: Application of flow-front estimation approach in a rectangular cavity with runners

Fig. 1 shows, indeed, the trustworthiness of the developed methodology in this case; the estimation is very accurate, with small deviations from the real front only next to the long sides, where, for numerical stability during the iterations, the algorithm code fits the flow-front shape with simple minimum distance segments.

In case of cavity with more complex geometry, the flow-front estimation algorithm operates a preliminary evaluation of the possible resin flow paths (resorting to transient simulations) and uses them as trajectories lines for moving the control points of the front. An example of this feature is reported in Fig. 2, where a geometry with a rounded side (fender-like) is considered.

In this case the lines connecting inlet and outlet cannot be straight as in Fig. 1, nonetheless the code is able to detect the actual flow paths and move the control points along them. As it can be seen, this feature allows a very precise approximation of the flow-front in such complex cavity shapes.

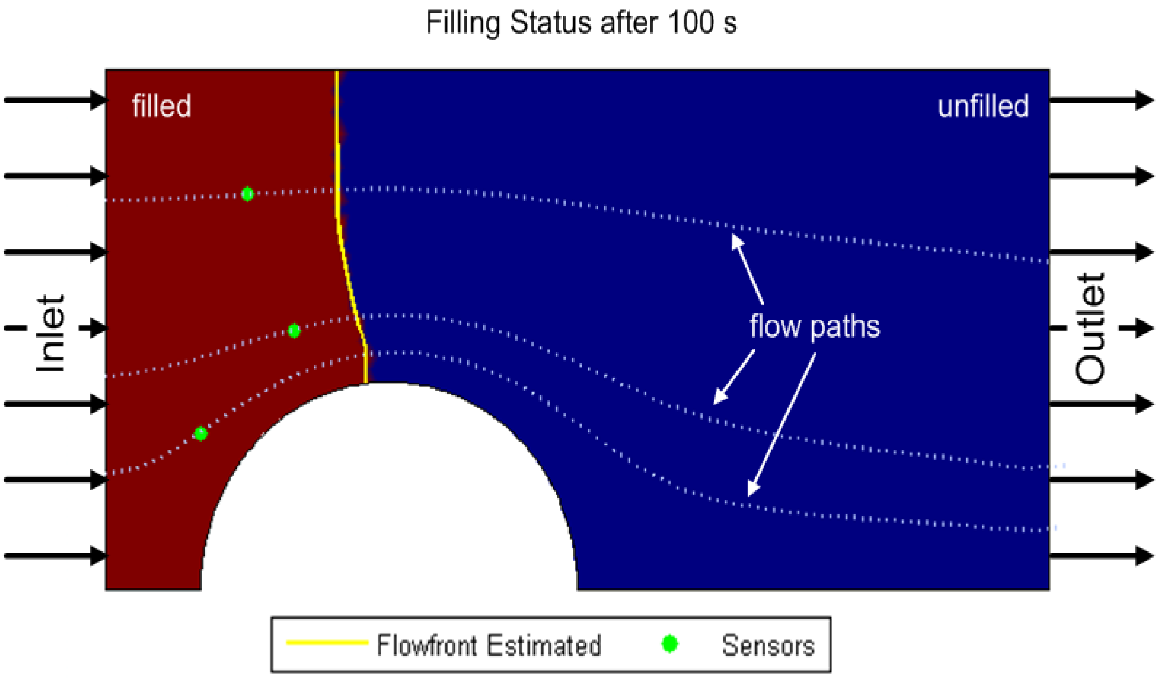

Figure 2: Application of flow-front estimation approach in fender-like geometry

The proposed approach for flow-front tracking permits to keep the effort by the sensing system's side low, since only a small amount of point sensors are required, if they are tactically placed in the mold, exploiting the benefits given by the flow paths' detection. In general, a strategic placement of the sensors can be done choosing their locations so that:

A. they stay as close as possible to the injection gates (at least one sensor for each gate), in order to maximize the use of data they provide;
B. each sensor belongs to a different flow path (unless a redundant system is required for security reasons);
C. these flow paths are spaced out to cover the widest laminate area and finish in the vent locations (not in "dead-ends").

Some considerations/constrains have to be added to the above stated rules:

a. the sensors should not be placed too close to the gates that $|p_i - p_{sens}|$ is lower than the measurement uncertainty at any time, otherwise no estimation can be made;
b. for the same reason above, more than one sensor have to be located along the same path, when the increment in fluid pressure becomes smaller than the experimental error;
c. extra sensors should be put in critical zones of the cavity or if the chosen path spacing provides an insufficient front resolution.

EXPERIMENTAL TESTS

Real tests have been performed to verify the effectiveness of the approach and validate the methodology. Plane rectangular and fender-like geometries for the mold cavity (size 250x500x2 mm) have been considered and vacuum driven injections have been carried out, using silicon oil and random glass fiber mat as testing materials. Piezoelectric pressure sensors type 6162AA, by Kistler AG, with an appropriate acquisition system, have been employed, similarly as in [9], to measure the fluid pressure in three selected points of the mold. At different experimental times, the data from sensors were analyzed and given as input to the flow-front estimation algorithm. Fig. 3 shows the whole arrangement for the rectangular geometry test and also the results of the flow-front estimation four subsequent injection times. As it is noticeable, the estimated fronts are very close to the real ones; the developed system is able to recognize rightly even small deviations from the ideal flow pattern.

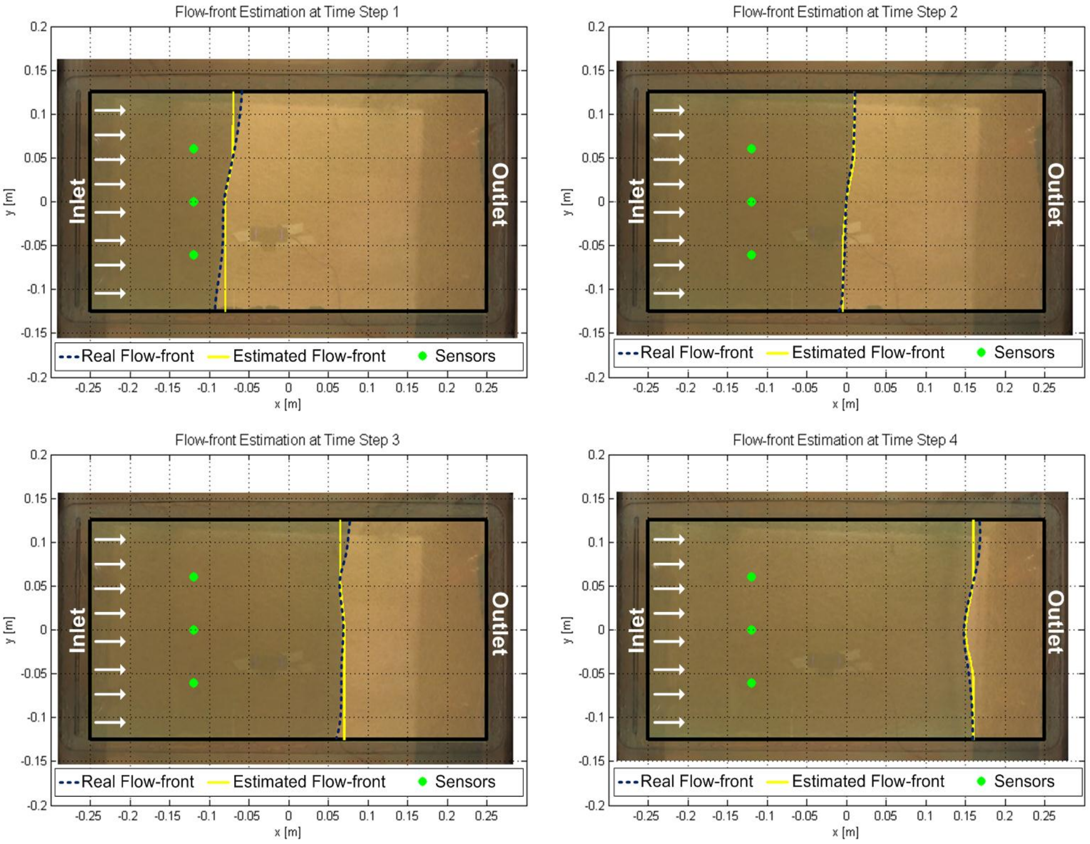

Figure 3: Rectangular geometry test configuration and results at different time steps

Fig. 4 illustrates the arrangements and results for the fender-like geometry test. Here the non-trivial mold design requires the detection of flow paths to apply the developed methodology. Also in this case, the proposed approach provides accurate estimations of the flow-fronts. Three sensors, placed in the highlighted strategic positions, assures already an acceptable flow-front resolution; the relative highest discrepancies from the real fronts can be observed only next to the cavity borders side, where, as mentioned before, minimum distance segments are used to locally approximate the flow-front shapes.

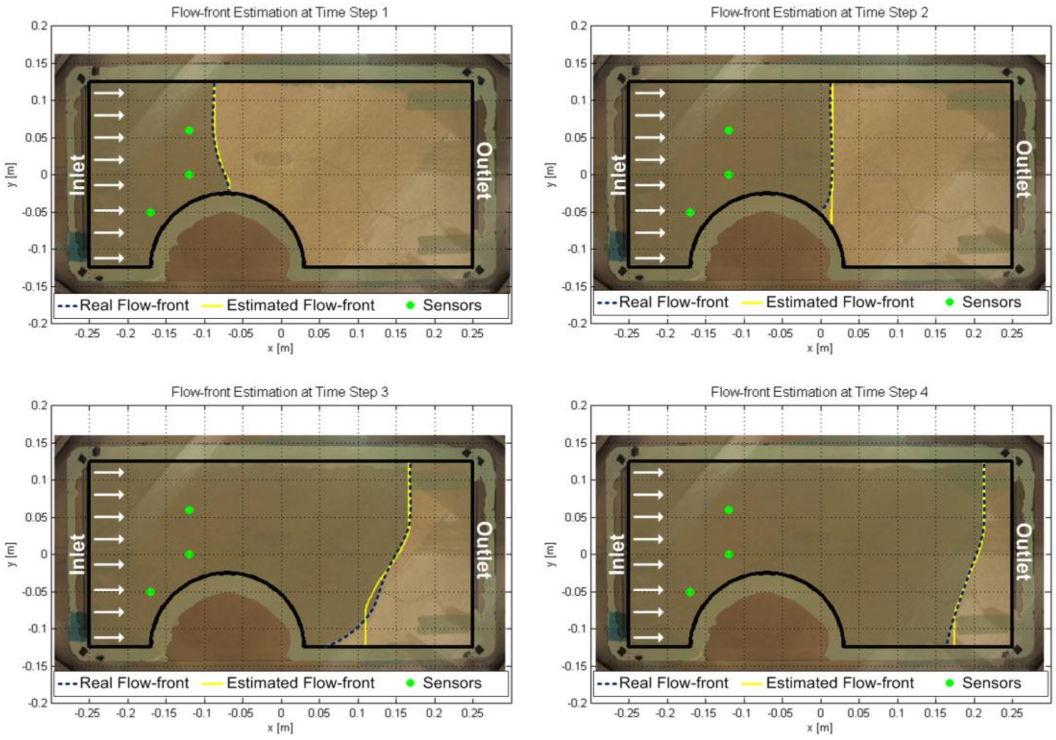

Figure 4: Fender-like geometry test configuration and results at different time steps

CONCLUSIONS

In this work a novel approach for tracking the flow-front in LCM-processes has been developed. The approach consists in a combined experimental/numerical methodology, which relies on using few, non-intrusive, and generally applicable pressure sensors, opportunely located in the mold cavity, for monitoring the correctness of flow progression. Data from sensors are entered as reference values in an optimization loop, where steady flow simulations are iteratively performed until the calculated pressures match the measured ones; at the end a suitable estimation for the flow-front position can be obtained for each process time. The algorithm code is moreover able to detect fluid flow paths, and use them to improve accuracy of front approximation; this feature makes the approach applicable to cavity with complex shapes. Real tests, with two different geometries, have been finally performed to validate the methodology. Results show a very good agreement between estimated and effective flow-front at various time steps; in addition, they indicate that only three sensors are sufficient to provide a satisfactory resolution of the flow-front profiles. Future work will tackle the issues to implement this approach in an actual in-line quality assessment system.

REFERENCES

1. Rudd CD, Long AC, Kendall KN and Mangin CGE (1997), Liquid moulding technologies, Woodhead Publishing Ltd.

2. Barlow D, Howe C, Clayton G and Brouwer S (2002), ‘Preliminary study on cost optimization of aircraft composite structures applicable to liquid moulding technologies’, *Composite Structures*, 57(1-4), 53-57.

3. Long AC and Endruweit A (2010), 'Prediction, measurement and significance of reinforcement permeability', *Keynote lecture in the 10th International Conference on Flow Processes in Composite Materials: (FPCM-10),* Ascona, Switzerland.

4. Zhang F, Cosson B, Comas-Cardona S and Binetruy C (2011), 'Efficient stochastic simulation approach for RTM process with random fibrous permeability', *Composites Science and Technology*, 71(12), 1478-1485.

5. Modi D, Correia N, Johnson M, Long AC, Rudd CD and Robitaille F (2007), 'Active control of the vacuum infusion process', *Composites Part A: Applied Science and Manufacturing,* 38(5), 1271-1287.

6. Johnson RJ and Pitchumani R (2008), 'Active Control of Reactive Resin Flow in a Vacuum Assisted Resin Transfer Molding (VARTM) Process', *Journal of Composite Materials*, 42(12), 1205-1229.

7. Sozer EM, Bickerton S and Advani SG (2000), 'On-line strategic control of liquid composite mould filling process', *Composites Part A: Applied Science and Manufacturing,* 31(12), 1383-1394.

8. Lawrence JM, Hughes P and Advani SG (2006), 'Experimental Validation of Dependence Map based Control in Liquid Composite Molding', *Journal of Composite Materials*, 40(13) 1137-1162.

9. Di Fratta C, Zogg M and Ermanni P (2011), 'A Combined Experimental/Numerical Approach for LCM-Process Quality Prediction', *Proc. of the Society for the Advancement of Material and Process Engineering: (SAMPE 11),* Long Beach, California.

10. Matsuzaki R, Kobayashi S, Todoroki A and Mizutani Y (2011), 'Full-field monitoring of resin flow using an area-sensor array in a VaRTM process', *Composites Part A: Applied Science and Manufacturing,* 42(5), 550-559.

11. Dunkers JP, Lenhart JL, Kueh, van Zanten JH, Advani SG and Parnas RS (2001), 'Fiber optic flow and cure sensing for liquid composite molding', *Optics and Lasers in Engineering,* 35(2), 91-104.

12. Carlone P and Palazzo GS (2012), 'Flow Monitoring and Permeability Measurement in LCM Processes by means of a Dielectric Sensor', *Key Engineering Materials,* 504, 289-294.

13. Tuncol G, Danisman M, Kaynar A and Sozer EM (2007), 'Constraints on monitoring resin flow in the resin transfer molding (RTM) process by using thermocouple sensors', *Composites Part A: Applied Science and Manufacturing,* 38(5), 1363-1386.

A MULTIFUNCTIONAL DEVICE FOR POLYMER/COMPOSITE CHARACTERIZATION

Xavier Tardif[1], Yasir Nawab[1,2], Nicolas Boyard[1], Vincent Sobotka[1], Pascal Casari[2], Frédéric Jacquemin[2] , Didier Delaunay[1]

[1]Université de Nantes, CNRS, Laboratoire de Thermocinétique de Nantes, UMR 6607, La Chantrerie, rue Christian Pauc, BP 50609, 44306 Nantes cedex 3 – France
[2] Université de Nantes, Institut de Recherche en Génie Civil et Mécanique, UMR CNRS 6183, 37 boulevard de l'Université, BP406, 44600 Saint-Nazaire, France

ABSTRACT: The control and optimization of heat transfers during the forming of composite parts is of primary importance since they directly impact the quality of final parts. The modelling of these transfers requires an accurate knowledge of the thermo-physical properties of the matrix and the reinforcement, but also of the parameters describing the phase change kinetics and associated shrinkage. The experimental determination of these parameters induces the use of many instruments, which is time consuming. To address this issue, a home-built instrumented mould, dedicated to thermoset and thermoplastic composites, was designed to measure and/or identify several properties from a single experiment. This "PvT-α" apparatus allows the moulding of circular samples of 40mm diameter and 6mm thick while controlling the applied pressure on the sample and the temperature cycle on its surfaces. This mould is designed such as heat transfer is 1D within the thickness of the sample. Variation of volume as well as heat transfer between the sample and the mould are recorded. Then a 1D conduction model with a moving boundary coupled to phase change kinetics is used to describe the behaviour of the sample. Specific volumes as well as transverse thermal conductivity in amorphous and glassy states can be estimated as function of temperature. Parameters of crystallization kinetic model are also identified for thermoplastics. The evolution of the shrinkage as a function of the phase change is determined. Finally, the impact of the fibre content on all these parameters is investigated. Our methodology is illustrated from results on a semi-crystalline thermoplastic and a thermosetting material.

KEYWORDS: *PVT-α mould, Thermo-physical properties, Shrinkage, Thermal expansion, Heat transfer*

INTRODUCTION

Simulation and optimization of forming processes of thermosetting and thermoplastic composites is essential to improve quality of parts and productivity. During the cycle, the composite undergoes the residual deformations and stresses, that can lead to dimensional instability, warpage, ply cracking, delamination and fibre buckling. These defaults depend mostly on the shrinkage behaviour of the polymer matrix from the point where shrinkage stresses cannot be relaxed anymore. The matrix shrinkage has several origins, but all are coupled with heat transfers. The thermal shrinkage comes from temperature variations during the cycle. In case of thermosetting polymer, the chemical shrinkage is a direct consequence of crosslinking of the resin whereas in case of thermoplastic polymer, the shrinkage is induced by crystallization. In both cases, the corresponding enthalpy released during the phase change, impacts on heat transfers. The consideration of coupled heat transfers in modelling is then of primary importance to accurately describe the composite part behaviour during the moulding. However, this modelling requires a good knowledge of thermo-physical properties as well as the phase change kinetics to provide coherent results. A complete characterization has to be done under well-controlled and as close as possible to process conditions. The work of characterization is time-consuming since several instruments are needed. Within this framework, we propose a methodology coupled to a home-made PvTα device that allows determination of the required parameters with a minimum of experiments contrary to other characterization protocols [1-3]. This methodology is first applied to a semi-crystalline thermoplastic matrix (polypropylene). Specific volume is directly obtained from measurements. Thermal conductivity is identified with a classical inverse algorithm [4] using the measurement of the temperature in the centre of the sample. The crystallization kinetics is identified with an instrumentation that is not invasive since it is based on the measurement of volume variation of the sample. The methodology is then applied to characterize an epoxy vinylester resin and associated cross-ply glass fibre (UD) composites with two fibre volume fractions. In this case, we emphasize on the characterization of the coefficients of thermal expansion, as well as the coefficients of chemical shrinkage.

DESCRIPTION OF THE DEVICE

The PVTα mould consists of a piston which can move in a cylindrical stainless steel cavity (Figure 1) in which polymer or composite sample is beforehand placed. The sample is about 6mm thick and 40mm in diameter.

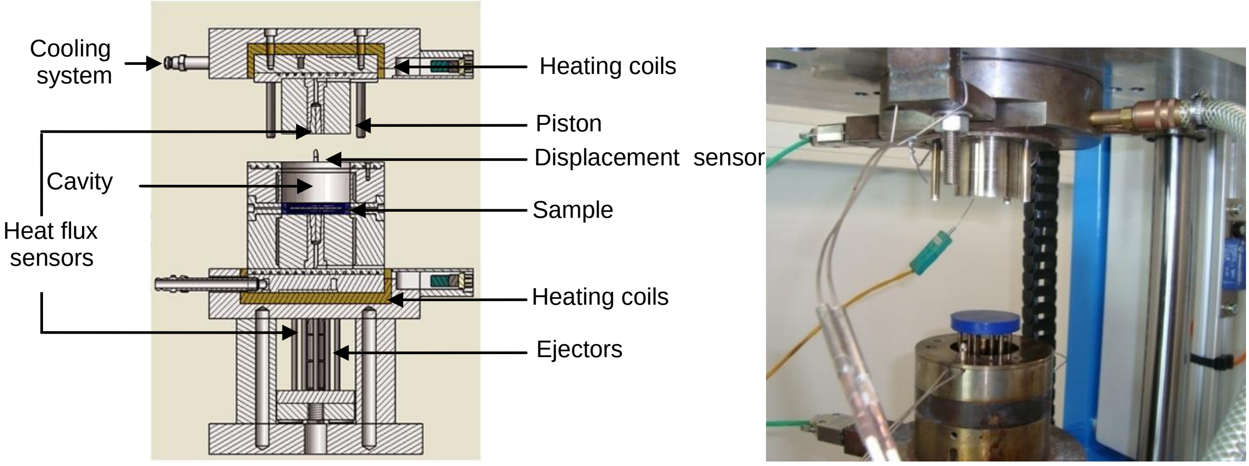

Fig. 1: Sketch and picture of the PvTα device

The mould is placed between two platens of an electric press that adjusts, in real time, the position of the piston to keep constant the applied pressure on the sample. The mould is designed so that heat transfers are 1D through the sample thickness unlike classical PvT. The heating is ensured by three heaters located at the top and bottom to heat the piston and cavity respectively. The cooling system consists of compressed air circuiting in the top and in the bottom of the mould. PID controllers allow the thermal regulation of the device. This device is instrumented with two heat flux sensors, one in the piston and the other in the moulding cavity. Each of them is composed of three thermocouples, placed at different locations from the surface and is manufactured in the same steel as the mould to be not intrusive. Data treatment with an inverse sequential algorithm [5] provides heat flux exchanged between the sample and the mould and the surface temperature of the sensor. Volume variations are recorded by LVDT-type displacement sensor with a precision of 1µm and a limit of 10mm. A complete description of this device is given in [6].Before starting PVTα experiment, the sample is sealed in an elastomer capsule. This low modulus elastomer is quasi-incompressible in the working pressure range. Since the polymer sample is placed in the deformable elastomer capsule, the pressure is assumed to be hydrostatic and the surface of the elastomer, on which the pressure is applied, does not vary. As a consequence, the measured thickness is directly related to the sample volume and its variations. To remove the impact of thermal expansion of the PvTα apparatus and the silicone capsule from the volume variation of the polymer, a baseline is performed with an aluminium reference material whose properties are known.

HEAT TRANSFER MODELING

A conduction model that takes into account volume variation is coupled to a phase change kinetics model (Eq.1b for crystallization and 1c for crosslinking) to describe heat transfer in the polymer (Eq. set 1). Crystallization is modelled by the differential form of Nakamura equation [7-8] (1b) and crosslinking by the Bailleul model [9]. It is a moving boundary problem. The domain used to represent the sample is a cylinder with a radius ‘r’ and a thickness ‘L’. However, heat transfer is only one dimensional through the thickness (x direction), the sample being isothermal along the radius at a given thickness.. Since ρ, Cp, λ depend on temperature and relative crystallinity or conversion degree, the problem to solve is non-linear. The silicon capsule is considered as a pure thermal resistance (R_{sil}). Initial temperature field is known.

$$(\rho Cp)(T,\alpha)\frac{\partial T}{\partial t}=\frac{\partial}{\partial x}\left(\lambda(T,\alpha).\frac{\partial T}{\partial x}\right)+\rho(T,\alpha).\Delta H.\frac{\partial \alpha(T,\alpha)}{\partial t},\ \mathrm{x}\in]0,\mathrm{L}(\mathrm{t})[,\ \forall \mathrm{t}>0 \tag{1a}$$

$$\frac{\partial \alpha}{\partial t}=n.K_{nak}(T).[1-\alpha(t)].[-\ln(1-\alpha(t))],\ \mathrm{x}\in]0,\mathrm{L}(\mathrm{t})[,\ \forall \mathrm{t}>0 \tag{1b}$$

$$\frac{\partial \alpha}{\partial \mathrm{t}}=\mathrm{W}(\nu(\mathrm{T})).\mathrm{K}(\mathrm{T}).\mathrm{G}(\alpha).\mathrm{F}_{\mathrm{diffusion}}(\alpha) \tag{1c}$$

$$-\lambda(T,\alpha).\left.\frac{\partial T}{\partial x}\right|_{x=0}=\frac{(T_{mold1}-T)}{R_{sil}},\ x=0,\ \forall \mathrm{t}>0 \tag{1d}$$

$$-\lambda(T,\alpha).\left.\frac{\partial T}{\partial x}\right|_{x=L}=\frac{(T-T_{mold2})}{R_{sil}},\ x=\mathrm{L}(\mathrm{t}),\ \forall \mathrm{t}>0 \tag{1e}$$

$$T(0,x)=T_{ini}(x),\ x\in]0,\mathrm{L}[,\ \mathrm{t}=0 \tag{1f}$$

In (1d) and (1e) T_{mold1} and T_{mold2} denote respectively mould surface temperatures at x=0 and x=L. α is the relative crystallinity or conversion degree. Thermal conductivity, specific heat and density are modelled by mixing laws. Finite volume method is used for the discretization of the set of equations (1), with a Cranck-Nicholson scheme.

CHARACTERIZATION OF THERMOPLASTIC

Material and experimental protocol

The material used for the experiment is a homopolymer polypropylene from Solvay: Eltex PP HV 252. Its thermal properties ([10], [11], [12]) and kinetics of crystallization [13], [14], [15]) have already been studied in previous papers. All these data will be useful for comparison purpose with our results. Polymer is first placed inside the elastomer capsule. Before sealing the capsule, a K-type thermocouple (∅ = 80µm) is inserted at half thickness of the sample. The recorded temperature will be used to identify thermal conductivity by solving an inverse heat conduction problem. Figure 2 gathers temperature and volume evolutions of the sample during an experiment. It consists in melting the polymer at 210°C during several minutes to delete thermal history of the material. Then, the melted PP is cooled at a constant cooling rate of 10K/min down to 100°C. The sample is then maintained in isothermal condition during more than 1000s to complete the crystallization. Finally, the polymer is cooled again at a constant cooling rate to the ambient. During the first cooling, between 100s and 800s, the identification of thermal conductivity is performed in the amorphous state (λ_a). At 1000s the temperature increase recorded by the thermocouple located in the middle of the sample is due the heat released during the crystallization. At the same time a change in the slope of the thickness occurs. This volume variation allows the identification of the kinetic function (K_{Nak}). The second cooling step, from 2600s to 5000s leads to the identification of thermal conductivity in the semi-crystalline state (λ_{sc}).

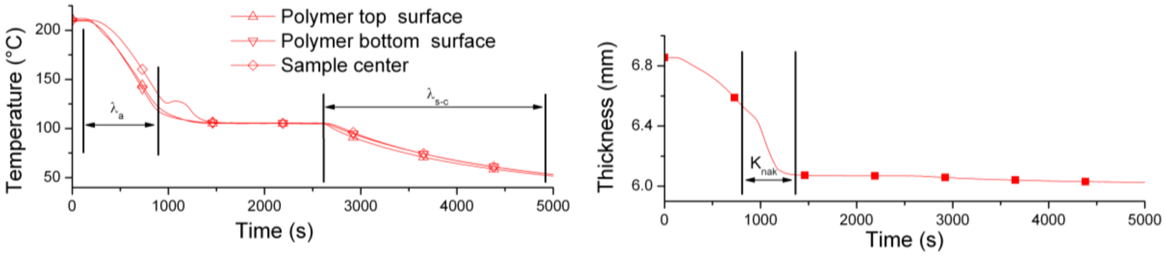

a b

Fig. 2: Recorded data: Temperature evolution (a); Thickness evolution (b)

Specific volume measurement

Specific volume of the polymer is directly obtained from an experiment that consists in melting the polymer at 210°C and cooling it down to the ambient while keeping a constant pressure. A cooling rate of 1K/min is imposed to the sample to minimize the thermal gradient within its thickness. Evolution of the specific volume (P=5MPa in the moulding cavity) is plotted in figure 3.

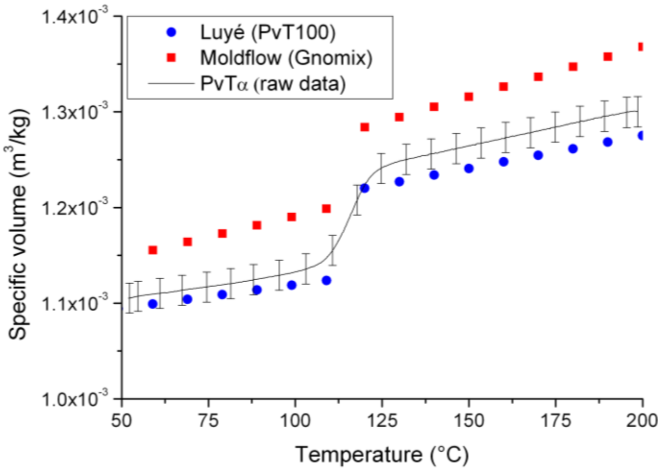

Fig. 3: PvT diagram of HV252 polypropylene at 5 MPa

Experimental data recorded by Luyé *et al* [12] and those provided by Moldflow© database are also superimposed in this figure. Values given by Luyé [12] are very close to PVTα measurements (about 1% difference) in both states. Deviations with Moldflow© values are larger with a gap that does not exceed 5%. The slopes of specific volume obtained by Luyé and those given by the PvTα are very close whereas those of Moldflow measurements are slightly larger. The total shrinkages due to the crystallization are quasi-identical for Luyé's and the PvTα results. Unlike specific volume determined by PvTα device, these curves, issued from literature, are extrapolated to 5MPa from measurements conducted under high pressure.

Thermal conductivity identification

The thermal conductivity is identified outside the crystallization zone as shown in figure 2. The inverse method used in this work has already been described by LeGoff *et al* [16]. The estimation consists in minimizing the least-square criterion (Eq.2) defined as the difference between the measured temperature (T_{exp}) in the centre of the sample and the calculated one (T_{num}) through the solving of the heat conduction equations (Eq 1a,1d-1f).

$$J(\bar{\boldsymbol{\lambda}}) = \frac{1}{2}\sum_{k=1}^{N_k}\left[T_{num}\left(t^k,\bar{\boldsymbol{\lambda}}\right) - T_{\exp}(t^k)\right]^2 \qquad (2)$$

With $\bar{\boldsymbol{\lambda}} = \left[\lambda_1,...,\lambda_j,...,\lambda_{JM}\right]^T$ a vector associated to an *a priori* given temperature table **T** $= \left[T_1,...,T_j,...,T_{JM}\right]^T$. A classical conjugate gradient algorithm coupled with a set of adjoint equations [4] is used to minimize the functional.

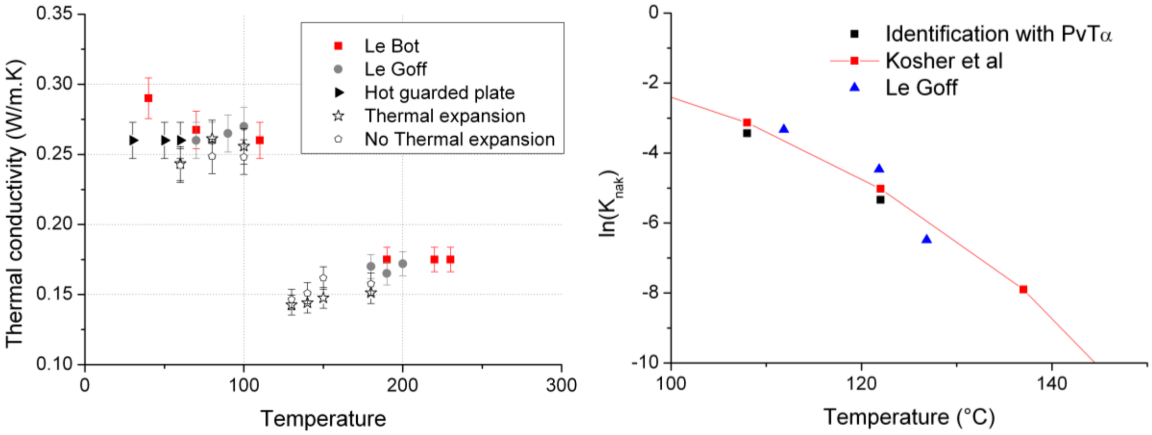

Fig. 4: a) Thermal conductivity of polypropylene HV252 and b) Kinetic function identified versus temperature (°C)

Figure 4a gathers values of thermal conductivity identified with the PvTα device. Two experiments with different sample were carried out. Results show a very good reproducibility. The values plotted in the figure correspond to the average values of both measurements. In this figure we also reported results obtained by Le Bot [11], Le Goff [17] and with hot guarded plate. The results are consistent, even if we observe some small deviation between values. In the melted state, the scattering remains small and our results are rather similar to previous studies. Moreover, we also observe a difference between thermal conductivity results when the variation of specific volume with temperature is taken into account ("thermal expansion" points) or not ("no thermal expansion" points). Let us note that as expected, thermal conductivity is overestimated when thermal shrinkage is not taken into account.

Crystallization kinetics identification

The kinetic function $K_{Nak}(T)$ can be determined by solving heat conduction problem (Eq. 1a, 1c-1f) coupled to crystallization kinetics model (Eq. 1b). The proposed methodology aims to minimize the difference between the experimental thickness (E_{exp}) and the computed one (E_{num}). The least-square criterion to be minimized, takes the form of Eq. (3):

$$J_2(\overline{\mathbf{K_{Nak}}}) = \frac{1}{2}\sum_{k=1}^{M_k}\left[E_{num}\left(t^k,\overline{\mathbf{K}}\right) - E_{\exp}(t^k)\right]^2 \tag{3}$$

With $\overline{\mathbf{K_{Nak}}} = \left[K_1,...,K_j,...,K_{JP}\right]^T$ a vector associated to an *a priori* given temperature table $\mathbf{T} = \left[T_1,...,T_j,...,T_{JP}\right]^T$. The same algorithm is used as for thermal conductivity to minimize J_2. This method is then non intrusive, no sensor inside the sample being necessary contrary to the classical method based on temperature measurement inside the sample [16]. In the proposed experiment, only two values have been identified, $K(128°C)$ and $K(108°C)$. Figure 4b presents identified parameters and kinetic function determined by Kosher [15] from DSC analysis. Le Goff *et al* [14] confirmed these values in a previous paper by using an inverse method based on temperature criterion. Deviation between bibliographic values and ours is small.

CHARACTERIZATION OF THERMOSET

Material and experimental protocol

Vinylester resin (DERAKANE MOMENTUM 411-350 epoxy vinyl ester) was used with 0.05wt% of initiator (Cobalt Naphthenate) and 1wt% of Catalyst (NOROX MEKP-925H Methylethylketone peroxide (MEKP)). These proportions were selected to get maximum gel time at room temperature (30 ± 10 min at 25°C). Unidirectional glass fibre having surface density of 300 g/m² was used as reinforcement [0/90] in composite. Two fibre volume fractions (32vol% and 49vol%) were selected to study the effect of fibre fraction on shrinkage. The following thermal cycle was used for the curing of samples in PVT-α mould at the pressure of 0.65MPa.

1. Maintaining the system at room temperature for 2 min.
2. Heating to 180°C at rate of 4°C/min and maintaining for 10min at that temperature.
3. Cooling to room temperature at 4°C/min.

Determination of CTE and CCS

In this part, we focus on the determination of the coefficients of thermal expansion (CTE) and of chemical shrinkage (CCS). These coefficients are determined by the evolution of the thickness variation of the resin during the thermal cycle [18]. This evolution and the associated heat flux data are presented in figure 5 during the heating (A→D) and cooling stages (D→F) of neat resin. A baseline was performed and substracted. The resulting heat flux corresponds only to the heat released by the crosslinking during the heating stage. Linear A-B part of thickness curve represents the thermal expansion of neat resin as reaction did not start yet. In the region between the points B and C, the chemical shrinkage of resin also appears in addition to thermal expansion and tends to decrease the sample thickness up to the point C where the resin is close to be fully cured. After the point C the only prominent effect is again thermal expansion so a linear behaviour of the displacement curve is observed between points C and D. During cooling step, the thickness curve is superimposed between C and D with the one plotted during the heating step. It implies that the thermal contraction coefficient is equal to the expansion coefficient. Then, between points C and E, the resin goes through the glass transition from the rubbery to glassy state as the curve slope changes. The difference between points A and F gives the total shrinkage of material at room temperature after curing and cooling. It is found that the global shrinkage for the resin is -2.1 vol%. The volume variation of an elementary volume mesh dV_i can be expressed by:

$$dV_i(T,\alpha)=dV_{0i}(1+CTE(T,\alpha).\Delta T+CCS.\Delta\alpha) \tag{4}$$

With dV_{0i} the initial volume, ΔT and $\Delta\alpha$ the variations between two timesteps. Assuming the cure shrinkage is a linear function of 'α' in each mesh for the neat resin and composite samples, we define a coefficient of chemical shrinkage (CCS) to describe this linear relationship. In order to get a value of thermal expansion coefficient CTE at each time step in region B-C, a mixing law (1) can be used:

$$CTE(\alpha) = CTE_{uncured}.(1-\alpha) + \alpha.\ CTE_{rubbery\_cured} \tag{5}$$

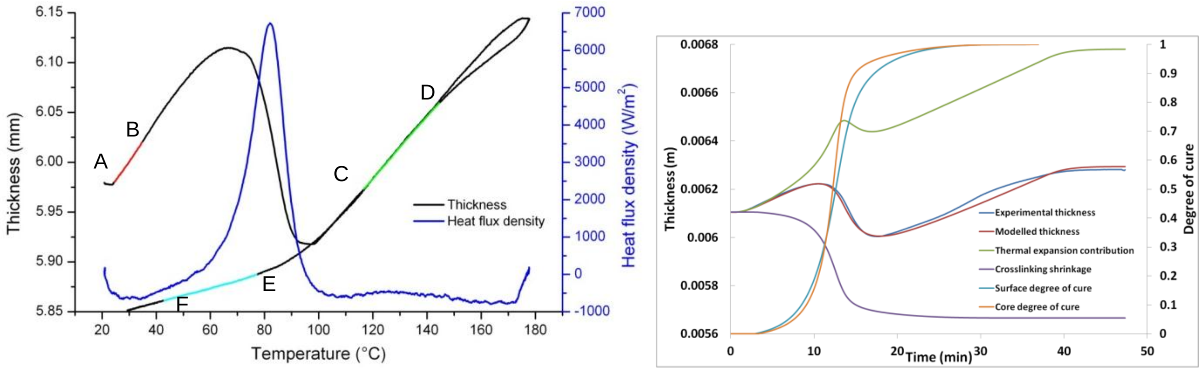

a b

Fig. 5. Evolution of measured (5a) and identified (5b) thickness variations

The coefficients CTE and CCS are determined by minimizing the gap between experimental and numerical (Eq set 1) thicknesses. By iterative calculation, thickness of each mesh is calculated according to its temperature and degree of cure and then added to get final thickness at each time step. Volume CTE are estimated outside the crosslinking zone in a consecutive way; from A to B for the uncured state (CTE = $6.37.10^{-4}$ K^{-1}), then from C to D for the rubbery cured state (CTE=$5.33.10^{-4}K^{-1}$) and finally from E to F for the glassy cured state (CTE= $1.24.10^{-4}$ K^{-1}).

When CTE are known, it becomes possible to estimate CCS. It is determined in Eq. 4 to fit experimental thickness with numerical one by solving the set of Eq 1. In figure 6 the experimental displacement curve and the modelled one for the neat resin are plotted, after identification of CCS. Thermal expansion contribution curve represents the thickness of sample with thermal expansion. Chemical shrinkage curve corresponds to the thickness evolution induced by resin crosslinking. From our calculations, the rapid kinetics leads a temperature increase between the surface and the core of the sample which can reach about 20°C and justify our approach. This result explains the peak observed on the "thermal expansion contribution" curve. Indeed, it also induces a gradient of the degree of cure (up to 0.15 between the surface and the core) since this parameter is strongly coupled to temperature field. Finally, the modelled curve superimposes very well the experimental thickness curve and validates the linear model to describe the resin cure shrinkage. The value of computed volume shrinkage for resin was found equal to -7.14vol%. The composite experiments were also treated in the same way. From the identified CCS values, the volume shrinkage induced by the crosslinking is equal to -4.40% for the composite with 32vol% of fibres and -2.76% for that containing 49vol% of fibres. The lower volume fraction of resin in composite samples leads to lower temperature and degree of cure gradients, as expected. The proposed shrinkage model, coupled to thermal effects can thus be used to simulate dilatometric behaviour of both resin and associated composites.

CONCLUSIONS

In the present work, a multifunctional mould PVT-α is used to characterize specific volumes, thermal conductivities, phase change kinetics, as well as shrinkage coefficients on neat thermosetting resin or thermoplastic polymer as well as on composites. This home-built apparatus is able to impose and quantify 1D heat transfer through the thickness of a bulk sample while controlling the applied pressure and measuring the volume variations. The associated moving boundary model takes into account the temperature and conversion degree gradients. Specific volume, thermal conductivity and crystallization kinetics were determined for a thermoplastic polymer. Comparison with literature shows very good agreement. Coefficients of thermal expansion and chemical shrinkage were determined for a thermosetting resin and for composites with two different fibre volume fractions. A linear behaviour was assumed for chemical shrinkage. The final chemical shrinkage value is found to be equal to -7.1vol% for the neat resin and decreases for the composites as expected. A new mould is currently under design to increase the temperature level, the applied pressure and the cooling rate to be representative of process conditions met with new materials.

REFERENCES

[1] Li C, Potter K, Wisnom MR, Stringer G. In-situ measurement of chemical shrinkage of MY750 epoxy resin by a novel gravimetric method. Composites Science and Technology. 2004;64(1):55-64.
[2] Shah DU, Schubel PJ. Evaluation of cure shrinkage measurement techniques for thermosetting resins. Polymer Testing.29(6):629-39.
[3] Schoch KF, Panackal PA, Frank PP. Real-time measurement of resin shrinkage during cure. Thermochimica Acta. 2004;417(1):115-8.
[4] Y. Jarny, “The adjoint method to compute the numerical solutions of inverse problems,” in Inverse Engineering handbook, K.A. Woodb., 2003.
[5] J. V. Beck, B. Blackwell, C. R. S. J. Clair, Inverse heat conduction III-Posed Problems, Wiley-Inte. 1985.
[6] X. Aduriz et al., “Quantitative control of RTM6 epoxy resin polymerisation by optical index determination,” Composites Science and Technology, vol. 67, no. 15-16, pp. 3196-3201, Dec. 2007.
[7] K.Nakamura, T. Watanabe, K.Katayama, and T.Amano, “Some aspect of non-isothermal crystallization of polymers I,” Journal of Applied Polymer Science, vol. 16, pp. 1077-1091, 1972.
[8] K.Nakamura, T.Amano, and K.Katayama, “Some aspects of nonisothermal crystallization of polymers II,” Journal of Applied Polymer Science, vol. 17, pp. 1031-1041, 1973.
[9] J-L. Bailleul, V. Sobotka, D. Delaunay, Y. Jarny. “Inverse algorithm for optimal processing of composite materials.” Composite Part A, 2003, 34 : 695-708.

[10] R. Le Goff, D. Delaunay, N. Boyard, Y. Jarny, T. Jurkowski, and R. Deterre, "On-line temperature measurements for polymer thermal conductivity estimation under injection molding conditions," International Journal of Heat and Mass Transfer, vol. 52, no. 5-6, pp. 1443-1450, 2009.

[11] P. Le Bot, "Comportement thermique des semi-cristallins injectés. Application à la prédiction des retraits," Nantes University, 1998.

[12] J.-F. Luyé, G. Régnier, P. Le Bot, D. Delaunay, and R. Fulchiron, "PVT measurement methodology for semicrystalline polymers to simulate injection-molding process," Journal of Applied Polymer Science, vol. 36, no. 2, pp. 302-311, Jan. 2000.

[13] R. Fulchiron, E. Koscher, G. Poutot, D. Delaunay, and G. Régnier, "Analysis of the Pressure Effect on the Crystallization Kinetics of Polypropylene: Dilatometric Measurements and Thermal Gradient Modeling," Journal of Macromolecular Science, Part B, vol. 40, no. 3, pp. 297-314, May 2001.

[14] R. Le Goff, G. Poutot, D. Delaunay, R. Fulchiron, and E. Kosher, "Study and modeling of heat transfer during the solidification of semi-crystalline polymers," International Journal of Heat and Mass Transfer, vol. 48, pp. 5417-5430, 2005.

[15] E. Koscher, "Effet du cisaillement sur la cristallisation du polypropylène HV252: aspects cinétiques et morphologiques," Université Claude Bernard - Lyon I, 2001.

[16] R. Le Goff, N. Boyard, V. Sobotka, N. Lefèvre, and D. Delaunay, "Inverse estimation of the crystallization kinetic function of semi-crystalline polymers and short fibre reinforced composites in moderate cooling conditions," Polymer Testing, vol. 30, no. 6, pp. 678-687, Sep. 2011.

[17] R. Le Goff, D. Delaunay, N. Boyard, Y. Jarny, T. Jurkowski, R. Deterre, "On-line temperature measurements for polymer thermal conductivity estimation under injection molding conditions," International Journal of Heat and Mass Transfer, vol. 52, no. 5-6, pp. 1443-1450, 2009.

[18] Y.Nawab, N. Boyard, V. Sobotka, P. Casari, F.Jaquemin, "Measurement and modelling of chemical shrinkage of thermoset Composites", Key Engineering Materials Vols. 504-506 (2012) pp 1129-1134

USING OPTICAL FIBRE-BASED SENSORS TO CHARACTERIZE RESIN FLOW AND MECHANICAL PROPERTIES IN LCM PROCESSES

Marc Waris, Pierre-Jacques Liotier and Sylvain Drapier

Département Mécanique et procédés d'élaboration, LCG UMR 5146, Ecole Nationale Supérieure des Mines de Saint-Étienne, Saint-Étienne.
Corresponding author's e-mail: drapier@emse.fr

ABSTRACT: This contribution aims at setting up physical solutions to track resin flow and conversion in LCM processes. We have demonstrated previously that thermocouples, along with optical fiber sensor (OFS), can be successfully employed to track resin flow front (Peng et al., J. Comp. Mat. 2010 and 2011). Also, in the case of simple plate geometries, distributed optical methods have proved to be efficient to assess the impregnation scenario of resin infusion (Peng et al., Composites/A 2010). Since then OFS such as Fiber Bragg Grating (FBG) and etched optical fiber sensor were developed and adapted to RTM processing. More precisely, OFS were embedded inside the preform, with an accurate placement in order to reduce the intrusiveness of the sensor. Moreover an efficient sealing with the mold cavity was achieved thanks to feedthrough systems. Specific cases were designed in order to study common issues faced by composites manufacturers, such as realizing thick composites parts or coping with "ply-drops" during the filling stage. OFS have shown great potential to monitor physical parameters such as temperature, degree of cure, and strain inside the part during the process. Responses provided by the sensors were compared to numerical simulation with the aim of having a better understanding of the phenomena occurring during the process. Finally a smart tooling concept was tested with OFS integrated inside composite tools. This concept has demonstrated some potential in monitoring RTM process without any perturbations of the sensors inside the part. This concept will be extended to two industrial applications.

KEYWORDS: *Liquid Composite Molding process (LCM), Process monitoring, Manufacturing process modeling, Optical fiber sensor (OFS), Composite mold.*

INTRODUCTION

In the process of mass reduction, such as met in aeronautics, the main challenge is manufacturing complex parts made out of composite materials with a high level of complexity, as for example shape geometry complexity or use of complex reinforcement (3D preform). Liquid composite molding (LCM) processes based on liquid resin infusion (Liquid Resin Infusion - LRI) or injection (Resin Transfer Molding - RTM) provide ideal responses in terms of cost reductions as well as mechanical performances of the final parts. Nevertheless, a proper characterization of the physical parameters of each component (matrix and reinforcement) and their change during the process must be proposed. Indeed, during the filling stage of LCM processes, uncertainties associated with the material parameters (permeability, resin viscosity) can affect the flow front, and result in the formation of dry spots. Then, during the curing stage, the shrinkage of the resin and the associated thermal contraction can lead to the formation of residual stresses. If the curing cycle is not properly tuned, residual stresses can alter the final mechanical performance, and sometimes create dimensional distortions.

In this paper we propose to study the process through both physical and numerical models of the process. This involves monitoring in real time with specific sensors and the development of numerical tools to predict the influence of input parameters on the quality of the final part. The comparison between the experimental measurements and data from the numerical tools provides relevant information to validate or to refine the models. A dedicated LCM demonstrator has been developed which allows us to manufacture composite part with a specific instrumentation system. This system is based on the technology of optical fiber sensors (OFS), very useful to monitor the physical parameters of composite part. In the case of the process they enable to measure the influence of input process parameter to the quality of the final part. They have been widely used for the monitoring of the resin behavior during the curing cycle [1], for the monitoring of physical parameters during the autoclave process [2], and recently for the monitoring of LCM process [3]. They have also demonstrated a good ability to monitor some process parameters like flow front resin, degree of cure and the mechanical state inside the part during each phase of the process.

The instrumentation is first applied to a LRI test-case in order to validate the flow modeling during the filling stage. Secondly, the instrumentation is extended to the monitoring of the Resin Transfer Molding (RTM), for the filling and the curing stages. Also a specific geometry is designed in order to study common issues faced by composites manufacturers, such as realizing thick composites parts or working out with “ply-drops” during the filling stage.

OPTICAL FIBER SENSORS (OFS)

OFS are suitable solution for monitoring composite material process, they give access to the physical parameters of interest with a low intrusiveness (125 µm in diameter). For example it is possible to increase the number of local measures along the same optical fiber (distributed measures), without introducing any new sensor inside the material. During this study we have developed two kinds of OFS. An etched fiber sensor was developed for the monitoring of the flow front and Fiber Bragg Grating for the monitoring of the mechanical state inside the part during the process.

Etched fiber sensor

This sensor provides useful information about the presence of the resin in specific location of the part. We can access the flow front propagation during the filling stage by extending the number of optical fiber output.

This sensor is based on the Fresnel reflection principle prevailing at the end of the optical fiber. A laser light source is injected on one end of the optical fiber, a small part of the incident light is reflected at the interface of the output fiber. The reflected light intensity is captured by a coupler 50/50 and a photodiode. This signal intensity is proportional to the Fresnel reflection coefficient which depends mainly on the refraction index of the environment. Therefore when the resin reaches the area close to the end of the optical fiber the refraction index changes from the air refraction index to the one of the resin.

Fig. 1 shows the responses of an OFS during the filling stage of the LRI process. One can notice a sudden drop of the optical signal when the resin approaches to the sensor and 15 s later a quick stabilization of the signal indicating that the sensor area is saturated by the resin. In the present case, a type K thermo-couple was placed close to the optical fiber to verify the detection capability by correlating both responses (resin temperature is fed in at 80°C while perform temperature is 120°C). The main advantage of the fiber sensor is that the signal is not affected by the thermal behavior of the materials, as measured made by thermocouple.

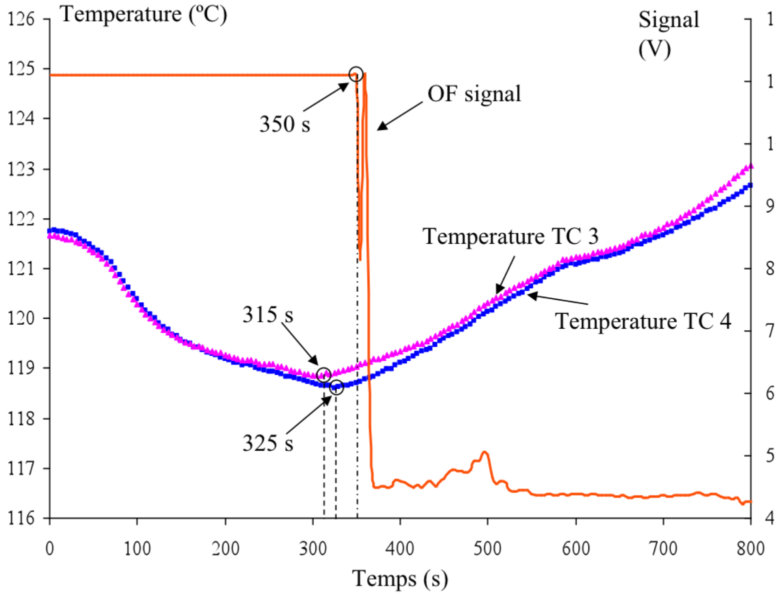

Fig. 1: Comparison between OFS and Thermocouple responses during the filling stage [5]

Fiber Bragg Grating (FBG)

This sensor allows to assess the internal mechanical state of composite parts. Residual strain and exothermic phenomena can then be monitored in thick composite parts. FBG usually consists in a periodic variation of the core refractive index along the optical fiber. The response of FBG to an incident broadband light source is a unique preferential wavelength which is called the Bragg's wavelength λ_B. The variation of λ_B depends on the FBG longitudinal strain and its temperature through a linear relationship:

$$\frac{\Delta\lambda_B}{\lambda_B} = K_T \cdot \Delta T + K_\varepsilon \cdot \Delta\varepsilon \qquad (1)$$

Therefore temperature and strain inside the composite material can be measured. The main challenge in using FBG for composite applications is the discrimination between strain and temperature, because the two of them are interacting. We have worked here on the dual Bragg Grating method with different types of FBGs, FBG type IA and type IIA. Despite good initial results showed by Shu et al. [4], this strategy seems difficult to apply to processes. Actually FBG Type IA and IIA appear to have a nonlinear behavior with temperature, this induces large errors in the discrimination operation. As a result, the discrimination was done with a temperature compensation measured by thermocouple.

Another challenge is the sensitivity of the FBG to the transverse loads. In fact transverse loads can strongly affect the spectral response of the FBG. It is thus difficult to assess an accurate value of the strain state. The solution is to get benefits of this complexity with thermo-mechanical analysis to capture the 3D mechanical state around the sensor. One application is the assessment of the residual stresses after the cooling stage.

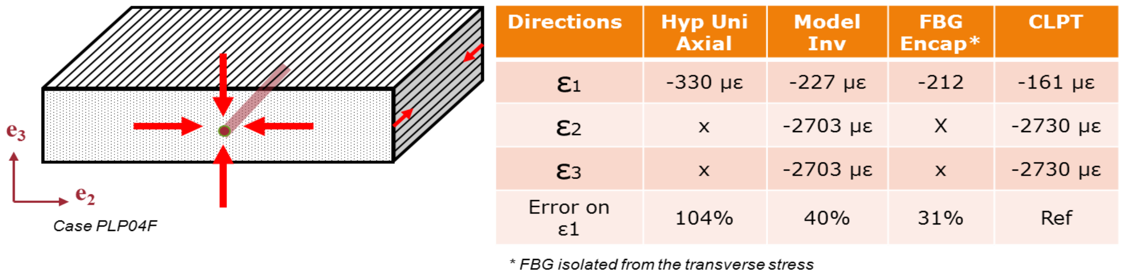

Directions	Hyp Uni Axial	Model Inv	FBG Encap*	CLPT
ε1	-330 με	-227 με	-212	-161 με
ε2	x	-2703 με	X	-2730 με
ε3	x	-2703 με	x	-2730 με
Error on ε1	104%	40%	31%	Ref

* *FBG isolated from the transverse stress*

Fig. 2: Example of the model application for the assessment of the residual strain during the cooling stage

Fig. 2 shows the analysis of the residual strain for the case of a plate made of carbon/epoxy with a unidirectional reinforcement. We can notice that taking the assumption of uni-axial stress state allows to have a quick result but with large error compared to the result coming from the classical laminate plate theory (CLPT). Hence, using results from FBG as input data is more accurate and allows achieving a more realistic assessment of the 3-dimensional residual strain state.

CASE STUDY OF LIQUID RESIN INFUSION (LRI) PROCESS MONITORING

Material and experimental set up

Experiments were conducted on a 24 plies composite preform with a $[0_6/90_6]_s$ stacking, made up of ‘‘UD fabric” (reference G1157 E01) produced by Hexcel Corp. These carbon fabrics are plain weave with 96% of weight in the warp direction and 4% of weight in the weft direction. The preform dimensions are 335 x 335 x 20 $mm^{3.}$ For the resin, the experimental LRI tests have been performed using an epoxy resin (HexFlow© RTM-6). Before injection, the resin is pre-heated at 80 °C in a heating chamber. The preform is heated at 120°C by a heating plate located below the semi-rigid mold. As for the external pressure prescribed over the stacking, it is uniform and equal to the local atmospheric pressure, induced by the vacuum ensured in the sealed system.

Flow monitoring

The purpose is to detect the resin flow by monitoring both temperature variation with thermocouples and refractive index of the OF sensors within the preform. The assumption of a purely transverse flow in well implemented LRI processes has been verified in previous works [5]. The purpose is thus to detect the resin flow through the thickness of the preform in order to estimate its filling time. These experimental results are presented in Fig. 4.

Discussions

Experimental results have been successfully compared to those obtained by a numerical model developed in our institution and now under industrial development by ESI Group [6]. This model is based on the coupling of Stokes equations, governing the behavior of the liquid region, and a Darcy's law, that rules the fibrous preform regions. To couple these two behaviors in a highly compressible preform, a modified Beaver–Saffman–Joseph condition has been included in an ALE formulation.

Fig. 3 shows a very good correlation between experimental measurements and numerical model predictions accounting for the process conditions. Those results thus tend to validate the LRI model, and it can be especially noticed that permeability must depend on porosity changes for the filling times to be properly predicted. It is one of the motivations of the proposed global framework of modelisation [6].

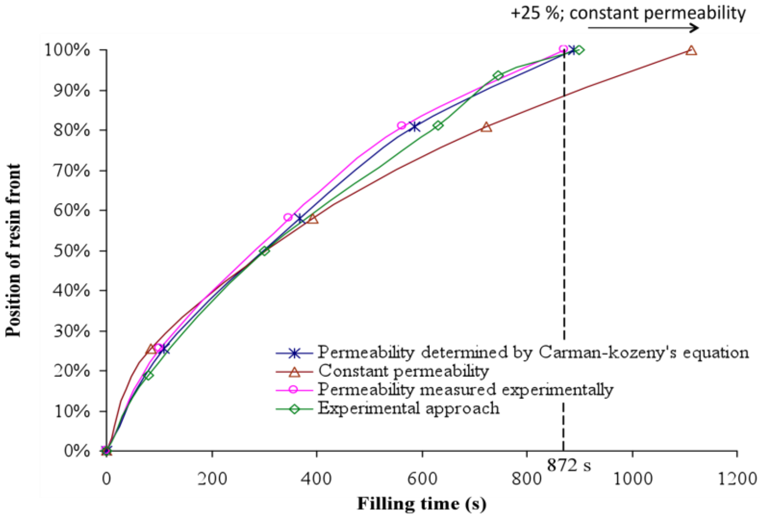

Fig. 3 Correlation between experimental and numerical results on a LRI process

CASE STUDY OF RESIN TRANSFER MOLDING (RTM) PROCESS MONITORING

Material and experimental set up

The preform here is composed of 7 Unidirectional carbon layers with the following sequence $[90_2, 0_3, 90_2]$. The size of the final plate is 430 x 430 x 4 mm^3.

The RTM6® resin is preheated at 80°C and injected with a constant rate inside the aluminum mold. The filling stage takes about 10 min. Then the cure cycle recommended by the supplier is applied to the mold to consolidate the material. The main process steps are:

- preforming and debulking of preform under vacuum (1);
- injection of resin through the preform inside the mold at 120°C (2);
- curing at 180°C during 90 min (3);
- cooling at room temperature (4).

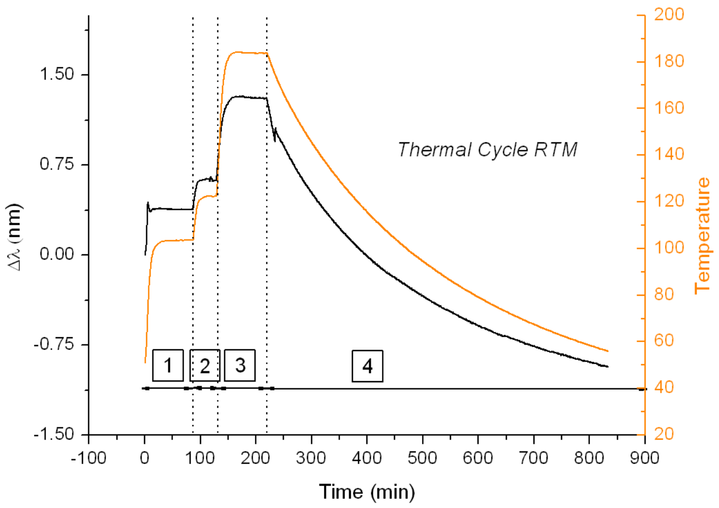

Fig. 4 Temperature and strain measurement during RTM process

Fig.4 shows the change in the Bragg's wavelength of the FBG embedded at the center of the composite material during the entire process. It is worth noting that the largest variation of the Bragg's wavelength, corresponding to the appearance of residual strains, occurs during the cooling stage

Embedded sensors

Optical fiber with FBG is embedded in the central part of the preform. A thermocouple is located near the FBG to achieve the temperature compensation. FBG is used to monitor the change of the strain inside the part, especially for the assessment of the residual strains. Besides, there are three OFSs based to the Fresnel reflexion embedded along the preform to monitor the flow front evolution.

Flow monitoring

The time corresponding to the OFS optical signal drops was recorded during the filling stage. Fig. 5 shows the comparison of the filling time between the experimental measures and the simulation. The simulation of the filling stage was computed Pam RTM software commercialized by ESI. We can notice a good correlation for this case, that demonstrates the capabilities of OFS to monitor the resin flow during the RTM process.

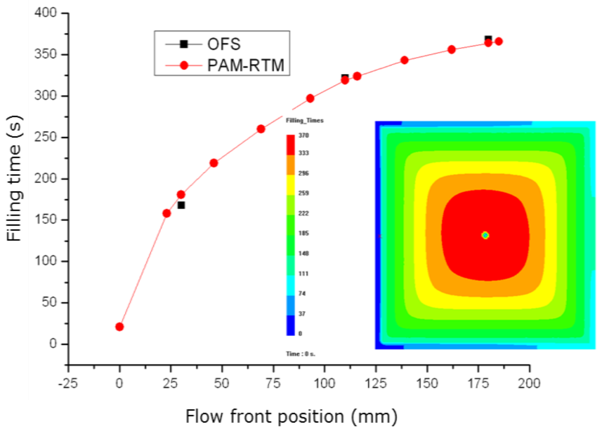

Fig. 5: Comparison between the experimental measures and the Pam RTM simulation

Assessment of residual strains

Residual strains during the cooling stage were compared with the Classical Laminate Plate Theory (CLTP). Table 1 illustrates the results. Although the experimental results in direction 2 may be questionable, results in direction 1 and 3 are in very good agreement with the CLPT. This demonstrates the potential of FBG to assess residual strains.

Table 1 Comparison of the residual strains with CLPT – system axes showed in Fig. 3.

Directions	Model Inv	CLPT
$\mathbf{e}_1$	-680 με	-600 με
$\mathbf{e}_2$	-940 με	-470 με
$\mathbf{e}_3$	-4770 με	-4990 με

Influence of the tool-part interaction

RTM composite mold made with the HexTool material was tested in order to compare with aluminum mold. A carbon/epoxy plate was manufactured with an asymmetric layup to demonstrate the minimization of residual stresses by using a composite mold. The first results prove that both residual strains measured by FBG and the final curvature of the plate (Fig. 6), are reduced with the HexTool mold. The part seems to be less constrained during the cooling stage, certainly because the thermal responses of both part and composite mold are very close.

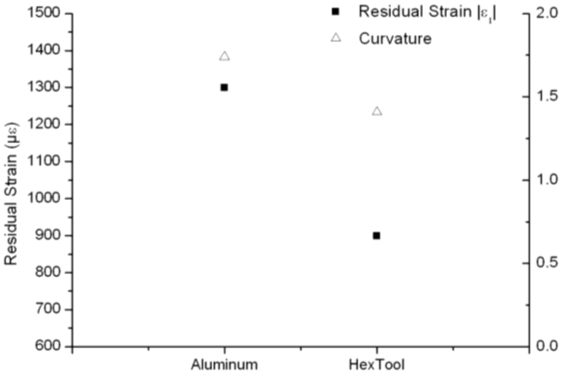

Fig. 6 Comparison of residual strain and curvature with the mold material

CONCLUSIONS

This study demonstrates the capabilities of the optical fiber sensors to monitor the main stages of LCM process. OFS do provide important information, in real time, about the flow and the mechanical state inside the material during the process. Nevertheless data treatment from OFS is rather difficult. The assessment of residual strains must be post-treated with a model to take into account the transverse effects which occurs during the cooling stage. Considering flat parts manufactured by infusion (LRI) and injection (RTM), good correlation between experimental data and simulations have been shown. In this study, the models used in the simulation of the LCM processes describe quite well the phenomena which take place during the process. However the comparison with the models was made for simple cases. Further investigations are required to verify the validity of the model in more severe conditions.

Besides, a first prototype with RTM composite mold was tested. A comparative study with aluminum mold demonstrated the potential of composite materials as HexTool for the reduction of residual stresses, caused by mold/preform interactions. This instrumentation method will be extended to the case of the manufacturing of complex parts.

ACKNOWLEDGEMENTS: This work was supported by the project LCM Smart, managed by Hexcel Company. The authors would like to acknowledge the support of all partners.

REFERENCES

1. V. Antonucci, M. Giordano, A. Cusano, J. Nasser, and L. Nicolais. Real time monitoring of cure and gelification of a thermoset matrix. *Manufacturing, Processing and Characterisations of Polymer Composites*, 66(16):3273–3280, janvier 2006.

2. George M. Maistros and Ivana K. Partridge. Monitoring autoclave cure in commercial carbon fibre/epoxy composites. *Composites Part B: Engineering*, 29(3):245–250, 1998.

3. L. Khoun, R. de Oliviera, V. Michaud, and P. Hubert. Measurement of process-induced strains by fibre bragg grating optical sensor in resin transfer moulding. *In ICCM* 17, 2009.

4. X. W. Shu, D. H. Zhao, L. Zhang, and I. Bennion. Use of dual-grating sensors formed by different types of fiber Bragg gratings for simultaneous temperature and strain measurements. *Applied Optics*, 43(10):2006–2012, 2004.

5. P. Wang. J. Molimard, S.Drapier, A.Vautrin, JC. Minni. Monitoring the resin infusion manufacturing process under industrial environment using distributed sensor. *Journal of composite materials*, 46(6):691-706, 2012.

6. P. Celle, S. Drapier, J.M. Bergheau. Numerical modelling of liquid infusion into fibrous media undergoing compaction. *European Journal of Mechanics A/Solids* 27 (2008) 647–661

CROSS-SECTIONAL MONITORING OF RESIN IMPREGNATION USING AN AREA-SENSOR ARRAY IN AN RTM PROCESS

Ryosuke Matsuzaki[1], Seiji Kobayashi [2], Akira Todoroki [2], and Yoshihiro Mizutani [2]

[1] *Tokyo University of Science, 2641 Yamazaki, Noda, Chiba, 278-8510 Japan.*
Corresponding author's e-mail: rmatsuza@rs.tus.ac.jp
[2] *Tokyo Institute of Technology, 2-12-1 Ookayama, Meguro, Tokyo, 152-8552 Japan.*

ABSTRACT: It is difficult to visualize the flow in the cross-section direction, and most conventional methods for monitoring resin flow are limited to the in-plane direction. This study investigates the monitoring of the cross-section of resin impregnation using an area-sensor array during a resin transfer molding (RTM) process. The area-sensor array is mounted on a thin polyimide film that is integrated with the inter-digital electrode array and associated wiring, and forms the bottom layer of the stacked composite laminates. Each area-sensor is square-shaped and measures the capacitance and electrical resistance of the sensor region. First, we constructed the equivalent electrical circuit model of in-plane and out-of-plane impregnation. The validity of the model was confirmed by comparison with the experimental results.

KEYWORDS: *Glass fibers, Electrical properties, Flow monitoring, Resin transfer molding (RTM).*

INTRODUCTION

Due to irregular resin flow caused by slight differences in the wrinkles of the vacuum bag or misalignment of the preform fabric during the vacuum-assisted resin transfer molding (VaRTM) process, an un-impregnated area called a dry spot sometimes occurs [1, 2]. When a distribution medium is used as a top layer to reduce the resin impregnation time, the impregnation does not have a uniform thickness. This may result in the occurrence of dry spots on the bottom layer. These dry spots can result in small voids that significantly degrade the mechanical properties of the structure [3-5].

In the present study, cross-sectional resin flow monitoring is proposed using an area-sensor array during the VaRTM process. We model an equivalent circuit model of the resin impregnation of the in-plane and out-of-plane (thickness direction) impregnation. The validity of the model is investigated by comparison with experimental results.

AREA-SENSOR ARRAY FOR MONITORING OF RESIN FLOW

A flexible substrate was used as a base for an area-sensor array to measure the resin flow front configuration. The pattern of electrodes and associated wiring made by photolithography is shown in Fig. 1. This work focused on non-conductive preforms such as GFRP. In case of conductive preforms like carbon fibers, spraying insulators such as silicon rubber on the sensor film is required. The configuration of the film was 200×200×0.013 mm^3. Because of its thinness, the sensor film was very flexible, and could easily be attached to complicated or curved molds [6]. Moreover, the film was stacked between the composite laminates and the mold. Consequently flow interference and decreased strength does not occur in the cured composites. The details of the in-plane monitoring using this sensor film are given in reference [7].

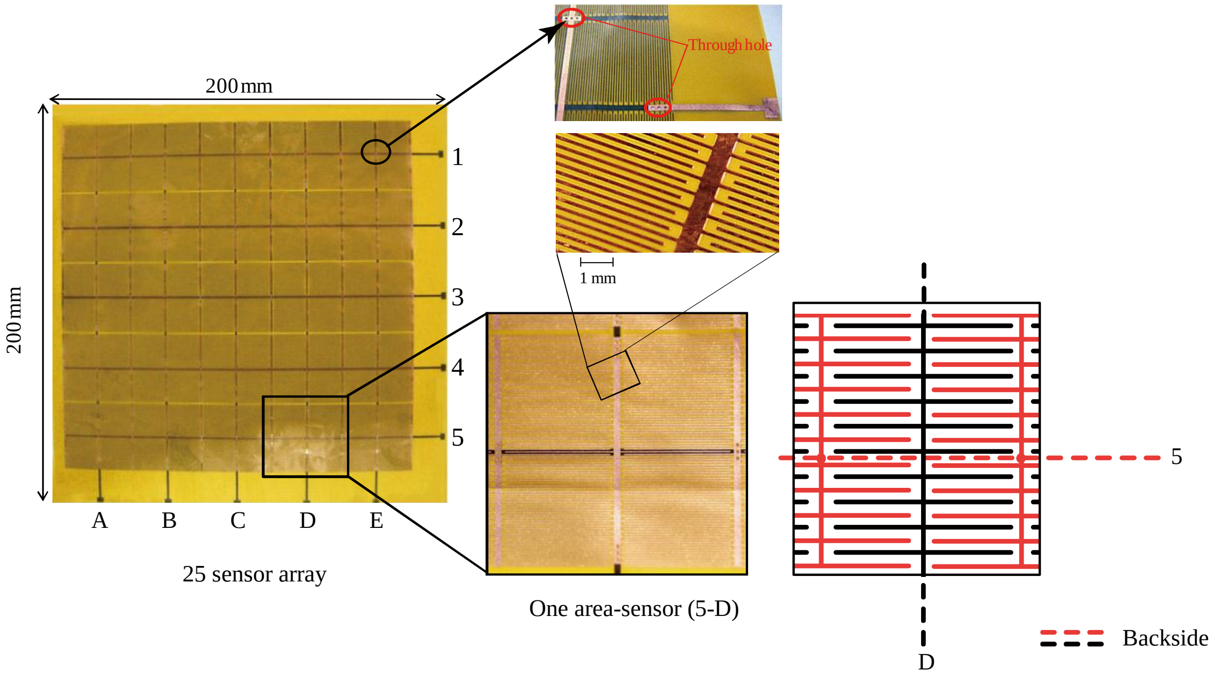

Fig. 1: Area-sensor array film for full field monitoring of resin flow.

ELECTRICAL PROPERTY CHANGE DUE TO IN-PLANE AND OUT-OF-PLANE IMPREGNATION

In-plane and out-of-plane impregnation

Figure 2 shows the two types of resin impregnation during the VaRTM process. In the case of thin laminates without a distribution medium, the dry fabrics are impregnated with resin from the side (in-plane impregnation), and the flow in the thickness direction is negligible as shown in Fig. 2 (i). In this case, the dry spot will penetrate in the thickness direction, and the precise flow front can be estimated using a sensor array film.

On the other hand, if a resin distribution medium is used to enhance the resin impregnation or in the case of through-thickness injection, the resin flows in the through-thickness direction (out-of-plane impregnation) exist as shown in Fig. 2 (ii), the dry spot does not penetrate in the thickness direction. To draw the precise dry spot configuration, the impregnated thickness must be estimated at each sensor. However, the method proposed in the previous study uses only the single parameter of impedance, thus it cannot identify the difference between in-plane and out-of-plane impregnation.

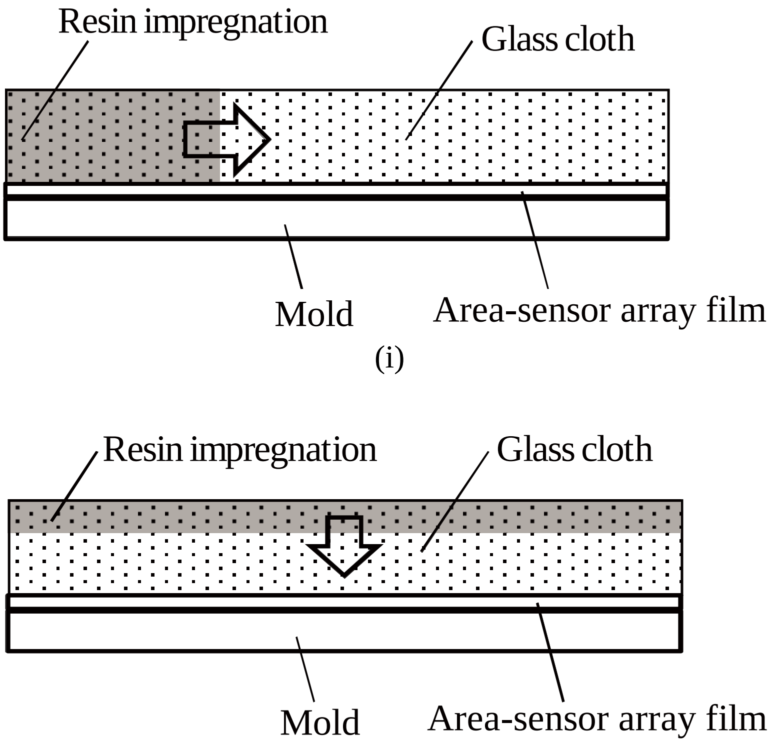

(i)

(ii)

Fig. 2: Resin impregnation during the RTM: (i) in-plane impregnation and (ii) out-of-plane impregnation.

Measurement of capacitance and electrical resistance

The electrical capacitance and resistance are measured when using glass cloth fabric impregnated with resin by in-plane or out-of-plane impregnation. The LCR meter (Hioki, 3532-50) is used for measuring the capacitance and electric resistance at 800 Hz. Figure 3 shows the experimental setup. One 35×35 mm^2 sensor is stacked on the acrylic plate. It should be noted that in the case of using a metallic mold, it is required to cover the electrode wires on the bottom surface of the sensor film with non-conductive thin layer. Eight layers of the 1K (1000 filaments/strand) glass fabric (Molymer SSP, YEM1801) are stacked on the sensor film, and an unsaturated polyester resin (DH material, Sundhoma PC-184-C) is impregnated. In the out-of-lane impregnation, the PVDC film (0.01 mm thickness) is inserted between the layers to separate the impregnated and un-impregnated layers. Electric capacitance and resistance are measured for four types of impregnated states: before impregnation, 1 layer impregnation, 7 layers impregnation, and full (8 layers, the thickness is about 2.0 mm) impregnation.

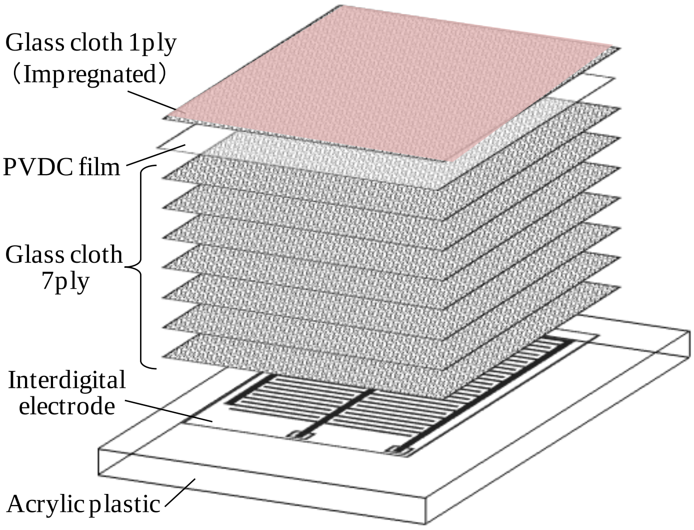

Fig. 3: Experimental setup for measuring the electrical resistance and capacitance for out-of-plane impregnation.

Experimental results and discussion

Figure 4 shows the electrical capacitance and resistance in the case of in-plane impregnation. The plots indicate the experimental capacitance and resistance change ratio $C_{\mathrm{exp}}/C_{\mathrm{exp\_0}}$ and $R_{\mathrm{exp}}/R_{\mathrm{exp\_0}}$ where $C_{\mathrm{exp\_0}}$ and $R_{\mathrm{exp\_0}}$ are the experimental initial capacitance and resistance before impregnation. The abscissa indicates the impregnated length divided by the sensor length: L=0 is the un-impregnated and L=1 is the fully impregnated state. The electric resistance decreases drastically when the resin touches a part of the inter-digital electrode, whereas the capacitance increase is almost proportional to the impregnated length L. This is because the resistivity ratio ρ_G/ρ_R is very high and the impregnated and un-impregnated glass fiber fabric can be modeled as a parallel circuit of electrical resistance. On the other hand, the permittivity ratio $\varepsilon_G/\varepsilon_R$ is not as high and a drastic change does not occur if the resin touches the electrode.

The plots in Fig. 5 show the experimental electrical capacitance and resistance in the case of out-of-plane impregnation from the top to the bottom layer. The abscissa indicates the impregnated thickness divided by the composite thickness: T=0 is un-impregnated and T=1 is the fully impregnated state. In the case of out-of-plane impregnation, the electrical resistance decreases and the capacitance increases gradually. The gradual decrease of the electrical resistance is derived from the series circuit model of electrical resistance of resin and glass fiber fabrics even when the resistivity ratio ρ_G/ρ_R is very high: one drastic electrical resistance decrease does not significantly affect the combined overall resistance.

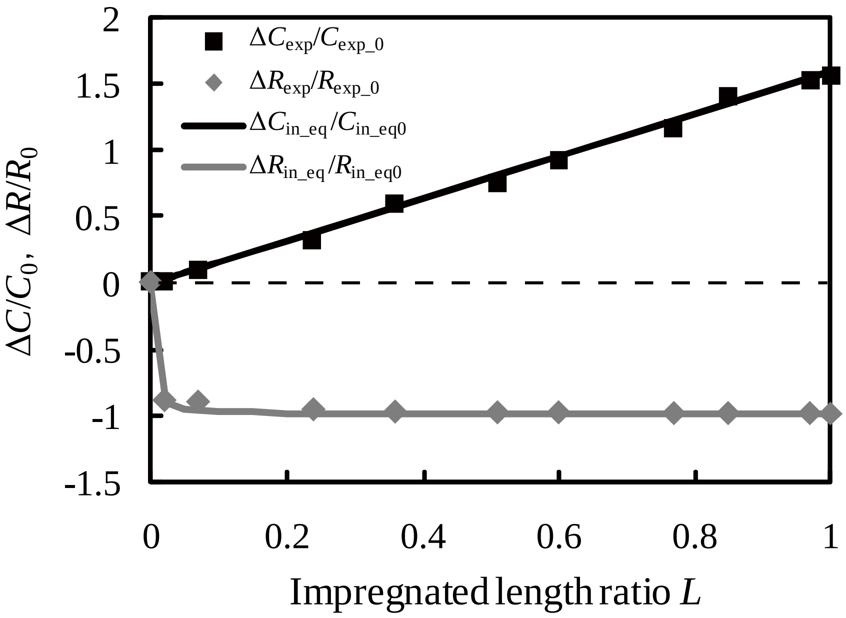

Fig. 4: Capacitance and resistance change ratio of experimental and calculated results using the equivalent circuit model during in-plane impregnation.

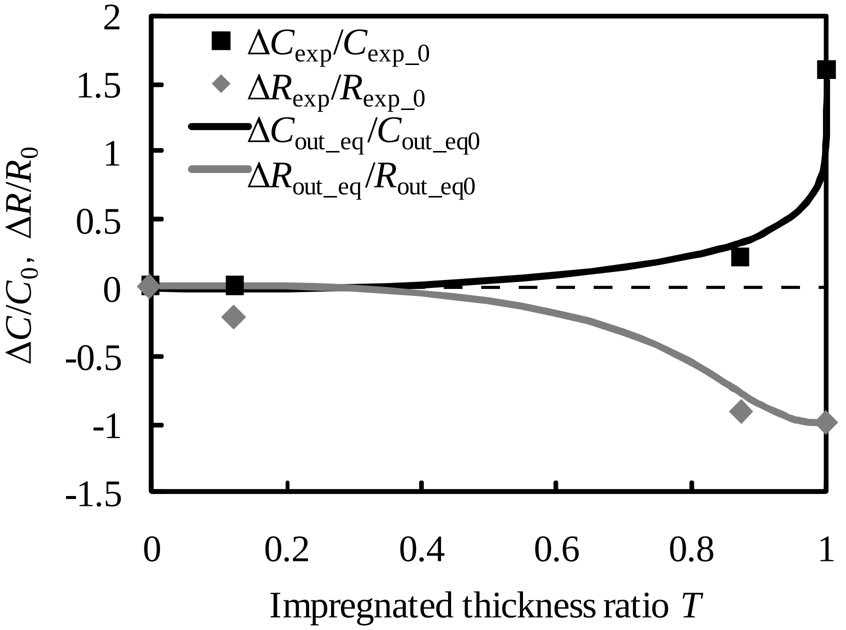

Fig. 5: Capacitance and resistance change ratio of experimental and calculated results using the equivalent circuit model during out-of-plane impregnation.

EQUIVALENT ELECTRICAL CIRCUIT MODEL

In-plane impregnation

By constructing equivalent circuit models when resin impregnating, the impregnated length *L* and thickness *T* can be monitored without preparing a data base of electric impedance and impregnated states. Figure 6 shows the equivalent circuit model in the case of in-plane impregnation. The impregnated and un-impregnated areas are modeled as a parallel circuit of capacitance and resistance. Let us consider the case where the impregnated length is *L* or the un-impregnated length is 1-*L*. Since the cross-section properties of the capacitance and resistance at the impregnated area change in proportion to the length *L*, the capacitance and resistance of the impregnated area, C_R and R_R, change in proportion and inverse proportion to the impregnated length *L*, respectively. Similarly, the capacitance and resistance of the un-impregnated area, C_G and R_G, change in proportion and inverse proportion to the un-impregnated length 1–*L*, respectively. Therefore, the capacitance and resistance of the impregnated area C_R and R_R and for the un-impregnated area C_G and R_G can be expressed as:

$$C_\mathrm{R} = \varepsilon_\mathrm{R} \frac{LS_\mathrm{R}}{l_\mathrm{R}}, \quad R_\mathrm{R} = \rho_\mathrm{R} \frac{l_\mathrm{R}}{LS_\mathrm{R}} \tag{1}$$

$$C_\mathrm{G} = \varepsilon_\mathrm{G} \frac{(1-L)S_\mathrm{G}}{l_\mathrm{G}}, \quad R_\mathrm{G} = \rho_\mathrm{G} \frac{l_\mathrm{G}}{(1-L)S_\mathrm{G}} \tag{2}$$

where l_R and S_R are the length and area parameters of the impregnated area while l_G and S_G are the length and area parameters of the un-impregnated area. It should be noted that the obtained capacitance and resistance are not the bulk resistivity and permittivity values of the dry or wet preforms.

Figure 4 also shows the theoretical values of the electrical capacitance and resistance when the in-plane impregnated length *L* changes. C_G and R_G were obtained using the capacitance $\varepsilon_\mathrm{G} S_\mathrm{G}/l_\mathrm{G}=2.6\times10^{-11}$ F and resistance $\rho_\mathrm{G} l_\mathrm{G}/S_\mathrm{G}=2.2\times10^{9}\ \Omega$ experimentally measured for the un-impregnated state (L=0) using the LCR meter. For C_R and R_R, the experimental values of the capacitance $\varepsilon_\mathrm{R} S_\mathrm{R}/l_\mathrm{R}=6.8\times10^{-11}$ F and resistance $\rho_\mathrm{R} l_\mathrm{R}/S_\mathrm{R}=5.2\times10^{6}\ \Omega$ at full impregnation (L=1) were used. As seen in Fig. 4, the theoretical values agree well with the experimental values; thus the validity of the equivalent model was confirmed.

Out-of-plane impregnation

Figure 7 shows the equivalent circuit model in the case of out-of-plane impregnation. The distance and area of the capacitor electrodes or resistor change with the impregnated thickness *T*. The capacitance and resistance C_1, R_1, C_2, R_2, C_3, R_3, C_4 and R_4 can be expressed as:

$$C_1 = \varepsilon_\mathrm{R} \frac{S'_R T}{\alpha L'_R}, \quad R_1 = \rho_R \frac{\alpha l'_R}{S'_R T} \tag{3}$$

$$C_2 = \varepsilon_\mathrm{R} \frac{S'_R}{l'_R T}, \quad R_2 = \rho_R \frac{l'_R T}{S'_R} \tag{4}$$

$$C_3 = \varepsilon_G \frac{S'_G(1-T)}{\beta l'_G}, \quad R_3 = \rho_G \frac{\beta l'_G}{S'_G(1-T)} \tag{5}$$

$$C_4 = \varepsilon_G \frac{S'_G}{l'_G(1-T)}, \quad R_4 = \rho_G \frac{l'_G(1-T)}{S'_G} \tag{6}$$

where L'_R and S'_R are the length and area parameters of the impregnated area, while L'_G and S'_G are the length and area parameters of the un-impregnated area. Here, α indicates the ratio of the length and area parameters of the out-of-plane area to that of the in-plane; β indicates the ratio of length and area parameters of the out-of-plane area to that of the in-plane.

The material parameters of α, β, $\varepsilon_R S'_R/l'_R$, $\rho_R\, l'_R/S'_R$, $\varepsilon_G S'_G/\, l'_G$, and $\rho_G\, l'_G/S'_G$ can be obtained by minimizing the residual sum of squares between the experimental values of $\Delta C_{exp}/C_{exp\_0}$ and $\Delta R_{exp}/R_{exp\_0}$ as

$$\text{minimize} \quad \sum\left[\left\{\left(\frac{\Delta C_{exp}}{C_{exp\_0}}\right)-\left(\frac{\Delta C_{out\_eq}}{C_{out\_eq0}}\right)\right\}^2+\left\{\left(\frac{\Delta R_{exp}}{R_{exp\_0}}\right)-\left(\frac{\Delta R_{out\_eq}}{R_{out\_eq0}}\right)\right\}^2\right] \tag{7}$$

As a result, the following material properties were obtained in this study: $\alpha = 0.95$, $\beta = 0.25$, $\varepsilon_R S'_R/l'_R = 1.4\times10^{-10}$ F, $\rho_R l'_R/S'_R = 2.4\times10^6\ \Omega$, $\varepsilon_G S'_G/l'_G = 3.3\times10^{-11}$ F, $\rho_G l'_G/S'_G = 1.6\times10^9\ \Omega$. Using these material properties, the capacitance and resistance change $\Delta C_{out\_eq}/C_{out\_eq0}$ and $\Delta R_{out\_eq}/R_{out\_eq0}$, when the out-of-plane impregnated thickness T changes, are calculated as shown in Fig. 5.

From Fig. 5, the capacitance increases and resistance decreases monotonically as T increases. The behavior of the calculated capacitance and resistance change agreed well with the experiments and the validity of the equivalent circuit was confirmed. The thickness T can be estimated from either the capacitance or resistance.

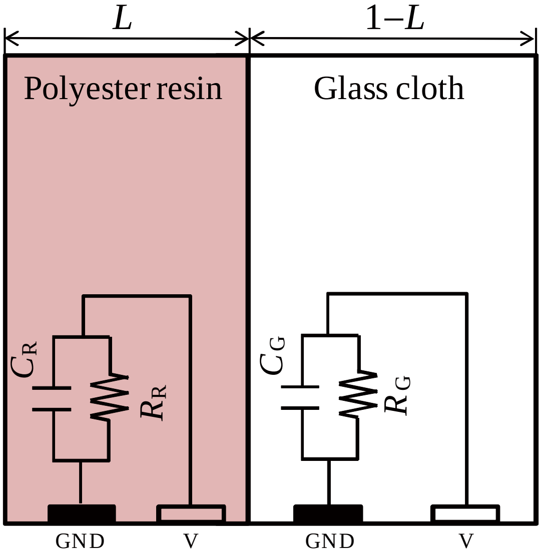

Fig. 6: Side impregnation model.

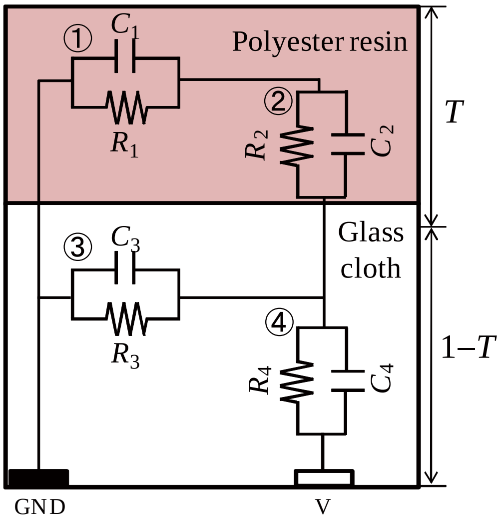

Fig. 7: Out-of-plane impregnation model.

CONCLUSIONS

Cross-sectional resin flow monitoring was proposed using the area-sensor array during the RTM process. The area-sensor array is mounted on a thin polyimide film integrated with an inter-digital electrode array and associated wiring, and formed the bottom layer of the stacked composite laminates. Each area-sensor is square-shaped and measures the capacitance and electrical resistance of the sensor region. We constructed the equivalent electrical circuit model of the in-plane and out-of-plane impregnation states, and the validity of the model was confirmed by comparison with the experimental results.

REFERENCES

1 Brouwer WD, van Herpt ECFC, Labordus A. Vacuum injection moulding for large structural applications. Composites Part a-Applied Science and Manufacturing. 2003;34(6):551-8.

2 Young WB, Chuang MT. Fabrication of T-Shaped Structural Composite through Resin Transfer Molding. Journal of Composite Materials. 1995;29(16):2192-214.

3 Ghiorse SR. Effect of void content on the mechanical properties of carbon/epoxy laminates. SAMPE Quarterly. 1993;24(2):54-9.

4 Goodwin AA, Howe CA, Paton RJ. The role of voids in reducing the interlaminar shear strength in RTM laminates. 11th International Conference on Composite Materials. Gold Coast, Australia1997. p. IV11-IV9.

5 Nancox NL. The effects of flaws and voids on the shear properties of CFRP. Journal of Materials Science. 1977;12:884-92.

6 Kobayashi S, Matsuzaki R, Todoroki A. Multipoint cure monitoring of CFRP laminates using a flexible matrix sensor. Compos Sci Technol. 2009;69(3-4):378-84.

7 Matsuzaki R, Kobayashi S, Todoroki A, Mizutani Y. Full-field monitoring of resin flow using an area-sensor array in a VaRTM process. Composites Part A: Applied Science and Manufacturing. 2011;42(5):550-9.

Section 5

Process Modelling and Simulation

MODELING THE CONSTITUTIVE RESPONSE OF AN ANISOTROPIC DUAL-SCALE FLOW

Mohammad Rouhi[1,2], Maciej Wysocki[1,2], Ragnar Larsson[2]

[1] *Swerea Sicomp, P.O. Box 104, 431 22 Molndal, Sweden*
[2] *Division of Material and Computational Mechanics, Department of Applied Mechanics,*
Chalmers University of Technology, SE-412 96 Göteborg, Sweden
Corresponding author's e-mail: mohammad.rouhi@swerea.se

ABSTRACT: Today's trend in composites manufacturing is to reduce cost by, among other things, cutting down the number of operations required to produce a component. For example all the steps of impregnating the reinforcement, consolidation, forming and finally curing may be, in some cases, combined into a single processing operation. This leads to increasingly complex manufacturing processes with many interacting sub-processes occurring simultaneously on different spatial and temporal scales. In this context we are developing a unified finite-strain continuum framework 1-4], which we recently adopted towards modeling of dual-scale flows in composite manufacturing 5]. In this context, in the present work we consider the manufacturing of the so called Engineering Vacuum Channel (EVaC) prepreg materials as discussed in e.g. 6]. Even though our numerical framework is capable of modeling all the interacting sub-processes at ones, the constitutive models for these are still rare and have not been generalised in a proper continuum context. In summary, the idea of the present work is to emanate from the existing model for fluid flow in a rectangular channel (the so called Poiseuille flow) and generalise it in the finite-strain continuum context. The major task is then to extend our framework to account for anisotropic Darcian interaction on the macro scale and implement the constitutive model into it, while the minor task is to examine the interaction between preform deformation on different scales and the process of micro infiltration and macro flow. The major task is accomplished by introducing the anisotropic permeability model to our coupled displacement-pressure, non-linear finite element model, while the minor task is approached using a representative numerical example, displaying the relevant interactions between the involved sub-processes. The algorithm is then tested for drained conditions, and results are compared to the one in 5] for isotropic flow.

KEYWORDS: *Anisotropic permeability, Finite Element Analysis (FEA), dual-scale flow, phase compressible continuum*

INTRODUCTION

Darcy's law is the most commonly used model for flow of resin in reinforcements during the processing of composite materials. This model describes the flow of Newtonian fluids in porous media and relates the volumetric flow rate Q to the pressure difference over the specimen ($\Delta p/L$), the viscosity μ and the permeability K defined as

$$Q = K\frac{A}{\mu}\frac{\Delta p}{L}. \tag{1}$$

Since both the mechanical properties and the permeability of composites are to a large extent determined by fiber volume fraction, it is common to study the permeability variation with fiber volume fraction, as proposed by Carman 7]. However, in the case of unidirectional reinforcement, where the transverse flow is much more constricted as compare to flow along the fibers, isotropic predictions of permeability are false. In this context, a permeability model of an idealised unidirectional reinforcement consisting of regularly ordered, parallel fibers was derived both for flow along and perpendicular to the fibers by Gebart 8]. In the present work we approach the problem in a similar way to Gebart; however, here we consider the partially impregnated layers of prepregs, the so called EvaC pregpregs 6]. In such a prepreg the fiber bed is kept dry and the matrix cover both sides of the preform, see Figure 1. Therefore, we assume that during the manufacturing processes two kinds of flow will develop; (i) the macroscopic flow between the layers and (ii) the infiltration flow into the dry fiber bed. In summary, the flow is restricted perpendicular to plies and fairly unrestricted parallel to plies.

The paper is organized as follows: formulation of homogenized theory of porous media in terms of governing equations is reiterated for completeness. The constitutive equations in terms of effective stress and fiber bed response along which the permeability model development is then described. Thereafter a compression relaxation test is done for a drained case and the results are compared to the one in 5] followed by discussion and concluding remarks.

HOMOGENIZED THEORY OF POROUS MEDIA

A composite material during a manufacturing operation may be described using a representative mixture (with volume V) consisting of three different micro scale constituents: (i) the incompressible solid particles p with the volume fraction ϕ^p, (ii) the incompressible liquid constituent l with volume fraction ϕ^l and void v with the volume fraction ϕ^v. We assume also that for the particular case of EVaC prepregs the motion of void may be associated with the motion of the solid particles. Motivated by this argument we conclude that the micro problem of three actual constituents is reduced to a two-phase continuum problem. Of course, both the constituents and phases must obey the saturation constraint defined as

$$n^s + n^f = 1 \qquad \text{with} \qquad n^s = \phi^p + \phi^v \text{ and } n^f = \phi^l. \tag{2}$$

In our model, the compaction of the solid phase is a function of the irreversible degree of saturation ξ (defining the degree of saturation within a representative fiber volume) and the reversible fiber packing volume fraction ϕ (which is obtained by considering the compaction of the dry portion of the representative fiber volume), see 2] for extensive derivations. Moreover, the total compaction strain ϵ were in 2] additively decomposed into a reversible compaction strain ϵ^e (related to the packing ϕ and the saturation state ξ) and the irreversible wetting compaction ϵ^p (related to the saturation degree ξ only) as

$$\epsilon = \epsilon^e + \epsilon^p \;\; \rightarrow \;\; \epsilon^e = log\left[\frac{\phi_0}{\phi}\frac{1-\xi(1-\phi)}{1-\xi(1-\phi_0)}\right],\; \epsilon^p = log[1-\xi(1-\phi_0)]. \tag{3}$$

Equation (3) provides a powerful relationship between the micromechanical measures of ϕ and ξ, and the continuum measures of the strains ϵ, ϵ^e and ϵ^p. At a later stage, this will allow us to define the continuum constitutive models using simple micromechanical relations. We thereby focus our attention to the formulation of a binary continuum model, consisting of a compressible solid phase s and an incompressible fluid phase f as followed by Larsson et. Al 2].

Governing equations

The total mass balance and the localized format of the momentum balance for quasi-static behaviour of our binary mixture are obtained, see 4] for details, as

$$\boldsymbol{\nabla} \cdot \boldsymbol{v} - n^s \dot{\epsilon} = -\boldsymbol{\nabla} \cdot \boldsymbol{v}^d, \tag{4}$$

$$\bar{\boldsymbol{\sigma}} \cdot \nabla + \hat{\rho}\boldsymbol{g} = \boldsymbol{0} \quad \forall x \in B, \tag{5}$$

where $\boldsymbol{v}^d$ is the Darcian velocity defined as $\boldsymbol{v}^d = n^f \boldsymbol{v}^r$, $\bar{\boldsymbol{\sigma}} = \boldsymbol{\sigma}^s + \boldsymbol{\sigma}^s$ is the total Cauchy stress. In turn, $\bar{\boldsymbol{\sigma}}$ is related to the effective (constitutive) stress $\boldsymbol{\sigma}$ and the fluid pressure p via the Terzaghi effective stress principle as $\bar{\boldsymbol{\sigma}} = \boldsymbol{\sigma} - p\mathbf{1}.$

CONSTITUTIVE RELATIONS

The total mechanical dissipation D interpreted in terms of a few independent phenomenological mechanisms of the mixture material.

$$D = \underbrace{\boldsymbol{\sigma}\colon \boldsymbol{l} - n^s p \dot{\epsilon} + \hat{\rho}^s \dot{\psi}}_{D^s} + \underbrace{\boldsymbol{v}^d \cdot (\underbrace{\rho^f \boldsymbol{g} - \boldsymbol{\nabla} \cdot p}_{\boldsymbol{h}_e^f})}_{D^i} \geq 0, \tag{6}$$

where $D^s \geq 0$ is the dissipation produced by the (homogenized) solid phase material, $D^i \geq 0$ represents dissipation induced by “drag” – interaction between the phases, $\boldsymbol{h}_e^f$ is the effective drag force and it may be noted that the effective stress felt by the continuum is represented by the Terzaghi stress $\boldsymbol{\sigma}$. Darcian velocity $\boldsymbol{v}^d$ is defined as $\boldsymbol{v}^d = n^f \boldsymbol{v}^r$, p is the fluid pressure, $\boldsymbol{l}$ is the spatial velocity gradient, $\hat{\rho}^s$ is the bulk density, ψ is free energy for the solid phase and $\mathbf{g}$ is gravity.

Guided by the dissipation inequality, we outline the constitutive relations of our two-phase continuum in respect to effective stress and fiber bed response.

Mechanical model

Assuming hyper-elasticity for the effective stress response for a Neo-Hookean elastic material we obtain the free energy $\psi\ [\boldsymbol{C}, \epsilon, \epsilon^p]$ for the solid phase which correspond constitutive state equations as

$$\boldsymbol{S} = 2\hat{\rho}_0^s \frac{\partial \psi_{mac}}{\partial \boldsymbol{C}}, \tag{7}$$

$$p = -\rho^s \frac{\partial \psi_{mic}}{\partial \epsilon}, \tag{8}$$

where $\boldsymbol{S} = \overline{\boldsymbol{S}} - J\boldsymbol{C}^{-1}p$ is the consequent effective second Piola Kirchhoff stress due to the Terzaghi effective stress principle.

Due to elastic packing induced by fluid pressure it was concluded in 2] that the solid phase compaction consists of an irreversible wetting corresponding to the exclusion of voids in the micro constituents and reversible component. The semi-empirical elastic fiber packing law proposed in Toll 9] is directly generalized to the compressive response of the non-saturated region of a fiber bundle consisting of voids and dry fibers as

$$p + p_0 = kE\phi^\alpha, \tag{9}$$

where p is the excess fluid pressure, relative to p_0, acting on a representative fiber bundles.
In view of the equation (8) we obtain "in compliance form" the compaction as a function of the wetting and the fluid pressure as

$$e^\epsilon = \frac{\left(\frac{p_0+p}{p_0}\right)^{-1/\alpha}\left(e^{\epsilon^p} - \phi_0\right) + (1 - e^{\epsilon^p})\phi_0}{1 - \phi_0}, \tag{10}$$

where it was used that the wetting is a diffusive process represented by the viscous evolution

$$\dot{\epsilon}^p = -\frac{p}{\mu}. \tag{11}$$

The parameter, μ, represents the viscous resistance for penetration of liquid into the bulk fibers while microscopic permeability for fiber bundles is calculated using Gebart equation as

$$\mu = \frac{\nu(1 - \phi_0)\zeta^2}{K_{fB}}, \tag{12}$$

$$K_{fB} = \frac{16r^2}{9\pi\sqrt{2}}\left[\sqrt{\frac{\pi}{2\left(\frac{\phi_0}{J}\right)\sqrt{3}}} - 1\right]^{\frac{5}{2}}, \tag{13}$$

where the liquid viscosity is chosen as $\nu = 100\ Pas$, the initial fiber content fraction is $\phi_0 = 0.55$, the wetting length is $\zeta = 50 \times 10^{-6}\ m$ and the fiber radius is $r = 3.5 \times 10^{-6}\ m$.

Permeability model

For the case of the partially impregnated prepregs, the so called EvaC pregpregs, we assume that during the manufacturing operation two flows will develop; (i) the macroscopic flow between the layers and (ii) the infiltration flow into the dry (microscopic) fiber bed. In this context, the generic flow in porous media may be described using the Darcy law as

$$\boldsymbol{v}^d = -\frac{1}{\nu(1-\phi^p)}\boldsymbol{K}\cdot\boldsymbol{h}_e^f, \qquad \boldsymbol{h}_e^f = \boldsymbol{\nabla}\mathrm{p}, \tag{14}$$

where $\boldsymbol{K}$ is the (anisotropic) permeability tensor and ν is liquid viscosity. In order to derive the permeability for the considered EvaC prepreg, we start by defining the structure tensor $\mathbf{M} = \mathbf{T} \otimes \mathbf{T}$ in the reference configuration $\in \mathrm{B}_0$, where $\mathbf{T}$ is unit vector as it is shown in Figure 1.

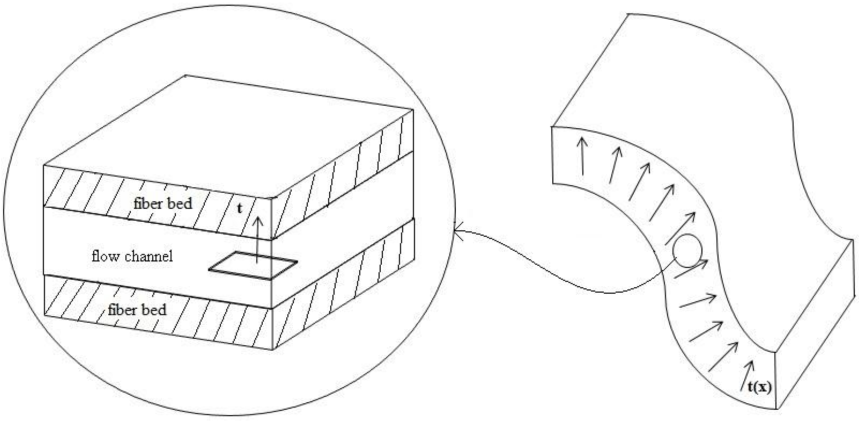

Figure 1: Flow channel and fiber bed stacks

Projecting the total Darcian flow onto the director field $\mathbf{T}$ and the plane perpendicular to $\mathbf{T}$ gives

$$\boldsymbol{v}^d = -\frac{1}{\nu(1-\phi^p)}\big(K_t(\mathbf{1}-\boldsymbol{M}) + K_{fB}\boldsymbol{M}\big)\cdot\boldsymbol{h}_e^f, \tag{15}$$

where $K_{\boldsymbol{fB}}$ is the permeability parallel to $\mathbf{T}$ and K_t is the permeability perpendicular to $\mathbf{T}$. Following the development in 10], the permeability K_t may be represented as $K_t = K_{fB}(1-\phi_l) + K_{Ch}\phi_l$, leading to

$$\boldsymbol{v}^d = -\frac{1}{\nu(1-\phi^p)}\Big(\big(K_{fB}(1-\phi_l)+K_{Ch}\phi_l\big)(\mathbf{1}-\boldsymbol{M})+K_{fB}\boldsymbol{M}\Big)\cdot \boldsymbol{h}_e^f, \tag{16}$$

where K_{fB} is the permeability through the fiber, K_{Ch} is the permeability through the channel and ϕ_l is liquid volume fraction.

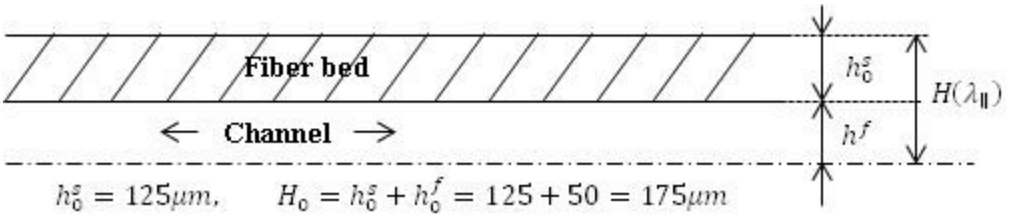

Figure 2: Distance between fiber layers and flow channel

The permeability through the fiber bed K_{fB} is represented using the Gebart equation (3). The permeability through the channel may be approximated considering the resistance to viscous flow within a rectangular channel, 10]

$$K_{Ch} = \frac{(h^f)^2}{12}, \tag{17}$$

where h^f is the channel height and it is a function of the continuum stretch parallel to **T** defined as

$$h^f = H(\lambda_{\|}) - h_0^s \;\rightarrow\; \{H(\lambda_{\|}) = H_0\lambda_{\|}\} \;\rightarrow\; h^f = H_0\lambda_{\|} - h_0^s, \tag{18}$$

where $\lambda_{\|}$ is the stretch in the direction of **T** given as

$$\lambda_{\|} = \sqrt{\boldsymbol{C}:\boldsymbol{M}}, \tag{19}$$

and $\boldsymbol{C}$ is the right Cauchy-Green deformation tensor, h_0^s is the fiber ply thickness (assumed constant at the moment) and $H_0 = h_0^s + h_0^f$. In consequence, the channel permeability reads

$$K_{Ch} = \frac{(H_0\lambda_{\|} - h_0^s)^2}{12}. \tag{20}$$

When the preform deforms, the size of the channel decreases, meaning that ϕ_l & $h^f \rightarrow 0$, which in that case K_{Ch} vanishes.

NUMERICAL RESULTS AND CONCLUDING REMARKS

A typical compression test, as defined in Figure 3, is performed using the same boundary conditions and material parameter as in Rouhi et. al. 5]. It is to assess the permeability model developed in this paper against our early isotropic attempts in 5].

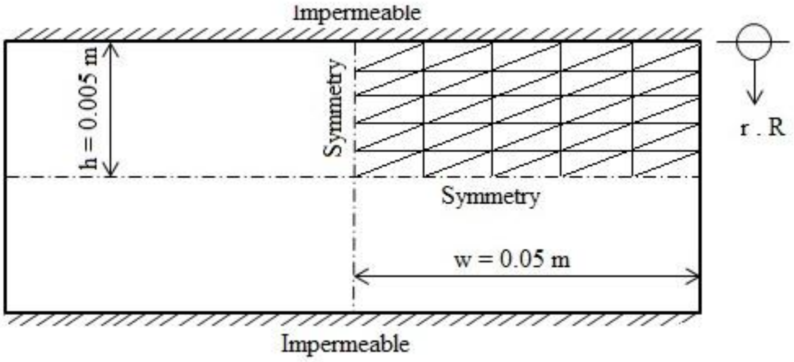

Figure 3: Analysed rectangular specimen with initial geometry and boundary conditions. Two cases are considered: 1) $p = 0$ along the vertical boundaries defining the partly drained condition and 2) The vertical boundaries are impermeable defining the globally undrained condition (corresponding to $p = unknown$ along the vertical boundaries).

Comparison between the two permeability models in this context is valid since the present boundary conditions allow only for in-plane macroscopic flow, i.e. in consequence isotropic in plane flow. Figure 4 shows the reaction forces and the global saturation degree versus time for the undrained case where all outer boundaries are modeled impermeable.

The behaviour of the process with the anisotropic permeability model is similar to the results from the isotropic permeability model in 5]. Figure 5 shows a comparison between the two models in case of saturation degree and reaction forces. In particular, using the same parameters the two curves coincides. The competition between the flow through the channel and the flow through the fibers is the key for the process. At the beginning of the process, the permeability through the fiber bed is much smaller than the permeability in the channel, resulting in higher flow in the channel. However, as the channel height vanishes and permeability decreases (as compaction increases) the situation reverses.

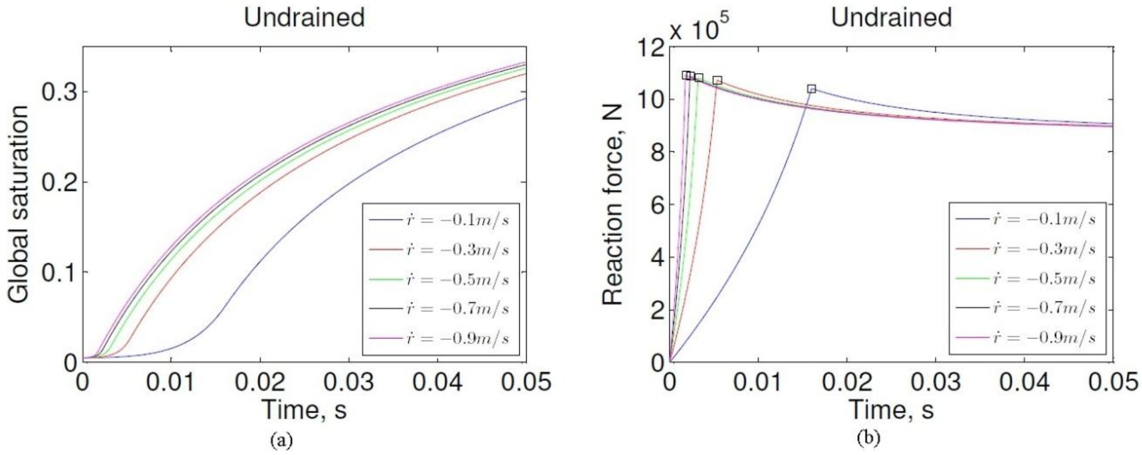

Figure 4: Relaxation test at globally undrained condition with respect to different initial loading rates, (a) Resulting global saturation degrees versus process time and (b) resulting reaction forces versus time

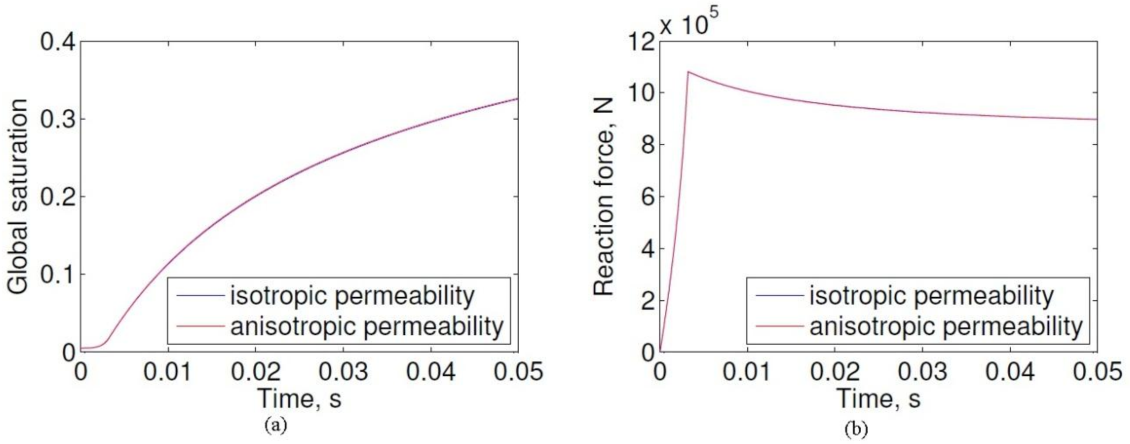

Figure 5: Comparison between relaxation tests for globally undrained conditions at the initial loading rate $\dot{r} = -0.5m/s$ for isotropic and anisotropic permeability model, (a) global saturation degree versus time and (b) reaction forces versus time

In summary, in the present work we developed a constitutive model for continuum FE modeling the manufacturing operation of a layered composite material. In particular, our focus was on modeling the processing of EVaC prepregs. Thus, an existing model for fluid follow in a rectangular channel (the so called Poiseuille flow) was generalized in a finite-strain continuum context and implemented to our two-phase continuum FE-software. The FE framework itself was extended to account for anisotropic Darcian interaction on the macro scale. The model was assessed against the results in 5] for isotropic permeability by enforcing appropriate boundary conditions. The results indicate that the model with anisotropic permeability behaves well and that the interaction between macro and micro flow dictates the degree of saturation and thus the quality of the final product. In particular, depending on the loading rate either microscopic or macroscopic flow develops, see Figure 4. This is due to the interaction between the flows, where although the permeability through the fiber bed is much smaller than the permeability in the channel, the fast loading will not allow for the macroscopic flow to develop.

REFERENCES

1. Larsson J and Larsson R (2002), ‘Nonlinear analysis of nearly saturated porous media: theoretical and numerical formulation’, *computer methods in applied mechanics and engineering,* 191 (36), pp. 3885-3907

2. Larsson R, Wysocki M and Toll S (2004), ‘Process-modeling of composites using two-phase porous media theory’, *European Journal of Mechanics, A/Solids,* 23 (1) , pp. 15-36

3. Wysocki M, Asp LE, Toll S and Larsson R (2009), ‘Two phase continuum modelling of composites consolidation’, *Plastics, Rubber and Composites,* 38 (2-4) , pp. 93-97

4. *Larsson R, Rouhi M and Wysocki M (2012), 'Free surface flow and preform deformation in* composites manufacturing based on porous media theory', *European Journal of Mechanics A/Solids,* 31 1-12

5. Rouhi M, Wysocki M and Larsson R (2012), 'Model development of two-scale porous media flow in composite process modeling'. To be submitted for publication in 2012

6. Thomas S, Bongiovanni C and Nutt SR (2008), 'In situ estimation of through-thickness resin flow using ultrasound', *Composites Science and Technology* 68 (15-16), pp. 3093-3098

7. *Carman PC (1937), 'Fluid flow through granular Bed', Transaction institution of chemical engineering,* 15:150-166.

8. Gebart BR (1992), 'Permeability of unidirectional reinforcement for RTM', *Journal of composite materials*, v 26, No. 8, p1100-1133

9. Toll S (1998), 'Packing mechanics of fiber reinforcements', *Polymer Engineering and Science*, 38(8), 1337-1350.

10. Bear J (1988), Dynamics of Fluids in Porous Media, New York: Elsevier Publishing Company, Inc.

MODEL DEVELOPMENT AND VERIFICATION OF THE VACUUM INFUSION PROCESS FOR COMPOSITE MANUFACTURING

Galyna Goncharova [1] , Mylène Deléglise [1] , Sébastien Comas-Cardona [1, 2] , Christophe Binétruy [1, 2]

[1] Department of Polymers and Composites Technology & Mechanical Engineering,
Ecole des Mines de Douai,
941 rue Charles Bourseul, BP10838, 59508 Douai Cedex, France.
[2] Research Institute in Civil Engineering and Mechanics (GeM), UMR CNRS 6183, Ecole Centrale de Nantes, 1 rue de la Noe, BP92101, 44321 Nantes Cedex 3, France.
Corresponding author's e-mail : mylene.deleglise@mines-douai.fr

ABSTRACT: A new analytical formulation of governing equations for hydro-mechanical coupled problem during single sided molding processes such as Vacuum Infusion (VI) is presented in this study. The main complexities of VI modeling are the presence of pressure changes and thickness evolution during fabric preform impregnation. The research is focused on the relations between flow progression and pressure changes inside the cavity. The main purpose of the presented studies aims at improving the manufacturing process of composite parts using a proposed mathematical model of moving-boundary problem. The derivation of a mathematical model of the VI process is proposed. Formulas of resin flow front position and pressure distribution with respect to longitudinal coordinate and time are proposed. The closed form analytical solution results are validated with one-dimensional fluid flow experimental data for two types of boundary conditions: constant and variable with time inlet pressure. This paper presents the comparison between the proposed model, experimental data from the literature and Correia's et al. [1] model for flow front position and pressure evolution. The results of the proposed model show better prediction for flow front position and pressure profile evolution over time than Correia's et al. [1]. The proposed model in this paper gives new look inside the hydro-mechanical coupled problems of the single sided molding processes. An improvement of the mathematical prediction of the VI process has been achieved.

KEYWORDS: *Vacuum Infusion, Analytical modelling, Numerical analysis.*

INTRODUCTION

Single sided molding processes such us vacuum infusion is a liquid composite molding process in which resin is infused under vacuum into fibrous preform. The mould top half is flexible. The liquid pressure acts against the atmospheric pressure during the impregnation process. This leads to a dynamic change in the thickness of the fiber reinforcement preform. Vacuum infusion is a growing composite manufacturing process, as it offers the possibility to produce large parts with good quality at a low-cost. The increasing amount of VI process applications for composite manufacturing is observed in different areas such as aerospace, marine or wind energy community. Each of these industries, require high quality composite material parts which results in the need of accurate VI process modeling. The above requirements orient the research on coupling mechanical problems to simulate the pressure distribution, the resin flow front position and the thickness profile distribution. For this reason the modeling of VI process is an important step for composite manufacturing. In this paper we propose new approaches for VI process modelling to be able to predict mechanical behaviour of fiber reinforcement preform. We present numerical results of flow front position and fluid pressure distribution, and comparison with experimental measurements.

PREVIOUS WORK

The final shape of a composite part produced with VI process depends on the strong coupling between the resin flow and the deformation of the fiber reinforcement during infusion process. The mathematical and numerical models give the understanding of physical mechanisms during the entire process. A very limited number of papers describe analytical solutions [1-6]. According to the literature, for one phase flow models the following set of equations are used for simulation of infusion process:

- Momentum equation (Darcy's law for unidirectional resin flow);
- Continuity equation (Gutowski et al. approach [7]);
- Stress equilibrium equation (Terzaghi’s law);
- Compaction model (experimental data from mechanical test);
- Permeability model (experimental data from infusion test).

The validity of describing statement of the problem can be realized using the comparison with experimental data. Works [2-6] presented correlation only with flow front position. Model, proposed by Correia et al. [1] was used in [8]. Authors presented comparison with experimental data for flow front position, pressure profile and change of thickness with respect to time. The difference between simulated and experimental filling time reaches 66 %. Figures 1 and 2 represent the comparison between model and experimental data for fluid pressure progression and preform thickness redistribution for different sensors locations.

The main drawbacks to the exist models [1-8] are:

- Strong assumption in continuity equation proposed by Gutowski et al. [7], which can be easily derived using comparison with mass conservation equation:

$$\left(h-\frac{h^2}{V_{f0}\,h_0}\right)\frac{\partial u_x}{\partial x}+u_x\frac{\partial h}{\partial x}=0 \qquad \text{for} \qquad 0\le x\le x_f\,, \tag{1}$$

where h is preform thickness, V_{f0} and h_0 are the initial fiber volume fraction and preform thickness after applied vacuum, u_x is Darcy’s velocity and x_f - flow front position.

- Permeability and compressibility are achieved separately from coupled hydro-mechanical processes. The change in permeability is usually represented as a function of thickness under steady-state flow. The compressibility level reached by the fiber preform is determined from function of the applied force, according to mechanical test characterization. The preform permeability and compressibility strongly vary with degree of impregnation of the material during vacuum infusion.

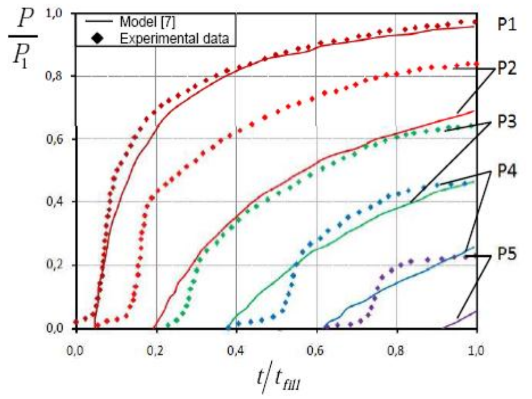

Fig. 1: Comparison between experimental data [8] and predicted distribution of fluid pressure using [1] model

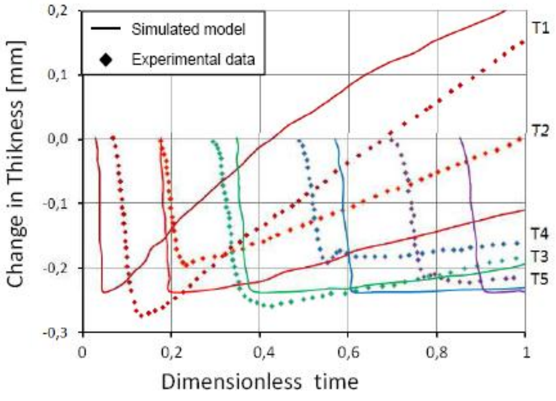

Fig. 2: Comparison between experimental data [8] and predicted thickness redistribution using [1] model

Therefore, the aim of presented work is:

a) To derive a complete initial-valued moving boundary problem with continuity approach based on mass conservation equation;
b) To receive an analytical solution without using explicit information of permeability and compressibility changes;
c) To verify the proposed model with experimental data comparison.

MATHEMATICAL FORMULATIONS AND ANALYTICAL SOLUTIONS

Continuity equation for fluid flow in deformable reinforcement

With assumptions that the saturation is perfect, fluid is incompressible, considering constant recovery compliance of impregnated fabrics $C^e(t)$, substituting Terzaghi's law into the mass conservation equation for unidirectional fluid flow, the continuity equation becomes:

$$\frac{\partial P}{\partial t} = \frac{\partial}{\partial x}\left(f(x,t)\frac{\partial P}{\partial x}\right), \qquad 0 \le x \le x_f \tag{2}$$

where P is fluid pressure, x_f - flow front, $f(x,t) = \frac{K_{xx}(x,t)}{\mu C^e(t)}$ is an unknown function, which depends on change of permeability and compressibility due to impregnation process.

The proposed second order differential equation (2) with moving-boundary must be closed with initial and boundary conditions.

Initial and boundary conditions

- Zero flow front position at t=0: $x_f(t=0)=0$;
- Zero fluid pressure at flow front position: $P(x=x_f,t)=0$;

- Flow front position will be simulated using Darcy’s law: $\frac{d\,x_f}{d\,t} = -\frac{K_f}{\mu\varphi_f}\frac{\partial P}{\partial x}$;
- Inlet pressure is constant and equal to P_1 : $P(x=0,t) = P_1 = Const$.

Let observe the influence of unknown function $f(x,t)$ on continuity Eq.(2) with initial and boundary conditions. From physics of process it is known that the fluid pressure function is: continuous, increasing at every point with time progression, decreasing with longitudinal coordinate at any particular point of time, the maximum value of function is limited to applied pressure.

The solution of Eq.(2) for resin transfer molding (RTM) process at any particular point of time will be one of presented graphics in Fig.(3a). As for RTM the upper mold is rigid, the thickness of the preform is invariable (function $f(x,t) = const$) and inlet pressure is not limited to atmospheric pressure as for VI. For this reasons, the steady-state solution for pressure profile will decrease linearly with flow front position.

According to experimental data [1, 8] the pressure for VI process at any particular point of time will be one from the graphics presented in Fig.(3b). The curve is concave due to present deformation in the thickness direction. The nature of fluid pressure leads to equilibrate atmospheric pressure with applied vacuum. As the maximum value of pressure limited and reaches at the inlet, at the equilibrium or at the steady-state condition pressure will give the extreme of pressure function at $x = 0$.

a

b

Fig. 3: Fluid pressure redistribution during: a) RTM; b) VI

Fig.(3) showed that the presence of function $f(x,t)$ is responsible for convexity of pressure curve. This convexity can be achieved solving Eq.(2) where the unknown function $f(x,t)$ replaced with additional boundary condition, because the pressure profile is continuous and unique. Additional condition can be applied in any edge of preform or even inside the geometry sample. For steady-state flow it has been mentioned the maximum and extreme of pressure function reaches at the inlet of the preform. In this case, proposed additional boundary condition: $\frac{\partial P}{\partial x}(x=0,t) = \varepsilon$, where $\varepsilon \to 0$.

The initial-valued moving boundary problem Eq.(2) assumed the constant inlet pressure. This proposal is true, when through the pipe enters enough fluid for Darcy’s flow rate. Presented system of boundary and initial conditions valued for case when there are Darcy's flow inside the preform. When radius of pipe is small and the inlet fluid pressure is gradually increased from zero to atmospheric one, rectilinear Poiseuille's flow observes inside the preform [9]. Following additional boundary condition can be used: $\frac{\partial P}{\partial x}\left(x = x_f, t\right) = \omega$, where $\omega = \frac{u_x \varphi_f \mu}{K_f}$.

Solution

From a mathematical point of view, proposed moving boundary problem Eq.(2) is equivalent to the one-dimensional Stefan problem [10]. The Goodman's integral method [10] is used to solve for this type of equation. The main idea of Goodman's integral method is to take the form of polynomial which is made to satisfy all the boundary conditions and an integrated form of the pressure Eq.(2). The position of the moving boundary is the solution of an ordinary differential equation with time as the independent variable.

In this case the functions for pressure and flow front position for constant inlet pressure:

$$P(x,t) = P_1 \left[1 - \left(\frac{x}{x_f}\right)^2\right] \tag{3}$$

$$x_f = 2\sqrt{\frac{K_f P_1}{\mu \varphi_f} t}\,, \tag{4}$$

The solution for pressure and flow front position in case with varied inlet pressure:

$$P(x,t) = \omega\left(x - x_f\right) + \frac{\omega x_f - P_1}{x_f^2}\left(x - x_f\right)^2 \tag{5}$$

$$x_f = -\frac{K_f \omega}{\mu \varphi_f} t \tag{6}$$

A predictive tool which is able to reproduce the pressure and flow front position has been proposed. Mathematical solutions for the calculations of the pressure and flow front position in the fiber preform during VI process with deformable media have been obtained.

RESULTS AND DISCUSSIONS

In order to validate proposed model, the numerical results will be compared with experimental data [8, 9] and solution proposed by Correia et al. [1]. The variation of the flow front position and fluid pressure with time during VI process will be discussed for two stated above cases: constant and varied with time inlet pressure.

Constant inlet pressure

Experimental data for four layers of random fabrics and one layer of embedded core fabric (preform was assumed as heterogeneous medium) for flow progression is shown in Fig.4 [8]. The parameters and material constants which were used for modelling [8]: permeability coefficient K_f = $0.76 \cdot 10^{-9}\ m^2$, porosity φ_f = 74%, resin viscosity $\mu = 0.35\ Pa\,s$, inlet pressure $P_1 = 90\ kPa$, preform length $L = 0.4\ m$. The analytical filling time is 153 s, whereas experimental injection is done in 150 s. Model data is also shown in Fig.4. Figure 5 shows the comparison between predicted and experimental fluid pressure profile induced by resin flow during impregnation of fiber reinforcements. P_1, P_2, P_3, P_4, P_5 denotes pressure at the distance $x = 0.08,\ 0.16,\ 0.22,\ 0.28,\ 0.34\,m$ from the inlet, respectively.

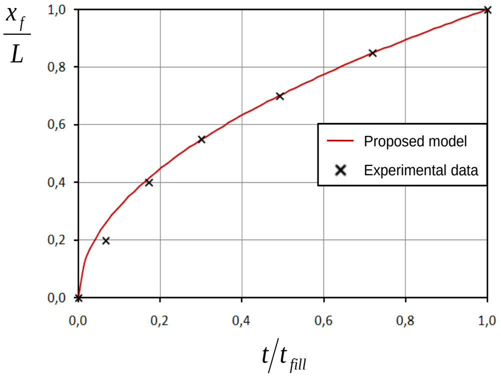

Figure 4. Comparison between experimental data [8] and predicted flow front position Eq.(4).

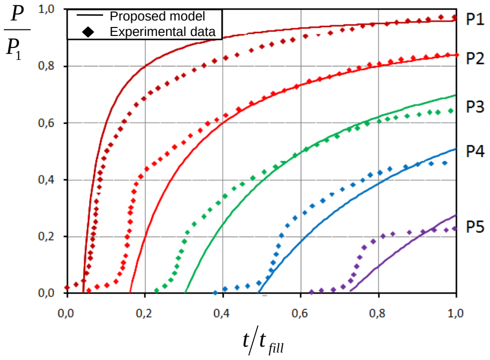

Figure 5. Comparison between experimental data [8] and predicted distribution of fluid pressure Eq.(3)

Varying inlet pressure

To validate proposed mathematical model with variable inlet pressure over time, the numerical results Eq.(5-6) will be compared with experimental data [9] and solution proposed at [1]. Experiment was done with four layers of U750/375. The parameters and materials constants which were used for modelling [9]: permeability coefficient K_f = $1 \cdot 10^{-9}\ m^2$, porosity φ_f = 78%, resin viscosity $\mu = 0.3\ Pa\,s$, inlet pressure $P_1 = 65\ kPa$, preform length $L = 0.39\ m$. Fluid velocity have been found by fitting Eq.(6) to the experimental data by a least-square minimization process u_x = $3.9 \cdot 10^{-3}\ m/s$. The experimental injection is done in 108 s whereas the analytical filling time is 100 s. Modi et al. [9] simulated VI process using Correia's model [1]. Fig. 6 shows the comparison of fluid pressure redistribution between experimental data, model proposed in this article (Eq.(5)) and Correia's one.

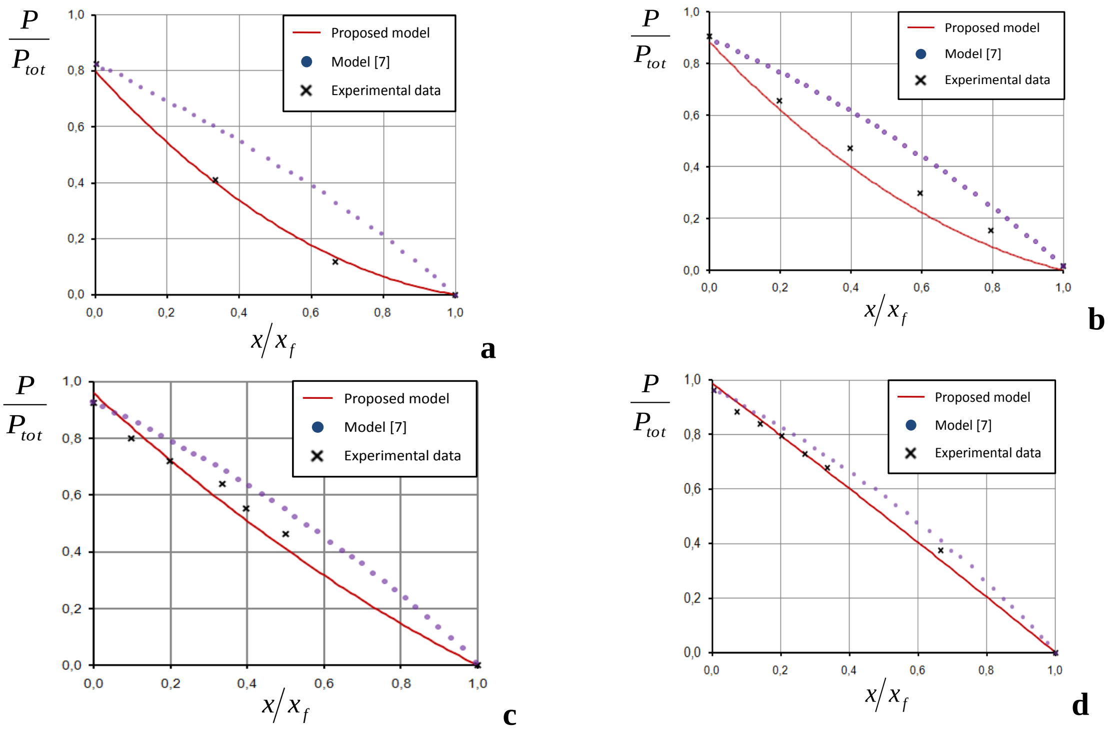

Figure.6. Fluid pressure profile evolution with flow progression in the rectilinear flow during VI process. (a) Infused length = 60 mm. (b) Infused length = 100 mm. (c) Infused length = 200 mm. (d) Infused length = 300 mm.

CONCLUSIONS

In this article we proposed analytical modeling and closed form solution for VI process. The flow front position and pressure evolution were obtained in closed form solution. It has been showed that the proposed solution gives good match with experimental data for flow front position and pressure redistribution over time. Two types of boundary conditions with respect to inlet pressure have been studied. Good agreement were obtained between theoretical analysis and infusion experiments for both cases: constant and varying with time inlet pressure. It has been shown that the pressure distribution can be found without explicit knowledge of the relationship between fiber volume fraction and compaction pressure as well as between preform permeability and fiber volume fraction. Consequently, mass conservation equation together with additional boundary condition gives simple and effective way to find a solution for flow front position and pressure distribution during single sided molding processes.

ACKNOWLEDGEMENTS: The authors wish to thank ANR (Agence Nationale de la Research) France for financing part of this work within the Numtiss project.

REFERENCES

1. Correia NC, Robitaille F, Long AC, Rudd CD, Simacek O and Advani SG (2005), ‘Analysis of the vacuum infusion moulding process: I. Analytical formulation’, *Composites: Part A*, 36, 1645-1656.

2. Hammami A and Gebart BR (2000), ‘Analysis of the Vacuum Infusion Molding Process’, *Polymer Composites*, Vol. 21, No. 1, 28-40.

3. Bayldon J and Daniel (2009), ‘IM Flow modeling in the VARTM process including progressive saturation effects’. *Composites: Part A*, 40, 1044-1052.

4. Park CH and Saouab A (2009), ‘Analytical Modeling of Composite Molding by Resin Infusion with Flexible Tooling : VARI and RFI processes’. *Journal of Composite Materials*, Vol. 43, No. 18, 1877-1900.

5. Acheson JA, Simacek P and Advani SG (2004), ‘The implications of fiber compaction and saturation on fully coupled VARTM simulation’. *Composites: Part A*, 35, 159-169.

6. Song YS and Youn JR (2008), ‘Modeling of Resin Infusion in Vacuum Assisted Resin Transfer Molding’. *Polymer Composites*, 390-395.

7. Gutowski TG and Dillon G (1997), The elastic deformation of fiber bundles. In: Gutowski T.G., editor. *Advanced composite manufacturing*. Willey; 1997. p. 138-147.

8. Yenilmez B, Senan M and Sozer EM (2009), ‘Variation of part thickness and compaction pressure in vacuum infusion process’. *Composite Science and Technology*, 69, 1710-1719.

9. Modi D, Johnson M, Long A and Rudd C. ‘Analysis of pressure profile and flow progression in the vacuum infusion process’. *Composite Science and Technology*, 69, 1458-1464.

10. Crank J (2005), Free and moving Boundary Problems. Oxford University Press, 425.

NEURAL NETWORK VERSUS KRIGING, SURROGATE MODELS FOR LCM PROCESS OPTIMIZATION

Abhishek Gupta [1], Piaras Kelly [1], Matthias Ehrgott [2] and Simon Bickerton [3]

[1] *Centre for Advanced Composite Materials, Department of Engineering Science, University of Auckland, Private Bag 92019, Auckland 1142, New Zealand, Corresponding author's e-mail: pa.kelly@auckland.ac.nz.*
[2] *Department of Engineering Science, University of Auckland, Private Bag 92019, Auckland 1142, New Zealand.*
[3] *Centre for Advanced Composite Materials, Department of Mechanical Engineering, University of Auckland, Private Bag 92019, Auckland 1142, New Zealand.*

ABSTRACT: In Liquid Composite Moulding (LCM) processes an optimal combination of a variety of manufacturing design variables must be chosen in order to minimize cycle time while keeping equipment, layout and running costs low. Such black-box function optimization can be achieved by integrating the process simulation algorithm with a meta-heuristic, such as a genetic algorithm (GA). However, the large number of function evaluations required by a GA combined with the computational expense of the simulations often makes this approach unaffordable. This issue is further emphasized when the filling and curing phases are coupled and an iterative optimization strategy becomes necessary. The use of a surrogate model, as a substitute to the expensive simulation algorithm, is a common technique for reducing the run-time of an optimization algorithm. Choosing such a model that suitably duplicates all the features and trends of the objective functions over the design space, is an important task. In this paper we compare two popular surrogate models, namely the artificial neural network (specifically the Cascade-Correlation Learning Architecture Neural Network) and kriging, and discuss their performance in terms of prediction accuracy and the run-time of the resultant optimization algorithm.

KEYWORDS: *Liquid Composite Moulding (LCM), Surrogate modelling, Kriging, Artificial Neural Networks.*

INTRODUCTION

The term Liquid Composite Moulding (LCM) is used to define a class of composite manufacturing processes in which a liquid thermosetting resin is introduced, under pressure, into a closed mould containing a dry fibrous reinforcement. In this study we focus on the optimization of the filling phase of the velocity-controlled Compression Resin Transfer Moulding (CRTM) process [1]. The CRTM process is a member of the LCM family and is characterized by the use of rigid tools which are assumed to undergo negligible deflection during the entire manufacturing cycle. The filling phase of this process can be divided into two parts: injection of the resin into a partially closed mould and complete mould closure, thereby compacting the wet fibres to the desired part thickness.

The design of the fill phase governs multiple objectives such as the fill time, the magnitude of the clamping force required (this plays a major role in determining the overall setup and running costs) and the existence of dry spots due to partial fibre impregnation. Minimization of such black-box objective functions can be achieved by implementing a genetic algorithm (GA) for multi-objective optimization. However, a GA typically requires a few thousand function evaluations to find good solutions, and the computational expense of a single simulation run can be very high. Together, these factors often render the implementation of a GA infeasible. This difficulty is further compounded in cases wherein the filling and curing phases are coupled, thus demanding an iterative solution strategy [2].

Surrogate modelling is a commonly used method for the efficient optimization of expensive black-box functions. Surrogate models attempt to learn the relationships between the design variables and the objective functions based on predictions made by the expensive simulation algorithm at a limited number of well distributed sample points in the design space. The exact number of points depends on the available computational budget and affects the particular choice of surrogate. During the model training period no consideration is given to the actual physics of the underlying process, solely the input-output behaviour is important. These models are computationally inexpensive and can therefore be used with large optimization algorithms. However, choosing a model that best duplicates the input-output relationship is a significant task. Artificial neural networks and kriging are two popular choices as surrogate models when no prior knowledge of the functional form is available. In this paper we compare these two models in terms of their prediction accuracies (when compared to the simulation algorithm) and the run-time of the final GA which uses them for function evaluations. It is believed that such models can be used to construct more elaborate optimization frameworks that allow coupling between the filling and curing phases of LCM processes. This would allow the complete composite manufacturing cycle to be fully optimized while expending minimum computational effort.

GOVERNING PDEs AND EMPIRICAL MODELS

Equation of fluid flow

Darcy's law is commonly used to model viscous flow through porous media. When combined with the equation for mass conservation it takes the following form;

$$\nabla \, . \, \left(h \, \frac{\boldsymbol{K}}{\mu} \, \nabla p \right) - \frac{\partial h}{\partial t} = 0 \, . \tag{1}$$

Here, the thickness h, resin pressure p and the permeability $\boldsymbol{K}$ are in general coupled. The viscosity μ is likely to vary spatially with the temperature and degree of resin conversion. This response can be captured by the following widely used rheological model;

$$\mu = A_\mu e^{E_\mu / R \, T_{abs}} \left(\frac{\alpha_g}{\alpha_g - \alpha} \right)^{a + b\alpha} , \tag{2}$$

where α_g is the resin gel conversion, E_μ is the activation energy, R is the universal gas constant, T_{abs} is the absolute resin temperature, α is the instantaneous resin conversion. A_μ, a and b are determined experimentally.

Energy equation

Assuming that the resin and fibre phases have the same local temperatures (often referred to as a lumped system) the volume averaged energy equation is;

$$\rho\, C_p \frac{\partial T}{\partial t} + \rho_r C_{pr} (\boldsymbol{u} \,.\nabla T) \;=\; \nabla.\,(k\,\nabla T) + \varphi\,\dot{H}. \tag{3}$$

The material properties ρ, C_p and k represent, respectively, the average density, specific heat capacity and thermal conductivity of the resin-fibre system. T is the local temperature, $\boldsymbol{u}$ is the volume averaged (or Darcy) velocity, t is the time, φ is the local reinforcement porosity and $\dot{H}$ is a source term representing the thermal energy generated by the resin as it cures. The average material properties are computed as follows;

$$\rho\, C_p = \;\varphi \rho_r C_{pr} + (1-\;\varphi)\rho_f C_{pf}, \tag{4}$$

$$\frac{1}{k} = \;\frac{\varphi}{k_r} + \frac{(1-\,\varphi)}{k_f}, \tag{5}$$

where the subscript *r* stands for resin and *f* stands for the fibres.

Species equation

The volume averaged species equation can be expressed as follows;

$$\varphi\,\frac{\partial \alpha}{\partial t} + \boldsymbol{u}.\nabla\alpha = \;\varphi\, R_\alpha. \tag{6}$$

To solve Eq. (6) the rate of resin polymerization (R_α) must be accurately modelled. Kamal and Sourour proposed a general model which is widely used to describe the polymerization reaction. It can be expressed as follows;

$$R_\alpha = \;\left(A_1\,.\;e^{(-E_1/R\,T_{abs})} + A_2\,.\;e^{(-E_2/R\,T_{abs})}.\,\alpha^{m_1}\right).(1-\;\alpha)^{m_2}, \tag{7}$$

where $A_1$and A_2 are constants; E_1 and E_2 are activation energies*;* m_1 and m_2 are catalytic constants.

Fibre Compaction Model

An accurate prediction of the clamping force requirements cannot be achieved without a fibre compaction model which suitably duplicates the response of the fibrous reinforcement being used in the particular process. In this study we use the mixed-elastic model which is described using four nonlinear stress-volume fraction curves – Dynamic & Dry", "Dynamic & Wet", "Static & Dry" and "Static & Wet". A five-term polynomial (Eq.8) provides excellent fit to the experimental data for a wide range of fibre volume fractions and may subsequently be implemented for the force simulations.

$$\sigma(V_f) = a'V_f^4 + b'V_f^3 + c'V_f^2 + d'V_f + e', \tag{8}$$

where σ is the fibre compaction stress, V_f is the fibre volume fraction. a', b', c', d' and e' are experimentally determined constants for the particular material in use. The values of these constants for a glass-fibre chopped strand mat (CSM) are given in Table 1.

Table 1: Mixed-elastic compaction model parameters [1].

	Dynamic dry	Dynamic wet	Static dry	Static wet
a’	4.68e+7	2.96e+7	2.97e+7	4.55e+7
b’	-5.14e+7	-2.65e+7	-3.60e+7	-5.80e+7
c’	2.27e+7	9.50e+7	1.72e+7	2.84e+7
d’	-4.62e+6	-1.54e+6	-3.68e+6	-6.17e+6
e’	3.58e+5	9.03e+4	2.943e+5	4.95e+5

NUMERICAL SIMULATION

The filling phase of the process is modelled using a hybrid Finite Element/Finite Difference (FE/FD) methodology, based on the algorithm proposed by Ruiz and Trochu [3] for the non-isothermal RTM simulation. A full description of the method and its extension to the CRTM case can be found in [3] and [4], respectively. The method assumes predominantly planar flows and is therefore valid for the process simulation of thin to moderately thick composite parts without an initial air cavity between the mould face and the preform during resin injection.

SURROGATE MODELLING

Before describing the individual surrogate models it should be mentioned that the sample points in the design space that are used for training the surrogate models are selected based on a maximin latin hypercube design. The number of sample points used depends on the computational budget available.

Artificial Neural Networks

In this study we implement the Cascade-Correlation Learning Architecture Neural Network (CCA-NN) [5] in place of the more common Multilayer Perceptron (MLP). The CCA-NN is preferred as it determines its own size and topology during the training procedure. This feature undermines the need for any prior knowledge of the function behaviour. MLP, on the other hand, requires the user to pre-specify the number of hidden neurons and the number of layers to be used. Therefore a lack of knowledge of the function behaviour often leads to either an inadequate number or too many hidden neurons to be specified.

Prior to building the CCA-NN it is assumed that hidden neurons have symmetric sigmoidal (hyperbolic tangent) activation functions whereas the output units just produce a linear sum of their weighted inputs. For problems in which a precise analog output is desired, like the present one, linear output units are often the best choice [5]. During training the quickprop algorithm [5] is used to adjust all the signal weights so as to minimize the error measure between the NN and the computational predictions.

Kriging

A thorough and intuitive description of the kriging approach applied to the analysis of computational experiments is provided in [6]. A brief overview of the method is presented herein.

In the kriging method the result obtained from a deterministic computer code is treated as the realisation of a stochastic process. Traditional stochastic processes are composed of a fundamental regression model together with an independent error term of mean zero and variance σ^2. In kriging, however, the errors are not assumed to be independent. In fact it is assumed that the error terms are correlated with the correlation between errors being related to the distance between the corresponding points. The correlation is high when the points are close and low when the points are far apart. Importantly, the mentioned distances are not necessarily equal to the Euclidean distance. The parameters used to compute the distance are obtained by solving a nonlinear unconstrained optimization problem so as to maximize a prescribed likelihood function [6]. In the present study a Nelder and Mead simplex algorithm has been used for this optimization problem. The algorithm is repeated 20 times in order to achieve a robust search of the parameter space.

An attractive feature of kriging is that it exactly reproduces the response of the computer code at the sampled locations.

SURROGATE MODEL COMPARISON

It is important to have a quantitative measure of the agreement between the surrogate model predictions and the actual computational function evaluations. For this purpose we use the correlation coefficient as a measure in this study.

After training the CCA-NN and the kriging model using the data at the sample points, these same sample points are reused to measure how well the surrogate models have learnt the relationship between the input and output variables. This method does not require computer simulations to be carried out at any additional points and is therefore in keeping with the computational budget limitations. The formula used to compute the correlation coefficient *R* is as follows;

$$R = \frac{\sum_{i=1}^{n}(X_i - \bar{X})(Y_i - \bar{Y})}{\sqrt{\sum_{i=1}^{n}(X_i - \bar{X})^2}\sqrt{\sum_{i=1}^{n}(Y_i - \bar{Y})^2}}, \quad (9)$$

where X_i is the computational prediction at the i^{th} sample point and Y_i is the corresponding surrogate model prediction. n is the total number of sample points used. From Eq. (9) it is clear that if the surrogate model predictions match exactly with the computational predictions, the correlation coefficient takes a value 1. Therefore the surrogate for which R is closer to 1 is considered to be superior for the problem at hand.

For the CCA-NN the Y_i values are obtained at the sample points right after training has been completed, without any adjustments required to the network. The closeness of the correlation coefficient to 1 depicts the efficiency of the training algorithm in minimizing the error in network predictions (implicitly maximizing the degree to which the network learns the features and trends in the function behaviour).

For kriging, the cross validation method, specified in [6], is used to make predictions at the sample points. In this method, once the model parameters have been obtained through the nonlinear optimization algorithm, the value X_i is left out while predicting Y_i based on the $n – 1$

remaining points. This step must be performed as otherwise the kriging prediction would exactly reproduce X_i, which would be a misleading representation of its predictive capability.

In this study we focus on two objective functions, the total fill time and the maximum compression force for the manufacture of a 1m diameter composite disc of 1.5cm thickness, under non-isothermal processing conditions. The CSM, introduced earlier, is assumed to be the preform material (35% final fibre volume fraction) and is injected with a reactive epoxy resin [4]. Since the manufacturing process under consideration is the velocity-controlled CRTM, the wet compaction time is known beforehand. Therefore the functions we approximate are the resin injection time, the maximum force during resin injection and the maximum force during wet compaction. The design variable space is 5 dimensional and includes the injection pressure, the injection height, the velocity of wet compaction, the resin temperature and the temperature of the mould. 300 sample points are used for surrogate training and analysis. Fig.1 depicts the comparison between the computational and the CCA-NN based predictions for the desired functions. Not only is the correlation between the two visually apparent, the value of the correlation coefficient is further justification of the same.

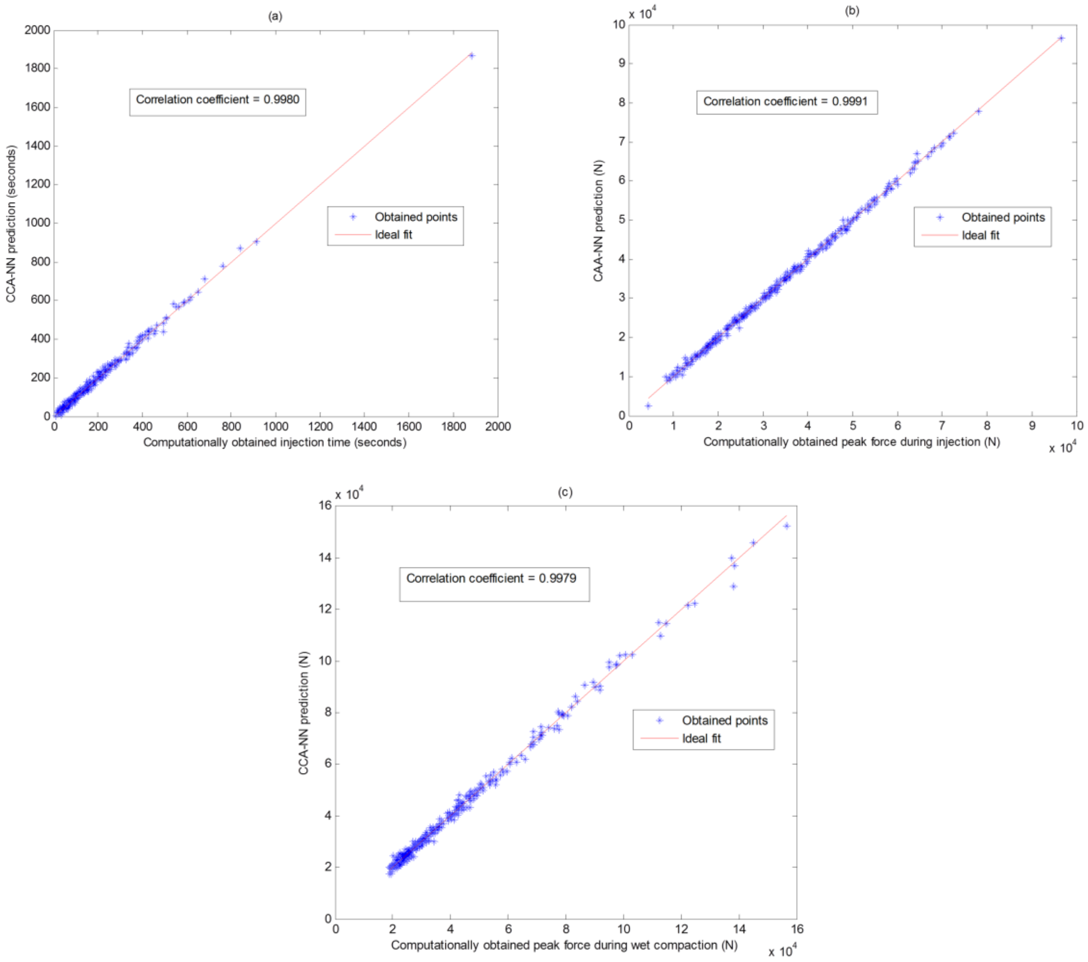

Fig.1: Comparison of CCA-NN predictions against actual function evaluations.

Fig .2 displays the comparison between the prediction of the kriging model and the computer simulation. Here, although the surrogate makes accurate comparisons in several cases, significant errors exist in many others. This fact is highlighted by the lower values of the correlation coefficient, as compared to the CCA-NN. However, it might be argued that leaving out an X_i would ordinarily require the model parameters to be re-evaluated, otherwise leading to the large prediction errors found. Even though dropping a single observation is known to have little effect on the maximum likelihood function [6], a second performance measurement criterion is used to confirm the superiority of the CCA-NN for the present problem.

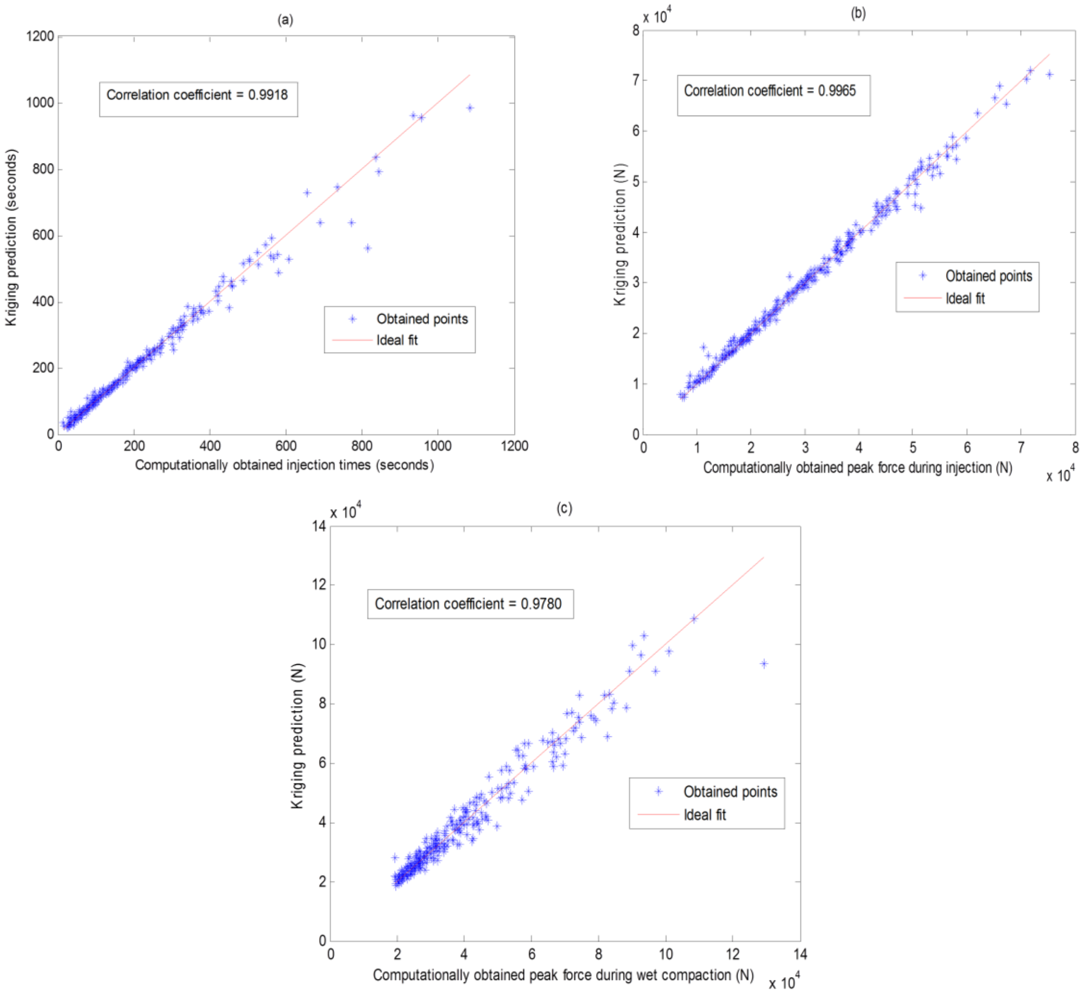

Fig. 2: Comparison of kriging predictions against actual function evaluations.

The total run-time of the resultant multi-objective GA that uses either surrogate for its function evaluations is a crucial factor. This is especially true in cases where the filling and curing phases are coupled and an iterative optimization strategy [2], which requires the filling phase to be repeatedly optimized, is employed. The design variable bounds for the GA are stated in Table 2. The mould temperature is assumed to be constant at 300 K and is not included as one of the design variables. The GA is run for 200 generations with a population size of 40.

Table 2: GA design variable bounds.

Description	*Lower bound*	*Upper bound*
Injection pressure (P_{inj})	200 KPa	450 KPa
Injection height (H_{inj})	1.6 cm	2 cm
Wet compaction velocity (V_{wet})	0.5 mm/min	2.5 mm/min
Resin temperature	293 K (20 ^{o}C)	348 K (75 ^{o}C)

Fig. 3a shows the Pareto front obtained by the GA using CCA-NN for its function evaluations and Fig. 3b shows the Pareto front when the kriging predictor is used. On close inspection it is found, not so surprisingly, that there is reasonably good agreement between the Pareto fronts obtained using either model. However, there is a significant difference in the run-times of the two optimization tasks. The CCA-NN based algorithm takes 14 seconds for one complete optimization run while the kriging based algorithm takes about 70 seconds for a serial computation on an Intel Core 3.33 GHz CPU (using the actual fill simulation would result in a run-time of at least a few hours for the same geometry).

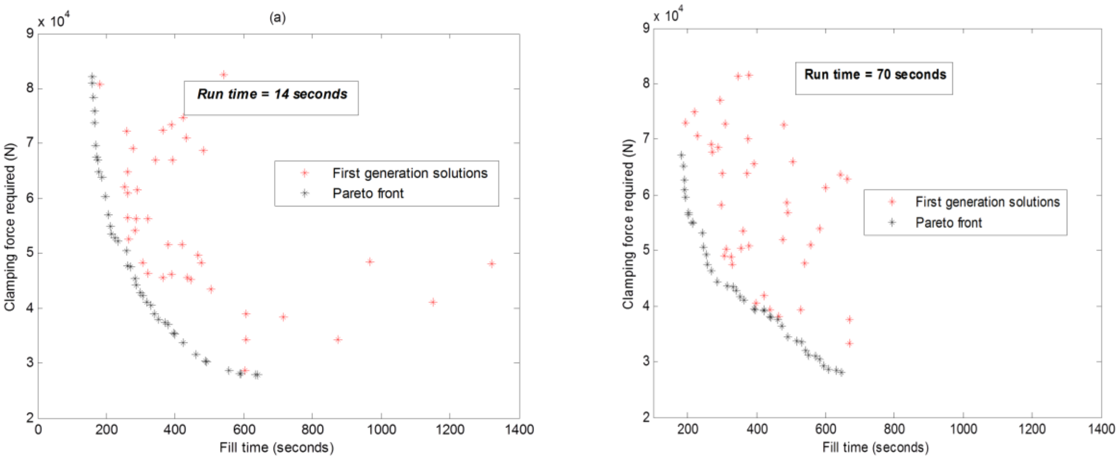

Fig. 3: (a) CCA-NN based Pareto approximation, (b) Kriging based Pareto approximation.

CONCLUSIONS

A comparison of two popular surrogate models is carried out in the present study with the aim of finding an accurate yet computationally cheap substitute for the fill simulation code. This study is considered to be of significant importance in terms of allowing the filling and curing phases of an LCM process to be coupled within a large optimization framework. We find that for the presented test case of an axisymmetric part the CCA-NN outperforms the kriging model in terms of both prediction accuracy and run-time. However, kriging models possess several interesting features, such as the ability to estimate expected improvements in their own predictions, which are not considered in this study. Therefore it is important to conduct a problem specific search over different surrogate models before choosing a particular one for the optimization algorithm.

REFERENCES

1. Walbran WA, Verleye B, Bickerton S, Kelly PA (2012), ‘Prediction and experimental verification of Normal Stress Distributions on Mould Tools During Liquid Composite Moulding’, Composites Part A: Applied Science and Manufacturing;43(1):138-149.

2. Ruiz E, Trochu F (2006), ‘Multi-criteria thermal optimization in liquid composite molding to reduce processing stresses and cycle time’, Composites Part A: Applied Science and Manufacturing;37: 913-924.

3. Ruiz E, Trochu F (2007). Coupled non-conforming finite element and finite difference approximation based on laminate extrapolation to simulate liquid composite molding

processes. Part II: Non-isothermal filling and curing. Science and Engineering of Composite Materials;14(2):113-144.

4. Gupta A, Kelly PA, Bickerton S, Walbran WA, Simulating the effect of temperature elevation on clamping force requirements during rigid-tool liquid composite moulding processes, *Under review, Composite Par A: Applied Science and Manufacturing*.

5. Fahlman SE, Lebiere C (1990), ‘The Cascade-Correlation Learning Architecture’.

6. Jones DR, Schonlau M, Welch WJ (1998),‘Efficient Global Optimization of Expensive Black-Box Functions’, Journal of Global Optimization;13: 455-492.

UNCERTAINTY QUANTIFICATION IN LIQUID COMPOSITE MOULDING PROCESSES

Bart Verleye [1], Dirk Nuyens [1], Andrew Walbran[3,2], and Ming Gan [2]

[1] *Dept. Computer Science, KU Leuven, Celestijnenlaan 200A, B-3001 Leuven, Belgium*
[2] *Centre for Advanced Composite Materials, University of Auckland, Private Bag 92019, Auckland, New Zealand*
[3]*Lehrstuhl für Carbon Composites, Technische Universität München, Boltzmannstraße 15, 85748 Garching bei München, Germany*
Corresponding author's e-mail: bart.verleye@cs.kuleuven.be

ABSTRACT: Variability of technical textiles plays an important role in Liquid Composite Moulding (LCM) processes and product quality. The numerical simulation of an LCM process depends strongly on the distribution of the volume fraction of the material. To obtain more realistic results, a distribution for the areal mass of the textile can be used as input, i.e., for every point of the mesh, an areal mass value is determined by a random field. The distribution used for the mathematical model has to be selected in agreement with the physical distribution. The random nature of the textile properties, make that different simulations have different results, although the simulations are created with the same macro parameters. This resembles the spread on experimental results and reveals the distribution of the output. To compute the average fill time or required tooling forces and their spreads, one can use the Monte Carlo (MC) method, being repeated random simulations, or the quasi-Monte Carlo (QMC) method, consisting of deterministic simulations of the random field. We show the QMC method to converge faster than the MC method and compare the obtained results with the results from a numerical simulation of the same LCM process without the usage of the random field to possibly differ a lot for certain outputs. One such output is the maximum fibre stress which is severely underestimated by the standard method.

KEYWORDS: *Variability, quasi-Monte Carlo, uncertainty quantification*

INTRODUCTION

Recently, variability and uncertainty quantification have been included in the simulation of LCM processes and textile qualification [2,3]. It has been shown that the variability of the permeability of the preform in a mould influences the fill time significantly [7]. Another example is the influence of the variability of textile parameters on the final part quality. To determine the influence of the variability, often experiments or simulations are performed and the average and variance are determined.

For the results presented here both the Monte Carlo (MC) method and the quasi-Monte Carlo (QMC) method have been used to generate instances of the random field. We show that the QMC method can give more reliable estimates using fewer simulations than the MC method. With these techniques, several parametric studies were performed to determine the influence of measured variability on the quality of the textile. These results are compared to the standard numerical simulation without using a random field for the areal mass. In such a simulation the random field values are replaced by the average value.

SIMULATION OF THE PROCESS

The process is modelled by applying *Darcy's law*, given by the elliptic PDE

$$\begin{cases} q + k\nabla p = q, \\ \nabla \cdot q = 0 \end{cases} \tag{1}$$

over a domain D in two physical dimensions. The flow solver uses a so-called 2.5D approach, the geometry is 3D but the flow in the through-thickness dimension is neglected [5]. For a point x in D, $p(x)$ denotes the *pressure head* of the fluid, $q(x)$ is the *filtration velocity* (or Darcy flux), $g(x)$ is the source term and the *hydraulic conductivity tensor* $k(x,\omega)$ is a random field dependent on a random event ω.

The conductivity tensor is assumed to follow a log-normal distribution with the following covariance function:

$$r(x,x') = \sigma^2 e^{\frac{-|x-x'|}{\lambda}} \qquad \text{for all } x, x' \text{ in } D \tag{2}$$

where $|x - x'|$ measures the Euclidean distance between the two points. The parameters σ^2 and λ are the *variance* and the *correlation length*. These two parameters are obtained from physical experiments (described in the next section) which specify the average m and standard deviation ν of the final field. The parameters for a normal random field with covariance from above are then obtained as

$$\sigma^2 = \log\left(\frac{\nu^2 + m^2}{m^2}\right) \tag{3}$$

$$\mu = \log(m) - \frac{\sigma^2}{2}, \tag{4}$$

and the final field is then constructed as

$$k(x,\omega) = e^{(\mu + K(x,\omega))}, \tag{5}$$

where $K(x,\omega)$ is simulated from the normal random field.

One way of solving this PDE is to generate random events ω in the form of random realizations of the conductivity tensor k by Monte Carlo simulations and then calculate the quantities of interest, which can be any linear or non-linear operator on q and p. It is then possible to undertake *uncertainty quantification* on these quantities of interest by calculating their mean, variance or any higher moments. The Monte Carlo method is compared to a method using a deterministic low-discrepancy sequence with few random shifts (to determine the accuracy of the simulation), called a randomized quasi-Monte Carlo method. This was recently studied in [4] and [6]. The simulated values are generated on a regular 2D grid using the technique of circulant embedding [1].

DETERMINING THE INPUT PARAMETERS

We now summarise the physical experimental measurements conducted to determine the *variance* and *correlation length* simulation parameters. The material selected for this study is a randomly orientated chopped strand mat (CSM), which exhibits random spatial variations in areal weight (AW) which is defined as the mass per unit area in units of grams per square meter (g/m^2). Further details of the selected material are provided in Table 1.

Table 1: Properties of the chopped strand mat, as provided by the supplier

Property	**Value**
Reinforcement type	Chopped strand mat
Manufacturer	Owens Corning
Suppplier code	M705-450 CSM
Nominal areal weight	450 g/m^2 +/- 10 %
Architecture type	Randomly orientated, emulsion bound

Spatial AW data for reinforcement layers is obtained using an experimental facility, consisting of a light box, digital camera and enclosure. See [3] for further details, experiments and AW maps figures. AW maps have been generated based on 290x450 mm^2 reinforcement samples, discretised using 7 mm sampling windows.

Based on six single layer samples of the CSM reinforcement, average (m) and standard deviation (ν) AW values of 445.32 g/m^2 and 91.65 g/m^2 respectively are obtained based on a Gaussian fit of the data. The *variance* can be calculated as the square of the standard deviation ν^2 =8399.72.

The mean AW is very close to the nominal value given in Table 1, however the standard deviation corresponds to a 21% variation from the mean, which is larger than that quoted by the supplier. Randomly orientated reinforcements are commonly employed for their homogeneity and isotropy, therefore it is important to quantify the level of variations as they can be used as a measure of quality when comparing reinforcements of similar AW.

The correlation length λ is determined more arbitrarily. The AW maps described above were compared with AW maps with different λ, generated as described in the previous section. A visual comparison resulted in λ = 0.007 as a good estimate. Fig. 1 shows an experimentally obtained AW map (left), and two generated AW maps, one with λ = 0.007 (middle) and one with λ = 0.02 (right). We clearly see that a too high λ results in too much clustering.

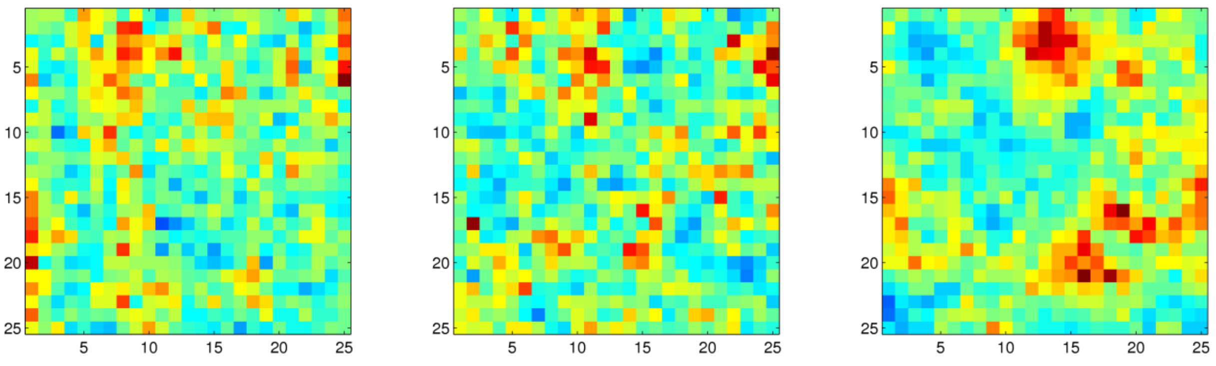

Fig. 1: Three areal mass maps: measured (left), for λ=0.007 (middle) and for λ=0.02 (right)

VALIDATION

In this section, the QMC method is validated for a realistic RTM application, and the convergence and accuracy of the QMC method compared to those of the MC method. With the technique described in the previous section, the average areal mass, standard deviation and correlation length were determined for the CSM (Table 1, $\lambda = 0.007$).

Table 2: Parameters of the injection simulations

Parameter	**Value**
Final height	3 mm
Injection pressure	87 kPa
Viscosity	0.19 Pa.s

With these numbers, eight independent simulations using 1024 random areal mass fields were created on a square domain with 25x25 grid points, both with the MC and the QMC method. For the Monte Carlo simulation this is the same as making 8x1024 = 8192 random simulations. For the randomized quasi-Monte Carlo method eight independent results are obtained based on 1024 deterministic samplings of the random field. These fields are input for the SimLCM software [5], which is used to simulate an RTM process with the parameters given in Table 2. From these simulations we retain two results: the time needed to fill the mould after the dry compression, and the maximum fibre stress after filling.

Fig. 2 presents the results of the simulations with both the MC (left) and QMC (middle) generated input fields for the fill time. In the left and middle panel the running average is plotted for each of the eight independent simulations. One can clearly see that the eight streams of approximations to the mean converge quickly towards each other in case of the QMC simulations. However, in the case of the MC simulation these results differ considerably. This is made clearer by the plot in the right panel which shows the convergence of the relative error on the average by plotting the standard error divided by the estimated value. The results show that the MC and QMC input result in the same average fill time, as expected, however, QMC yields a faster convergence to the result.

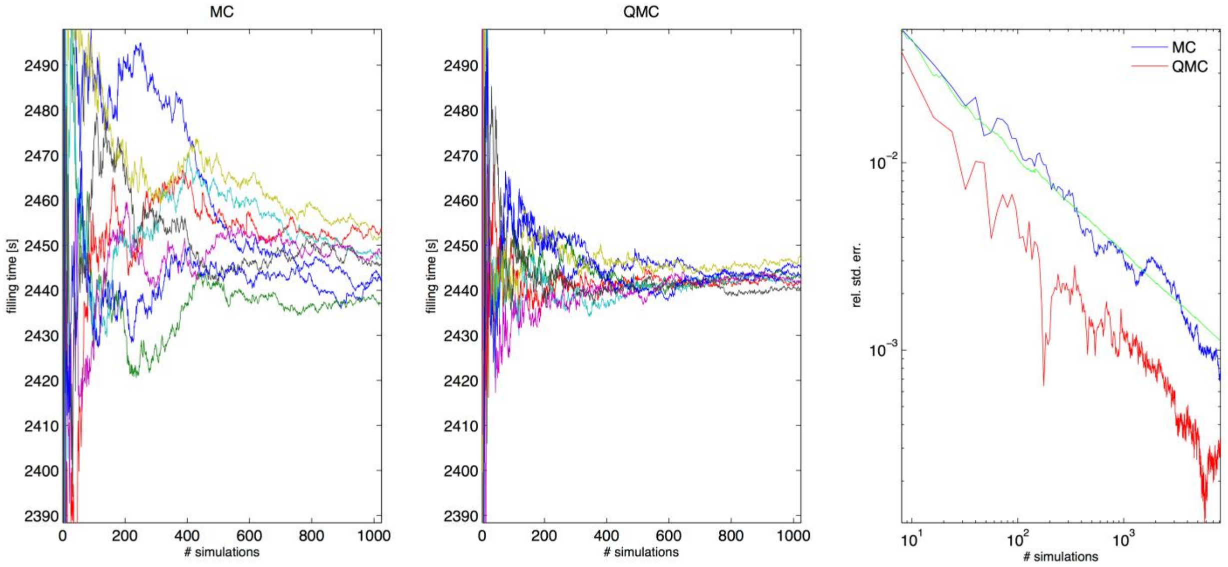

Fig. 2: Results of the Monte Carlo (left) and quasi-Monte Carlo (middle) simulation, the running average of the filling time. The convergence for both methods is shown on the right.

The fill time computed with a constant areal mass of 450 g/m^2 over the whole domain is 2432s, which is not significantly different from the average fill time of the experiments with a variational areal mass (Table 3). In this case, the inclusion of variability does not give us a better estimation of the average fill time, however, the variance on the fill time is an interesting parameter as it can be used to determine a confidence interval from which a maximum filling time could be set which leads to success in e.g. 98% of the cases.

The maximum preform stress at the end of the filling, computed for a constant areal mass of 450 g/m^2 using the standard LCM-processes simulation is 125 kPa. As can be seen in Table 3, this is much less than the average maximum computed with variability using the QMC method, and is certainly much less than the absolute maximum appearing in the simulation. In this case, the use of variability gives us much more information while the result of the standard LCM calculation is almost useless.

While only the maximum stress and the fill time have been discussed here, similar results for the minimum stress, variance of stress over the mould, etc. can be obtained using the QMC method. Moreover, for more complicated geometries, also the influence on the robustness of a particular injection scheme can be considered.

Table 3: Results of the QMC simulations with an average AW of 450 g/m^2 and both 10% variance (top row) and 20% variance (bottom row)

	Standard method	**Random field simulation by QMC method**				
		Average	Median	Min	Max	σ^2 (σ)
Fill time (s)	2432	2437	2433	2064	2930	11330 (106)
		2443	2425	1831	3747	48070 (219)
Max. preform stress (Pa)	1.25 E5	5.27 E5	5.08 E5	3.09 E5	1.33 E6	1.13 E10 (1.06 E5)
		2.03 E6	1.84 E6	6.07 E5	1.14 E7	7.07 E11 (8.40 E5)

PARAMETRIC STUDY

Fig. 3 shows the computed histograms of the fill time for three different cases. The left subfigure is the result of a simulation with an AW of 250 g/m^2 ± 10%. The middle figure is for an AW of 450 g/m^2 ± 10%. The right figure is the histogram of the above discussed simulation, with the areal weight 450 g/m^2 ± 20%. As expected, the average fill time for the lower AW is less than in the case of the higher AW. The histogram for the AW of 250 g/m^2 is not symmetric, as for very low AW, the fill time converges to the one of an empty mould. Note that the bins for the left and right figure were generated automatically, but that for the middle figure the bins of the right figure were used to allow comparison.

For the study with higher variance, the average fill time and maximum of the preform stress are also mentioned in Table 3. Also in Table 3 are the medium, the minimum, the maximum and variance of these parameters for both the low and high variance input. For the fill time, we can conclude that the variance on the AW has little influence on the average, however, the spread on the fill time is much larger for a highly variable AW. For the maximum of the preform stress, the variance on the input has a significant influence on both the average and the spread of the maximum. Introducing a variance of 10% results in a four times larger average. Going from a 10% to a 20% variance also doubles the resulting average maximum stress. This shows that variance is an important parameter to consider in simulations that help to choose materials and tooling.

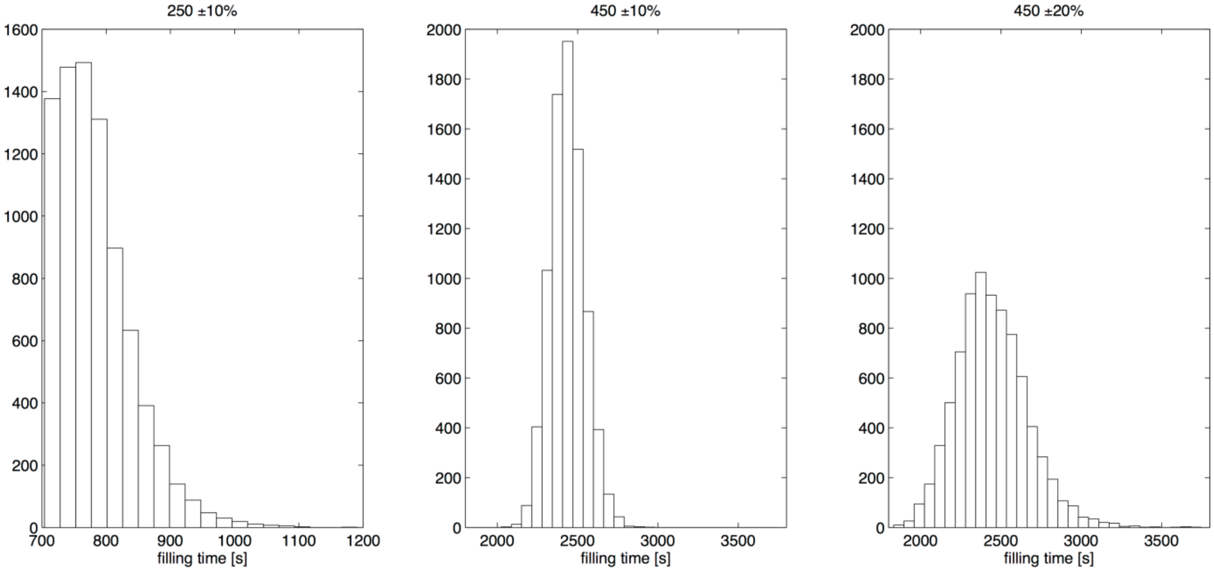

Fig. 3: Histograms of the fill time for three different simulations. The middle panel shows the results of the simulations with the parameters provided by the manufacturer (Table 1). For the left panel the AW was changed to 250 g/m^2, for the right panel the variance was changed to 20%.

CONCLUSIONS

The variability of the areal mass of a preform, has a significant influence on LCM processes. To predict robustness and quality of production lines, variability must be included into the simulations. In this paper we presented the use of the quasi-Monte Carlo method to introduce the variability, and showed to have faster convergence than with the often used Monte Carlo method in the case of computing the fill time.

It was shown that the variability of the areal weight has little influence on the average fill time, however, it does have an influence on the spread of the fill time. The maximal stress in the preform is highly influenced by the variability of the input. In this case, introducing a variability of 10%, results in a four times higher average compared to a standard simulation with constant areal mass.

REFERENCES

1. Dietrich CR and Newsam GH (1997), ‘Fast and exact simulation of stationary Gaussian processes through circulant embedding of the covariance matrix’, *SIAM Journal on Scientific Computing*, 18(4), 1088-1107.

2. Endruweit A and Long AC (2006), ‘Influence of stochastic variations in the fibre spacing on the permeability of bi-directional textile fabrics’, *Composites Part A*, 37(5), 679.

3. Gan JM, Bickerton S, Battley M (2012), ‘Quantifying variability within glass fiber reinforcements using an automated optical method’, *Composites Part A*, accepted, http://dx.doi.org/10.1016/j.compositesa.2012.03.024

4. Graham IG, Kuo FY, Nuyens D, Scheichl R and Sloan IH (2011), ‘Quasi-Monte Carlo methods for elliptic PDEs with random coefficients and applications’, *Journal of Computational Physics*, 230(10), 3668-3694.

5. Kelly PA and Bickerton SA (2009), ‘Comprehensive filling and tooling force analysis for rigid mold LCM processes’, *Composites Part A*, 40(10).

6. Kuo FY, Schwab C and Sloan IH (2012), ‘Quasi-Monte Carlo finite element methods for a class of elliptic partial differential equations with random coefficients’, Hausdorff Institute for Mathematics Preprint #2011b08, Bonn, Germany.

7. Sriramula S, Chryssanthopoulos MK (2009), ‘Quantification of uncertainty modelling in stochastic analysis of FRP composites’, *Composites Part A*, 40(11):1673–84.

NUMERICAL ANALYSIS OF POST FILLING FLOWS USING COMPLIANT TOOLS

Florian Klunker [1] , Widyanto Surjoseputro [2], Santiago Aranda [2],
Daniel Beermann [2] and Gerhard Ziegmann [2]

[1] *Centre of Structure Technologies, Swiss Federal Institute of Technology Zurich, Leonhardstrasse 27, CH-8092 Zurich, Switzerland.*
[2] *Institute of Polymer Materials and Plastics Engineering, Clausthal University of Technology, Agricolastrasse 6, D-38678 Clausthal-Zellerfeld, Germany. Corresponding author's e-mail: widyanto.surjoseputro@tu-clausthal.de*

ABSTRACT: A methodology for a fully coupled post filling flow is applied. This methodology can be extended in future works to different processes like the impregnation of textiles in vacuum assisted resin infusion (VARI), compression RTM or similar processes, where the flow is affected by the transversal deformation of the textile. As in this paper the post filling flow is addressed, the results can be used e.g. for the post filling phase in VARI or for the compression phase in prepreg processes. The results indicate that in unconstrained 1D-flows an up-scaling rule can be applied, meaning by knowing the post-filling flow for small samples, the result in larger structures can be predicted by simple rules: If the textile shows elastic properties, the ratio of processing times for reaching a certain post-filling stage (final thickness, pressure distribution) is increasing with the square of the ratio of part length.

KEYWORDS: *Post-filling flow, flow simulation, thickness equilibration, up-scaling, vacuum assisted resin infusion.*

INTRODUCTION

Recent trend in the composite industries, especially in aircraft industries, shows a tendency toward large complex composite structures. Some large industrial applications like in aeronautics, shipbuilding or wind-energy are commonly manufactured using composite manufacturing process involving compliant tools such as the vacuum bag in Vacuum Assisted Resin Infusion (VARI). In the development, it is strived to manufacture large complex composite structure entirely in VARI in just one infusion step. Fig. **1** shows an example of the complexity of an aircraft fuselage for possible future manufacturing in one-shot VARI. Here, choosing the right infusion strategy is one of the big challenges, since it must assure the full impregnation of the whole structure in the targeted time and minimize the risk of a failed process.

The main particularity of VARI compared to other LCM processes is that the thickness of the part changes throughout the entire process, depending on the governing stresses applied on the preform. Thus, the pressure gradient as driving force for flow during the infusion also means thickness gradient on the entire part. As it is known, thickness and respectively the fibre volume fraction are decisive for the mechanical properties of the final parts [1]. Therefore in VARI, the post-filling stage or the time period right after the closing of infusion line is very important, since the final thickness of the part depends on the pressure equalization taking place in this stage. In practice, the post-filling stage is limited by the gel time of the resin.

Fig. 1: Segment of Airbus A350XWB fuselage (Source: Premium Aerotech)

In the past, the post-filling flow has already been investigated. In [2], an approach for simulating the post-filling behaviour has been introduced. In the investigation, post-filling flows mainly in membrane VARTM with various venting strategies was observed. However, the investigation was limited on a single fabric dimension. In the simulation it was assumed that there is no plastic or viscous component in the deformation model [2]. It was also mentioned that in the validation experiments a better compaction characterization is needed to diminish some inaccuracies in the comparison between predicted and measured values [3].

Further investigations on post-filling are necessary, since flow simulation of infusion and post-filling flow for a large complex structure is related with high modelling effort and calculating time. Any simplification that can allow a prediction of flow behaviour in large complex structure based on a smaller and simpler model will reduce the simulation efforts. While in the infusion stage simulation an up-scale rule can be applied to the infusion behaviour [4], for post-filling flow such an approach until now has not yet been investigated. This paper addresses the up-scaling methodology for post-filling flow.

SIMULATION OF POST-FILLING FLOW

The flow in textiles is modelled as flow in porous media. An important relationship to describe the flow in porous media is Darcy’s Law:

$$v = -\frac{K}{\eta}\nabla p \qquad (1)$$

where v is the volume averaged fluid velocity, K the permeability tensor, η the resin viscosity and p the pressure field in the fluid.

In VARI like processes with involving one-sided tooling, flow in textiles is considered as flow in deformable porous media. Thus, Darcy’s Law has to be combined with the mass balance. In case of incompressible fluids it can be rewritten as [2]:

$$\nabla \cdot v = -\dot{\varepsilon} = -\frac{\dot{V}}{V} \tag{2}$$

where $\dot{\varepsilon}$ is the volumetric linear strain rate which can also be expressed as the relative change of an elementary volume V. For the evaluation of the volume change the flow is coupled with structural analysis. Assuming that the deformation of a textile is only in the through thickness direction, its Young's Modulus is defined by

$$E = \frac{\sigma}{\varepsilon} \tag{3}$$

where σ describes the stress acting on the fibre due to the compaction, which are determined in compaction experiments. For this paper, the Poisson ratio is set to 0.

The stress acting on a textile can be described according to Terzhagi's principle of effective stress [2,5]. The Terzaghi`s principle describes the interaction between the solid phase of a porous medium (the fibre reinforcement) and the porous phase (the matrix). This principle states that the effective stress applied on the fibre reinforcement is the difference between the total stress applied on the porous medium and the stress from fluid pressure of the matrix surrounding the fibres. Assuming the compressibility of the reinforcement and the absence of internal forces, the result is that any change in this equilibrium produces a deformation (in this case transversal deformation) of the porous medium. Particularised for the case of a resin infusion, the Terzaghi`s principle can be expressed as:

$$\sigma_{fib.} = \sigma_{ext.} - \sigma_{fluid} \tag{4}$$

where σ_{fib} is the stress from compaction on the fibre reinforcement, σ_{ext} is the stress from outside the cavity (usually atmospheric pressure) and σ_{fluid} is the stress from the pressure of the fluid in which the fibres are embedded. Thus, σ_{fluid} is the vacuum pressure before the impregnation and the resin pressure after the impregnation. The pressure difference of atmospheric pressure and fluid pressure acts as force constraint on the top of the part, causing reinforcement deformation, depending on the initial condition of the part.

UPSCALING RULES FOR 1D-POST FILLING FLOWS

An example of a simulation is shown in Fig. 2. A rectangular plate, representing the wetted textile preform, is fixed on the bottom, the top of the plate represents the side with the vacuum bag, the vent is located on the left side of the plate and the right side is a symmetric boundary condition. The colour represents the pressure distribution in the plate. The figure shows the situation, that a fully saturated textile with a homogeneous fluid pressure and therefore with a constant thickness is vented to a lower pressure level, which results in a time depending decrease of thickness going from the left to the right.

For evaluating and comparing results, two normalized positions are introduced (see Fig. 2):

(i) The normalized position $\beta = x/c_f\,(t)$, where $c_f(t)$, describes the compaction front. For the definition of the compaction front a pressure value close to maximum pressure was set. This is further referred to as reference pressure. The value of this pressure was chosen to be 99750 Pa, so close to the absolute atmospheric pressure of 1x10^5 Pa. According to this reference pressure for different pre-defined reference time t_r (10 s to 40 s in steps of

10 s), the point with a pressure value closest to the reference pressure was chosen to be the reference point. This reference point is defined as $x/c_f\,(t_r) = 1$.

(ii) The referential coordinate $\alpha = x/L$, where L is the length of the part.

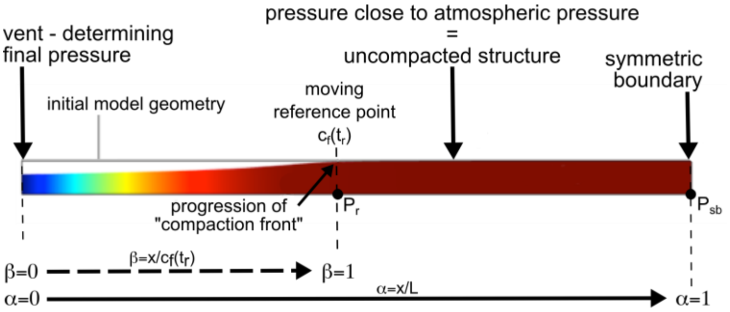

Fig. 2: Sketch of the simulation model for post-filling flow

In Fig. 3 (left) the pressure distribution is shown as a function of a normalized position β for t_r. As it can be seen, the simulation shows a perfect match of the pressure curves, which indicates, that an up-scaling law can be applied, as e.g. it was done for vacuum infusion processes [4].

The same simulation was also conducted with different lengths and heights. Fig. 3 (right) shows the comparison of the pressure course from different lengths and heights as a function of normalized time t_n. Instead of measuring the pressure at the reference point, the pressure was evaluated at the bottom of the symmetry boundary (at P_{sb} Fig. 2). The normalized time is defined as $t_n = t/t_r$, with t_r denoting the reference time which is needed, until the pressure at P_{sb} decreased to less than 500 Pa. Also here a good match can be observed.

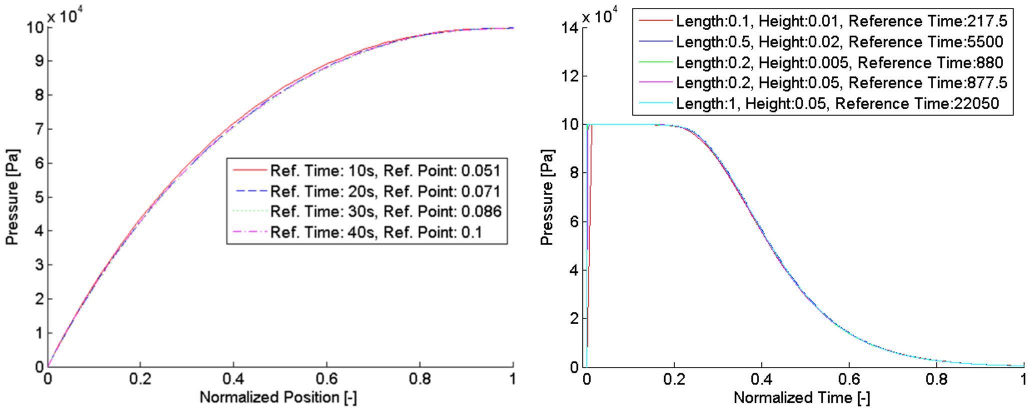

Fig. 3: Pressure distribution in post-filling flow simulation (left: normalized position for different times, right: normalized time for different length and height)

The results lead to the conclusion, that a similar behaviour to unconstrained flow in VARI is taking place in this process. Comparing the ratios of the reference times and reference points provide the validation of this observation: If the position of the point of interest doubles, the time will be four times higher to reach the same pressure status. Thus, in 1D-flows for various lengths these up-scaling rules can be applied, if the textile has elastic properties and a compaction is possible which is not constrained by the mould:

$$p\left(k_l x, {k_l}^2 t\right) = p(x,t), \tag{5}$$
$$t\left(k_l x, {k_l}^2 t\right) = t(x,t), \tag{6}$$

where p is the fluid pressure, t the part thickness, x the position of interest in the part, t the time and k_l the up-scaling factor in length. Theoretically, changing the height does not affect the duration of the post filling flows in 1D-flows. Therefore, it has to be noticed that an ideal assumption was used in the simulation, not taking shear forces into account. In the reality, factors such as mechanical interaction of textile layers, especially for thick laminate, could show different results. This has to be investigated in future works.

EXPERIMENTAL VALIDATION OF POST-FILLING FLOW

Materials

The textile was an unbound random E-glass fibre mat (S415N from Quadrant Plastic Composite AG) with an approximate areal weight of 415 g/m^2. The fluid was the silicon oil Rhodorsil huile 47 V 100 HT with a viscosity of 0.1 Pas.

Analysis of the compaction behaviour

It has been already reported in several works, that the fibre reinforcement under transversal compaction behaves in a viscoplastic-elastic way [6,7]. Repeating cyclic compaction experiments were performed in a universal testing machine in order to understand the compaction behaviour of the textile under repeated loading. Each cycle consists of three stages (see Fig. 4, left): a compression stage at constant pressure rate change until a maximum pressure of 0.1 MPa, a creep phase, where the porous medium can deform under constant maximum pressure for a given time (ten minutes) and a last release phase where the compressing load is discarded evenly at a constant rate.

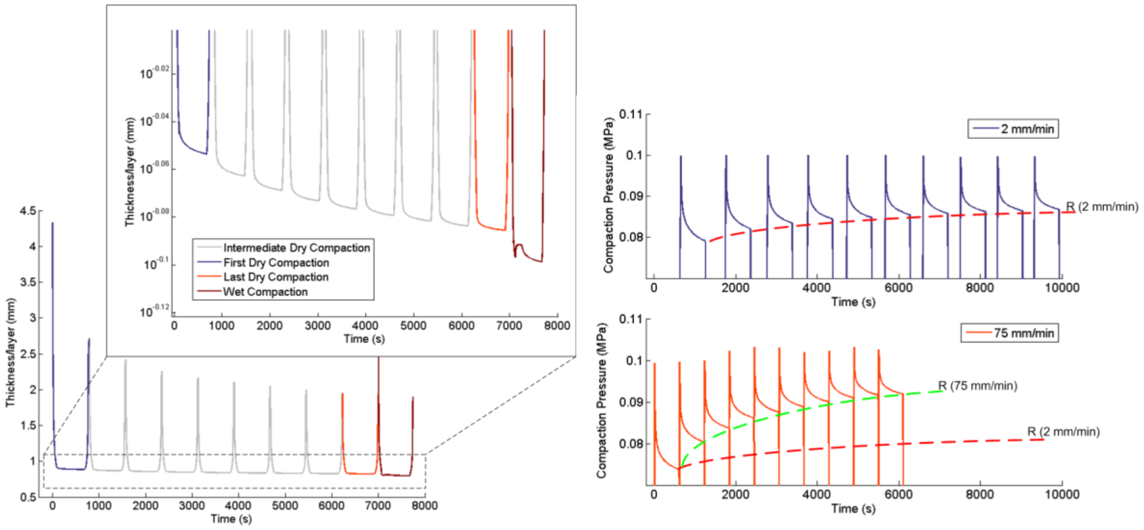

Fig. 4: Cyclic compaction of the glass fibre random mat. Left side (force controlled compaction): asymptotic thickness reduction during the creep intervals in cyclic dry/wet compaction. Right side (deformation speed controlled): mitigation of the time-dependent behaviour in dry compaction/relaxation cycles.

The experiment consisted of ten repetitions of the described cycle. The first nine cycles run under dry conditions. Between the ninth and the tenth compactions, the fibre was impregnated with a natural oil, so that the last cycle can be considered a wet compaction cycle. Additional experiments at constant deformation speed conditions were carried out in order to study the relaxation behaviour under constant deformation (see Fig. 4, right).

Fig. 4 shows that after nine compaction cycles a virtually repeatable compaction hysteresis is reached, suggesting an almost exclusive entirely visco-elastic behaviour. In fact, the last dry compaction cycles give almost the same curve σ/ε producing no significant permanent deformation after each compaction cycle. Additionally, the analysis of the experiments leads to the conclusion that the repeated compaction cycles reduce the time-dependent behaviour (viscoelasticity) of the material. Through these repeated cycles, the textile is prepared for a reproducible impregnation phase, where the compaction history of the material has been reset. That leads to more reproducible results in the post-filling stage, which is definitely decisive for the final thickness of the laminate.

Experimental setup

For the post-filling flow experiments, a metal tool with seven integrated pressure sensors, not in contact with the textile, was used to monitor the pressure at different locations during the experiments (Fig. 5). The pressure changes were measured at one-second intervals and monitored using LabView data acquisition software. It has to be noticed that in the experiments conducted in this study the thickness change is not observed.

In each experiment, eight layers of textile were placed at the centre of the tool and bagged with a flexible vacuum film. Three different fabric dimensions of 15 cm, 20 cm and 30 cm were chosen for the experiments. All layers have the same width of 20 cm to ensure that no boundary effect is affecting the measurement. Silicone oil as non-curing infusion liquid allowed a pressure equilibration without flow time restrictions. The position of the infusion bucket was on the laboratory floor, approx. one meter below the tool.

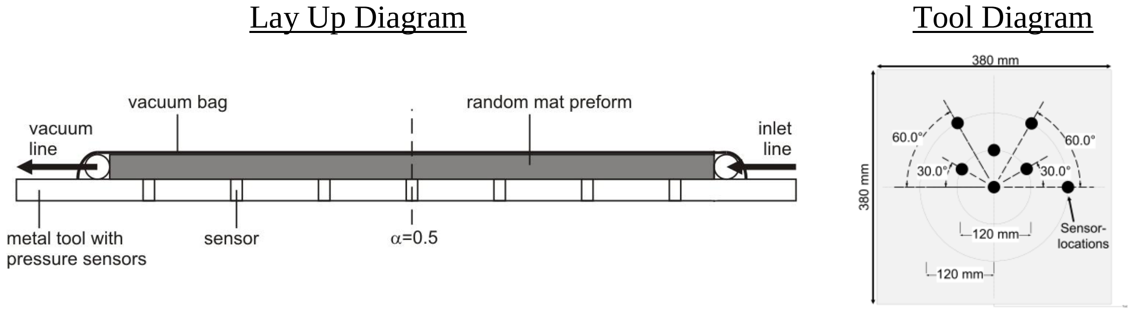
Lay Up Diagram

Tool Diagram

Fig. 5: Experimental setup and sketch of sensor locations

Experimental procedure

In each experiment, prior to the infusion, the textile stack is being pre-conditioned by conducting ten cycles of dry compaction. The setup of vacuum equipment allowed a quick switch of the relative pressure from -200 mbar to -500 mbar and vice versa. One cycle of compaction means here that the fabric is compacted from -200 mbar to -500 mbar and then released to -200 mbar. In the experiments ten cycles of dry compaction were applied on the fabric.

After the pre-compaction, silicon oil was injected at -200 mbar. Like in conventional VARI, the liquid injection line was closed after the infusion was completed. With the closing of the injection line, the first post-filling stage started to take place until the liquid pressure is equalized at the vent vacuum level of -200 mbar. From this equally distributed pressure field, the vent vacuum level was increased to -500 mbar, allowing the post-filling flow to continue until this new vacuum level was reached. At the end of the second post-filling flow, the vacuum pressure level was switched back to -200 mbar and the injection line was opened again allowing second infusion cycle to take place in order to increase thickness. After this, the fluid pressure was again equalized at -200 mbar and -500 mbar, as mentioned above. The experiment is conducted for three different fabric lengths of 15 cm, 20 cm and 30 cm.

RESULTS AND DISCUSSION

The referential coordinates α of the sensors is depending on the preform length L. For validation of the Eqn. 5, the pressure sensor signals from similar α-values have been compared in the second equilibration stage, i.e. the decrease from -200 mbar to -500 mbar.

The original curves of pressure courses during the post-filling flow in the two cycles for three different lengths for $\alpha = 0.5$ can be seen in Fig. 6 (a). According to Eqn. 5, the ratio of the times needed to reach a certain pressure level is equal to the square of the ratio k_l of the lengths of two parts, which is applied here to normalize the time by multiplication of ${k_l}^2$. Applying this to the pressure curves in Fig. 6 (a) with 20 cm length as a reference length will give a new diagram with the normalized relative pressure $p/\max(abs(p))$ as a function of normalized time as seen in Fig. 6 (b).
Fig. 6 (c) shows the normalized values for a relative position of within the interval of 0.775 to 0.925.

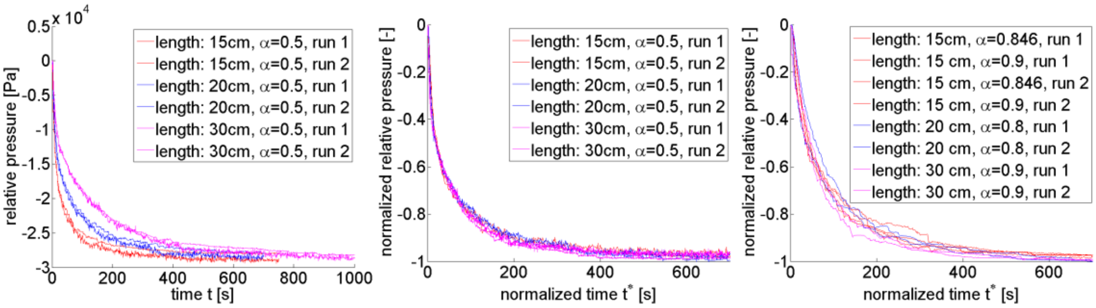

(a) (b) (c)

Fig. 6: Pressure courses during post-filling flows for different lengths. (a) $\alpha = 0.5$, in original time; (b) $\alpha = 0.5$, in modified time scale; (c) $\alpha = 0.85 \pm 0.075$, in modified time scale

Fig. 6 (b,c) show that the normalized curves match each other, despite the various lengths and the positions within the samples. Given the fact that these experimental results resemble the simulation result (see Fig. 3), it can be concluded that in case of elastic textile properties it is possible to apply an up-scaling function to predict post-filling behaviour of various lengths of part.

As it can be seen at Fig. 6 (a), the pressure is immediately decreasing after switching the pressure level, which is also the case at all positions in the setup. With totally elastic properties of the textile this behaviour cannot be predicted, as the simulation showed the development of a "compaction front" (see Fig.3, left and right). First trials with a time dependent Young's modulus show, that this pressure decrease, starting at the same time in all locations can be due to viscoelastic effects, which has to be investigated further. Nevertheless, due to pre-compaction cycles, this effect could be minimized, so that the up-scaling laws could be validated.

CONCLUSIONS

In processes involving compliant tool, up-scaling rules can be applied for post-filling flow stage, provided that the textile show elastic behaviour. Experiments using random glass fibre mat have shown that these rules are not applicable for un-compacted textiles, due to its viscoplastic-elastic behaviour, which depend strongly on the compaction history. A pre-conditioning of the reinforcement as a part of a preforming process consisting of repeated compression/release cycles will diminish their plastic deformation during each compaction as well as the visco-elasticity, which will lead to a more reproducible and predictable post-filling stage.

The up-scaling rules can be use to predict the post-filling stage for various lengths of part. However, further investigations are needed regarding the effect of thickness and other textiles on the scalability of post-filling flow.

REFERENCES

1. Rudd CD, Long AC, Kendall KN and Mangin CGE (1997), Liquid Moulding Technologies, Cambridge: Woodhead Publishing Ltd..

2. Simacek P, Heider D, Gillespie Jr. JW and Advani S (2009), 'Post-filling flow in vacuum assisted resin transfer molding processes: Theoretical analysis', *Composites Part A: Applied Science and Manufacturing*, 40, 913-924.

3. Simacek P, Eksik Ö, Heider D, Gillespie Jr. JW and Advani S (2012), 'Experimental validation of post-filling flow in vacuum assisted resin transfer molding processes', *Composites Part A: Applied Science and Manufacturing*, 43, 370-380.

4. Correia NC, Robitaille F, Long AC, Rudd CD, Simacek P, Advani S (2005), 'Analysis of the vacuum infusion moulding process: I. Analytical formulation', *Composites Part A: Applied Science and Manufacturing*, 36, 1645-1656.

5. Lancellota R, Ehlers W and Bluhm J (Eds.) (2002) Coupling between the evolution of a deformable porous medium and the motion of fluids in the connected porosity. In Porous Media. Theory, Experiments and Numerical Applications. Berlin Heidelberg: Springer-Verlag.

6. Kelly PA, Umer R, Bickerton S (2006), 'Viscoelastic response of dry and wet fibrous materials during infusion process', *Composites Part A: Applied Science and Manufacturing*, 37, 868–873.

7. Comas-Cardona S, Le Grognec P, Binetruy C and Krawczak P (2007): Unidirectional compression of fibre reinforcements. Part 1: A non-linear elastic-plastic behaviour. *Composites Science and Technology*, 67, 504–517.

MONOLITHIC VERSUS DECOUPLED APPROACH TO COUPLE STOKES/DARCY FLOWS IN EXTREME REGIMES FOR LCM PROCESS MODELLING

L. Abou Orm[1], R. Troian[1,2], J. Bruchon[1], N. Moulin[1,2], P.-J. Liotier[1] and S. Drapier[1]

[1] *Mechanics and Materials Science Division & LTDS UMR CNRS 5513, Ecole Nationale Superieure des Mines de Saint-Etienne, Saint-Etienne, France.*
[2] *ARMINES, Paris, France*
Corresponding author's e-mail : drapier@emse.fr

ABSTRACT: The present contribution is devoted to developing robust finite element solutions for coupling flows in both purely fluid region, ruled by Stokes equations, and fibrous preform region governed by a Darcy's law. Particularly the cases of low permeability of preform, down to 1E-15 m^2, are of interest to model LCM processes. Both a decoupled approach, as proposed by Celle et al.[1], and a monolithic approach, as proposed by Pacquaut et al. [2] are investigated in severe regimes. Flows are solved using mixed finite elements, stabilized respectively with a bubble function (P1+/P1 mini-elements) and a sub-grid scale stabilization technique (ASGS) [3]. A special attention is paid to the interface conditions, namely normal stress and velocity continuity and tangential velocity constraint similar to a Beaver-Joseph-Saffman's condition. First, in the cases of flows normal and tangential to the Stokes-Darcy interface convergence rates are investigated, and a comparison with available analytical solutions is carried out. Second, the Method of Manufactured Solution is used to assess the convergence rate along with the solution robustness. From this comparison, it is shown that provided a very special attention is paid to the coupling conditions, very precise results can be obtained. More precisely, the decoupled approach has been stabilized regarding the system conditioning, with appropriate penalty factors which depend now on the physics of the problem. This approach is under validation in an industrial framework. As for the monolithic approach, it is now perfectly robust due to the introduction of the ASGS sub-grid scale stabilization, and is being assembled with thermo-physico-chemistry of the resin.

KEYWORDS: *Stokes, Darcy, decoupled approach, monolithic approach, rates of convergence, manufactured solutions.*

INTRODUCTION

Resin infusion-based processes are used for manufacturing large structures of good quality (low void content) with high fiber volume fraction. For instance, to manufacture rotor blades or boat hulls, these processes have been developed to solve the filling problems associated with the Resin Transfer Molding processes (RTM). Resin infusion-based processes consist of infusing liquid resin through the thickness of the reinforcement rather than in the plane. They can be modeled as follows: a mold contains initially the resin (a purely fluid domain) and preforms (a porous medium). Under the effect of a mechanical pressure applied on the whole stacking, the resin flows into the preforms which can be seen as a porous medium undergoing large deformations.

This paper proposes to focus on the Stokes–Darcy coupled problem, the main coupled problem to be validated prior to simulate numerically the filling stage in resin infusion-based processes using the finite element method. The Stokes–Darcy coupled problem has been studied by many researchers and is still a great challenge in many fields of engineering. The main strategies found in the literature to solve the coupled problem are either a decoupled strategy which consists of using two different structured meshes to solve the Stokes and the Darcy equations [1], or a monolithic strategy which consists of using a single non-necessarily structured mesh [2].

MATHEMATICAL FORMULATION

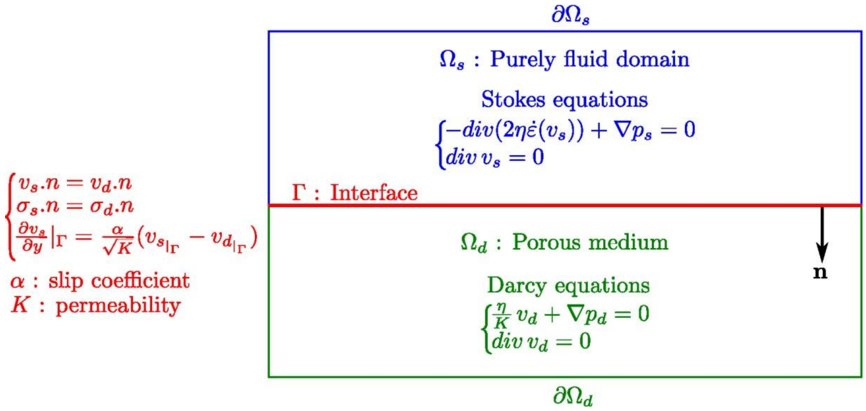

Fig. 1: Stokes-Darcy coupling. Governing equations and interface conditions.

In order to model Stokes/Darcy coupling let us consider a bounded domain Ω formed by two non-overlapping subdomains Ω_s and Ω_d separated by a surface $\Gamma = \partial\Omega_s \cap \partial\Omega_d$ (Fig. 1). Index s is used to denote everything that concerns the purely fluid part (Stokes' domain), and index d for modeling porous medium (Darcy's domain of permeability K). Ω_s is the region occupied by the fluid, the motion of which is described by completing the Stokes equations with the equation of mass conservation, and the incompressible Newtonian fluid flow in Ω_d, the porous medium with low permeability, is governed by a Darcy law of momentum conservation (Fig. 1). Moreover boundary conditions must be considered on the interface Γ. These conditions are continuity of normal velocity, continuity of normal stresses and the Beaver-Joseph-Saffman condition (α is equivalent to an apparent friction).

The general method for dealing with incompressible flow and solving Stokes and Darcy equations in steady state is classically based on mixed velocity-pressure formulation to cope with mass conservation issues. Although the form of Darcy's equation permits to solve separately for velocity and pressure, for consistency mixed formulations are considered also. In our case, linear approximations for velocity as well as pressures are chosen.

MONOLITHIC APPROACH

This section is focused on coupling Stokes-Darcy by using one single mesh for the fluid and the porous domains. A level set method is used to represent the Stokes-Darcy interface and to capture the moving flow front. The discretization is ensured by using a mixed velocity-pressure formulation. Velocity and pressure are approximated by linear and continuous element stabilized with an ASGS (Algebraic Subgrid Scale) method [3].

The basic idea of this method is to approximate the effect of the component of the continuous solution which cannot be captured by the finite element solution. It consists in splitting the continuous solution for velocity and pressure into two components, one coarse corresponding to the finite element scale (v_h and p_h), and a finer scale ($v'$and p') corresponding to lower scales for resolutions. The velocity is approximated as $v = v_h + v'$ and the pressure field is approximated as $p = p_h + p'$. Among the sub-grid scales methods, the ASGS method consists in taking the projection operator onto the fine scales as the identity operator when acting on the finite element residual [3].

The whole computational domain $\Omega \subset R^d$is discretized with one single unstructured mesh. This mesh is made up of triangles if $d = 2$ and of tetrahedrons if $d = 3$. Velocity and pressure fields are approximated by the continuous fields v_h and p_h, which are piecewise linear. For the sake of simplicity, we choose to write the inner product on L^2 as $< >$. The variational formulation of the problems consists in finding a velocity-pressure pair $[v_h, p_h]$such that

$$B_s([v_h, p_h], [w_h, q_h]) = L_s([w_h, q_h])$$

for any test function $[w_h, q_h]$, where the bilinear stabilized form B_s and the linear form L_s are defined in Stokes by (c_1 is a numerical constant to be determined and h_k is a characteristic of the mesh element size):

$$\begin{aligned} B_s([v_h, p_h][w_h, q_h]) = 2\mu\langle\dot{\epsilon}(v_h), \dot{\epsilon}(w_h)\rangle - \langle\nabla.w_h, p_h\rangle - \langle\nabla.v_h, q_h\rangle + \\ +\tau_p \textstyle\sum_K \langle\nabla.v_h, \nabla.w_h\rangle + \tau_u \textstyle\sum_K \langle-\mu\Delta v_h + \nabla p_h, \mu\Delta w_h - \nabla q_h\rangle, \\ L_s([w_h, q_h]) = \langle f, w_h\rangle + \langle h, q_h\rangle + \tau_p\langle h, \nabla.w_h\rangle - \tau_u\langle f, \nabla q_h\rangle, \\ f = -\nabla.\big(2\mu\dot{\epsilon}(v)\big) + \nabla p, h = -\nabla.v, \tau_u = {h_k}^2 c_1\mu, \tau_p = c_1\mu \end{aligned} \tag{1}$$

and in Darcy by (l_u and l_p are characteristic lengths):

$$\begin{aligned} B_s([v_h, p_h], [w_h, q_h]) = \frac{\mu}{k}\langle w_h, v_h\rangle - \langle\nabla.w_h, p_h\rangle - \langle\nabla.v_h, q_h\rangle + \\ +\tau_u \textstyle\sum_K \langle\frac{\mu}{k} v_h + \nabla p_h, -\frac{\mu}{k} w_h - \nabla q_h\rangle + \tau_p \textstyle\sum_K \langle\nabla.v_h, \nabla.w_h\rangle, \\ L_s([w_h, q_h]) = \langle f, w_h\rangle + \langle h, q_h\rangle + \tau_p\langle h, \nabla.w_h\rangle - \tau_u\langle f, \nabla.q_h\rangle, \\ f = \frac{-\mu}{k} v + \nabla p, h = -\nabla.v, \tau_u = {h_k}^2 \frac{k}{\mu}\frac{1}{l_u^2}, \tau_p = \frac{\mu}{k} l_p^2. \end{aligned} \tag{2}$$

For Stokes and Darcy flow coupled through interfaces, the three boundary conditions that must be enforced are: continuity of normal velocity, continuity of normal stresses and Beavers-Joseph-Saffman condition which describes the relationship between the stress vector in Stokes $\boldsymbol{t_s}$ and the differential in velocity on either side of the interface of tangent $\boldsymbol{\tau}$:

$$-\frac{\boldsymbol{t}_s.\boldsymbol{\tau}_j}{\eta} = \frac{\alpha}{\sqrt{K}}(\boldsymbol{v}_s|_\Gamma - \boldsymbol{v}_d|_\Gamma).\boldsymbol{\tau}_j$$

.

The bilinear form B_s and the linear form L_s are defined in Stokes-Darcy by:

$$B_s([v_h, p_h], [w_h, q_h]) = 2\mu\int_\Omega H_s\dot{\epsilon}(v_h):\epsilon(w_h) + \frac{\mu}{k}\int_\Omega H_d w_h v_h - \int_\Omega \nabla.w_h p_h - \int_\Omega \nabla.v_h q_h +$$

$$+\tau_p \int_\Omega \nabla . v_h \nabla . w_h + \tau_u \int_\Omega \langle -\Delta v_h + \frac{\mu}{k} v_h + \nabla p_h, \mu \Delta w_h - \frac{\mu}{k} w_h - \nabla q_h \rangle + \quad (3)$$

$$+ \int_\Gamma \alpha \frac{\mu}{\sqrt{k}} (v_{h.} \tau)(w_{h.} \tau),$$

$$L_s([w_h, q_h]) = \langle f, w_h \rangle + \langle h, q_h \rangle + \tau_p \langle h, \nabla . w_h \rangle + \tau_u \langle f, \mu \Delta v_h - \frac{\mu}{k} v_h - \nabla q_h \rangle.$$

Where H_i is a Heaviside function, equal to 1 in domain I and vanishing elsewhere. The surface integral $\int_\Gamma \alpha \frac{\mu}{k} (v_h . \tau)(w_h . \tau)$ is turned into a volume integral for calculation simplification.

DECOUPLED APPROACH

Weak formulation

The mixed formulation of the equations of Stokes and Darcy can take two different forms in which the boundary conditions on the pressure are imposed as Dirichlet conditions or weakly, but more importantly are stable or not. Consequently, the stable dual mixed formulation is chosen for Stokes and the primal mixed formulation is kept for Darcy.The model developed here is based on modeling the liquid flow across the deformable porous medium in which finite strains are accounted for with an updated Lagrangian scheme. The regions where Stokes and Darcy flows prevail are considered independently and an iterative process ensures the equilibrium between these two regions where the flows have been solved.

Finite element approximation.

The computational domains $\Omega_s \subset R^d$ and $\Omega_d \subset R^d$ are discretized with not-necessarily structured meshes but coincident discretisation on the interface. These meshes are made up of triangles if $d = 2$ and of tetrahedrons if $d = 3$. Velocity and pressure fields are approximated by the discrete fields $v_{s,h}$, $p_{s,h}$ and $v_{d,h}$, $p_{d,h}$ for Stokes and Darcy regions respectively, which are piecewise linear and belong to the same finite element spaces.

The discretised form of the Stokes variational formulation consists in finding a velocity-pressure pair $[v_{s,h}, p_{s,h}]$ such that

$$B([v_{s,h}, p_{s,h}], [w_{s,h}, q_{s,h}]) = L([w_{s,h}, q_{s,h}]) \quad (4)$$

for any test function $[w_{s,h}, q_{s,h}]$, where the bilinear form B and the linear form L are defined by:

$$B([v_{s,h}, p_{s,h}][w_{s,h}, q_{s,h}]) = 2\mu \langle \dot{\epsilon}(v_{s,h}), \dot{\epsilon}(w_{s,h}) \rangle - \langle \nabla w_{s,h}, p_{s,h} \rangle - \langle \nabla v_{s,h}, q_{s,h} \rangle$$

$$L([w_{s,h}, q_{s,h}]) = \langle f_s, w_{s,h} \rangle + \langle h_s, q_{s,h} \rangle, \quad (5)$$

$$f_s = -\nabla(2\mu \dot{\epsilon}(v_s)) + \nabla p_s,\ h_s = -\nabla v_s.$$

Similarly, the discretised form of the Darcy variational formulation consists in finding a velocity-pressure pair $[v_{d,h}, p_{d,h}]$ such that

$$B([v_{d,h}, p_{d,h}], [w_{d,h}, q_{d,h}]) = L([w_{d,h}, q_{d,h}]) \quad (6)$$

for any test function $[w_{d,h}, q_{d,h}]$, where:

$$B([v_{d,h}, p_{d,h}][w_{d,h}, q_{d,h}]) = \frac{\mu}{k} \langle w_{d,h}, v_{d,h} \rangle + \langle \nabla p_{d,h}, w_{d,h} \rangle + \langle \nabla q_{d,h}, v_{d,h} \rangle$$

$$L([w_{s,h}, q_{s,h}]) = \langle f_d, w_{s,h} \rangle + \langle h_d, q_{s,h} \rangle, \quad 7)$$

$$f_d = \frac{-\mu}{k} v_d + \nabla p_d,\ h_d = -\nabla v_d.$$

The elements used for numerical integration of Stokes and Darcy equations are the Mini-elements P1+/P1 introduced by [4]. These elements are based on the enrichment of the discretisation with a bubble function representing a local contribution at the elementary level. This produces a stabilized-like formulation, in which the stability parameter is given by the shape of the bubble function and depends also on the physics of the problem solved.

Coupling conditions.

Conditions on the interface are prescribed in two different manners. Continuity of pressure (prescribed in Darcy as Dirichlet condition) is fulfilled naturally. Condition of normal velocity continuity and condition on tangential velocity are prescribed by penalization in Stokes region.

Method for prescribing normal velocity continuity was first considered. It was found out that permeability eliminates the effect of penalization. Consequently, this condition on normal velocity is now prescribed by using coefficient of penalization λ that depends on the perform permeability K : $\lambda=10^5/K$. Tests successfully proved the robustness and efficiency of this new approach, for variable values of permeability (down to 1e-15 m^2), coefficients of viscosity, and thickness of the fluid layer.

Then it appeared that the tangential velocity had to be controlled at the Stokes-Darcy interface for the velocity profile in Stokes to be properly described. Condition on the tangential velocity on the interface is now prescribed following the analytical solution given for the BJS condition. Results obtained with this BJS-like condition on the tangential velocity show that computed and analytical velocities coincide provided the mesh size around the interface is sufficiently ‘coarse’, *i.e.* is such that $h_k > \sqrt{K}$. Results were verified for various values of permeability and thickness of fluid layer.

COMPARISON OF BOTH METHODS

Numerical validation.

To study the influence of physical and numerical parameters on the solution computed from both methods various tests were chosen, and results of these tests were also investigated to evaluate the robustness and precision of the methods. For example, the stationary case, presented in Fig. 2, illustrates the capability of representing realistic geometries with the decoupled approach.

The test case of a fluid flow perpendicular to the interface validated the continuity of the normal velocity, meanwhile test case of the parallel flow validated the fulfilling of the BJS condition imposed on tangential velocity. Also several tests for more complex geometry (inclined straight interface) were conducted, to justify the use of the developed methods. Simulations were also run successfully for complex 3D transient (filling) cases (Fig. 2).

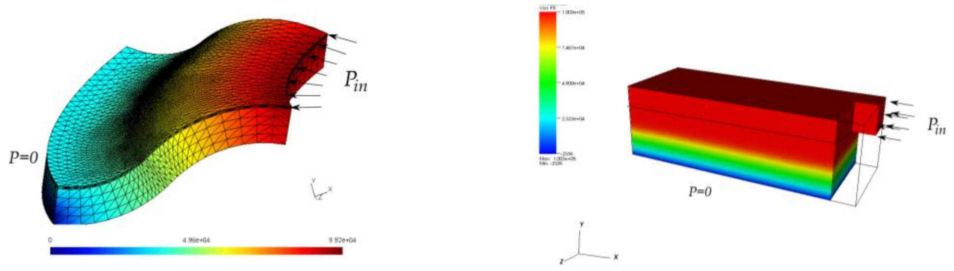

(a) (b)

Fig. 2: Injection of a 3D part, pressure field in Pa – permeability K=1e-14 m^2: (a) decoupled approach and (b) monolithic approach

Perpendicular flow. Relative errors.

The convergence of the solution, as well as its robustness, has been considered for the test case of a flow perpendicular to the interface of normal **y** in the global frame. Let us consider a domain $\Omega = [0; 5] \times [0; 2]$ m^2 composed of two sub-domains: a pure fluid domain $\Omega_s = [0; 5] \times [1; 2]$ m^2 and porous medium $\Omega_d = [0; 5] \times [0; 1]$ m^2. A pressure gradient of 1 bar is applied along the y-axis. Other boundary conditions are zero normal velocity on the left and right hand sides of the geometry. The obtained numerical results were compared with known analytical ones, where $v_{x,s} = v_{x,d} = 0, v_{y,s} = v_{y,d} = -\frac{K}{\eta}\nabla p, p_d = p_1, p_d = p_1 y$.
The errors were computed: $\|u_{error}\| = \frac{\|u-u_h\|_{L^2}}{\|u\|_{L^2}}$, where u is the analytical solution and u_h is the obtained numerical solution, $\|u\|_{L^2} = (\int_\Omega u^2 d\Omega)^{1/2}$- norm L^2. Results for the case of perpendicular flow for different size of the mesh were obtained, when η = 1 Pa.s, K = 10e-14 m^2 and presented in Table 1. It can be verified that both methods are robust and lead to very similar relative error which become smaller when the mesh becomes finer.

Table 1: Relative errors for the test case of perpendicular flow, K=1e-14 m^2

Mesh	$\|V_{y,s}\|$, monolithic approach, %	$\|V_{y,s}\|$, decoupled approach, %
100×25	0.468	0.401
100×50	0.231	0.211
100×100	0.141	0.109
100×200	0.111	0.099

Inclined interface.

To compare both methods for more complex problems, the case of an inclined interface is considered (Fig. 3). A domain $\Omega = [0; 1] \times [0; 1]$ m^2 is composed of two sub-domains: a pure fluid domain Ω_s and porous medium Ω_d, $H_s = [0.2; 0.8]$ m. A 1 bar pressure gradient is applied along the **y** axis. The other boundary conditions are zero normal velocity on the left and right hand sides of the geometry. Pressure and normalized velocities for the middle section of the domain for the interface at point (0.5; 0.5) are presented in Fig. 3. It is clear that pressures are perfectly represented by both methods, while velocities are almost perfectly coincident; one will notice that velocities represented in Fig. 3-b are of the order of 1e-11 m.s^{-1}. These results demonstrate the ability of both methods to represent the Stokes-Darcy coupling for locally defined interfaces.

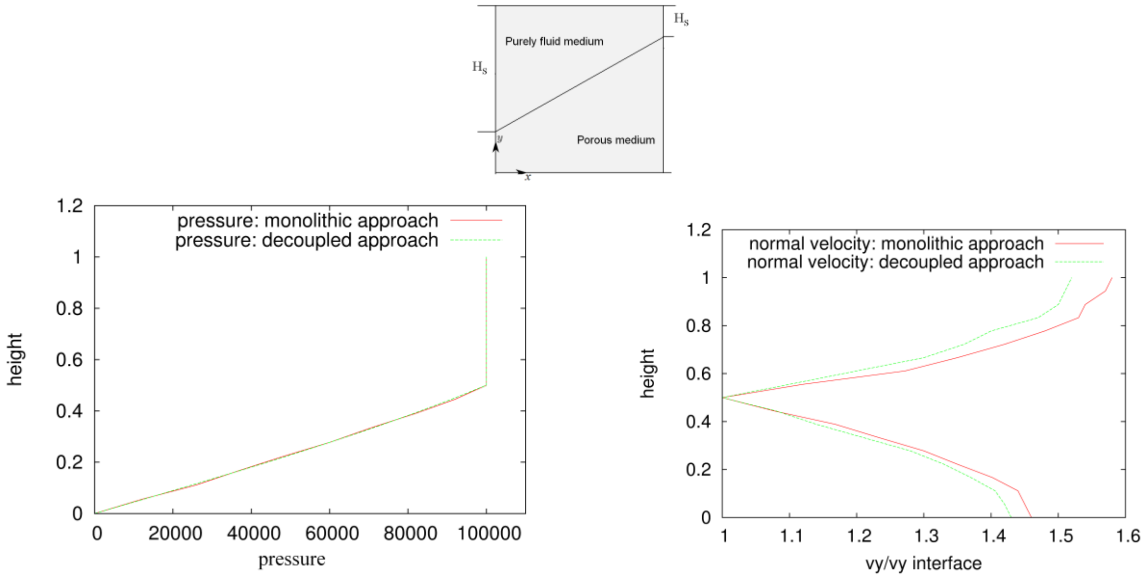

a) b)

Fig. 3: Pressure (a) and normalized velocities (a), when η = 1 Pa.s, K = 1e-15 m^2.

Manufactured solution.

Finally, to verify both implementation and convergence of the approach the method of manufactured solution was used [5]. It consists in building an analytical solution that is fed into the system of equations under consideration and permits to calculate the corresponding source term. Then, this source term is implemented into the numerical code to obtain the numerical solution of the discretised problem. Eventually the difference between the initial analytical solution and the numerical one is calculated and permits to measure the capability of the method implementation to solve the PDE sets of equations.

In the domain $\Omega = [0;1] \times [0;1]$ with $\Omega_s = [0;0.5] \times [0;1]$, $\Omega_d = [0.5;1] \times [0,1]$, we consider the following velocity and pressure fields:

$p_d = -y^4 e^x$, $v_{x,d} = y^4 e^x$, $v_{y,d} = \frac{-1}{5} y^3 e^x$,

$p_s = -y^4 e^x$, $v_{x,s} = y^4 e^x$, $v_{y,s} = \frac{-1}{5} y^5 e^x$.

Each area Ω_s and Ω_d is divided into squares, h is the mesh size. Each square is itself divided into two triangles leading to meshes 20×20, 40×40, 80×80. Each grid corresponds to a more refined version of previous. Homogeneous Dirichlet conditions are prescribed on the overall boundary of the domain Ω.

The convergence of the error for both pressure and velocity is represented in log scale in Fig. 4. For the pressure in Stokes region (Fig. 4-a), convergence rates are in perfect agreement for both methods [2.5; 1.2], and even better than the theoretical convergence rate of order 1. As for Stokes velocity (Fig. 4-b) the convergence rate is [3; 1.33] for the monolithic approach and [2.5; 2] for the decoupled approach (theoretical rate is of order 2). For the Darcy region, the convergence rates for pressure are [3.6; 1] for the monolithic approach and [2.4; 1.4] for the decoupled approach (theoretical rate is of order 2), and for the velocity it is [3.25; 1] for the monolithic approach and [2.4; 1.6] for the decoupled approach (theoretically it is of order

2). For the monolithic approach, the rate of convergence is relatively high due to the ‘optimal’ choice of constants c_p, c_u and c_1 in the stabilization terms τ_u and τ_p (Eq. 1).

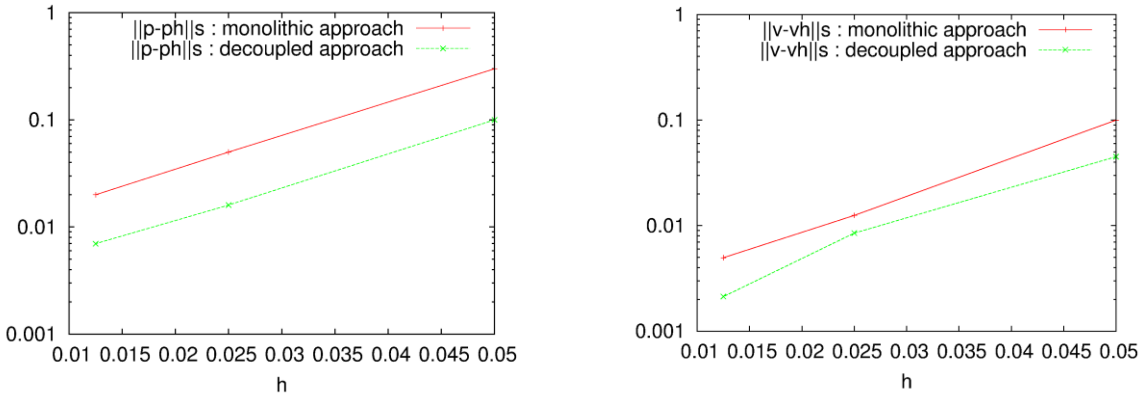

a) b)

Fig. 4: Convergence of the error for the pressure (a) and velocity (b) in Stokes domain for monolithic and decoupled approaches for the problem with $\eta = 1$ Pa.s, $K = 1\ m^2$.

CONCLUSIONS

Monolithic and decoupled strategies have been developed to solve the Stokes–Darcy coupled problem. Both approaches were validated by numerical test and method of manufactured solution was used to calculate the rates of convergence. The comparison of two approaches showed that both of them could be successfully used to solve the coupled Stokes-Darcy problem for permeabilities down to 1e-15 m^2.

AKNOWLEDGEMENTS: Dr R. Troian’s work on Stokes-Dacy coupling stabilisation in the decoupled approach was supported through the FP7 INFUCOMP program; which is greatly acknowledged by the authors.

REFERENCES

1. P. Celle, S. Drapier, and JM. Bergheau (2008), Numerical modelling of liquid infusion into fibrous media undergoing compaction. *European Journal of Mechanics*, A/Solids(27), 647-661.

2. G.Pacquaut, S.Drapier, J.Bruchon, and N.Moulin (2011), Combining a level set method and a mixed stabilized p1/p1 formulation for coupling stokes-darcy flows. *International Journal for Numerical methods in Fluids*, DOI: 10.1002/fld.2569.

3. S.Badia and R.Codina (2008), Unified stabilized finite element formulation for the stokes and the darcy problems. *SIAM journal on Numerical Analysis*, 47, 1971–2000.

4. D.N. Arnold, F. Brezzi, and M. Fortin (1984), A stable finite element for the Stokes equations. *Estratto da Calcolo*, 21(4), 337-344.

5. K. Salari et P. Knupp : Code verification by the method of manufactured solutions. Technical report, Sandia National Laboratories, 2000.

NUMERICAL STUDY ON CONSOLIDATION PROCESS OF T-STIFFENED SKIN IN AUTOCLAVE

Yanxia Li*, Min Li, Yizhuo Gu, Zuoguang Zhang

Key Laboratory of Aerospace Materials and Performance (Ministry of Education),
Beihang University, Beijing 100191, China
Corresponding author's e-mail: liyanxia@buaa.edu.cn

ABSTRACT: Numerical models were developed to study the consolidation process of anisotropic T-stiffened skin in autoclave cocuring process. Resin pressure and resin flow were analyzed. The predicted results showed that the resin flow in the plane direction was obvious and the total quantity of resin flow out in the corner was larger than in the web and flange. At the same time, the experimental data validated the predicted resin flow during the consolidation process of T-stiffener skin in autoclave process. The results of this study will be attributed to promote the manufacturing quality of the integral molding technology and ultimately lead to optimized skin/stiffener designs.

KEYWORDS: *Polymer-matrix composites; Autoclave ;;Numerical Simulation; Consolidatio*

INTRODUCTION

Integral moding technologies of cocuring and cobonding, improving the quality and largely reducing the numbers of fastener and components, impetus the potential use of composite materials in the primary structure. Particularly, utilization of the stiffeners cocured with skins is finding frequently implemented in an extensive number of new aircraft designs. T-stiffener, which is the simplest unit of a stiffened panel, can be developed into other stiffeners. A large body of experimental and analytical work performed by a number of researchers has focused on the failure behavior of stiffened structures during postbuckling and pull-off conditions [1-4]. Particular emphasis was placed on identifying the failure processes, which lead to catastrophic failure. Compared to the molding process of these structural components, such as flat laminates and L-shaped laminates, the resin flow and fiber compaction behavior is more complex, that evidently influences its manufacturing quality. This study is to analyze the resin flow and fiber compaction in the T-stiffened skins during the autoclave cocuring process by numerical simulation, the experimental data also provided and validated the predicted resin flow in the T-stiffened skins. The results of this study will be attributed to promote the manufacturing quality of the integral molding technology and ultimately lead to optimized skin/stiffener designs.

NUMERICAL SIMULATION MODELS

Assumptions

The following basic assumptions are made in the present model:

(1) The composite material is idealized as a void free fiber bed fully saturated resin.
(2) The resin is assumed to behave as an incompressible Newtonian fluid.
(3) The resin flow in the porous fiber bed obeys Darcy's law.
(4) The individual fibers are incompressible.
(5) Body forces such as self weight are negligible.

Flow and compaction model

Biot [5] developed the theory of three-dimensional consolidation for isotropic material and extended the theory to the most general case of anisotropic material in 1955. It was also called the 'real 3D consolidation theory' and was used in soil and rock mechanics field widely. In this paper, the Boit consolidation model was accepted to simulate the resin flow and fiber compaction during the autoclave process of composites and the force equilibrium equation for a differential element of the composites is written as [6,7]:

$$\frac{\partial \sigma_{ij}}{\partial x_j} + \frac{\partial P}{\partial x_i} = 0 \tag{1}$$

where σ_{ij} and P are the fiber effective stress and resin pressure, respectively. Subscript i and j stand for x or z Cartesian coordinates.

The constitutive equation of the fiber bed is simplified and expressed as

$$\begin{Bmatrix} \sigma_{xx} \\ \sigma_{zz} \\ \tau_{xz} \end{Bmatrix} = \begin{bmatrix} E_{xx} & & \\ & E_{zz} & \\ & & G_{xz} \end{bmatrix} \begin{Bmatrix} \varepsilon_{xx} \\ \varepsilon_{zz} \\ \gamma_{xz} \end{Bmatrix} \tag{2}$$

which is further expanded as

$$\begin{aligned} \sigma_{xx} &= V_f E \varepsilon_{xx} \\ \sigma_{zz} &= As \cdot \left(1 - \sqrt{V_f / V_0}\right) \Big/ \left(\sqrt{V_a / V_f} - 1\right)^4 \\ \tau_{xz} &= G_{xz} \gamma_{xz} \end{aligned} \tag{3}$$

where E_{xx}, E_{zz} and G_{xz} are the fiber bundle elastic constants, ε_{xx}, ε_{zz} and γ_{xz} are the strains, V_{f} is the fiber volume fraction, E is Young's modulus of the fiber, V_{a} is the possible maximum fiber volume fraction, V_0 is the initial fiber volume fraction, As is a spring constant.

At the same time, the mass conservation of the representative element requires:

$$\left[\frac{\partial(\rho_r v_x)}{\partial x} + \frac{\partial(\rho_r v_y)}{\partial y} + \frac{\partial(\rho_r v_z)}{\partial z} \right] dxdydz = \frac{\partial(e\rho_r dxdydz)}{\partial t} \tag{4}$$

where the left item of the equation is the total flow in the unit element, the right item of the equation is the change rate of fluid mass, v_x, v_y and v_z are the seepage velocities of the resin within the composite in the x, y and z directions, ρ_r, e and $e\rho_r dxdydz$ are resin density, porosity, and the resin mass of the representative element.

The resin flow in the porous fiber bed obeys Darcy's law and it is assumed that the fixed global coordinate system is consistent with the principal material coordinate system. The differential continuity equation of resin flow in the anisotropic composite is:

$$-\left[\frac{\partial\rho_r}{\partial x}\left(\frac{K_{xx}}{\mu}\frac{\partial P}{\partial x}\right)+\frac{\partial\rho_r}{\partial y}\left(\frac{K_{yy}}{\mu}\frac{\partial P}{\partial y}\right)+\frac{\partial\rho_r}{\partial z}\left(\frac{K_{zz}}{\mu}\frac{\partial P}{\partial z}\right)\right]dxdydz=\frac{\partial(e\rho_r dxdydz)}{\partial t} \tag{5}$$

where K_{xx}, K_{yy} and K_{zz} are the fiber bed permeability which varies with varying fiber volume fraction, μ is resin viscosity.

At the same time, it is also assumed that the resin density ρ_r is constant and the fiber is incompressible. Therefore, the bulk strain rate is equal to the change rate of porosity. The final flow continuity equation can be written as:

$$\frac{\partial\varepsilon_v}{\partial t}=-\nabla\left(\frac{K}{\mu}\nabla P\right) \tag{6}$$

where ε_v is the bulk strain, K is the fiber bed permeability tensor.

Initial and boundary conditions

It is assumed that displacement and resin pressure are zero in the whole domain before the external pressure is exerted.

Resin pressure in the side of the bleeder plies is supposed to be zero, while in the tool side, the resin cannot flow out and no normal displacement is allowed. Table 1 presents the boundary conditions of the flow-compaction model.

Table 1: Summary of the boundary conditions for the flow-compaction model

Boundary conditions, for t >0, on the surface		
Displacement	External applied pressure	Flow
Free	P_a	$P=0$
Fixed	$\partial P/\partial n=0$	

Geometry and boundary conditions of the T-stiffened skin

Fig.1 is the schematic of the T-shaped structure element, including two L-shaped stiffeners and one skin, in which the yellow triangle area is filled with the unidirectional prepreg. Definition of boundary conditions is shown in Fig.2. In Fig.2 (a), the yellow line is defined as free flow boundary with no displacement constraint; the purple line is defined as no permeable boundary with displacement constraint. The external pressure is applied on the green line in the normal direction in Fig.2 (b).

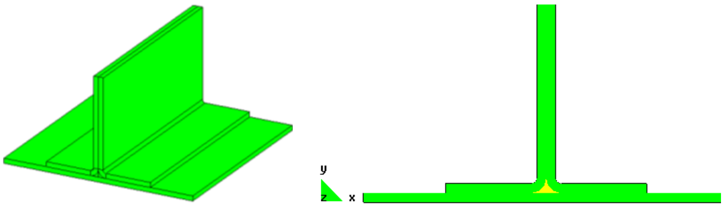

(a) 3D model (b) 2D structure

Fig.1: Schematic of T-shaped structure element laminate

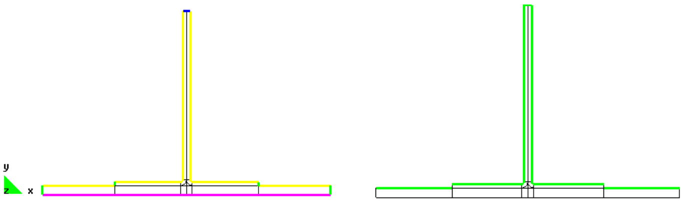

(a) Displacement and flow boundaries (b) external pressure boundary

Fig.2: Definition of boundary conditions

SIMULATED RESULTS ANALYSIS

In this part, the resin pressure distribution and resin flow out at different positions are presented and simply analyzed in the abstract paper. Fig.3 was the simulated resin pressure distribution in the lay-up at different time. Resin pressure decreased in the corner part firstly and the resin pressure quickly decreased in the thinner stiffener part.

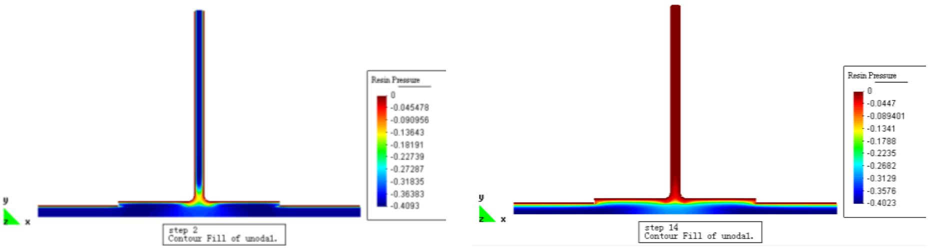

(a) time =120s (b) time = 840s

Fig.3: Resin pressure distribution in the lay-up at different time

Fig. 4 showed the total quantity of resin flow out at the typical points according the simulated results. The amount of resin flow out in the P2 position was much larger than P1 and P3 positions which showed that the resin flow in the plane direction was obvious, then affect the resin distribution and laminate thickness.

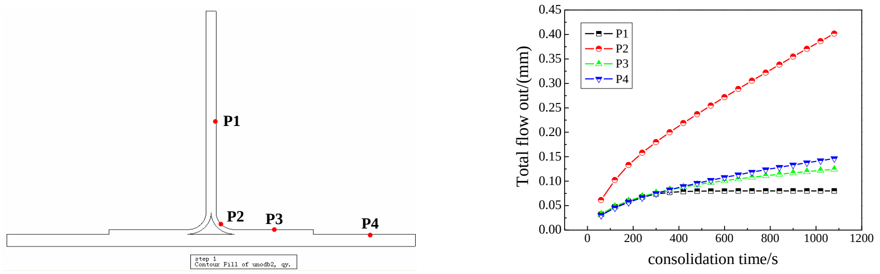

(a) Positions for results analysis (b) resin flow out results

Fig.4: Resin flow out at different positions

The pressure measurement method using the transferring pressure film is executed to obtain pressure distribution in different sections of T-stiffener[8]. From Fig.6, nonuniform pressure obviously distributes in T-stiffeners, the lowest pressure exists in stifferner corner and higher pressure is transferred into flange and web sections. The results of pressure measurement above have indicated that the lowest pressure appears in stiffener corner. So it can be concluded that there is pressure difference in the plane which cause resin flow from web and flange sections to stiffener corner. To further understanding the resin flow in T-stiffeners, the bleeding quantity of bleeding cloth in different stiffener sections are given in Fig.7. Compared to the bleeding quantity in web and flange sections, more resin was absorbed by the bleeding cloth in the corner due to the plane and thickness direction resin flow. It's coordinate with the results in Fig.5, i.e the total quantity of resin flow out being larger in the corner.

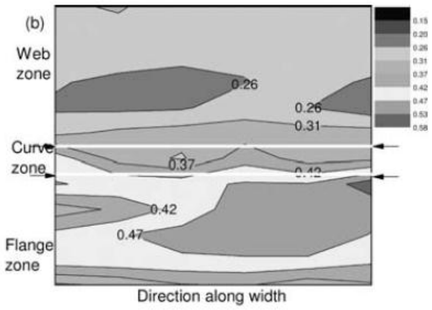

Fig.5: Pressure distribution in the stiffeners

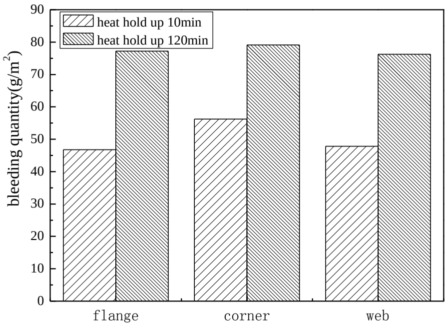

Fig.6: bleeding quantity distribution in the stiffeners

CONCLUSIONS

In this paper, we studied the resin flow and fiber compaction simulation for the T-stiffener skin with the numerical simulation method. The predicted results showed that the resin flow in the plane direction was obvious and the total quantity of resin flow out in the corner was larger than in the web and flange. At the same time, the experimental data validated the predicted resin flow during the consolidation process of T-stiffener skin in autoclave process.

REFERENCES

1. K.A. Stevens, G.Davies, and R.Ricci, In 19th ICAS conference, *ICAS*94-9.8.3, Anaheim, California, 2975(1994).

2. K.A. Stevens, R.Ricci, and G.Davies, *Composites*, 26, 189(1995).

3. K.A.Stevens, S.Specht, and G.Davies, *ICCM-1*1, Gold Coast, Austalia(1997).

4. B.G.Falzon, K.A. Stevens, and G.Davies, *Composites Part A*, 31, 459(2000).

5. Biot M.A.(1941), ‘General Theory of Three-Dimensional Consolidation’, *Journal of Applied Physics*, 12(2):155-164.

6. Smith G.D., Poursartip A(1993), ‘A comparison of two resin flow models for laminate processing’, *Composite Materials*, 1993; 27(17): 1695-1711.

7. Li M, Li YX, Zhang ZG, et al(2008), ‘Numerical simulation of two-dimensional flow and compaction during the consolidation of laminated composites’, *Polymer Composites*, 29(5): 560-568.

8. Xueming Wang, Fuyuan Xie, Min Li, et al(2010), ‘Influence of core fillers on resin flow and fiber compaction of cocured skin-to-stiffener structures’, *Polymer Composites*, 31(8): 1360-1368.

A 2.5D SIMULATION OF THE FILLING AND POST-FILLING STAGES OF THE RESIN INFUSION PROCESS

Quentin Govignon[1*], Lucas Maes[3], Bart Verleye[1,2,3], Simon Bickerton[1], and Piaras Kelly[2]

[1]*Department of Mechanical Engineering, Centre for Advanced Composite Materials, The University of Auckland, New Zealand*
[2]*Department of Engineering Science, Centre for Advanced Composite Materials, The University of Auckland, New Zealand*
[3] *Department of Metallurgy and Materials Engineering, Composite Material Group, Katholieke Universiteit Leuven, Belgium*

ABSTRACT: The Resin Infusion process (RI, also known as VARTM) is a subclass of the Liquid Composite Moulding (LCM) collective, which is increasingly applied in industry. As opposed to the other LCM processes, RI utilises only one rigid mould half, the upper mould half of the mould being a flexible plastic bag. This greatly reduces tooling costs, and makes the process suitable for medium to very large sized parts. However, the interaction between a flexible bag and the infusion of the laminate within, presents a significant challenge to model and understand. The University of Auckland LCM research group is developing SimLCM as a generic LCM mould filling simulation. SimLCM has recently been extended to simulate RI, focusing on resin flow and laminate thickness predictions throughout the process. To accurately predict filling times, and the evolution of fluid pressure and laminate thickness during filling and post-filling phases, a detailed knowledge is required of the complex compaction response of the fibre reinforcement. While significant research has been published on modelling of the filling in RI, the post-filling period has received much less attention. This phase is, however, significant as spatial variations in laminate thickness are removed, preferably before the infused resin gels. Extending on previous work on rectilinear filling, this paper will present a program of RI experiments in a range of 2D flow geometries and the results will be compared to the predictions made using SimLCM. Special attention is given to the post-filling stage, and the validation of the new models developed for SimLCM. A selection of radial, peripheral and more complex filling situations have been addressed.

KEYWORDS: *Resin Infusion, VARTM, Liquid Composite Moulding, simulation*

INTRODUCTION

Resin Infusion (RI) is part of the Liquid Composite Moulding (LCM) process family. The term LCM describes the closed mould processes in which a liquid polymeric resin is impregnated through a fibrous reinforcement. Commonly applied LCM processes include Resin Transfer Moulding (RTM), Compression RTM (CRTM), RTMLight and Resin Infusion.

During manufacture with an LCM process, the operator typically has little control over the advancement of the flow, and successful process development by trial and error requires experience and can be long and expensive. Reduction of development costs requires a good understanding of the process physics, and can benefit from development of an accurate simulation tool. Significant effort has been placed into establishment of RTM and CRTM simulations that accurately predict fill time, flow front advancement and dry spot formation [1-4]. These two processes, through the use of rigid mould tools, allow for accurate control of the laminate thickness and therefore of the fibre volume fraction. A simulation tool therefore only requires an acceptable reinforcement permeability model to provide flow data.

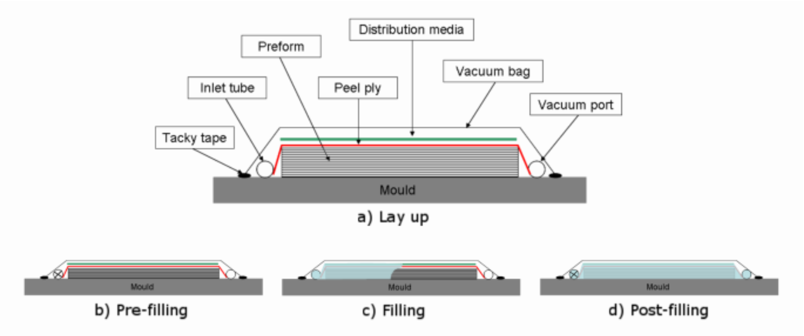

Figure 1: Steps of the RI Process.

As opposed to RTM and CRTM, RI uses a single sided mould, the reinforcement being contained within a cavity formed and sealed by a vacuum bag. As the vacuum bag employed during the process provides minimal flexural rigidity, local compaction of the fibrous reinforcement is governed by the pressure difference between the inside of the cavity and the external atmospheric pressure. Local laminate thickness will vary in relation to the resin pressure inside the cavity, as will the reinforcement permeability which is governed by the local reinforcement architecture [5-9]. Not only is the resin flow affected by these changes in laminate properties, but it is also crucial to understand and simulate these variations in order to be able to predict and control the final part quality [9-12].

If infusion is to be used in the aeronautics industry as a replacement for prepregs and autoclave processes, simulation tools will have to not only predict the flow during the filling stage but also the evolution of the laminate throughout the filling and post-filling up to the curing of the resin. This paper presents experimental and numerical results, from a program aimed at developing SimLCM, a generic LCM process simulation.

DEVELOPMENT OF THE SIMULATION

SimLCM is a simulation tool developed at the University of Auckland, capable of simulating rigid moulding process such as RTM and CRTM. It is currently being developed for simulation of LCM processes using bags and semi-rigid tooling in order to offer a generic LCM process simulation tool. Laminate thickness evolution is coupled strongly with mould deflections and fluid pressure. It affects the permeability of the reinforcement and flow of the resin as well as the final mechanical properties of the composite. The simulation presented here aims to take into account those effects and offers prediction of the flow and laminate properties through both filling and post-filling, addressing what final laminate composition and thickness will settle to, and the time required. Comparisons are made here to the filling and post-filling phases for infusion of moderately complex geometries. Empirical permeability and compaction models for the CSM have been described previously [7, 12].

Theory

Resin flow through a fibrous reinforcement is usually described using Darcy's law;

$$\mathbf{q} = -\frac{\mathbf{K}}{\mu}\nabla P\ , \tag{1}$$

where $\mathbf{q}$ represents the volume-averaged velocity, $\mathbf{K}$ is the permeability tensor of the preform, μ is the fluid viscosity and P is the local fluid pressure. The conservation of solid and fluid mass imposes:

$$\nabla(h\mathbf{q}) = -\frac{\partial h}{\partial t}, \tag{2}$$

where h is the local laminate thickness. Combining Eqns. 1 and 2 gives;

$$\nabla\left(\frac{\mathbf{K}}{\mu}h\nabla P\right) = -\frac{\partial h}{\partial t}. \tag{3}$$

Solution strategy:

In Eqn. 3, the permeability is a coupled to the fibre volume fraction (V_f) which can be expressed as a function of the thickness. The fluid pressure can also be linked to the thickness through Terzaghi's relation:

$$\mathrm{P} = P_{ext} - \sigma_f, \tag{4}$$

where P_{ext} is the external pressure applied on the vacuum bag (in general atmospheric pressure), and σ_f is the stress taken by the fibrous preform which is related to the V_f through the reinforcement compaction model. Eqn. 3 can therefore be rewritten as:

$$\nabla\left(\frac{\mathbf{K}(h)}{\mu}h\frac{\partial P}{\partial h}\nabla h\right) = -\frac{\partial h}{\partial t}. \tag{5}$$

Eqn. 5 is then expressed in a matrix form as

$$\mathbf{K}_{el}(h^t) + \mathbf{C}_{el}(\dot{h}^t) = \mathbf{F}_{el}(h^t), \tag{6}$$

with $\mathbf{K}_{el}$, the elemental stiffness vector, $\mathbf{C}_{el}$ the capacitance matix, and $\mathbf{F}_{el}$ the element force vector. To be solved using the Newton-Raphson Algorithm by using a backward finite difference approximation for the first derivative of the height:

$$\frac{\partial h}{\partial t} \approx \frac{h^t - h^{t-\Delta t}}{\Delta t}, \tag{7}$$

EXPERIMENTAL OBSERVATIONS

Plan of Experiments

To provide challenging validation cases for SimLCM, three different 2D shapes were infused. Two shapes were based on a 380x202 mm rectangular preform. The 'Square-hole' shape has a 100x100 mm square removed at the centre; the 'Dumbbell' has 100x50 mm cut-outs on each side halfway along the length. Schematics and dimensions of the preform shapes are depicted in **Error! Reference source not found.**. The third geometry chosen was a disc with a 225 mm outer radius and a 7.5 mm inner radius, infusions were performed with radial divergent flow and peripheral convergent flow as presented in [13, 14]. The 'dumbbell' and 'square-hole' are identical regards simulation. Completing both experiments allows for pressure data to be taken along two paths, without adding more pressure transducers to the mould.

All experiments were performed with the inlet at atmospheric pressure, and the vent at 4.7 mbar. The preform consisted of 10 layers of a 450 g/m2 Chopped Strand Mat (CSM) that was characterised for compaction and permeability [9,10]. The test fluid was a mineral oil, Mobil DTE Heavy, with a viscosity of 0.2 Pa.s at 20°C.

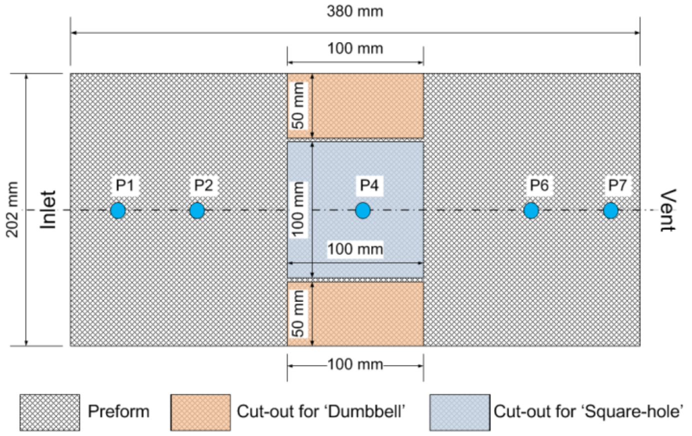

Figure 2: Schematic description of the preform shapes.

Setup

The RI monitoring setup used for the experiments presented here was described in [7, 12, 14]. As well as recording inlet and vent pressure, fluid pressure was recorded at five points along the laminate (35, 90, 200, 310, and 365 mm from the inlet, P1, P2, P3, P4, and P5 respectively) for the rectangular infusion and three points along the laminate for the circular preform (56, 113 and 169 mm from the centre for P1, P2 P3 respectively), using 6001A4-FL pressure transducers. Laminate thickness was measured across the whole surface using a stereophotogrammetry system [6,8].

Observations

When comparing the 'square-hole' and 'dumbbell' at the same relative fill time, it is observed that the thickness distribution and flow front shape and position are very similar. In Figure 3, the thickness map of the 'dumbbell' experiment (top) was overlaid on the processed image of the 'square-hole' experiment (bottom), lining up the cut-out of the dumbbell with the top half of the square hole. It is therefore possible to assume pressures measured along the centreline of the ‘square-hole’ infusion are equivalent to those along the outside edge of the ‘dumbbell’ infusion, and vice-versa.

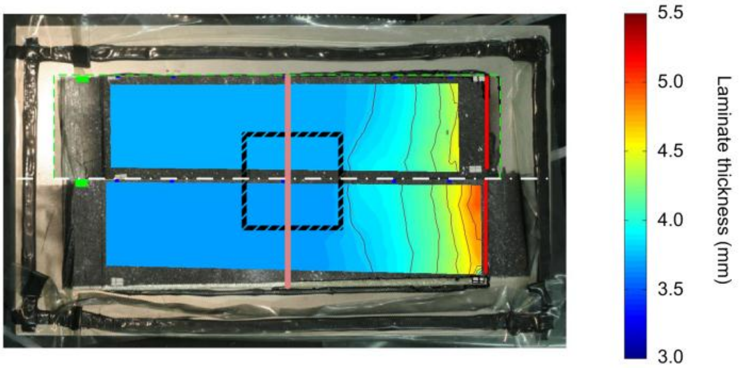

Figure 3: Comparison of the thickness distribution in the ‘dumbbell’ (top) and ‘square-hole’ (bottom) when the flow front (in pink) reaches 200 mm from the inlet.

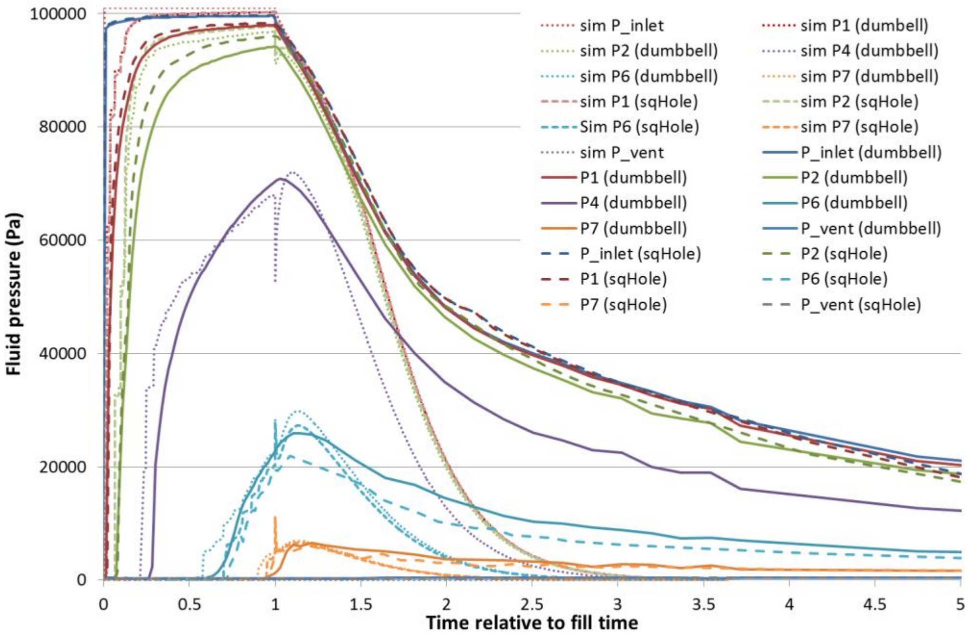

Figure 4: Comparison of the fluid pressure evolution in the rectangular infusion experiments and simulation.

Figure 4 presents the evolution of the fluid pressure along the centreline of both ‘dumbbell’ and ‘square hole’ experiments. To eliminate the variations in time due to variability of the process and fluid viscosity, the time was normalised to the fill time. Until 0.15 fill time, before the flow front reaches the cut-out, the fluid pressures in both experiments matches very well. After the flow front reaches the beginning of the cut-out, the fluid pressures at P1 and P2 diverges with a steeper rise and higher maximum along the centreline of the ‘square hole’ experiment, the rise being more pronounced at P2 that at P1. This effect can also be observed in Figure 3 where the thickness appears to be higher just upstream of the cut-out as compared to the area where the preform is continued. While there is a lag between the pressure rise at P6 between the two experiments, the pressure at the centreline of the ‘dumbbell’ experiment rising earlier and to a higher peak than that of the ‘square hole’ experiment, the difference is not noticeable anymore at P7.

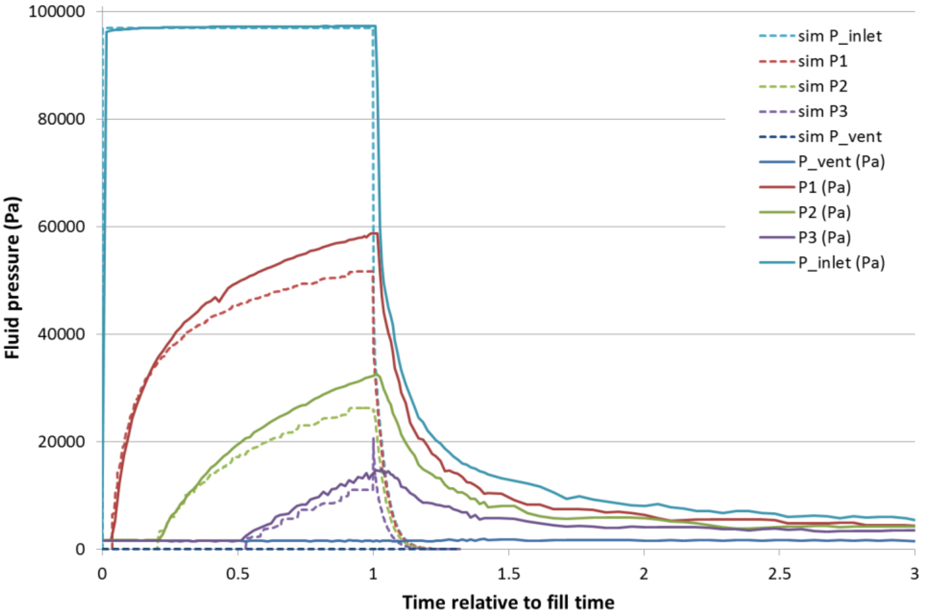

Figure 5: Comparison of the fluid pressure evolution during the radial infusion between the simulation and experiment.

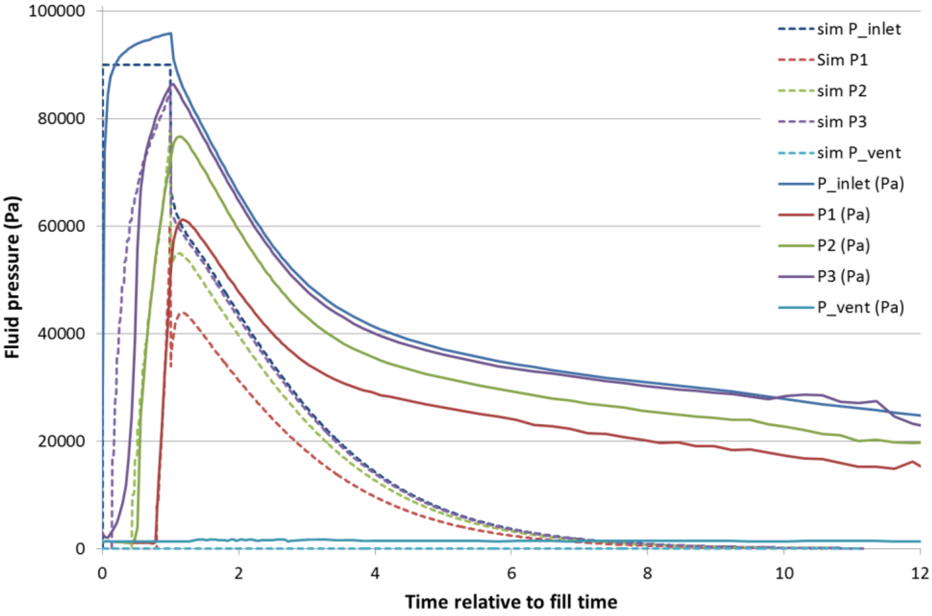

Figure 6: Comparison of the fluid pressure evolution between the experiment and simulation for the peripheral infusion.

Figure 5 and Figure **6** present the fluid pressure evolution during the radial and peripheral infusions. Table 1 presents the fill time for all experiments and the corresponding simulation. It can be observed that while the peripheral infusion has a much reduced fill time, the time necessary for post-filling is much longer, in fact the total cycle time is slightly longer than in the radial infusion case. On the other hand while the radial infusion has a relatively long fill time, the post-filling occurs much faster than for peripheral or linear infusion. It can also be observed that while the inlet pressure didn't reach a stable maximum during filling for the peripheral infusion, the pressures at P1, P2 and P3 reached a much higher peak as compared to the radial infusion.

Table 1: Comparison of the experimental and simulated fill time for all experiments

	Dumbbell	Square hole	Radial	Peripheral
experimental fill time (s)	1055	1660	1247	227
Simulation fill time (s)		1523	1180	249

SIMULATION RESULTS

As was discussed in [12], fibrous reinforcements displays a complex compaction behaviour. The reinforcements do not behave in the same way in loading and unloading or when they are wet and or dry. Three compaction models were therefore implemented in the simulation, one representing the compaction of dry fibre, one representing the progressive unloading of a saturated reinforcement for the filling stage, and one modelling the compaction of saturated reinforcement during post-filling. However this causes some discontinuity in the pressure and laminate thickness at the onset of post-filling as can be seen in Figure 4 to 6.

It can be observed from Figure 4 to 6 that the simulation appears to capture very well the filling stage of the resin infusion process in various scenarios providing some level of complexity. The simulation of the post filling appears however to predict much quicker changes than what is observed during the experiments. The pressure profile across the parts however, appear to match relatively well. For the rectangular infusions, the rate of pressure decay predicted at the beginning of post-filling match relatively well that observed in the experiments. Once the fluid pressure reaches below 60000 Pa near the inlet however, the experimental rates of pressure decay decrease dramatically while the simulation does not pick this up. This could be the sign of a stiffening of the reinforcement that was not observed during the reinforcement characterisation. Another possible explanation could be due to small irregularities at the edges of the preform in the experiments that might reduce the flow out to the vent.

The developments of simLCM for the resin infusion can now also account for turning the inlet into a vent at the onset of post-filling, and the possibility of having multiple zones with different materials or number of layers is being implemented into the infusion model.

CONCLUSION

This paper has presented recent development of the process simulation software SimLCM to address resin infusion. Several complex scenarios were presented, and compared to detailed experiments for validation. The simulation provides good predictions of flow progression and laminate thickness evolution, and provides a deeper analysis than that possible using a simple RTM simulation. While the experimental post-filling appears to be slower than forecasted by the simulation, it has to be noted that the post-filling simulation is very sensitive to the compaction behaviour model used; a refined compaction model could provide more satisfactory results. On-going work is focused on amelioration of the predictions through the post-filling stage of RI and improvement of the reinforcement's compaction behaviour model.

REFERENCES

[1] Liu B, Bickerton S, Advani SG. Modelling and simulation of resin transfer moulding (RTM)--gate control, venting and dry spot prediction. Composites Part A: Applied Science and Manufacturing. 1996;27(2):135-41.

[2] Gokce A, Advani SG. Simultaneous gate and vent location optimization in liquid composite molding processes. Composites Part A: Applied Science and Manufacturing. 2004;35(12):1419-32.

[3] Simacek P, Advani SG. Desirable features in mold filling simulations for Liquid Composite Molding processes. Polymer Composites. 2004;25(4):355-67.

[4] Soukane S, Trochu F. New Remeshing Applications in Resin Transfer Molding. Journal of Reinforced Plastics and Composites. 2005;24(15):1629-53.

[5] Govignon Q, Bickerton S, Morris J, Lin J. A stereo photography system for monitoring full field thickness variation during resin infusion. In: Binetruy C, editor. FPCM8. Douais, france: Ecole des Mines de Douai; 2006. p. 231-9.

[6] Tackitt K, Walsh S. Experimental Study of Thickness Gradient Formation in the Vartm Process. Materials & Manufacturing Processes. 2005;20(4):607-27.

[7] Govignon Q, Bickerton S, Morris J, Kelly PA. Full field monitoring of the resin flow and laminate properties during the resin infusion process. Composites Part A: Applied Science and Manufacturing. 2008;39(9):1412-26.

[8] Li J, Zhang C, Liang R, Wang B, Walsh S. Modeling and analysis of thickness gradient and variations in vacuum-assisted resin transfer molding process. Polymer Composites. 2008;29(5):473-82.

[9] Kessels JFA, Jonker AS, Akkerman R. Fully 2 1/2D flow modeling of resin infusion under flexible tooling using unstructured meshes and wet and dry compaction properties. Composites Part A: Applied Science and Manufacturing. 2007;38(1):51-60.

[10] Andersson HM, Lundstrom TS, Gebart BR. Numerical model for vacuum infusion manufacturing of polymer composites. International Journal of Numerical Methods for Heat & Fluid Flow. 2003;13(3):383-94.

[11] Govignon Q, Bickerton S, Kelly PA. Simulation of the Complete Resin Infusion Process. (9th International Conference on Flow Processes in Composite Materials (FPCM9). Montreal (Quebec) Canada2008.

[12] Govignon Q, Bickerton S, Kelly PA. Simulation of the reinforcement compaction and resin flow during the complete resin infusion process. Composites Part A: Applied Science and Manufacturing. 2010;41(1):45-57.

[13] Timms J, Govignon Q, Bickerton S, Kelly PA. Observation from the Filling and Post-Filling Stages of Axisymmetric Liquid Composite Moulding with Flexible Tooling. 10th International Conference on Flow Processes in Composite Materials (FPCM10). Monte-Verita, Switzerland2010.

[14] Timms J, Bickerton S, Kelly PA. Laminate thickness and resin pressure evolution during axisymmetric liquid composite moulding with flexible tooling. Composites Part A: Applied Science and Manufacturing. 2012;43(4):621-30.

NUMERICAL SIMULATION OF RESIN FLOW, MOULD DEFLECTION AND REINFORCEMENT DEFORMATION IN RTM LIGHT PROCESSING

Jamie G. Timms[1], Simon Bickerton[1] and Piaras A. Kelly[2],

[1]*Centre for Advanced Composite Materials, Department of Mechanical Engineering*
[2]*Department of Engineering Science*
The University of Auckland, Auckland, New Zealand
Corresponding author's e-mail: jtim009@aucklanduni.ac.nz

ABSTRACT: A numerical simulation of the RTM Light manufacturing process must capture the interactions between resin flow, preform deformation and mould deflection that occur during filling and post-filling. From a numerical solution perspective, RTM Light is similar to the fluid-structure interaction (FSI) class of problems, where the 'fluid' is a saturating deformable porous media and the structure is a compliant mould. Previous implementations of RTM Light simulations have been based on a partitioned solution procedure, using independent solvers for the flow and structure modules and a fixed point iteration coupling method. While this type of coupling has been successfully implemented in the solution of a number of FSI problems, it is prone to instability when coupling between the subdomains is strong, as is the case in RTM Light. This paper presents the development of a finite element RTM light simulation and compares performance of a number of partitioned and monolithic solution approaches for solving the coupled structural and flow problem. The flexibility of the code is demonstrated by simulating the limiting cases of zero mould compliance (i.e. RTM) and complete compliance (i.e. Resin Infusion/VARTM), along with the intermediate case of RTM Light.

KEYWORDS: *RTM Light, simulation, deformable porous media, coupled systems*

INTRODUCTION

Although all Liquid Composite Moulding (LCM) processes employ closed moulds, the construction and mechanical properties of those moulds can vary widely, from rigid tooling, as used in Resin Transfer Moulding (RTM) and Compression RTM, to fully compliant films used in Resin Infusion (a.k.a. VARTM). The RTM Light manufacturing process differs from RTM by replacing one rigid mould half with a lighter, less rigid component. The lighter mould half is often an isotropic glass fibre composite, and clamping is usually provided by application of vacuum to a region at the periphery of the mould cavity. Resin flow is driven by a cavity vacuum, an external injection system, or a combination of the two. RTM Light can provide significant reductions in setup costs when compared to RTM, while at the same time allowing for higher injection pressures, higher volume fractions, and reduced cycle times when compared to flexible film processes [1]. However, the coupled interactions between mould flexure, reinforcement deformation and the evolution of the saturating resin phase complicate the development of efficient numerical simulations for RTM Light processing.

MODEL DEVELOPMENT

Assumptions and governing equations

Deformable porous media equations

In a full 3D problem, the porous media may be modelled as an elasto-porous solid, but assuming that the parts are thin allows the model to be simplified considerably through the introduction of the parameter *h*, the transverse part thickness [2]. The porous media domain is split into saturated and unsaturated subdomains, with the unsaturated domain assumed to be at constant pressure. For the saturated subdomain the fluid flow is governed by Darcy's law:

$$v_i = -\frac{K_{ij}}{\mu} p_{,j} \qquad \text{in } \Omega_F \qquad (1)$$

where K is the permeability, μ is the viscosity, v is the Darcy velocity and p is the resin pressure. Conservation of fluid and fibre mass leads to the continuity equation:

$$\dot{h} + (hv_i)_{,i} = 0 \qquad \text{in } \Omega_F \qquad (2)$$

Terzaghi's principle relates the effective stress on the fibre bed $\bar{\sigma}$ to the fluid pressure and the total stress σ applied to the porous media:

$$\sigma_{ij} = \bar{\sigma}_{ij} - \delta_{ij} p \qquad \text{in } \Omega_F \qquad (3)$$

Structural equations

For the model of the mould structure we assume strains and rotations to be small, and the mould to be constructed from a linear elastic material. Therefore, the governing equations of the structure are those of linear elasto-statics [3]:

Internal equilibrium of the stresses τ and the body forces b:

$$\tau_{ij,j} + b_i = 0 \qquad \text{in } \Omega_S \qquad (4)$$

Strain-displacement equations:

$$e_{ij} = \tfrac{1}{2}\left(u_{i,j} + u_{j,i}\right) \qquad \text{in } \Omega_S \qquad (5)$$

Stress-strain equations, where E_{ijkl} are the elastic moduli:

$$\tau_{ij} = E_{ijkl} e_{kl} \qquad \text{in } \Omega_S \qquad (6)$$

Coupling equations

The boundary conditions at the interface Γ_I between the porous media and the flexible mould are of particular importance because they determine the nature of the coupling between the two domains. There are two conditions; the first is compatibility of displacement:

$$h - h_0 = u_i n_i \qquad \text{on } \Gamma_I \tag{7}$$

where h_0 is the initial porous media thickness and **n** is the unit normal vector to the part (i.e. the local thickness direction). The second condition is equilibrium of surface tractions:

$$\begin{aligned} \tau_{ij} n_j &= \sigma_{ij} n_j \\ &= \bar{\sigma}_{ij} n_j - \delta_{ij} p \end{aligned} \qquad \text{on } \Gamma_I \tag{8}$$

This implies that at the interface the normal surface traction on the mould is equal to the total stress on the porous media.

Resin front propagation

The propagation of the resin front is governed by the interstitial fluid velocity normal to the front interface Γ_F:

$$\dot{x}_n = -\frac{K_{ij}}{\phi\mu} p_{,j} n_i \qquad \text{on } \Gamma_F \tag{9}$$

Constitutive equations

There are two important constitutive equations for the fibre bed that are required to complete the model. The first is the permeability function:

$$K_{ij} = K_{ij}(V_f) \tag{10}$$

where V_f is the fibre volume fraction. The second is the reinforcement compaction function, which relates fibre deformation to effective stress:

$$\bar{\sigma}_{ij} = \bar{\sigma}_{ij}\left(V_f, \dot{V}_f, \text{history}\right) \tag{11}$$

Fibrous reinforcements used in LCM processes exhibit a complex combination of nonlinear elastic, viscoelastic and plastic behaviour under loading, with several models of varying complexity having been proposed to date [2,4]. For the purposes of this paper, the response is assumed to be nonlinear elastic only, but the procedures described here can be extended to more general compaction models.

Finite element discretisation

The finite element method is used to perform the spatial discretisation of the governing equations for the mould structure and the deformable porous media. Weighted residual methods (e.g. Galerkin) are used for the porous media while the structural domain can be discretised with either weighted residual or variational methods [3]. There is a great deal of flexibility in the choice of elements for either domain, depending on the geometry, dimensionality and mould construction of the problem at hand. Table 1 provides a summary of the implemented combinations, but extensions to a wider variety of problems beyond those listed follow naturally.

Table 1: Elements for simulation problem types

Description	**Pressure Element**	**Structural Element**
1D Rectilinear	Cubic-Hermite (C-H)	Euler-Bernoulli Beam
1D Axisymmetric	Axisymmetric C-H	1D Kirchhoff Plate
2D	Bilinear Quad / Linear Tri	Discrete Kirchhoff Tri

Applying the spatial discretisation results in a coupled set of nonlinear differential-algebraic equations for the two domains:

$$\begin{aligned} \mathbf{C}_1\dot{\mathbf{h}} + \mathbf{K}_1(\mathbf{h})\mathbf{p} &= \mathbf{f}_1 \\ \mathbf{K}_2\mathbf{h} - \mathbf{f}_f(\mathbf{h}) - \mathbf{f}_p\mathbf{p} &= \mathbf{f}_2 \end{aligned}, \tag{12a-b}$$

where **h** and **p** are vectors of the structural and porous media freedoms. Introducing an implicit time discretisation,

$$\dot{\mathbf{h}}_t = \frac{\mathbf{h}_t - \mathbf{h}_{t-\Delta t}}{\Delta t}, \tag{13}$$

reduces Eqns. 12a-b to a set of nonlinear algebraic equations at each time step.

COUPLING AND SOLUTION PROCEDURES

Coupled problems are typically solved using one of three approaches: field elimination, monolithic (direct) treatment or partitioned (iterative) treatment [5]. Elimination involves removing one or more fields from the governing equations through manipulation and transformation before solving for the remaining variable(s). This technique is appropriate for the limited number of problems where elimination is possible. The monolithic approach combines the coupled subsystems into a single problem and solves for all variables simultaneously, whereas the partitioned approach solves the systems separately while transmitting the coupling interactions through boundary, forcing or property terms. Partitioned approaches are attractive because of their potential computational efficiency and the ability to reuse existing codes for each subsystem, but can often lack the robustness and stability of a monolithic approach [6].

Partitioned solution procedures

Partitioned solution procedures are expedited by representing Eqns. 12a-b in ‘black-box’ form:

$$\begin{aligned} \mathbf{p} &= F(\mathbf{h}) \\ \mathbf{h} &= S(\mathbf{p}) \end{aligned} \tag{14a-b}$$

This allows a fixed point equation for **p** (or **h**) to be written as

$$\mathbf{r}(\mathbf{p}) = F \circ S(\mathbf{p}) - \mathbf{p} = \mathbf{0} \tag{15}$$

Fixed-point iteration with under-relaxation (UR)

The most straightforward solution procedure of Eqn. 15 is fixed-point iteration:

$$\mathbf{p}^{k+1} = F \circ S(\mathbf{p}^{k}) \tag{16}$$

This technique is prone to instability when the coupling between the subsystems is strong; for the RTM Light problem convergence can be obtained by introducing a relaxation parameter:

$$\mathbf{p}^{k+1} = (1-\omega)\mathbf{p}^{k} + \omega(F \circ S(\mathbf{p}^{k})) \qquad 0 < \omega \leq 1 \tag{17}$$

Fixed-point with Aitken relaxation

Fixed-point iteration with Aitken relaxation [7] introduces a dynamic relaxation factor, such that the next estimate of **p** is a linear combination of the two prior estimates:

$$\begin{aligned} \mathbf{p}^{k+1} &= \mathbf{p}^{\mathbf{k}} + \omega^{k}\mathbf{r}^{\mathbf{k}} \\ \mathbf{r}^{k} &= F \circ S(\mathbf{p}^{k}) - \mathbf{p}^{k} \\ \omega^{k} &= -\omega^{k-1}\frac{(\mathbf{r}^{k-1})^{\mathrm{T}}(\mathbf{r}^{k}-\mathbf{r}^{k-1})}{(\mathbf{r}^{k}-\mathbf{r}^{k-1})^{\mathrm{T}}(\mathbf{r}^{k}-\mathbf{r}^{k-1})} \end{aligned} \tag{18a-c}$$

IQN-ILS

The final and most sophisticated partitioned technique presented here is the quasi-Newton technique based on a least squares approximation of the Jacobian (IQN-ILS) by Degroote et al. [8]. The method requires taking the pressure residual in Eqn. 15 and forming a Newton-Raphson iteration step:

$$\frac{d\mathbf{r}^{k}}{d\mathbf{p}^{k}}\Delta\mathbf{p}^{k+1} = -\mathbf{r}^{k} \tag{19}$$

The formation and subsequent solution of Eqn. 19 is a costly operation, which the IQN-ILS method avoids by developing an approximation to the inverse of the Jacobian based on the previous residual and state vector updates:

$$\begin{aligned} \mathbf{V}^{k} &= \left[\Delta\mathbf{r}^{k-1}, \Delta\mathbf{r}^{k-2}, \dots , \Delta\mathbf{r}^{0}\right] \\ \mathbf{W}^{k} &= \left[\Delta\mathbf{p}^{k-1}, \Delta\mathbf{p}^{k-2}, \dots , \Delta\mathbf{p}^{0}\right] \end{aligned} \tag{20a-b}$$

The least squares problem is solved by performing a QR decomposition on V:

$$\mathbf{V}^{k} = \mathbf{Q}^{k}\mathbf{R}^{k}, \tag{21}$$

which is used to form an approximation to the inverse Jacobian:

$$\left(\frac{d\mathbf{r}^{k}}{d\mathbf{p}^{k}}\right)^{-1} \approx \mathbf{W}^{k}(\mathbf{R}^{k})^{-1}(\mathbf{Q}^{k})^{\mathrm{T}} - \mathbf{I} \tag{22}$$

Monolithic solution procedures

Newton-Raphson (NR)

Rewriting Eqns. 12a-b in residual form and taking the derivatives provides the basis of the Newton-Raphson method:

$$\begin{aligned}\mathbf{r}_1 &= \frac{\mathbf{C}_1}{\Delta t}(\mathbf{h}-\mathbf{h}_{t\text{-}\Delta t}) - \mathbf{K}_1(\mathbf{h})\mathbf{p} - \mathbf{f}_1 = \mathbf{0} \\ \mathbf{r}_2 &= \mathbf{K}_2\mathbf{h} - \mathbf{f}_f(\mathbf{h}) - \mathbf{f}_p\mathbf{p} - \mathbf{f}_2 = \mathbf{0}\end{aligned} \tag{23a-b}$$

$$\begin{bmatrix} \dfrac{\partial \mathbf{r}_1}{\partial \mathbf{p}} & \dfrac{\partial \mathbf{r}_1}{\partial \mathbf{h}} \\ \dfrac{\partial \mathbf{r}_2}{\partial \mathbf{p}} & \dfrac{\partial \mathbf{r}_2}{\partial \mathbf{h}} \end{bmatrix}^k \begin{bmatrix} \Delta\mathbf{p} \\ \Delta\mathbf{h} \end{bmatrix}^{k+1} = -\begin{bmatrix} \mathbf{r}_1 \\ \mathbf{r}_2 \end{bmatrix}^k \tag{24}$$

Newton-Raphson with time step substitution (NR-S)

The vast majority of LCM mould filling simulations use a volume of fluid technique to capture the resin front propagation. However, one of the drawbacks of this approach is the dependence of the time step on the state variables. The full formulation of the Jacobian accounts for this dependence, but this may create a considerable computational overhead. As an alternative approach, the time step may be updated by simple substitution at each iteration.

NUMERICAL EXPERIMENTS

The comparative performance of the solution procedures is demonstrated through a 1D test problem described in Fig. 1. The resin pressure and laminate thickness at the end of filling for RTM, RTM Light, and VARTM are shown in Fig. 2, demonstrating the variety of processes able to be simulated under this framework. The results are generated with a 100 element mesh using the NR-S solution procedure.

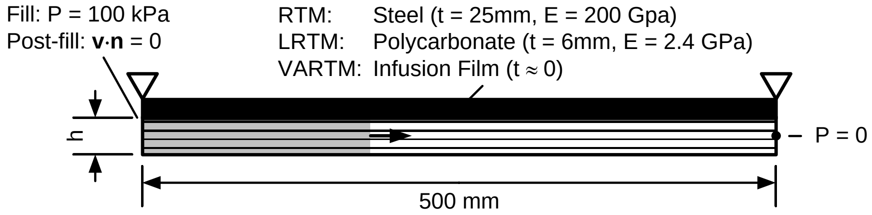

Fig. 1: Schematic of 1D example problem

Discussion

Comparisons between the monolithic and partitioned solution procedures are presented for the 1D example problem using a 100 element mesh and convergence tolerances between 10^{-3} and 10^{-8}. Fig. 3 shows the convergence rates at the final time step and Fig. 4 demonstrates the computational effort required for each approach in terms of average iterations and total solution time. It is clear that the quadratic convergence of the full Newton-Raphson technique is degraded by introducing the time step substitution, although it still outperforms the partitioned procedures. The IQN-ILS technique is the best performed partitioned procedure, particularly as the tolerance tightens (or the problem size increases), while the simple under-relaxation approach fails to converge within 20 iterations.

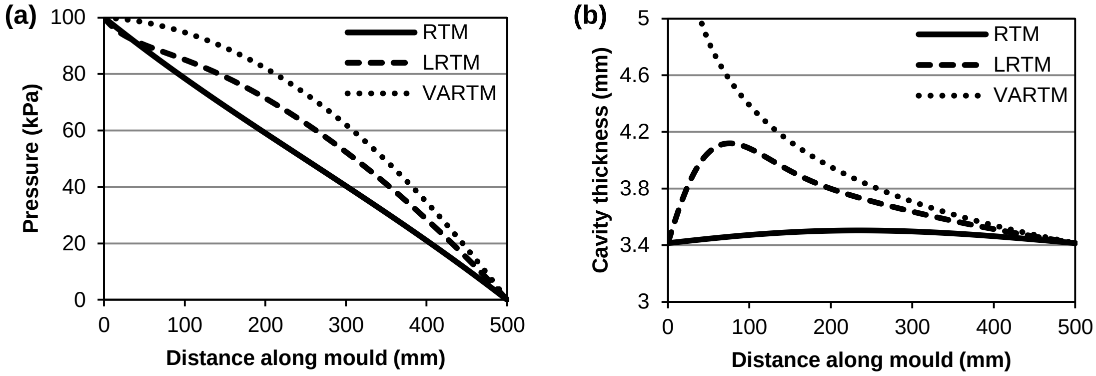

Fig. 2: Resin pressure and mould cavity thickness at the end of filling

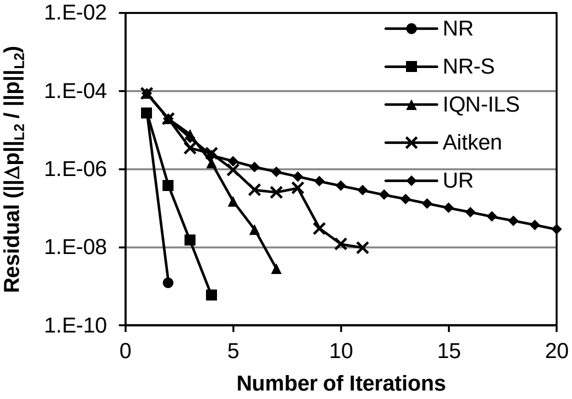

Fig. 3: Final time step convergence rates for pressure update tolerance of 10^{-8}

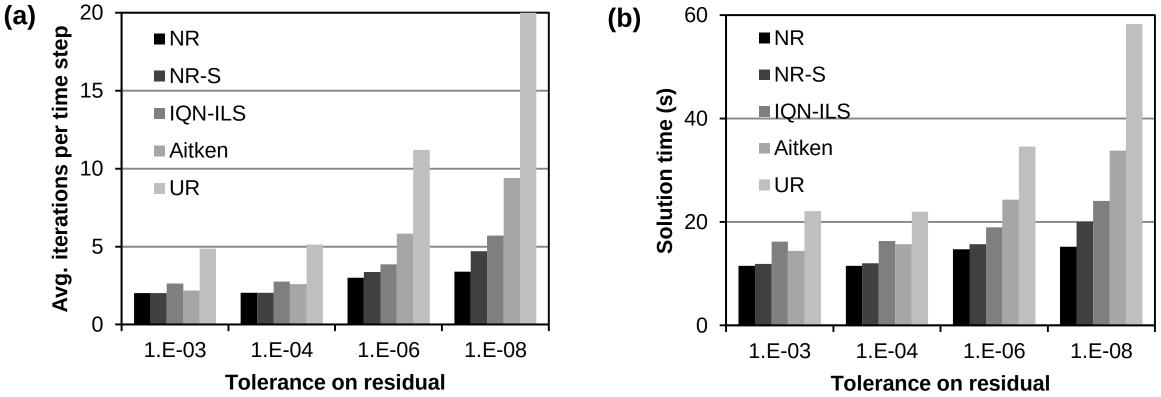

Fig. 4: Computational effort: (a) average iterations to converge, (b) solution time.

The monolithic procedures were also found to be the most robust, followed by the IQN-ILS and dynamic relaxation approaches. The static under-relaxation was the least reliable, with divergence occurring for certain values of ω.

CONCLUSIONS

A coupled finite element simulation of the RTM Light process has been developed along with a number of monolithic and partitioned coupled solution procedures. The solution procedures have been compared for a 1D example problem. The IQN-ILS technique was the most effective partitioned approach, but was superseded in performance by the monolithic approach for small problem sizes. However, any choice of algorithm must consider the relative importance of computational efficiency, robustness, and software modularity for the problem of interest.

REFERENCES

1. Timms J, Bickerton S and Kelly PA (2012), ‘Laminate thickness and resin pressure evolution during axisymmetric liquid composite moulding with flexible tooling’, *Composites Part A: Applied Science and Manufacturing*, 43(4), 621-630.

2. Kelly PA and Bickerton S (2009), ‘A comprehensive filling and tooling force analysis for rigid mould LCM processes’, *Composites Part A: Applied Science and Manufacturing,* 40(11), 1685-1697.

3. Bathe KJ (1996), Finite Element Procedures, New Jersey: Prentice-Hall.

4. Cheng JJ Kelly PA and Bickerton S (2012), ‘A rate-independent thermomechanical constitutive model for fiber reinforcements’, *Journal of Composite Materials*, 45(2), 247-256.

5. Felippa CA, Park KC and Farhat C (2001), ‘Partitioned analysis of coupled mechanical systems’, *Comput. Methods Appl. Mech. Engrg.*, 190, 3247-3270.

6. Matthies HG, Niekamp R and Steindorf J (2006), ‘Algorithms for strong coupling procedures’, *Comput. Methods Appl. Mech. Engrg.*, 195, 2028-2049.

7. Küttler U and Wall W (2008) ‘Fixed-point fluid-structure interaction solvers with dynamic relaxation’, *Computational Mechanics*, 43(1), 61-72.

8. Degroote J, Bathe KJ and Vierendeels J (2009), ‘Performance of a new partitioned procedure versus a monolithic procedure in fluid-structure interaction’, *Computers and Structures*, 87, 793-801.

Section 6

Thermoplastics

PROCESSING OF LONG-POLYMER-FIBER-REINFORCED THERMOPLASTIC PELLETS BY COMPRESSION MOLDING

Thomas Bayerl, Hristo Valchev, Erhard Natter, Peter Mitschang

Institut für Verbundwerkstoffe, Erwin-Schrödinger-Str.Geb. 58, 67663 Kaiserslautern, Germany. Corresponding author's e-mail: thomas.bayerl@ivw.uni-kl.de

ABSTRACT: Polymer-polymer materials consist of a matrix and a reinforcement which originate from the same thermoplastic family. Recent research activities concentrate on the manufacturing of semi-finished polymer-polymer materials in other shapes than the commercially available tapes and sheet-like semi-finished products. A pellet-like form allows the possibility of processing the polymer-polymer material by injection and compression molding. The component design variety offered by these processes is almost unlimited. Nevertheless, the thermoplastic reinforcement is vulnerable to excessive heat. This problem has not been addressed yet since it does not appear with the use of inorganic reinforcements such as glass and carbon fibers. This study deals with the processing of long-polymer-fiber reinforced thermoplastics, in this case polypropylene-polyethylene terephthalate (PP-PET) and a self-reinforced polyethylene terephthalate (PET-PET), by extrusion for compression molding applications. The influence of extruder temperature on fiber reinforcement and processability is discussed by means of built-in-press rheometry. The impact of the heating process on mechanical properties, such as tensile strength, Young's modulus, and impact strength, is also addressed. The results revealed that the use of a common long fiber reinforced thermoplastic (LFT) process chain is adaptable for the newly developed polymer-polymer material in order to manufacture a complex shaped component. The flow characteristics of the material as well as the preservation of the polymer reinforcement can be handled by means of accurate temperature control.

KEYWORDS: *Polymer-Polymer Composites, Compression Molding, Long-Fiber Reinforced Thermoplastic (LFT), Impact Resistance, Polymer Heating, Self-Reinforced, Sustainability*

INTRODUCTION

First attempts to manufacture polymer-polymer, and especially single-polymer, materials have been made since the 1970s [1,2]. In contrast to usual fiber reinforced polymer composites which mainly benefit from the combination of a polymer matrix and inorganic fibers, polymer-polymer materials consist of a polymer matrix phase and a polymeric reinforcement. The used components can be chosen amongst the variety of all polymers available on the market, whereas mainly thermoplastic versions are nowadays in use. For conforming to the term self-reinforced polymer (SRP), matrix and reinforcement of such materials have to originate from the same polymer type (e.g. polypropylene, PP, matrix and PP fiber). In literature and recent research, the definition of self-reinforced polymers refers also to reinforced materials which consist of a polymer matrix and reinforcement from the same polymer family (e.g. for polyolefins: a combination of high density polyethylene, HDPE, and PP). To distinguish between these types, the concurrent definition of single-component (same polymer) and multi-component (same polymer family) SRP is applied. Further classifications respect the production process steps (single or multi) and the spatial distribution of the reinforcement (1D, 2D, 3D) [3].

Commercial SRP materials are already available from a small amount of manufacturers but they are all based on polyolefins. The all-polypropylene materials named Curv®, PURE®, Tegris^{TM}, and Armordon® offer outstanding mechanical properties at extreme light-weight [4,5,6,7]. Besides them, a HDPE self-reinforced composite has recently appeared on the market: kaypla® from Nextrusion GmbH [8]. All products offered on the market have in common that they are only available in sheet-like or tape-like form.

In contrast, recently developed polymer fiber reinforced thermoplastic pellets offer the possibility for injection and compression molding process with a higher freedom of design [9,10] Nevertheless, the application of standard machinery using screws for heating may significantly harm the reinforcement and decrease its integrity. Therefore, the objective of this work was to investigate the feasibility of self-reinforced pellets in a long-fiber reinforced thermoplastic (LFT) compression molding process with standard equipment.

MATERIALS & METHODS

A self-reinforced polyester system (srPET) consisting of an amorphous polyethylene therephthalate (PET) matrix and crystalline PET fibers as well as a PP-PET compound were applied in this feasibility study (Table 1). The PP-PET compound served as model system for a self-reinforced composite providing a large temperature gap between matrix and fiber melting point. Both materials were dried at 40 °C for a minimum of 24 h prior to the processing in the extruder. Each compound contained a fiber fraction of approximately 30 wt-%.

Table 1: Investigated materials

Material	Manufacturer	Pellet length [mm]	Reinforcement fraction [wt-%]
PP-PET30	Celstran GmbH, Germany	7	30
LPET-HTPET31 (srPET)	Comfil ApS, Denmark	5	31

For the pellet melting, a Kannegiesser KMH60S (Kannegiesser, Germany) screw extruder was applied. By adjusting the extruder’s six heating zones, distinct mass temperatures could be realized. All other parameters like back pressure or speed were kept on a constant level (Table 2). The amount of mass, which was heated within a cycle of approx. 3 min 30 s, was 500 g per shot. The material dough was manually transported and placed into the mold.

For the molding of the preheated dough, a Dieffenbacher hydraulic press (J. Dieffenbacher GmbH, Germany) was able to realize a maximum press force of 8000 kN (800 t) and is regarded as an industrial standard machine. Several molds were used for the trials which included, besides the rheometer setup, a shear edge mold for a sheet (540 x 540 mm²), and a complex shaped tool with ribs for the manufacturing of an automotive demonstrator part.

Table 2: Important extruder parameters

Max. pressure	150 bar
Nozzle diameter	55 mm
Speed	10 min^{-1}
Back pressure	40 bar
Material mass	Approx. 500 g
Cycle time	3 min 30 s

The experimental series contained an analysis of the compounds' rheological properties, namely the viscosity in reference to the process temperature. The viscosity was measured by a rheometer setup which was directly mounted in the press (Fig. 1). The setup consisted of two disks with a diameter of 250 mm. After placing the dough between the heated disks (160 °C), the press was closed. The disk temperature was chosen higher than the usual mold temperature to enable an isothermal material flow without freezing effects on the disk. By analyzing the obtained press data, which contained closing speed, press force, and distance between the disks, the shear rate as well as the viscosity could be calculated according to the given equations (Eqn. 1 and Eqn. 2) [11]. The closing speed was preset to 5 mm/s and a maximum force of 1500 kN was applied after complete closure.

$$\text{Shear rate } \gamma = \frac{2 \cdot v \cdot R}{h^2} \tag{1}$$

$$\text{Viscosity } \eta = \frac{2 \cdot F \cdot h^3}{3 \cdot \pi \cdot v \cdot R^4} \tag{2}$$

v = closing speed (5 mm/s)	F = press force
h = distance between disks	R = radius of the disks (125 mm)

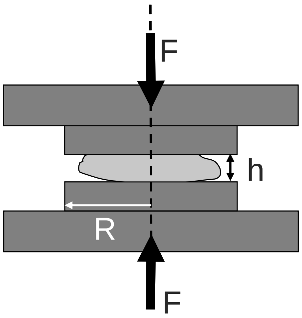

Fig. 1: Rheometry setup

For the mechanical analysis, tensile tests with cut samples from compressed sheets according to DIN EN ISO 527 and dart impact experiments according to DIN EN ISO 6603-2 were performed. Furthermore, specimen bars were cut for the use with a Charpy impact testing device according to DIN EN ISO 179-1eA.

RESULTS

General Observations and Rheometry Results

For both investigated compounds, various mass temperatures have been tested on their feasibility. The range for PP-PET included temperatures from 170 °C to 250 °C, the srPET experiments covered the range from 180 °C to 260 °C (Table 3). The viscosity was revealed to be too high in case of a mass temperature of 170 °C for PP-PET. The extruder was not able to transport the high viscous mass sufficiently. An identical behavior was observed with srPET at 180 °C and 200 °C.

Table 3: Investigated mass temperatures

PP-PET	(170 °C)	180 °C	190 °C	200 °C	220 °C	-	250 °C	-
srPET	-	(180 °C)	-	(200 °C)	220 °C	240 °C	-	260 °C

In case of PP-PET, all examined mass temperatures led to a dough-like viscous material, whereas the srPET system was found in a honey-like, low viscous state at 260 °C. Lower temperatures resulted in high viscous doughs for the polyester as well.

The optical impression of the viscosity changes caused by the different process temperatures was verified by the rheological analysis.

The PP-PET system revealed a maximum viscosity below 1000 Pas which is in the range of competing glass-fiber filled PP compounds (Fig. 2) [12]. The viscosity declined with increasing mass temperature whereas the flowability nearly showed the same results between 180 °C to 220 °C. The highest temperature of 250 °C already indicated that the PET fibers might be damaged during the heating process, which could be verified in a subsequent mechanical analysis.

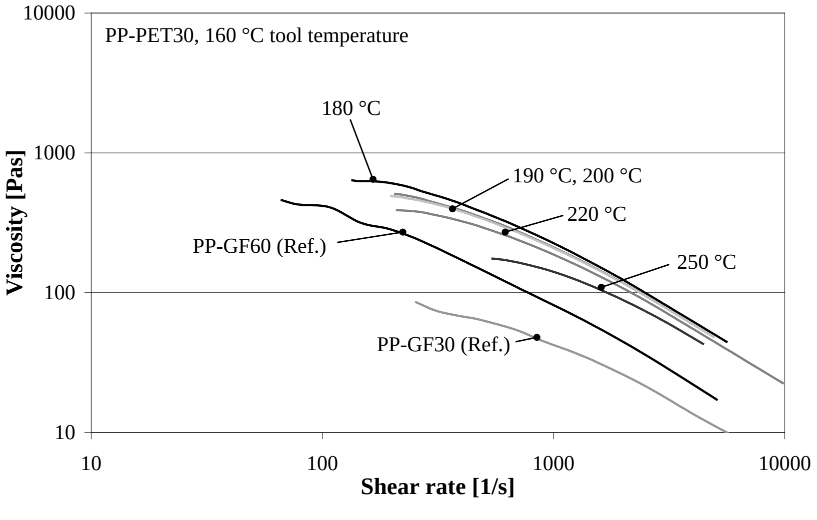

Fig. 2: Viscosity data obtained from the study for PP-PET model compound

The viscosity of the PET-PET system was measured to be significantly higher than the PP-PET material combination (Fig. 3). The minimum processible temperature of 220 °C demonstrated a viscosity in the range of 10000 Pas which was ten times higher than the PP-PET. Only the low viscous, honey-like state at 260 °C, in which significant fibre damage was expected, revealed a viscosity in the range of the PP-PET model compound.

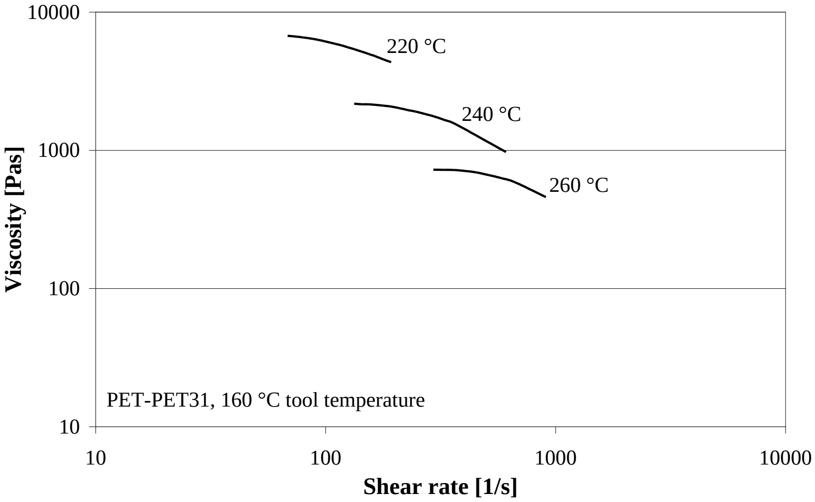

Fig. 3: Viscosity results for the srPET system

By concluding from the rheometry results, a significantly better flow processability in complex molds was expected from the PP-PET. Despite this, both compounds could be processed by standard equipment.

Manufacturing of Plates and Mechanical Testing

After the rheological data had been obtained, a shear edge mold for the manufacturing of sheets was applied. Several plates were manufactured at different process temperatures to investigate the influence of mass temperature on the mechanical performance of SRP. The specimens for the mechanical tests were obtained from these sheets.

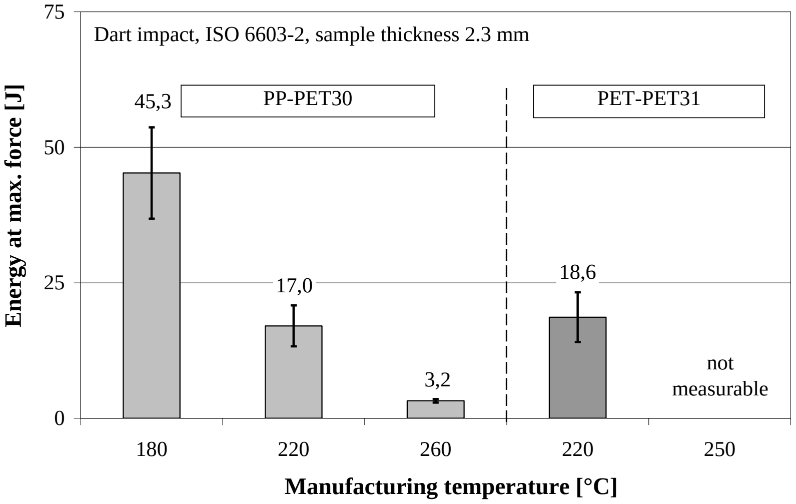

Fig. 4: Drop impact energy obtained from samples from the compressed sheets

The dart impact resistance decreased for both material combinations with increasing process temperature (Fig. 4). Although the second sample of the srPET at 260 °C did not deliver a measurable result, the sample behavior itself revealed a very weak condition. The 260 °C heated srPET sheets had a transparent, glassy morphology which was so brittle that the forces during the impact test were not high enough to exceed the random noise of the load cell. In contrast to srPET, the PP-PET indicated the expected behavior of higher mass temperatures resulting in increased fiber damage and, thus, in lower impact resistance. This behavior could be validated with notched Charpy impact samples (Fig. 5). By concluding from the impact results, the lowest mass temperature of 180 °C should be applied for processing, whereas the corresponding process temperature for srPET should not be higher than 220 °C. In general, the lowest possible process temperature should be applied to preserve the reinforcement integrity.

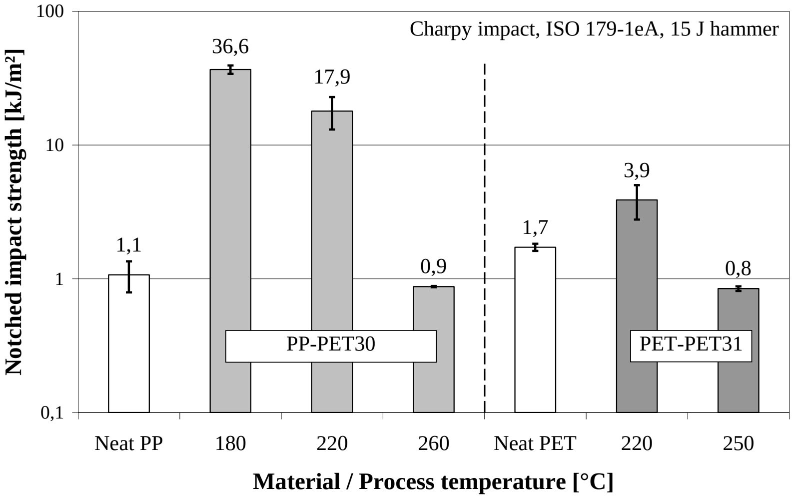

Fig. 5: Results of notched Charpy impact tests

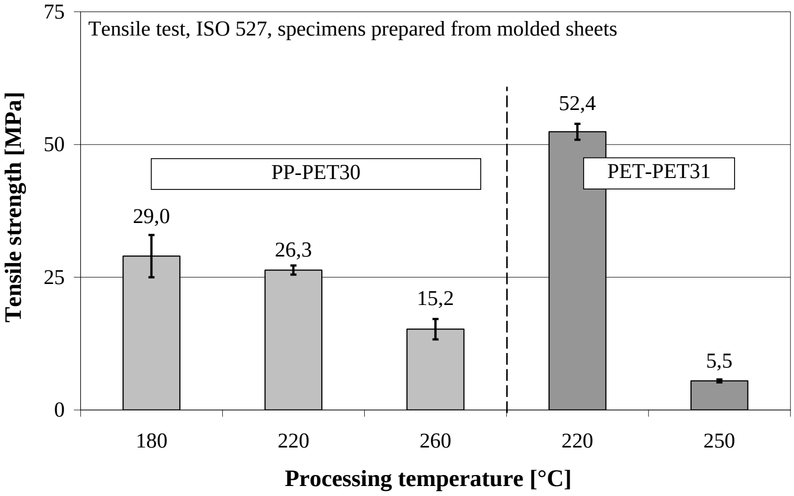

Fig. 6: Tensile strength in comparison to manufacturing temperature for PP-PET and LPET-HTPET

Similar trends in comparison to the results of the impact tests were obtained from the tensile tests (Fig. 6). The highest performance was measured from samples with the lowest mass temperature during processing. This conclusion is valid for PP-PET as well as srPET. The tensile experiments revealed a significant higher tensile strength and modulus for the PET-PET compounds than for the PP-PET. Nevertheless, the strain at maximum force was significantly higher for the PP-PET.

Manufacturing of Complex Shaped Demonstrators

The applied demonstrator mold was a Y-shape geometry containing several ribbings for examining the flowability of the dough. For a complete mold filling, a mass of 1 kg was calculated for PP-PET, whereas 1.3 kg was needed for srPET. The mold was preheated to 90 – 100 °C when the dough was placed in front of the cavity on the lower mold part.

For improving the material flowability, PP-PET was used at a temperature of 195-200 °C. Since the mold filling was executed in a semi-continuous concept, due to the larger amount of melted material, a higher temperature than previously measured for the best rheological and mechanical performance was necessary to compensate thermal losses. Besides the higher temperature, the processability was unproblematic with PP-PET – the mold could be completely filled without voids resulting in a good demonstrator surface quality.

In contrast to the PP-PET model system, the processing of the self-reinforced polyester was challenging and less successful. The high viscosity led to an incomplete mold filling which resulted in frozen melt flow fronts and voids within the demonstrator. Besides this, also shrunken parts were observed. As consequence, the PET-PET system is assumed to be predestined and more efficient with less complex molds.

CONCLUSION

Within this study was demonstrated that the processing of the newly developed SRP pellets in a LFT compression molding process chain is feasible. The PP based material system revealed good rheological properties resulting in a well-processed demonstrator. The viscosity of the material enabled the filling of complex cavities. The self-reinforced polyester demonstrated higher mechanical properties than the investigated PP-PET system but resulted also in a higher viscosity. The viscosity was measured in the range of 10000 Pas and did not allow a sufficient flow processing within the complex mold. Despite this, the filling of sheet-like molds was possible.

By concluding from the obtained results, the mass temperature of self-reinforced materials has to be chosen to a minimum to preserve the performance of the polymeric reinforcement. Nevertheless, a compromise has to be made since a lower mass temperature simultaneously causes a higher viscosity which limits the application of the respective material within complex tools.

ACKNOWLEDGMENTS: The research leading to these results has received funding from the European Community’s Seventh Framework Programme (FP7), Theme NMP2007, under the grant agreement no. 214355.

REFERENCES

1. Mead, WT, Porter, RS (1978), 'The Preparation and Tensile Properties of Polyethylene Composites', *Journal of Applied Polymer Science*, 22, 3249–3265.

2. Capiati, NJ, Porter, RS (1975), 'The concept of one polymer composites modelled with high density polyethylene', *Journal of Materials Science*, 10, 1671–1677.

3. Kmetty Á, Bárány T, Karger-Kocsis J (2010), 'Self-reinforced polymeric materials: A review', *Progress in Polymer Science*, 35, 1288–1310.

4. Don & Low Ltd (2011), 'Armordon Self Reinforcing Polypropylene (srPP) – panels', company publication, *http://www.armordon.com/wpcontent/uploads/ 2009/04/panels-insert.pdf*.

5. Propex Fabrics (2011), 'Curv® – Technical Data Sheet C100A', company publication, *http://www.curvonline.com/deutsch/pdf/datasheet_long.pdf*.

6. Lankhorst Pure Composites bv (2007), 'PURE® - Technical Data Sheet, PURE® - sheets', company publication, version 30-03-07.

7. Milliken & Co (2007), 'Tegris Sheet Stock, Technical Data Sheet', company publication.

8. Nextrusion GmbH (2011), 'Product Information kaypla®, High-Performance Tapes', company publication, *http://www.kaypla.de/fileadmin/user_upload/kaypla_doc/ product_informations/product_information_kaypla_tapes.pdf*.

9. Hare C (ed) (2010), 'Esprit – a new project launched to expand the versatility of Self Reinforced Plastics with partners from across Europe', Technical Bulletin, *www.espritproject.eu*.

10. Hare C (ed) (2010), 'Self Reinforced Polymer composites with impact!', Technical Bulletin, *www.espritproject.eu.*

11. Edelmann K (2001), Prozessintegrierte Analyse des Fliessverhaltens von faserverstärkten thermoplastischen Pressmassen für die Serienfertigung, dissertation, TU Kaiserslautern.

12. Sommer M (2006), Eigenschaftserweiterung von langfaserverstärkten thermoplastischen Fließpresshalbzeugen, dissertation, TU Kaiserslautern.

SHEAR CHARACTERISATION OF UD THERMOPLASTIC COMPOSITES

S.P. Haanappel[1,2], B. Rietman[1], and R. Akkerman[1,2]
[1]*Faculty of Engineering Technology, Chair of Production Technology, University of Twente*
P.O. Box 217, 7500AE Enschede, the Netherlands, s.p.haanappel@utwente.nl
[2]*ThermoPlastic composite Research Centre (TPRC), Palatijn 15, P.O. Box 770, 7500AT*
Enschede, the Netherlands

ABSTRACT: Intra-ply shear is one of the main mechanisms to accumulate deformations in thermoplastic composites forming processes. In this paper a shear characterisation method for uni-directionally (UD) reinforced thermoplastics in their molten configuration is presented. Bar-like specimens made from UD carbon PEEK material are subjected to oscillating torsional loads. By utilising linear visco-elastic theory, the small strain oscillatory responses are translated to storage and loss shear moduli. The frequency dependent moduli are subsequently translated to the transient domain and show a close-to elastic response for the considered instantaneous strain rates. The application of such characterisation data is demonstrated by modelling the stamp forming process of a complex shaped product with the aid of the finite element method. The process considered deals with an initially flat quasi-isotropic laminate consisting of eight plies, which is formed at high temperatures. Predicted intra-ply shear strains are compared with those measured by photogrammetry in a real formed part. Predicted and measured shear strain distributions and their magnitudes were in good agreement. Moreover, critical regions in which small wrinkles develop were indeed indicated by the forming predictions.

KEYWORDS: *thermoplastic, laminates, uni-directional, shear, characterization, forming, experiments, modeling*

INTRODUCTION

Hot stamp forming of fibre reinforced thermoplastic laminates is ideally suited for the production of thin shelled products with complex curvatures. Nevertheless, process induced defects such as local buckling and subsequent wrinkling appear frequently and disqualify the final product. Better anticipation on these defects results in lead-time reductions and can be achieved by predicting such defects in the early product design stages.

Simulation tools for the stamp forming process of uni-directional (UD) fibre reinforced thermoplastics aim to reduce the number of optimisation cycles during the development phase of a product. Constitutive models are needed to describe the occurring deformation mechanisms, such as intra-ply shear, out-of plane bending, and ply-ply and tool-ply friction. These models subsequently require reliable material property data and corresponding characterization methods.

An alternative method for intra-ply shear characterization by means of torsion is presented. The measured data is subjected to some conversions, such that it can be used in forming simulations. Indeed, the forming process of a complex product is simulated as a next step, with the obtained characterization data involved. The other deformation mechanisms are characterised by other methods and are not considered here. The simulation results are then briefly compared with a real stamp formed product.

SHEAR CHARACTERISATION

The published methods for intra-ply shear characterisation of UD fibre reinforced polymer melts result in distinctly different material parameters, as was summarised clearly by Harrison [1]. For example, a difference of several orders of magnitude was found between plate-plate rheology [2] and picture frame experiments [3]. Therefore, the development of an alternative shear characterisation technique is desired. Reliability, repeatability, and easy accessibility are the desired properties of the envisioned test. The method shown here comprises a straight rectangular bar that is subjected to a torsional load. The set-up makes use of a commercially available rheometer. A set of slightly modified standard fixtures is used, which are generally applied to bar like specimens in their solid to rubbery material state.

Torsion of bars with a rectangular cross section

The method presented here deals with a prismatic bar that is subjected to torsion. The bar has a constant rectangular cross section, as shown in Fig. 1. It is assumed that the bar consists of UD fibres that run parallel to the rotation axis. Torsional loads are introduced via clamps that are attached to both ends of the specimen. At each end the specimen is clamped by two clamping surfaces parallel to the axis of rotation.

Considering an elastic rectangular bar with length *L*, the torque *M* can be related to the rotation angle ϕ and a shear modulus *G* via [4]:

$$M = GJ\frac{\phi}{L} \tag{1}$$

The torsional rigidity *J* for a rectangular cross section with dimensions *t* and *w* reads:

$$J(t,w) = \tfrac{1}{3}t^3 w\left(1 - \frac{192}{\pi^5}\cdot\frac{t}{w}\cdot\sum_{k=1}^{\infty}\frac{1}{(2k-1)^5}\cdot\tanh\left(\frac{(2k-1)\pi w}{2t}\right)\right) \tag{2}$$

It is aimed to subject the rectangular bar to dynamical mechanical tests that involve small amplitude oscillatory deformations through a range of frequencies. Such tests are generally used for the characterisation of visco-elastic materials. Sinusoidally oscillating loads can be represented by replacing the variables in Eqn. (1) with their complex variants. The following relation to determine the complex shear modulus of the tested material then yields:

$$G^* = G' + iG'' = \frac{M^*}{J}\frac{L}{\phi^*} \qquad \text{with} \quad \phi^* = \phi_0 e^{i\omega t} \quad \text{and} \quad M^* = M_0 e^{i(\omega t+\delta)} \tag{3}$$

and can straightforwardly be applied to the measured responses of the device at hand.

Specimen preparation and experiments

Torsion bar specimens were produced with polyether ether ketone (PEEK) UD carbon fibre prepreg, commercially available as CETEX Thermo-Lite® from Ten Cate. The specimen production comprises the hot pressurised consolidation of a stack of 80 equally orientated plies, resulting in an 11 mm thick laminate with a 59±3 % fibre volume fraction. The laminate was subsequently cut with a diamond wheel saw to yield specimens with a width and length of 13.0±0.1 mm and 60.6±0.1 mm, respectively. Thick bar-like specimens are preferred, because thin strip-like specimens are more sensitive to unwanted fibre tensions that might occur [5].

Once the specimen is accurately positioned within the fixtures as in Fig. 1 (centre), it is enclosed by a temperature controlled chamber or cavity. The specimen is heated to 390^{o}C and gentle flow of nitrogen gas is applied within the cavity in order to avoid polymer degradation effects that are driven by the presence of oxygen. Strain sweeps are performed to explore the linear region of the material response. The maximum shear strain that appears in the rectangular cross section is used as a reference throughout all the analyses and appears at the centre of the longest side of the rectangular cross section. Frequency sweeps are carried out to investigate the material response for a range of loading rates.

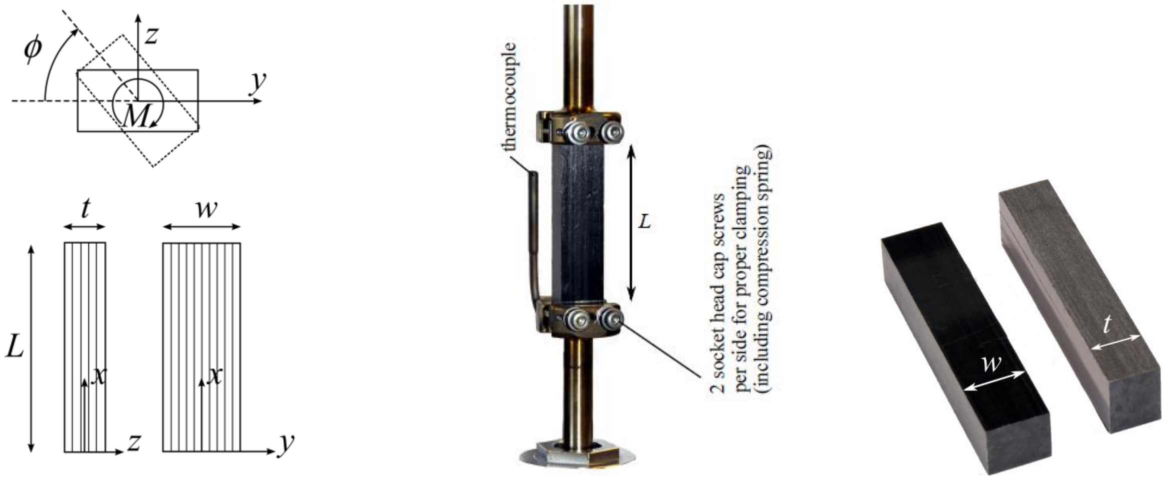

Fig. 1: Left: schematic representation of the UD reinforced straight bar. Centre: fixtures with a mounted specimen. Length *L* indicates the length between the clamps, not the specimen's length itself. Right: typical geometry of the specimens.

Results and discussion

Fig. 2 shows the averaged results of both the amplitude and frequency sweeps for five specimens. The strain range covered during the amplitude sweep is approximately one decade only (Fig. 2, left). This was chosen in order to minimise effects such as fibre migration, which might occur for larger deformations. Such interesting non-linear phenomena could probably lead to deviating responses but are not considered here. The measured shear moduli are constant for the investigated shear strain range. Together with the waveform data that looks visually good, this implies linear visco-elastic material behaviour and thus Eqn. (3) can be applied straightforwardly.

Frequency sweeps were carried out subsequently with shear strain amplitudes of $\gamma_0 = 0.1\%$. The measured moduli are weakly dependent on frequency. A constantly increasing slope can be deduced for the considered range of frequencies. The storage terms are consistently larger than the loss terms within the range of investigated parameters. This behaviour is substantially different from the polymer characteristics without the presence of fibres. The neat polymer characteristics show increasing storage and loss moduli for increasing angular frequencies, as well as a dominating loss modulus. The elastic dominance of the tested composite system here is most likely caused by the presence of the fibres. Multiple fibre-fibre interactions will be present and it is supposed that these invoke elastic effects during material loadings [6].

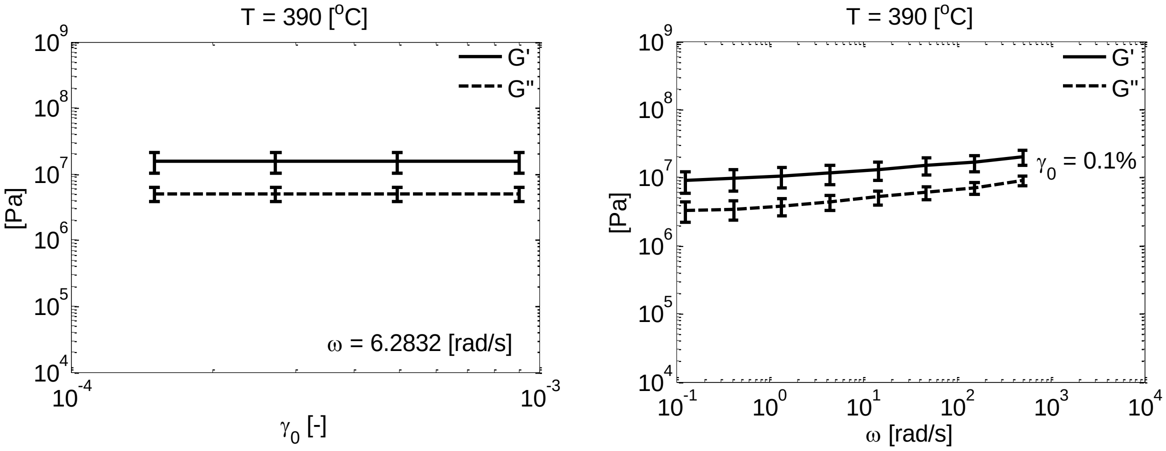

Fig. 2: Storage G’ and loss G’’ moduli, as function of strain amplitude γ_0 (left), and as function of angular frequency ω (right).

Translation to the transient domain

The shear behaviour for small strains is now known in the frequency domain. Since the forming process takes place in the transient time domain, the measured characteristics in Fig. 2 have to be translated. The well-known empirical Cox-Merz relationship is often used for neat polymer melts with a dominating loss modulus. It relates the complex viscosity as a function of the angular frequency, to the steady shear viscosity as a function of shear rate. Generally, this relationship cannot be applied for dispersed media. This was for example shown by Kitano [7] for short glass fibre filled polyethylene (PE). Generally, transient deformations of linear visco-elastic materials are described via the following constitutive relationship from linear visco-elasticity theory (LVE) [8]:

$$\tau(t) = \int_{s=-\infty}^{s=t} G(t-s)\dot{\gamma}(s)ds \qquad (4)$$

where τ is the shear stress, $\dot{\gamma}$ the shear rate, and $G(t)$ is the shear relaxation modulus. The integration is carried out over all past times s up to the current time t. The shear relaxation modulus needs to be determined to describe the transient interaction between shear stress and shear strain and its rate.

Another relation from LVE theory relates this relaxation modulus to the frequency dependent loss modulus [8] via:

$$G(t) = \frac{2}{\pi} \int_0^\infty \frac{G''}{\omega} \cos(\omega t) d\omega \tag{5}$$

where we recognise the inverse Fourier cosine transform. Since the loss modulus shows a straight line in the frequency plot, it can be approximated by a power law function as shown in Fig. 3 (left). Following a similar procedure as was done by Campanella [9], substitution of this fairly simple relation into Eqn. (5) allows for its analytical evaluation. Substitution of the resulting analytical expression into the constitutive relationship from the LVE theory in Eqn. (4), finally results in the following shear stress response for an instantaneously applied constant shear rate $\dot{\gamma}_n$:

$$\tau(t) = \frac{2}{\pi} \dot{\gamma}_n a \Gamma(1-p) \sin\left(\frac{p\pi}{2}\right) \frac{t^p}{p} \tag{6}$$

in which Γ is the error function. In this analysis, the equilibrium modulus has been omitted for now. It will be accounted for in future analyses, together with a more representative description of both the moduli. Fig. 3 (right) shows these stress responses for three different shear strain rates, which are typically the magnitudes as they appear in stamp forming processes. The material shows a close to elastic response, however, slightly dependent on shear rate. Nevertheless, the material will be regarded as behaving elastically within the range of shear rates that appear during the stamp forming processes considered here. Such behaviour has been assumed earlier by Scobbo [10], who states that within the considered range of shear rates the material indeed acts as an elastic solid. Or as cited from [11]: “Although hot rubbery polymers exhibit both solid rubbery and rubbery liquid characteristics, in the limit, thermoforming is a solid phase deformation process”.

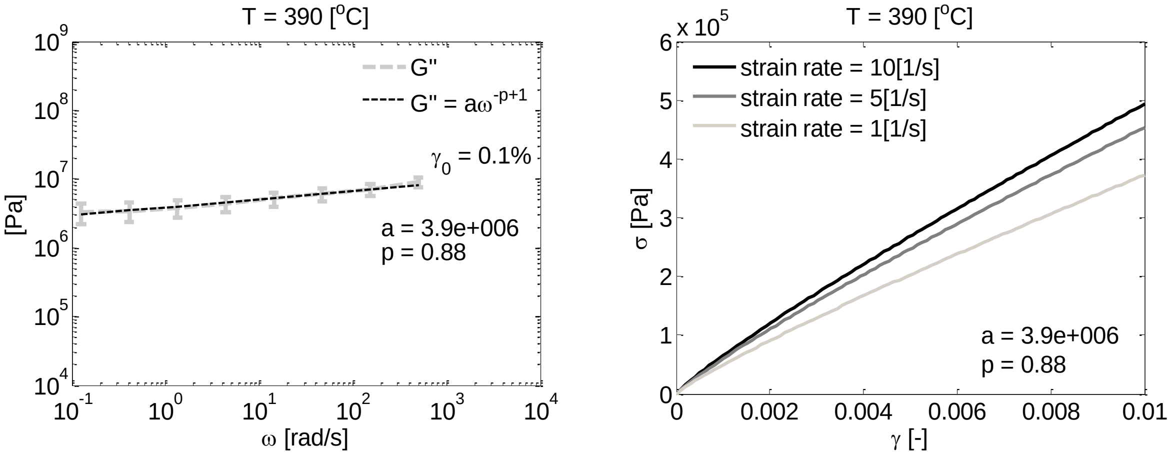

Fig. 3: Left: straight line approximation for the loss modulus. Right: calculated stress-strain response from Eqn. (6) as a result of a instantaneously applied constant shear strain rate.

APPLICATION

The measured shear characteristics find their application in forming simulations. This section shows such an application for which a fairly complex product was selected. It comprises a stiffening rib with features such as flanges and double curvatures as displayed in the centre of Fig. 4. It is one of the many parts of the wing fixed leading edge assembly, designed and built by Fokker Aerostructures. Although the product design is tailored for the stamp forming process of flat sheets of another conventional composite material, we consider an eight layered quasi-isotropically stacked laminate (Fig.4, left) with the UD carbon PEEK material for this research. Firstly, the forming process and the resulting product shape will be shown. Secondly, the modelling and the resulting predictions of the intra-ply shear strains will be discussed.

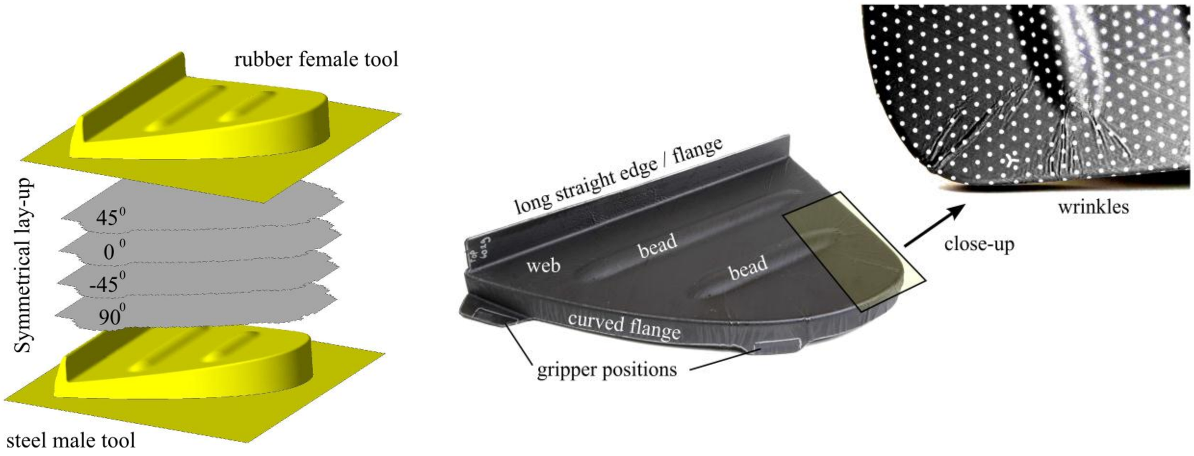

Fig. 4: Left: stamp forming set-up as used for forming experiments and process modelling, the laminate consists of eight plies in total. Centre: the resulting J-nose stiffener with the definition of some features. Right: partial close-up showing process induced defects.

Forming experiment

A flat blank with a shape as shown in Fig. 4 (left) was cut out of a flat pre-consolidated laminate. The blank is subsequently heated in an infra-red oven and transported between a pre-heated steel male and a cold rubber female tool. Subsequently, the hot blank is formed by the downwards movement of the female tool with a typical speed of 20 mm/s. A detailed process analysis was performed in [12]. The resulting product shape is shown in the centre of Fig. 4. The close-up on the right of Fig. 4 shows small wrinkles mainly occurring in the web and originating from the doubly curved bead ends.

As can be seen in the close-up in Fig. 4, blanks were prepared with a white dot pattern. This was applied with paint brush tooling in order to quantify the intra-ply strains. The position of the dots before and after forming was measured with the aid of photogrammetry software. Intra-ply strain components were subsequently determined by calculating the deformation gradients for each triangle, as determined by the dots. The resulting shear strain components of the top ply are shown in Fig. 5 (left). Dominating shear strains are visible near the bead ends, however, these mainly have an apparent character due to the presence of wrinkles in those areas (Fig. 4, right). The strain measures correctly represent the intra-ply shear strains for the regions without wrinkles and vary between -0.02 and 0.02, corresponding to fibre shear angles between $\approx -1^{\circ}$ and 1°.

Forming predictions and discussion

The AniForm finite element software was employed to model the iso-thermal forming process according to the virtual set-up in Fig. 4 (left). A similar modelling methodology was described in a previous publication [13]. The male and female tools are modelled as rigid surfaces, each containing 37.000 elements. Eight individual plies were modelled separately with 17.000 elements each. These plies consist of 3-node triangular shell elements (discrete Kirchhoff triangles, DKT). An elastic fibre model in combination with the characterised intra-ply shear behaviour was modelled for the in-plane material responses. The characteristics in Fig. 3 (right) were assumed to be elastic and are represented with a Mooney-Rivlin model. An orthotropic elastic model is used for the DKTs to model the bending behaviour of the plies. Tool-ply friction was measured with an in-house developed friction tester [14] and the characteristics were processed in the models that describe contact logic at the modelled interfaces.

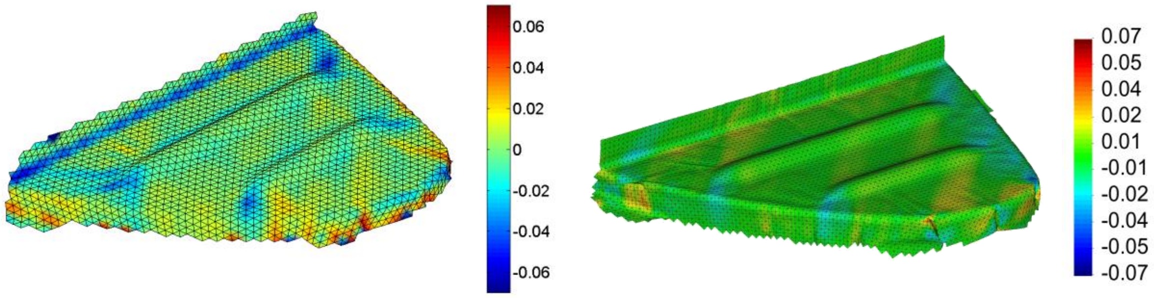

Fig.5: Intra-ply shear distributions of the top ply, expressed in the shear component of the Green-Lagrange strain tensor $\varepsilon_{xy} = \gamma/2$. Left: experimental result, determined with photogrammetry. Right: forming simulation result.

Fig. 5 (right) shows the predicted product shape and intra-ply shear strains of the top ply. A small contribution of intra-ply shear mechanisms is indicated, which was also concluded from the photogrammetry results in Fig.5 (left). Some wrinkles or waves are predicted as well near the bead ends, however, the real process induced defects are too small to be represented with a typical finite element mesh size. Nevertheless, the predicted wrinkles or waves indicate potential problematic areas.

During the forming process of the considered geometry in combination with the quasi-isotropic layup, out-of-plane bending is the most pronounced of all mechanisms that appear. The experiment suggests that probably more energy is required for intra-ply shearing, compared to the local out-of-plane bending. The latter will eventually develop and consequently results in wrinkles. The model prediction indicates this as well, which suggests that the magnitude of the measured intra-ply shear characteristics, as well as the elastic behaviour approximation, is likely to be a good approach.

CONCLUSIONS

An alternative shear characterisation method has been shown. Rectangular bar shaped specimens comprising a UD carbon PEEK material were subjected to oscillatory torsional loads. The measured responses show a storage modulus that is consistently larger than the loss modulus. Moreover, a weak frequency dependency was found which suggests that the material behaves like a solid or weak gel [15]. The frequency dependent moduli were subsequently translated to the transient domain in order to be used in a stamp forming model.

An iso-thermal stamp forming process was modelled by means of the finite element method. A complex product was selected and forming of a quasi-isotropic UD carbon PEEK laminate was simulated. Predicted intra-ply shear strains were compared with these strains in a real-life product. Stamp forming experiments were conducted and strains were extracted with the aid of photogrammetry. Both the simulation and experiment show small intra-ply shear strains, their distribution and order of magnitude in agreement. Local out-of-plane bending was the pronounced mechanism and results in small wrinkles in practise. Simulations were able to indicate these potential problematic regions, which is among others the result of proper modelling of the intra-ply shear behaviour.

ACKNOWLEDGMENTS: The author would like to thank the employees from Ten Cate and Fokker for their excellent support and guidance in preparing and performing the thermoforming experiments. This project is funded by the Thermoplastic Composite Research Centre (TPRC). The support of the Region Twente and the Gelderland & Overijssel team for the TPRC, by means of the GO Programme EFRO 2007-2013, is also gratefully acknowledged.

REFERENCES

1. Harrison P, Clifford MJ (2005), In Design and manufacture of textile composites, Chapter 4, Rheological behaviour of pre-impregnated textiles. ed. Long AC, Woodhead Publishing Ltd., Cambridge, UK.
2. Groves DJ, Stocks DM (1991). Rheology of thermoplastic-carbon fibre composite in the elastic and viscoelastic states. *Composites Manufacturing*, 2(3-4), 179-184.
3. Ó Brádaigh C.M. (1994), Sheet forming of composite materials, in chapter 13 of Flow and Rheology in Polymer Composites Manufacturing, volume 10 of book series: Composite Materials, editor: S.G. Advani, Elsevier Science Publishers, Amsterdam.
4. Timoshenko SP, Goodier JN (1970), Theory of Elasticity, 3rd ed., McGraw-Hill.
5. Haanappel SP, ten Thije RHW, Rietman AD, Akkerman R (2011), In-plane shear characterisation of uni-directionally reinforced thermoplastic melts, *Proceedings of Esaform 2011, Belfast, Ireland*.
6. Gutowski TG (1985), Resin flow/fiber deformation model for composites, *S.A.M.P.E. quarterly*, 16, 58-64.
7. Kitano T, Kataoka T. and Nagatsuka Y (1984), Dynamic flow properties of vinylon fibre and glass fiber reinforced polyethylene melts, *Rheologica Acta*, 23, 408-416.
8. Ferry J (1980), Viscoelastic properties of polymers, 3rd ed, John Wiley & Sons.
9. Campanella OH, Peleg M (1987), On the relationship between the dynamic viscosity and the relaxation modulus of visco-elastic liquids, *Journal of Rheology*, 31, 511-513.
10. Scobbo Jr J, Nakajima N (1989), Dynamic mechanical analysis of molten thermoplastic/continuous graphite fiber composites in simple shear deformation, *Proceedings of National SAMPE Technical Conference*, 21, 730-743.
11. Throne J (1996), Technology of Thermoforming, Hanser Publishers.
12. Haanappel SP, Sachs U, ten Thije RHW, Rietman B, Akkerman R (2012), Forming of thermoplastic composites, *Proceedings of Esaform 2012, Erlangen, Germany*.
13. Haanappel SP, ten Thije RHW, Akkerman R (2010), Forming predictions of UD reinforced thermoplastic laminates, *Proceedings of ECCM 14, Budapest, Hungary*.
14. Sachs U, Haanappel SP, Rietman B, Akkerman R (2011), Friction testing of thermoplastic composites, *Proceedings of SEICO 2011*, Paris, France.
15. Citerne GP, Carreau PJ, Moan M (2001), Rheological properties of peanut butter, *Rheologica Acta*, 40, 86-96.

MODELLING OF LASER WELDING PROCESS ON THERMOPLASTIC COMPOSITES

Benoit Cosson[1], Mylène Deléglise[1], Wolfgang Knapp[2], Philippe Castaing[3], Christophe Binétruy[1]

[1]Ecole des Mines de Douai, Lille Eurorégion, 941 rue Charles Bourseul,
BP410838, 59508 Douai cedex, France
[2]CLFA, Fraunhofer ILT, c/o Armines MINES ParisTech, 60 bld. Saint-Michel,
75272 PARIS cedex 6, FRANCE
[3]CETIM, 74, Route de la Jonelière - BP 82617, 44326 NANTES Cedex 03

ABSTRACT: Thermoplastics composites for structural applications are under growing development from the aerospace (carbon fibers with PEI, PPS or PEEK matrices mainly) to the automotive industry (glass and carbon fibers with PP, PA). The plastic deformation they can provide and the assembly facilities through welding techniques are well appreciated. Among the available welding technics, laser offers the possibility to assemble materials in a precise and localized manner and can be easily automated. However, due to the presence of continuous fibers at a high fiber volume fraction, propagation of the laser energy through the composite that present local variation of fiber volume fraction is not as straight forward as in an homogeneous material. Modelling of the laser welding of a PA/continuous glass fiber is considered here. The study takes into account the microstructure of the composite in order to evaluate changes in local energy absorption and divergence directly linked with the local fiber volume fraction value. Modelling of the welding process is developed from the representation of the moving laser beam. The beam propagation through the composite thickness is considered thanks to the ray tracing method. The local polymer rheology is defined through the resultant temperature profile obtained at the interface and taking into account the influence of the local fiber volume fraction. When applied to non continuous fibrous structure, local fluid flow induced during the welding process is greatly influenced by the influence of temperature on the viscosity coefficient, affecting the weld line quality and geometry. Variability of welding seam geometry and quality along with the composites structures variability is then shown.

KEYWORDS: *Laser welding, modelling, microstructure, thermoplastic composites*

INTRODUCTION

Structural thermoplastics composites are investigated to replace metallic parts in transport industries in order to reduce weight while providing good mechanical properties and better part recyclability. Apart from the manufacturing concerns, adapted bonding techniques need to be developed for fast and reliable assembly of different part. Thanks to the capability of thermoplastics to be melted, welding techniques can be considered.

Welding of two thermoplastic composite consists in bringing a sufficient amount of energy at the interface between two substrates in contact to melt the local thermoplastic. According to the applied pressure and the contact between the two substrates, polymer macromolecules from both substrates move locally to create an interpenetrated network that will ensure the strength of the created bond after cooling [1].

Fusion bonding can be performed in a number of ways depending on how heat is provided to the system [2-10], using compression, resistive, electro magnetic, vibration, ultrasonic, infrared or laser energy source. These techniques have in common that an intimate contact must exist between the two substrates. Smooth surface and sufficient applied pressure are guarantee of the final welded joint quality. InfraRed and laser are light sources with a large wave length spectrum (IR rays) or a given wave length (laser). The light acts as an excitation wave when absorbed by the material, generating heat. For better results, one of the substrate should be transparent to light and the interface should have good absorption properties (usually called “black” material). Laser is a light energy more simple than the IR light beam as it is composed of only one wave length and is a focused beam, with a homogeneous energy distribution. IR are generated by lamps that produce light in all the directions.

Laser welding method shows a great potential for industrial use. It has the advantage of avoiding complex settings and mechanical resistance issue involved in US and vibration welding and to respect the substrate integrity that can not be guaranteed with compression welding. Moreover, it is more flexible than in resistive welding where a relatively thick interface might be inserted at the welding interface. Moreover, the focused energy source is an advantage in terms of final part aesthetics. The objective of this work is to develop an affordable non-intrusive numerical simulation of the laser welding process modeled with adapted physics mechanism and taking into account the microstructure heterogeneity of the considered materials. The flow of melted polymer at the welding interface is governed by the pressure applied on the two substrates and on the local viscosity of the melted polymer itself that depends on the local temperature and on the fibrous microstructure.

LASER WELDING PROCESS

A laser is composed of a light generator that generally produces only one wavelength from 900 to 1800 nm. For thermoplastic welding application low power lasers can be used, so diode laser will be considered here. Diode offers the possibility to conduct the laser beam to any places by optical fibers. The generated beam is then focused by lenses and mirrors. Constant energy during welding is insured by the pyrometer that measures surface temperature continuously. A clamping system to insure close contact between the two parts is required, either by using flat transparent plates or punctual pressure devices.

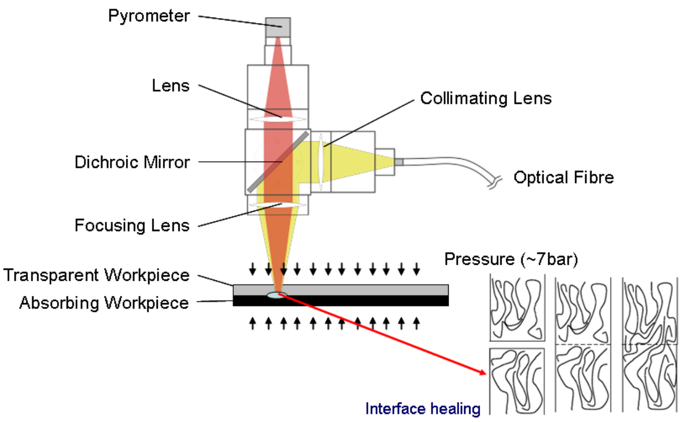

Figure 2: Laser welding system

The applicability of the laser welding process essentially depends on the optical properties of the polymers with regard to the laser wavelength, especially absorption or transmission rate of laser radiation. For absorbing materials, the entire laser energy can be considered absorbed on the surface. On the contrary, for semi-transparent media (PA, PS, PMMA, PC, etc.), laser beam energy can be deposited into the structure [11-12]. For better quality results, the first substrate should be transparent so that most of the energy attains the interface layer. Likewise, the second substrate should be highly absorbent; the energy is thus immediately absorbed at the interface level. If both substrate are transparent, a third black (absorbent) component should be added and play the role of the interface layer.

In this study, UD composite with PA66 polymer is considered. The second substrate is charged with black carbon to obtain absorbent properties [13-15].

When laser beam passes through the substrate, part of the energy is reflected at the composite surface (10% of the initial laser beam energy), then part is absorbed and part is refracted at each fiber/polymer interface. In this paper, divergence of the laser beam through the composite substrate and the resulting energy profile at the welding interface are presented to highlight the influence of the microstructure variability on the final welding seam geometry.

LASER BEAM MODELING: RAY TRACING METHOD

The method chosen here to model the laser beam propagation through the material is the ray tracing method. Usually, only absorption is used associated with a diffusive parameter defined experimentally. The ray tracing method allows taking into account the variability of the resulting heat energy profile at the welded interface with respect to the fiber volume fraction mapping (presented in Figure 5) and the local fiber distribution.

Ray tracing method was initially developed for light effects in numerical animation for video games. The principle is to propagate a sufficient number of rays to represent a light beam through a material, according to the reflection indices of the different materials encountered. In the case of composite materials, laser beam diffuses through the heterogeneous material composed of the polymer and the fibers. Laser shape is considered purely cylindrical before entering the material with rays strictly perpendicular to the composite surface. The composite surface is considered perfectly flat, so that no diffraction due to surface roughness is considered. To include heat loss due to surface roughness, a corrective coefficient can be taken to be around 10%, which includes energy losses due to surface roughness and to reflection of the beam ray when beam enters the composite. Indices of reflection for the polymer and the glass are respectively 1.49 and 1.53. Snell-Descartes law is used to calculate the change in angle direction of each ray. Each time a ray encounters a new material, it is slightly deviated. Reflected beams are not taken into account here as reflection is negligible in front of refraction to lower the computation costs.

$$n_1 \sin\theta_1 = n_2 \sin\theta_2 \,. \tag{2}$$

Where n is the refraction index and θ is the incident angle. The different indexes represent the different materials.

Ray tracing method is implemented using Finite Element program developed under COMSOL Multiphysics. The mesh is defined on a representative periodic composite cell, so that only one cell repeated until the desired length and thickness is reached is used. This allows to greatly reducing the computation cost as the computation cost is directly linked to the number of ray considered. The laser beam is represented by thousands of rays uniformly distributed on a predefined incident surface, assuming a perfectly collimated beam, so that the energy is homogeneous over the laser beam and that the beam is strictly normal to the composite surface. Each ray thus enters the composite surface along the same direction. Ray orientation evolution is calculated at each separating wall between two elements. Elements belong either to a fiber or to the matrix, each family having a different refractive index. If two adjacent elements have the same refraction index, the ray's direction stays unchanged. If they are different, Snell Descartes law applies to the ray direction. An illustration of the ray tracing method is shown in Figure 3, along with the resulting energy profile obtained for a thousand rays crossing a small unit cell, showing that the energy profile rapidly deviates from the original uniform energy distribution. Convergence of the model is defined during the calculation. New rays are generated until the resulting total energy at the welding interface does not vary.

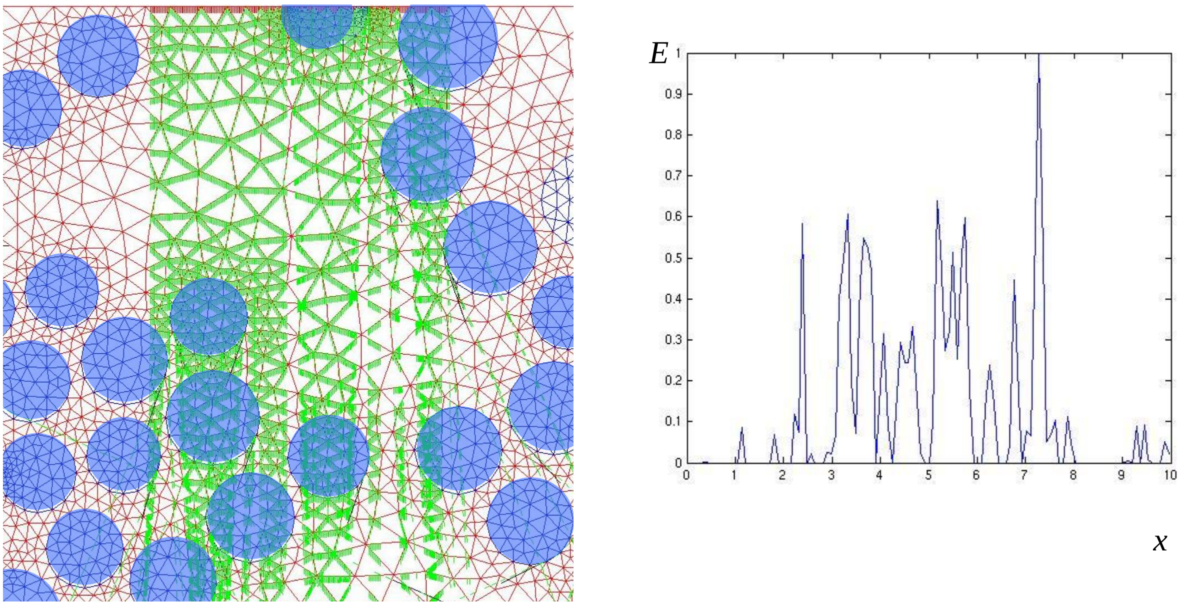

Figure 3: Ray tracing modeling example on a unit cell.
Left : ray propagation through a unit cell.
Right : beam intensity obtained after propagation through the represented FE cell

Ray tracing method is thus a line propagation simulation with change of direction according to the traversed medium. Thanks to the periodic representation of the cells with the highest possible fiber volume fraction reached using the Delaunay and Voronoï geometrical principal for unit cell partitions, it is then easy to pile up the reference cells varying their global fiber volume fraction property and create a random fiber organization. The second advantage is to reduce computational costs, as only one reference cell is considered.

Laser beam diffraction is thus obtained. Results for different composite thicknesses are presented in Figure 4 for a laser beam with a 1mm diameter. For a thin plate (0.2mm) the energy distribution is nearly uniform and the laser beam size stay unchanged. On the contrary, when considering thick panels (5mm), the resulting energy profile spreads on a circle 13 times bigger than the original beam diameter and cannot be considered uniform anymore. The laser energy is then reduced by refraction effects, showing that the laser welding technique is limited to thin panels.

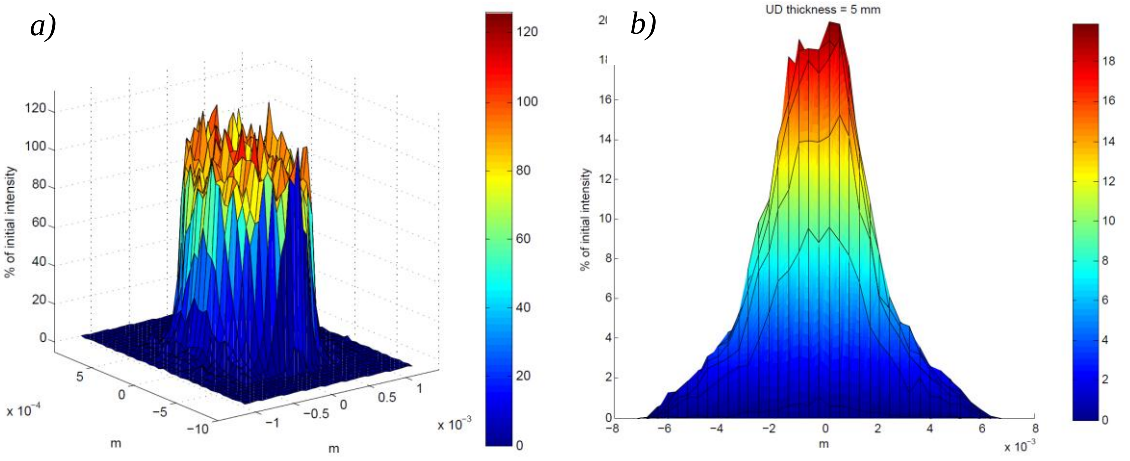

Figure 4: Resulting laser beam energy profile after passing
through a composite plate of different thickness, a) 0,2mm, b) 5mm.

TEMPERATURE PROFILE MODELING

For any light source, the final energy absorbed in the second substrate is defined according to the incident ray density. The heat source generated is defined as an integral over the wave length spectra [21-25]:

$$\nabla \cdot q_r(x) = -\int_0^{\infty} \kappa^{\lambda} M^{\lambda}(x_p) e^{-\kappa^{\lambda}(x-x_p)} d\lambda \tag{3}$$

where λ is the wave length, κ is the absorption coefficient and M is the incident emissive power, and x-x_p represents the ray travel length. In the special case of a laser light source, only one wavelength is considered and thus the previous equation become :

$$\nabla \cdot q_r(x) = \kappa M(x_p) e^{-\kappa(x-x_p)} \tag{4}$$

Lasers are generally composed of one wavelength, if generated from only one kind of diode. This heat source can then be integrated in the heat balance equation as a source term:

$$\rho C_p \frac{dT}{dt} = \nabla \cdot (k \nabla T) - \nabla \cdot q_r \tag{5}$$

Where k.is heat conduction, ρ the material density and C_p the material heat capacity.
The total energy absorbed at the interface is then defined in the area of interest by:

$$E = \int dI^{\lambda}(y) \cdot dx \tag{6}$$

Absorption of the energy is in a first step considered taking place at the interface line. The resulting temperature profile, shown in Figure 15, is thus symmetrical, the welding interface being the symmetry plane. A dynamic welding is also considered in Figure 5 with a laser velocity displacement of 0.04 m.s^{-1}. Heat conduction through the composite is slower than the velocity of the welding process, leading to a delay in response at the interface of the welding process. Welding parameters such as velocity and laser power should be optimized according to the level of temperature than can be reached in the composite and at the composite surface, especially for aspect consideration of painted or prepared for painting structures. The modeling algorithm developed here can help in this matter.

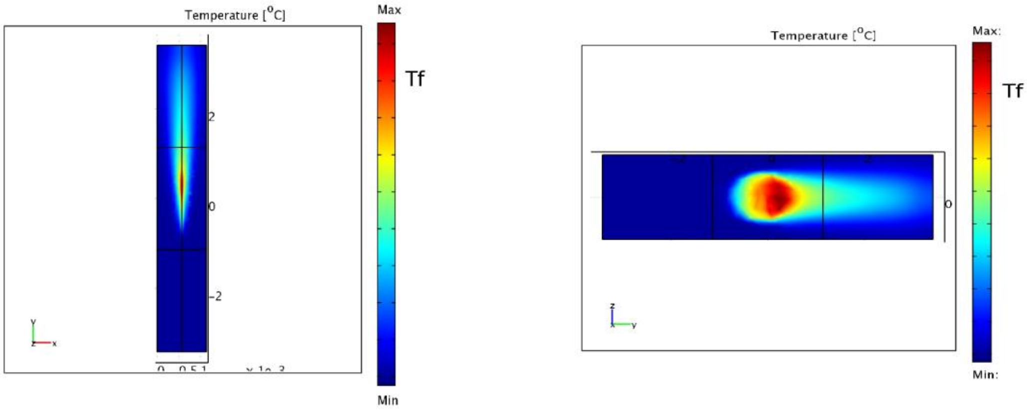

Figure 5: Dynamic welding
a) composite section b) temperature profile at the interface

WELDED INTERFACE FINAL GEOMETRY

Application of the welded simulation is conducted on a structure showing the variability of the composite through the fiber volume fraction parameter (mean value : 35%). Objective is to obtain the temperature profile at the welding interface. A continuous weld seam is generated by displacement of a 40W laser over the structure on a straight line at constant velocity (0.04 m.s^{-1}). Simulation results presented in Figure 6 shows the interface 2D plane (simulation time convergence was checked). Light color represents the integration point location where temperature reached the polymer melting temperature (or higher) during the process. We can then assume that good welding is obtained at those points. Analysis of this profile shows the irregularity of the weld seam edges, directly due to the fiber volume fraction variability in the substrate. In this present case, conduction is not sufficient to homogenize the temperature at the interface. Due to the irregular temperature profile, one could also expect variability in polymer viscosity profile, inducing different flow behavior at the edges of the weld seam. A squeeze flow model is thus generated at the end of the weld seam.

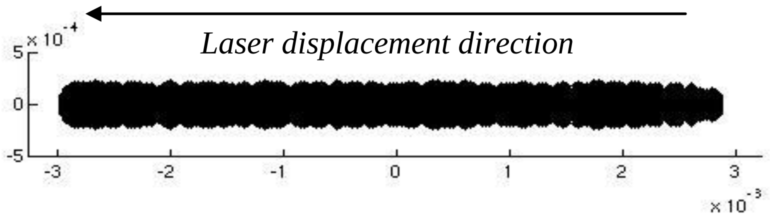

Figure 6: Resulting weld line geometry

CONCLUSION

A complete and original modeling of the laser technology for thermoplastic composite welding is proposed here, from the laser beam geometry to the resulting weld line geometry. An important divergence is generated due to the fibrous structure of the composite, increasing the weld line mean width and reducing the welding energy. Variability in fiber volume fraction has an important influence on the weld line aesthetics. This model can be used for optimization of the welding process parameters for industrial applications according to material characteristics and microstructure organization to improve weld line quality (amount of melted polymer) and aesthetics.

ACKNOWLEDGEMENTS: This project was funded by the French National Research Agency (ANR) under grant number 07- P2IC-003-001.

REFERENCES

1 P-G de Gennes, Reptation of a polymer chain in the presence of fixed obstacles, Journal of Chemical Physics, Vol 55(2),1971, pp572-579

2 Grewell DA, Benatar A, Park JB. Plastics and composites welding handbook. New York: Academic Press; 2003.

3 J.S.U. Schell, J. Guilleminot, C. Binetruy, P. Krawczak, Computational and experimental analysis of fusion bonding in thermoplastic composites: Influence of process parameters, Journal of Materials Processing Technology, Volume 209, Issue 11, 21 June 2009, Pages 5211-5219

4 Klinkmuller V, Um M-K, Steffens M, Friedrich K, Kim B-S: A new model for impregnation of different GF/PP commingled yarns. Appl Compos Mater, 1, 351-371 (1995).

5 C. Ageorgesa, L. Yea,*, M. Houb, Advances in fusion bonding techniques for joining thermoplastic matrix composites: a review, Composites: Part A 32 (2001) 839±857
6 Hou M, Ye L, Mai YW. An experimental study of resistance welding of carbon fibre fabric reinforced polyetherimide (CF Fabric/PEI) composite material, Appl Compos Mater 1999;6:35–49.

7 Don RC, Bastien L, Jakobsen TB, Gillespie Jr. JW. Fusion bonding of thermoplastic composites by resistance heating. SAMPE J 1990; Jan–Feb:59–66.
8 D. Stavrov*, H.E.N. Bersee, Resistance welding of thermoplastic composites-an overview, Composites: Part A 36 (2005) 39–54

9 Z.S. Colak, F. Sonmez, O.V. Kalenderoglu, Process modeling and optimization of resistance welding for thermoplastic composites, Journal of Composite Materials, 36 (2002), pp. 721–744

10 Stratov D. and al. (2005), Resistance welding of thermoplastic composites- an overview, Composites: Part a 36, 39-54.

11 Rosselli F. and al. (1997) Effect of processing on laser assisted thermoplastic tape consolidation, Composites: Part A 28A, 1023-1033.

12 Atanasov, P. A .(1995), Laser welding of plastics – the theory and experiment. Optical Eng. 34/10, 2976-2980

13 Bachmann FG, Russek U-A. Laser welding of polymers using high power diode lasers. In: Proceedings of the Photonics West conference, San Jose, CA, USA, 2002.

14 Duley WW, Olfert M, Bridger P, Bird J, Mueller RE. Basic physical phenomena during laser processing of materials. In Proceedings of the international conference on laser advanced material processing' 92, Nagaoka, 1992. p. 261–268.

15 Peter A Atanasov. Laser welding of plastics: theory and experiments, Opt Eng 1995; 34(10):2976–80.

21 M.T. Abadi, Rheological characterization of continuous fibre-reinforced viscous fluid. J. Non-Newtonian Fluid Mech. 165(2010) 914-922.

22 Yasuo Kurosaki. Radiative heat transfer in plastic welding process, J Quant Spectrosc Radiat Transfer 2005;93:25–41.

23 Monteix S, Schmidt F, Maoult YL, Yedder RB, DiraddoRW, Laroche D (2001) Experimental study and numerical simulation of perform or sheet exposed to infrared radiative heating. J Mater Process Technol 119(1-3): 90-97

24 Kneip JC, Martin B, Loredo A, Matteı¨ S, Grevey D. Heat transfer in semi-transparent materials during laser interaction. J Mater Process Technol 2004;155–156:1805–9.

25 J.C. Kneip, B. Martin, A. Loredo, S. Mattei, D. Grevey, Heat transfer in semi-transparent materials during laser interaction, Journal of Materials Processing Technology 155–156 (2004) 1805–1809.

SYNTHESIS AND CHARACTERIZATION OF MULTI-WALLED CARBON NANOTUBE REINFORCED POLY ETHER ETHER KETONE COMPOSITE

Nikhil Shaun Mepurathu[1], Gavin Lawes[2], Akila Deeghayu Kumarasiri[2] and Susil K. Putatunda[3]

[1] *Department of Mechanical Engineering, Wayne State University, Detroit, MI 48202, USA*
[2]*Department of Physics and Astronomy, Wayne State University, Detroit, MI 48201, USA*
[3]*Department of Chemical Engineering and Materials Science, Wayne State University, Detroit, MI 48202, USA.*
Corresponding author's email:sputa@eng.wayne.edu

ABSTRACT: The primary focus of this study was to investigate the synthesis of homogenous multi-walled carbon nanotube (MWCNT) reinforced Polyether-ether ketone (PEEK) using a novel melt processing technique. The secondary objective was to characterize the mechanical and physical properties of this MWCNT reinforced composite. Multi-walled carbon nanotube reinforced PEEK composites having different weight percentages such as 1%, 5% and 10% of MWCNT were synthesized using a novel melt-processing method. The microstructures of these samples were analyzed using a scanning electron microscope to confirm the uniform distribution of carbon nanotubes in the polymer matrix. The mechanical properties of these samples, including toughness and yield strength were determined using ASTM standards. The transport properties of these composites such as electrical and thermal conductivity and magnetic properties were measured as a function of carbon nanotube content and compared with those of pure PEEK. The test results show that there was a uniform, homogenous distribution of carbon nanotube in this polymer composite up to 5 wt. %. The mechanical, electrical and thermal properties increased with increasing carbon nanotube content up to 5 wt. %. Beyond this MWCNT fraction, there was no significant improvement in properties.

KEYWORDS: *Poly ether ether ketone, Yield strength, Multi walled carbon nanotubes, Toughness, Polymer.*

INTRODUCTION

Poly ether ether ketone (PEEK) is a semi-crystalline, high temperature resistant thermoplastic polymer. It has many desirable properties including a combination of high thermal stability, good chemical and solvent resistance, and excellent mechanical properties over a wide range of temperatures. In addition to this, it has excellent fire resistance [1, 2]. Because of these attractive properties, PEEK is a highly desirable material for use in critical structural components in aerospace and automotive applications. PEEK has also other potential applications such as high temperature wiring, tribology, and biomedical applications [3].

Unfortunately, the fracture resistances, and electrical and thermal properties of PEEK are comparatively poor compared to other polymeric materials, which limits the incorporation of this polymer in certain applications. However, by reinforcing the parent PEEK matrix by carbon nanotubes, it may be possible to significantly improve the transport and fracture resistance of this material. The incorporation of multi-walled carbon nano-tubes (MWCNT) into a PEEK matrix can provide structural materials with dramatically increased modulus and strength [4].Improving the properties of PEEK by fabricating composite systems including carbon nanotubes would also increase their toughness , which could increase the use of this material in applications that require both high strength and toughness e.g. the automotive and aerospace industries. These PEEK/MWCNT composites could also possibly replace metal parts where a certain level of conductivity is needed for electrostatic painting [5].

Carbon nanotubes have emerged as an important engineering material in recent years. Multi-walled carbon nanotubes consist of two or more concentric cylindrical shells of graphene sheets coaxially arranged around a central hollow core with the same interlayer separations as in graphite. CNTs have extremely high values of Young’s modulus, (up to 1TPa) and tensile strength approaching 60GPa [6-8]. Carbon nanotubes also have high geometric aspect ratio, stiffness-to-weight ratio and strength -to-weight ratio. CNTs are thermally stable until 2800°C in vacuum and have thermal conductivity almost twice as large as diamond and electrical current carrying capacity almost 1000 times as that of copper [9]. Carbon nanotubes exhibit good electrical and thermal conductivity due their graphite like structure. These properties, combined with their good aspect ratio of up to several thousand make carbon nanotubes an ideal candidate for the development of electrically and thermally conductive composites having improved mechanical properties, while using a very small amount of reinforcing material[10].

The properties of composites reinforced with carbon nanotubes, depend strongly on the polymer matrix and the processing methods used to process the composites [11]. Ensuring a uniform dispersion of carbon nanotube in a polymer matrix is difficult because of the high probability of agglomeration for the CNTs. At the same time, nanotube agglomeration can limit the mechanical and transport properties of this composite [12]. Therefore, there is a significant need to develop a robust, versatile, and scalable process to prepare polymer composite systems containing a composite with homogenous distribution of CNT embedded in the matrix. In this investigation we used a novel melt processing method to develop a homogenous and uniform mixture of CNT reinforced PEEK.

OBJECTIVES

The primary focus of this investigation was to synthesize multi walled carbon nanotube reinforced PEEK composites. We focused this study on MWCNT as these are less expensive than single walled carbon nanotubes, leading to a more affordable commercial product. The secondary objective was to characterize the physical and mechanical properties of this composite as a function of nanotube content. Towards this objective, we measured the physical properties such as; electrical and thermal conductivity of the MWCNT reinforced PEEK. We confined this study to low volume fraction composite to limit the processing cost associated with the MWCNT and to restrict the investigation to electrically insulating composites below the percolation threshold.

EXPERIMENTAL PROCEDURE

Materials

A Brabender Plasticorder internal mixer with a mixing chamber volume of 85cc was used for blending PEEK with different loadings of CNT. A fill factor of 0.7 was used during the mixing. Prior to mixing, all ingredients were dried for 24 hours at 80 ^{o}C in vacuum to remove any residual moisture. The PEEK was first melted in the mixer and then the CNTs were added as a dry powder. The ingredients were mixed for 5 minutes at 350 ^{o}C at a rotor speed of 80 rpm. A batch mixing time of total 10 minutes (including polymer melting) was used for the preparation of the composite. The resultant compounds were cooled down to room temperature and ground into small pellets for further analysis. This synthesis process resulted in a homogenous mixture with a uniform distribution of carbon nanotubes embedded in the polymer matrix.

Molding operation

Dog bone shaped bars were prepared for mechanical property testing through vacuum compression molding (Technical machine products corporation, Cleveland, OH) at ~ 350^{o}C. The pellets were added to the mold and compressed in between kapton films at a pressure of 10,000 psi for at least 5 minutes. After taking out the mold, it was cooled down between cold platens. A minimum of five specimens were prepared for each composition. The samples used for this study are about 20cm in length, but this technique can be used to prepare larger size samples limited only by the size of the mold.

Tensile testing

Tensile test specimens were prepared according to ASTM standard for plastics [13] . The tensile tests were carried out using a servo hydraulic MTS test machine at room temperature and ambient atmosphere at a constant displacement rate of 1mm/min. Three identical samples were tested and the load displacement diagrams were obtained on an X-Y plot. From these load displacement diagrams, yield and tensile strength, percentage elongation and fracture strength were determined. The average values from three identical test samples are reported in this paper.

Electrical, thermal and magnetic properties

In order to determine the electrical resistivity of the materials, samples of size 5mm by 5mm and 1 mm in thickness were prepared. Silver paint was used to fabricate the electrodes used for the measurements, which were done at room temperature. The heat capacity measurements were carried out using a standard option on a Quantum Design Physical Property Measurement System (PPMS), with the measurement done over a temperature range of 5 to 60 K in order to investigate the low temperature vibrational modes. The room temperature magnetic properties were measured using a SQUID based Quantum Design Magnetic Property Measurement System (MPMS).

Microstructural analysis

The microstructural analyses of the samples were carried out using FEI Field Emission Scanning Electron Microscope. The SEM images of composite samples with different CNT contents were examined at various magnifications to determine the dispersion of the CNTs in the PEEK matrix.

RESULTS AND DISCUSSION

Microstructures

Figure 1(a) shows the SEM image of pure PEEK and Figures 1(b), 1(c) and 1(d) shows the SEM images with 1%, 5% and 10 % CNT respectively. A nearly homogenous sample having a uniform distribution of carbon nanotubes in the polymer matrix was observed. However, some small patches indicating nanotube agglomerations can be observed in the images for the 5% and 10% samples.

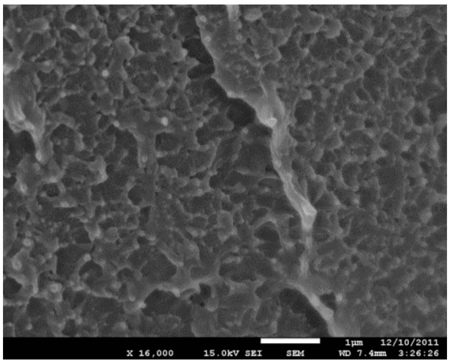

Fig. 1(a): Pure PEEK

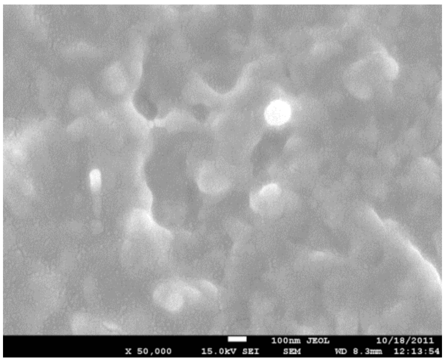

Fig. 1(b): PEEK with 1% CNT

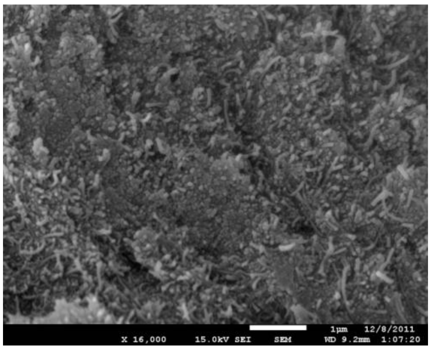

Fig. 1(c): PEEK with 5% CNT

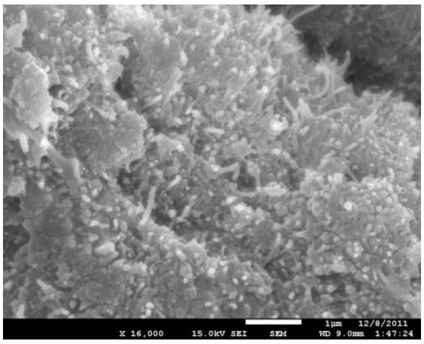

Fig. 1(d): PEEK with 10% CNT

Mechanical properties

In order to completely characterize the mechanical response of these composite materials, we determined the stress-strain response curves. These curves are shown in Fig.2. These curves show an approximately linear stress strain relation, confirming the brittle nature of the polymer. With increasing CNT content the stress strain diagram limit increases demonstrating an increased toughness of the composite on reinforcement with carbon nanotubes.

Figure 3 shows the yield strength of the composites as a function of carbon nanotube content. It is evident that the yield strength increases monotonically with CNT fraction up to a nanotube fraction of 5%. However, beyond the 5% composition there was no significant improvement in the yield strength of the material with increasing CNT fraction.

We observed a similar behavior for the ductility of the composites. Figure 4 is a plot of ductility (in terms of percentage elongation) against CNT fractions. These measurements confirm that there is a marginal improvement in ductility on reinforcement of carbon nanotubes, with this increase in performance also saturating at a composition of CNT of 5 wt%. It is interesting to note that in these materials, incorporating carbon nanotubes increases both the strength and ductility. This observation is contrary to most composite materials, for which the yield strength typically increases with reinforcement but the ductility decreases.

The tensile toughness of the materials with different % of carbon nanotubes were estimated using the following relationship:

$$\text{Tensile toughness} = \frac{\sigma_{ys} + \sigma_{uts}}{2}\,\varepsilon_f$$

Where σ_{ys} and $\sigma_{uts}$the yield and tensile strengths are for the material while ε_f is the fracture strain. These estimated values are reported in Table 1. Table 1 shows systematic improvement in tensile toughness with CNT reinforcement. The uniform and homogenous mixture of CNT in the bare polymer matrix has resulted in an improvement of the tensile toughness in the material. Table 1 also reports the energy for fracture of the material. We observe significant improvement in fracture energy with CNT reinforcement. These simultaneous improvements in toughness and strength make CNT reinforced PEEK an ideal composite material for structural applications requiring both high toughness and strength. Interestingly we find that while the toughness increased by a factor of 2 with the addition of CNT, the strength also increased by about 27%.

The Young's modulus of the material as a function of CNT content is reported in Table 2. The modulus of PEEK increased by about 10% with CNT reinforcement. The modulus is a measure of stiffness of the material, with a higher modulus indicating higher stiffness and resistance to buckling. The systematic increase of Young's modulus with CNT content confirms the improvement in buckling resistance of the material.

These improvement in physical properties suggest significant weight reduction can be achieved using CNT reinforced PEEK with allowing approximately 1/3rd reduction in the material used to attain the same strength without reduction in the toughness.

Table 1: Tensile toughness and Fracture energy

	Pure PEEK	1% CNT	5% CNT	10%CNT
Tensile toughness (MPa)	0.68	0.75	0.90	1.10
Fracture energy (Joules/m^3)	0.35	0.44	0.52	0.61

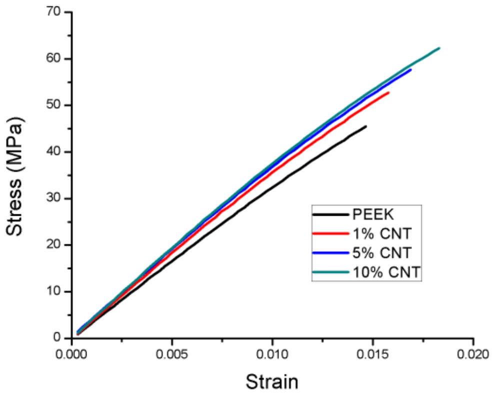

Fig.2: Stress strain curve for different CNT compositions.

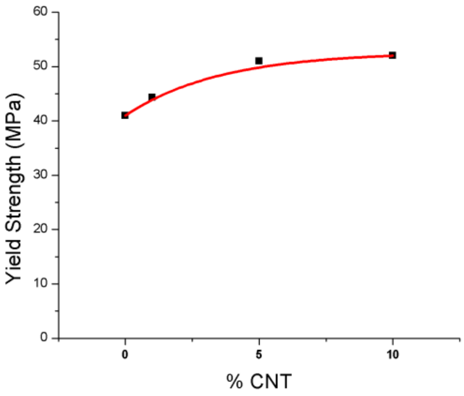

Fig.3: Influence of percentage of CNT on Yield strength

Table 2: Modulus of Elasticity

	Pure PEEK	1% CNT	5% CNT	10 % CNT
Young's Modulus (in MPa)	3128.05	3370.50	3418.67	3424.59

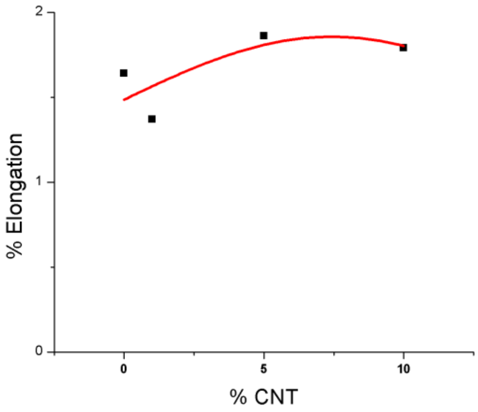

.

Fig.4: Influence of CNTs on percentage elongation

Electrical properties

The IV measurements showed an increased value of conductivity with the increasing percentage of CNT content in the sample as shown in figure 5. There was an increase in the conductivity values between pure PEEK and 1% CNT PEEK. The difference in the conductivity values between 1% and 5% CNT reinforced samples was small. However, in the case of 10% CNT sample, a huge increase in the conductivity value was observed. It may be possible that the percolation threshold of CNT reinforced PEEK might be in the range of 5% to 10% which result in conductive paths making the samples much more conductive. The percolation threshold of the composites has been found to depend on the viscosity of the polymer matrix. PEEK with its high viscosity is expected to have a low percolation threshold [5]. This study suggests the CNT fractions in the composite should be held or maintained below 10% for applications requiring insulating materials. CNT fractions above this limit will produce more conducting composites which may be suitable for electrostatic painting.

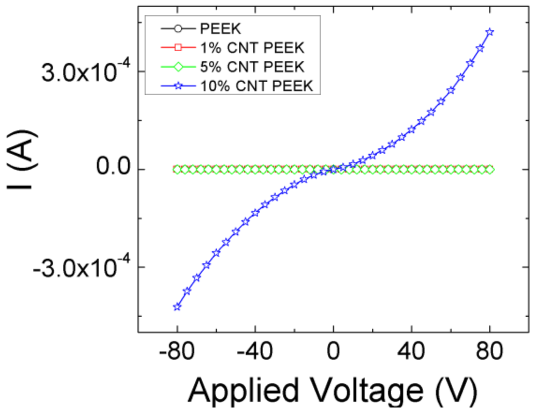

Fig.5: IV curves for different CNT compositions

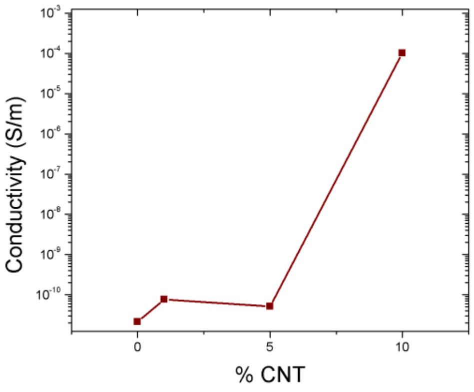

Fig.6: Effect of CNT on Electrical Conductivity

Thermal properties

The heat capacity measurements show that the heat capacity values for pure PEEK and 5% CNT reinforced PEEK samples are very similar as shown in figure 7. This suggests that the contribution of nanotubes towards heat capacity of the sample is minimal. The low temperature heat capacity varies like T^2 rather than the T^3 dependence in crystalline material. The straight line portion of the diagram shows the T^2 dependency of heat capacity at low temperatures.

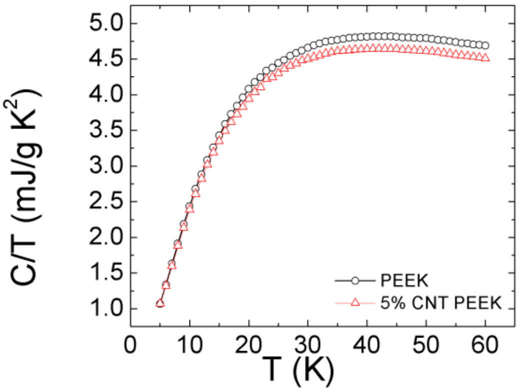

Fig. 7: C/T vs. Temperature

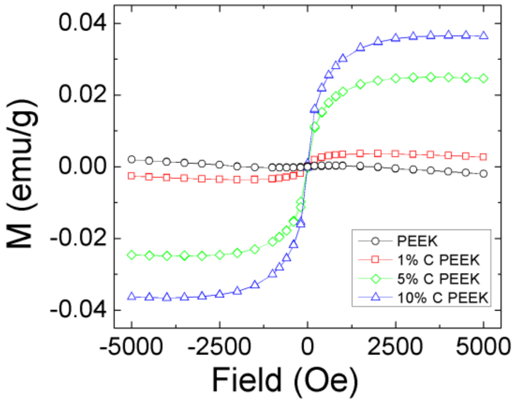

Fig. 8: M-H curves for pure PEEK and different CNT compositions

Magnetic Properties

The M-H curves in figure 8 show increasing saturation values of the magnetic moment with the increase in the percentage of carbon nanotubes. The pure sample shows diamagnetic behavior, whereas the nanotube reinforced composites show increasing ferromagnetic behavior with the increasing weight percentage of reinforcement. It is also noted that the increase in the magnetic saturation value between the 1% and 5% is more than that in the case of between 5% and 10% samples. The saturation magnetization ratios between the 1%, 5% and 10% CNT doped samples are 1:6.8:9.8. This suggests the samples are nearly homogeneous with the 5% sample having a slightly higher CNT concentration than expected. These magnetization measurements were performed on samples of length scale of 1mm. Therefore this technique can be used to characterize inhomogeneity in the composite samples on this length scale. Magnetization measurements can therefore complement electron microscopy studies as a tool to measure inhomogeneity in the samples.

CONCLUSIONS

1. By processing PEEK with a novel melt processing technique, we prepared a nearly homogeneous and uniform mixture of CNT in PEEK.
2. The reinforcement of PEEK with multi walled carbon nanotubes resulted in simultaneous improvement of strength and toughness, with increase of about 27% in strength and 100% in toughness.
3. While the improvement in mechanical properties was significant up to 5 wt. % CNT, beyond 5 wt%, larger CNT fractions did not lead to any further improvement.
4. The electrical conductivity increased considerably between the 5% and the 10% sample. This may be because of reaching the percolation threshold of the composite. The composites having high CNT fractions could be used for electro-static painting.
5. These composites could be used as structural components in applications requiring both high strength and high toughness.

6. This novel melt processing technique can also be suitable for preparation of other type of homogenous polymer composite.

REFERENCES

1. K.J Dahl, Jansons.V., *Polymers and other advanced materials: Emerging technologies and business opportunities.* (1995): p. 69-81.
2. Staniland, P.A., *Poly (ether ketones).* Comprehensive polymer science, 1989. **5**: p. 484-497.
3. Jones, D.P., D.C. Leach, and D.R. Moore, *Mechanical properties of poly(ether-ether-ketone) for engineering applications.* Polymer, 1985. **26**(9): p. 1385-1393.
4. Atodaria, D.R., *Fatigue crack growth behavior of carbon fiber reinforced polymer composite polyether-ether ketone (PEEK).* Proceedings of the International Conference on Composite Materials, 10th, Whistler, B. C., Aug. 14-18, 1995, 1995. **1**: p. 665.
5. Socher, R., et al., *The influence of matrix viscosity on MWCNT dispersion and electrical properties in different thermoplastic nanocomposites.* Polymer, 2012. **53**(2): p. 495-504.
6. Salvetat, J.P., et al., *Mechanical properties of carbon nanotubes.* Applied Physics A: Materials Science & Processing, 1999. **69**(3): p. 255-260.
7. Treacy, M.M.J., T.W. Ebbesen, and J.M. Gibson, *Exceptionally high Young's modulus observed for individual carbon nanotubes.* Nature, 1996. **381**(6584): p. 678-680.
8. Yu, M.-F., et al., *Strength and Breaking Mechanism of Multiwalled Carbon Nanotubes Under Tensile Load.* Science, 2000. **287**(5453): p. 637-640.
9. Blundell, D.J. and B.N. Osborn, *The morphology of poly(aryl-ether-ether-ketone).* Polymer, 1983. **24**(8): p. 953-958.
10. Coleman, J.N., et al., *Small but strong: A review of the mechanical properties of carbon nanotube–polymer composites.* Carbon, 2006. **44**(9): p. 1624-1652.
11. Thostenson, E.T., Z. Ren, and T.-W. Chou, *Advances in the science and technology of carbon nanotubes and their composites: a review.* Composites Science and Technology, 2001. **61**(13): p. 1899-1912.
12. Ajayan, P.M. and J.M. Tour, *Materials Science: Nanotube composites.* Nature, 2007. **447**(7148): p. 1066-1068.
13. American Society for Testing and Materials, P., USA, *Standard test method for tensile properties of plastics.* ASTM standard D 638, 2003.

TEXTILE IMPREGNATION WITH THERMOPLASTIC RESIN – MODELS AND APPLICATION

Richard Loendersloot[1], Wouter Grouve[2], Edwin Lamers[3] and Sebastiaan Wijskamp[4]

[1] *Applied Mechanics, University of Twente, P.O. Box 217, 7500AE, Enschede, The Netherlands. Corresponding author's e-mail: r.loendersloot@utwente.nl*
[2] *Production Technology, University of Twente, P.O. Box 217, 7500AE, Enschede, The Netherlands.*
[3] *Reden – Research Development Nederland, Twekkelerweg 263, 7553LZ, Hengelo, The Netherlands.*
[4] *Ten Cate Advanced Composites, Campbellweg 30, 7443PV, Nijverdal, The Netherlands.*

ABSTRACT: One of the key issues of the development of cost-effective thermoplastic composites for the aerospace industry is the process quality control. A complete, void free impregnation of the textile reinforcement by the thermoplastic resin is an important measure of the quality of composites. The introduction of new, more thermal resistant and tougher polymers is accompanied by a large number of trial and error cycles to optimise the production process, since the polymer grade strongly influences the processing conditions. Therefore, a study on the impregnation is performed. Thermoplastic manufacturing processes are often based on pressure driven, transverse impregnation, that can be described as a transient, non-isothermal flow of a non-Newtonian fluid, where a dual scale porosity is assumed for the reinforcement's internal geometry. Meso- and micro scale models of isothermal flow revealed a limited sensitivity to the process conditions at the bundle scale for high pressure processes such as plate pressing, with an increasing sensitivity for lower pressures as apply for autoclave processes. The process conditions are significant for the quality of impregnation at filament scale. Specific combinations of pressure, viscosity and bundle compressibility can lead to void formation inside the bundles, as confirmed by microscopic analysis. The methodology developed has been translated to a ready-to-use design tool for the implementation of new polymers.

KEYWORDS: *transverse impregnation, micro impregnation, non-Newtonian, thermoplastic manufacturing process, design tool,*

INTRODUCTION

The application of thermoplastic composites offer a wide variety of opportunities for various industries, but most particularly the aerospace industry. A key issue for this industry is the product quality, which by itself is not a problem: a more than sufficient product quality can be achieved by the current state-of-the-art production technologies. However, once new materials are used, such as improved thermoplastics, a trial-and-error process has to be followed to obtain the production process settings to achieve the quality required. The bottleneck is a sound understanding of the processes occurring during the production of the thermoplastic product.

Thermoplastic composite production processes differ from thermoset composite production processes due to the constraints set by the higher viscosity. In general, dry or pre-impregnated (but not void free) fabric is consolidated using a combined heat and pressure cycle. The focus here is on the plate pressing process as applied by Ten Cate Advanced Composites for the production of the thermoplastic sheet material Cetex©, a woven glass reinforced PPS sheet material. The procedures described in this paper are also valid for other thermoplastic composite production processes.

The fabric is placed between foils of thermoplastic material, as shown in Fig. 1. The mould is heated, the thermoplastic material becomes viscous and impregnates the fabric after the pressure is applied. The matrix material solidifies during the cooling cycle, resulting in the fully impregnated product. Note that both woven fabrics and (stacks of) uni-directional fabrics can be used.

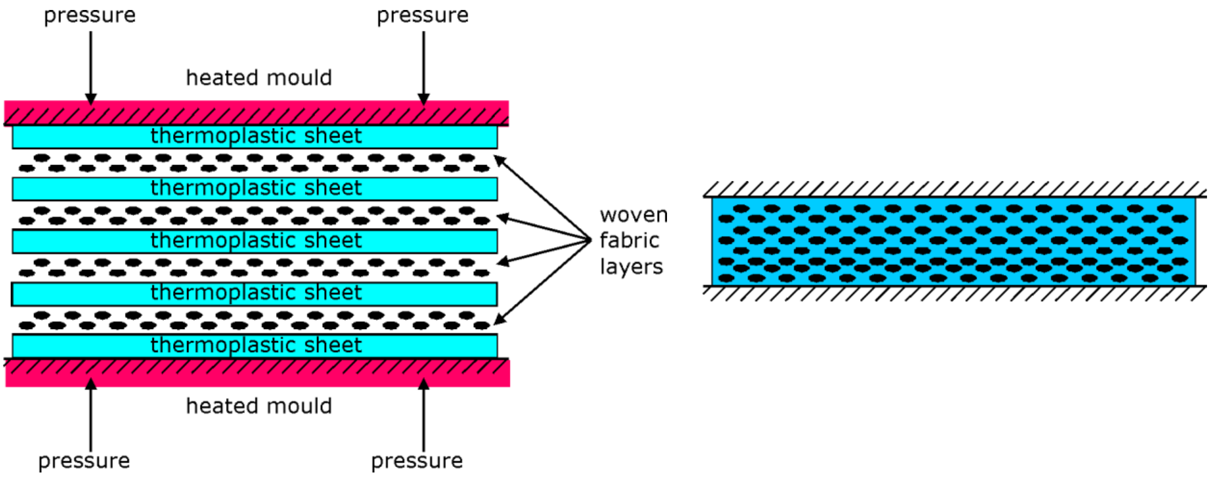

a. Stack of thermoplastic sheets and woven fabric layers, prior to the pressurized consolidation process.

b. Fully impregnated fabric at the end of the production cycle.

Fig. 1: Hot press production for thermoplastic material.

The process described sets the following requirements to the model: A thermal cycle has to be included as well as a two-level flow model. The two levels are defined at the length scale of the fibre bundles (interbundle) and the fibre filaments (intrabundle). Voids are generally formed at the intrabundle level. Complications are furthermore found in the fact that the thermoplastic material generally exhibits a strain rate dependent viscosity (non-Newtonian behaviour).

Grouve and Akkerman [1] showed that three different steps in the production cycle can be recognized (see Fig. 2) and can be treated independently for the process investigated:

1. Elevate temperature, to lower the viscosity of the matrix material.
2. Increase the pressure, to force the matrix material to impregnate the fabric.
3. Cooling and solidification of the laminate.

They stated that the interbundle space is filled during the first phase of the production process. The thermoplastic material is sufficiently viscous to flow around the fibre bundles (Fig. 2 state A), but too viscous to impregnate the fibres. This is only achieved after applying pressure to the mould (Fig. 2: B to C). The applied pressure is distributed over the resin and the textile, resulting in impregnation of the fibres accompanied by compaction of the fabric.

Interbundle and intrabundle flow models are discussed in this paper, explaining the observation by Grouve and Akkerman [1]. The thermal modelling is not addressed here, but is incorporated in the design tool that has resulted from this research. Details are found in ref [1].

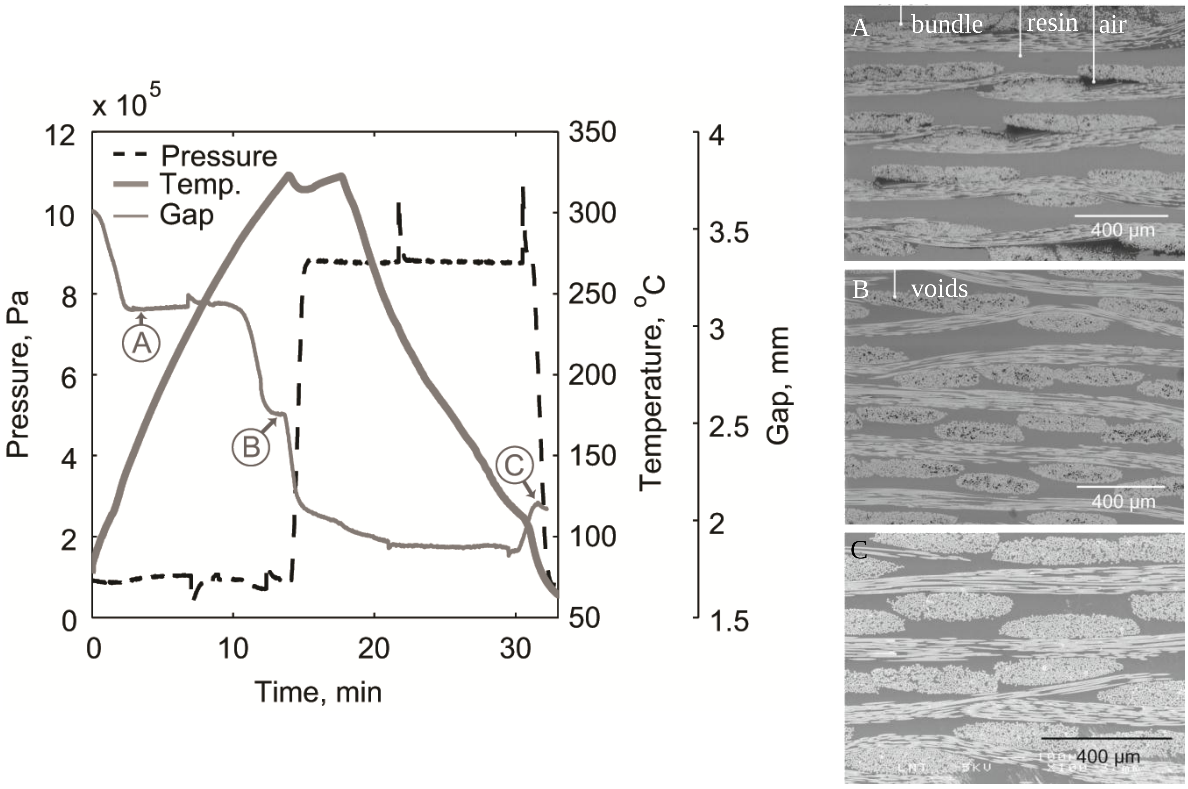

Fig. 2: Process variables measured during the production of a glass/PPS laminate and the micrographs of cross-sections of the laminate at the three points during the process cycle.

THEORY

The interbundle flow is initially analysed employing a transient, isothermal, two dimensional analysis in Comsol. This multiphysics software package numerically solves the Navier-Stokes equation:

$$\rho\frac{\partial \boldsymbol{u}}{\partial t} + \rho\boldsymbol{u}\cdot\boldsymbol{\nabla}\boldsymbol{u} = \boldsymbol{\nabla}\cdot\left(-p\boldsymbol{I} + \eta(\boldsymbol{\nabla}\boldsymbol{u} + \boldsymbol{u}\boldsymbol{\nabla})\right) + \boldsymbol{f} \qquad (1)$$

With ρ the density, $\boldsymbol{u}$ the velocity vector, t the time, p the pressure, $\boldsymbol{I}$ the identity tensor, η the dynamic viscosity and $\boldsymbol{f}$ the vector of body forces. The Carreau model for the viscosity [2] was used, to account for the shear thinning properties of the fluid during the initial phase of the impregnation. According to this model, the effective dynamic viscosity η_{eff} is defined as:

$$\eta_{\text{eff}}(\dot{\gamma}) = \eta_\infty + (\eta_0 - \eta_\infty)(1 + (\lambda\dot{\gamma})^2)^{\frac{n-1}{2}} \qquad (2)$$

With η_0 and η_∞ the viscosity at zero strain rate and infinite strain rate respectively. The parameters n and λ are to be determined experimentally. The Carreau model performs well for lower shear rates (~$10^3 s^{-1}$) to reasonable for shear rates in the range of $10^5 s^{-1}$. Often, a power-law function is used, but this significantly overestimates the viscosity at lower shear rates, which was judged undesirable in this case. The viscosity as a function of the shear rate is shown in Fig 3.

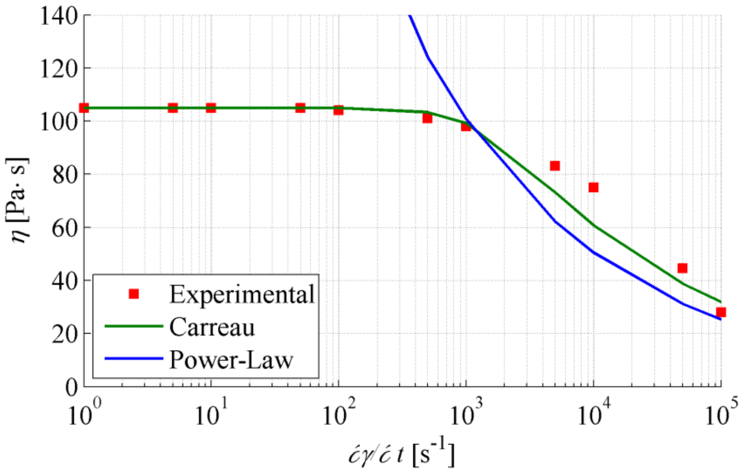

η_0 = 105Pa·s
η_∞ = 0Pa·s
λ = $7{\cdot}10^{-4}$s
n = 0.72

Fig.3: Measured viscosity of PPS as a function of the shear rate compared to a Carreau (coefficients are indicated to the right of the graph) and a power-law model for the viscosity.

The impregnation is governed by a transverse flow across aligned fibre bundles (interbundle flow) or fibres (intrabundle flow). It is assumed that there is no significant flow in axial direction due to the absence of a pressure gradient in the plane of the textile. The pressure distributions in a lab-scale press (width: 0.25m) and an industrial press (width: 1m) were measured revealing a nearly constant pressure over the width for the industrial press, though a significant pressure gradient was observed in the lab scale press. For the bundle impregnation, it is assumed firstly that the flow front is essentially oriented in radial inward direction and secondly that the flow obeys Darcy's law, thus reading for the fluid superficial velocity u:

$$u = \frac{K}{\eta}\frac{\partial p}{\partial r} \tag{3}$$

With K the permeability, η the viscosity, p the pressure and r the radial coordinate. The bundle shape is elliptical in general and therefore an equivalent radius r_{eq} is employed, which reads [3]:

$$r_{eq} = \sqrt{2}\frac{r_1 r_2}{\sqrt{(r_1^2 + r_1^2)}} \tag{4}$$

With r_1 and r_2 the minor and major radii of the ellipse representing the cross-sectional shape of the fibre bundle. The bundle permeability is assumed to be constant, despite a certain distribution of the fibre filaments in the bundle. Gebart's formulation for hexagonally packed fibre bundles [4] is employed to estimate the bundle permeability K:

$$K = \frac{16}{9\pi\sqrt{2}}\left(\sqrt{\frac{V_{fmax}}{V_f}} - 1\right)^{\frac{5}{2}} r_f^2 \tag{5}$$

With V_f and V_{fmax} the actual and maximum fibre volume fraction in the bundle respectively and r_f the filament radius. These properties are determined by using micrographs.

RESULTS & DISCUSSION

Firstly, the interbundle flow is investigated using a 2D model. An elliptically shaped bundle is assumed [5], as shown in Fig 4. A transient analysis is employed to model the wetting process. The air initially surrounding the bundle is modelled as a thin fluid. A transition region must be set to obtain numerical stability. The resin pushes the air out of the domain by prescribing a velocity condition on the inflow boundary. Symmetry boundary conditions are applied to model to obtain periodicity of the geometry. Dirichlet boundary conditions are applied at the bundle interface. A limited sensitivity to the boundary conditions was observed. Detailed modelling of the boundary conditions at the bundle interface is discussed in Grouve and Akkerman [6].

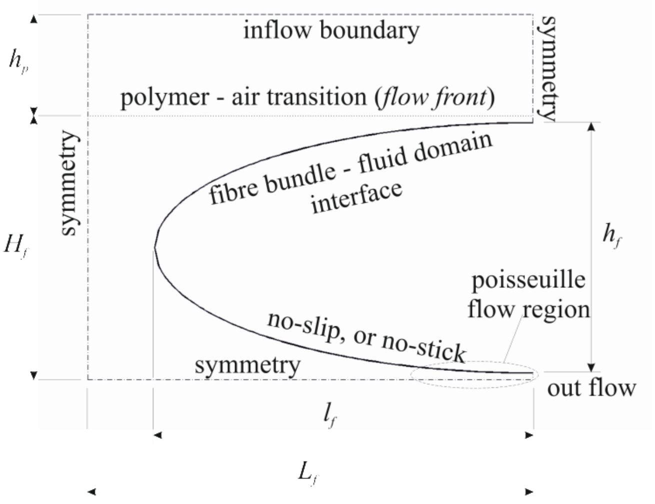

Bundle width	l_f	0.1866	mm
Bundle height	h_f	0.1170	mm
Cell width	L_f	0.2195	mm
Cell height	H_f	0.13	mm
Polymer height	h_p	0.05	mm

Fig. 4: Cross-sectional shape of the flow domain. The dimensions are obtained from microscopy images.

The progression of the flow front is visualised in Fig. 5 for three different inflow velocities. The colour in the graphs indicates the shear rate. The shear rate is relatively low for the main part of the domain, but the maximum increases nearly proportional to the inflow velocity.

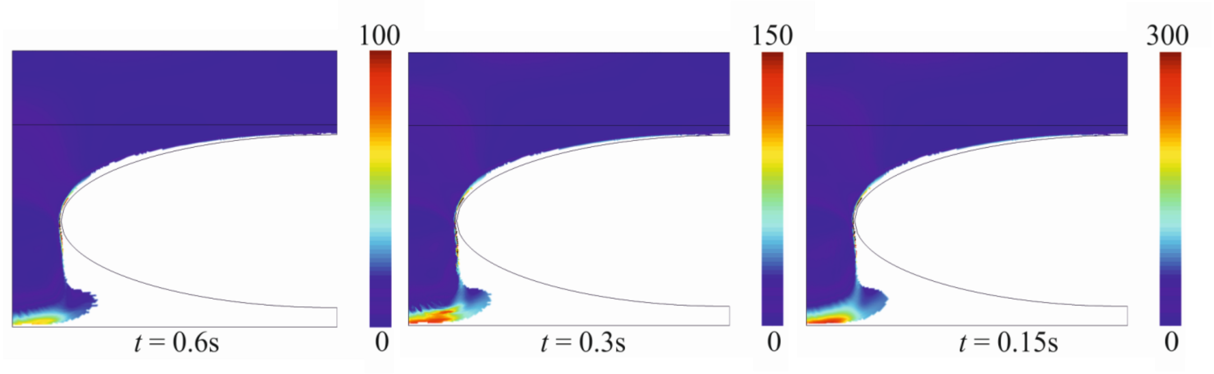

Fig. 5: Flow front progression at three different prescribed velocities ($0.05\text{mm}\cdot\text{s}^{-1}$, $0.1\text{mm}\cdot\text{s}^{-1}$ and $0.2\text{mm}\cdot\text{s}^{-1}$), at similar relative impregnation stages. The colour indicates the shear rate.

A thin layer of air remains present at the bundle interface. This results from the transition region combined with the overestimated fluid viscosity of the air, required to obtain numerical stability; The air is modelled as a thin Newtonian fluid, being significantly more viscous than in reality (10^{-4} Pa·s), but still orders of magnitude lower than the PPS viscosity (~10^2). A number of tests showed that the viscosity selected for air contributes positively to the stability of the solution, but does not affect the results.

The significant difference in the inflow velocity causes significantly higher shear rates, but the maximum shear rate remains below the limit where shear thinning becomes relevant (see Fig. 3). Hence, there is also no significant difference in the flow front progression. The conclusion can be drawn that shear-thinning is not relevant for the process settings used here. The analysis of 3D models resulted in the same conclusion.

The second stage in the filling process is the intrabundle impregnation. The resin has become sufficiently thin to flow around the filaments of the fibre. The bundle is surrounded by resin, resulting in an inward oriented impregnation, accompanied by a compressive pressure on the fibre bundle (see also ref. [7]). The applied compressive force F_A is split in a part related to the compaction stress σ_f of the fibre and the resin pressure p_r, effectively driving the impregnation:

$$F_A = \int_{A_f} \sigma_f \, \mathrm{d}A + \int_{A_r} p_r \, \mathrm{d}A \tag{7}$$

The compaction stress can be modelled with a power-law function [1], where the coefficients c_0 and c_1 are determined by experiments ($1.15 \cdot 10^7$ and 2.68 for the glass fabric investigated):

$$\sigma_f\big(\varepsilon_z(h)\big) = c_0 \varepsilon_z^{c_1}(h) = c_0 \left(\frac{h - h_0}{h_0}\right)^{c_1} \tag{8}$$

The uncompressed thickness h_0 was measured to be 0.3mm, h is the compressed thickness. The compaction results in an increase of the bundle fibre content (V_f in Eqn. 5). A Comsol model with an array of fibre filaments is used to investigate this effect. A minimum size repetitive unit is modelled, consisting of a single full fibre filament and three halve filament sections. The fibre filament radius is set to 3μm, based on microscopic images. Symmetry boundary conditions are applied to the upper and lower boundaries, whereas a zero-pressure is set at the outflow on the right hand side. A velocity is prescribed at the inflow ($0.1\text{mm}\cdot\text{s}^{-1}$) on the left hand side. The bundle can move, but no-slip boundary conditions are applied at the interface between fibre and fluid. The fibre filaments are connected to each other with truss elements, representing the bundle compressibility. The truss stiffness is set such that the compaction stress of the bundle is approximated.

Once again, the Carreau model for the viscosity is employed but non-Newtonian fluid behaviour is only observed at small areas close to the filament interfaces. The shear rate hardly exceeds the value of 2000: the resin still behaves as a Newtonian fluid according to the viscosity versus shear rate graph of Fig 3. Hence, a viscosity that only depends on the process temperature can be used.

The results show a small movement of the fibres, but no full closure of the intra bundle space: the resin can continue to flow through the bundle, resulting in a full impregnation and a void free final product. Fibre bundles with a low compaction stiffness can be difficult to impregnate void free. Generally, bundles in a woven fabric have an certain amount of twist [8], resulting in a (geometrical) compaction stiffness. However, some fabrics, and in particular unidirectional fabrics can show a low amount of twist, hence may suffer from a non-void free impregnation.

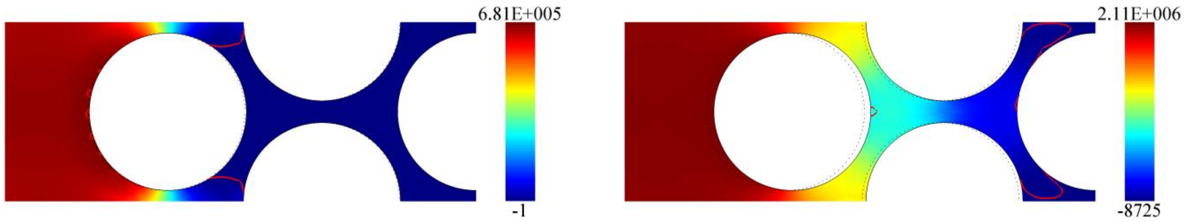

a. Pressure distribution at t = 0.025s. b. Pressure distribution at t = 0.050s.

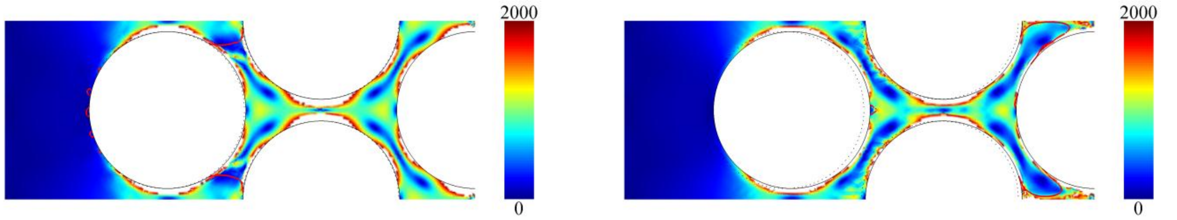

c. Shear rate at t = 0.025s. d. Shear rate at t = 0.050s.

Fig. 6: The pressure distribution and the shear rate at t = 0.025s and t = 0.05s (end of impregnation). The solid red line indicates the flow front. The shear rate in the uncoloured areas of the flow domain is higher than 2000s^{-1}.

The results suggest similar impregnation times and therefore a simultaneous impregnation of the interbundle and intrabundle space. However, the flow velocity component at the bundle interface in normal inward direction, is small compared to the tangential flow component, due to the difference in inter- and intrabundle permeability. The result is a sequential impregnation of the two domains, for this case. This situation alters if the inflow velocity (and hence the applied pressure) is substantially lower, as for example occurs in autoclave processes.

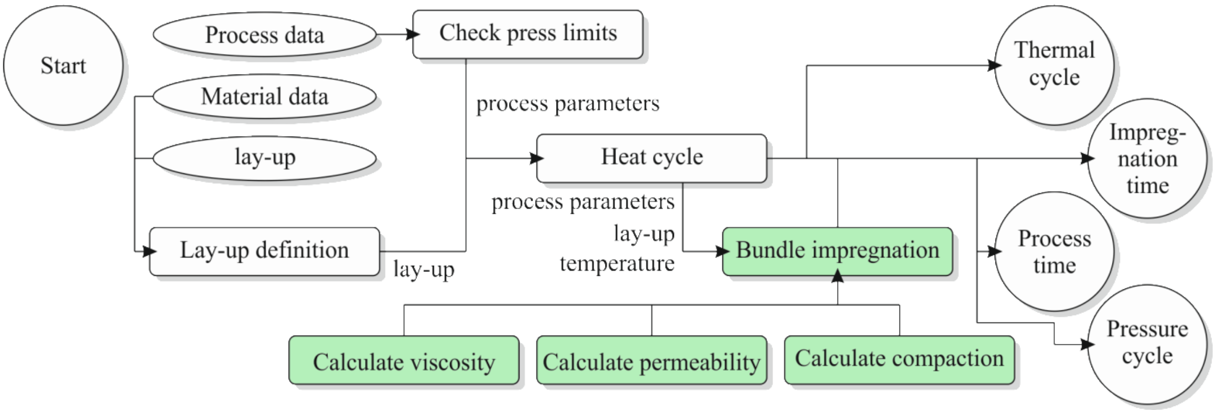

Fig. 7: Flow diagram of the design tool. The ovals indicate user input, the circles to the right refer to the output of the tool and the coloured rectangles correspond to the items of the tool discussed in this paper.

The results of this analysis were implemented in a design tool for film stacking processes. A flow diagram is presented in Fig. 7. The user needs to specify the material properties, the process cycle settings and the lay-up of the fabric and thermoplastic sheets in the mould. The algorithms in the tool subsequently determines the process characteristics, including the void content in the final product. This has led to a significant reduction in process time, since the process time was consciously overestimated to ensure a void free product. The tool also allows to investigate the effect of new materials on the process characteristics and the quality of the final product.

CONCLUSIONS

A design tool was developed for manufacturing processes of thermoplastic based composites. Transverse impregnation of the textile reinforcement can lead to void formation and a resulting poor product quality, if the process settings are not set appropriately. The resin, being above the glass-transition temperature but below the melting temperature, is sufficiently viscous to fill all interbundle spaces, but the intrabundle spaces are filled only once a pressure is applied and the temperature rises above the melting temperature. It is shown that shear thinning does not play a significant role for glass/PPS and that compaction of the fibre bundle for this material does not cause the formation of voids due to closure of the intrabundle space. The tool is developed for the plate pressing production process, in which the results are included. It allows the exploration of new thermoplastic materials without costly trial and error programs, but also sets requirements for the materials to be developed.

ACKNOWLEDGMENTS: This work was performed with the support of the Netherlands Agency for Aerospace Programs (NIVR) under contract number SRP-59621UT. This support is gratefully acknowledged by the authors.

REFERENCES

1. Grouve WJB and Akkerman R (2010), ‘Consolidation process model for film stacking glass/PPS laminates’, *Plastics, Rubber and Composites*, 39(3-5):208-214.

2. Osswald TA and Menges G (2003), *Material Science of Polymers for Engineers*, Carl Hanser Verlag, 2nd edition, ISBN 3-446-22464-5

3. West BP van, Pipes RB, Keefe M and Advani SG (1991), ‘The draping and consolidation of commingled fabrics’, *Composites Manufacturing*, 2(1):10-22.

4. Gebart BR (1992), ‘Permeability of unidirectional reinforcements for RTM’, *Journal of Composite Materials*, 26(8):1100-1133.

5. Lamers EAD (2004), *Shape Distortins in Fabric Reinforced Composite Products due to Processing Induced Fibre Reorientation*, PhD-Thesis, University of Twente, ISBN 90-365-2043-6, http://doc.utwente.nl/41422/1/thesis_Lamers.pdf

6. Grouve WJB and Akkerman R (2008), ‘An idealised BC for the meso scale analysis of textile impregnation processes’, *Proceedings of FPCM-9*, Montréal, Canada, 8 pages.

7. Endruweit A, Luthy Th, Ermanni P, ‘Investigation of the Influence of Textile Compression on the Out-of-Plane Permeability of a Bidirectional Glass Fiber Fabric’, *Polymer Composites*, 23(4):538-554

8. Lomov SV, Huysmans G, Luo Y, Parnas RS, Prodromou A, Verpoest I, Phelan FR (2001), ‘Textile composites: modelling strategies’, *Composites Part A*, 32:1379-1394

OIL PALM BIOMASS REINFORCED POLYPROPYLENE COMPOSITES

Ridzuan Ramli [1], Rosli M.Yunus[2], Beg M.D.H[2], Rohaya Mohamed Halim[1], Astimar A. Aziz[1], Ropandi Mamat[1] and Zawawi Ibrahim[1]

[1]*Malaysian Palm Oil Board (MPOB), P.O.Box 50720 Kuala Lumpur.*
[2]*Faculty of Chemical and Natural Resources Engineering, University of Malaysia Pahang, Gambang- 26300, Kuantan, Pahang Darul Makmur, Malaysia.*
Corresponding author's e-mail: ridzco@gmail.com

ABSTRACT: Oil palm empty fruit bunch (EFB) fibre and oil palm clinker (OPC) reinforced polypropylene (PP) composites were prepared by the melt-cast technique. Grinded EFB fibre and crushed OPC was compounded separately into polypropylene using a twin-screw compounder, with fiber contents of 10-40 wt% as well as without coupling agent and with 2-4 wt% coupling agent. The extrudates were then injection moulded to fabricate composites. The composites were characterized by mechanical, melt flow index (MFI), surface morphological and thermal tests. The mixing torque for PP and PP/EFB composites was found to be very close, whereas the torque of PP/OPC shows higher value than that of PP/EFB. The MFI of PP drops from 8 g/10 min to 5.2 for EFB/PP and to 4.2 for OPC/PP composites with increasing fibre content. Interestingly, the heat distortion temperature increases for the composites as compared to the pure PP. Incorporation of coupling agent in the composite exhibits better mechanical and thermal performances than without coupling agent due to better interfacial adhesion between fibers and PP matrix.

KEYWORDS: *Oil palm empty fruit bunch (EFB), oil palm clinker (OPC), polypropylene composite, coupling agent.*

INTRODUCTION

The incorporation of inorganic fillers has been proven to be an effective way for the improvement of mechanical properties, in particular the toughness of polymeric materials [1]. However, the particle loading in polymer inevitably adversely affects the processability of the compounds and results in much higher weight of the end-products. These limit various applications of the processed materials in automotive industries. To address these limitations due to particle loading, synthesis of composites using novel particles with improved properties is highly desirable. In this context, the oil palm biomass is a newly developed polymer reinforcing material consisting of inorganic oxides reportedly playing important roles [2]. Oil palm biomass (empty fruit bunch) is an industrial waste product and hence available at minimal cost. About 30 million tonnes of empty fruit bunches are produced in the world each year and these are considered by-products of agriculture [3]. Since Malaysia is one of the largest producers of palm oil, a huge amount of lignocellulose fibre can be obtained from the palm oil industry.

However, the main disadvantage of using oil palm biomass is its hydrophilic nature, which lowers its compatibility with hydrophobic polymeric matrices. Besides, oil palm biomass has poor environmental and dimensional stability that prevents its wider use in composites [2]. Cellulose fibres contain many hydroxyl groups (-OH) and interact readily with water molecules by hydrogen bonding. Absorption of water leads to micro-cracking of composites and expedites degradation of mechanical properties. It is difficult to entirely resist the absorption of moisture in composites without using expensive surface barriers [4]. Optimization of interfacial adhesion between cellulose-based fibres and thermoplastics has been the focus of research interests [5]. Coupling agents play an important role in improving compatibility and adhesion between polar fibre and non-polar polymer matrices by forming chemical bonds [6]. Although coupling agents have been reported to have been efficiently used in wood plastic composites [7, 8], not much work has been conducted on oil palm biomass reinforced with coupling agents. Therefore, the specific objectives of this work were to study the effects of oil palm EFB and oil palm clinker loading in PP and study the effects of coupling agents on the mechanical and melt flow properties of the resulting composites.

EXPERIMENTAL

Materials and methods

Oil palm empty fruit bunches (EFB) were obtained from Biomass Section, Malaysian Palm Oil Board. The oil palm clinker (OPC) was collected from a palm oil mill in Dengkil, Malaysia. The EFB and the clinkers were crushed into the required size. The polypropylene (PP) with a density specified as 0.90 g/cm^3 and melt index as 8 g/10min was a homopolymer, purchased from Cosmoplene. The coupling agent used was maleated polypropylene, Epolene (E43), produced by Eastman Chemical Company. Molecular weight and acid number of E-43 was 9100 and 45 respectively. The EFB and OPC were dried at 80^{o}C and introduced individually into PP by means of a Brabender DSK 42/7 twin-screw extruder having barrel temperatures from 170^{o}C to 190^{o}C from the feeding zone to the die zone respectively. The incorporated EFB and OPC contents in PP were 10, 20, 30, and 40 wt%. The compounded samples were prepared into ultimate composites by an injection moulder using a 20-ton Battenfeld BA 200CD Plus machine, with a UNILOG 4000 control system.

Tensile tests were carried out using an Instron machine with a load cell of 5 kN, in accordance with the ASTM D 638 - Type I standard. The gauge length and the crosshead speed for testing was 50 mm and 50 mm/min, respectively. The flexural test was conducted according to the ASTM D790-86: Test Method 1, at a speed of 2 mm/min by a 100N load with the support span of 50 mm. The diameters of the loading nose and supports were 20 mm and 10 mm respectively. Izod impact test was performed on a Ceast 6456 Izod pendulum impact tester. Notching (45^o) was produced on the impact specimens using Davenport notch cutting apparatus. This test was conducted based on ASTM D256-88. Melt flow index (MFI) of each sample was determined according to ASTM D1238 (230^{o}C per 2.16Kg) using Zwick D7900 melt flow indexer. The thermogravimetric analysis (TGA) was carried out by a SDT 2960 Simultaneous DTA-TGA analyser. Thermal measurements were taken with a constant heating rate of 20^{o}C/min at a scanning temperature range of 25^{o}C – 700^{o}C, whilst maintaining a static airflow of 150 ml/. A scanning electron microscope (SEM) (Leica, S360) was used to analyze the surface morphology of the fractured composites. The tensile fractured samples were sputtered coated before viewing under the microscope.

RESULTS AND DISCUSSION

Flow behaviour of PP and PP/EFB composites

The melt flow characteristics of neat PP and 30wt% EFB-fibre loaded PP are noted after 10 minutes and the data are introduced in Table 1. While the torque of the PP/EFB composite is almost the same as that of the neat PP in term of its energy requirement, the MFI of the composite shows a lower value and higher heat distortion temperature. The lower flow of the composite as compared to that of PP can be assigned to the presence of viscous components in the fibres.

Table 1: Test results of PP and PP/EFB composites.

Properties	PP	PP/EFB
Mixing torque (NM)	7.0	8.8
Melt flow index (g/10min)	8.0	5.2
Heat distortion temperature (ºC)	99	130

Mechanical properties

The tensile strength (TS) of virgin PP is found to be 37 MPa and that of the PP/EFB composite prepared without coupling agent (E-43) decreases from 29.26 MPa to 26 MPa with fiber loading from 10 to 40 wt%, respectively. This decreasing nature is due to the weak interfacial adhesion between the EFB and PP. Poor interfacial interaction is generally responsible for the inefficient stress transfer when load is applied to the sample.

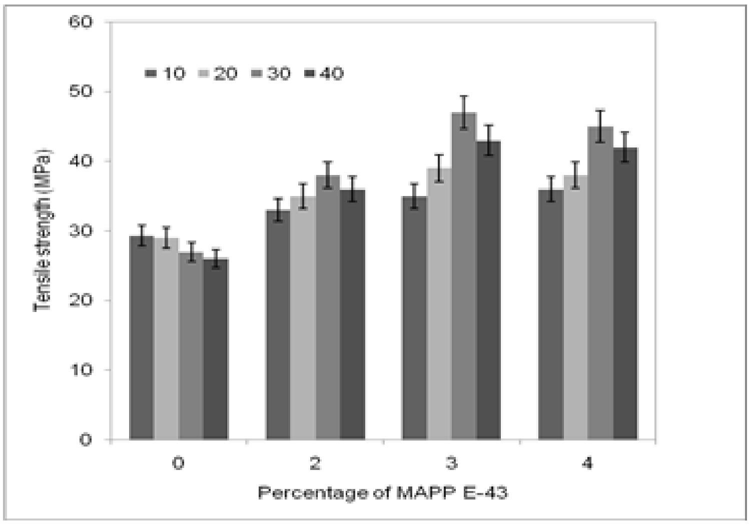

Figure 1: TS of EFB/PP composites for various amount of coupling agent and EFB fibres.

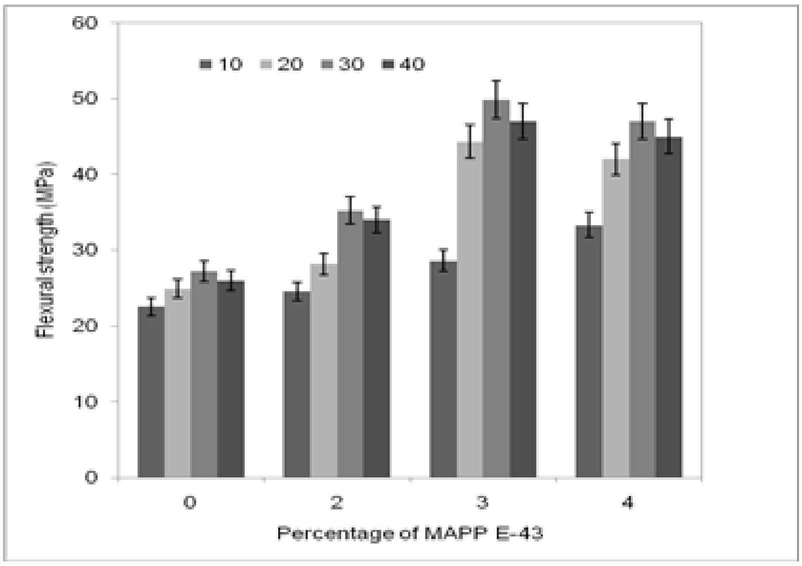

Figure 2: The FS of EFB/PP composites for various amount of coupling agent and EFB fibres.

Fig. 1 illustrates the TS of EFB/PP composites with various contents of E-43 including the fibre loading of 10 to 40 wt%. The TS of composites significantly increases both with increasing the amount of coupling agents (until 3%) and the fibre content (until 30%). A few researchers have disclosed a decrease of TS with increasing the fibre content in natural fibres reinforced polyolefines composites, while other researchers have found an opposite trend [9-11]. The irregular shaped EFB fibres with shorter fibre length used in this study may not be able to support stresses transferred from the polymer matrix to the fibres, thereby reducing TS as the fiber loading increases. It is obvious that 3wt% E-43 and 30wt% EFB shows the maximum TS value of 47 MPa among all other contents of fibre and E-43 used.

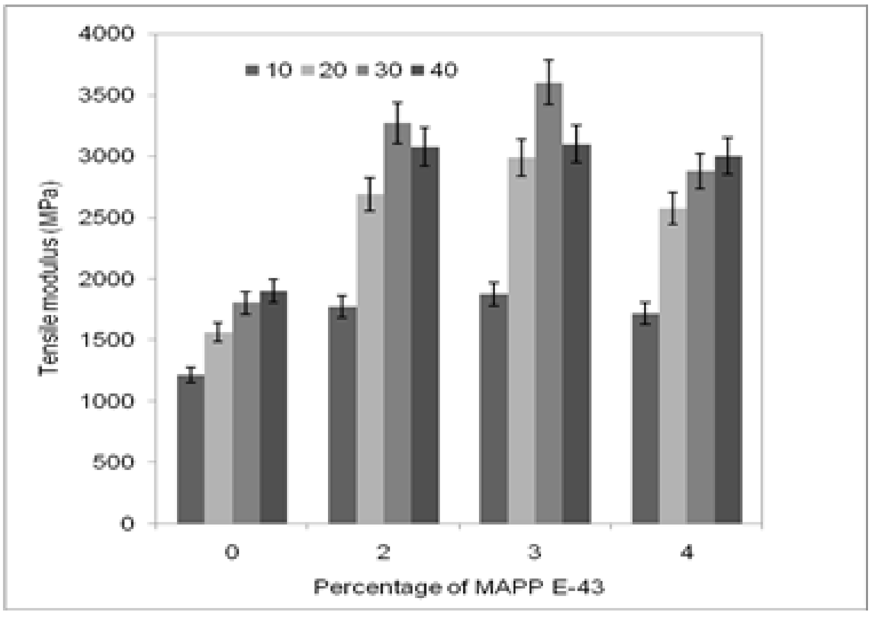

Figure 3: The TM of EFB/PP composites for various amount of coupling agent and EFB fibres.

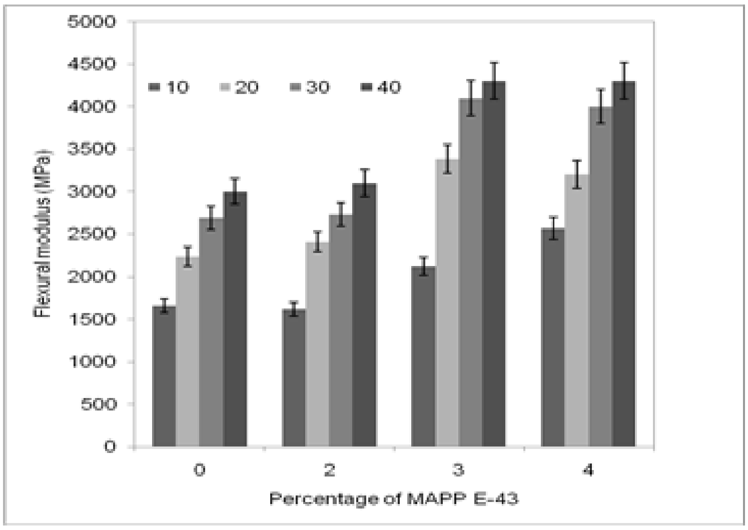

Figure 4: The FM of EFB/PP composites in presence of E-43 coupling agent and EFB contents.

The change of flexural strength (FS), as shown in Fig.2, is quite similar to that of TS. The highest FS is obtained by the incorporation of 3 wt% coupling agent and 30 wt% EFB fibre content. Fig. 3 represents the tensile modulus (TM) of the EFB/PP composites. The increase of TM with increasing the fibre content and the amount of coupling agent is noteworthy. The highest TM of 3600 MPa is obtained at 3 wt% E-43 and 30 wt% EFB content. The flexural modulus (FM) of the composites at various E-43 contents is shown in Fig. 4, where the highest measured value of FM is 4300 MPa. A similar trend of FS and FM changes as those of TS and TM is also found. The reason for this similarity may be due to chemical and physical characteristics of fibre reinforcement with PP.

Table 2 represents the values of Impact Strength (IS) and Melt Flow Index (MFI) of EFB/PP composites prepared at 3 wt% E-43. With respect to increasing EFB fibre content, the IS increases initially, shows the highest value at 30% fibre content and then decreases. On the other hand, the MFI progressively declines with increasing the fibre content. These results can be described by the fact that the inclusion of EFB fibres increases the stiffness and rigidity of the composite, thereby reducing the impact resistance due to initiation of cracks. If the amount of reinforcing fibre increases considerably, the fibres tend to stop crack propagation, leading to higher impact strength [12].

Table 2: The IS and MFI values of EFB/PP composites in presence of 3 wt% coupling agent.

% EFB fiber content	IS (J/m)	MFI (g/10min)
10	26.90	6.14
20	34.81	3.26
30	37.97	3.04
40	30.59	2.83

The values of IS and MFI for PP/EFB and PP/OPC composites are presented in Table 3, where a significant difference of IS and MFI values for these two fibres are observed. The IS and MFI values for the PP/EFB composite are found higher than those for the PP/OPC composite.

Table 3: IS and MFI of the composites at different loadings of fibre and coupling agent.

Agent	Filler	PP/EFB		PP/OPC	
%	%	Impact (J/m^2)	MFI (g/10min)	Impact (J/m^2)	MFI (g/10min)
0	10	22.15	4.27	21.62	3.45
0	20	22.15	4.24	25.32	3.01
0	30	25.32	4.00	26.37	2.5
0	40	23.21	3.14	20.04	2.76
2	10	15.3	6.73	19.52	5.1
2	20	20.57	5.5	18.46	5.5
2	30	23.45	3.81	20.57	5.32
2	40	21.62	3.35	18.99	4.38
3	10	18.48	6.75	21.62	6.34
3	20	20.57	5.46	26.37	5.71
3	30	27.32	2.9	28.48	5.3
3	40	22.15	2.32	18.99	5.01
4	10	20.05	6.35	25.15	6.11
4	20	20.05	4.96	25.15	6.72
4	30	21.55	3.29	26.9	5.66
4	40	18.99	2.54	19.52	5.08

Figs. 5 and 6 show the SEM images from the fracture surface of PP/OPC and PP/EFB composites without coupling agent and at 30 wt% fibre loading, respectively. Holes and void spaces are visible on both images, implying a poor adhesion between OPC and matrix. The fibres seem to be pulled out from the matrix and are not well dispersed. Comparing both images, the EFB reinforcements show less holes and cavities. This possibly renders higher mechanical performance of the EFB reinforced composites. The occurrence of feathering in the micrographs of composites prepared without coupling agent indicates the ductility of OPC/PP matrix. However, these protrusions are less for composites with 3% coupling agent. The presence of voids may create stress concentration points which in turn reduce the strength of the samples.

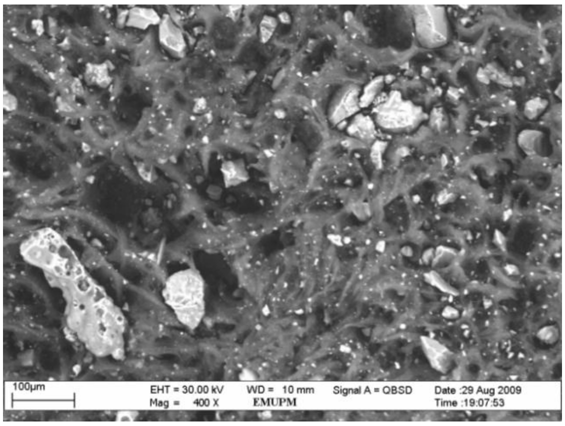

Figure 5: SEM image for the PP/OPC composite at 30 wt% fibre loading.

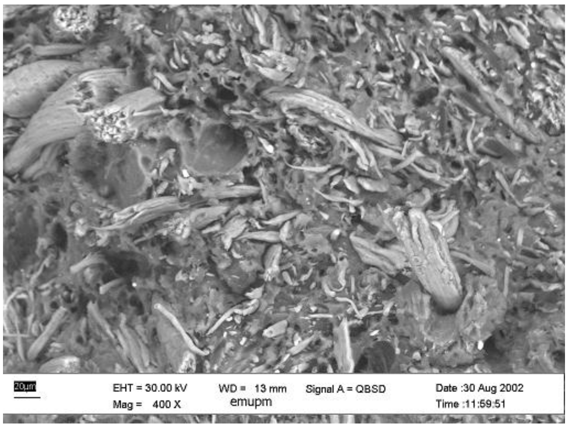

Figure 6: SEM image for the PP/EFB composite at 30 wt% fibre loading.

Fig. 7 demonstrates the fracture surface of PP/OPC composites with 3 wt% E-43 and 30% fibre loading. The surface micrographs of composite materials with coupling agent are relatively smooth as compared to those without coupling agent. The OPCs are observed to disperse well within the matrix and fewer holes are noticeable on the micrographs. The reinforcing OPC shows cleavage rather than pull-out.

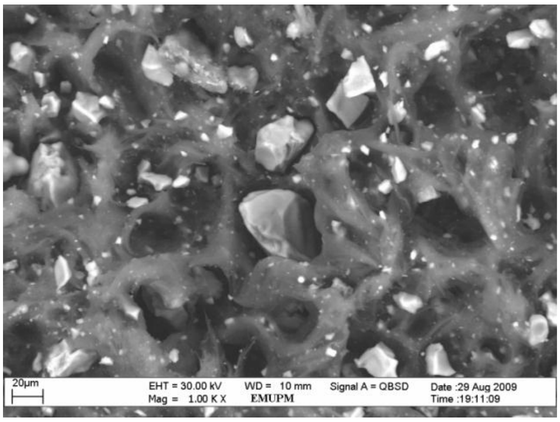

Figure 7: SEM micrograph of the PP/OPC composite with 3 wt% coupling agent.

Thermal properties

TGA thermograms of PP and the composites are shown in Fig. 9. From TGA analyses, the temperature range of degradation, amount of residue and the activation energy estimated are tabulated in Table 4. With the addition of fibres, the decomposition temperature increases. This increase of decomposition temperature has been reported to be due to the hindered diffusion (i.e., barrier effect) of volatile decomposition products caused by the dispersion of fibres in the PP matrix [13]. Composites with coupling agent show higher temperatures. This apparent improvement in thermal stability of the treated fibre composite could be attributed to bond formation between the coupling agent and the fibres. Thermal degradation kinetics of the samples were determined from the TGA data using the following relation [15]:

$$\ln\left[\ln\frac{1}{y}\right] = -\frac{E_a}{RT} + \ln\left[\frac{RZ}{E_a\beta}T_{\max}{}^{2}\right] \tag{1}$$

where, y is the fraction of nonvolatilized material not yet decomposed, T_{max} is the temperature at maximum reaction rate, β is the heating rate, Z is the frequency factor and E_a is the activation energy. The activation energy, E_a, determined from slopes of the ln[ln (1/y)] versus 1/T plots are also tabulated (Table 4).

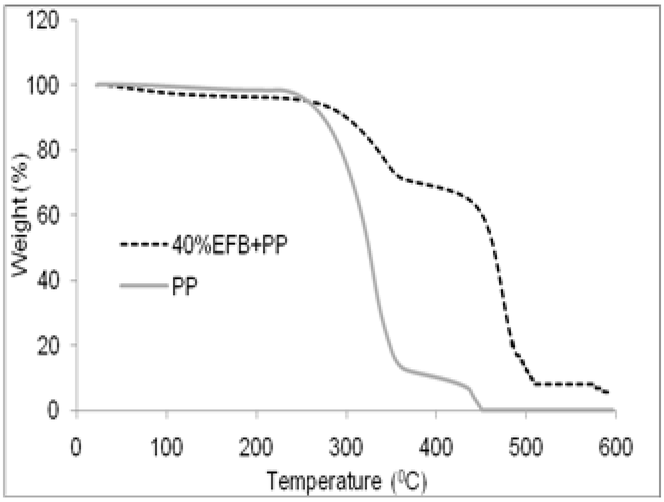

Figure 9: TGA thermograms of PP and EFB/PP composites (with 40 wt% EFB).

The calculated activation energy for pure PP is 99 kJ/mol, whereas for 10wt% fibre loaded composites the values for 1st stage and 2nd stage decomposition are 23kJ/mol and 64 kJ/mol. With increasing fibre content, the activation energy for 1st stage increases and 2nd stage decreases, and the value is even higher for composites with MAPP.

Formulation	Stage	Temperature range(^{0}C)	T_{max}	Residue (%)	Activation Energy kJ/mol
Pure PP	1st	267-472	420	0.012	99.41
10%EFB+PP	1st	210-351	325	2.8	23.39
	2nd	377-490	464		64.62
40%EFB+PP	1st	214-361	331	5.78	65.37
	2nd	389-496	470		35.88
PP+40%EFB+MAPP	1st	223-371	339	5.47	71.35
	2nd	392-499	472		40.06

Table 4: Thermal properties of composites

CONCLUSION

Significant improvement of mechanical properties, such as TS and TM, has been found at 30 wt% fibre loading and 3 wt% coupling agent. Strong adhesion between fibres and matrix has also been found for this composition by scanning electron microscopy. The effect of OPC on composite properties is less than that of EFB. Melt flow index shows a negative trend with the incorporation of fibres and coupling agent. With increasing fibre content, the activation energy for 1st stage increases and 2nd stage decreases and the values are found to be higher for composites with E-43.

ACKNOWLEDGMENTS: The authors would like to thank the Director General of MPOB for permission to publish this paper. The authors also wish to gratefully acknowledge the funding from MPOB for this study.

REFERENCES

1. Pukanszky B. (1999). Particulate filled polypropylene composites. In: Karger- Kocsis J, editor. Polypropylene: an A–Z reference, Dordrecht: Kluwer Academic Publishers, pp. 574–80.

2. Shinoz S., Visvanathan R., Panigrahi S., Kochubabu M. (2001). Oil palm fibre (OPF) and its composites, *Industrial Crops and Production*, **33**: 7–22.

3. Rozman H.D., Ismail H., Jaffri R.M., Aminullah A.A., Mohd Ishak Z.A. (1998). Mechanical properties of polyethylene-oil palm empty fruit bunch composites, *Polymer Plastic Technology Engineering*, **37**: 495–507.

4. Rowell R.M., Tillman A.M., Simonson R.J. (1986). A simplified procedure for the acetylation of hardwood and softwood flakes for flake board production *Journal of Wood Cheistry Technology* **6**: 427-448.

5. Weyenberg I. Van de, Ivens J., Coster A., Kino De B., Baetens E., Verpoest I. (2003). Influence of processing and chemical treatment of flax fibres on their composites, *Composites Science and Technology*, **63**(9): 1241-1246.

6. Lu J.Z., Wu Q., Harold S. (2005). Chemical coupling in wood fibre and polymer composites: a review of coupling agents and treatments, *Wood and Fibre Science* 2000, **32** (1): 88 – 104.

7. Bledzki A.K., Faruk O., Huque, M. (2002). Physico-mechanical studies of wood fiber reinforced composites. *Polym Plast Techn Eng* , **41**(3): 435–451.

8. Kazayawoko M., Balatinecz J.J., Matuana L.M. (1999). Surface modification and adhesion mechanism in woodfiber-polypropylene composites, *J Mater Sci*, **34**(24): 6189–6199.

9. Beg M. D. H., Pickering K. L. (2006) . Fibre Pre-Treatment and Its Effects on Wood Fibre Reinforced Polypropylene Composites. *Materials and Manufacturing Processes*, **21**: 303–307.

10. Rozman H.D., Saad M.J., Mohd Ishak Z.A. (2003). Flexural and impact properties of oil palm empty fruit bunch (EFB)-polypropylene composites- the effect of maleic anhydride chemical modification of EFB. *Polymer Testing*. **22(3)**: 335–341.

11. Khalil H.P.S, Issam A.vM., Ahmad Shakri M.T., Suriani R., Awang A.Y. (2007). Conventional agro-composites from chemically modified fibres. *Industrial Crops and Products*. **26**: 315–32

12. Khalid M., Ratnam C.T., Chuah T.G., Ali S., Choong T.S.Y. (2008). Comparative study of polypropylene composites reinforced with oil palm empty fruit bunch fiber and oil palm derived cellulose. *Materials and Design.* **29(1)**: 173–178.

13. Abu Sharkh B.F., Hamid, H. (2004). Degradation study of date palm fibre/polypropylene composites in natural and artificial weathering mechanical and thermal analysis. *Polymer Degradation and Stability*, **85**: 967–973.

14. Broido A. (1959). A simple sensitive graphical method of treating thermogravimetric analysis data. *Journal of Polymer Science,* Part A, **7**, 1761–1773.

ELASTIC PROPERTIES OF SHORT FIBRES REINFORCED POLYMERS IN THE VICINITY OF A WELD LINE

Gilles Dusserre

Université de Toulouse ; Mines Albi, INSA, UPS, ISAE, ICA (Institut Clément ADER) ;
Campus Jarlard, F-81013 Albi cedex 09, France.
Corresponding author's e-mail: gilles.dusserre@mines-albi.fr

ABSTRACT: Short fibres reinforced thermoplastic polymers are currently processed by injection moulding. Net-shape complex parts are produced at a high rate and the fibres allow to reach interesting mechanical properties compared to non-reinforced polymers. The fibres orientation distribution in the part is the result of flow processes involved while filling the mould. The final material is then heterogeneous with anisotropic material properties. These heterogeneities are particularly important in the weld lines, resulting from the merging of two flow fronts. In non-reinforced polymers, it is possible to keep non-affected properties in these areas if the material is hot enough to weld properly when the fronts merge. However it is not the case in reinforced materials since the fibres orientation is very significantly different in the flow front as in the bulk material due to the lack of shear, resulting in a poor mechanical properties area. A characterisation of the elastic properties of the weld line is here proposed. Tensile tests performed on specimen with and without weld lines are performed showing a significant decrease of properties in the first case, and 3D-Digital Image Correlation method is used to identify the evolution of the mean elastic modulus as a function of the distance to the weld line. The results are analysed by comparing the experimental values to those given by the commercial software Moldflow®, based on the Mori-Tanaka micro-mechanical model and the Folgar-Tucker model, which evaluates the second-order orientation tensor proposed by Advani and Tucker.

KEYWORDS: *Short Fibers Reinforced Polymers, Injection Molding, Weld Lines, Elastic properties, 3D Digital Image Correlation.*

INTRODUCTION

Injection molding is widely used by the manufacturing industry to form plastic parts at a high production rate. In most cases, limited mechanical properties are required for large diffusion products. The reinforcement of these materials by short fibers allows to increase the mechanical properties without necessitating to change the process. Short fibers reinforced polymers have become more and more performing from a mechanical point of view, thanks to the development of formulations exhibiting interesting mechanical properties up to 200 °C. This is the case of polyetherimide resin, PEI. The injection molding of polymers can produce net-shape parts with a high level of geometrical complexity. As a consequence of the complex flow involved, several flow fronts may merge creating a weld line. The influence of the weld lines on the mechanical properties of the material can be limited if the temperature of the merging fronts is high enough to allow a sufficient welding of the matter. Nevertheless in the case of short fibers reinforced polymers, the welding of the fronts is disturbed by the fibers (lower local packing pressure [1], partial welding of the matrix [2]). Moreover the local fibers orientation are affected in the vicinity of the flow front inducing material heterogeneity [3]. Hence the weld lines remain weakness areas, in particular for high fiber fraction [4], necessitating to be accounted for in the mechanical design of the part when the presence of weld lines could not be avoided. This can be achieved thanks to process simulation performing flow modeling to predict the location of the weld lines and the fibers orientation field. Autodesk® Moldflow® Insight is a widely used software package developed for the simulation of injection molding processes. It performs flow simulation using different assumptions (Hele-Shaw, 3D, Dual Domain [5]) and evaluates the fibers orientation tensor in each element. The Folgar-Tucker model [6] is used under its form proposed by Advani and Tucker [7] with a closure approximation that reduces fourth order tensor to second order tensor [7]. The error committed by this closure approximation is weakened by a “thickness moment of interaction coefficient” [5]. A micromechanical homogenization model is then applied to calculate the part effective properties. In this paper, full-field strain measurements are performed using the 3D Digital Image Correlation technique (3D-DIC). The in-plane elastic properties variation across the weld lines is then assessed. These experimental results are compared to the elastic properties computed using Moldflow®. X-ray tomography cross sections of the weld line area validate the fiber orientation computation.

MATERIAL AND METHODS

Material and specimen fabrication

The material under study is a 30 wt.% glass fiber reinforced PEI, well known under its commercial designation Ultem® 2310. The pellets are dried at 140°C for 4 hours before injection. The parts under study are ISO 3167 [8] test specimens and were molded using a 175 tons DK-Codim® press. The nominal section of the tensile specimen is 4×10 mm². Two batches of specimen were molded using a modular tooling [9] allowing to inject specimen with and without weld line.

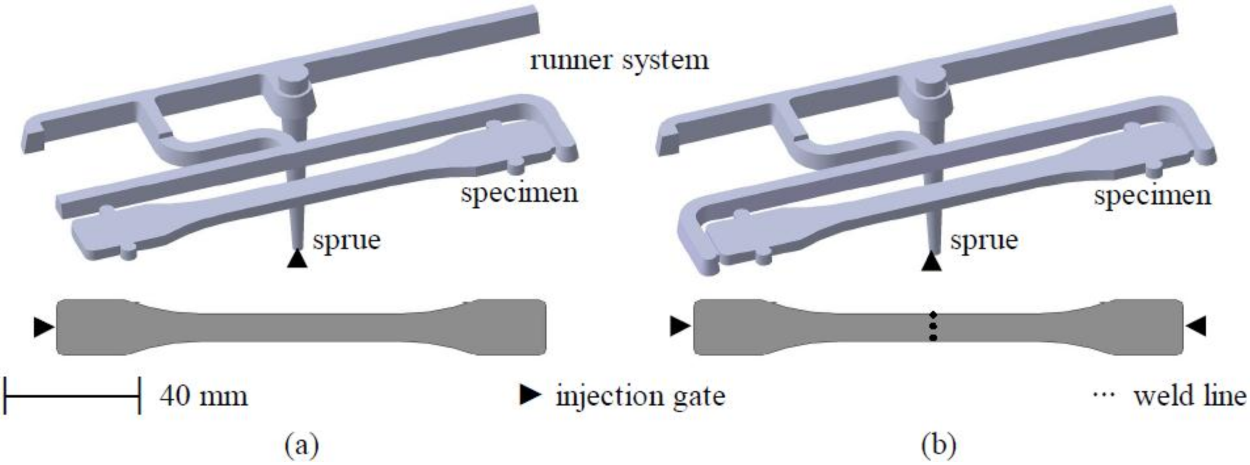

Fig. 1: Short fibers reinforced polymer specimens: without (a) or with (b) weld line

The first geometry involves a single injection gate in order to obtain specimen without weld line, Fig. 1.a. The second geometry involves a runner system allowing to fill the part from two injection gates located at each extremity of the specimen, Fig. 1.b. A weld line is then obtained in the middle of the specimen by the merging of the two flow fronts.

Tensile tests

Tensile tests were performed at room temperature and 80 °C using an Instron® 5800R electromechanical testing machine fitted out with a 30 kN load cell and a 12.5 mm gauge length extensometer. The tests are controlled at a crosshead displacement rate of 1 mm.min^{-1}.

3D Digital Image Correlation

In order to assess the material heterogeneity, kinematical full-field were measured using the 3D DIC technique. The surface of the specimen was patterned by a projection of white paint drops on a black background and images were acquired using two synchronized Qimaging® Qicam CCD cameras (resolution 1360×1036 pixels) with Nikkor Nikon 50 mm f1.8 macro lenses. The typical magnification factor is 50 pixels/mm. The correlation subset size is of 15 pixels. The strain calculation subset size is 0.25 mm.

EXPERIMENTAL RESULTS

Tensile behavior of the material

The tensile tests performed on the samples without weld line show that the mechanical behavior of the material under study is elasto-plastic. The linear range of the tensile curve (Fig. 2) is very limited, up to 40 MPa approximately. The Young's modulus is about 10 GPa and is sensitive to temperature: it is 6.5 % lower at 80 °C than at room temperature (Table 1 and Fig. 2). However the mechanical characteristic the most sensitive to temperature is the ultimate strength since it decreases about 20 % between room temperature and 80 °C.

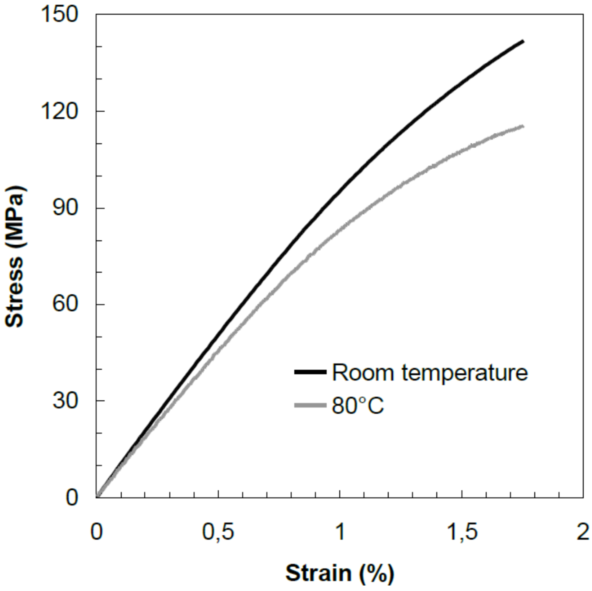

Fig. 2: Tensile behavior of Ultem® 2310 at room temperature and 80 °C

Table 1: Mechanical properties of Ultem® 2310 at room temperature and 80 °C

Temperature	Young's Modulus	Ultimate tensile strength	Tensile strain at break
°C	GPa	MPa	%
25	10	145	1.75
80	9.35	115	1.75

Influence of the weld line

The Fig. 3 emphasizes the influence of the weld line on the mechanical behavior of the material by comparing the load-displacement curves obtained in each case at room temperature (Fig. 3.a) and at 80 °C (Fig. 3b). The stiffness of the specimen is not significantly affected by the weld line which is not surprising because the affected area is a few millimeters long, which is small compared to the distance between the specimen shoulders (80 mm). The influence of the weld line is much more significant on the ultimate tensile strength. The ultimate strength of a specimen with a weld line is 42 % lower at room temperature and 29 % lower at 80 °C, with a specimen break occurring on the weld line.

Full-field measurement

The strain field measured by 3D-DIC on the tensile specimens with and without weld line are compared in Fig. 4. The specimen without weld line strains almost homogeneously: the longitudinal (parallel to loading direction) and transversal (perpendicular to loading direction) strain variations are respectively of ± 10 % and ± 20 % of the mean value. The strain field seems to be stochastic and doesn't reveal any particular strain mechanism. At the contrary the specimens with a weld line undergo a significant strain localization: the longitudinal and transversal strains are respectively about 35 % and 48 % higher in the weld line area than elsewhere on the area of interest. The weld line area seems to involve a higher Poisson's effect on the edge of the specimen where the compressive transversal strain reaches a maximum. This phenomenon results in a heterogeneous in-plane shear strain field.

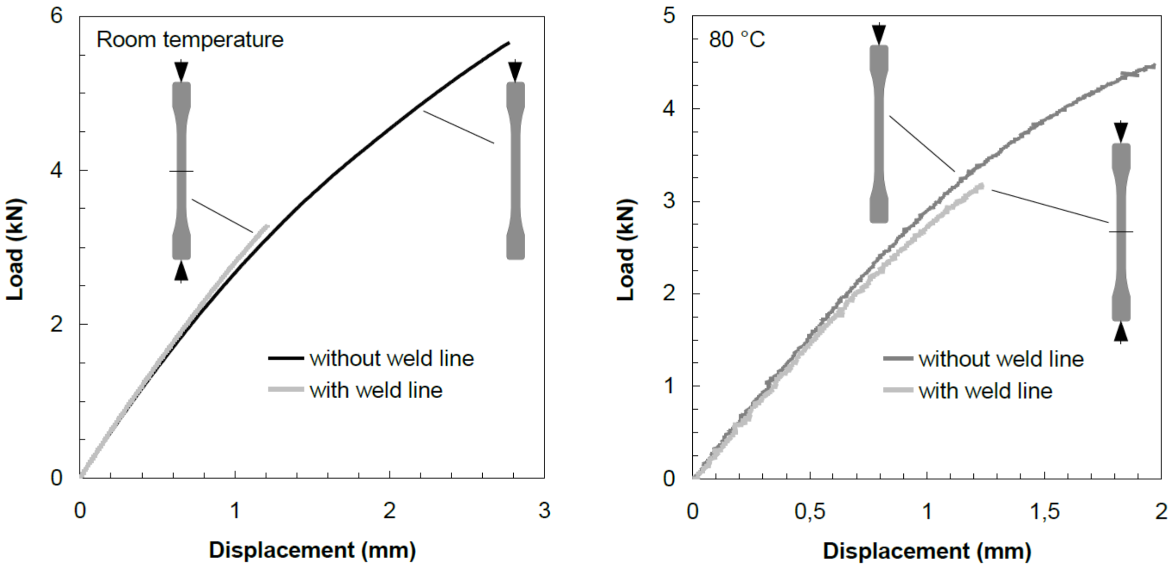

(a) (b)

Fig. 3: Influence of the weld line Ultem® 2310 behavior at room temperature (a) and 80 °C (b)

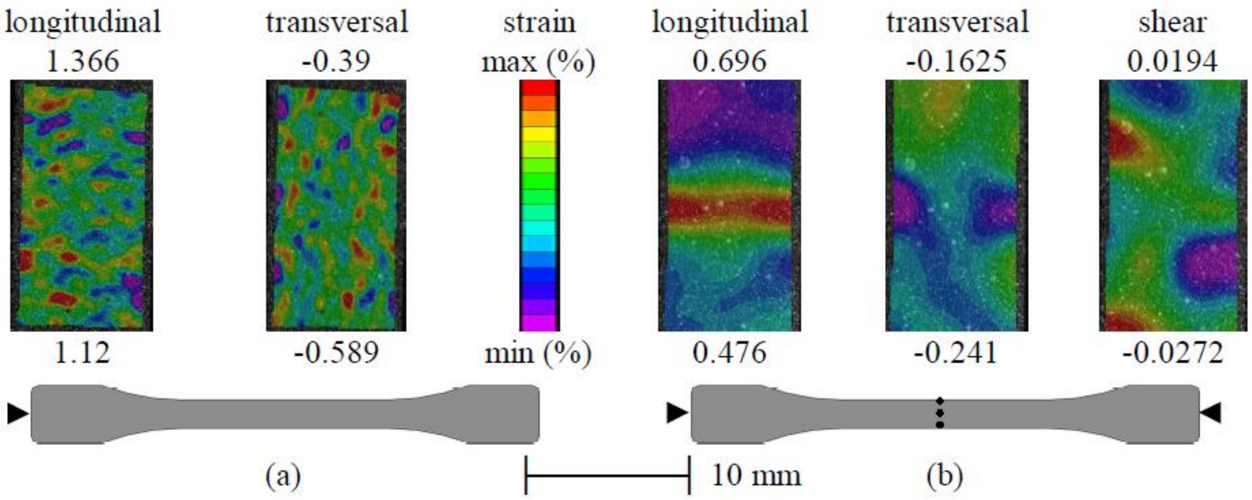

Fig. 4: Strain field measured by 3D-DIC: without (a) or with (b) weld line

PROCESS NUMERICAL SIMULATION AND ELASTIC PROPERTIES MODELLING

Process numerical simulation

The part injection was simulated using the FEM software package Autodesk® Moldflow® Insight. The geometry under study is a plane specimen (Fig. 5). It is meshed using triangular elements thanks to a midplane procedure (Hele-Shaw approximation). The first mesh is used to analyze a specimen without weld line (uniform element size of 3 mm in this case, Fig. 5.a). A second mesh was used to analyze the part with weld line. In this mesh a refinement was performed around the weld line area to reach a size about 0.25 mm in the middle of the specimen (Fig. 5.b). The Ultem® 2310 properties necessary to perform flow, fiber orientation and elastic properties analysis are available in the software database. The injection gates are located at one or both extremities of the part in order to obtain a part without weld line or with a weld line in the middle of the specimen. The process parameters were set to the values used for the fabrication of the tensile test specimens (recommended processing conditions). The analysis performed involves a filling step and a packing step.

Elastic properties computation

The fiber orientation is evaluated [6,7] from flow analysis. A Mori-Tanaka micromechanical model is used [10] to compute the local elastic properties of the part at each element. The Fig. 5 compares the local elastic properties computed with and without weld line. As expected, the specimen without weld line exhibits very anisotropic but uniform properties between the specimen shoulders. The elasticity modulus in the first principal direction is significantly overestimated, about 30 %, compared to the measured longitudinal modulus (extensometer, Table 1). This can be explained by the Hele-Shaw assumption that doesn’t consider any through thickness flow and overestimates the in-plane properties. In the weld line area, Fig. 5.b, the longitudinal modulus decreases about 40 % compared to the maximal value. The elastic properties are directly related to the fiber orientation tensor, and the area affected by the weld line is of the same length, about 10 mm, as measured using 3D-DIC (Fig. 4). This weld line area is characterized by almost isotropic but very heterogeneous properties.

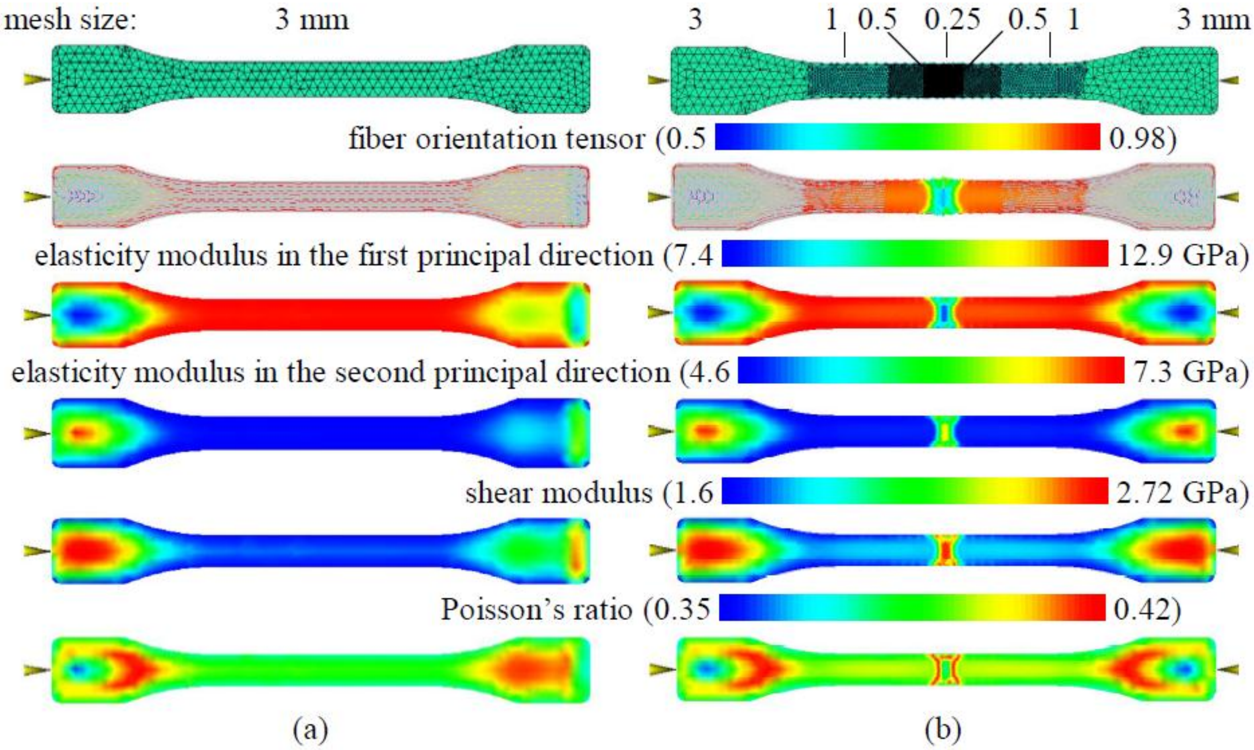

Fig. 5: Local fiber orientation and elastic properties computed using Autodesk® Moldflow® Insight in the specimens without (a) and with (b) weld line

DISCUSSION

The Fig. 6.a and Fig. 6.b compare respectively the evolution of the longitudinal modulus and Poisson's ratio across the weld line computed using Autodesk® Moldflow® Insight, to the experimental values. The numerical results are taken in the middle of the specimen whereas experimental values are averaged across the width of the specimen in order to get smooth plots. The results are plotted for two specimens with a weld line and an other curve shows the results obtained with a sample without weld line. The results (Fig. 6.a) show a good agreement of the simulated and measured length of the area affected by the weld line, about 10 mm. However, the influence of the weld line on the modulus decrease is overestimated by the simulation: 40 % instead of less than 30 % in the experimental results. Nevertheless it turns out that this discrepancy between simulation and experiment is the result of a good agreement of the elastic properties evaluated in the non affected area with the properties of the specimen without weld line (lower than 10 %) and a fair agreement of the local properties of the weld line with the experimental one (lower than 15 %). It could be concluded that the resulting elastic properties are also affected by the previous flow and that this influence is underestimated by the simulation. This can be explained by the Hele-Shaw assumption that provides a plane orientation tensor. A Poisson's ratio between 0.35 and 0.4 is obtained in each case outside the weld line area. In the weld line vicinity the computed Poisson's ratio increases and then decreases up to a minimum about 0.37 whereas the experiment provides a continuous decrease up to 0.3 in the weld line.

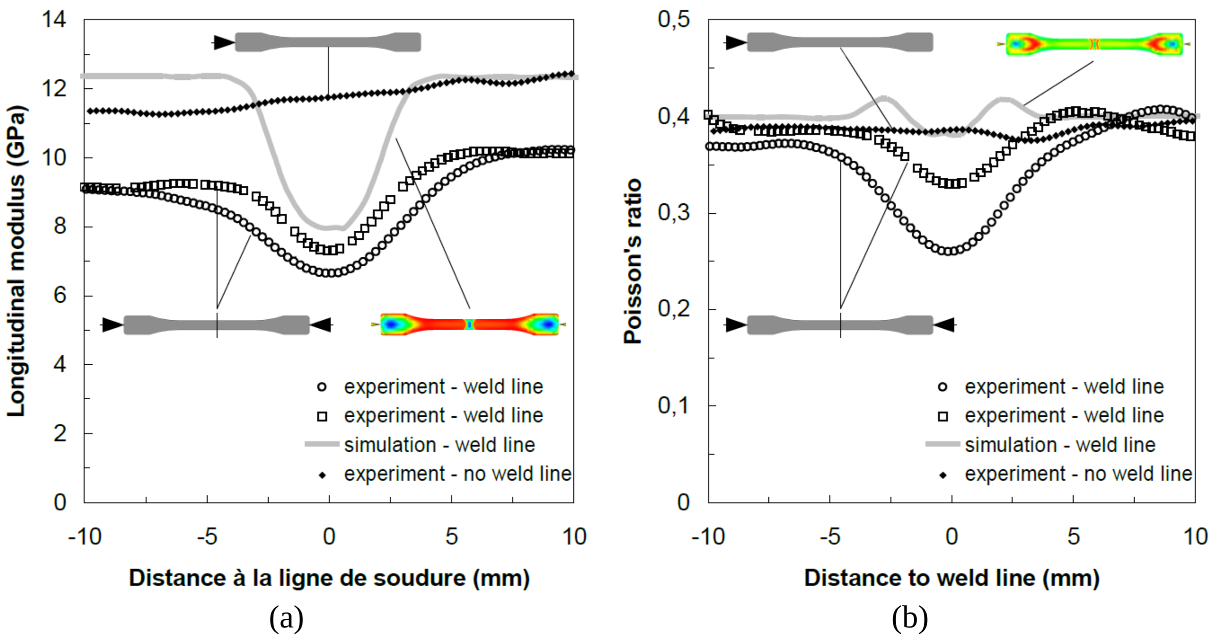

Fig. 6: Longitudinal modulus (a) and Poisson's ratio (b) measured by 3D-DIC for specimen with and without weld line and comparison with simulation

X-ray tomography cross sections of a 4 mm edge cube sampled symmetrically across the weld line are shown in Fig. 7. The cross section near the weld line shows that the fiber are most likely oriented in the cutting plane except in the area near the mold where the preferential orientation is parallel to the flow. When the cutting plane get further and further away from the weld line, the thickness of the area where the fibers are oriented in the flow direction increases. This occurs up to a distance about 1.5 mm from the weld line: the area where the fibers are stochastically oriented has then almost completely disappeared. This is consistent with the computation results of the Fig. 5.b (fiber orientation tensor).

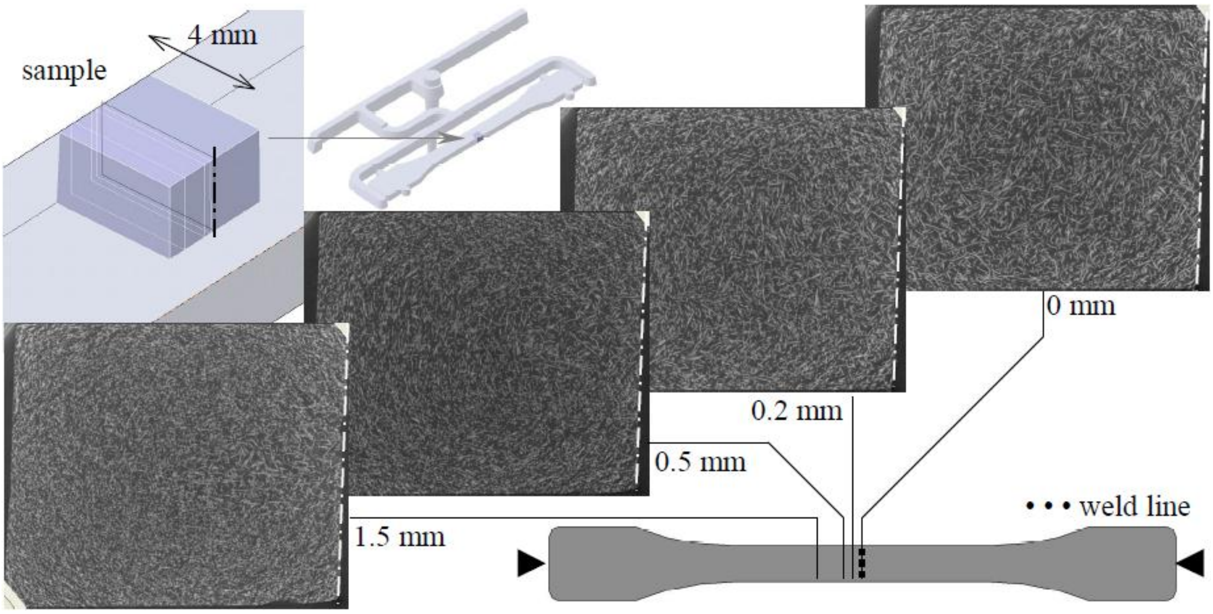

Fig. 7: X-ray tomography cross sections of the material in the vicinity of the weld line

CONCLUSIONS

Tensile tests have shown that weld lines drastically affects the ultimate stress of the material, but its influence on the part stiffness is weak. An experimental and theoretical study of the weld line area provides a local elasticity modulus assessment. The decrease of the experimental longitudinal modulus in the vicinity of the weld line arises 30 % in the weld line. The simulation results slightly overestimate this decrease but this bias can be mainly attributed by the over estimation of the modulus in the non affected area, probably due to the Hele-shaw assumptions. A less fair agreement is obtained on the Poisson's ratio. However, it turns out that the heterogeneity of the elastic properties of the material in the vicinity of the weld line is related to the fiber orientation distribution since X-ray tomography cross sections of the weld line area fairly agree the predictions of the simulation.

ACKNOWLEDGMENTS: the author greatly acknowledges Mrs. Christine Rolland who performed micro tomography characterizations.

REFERENCES

1. Fellali S, Meddad A, Fisa B and Favis BD (1995), 'Weldlines in injection molded parts: A review', *Advances in Polymer Technology,* 14(3), 169-195.

2. De Gennes PG (1971), 'Reptation of a polymer chain in the presence of fixed obstacles', *The Journal of Chemical Physics,* 55(2), 572-579.

3. Yang B, Ouyang J and Li X (2011), 'Simulation of fiber reinforced composite materials mold filling process and mechanical properties analysis', *Journal of Non-Newtonian Fluid Mechanics,* 166(19-20), 1129-1136.

4. Vaxman A, Narkis M, Siegmann A and Kenig S (1991), 'Weld-line characteristics in short fiber reinforced thermoplastics', *Polymer Composites,* 12(3), 161-168.

5. Autodesk® Moldflow® Insight 2010 Help

6. Folgar FP and Tucker CL (1984), 'Orientation behavior of fibers in concentrated suspensions', *Journal of Reinforced Plastics and Composites,* 3(2), 98-119.

7. Advani SG and Tucker CL (1987), 'The use of tensors to describe and predict fiber orientation in short fiber composites', *Journal of Rheology,* 31(8), 751-784.

8. Plastics - Multipurpose test specimens. ISO 3167:2002.

9. Saint-Martin G (2003), Etude Typologique des defauts structuraux generes au cours de la mise en forme pas injection de composites a matrice polymere thermostable renforces par fibres de verre courtes, PhD Thesis, Ecole des Mines de Paris, France, in french.

10. Tucker CL and Liang E (1999), 'Stiffness predictions for unidirectional short fiber composites: review and evaluation', *Composite Science and Technology*, 59(5), 655-671.

PULTRUSION SYSTEM FOR CONTINUOUS FIBER REINFORCED THERMOPLASTIC COMPOSITE

Anin Memon[1], Toshihiro Motochika[1], Daisuke Hatano[1], Asami Nakai[2] and Akio Ohtani[2]

[1] Department of Advanced Fibro-Science, Kyoto Institute of Technology,
Matsugasaki, Sakyo-ku, Kyoto, 606-8585, JAPAN
[2] Department of Mechanical Engineering, Gifu University,
1-1 Yanagido, Gifu, 501-1193, JAPAN

ABSTRACT: In this study, the pultrusion system for continuous fiber reinforced thermoplastic composite was presented. The design concept of pultrusion systems were described in the term of materials design, structure design and processing design. The materials design were used hybridization of glass fiber with jute fiber reinforced PLA and carbon fiber with aramid fiber reinforced PA66. The braiding technique manufactured a hybrid yarn arrangement in tubular preforms. The braided preforms were pulled through a heated die where the consolidation flow took place due to reduced matrix viscosity and pressure. The pultrusion experiments were fabricated the tubular hybrid composite. Impregnation quality was evaluated by microscope observation of the pultruded cross-sections. The flexural mechanical properties of the beams were measured by 4-point bending test.

KEYWORDS: *FRTP, Braided composite, Pultrusion molding, Tubular hybrid composite*

INTRODUCTION

Many of common composite production methods are unsuitable for mass production. One exception is the pultrusion process, it is possible to maintain a continuous production of straight profile with constant cross-sections. Pultrusion is a manufacturing process in which reinforcing fibers impregnation with matrix are pulled through a die to form composites of a constant cross-section. Generally, the unidirectional fibers are impregnated with low viscosity thermosetting resins before passing through a series of die for shaping and curing during pultrusion process [1,2,3]. While thermoset pultrusion is a well known and commercially established manufacturing method, there is less knowledge about the thermoplastic pultrusion. In contrast to thermosets, thermoplastic matrix are generally polymerized, no further chemical reaction are necessary, therefore the processing is reduced to first melting the matrix, then shaping the composite under pressure and finally cooling it to preserve the new shape. Thermoplastic resins contain very high melt viscosities, which make in-process melt impregnation of the reinforcement difficult. For this reason, various intermediate materials have been developed to overcome these problem such as micro-braided yarn commingled yarn and parallel configuration yarn as shown in Figure 1. The schematic of tubular braiding fabric are showed in Figure 2, all fiber bundles are diagonally oriented, and the angle (θ) of the fiber bundle to the longitudinal direction can be adjusted freely. Also, the fiber bundle called the middle-end-yarn (MEY) can be inserted into the braiding yarns along the longitudinal direction. For this reason, the braiding technique can control the anisotropic of pultrusion molding.

In the early stage of thermoplastic braided composite by pultrusion molding with various form of materials have been widely studied [3, 4, 5]. Anin and Asami [2] proposed the structure and processing design of braided jute spun yarns/PLA composite by pultrusion molding. The intermediate materials were prepared by micro-braided yarn and parallel configuration yarns. Successful tubular braided composite realized using glass fiber for middle end yarns in the braided structure. It was found that successful tubular braided composite realized using glass fiber 1,150 tex for middle end yarns in the braided structure. The highest bending strength and modulus were found in the specimen using parallel yarn configuration. [5]. Yoshitaka Tanaka et al. [4] developed the thermoplastic pultrusion braided composite in L-shape. Commingled yarn carbon fibers and PA66 were used as intermediate materials. It was found that the un-impregnation area increased with increasing the molding speed.

The objective of this study was to establish a method of thermoplastic pultrusion molding of braided composite hybrid glass fiber with jute fiber reinforced PLA and carbon fiber with aramid fiber reinforced PA66. Figure 3 shows the schematic of pultrusion process of braided composite in this study. The commingled yarns were used as intermediate materials to prepare the pultrusion preform by braiding technique. The fabrication quality of pultrusion process was evaluated by cross-section observation and mechanical properties evaluated by four-points bending test.

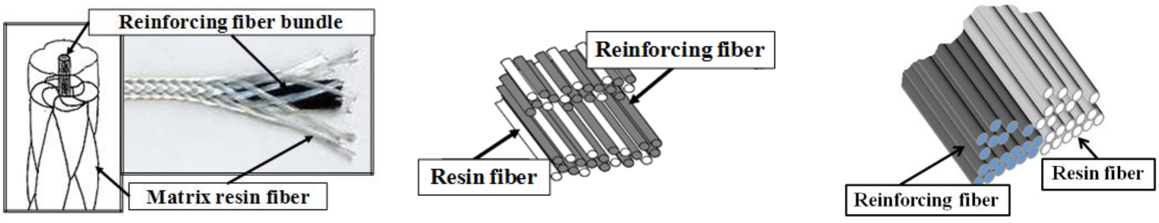

a) Micro-braided yarns b) Comingled yarns c) Pararelled yarns

Figure 1 Schematic of intermediate material

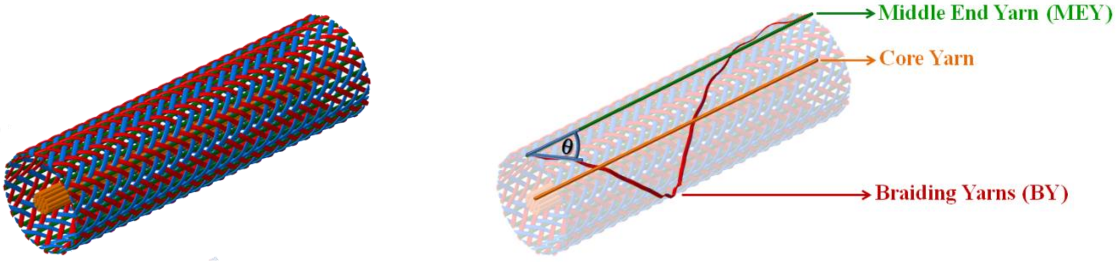

Fig. 2 The Schematic of tubular braiding fabric

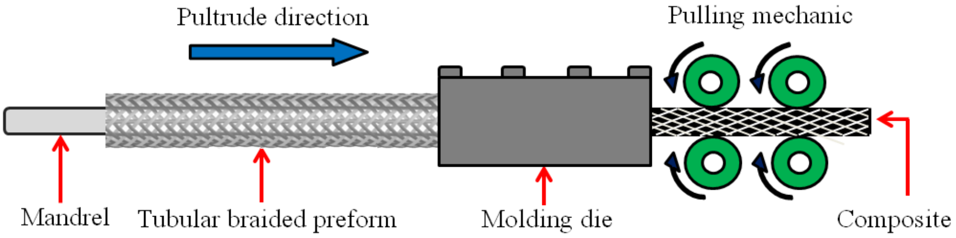

Fig. 3 The schematic of pultrusion process of braided composite

MATERIALS AND EXPERIMENT

Design concept

In this paper, the designed concept of braided composite by pultrusion molding is described. The designed concept involves the materials design, structure design and processing design as shown in figure 4. Material designs consisted of interface such as surface treatment on reinforcement fiber, volume fraction and configuration of yarn on intermediate materials. Braiding angle, gap between braiding yarns and filling ratio, are the important parameter of the structure design. Meanwhile, the processing designs were consisted of pultrusion temperature, pulling speed and pulling force.

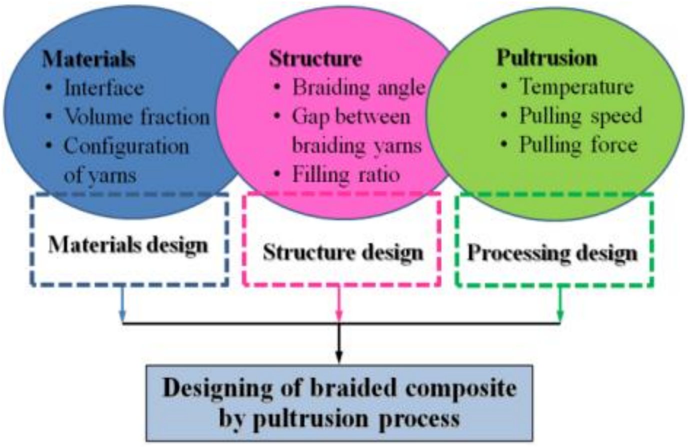

Fig. 4 Design concept of braided composite by pultrusion molding

Materials

In this study, the materials were used hybridization of glass fiber with jute fiber reinforced PLA and carbon fiber with aramid fiber reinforced PA66. Jute and PLA composites have been fabricated with good impregnation quality and mechanical properties using compression of micro-braided yarns [6]. Following the designed concept in this study, jute fiber tows were comingled with polylactic acid fiber. Figure 5 showed the commingle technique for mix the resin fiber with reinforced fiber. The jute spun yarns having a fineness of ~400 tex (Bangladesh Janata Jute Mills Ltd.) were used as reinforcement fibers. The continuously PLA fibers in a tow configuration were used as resin fiber, having a fineness of ~56 tex (84T-26-LA10, Toray Co.,Ltd). Glass fiber yarns having a fineness of 520, 600, 720 and 1,150 tex (Nippon Electric Glass Co. Ltd.) were also used as the middle end yarn to enhance the strength of braided fabric. The PA66 resin fiber bundles having a fineness of 23.5 tex were used as the matrix resin. Carbon fibers (T700 – 50C – 12, Toray Co.,Ltd) having a fineness of 800 tex were commingled with PA66 resin fiber bundles. Aramid fiber (East co., Ltd. Rede~yupon, Kevlar29 – 6K,) having a fineness of 330 tex and also commingled with PA66. They were used as intermediate materials. The braided fabric preforms for pultrusion was fabricated using 48 braiding yarns (BY) and 24 MEY in a tubular braiding machine with a 48 carriers (Murata Machinery). The braids were done using braiding ring with diameter of 30 mm and mandrel with diameter of 20 mm, and the braiding angle was 30-45 degree and layer quantities of braided fabric was superposed of 2 layers. The lists of the different braided preforms were shown in table 1. The resin fibers of the braided preform were melted and impregnated with reinforcing fibers in the hot die, two-layered braided composites with tubular cross section were molded.

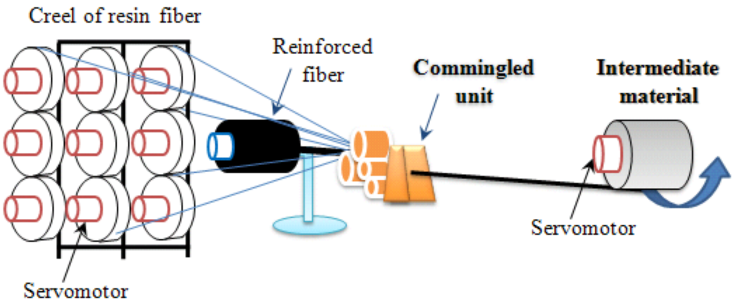

Fig. 5 Comingle technique

Table 1 Lists of the different braided preforms.

Preform	Braiding angle (°)	Vf of Composite (%)	Filling ratio (%)
PLA resin fiber group			
1) J / GF520	38	43	100
2) J / GF600	38	46	100
3) J / GF720	35	46	100
4) J / GF1150	30	53	104
PA66 resin fiber group			
5) C / C	45	48	106
6) A,C / C	45	49	106
7) A / C	45	49	106
8) A / A	45	49	107

J : Jute, GF, Glass fiber, C : Carbon fiber, A : Aramid fiber

Processing design

The tubular pultrusion molding assembly was shown in Figure 6, consisting of the preheater, the pultrusion die and pulling mechanic unit. Prior to pultrusion, the preforms were dried in convection oven. The preforms were pre-heated in the preheating die for easier impregnation. The tubular molding die had outside diameter of 23 mm, inside (mandrel) diameter of 20 mm and the thickness of 1.5 mm can be produced. The length of the molding die was 270 mm, which was separated into four heating zones. The die shape was large at the consolidation die entrance and gradually reduces in 50 mm taper region until constant thickness 1.5 mm was reached. The temperature at each part of the die can be precisely controlled during pultrusion. The temperature at each sections of the die was set as shown in Table 2. The braided preforms were pulled through the forming assembly die by a pulling mechanic at a speed of ~18-20 mm/min.

Generally, glass fiber was used as MEY to enhance the strength of braided preform for pultrusion molding in PLA resin fiber group, carbon fiber and aramid fiber were used as MEY to enhance the strength of braided preform for pultrusion molding in PA66 resin fiber group. This study will select the preform which use the minimize glass fibers in braided preform to examine the effect of molding temperature in case corresponding with the green composite. For the tubular composite in PA66 resin fiber group, the preform which given the good mechanical properties and impregnation will be selected to examine the effect of molding temperature in case corresponding with the high strength composite. These preform were molded by changing the pultrusion temperature in molding die zone1 and zone 2 with constant molding speed. The changing of pultrusion temperature for PLA resin fiber group are 195, 210, 215 and 225 ^{o}C. And the changing of pultrusion temperature for PA66 resin fiber group are 290, 300, 310 and 320 ^{o}C. After the molding, the specimens were cut and polished in a direction perpendicular to longitudinal direction for the cross-section observation in order to investigate the internal state of the molding with optical microscopic.

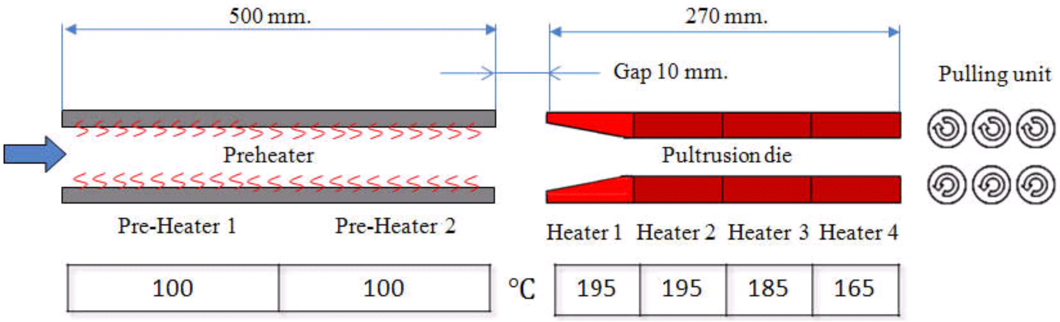

Fig. 6 The Schematic of tubular braiding fabric

Table 2 The pultrusion temperature

Preform	Pre-heater (°C)		Molding die heater (°C)				Mandrel temp. (°C)	Pulling speed (mm/min)
	PH-1	PH-2	H-1	H-2	H-3	H-4		
PLA resin fiber group 1) J / GF520 2) J / GF600 3) J / GF720 4) J / GF1150	100	100	195	195	185	165	165	18
PA66 resin fiber group 5) C / C 6) A / C 7) A / A	230	230	290	290	275	230	230	20

PH-1 ; Pre-Heater, H ; Heater

Experiments

The four-point bending test was performed by using the pulley unit and the metal solid bar as shown in the Figure 7. The pulley unit and steel bar are capable of decreasing the stress concentration generated at the point for support and loading nose. The bending test was performed by using an INSTRON universal testing machine with a span length of 300 mm and cross-head speed of 1mm/min.

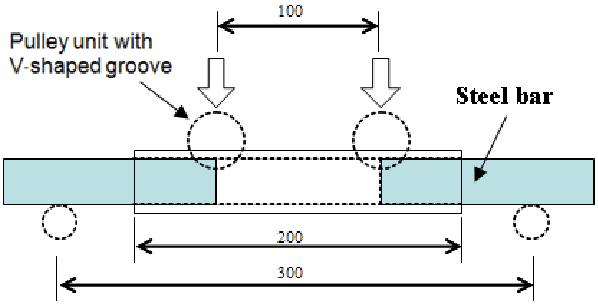

Figure 7 The schematic of four–point bending test

RESULTS AND DISCUSSION

From Table 3, the plutrusion of preforms of PLA resin fiber group with J/GF520 and J/GF600 were interrupted due to the MEY breakage inside the pultrusion die. The preform with J/GF720 and J/GF1150 were fabricated without the problem because the preform had enough strength for pultrusion. The minimized usage of glass fiber was found in preform J/GF720. Therefore, it was selected for the experiment with the different pultrusion temperature. For PA66 resin fiber group, all preforms were successful pultruded and the highest mechanical properties were found in preform C/C because the high strength of carbon fiber in the braided structure. Figure 8 showed the un-impregnation area of tubular braided composite in this group. In the other hand, when compare with the impregnation quality, preform A/A showed the best impregnation quality because of aramid fiber was the same group of thermoplastic with PA but this tubular composite had the lowest mechanical properties than other in this group. In case hybrid tubular composite A/C, it was found that the un-impregnation area slightly increase with the good mechanical properties than A/A. Therefore, the hybrid preform A/C was interested to select for the experiment with the different pultrusion temperature.

The specimens with different molding temperature were successfully pultruded in both groups, the hybrid tubular J/GF720 and A/C were showed in figure 9. The cross-section photographs of specimens J/GF720 and A/C are shown in Figure 10. From the photograph, the dark regions between the fiber bundles indicate macro void and the dark regions inside of fiber bundles indicate un-impregnation area. In case of pultrusion molding J/GF720 with increasing molding temperature, the modulus was decreased due to the high temperature affected the degradation of jute spun yarns as shown the comparison in the relationship between un-impregnation and molding temperature as shown in Figure 11. Therefore, the molding temperature of 205 °C is the optimum temperature for fabrication the tubular hybrid jute spun yarn/PLA braided composite. For hybrid tubular A/C, the un-impregnation was decrease and constantly at the temperature ~300-320 ^{o}C as shown Figure 12. Therefore, the molding temperature of 300 °C is the optimum temperature for fabrication the hybrid tubular A/C braided composite. From these results, the impregnation quality was increased when the molding temperature increased with constant molding speed because the matrix viscosity was reduced at higher temperature.

Table 3 The results from 4 point bending test with different braided preforms.

Preform	Braiding angle (°)	Vf of Composite (%)	Filling ratio (%)	Molding temp. (^{o}C)	Modulus (GPa)	Strength (MPa)
PLA resin fiber group						
1) J / GF520	38	43	101	195	Un-successful	Un-successful
2) J / GF600	38	46	101		Un-successful	Un-successful
3) J / GF720	35	46	101		8.9	29.0
4) J / GF1150	30	53	104		15.4	28.3
PA66 resin fiber group						
5) C / C	45	48	106	290	54.7	170
6) A / C	45	49	106		42.6	102
7) A / A	45	49	107		18.1	111

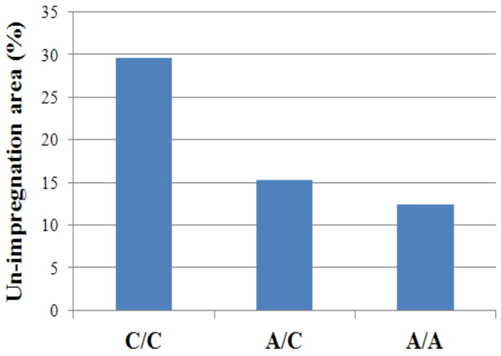

Fig. 8 The un-impregnation area of tubular braided composite in group of PA66 resin fiber

a) Tubular braided composite J/GF720 a) Tubular braided composite A/C

Fig. 9 The tubular braided composite

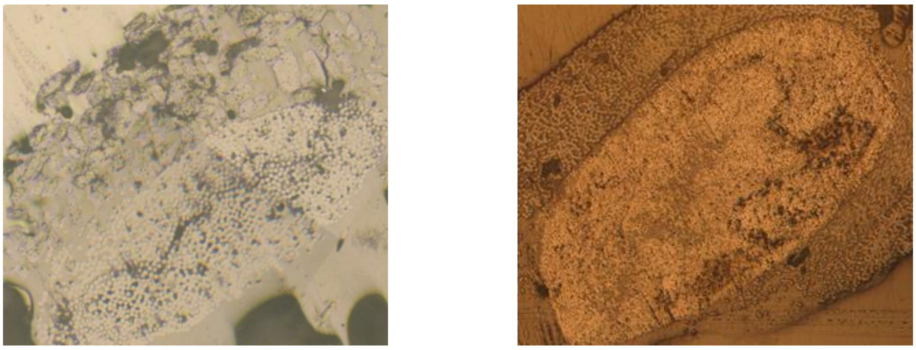

a) J/GF720 (205 °C) b) A/C (300 °C)

Fig. 10 The cross-section observation of specimens

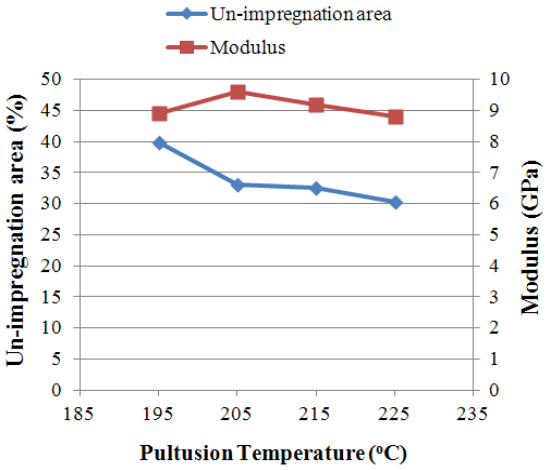

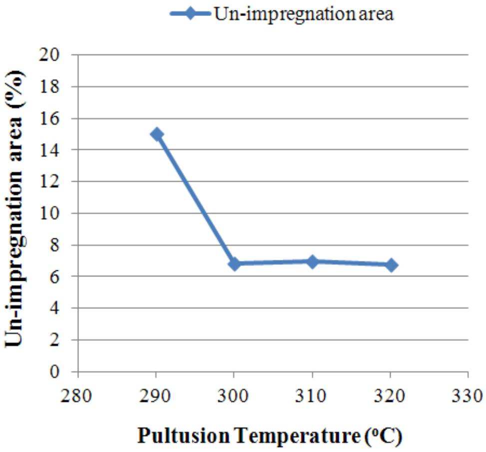

Fig. 11 Relationship between un-impregnation and molding temperature of tubular braided composite in PLA resin fiber group

Fig. 12 Relationship between un-impregnation and molding temperature of tubular braided composite in PA66 resin fiber group

CONCLUSION

In this study investigated the pultrusion system for continuous fiber reinforced thermoplastic composite using hybridization of glass fiber with jute fiber reinforced PLA and carbon fiber with aramid fiber reinforced PA66. The comingle technique was used to mixed the resin fiber and reinforcing fiber. The pultrusion system of hybrid tubular braided composite with PLA resin fiber group showed best mechanical properties and impregnation quality with hybrid jute and glass fiber 720 tex, using molding temperature 205 °C. The system with PA66 resin fiber group showed best impregnation with hybrid aramid fiber and carbon fiber, using molding temperature 300 °C. It was clarified that the un-impregnation area was decreased when the pultrusion temperature increased. The pultrusion system of hybrid tubular braided composite investigated in this study is an importance step towards the economically viable production of high performance the composite products.

REFERENCES

1. G. Bechtold, S. Weidmer and K. Friedrich, “Pultrusion of thermoplastic composite-New delopement and modeling studies”, *Thermoplastic composite materials*, Vol. 15-September (2002), 443-465.
2. Andreas Carisson, B. Tomas Astrom, “Experimental investigation of pultrusion of glass fibre reinforced polypropylene composites”, *Composite Part A*, 29A (1998), 585-593.
3. Dae-Hwan Kim, Woo Il Lee and Klaus Friedrich, “A model for a thermoplastic pultrusion process using momingled yarns”, *Composites Science and Technology*, 61 (2001), 1065-1077.
4. Yoshitaka Tanaka, Naoyuki Shikamoto, Akio Ohtani, Asami Nakai and Hiroyuki Hamada, “Development of pultrusion system for carbon fiber reinforced thermoplastic composite”, *International Conference on Composite Materials 17th*,(2009).
5. Anin memon and Asumi Nakai, “Structure and processing design of jute spun yarns/PLA composite by pultrusion molding”, *ANTEC 2012*.
6. Shikamoto N, Wongsriraksa P, Ohtani A, Leong Y W, and Nakai A, “Processing and mechanical properties of jute reinforced PLA composite”, *Soc. for the Advancement of Material and Process Engineering*, (2008).

INFLUENCE OF PROCESSING CONDITIONS ON THE PERMEABILITY OF MICROFIBRIL-REINFORCED COMPOSITES

Sylvester Tan [1], Arcot A. Somashekar [1] and Debes Bhattacharyya [1]

[1] *Centre for Advanced Composite Materials, Department of Mechanical Engineering, The University of Auckland, Private Bag 92019, Victoria Street West, Auckland 1142, New Zealand. Corresponding author's e-mail: a.somashekar@auckland.ac.nz*

ABSTRACT: In-situ microfibril-reinforced composites (MFCs) that consist of linear low density polyethylene (LLDPE) and polyethylene terephthalate (PET) were manufactured by industrial processing methods, such as compression moulding, extrusion blow moulding, slit-die extrusion with calendering, and injection moulding. The objective of this work was to investigate the effects of processing methods on the oxygen permeability of the manufactured MFCs.

A comparison of the processing methods showed that compression moulded MFC film displayed the greatest improvement in barrier property (48%), when compared to neat LLDPE film. Calendered MFC films and injection moulded MFC containers showed slight improvements of 18% and 25%, respectively, over plain LLDPE. Extrusion blow-moulded films produced mixed results due to the presence of voids in the LLDPE matrix.

An investigation into the cooling conditions was performed on the compression moulding unit. Films cooled under no pressure provided a 20% improvement, in comparison to the 48% improvement found in films cooled under pressure. The reduction in improvement observed in the other processing methods is most likely due to the rapid cooling or lack of applied pressure during the cooling process.

KEYWORDS: *microfibril-reinforced composite, oxygen permeability, processing methods*

INTRODUCTION

The demand for polymers has grown substantially over the past few decades. As it is in most cases, a single polymer rarely meets all the requirements of a particular application. Polymers which possess the greatest functional properties, such as mechanical, electrical and gas barrier, are expensive. For this reason researchers around the world have been investigating other ways to improve polymers of interest, in particular through the use of reinforcements.

There are two popular methods found in literature. Using a reinforcing additive, like fillers and fibres, is a common method not only in polymer processing but also in metals. Depending on the additive used, any one of the functional properties can be improved. The other method is blending two or more polymers together, in order to obtain the best properties from each polymer.

A relatively new concept developed in the 1990s utilises both these techniques. A microfibril-reinforced composite is formed by drawing a polymer blend and transforming a predominantly spherical morphology into highly orientated microfibrils. Fibre-reinforced composites are formed by manually distributing the fibres in an isotropic matrix whereas in the case of MFCs this is done by in-situ during the drawing process.

Manufacturing MFCs involves three steps - the first step is the standard procedure used for manufacturing polymer blends where crystallisation takes place in an isotropic state [1]. Unlike traditional reinforcements, such as glass fibres, microfibrils are not produced as separate materials; they are formed in-situ by drawing the filament produced in step one. The next step is the fibrillisation where the spherical particles are transformed into high aspect ratio microfibrils through coalescence. The isotropisation stage is the final step which usually takes place through one of the numerous processing methods available whereby the matrix is transformed into an isotropic state by heating at a temperature between the melting points of the two polymers. Temperature is the key parameter in ensuring that microfibrils produced are maintained in the end product.

Previous studies have looked into the mechanical and oxygen barrier properties of MFCs, and also on modelling fibre formation and permeability [2,3]. This work explores the applicability of common processing methods, such as compression moulding, slit-die extrusion, injection moulding and blown film extrusion for use with MFCs and the effects these methods have on the gas barrier properties.

MANUFACTURING

Materials

Qamar linear low density polyethylene, grade FC21HN, manufactured by Eastern Petrochemical Company (SHARQ), Saudi Arabia, was chosen as the matrix. Polyethylene terephthalate manufactured by Shinkong Synthetic Fibres Corporation, Taiwan, material grade Shinpet 5015W, was used as the reinforcement.

Blending

A Brabender DSE 25 twin screw extruder with a screw diameter of 20 mm, barrel length of 42 D and a circular die of 2 mm diameter was used for blending. Both polymers were dried for a minimum period of 6 hours. Drying of PET is particularly necessary to avoid the risk of hydrolysis [4]. The dried polymers were mixed by hand in the desired blend ratio. The extrusion zone temperature was varied from 220 to 280°C, with an increasing temperature gradient from the heating zone near the hopper to the die. The screw speed was varied between 12-15 rpm to ensure the torque remained below 200 Nm (recommended maximum torque for the extruder). Upon exiting the extruder the blended filament was cooled in a water bath and collected on a spool through the use of a winder.

Drawing

Drawing was performed in a laboratory constructed drawing unit which had four heating zones consisting of eight infrared lamps, each of 500 W heating capacity. The temperature was set between 80-90°C.

The material from the spool was put through two sets of rollers which were used to control the draw ratio. The roller on the supply motor (slow roller) controlled the length of time the filament spent inside the heating unit. The roller on the take-up side (fast roller) controlled the pulling force. The supply motor was set to 1.6-1.8 rpm and the take-up motor was set to 14 rpm. After drawing the material was recollected on a separate spool.

Processing methods

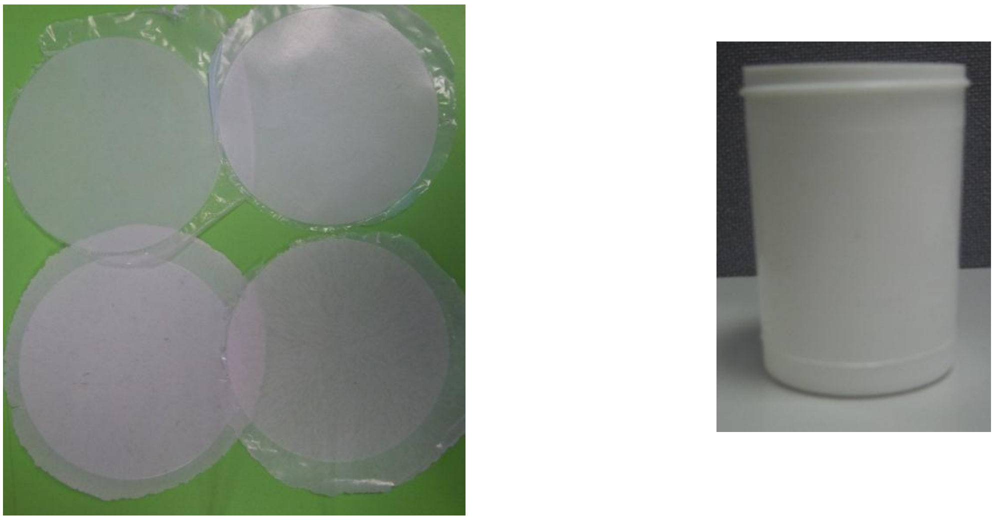

Compression moulded film

Injection moulded container

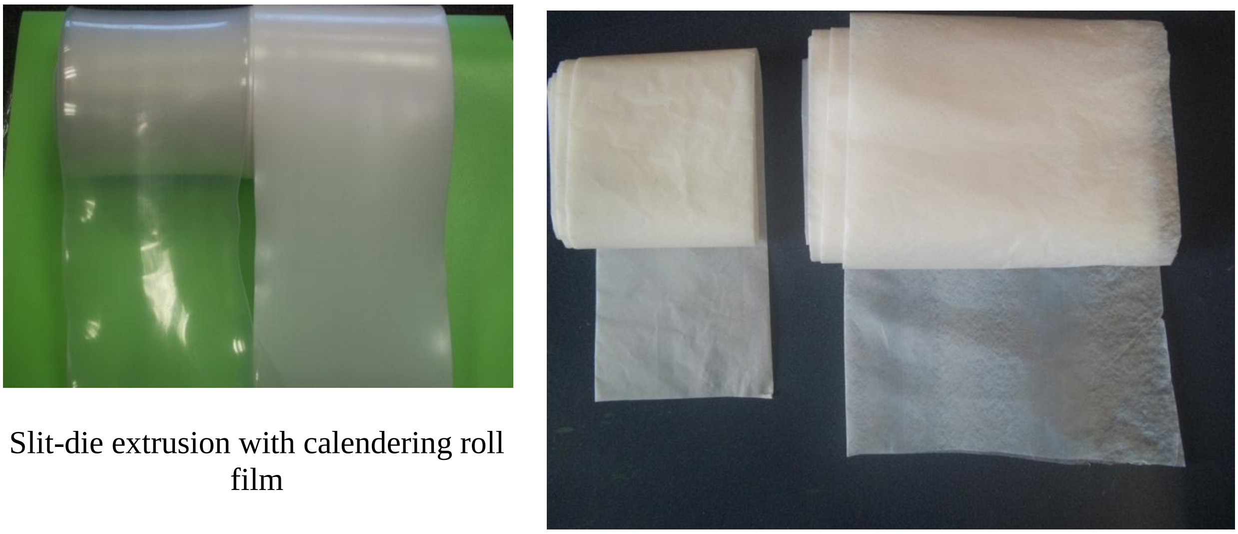

Slit-die extrusion with calendering roll film

Extrusion blow moulded film

Fig. 1: Photographs of end product from each processing method

Fig. 1 presents sample images of MFC products manufactured using different methods. Compression moulding was performed on a Carver hydraulic press manufactured in the USA. Films were created from continuous filament or pellets using a frame or circular pressing plate. The drawn material was heated to 180°C and a pressure of 3, 5 and 9 metric tonnes was applied in 2 minute intervals after which the film was left to cool under pressure for at least 30 minutes. Films manufactured were in the range of 0.2-0.25 mm in thickness.

Slit-die extrusion was done on a single screw extruder (model JW45/30, manufactured in China) used in conjunction with calender rolls (Wayne, 12 inch sheet line, USA) to reduce the thickness of the sheet. The slit-die was 100 mm wide and 0.8 mm high. The heating zones were set to 180°C and the die was set to 195°C. The thickness of the sheet was between 0.4-0.5 mm.

Containers and tensile specimens are two products which can be formed using injection moulding. As there was no mould to create injection moulded films, containers were manufactured for permeability testing using a Boy 50A injection moulding machine, made in Germany. There were 3 heating zones plus the nozzle temperature which were set to 200, 205, 210 and 210°C, respectively. The screw speed was 8 rpm, holding pressure 2 MPa and injection speed 26-35 m/s.

Permeability

Permeation measurements for films were performed on a Mocon OX-TRAN machine, model 2/10, manufactured in the USA. The carrier gas (nitrogen and hydrogen) is passed through the inner half of the testing cell. Typically the carrier gas will have between 1-3% hydrogen which is used as a catalyst to react with any oxygen that may be present in the carrier gas, ensuring no oxygen proceeds to the inner cell due to the carrier gas. The outer half of the testing cell contains the test gas (oxygen) which flows continuously throughout the test [5].

Containers were tested on a permeability rig that was built in-house. This was based on ASTM Standard D3985-02 (Standard Test Method for Oxygen Gas Transmission Rate Through Plastic Film and Sheeting Using a Coulometric Sensor). There are a variety of standard references in use; for this work, the International Union of Pure and Applied Chemistry (IUPAC) standard has been used. This defines the standard temperature as 0°C and pressure as 100 kPa.

RESULTS AND DISCUSSION

For permeability testing, three processing methods were used to manufacture films (<0.5 mm). To cover the injection moulding process, containers were manufactured and tested. This ensured that the main processing methods which others have used in the literature have been covered. The compression moulding process represents the main method used in this study because it was easy to use and only required 3g of material per sample. In contrast, the other methods were continuous processes and hence required a larger amount of starting material.

Compression moulding

Films were prepared from LLDPE/PET with blend ratios of 90/10, 85/15, 80/20, 75/25, 70/30 and 65/35. There is a 30% improvement in permeability for the 90/10 LLDPE/PET combination, in comparison to neat LLDPE (Fig. 2). The next increment in PET content (the 85/15 ratio) shows a 13% improvement in relation to the 90/10 combination. However, after this the influence of PET content on permeability is about 5% improvement for each additional increment of PET. Since the 75/25 LLDPE/PET blend was the first to be manufactured, non-optimum settings and procedures may have been the reason why, on average, the permeability was higher than the 20% composition. It should be noted that the lowest permeability value for the 25% PET was less than the lowest permeability value for the 20% PET.

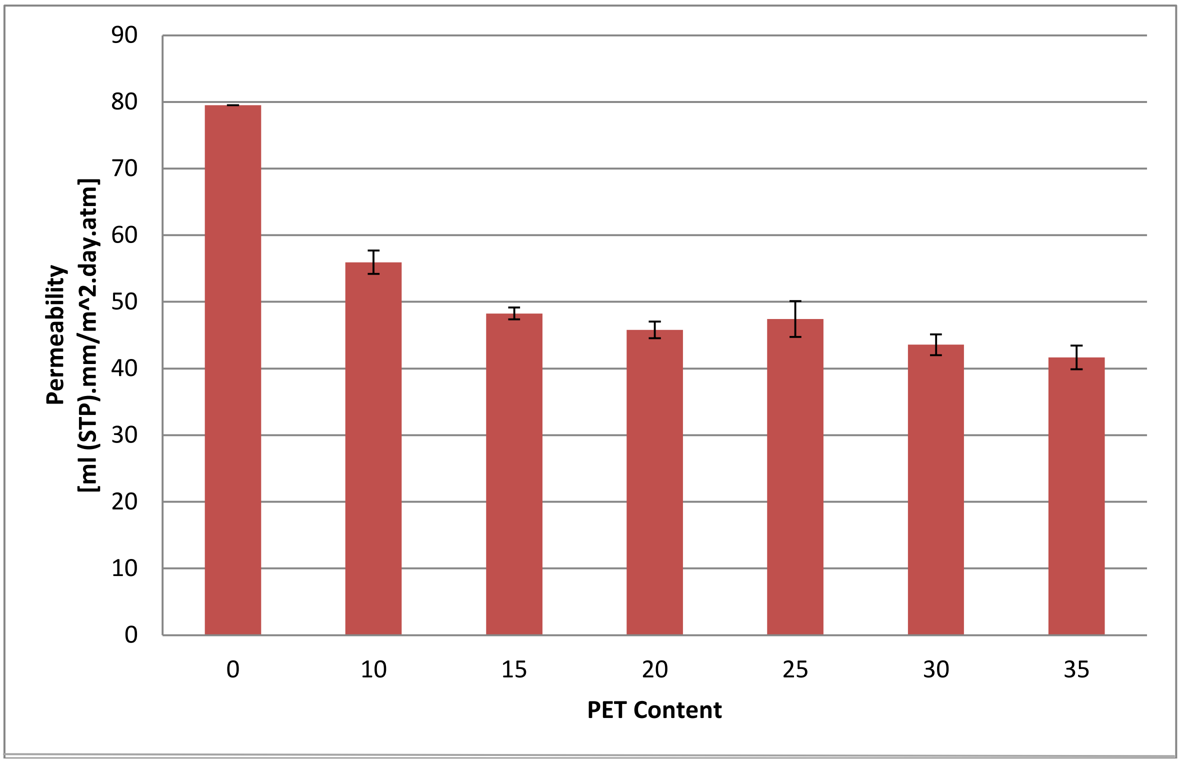

Fig. 2: Permeability of compression moulded MFC films with one hour cooling

Processing conditions have a significant effect on permeability as Shields [2] pointed out, in particular, the rate of cooling, which produced a large variation in results. This was investigated by manufacturing (and then testing) films that were taken straight from the press (no cooling and no pressure), cooled to 100°C under pressure and cooled to 60°C under pressure. These corresponded to cooling times of 0, 30 and 60 minutes respectively.

Table 1: Permeability of 65/35 LLDPE/PET MFC films from different cooling times

Manufacturing Condition	**Cooling Time (minutes)**	**Permeability [ml.(STP).mm/m^2.day.atm]**					
		1	2	3	4	5	Average
No pressure, no cooling	0	70.9	65.7	58.2	59.8	65.1	63.9
Cooled to 100°C under pressure	30	42.0	41.7	39.2	42.7	42.3	41.6
Cooled to 60°C under pressure	60	42.1	42.4	38.7	41.7	43.5	41.7

The results of this investigation are shown in Table 1. For no pressure cooled films, the permeability almost returned to the value for neat LLDPE and showed large variation between samples. This is because no pressure was applied while cooling and this leads to the relaxing of the polymer chains and possibly the microfibrils. This relaxation results in the polymer chains aligning in their preferred directions rather than the optimal orientations for permeability. Hence this also results in more variation in how the chains align, which would help explain the variation in permeability for films cooled under no pressure.

After 30 minutes under pressure, the sample temperature dropped below 100°C. These films had the same permeability as films cooled for an additional 30 minutes under pressure. The reason for this is that the crystallisation temperature is about 105°C, which means the alignment of the polymer chains below this point becomes more difficult. Hence the semi-crystalline regions would be relatively similar for films cooled down to 100°C and cooled down to 60°C.

These findings indicate that the temperature at which the film is removed influences the morphology found in the sample, and hence the permeability. Films removed above the crystallisation temperature had a higher oxygen transmission rate while films removed below the crystallisation temperature had a reduced rate.

Slit-die extrusion with calendering rolls

Calendering is essentially a continuous version of compression moulding, with the compression occurring through the calendering rollers. The main difference is the lack of control over the processing conditions; in particular, there is no control over the exact pressure applied on the rollers of the calendering machine used to manufacture MFC films. There is also very little room for cooling once the material leaves the extruder, as it is basically quenched once it touches the calendering rolls.

Table 2: Permeability of calendered films

Composition	**Permeability [ml.(STP).mm/m^2.day.atm]**				
	1	2	3	Average	Standard deviation
Neat LLDPE	96.7	90.9	93.9	93.8	2.9
LLDPE/PET 75/25 Drawn	77.6	77.1	77.3	77.3	0.3

Table 2 shows there is an 18% improvement in barrier property when 25% PET is added to LLDPE, compared to plain LLDPE film. In comparison, for compression moulded films there was an improvement of 41% for the same composition. On the other hand, no pressure cooled compression moulded films exhibited a 19.6% improvement over neat LLDPE film. This is expected since the molten material leaves the slit-die under no pressure and above the crystallisation temperature. In this state, it is cooled under ambient conditions till it reaches the calendering rolls, where the material is cooled down to room temperature.

Extrusion blown film

Permeability tests were performed on extrusion blow moulded films which were manufactured as part of an earlier research project [6] and provided for use in this work. There was no control sample (plain LLDPE) manufactured; therefore it was hard to judge if there was any improvement for MFC blown films.

The 80/20 MFC batch had a blow ratio of three and was the only one that provided consistent results. 75/25 drawn film was not homogenous as different blow ratios were used. The film with a blow ratio of four contained sections dominated by LLDPE, which produced large variations in permeability when different sections of the film were tested. A blow ratio of two resulted in better dispersion and improved film quality. This value has been reported in Table 3; it is slightly higher than the permeability for 80/20 drawn film. This may have been because this composition was the first to be manufactured, before the ideal settings were determined.

Table 3: Permeability values for extrusion blow moulded film

Composition	**Permeability [ml.(STP).mm/m^2.day.atm]**		
	1	2	3
LLDPE/PET 80/20 Drawn	109.6	111.4	112.1
LLDPE/PET 75/25 Drawn	121.5	-	-

Fakirov et al. [7] investigated the applicability of extrusion blown films for MFC and they also observed the permeability results from MFC blown films to be inconsistent and in some instances worse than the permeability of the matrix. They put these down to the presence of voids in the morphology.

Injection moulding

Injection moulding is the most common processing method used for MFC. The majority of researchers have used this method for manufacturing tensile specimens. For this work containers were manufactured for permeability testing.

The thickness of the containers was significantly greater than the films produced earlier; however, this was not an issue since permeability takes into account thickness. The results for 75/25 LLDPE/PET MFC and plain LLDPE are shown in Table 4.

Table 4: Permeability of LLDPE/PET MFC and plain LLDPE injection moulded containers

Composition	**Permeability [ml.(STP).mm/m^2.day.atm]**				
	1	2	3	Average	Standard deviation
LLDPE/PET 75/25 Drawn	128.5	141.3	111.3	127.0	15.0
Neat LLDPE				169.4	

There is a 25% improvement in permeability for 75/25 LLDPE/PET MFC containers, when compared to neat LLDPE containers. The percentage improvement in permeability compares favourably to calendered films that provided an improvement of 18%. With injection moulding, the mould is water cooled (quenched) with the pressure maintained as it is, after the cavity has been filled. Friedrich et al. [8] reported that PET fibrils relax greatly during injection moulding, and this may explain the drop in improvement compared to compression moulding.

CONCLUSIONS

This research investigated the influence of processing methods on oxygen permeability of manufactured MFC products. Processing methods had a noticeable influence on the effectiveness of creating a difficult path for the oxygen molecules. Compression moulded films which were cooled under pressure displayed the best oxygen barrier properties. Calendered films showed an improvement over neat LLDPE; however the improvement is noticeably less than what is found in compression moulding. A comparison between the permeability of calendered films and compression moulded films cooled under no pressure shows a similar improvement over plain LLDPE. As suggested earlier, this implies that the cooling methods are similar. This is reasonable as the molten material leaves the extruder under no pressure before touching the calendering roll. It is anticipated that extrusion blown films would also encounter this problem if the voids found in the morphology are removed. Injection moulded containers were cooled under pressure; however the cooling rate is much higher than compression moulding. It appears the cooling rate affects the microstructure in injection moulded specimens.

ACKNOWLEDGMENTS: The authors would like to thank the Ministry of Science and Innovation for funding this research. They would also like to acknowledge the contribution of the technical staff, in particular, Mr Jimmy Thomas.

REFERENCES

1. Evstatiev M, Fakirov S, Krasteva B, Friedrich K, Covas JA and Cunha AM (2002), ‘Recycling of poly(ethylene terephthalate) as polymer-polymer composites’, *Polymer Engineering & Science,* 42(4), 826-835.

2. Shields RJ (2008), Characterisation of the Mechanical and Oxygen Barrier Properties of Microfibril Reinforced Composites, PhD Thesis, The University of Auckland.

3. Bhattacharyya D and Shields RJ (2010), ‘Modeling of fibre formation and oxygen permeability in micro-fibrillar polymer-polymer composites’, *International Union of Theoretical and Applied Mechanics Symposium on Multi-functional Material Structures and Systems,* IUTAM Book Series (ed. B. Dattaguru, S. Gopalakrishnan and V.K. Aatre), London: Springer, 111-122.

4. Giles HF, Wagner JR and Mount EM, (2005), Extrusion: The Definitive Processing Guide and Handbook, William Andrew Pub.

5. Mocon, OX-TRAN Model 2/10 Modular System Operator’s Manual, Minneapolis.

6. Somashekar AA and Bhattacharyya D (2010), ‘Improved mechanical and functional properties in microfibrillar polyethylene/polyethylene terephthalate composites’, *Proc of the Nineteenth International Conference on Processing and Fabrication of Advanced Materials (PFAM XIX),* 3.30, 568-581.

7. Fakirov S, Shields RJ, Fuchs C, Friedrich K and Bhattacharyya D, (2008), ‘Polyolefin/PET microplates–reinforced composites with improved barrier properties’, *International Journal of Polymeric Materials,* 57(1), 33-53.

8. Friedrich K, Evstatiev M, Fakirov S, Evstatiev O, Ishii M and Harrass M, (2005), ‘Microfibrillar reinforced composites from PET/PP blends: processing, morphology and mechanical properties’, *Composites Science and Technology,* 65(1), 107-116.

Section 7

Natural Fibres and Green Composites

BIOBASED THERMOSET RESINS AND FLAX FIBRE REINFORCEMENTS PROCESSED BY VACUUM ASSISTED RESIN TRANSFER MOULDING

Jens Schuster[1], Quentin. Govignon[2], Simon. Bickerton[2]
[1] Institut for Kunststofftechnik Westpfalz, University of Applied Sciences Kaiserslautern, 66953 Pirmasens, Germany, Corresponding author´s e-mail: jens.schuster@fh-kl.de
[2] Centre for Advanced Composite Materials, The University of Auckland, Auckland, 1142 Glenn Innes, New Zealand

ABSTRACT: Biocomposite panels consisting of biobased thermoset resins (EP, UP, and tannin) and flax fibre reinforcements were produced using the vacuum assisted resin transfer moulding process. Panels based on a conventional chemical-based resin matrix were also produced, and investigated comparatively. Rheometric analyses were performed to evaluate the suitability of these resins for liquid composite moulding. Tensile, shear, and impact-bending tests have been carried out to assess the quality and mechanical performance of manufactured laminates. The impregnation quality was assessed by means of ultrasonic-C-scanning and microscopy. It turned out that the properties of the biobased composite panels made of biobased epoxy resin and a biobased UP-resin from the company Nuplex in New Zealand were only slightly inferior to those produced with a conventional epoxy resin. A biobased UP-resin from the company USSC in the USA developed voids during curing. A tannin based resin containing of formaldehyde was not processable.

KEYWORDS: *Biocomposites, Rheological properties, Mechanical properties, Resin transfer Moulding (RTM)*

INTRODUCTION

Conventional mineral oil-based thermoset materials have been used as matrix materials for natural fibres such as flax and hemp for more than a decade. Since mineral oil should not be regarded as a renewable resource, due to the length of time required for natural creation and shrinking world reserves, attempts have been made to produce bio-based versions of unsaturated polyester (UP), epoxy, and tannin resins [1-3]. Combining these bio-based resins with natural fibres result in composite materials, made only from renewable resources, which can be called bio-composites or green composites. However, some of the so-called bio-resins have a bio-content of just 50% or lower, and very few have achieved 100% bio-content.

Since the turn of the millennium, an increasing amount of research has been conducted on bio-composites with an emphasis on thermoplastic matrices such as starch, poly(lactic acid) (PLA), and poly(ε-caprolactone) (PCL) [4 – 10]. However, quite a few publications exist in the field of biothermoset-based natural fibre composites [11–15] which have been applied for some prototype applications in the fields of civil and transport engineering [16–18].

Natural fibres such as flax, jute, sisal, hemp, and ramie, are currently being used as reinforcements in composite manufacturing. Flax fibres in particular possess a Young´s modulus comparable to glass fibres [19, 20] and have also been investigated as reinforcement for bio-based thermoset resins [14, 21-23]. The predominant methods explored in the literature to process these systems of natural fibre and bio-based thermoset resins are compression moulding and hot-pressing [12, 14, 21, 22]. Only Dweib et.al. used the Vacuum Assisted Resin Transfer Moulding (VARTM) to impregnate flax mats in comparison to other reinforcements with a soybean oil based resin [23].

OBJECTIVES

In this study a selection of bio-based resins were applied in an VARTM-process to impregnate a unidirectional flax fibre perform in order to assess the processability of biobased resins.

EXPERIMENTAL

Four different bio-based thermoset resins were investigated in this study, including one epoxy, two UP-resins, and a tannin resin. A hot curing biobased epoxy was purchased from B.A.M Biocomposites And More GmbH in Germany, consisting of epoxidised triglycerides derived from plant oil and plant based polycarboxylicanhydride. Resin and hardener were mixed to a weight ratio of 114:85, and 1.5 – 5% of catalyst was added to the mixture. Two cold curing resins were delivered by Urethane Soy Systems Co. (USSC) in the United States, and Nuplex Industries in New Zealand. The USSC resin is a soy-based two-component urethane-system (A and B) to be mixed in a weight ratio of 88:100 and is 100% from renewable resources. The origin of the Nuplex resin was kept confidential by the company Nuplex and it is not known by the authors. It is a one-component 70% biobased system, which is catalysed with methyl ethyl ketone peroxide (MEKP, 1 wt-%) and cobalt octate (0.3 wt-%). Colatan CDM GT5, the base for the tannin resin, was supplied by Christian D. Markmann GmbH in Germany. It is a natural polyphenol extracted from Quebracho Colorado (Schinopsis Lorentzii), a tree that grows in the northern area of Argentina. To prepare the resin, 44 wt-% of GT5 is dissolved in 100 wt-% formaldehyde solution (38%). Tannin is a hot curing system and is mainly used for gluing of chipboards during a hot-press operation [1, 2]. A standard chemical based cold curing epoxy-resin (Prime 20 from Gurit) developed for liquid composite moulding, was used as a benchmark. This system was mixed to a weight ratio of 100:26, resin to hardener.

A 305 g/m^2 unidirectional flax reinforcement has been used due to the good mechanical properties of the flax fibres. The reinforcement was supplied by Libeco-Lagae, Belgium, and was cut into samples measuring 250 x 400 mm. In order to derive a final part thickness of approximately 4 mm, 8 layers were arranged in a unidirectional lay-up. Concerns due to possible thermal degradation of flax due to exposure to high temperatures during processing of hot curing resins can be neglected, because flax is thermally stable up to a temperature of 120 °C. Above 120 °C degradation processes will be initiated [24].

Viscosity measurements were made on all resins using an AR-G2 rheometer with a Peltier plate arrangement from TA Instruments. Each resin was subjected to a time sweep at 25°C for

1 hour, and a temperature sweep between 20°C and 120 °C with a heating rate of 5 K/min. The resins were subjected to a frequency of 1 Hz and at strain of 15% without normal load.

Differential Scanning Calorimetry (DSC) analyses were performed to determine if the resins studied cured completely after being subjected to the recommended temperature-time cycle. Using a DSC-Q-1000 calorimeter from TA Instruments, the cold curing resins were processed at a 65 °C post-curing temperature, and the hot curing systems at 120 °C. The duration of all analyses was three hours. The heating rate was set at 20K/min.

After drying for 4 h at 120 °C, the flax fibre reinforcements were arranged with a $[0°]_8$ stacking sequence. The fibre reinforcements have not been subjected to a particular surface treatment, because bonding agents have a different impact on mechanical properties of the composite according to the resin type used. Before infusion, the mixed resin was degassed in a pressure pot under vacuum for 10 min to reduce the air content in the resin. The maximum vacuum level was reached after a slow gradual decrease of pressure to avoid boiling of the resin. After degassing, ambient pressure was applied, forcing the resin to move into the still clamped inlet tube. Upon unclamping of the inlet, the resin flowed through the distribution media and impregnated transversely the flax preform. The last five centimetres of the preform were not covered with the distribution media, to prevent resin exiting at the vent before complete saturation of the preform, which may lead to macro void entrapment. Once the flow front had reached the end of preform, the post-filling stage was initiated, pressure at the inlet and vent being set to 50 kPa. Laminate thickness and resin pressure gradients gradually dissipate, and the pressure boundary conditions were maintained until the resin was cured. Subsequently, the cold curing resins were post-cured for seven hours at 65°C. The infusion of the hot curing resins took place in an oven, at room temperature. The hot curing cycle of one hour heating up to 120 °C, a one hour hold at 120 °C, and one hour cool down was started simultaneously with the post-filling stage. Four samples with best achievable quality were produced with each resin except the tannin system.

Specimens with a length of 250 mm and a width of 25 mm were cut out of the cured panels in 0°- and 90°- direction. The tensile strength, stiffness, and elongation properties were measured according to EN ISO 527, using a tensile testing machine from Instron (model 5500R 1186). The cross-head-speed was 1 mm/min until an elongation of 0.3% and 5 mm/min until failure.

Shear tests were performed with a custom built lateral working shear testing device situated in a universal testing machine (Zwick 1445). It was constructed according to a device suggested by Lauke for curved specimens [25]. Five specimens of each fibre direction with a size of 10 x 10 mm were sheared in the middle plane, with a cross-head-speed of 5 mm/min. The ultimate shear strength is computed by dividing the maximum measured shear force by the sheared area of the sample (approximately 10 x 10 mm^2).

The determination of Charpy impact strength (impact bending) was carried out according to EN ISO 179. Specimens with a length of 80 mm and a width of 10 mm were tested in an instrumented Hesscon impact tester with an impact energy of 1 J for the Nuplex sample and 4 J for the B.A.M., USSC, and Prime20 resins. The striking area was placed perpendicular to the fibres. The tannin sample could not be tested because the necessary impact energy was below the minimum limit of the impact tester.

The microscopy analyses were performed with a magnification of 15 times using an optical microscope. The void contents were measured with the Vision XXL image processing system.

RESULTS

The measured viscosity data is summarised in Table 1. It can be seen that all resins have an initial mix viscosity in the range up to 1 Pa.s. Since viscosities above 1.5 Pa.s are regarded to not be suitable for liquid composite moulding, it is clear that all of the resins studied are applicable to LCM-processes. In addition, it turned out that only the USSC UP-resin viscosity of 2.59 Pa.s exceeds this threshold within the duration of infusion (max. 20 min), which led to a very slow flow front propagation during panel manufacture.

Table 1: Measured viscosities of the studied resin systems

Resins	Viscosity η at 20°C after 0 s in [Pa.s]	Viscosity η at 25°C after 0 s in [Pa.s]	Viscosity η at 25°C after 1200 s in [Pa.s]
B.A.M. epoxy	0.43	0.41	0.57
USSC resin	1.00	0.70	2.59
Nuplex UP-resin	0.91	0.65	1.06
Tannin	0.056	0.047	0.030
Prime 20	0.50	0.39	0.60

Careful observations were made during resin infusion considering two main factors; does the resin boil during degassing or curing, and will the infusion process compare well to infusion using the benchmark synthetic resin? In contrast to the other bio-based resins, the degassing of the Nuplex UP-resin proceeded without boiling. The other three resins boiled even under careful treatment, leading to overflow out of the mixing cup inside the pressure pot. Subsequently, all panel infusions proceeded without problems. Due to boiling during degassing, the tannin resin experienced a significant increase in viscosity, which resulted in a slower flow front progression than was expected. However, a complete infusion was possible. According to their relatively high viscosities, the infusions with both UP-resins were significantly slower than those with both epoxy resins (Table 2).

Table 2: Measured filling times during manufacture by VARTM

Resins	B.A.M. epoxy	USSC resin	Nuplex UP-resin	Tannin	Prime 20
Filling time [min]	4	21	10	12	3

As observed from the rheometry studies, the viscosities of the UP-resins increased very soon after mixing due to a rapid start to the curing process. This slowed down the flow front speed even more. The propagation of the USSC Bio resin was almost brought to a complete stop. Due to their low viscosities, the infusion with the epoxy resins took place within three and four minutes (Table 2). Since the hot curing B.A.M. epoxy does not cure at ambient temperature, the handling of this resin was very convenient and not time critical.

The post-filling and post-curing of the Nuplex UP-resin and the hot curing B.A.M. epoxy resin proceeded without problems. The USSC Bio resin started boiling during the post-filling phase under a pressure of 500 mbar. Exploratory experiments showed that this resin also boils at ambient pressure, which leads to the conclusion that the gas bubbles are produced as a side product of the curing process. The tannin resin infused preform distorted during curing at 120 °C in the oven and cracked the vacuum bag. During resin cure, a harmful gas, causing immediate eye burn, was created. Keeping in mind that the intention of a green composite should not be harmful in any regard, further tannin infusions were not undertaken. Fortunately, it was possible to cut samples for mechanical testing from relatively flat sections of the distorted panel. DSC-analyses had proven that all resins were cured after 3 hours at recommended curing temperatures.

The measurement of the Young´s moduli in fibre direction (0°) revealed an equal stiffness of the hot curing B.A.M. epoxy and the benchmark epoxy system as shown in Fig. 1a. Furthermore, the Young´s modulus of the Nuplex UP-resin appeared to be higher than the value of the USSC Bio resin. As expected from the very flexible appearance of the tannin samples, the stiffness was significantly lower than for the other resins. Very similar trends were derived transverse to the fibre direction (Fig. 1b) with slightly higher values of the conventional Prime 20 resin. It is clear that the stiffness properties of the epoxy resins are superior to those of the UP-resins.

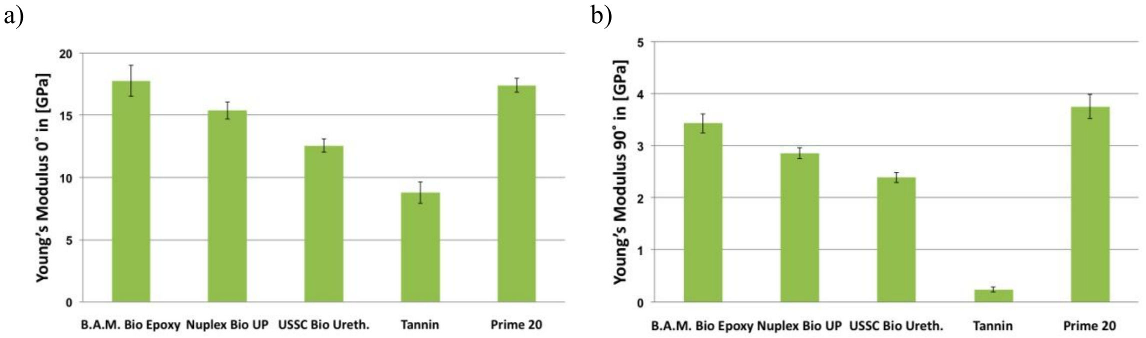

Fig.1: Measured Young´s moduli; a) in fibre direction; b) perpendicular to fibre direction

The 0°-tensile strength data showed no significant difference between the properties of the UP- and epoxy resins, with the lowest values for the hot curing system (Fig. 2a), which is due to a its more brittle behaviour (Fig. 3a). According to the stiffness measurements, the tannin had very low tensile modulus along with a high elongation. In addition, the failure mode of tannin was quite different to those of the other systems. The epoxy and UP-resins failed due to initial longitudinal cracks in the fibre direction, leading to transverse cracks.

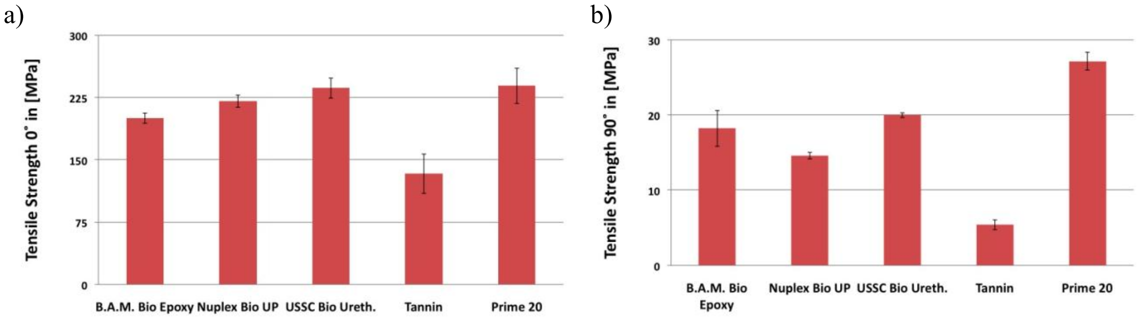

Fig.2: Measured tensile strength; a) in fibre direction; b) perpendicular to fibre direction

The tannin sample delaminated between the single plies proving a weak interfacial bonding. This is also confirmed by the transverse tensile tests depicted in Fig. 2b and the transverse ultimate elongation results in Fig. 3b. The Prime 20 epoxy possesses superior interfacial properties in comparison to the other resins. As demonstrated by the data on elongation (Fig. 3), the B.A.M. epoxy is more brittle than the other epoxy and the UP-resins.

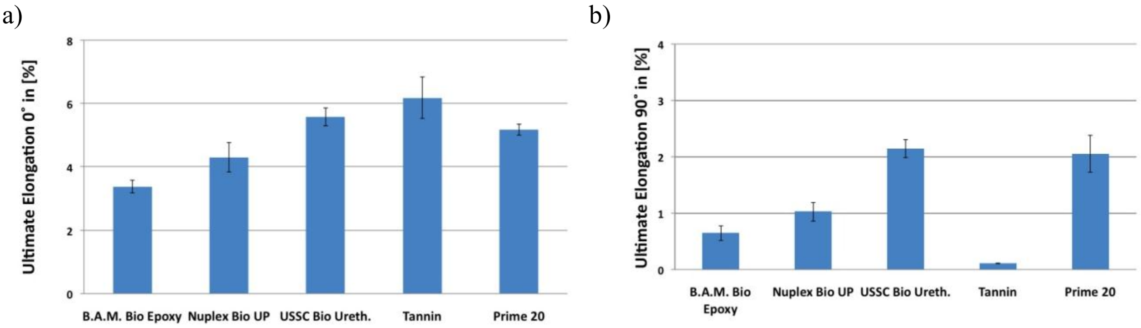

Fig.3: Measured ultimate elongations; a) in fibre direction; b) perpendicular to fibre direction

The measured shear strength, as an indicator for the interfacial shear strength, is twice as high for the Nuplex UP resin than for the other resins. It was not possible to measure values for the Tannin samples (Fig. 4).

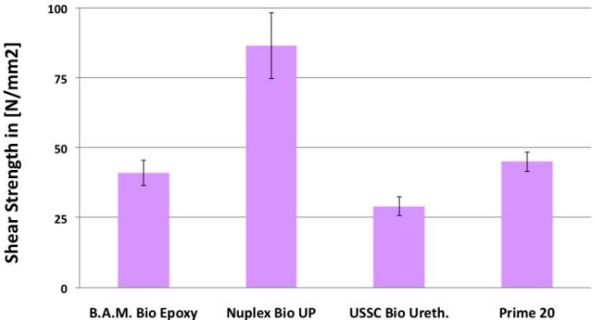

Fig.4: Measured shear strength

The impact bending tests show a high impact strength for the Nuplex resin, and lower impact resistance for the other three tested resins, as depicted in Fig. 5.

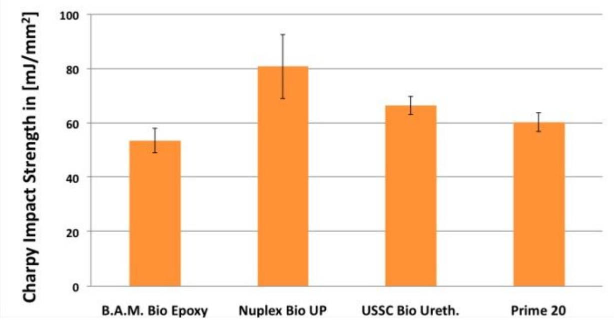

Fig.5: Measured Charpy impact strength

Evaluations of cross-sections lead to void contents of material under inspection (Table 3). It can be seen in accordance with Fig. 6, that the Nuplex resin and the B.A.M. epoxy resin have the lowest void contents in comparison to other resins. The standard epoxy resin Prime 20 contained more voids than expected.

Table 3: Measured fibre volume fraction and void content

Resins	B.A.M. epoxy	USSC resin	Nuplex UP-resin	Tannin	Prime 20
Fibre volume fraction [%]	38.9	32.1	41.1	56.3	40.8
Void content [%]	1.8	16.2	3.4	10.0	4.1

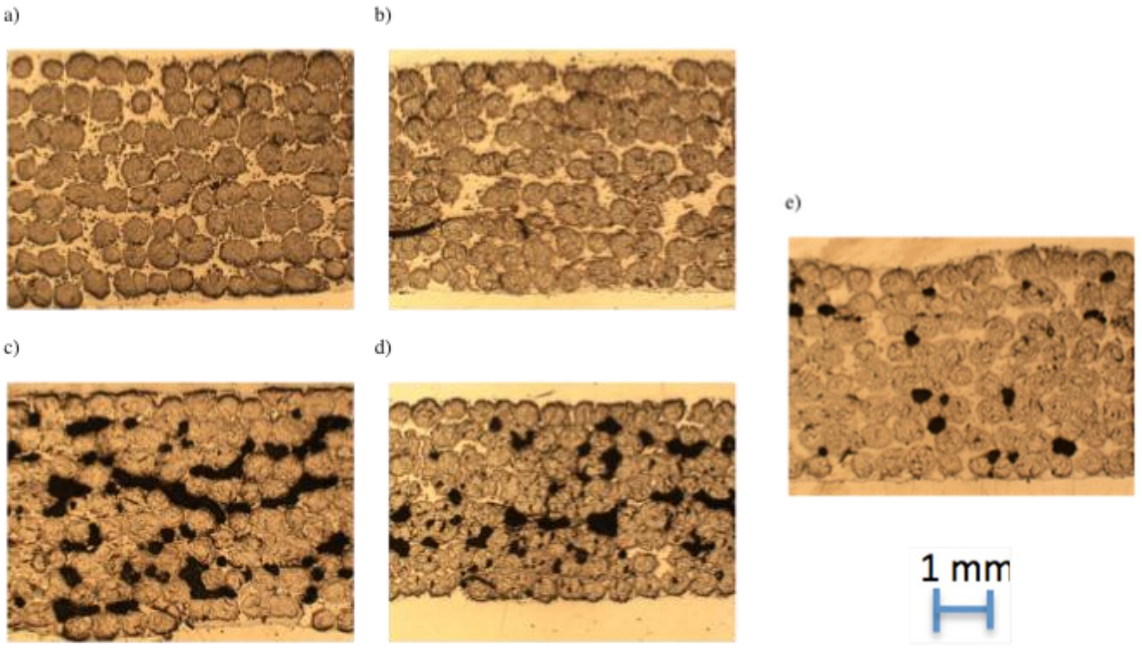

Fig.6: Microscopy images from the flax fibre panels produced from a) B.A.M. Bio epoxy, b) Nuplex Bio UP, c) USSC Bio resin, d) Tannin, e) Prime 20

DISCUSSION

The hot curing B.A.M. bio-epoxy resin and the cold curing bio-UP-resins are processable using the VARTM-process due to their viscosities being in an appropriate range. The tannin resin cannot be used for VARTM because it needs a solid die to avoid distortion of the infused part during curing. Therefore, it will not be regarded further. The USSC Bio resin is not suitable for the infusion of larger parts because the viscosity increases from an already high level of 1 Pa.s (at 25 °C) within 20 min to 2.59 Pa.s. In addition, the boiling of the resin during the post-filling phase resulted in an estimated void content of more than 16 %. Even with tensile and impact properties in the range of the other resins, the shear strength and the Young´s Modulus are lower due to void induced softening. The composite panels produced with the B.A.M. resin and the Nuplex UP resin contained only a few voids (2 – 3.5 %), and had good mechanical properties in the range of those produced with mineral oil based benchmark resin Prime20. The epoxy resins are stiffer than the UP resin, while the UP resin proved superior in terms of shear strength and impact properties.

CONCLUSIONS AND PERSPECTIVES

The processability and mechanical property comparison of four bio-based thermoset resins with a conventional mineral oil based resin has led to the conclusion that two bio-based resins (the B.A.M. epoxy and Nuplex UP resins) can potentially be used as a substitute for the benchmark resin. These bio-based resins have been used successfully to impregnate natural fibres using the VARTM process, without the need for further chemically based improvements such as dilutants to reduce the viscosity. Such dilutants would have had negative impact on the biocontent. Application of the USSC Bio resin to VARTM does not seem to be reasonable, due to a high void content caused by resin boiling during the post-filling phase, and a relatively high viscosity. This boiling could not be avoided by ana means. Tannin cannot be used with a VARTM process because the infused preform distorts during curing. In addition, the high content of formaldehyde of tannin resin makes the material hazardous to work with, and challenges the concept of an ecologically beneficial bio-based material. Finally, it can be concluded that the B.A.M. epoxy and Nuplex UP, two currently existing biobased thermoset resins, are ready to be used for industrial applications.

During this research the interface between fibre and matrix was not under investigation and was thus not altered. However, it is well known that the use of compatibilising agents increases the mechanical properties such materials [26, 27]. As described in these references, the fibre treatment procedures are not easy to perform, and are quite time consuming. Improvements of the interface between flax fibres and bio-based thermoset resins will be a topic for further work. In addition, the infusion of bidirectional reinforcements with biobased resin will be investigated.

ACKNOWLEDGEMENTS

Prof. Schuster thanks the Centre for Advanced Composite Materials (CACM) for its kind hospitality during his sabbatical stay, enabling this piece of research described here. Financial support of the DAAD (D/10/03896) is gratefully acknowledged. The Sustainable Composites research programme at the CACM is generously supported by the Ministry for Science and Innovation, New Zealand.

REFERENCES

1. Shibata M and Nakai K (2008), ‘Preparation and properties of biocomposites composed of bio-based epoxy resin, tannin acid, and microfibrillated cellulose’, *J of Polymer Science: Part B: Polymer Physics,* 48 (4), 425 – 433.

2. Stashevski AM and Deppe HJ (1973), ‘The application of tannine resins as adhesives for wood particle boards’, *HOLZ als Roh- und Werkstoff,* 31 (11), 417-419.

3. Wang C, Yang L and Ni B, Wang L (2009), ‘Thermal and mechanical properties of cast polyurethane resin based on soybean oil’, *J of Appl Polym Sci,* 112 (3), 1122-1127.

4. Mohanty AK, Misra M and Hinrichsen G (2000), ‘Biofibres, biodegradable polymers and biocomposites: an overview’, *Macromol Eng,* 276 (3-4), 1-24.

5. Pan P, Zhu B, Dong T, Serizawa S, Iji M and Inoue Y (2008), 'Kenaf fiber/Poly(ε-caprolactone) biocomposite with enhanced crystallization rate and mechanical properties', *J of Appl Polym Sci*, 107 (6), 3512-3519

6. John MJ and Thomas S (2008), 'Biofibres and biocomposites', *Carbohydr Polym* 71 (3), 343–364.

7. Cheung HY, Lau KT, Pow YF, Zhao YQ and Hui D (2010), Biodegradation of a silkworm silk/PLA composite', *Composites Part: B*, 41 (3), 223-228.

8. Majhi SK, Nayak SK, Mohanty S and Unnikrishnan L (2010), 'Mechanical and fracture behavior of banana fiber reinforced Polylactic acid biocomposites', *Int J Plast Technnol* DOI.

9. Le Duiqou A, Davies P and Baley C (2010), 'Analyse du cyvle de vie d´un biocomposite', *Matériaux & Techniques*, 98 (2), 143-150.

10. Moriana R, Vilaplana F, Karlsson S and Ribes-Greus A (2011), 'Improved thermo-mechanical properties by the addition of natural fibres in starch based sustainable biocomposites', *Composites Part: A*, 42 (1), 30 – 40.

11. Liu W, Drzal LT, Mohanty AK and Misra M (2007), 'Influence of processing methods and finflu length on physical properties of kenaf fiber reinforced soy based biocomposites', *Composites Part: B*, 38 (3), 352-359.

12. Liu Z and Erhan SZ (2008), 'Green composites and nanocomposites from soybean oil', *Mat Sci and Eng A*, 483-484 (1), 708-711.

13. Müssig J (2008), 'Cotton fibre reinforced thermosets versus ramie composites: a comparative study using petrochemical- and agro-based resins', *J Polym and the Environ*, 16 (2), 94-102.

14. Adekunle K, Åkesson D and Skrifvars, M (2010), 'Biobased composites prepared by compression molding with a novel thermoset resin from soybean oil and a natural-fiber reinforcement', *J of Appl Polym Sci*, 116 (3), 1759-1765.

15. Kim JT and Netravali AN (2010), 'Mechanical and thermal properties of sisal fiber-reinforced green composites with soy protein/gelatin resins', *J of Biobased Mat and Bioenergy*, 4 (4), 338-345.

16. Mehta G, Mohanty AK, Thayer K, Misra M and Drzal LT (2005), 'Novel biocomposites sheet molding compounds for low cost housing panel applications', *J of Polym and the Environ*,13 (2), 169-175.

17. Dweib MA, Hu B, Shenton III HW and Wool RP (2006), 'Bio-based composite roof structure: manufacturing and processing issues', *Comp Struc* 74 (4), 379-388.

18. Müssig J (2007), 'Karosserie aus Naturfasern und Pflanzenöl', *Kunststoffe*, 97 (3), 78-83.

19. Satyanarayana K and Wypych F. (2007), ‘Characterization of natural fibers’, *In: Fakirov S, Bhattacharrya D, editors. Handbook of engineering biopolymers: homopolymers, blends and composites. Hanser Gardner Publications:* p. 34.

20. Reußmann T (2003), ‘Entwicklung eines Verfahrens zur Herstellung von Langfasergranulat mit Naturfaserverstärkung’ *Ph.D.-thesis, Technische Universität Chemnitz Germany*, p.22.

21. Chabba S, Matthews GF and Netravali AN (2005), ‘Green´composites using cross-linked soy flour and flax yarns’, *Green Chem*, 7 (8), 576-581.

22. Alix S, Marais S, Morvan C and Lebrun L (2008), ‘Biocomposite materials from flax plants: Preparation and properties’, *Composites Part: A*, 39 (12), 1793-1801.

23. Dweib MA, Hu B, O´Donnell A, Shenton HW and Wool RP (2004), ‘All natural composite sandwich beams for structural applications’, *Comp. Struct.*, 63 (2), 147 – 157.

24. Van de Velde K and Baetens E (2001), ‘Thermal and mechanical properties of flax fibres as potential composite reinforcements’, *Macrom Mat and Eng*, 286 (6), 342 – 349.

25. Lauke B, Beckert W and Schneider K (1994), ‘Interlaminar shear strength evaluation of curved composite samples’, *Appl Comp Mat* 1 (1), 267-271.

26. Lui Q, Stuart T, Hughes M, Sharma H H and Lyons G (2007), ‘Structural biocomposites from flax – part II: The use of PEG and PVA as interfacial compatibilising agents’, *Composites: Part A*, 5 (38), 1403 – 1413.

27. Gassan, J, Dietz T and Bledzki A (2000), ‘Effect of silicone interphase on the mechanical properties of flax-polyurethane composites’, *Comp. Interf.*, 2 (7), 103 – 115.

AN EXPERIMENTAL ESTIMATION OF LIQUID ABSORPTION COEFFICIENT FOR CELLULOSE NANO-FIBER FILMS

A. Javadi[1], K.M. Pillai[1] and R. Sabo[2]

[1]*Laboratory for Flow and Transport Studies in Porous Media, Dept. of Mechanical Engineering, University of Wisconsin-Milwaukee, 3200 N. Cramer St., Milwaukee, WI 53211, USA.*
[2]*USDA, Forest Products Laboratory, One Gifford Pinchot Dr., Madison, WI 53726, USA.*

ABSTRACT: While making polymer composites from natural fibers using the liquid composites molding (LCM) process, the fibrous porous medium inside the LCM mold undergoes swelling and porosity reduction as a result of enlargement of natural fibers due to liquid absorption. The preforms made from plant-derived cellulose nanofibers (CNF) have a potential for creating higher-quality and bio-based green composites. The absorption coefficient, b, plays a very important role in the modified continuity equation that is proposed for such swelling media for conducting LCM mold-filling simulations. Past research has shown that an ad-hoc value of unity for b is quite good for modeling flows in LCM molds packed with natural fibers. In this paper, a simple dipping experiment is proposed to estimate b directly using a microbalance. The final results indicate that b is indeed one for CNF preforms as measured with water as the wetting liquid.

INTRODUCTION

The usage of glass, carbon or kevlar fibers for providing reinforcement in polymer composites has been increasing for the past few decades. Due to several disadvantages associated with such composites including adverse environmental impact, difficult recycling, and high amount of energy needed for processing and recycling, there has been a trend of using natural fibers such as flax, kenaf and jute as reinforcement in polymer composites [1]. Natural fibers are preferred since they are biobased and biodegradable. However, the usage of natural fibers in polymer composites has some drawbacks including lower mechanical properties, degradation due to moisture absorption, and inconsistent reinforcement properties due to natural variability in fibers [2].

Cellulose nanofibers (CNFs), a new type of nanoscale fibers made of cellulose molecules and derived from plant sources, have very high mechanical properties compared to the natural or inorganic reinforcing fibers. Recent reduction in costs of producing CNFs due to the development of new chemistry-based processing methods [3, 4] has made it possible to use such fibers as reinforcement for nanocomposites. However, the CNF based nanocomposites remain confined to labs since there remain several hurdles in scaling-up their production [5]. A research collaboration between USDA Forest Products Laboratory at Madison, WI and University of Wisconsin-Milwaukee has been investigating the possibility of producing scalable CNF based composites through the use of CNF as reinforcement in liquid composites molding processes [6]. Preliminary wetting tests with various liquids have indicated that CNF sheets [Figure 1] absorb liquid and swell at a rapid pace [7].

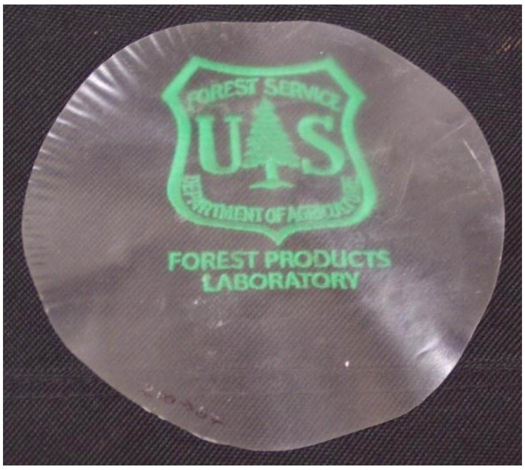

Figure 1: Transparent CNF film produced at USDA Forest Product Laboratory, Madison, WI.

MODELING RESIN FLOW IN SWELLING, LIQUID ABSORBING POROUS MEDIUM

For modeling single-phase flows in swelling porous media [1], the Darcy's law can be still considered to be valid:

$$< V > = -\frac{K}{\mu}\nabla < P >^{f} \tag{1}$$

Here $< V >$ is the phase average velocity, K is the porous-medium permeability, μ is the resin viscosity, and $< P >^{f}$ is the intrinsic phase average pressure. Unlike the non-swelling porous media formed by glass or carbon fibers, the permeability of a porous medium formed by CNF will be a function of both time and space due to swelling of solid matrix as a result of liquid absorption. Borrowing from the flow model for liquid flows in liquid-absorbing, swelling porous medium formed by paper [8] or natural fibers [9], the continuity equation for flow in porous media made from CNF reinforcement can be described as

$$\nabla . < V > = -S - \frac{\partial \varepsilon}{\partial t} \tag{2}$$

where S is the liquid absorption rate and $\boldsymbol{\varepsilon}$ is the porosity. In contrast to the traditional continuity equation $\nabla . < V > = 0$ employed by non-swelling glass or carbon fibers in rigid-mold LCM processes, Eqn. 2 has S as the sink term and $-\ \partial\varepsilon/\partial t$ as the source term (note that this term is positive since the porosity reduces with time in a swelling porous medium). A detailed derivation Eqn. (2) using the respected volume averaging method is presented in [9]. So the resin will either decelerate or accelerate depending upon whether the right hand side of Eqn. 2 is negative or positive, respectively.

Let us now present a modification of the continuity equation which has produced impressive results while modeling flows in swelling porous media, irrespective of whether it is the capillary-pressure driven wicking flow [8], or the injection-pressure driven flow in an RTM mold [9, 10]. Let v be the fiber volume fraction in our CNF based porous medium. Since S is the rate of liquid absorption by fibers and since dv / dt is directly related to the rate of increase of fiber volume, then S is anticipated to be proportional to dv/dt. As a first approximation, we assume S to be linearly proportional to dv/dt, i.e.,

$$S = b\frac{dv}{dt} \tag{3}$$

where b is the *absorption coefficient* that is expected to fall in the range $0 < b < 1$. Note that $b = 0$ indicates zero absorption of liquid by the porous medium, while $b=1$ implies that the rate of increase in the volume of solid matrix is equal to the volumetric rate of liquid absorption by the matrix during the resin-flow process.

The assumption $b = 1$, i.e., the volume of liquid absorbed by the solid matrix in a given time period is equal to the increase in the matrix volume during the same period, has yielded impressive results while predicting the moving liquid-front location during wicking in a liquid-absorbing, swelling paper-like medium [8]. This same assumption proved effective even for predicting the pressure and flow-front location in fiber mats made from natural fibers such as jute that absorb liquid and swell during 1-D RTM mold-filling experiments [9, 10]. It is important to note that though the assumption $b = 1$ has proven to be effective, *it has not be established through a direct measurement of volume of liquid absorbed along with volume change in the solid matrix.* In this paper, an attempt will be made to directly estimate the absorption coefficient b using a microbalance available within a Tensiometer, also called DCA (Dynamic Contact-Angle Analyzer). To test the proposed methodology, water is used as the fluid instead of an actual resin.

THEORY: MEASURING THE ABSORPTION COEFFICIENT THROUGH A MICROBALANCE

A small rectangular CNF sheet is suspended from a hook attached to the microbalance. The reading of the microbalance gives the weight of the dry sheet. A container of water resting on the moving platform is raised to immerse the sheet (Figure 2). After this immersion, the microbalance reading is reduced as a result of the buoyancy force acting on the immersed sheet. As shown below through our derivation, the readings before and after the immersion can be used to estimate the values of the absorption coefficient.

The various forces acting on the submerged CNF sheet (Figure 3) follow the relation

$$T + F_b = W \tag{4}$$

where T is tension in the string suspending the sheet and which is read as the reading of the microbalance, W is the weight of the specimen along with that of the water absorbed by it. Note that the buoyant force, F_b, can be estimated as

$$F_b = \rho V g \tag{5}$$

where ρ is the density of water (= 998 kg/m^3), V is the volume of water displaced by the CNF sample (which is nothing but the sample volume), and g is the acceleration due to gravity (=9.8 m/s^2). The use of Eqns. (4) and (5) leads to the following relation at the initial time $t = 0$:

$$T_o + \rho V_o g = W_o \tag{6}$$

Here the subscript o signify the initial ($t = 0$) quantities.

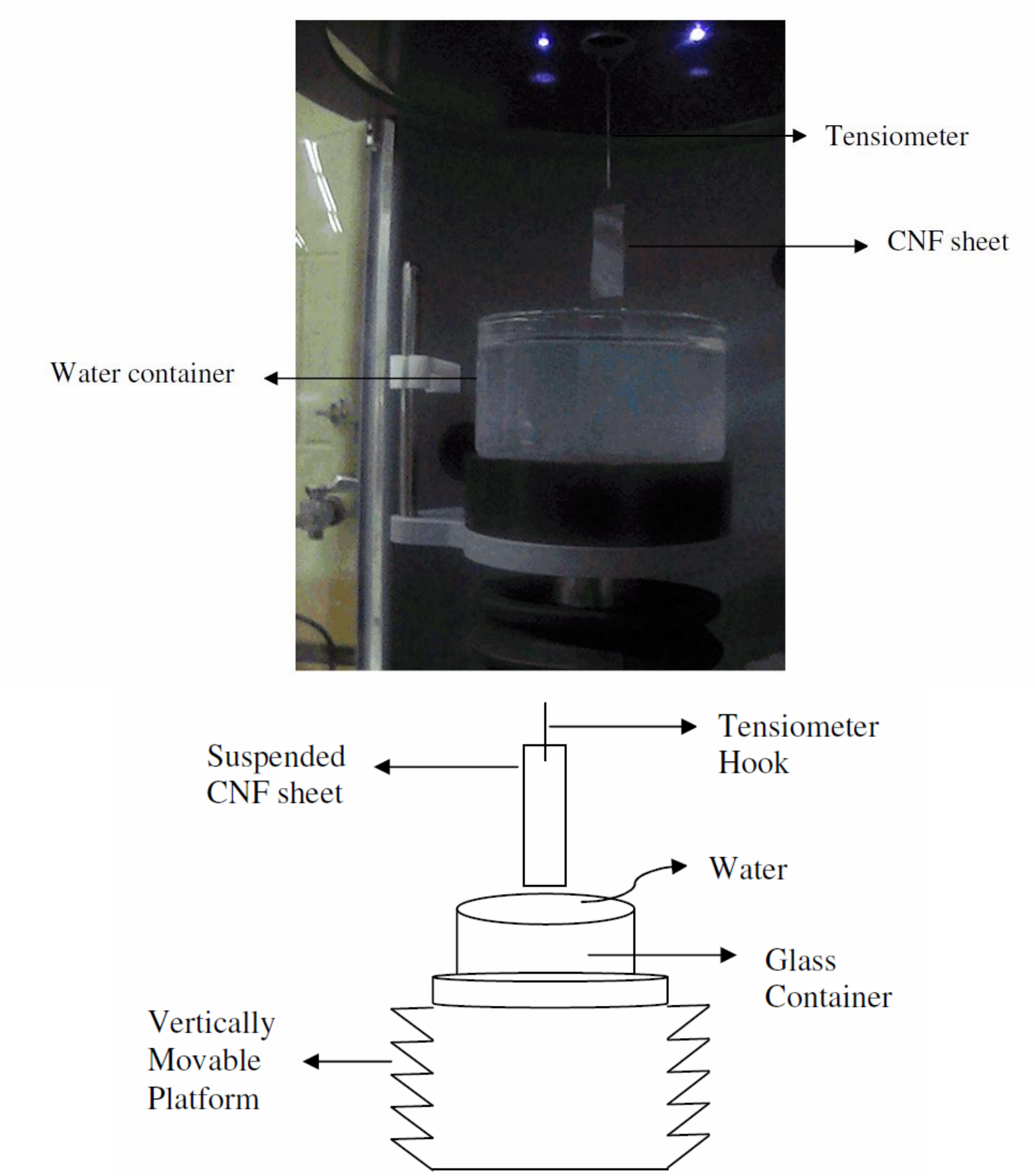

Figure 2: (Top) A photograph of the experimental setup used for estimating the absorption coefficient using the microbalance of tensiometer (DCA). (Bottom) A schematic of the setup showing the details.

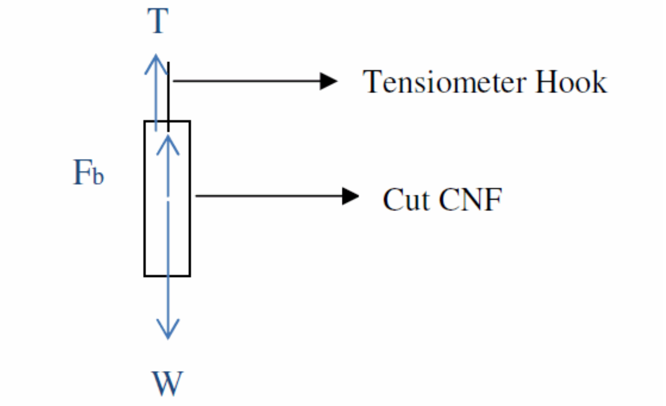

Figure 3: A Free Body Diagram depicting various forces on the CNF sheet hung with a hook in the microbalance while submerged in water.

Note that W_o is the weight of the CNF sample before it is submerged into water and was measured by a sensitive, two-digit electronic balance, while T_o is obtained from the microbalance. Since g and ρ are easily-determinable constants, we are able to estimate the initial sample volume, V_o , by using Eqn.6.

Since Eqn. 4 is a general equation valid at any given time, t, after the sample has been dipped into water, we can present it again as

$$T(t) + \rho V(t) g = W(t) \tag{7}$$

where $T(t)$ is the tension reading measure by the microbalance, and $W(t)$ is the CNF sample weight. ($W(t)$ after time t was obtained by taking the sample out from water, blowing air into it to shake-off the water sticking to it, and then using the electronic balance.)

On subtracting Eqn. (6) from Eqn. (7), we have

$$T(t) - T_o + \rho g \left(V(t) - V_o \right) = W(t) - W_o \tag{8}$$

By using the values of $T(t)$, T_o, $W(t)$, W_o, and V_o obtained from the previous equations, and employing the assumed values of ρ and g, we can calculate the current volume of the CNF sample, $V(t)$, from Eqn. 8.

Using $W_o = m_c g$, where m_c is the original (dry) mass of the CNF sample, and $W(t) = (m_c + m_w(t)) g$, where m_w is the mass of water absorbed by the sample since the start of the experiment, we obtain

$$V_w(t) = (W(t) - W_o)/\rho g \tag{9}$$

Thus we can calculate the volume of water absorbed by the CNF sample as a function of time during the course of the experiment.

Using Eqn. 3, we can set the definition of the absorption coefficient, b, as

$$b = \frac{\mathrm{S}}{\mathrm{dv/dt}} = \frac{\text{rate at which liquid volume is absorbed per unit porous−medium volume}}{\text{rate of change of fiber (solid−matrix) volume fraction}} \tag{10}$$

Now the fiber (solid-matrix created from CNF in an LCM mold) volume fraction can be defined as

$$v = \frac{V_f}{\mathrm{V}} \tag{11}$$

where V_f is the fiber volume within an REV (representative elementary volume) used for deriving macroscopic governing equations through the method of volume averaging [11]. $\mathrm{V_{REV}}$ is the REV volume that remains fixed with time. Taking the derivative of Eqn.11 with respect to time results in

$$\frac{\mathrm{d}v}{\mathrm{dt}} = \frac{1}{\mathrm{V_{REV}}} \frac{\mathrm{d}V_f}{\mathrm{dt}} \tag{12}$$

If we define the sink term of Eqns. 2 and 3 as the rate of depletion of water within an REV, then it can be expressed as

$$S = \frac{1}{\mathrm{V_{REV}}} \frac{d\,\mathrm{V_w}}{dt} \tag{13}$$

where $d\,\mathrm{V_w}$ is the differential reduction in the surrounding water volume due to absorption. On substituting Eqns. 12 and 13 in Eqn. 10, we get the definition of the absorption coefficient, b, as the ratio of the volume of water absorbed to the change in fiber or solid-matrix volume in a given differential time-interval:

$$b = \frac{d\,\mathrm{V_w}}{\mathrm{d\,V_f}} \tag{14}$$

The coefficient b as defined above is rather difficult to measure experimentally. Instead, we found it convenient to measure a quantity b' that is defined as

$$b' = \mathrm{V}_w(t)\,/[V(t) - V_o] \tag{15}$$

which is the ratio of total volume of water absorbed by the CNF sample to change in the sample volume due to swelling. It turns out that, by taking the differential of Eqn. 15 and by conducting some algebraic manipulations, one can relate b to b' through the relation

$$b = [V(t) - V_o]\,\frac{d\,b'}{d\,V} + b' \tag{16}$$

In this paper, we intend to plot b' as a function of $[V(t) - V_o]$ such that the slope and value at any point of the curve will yield the value of b. (Note that $d\,b'/d\,V = d\,b'/d\,[V(t) - V_o]$.)

EXPERIMENTAL DETAILS AND DATA ANALYSIS

Samples were developed from the CNF sheets made at USDA forest product laboratory at Madison, WI [Figure 1]. The CNF sheet were cut in rectangular shape for the experiment. Tensiometer (DCA) was used for this purpose; the microbalance of the device was calibrated afresh at the start of these experiments. Note that the Tensiometer, which is designed to measure surface tension, was adapted suitably for our experiment—its inbuilt software that translates the microbalance measurements into surface tension values was manipulated to yield the force/weight values. A total of 11 CNF samples of varying sizes were used in our experiments. Each sample was subjected to a cyclical dipping process of 30 seconds time-period for 20 minutes. At the end of this period, it was observed that all CNF samples had reached their maximum-possible saturation states such that they were no longer absorbing any more water. Then the final value of tension in the string, T(t), as well as the final weight of the specimen, W(t), were measured. Using Eqn. 8, the change in the volume of the CNF specimens, $V - V_o$, was estimated; using Eqn. 9, the volume of water absorbed by the CNF specimen, V_w, was evaluated. Using these two values, b' was estimated using Eqn. 15. Thus a total of eleven ordered pairs of the form $(b',\ [V(t) - V_o]\ )$ were developed from the same number of CNF samples. (Table 1 lists details of five of these randomly-chosen samples.) These ordered pairs were then used to plot the graph shown in Figure 4 which then furnished the slope $d\,b'/d\,V\ or\ \ d\,b'/d\,[V(t) - V_o]$ that was used in Eqn. 16 to get the final value of the absorption coefficient b.

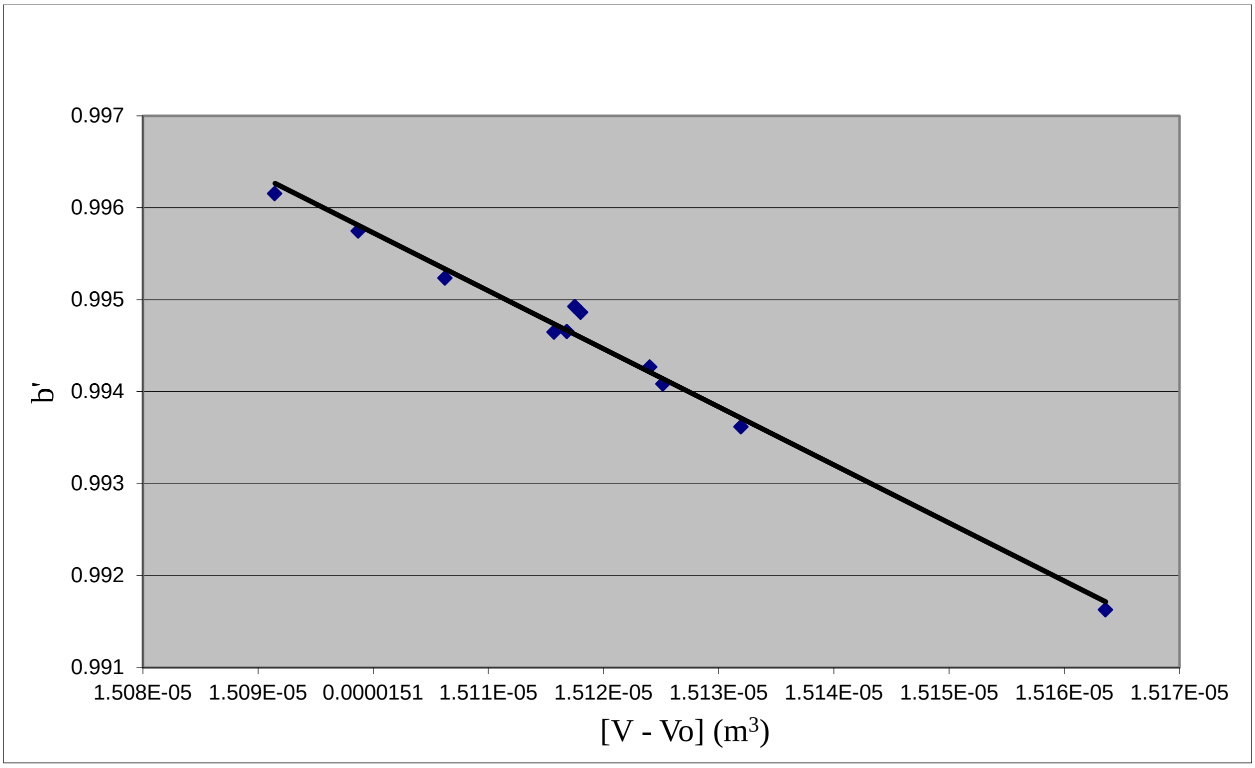

Figure 4: A plot b' as a function of $[V(t) - V_o]$ as observed for 11 different CNF samples.

CNF Sample Number	initial weight (mg)	Change in sample volume $[V - V_o]$ (m^3)	Volume of water absorbed by the sample (V_w)	b'
1	20.8	1.512E-05	1.5037E-05	0.994268362
2	31.8	1.51636E-05	1.504E-05	0.991626175
3	17.8	1.5132E-05	1.5035E-05	0993616028
4	18.7	1.51252E-05	1.5034E-05	0.995234051
5	21.1	1.51157E-05	1.5036E-05	0.994651994

Table 1: Some details of the experiments conducted with five randomly-chosen CNF samples out of a total of eleven.

RESULTS, CONCLUSIONS AND FUTURE WORK

The plot of Figure 4 furnished the final value b = 0.9942 that was an average of the b value obtained for each of the eleven samples using Eqn. 16. These b values were virtually indistinguishable from the b' estimated for the eleven samples. This close convergence clearly indicates that the liquid volume absorbed by samples and the corresponding changes in sample volumes, as indicated by Eqns. 14 and 15, are clearly equal. In other words, *change in the volume of CNF preforms during swelling is entirely due to the volume of water absorbed by it*. This implies that our earlier ad-hoc assumption of using b as unity for flow models in swelling porous media is correct at least for the CNF preforms.

We reiterate that the b' versus $[V(t) - V_o]$ plot, as shown in Figure 4, was done using $V - V_o$ or V_w values obtained after achieving a full saturation in CNF samples. Our attempts to get a similar plot in real time, after measuring these variables as a function of time, met with failure due to the rapid rate of swelling in CNF samples during the earlier part of the wetting process—the method of pulling out the sample from water, blowing air on it to shake-off the sticking liquid, and then measuring it using a weighing scale, is simply too slow to capture the fast changes happening in CNF during the dipping process. New techniques have to be developed to capture such changes in real time so that changes in the values of b as a function of time can also be studied.

The current work was based on using water for this preliminary study. In future, it would be instructive to measure b for the various resins used for making composites or for various test liquids used for studying flow and characterizing permeability.

It is also important to note that in a real LCM mold, the CNF solid matrix will be under compressive stress due to mold closure as well as liquid pressurization. New tests need to be developed to measure the absorption coefficient b under such conditions in order to check if the findings of the present paper are going to be valid for such in *in-situ* situations as well.

ACKNOWLEDGEMENTS

The financial support from Forest Products Laboratory, Madison as well as from College of Engineering and Applied Science, University of Wisconsin-Milwaukee through its undergraduate research scholarship program is gratefully acknowledged.

References

1. Masoodi, R. and Pillai, K.M., “Modeling the Processing of Natural Fiber Composites made using Liquid Composites Molding,” in, Handbook of Bioplastics and Biocomposites Engineering Applications, ed. by S. Pilla, Scrivener-Wiley, 2011.
2. Joshi, S.V., Drzal, L.T., Mohanty, A.K., Arora, S., “Are natural fiber composites environmentally superior to glass fiber reinforced composites?” *Composites Part A*, 35(2004): 371-376.
3. Saito T, Hirota M, Tamura N, Kimura S, Fukuzumi H, Heux L, Isogai A., “Individualization of nano-sized plant cellulose fibrils by direct surface carboxylation.” *Biomacromolecules* 10 (2009):1992–1996.
4. Saito, T.; Isogai, A., “Introduction of aldehyde groups on surfaces of native cellulose fibers by TEMPO-mediated oxidation.” *Colloids and Surfaces A: Physicochem. Eng. Aspects.* 289 (2006): 219-225.
5. Siró, I., Plackett, D., “Microfibrillated cellulose and new nanocomposite materials: a review,” *Cellulose*, 17(2010): 459-494.
6. R. Masoodi, R.E. Hajjar, K.M. Pillai, and R. Sabo, “Mechanical response of a cellulose nanofiber/bio-derived epoxy composite,” *Materials and Design*, accepted for publication.
7. R. Masoodi, R. Javadi, K.M. Pillai, R. Sabo, “An Experimental Study on Swelling of Cellulose Nano-Fiber Films in Epoxy Resins and Water,” Proceedings of SAMPE 2011, Long Beach CA.
8. Masoodi, R., Tan. H., and Pillai, K.M., “Numerical Simulation of Liquid Absorption in Paper-Like Swelling Porous Media,” *AIChE Journal*, v 56, n 9, pp. 2257-2267, Sep 2010.
9. “Numerical Simulation of LCM Mold-Filling during the Manufacture of Natural Fiber Composites,” R. Masoodi, K.M. Pillai, N. Grahl, and H. Tan, *Journal of Reinforced Plastics and Composites*, v31, issue 6, March 2012.
10. Masoodi, R., Pillai, K.M. and Verhagen, M.A., “Flow Modeling in Natural-Fiber Preforms used in Liquid Composite Molding,” Proc. 1st joint American-Canadian International Conference on Composites, Newark, Delaware, USA, September 15-17, 2009.
11. Tucker III, C.L. and Dessenberger, R.B., Governing equations for flow and heat transfer in stationary fiber beds, *Flow and rheology in polymer composites manufacturing*, Elsevier, Amsterdam, pp. 257-323, 1994.

INVESTIGATION OF RESIN FLOW IN WOVEN (DUAL-SCALE) JUTE FABRICS THROUGH THE TWO-COLOR EXPERIMENT

R. Masoodi [2], A. Javadi [1], K.M. Pillai[1]

[1]*Laboratory for Flow and Transport Studies in Porous Media*
Department of Mechanical Engineering, University of Wisconsin-Milwaukee
3200 North Cramer St., Milwaukee, WI53211, USA, http://www4.uwm.edu/porous/
[2]*School of Design and Engineering, Philadelphia University*
4201 Henry Ave, Philadelphia, PA 19144, USA.

ABSTRACT: The current breed of natural-fiber based polymer composites offer ‘green’ alternatives for the automotive and other engineering applications. Jute, one of the most useful and inexpensive of all the natural fibers, is usually available as woven fabrics, often in the form of gunny sacks. Many polymer composite parts are made by the liquid composite molding (LCM) process where accurate mold-filling simulations are often employed to optimize mold design. However, the use of natural fiber preforms made from woven jute fabrics adds several hitherto unexplored complexities to the LCM mold-filling physics. One such complexity arises from the flow of resin in a dual-scale porous medium created by woven fabrics in LCM molds. In this paper, we study the effect of the dual-scale architecture on resin flow in LCM using a two-color experiment. During the making of a jute part using epoxy resin, injection of a colored resin is followed by the injection of resin of another color. Trapping of the earlier-injected resin inside fiber tows of the jute fabric is clearly demonstrated through this experiment. Such a result, also seen in the conventional glass fabrics, has tremendous implications as far as modeling of temperature and cure during LCM mold-filling in concerned.

INTRODUCTION

The quality of composite parts made using the liquid composite molding (LCM) process and the efficiency of the process depend strongly on the wetting of fiber preform during the mold-filling stage of LCM. The mold-filling simulation is one of the most effective approaches to optimize the LCM process and mold design. For single-scale fiber preforms (the ones made from random fiber mats), the liquid resin impregnating the dry fibers in LCM can be modeled by using the Darcy’s law ($\mathbf{v}=-\mathbf{K}/\mu\cdot\nabla p$where $\mathbf{v}$ is the volume-averaged velocity of resin, p is the pore-averaged resin pressure, $\mathbf{K}$ is the permeability tensor for the fiber preform, and μ is the resin viscosity) with the continuity equation ($\nabla\cdot\mathbf{v}=0$) [1]. However, recent studies have shown that such a modeling approach faces difficulties in accurately predicting the wetting of the dual-scale fiber preforms made from woven and stitched fabrics [2-6].

The dual-scale fabrics are characterized by an order-of-magnitude difference in the pore length-scales of the larger gaps between fiber tows and the smaller pores inside fiber tows. During LCM mold-filling, the resin flow through a dual-scale fiber preform is quite different

---

[1] The author to whom correspondence should be addressed.
(Email:krishna@uwm.edu, Tel: 414 229 6535 Fax: 414 229 6958)

from the flow in a single-scale preform. The liquid resin flowing through the dual-scale media is characterized by delayed impregnation of fiber tows due to a higher flow-resistance inside the tows. Moreover, the order-of-magnitude decrease in permeability inside tows ensures that the resin inside the tows is practically stationary with respect to the resin traveling through the gaps around the tows. Such an effect has been demonstrated through a two-color injection experiment for *glass* mats [6], where a green-color resin is initially injected into a dry mold [Fig 1(a)] packed with either random mats or stitched biaxial fabrics and is then followed by the injection of a blue-color resin. The color distribution in the cross-section of a composites panel made from random mats clearly indicates that the earlier-injected green resin is almost completely replaced by the later-injected blue resin [Fig 1(b)]. However, the corresponding color distribution in a woven fabric clearly indicates that the earlier-injected green resin is absorbed and trapped by fiber tows while the later-injected blue resin pushes out the green resin in gaps present between tows [Fig 1(c)]. Shih and Lee [7] carried out a similar experiment where a light-colored liquid, followed by a dark-colored liquid, were injected into a unidirectional stitched fabric. They observed that the later-injected dark liquid traveled through the gaps to the resin front, bypassing the earlier-injected light liquid trapped inside the tows. These two separate observations made by two different research groups provide a strong justification for establishing a new flow modeling approach for the dual-scale fabrics.

In recent years, the interest in using eco-friendly materials in engineering has increased due to a growing environmental awareness. As a result, researchers are looking for ‘green’ composites, such as natural-fiber based composites, to replace some of the traditional engineering composites that are not environmentally friendly [8]. However, the use of natural-fiber based fiber mats, such as the woven jute fabrics, adds many new complexities to the LCM mold-filling physics [9]; one such complexity arises due to resin flow in the dual-scale woven jute fabrics. Till date, no one has reported an experiment to highlight this difference.

In this paper, we report the results a two-color experiment conducted with epoxy and a jute fabric in an LCM mold. Our aim is to study if the dual-scale nature of woven jute fabrics leads to the same effects during the two-color experiment as seen in the case of glass fabrics.

EXPERIMENTS

A set of experiments were performed to study the flow of resin in a dual-scale porous medium created by a woven jute fabric and compare it with the flow in a single-scale porous medium created by a random fiber mat. We wanted to test the hypothesis that *resin is absorbed and retained by tows in the dual-scale media for natural fibers also*. According to this hypothesis, the earlier injected resin would always flow in front of the later injected resin in the case of a single-scale porous medium. But in the case of a dual-scale porous medium, the earlier-injected resin would be absorbed by the fiber tows and get ‘locked-in’ inside tows, while the later-injected resin would flow past the saturated tows through the inter-tow gaps to the moving front. Hence two resins of different colors were injected one after the other during the course of a radial injection experiment, and their distribution was studied after their curing in order to test the proposed hypothesis.

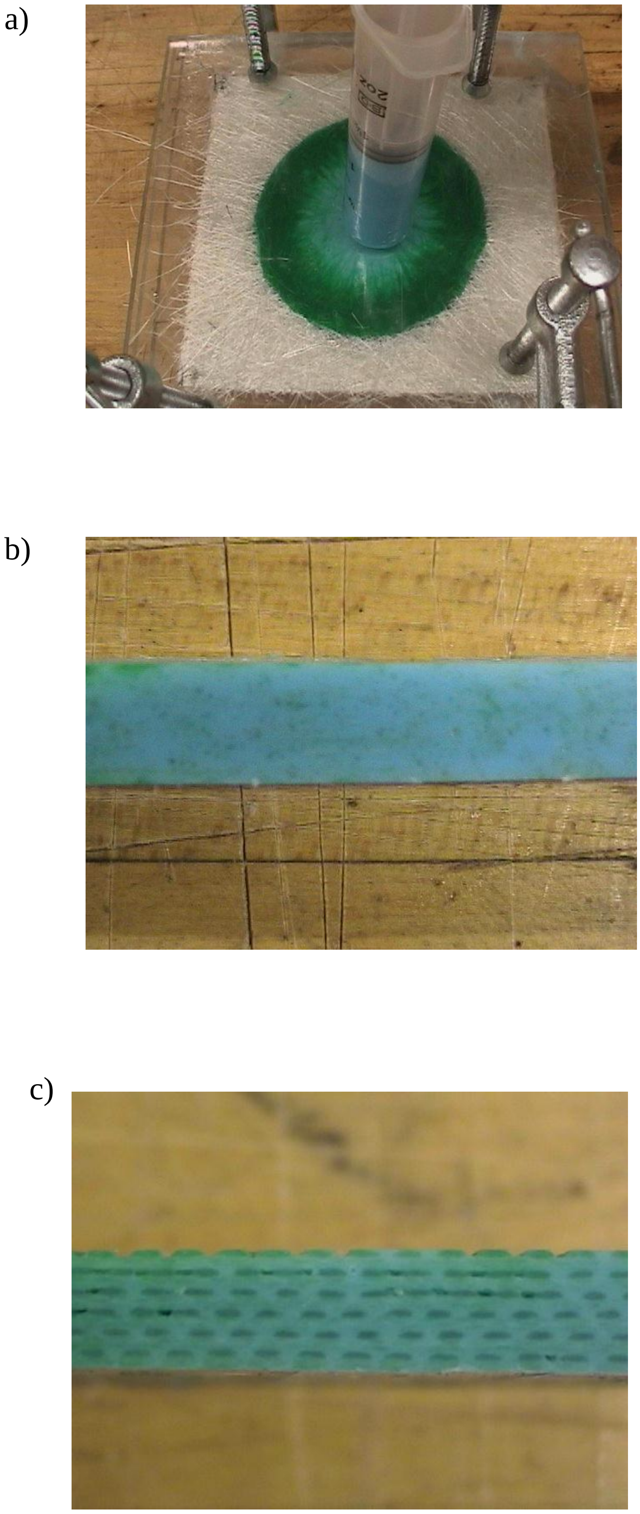

Fig 1: Two-color injection experiment in *glass* fiber mats: (a) injection of a green-color resin is followed by a blue-color resin (random fiber mat); (b) cross-section of a composites panel made from the random fiber mat; (c) cross-section of a composite panel made from a woven fabric.

In these experiments, discarded coffee bags were used as the source of woven jute fabrics (dual-scale media) while preparing the test specimen (Figure 2a). The randomly-laid out and machine-arranged fibers of kenaf (Figure 2b) were used for comparison as the single-scale random mat. The thermoset resin used in our study is an epoxy resin/hardener system of the name System 2000/hardener 2020 from FibreGlast Development Corporation. According to the manufacturer, the recommended resin-to-hardener ratio for this resin is 3:1 by volume. An unheated mold with a rectangular mold-cavity of size 200×100×3.2 mm was used to make flat composites panels. A low-pressure injection was used to make the test specimens from the dual- and single-scale media. First, one layer of mold release was coated on the inner side of the mold and was allowed to cure. Then enough layers of fabrics/mats were stacked in the bottom (female) part of the mold. The mold was closed subsequently and a yellow-colored epoxy was injected into the mold to fill the half of it; injection of a blue-colored epoxy followed it to fill the remaining mold-cavity. (The colored epoxies were created by mixing suitable dyes with the almost-colorless resin.) The mold was left alone for at least 24 hours for curing and then opened.

Fig 2: Different natural fibers used in this study: (a) Woven jute fabric in the form of a dual-scale porous medium; (b) Random laid-out kenaf fibers representing a single-scale porous medium.

After the cure, the extracted flat composite panels were cut into smaller pieces in order to observe the distribution of colored resins inside and between fiber tows. Several narrow strips were cut from the panels and polished to prepare for a microscopic examination. An American Scope ME300 metallographic microscope at a magnification of 100X, along with a live-capture camera system, was then used to take magnified photos of cross-sections of our natural-fiber-epoxy composites panels.

RESULTS AND DISCUSSIONS

Figure 3 shows a sample that was made from the woven jute fabric and two-color epoxy resin. The yellow epoxy, the first-injected colored resin, was introduced from the bottom of the picture; the blue epoxy was injected subsequently from the bottom as well. It appears that the later-injected blue epoxy is beginning to replace the earlier-injected yellow epoxy (Figure 3). However, the magnified photographs of the cross-section of this sample (Figure 4) show that the latter was not completely washed off—it is clear that the blue resin flushed-off the yellow resin in the inter-tow gaps surrounding the fiber tows, which was occupied by the yellow resin initially. However, in case of the random fiber mat (Figure 5), the blue resin almost completely drives away the yellow resin as there are no fiber tows to absorb and hold the latter.

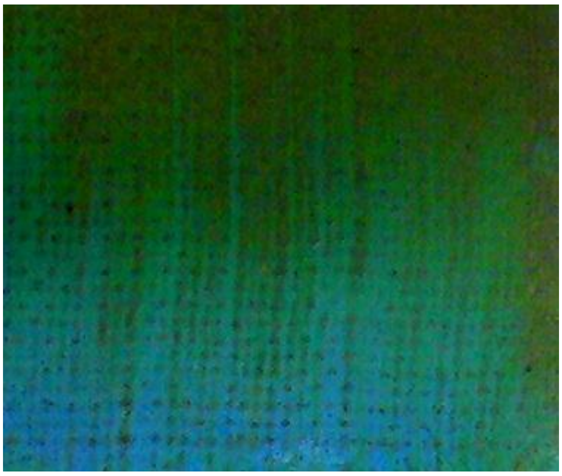

Fig 3: Top view of a flat composites panel made from woven (dual-scale) jute fabric and the earlier-injected yellow epoxy resin followed by the later-injected blue epoxy resin. (Injection was from the bottom.)

This experiment clearly shows that the resin flow-pattern in woven jute fabrics is fundamentally different from the flow observed in the random (kenaf) fiber mats. In the woven (dual-scale) medium, it is clearly seen that the earlier injected resin is absorbed and retained by the tows as the later injected resin moves to the front after bypassing the saturated tows (Figure 4). It is noteworthy that the trapping of resin by tows is similar to the trapping seen for glass fabrics [Figure 1c].

In woven jute fabrics, the jute fibers are around 100 microns (0.1 mm) in diameter [9] and are one order-of-magnitude larger than the typical glass fibers of around 10 microns in diameter. The tows size (both for jute and glass) are on the order of millimeters. Since permeability of a fibrous porous medium is proportional to the square of fiber diameter, it is clear that the intra-tow (tow) permeability is two orders-of-magnitude higher for the jute fabrics compared to the glass fabrics, while the inter-tow (gap) permeability remains comparable. This means that the gap-to-tow permeability ratio is lower in jute fabrics compared to the glass fabrics. Since this gap-to-tow permeability ratio has been found to be very significant in creating the sink effect in dual-scale porous media [13], it is interesting to see that, despite having a lower gap-to-tow permeability ratio as well as exhibiting the fiber-swelling phenomenon due to resin absorption [9], the jute fabrics exhibit all the 'symptoms' of the unsaturated flow observed in glass fabrics. (The effect of the gap-to-tow permeability ratio can be correlated with the effect of the pore volume ratio, another parameter found important for flows in dual-scale fabrics [10, 11, 12].)

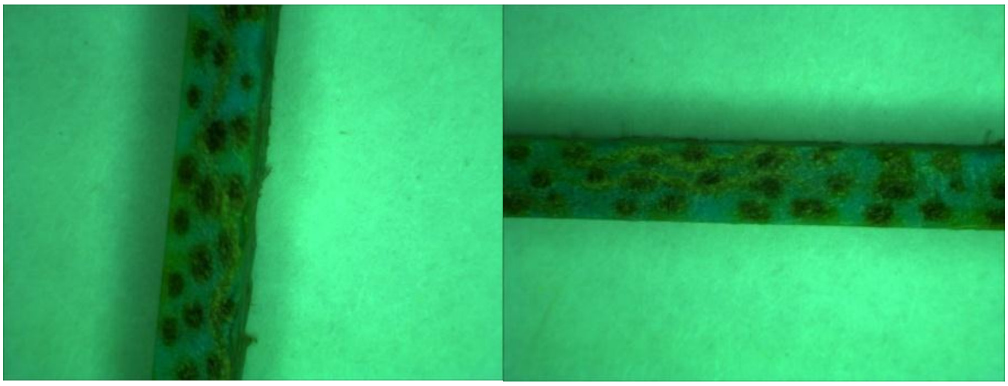

Fig 4: Magnified pictures of typical cross-sections of the flat panels made from the woven (dual-scale) jute fabric and the two-color resin system. The earlier injected yellow resin is seen to be lodged inside fiber tows while the later injected blue resin is surrounding it. (Due to the use of a color filter during the taking of photographs, the yellow color appears darker while the blue color appears lighter.)

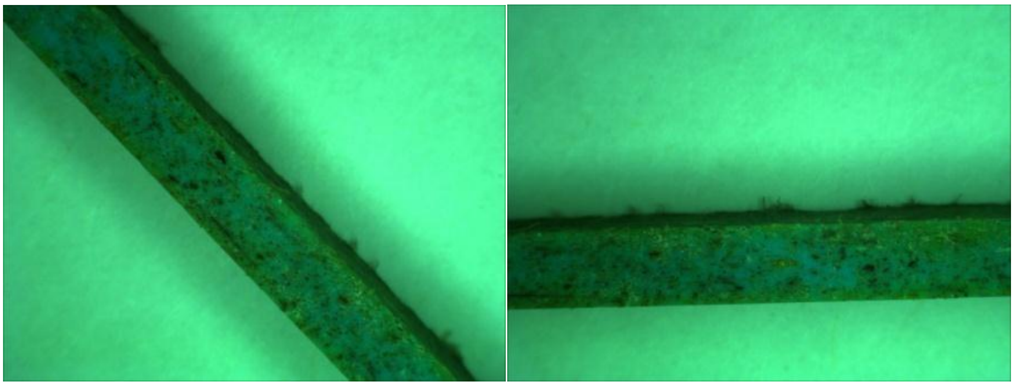

Fig 5: Magnified pictures of typical cross-sections of the flat panels made from the random (single-scale) kenaf fiber mat and the two-color resin system. The later injected blue resin seems to have completely replaced the earlier injected yellow resin.

The discussion given above clearly highlights the need for treating the resin flow through jute fabrics during LCM as the flow through a dual-scale porous medium. In such media, when a resin is injected into an LCM mold, it quickly passes through the inter-tow gap region without impregnating the tows completely. After the resin-front has passed, resin from the surrounding gap region continues to impregnate the tows due to the local resin pressure and the wetting capillary (suction) pressure. This delayed impregnation of tows leads to the *unsaturated* flow in LCM process characterized by partial saturation near the resin front. Significant work has been done in modeling such unsaturated flows in glass fabrics [14, 15]. Success has also been achieved in simulating such flows through numerical means [10, 16]. Simulation of the unsaturated flows in dual-scale porous media after including the thermal and resin-curing effects [11, 12] indicates that the *effect of such phenomena is not confined to a small partially-saturated region near the resin front, but instead extends to almost whole of the mold*.

SUMMARY AND CONCLUSION

We experimentally studied resin flow in a woven fabric made from jute and a random mat made from kenaf. The two-color experiment, which involved injecting two different color resins one after the other, clearly established the differences in resin flow patterns observed in the single-scale (kenaf) and dual-scale (jute) fiber mats. In the dual-scale mats, the earlier injected resin is absorbed and retained by the tows while the later injected resin moves to the front after by bypassing the saturated tows. Such a trapping of the older resin is not observed in the single-scale mats. These results match the results obtained previously for glass fiber mats.

This clearly highlights the need for using the dual-scale (or ‘sink’) approach for modeling LCM flows in the woven jute fiber mats.

REFERENCES

1. C.I. Tucker and R.B. Dessenberger, ”Governing Equation for Flow and Heat Transfer in Stationary Fiber beds” In SG Advani ed., *Flow and Rheology in Polymer Composites Manufacturing*, Ch. 8, Elsevier Science, Amsterdam, 1994.
2. K.M. Pillai and S.G. Advani, A model for Unsaturated Flow in Woven Fiber Preforms during Mold Fillings in Resin Transfer Molding, *Journal of Composite Materials*, Vol 32, no 19, 1998.
3. B.Z. Babu and K.M. Pillai, Experimental investigation of the effect of fiber-mat architecture on the unsaturated flow in liquid composite molding, *Journal of Composite Materials*, Vol 38, No. 1, 2004.
4. K.M. Pillai, “Unsaturated Flow in Liquid Composite Molding Processes: A Review and Some Thoughts,” *Journal of Composites Materials,* Vol. 38(23), pp. 2097–2118, 2004.
5. K.M. Pillai, T. L. Luce, M. V. Bruschke, R. S. Parnas, and S. G. Advani, “Modeling the Heterogeneities Present in Preforms During Mold Filling in RTM,” *Advanced Materials: Expanding the Horizons*, Vol. 25, 25th International SAMPE Technical Conference, Boston, MA, USA, 1993.
6. T. Roy, C. Dulmes, and K.M. Pillai, ``Experimental investigations of the unsaturated flow in Liquid Composite Molding"Proceedings of the 5th Canadian-International Conference in Vancouver, Canada, August 16-19, 2005

7. C.-H. Shih, L.J. Lee, "Effect of fiber architecture on permeability in liquid composite molding, *Polymer Composites*, 19 (5) (1998), pp. 626–639
8. Masoodi, R. and Pillai, K.M.., "A study on moisture absorption and swelling in bio-based jute-epoxy composites", *Journal of Reinforced Plastics and Composites*, 31(5): 285–294, 2012.
9. Masoodi, R., Pillai, K.M.., Grahl, N., and Tan, H., "Numerical simulation of LCM mold-filling during the manufacture of natural fiber composites", *Journal of Reinforced Plastics and Composites*, 31(6): 363–378, 2012.
10. Hua Tan and K.M. Pillai, "Multiscale Modeling of Unsaturated Flow in Dual-Dcale Fiber Preforms of Liquid Composite Molding I: Isothermal Flows," *Composites Part A: Applied Science and Manufacturing*, v 43, n 1, pp. 1-13, Jan 2012.
11. Hua Tan and K.M. Pillai, "Multiscale Modeling of Unsaturated Flow in Dual-Dcale Fiber Preforms of Liquid Composite Molding II: Non-isothermal Flows," *Composites Part A: Applied Science and Manufacturing*, v 43, n 1, p 14-28, Jan 2012.
12. Hua Tan and K.M. Pillai, "Multiscale Modeling of Unsaturated Flow in Dual-Dcale Fiber Preforms of Liquid Composite Molding III: Reactive Flows," *Composites Part A: Applied Science and Manufacturing*, v 43, n 1, pp. 29-44, Jan 2012.
13. J. Slade, K. M. Pillai and S. G. Advani, "Investigation of Unsaturated Flow in woven, braided and stitched fiber mats during mold filling in Resin Transfer Molding", *Polymer Composites*, v 22, no. 4, Aug. 2001, p 491-505.
14. K. M. Pillai "Governing Equations for Unsaturated Flow through Woven Fiber Mats: Part 1 Isothermal Flows", *Composites Part A: Applied Science and Manufacturing*, v33, 2002, p 1007-1019.
15. K.M. Pillai and M.S. Munagavalsa, "Governing equations for unsaturated flow through woven fiber mats, Part 2: Nonisothermal reactive flows", *Composites Part A: Applied Science and Manufacturing*, v 35, 2004, p403-415.
16. H. Tan and K.M. Pillai, "Fast Liquid Composite Molding Simulation of Unsaturated Flow in Dual-Scale Fiber Mats Using the Imbibition Characteristics of a Fabric-Based Unit Cell", *Polymer Composites*, vol. 31, issue 10, p 1790-1807, 2010.

EFFECT OF ULTRASONIC TREATMENT ON THE COMPATIBILITY AND MECHANICAL PROPERTIES OF OIL PALM EMPTY FRUIT BUNCH (EFB) FIBER REINFORCED POLYLACTIC ACID COMPOSITES

A.K.M.M. Alam, M.D.H. Beg, D. M.R. Prasad and R. M. Yunus

Faculty of Chemical and Natural Resources Engineering, Universiti Malaysia Pahang, Gambang 26300, Kuantan, Malaysia,Corresponding author: rmy@ump.edu.my, Phone: +6095492004

ABSTRACT: In this research, environmentally friendly composites were prepared by renewable materials such as oil palm empty fruit bunch (EFB) fiber and poly lactic acid (PLA). Fibers contents in the range 10-40 wt% were incorporated in PLA using extrusion followed by injection molding to prepare EFB/PLA composites. In order to improve the compatibility between EFB and PLA, EFB was treated by ultrasonic method in presence of alkali solution. The EFB fiber content was optimized on the basis of tensile strength (TS) and tensile modulus (TM) tests. The melt flow index (MFI) of treated fiber incorporated composites was found to be higher than that of the Raw EFB/PLA composite. A significant improvement of the TS, TM and impact strength (IS) values of the composites were observed after simultaneous ultrasonic and alkaline treated EFB fiber reinforced PLA composites. These composites showed more thermal stability as examined by thermogravimetric analysis. Distinct fracture surface morphologies such as fiber breaking, fiber pull out, fiber-matrix adhesion of the samples were clearly observed by the scanning electron microscopy.

Keywords: *Empty fruit bunch fiber, Poly lactic acid (PLA), ultrasonic treatment, melt flow index, mechanical and thermal properties.*

INTRODUCTION

Natural fiber reinforced polymer composites are known as biocomposites with environment-friendly nature [1]. At present the application of natural fiber reinforced polymer composites increased noticeably to reduce the dependence on petroleum based polymer products. For this reason, attention has been paid to the renewable polymer matrices. Polylactic acid (PLA) is the first commodity plastic produced from renewable resources. It is an economically feasible material, placed at the forefront of the emerging plastic industries [2,3,4,5]. It is a promising biodegradable and compostable polymer with ease of processability and can evolve harmless natural products by simple hydrolysis [6]. Despite its many advantages, it has a relatively low toughness and a narrow processing window, which restrict its widespread applications in the area of structural components and packaging. The toughness of PLA has been observed to increase to some extents by addition of natural fibers [7]. The EFB fiber has potential to yield up to 73% fibers [8] and is preferable in terms of availability and cost for composite fabrication. However, natural fibers have some drawbacks, because they are known to consist of different natural substances such as cellulose, hemicelluloses, lignin, pectin and waxes. Since empty fruit bunch (FFB) fiber is a natural fiber, it consists of these ingredients that play adverse roles to interact fibers well with polymer matrix [9]. Therefore, removal of these components from EFB fibers has been an essential interest of scientific research. In this respect, a useful approach for lowering these components from fibers has been performed by alkali treatment [10]. The notable other methods used by numerous researchers to improve polymer fiber adhesion are radio frequency, microwave energy, infrared heating and ultrasound treatments [11]. Of these, use of ultrasonic energy is noteworthy, because ultrasound causes cavitation, which is generally considered as a significant post-indicator of modifying fibers surface. In spite of following individual treatment either by alkali or by ultrasound in water, the present research have been focused on simultaneous alkaline and ultrasound treatments of fibers for developing EFB/PLA-based materials in order to observe the effects of treatment parameters on their viscoelastic and melt flow properties.

MATERIALS AND METHODS

Materials

Poly(lactic acid) thermoplastic resin used in this study was a product of Nature Works® PLA, 2002D, Germany with melt index of 5-7 g/10 min at a temperature210°C and specific gravity of 1.24, derived from renewable resources. Oil palm empty fruit bunch (EFB) fibers were obtained from FELDA Palm Oil refinery, Pahang, Malaysia. Other important chemicals used in this work were sodium hydroxide (NaOH) and acetic acid of Merck, Germany.

Methods

Fibers treatments and composites fabrication

Raw EFB fibers contained several impurities which were washed out with water-flow, and the washed EFB fibers were dried under sun light. The dried fibers were chopped into short fiber in random size of 5 -10 mm. During composites fabrication, 10, 20, 30, and 40 wt% EFB fiber contents were compounded with PLA by a twin screw extruder (Thermo Scientific Prism Eurolab-16, Germany). The extrudates were pelletized and dried at 80°C for overnight. Tests samples were prepared by a BOY15-S, Germany injection molding machine.

Mechanical properties as examined by the tensile test was found to be the highest for composites with 30 wt% EFB fibers, which were considered as the optimized fiber contents in the present study. The EFB fibers were then subject to ultrasonic treatments, using a Daihan Ultrasonic bath, separately in water and alkaline media. Ultrasound treatment of EFB fibers was carried out in water medium at 30°C for 30 min, this treatment was performed in 3 wt% NaOH solutions with 80°C temperature and 90 min exposing time as well as with weight ratio for EFB and NaOH of 1:10. For uniform agitation, vibration of the bath was set at resonance condition. After treatments, fibers were washed thoroughly with water-flow to remove alkali solution from the fiber surface and subsequently neutralized to p^H 7 with a few drops of acetic acid solution and then dried in an oven at 70° C. These EFB fibers were loaded in PLA to fabricate composites. Thus, the samples prepared for subsequent studies were raw EFB (REFB) fibers, ultrasound-water treated EFB (UEFB) fibers, ultrasound-alkali treated EFB (UAEFB) fibers, a virgin PLA (PLA), REFB-fibers reinforced PLA composites (REPC), UEFB-fibers reinforced PLA composites (UEPC) and UAEFB-fibers reinforced PLA composites (UAEPC).

Melt Flow Index (MFI)

The melt flow index (MFI) measurement was carried out using a Dynisco MFI2 melt flow indexer following ASTM D1238 with an applied load of 2.16 kg at 210^{0}C. Three independent tests were carried out on each sample.

Tensile testing of composites

Tensile testing was conducted according to ASTM 638-08, using a Shemadzu Universal tensile testing machine fitted with a 5 kN load and operated at a cross-head speed of 10 mm/min. Five samples of each category were tested for tensile strength (*TS*) and tensile modulus (*TM*) measurements, keeping 65 mm gauge length.

Impact testing

The impact testing was carried out according to the EN ISO 179 by a Ray-Ran Pendulum Charpy Impact System. The impact velocity was 2.9 m/s with hammer weight of 0.475 kg. Dimensions of the samples were 80mm × 8mm × 3.5 mm with a single notch of 0.25 mm. Five replicates were evaluated for each type of samples to obtain impact strength (*IS*).

Scanning electron microscopy (SEM)

Composites fracture surfaces were investigated by using a (ZEISS, EVO50, Germany) scanning electron microscope. Samples were mounted with carbon tape on aluminium stubs and then sputter coated with platinum to make them conductive prior to SEM observation.

Thermogravimetric analysis (TGA)

Thermogravimetric measurements were performed by a TGA Q500 V6.4, Germany in a platinum crucible under nitrogen atmosphere (flow rate 60 ml/min) with a heating rate of 20°C /min. The temperature range was scanned from 25 to 600° C.

RESULTS AND DISCUSSION

Mechanical Properties

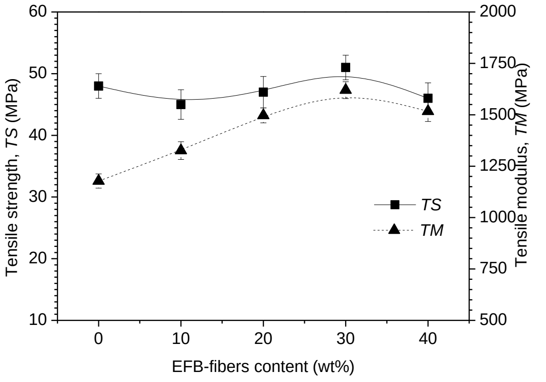

Fig.1: Tensile strength and tensile modulus as a function of REFB content in REPC

The variation of *TS* and *TM* with respect to REFB fibers content is plotted in Fig. 1, where the 30 wt% EFB fibers reinforced PLA composite exhibits the highest mechanical properties among all others. Considering optimized fiber content in the composites, fibers were subjected to treatments in 3 wt% alkali solution for 90 minute exposing time and 80°C temperatures. The change of *TS*, *TM* of treated EFB fibers incorporated PLA composites is shown in Fig. 2, along with *IS* as represented in Fig. 3.It is found that the maximum *TS TM* and *IS* values are obtained in case of UAEPC.

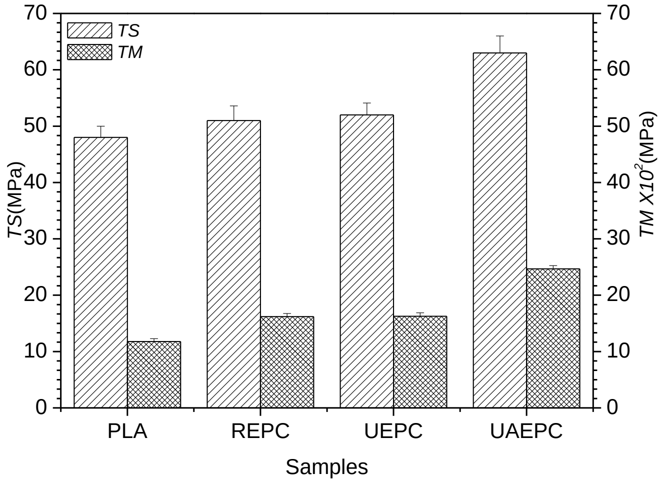

Fig. 2: Tensile strength and tensile modulus of PLA and different EFB/PLA composites

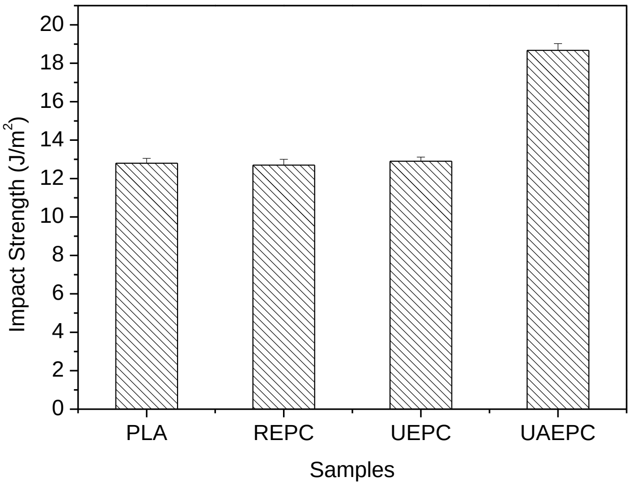

Fig. 3: Impact strength of PLA and different EFB/PLA composites

This better performance of the resulting composites can be attributed to the increased compatibility between EFB fibers and PLA because of the modification of EFB fibers surface by alkali treatments in ultrasonic bath. On the other hand, the increase of *TS* and *TM* in the composites merely for the inclusion of REFB fibers content may be assigned to the strong *TS* and *TM* values of the individual EFB fiber [12]. However, when EFB fiber content is greater than 30 wt%, the composites become inhomogeneous because of the fiber-fiber interaction whose effect may cause to develop fiber-agglomeration in the composites, as reported elsewhere [13].

Surface morphology

The fracture surface morphology of the fibres reinforced PLA composites is presented in Fig. 4, where fiber-fracture and holes are highlighted with circles and arrows. Noticeable fibers seem to be pulled out from the matrix, and holes or gaps are formed in between the fibres and the PLA matrix, as shown. These results could be due to either de-bonding during tensile testing or poor adhesion. Poor adhesion is a result of the presence of wax, pectin and other impurities in the surface of untreated fibres. Fibre fracture and fiber pull-out are supposed to be good indicators of stress transfer from the matrix to the fibres. In case of UAEPC, fibres are found to be fractured rather than pulled out. Thus, the stress is transformed from the matrix to fibres efficiently when the load is applied, suggesting good adhesion in between these fibres and matrix. These observations suggest a relatively poor interfacial adhesion in the REPC composites when compared with the other treated fibre/PLA composites.

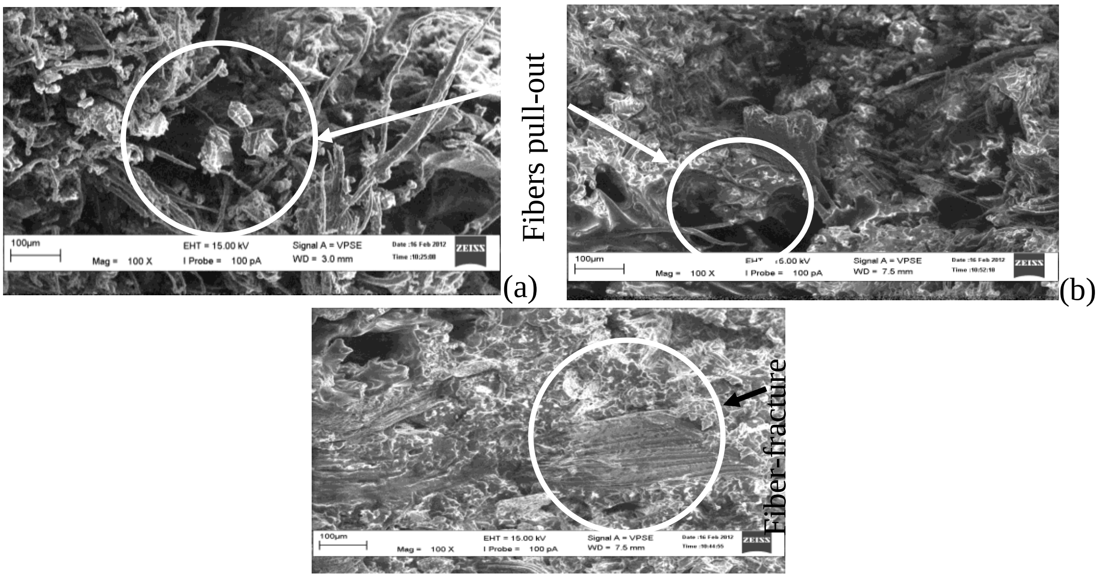

(a)

(b)

(c)

Fig. 4: SEM micrographs of (a) REPC, (b) UEPC and (c) UAEPC

Melt flow index

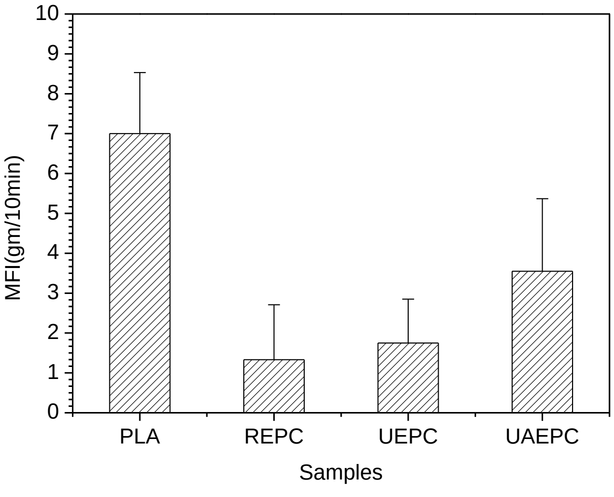

Fig. 5: Melt flow index of PLA and different EFB/PLA composites

The melt flow behavior of fibres reinforced PLA composites is presented in Fig. 5. It is found that *MFI* value of UAEPC is the maximum compared to those of other composites. This better flow behavior of the UAEPC can be considered as good dispersion of fibers into matrix as well as increased compatibility between EFB fibers and PLA due to removal of noncellulosic components of EFB fibers with ultrasonic treatment in presence of alkali solution.

Thermogravimetric analysis

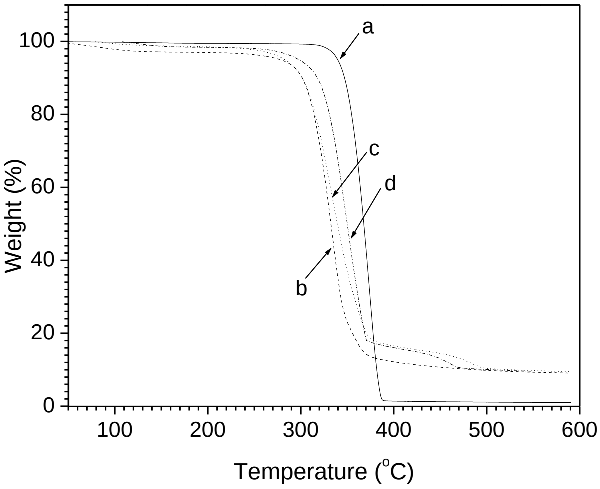

Fig. 6: TGA thermograms of **(**a) PLA, (b) REPC, (c) UEPC and (d) UAEPC

Fig. 6 illustrates the thermal degradation of the samples investigated in a temperature range of 50–550 °C. TGA generally involves the release of absorbed water (if any) from a sample, the “onset” of degradation of molecules in the sample, the steps of degradation and the presence of residual char. The thermal degradation of neat PLA takes place in one step in which the onset of weight-loss occurs at about 330°C and finishes at 390°C. On the other hand, this degradation in composites commences at relatively lower temperature than that found in PLA. The TGA traces of composites seem to fall at 100°C, indicating the emission of absorbed moisture. Besides, the TGA sharp-fall, which occurs at 289°C for composites look quite distinct from that for PLA, showing a two-step process in the temperature ranges of 275-375°C and 375-484°C. This may be connected to the decomposition behavior of the molecules of EFB fibers in the differently treated composites. The degradation of natural fiber has been ascribed by the dissociation of C−C chain bonds along with H–abstraction at the site of dissociation [14].

CONCLUSIONS

Studies on optimization of EFB fiber content in fabrication of biodegradable PLA composites have been performed by means of mechanical test. Optimized EFB fibers thus obtained were treated with ultrasonic method in presence of alkali solution. The highest mechanical performances has been shown by the EFB fibers when their content in the composites is 30 wt%, and their treatment parameters such as concentration, time and temperature are 3wt%, 90 min and 60°C, respectively. The melt flow index of the composites has also been found to improve by the aforesaid treatment procedure. All these results strongly indicate a significant enhancement of materials properties by ultrasound and alkali treatment of EFB fibers. SEM analysis has confirmed increased compatibility between PLA and treated EFB fibers.

REFERENCES

1. John MJ and Thomas S (2008), 'Biofibers and biocomposites', *Carbohydrate Polymer,* 71, 343–364.

2. Mohanty AK, Misra M and Drzal LT (2005), 'Natural fibers, biopolymers, and biocomposites' Taylor and Francis: CRC press.

3. Sinha Ray S and Okamoto M (2003), 'Biodegradable polylactide and its nanocomposites: opening a new dimension for plastics and composites', *Macromol Rapid Commun,* 24,815–40.

4. Solarski S, Ferreira M and Devaux E. (2005), 'Characterization of the thermal properties of PLA fibers by modulated differential scanning calorimetry', *Polymer,* 46,11187–92.

5. Sawpan MA, Pickering KL and Fernyhough A (2009), 'Characterisation of hemp fibre reinforced poly(lactic acid) composites', *Int J Mater Product Technol,* 36:229–40.

6. Donald Garlotta (2001), 'A Literature review of poly (lactic acid)', *Journal of Polymers and the Environment*, 9(2): 63-84.

7. Cai H, Dave V, Gross RA and McCarthy SP (1996), 'Effects of physical aging, crystallinity, and orientation on the enzymatic degradation of poly(lactic acid)', *Journal of Polymer Science, Part B: Polymer Physics,* 34, 2701.

8. Wirjosentono B, Guritno P, and Ismail H (2004), 'Oil palm empty fruit bunch filled polypropylene composites', *Inernational Journal of Polymer Materials,* 53, 295–306.

9. Shibata M, Ozawa K, Teramoto N, Yosomiya R and Takeishi H (2003), 'Biocomposites made from short abaca fiber and biodegradable polyesters'. *Macromolecular Materials and Engineering,* 288: 35.

10. Islam MS, Pickering KL and Foreman NJ (2010), 'Influence of alkali treatment on the interfacial and physico-mechanical properties of industrial hemp fibre reinforced polylactic acid composites', *Composites: Part A,* 41, 596–603.

11. Thakore KA, Smith CB and Clapp TG (1990), 'Application of ultrasound to textile wet processing', *Am. Dyestuff Rep,* 79(10), 32-38.

12. Shinji Ochi (2008), 'Mechanical properties of kenaf fibers and kenaf/PLA composites', *Mechanics of Materials,* 40, 446–452.

13. Joseph S, Joseph K and Thomas S (2006), 'Green composites from natural rubber and oil palm fiber: physical and mechanical properties', *International Journal of Polymer Materials,* 55, 925–945.

14. Joseph PV, Joseph K, Thomas Pillai CKS, Prasad VS, Groeninckx G and Sarkissova M (2003), 'The thermal and crystallization studies of short sisal fiber reinforced polypropylene composite', *Composite: Part A,* 34(3), 253-266.

EFFECTS OF ENZYMATIC FIBRE TREATMENT ON KENAF FIBRE REINFORCED RECYCLED POLYPROPYLENE COMPOSITES

M.R. Islam, M.D.H. Beg* and A. Gupta

Faculty of Chemical and Natural Resources Engineering, Universiti Malaysia Pahang,
26300 Gambang, Kuantan, Malaysia.
**Corresponding author: dhbeg@yahoo.com, Phone: +6095492816, Fax: +6095492889*

ABSTRACT: In this work, environmentally friendly enzymatic pre-treatment of fibre to improve the interfacial bonding and adhesion between fibre and matrix were carried out for kenaf fibre reinforced recycled polypropylene (RPP) composites. Composites were produced using twin screw extruder followed by injection moulding. Maleic anhydride grafted polypropylene (MAPP) was used as coupling agent in the blend. Fibre tensile property, density and morphological changes due to treatment were compared with untreated fibre and effects of those properties on composites properties were analyzed. Composites were characterized by various mechanical tests such as tensile and flexural testing. It was found that, TS of composites increased by 40% due to enzyme treatment of fibre. Processability of composites was studied by measuring melt flow index (MFI). It was found that by increasing the fibre volume, increased shear stress and torque during extrusion and moulding, as a result 40% fibre was found to be optimum loading. Thermal stability was analyzed through thermogravimetric analysis (TGA). Activation energy was calculated from TGA analysis using Broido's equation. It was found that enzymatic treatment increased the activation energies of the composites at the second stage of degradation. To understand any morphological changes due to treatment and reactive processing of the materials, scanning electron microscope (SEM) were examined. Environmental stability of composites was studied by measuring water absorption for different time intervals.

KEYWORDS: Composites, kenaf fibre, Laccase enzyme, activation energy.

INTRODUCTION

Cellulose based natural fibres like henequen, sisal, coconut fibre (coir), jute, palm, bamboo, wood, paper etc. have been used as reinforcing agents in the thermoplastic and thermosetting polymer matrices [1]. Previous research revealed that, fibre loading increased composites' strength up to a certain limit and coupling agent enhanced the mechanical properties of the composites [2]. Natural fibres are polar in nature, whereas polymer matrices are non-polar and due to that a very low compatibility has found between fibre and matrices [3]. Interactions between the anhydride groups of maleated coupling agents and the hydroxyl groups of natural fibres can overcome the incompatibility problem and increase tensile and flexural strengths of natural fibre thermoplastic composites [4]. Except using coupling agent, fibre surface modification or treatment are also in practice. Natural fibre treatments by means of the enzyme are now drawing attention to the researchers as the treatments include cost reduction, energy and water saving, improved product quality and potential process integration [5]. According to Bledzki, a major reason for embracing this technology is the fact that application of the enzyme is regard as environmental friendly and the reactions catalysed are very specific with a focussed performance as a consequence [6].

However, enzymatic treatment of fibre were used in this study to find the alternative way of treatment as environment friendly and quick process. Addition to the flow behaviour of the composites, various mechanical and thermal analyses with morphological observations were also carried out to characterize the kenaf/RPP composites in this study.

EXPERIMENTAL

Materials

Kenaf fibre and recycled polypropylene

Kenaf fibre was supplied by a local company, Kampung Merchong, Endau Rompin, Pekan, Pahang, Malaysia. Recycled polypropylene (RPP) was chosen as the polymer matrix for this experiment. Recycled polypropylene, which was recycled mainly from waste based vehicle battery cases and car bumpers which is commercially available as PP Black copo supplied by Efficient Growth Sdn. Bhd., Selangor, Malaysia.

Coupling agent

Maleic anhydride grafted polypropylene (MAPP), a very common type of coupling agent was chosen for this experiment and supplied by MTBE (M) Sdn. Bhd., Gebeng, Kuantan, Pahang.

Methods

Fibre treatment through laccase enzyme

Kenaf fibres were treated by laccase enzyme solution of enzyme activity 80 U/ml for 4hrs of soaking time. Weak acetic acid was used to control the p^H of the solution at 5.5. After that, fibre was washed by tape water until p^H reached 7. Fibre was air dried for 1 day and then put in an oven at 70 ^oC for another day.

Preparation of the composites

Air dried kenaf fibre was shredded into small size (2 to 5 mm) by a plastic crusher. Shredded fibre was dried at 70 ^oC in an oven until reached the moisture content below 5%. Both untreated and treated fibre were individually compounded into RPP with and without coupling agent by means of a Prism Eurolab 16 twin-screw compounder having barrel temperatures from 170 ^oC to 190 ^oC from the feeding zone to the die zone, respectively. The fibre to coupling agent ratio was 10:1. The incorporated fibre contents in composites were

40% (by weight). The compounded samples were prepared into test specimens by injection moulder using NESSEI injection molding machine model- PNX60 machine.

SEM analysis

The morphological structure of kenaf fibres and kenaf-RPP composites were analyzed by using a scanning electron microscope (model-ZEISS, EVO 50). The samples were air dried before testing. Prior to SEM observation, samples were coated with gold with the help of vacuum sputter-coater for ease of conduction. The coated sample was then taken for microscopy, operated at 300 kV. The microstructures of materials were compared by observing the fractured surfaces of the composites.

TGA analysis

TGA measurements were carried out using thermogravimetric analyzer (TA instrument, TGA Q500). Each specimen was weighed about 5 ± 2 mg and analyzed at scanning temperature range of 25 – 600 ^{o}C and heating rate of 20 ^{0}C/min. TGA was conducted with the compounds placed in a platinum crucible under nitrogen atmosphere at a flow rate of 40 ml/min to avoid unwanted oxidation. Kinetic parameters for the thermal degradation were determined from the TGA graphs using the following equation (Eqn 1), given by Broido [7]:

$$\ln\left(ln\frac{1}{y}\right) = -\frac{E_a}{RT} + \ln\left(\frac{RZ}{E_a\beta}T_{max}^2\right) \tag{1}$$

Where,
y = Fraction of non volatilized material not yet decomposed,
T_{max} = Temperature of maximum reaction rate (^{o}C),
β= Heating rate (^{o}C/min),
Z= Frequency factor,
E_a= Activation energy (J/mol),
R= Gas constant (8.314 J/mol.K).

From the TGA data, the values of y have been taken, and calculated values of lnln (1/y) and was plotted in Y axis, whereas temperatures as 1/T in Kelvin scale were plotted in X axis. Finally from the slope of the trend line the activation energy of the composite has been calculated.

MFI measurement

The MFI was determined by using melt flow index tester (Dynisco Instrument) with sample weight approximately about 5 to 8 g at 230 ^{o}C and with a standard weight of 2.16 kg.

Density measurement

A gas pycnometer (model-micromeritics, AccuPyc II 1340) was used to determine the volume of the materials in order to calculate the density of the materials. Approximately 2 to 3 g of each material was measured by using a digital balance machine up to four decimal. Five replicates of analysis were considered for each category of sample, and an average value was taken for data analysis.

Tensile properties measurement

The tensile tests were carried out according to ASTM D638-Type I using SHIMADZU (MODEL AG-1) universal testing machine with load cell of 5 kN, using crosshead speed of 10 mm/min and with a gauge length of 65 mm. Eight specimens were tested, and at least five specimens were presented as an average of tested specimens.

Flexural properties analysis

The flexural test was conducted according to ASTM D790-97 standard using Universal Testing Machine (model- SHIMADZU, AG-1) with static load cell of 1 kN. The support was set at 50 mm, and the crosshead speed was fixed at 10 mm/min. Eight specimens were tested, and at least five specimens were presented as an average of tested specimens.

RESULTS AND DISCUSSION

MFI of the composites

The MFI of the composites are presented in Table 1. RPP itself shows a MFI of 5.58 g/10 min, whereas untreated fibre based composites showed 0.40 g/10 min. The MFI of RPP/Kenaf composite based on untreated fibre in the presence of coupling agent was found to be at 0.33 g/10 min, Enzyme treated kenaf fibre reinforced RPP composites show a MFI of 0.22 g/10min. More hydroxyl groups are exposed due to enzymatic treatment reacts with polymer matrix in the presence of MAPP. This strong chemical bonding may reduce the flow of the melt, which results in a low MFI. Treatment of fibre in the presence of coupling agent enhances the viscosity, which further decreases the flow rate.

Table 1: Density, MFI, FS and FM of the composites

Formulation	Density (g/cm^3)	MFI (g/10 min)	FS	FM
RPP	0.91	5.58	13.98	133
kenaf(raw)+RPP	1.07	0.40	27.72	409
kenaf(raw)+RPP+MAPP	1.12	0.33	32.09	759
kenaf(enzyme treated)+RPP+MAPP	1.10	0.22	33.9	806

Densities of the composites

The densities of the composites are presented in Table 1. The density for the case of laccase enzyme treated composites is found to be 1.10 g/cc, whereas composite with untreated fibre in the presence of coupling agent is 1.12 g/cc.

Tensile properties of the composites

Fig. 1 shows the analysis of tensile strength (TS) and tensile modulus (TM) of RPP, untreated and treated fibre based composites with coupling agent. Data analysis reveals that, TS value of composites with untreated fibre with coupling agent show TS of 25.17 MPa, whereas enzyme treatment showed TS of 25.77 Mpa. Enzyme treatment with coupling agent improves TS by 40%. On the other hand, TM was found to be 1078 MPa for the case of enzyme treated fibre based composites.

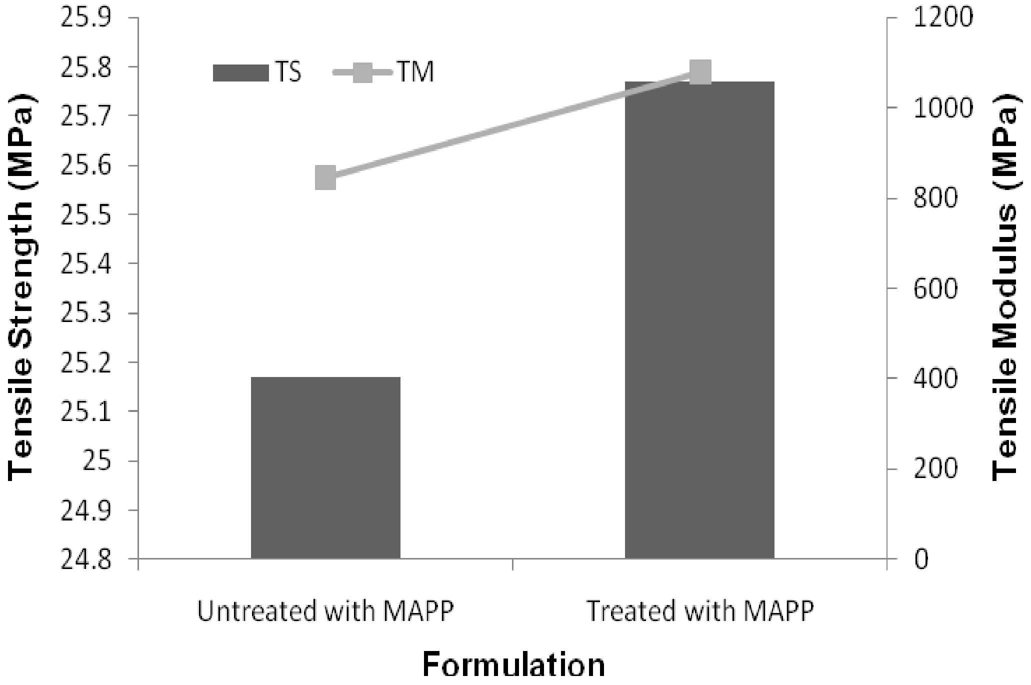

Fig. 1: TS and TM of RPP and composites based on untreated and treated fibres with coupling agent at various percentages of fibre loading.

Flexural properties of the composites

Flexural strength (FS) and flexural modulus (FM) of kenaf/RPP composites are presented in Table 1. It is found that fibre loading (40%) increases FS from 13.98 to 27.72 MPa and FM from 133 to 409 MPa, respectively. Furthermore, FS and FM increase from 27.72 to 32.09 MPa and from 409 to 759 MPa, respectively in the presence of coupling agent for the case of untreated fibre based composites. Incorporation of fibre usually increases the stiffness of the resultant composites. Enzyme treated fibre based composites show FS and FM of 33.09 and 806 MPa. The anhydride group of MAPP reacts with hydroxyl groups of natural fibre, whereas its PP part is adhered to the polymer matrix resulting in better coupling and chemical bonds in between fibre and matrix. Thus, strong chemical bonding due to the presence of coupling agent resist the higher bending force as a result of increased FS and FM.

Thermogravimetric analysis of the composites

Thermal properties of the RPP, composite with untreated fibres and composite with untreated and treated fibre in the presence of coupling agent are shown in Table 2. It can be seen that use of fibre makes the composites degrade at two stages [10], whereas RPP degrades at only one stage. Using MAPP does not show any significant improvement regarding thermal stability. The residues were found to be increasing with the fibre loading. It is found that, the activation energies of the composites at the first stage of degradation are almost 44 kJ/mol, and in the second stage, it is decreasing with higher fibre loading. The first stage of degradation is only due to fibre which has lower thermal stability than the matrix and found the activation energy is not affected much due to fibre content, which is also reported by [10]. Increased fibre volume fraction as a result of decreased activation energy has been found in the second stage of degradation [10]. This may be due to the reason of diffusion of fibres at higher loading in the composites. Enzyme treated fibre based composites in the presence of coupling agent is found to improve the activation energies at the second stages of degradation.

Table 2**:** Thermal properties of the composites

Formulation	**Stage**	**Temperature range (^oC)**	**T_{max} (^oC)**	**Activation energies (kJ/ mol)**	**Residue (wt %)**
RPP	1st	267-472	420	99.41	7.58
40%kenaf(raw)+RPP	1st	221-391	365	44.37	12.34
	2nd	392-501	473	67.44	
kenaf(raw)+RPP+MAPP	1st	247-381	351	50.90	12.43
	2nd	406-502	477	61.75	
kenaf(enzyme treated) + RPP + MAPP	1st	229-379	343	46.28	11.88
	2nd	389-501	470	87.71	

SEM of the composites

SEM micrographs for the composites based on untreated and treated fibre are shown in Fig. 2. SEM examination of fractured surfaces for the case of untreated and untreated/coupled based composite revealed poor interfacial bonding as compared to treated/coupled based ones. Micrographs indicate fibre pull-out, debonding and delimitation comparatively high for the case of untreated based one (Fig. 2-a & 2-b). In the Fig. 2-a & 2-b, the presence of voids, as shown may create stress concentrations which in turn reduce the strength of the samples. Evidence of good interfacial adhesion between the fibre surface and the matrix (Fig. 2-c) for the case of using treated fibre with coupling agent is shown.

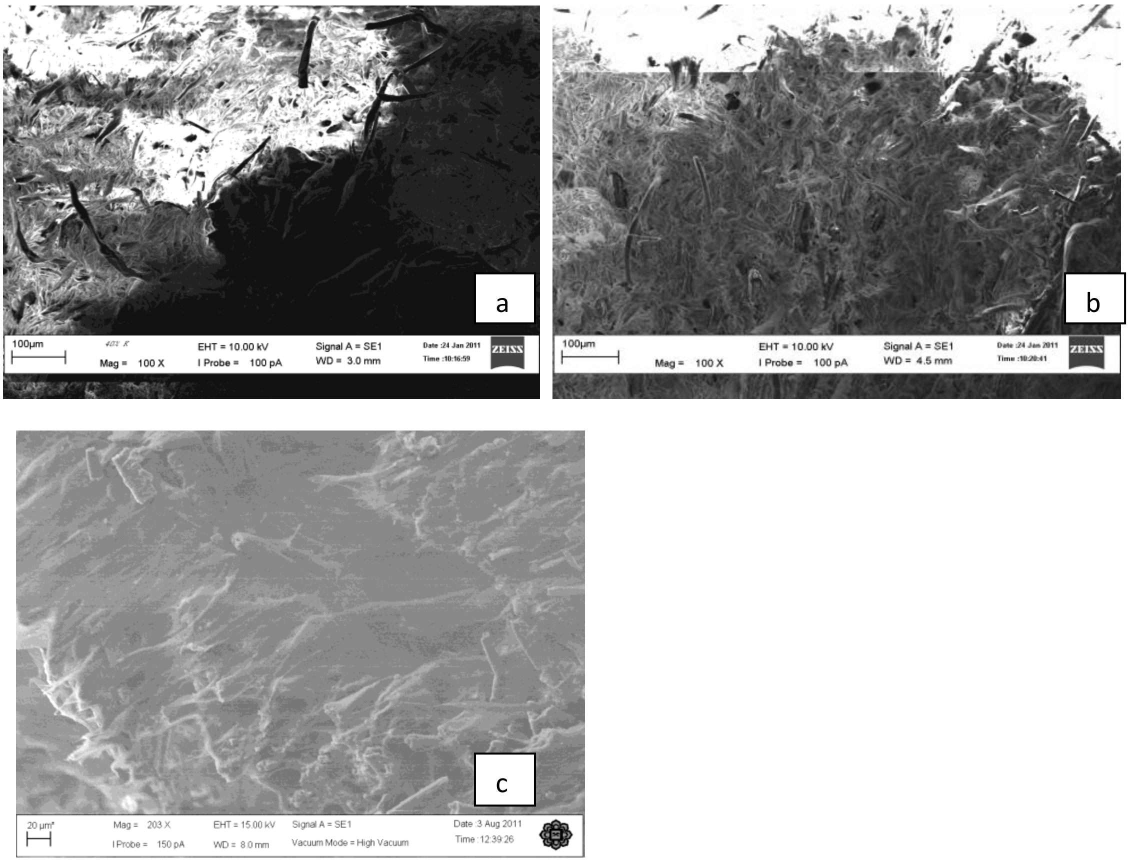

Fig. 2: SEM observations of the fractured surfaces of composites based on untreated (a), untreated –coupled (b) and enzyme (c) treated formulation.

CONCLUSION

Incorporation of fibre increases 18% of TS of the composites than from RPP. After that, MAPP was introduced as a coupling agent with the untreated fibre. Then TS is increased by 37%. TS is found to be 25.77 MPa, which is almost 40% higher than that of untreated/uncouple formulation based composite. Thus, strong chemical bonding may results good interfacial adhesion. MFI decreases at a greater extend, whereas density increases for the case of treated/coupled based composite. Melt flow index shows a negative trend with the incorporation of fibre and addition of coupling agent. Treatment of fibres enhances the thermal stability as well as activation energy of the composites in the presence of coupling agent. Degradation of composites is found to occur at two stages, while recycled polypropylene at one stage.

ACKNOWLEDGEMENTS: University of Malaysia is highly acknowledged for providing fund through PRGS RDU100339 for this project.

REFERENCES

1. P.J Herrera-Franco, A Valadez-González. Mechanical properties of continuous natural fibre-reinforced polymer composites. Composites *Part A: Applied Science and Manufacturing*, *Volume 35, Issue 3, March 2004, Pages 339-345.*

2. Suradi, S.S., Younus, R.M. and Beg, M.D.H. 2010. Oil palm bio-fibre-reinforced polypropylene composites: effects of alkali fibre treatment and coupling agent. *Journal of composites materials*, DOI: 10.1177/0021998310387686.

3. Bledzki A. K., Gassan, J. and Theis, S. 1998. Wood-filled thermoplastic composites. *Mech Compos Mater*. **34**: 563–8.

4. Keener, T.J, Stuart, R.K, Brown, T.K. 2004. Maleated coupling agents for natural fibre composites. *Composites Part A: Applied Science and Manufacturing*. **35**(3): 357-362.

5. Aehle, W. 2004. *Enzyme in industry: production and application, ''industrial enzymes*". Weinheim: Wiley-VCH verlag.

6. Bledzki, Andrzej K., Mamun, Abdullah A., Jaszkiewicz, Adam and Erdmann Karsten. 2010. Polypropylene composites with enzyme modified abaca fibre. *Composites Science and Technology*. 70(5): 854-860.

7. Broido, A. (1969). A simple, sensitive graphical method of treating thermogravimetric analysis data. *Journal of Polymer Science* Part A-2, 7: 1761.

8. Jarukumjorn K and Suppakarn N. 2009. Effect of glass fibre hybridization of sisal fibre-polypropylene composites. *Composite: Part B.* 40(7): 623-627.

THE MANUFACTURE AND MECHANICAL PROPERTIES OF ALIGNED LONG HARAKEKE FIBRE REINFORCED EPOXY COMPOSITES

Tan Le [1] and K.L. Pickering [2]

[1, 2] School of Engineering, The University of Waikato, Hamilton, New Zealand.
Email: tml14@waikato.ac.nz; klp@waikato.ac.nz

ASTRACT: Aligned long harakeke fibre reinforced epoxy composites were prepared using hand lay-up followed by compression moulding. Densities of harakeke fibre and epoxy resin were determined for the purpose of composite design. The evenness of composites fabricated by two different size moulds was compared. It was found that more even composites were produced when using a small mould than a big mould. In this work, the dependence of tensile and flexural properties of harakeke/epoxy composites on fibre content was also investigated. The results showed that the addition of fibre enhanced tensile properties of epoxy. The tensile strength and Young's modulus increased with the volume fraction of harakeke fibre. The flexural strength and flexural modulus increased as the fibre volume fraction increased up to 0.4. Further addition of fibre did not result in an improvement of composite flexural properties.

KEYWORDS: *harakeke fibre, tensile properties, flexural properties, mould size, fibre volume fraction, epoxy resin, compression moulding.*

INTRODUCTION

Harakeke is the Maori name for the New Zealand native plant commonly known as New Zealand flax. The name "flax" is actually a misnomer here because harakeke is not biologically related to European flax [1]. Long fibre extracted from the harakeke leaves has a long history of use for production of clothes, sacking and rope. Harakeke products used to account for around 20% of the total export income of New Zealand in the early 1920s [1]. Sales decreased during the 20th century due to the presence of synthetic fibres and the expansion of the sisal industry, and the current use of harakeke is confined to crafts [2]. Harakeke fibre has similar properties to sisal – another leaf fibre [1, 2]. While the application of sisal fibre in composites has been reported by a variety of papers [3], harakeke fibre has only been recently studied for composites [1, 2, 4-8]. The specific tensile strength of composites reinforced with aligned long harakeke fibre has been found to be comparable to that of composites reinforced with other plant fibres, while it is poor relative to glass fibre reinforced composites [5]. Other mechanical properties of aligned long harakeke fibre reinforced composites have not been reported. Therefore, further studies should be conducted to show the potential of harakeke fibre for use in composite.

In this work, the uniformity of harakeke/epoxy composites made using two different size moulds was assessed by comparing the coefficient of variation (CVs %) of tensile strength and Young's modulus to find out the optimal mould to use for further research. The tensile and flexural properties of aligned long harakeke reinforced epoxy composites manufactured using the chosen mould with various fibre volume fractions were also evaluated.

EXPERIMENTAL

Materials

Harakeke fibre was obtained from Templeton Flax Mill, Riverton, New Zealand. The fibre bundles were combed manually in a single direction before being cut into the same length to fit the size of compression mould, and then dried at 80^{o}C overnight before composite fabrication.

The matrix was a low viscosity epoxy system comprised of Nuplex resin R180 and Nuplex standard hardener H180 (mixing ratio 5:1 by weight).

Density measurement

Natural fibre density can be measured by one of five methods: (1) diameter and linear density, (2) Archimedes, (3) helium pycnometry, (4) gradient column and (5) liquid pycnometry. Among them, Archimedes using canola oil as an immersion fluid was recommended because it is simple, quick to give the test results and bears lowest cost [9]. Testing was based on ASTM D3800-99 (Standard Test Method for Density of High-Modulus Fibers). Three specimens of harakeke fibre bundles weighing about 1 g were oven dried at 60^{o} C for 72 hours and then placed in a vacuum oven at room temperature for 5 minutes to remove trapped air between fibre cells before testing. The average density was calculated and reported.

The density measurement of cured epoxy resin was based on ASTM 792-00 (Standard Test Methods for Density and Specific Gravity (Relative Density) of Plastics by Displacement). Distilled water was used as an immersion fluid. Densities of five cured epoxy specimens were measured. The average density was calculated and reported.

Composite manufacture

The fabrication of harakeke/epoxy composites was similar to that which has been used to make flax/epoxy composites [10]. Combed and dried fibre was hand laid into simple rectangular moulds which had been covered by a Teflon sheet to form a fibre mat. Six different fibre volume fractions were used (0.1, 0.2, 0.3, 0.4, 0.5 and 0.6) to make composites in two different size moulds (28 x 22 x 0.3 cm^3 and 22 x 15 x 0.3 cm^3). The essential mass of fibre appropriate to each fibre volume fraction is indicated in Table 2. The epoxy resin and hardener were thoroughly mixed in a plastic cup and then degassed in a vacuum oven at room temperature for 10 minutes (longer degassing time may accelerate the curing reaction). The epoxy mixture was poured over the fibre and then was left to soak into the mat for 20 minutes. A wide flat ended metal scraper was used to squeeze out trapped air of the fibre mat. The mould with fibre and resin was degassed in a vacuum environment for 5 minutes to remove trapped air from the resin impregnated fibre mat. A steel plate was then laid on the top of the mould. Finally the mould was place into a compression moulder and then the epoxy soaked fibre mat was pressed until the mould closed and was left for curing for 24 hours. The composite sheet was removed from the mould and post cured for 4 hours in an oven at 80 ^{o}C.

Tensile testing

Composite tensile testing was based on ASTM D 3039 (Standard Test Method for Tensile Properties of Polymer Matrix Composite Materials) using abrasive paper tabs. Six composite specimens with nominal dimensions of 200 x 15 x 3 mm^3 were cut from cured composite sheets using a circular saw. The tensile properties of neat epoxy were measured according to ASTM D 638 - 03 (Standard Test Method for Tensile Properties of Plastics). Six dumbbell-shaped epoxy specimens were cast and cured in a silicone mould for 24 hours and then post cured at 80^{o}C in an oven for 4 hours. All tensile specimens were conditioned at 23^{o} ± 3^{o} C and 50% ± 5% relative humidity for 40 hours and then tested on an Instron-4204 universal testing machine fitted with a 50 kN load cell at a crosshead speed of 5 mm/min. Strain was measured by Instron 2630-112 extensometer with a 50 mm gauge length. The mean value of densities of composites and neat epoxy were calculated and reported.

Flexural testing

Cured composites were cut into six flexural test specimens with nominal dimension of 85 x 12 x 3 mm^3 using a circular saw. The flexural test (three-point bending) was carried out in accordance with ASTM D 790-03 (Standard Test Methods for Flexural Properties of Unreinforced and Reinforced Plastics and Electrical Insulating Materials) on an Instron-4204 fitted with a 5 kN load cell. A support span-to-depth ratio of 16:1 and a crosshead speed of 2 mm/min were used. The average density was calculated and reported.

RESULTS AND DISCUSSION

Harakeke fibre and epoxy densities

The densities of harekeke fibre and cured epoxy matrix are presented in Table.1. Fibre weight fraction, fibre mass and composite densities were calculated and are indicated in the Table 2.

Table 1: Densities of cured epoxy and harakeke fibre

Density (g/cm^3)	Cured epoxy	Harakeke fibre
	1.1575	1.2741

Comparison of composites manufactured by two different size moulds

Coefficients of variation (CVs) of tensile strengths and Young’s modulus were calculated for the composites fabricated by two different mould sizes and are presented in Figs 1 and 2, respectively. It was found that composites made using the big mould possessed higher CVs for both tensile strength and Young’s modulus than those of composites made using the small mould.

This suggests that composites with better uniformity were produced using the smaller mould. The composite unifrormity can be affected by variation of fibre mat thickness crossing the mould. The fibre mat was prepared using hand layup, so the fibre mat thickness was mainly controlled by the worker. Therefore, the variation of fibre mat thickness can be considered as human error which can be less in the case of smaller mould.

Table 2: Composite design for two different size moulds

				Mould size 28 x 22 x 0.3 = 184.8 cm^3		Mould size 22 x 15 x 0.3 = 99 cm^3	
No.	v_f	p_c (g/cm^3)	w_f	m_c (g)	m_f (g)	m_c (g)	m_f (g)
1	0.1	1.17	0.11	216	24	116	13
2	0.2	1.18	0.22	218	47	117	25
3	0.3	1.19	0.32	220	71	118	38
4	0.4	1.20	0.42	223	94	119	50
5	0.5	1.22	0.52	225	118	120	63
6	0.6	1.23	0.62	227	141	122	76

Where, v_f = fibre volume faction; v_m = matrix volume fraction; p_c = composite density; m_c = composite mass; m_f = fibre mass.

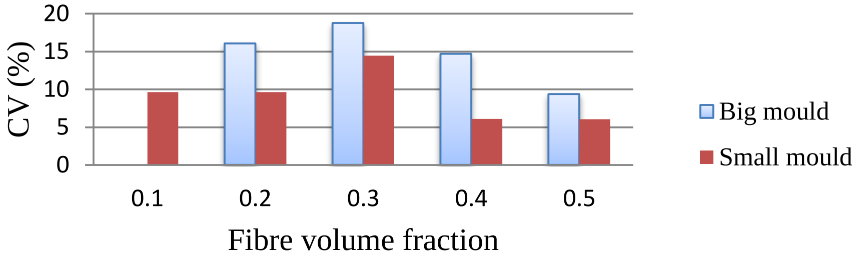

Fig. 1: Tensile strength CV versus fibre volume fraction for uniformity assessment

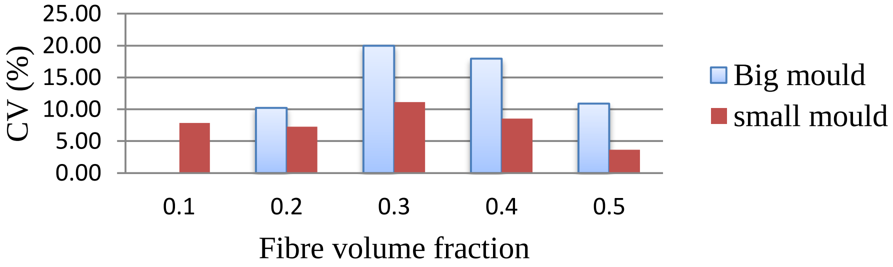

Fig. 2: Young's modulus CV versus fibre volume fraction for uniformity assessment

Tensile properties

Average tensile strength and Young's modulus of composite specimens with different fibre volume fractions (0.1, 0.2, 0.3, 0.4 and 0.5) and cured epoxy specimens were calculated and are presented in Figs 3 and 4, respectively. These figures show that the addition of harakeke fibre makes epoxy matrix stronger and stiffer. Both figures share the same trend such that the increase in fibre volume fraction increases the tensile strength and Young's modulus of composites. A least-squares best fit line was drawn through all data points with presenting a regression equation and high R-square for both the tensile strength and Young's modulus. The high R^2 shows a high correlation between tensile strength and fibre volume fraction.

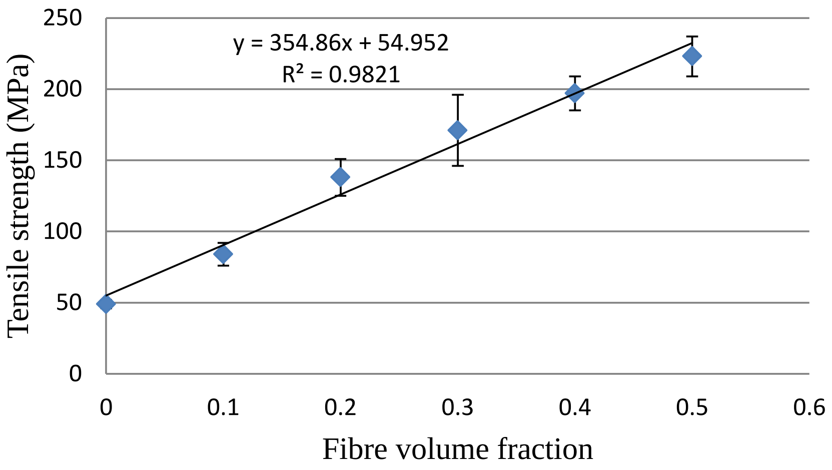

Fig. 3: Tensile strength of harekeke/epoxy composites versus fibre volume fraction showing least-square best fit line and R^2

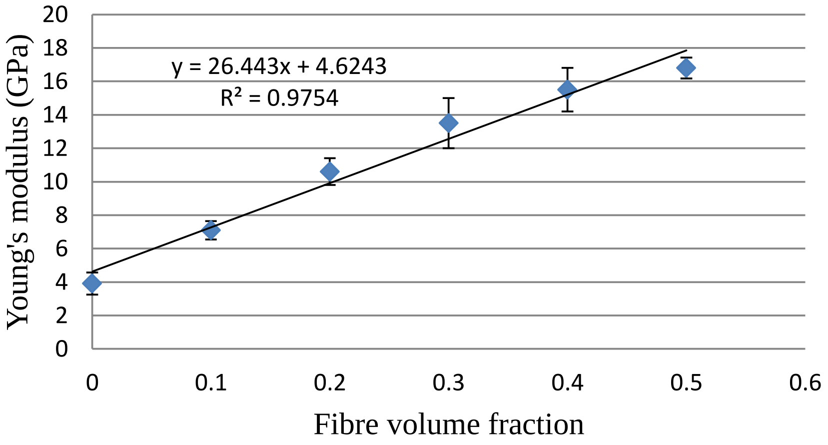

Fig. 4: Young's modulus of harekeke/epoxy composites versus fibre volume fractions showing least-square best fit line and R^2.

Flexural properties

Average flexural strength and flexural modulus of composite specimens with different volume fractions of harakeke fibre (0.1, 0.2, 0.3, 0.4, 0.5 and 0.6) were calculated and are presented in Figs 5 and 6, respectively. It can be seen that the flexural strength and flexural modulus of harakeke/epoxy composites increases as the volume fraction of harakeke fibre increases up to 0.4; at this volume fraction, the flexural strength and flexural modulus of composites are 223MPa and 13.7 GPa. Further addition of harakeke fibre did not bring about improvement of these flexural properties.

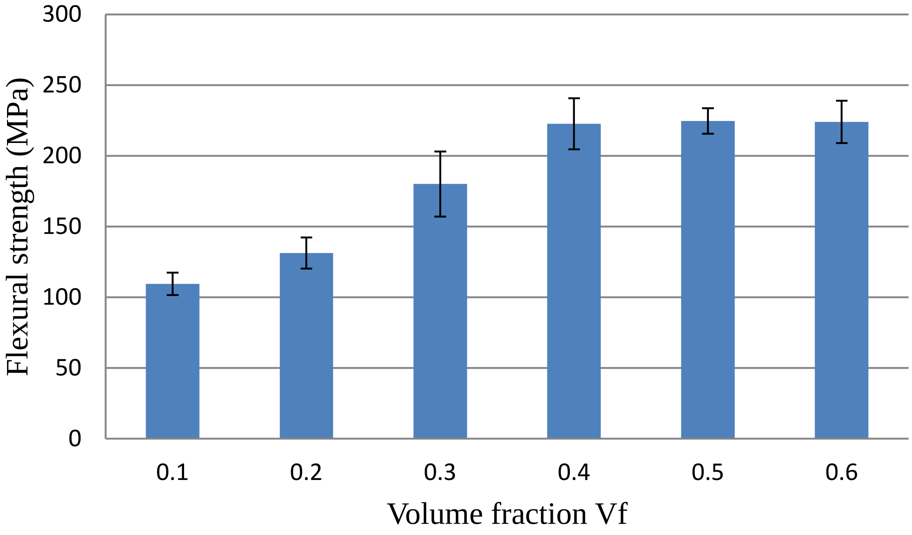

Fig. 5: Flexural strength of harakeke/epoxy composites versus fibre volume fraction.

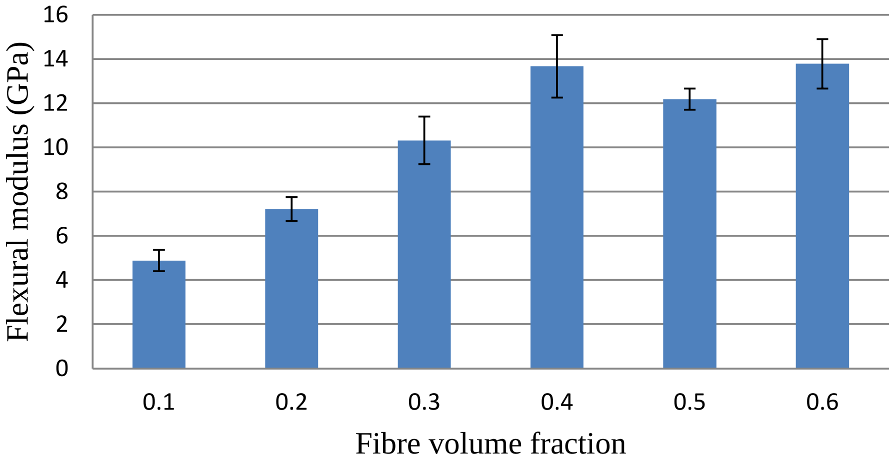

Fig. 6: Flexural modulus of harakeke/epoxy composites versus fibre volume fractions.

CONCLUSION

The uniformity of aligned long harakeke fibre reinforced epoxy composites fabricated using two moulds with different size was compared. The results suggest that the smaller mould creates more uniform composites. It can be due to less human error occurring for smaller mould when the fibre mat is prepared using hand layup.

The addition of aligned long harakeke fibre enhances the tensile strength and Young's modulus of epoxy significantly. These tensile properties increase with volume fraction of harakeke fibre. For flexural properties, it was found that the fibre volume fraction of 0.4 is optimal for aligned long harakeke fibre reinforced epoxy composites with flexural strength of 223MPa and flexural modulus of 13.7 GPa.

REFERENCES

1. Duchemin, B. and M. Staiger, *Treatment of Harakeke fiber for biocomposites.* Journal of Applied Polymer Science, 2009. **112**(5): p. 2710-2715.

2. Newman, R., et al., *Epoxy composites reinforced with deacetylated Phormium tenax leaf fibres.* Composites Part A, 2007. **38**(10): p. 2164-2170.

3. Li, Y., Y. Mai, and L. Ye, *Sisal fibre and its composites: a review of recent developments.* Composites Science and Technology, 2000. **60**(11): p. 2037-2055.

4. Dalu, L., et al., *Acoustic emission monitoring of cyclic flexural tests on phormium/epoxy composites.* E-Journal of Non Distructive Testing, 2009. **14**(2).

5. Newman, R., et al., *Failure mechanisms in composites reinforced with unidirectional Phormium leaf fibre.* Composites Part A, 2009.

6. Duchemin, B., K. Van Luijk, and M. Staiger, *New Zealand flax (Phormium tenax) reinforced eco-composites.* Proc of EcoComp, 2003: p. 1–2.

7. Le Guen MJ and Newman RH, *Pulped Phormium tenax leaf fibres as reinforcement for epoxy composites.* Composites Part A, 2007. **38**(10): p. 2109-2115.

8. De Rosa IM, Santulli C, and Sarasini F, *Mechanical and thermal characterization of epoxy composites reinforced with random and quasi-unidirectional untreated Phormium tenax leaf fibers.* Materials and Design, 2009.

9. Truong, M., et al., *A comparative study on natural fibre density measurement.* The Journal of The Textile Institute, 2009. **100**(6): p. 525-529.

10. Hepworth, D., et al., *The manufacture and mechanical testing of thermosetting natural fibre composites.* Journal of materials science, 2000. **35**(2): p. 293-298.

EFFECT OF COMMON CHEMICAL TREATMENTS ON THE PROCESS KINETICS AND MECHANICAL PROPERTIES OF FLAX/EPOXY COMPOSITES MANUFACTURED BY RESIN INFUSION

Steven Phillips[1], Pei-Yu Kuo[2], Larry Lessard[1], Mohini Sain[2] and Pascal Hubert[1]

[1] *Department of Mechanical Engineering, McGill University, 817 Sherbrooke Street West, Montreal, Canada, H3A 0C3. Corresponding author's e-mail: pascal.hubert@mcgill.ca*
[2] *Faculty of Forestry, University of Toronto, 33 Willcocks Street, Toronto, Canada, M5S 3B3.*

ABSTRACT: The chemical treatment of cellulose-based fibres such as flax is an important step in improving their adhesion with common resin systems in the production of bio-based composites. However, the implications of these treatments on processing behaviour are not yet fully understood. This study investigated the effect of common chemical treatments on the flow and compaction behavior of woven flax fabrics during the resin infusion process. Woven flax fabrics were treated by acetone, alkaline, silane and diluted epoxy based on previously proposed methods. The treated fabrics were then infused with resin during which the evolution of flow front and preform thickness was monitored. The cured laminates were finally subjected to flexural testing, edgewise parallel Charpy impact and void analysis by optical microscopy. The results suggest that the studied chemical treatments increased the effective permeability of the flax fabrics. This was most apparent for the alkaline treatment which showed a 50% increase in effective permeability mostly due to an increase in porosity caused by fibre swelling. The latter observation suggested that the tension in the fibres during alkaline treatment is an important parameter in the context of composite processing. The results from flexural testing demonstrated the negative effect of voids on flexural properties. On the other hand, results from Charpy test revealed no clear trends. For the treatments studied, the diluted epoxy provided the best balance between mechanical properties and process-ability.

KEYWORDS: *flax; permeability; compaction; chemical treatments; mechanical properties*

INTRODUCTION

Flax fibres among other bast fibres have shown good potential in the reinforcement of polymers to produce a class of eco-friendly composite materials. A major drawback of this type of material is their limited strength which has led to a wide body of work in improving the adhesion of cellulose-based fibres with conventional resin systems. Of the several methods proposed, chemical treatment, is the most widely used that has shown improvement in mechanical properties [1]. Although much attention has been given to the influence of these treatments on mechanical properties, little is known about their influence on processing behaviour such as permeability and compaction response. The current paper aims to help fill the gap between these two areas.

Several factors have been shown to influence the wetting behaviour and consequently permeability of cellulose-based reinforcements, including fibre modification such as chemical treatment [2] as well as reinforcement architecture such as yarn length and diameter [3]. This class of fibres has also been observed to exhibit complex behaviour such as swelling and sink effects [4] therefore predicting their behaviour during liquid composite moulding is not straightforward. These phenomenon are just beginning to be fully understood and a recently proposed model by Masoodi *et al* helps to describe these issues [5]. The impact of chemical treatments on permeability and accompanying flow phenomena has received little attention. As a step in addressing this topic, the current study investigated the effect of common chemical treatments on the process kinetics and mechanical properties of flax/epoxy composites manufactured by the resin infusion process.

SAMPLE PREPARATION

Materials

Woven flax fabrics (2x2 twill) with an areal weight of 550 g/m^2 were kindly supplied by Lineo NV. An epoxy resin system with low viscosity and long pot life was selected for the experiments (Araldite LY1564 and Aradur 3486). The viscosity of the resin system was determined in the temperature range of interest by a flow test on a TA AR2000 rheometer equipped with a cone and plate type geometry.

Chemical treatment

Four chemical treatments were selected based on the work of Van de Weyenberg *et al* [1]. All treatments involved a two hour soak in a corresponding solution at room temperature. The first solution was acetone which was intended to remove potential impurities from the as supplied fabrics. The second was a 4% NaOH aqueous solution (alkaline treatment). This treatment was followed by washing with distilled water until a balanced pH level was measured by litmus paper. The third treatment was a 1% silane of type gamma-glycidoxypropyltrimethoxysilane in a solution of 60% ethanol and 40% distilled water (pH between 3.5 and 4). The final treatment was a 3% diluted epoxy in acetone. The epoxy monomer and hardener were first mixed in acetone into which the fabrics were added. Following all treatments, the fabrics were dried for 12 hours at 80 °C in a convection oven. An exception was the diluted epoxy treatment which was dried at ambient conditions.

SAMPLE MANUFACTURING

Experimental Setup

An instrumented tool plate suitable for resin infusion was constructed for the experiments. The setup was attached to a hot plate to accelerate curing of the resin. A pressure transducer (Wika Eco-Tronic) was connected to a resin trap at the outlet to monitor the vacuum pressure. Laser thickness sensors (Banner LG5A65NIQ) were installed at two positions as denoted by L_1 and L_2 in Fig. 1. The flow front was tracked visually at 2 cm intervals. To prevent race tracking, the sides of the preforms were lined with sealant tape.

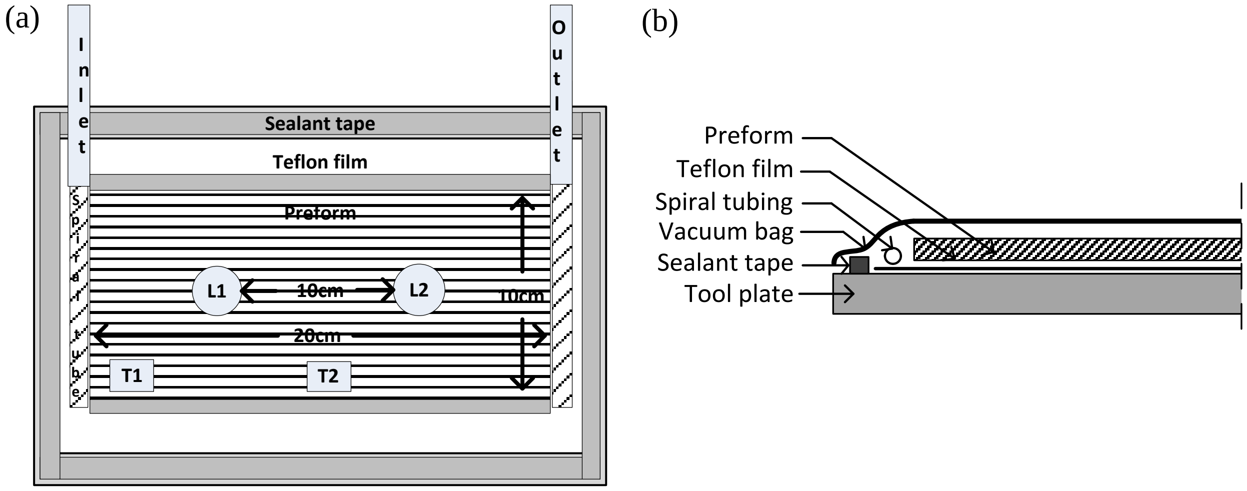

Fig. 1: Schematic of Experimental Setup; (a) Top View and (b) Side View

Experimental Procedure

Each test began with a leak check consisting of detaching the vacuum line and monitoring the pressure in the resin trap. An increase of approximately 0.05 kPa over ten minutes was observed which was deemed acceptable. The dry compaction stage was then recorded (the consolidation rate dictated by the starting capacity of the pump). A one hour de-bulk was then performed to encourage moisture removal. The resin was mixed by hand for 5 minutes and degassed for 30 minutes during this stage. The infusion then took place during which the flow front was tracked and the thickness evolution was monitored. The system was finally held for one hour at ambient conditions to monitor the post-fill stage before starting the heaters at step 7. A cure temperature and time of 50 °C and 12 hours respectively were selected.

Preliminary experiments revealed that the resin tended to de-gas under very low outlet pressures. To alleviate this issue, the resin was degassed at a slightly lower pressure (~0.5kPa) than that which was set during the experiments. Furthermore, two additional post-fill pressures (25 and 50 kPa) were included in the experiments to produce composites of varying void content to study the effect of voids on flexural and Charpy impact properties.

Process kinetics

Dry compaction stage

Representative dry compaction curves are shown in Fig. 2 with the fibre volume fractions before and after compaction in Table 1. The fibre volume fraction was calculated assuming a fibre density of 1.5 g/cm^3 and fabric areal weight of 543 g/ m^2. The latter was measured after drying at 80 °C for 1 hour in a convection oven. The areal weight of the fabrics and fibre density were assumed to be constant for the different treatments. The former was measured at ambient condition and remained relatively constant. However, the dependence of the latter on the treatments was unknown at the time of this writing and will be addressed in future work. The fibre volume fraction before pressure application, shown in Table 1, was taken to be that measured at a compaction pressure of 1.5 kPa. Since the curves were measured following the leak test, they represent the behaviour of the fibre bed after one compaction cycle.

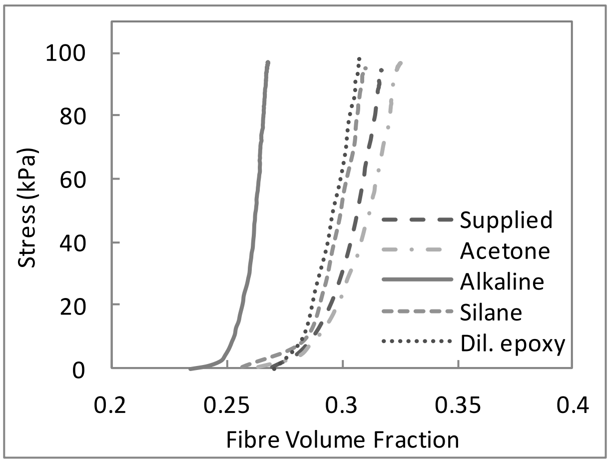

Fig. 2: Representative data from dry compaction stage

Table 1: Fibre volume fraction before and after dry compaction stage

	V_f before (σ=1.5 kPa)	V_f after (σ=97 kPa)
As supplied	27.4 ± 0.6	31.5 ± 0.7
Acetone	27.6 ± 0.8	31.7 ± 1.3
Alkaline	24.4 ± 0.1	26.9 ± 0.4
Silane	27.5 ± 0.4	31.8 ± 0.6
Diluted epoxy	27.5 ± 0.8	30.9 ± 1.0

The results show that the treatments did not generally affect the dry compaction behaviour. An exception, however, was the alkaline treatment which showed a dramatic drop in fibre volume fraction for the applied pressure cycle. This is likely due to the significant amount of swelling which alkaline treatments induce in cellulose fibres. This effect is commonly avoided by tensioning the fabrics during treatment [6]. Thus, it can be concluded that for the purpose of composite processing, the fabric boundary condition during the alkaline treatment plays a key role.

Filling and post-filling stage

The evolution of fibre volume fraction for the as supplied fabrics during the filling and post filling stages are shown in Fig. 3. The behavior was typical of that observed during the resin infusion process. Upon experiencing the flow front, the fabrics underwent a wet relaxation stage, followed by a wet compaction stage after clamping of the outlet. As shown in Fig. 3 (b), the fibre volume fraction tended to decrease with increasing post-fill pressures due to the removal of less resin.

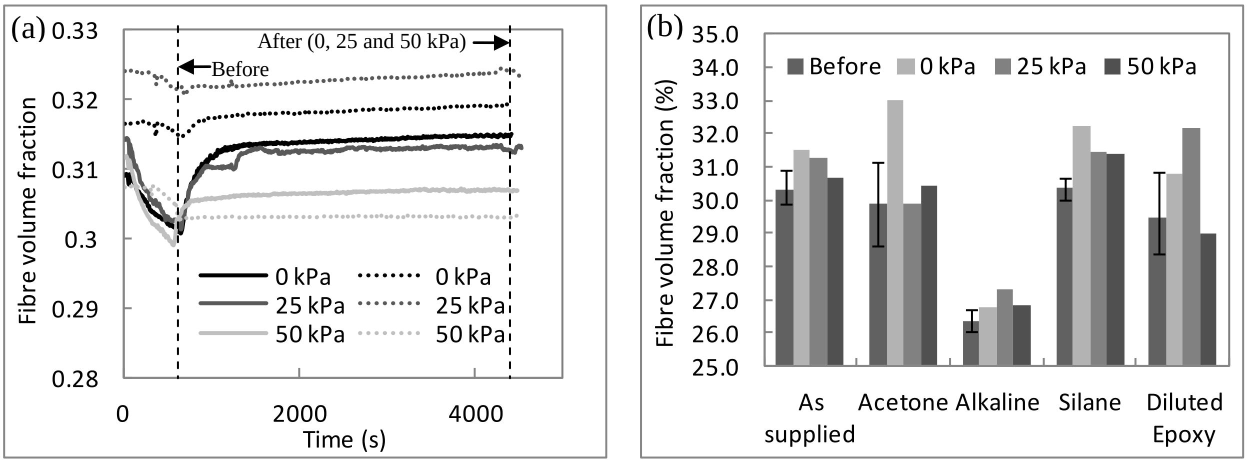

Fig. 3: Filling and post-filling stage fibre volume fraction evolution (a) as supplied fabric (b) before and after post-fill stage

Due to high variability in the fabrics, the difference in behaviour for most of the treatments was not apparent. However, similar to the dry compaction stage, the alkaline treatment clearly exhibited much lower fibre volume fractions. Future testing will include monitoring the resin pressure so that the fibre bed behaviour can be better compared and related to permeability.

Effective permeability

Flow during the resin infusion process is generally described using Darcy's law. A critical parameter in this relationship is permeability. Assuming full saturation behind the flow front, the effective permeability can be derived as:

$$K_{eff} = \frac{m \cdot \Phi \cdot \mu}{2 \cdot \Delta p} \qquad (1)$$

where m is the slope of flow front position squared versus time, Φ is the porosity, μ is the viscosity and Δp is the pressure difference between the inlet and outlet. The effective values for permeability obtained from the experiments are summarized in Fig. 4.

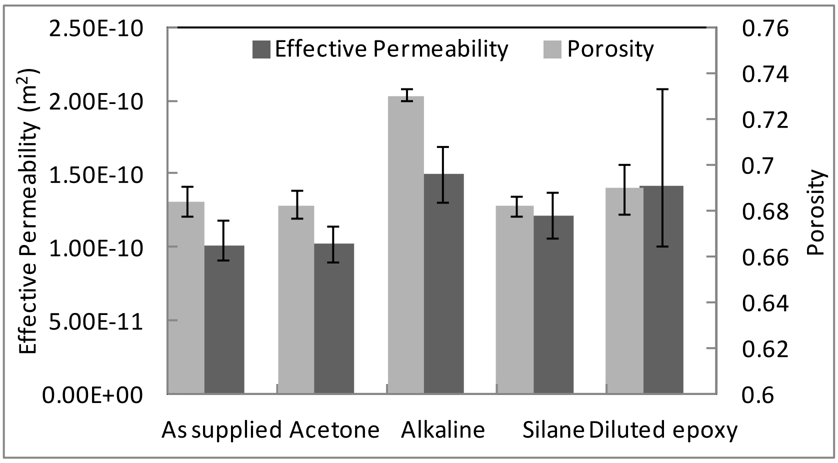

Fig. 4: Effective permeability and porosity during resin infusion process for flax fabrics treated by common surface treatments

The results revealed that the use of chemical treatments resulted in measureable changes in effective permeability. Due to an increase in porosity, this was most apparent for the alkaline treatments. In the case of the silane and diluted epoxy treatments, an increase in permeability was observed for a negligible change in porosity. However, in the case of the diluted epoxy treatment, this was accompanied by a large degree of scatter which was likely a result of non-uniformity of the applied treatment. This was confirmed by visual inspection of the fabrics. Therefore, similar to the alkaline treatment, the method of treatment must be chosen appropriately in order to obtain the desired result.

It should be noted that in computing the effective permeability, the pressure drop along the preform was assumed to be the difference between atmospheric pressure and that in the resin trap. However, due to changes in surface energy and the low pressures involved, it is likely that capillary pressure played a role. Thus, the measured parameters are simply effective permeability values that neglect capillary forces. Similarly, inherent changes in porosity in the resin infusion process as well as swelling effects were neglected and a constant porosity level, equal to that measured just prior to infusion, was assumed. Future work will be focused on measuring the surface energy and swelling changes due to the treatments.

MECHANICAL CHARACTERISATION

Void analysis

Void analysis was carried out by optical microscopy and image analysis on a 5 cm long polished cross section from the center of each laminate. Due to the limited contrast between the voids and the rest of the laminate, the voids were manually filled with black pixels. The void percentage was then determined using a threshold function in the image analysis software, ImageJ. A summary of the measured void contents along with a sample cross-section is given in Fig. 5. The results confirmed that with increasing pressure at the outlet, the degassing effect was minimized and the overall void content tended to decrease.

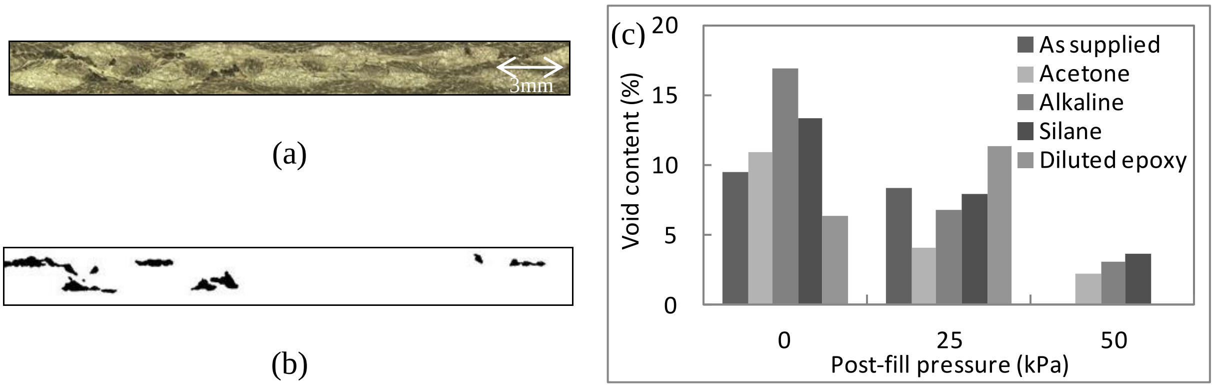

(a)

(b)

Fig. 5: Void analysis results; a) selected cross-section, b) cross-section after thresholding and c) void content versus post-fill pressure

Flexural

Flexural testing was carried out in accordance with ASTM D790 on an MTS Insight load testing machine with a 5 kN load cell. A sample area of 12.7 x 80 mm^2, span of 64mm and loading rate of 2 mm/min were selected. The results are summarized in Fig. 6.

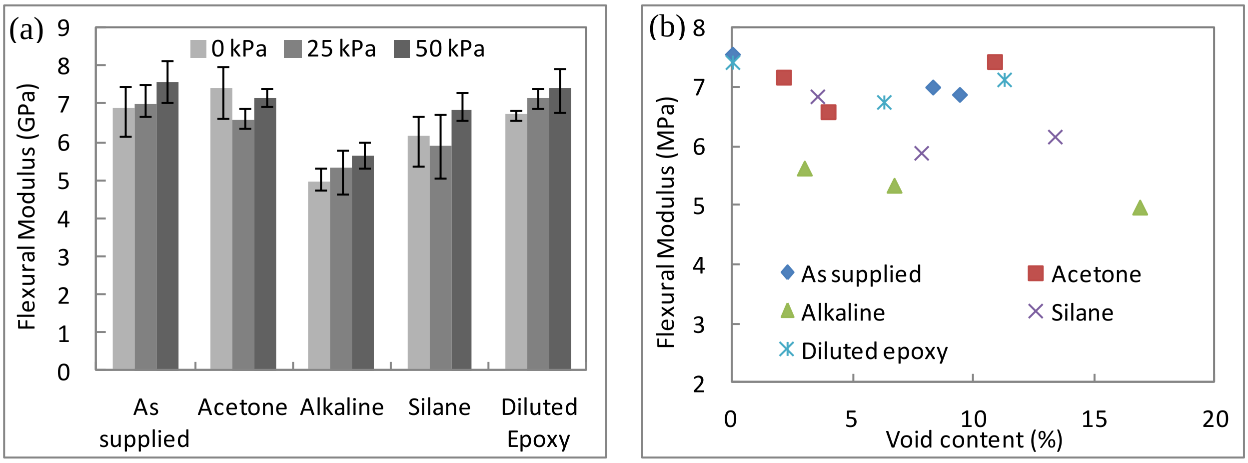

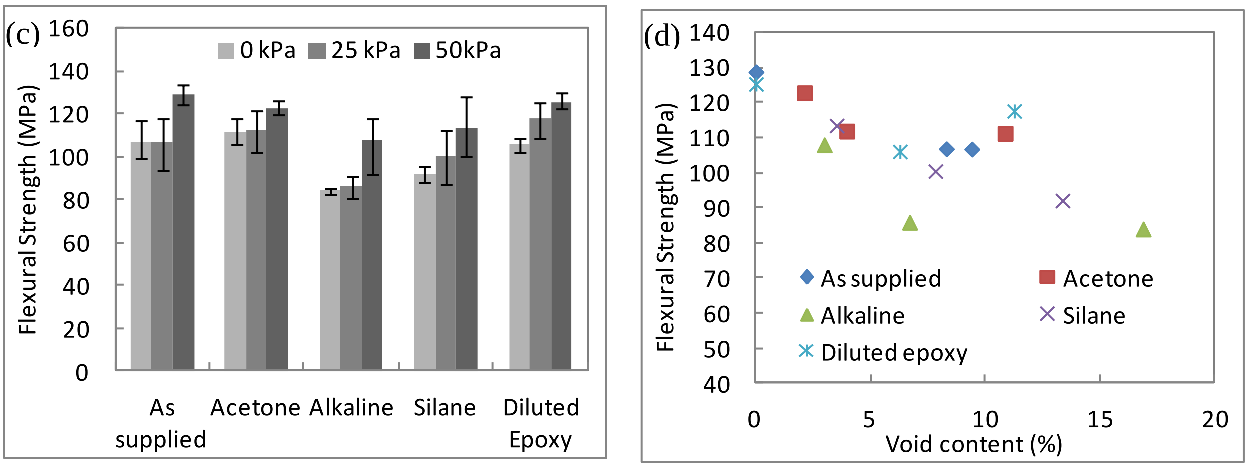

Fig. 6: Flexural properties of flax/epoxy composites manufactured by resin infusion at different post-fill pressures using common chemical treatments: a) modulus, b) modulus versus void content, c) strength and b) strength versus void content

Two key findings were revealed by the flexural testing. First, among the studied treatments, the as supplied and diluted epoxy resulted in the best flexural properties. On the other hand, the lowest properties were exhibited by the alkaline treatment, likely due to a lower fibre volume fraction. The second finding was that with increasing void content the flexural properties of the composites decreased. This is consistent with the findings of other studies for conventional composites [7].

Charpy impact

Charpy impact testing was carried out in accordance with ISO 179 in an edgewise parallel configuration. A sample area of 12.7 x 80 mm^2 was selected with a span of 60 mm. The frictional loss induced by the setup was measured prior to the tests and taken into account. The results are shown in Fig. 7.

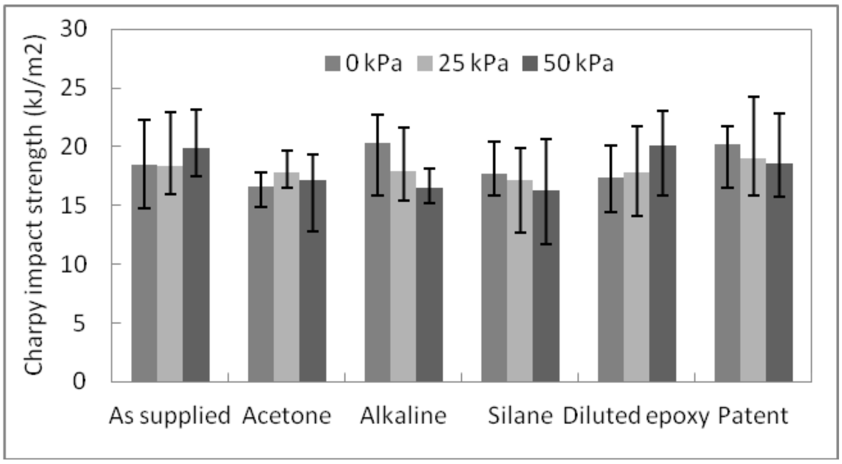

Fig. 7: Charpy impact properties of flax/epoxy composites manufactured by resin infusion at different post-fill pressures using common chemical treatments

Fig. 7 suggests that there was no clear trend between the various treatments and the measured Charpy impact strengths. The same was indicated for the effect of voids on the Charpy impact properties. However, the large coefficient of variance (~ 15%) indicates that a more suitable impact test configuration may be required for this type of material.

CONCLUSIONS

The application of alkaline, silane and diluted epoxy treatments to flax fabrics were shown to result in measureable changes in effective permeability. Furthermore, in the case of the alkaline treatment a significant change in dry compaction behaviour was observed. This was attributed to fibre swelling and suggests that the boundary condition of the fabric during this treatment is an important parameter in the context of composite processing. Flexural and Charpy impact tests were finally carried out on the manufactured panels. The former test demonstrated the negative impact of voids on flexural strength and modulus. However, the latter test did not reveal any clear relationships and the results were fraught with scatter. Based on the results of this study, a diluted epoxy treatment provided the best balance between process-ability and flexural properties.

ACKNOWLEDGMENTS: The financial support of the Network for Innovative Plastic Materials and Manufacturing Processes (NIPMMP) is acknowledged. The authors would also like to thank Lineo NV for supplying materials.

REFERENCES

1. Van de Weyenberg I, Ivens J, De Coster A, Kino B, Baetens E, Verpoest I (2003), 'Influence of processing and chemical treatment of flax fibres on their composites', *Composites Science and Technology*, 63(9), 1241-6.

2. Cantero G, Arbelaiz A, Llano-Ponte R, Mondragon I (2003), 'Effects of fibre treatment on wettability and mechanical behaviour of flax/polypropylene composites', *Composites Science and Technology*, 63(9), 1247-54.

3. Umer R, Bickerton S, Fernyhough A (2011), 'The effect of yarn length and diameter on permeability and compaction response of flax fibre mats', *Composites Part A: Applied Science and Manufacturing*, 42(7), 723-32.

4. Francucci G, Rodríguez ES, Vázquez A (2010), 'Study of saturated and unsaturated permeability in natural fiber fabrics', *Composites Part A: Applied Science and Manufacturing*, 41(1), 16-21.

5. Masoodi R, Pillai KM (2011), 'Modeling the Processing of Natural Fiber Composites Made Using Liquid Composite Molding', Handbook of Bioplastics and Biocomposites Engineering Applications, Hoboken: John Wiley & Sons, 43-73.

6. Karmakar SR (1999), Chemical technology in the pre-treatment processes of textiles, Amsterdam: Elsevier.

7. Olivier P, Cottu JP, Ferret B (1995), 'Effects of cure cycle pressure and voids on some mechanical properties of carbon/epoxy laminates', *Composites*, 26(7), 509-15.

OPTIMUM PROCESSING CONDITIONS FOR THE MANUFACTURE OF BAMBOO FABRIC-POLYPROPYLENE COMPOSITES

Nurul Fazita Mohammad Rawi, Krishnan Jayaraman, Debes Bhattacharyya

Centre for Advanced Composite Materials (CACM),
Department of Mechanical Engineering, The University of Auckland,
Private Bag 92019, Auckland, New Zealand
Corresponding author's e-mail:nmoh144@aucklanduni.ac.nz

ABSTRACT: Bamboo is one of the world's best known natural materials and one of the fastest growing plants. Bamboo fibres have attracted global attention as a potential alternative for synthetic fibres such as glass or carbon fibres because of their low-density and high specific stiffness and strength. Research on bamboo fibre-reinforced composites has generally been focused on the use of short fibres. However, long bamboo fibres possess many excellent properties when used as fabric such as high strength and modulus due to continuous fibres oriented on at least two axes. In this study, bamboo fabric was consolidated between polypropylene sheets by compression moulding under various processing conditions. Compression moulding was used as it is a suitable and easy way to consolidate polypropylene sheets with bamboo fabric. The effects of three compression moulding parameters; processing temperature, pressure and time, on the tensile, flexural and impact properties of the composite sheets were evaluated. The Taguchi method was adopted to determine the optimum set of the compression moulding parameters to achieve the maximum mechanical properties of the composites. It is observed that processing temperature significantly affects the mechanical performance of compression moulded bamboo fabric-polypropylene composites. A viscosity test was conducted and the results showed that higher processing temperature gives better flow of the polypropylene. High pressure and short processing time resulted in better mechanical properties of the bamboo fabric-polypropylene composites.

KEYWORDS: *Compression moulding, Taguchi method, Polypropylene sheet, Bamboo fabric, Mechanical properties*

INTRODUCTION

In recent years, industry is attempting to decrease its dependence on petroleum based fuels and products due to increased environmental consciousness. This is leading to the need to investigate environmentally friendly, sustainable materials to replace existing ones. Currently the most feasible way toward eco-friendly composites is the use of natural fibres as reinforcement. Natural fibre composites possess advantages such as easy availability, renewability of raw materials, low density, and high specific strength and stiffness [1].

Bamboo is one of the world's best known natural engineering materials and it is also one of the most under-utilised natural resources available abundantly in Southeast Asian countries.

The total bamboo forest area in the world has reached 22 million hectares currently and worldwide availability of bamboo fibre is over 30 million tons per year [2]. Bamboo is one of the fastest growing plants with a maturity cycle of 3–4 years and it has excellent mechanical properties such as low-density, high tensile modulus, low elongation at break and its specific stiffness and strength are comparable to those of glass fibres. Bamboo fibres possess many excellent properties when used as textile materials, such as high tenacity, resistance to bacteria, high strength and stiffness due to continuous fibres oriented on at least 2 axes [3]. Petroleum based polypropylene (PP) is an important thermoplastic resin and has great potential for composites because it can be processed by conventional technologies, such as extrusion, compression and injection moulding, in many applications [4].

Compression moulding was used as it is a suitable and easy way to consolidate polypropylene sheets with bamboo fabric. Compression moulding is a common and economically sensible consolidation technique. It employs one or more hydraulic presses and consolidates the prepreg stack between parallel platens, possibly using a picture frame mould to prevent resin bleeding from the edges of the laminate. In this study, the effects of three compression moulding parameters; processing temperature, pressure and time, on the tensile, flexural and impact properties of the composite sheets were evaluated. The Taguchi method was adopted to determine the optimum set of the compression moulding parameters to achieve the maximum mechanical properties of the composites.

MATERIALS AND METHODS

Materials

Polypropylene sheets of random copolymer MOPLEN RP241G with 0.38 mm thickness manufactured by Lyondell Basell Industries, was supplied by Field International Ltd., Auckland, New Zealand. The plain woven bamboo fabric as shown in Fig. 1 (2 warps x 1 weft) was supplied by Industrial Textiles Limited, Auckland, New Zealand. The yarn thickness is 20 x 14 (km/kg) according to the metric numbering system with the lower number indicating thicker yarn while the yarn count is 104 x 56 per square inch.

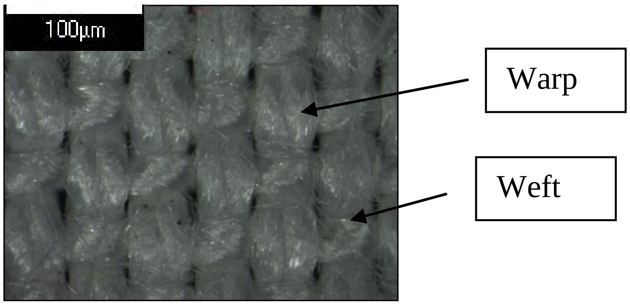

Fig. 1: Woven bamboo fabric

Fabrication of composites

Bamboo fabric and polypropylene sheet were cut into 390 mm x 390 mm dimensions. A clearance of 10 mm from the edges of the mould cavity allows for the overflow of excess matrix. The weights of polypropylene sheets and bamboo fabric were taken prior to composite fabrication so as to determine the wt% of fibre and matrix of the resulting composite. Before the manufacture of composite sheets, the bamboo fabric was dried for 24 hours at 80°C in the Moreto vacuum dryer to reduce its moisture content. Composite sheets consist of four layers of bamboo fabric and five layers of polypropylene sheets. The composite sheets were produced using a film-stacking procedure. The layers of bamboo fabric and polypropylene sheets were arranged alternately as shown in Fig. 2. The fibre weight fraction of the composite sheets was 0.32. Layers of the bamboo fabrics all oriented in the same direction (warp wise) were compression moulded using a 100 ton hydraulic hot press with a square mould of dimensions 400 mm x 400 mm and a maximum oil heater temperature of 250°C.

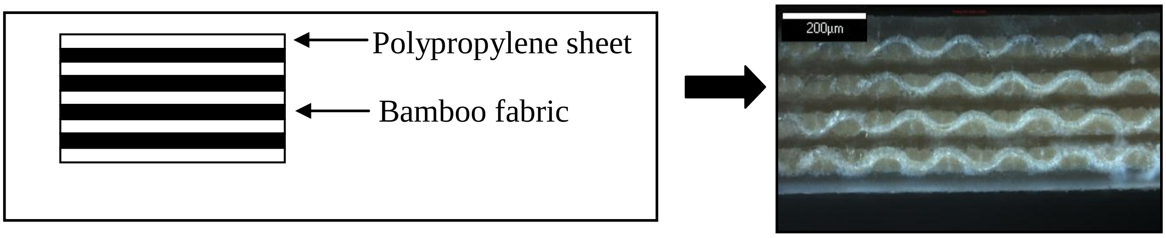

Fig. 2: Arrangement of bamboo fabric-polypropylene composite sheet

The mould was heated using electrical and oil heaters to the desired temperature. A thermocouple was placed outside of the square mould in order to monitor the temperature. Once the mould reached the desired temperature, the upper platen was opened and bamboo fabric-polypropylene sheet assembly was quickly placed inside the mould. Then, the mould was closed without pressure for first two minutes to allow permeation of the polypropylene through the fabric, followed by the application of pressure and heating time according to the Taguchi table. The temperature was held at the required level; after the set heating time, the mould was then cooled by circulating cold water. The sample was kept under set pressure until it cooled to 25°C. The platen was opened and the composite was removed from the press. Fig. 3 shows the simplified manufacturing method for the composites.

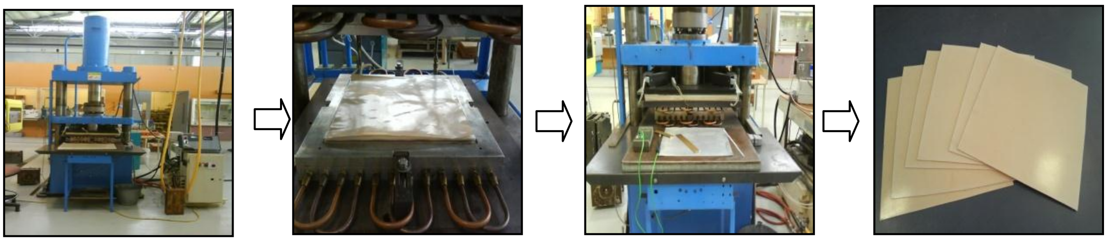

Fig. 3: Manufacturing method for bamboo fabric-polypropylene composite sheets

Mechanical properties

Tensile tests for composite sheets were performed according to ASTM D638-10. The flexural tests were performed according to ASTM D790-10 (Procedure B) and Charpy impact test was carried out using a Ceast pendulum impact tester as per ASTM D6110-10.

Design of experiment by Taguchi method

The Taguchi design of the consolidation parameters considered three control factors, namely consolidation temperature, pressure and time and each of the parameters was assigned two levels while the tensile, flexural and impact properties were chosen as the responses. Table 1 lists four runs based on an orthogonal array L4 (2^{3-1}) and the experimental results.

Table 1: Orthogonal array L4 (2^{3-1}) of the experimental runs and results.

	Control factors			Tensile strength (MPa)		Tensile modulus (GPa)		Flexural strength (MPa)		Flexural modulus (GPa)		Impact strength (J/m)	
Run	Temperature (°C)	Pressure (MPa)	Time (min)	W	F	W	F	W	F	W	F	W	F
1	175-180	0.39	5	49.7	36.9	2.08	1.53	48.0	37.4	1.82	1.43	257	267
2	175-180	0.66	10	48.8	38.7	2.18	1.67	44.6	38.4	1.72	1.44	260	273
3	195-200	0.39	10	47.5	36.3	1.82	1.45	42.8	36.9	1.69	1.35	261	278
4	195-200	0.66	5	48.8	35.5	2.03	1.4	45.7	37.0	1.76	1.38	242	261

*W = warp, F = weft

To improve the consolidation process and obtain higher tensile, flexural and impact properties, further investigation was done by using Taguchi orthogonal array L9 (3^2) with three logical levels for each parameter. The two parameters identified as processing factors affecting tensile, flexural and impact properties were consolidation pressure and time based on analysis of Taguchi L9 with the temperature maintained at 195-200 °C. The experimental runs and results are shown in Table 2.

Table 2: Orthogonal array L9 (3^2) of the experimental runs and results.

	Control factors		Tensile strength (MPa)		Tensile modulus (GPa)		Flexural strength (MPa)		Flexural modulus (GPa)		Impact strength (J/m)	
Run	Pressure (MPa)	Time (min)	W	F	W	F	W	F	W	F	W	F
1	0.39	3	56.9	41.4	2.40	1.80	60.2	47.9	1.96	1.63	198	229
2	0.39	5	54.5	42.2	2.35	1.75	59.5	49.2	2.00	1.68	219	210
3	0.39	10	48.0	36.4	1.88	1.45	44.2	38.5	1.63	1.32	262	278
4	0.66	3	56.9	42.9	2.38	1.82	61.0	49.7	1.99	1.67	219	222
5	0.66	5	48.6	48.0	1.97	1.43	47.2	39.1	1.77	1.40	243	262
6	0.66	10	56.8	56.9	2.51	1.67	60.8	48.4	2.01	1.64	204	227
7	1.05	3	53.4	35.8	2.18	1.61	54.6	44.2	2.02	1.68	183	237
8	1.05	5	61.1	41.9	2.78	2.05	61.9	49.4	1.99	1.64	192	210
9	1.05	10	58.9	41.0	2.75	1.91	62.4	48.4	2.06	1.64	192	207

*W = warp, F = weft

RESULTS AND DISCUSSION

Fig. 4 illustrates the effects of the control factors by showing the weft flexural strength values at the two level settings of each factor. The calculated means related to the response can be used to identify the optimal set of conditions to achieve the greatest performance of the bamboo fabric-polypropylene composite sheets. Because each factor was studied at two levels; level 1 denotes low level of a factor setting and level 2 represents the high level setting. The factor settings at highest values should be the optimum set of process conditions. The negative net effect shown is due to the "low" factor level resulting in a higher flexural strength than the “high” factor level.

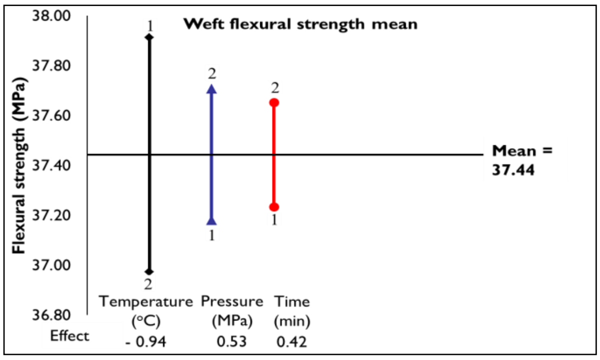

Fig. 4: Weft flexural strength graph for means (Taguchi L4)

The higher effect value represents the higher influence of the control factor on the performance of the composite sheets. As can be seen from Fig. 4, consolidation temperature has the greatest effect on the flexural strength followed by consolidation pressure and time. In order to decide which level is best for the maximum value of the response, the values at two level settings of each factor are compared. From the means figures, the best combination of the processing condition was concluded as shown in Table 3. Tensile strength and modulus, flexural strength and modulus, and impact strength for warp and weft directions showed the highest value for lower level of consolidation temperature (175-180°C). The high effect value of consolidation temperature shows that this factor has greater influence on the weft flexural strength as can be seen in Fig. 4. This result therefore suggests that this parameter must be more tightly controlled during hot pressing.

Table 3: Summary of consolidation parameters for maximum properties (Taguchi L4)

	Properties Consolidation Factor	Tensile modulus	Tensile strength	Flexural modulus	Flexural strength	Impact strength
Warp	Temperature (°C)	175-180	175-180	175-180	175-180	175-180
	Pressure (MPa)	0.66	0.66	0.39	0.39	0.39
	Time (min)	5	5	5	5	10
Weft	Temperature (°C)	175-180	175-180	175-180	175-180	175-180
	Pressure (MPa)	0.66	0.66	0.66	0.66	0.39
	Time (min)	10	10	5	5	10

From Fig. 4, it is observed that the effect of consolidation pressure is also significant on the weft flexural strength. It shows that the high level of consolidation pressure (0.66 MPa) gives a higher value for the weft flexural strength. Table 3 indicates the effect of consolidation pressure on tensile, flexural and impact properties of composite sheets. Pressure during the consolidation process provides the driving force to put the layers in intimate contact pushes them together and further helps to impregnate the resins into the fabric. The pressure can also reduce the void content and complete the consolidation followed by cooling under pressure. However, simple increases in pressure are likely to be counter-productive since this will also reduce the transverse permeability of the fibre bundles. Therefore, sufficient pressure is needed which also depends on the consolidation temperature and time. Fig. 4 shows that the consolidation time to achieve maximum weft flexural strength is ten minutes. Tensile strength and modulus for weft direction and impact strength for both warp and weft directions also show the same results. The time for successful consolidation in the film-stacking process becomes even longer if the viscosity of the polymer is high, since high viscosity polymers have a greater resistance to flow [5]. This can explain the fact that a longer consolidation time (ten minutes) gives maximum value to certain mechanical properties. However, for efficiency during manufacturing, the consolidation time should be minimised.

Reduction in consolidation time and increase in mechanical performance

From the L4 Taguchi analysis, the results indicated that a low consolidation temperature gives higher mechanical properties. This resulted in a longer consolidation time (ten minutes) to maximise certain mechanical properties of the bamboo fabric polypropylene sheets. However, consolidation time of ten minutes will result in higher cost during production. Hence, the higher consolidation temperature and pressure with lower consolidation time conditions are suggested for further study. In order to achieve these conditions, further analysis was done on consolidation temperature by conducting a rheology test on the polypropylene sheet at low (185^{o}C) and high (195^{o}C) temperatures. The test was done to see whether there is a significant difference in viscosity between these two temperatures. The lower viscosity of the polypropylene sheet will give better flow and hence will result in better consolidation. Therefore, improvement in mechanical properties is also expected from this new set of conditions. In a polymer melt, the viscosity decreases with increasing temperature due to greater free space available for molecular chain motion at higher temperature [6]. From the viscosity test, it is clear that the consolidation temperature of 195^{o}C showed better flow compared to 185^{o}C, which was expected. Fig. 5 shows that there is a significant difference in viscosity between 185^{o}C and 195^{o}C. The viscosity of polypropylene at 185^{o}C is 45 Pa.s while at 195^{o}C, the viscosity is 2.4 Pa.s. This is the reason that certain mechanical properties required higher consolidation time when 185^{o}C was used during the consolidation process, since this temperature was not enough to give better flow of polypropylene through the bamboo fabric. Therefore, further studies were carried out using 195^{o}C due to the better flow of polymer and shorter consolidation time.

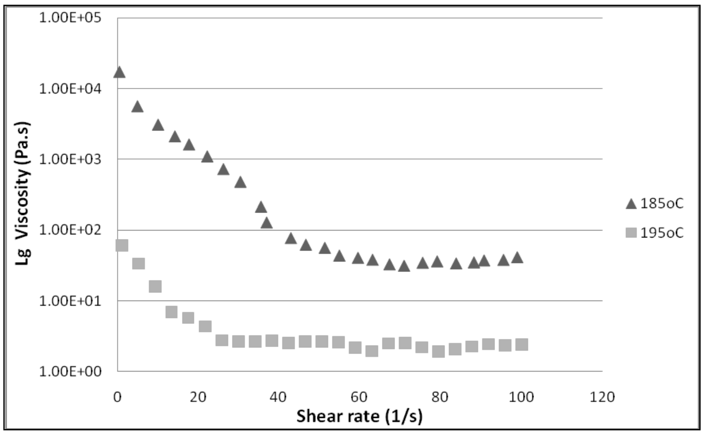

Fig. 5: The viscosity of polypropylene as a function of shear rate at different temperature

Fig. 6 presents the effects of the control factors by showing the means related to the warp tensile modulus values at the three level settings of each factor. Because each factor was studied at three levels, level 1 denotes the low level of a factor setting, level 2 denotes the medium level setting and level 3 represents the high level setting. Fig. 6 shows consolidation pressure has a greater effect on the tensile modulus than consolidation time. However, the interaction between pressure and time should be considered since the interaction also shows a large effect on the tensile modulus.

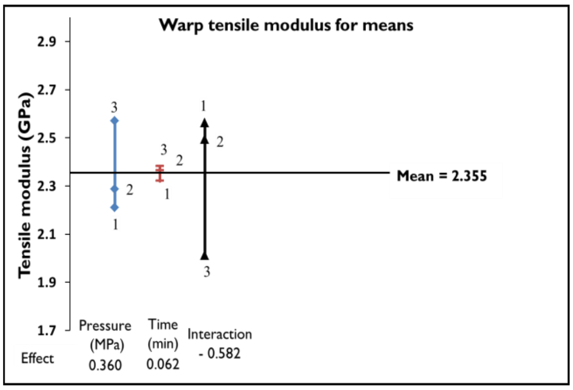

Fig. 6: Warp tensile modulus graph for Means (Taguchi L9)

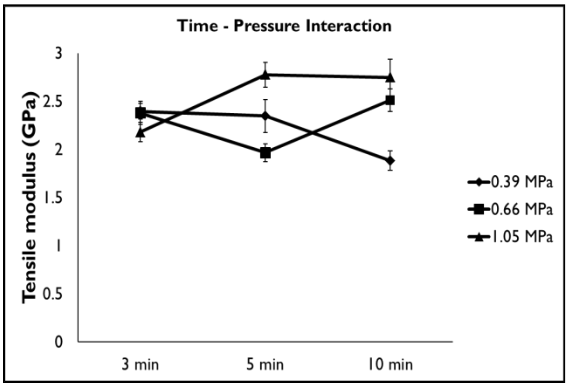

Fig. 7: Time-Pressure interaction (Taguchi L9)

Processing parameters required to achieve maximum properties for warp and weft directions are summarised in Table 4. Interaction of consolidation pressure and time show different conditions compared to main factors of tensile and flexural properties for warp and flexural strength for weft directions. This condition occurs frequently with the Taguchi method. The main disadvantage of this method is that the results obtained are only relative and do not exactly indicate which parameter has the highest effect on the performance characteristic value. It also does not account for how the variables affect each other.

Table 4: Summary of consolidation parameters for maximum properties (Taguchi L9)

	Properties Consolidation Factor	Tensile modulus	Tensile strength	Flexural modulus	Flexural strength	Impact strength
Warp	Pressure (MPa)	1.05	1.05	1.05	1.05	0.39
	Time (min)	10	3	3	3	10
	Interaction pressure and time	1.05 MPa, 5 min	1.05 MPa, 5 min	1.05 MPa, 10 min	1.05 MPa, 5 min	0.39 MPa, 10 min
Weft	Pressure (MPa)	1.05	0.66	1.05	1.05	0.39
	Time (min)	5	10	3	3	10
	Interaction pressure and time	1.05 MPa, 5 min	0.66 MPa, 10 min	1.05 MPa, 3 min	1.05 MPa, 5 min	0.39 MPa, 10 min

From Fig. 6, it can be seen that consolidation pressure has a significant effect on the warp tensile modulus. It can be seen from Table 4 that all mechanical properties have the highest value when 1.05 MPa consolidation pressure is used during the consolidation process except for tensile strength for weft direction and impact strength for both warp and weft directions. Hence, the consolidation pressure of 1.05 MPa was chosen as optimum consolidation pressure. As observed in Table 4, the lower consolidation time (three minutes) gives higher value for flexural strength and modulus for warp and weft directions and tensile strength in warp direction; while ten minutes consolidation time gives maximum value to the tensile modulus (warp), tensile strength (weft) and impact strength for warp and weft directions. These results caused difficulties in choosing which level gives better consolidation to the bamboo fabric-polypropylene composite sheets. Again, the effect of the means is identified to see the significance of the different levels of the consolidation time. From Fig. 6, it can be concluded that the means effects of the consolidation time between three and ten minutes are very small. This means that there is not a huge difference in mechanical properties between those two consolidation times while interaction between pressure and time showed enormous effect on the tensile modulus of the composites. From Fig. 7, the interaction between pressure and time shows five minutes and 1.05 MPa pressure gives higher values for the tensile modulus. The mechanical properties of the bamboo fabric-polypropylene composites are higher than the short bamboo fibre polypropylene composites (30 wt%) except for flexural modulus as compared to the results reported by Lee *et al.* [7].

CONCLUSIONS

It is observed that processing temperature significantly affects the mechanical performance of compression moulded bamboo fabric-polypropylene composites. Viscosity test results showed that higher processing temperature (195^{o}C) gives better flow of the polypropylene. High pressure (1.05 MPa) and short processing time (five minutes) resulted in better mechanical properties of the bamboo fabric-polypropylene composites.

ACKNOWLEDGMENTS: This work is supported by Universiti Sains Malaysia (USM), Malaysia and Ministry of Higher Education (MOHE), Malaysia. Thanks also go to the staff at CACM, The University of Auckland, New Zealand.

REFERENCES

1. Shubhra Q, Alam A, Gafur M, Shamsuddin S, Khan M, Saha M, Saha D, Quaiyyum M, Khan J and Ashaduzzaman M (2010), ‘Characterization of plant and animal based natural fibers reinforced polypropylene composites and their comparative study’, *Fiber Polym*, 11(5), 725-731.

2. Han G, Lei Y, Wu Q, Kojima Y and Suzuki S (2008), ‘Bamboo-fiber filled high density polyethylene composites: Effect of coupling treatment and nanoclay’, *J Polym Environ,* 16(2), 123-130.

3. Liu Y and Hu H (2008), ‘X-ray diffraction study of bamboo fibers treated with NaOH’, *Fiber Polym,* 9(6), 735-739.

4. Haydaruzzaman Khan AH, Hossain MA, Khan MA, Khan RA and Hakim MA (2010), ‘Fabrication and characterization of jute reinforced polypropylene composite: Effectiveness of coupling agents’, *J. Compos. Mater.,* 44(16), 1945-1963.

5. Campbell FC (2010), ‘Thermoplastic composite fabrication processes’, *Structural Composite Materials,* Campbell FC (Ed.), USA: ASM International.

6. Muksing N, Nithitanakul M, Grady BP, and Magaraphan R (2008), ‘Melt rheology and extrudate swell of organobentonite-filled polypropylene nanocomposites’, *Polym. Test.,* 27(4), 470-479.

7. Lee SY, Chun SJ, Doh GH, Kang IA, Lee S and Paik KH (2009), ‘Influence of Chemical Modification and Filler Loading on Fundamental Properties of Bamboo Fibers Reinforced Polypropylene Composites’, *J. Compos. Mater.,* 43(15), 1639-1657.

OPTIMIZATION OF THE MANUFACTURING OF TWILL BAMBOO FABRIC REINFORCED POLYPROPYLENE HYBRID COMPOSITES LAMINATES

Nurul Mahmud Zuhudi[1], Xiaowen Yuan[1], Krishnan Jayaraman[1]

[1]Centre of Advanced Composite Material (CACM), Department of Mechanical Engineering, School of Engineering, University of Auckland, Private Bag 92019, Auckland 1142, New Zealand. Corresponding author's e-mail: nmah047@auckland.ac.nz

ABSTRACT: In recent years, natural fabric thermoplastic composites have received much attention especially bamboo due to its attractive capabilities for structural applications. It is crucial to study the processing of bamboo fabric materials in order to achieve quality and cost-effectiveness in fibre reinforced composites. Though bamboo fabric has been widely utilized for several years in composite applications due to its high strength and abundance, much work has been concentrated on short bamboo fibre and very little work on using bamboo fabric. The effectiveness of twill bamboo fabric is expected to give higher strength performance due to its structure but the processing needs to be optimised. Bamboo fabric composites were fabricated using compression moulding due to its simplicity, gives good surface finish and relatively low cost in terms of labour and production. Further, the impregnation of the polymer into the fabric is easier in this process. As the fabric weave structure contributes to the impregnation quality which leads to the overall performance, the processing parameters of consolidation i.e. pressure, time, and weight fraction of fabric were optimized using the Taguchi method. This optimization enhances the consolidation quality of the composite by improving the composite mechanical properties, three main tests were conducted i.e. tensile, flexural and impact test. It is observed that the processing parameter significantly affected the consolidation and quality of composite. Hybrid bamboo glass polypropylene composite sheets were also fabricated using the optimum processing parameters found out for the bamboo polypropylene composites and mechanical tests were performed on hybrid composites.

KEYWORDS: *twill bamboo fabric, processing parameters, optimization, compression moulding process, bamboo-glass hybrid laminates,*

INTRODUCTION

In the past few decades, natural fibres have attracted more interest among researchers and industries for non-structural and structural applications. The combination of natural fibres like oil palm, kenaf, hemp, flax, jute, pineapple leaf fibre, sisal, wood and others with polymer matrices from both non-renewable and renewable resources can be used to produce composite materials. The selection of bamboo as reinforcement is mainly due to the abundance and renewability [1].

Bamboo in woven fabrics forms are embedded in the materials system as it is expected to give easier material handling and reduce manufacturing cost. In this research, bamboo has been investigated as reinforcement in an effort to partly reduce the usage of non-renewable synthetic fibres. Currently, synthetic reinforced fabric forms are commonly being used in composite manufacturing which mitigates the difficulty in matrix consolidation and reduces impact damage with improved energy absorption and structural integrity. Despite the advantages mentioned above, the usage of bamboo fibres in thermoplastics has not been extensive due to their limited thermal stability, higher moisture absorption, low degree of dispersion and poor interfacial bonding between fibre and polymer matrix [2]. However, research on property optimization may enable natural fibre and polymer composites to compete with well-established glass and carbon fibre. The hybridization of synthetic fibres such as glass with bamboo fabrics polymer improves the mechanical properties, and is economic and environmentally friendly. Various attempts have been made to manufacture glass reinforced natural fibre hybrid composites, such as glass/bamboo, glass/hemp, glass/jute, glass/sisal, glass/oil palm, glass/coir, glass/pineapple leaf and others [3-6].

In connection with the use of woven fabric, the compression method is very popular in the manufacturing of natural fibre composites because of its high reproducibility and low cycle time. However, there is a need to optimize the processing parameters used for manufacturing in order to produce a high quality composite laminate. The impregnations of bamboo fabrics with polymer matrix can be further studied by considering the effects of the consolidation process, of the fabrics architecture and deformation as well as void content reduction [7]. Several authors studied the optimum processing parameters of compression moulding for various materials [8]. Currently, the Taguchi method of experimental design [9], which is gaining popularity in optimization studies, has been applied in this work. The reasons for using this approach for experimental design are to reduce the number of actual experiments; make both the processing and property analyses of the product insensitive to the variation in uncontrolled factors; and investigate the influence of factors on the variability of a given response and makes the process more robust [10].

The details objectives of this research were:

i. To establish a process for manufacturing high quality bamboo reinforced polypropylene composite laminates and optimize their processing parameters using the compression moulding process.
ii. To assess the effect of the hybridization with glass and evaluate the potential of the bamboo-glass hybrid composite laminates.

MATERIALS AND METHODS

Materials

The twill bamboo fabrics woven pattern of 100% bamboo fabric was obtained from Xinchang Textiles, Co.Ltd Guangzhou China. The fabrics used have breaking force of 725N (±33.5) and 416N (±14.8) for warp and weft respectively according to ATSM 5034 Grab Test. The bamboo fabrics with a width of 1500mm and weight of 220gsm were used, having specification of 20*20 and 108*58 for yarn count and density respectively. Figure 1 shows the material directionality using optical microscopy. The matrix used was, Polypropylene Random Copolymer (PP) supplied from LyondellBasell Industries in sheet form. This product, typically has mechanical properties of 28MPa (ISO 527-2) for tensile stress, 1050MPa (ISO 178) for flexural modulus and density of 0.900g/cm^3 (ISO 1183D) as per material specification. The melting temperature given from the supplier is 145°C.

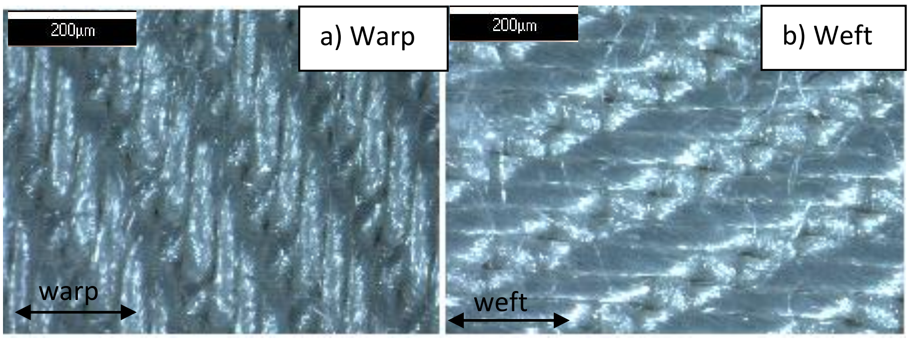

Fig. 1: Material directionality of bamboo fabric under optical microscopy

Fabrication Process

The compression moulding experiments were carried out using a hot press 200kN upstroking hydraulic press. This compression equipment is composed of a heating press with oil and electrically heated platens and a cooling press with water-cooled platens. 400 x 400 mm^2 flat composite sheets were manufactured in a moulding frame. Aluminium plates were added on the frame to produce a sheet of about 2-3 mm theoretical thickness. The bamboo fabrics were cut to the required dimensions. The bamboo fabrics were dried in the vacuum dryer at 80°C for 48 hours to remove the moisture contents and reduce void content formation in the composite sheets produced. The polypropylene sheets were cut to the same size as the fabrics and did not require any preparation.

In order to produce a high quality composite laminate, ply stacking was arranged prior to placement in the hot press to prevent the fabric from re-absorbing any moisture while the mould heated to the required consolidation temperature. The fabrics were taken out from the dryer prior to the assembly of ply stacking for each sheet fabricated. The weight of the dried fabric was measured and the fabric contents relative to the sheets weights were recorded.

Polymer incorporation was achieved by sandwiching six plies bamboo fabric with 0.38 mm polypropylene sheets at the top and bottom and another 0.6 mm polypropylene sheet in between the bamboo fabrics, the latter acting as mid ply to produce a symmetrical laminate. The bamboo fabrics were interleaved between PP sheets intended to fully achieve impregnation of the polymer through the fabric thickness, thus producing good quality composite sheets with nominal thickness in the range of 2.2 to 2.5mm.

The manufacturing process to produce a high quality composite laminate is illustrated in Figure 2. Figure 3 shows the manufacturing cycle for processing the composite laminates. The thermocouples used were placed on the mould in order to check the evolution of the temperature profile through the processing cycle. The mould was heated for about 30 to 45 minutes to temperature 185°C and while the mould was heated, the ply stacking assembly was prepared five minutes prior to inserting into the hot mould. When the mould reached the required temperature, it was opened and the ply stacking assembly was quickly put into the mould. An aluminium sheet was used to transfer the ply stacking into the hot mould prior to reducing heat loss. Then, the upper and lower hot platens were quickly closed. In the pre heating stage, the mould was heated for about five minutes because a little heat loss occurs during opening. However, there was no pressure applied during the pre-heating stage as the polypropylene was expected to start melting and achieved full impregnation in this stage.

The ply stacking assembly was heated to a temperature of 185°C (about five minutes) and the consolidation pressure was then applied once the temperature was reached. The temperature and pressure were held steadily for the required consolidation time. The polymer was allowed to be fully impregnated inside the fabrics. This stage is also known as the impregnation stage during which the pressure was applied to remove water vapour and volatiles resulting from the heating process and force the molten polymer into the fabrics. The oil and electric heaters were switched off at the end of the consolidation time and a cooling press with water-cooled platens was used. During the cooling period, the pressure applied was maintained until the fabricated composite sheet reached 40^{o}C, or lower, at which stage it could be removed from the mould to prevent deconsolidation and distortion of the sheets. At this stage, the polymer was crystallized and solidified to complete the cycle.

In manufacturing using a hot mould, various factors need to be considered to produce a high quality composite laminate. In this research, the effects of the processing parameters used during manufacturing were studied and optimized. However, good consolidation of polymer composites was also associated with impregnation of the polymer into the fabrics, the effect of fabric deformation on consolidation and void content reduction. The effect of fabric architecture on the polymer consolidation was needed to be further studied in order to obtain a high quality and good surface finish of the composite laminate.

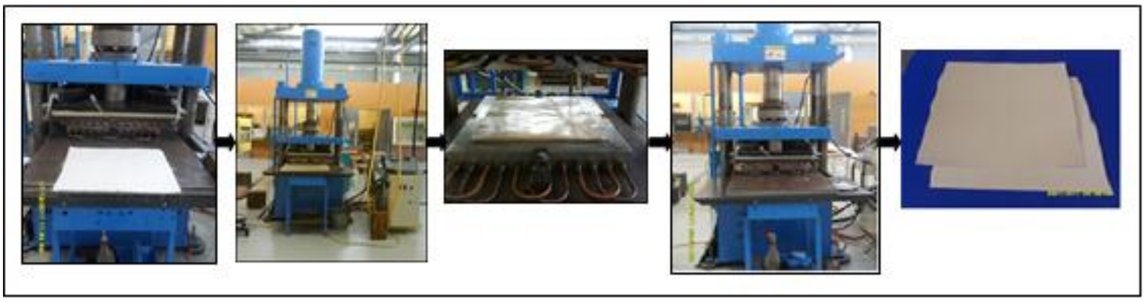

Fig. 2: Fabrication flow chart

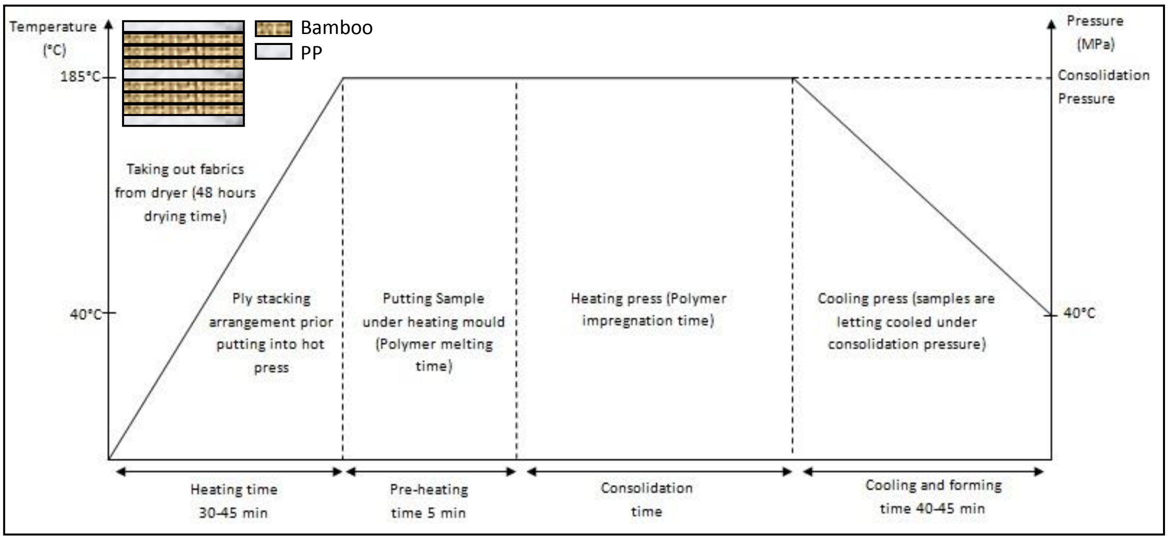

Fig. 3: Manufacturing cycle for thermoplastic composite processing

Optimization using Taguchi Method L9

The main objective of this stage was to optimize and produce fully consolidated sheets of bamboo-polypropylene (BP).The Taguchi quality design using L9 was applied for parameter design. The fabrication of BP composites sheets were intended to produce consolidation processing conditions such that the optimum strength and stiffness of composite sheets could be achieved; moreover significant processing factors could be determined. The details of specimens and processing condition used were according to Table 1 below:

Table 1: Taguchi design matrix of L9

Trial	Sample Name	Fibre Weight Fraction, W_f(%)	Pressure, P (MPa)	Time, t (min)	Temp, T(°C)
1	L9_1	31.5	0.33	3	185
2	L9_2	31.5	0.66	6	185
3	L9_3	31.5	0.80	9	185
4	L9_4	41.5	0.33	6	185
5	L9_5	41.5	0.66	9	185
6	L9_6	41.5	0.80	3	185
7	L9_7	47.5	0.33	9	185
8	L9_8	47.5	0.66	3	185
9	L9_9	47.5	0.80	6	185

The Taguchi design of consolidation parameters considered three factors namely weight fraction, consolidation pressure, and time and each of the parameters was assigned three levels. For the responses, tensile and flexural were chosen in the study. The experimental trials which were arranged in a Taguchi L9 orthogonal array (OA) consisted of nine experiments. The selected optimal consolidation processing conditions found, using the Taguchi method were then used to fabricate bamboo-glass hybrid (BG) polypropylene in the later stage.

RESULTS AND DISCUSSIONS

Effect of processing parameters

The mechanical property results of the tensile and flexural tests of L9 orthogonal array were analysed to maximize the response. The effects of each processing parameters for each of the responses were investigated to determine the level of each parameters which lead to the optimum processing condition. In order to analyse the effect of one specific processing parameter, the average value of tensile strength, its modulus, flexural strength, and its modulus were compared to compensate for the variation of other processing parameters. For L9 orthogonal array experimental results, the mechanical properties of the composites are shown in Table 2. A similar trend occurred for all other responses. The mechanical properties gave the highest value as the weight fraction of bamboo fabric is increased up to 47.5%.

To further study the magnitude of each factor's contribution to the responses, plot of average values is given in Figure 4. The larger the effect magnitude represents the higher influence of the processing parameters on the composite laminates. The weight fraction has a significant effect on tensile modulus as expected. However, main objective for this Taguchi analysis is to determine which consolidation pressure and time give full impregnation as the weight fraction increased up to 47.5%. The effects of pressure and time have been considered further because they significantly affected the properties. It is clear that the highest pressure and longest consolidation time give maximum tensile modulus. The same profiles are observed for most of the responses i.e. tensile and flexural strength, and their modulus. This means that the cost of production increases with manufacturing time. In order to reduce manufacturing time, the effect of the pressure applied to the twill fabric architecture was investigated. A full impregnation of the matrix inside the fabric is very dependent on the pressure applied. This is further compared. The result shows a very small drop (less than about 10%) for each sample in terms of its tensile, flexural strength and their modulus. In conclusion, the shortest time (three minutes) and highest pressure (0.80MPa) were chosen at 47.5% weight fraction of reinforcement to be used to obtain optimum properties with reasonable processing cost.

In order to validate the selection of Taguchi parameters; an identical stacking sequence of composite sheets was fabricated using selected processing parameters. Five tensile specimens were tested using the testing condition and it was found that the properties were within 10% compared to the longest time (nine minutes) i.e. ultimate tensile strength of 63 MPa and its modulus of 2.5GPa. This result established the selection of the processing parameters from Taguchi and this condition has been used throughout the manufacture of the Bamboo-Glass (BG) hybrid composites for preliminary study of the potential of the hybrid effects on the composites system.

Table 2: Mechanical properties of bamboo fabric reinforced polypropylene composites

Sample Name	Tensile Strength (MPa)	Tensile Modulus (GPa)	Flexural Strength (MPa)	Flexural Modulus (GPa)
L9_1	44±2.13	2.3±0.06	52.5±4.22	1524±136.9
L9_2	48±2.00	2.4±0.09	57.8±2.43	1715±152.7
L9_3	50±0.98	2.5±0.08	52.6±1.62	1554±58.59
L9_4	58±1.35	2.6±0.1	45.3±0.85	1548±50.11
L9_5	56±1.77	2.6±0.14	49.4±1.26	1672±87.73
L9_6	57±2.67	2.6±0.10	52.9±1.60	1805±56.33
L9_7	64±1.81	2.8±0.36	68.4±1.98	2550±102.4
L9_8	66±3.92	2.5±0.17	57.9±1.36	1795±61.05
L9_9	61±0.17	2.8±0.14	61.5±3.89	1876±205.6
Polypropylene	22±0.09	1.0±0.04	24.5±2.38	1007±42.62

*± indicates standard deviation

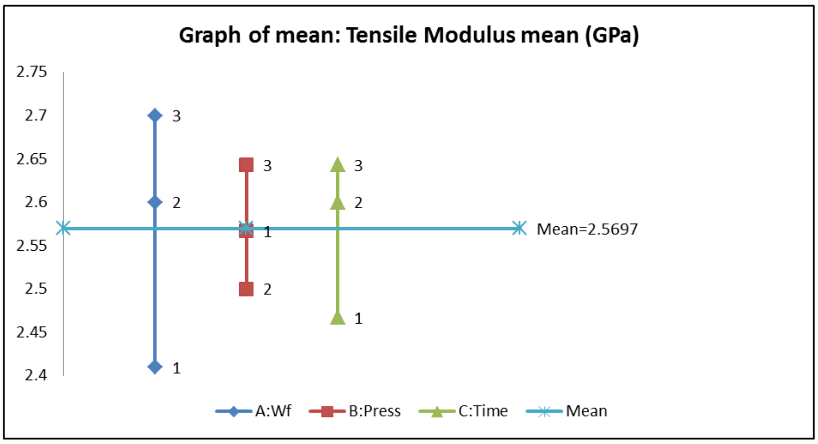

Fig. 4: Tensile modulus graph of means for L9 orthogonal array of BP composites

Effect hybridization with glass

The tensile strength and modulus of pure polypropylene (PP), BP, and BG composites are presented in Table 3. Incorporation of bamboo fabrics into the composite system results in a linear increase in tensile strength of PP matrix Tensile strength of BP composites improves to 238% as compared to pure PP. A similar trend is also revealed for BG composites for BG_0° (glass fibre orientation parallel to the loading direction). It is illustrated that BG_0° increase about 91% as compared to BP composite. It is obvious that the tensile modulus has a similar trend to that of its strength.

The effect of hybridization of glass with BP composites is evident by incremental about 136MPa in tensile properties of BG. This improved performance is attributed to the addition of the unidirectional glass Plytron® sheets which are oriented at the same loading conditions. However, deterioration in tensile strength at BG_90° (glass fibre orientation perpendicular to the loading direction) to 58 MPa is a direct consequence of the perpendicular orientation (90°) of the unidirectional glass Plytron® sheets to the loading condition and also may be caused by a poor fibre/matrix adhesion.

The variation of flexural strength and impact strength is presented in Table 3. The flexural properties displayed similar characteristics as observed for the tensile strength and modulus. The flexural strength and its modulus of BP composites are 70MPa and 2668 MPa respectively. For BG_0°, the flexural properties show increased values of 312 MPa and 11784 MPa respectively. Compared to BP composites, the flexural modulus for BG_90° is decreased to 2172 MPa. A linear increment with the addition of unidirectional glass Plytron® sheets for BG_0° gives impact resistance up to 905.4 J/m compared to 530.9 J/m of BP. However, BG_90° samples show a negative effect of glass hybridization to the material system.

Table 3: Mechanical properties of bamboo-glass hybrid composites

No	**Sample code**	**Tensile Strength (MPa)**	**Tensile Modulus (GPa)**	**Flexural Strength (MPa)**	**Flexural Modulus (MPa)**	**Impact Strength (J/m)**
1	PP	21.7±0.09	1.02±0.04	24.5±2.4	1007±42.6	204.1±8.2
2	BP	71±1.25	2.1±1.3	70±0.8	2668±28.9	530.9±94.3
3	BG_0°	136±7.02	6.9±0.94	312±24.7	11784±1146.5	905.4±79.5
4	BG_90°	58±1.7	2.1±0.1	63±1.4	2172±40.7	407.7±13.6
***± indicate standard deviations**						

CONCLUSIONS

High quality bamboo reinforced polypropylene composites laminates with good surface finish were successfully manufactured using the compression moulding process. This optimization of the processing parameters allowed full impregnation of the matrix inside the fabrics when the best possible mechanical properties were achieved. Glass hybrid was shown to enhance the mechanical properties of the composites, which showed a potential for bamboo-glass hybrid composites to be further developed. However, further study on the effect of different stacking sequences and weight fractions is needed.

ACKNOWLEDGEMENTS

The author would like to thank the Technical University of MARA (University of Kuala Lumpur-Malaysian Institute of Aviation Technology), Malaysia for providing the scholarship and the Centre of Advanced Composite Material (CACM), University of Auckland for providing resources and equipment.

REFERENCES

[1] Jawaid M and Abdul Khalil HPS (2011), ‘Cellulosic/synthetic fibre reinforced polymer hybrid composites: A review’, Carbohydrate Polymers 86, 1-18.

[2] Nayak SK and Mohanty S (2010), ‘Sisal glass fibre reinforced PP hybrid composites: Effect of MAPP on the dynamic mechanical and thermal properties’, Journal of Reinforced Plastics and Composites, 29(10), 1551–1568.

[3] Mandal S, Alam S, Varma IK and Maiti SN (2010), ‘Studies on bamboo/glass fibre reinforced USP and VE resin’, Journal of Reinforced Plastics and Composites, 29(1), 43–51.

[4] Kushwaha PK and Kumar R (2010), ‘The studies on performance of epoxy and polyester-based composites reinforced with bamboo and glass fibres’, Journal of Reinforced Plastics and Composites, 29(13), 1952–1962.

[5] Venkata Subba RE, Varada RA, Hemachandra RK, and Ramachandra RG (2010), ‘Chemical resistance and tensile properties of glass and bamboo fibers reinforced polyester hybrid composites’, Journal of Reinforced Plastics and Composites, 29(14), 2119–2123.

[6] Nayak SK, Mohanty S, and Samal SK (2010a), ‘Hybridization effect of glass fibre on mechanical, morphological and thermal properties of polypropylene–bamboo/glass fibre hybrid composites’, Polymers and Polymer Composites, 18(4), 205–218.

[7] Bledzki AK, Jaszkiewicz A, Murr M, ‘Processing techniques for natural- and wood-fibre composites’, In Properties and performance of natural-fibre composites, Pickering, K. (Ed.) 301-329, Abington Hall, Abington, Cambridge, England: Woodhead Publishing Limited

[8] Onal L and Adanur S (2005), ‘Optimization of Compression Molding Process in Laminated Woven Composites’. Journal of Reinforced Plastic and Composites, Vol. 24,7

[9] Clarke GM and Kempson RE (Eds) (1997), Introduction to the Design and Analysis of Experiments, New York: Wiley

[10] Lochner RH and Matar JE (Eds) (1990), Designing for Quality: An Introduction to the Best of Taguchi and Western Methods of Statistical Experimental Design. Quality Resources, White Plains, New York

FIBER ORIENTATION OBSERVATION OF JUTE FIBER FILLED INJECTION MOLDINGS

Yuqiu Yang[1], Putinun Uawongsuwan[2], Cuntao Wang[2],
Masuo Murakami[2], Hiroyuki Hamada[2], Asami Nakai[3]

[1] *Donghua University, Shanghai, China*
[2] *Kyoto Institute of Technology, Kyoto, Japan*
[3]*Gifu University, Gifu, Japan*
Corresponding author's e-mail: amy_yuqiu_yang@hotmail.com

ABSTRACT: Natural fiber composites are considered to be very promising materials for the future. However, the mechanical properties of natural fiber composites are still comparatively low and highly scattered. In the study, the hybrid fiber concept was introduced whereby Jute and glass fibers were simultaneously incorporated to enhance the mechanical properties of the composite. And long fiber pellet pultrusion technique was adopted to prepare glass/PP or Jute/PP pellets. Because it is a new method which is able to fabricate composite pellets with relative long length fibers for injection molding process, where, glass/jute yarns were continuously pulled and coated with PP resin. A non-linear correlation between the fiber contents and tensile strength in the hybrid composites could be observed whereby the optimum hybridization of GF 10 wt% and JF 20 wt%. In particularly, fiber orientation of both jute and glass fibers are analyzed based on the SEM and X-CT observation results. Additionally, the fiber alignment correction factors of all the injection molded composites were calculated from the experimental tensile modulus. It is found that the fiber orientation was improved and more of them were aligned to MD direction under the hybrid effect. It is interested that with the addition of glass fiber into jute system material, both glass fiber and jute fiber could get better orientation. Therefore high modulus can be obtained even put small jute fiber into glass fiber/PP material system, for the soft jute fiber have help the rigid glass fiber orientated to flowing direction.

KEYWORDS: *Hybrid, fiber orientation, tensile modulus*

INTRODUCTION

In the recent decades, natural fibers as an alternative reinforcement in polymer composites have attracted attentions of many researchers and scientists due to their advantages over conventional glass and carbon fibers. However, the certain drawback of natural fibers/polymers composites is the incompatibility between the hydrophilic natural fibers and the hydrophobic thermoplastic matrices. This leads to undesirable properties of the composites [1]. At present, a whole green composite is not satisfied the needs of society. Therefore, in automobile factories of Japan, a green composite with green degree or weight content of natural components of 30 wt% is required.

The properties of the natural fiber reinforced composites can be improved by hybridizing with high strength synthetic fibers. Interspersing the two or more kinds of fiber in a common matrix forms the hybrid composites. The concept of hybridization gives flexibility to the design engineer to tailor the material properties according to the requirements, which is one of the major advantages of the composites. Arbelaiz A. et al. [2] found that flax fiber/glass fiber/polypropylene hybrid composites displayed higher strength values than those for flax fiber bundle/PP composites. Thwe M.M. and Liao K.[3] was found that the hybrid approach of blending more durable glass fiber with bamboo fiber is an effective way to improve the durability of natural fiber composite under environmental aging. G. Cicala et al. [4] investigated the hybridization of glass fibers with natural fibers for applications in the piping industry. The adoption of hybrid design allowed for a cost reduction of 20% and a weight saving of 23% compared to the current commercial solution.

Several factors affect the modulus of short fiber reinforced thermoplastics such as the characteristics of matrix and fiber, interfacial bonding, fiber content, void volume, fiber orientation distribution and fiber length distribution. During injection molding process, the distributions of fiber length and fiber orientation are governed by various factors [5]. Moreover, one of the main problems of fabrication of short fiber reinforced composites is the fiber breakage during compounding and processing and resulting composites have short fiber length distribution [6]. In addition, generally, synthetic like glass fiber/thermoplastic can be fabricated by side feed compound. However this method can not be used for natural fiber. Besides large bulk density, the rough surface of natural fibers can not be feed into resin consistently. Therefore, the long fiber pellet production technology [7] was adopted in the paper to resolve the compounding difficulties, fiber breakage during compounding and precisely controlled of fiber volume fraction in the pellet.

Several models for prediction of elastic properties of composites have also been proposed by many researchers. One of the major approaches to mechanical property prediction for short fiber reinforced composite is the modified rule of mixture (MROM), which has been mostly used to predict the modulus and strength of short fiber composite by taking into consideration the effects of fiber length and orientation distribution [8-10]. The other major approach is “laminate analogy” which combines the micromechanics of combining different phases with the macromechanics of lamination theory [11]. K.S.Ahmed and S.Vijayarangan [12] applied CLT to predict the elastic properties of jute-glass fiber hybrid laminate composite. The prediction by CLT showed close agreement with experimental values with a maximum deviation of 20%. However, most of CLT models were used for prediction of the laminate composite.

In this work, the mechanical properties of glass/jute/polypropylene hybrid injection molded composite were investigated related to the “Green degree”. The theoretical prediction based on classical lamination theory and determination of fiber orientation from fracture surface observation method is proposed to predict elastic modulus of the hybrid injection molded specimen. The predicted values from classical lamination theory are compared with the experimental values and the results are discussed.

MATERIAL AND EXPERIMENTAL

Materials and specimen preparation

In this study, two types of long fiber pellets including jute fiber/polypropylene (JF/PP) and glass fiber/polypropylene (GF/PP) were prepared by long fiber pultrusion technology. The schematic illustration of the long pellet making machine is shown in Figure 1. The lengths of the pellets in this study were 8 mm for JF/PP and 11 mm for GF/PP, respectively.

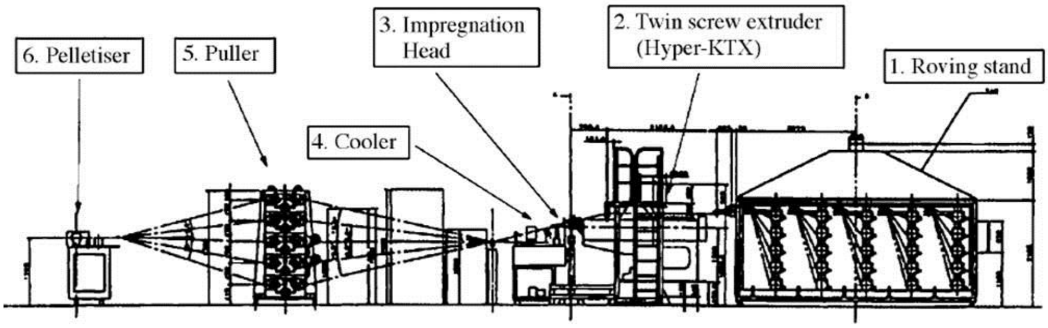

Fig. 1: Long fiber pellet pultrusion technology.

The pellets were dried at 80oC for 24 hours before molding to remove the moisture and then mixed to obtain the desired composite according to specimen designation in Table 1. The 50 tons injection molding machine (PO YUEN UM50) was used for specimen fabrication. The barrel temperature was set at 200oC while injection and holding pressure were 85 and 75 MPa, respectively. In this work, the “Green degree” is introduced which is defined as the weight fraction of natural component in a composite material.

Table 1: Specimens and material content of composites.

Specimen ID	**GF (wt.%)**	**JF (wt.%)**	**PP (wt.%)**	**Green degree (%)**
G10J0	10	0	90	0
G10J10	10	10	80	10
G10J20	10	20	70	20
G10J30	10	30	60	30

Mechanical test

Tensile tests were carried out by Instron universal testing machine with testing speed 1 mm/min and grip distance of 115 mm in accordance with ISO-527. The tensile modulus of elasticity was measured by using 10 mm gage length strain gauge (KYOWA, KFG-10-120-C1-11).

Scanning electron microscopy (SEM)

Scanning electron microscopic studied (SEM, JEOL: JSM 5200) were conducted to analyze the fiber orientation. The fracture ends of the tensile specimens were mounted on copper stubs and gold coated to avoid electrical charging during examination.

RESULTS

The tensile properties of all composite are shown is Figures 3 and 4. The modulus of hybrid composite increased linearly with increasing jute fiber content and green degree. Based on the observation on the fracture, it is found that the jute and glass fiber are oriented in many directions and jute fiber show slight screw which is considered due to the twist in jute yarn.The y-intercept value of linear trend line of increasing in modulus still shows higher modulus than the 10 wt% glass fiber composite. This indicates that there is a synergistic contribution from both the jute and glass fibers in enhancing the tensile modulus of hybrid composite.

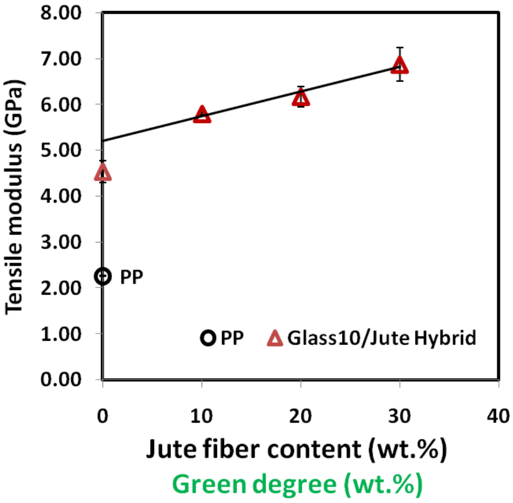

Fig. 2: Relationship between tensile modulus and jute fiber content i.e. green degree.

THEORETICAL PREDICTIONS

Laminate analogy from hybrid injection molded specimen

The design format for predicting modulus for short fiber hybrid systems is well developed for 2-dimensional structures. First, the 3-dimensional orientation of short hybrid fiber is transformed to the 2-dimensional laminate structure. In this study, only two main fiber orientation directions are considered as 0^o and 90^o to the flow direction, respectively. The schematic of laminate analogy was shown in Figure 3.

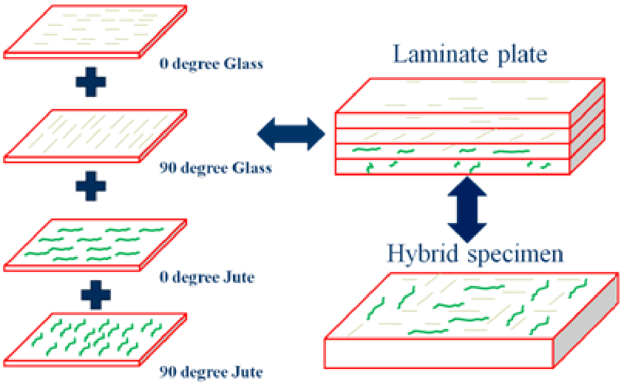

Fig. 3: Schematic of laminate analogy for predicting mechanical properties of 2-dimensional short fiber composites.

Elastic properties of unidirectional fiber lamina

The elastic properties of unidirectional G0, G90, J0 and J90 laminas were predicted using simple rule of mixture relationships from the mechanics of materials approach.

$$E_{l,i} = E_{f,i}V_{f,i} + E_{m,i}V_{m,i} \qquad (1)$$

$$\nu_{lt,i} = \upsilon_{f,i}V_{f,i} + \upsilon_{m,i}V_{m,i} \qquad (2)$$

$$\frac{1}{E_{t,i}} = \frac{V_{f,i}}{E_{f,i}} + \frac{V_{m,i}}{E_{m,i}} \qquad (3)$$

$$\frac{1}{G_{lt,i}} = \frac{V_{f,i}}{G_{f,i}} + \frac{V_{m,i}}{G_{m,i}} \qquad (4)$$

Where $E_{f,i}$, $\nu_{f,i}$, $G_{f,i}$ and $V_{f,i}$ are elastic modulus, Poisson’s ratio, shear modulus and volume fraction of fiber in i layer, respectively. $E_{m,i}$, $\nu_{m,i}$, $G_{m,i}$ and $V_{m,i}$ are elastic modulus, poisson’s ratio, shear modulus and volume fraction of matrix in i layer, respectively. The material’s constant are provided in Table 2.

Table 2: Material’s constant using in elastic modulus prediction

Properties	**Glass fiber**	**Jute fiber**	**PP**
Young’s modulus (GPa)	76	55	2.26
Shear modulus (GPa)	0.2	0.38	0.42
Poisson’s ratio	30	7.24	0.42
Density (g/cm^3)	2.58	1.52	0.9

Lamina stress-strain relations

A laminate is composed of unidirectionally-reinforced lamina orientated in various directions with respect to the axes of the laminate. For in-plane (*l*-*t* axis) stress state, the reduced lamina stiffness matrix is defined as

$$[Q] = \begin{bmatrix} Q_{11} & Q_{12} & 0 \\ Q_{12} & Q_{22} & 0 \\ 0 & 0 & Q_{66} \end{bmatrix} \qquad (5)$$

Where,

$$Q_{11} = \frac{E_l}{1-\nu_{lt}^2 \frac{E_t}{E_l}},\ Q_{22} = \frac{E_t}{1-\nu_{lt}^2 \frac{E_t}{E_l}},\ Q_{12} = \frac{\nu_{lt} E_t}{1-\nu_{lt}^2 \frac{E_t}{E_l}}, \qquad (6)$$

$$Q_{66} = G_{lt}$$

The transformed reduced stiffness matrix in any x-y directions is defined as

$$[\bar{Q}] = \begin{bmatrix} \bar{Q}_{11} & \bar{Q}_{12} & 0 \\ \bar{Q}_{12} & \bar{Q}_{22} & 0 \\ 0 & 0 & \bar{Q}_{66} \end{bmatrix} \qquad (7)$$

For 0^o unidirectional lamina, the transform reduced stiffness is defined as

$$[\bar{Q}_0] = \begin{bmatrix} Q_{11} & Q_{12} & 0 \\ Q_{12} & Q_{22} & 0 \\ 0 & 0 & Q_{66} \end{bmatrix} \qquad (8)$$

For 90^o unidirectional lamina, the transform reduced stiffness is defined as

$$[\bar{Q}_{90}] = \begin{bmatrix} Q_{22} & Q_{12} & 0 \\ Q_{12} & Q_{11} & 0 \\ 0 & 0 & Q_{66} \end{bmatrix} \qquad (9)$$

From classical lamination theory, extensional stiffness matrix for hybrid laminate can be written as

$$\lfloor A_{ij} \rfloor = \lfloor \bar{Q}_{ij} \rfloor_{0J} (n_{0J} t_{0J}) + \lfloor \bar{Q}_{ij} \rfloor_{90J} (n_{90J} t_{90J}) + \lfloor \bar{Q}_{ij} \rfloor_{0G} (n_{0G} t_{0G}) \qquad (10)$$
$$+ \lfloor \bar{Q}_{ij} \rfloor_{90G} (n_{90G} t_{90G})$$

Where, n_{0J}, n_{90J}, n_{0G}, and n_{90G} are number of jute 0^o, jute 90^o, glass 0^o and glass 90^o layer in the laminate, respectively. The parameters t_{0J}, t_{90J}, t_{0G} and t_{90G} are thickness of jute 0^o, jute 90^o, glass 0^o and glass 90^o layer in the laminate, respectively.

The laminate elastic modulus was estimated using the relation

$$E_x = \frac{A_{11}A_{22} - A_{12}^2}{tA_{22}} \qquad (11)$$

Theoretically elastic modulus prediction

- Fiber volume fraction determination

The observation of fracture surface from SEM micrograph was proposed as the fiber orientation observation method. The fiber orientation was simplified to only two orientation direction as 0 and 90 degree to the flow direction as shown in Figure 4.

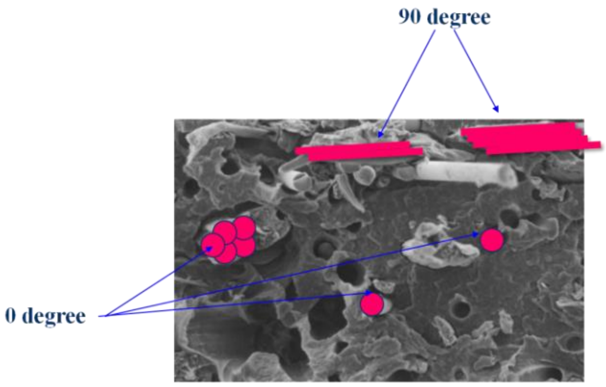

Fig. 4: The example of marking of fiber orientations on SEM micrograph of fracture surface.

For glass fiber, the fiber were marked related to 0 and 90 degree direction as shown in Figure 5. Then the number of marked fiber in 0 and 90 degree direction were counted and calculated to volume fraction by the following equations

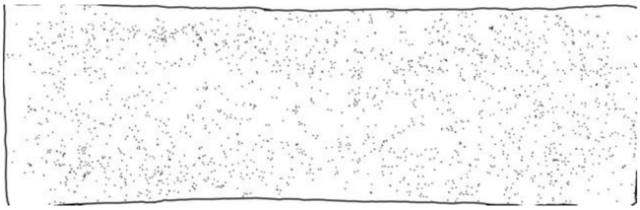

(a) G0 direction

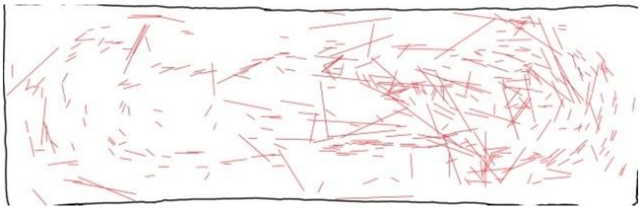

(b) G90 direction

Fig. 5: The glass fiber marking of G10J30 specimen :
(a) 0 degree and (b) 90 degree direction.

For volume of 0^o direction glass fiber

$$V_{G0} = V_{G,total} \frac{N_{G0}}{N_{G0} + N_{G90}} \tag{13}$$

For volume of 90^o direction glass fiber

$$V_{G90} = V_{G,total} \frac{N_{G90}}{N_{G0} + N_{G90}} \tag{14}$$

Where, N_{G0} and N_{G90} are the number of glass fiber in 0^o and 90^o direction, respectively.

For jute fiber, the cross-section area 0 degree direction of jute were marked as shown in Figure 6.

Fig. 6: Jute fiber marking in 0 degree direction of G10J30 specimen.

The area of marked jute fiber in 0 direction was measured and using area fraction for calculate the volume of jute fiber in 0 degree direction as following equation

For volume of 0^o direction jute fiber

$$V_{J0} = \frac{A_{J0}}{A_{specimen}} \times 100 \qquad (15)$$

For volume of 90^o direction jute fiber

$$V_{J90} = V_{J,total} - V_{J0} \qquad (16)$$

Where, A_{J0}, $A_{specimen}$ and $V_{J,total}$ are area of marked 0^o jute fiber, total area of fracture surface and total volume of jute fiber, respectively.

Then the volume of matrix in each lamina layer can be calculated by the following equations

For 0^o direction glass fiber layer

$$V_{matrix,G0} = V_{matrix,total} \frac{V_{G0}}{V_{G0} + V_{G90} + V_{J0} + V_{J90}} \qquad (17)$$

For 90^o direction glass fiber layer

$$V_{matrix,G90} = V_{matrix,total} \frac{V_{G90}}{V_{G0} + V_{G90} + V_{J0} + V_{J90}} \qquad (18)$$

For 0^o direction jute fiber layer

$$V_{matrix,J0} = V_{matrix,total} \frac{V_{J0}}{V_{G0} + V_{G90} + V_{J0} + V_{J90}} \qquad (19)$$

For 90^o direction jute fiber layer

$$V_{matrix,J90} = V_{matrix,total} \frac{V_{J90}}{V_{G0} + V_{G90} + V_{J0} + V_{J90}} \qquad (20)$$

The fiber volume fraction of each lamina can be calculated by equation (21) to equation (24)

For 0^o direction glass fiber layer

$$V_{f\ of\ G0} = \frac{V_{G0}}{V_{G0} + V_{matrix\ of\ G0}} \qquad (21)$$

For 90^o direction glass fiber layer

$$V_{f\ of\ G90} = \frac{V_{G90}}{V_{G90} + V_{matrix\ of\ G90}} \qquad (22)$$

For 0^o direction jute fiber layer

$$V_{f\ of\ J0} = \frac{V_{J0}}{V_{J0} + V_{matrix\ of\ J0}} \tag{23}$$

For 90° direction jute fiber layer

$$V_{f\ of\ J90} = \frac{V_{J90}}{V_{J90} + V_{matrix\ of\ J90}} \tag{24}$$

For determination of thickness of each lamina layer, the fiber fraction ratio was used to calculate as show in equation (25) to equation (28) and the calculated results of volume and thickness of all lamina layers are shown in Table 3.

For 0° direction glass fiber layer

$$t_{G0} = \frac{V_{G0}}{V_{fiber,total}} \times t_{total} \tag{25}$$

For 90° direction glass fiber layer

$$t_{G90} = \frac{V_{G90}}{V_{fiber,total}} \times t_{total} \tag{26}$$

For 0° direction jute fiber layer

$$t_{J0} = \frac{V_{J0}}{V_{fiber,total}} \times t_{total} \tag{27}$$

For 90° direction jute fiber layer

$$t_{J90} = \frac{V_{J90}}{V_{fiber,total}} \times t_{total} \tag{28}$$

Table 3: The calculated value of volume and thickness of each lamina layer of composites.

Code	V_{G0}	V_{G90}	V_{J0}	V_{J90}	t_{G0}	t_{G90}	t_{J0}	t_{J90}
G10J0	2.75	0.98	0	0	2.20	0.78	0	0
G10J10	3.07	0.83	1.42	5.19	0.87	0.24	0.40	1.47
G10J20	3.30	0.79	2.10	11.75	0.55	0.13	0.35	1.95
G10J30	3.43	0.86	3.07	18.76	0.39	0.10	0.35	2.14

The laminate elastic modulus for hybrid injection molded specimen can be calculated by using equation (10) and (11) and the results are shown in table 4. Good agreement between the values predicted by classical lamination theory and experimental results are obtained. The deviation between the experimental and predicted values was found to be up to 5.6%. The deviation may be attributed by the fiber distribution effects which are not included in this calculation.

Table 4. Predicted value by CLT and deviation between prediction and experimental.

Specimen ID	**Predicted modulus (GPa)**	**Experimental modulus (GPa)**	**Deviation (%)**
G10J0	4.28	4.53	-5.62
G10J10	5.49	5.80	-5.38
G10J20	6.20	6.18	+0.32
G10J30	7.05	6.88	+2.42

CONCLUSIONS

In this paper, the effect of hybridization on tensile properties of jute-glass hybrid injection molded composites is described. The tensile modulus of hybrid composite increased with increasing jute fiber content. The elastic modulus is predicted by using classical lamination theory. The theoretical approach with laminate analogy concept in this paper can be applied to jute-glass hybrid injection molded composites, with a deviation up to about 5% with the experimental results.

REFERENCES

1. H. Ku, H. Wang, N. Pattarachaiyakoop and M. Trada, (2011), *Composites: Part B*, 42, 856-873.
2. A. Arbelaiz, B. Fernandez, G. Cantero, R.L. Ponte and I. Mondragon (2005), *Composites : Part A*, 36, 1637-1644.
3. M.M. Thwe and K. Liao, (2002), *Composites : Part A*, 33, 43-52.
4. G. Cicala, G. Cristaldi, G. Recca, G. Ziegmann, A. El-Sabbagh and M. Dickert, (2009), *Materials and Design*, 30, 2538-2542.
5. N.O. Ahmed, M.S.A. Ahmed and B.M. Othman, *International Journal of Mechanical & Mechatronics*, 9, 361-367.
6. S. Patcharaphun and G. Opaskornkul, Kasetsart, (2008), *J. (Nat. Sci.)*, 42, 392-397.
7. T. Ohta, Y. Takai, Y.W. Leong and H. Hamada, (2009), *Polymers and Polymer Composites*, 17, 467-474.
8. S.W. Jung, S.Y. Kim, H.W. Nam and K.S. Han, (2001), *Composites Science and Technology*, 61, 107-116.
9. S. Patcharaphun and G. Mennig, (2007), *Journal of Metals, Materials and Minerals*, 17, pp.9-16.
10. G. Zak, M. Haberer, C.B. Park, B. Benhabib, (2000), *Rapid Prototyping Journal*, 6, 107 – 118.
11. J.L. Kardos, (1985), *Pure & Appl. Chem.* 57, 1651-1657.
12. K.S.Ahmed and S.Vijayarangan, (2006), *Indian Journal of Engineering and Materials Sciences*, 13, 435-442.

INFLUENCE OF THE TYPE OF FLUID AND INJECTION CONDITIONS ON THE PROCESSING OF NATURAL FIBER COMPOSITES

Gaston M. Francucci [1], Analia Vazquez [2], Edu Ruiz [3] and Exequiel S. Rodriguez [1]

[1] Composite Materials Group, Research Institute of Material Science and Technology (INTEMA-CONICET). Materials Engineering Department, Engineering Faculty, National University of Mar del Plata. J. B. Justo 4302, B7608FDQ, Mar del Plata, Argentina.
Corresponding author's e-mail: erodriguez@fi.mdp.edu.ar
[2] Polymer and Composite Material Group- INTECIN-CONICET – University of Buenos Aires. Las Heras 2214, CP 1127, Buenos Aires, Argentina.
[3] Chaire sur Composites à Haute Performance (CCHP), Centre de recherches en plasturgie et composites (CREPEC), Ècole Polytechnique de Montreal, C.P. 6079, Station Centre-Ville Montréal (Québec), H3C 3A7, Canada.

ABSTRACT: In composites manufacturing, proper impregnation of the fibrous reinforcement is key for obtaining consistent mechanical properties of the components. The capillary flow taking place during resin injection is an important driving force for the infiltration of the fibers. Capillary flow is also a main mechanism on the void formation during resin injection. In the case of natural fibers, important capillary effects appear due to the hollow structure of the fibers, small diameter and molecular polarity. In a previous work presented at FPCM10, the authors have shown the characterization of the capillary effects arising during the infiltration of natural fiber preforms. In this work, the effect of the type of fluid used for the permeability test on the unsaturated permeability value was estimated and related to the capillary effects developed during the infiltration. In addition, the permeability of the fabrics was measured under different injection conditions, constant flow rate and constant pressure, and the differences observed could be explained taking into account the capillary effects developed in each case. Finally, the capillary pressure obtained in the constant pressure experiments was used to correct the applied pressure gradient in the transient unsaturated permeability tests and thus a corrected value of permeability independent of the tests fluid was obtained. The results obtained suggested that the processing conditions, such as type of fluid, injection method and flow velocity could affect significantly the measurements of unsaturated permeability.

KEYWORDS: *capillary effects, permeability, natural fiber fabrics, bio-composites, liquid composite molding.*

INTRODUCTION

Natural reinforcements have the advantage of being renewable, abundant and cheaper than synthetic fibers. In addition, natural fibers are more environmentally friendly than synthetic and ceramic fibers. They also possess good specific mechanical properties. At the same time, natural fibers consume the same amount of CO_2 during the plant growing than the produced during fibers degradation. Liquid composite molding techniques have proven to be suitable for processing natural fiber composites [1]. In previous works [2-3], the relationship between saturated and unsaturated permeability and the compaction response of natural fiber fabrics were studied. Nevertheless, still there are some practical issues regarding the infusion of natural reinforcements, for example, the difficulty to impregnate the fibers under vacuum at room temperature leading to important voids formation within the tows.

Capillary effects have shown to be determinant in the mechanism of void formation during infiltration of fabrics [4-9]. Residual porosity has a detrimental effect on the mechanical properties of composites materials. Capillary pressure is also important at low impregnation rates since it acts as the driving force for the impregnation of the reinforcement [10]. In general, capillary pressure is dependent on flow velocity, and for a certain fiber-fluid system, it can vary from negative values (wetting case, where flow is enhanced) to positive values (non-wetting case; flow is retarded) when the velocity is increased.

Several studies have been conducted in order to determine the magnitude of the capillary pressure developed in synthetic fabrics infiltration. Batch et al. [7] investigated the capillary impregnation of aligned fibrous beds and found an optimal fluid speed for which micro and macro flow have the same rate and the void formation is minimized. Capillary pressures obtained for DOP fluid (dioctyl phthalate) and glass fiber (40-60 vol%) were in the order of 10 kPa. Patel et al. [4] found, as a general trend, an increase in the capillary pressure with the decrease in matrix surface tension. Also Bayramli et al. [11] found that high fluid velocities give large dynamic contact angles, which can adversely affect impregnation. Verrey et al. [12] conducted infiltration experiments in non-crimp fabrics with different test fluids. They found negative values of capillary pressure for polyethylene glycol and lauryllactam 12 and positive values for epoxy resin. Other authors have used different approaches to model the capillary forces acting in fiber performs. Also, Dimitrovova and Advani [13] modeled the capillary pressure for the flow across an array of aligned cylindrical fibers. By means of a free boundary program, they concluded that surface tension as well as viscous forces influences relative permeability and capillary pressure.

In the case of vegetable fibers (like jute) capillary effects are increased due to the hollow structure, low diameter and a polar character of the fibers [14]. Nevertheless, insufficient information can be found about the impact of the capillary effects on the LCM processing of natural fiber preforms. In this work, the effect of the capillary pressure developed during the infusion of jute woven fabrics with vinyl ester resin and a water/glycerin solution on the fabric transient unsaturated permeability measurements was analyzed. In addition, the effect of the injection method on the capillary pressure and the permeability measurements was studied.

EXPERIMENTAL PROCEDURE

Materials

In this work, commercial bidirectional woven jute fabrics (Castanhal Textil, Brasil; surface density = 300 g/m2) were used. The fabrics were washed with a 2% V/V distilled water and detergent solution, and then dried under vacuum at 70º C for 24 h to remove contaminants and normalize the fabrics conditions for all the injections. The test fluids used were a 22 % V/V water/glycerin solution (surface tension = 63 ± 0.1 mN/m) and a vinyl ester resin (Derakane

411-350, from Ashland, surface tension = 37 ± 0.1 mN/m). The surface tension was measured using the ring method, and the viscosity of the fluids was measured before every infusion by means of a Brookfield DV–II+ cone and plate viscometer (precision ± 0.0025 Pa.s).

Methods

Transient unsaturated permeability tests were carried out on jute bidirectional woven fabrics (surface density equal to 0.03 gr/cm^2) by using two different test fluids: a 22 % V/V water/glycerin solution (viscosity values near 0.150 Pa.s), and a vinyl ester resin (Derakane 411-350 from Ashland, viscosity values near 0.5 Pa.s). Prior to the permeability tests, the fabrics were washed with a 2% V/V distilled water and detergent solution, to remove contaminants and normalize the fabrics conditions for all the injections. Unidirectional injection experiments were performed in a rectangular metallic mold (500mm x 100mm) with an acrylic lid. The depth of the mold cavity used for each injection was set with metallic spacers in order to obtain the desired values of porosity. Mold deflection during the infiltration tests was avoided by using a 3 cm in thickness acrylic lid. Two injections were conducted for each porosity and type of fabric. The viscosity of the fluid used was measured before every infusion by means of a Brookfield DV–II+ cone and plate viscometer. In addition, in the tests performed with vinyl ester resin constant pressure and constant flow rate experimental configurations were used. In the former, a vacuum pump was used to force the fluid flow though the mold cavity, while in the latter the fluid was injected into the mold by a machine capable of keeping the injection flow rate constant.

RESULTS AND DISCUSSION

Regarding the capillary effects developed during the infiltration of natural fiber reinforcements, it was found in previous investigations [14] that capillary forces are strong due to the hollow structure, low diameter and a polar character of the fibers. When the fiber volume fraction increases, the capillary forces grow. Also, when a polar fluid (water/glycerin solution) was used negative capillary pressure values were obtained (enhancing flow) while when vinyl ester resin was used the capillary pressure value was positive (no spontaneous infiltration takes place).

Effect of the type of fluid on the unsaturated permeability measurements

In this work, the impact of capillary effects on the measured value of transient unsaturated permeability was investigated. Fig. 1 shows the permeability of the jute fabric for different porosities measured with the two different test fluids. As observed by other authors [15-16] the dependence of permeability on the type of fluid is an evidence of the importance of the wetting behavior and capillary forces acting in the infiltration process. In addition, the permeability measured with vinyl ester resin should be higher than the one measured with the water/glycerin solution, because the latter causes fiber swelling and therefore the permeability of the perform decreases as the injection takes place [2]. However, an opposite trend was experimentally observed, suggesting that capillary effects could have been responsible of the differences observed between experiments. Although the saturated permeability is not dependent on the pressure field or the capillary pressure developed at the flow front, the transient (unsaturated) value of this property does depend on the pressure distribution along the fiber bed. This issue arises by the calculus procedure used to obtain the transient permeability, in which the pressure gradient taken into account in Darcy's Law ignores the capillary pressure contribution to the flow movement. Therefore, if the magnitude of the capillary pressure is important, the permeability could be sub estimated if the capillary pressure opposes to the flow and overestimated if it enhances flow.

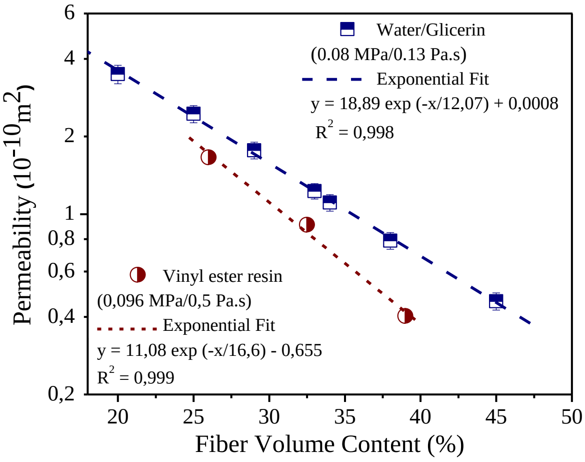

Fig. 1: Permeability results of jute fibers measured with different test fluids.

Due to its chemical composition, glycerin solution has higher polar character than the vinyl ester resin. Unlike synthetic fibers, natural fibers have hydroxyl groups in the surface, which make them more compatible with polar fluids. Therefore, as shown in [14], the capillary pressure was negative and enhanced flow when the reinforcement was injected with a water/glycerin solution, while it was positive (against flow) when vinyl-ester resin was used. This difference in the capillary pressure sign leads to an increase on the measured fabric permeability value when the test fluid is injected and a lower permeability value when vinyl ester resin is used.

From the previous observations of the differences obtained in the permeability measures with different fluids, it was suggested that unsaturated permeability data can be corrected if one knows the capillary forces acting at the fluid front. A correction was carried out for the permeability values obtained for a fiber volume content of 40 %. To correct these permeability values, the capillary pressures measured for the same fiber volume content were added to the measured pressure gradient during the permeability test. The results of the permeability correction for a fiber volume fraction of 40% are presented in Table 1. It results from this calculation that the difference between the corrected permeability values is below 5%. In addition, although this permeability value could be considered independent of the fluid used in the test, the corrected permeability value for the vinylester resin was higher than the one for the water/glycerin solution, which is consistent with previous investigations about the effect of fluid absorption and fiber swelling on the permeability of the preform [2].

Table 1: Corrected permeabilities for a V_f=40%.

	Water/Glycerin	**Vinylester Resin**
Original pressure gradient - ΔP (MPa)	- 0.08	- 0.096
Measured Capillary Pressure $\Delta P\gamma$ (MPa) [14]	-0.025	+0.036
Corrected pressure gradient considering capillary effects (MPa)	- 0.105	- 0.06
Original permeability (m^2)	6.95 E-11	3.48 E-11
Corrected permeability considering capillary effects (m^2)	5.3 E-11	5.57 E-11

Effect of the injection method on the permeability measurements

It has been stated that capillary effects depend on the dynamic contact angle, which is affected by the flow front velocity as described by the Hoffman–Voinov–Tanner law [17]. Verrey et al [12] verified experimentally the validity of the Hoffman–Voinov–Tanner law on epoxy resin, and they found that the capillary pressure increased with the capillary number. The equilibrium capillary pressure was negative, thus at a capillary number about 0.014 the capillary pressure was zero and above that value the behavior of the resin changed from wetting to non wetting.

In accordance to Verrey et al[12], the capillary pressure calculated with the constant flow rate procedure was higher than the calculated with the constant pressure test, as presented in a previous work [14]. This difference can be explained considering the influence of the capillary number on the capillary pressure. Constant pressure experiments lead to a wide range of capillary numbers because the fluid velocity decreased as the front moved further in the preform and also, the experiments were done with different applied pressure gradients. On the other hand, the capillary number is constant through all the preform during the constant flow rate experiments. Fig. 2 shows the capillary numbers obtained during the constant pressure and constant flow rate experiments, as a function of the percentage of the preform impregnated by the liquid flow. It can be seen that the capillary number was lower in the constant pressure experiments in more than 60% of the flow distance in the tests performed with the maximum pressure gradient (95 KPa), and more than 75% in the tests performed with the lowest pressure gradient (73 KPa). Consequently, as the vinyl-ester resin behavior was non wetting in both cases, the constant flow rate experiments leaded to a higher capillary pressure than the constant pressure tests, because the resin flow reached higher capillary numbers.

The unsaturated permeability of the jute woven fabric calculated from the constant pressure experiments was higher than the calculated with the constant flow rate procedure, as shown in Fig. 3. These results are consistent with the capillary pressure values found in both tests. This pressure drop is positive in both cases, so the lower capillary pressure developed in the constant pressure experiments had less effect on delaying the flow front, and the measured unsaturated permeability resulted higher. These results show, in accordance to other authors [18-22], that the injection method and flow rate affect the measured permeability values, and therefore all the experimental conditions should be reported together with permeability results.

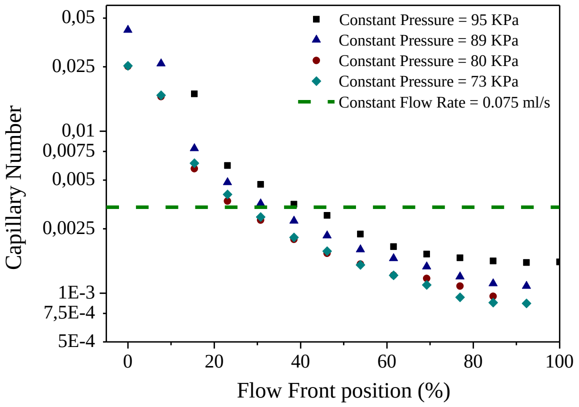

Fig. 2: Capillary numbers obtained in constant pressure and the constant flow rate tests, as a function of the flow front position.

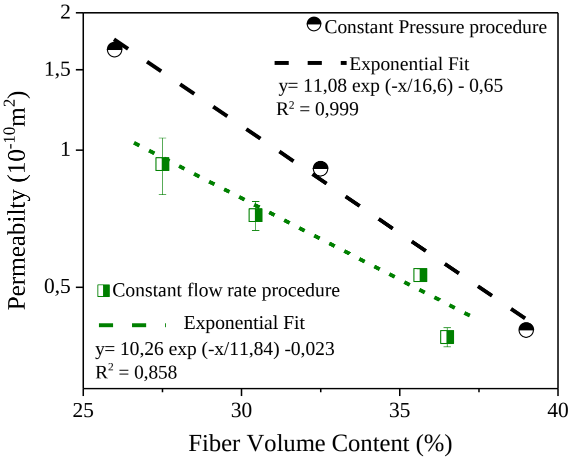

Fig. 3: Permeability vs. porosity curve determined with different injection methods: constant flow rate and constant applied pressure.

CONCLUSIONS

The capillary pressure drop developed at the flow front during infusion of jute woven fabric was calculated using the methods proposed by Verrey et al. [12]. These methods were chosen because they allow the capillary pressure to be estimated under dynamic conditions, which is more representative of the real infusion process. Both, constant flow rate and constant applied pressure experiments were performed. However, it was found, in accordance to the same authors, that the capillary pressure drop depends on the capillary number, thus the results obtained from the constant pressure experiments represent an average capillary pressure, because it changes strongly during impregnation of the fiber bed.

Although unsaturated permeability of preform is supposed to be a property of the reinforcement, it was found that it was affected by the injection fluid and the procedure used to measure this property. If the magnitude of the capillary pressure drop is significant (as it is in natural fiber fabrics) the unsaturated permeability measured using fluids more compatibles with the fibers will be higher than the measured with less compatible liquids. In this study, the measured capillary pressure was used to correct the pressure gradient applied in the permeability tests. Consequently, a corrected transient unsaturated permeability independent of the test fluid was obtained.

In addition, it was found that the injection method affects the capillary number and therefore, the capillary pressure drop. As a consequence, the measured unsaturated permeability values depend on the injection method. It was found that the lower capillary pressure developed in the constant pressure experiments had less effect on delaying the flow front, and thus the measured transient unsaturated permeability resulted higher than the obtained with the constant flow rate experiments.

ACKNOWLEDGMENTS: The authors acknowledge to the National Research Council of Argentina (CONICET) for the financial support, as well as the SECYT (PICT06 1560). In addition the authors acknowledge to the Government of Canada as part of the Canadian Commonwealth Scholarship Program (CCSP) and Government of Canada Awards (GCA).

REFERENCES

1. Rodríguez E, Petrucci R, Puglia D, Kenny J, Vázquez A (2005), ‘Characterization of different composites based on natural and glass fibres obtained by vacuum infusion’, *Journal of Composite Materials,* 39(3), 265-282.

2. Francucci G, Rodríguez ES, Vázquez A (2010), ‘Study of saturated and unsaturated permeability in natural fiber fabrics’, *Composites Part A: Applied Science and Manufacturing,* 41(1), 16-21.

3. Francucci G, Rodriguez E, Vázquez A. Experimental study of the compaction response of jute fabrics in liquid composite molding processes (2011), Journal of Composite Materials ; Published Online, DOI: 10.1177/0021998311410484.

4. Patel N, Lee LJ (1996), ‘Modeling of void formation and removal in liquid composite molding. Part I: Wettability analysis’, *Polymer Composites,* 17(1), 96-103.

5. Patel N, Lee LJ (1996), ‘Modeling of void formation and removal in liquid composite molding. Part II: Model development and implementation’, *Polymer Composites*, 17(1), 104-114.

6. Patel N, Rohatgi V, Lee LJ (1995). ‘Micro scale flow behavior and void formation mechanism during impregnation through a unidirectional stitched fiberglass mat’, *Polymer Engineer Science,* 35(10): 837-851.

7. Batch GL, Chen YT, Macosko CW (1996), ‘Capillary impregnation of aligned fibrous beds: Experiments and model’, *Journal of Reinforced Plastics and Composites,* 15(10), 1027-1051.

8. Binetruy C, Hilaire B, Pabiot J (2000), ‘The influence of fiber wetting in Resin Transfer Molding: Scale effects’, *Polymer Composites*, 33(4), 267.

9. Ruiz E, Achim V, Soukane S, Trochu F, Bréard J (2006), 'Optimization of injection flow rate to minimize micro/macro-voids formation in resin transfer molded composites', *Composites Science and Technology,* 66(3-4), 475-486.

10. Amico S, Lekakou C (2001), 'An experimental study of the permeability and capillary pressure in resin-transfer moulding', *Composites Science and Technology*; 61(13), 1945-1959.
11. Bayramli E, Powell RL (1992), 'Impregnation dynamics of carbon fiber tows', *Journal of Composite Materials,* 26(10), 1427-1442.

12. Verrey J, Michaud V, Månson JAE (2006), 'Dynamic capillary effects in liquid composite moulding with non-crimp fabrics', *Composites Part A: Applied Science and Manufacturing*; 37(1), 92-102.

13. Dimitrovova Z, Advani S (2002), 'Analysis and characterization of relative permeability and capillary pressure for free surface flow of a viscous fluid across an array of aligned cylindrical fibers', *Journal of Colloid and Interface Science,* 245(2), 325-337.

14. Francucci G, Vazquez A, Rodriguez ES, Ruiz E (2010), 'Capillary effects in vacuum assisted resin transfer molding with natural fibers' *Proc. of The 10th International Conference on Flow Processes in Composite Materials (FPCM-10),* Ascona Switzerland.

15. Griffin PR, Grove SM, Russell P, Short D, Summerscales J, Guild FJ, and Taylor E (1995), 'The effect of reinforcement architecture on the long-range flow in fibrous reinforcements', *Composites Manufacturing,* 6(3-4), 221-235.

16. Steenkamer DA, Wilkins DJ, and Karbhari VM (1993), 'Influence of test fluid on fabric permeability measurements and implications for processing of liquid moulded composites', *Journal of Material Science Letters,* 12(13), 971-973.

17. Kistler SF and Berg JC (ed.) (1993). Hydrodynamics of wetting, in Wettability, New York: Marcel Dekker.

18. Visconti IC, Langella A, and Durante M (1998), 'The influence of injection pressure on the permeability of unidirectional fibre preforms in RTM', *Proc. of The 8th European Conference on Composite Materials (ECCM-8),* Naples, Italy.

19. Gauvin R, Trochu F, Lemenn Y, and Diallo L (1996), 'Permeability measurement and flow simulation through fiber reinforcement', *Polymer Composites,* 17(1), 34-42.

20. Chan AW, Larive DE, and Morgan RJ (1993). 'Anisotropic permeability of fiber preforms: Constant flow rate measurement', *Journal of Composite Materials,* 27(10), 996-1008.

21. Dave´ R (1990), 'A unified approach to modelling resin flow during composite processing', *Journal of Composite Materials,* 24(1), 22–41.

22. Kim SK, and Daniel IM (2007), 'Observation of permeability dependence on flow rate and implications for liquid composite molding', *Journal of Composite Materials,* 41(7), 837-849.

DEVELOPING A NOVEL MANUFACTURING TECHNIQUE FOR MANUFACTURING NATURAL FIBRE REINFORCED THERMOPLASTICS

S.M.R. Kazmi, R. Das, S. Bickerton, Q. Govignon and K. Jayaraman

Department of Mechanical Engineering, Faculty of Engineering, University of Auckland,
Private Bag 92019, Auckland 1142, New Zealand. Corresponding author's e-mail:
skaz012@aucklanduni.ac.nz

ABSTRACT: Natural fiber reinforced thermoplastics have gained importance because of their light weight, good mechanical properties and sustainability. Many techniques to manufacture these composites use matched moulds and presses, requiring high setup cost. The focus of this study is to develop a novel manufacturing technique for fibre reinforced thermoplastics, which involves consolidation of laminates under a flexible vacuum bag inside an oven. With a comparatively lesser capital expenditure, this technique is expected to be cost effective in producing complex shaped parts. It would be too expensive to invest on matched moulds for parts that are not produced at a large scale (e.g. one-off production). An experimental study is presented on flax fibre reinforcement, consolidated with PP (PP). Thickness, pressure and temperature of laminates along with the applied temperature and pressure were monitored during the experiment. Thicknesses of manufactured laminates were measured with a micrometer to calculate the achieved fiber volume fraction. The cross-sections of laminates were examined under an optimal microscope to examine the quality of consolidation. Two variations in the manufacturing technique were explored, where vacuum was applied to the mould differently with respect to time and quantity. The results showed that this manufacturing technique can produce parts at the highest possible fibre volume fraction. There was no significant difference in achieved thickness/fibre volume fraction for the two variations/methods studied. One of the two methods was recommended because of its convenience. Moreover, the importance of flax and PP sheet layup was found during this study. This work will contribute to developing a practical method to produce natural fiber reinforced thermoplastic composites with double curved surfaces and desired mechanical properties.

KEYWORDS: *Sheet consolidation, vacuum compaction, natural fibre, thermoplastics*

INTRODUCTION

Thermoplastic composites are widely used in industry due to their lighter weight, higher toughness, higher impact strength [1], lower processing times [2] and recyclability [3], as compared to most thermoset composites. Two reinforcements used in composites are mainly natural or glass fibres. Natural fibres are light weight, environment friendly and have a higher fibre content for the same mass [4], compared to glass fibres. Hence natural fibre reinforced thermoplastics (NFRTs) have significant potential to replace other composite types in applications where composite weight has significant importance..

The required geometry, size, mechanical performance and scale of production of a component or a mechanical part govern the manufacturing process to be used [5]. It is not practically feasible for a certain manufacturing process to be cost effective as well as time efficient for all types of applications. A manufacturing process can only target one or few industry or product type/s. Hence there is always a trade-off while selecting a manufacturing process for a specific product.

This paper develops a manufacturing technique extending from the basic approach of compression moulding [6] in order to manufacture natural fibre reinforced thermoplastics (NFRTs). This technique additionally involves the use of a flexible bag as the upper mould where compaction is achieved by applying vacuum inside the mould similar to that used in resin infusion [7]. The mould is kept inside an oven so that its temperature can be raised above the melting point of the thermoplastic to consolidate the natural fibres. The oven temperature and vacuum pressure were controlled and measured along with the thickness of the laminate produced.

This technique will be targeted towards a small scale or one-off production of large natural fibre reinforced thermoplastics comparable to a volume of one meter cube. This technique will need lesser tooling costs compared to compression moulding that will require huge presses and moulds to manufacture these large parts. The flexible bagging will ease the production of parts with double curvatures due to its in-experiment adjustability. Whereas a rigid mould cannot be changed once it is manufactured. This technique will also aim to cater demands for aircraft interior structures such as light weight and intricate designs.

This paper aims to evaluate two oven cycles in the manufacturing technique and evaluate its potential to produce sheet consolidated natural fibre reinforced thermoplastic composites. The experimental program, procedure and setup are given along with a discussion on factors affecting the consolidation quality of the manufactured parts.

MATERIALS AND PROCEDURE

Flax was used as the reinforcement and Polypropylene (PP) as the polymer/matrix to consolidate the reinforcement. The reasons for choosing this material system are as follows. Flax along with Kenaf is one of the most promising natural fibres. This is because flax composites have a higher fibre content and better mechanical properties compared to other natural fibres [8]. PP has a low viscosity amongst thermoplastics, reasonably good mechanical properties, dimensional stability and impact strength [9]. Three flax types (density 1.49 g/cm^3 from the supplier Libeco Lagae - Belgium), unidirectional, fine twill and coarse twill, were used with areal densities 0.031, 0.033 and 0.058 g/cm^2, respectively. The areal densities were calculated by weighing the respective flax sheets of known areas. Polypropylene (density - 0.9g/cm^3 and grade - Moplen HP548S) was supplied by Field International (New Zealand) in the form of 0.365 mm thick sheets. The melt flow rate of polypropylene used was found to be 7.43 g/10min at 230°C.

Figure 1 presents a schematic diagram of the experimental setup and material layout, with an example of unidirectional flax sheets inside an oven. PP and flax sheets of 100 x 100 mm^2 were kept together alternately to obtain a homogeneous laminate. A nylon bag was used to create a flexible upper mould. A breather is used to apply the vacuum inside the mould, and a

Teflon sheet separates the laminate from the nylon bag. The elevated temperature inside the oven melts PP, and the applied vacuum consolidates the PP and the flax sheets.

A setup for analysing out of autoclave prepreg (designed in-house) was used to measure the thickness and pressure variation in the laminate during the experiment. An eddy current transducer (Lion Precision Eddy Current Sensor: *Driver: P016-5090 NR*, Probe: *P015-6005*) was used to measure laminate thickness variation during the composite consolidation. The movement of the aluminium foil (shown in Figure 1) during the process was tracked by the eddy current sensor. The pressure transducer (Cerabar *M PMP48*) measured pressure inside the laminate as shown in Figure 1. The temperatures of the laminate and the oven were measured using high temperature thermocouples. The applied vacuum pressure was also measured using another pressure transducer (Edwards ASG 1000 mbar, supplied by VABS).

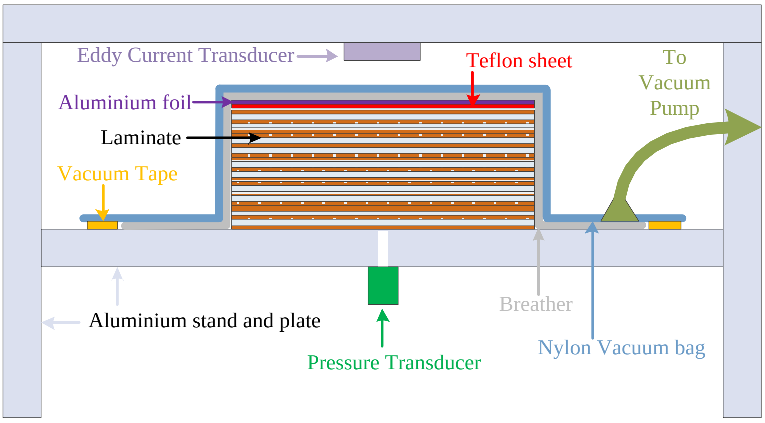

Figure 1: Schematic of the experimental setup to produce sheet consolidated NFRT

Thicknesses at different points of the manufactured laminates were measured. Fibre volume fraction of each manufactured laminate was calculated by using its average thickness. Cross-sectional views of the laminates were examined under a reflected light compound optical microscope (*Manufacturer: Olympus*, *Model # BX-60*) to examine the quality of consolidation.

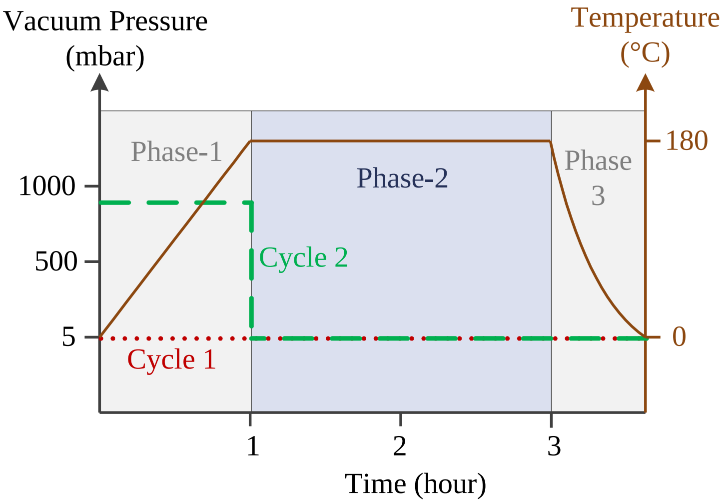

Figure 2: Schematic to describe different cycles employed and phases involved in the manufacturing technique

The second cycle (Cycle-2) is similar to a compression moulding cycle where the temperature of the mould was raised to 180°C before compaction was applied although there were two differences. The applied compaction pressure was limited to atmospheric pressure and the upper part of the mould was flexible. In the first phase, flax and PP sheets were kept under a nominal vacuum compaction pressure of 100mbar. Full vacuum was applied at 180°C in phase-2.

Table 1: Experimental program with target and achieved manufacturing details of FRP

	Target FVF	**Target Thickness (mm)**	**Flax sheets**	**PP sheets**	**Layup** Flax 0 ▤ Flax 90 ▨ PP □	**Achieved FVF**
Cycle-1_Uni	0.44	7	15	10	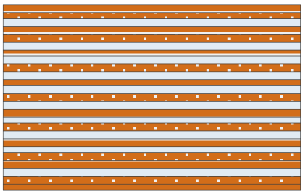	0.48
Cycle-2_Uni						0.47
Cycle-1r_Uni					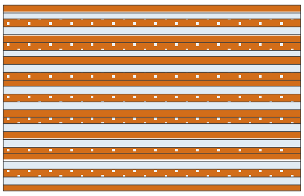	0.44
Cycle-1_Fine	0.32		10	12	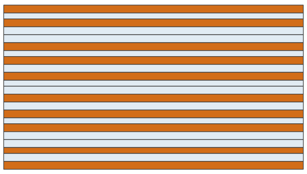	0.34
Cycle-2_Fine						0.31
Cycle-1_Coarse	0.40		7	11		0.41
Cycle-2_Coarse						0.41

Table 1 presents the experimental program and details for the manufacture of flax reinforced polypropylene (FRP). A set of seven experiments were carried out on three flax reinforcements (unidirectional, fine twill and coarse twill) based on cycles 1 and 2. Thickness and fibre volume fraction of the manufactured laminate depends on the number of fibre and polymer sheets. To achieve a certain part fibre volume fractions and thickness the number of flax and PP sheets had to be calculated. Based on this targeted fibre volume fraction, the laminate thickness and the available material dimensions, the number of flax and PP sheets were calculated for the respective experiments. This target fibre volume fraction was actually the maximum achievable fibre volume fraction for the three flax types under vacuum. The results of compaction characterization of the three flax types carried out earlier were used for this matter. Sheet layup and other details can be found in Table 1. Three flax reinforcements were used to confirm repeatability of the study. To keep the laminate symmetrical, a 0°/90° alternate layup was employed for the unidirectional fabric.

For Cycle-1 experiments with unidirectional flax, the PP sheets were concentrated in the centre of the laminate. Another cycle (Cycle-1r in Table 1), used for unidirectional flax only, was exactly similar to Cycle-1, except it had a slightly different layup of flax and PP sheets to monitor the difference in consolidation of the laminate. For cycle-1r experiments, the 10 PP layers were adjusted with respect to the 15 flax layers as shown in Table 1. Consequently, compared to Cycle-1, flax and PP sheets in Cycle-1r were distributed more homogeneously through the thickness. The results showed that there was not much fibre volume fraction difference between laminates produced by cycles 1 and 2.

Cooling in phase 3 was forced by a fan incorporated inside the oven. This practice reduced the overall manufacturing time and the final achieved thickness of the part. The thickness reduction occurred due to a rapid temperature drop as smaller matrix/resin/PP crystals were formed resulting in a more compact laminate. Laminate temperature in cycle-1r was forced to decrease at a slower rate than that for cycles 1 and 2. The reason behind this was to check whether there is any significant change in the thickness drop of the laminate or not.

RESULTS AND DISCUSSION

Figure 3 shows the laminate thickness, temperature and pressure along with the applied vacuum pressure during the three experiments to produce unidirectional flax reinforced polypropylene (UFRP). There are five separators drawn on Figure 3 to divide Phase-2 into three and Phase-3 into two parts.

It can be observed from the laminate thickness profile (Figure 3) during the experiments that there are two major reductions in the laminate thickness. The first one occurs when PP appears to melt and flow through the majority of the reinforcement thickness (Phase-2A) over a period of 45 minutes. There is a quick drop during the first 10 minutes and then a decrease at a slower rate for the next 35 minutes. During Phase-2A PP starts flowing as melted liquid. The fiber volume fraction increased from 0.28 to 0.37 for cycle-1 laminate and from 0.24 to 0.37 for cycle-2 laminate. For cycle-1b laminate, the fiber volume fraction increased from 0.28 to 0.39 during the same period of time. The second thickness reduction occurs when the laminate is cooled (Phase 3A) over a period of approximately 30 minutes. For cycle-1, fiber volume fraction of the laminate increased from 0.43 to 0.48, whereas for cycle-2 it increased from 0.43 to 0.47. Laminate thickness reduction while PP was melting, was smoother for cycle-1, compared to that for cycle-2. However, there was not any considerable difference between the final achieved thicknesses for cycles 1 and 2. During phase-2B there is a negligible thickness reduction for all cycles. Hence, it can be expected that decreasing this time would not affect the achieved laminate thickness. However, this act would certainly decrease the overall manufacturing time. Moreover, it could be seen in the curves that a sudden temperature drop after consolidation of the materials, also decreases the thickness considerably.

It can be seen in Figure 3 that during Phase-2c there is an unexpected laminate thickness increase for cycle-1r. Moreover after 13000 seconds there is a significantly slower thickness drop for cycle-1r as compared to that for cycles 1 and 2. These can be the reasons for a lower fibre volume fraction of the laminate produced by cycle-1r than those produced by cycle-1 and cycle-2.

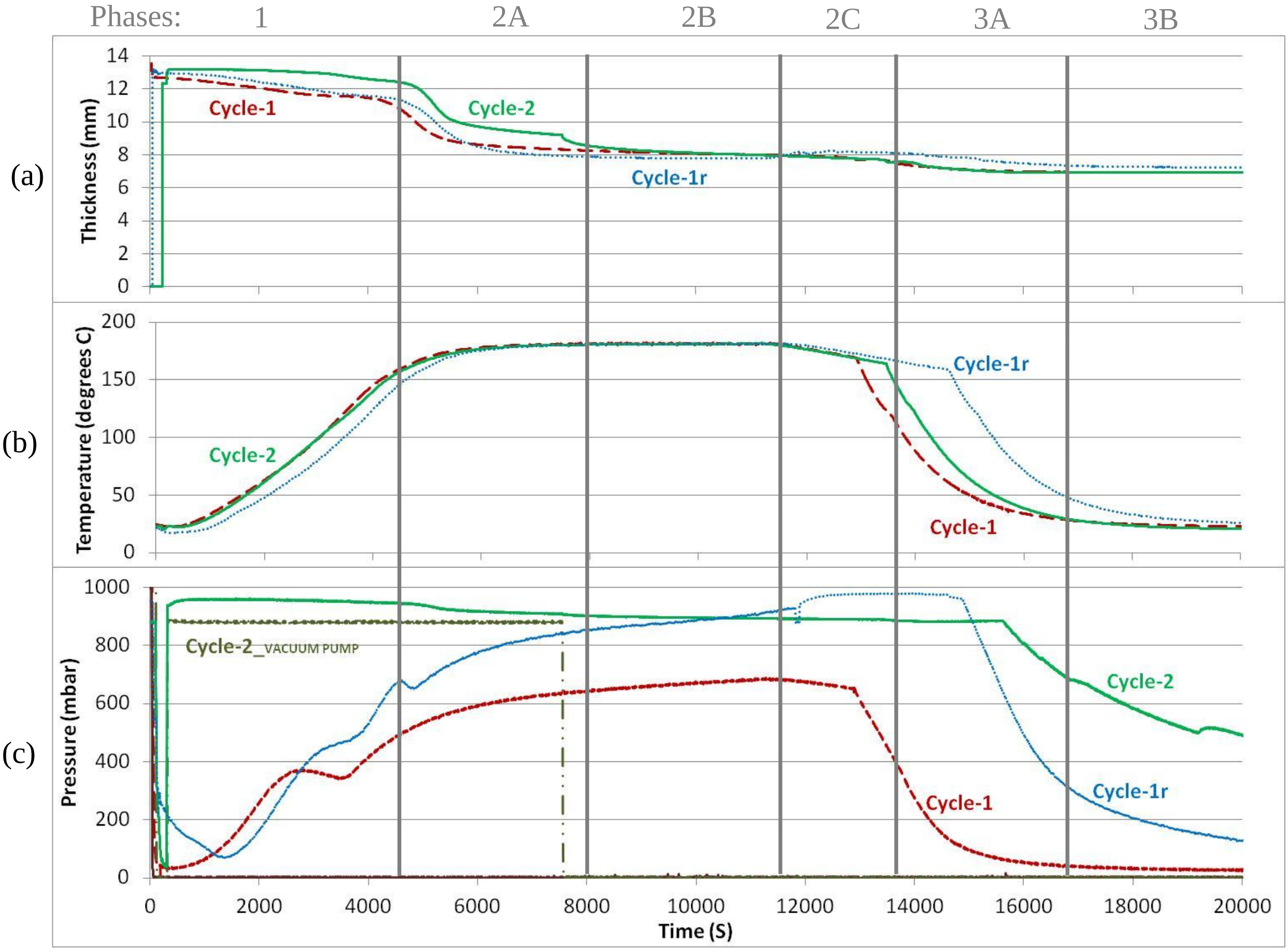

Figure 3: Measured quantities during the production of UFRP for both cycles
(a) Thickness, (b) Temperature and (c) Pressure

Laminate pressure for all the cycles could not be fully controlled by the applied vacuum. This implies that the PP sheets were not letting vacuum to be established on the side of the mould adjacent to the pressure transducer. There was also an increase in the mould pressure while PP was heated. This pressure increased to approximately equal to atmospheric pressure while it melted. When the semi consolidated sheets were left to cool, the mould pressure went down to below 50 mbar. This pressure came down at a much slower rate for cycle-2 as compared to cycle-1. Moreover there was no significant change in the mould pressure after full vacuum pressure was applied in cycle-2. Hence not much can be commented on the consolidation differences between the two cycles with the help of the pressure data. Achieved fibre volume fraction of the manufactured part for cycle-1 is not significantly higher than that for cycle-2. Hence, it is hard to deduce that keeping the preform under full vacuum from beginning of the experiment helps to better consolidate the fibres and polymer sheets together. However, cycle-1 is significantly more convenient than cycle-2 as lesser labour intervention/time is required for cycle-1.

Figure 4 shows images of unidirectional/PP laminate cross-sections, recorded using the optical microscope. The dark brown lines that can be seen are the fibre bundles along the plain of this 2D image. Almost circularly shaped collection of brown dots is actually the fiber bundles coming out of the plane of this image. The pure golden area is resin or matrix (i.e. PP). The circles in Figure 4 highlight the resin rich areas. Looking at the images, resin rich areas are considerably higher for parts produced with cycle-2 than those produced with cycle-1. It was noted that more than the cycle difference, it was the symmetrical layup of fibres and polymer that led to a better consolidation of the final part. Looking closely at figure 3 (a) and (b), it can be deduced that there are two resin rich layers for cycle-1 part. For cycle-1r part, there is a spread of resin rich areas but there is no complete resin rich layer.

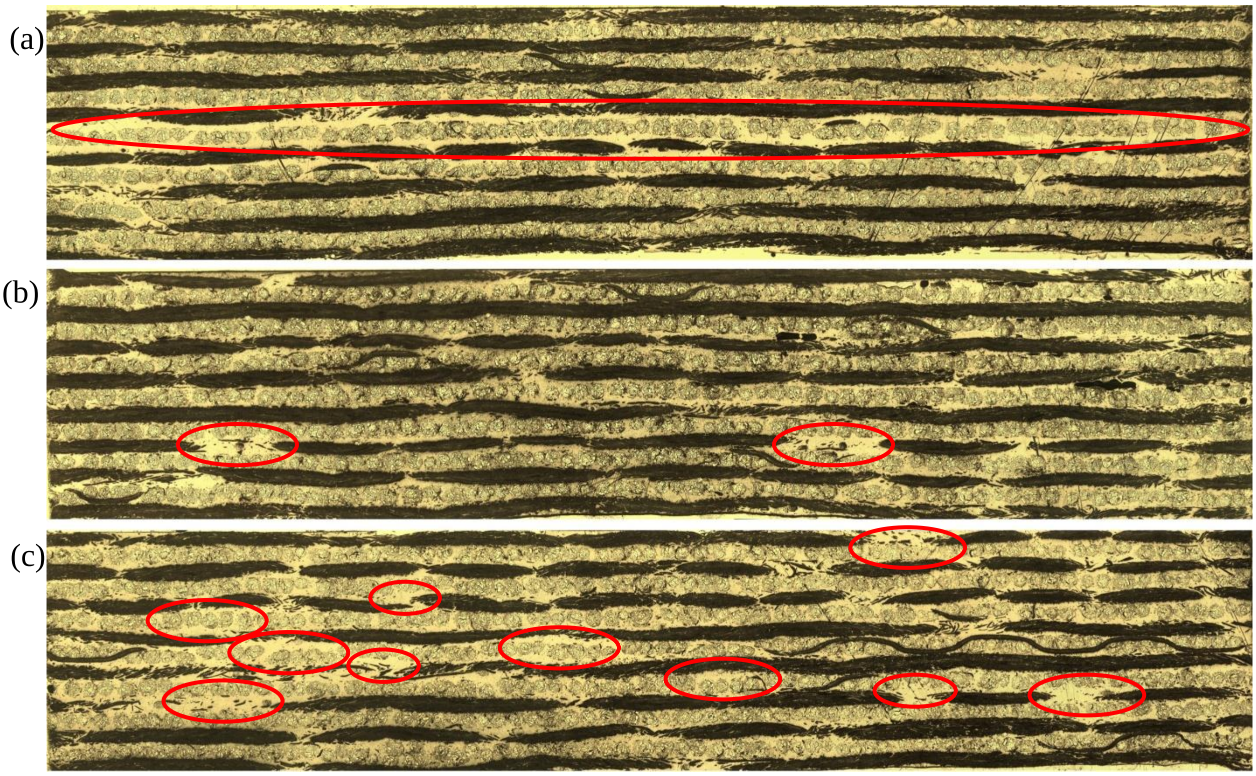

Figure 4: Microscopic view of manufactured UFRPs' cross-section
(a) Cycle-1, (b) Cycle-1r, (c) Cycle-2

CONCLUSIONS AND RECOMMENDATIONS

This paper has presented an experimental study on oven processed vacuum consolidation of natural fibre reinforced thermoplastics (NFRTs). Two distinct oven cycles were employed, and both of them produced parts of similar quality. However, cycle-1 was considered to be better because it required lesser human intervention during manufacture. It was found that this manufacturing technique has the ability to produce parts with the highest achievable fibre volume fraction possible under vacuum compaction. No significant change in part thickness was observed during the first two phases for all cycles. Moreover, in the holding phase (phase-2A), the thickness reduces gradually in cycle-1, compared to cycle-2. This might contribute to a slightly higher fibre volume fraction and lower resin rich areas for parts manufactured with cycle-1, as compared to those produced by cycle-2. This also results in different final thicknesses produced by the two cycles. Furthermore, cycle-2 laminates will be more porous, because full vacuum was applied at a later stage in cycle-2. It is shown that the fibre and polymer sheets must be alternately distributed in such a way that each polymer sheet has to flow as less than the full thickness of the adjacent fibre sheet as possible. This would enhance polymer impregnation in the fibres so as to induce an improved laminate consolidation. The cooling rate (Phase-3) also has considerable effect on the achieved fibre volume fraction. An increase in cooling rate produces thinner laminates (with higher fibre volume fractions).

In the future, two sets of experiments will be carried out to assess the effect of reduced manufacturing time on consolidation quality of the composites. Polymers with different viscosities will be used to study their effect on the consolidation quality. Different fibres will be used to study the variability of fibres on the manufacturing process. Through thickness permeability tests for different fibres will be carried out to understand the polymer flow pattern through the fibres. Tensile and short beam testing of manufactured parts will be carried out to compare the mechanical properties of parts produced from this technique and others (i.e. compression moulding). It is important to note that the focus of this work was to develop a manufacturing process, rather than finding the best combination of materials for a targeted manufacturing industry. There is scope to find potential in different combinations of natural fibre and thermoplastics that can be used with this manufacturing technique.

ACKNOWLEDGMENTS:

1. **HEC Pakistan** PhD scholarship (Monis Kazmi)
2. **Mr. Chris Hickey** for designing the out of autoclave prepreg to measure laminate thickness and pressure
3. **Mr. Ian Wright** for compaction characterization of unidirectional, coarse twill and fine twill flax.

REFERENCES

1. Talreja R, M.J. (2001), ed. Polymer matrix composites. Oxford: Elsevier Science Ltd.

2. Van Rijswijk, K. and H.E.N. Bersee (2007), Reactive processing of textile fiber-reinforced thermoplastic composites - An overview. Composites Part A: Applied Science and Manufacturing. **38**(3): p. 666-681.

3. Steenkamer, D.A. and J.L. Sullivan (1998), On the recyclability of a cyclic thermoplastic composite material. Composites Part B: Engineering. **29**(6): p. 745-752.

4. Joshi, S.V., et al. (2004), Are natural fiber composites environmentally superior to glass fiber reinforced composites? Composites Part A: Applied Science and Manufacturing. **35**(3): p. 371-376.

5. Bader, M.G. (2002), Selection of composite materials and manufacturing routes for cost-effective performance. Composites Part A: Applied Science and Manufacturing. **33**(7): p. 913-934.

6. Baekeland (1915), Method of making a plastic body. U.S. Patent No. 1,160,362. United States Patent Office, New York, U.S.A

7. Williams, C., J. Summerscales, and S. Grove (1996), Resin infusion under flexible tooling (RIFT): A review. Composites Part A: Applied Science and Manufacturing. **27**(7 PART A): p. 517-524.

8. Joffe, R. and J. Andersons (2008), Mechanical performance of thermoplastic matrix natural-fibre composites, in Properties and performance of natural-fibre composites. p. 402-459.

9. George, J., M.S. Sreekala, and S. Thomas (2001), A review on interface modification and characterization of natural fiber reinforced plastic composites. Polymer Engineering and Science. **41**(9): p. 1471-1485.

Section 8

Applications and Industry

FAST IMPREGNATION OF COMPLEX SHAPES FOR THE MANUFACTURING OF HIGH PERFORMANCE COMPOSITES AND ITS ASSOCIATED TOOLING

Clemens Dransfeld [1], Kunal Masania [1], Erich Kramer [1], Marcel Siegfried [2],
and Stefan Klauser [3]

[1] *University of Applied Sciences and Arts Northwestern Switzerland FHNW, Institute of Polymer Engineering, Klosterzelgstrasse 2, 5210 Windisch, Switzerland.*
[2] *formerly FHNW, now at Katholieke Universiteit Leuven, Belgium.*
[3] *RUAG Schweiz AG, RUAG Technology, Seetalstrasse 175, 6032 Emmen, Switzerland.*
Corresponding author's e-mail: clemens.dransfeld@fhnw.ch

ABSTRACT: Today's application of composites structures in aeronautical industry is limited by the high manufacturing cost due to the labour intensive character of the current manufacturing processes as well as the long processing times. When considering the resin transfer process (RTM) the cycle time is limited by two distinct phases: the impregnation phase and the curing phase. The compression resin transfer moulding (CRTM) process is characterized by the fact that injection is done in a partially opened cavity, thus permitting a faster distribution of the resin offering large potential to shorten the impregnation phase. This work aimed at investigating the underlying principles of CRTM and to understand how this process can be applied to complex aeronautical composite profiles, such as frames and beams. Starting from a plate tool with dwell pressure moulding capabilities, the principle of CRTM was successfully transferred to two different geometries, a closed rectangular overbraided section with a compliant core mechanism (denominated FX-core), and open C-section based on automated tooling with drawer. It was demonstrated that a reduction of impregnation time of several order of magnitudes could be confirmed. As an additional benefit the interfacial properties of the composite could be increased with this fast processing route.

KEYWORDS: *Resin transfer moulding, compression moulding, resin flow, carbon fibre reinforced polymers (CFRPs).*

INTRODUCTION

Several markets for advanced composites structures face a manufacturing challenge as current prepreg autoclave techniques are too labour intensive and time consuming, thus limiting further growth. A simple analysis of existing process steps (Fig. 1) shows that the variation of sequence of fibre positioning, fibre impregnation and fibre compaction is the most characteristic parameter of novel manufacturing approaches.

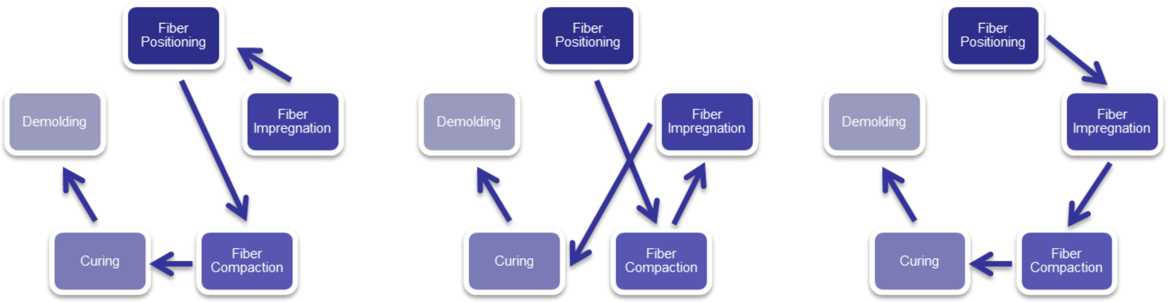

Prepreg / SMC / Filament winding *Resin Transfer Molding* *Compression RTM*

Fig. 1: Sequence of processing steps in various composite manufacturing processes

The resin transfer moulding process (RTM) is one attractive alternative where dry textile reinforcements are impregnated in direction of its plane in its compacted state in a closed cavity. The drawback of this technique is that the resin is being forced through a compacted preform over a considerable length resulting in several technological and scientific challenges related to the low permeability [1].

One appealing alternative to overcome above issues is the compression resin transfer moulding process (CRTM). In this process the cavity is not fully closed resulting in a reduced compaction of the preform and hence an increased permeability – or at best in a void space above the preform - for free flow distribution. In an idealized approach the flow length will only correspond to the thickness of the laminate rather than the length, which typically corresponds up to two orders of magnitude, as schematically shown in Fig. 2.

Fig. 2: Infiltration approach of conventional RTM versus Compression RTM

One limitation of this approach was based on the assumption that the CRTM process is limited to rather planar shapes. One aim of this work was to assess the benefits of such process in geometries of increasing complexity.

PLATE TOOL

A rectangular plate with the dimension of 180 mm by 380 mm was chosen for further investigation. In order to mould such geometry, a tooling concept based on vertical shut-off was selected. The corresponding process sequence is depicted in Fig. 3.

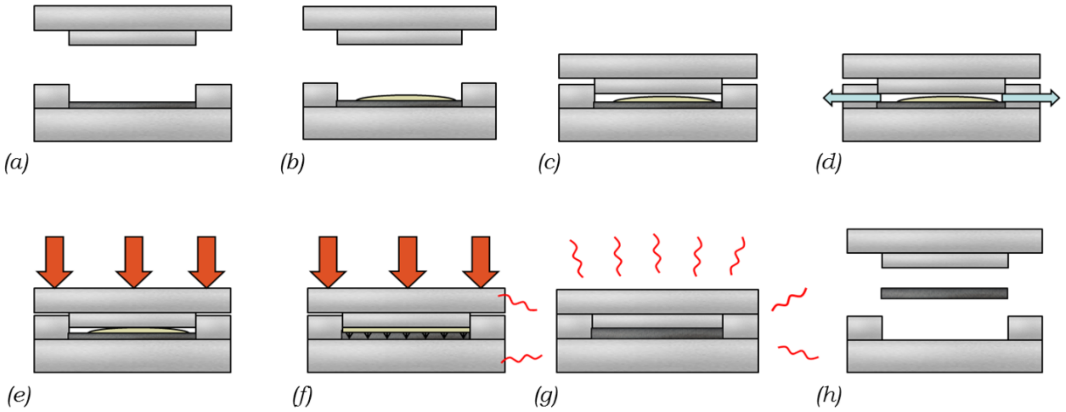

Fig. 3: Principle of compression resin transfer moulding: (a) reinforcement is placed into mould, (b) resin is dosed, (c, d) cavity is closed to intermediate position and evacuated, (e, f) pressure on the mould impregnates the reinforcement through the thickness, allowing a particularly high dwell pressure, (g) curing and (h) demoulding.

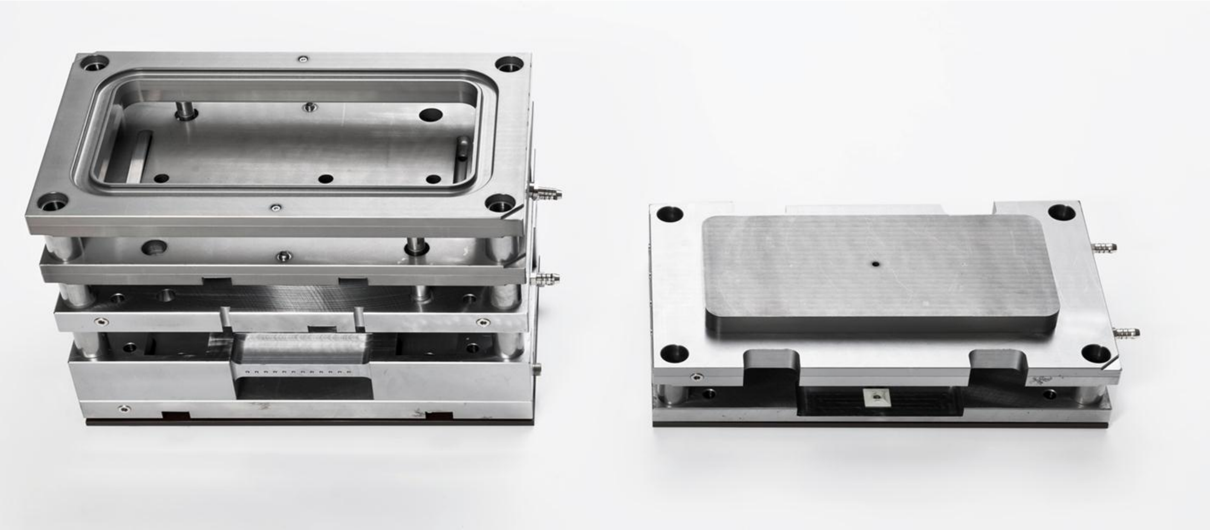

Fig. 4: Plate tool for the compression resin transfer moulding process. On the left side is the lower cavity with its frame in the ejected position, on the right side is the upper cavity.

By having a vertical shut off avoids the entrapment of an un-compacted preform in the parting line and supports an accurate positioning. After, or while dispensing the right amount of resin quantity, the tools is closed, but not to its final position leaving a void space above the reinforcement. It is now important to have a seal design that allows a full evacuation of the cavity in the position prior to full compaction. In the following compression step, the resin infiltrates the preform through the thickness and the preform is simultaneously compacted to its final thickness. Fig. 5 illustrates the dwell pressure acting over the whole cavity. The modelling of such flow phenomena is subject of various investigations [2].

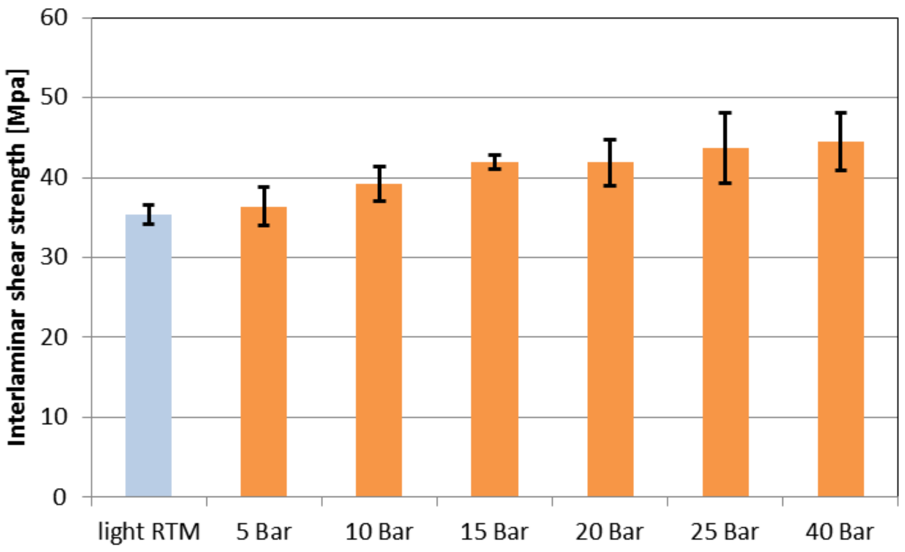

Fig. 5: The effect of CRTM dwell pressure on the interlaminar shear strength.

Compression RTM experiments have been carried out on RTM6 resin and carbon fiber non-crimped-fabric (NCF) with variations on dwell pressure. As shown in Fig. 5, it could be observed that the interface driven properties are slightly positively influenced by this new means of fast impregnation (at constant fiber volume content).

C-BEAM TOOL

By selecting a straight C-Profile, it was intended to assess whether the principle of compression RTM could be transferred to a rather complex geometry not having a main direction of consolidation. The principle chosen, as shown in Fig. 6 was based on a slide mold operated by springs and inclined planes. This offers the additional advantage to avoid pinching of the textile preform during closing and compaction. Particular attention was given to the sealing and ejection methods as the evacuation of the cavity had to be enabled before full closure of the mold. Heating was achieved with liquid, a method well established in injection molding.

The following experimental scenarios where further investigated with this tool.

- Conventional RTM
- Gap injection: resin is infiltrated by vacuum only in the gap position.
- Compression RTM

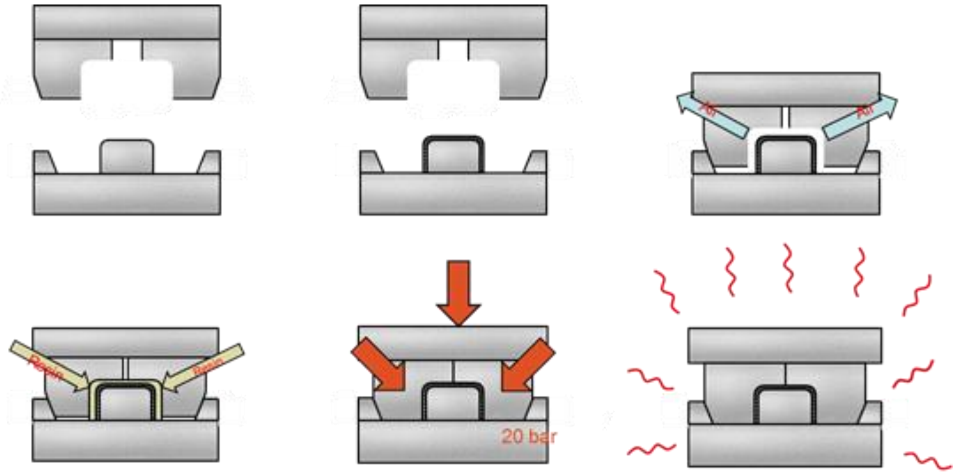

Fig. 6: Process sequence with compression RTM of a C-beam geometry.

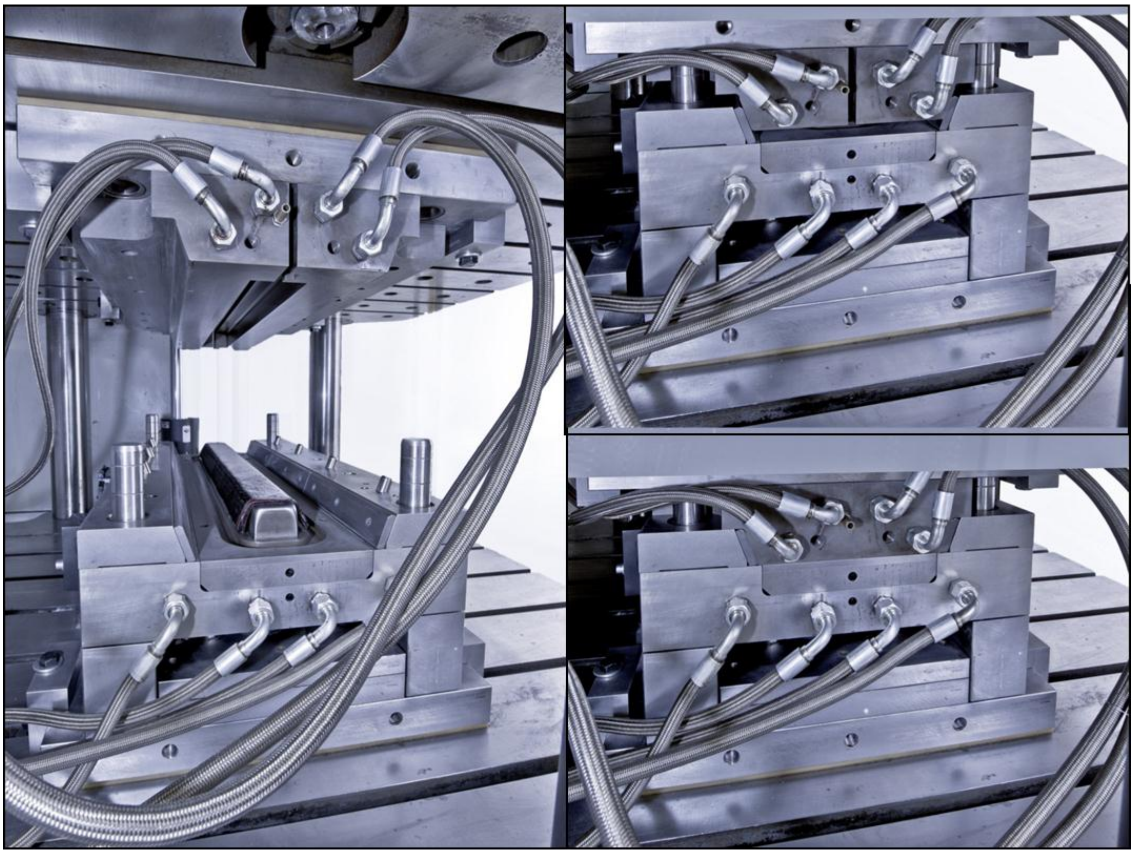

Fig. 7: Closing sequence of C-beam tool over preform.

Overall, changing from a classical RTM process with the prescribed temperatures ramps, to an isothermal cycle with CRTM reduced the cycle time from 7.5 to 2 hours. As shown in Fig. 8 the CRTM variant shows some impregnation problems on the inner mold line which points at potential problems related to the very high lateral impregnation speed. It could nevertheless be demonstrated that the principles of CRTM can be applied to a complex shape and the potential for high volume production could be confirmed.

Fig. 8: Inner mold surface of C-beam, left with gap injection (good wetting), right CRTM (dry spots resulting from to high impregnation speed).

HOLLOW SECTION TOOL (FX-CORE)

Another attractive approach to make C-profile is to make a rectangular profile based on the braiding process, which is then cut into two profiles in a consecutive step. The motivation for this being that the braiding process allows defined control of fibre angles and is characterized by minimal fibre wastage. The question was, whether the principle of CRTM could be applied to hollow section ideal wise with a functional mandrel to be used for braiding as well as curing.

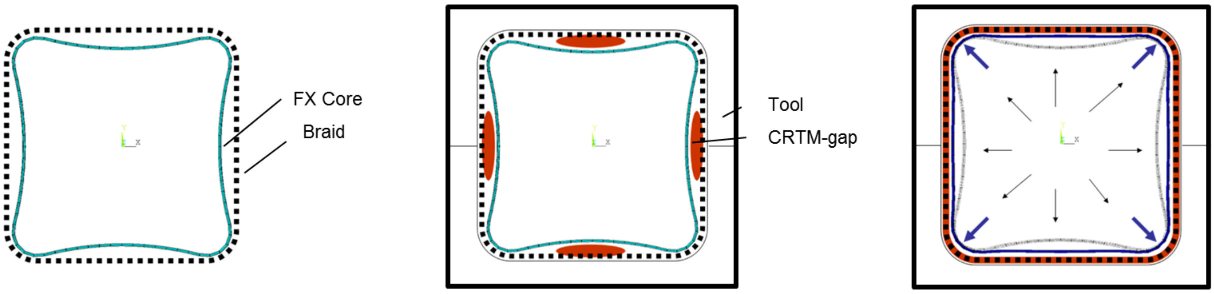

Fig. 9: Principle of functional core with compliant bending (FX Core)

The concept (Fig. 9) is based on a hollow braiding mandrel with concave sides made of a thin GRP skin resulting in high membrane stiffness, but locally compliant in bending. The core has enough stability to be handled on a braiding machine; when inserted into the curing tool, the concave hollows serve as “gap” during the resin injection. The compression step is achieved by inflating the core; this leads to the out-of-plane impregnation of the laminate characteristic to CRTM. Furthermore due to the properties of the core the braid is stretched and is particularly well consolidated in the corners (Fig. 10) where bridging would usually occur with a rubber core.

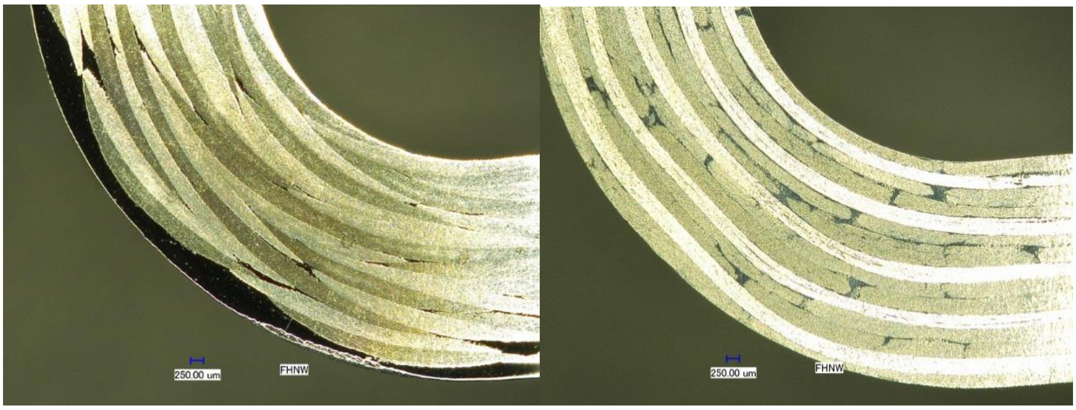

Fig. 10: Micrograph of braided profile corner (left) compared to a corner from a profile made of discontinuous layers of non-crimp fabric, the scale bar is 250 µm.

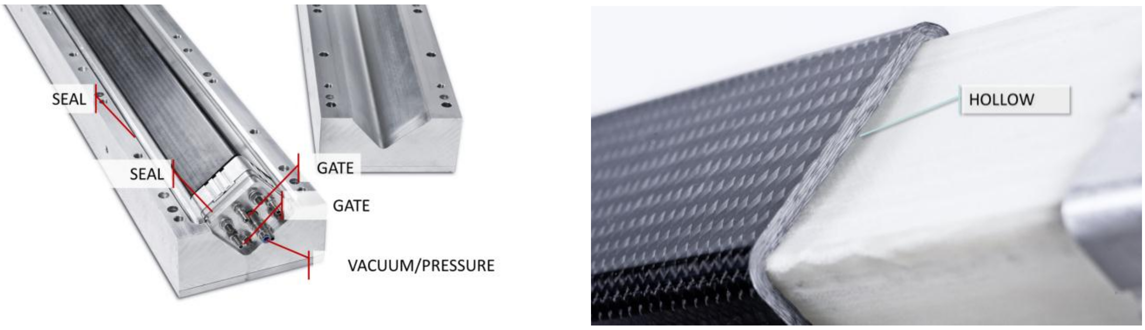

Fig. 11: Details of FX-core impregnation tool

The thickness distribution has been validated over the length of the profile at the four sides (Fig. 12). Two observations were made: first the compliance of the core is affected on the sides by the end cap with the gates, second, the longer sides 1 and 3 are stronger compacted than the short ones.

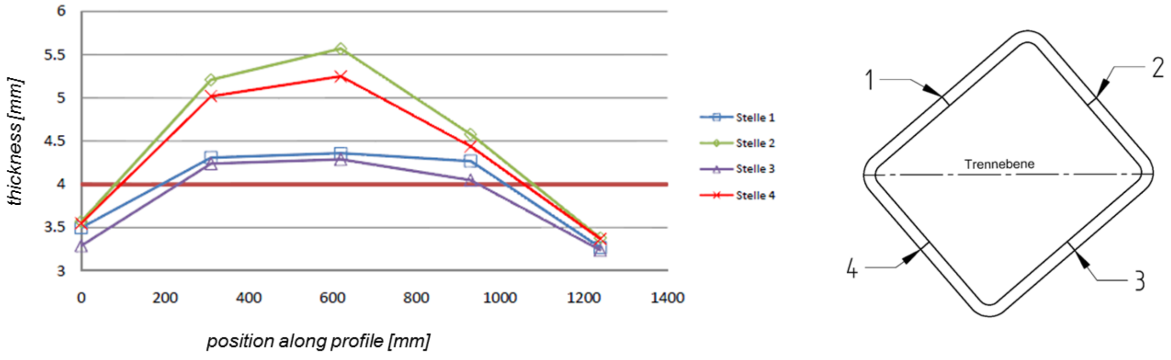

Fig. 12: Thickness distribution over profile.

CONCLUSIONS

The cycle time in liquid composite molding is limited by two distinct phases: the impregnation phase and the curing phase. In the scope of this work it was demonstrated that the impregnation phase could be substantially reduced by the Compression RTM process. It was furthermore demonstrated, that this processing approach can be transferred to geometries of various complexity and represents a promising technique for high volume production of advanced composites.

Future work will have to focus on increasing the technology readiness level of the various approaches. The additional processing parameters need further investigations with respect to their effect on structure property relationship.

ACKNOWLEDGMENTS: A special thanks goes to Karin Birkefeld and Tjark van Reden from Stuttgart University, Institute of Aircraft Design for kindly supporting the braiding activity. The plate and C-beam tool where manufactured by Alpex technologies (Austria). The FX-core tool was manufactured with support from RUAG Technologies. Parts of this work were funded by the European Commission, grant agreement no. 212014, within the Seventh Framework Programme in the collaborative project Imac-Pro (Industrialization of Manufacturing Technologies for Composite Profiles for Aerospace Applications).

REFERENCES

1. Rudd CD, Long AC, K. N. Kendall KN and Mangin CG (1997), 'Liquid moulding technologies', Woodhead Publishing.

2. Merotte J, Simacek P and Advani SG (2010), 'Resin flow analysis with fiber preform deformation during Compression Resin Transfer Molding', *Composites: Part A*, pp. 881-887.

3. Dransfeld C and et al. (2011), 'Fast impregnation of complex shapes for the manufacturing of high performance composites and its associated tooling', *SETEC 2011 - SAMPE Europe Technical Conference*, Leiden.

4. Dransfeld C, Siegfried M, Birkefeld K and Van Reden T (2012), 'FX-Core: Functional Braiding Mandrel for the compression resin transfer moulding of profiles', *SEICO 2012 - SAMPE Europe International Technical Conference*, Paris, France.

MULTI-COMPONENT LCM PROCESSING FOR AERONAUTICAL STRUCTURAL APPLICATIONS – THE INFLUENCE OF DEFLECTION IN METERING AND HOMOGENIZATION

Florian Springl [1], Patrik Welz [2], Swen Zaremba [1]; Christian Weimer [2] and Klaus Drechsler [1]

[1] *Technical University of Munich, Institute for Carbon Composites, Boltzmannstraße 15, 85748 Garching, Germany. Corresponding author's e-mail: springl@lcc.mw.tum.de*
[2] *Eurocopter Deutschland GmbH, Production Technologies and Project, 81663 Ottobrunn, Germany. Corresponding author's e-mail: christian.weimer@eurocopter.com*

ABSTRACT: This paper summarizes important facts and their consequences for the introduction of a multi-component resin system for aeronautical LCM processes. A generic comparison of the cost impact of the change from one to multi-component resin system for LCM is given. Furthermore, this paper presents results regarding the influence of varying metering and mixing conditions of a thermo set resin on the quality of performance of the composite material. Finally a potential method for inline process monitoring of the homogeneity is presented.

KEYWORDS: liquid composite moulding, resin transfer moulding, process monitoring, mixing ratio, multi-component thermo set resin,

INTRODUCTION

Manufacturing of carbon-fibre-reinforced plastic (CFRP) composite structures, using the liquid composite moulding (LCM) process increases the quality of such structures by a higher automation and less manual production steps. This matches hand in hand the requirement for higher production volumes. For LCM processes in aeronautics today, premixed single-component material systems are used. Multi-component material systems are coming into the focus of the aircraft industries, due to obsolescence matters, cost, reduced logistical efforts, specific functionalisation and further increase in volumes.

A further disadvantage of such exothermal single-component resin systems are the storage or transport regulations, which have to be fulfilled due to health and safety executive (HSE) requirements.

Consequently new productions steps such as metering and mixing of multi-component resin systems must be introduced in order to prepare multi-component resin systems for their use in aerospace LCM applications. However, high quality, high repeatability and robust processes are required to enable a future qualification of such processes.

MOTIVATION FOR NEW COST-EFFECTIVE PROCESSES TO MANUFACTURE WITH MULTI-COMPONENT RESIN SYSTEMS

This study shows the cost-reducing potential and the main cost drivers for multi-component epoxy resin processes compared with single-component epoxy resin processes in the continuous and discontinuous process chain. Therefore three thermo set resins, suitable for aircraft applications, were chosen; one single-component (A) with the corresponding multi-component high temperature amine system (B) and one anhydride thermoset multi-component system (C).

Table 1: Investigated material systems

	A	B	C
Material system	single-component, amine system	multi-component amine system	multi-component anhydride system

All manufacturing steps for a helicopter main rotor blade system, beginning with the ordering of materials to the infiltration were investigated. Especially the quality safety tests in the continuous and discontinuous process were regarded. The results of the cost development for each manufactured main rotor blade, in terms of several general requirements, are presented in Figure 1.

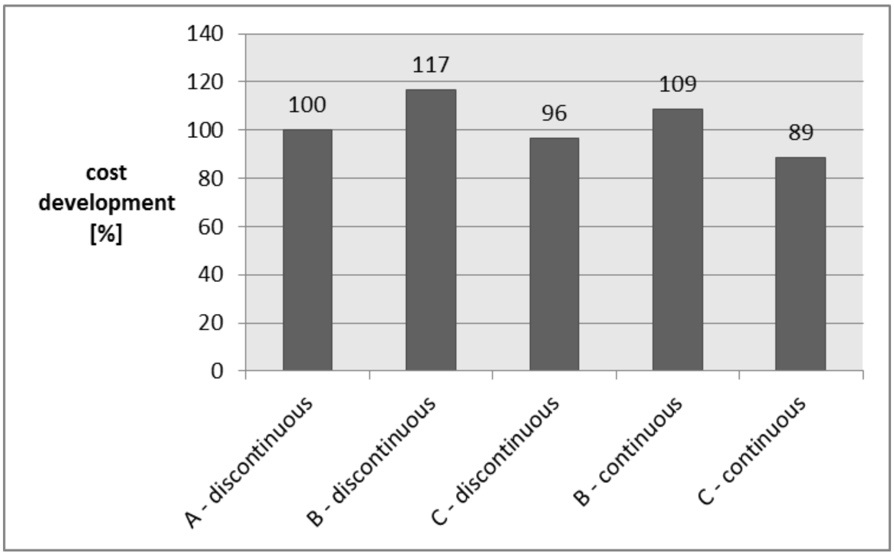

Fig. 1: Results of the cost development by using multi component resin systems compared with single component resin systems

The current RTM-production for helicopter parts at Eurocopter, Germany is a discontinuous manufacturing with the high-temperature single-component resin system and defines the 100%-costs value. The discontinuous production in which the metering and mixing step is separated and the continuous production in which the metering and mixing step is proceeded inline are in the focus of this study.

The main result of this investigation is that not just a change to multi-component processes leads to an effective manufacturing. A combination of an automated production with cost-effective multi-component resin systems and a continuous inline quality management reaches the most promising results.

REQUIREMENTS FOR MATERIAL OR PROCESS QUALIFICATION

To introduce new processes or material systems for the production of parts, a material and process qualification is necessary. “This step proves the ability of a given material/process to meet the requirements of a material specification; it is also the process of establishing the original specification requirement values. Rigorous material qualification testing considers the statistics of the data and is ideally a subset of, or directly related to, the design allowable testing performed to satisfy structural substantiation requirements” [1]. Regarding the role of the produced component, safety factors are defined by the national aviation authorities, such as the Federal Aviation Administration (FAA), the German Luftfahrtbundesamt (LBA) or the European Aviation Safety Agency (EASA). To fulfil the requirements concerning a qualification the examples to determine A-Values and B-Values are shown.

These commonly used aerospace tolerance limits are defined as:

- A-basis: At least 99% of the population of a respective property is expected to equal or exceed this tolerance limit with 95% confidence. FAR Sec. 25.613: A-basis values must be used where applied loads are eventually distributed through a single member within an assembly, the failure of which would result in a loss of structural integrity of the component.
- B-basis: At least 90% of the population of a respective property is expected to equal or exceed this tolerance limit with 95% confidence. FAR Sec. 25.613: B-basis values must be used for redundant structures in which the failure of individual elements would result in applied loads being safely distributed to other load-carrying members.

In order to compute a basis value for a normally distributed population, it is necessary to obtain estimates of the population mean $\bar{x}$ and standard deviation s, depending on the number of repetitions n [1].

$$\bar{x} = \frac{1}{n}\sum_{i=1}^{n} x_i \tag{1}$$

$$s = \sqrt{\frac{1}{n-1}\sum_{i=1}^{n}\left(x_i - \bar{x}\right)^2} \tag{2}$$

To calculate the basis values the following equations are used:

$$A = \bar{x} - k_a \cdot s \tag{3}$$

with k_a as one-sided tolerance limit factor

$$B = \bar{x} - k_b \cdot s \tag{4}$$

with k_b as one-sided tolerance limit factor.

The one-sided tolerance limit factor k depends on the number n of repetitions of each test. An approximation is given for normal distribution.

$$k_a \approx 2{,}326 + \exp(1{,}34 - 0{,}522 \cdot \ln(n) + \frac{3{,}87}{n}) \qquad (5)$$

$$k_b \approx 1{,}282 + \exp(0{,}958 - 0{,}520 \cdot \ln(n) + \frac{3{,}19}{n}) \qquad (6)$$

To determine the maximum potential of a material system in order to reach an optimum of light weight construction demands many iterations of n tests or a small standard deviation with robust processes. Increasing the number of tests to the infinite leads to the standard process-induced deviations. Therefore the influence of mixing deviation and the effect of an inhomogeneous material system is investigated.

THE INFLUENCE OF MIXING DEVIATIONS ON THE GLASS TRANSITION TEMPERATURE

In the context of the effect of metering deviation on the glass transition temperature T_g a study was implemented to investigate the influence. A commercially available epoxy infusion resin was tested with the differential scanning calorimetry (DSC) method (DIN 53765 1994: Testing of plastics and elastomeres; Thermal analysis; DSC-method). The DSC equipment was a Q200 of TA Instruments, New Castle, USA. The cooling unit is a RCS-90 of TA Instruments, New Castle, USA.

Under the focus of metering deviations of +5% and +10%, the glass transition temperature was determined. The results of the measurements are shown in Figure 2.

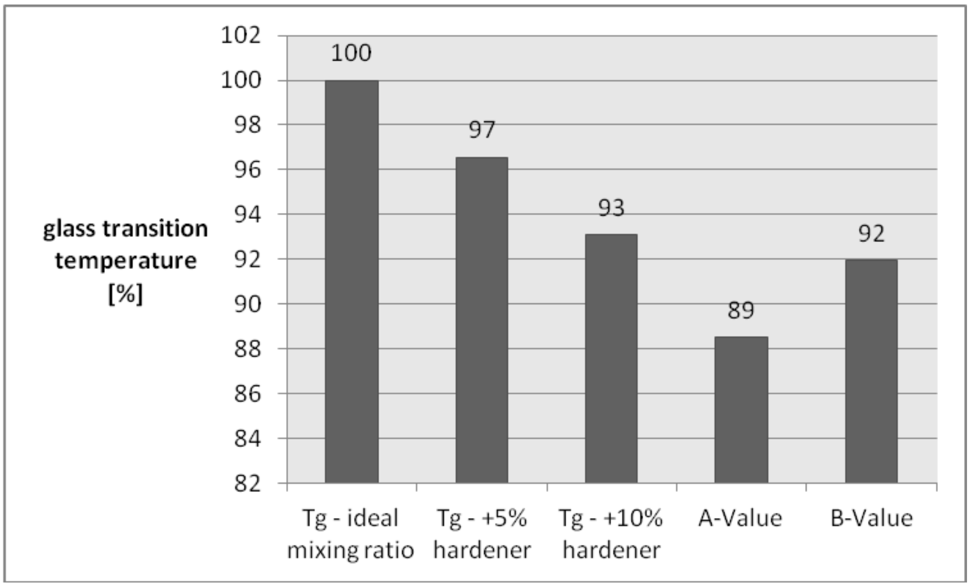

Fig. 2: Results of the differential scanning calorimetry (DSC) method (DIN 53765 1994) and the T_g development by varying the mixing ratio from ideal to +5% and +10% of hardener

The glass transition temperature is sensitive to metering deviations. Due to the correlation of the degree of cure and the glass transition temperature, the T_g depends on the quality of metering and mixing. The examination proves that the glass transition temperature drops from 100% at an optimum mix down to 97% by varying the amount of hardener by 5%. A variation of 10% of hardener causes a T_g reduction of 7 %.

With the population including deviation up to +5% and +10 % the T_g for part design is reduced by the A- and B-Value, as explained in the previous chapter. The statistic evaluation leads to a glass transition temperature for the A-Basis component of 89% of the origin T_g and for the B-Basis component of 92%.

To increase the statistical value, a higher number of tests or a reduction of the standard deviation is possible. Increasing the number of tests affects the material qualification time and therefore the costs. The other possibility is to manufacture with robust processes and online monitoring systems to guarantee the quality, or a small standard deviation.

THE INFLUENCE OF MIXING DEVIATIONS ON MECHANICAL PROPERTIES

The influence of metering deviation was investigated with the anhydride epoxy resin system (C) as used in the first chapter. For the examination the three-point bending test (DIN EN ISO 178) with multipurpose test specimens (DIN EN ISO 3167:2002 – Plastics – multi-purpose test specimens) was used. This standard is applicable to use the same specimens for tensile tests as well for pressure, bending and notch impact test with a simple modification. The equipment was an Inspekt 250 universal testing machine and a video extensiometer RTSS, Hegewald und Peschke, Nossen, Germany.

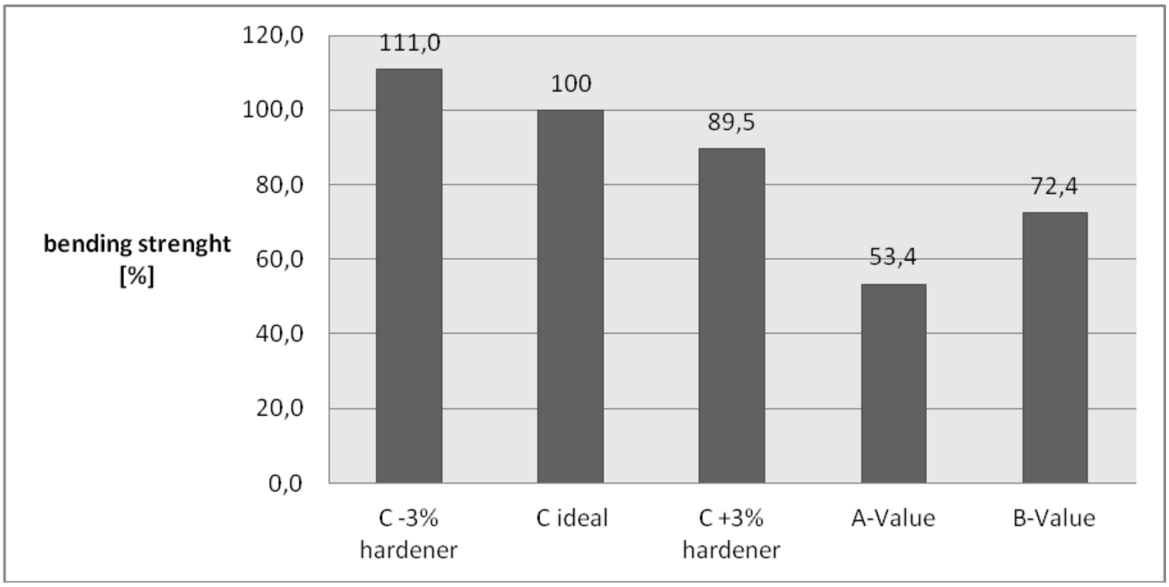

Fig. 3: Results of the three-point bending test (bending strength) development by varying the mixing ratio from ideal to -3% and +3% of hardener

The results of the three-point bending test show that a reduction of the hardener increases the bending strength of 11%. A higher amount of 3% of hardener leads to a reduction of 10.5%

bending strength. One possible explanation is that a higher degree of cure is achieved due to a higher amount of hardener. Therefore the specimen becomes more brittle and a pre-damaging of the specimens is induced by de-moulding. In this study 8 specimens for each configuration were tested.

With the population including deviation up to ±3% the bending strength for part design is reduced by the A- and B-Value thematic. For an exemplary material test 53.4% respectively 72.4% of the origin bending strength must be used for a part dimensioning.
For an optimisation of the test results the same methods should be used as mentioned before.

To increase the A / B – values the above investigation shows it is necessary to decrease the process-induced standard deviation. One solution is an inline process monitoring system presented in the next chapter. The global goal is to integrate this monitoring system into the continuous inline production chain of multi-component thermo set resin systems. The automation leads to an increase in quality, increased material properties (A/B – value) and finally a reduced part weight.

THE METHOD OF MONITORING THE MIXING CONDITIONS BY USING ULTRASOUND TECHNOLOGY

Online process monitoring in the production chain of CFRP components occupies a central role and is the focus of current research studies, as well as in industrial applications. Techniques such as di-electrical analysis (DEA) [3], direct current resistance (DCR) [4], Fourier transformed infrared spectroscopy (FTIR) [5] or the refractive index technology [6] are investigated for different purposes. The ultrasound technology is used to monitor the progress of resin cure and flow front progression. The cross linking process, the vitrification and the glass transition temperature are determined by ultrasound process inspection, measuring the ultrasound velocity c [2]. For liquids

$$c = \sqrt{\frac{\kappa}{\rho}} \tag{7}$$

and for solids

$$c = \sqrt{\frac{E(1-\mu)}{\rho(1-\mu-\mu^2)}} \tag{8}$$

is valid (μ =Poisson value; E = E-Modulus).

To obtain information on the resin and hardener distribution in the mixture, relevant velocity differences in the single-components are required. In most cases the resin has an equal density ρ to the hardener. Only the compression modulus κ can afford a different sound velocity of the liquids, as shown in equation 7.

For the investigation of the ultrasonic speed in the single-components of a resin system as well as in the mixture of each, respectively with mixing deviation a heatable press with oppositely integrated sonotrodes was used.

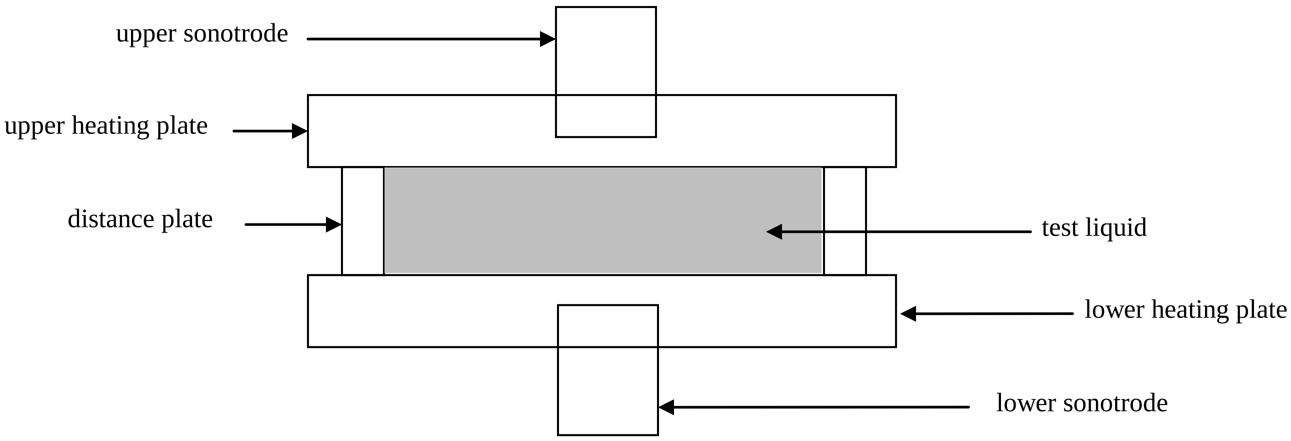

Fig. 4: Drawing of ultrasound test equipment used for sound velocity measurement in thermo set resin systems

With the defined gap between both heating plates the determination of the sound velocity c is possible. The results are summarised in Figure 4.

The single-components, resin and hardener, the ideal mixture and a mix with 3% more hardener was measured. The temperature was applied from 30 °C up to 130°C with a heating rate of 2.5 °C/min.

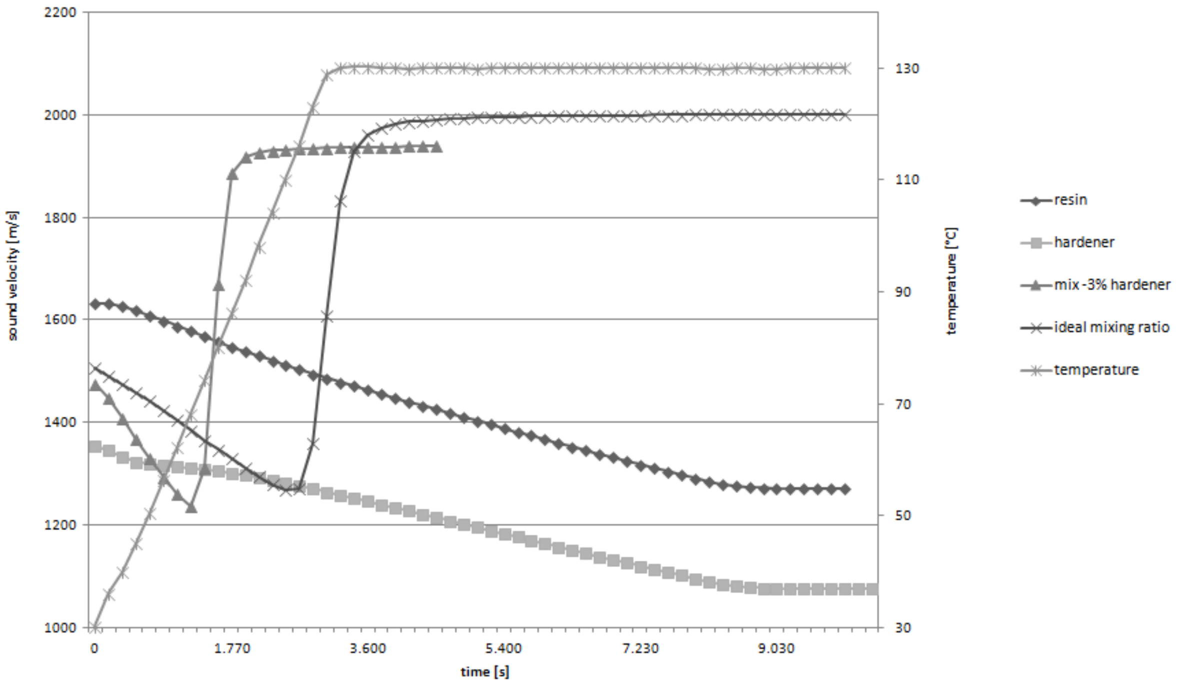

Fig. 5: Results of ultrasound testing with resin, hardener, ideal mixture and a mix with +3% hardener and a temperature profile from 30°C to 130°C (heating rate: 2.5°C/min)

Figure 5 shows that the initial sound velocity of the resin is approximately 1,640 m/s and that the hardener 1,360 m/s at 30 °C. By increasing the temperature a linear correlation is visible by a reduction of the sound velocity.

In the ideal mix (1:1) the initial velocity is 1,500 m/s at 30 °C. The cross linking process can be followed. The viscosity is reduced to 1,600 s after starting. The reaction between the resin and the hardener is visible by 1,800 s after the start. The same procedure was applied to the mix with +3 % of hardener. The reaction starts at 3,200 s, ends at 3,600 s and reaches a higher end velocity, due to a higher degree of resin cure.

CONCLUSIONS

The results of this paper present the economic and technological motivation for an introduction of multi-component resin systems in the production process of CFRP components for aeronautical applications. The introduction of multi-component resin systems needs a material qualification. In this context the achievable material values for part design are influenced by the statistical evaluation (A/B -values), required by the governmental organisations.

One issue of a successful implementation of a multi-component resin system is a simple and cost effective method for process monitoring. Many methods, such as DEA or DCR are discussed in the literature. For the measurement of the homogeneity of reactive epoxy resin components in particular, the ultrasonic method is investigated in this paper. The advantage of this method is a contactless measurement of the process. Due to this, no time-intensive cleaning with solvents and no complex maintenance of the sensors is necessary. Amongst others the ultrasonic method can be used for monitoring the mixing ratio, the flow front in the closed mould [7], the curing process [2] and a post-curing inspection of the glass transition temperature [7].

REFERENCES

1. Composite Materials Handbook. Volume 1: Polymer Matrix Composites Guidelines for Characterization of Structural Materials. MIL-HDBK-17-1F (2002).

2. Töpker J and Michaeli W (2001), ‘Process Control of RTM by Ultrasonic’, Long Beach: SAMPE International.

3. Day D (1988), ‘Effects of Stoichiometric Mixing Ratio an Epoxy Cure – A Dielectric Analysis’, *Journal of Reinforced Plastics and Composites*, 7:475

4. N. Pantelelis, “PROCESS MONITORING AND CONTROL FOR THE PRODUCTION OF CFRP COMPONENTS”, National Technical University of Athens

5. Eibl S (2008), ‘Observing In-homogeneity of Plastic Components in Carbon Fiber Reinforced Polymer Materials by ATR-FTIR Spectroscopy in the Micrometer Scale’, *Journal of Composite Materials*, 42: 1231.

6. Kim CB (2004), ‘Measurement of the refractive index of liquids at 1.3 and 1.5 micron using a fibre optic Fresnel ratio meter’, *Measurement Science and Technologie*.

7. Springl F, Theilmann Ph and Drechsler K (2012), ‘Konstruktion eines RTM Werkzeuges zur Fließfrontdetektion mittels Ultraschalltechnik‘ Technische Universität München, Lehrstuhl für Carbon Composites, Bachelor Thesis.

ONLINE PROCESS MONITORING SYSTEMS – BENCHMARK AND TEST STUDY

Reinhold Meier [1], Swen Zaremba [1], Florian Springl [1], Klaus Drechsler [1], Fabrice Gaille [2] and Christian Weimer [2]

[1] *Institute for Carbon Composites, TU Munich, Boltzmannstraße 15, 85748 Garching, Germany. Corresponding author's e-mail: meier@lcc.mw.tum.de*
[2] *Eurocopter Deutschland GmbH, Industriestraße 4, 86609 Donauwörth*

ABSTRACT: Despite the ambitions for increasing numbers of Carbon Fiber Reinforced Plastics (CFRP) parts no reductions in quality aspects can be accepted. Therefore new quality inspection methods have been taken into account. Online Process Monitoring (OPM) systems offer the opportunity to monitor process data, compare them with the ideal course of the process and draw conclusions about part quality. In this study three commercially available OPM systems - Dielectrical Analysis (DEA), Direct Current Resistivity measurements (DCR) and Ultrasonic Technology (US) - are discussed for use in series production. DEA measures the change in dielectrical properties of the resin, DCR is based on resistivity changes of the resin during processing and US analyses changes in ultrasonic speed of the matrix material. All systems monitor flow front arrival, in-mold viscosity and curing. Furthermore effects of aged resin and varying mixing ratios and detection of toughening thermoplastics are investigated. For ideal comparison of the different OPM systems an RTM tool was designed in which all three OPM sensors are installed at the same time thus the compared data are simultaneously gathered within the same experiment. Finally, the systems are evaluated with respect to the above-mentioned criteria in order to support the choice of a dedicated OPM system depending on the specific case of operation.

KEYWORDS: *Resin Transfer Molding, Online Process Monitoring, Flow Front Tracking, Viscosity Monitoring, Cure Monitoring, Dielectrical Analysis, Resin Resistivity, Ultrasonic Technology*

INTRODUCTION

In aerospace as well as the automotive industry an increasing production rate of CFRP parts can be observed driven by the need for more energy-efficient vehicles. Further applications of CFRP are often limited by high costs and long cycle times. OPM systems offer high potentials to meet the requirements in efficiency, cycle time and costs by comparison of monitored process data with the ideal course of the process. Hence, part production and quality management run simultaneously so that cycle time is reduced and no or less additive quality assurance measures are needed. In a next step the production process of each part can be adapted to the specific process conditions based on gathered process data, so that processing energy is saved by reduction of process tolerances and reduced cycle times. In this study state of the art OPM systems are tested in a benchmark study, the Dielectrical Analysis DEA 230 from NETZSCH, Optimold from SYNTHESITES, and US-Plus from SENSOR UND

LASERTECHNIK. The goal is to compare the identified OPM systems and evaluate their functionality for use under series production conditions.

OPM SYSTEMS

Dielectrical Analysis - DEA

In dielectrical measurements, an AC-voltage is applied to the inspected material. The established electric field and the resulting current depend on the ion conductivity and the dielectrical polarization of the sample. During curing of thermoset resins, the number and mobility of free ions and molecules change due to the growing molecular network which can be measured by analyzing amplitude and phase shift of the voltage and current signal. Based on the changes in amplitude and phase shift the complex dielectric constant is determined [1]. In a further step ion conductivity σ can be calculated from the following equation (Eqn.1) in which ε'' is the loss factor (imaginary part of the complex dielectric constant), ε_o is the dielectric constant for vacuum and ω is the angular frequency [2]:

$$\sigma = \varepsilon'' \cdot \omega \cdot \varepsilon_o \qquad (1)$$

The reciprocal value of the ion conductivity is the ion viscosity which is directly related to viscosity changes of thermoset resins [1].

As DEA measurements are based on electrical properties of the resin DEA sensors have to be insulated from electrically conductive materials such as carbon fibers. Furthermore DEA measurements are not ideal for condensation polymerizations since changes in dielectrical properties of the resin are superimposed by the released reaction products such as water which is dissociated in ions.

Direct Current Resistivity Sensing - DCR

The Optimold system is based on correlations between resistivity and state of curing which was first investigated for thermoset resins in the 1960s [3]. Resistivity ρ of a polymer is determined by measurement of the potential drop U across the sample and the electric current I applied to the sample. With knowledge of the distance l and the area A perpendicular to the potential gradient, the resistivity ρ can be calculated from Eqn. 2 [3]:

$$\rho = \frac{U \cdot A}{I \cdot l} \qquad (2)$$

DCR sensing is also based on electrical properties of the resin system. Hence, the same limitations concerning insulation from carbon fibers and condensation polymerization are valid as already discussed for the DEA.

Ultrasonic Technology - US

US-Plus uses ultrasonic technology which is already well known in the composite industry as a non-destructive testing technique. Generally it can be divided into transmission and pulse-echo methods, whereas in this study only the former is relevant. In transmission measurements, ultrasonic transducers are placed face to face with each other so that the bulk material in-between is inspected. An ultrasonic signal is generated by a piezo-electric transducer (emitter) and coupled into the material under test. The transmitted longitudinal wave is detected by the second piezo-electric transducer (receiver). By measuring the time of flight of the ultrasonic signal in the inspected material and with knowledge of the part thickness the speed of sound is calculated. Changes in the speed of sound correlate with changes in viscosity and curing state of thermoset resins [4]. Furthermore the attenuation of the ultrasonic signal contains information about the presence of flaws such as entrapped air (porosity) or delamination in composite materials.

EXPERIMENTAL DETAILS

Test Plan

When OPM systems are used for quality inspection purposes, repeatability necessarily becomes a crucial criterion. Therefore several experiments were conducted at least twice in an identical manner for each resin system. One room temperature curing resin system - MGS® RIM 135 Infusion Resin and MGS® RIMH 1366 hardener both from HEXION - and one hot curing resin system - RTM6 from HEXCEL Composites - were used in this study.

The former resin system was used for investigation of the OPM systems sensitivities to *flow front arrival*, detection of *race tracking* - preferential resin propagation in flow channels formed by the preform and the cavity, effects of varying *mixing ratios* and *porosity* content. RTM6 was used for the investigation of effects of *aged mono-component resins* and the detection of *thermoplastic materials* in terms of a thermoplastic film and a thermoplastic fleece, which are soluble in RTM6 to a certain degree. For comparison reasons reference measurements with each resin system have been carried out at least two times, in which the ideal mixing ratio and fresh resin was used, respectively.

Flow front arrival is crucial for improved understanding of filling patterns which becomes interesting especially for complex parts. In this study flow front arrival was optically validated by using a transparent polycarbonate mold insert. Detection of *race tracking* is a special case of detection of the arriving flow front localized to cavity walls. Hence, the use of the different OPM sensors close to cavity edges is proven in the race tracking trial.

The *mixing ratio* of the matrix material is mandatory for the mechanical properties of the final part. Consequently, ideal OPM systems are capable of detecting deviations from recommended mixing ratios. In this study the amount of hardener was varied by ±5% in weight resulting in ratios of 100:35 and 100:25 proportions of resin to hardener. The required mixing ratio of RIM 135 is 100:30 and was used in the reference trials. The race tracking trial was carried out with a ratio of 100:35 in order to reduce the viscosity of the injected resin and thus enhance the race tracking effect.

As well as the correct mixing ratio, low *porosity* is essential for achieving the desired mechanical properties. In one trial of the study porosity was provoked by injection of non-degassed resin. Furthermore the mixing ratio was set to 100:25 as air bubbles tend to rise faster in less viscous fluids.

Aging of mono-component resins leads to dumping of expensive thermoset mono component-resin as the minimum viscosity for optimum infiltration cannot be guaranteed when the expiry date is exceeded. Sensors for determination of the degree of precrosslinking or for the detection of the effects of aged resin during manufacture can reduce the amount of dumped material. Hence, the infiltration and curing process of RTM6 resin which was stored for 16 days at room temperature - 15 days maximum shelf life at 23°C - was monitored and compared to reference trials with fresh resin.

Test Setup and Experimental Description

A stand-alone RTM plate tool in frame construction (Fig. 1) was designed for the benchmark study and placed in an oven (Fig. 2) for the hot as well as the room temperature curing resin system tests in order to guarantee identical process conditions. The mixed and degassed resin was injected with constant injection pressure at 3.5bars by means of a pressure pot and was preheated to 80°C for the RTM6 trials. RIM 135 was injected at room temperature. Before injection the tool was heated to 30°C for the RIM 135 and to 120°C for the RTM6 trials. In the case of the RIM 135 experiments, the progressing flow front was monitored by a camera placed above the transparent polycarbonate mold insert. Curing temperature in the case of the RIM 135 trials was set to 65°C and 170°C for the RTM6 trials. Tool Mounted Sensors (TMS) were used in the case of the DCR and US measurements. The single-side DCR sensor was mounted in the bottom plate whereas one US transducer (K4V1) was placed in every mold half. In terms of the DEA, insulated disposable comb sensors, so-called filtered IDEX (interdigitated) sensors, were fixed onto the polycarbonate top mold with adhesive tape. In addition to the OPM sensors, pressure sensors - PXM600MU-14BARGV from OMEGA - and thermocouples (Type-K) were placed at the linear inlet and outlet of the mold.

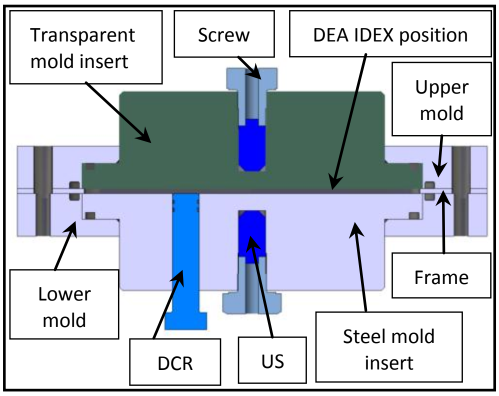

Fig. 1: Sectional drawing of the tool

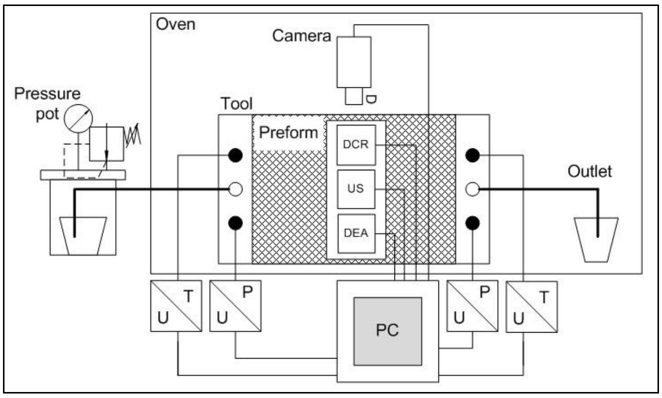

Fig. 2: Experimental setup

The general layup of the preforms was identical for all the experiments and consisted of one insulation glass layer next to the DCR TMS and 12 layers of biaxial carbon NCF resulting in a fiber volume content of around 58%v. In the experiments with thermoplastic layers one thermoplastic film was placed between the preform and the sensors' surfaces as top and bottom layer and one thermoplastic fleece layer was placed between each textile layer, respectively. For the race tracking trial flow channels were provoked by cutting the preform into two intentionally undersize strips and placing metal inlays between them so that a cavity edge and a small flow channel was formed at each OPM sensor.

Process Data Acquisition

For accurate and sensitive data acquisition in terms of the DEA and the US system correct and adapted systems settings are required. Apart from the general systems setup no experimental specific settings are needed in case of the DCR system.

In order to achieve optimum results, the frequency dependency of the DEA must be accounted according to the process parameter required. For epoxy resin systems, frequencies from 0.1-10000Hz are suggested, depending primarily on the resin viscosity. With decreasing frequency the sampling time for calculation of one data point increases, ranging from around 4s at 10kHz to around 40s at 0.1Hz. Furthermore each type of sensor has a preferred frequency at which comparisons between different resin systems should be made. The DEA IDEX sensors used in this study have a preferred measurement frequency of 10Hz. Since resin viscosity is lowest during injection and immediate detection of the flow front is crucial in this study the measurement frequencies were set to 10, 1 and 0.1kHz during the infiltration stage. After curing set in, measurements with 10, 1 and 0.1Hz were added to account for the higher viscosity levels. With increasing viscosity, lower frequencies are recommended as molecules and ions are hindered in their mobility due to the growing molecular network of the polymer. Measurements at the different chosen frequencies were carried out automatically by the system one after the other, starting at the lowest frequency.

For calculation of the ultrasonic speed in the investigated sample, the time of flight of the ultrasonic wave through the bare tool must be determined. Therefore measurements without placing a frame between the upper and the lower mold were carried out.

The US system has an internal repetition rate up to 1000 pulses per second and an adjustable number of averaging (typical 200 to 1000). Each data point represents a mean value of an adjustable minimum number of single measurements, 1000 in this study. This fact results in a maximum time resolution depending also on the investigated material. In the system settings a cycle time is asked from the user which must be longer than the sampling time, otherwise no data point can be calculated. This cycle time is a crucial parameter during infiltration especially when sensitivity to resin arrival is evaluated like in this study. Consequently the cycle time was set to 1.5s, which was close to the system’s sampling time needed for the set number of averaging. Before starting the curing cycle, data acquisition was stopped and restarted with a cycle time of 10s for reducing memory capacity.

In addition to the digital signal - resin arrival “yes” or “no” - information about the degree of saturation of the sensed preform volume are gathered by the US system due to the transmission character of the measurement. The received ultrasonic signal is connected to an automatic gain controlled preamplifier for using the full dynamic range of the Analog to Digital converter. The actual gain value is saved and can be displayed (see Fig. 3). This means that received signals with lower magnitudes are amplified more than signals with higher magnitudes. As long as the preform is dry, the ultrasonic wave is almost completely reflected at the tool cavity interface, no acoustic signal reaches the receiver and the gain is high. With increasing saturation of the preform, the acoustic impedance of the preform also increases, and the arriving ultrasonic signal at the receiver is less damped. Nearly constant system amplification indicates completed saturation of the preform (compare Fig. 3).

RESULTS AND DISCUSSION

All OPM systems considered reliably detected *resin arrival* in every trial of the study. A clear jump in the signals collected was registered for every system (see Fig. 4). Comparison of the videos taken and the signals collected show that the flow front was immediately detected by the DCR and the US system. In case of the DEA-IDEX sensors, approximately half of the sensor surface area had to be wetted before resin arrival was signaled. This is explained by the additional glass layers between the electrodes and the carbon fibers which are necessary for sufficient insulation of the DEA sensors.

Every OPM system monitored the development of the *resin viscosity*. As soon as the temperature was increased for the curing cycle, the viscosity started to decrease until curing becomes dominant (Fig. 4). With increasing degree of curing, the systems' signals also increase. End of curing for the given temperature is signaled by a constant signal. The 100Hz as well as the 10Hz graphs of the DEA are shown in Fig. 4. Higher frequencies are suitable for immediate detection of the flow front and for low viscosity stages. Therefore, lower frequencies (10Hz, 1Hz and 0.1Hz) were added in later stages of curing to account for the increasing viscosity of the curing resin.

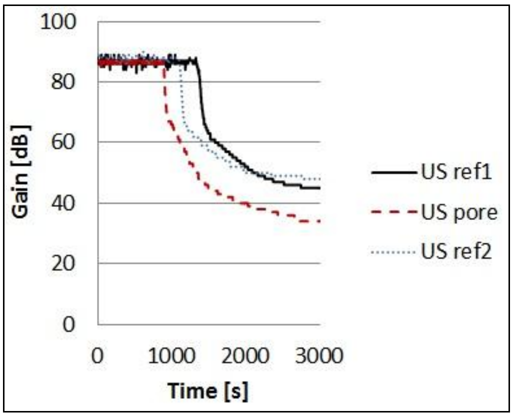

Fig. 3: Development of US gain

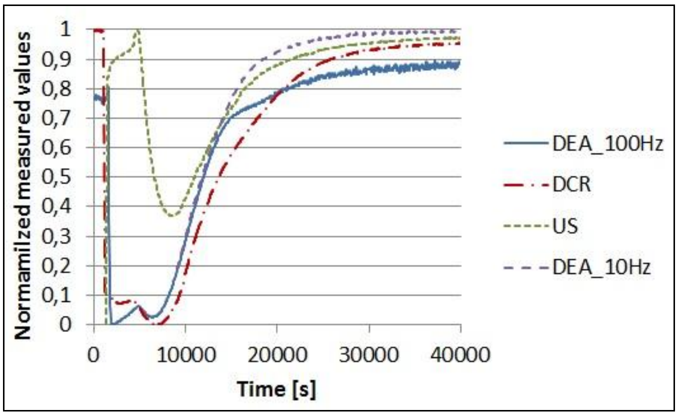

Fig. 4: Signal sequences of reference trial 1

As can also be observed in Fig. 2, minimum viscosity was detected by the different OPM systems at different times. In all trials, minimum viscosity was first signaled by the DEA, followed by the DCR and finally by the US. This might be due to the different positions of the DEA and the DCR sensor and the bulk measurement in terms of the US system.

The different *mixing ratios* lead to different reaction rates, which was registered by every OPM system. Higher amounts of hardener lead to higher gradients, meaning higher reaction rates and vice versa when the sensors' signals are plotted over time compared to the ideal mixing ratio. Almost congruent runs were observed for the same mixing ratios with respect to the DCR and the DEA system. In terms of the US system, only the curves for ideal mixing ratios could be compared with each other due to the differences in the experimental setup in the race tracking and the porosity trial. Together with the reference trials with RTM6, fair *repeatability* can be concluded for the US system.

The metal inlay, filling half of the sensed volume in the *race tracking trial*, leaded to huge jumps in the measured ultrasonic speed. No correlations with material parameters can be made. Nevertheless, US sensors can be used for detection of race tracking in the assembly considered. The DCR TMS can be used close to cavity edges for flow front arrival as well as curing monitoring without restriction. An IDEX sensor has not been applied in the race tracking trial due to incompatibility of the sensor's cable with the metal inlay.

The speed of sound in the *porosity* trial was clearly lower compared to the other trials. Therefore the porosity contents of references trials 1 and 2 and of the porosity trial were determined by acid digestion (EN 2564:1998). The specimens were taken from those spots of the manufactured plates which were investigated by the US device. The results are listed in Table 1, and show that the lowest porosity as well as the lowest fiber volume content was measured for the porosity trial. Hence, the lower ultrasonic speed is not due to entrapped air in the sensed volume but due to the lower fiber volume content. Dependency of the ultrasonic speed on the fiber volume content has already been investigated in other studies [4].

Table 1: Results of acid digestion of room temperature curing resin samples

	Porosity content [%V]	Fiber volume content [%V]
Reference trial 1	5.2	57.41
Reference trial 2	5.27	56.98
Porosity trial	0.7	53.18

The results of the acid digestion from Table 1 are reinforced by the gain values of the ultrasonic signals exhibited in Fig. 3. This can be seen by the systems amplification development of the received ultrasonic signal of the different trials. The final gain values in the reference trials are similar, which is in agreement with the porosity values of Tab. 1. The clearly lower porosity content of the porosity sample, and hence a higher degree of preform saturation is signaled by the clearly lower gain values of Fig. 3.

In terms of the DEA with the used filtered IDEX sensors and the DCR system, no differences in the porosity trial were found in comparison to other measurements.

Concerning the *detection of thermoplastic materials* only the thermoplastic film leaded to different signals in terms of the DEA and the DCR system. Whereas the flow front and the curing reaction were also monitored by the DEA, this information was masked by the thermoplastic film in terms of the DCR. After resin arrival and during early stages of curing, ion viscosity is about half an order of magnitude higher compared to the reference measurements. With ongoing curing the graphs of the film trial converge with the reference graphs. With respect to the US system no thermoplastic materials could be observed.

None of the OPM systems considered could monitor any significant differences during injection or curing of *aged resin* compared to the trials with fresh RTM6 resin. The US curve lay between the reference curves. The curves of the DCR and the DEA signaled higher resistivity and lower ion viscosity values, respectively, during the liquid state.

Concerning the repeatability in the RTM6 trials, the best results were obtained by the DEA followed by the US. In terms of the DCR, more noisy signals were measured due to presence of conductive carbon fibers. Furthermore a thin film of cured resin was observed on the sensor's surface after the last trial resulting in clearly higher resistivity values.

CONCLUSIONS

Apart from the detection of thermoplastic materials the OPM systems considered met the expectations. Concerning the in-mold detection of aged resin no significant differences were observed compared to fresh resin. Either the storage time at room temperature was too short to cause any changes or the resulting differences were masked by the influence of the conductive fibers. More experiments are suggested to draw further conclusions concerning resin aging.

The striking differences of the OPM systems are restricted to more general aspects. The DEA with the used IDEX sensors and the DCR system are limited to part surface measurements, whereas the US technology gathers information from the bulk material. But available inlay sensors for the DEA and the DCR system can be used to monitor process parameters inside the part. Furthermore, these sensors do not need any additional design space in comparison to the US sensors. The latter have to be mounted on both sides of the parts and must be installed at positions where the ultrasonic signals perpendicularly meet the cavity and part surfaces within certain tolerances.

Hence, as a final conclusion it can be said that the correct choice of an OPM system is mainly dependent on the surrounding process conditions such as available design space or desired sensor positions and the process parameters required such as flow front arrival or degree of saturation. The following table summarizes important criteria for the choice of an appropriate OPM system and can be used as decision guidance.

Table 2: Overview of system characteristics

Criteria	DEA with IDEX sensors	US	DCR
Resin arrival	+	+	+
Race tracking	%	+	+
Preform saturation	-	+	-
Porosity	-	+	-
In-mold viscosity development	+	+	+
In-mold quantification of mixing ratio	-	-	-
In-mold detection of aged resin	-	-	-
Reactivity	+	+	+
End of curing	+	+	+
Detection of thermoplastic film (top layer)	+	-	+
Detection of thermoplastic fleece (between layers)	-	-	-
Condensation polymerization*	-	+	-
Contact free measurement	-	+	-
Signal penetration depth	low	high	low
Effort for sensor insulation from carbon	higher	low	moderate
Design space	low	high	low
System installation effort	higher	higher	low
Repeatability	higher	fair	fair
Frequency dependency	yes	no	no
%... No statement possible, -...impossible , +... possible, * Material dependent			

ACKNOWLEDGEMENTS: We would like to express our thanks to EUROCOPTER Germany GmbH for funding this work and the possibility to publish the results, to Mr. Knappe of NETZSCH, Mr. Lange of SENSOR- UND LASERTECHNIK and Mr. Pantelelis of SYNTHESITES for their assistance in running their systems and Mr. Theilmann and Mr. Esquisabel for their experimental support.

REFERENCES

1. Senturia SD and Sheppard NF Jr (1986), ‘Dielectric Analysis of Thermoset Cure’, *Advances in Polymer Science*, Vol. 80, Berlin Heidelberg, Springer Verlag

2. Simpson JO and Bidstrup SA (1995), ‘Rheological and Dielectric Changes During Isothermal Epoxy-Amine Cure’, *Journal of Polymer Science: Part B: Polymer Physics*, Vol. 33, 55-62.

3. Warfield RW (1962), ‘Properties of Crosslinked Polymers as Evidenced by Electrical Resistivity Measurements’, *Macromolecular Chemistry*.Vol. 58.

4. Töpker HJ (2002), Ultrasonic Measurement Technique for Online Control and Analysis of the Impregnation and Curing Process by Resin Transfer Moulding, Aachen, Verlag Mainz

RESIN FLOW SIMULATION BASED ON ADVANCED REINFORCEMENT GEOMETRY MODELLING FROM YARN-SCALE TO COMPONENT-SCALE

Andreas Endruweit, Frank Gommer, Joel Hutchinson, Spiridon Koutsonas, Andrew C. Long,
Peter Schubel, Xueliang Xiao, Xuesen Zeng

Faculty of Engineering – Division of Materials, Mechanics & Structures,
University of Nottingham, University Park, Nottingham, NG7 2RD, U.K.
Corresponding author's e-mail: andreas.endruweit@nottingham.ac.uk

ABSTRACT: The architectures of textile reinforcements were characterised experimentally at different length scales. The obtained data allowed geometrical models to be generated, for which impregnating resin flow was simulated. Transverse yarn permeabilities for random filament arrangements, modelled based on typical nearest neighbour distributions, are log-normally distributed and significantly smaller than permeabilities for uniform yarns. Flow velocity fields indicate probabilities for intra-yarn dry spot formation. Detailed modelling of flow channel geometries in unit cells of fabrics with complex architectures allowed in-plane and through-thickness permeabilities to be obtained, which are in good quantitative agreement with experimental data. For non-uniform fabrics characterised by distributions of fibre angles, typical mould filling patterns were predicted. Global permeabilities were determined, which showed variability in the same order as typical experimental results. Analysis of gaps between the reinforcement and the surface of a moulding tool at bends in the component geometry indicated racetracking at the outer radius of the bend and lagging of the flow front at the inner radius, as observed experimentally. Realistic simulation of the impregnation of preforms with dynamically varying thickness in processes with flexible tooling was enabled by combination of flow and compression modelling.

KEYWORDS: *Liquid Composite Moulding, resin flow, numerical analysis, permeability, textile modelling*

INTRODUCTION

In Liquid Composite Moulding (LCM) processes, the impregnation of a textile reinforcement with liquid resin is affected by the reinforcement properties at different length scales. Effects of, e.g., capillary pressure (yarn-scale), defined fibre shear (unit cell/component-scale) and uniform compaction (component-scale) have been discussed extensively in the literature. Additional subjects of study are related to process-induced reinforcement non-uniformity and stochastic properties, which can influence the outcomes of resin injections at the component-scale. This overview summarises recent developments and current activities at the University of Nottingham in modelling reinforcement properties at different scales and their influence on resin flow in LCM processes.

YARN-SCALE

The formation of inter-filament voids during impregnation, which can affect (matrix-dominated) mechanical properties of a composite, is related to random filament distributions in yarns and the resulting non-uniform resin flow velocity fields. Based on microscopic analysis of moulded and cured composite specimens, local distributions of filaments in yarns were characterised statistically at different fibre volume fractions. The distributions were described by the typical distance between a filament and its *n*-the nearest neighbour (Fig. 1). This allows instances of filament arrangements representative of the actual random bundles to be reconstructed.

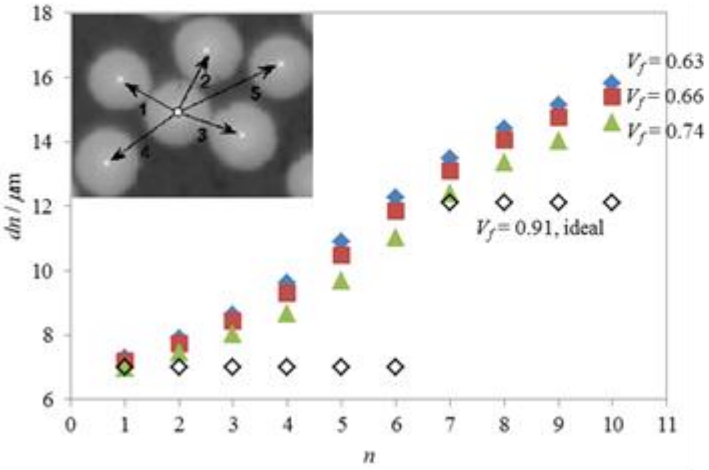

Fig. 1: Typical distances, *dn*, between any filament and its *n*-th nearest neighbours at different fibre volume fractions V_f (for the example of a unidirectional carbon fibre fabric)

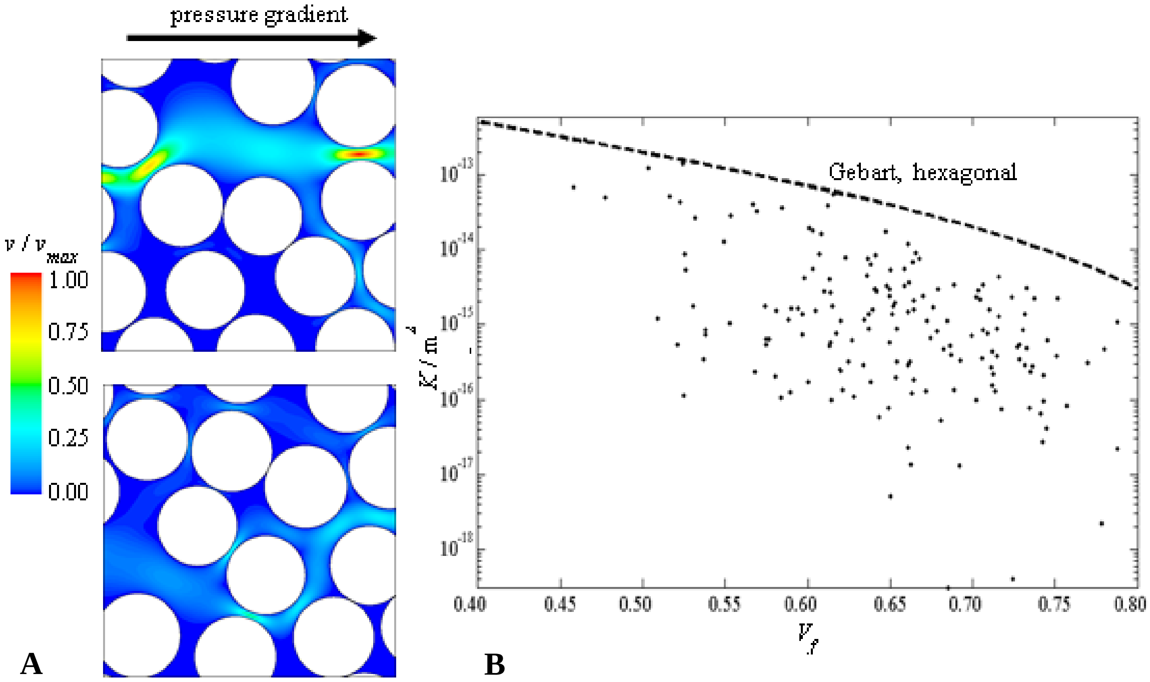

Fig. 2: A: simulated transverse flow velocity field for two different instances of random filament arrangements at $V_f = 0.63$; B: calculated transverse permeability as a function of V_f

Using the commercial Computational Fluid Dynamics (CFD) package Fluent^{TM}, steady-state transverse flow through these random filament arrangements was simulated numerically. Transverse permeabilities, derived from the applied pressure gradients and the calculated flow velocity fields (Fig. 2A), are log-normally distributed at any given fibre volume fraction. As the average permeabilities decrease with increasing fibre volume fraction, their scatter tends to decrease due to a reduction of the filament mobility. The fact that the permeability tends to be significantly smaller than the permeability for ideal uniform filament arrangements (Fig. 2B) according to Gebart [1] indicates clearly the limitations of numerical permeability predictions based on small periodic unit cells and the need to account for the statistical distribution of filaments within yarns.

Maps of the flow velocity fields (Fig. 2A) indicate that the majority of fluid flows through a limited number of inter-filament channels. Zones of low flow velocity in steady-state saturated flow are related to high local filament density and indicate high probability for void formation in impregnating transient flow. Thus, evaluation of the flow velocity distribution can help to estimate the probable void content.

UNIT CELL-SCALE

For 3D weaves as examples for reinforcement fabrics with geometrically complex architectures, detailed geometry data were acquired by x-ray micro-Computed Tomography (CT) scanning of composite specimens (Fig. 3A). These data were converted to accurate unit cell geometry model (Fig. 3B) using the TexGen software [2]. The unit cell domains were meshed with uniform hexahedral voxels. Steady-state flow through pore spaces was simulated using the commercial CFD package Ansys CFX^{TM} (Fig. 3C).

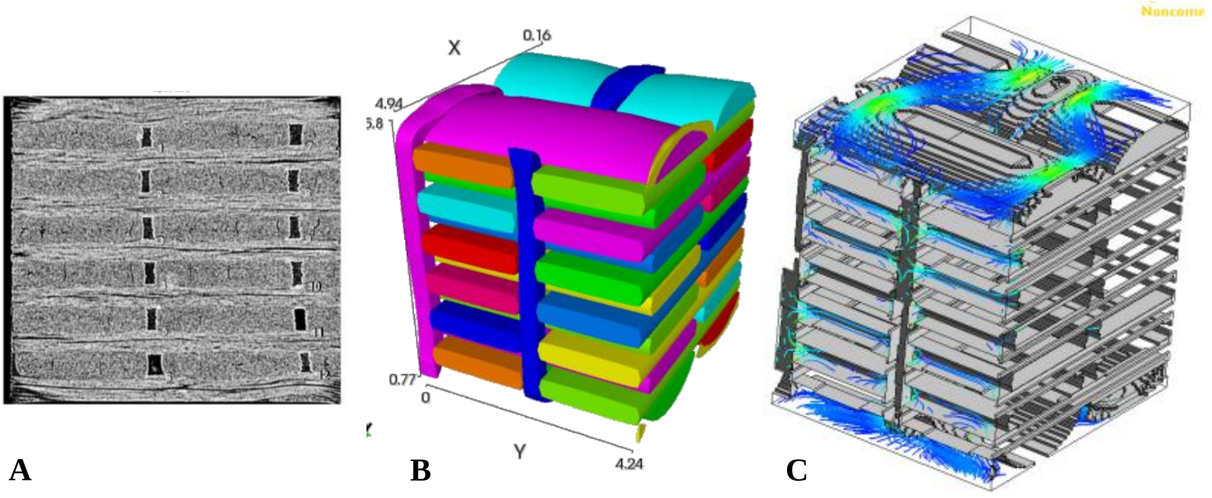

Fig. 3: 3D orthogonal carbon fibre weave; A: slice from micro-CT 3D data set (flow channels in warp direction appear black); B: TexGen model of unit cell geometry; C: streamlines from CFD simulation of flow in warp-direction

For the example of a 3D orthogonal weave, the results suggest that flow is dominated by the binder yarn arrangement. On the surfaces of the weave, dimples form at crossover points of the binder with weft yarns due to localised compaction. Confirming the suggestions from an experimental study [3], they connect to form flow channels on the fabric surfaces (Fig. 3C). In the layers of aligned yarns in the fabric, the binder blocks gaps between warp yarns while open gaps remain in the weft direction. From the applied pressure gradients along different fabric directions and the calculated flow velocities, in-plane and through-thickness permeabilities were determined. In agreement with experimental observations [3], the in-plane permeability in the warp direction was found to be significantly lower than in the weft direction. Accurate modelling of variations in yarn cross-sections allowed good quantitative agreement with experimental data to be obtained.

COMPONENT-SCALE

Transient impregnating flow in porous media can be described by combining Darcy's law and the equation of continuity, which are implemented in several simulation codes. In this study, the commercial code PAM-RTM^{TM} is used for resin flow simulation at the component-scale.

To predict typical mould filling patterns and estimate ranges for global permeability values, fabric non-uniformity related to yarn in-plane waviness was taken into account in flow simulations. Continuous random fields describing the yarn spacing for the example of bi-directional non-crimp fabrics (Fig. 4A) were generated based on trigonometric functions with the random parameters frequency and phase. Maximum values of the random frequencies (in non-crimp fabrics determined mainly by the stitching pattern) are determined from fibre angle variations observed in actual fabrics (Fig. 4B). From the functions describing the yarn spacing, continuous distributions of the local fibre volume fraction are calculated. Permeability fields are estimated based on local homogenisation and the Kozeny-Carman equation [4].

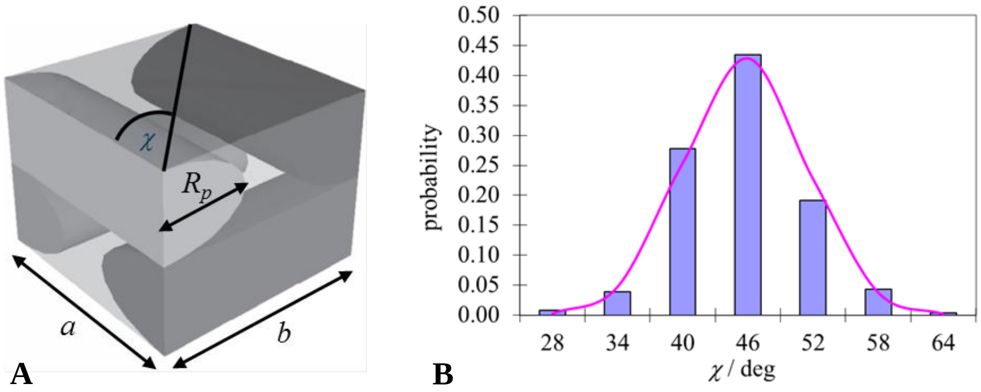

Fig. 4: Example of ±45° non-crimp (glass fibre) fabric; A: unit cell; B: experimentally determined distribution of angles between local fibre direction and fabric warp direction

Flow front shapes obtained from resin injection simulations with non-uniform porosity and permeability fields (Fig. 5) were found to be similar to those observed experimentally. The variability in global permeability increases with increasing average gap size between adjacent yarns in the fabric. It also tends to increase with increasing variability in fibre angles, but then decreases again after passing through a maximum. In summary, variations of the global permeability decrease with decreasing ratio of dimensions of fabric non-uniformity and specimen dimensions [5]. The global permeability variations derived from the series of simulations at realistic degrees of non-uniformity were found to be in the order of magnitude of typical experimental results, between 10 % and 20 %. While the stochastic description of the textile structure is focussed on non-crimp fabrics, similar considerations apply to any bi-directional fabrics (with higher accuracy the lower the degree of crimp).

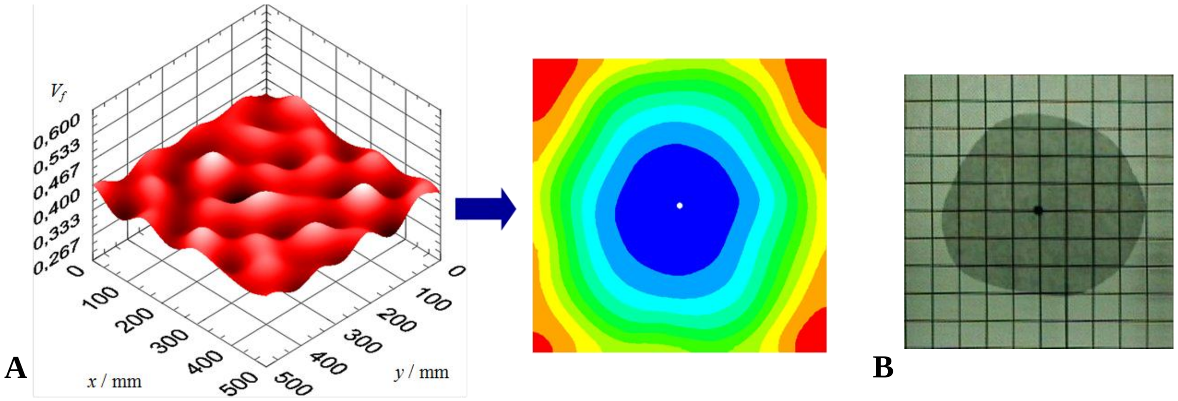

Fig. 5: A: Example for random field of local fibre volume fractions; corresponding flow front shapes at different injection times in radial injection at constant injection pressure; B: typical experimentally observed flow front shape for qualitative comparison

In LCM processes employing stiff moulding tools, e.g. Resin Transfer Moulding (RTM), gaps form between the reinforcement and the tool surface due to local compression at sharp bends in the component geometry. The gap size is affected by the bend geometry (radius and angle), the tool closing force and the reinforcement parameters compressibility and coefficient of friction (on the tool surface). Experimental observations in a transparent Perspex tool with a 90° bend suggest that, during resin injection, the gap between reinforcement and tool results in racetracking at the outer radius of the bend, while the locally increased fibre volume fraction of the compressed reinforcement results in lagging of the flow front at the inner radius of the bend (Fig. 6).

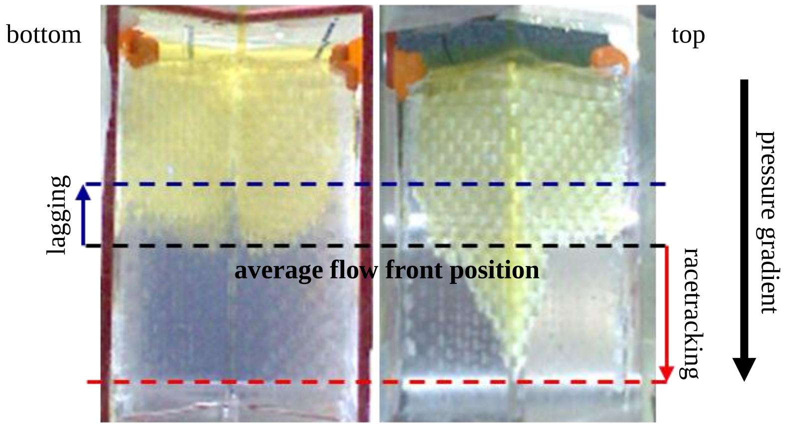

Fig. 6: Experimentally observed flow front shapes on top and bottom of a 90° bend during impregnation of a plain weave glass fibre fabric

Experimental analysis of localised fabric compression indicates that the gap height along the bend can be modelled as a parabola. Based on this model, the bend can be segmented into material zones with different average gap height and fabric thickness (Fig. 7A). The equivalent permeability of the gap can be estimated, and the permeability of the compressed reinforcement can be determined from interpolation of the permeability measured at different compaction levels. As input for 2D flow simulations, thickness-weighted averaging of the equivalent gap permeability and the permeability of the compressed fabric allows the effective permeability for each segment of the bend to be estimated. The simulated flow front shapes reflect the dominating effect of racetracking in the gap. To obtain more accurate results, through-thickness variations in permeability need to be taken into account in 3D flow simulation. The results indicate racetracking at the outer radius of the bend and lagging of the flow front at the inner radius (Fig. 7B), similar as observed experimentally. However, the fine discretisation required for accurate modelling of the gap and definition of material zones with different properties causes issues for 3D mesh generation which still need to be addressed.

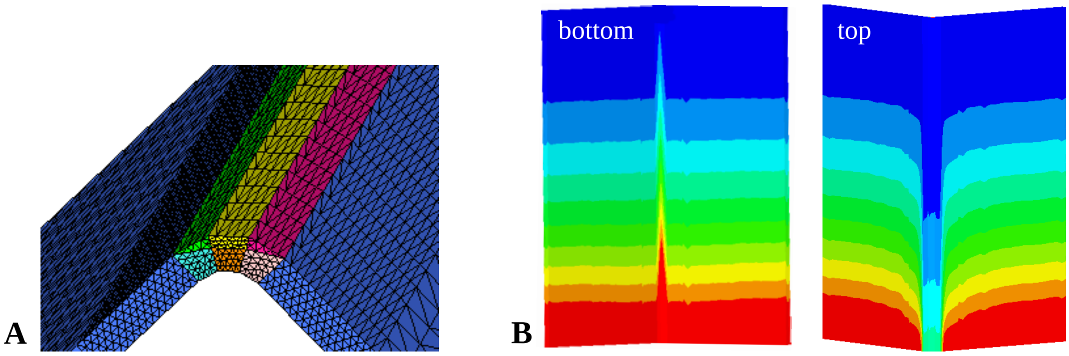

Fig. 7: A: 3D finite element model of 90° bend segmented into zones with different properties; B: resulting flow front patterns at different injection times (input parameters not related to the fabric in Fig. 6)

In Light RTM processing of composite components, semi-flexible composite tools are used. Compared to stiff (metallic) tools used in RTM, their cost is significantly lower, and they are easier to handle due to reduced weight. Compared to Vacuum Infusion under flexible vacuum bags, the achievable dimensional accuracy is higher, and component manufacturing costs are reduced since no consumables (vacuum bag, breather, peel ply, sealant) are used. However, relatively low stiffness of the tools may result in deformation affecting control of the resin injection and dimensional accuracy of the finished component.

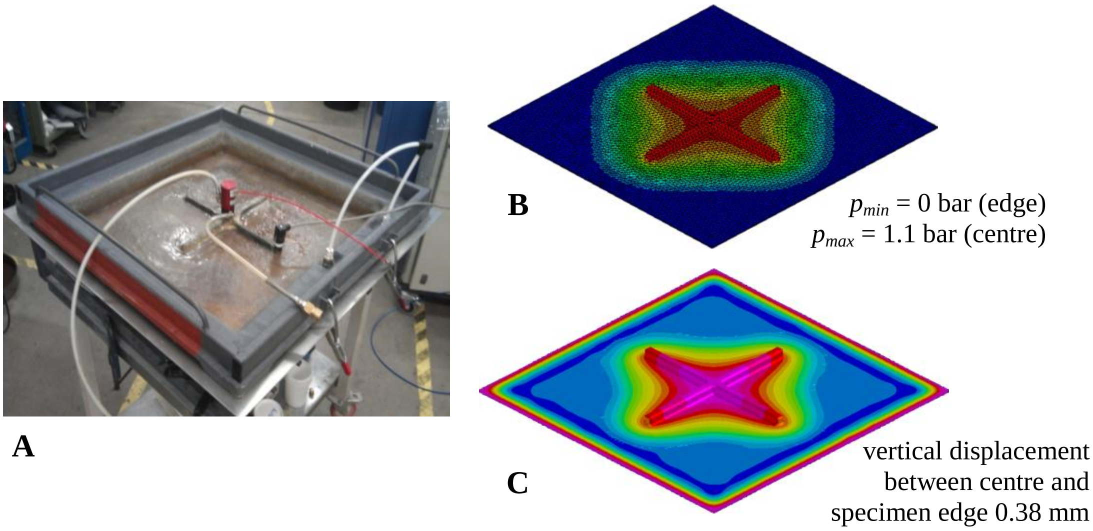

Fig. 8: A: Light RTM demonstrator tool; B: simulated fluid pressure distribution at a given injection time; C: corresponding simulated tool deflection

Reinforcement impregnation in Light RTM was simulated step-wise. In a first step, closing of the tool and compression of the dry reinforcement were simulated based on experimentally determined compaction curves. After this initial step, flow front positions of the impregnating fluid and the corresponding fluid pressure fields were determined on a 3D mesh assuming Darcy flow (Fig. 8). Then the pressure-induced deflection of the tool (of given stiffness) was calculated in PAM-CRASH^{TM} (Fig. 8). Finally, the permeability field was updated as input for the next step of flow simulation by interpolation of experimentally determined data for the local textile thickness. This procedure allows realistic simulation of the Light RTM process enabling optimisation of the tool design, in particular with respect to component thickness control, and selection of the reinforcement based on its impregnation properties. Application to the manufacture of large composite components is illustrated in Fig. 9.

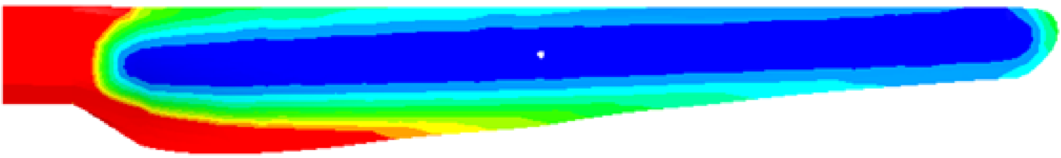

Fig. 9: Simulated flow front patterns at different injection times for Light RTM manufacture of a 6 kW wind turbine blade (linear injection gate along blade axis)

CONCLUSIONS

At different length scales, the architecture of reinforcements was characterised experimentally and converted into geometrical models, for which impregnating resin flow was analysed.

At the yarn-scale, models representing random filament distributions were generated based on typical nearest neighbour distributions. Simulation of flow through these models allowed realistic transverse yarn permeabilities, which were found to be log-normally distributed and significantly smaller than permeabilities for ideal uniform yarns, to be determined. Flow velocity fields give an indication for probable intra-yarn dry spot formation.

At the unit cell-scale, flow channel geometries were analysed and modelled in detail for complex fabric architectures. In-plane and through-thickness permeabilities, calculated based on flow simulations, were found to be in good quantitative agreement with experimental data.

At the component-scale, impregnating flow was simulated for non-uniform fabrics characterised by distributions of fibre angles. Typical mould filling patterns were predicted, and global permeabilities were determined. Global permeability variations at realistic degrees of non-uniformity were in the same order as typical experimental results, between 10 % and 20 %. The geometry of gaps between the reinforcement and the surface of a stiff moulding tool, occurring at sharp bends in the component geometry, was analysed. The equivalent permeability of gaps and the permeability of locally compressed fabrics were estimated. Mould filling simulations show flow fronts affected by race-tracking and lagging effects, similar as observed experimentally. Combination of flow and reinforcement compaction modelling allowed realistic simulation of the impregnation of preforms with dynamically varying thickness, as observed in LCM processes with flexible tooling.

A challenge for future work is integration of the different approaches into one unified fabric geometry model.

ACKNOWLEDGEMENTS: This work was partially funded by the Engineering and Physical Science Research Council as part of Platform Grant EP/F02911X/1, the Nottingham Innovative Manufacturing Research Centre (EP/E001904/1) and various projects funded by the Technology Strategy Board. Software licences and technical support for PAM-RTM^{TM} and PAM-CRASH^{TM} were provided by ESI Group.

REFERENCES

1. Gebart BR (1992), 'Permeability of Unidirectional Reinforcements for RTM', *J Compos Mater*, 26(8), 1100-1133.

2. TexGen (Version 3.5.0). University of Nottingham (2011). http://texgen.sourceforge.net (Viewed 31 January 2012).

3. Endruweit A and Long AC (2010), 'Analysis of Compressibility and Permeability of Selected 3D Woven Reinforcements', *J Compos Mater*, 44(24), 2833-2862.

4. Carman PC (1937), 'Fluid Flow through Granular Beds', *T I Chem Eng-Lond*, 15, 150-156.

5. Endruweit A and Long AC (2006), 'Influence of stochastic variations in the fibre spacing on the permeability of bi-directional textile fabrics', *Compos Part A-Appl S*, 37(5), 679-694.

VARIABILITY OF FIBROUS MATERIALS: EXPERIMENTAL AND THEORETICAL STUDY

F. Zhang[1], S. Comas-Cardona[1,2], C. Binetruy[1,2]

[1]*Ecole des Mines de Douai, Polymers and Composites Technology & Mechanical Engineering Department, 941 rue Charles Bourseul, 59508 Douai, France*
[2] *Ecole Centrale de Nantes, Research Institute in Civil Engineering and Mechanics (GeM) UMR CNRS 6183, 1 rue de la Noe, 44321 Nantes, France*
Corresponding author: sebastien.comas@ec-nantes.fr

ABSTRACT: Different types of fibrous reinforcement used for structural composites are available, e.g. woven, non-woven or non-crimp fabrics. The architectures of woven and non-crimp fabrics exhibit a quasi-periodic repetition of basic unit cell. As a result, local mechanical and transport properties can be represented by the effective properties of a typical unit cell. In the case of non-woven or random fibrous reinforcement, the statistical properties, such as the distribution of pore sizes and shapes, the degree of correlation and the interconnectivity of pores, govern the transport process and the macroscopic material properties. Therefore, accurate prediction of fibrous media properties depends on appropriate description and representation of the microstructure. As observed by experimental studies, for instance, the permeability is very sensitive to such variation and greatly affects composite manufacturing. The study is based on image analyses of a random mat fibrous architecture which is then used as input in the prediction algorithm for the effective permeability of a region of interest. By defining suitable sampling size in the fabric sample, a permeability field can be obtained from each sample and validated with the experimental radial injection results in terms of flow front geometry. The random field model of permeability is then constructed by statistical characterization techniques.

KEYWORDS: *permeability, variability, probability density functions*

INTRODUCTION

The Chopped Strand Mat (CSM), manufactured by stitching a random distribution of chopped strands of glass fiber into a uniform mat, is a fibrous reinforcement used for composite parts. The manufacturing of composites using CSM reinforcement requires the use of resin injection techniques such as any of the Liquid Composites Molding (LCM) for instance. During such process, the resin flows within the fibrous media. This stage is widely modeled and simulated using Darcy's law:

$$q = -\frac{K}{\mu}\nabla p \tag{1}$$

where q is the Darcy's velocity, μ the viscosity, K the Darcian permeability and p the fluid pressure. Modeling such injection-based manufacturing requires a good knowledge of the permeability K.

On one hand, measurements have been shown to be a tedious task which still shows high discrepancies. On the other hand, the permeability is not spatially constant in a sample or in a preform. There is an inherent variability contained within the sample and its microstructure because of the fibrous reinforcement manufacturing or handling. This microstructural variability will lead to fluctuations in transport properties, manufacturing and mechanical properties. A previous study focused on the propagation of the variability during the injection stage of composites manufacturing [1], this study is devoted to characterizing the variability of CSM (non woven materials) that are required input for stochastic simulation tools.

The approach followed in this study will address the variability of the microstructure and permeability of CSM. The methodology is based on fibrous reinforcement digital imaging coupled with various numerical techniques to estimate permeability. First, the treatment of digital images, including the sampling method and statistical characterization of the random microstructure, are explained. Then the obtained statistical properties are employed in two different modeling approaches of effective permeability field, followed by the validation by means of the mold-filling simulation. Finally, the statistical properties of the permeability field are quantified.

RANDOM MICROSTRUCTURE CHARACTERISATION

Materials and experimental procedure

The material used in this study is a CSM (M705450, Owens Corning) composed of E-glass with an areal weight of 457g/m^2 (coefficient of variation CV=5%). A total number of 37 samples of size 0.265m×0.265m are randomly selected in a roll as realizations of the random fabric. Digital grayscale images of samples were acquired using a lightbox device [2]. Then image processing is performed to correct the barrel distortion and to remove any uneven lighting (Fig. 1(a)). Also a calibration relationship from [2] is used to relate pixel intensity to the CSM areal weight.

Once the microstructure of each CSM sample has been recorded, the samples are then subjected to a central injection experiment. The injection is realized with a mineral oil. The injection pressure is constant P_{inj}=0.05 MPa. The thickness of the mold cavity is adjusted to maintain an average fiber volume fraction V_f at 38% (+/-0.6%). The bottom mold platen is made of glass and allows image recording. During the injection of each sample, several images are recorded. After appropriate image processing, the transient flow front evolution is extracted. To ease the reading of fluctuations, the flow fronts (close to circles in the Cartesian coordinates Fig. 1(a) are plotted in cylindrical coordinates (θ,r) (Fig. 1(b)). The flow front profiles will be used in the validation section of this article.

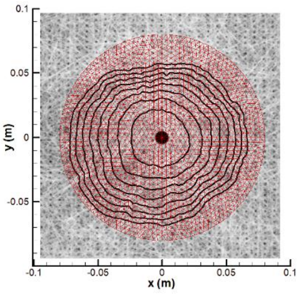

Fig. 1(a): Fabric (background) and experimental flow front positions (black)

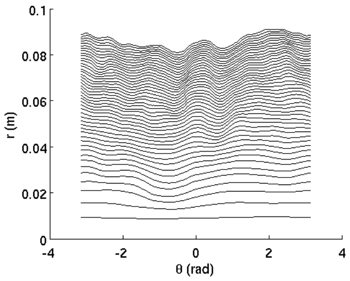

Fig. 1(b): Experimental flow front positions in radial coordinates

Image sampling

The digital grayscale images obtained from the lightbox are used. To obtain permeability fields, a sampling strategy (Fig. 2) is defined on the original grayscale image (of size N^2 in pixels) where $N = U \times N_I \times N_A$, where U (pixel) is the size of a single-phase unit as defined above, N_I^2 is the number of units in each sampling region (S), and N_A^2 is the number of sampling regions in the image. In the end, the permeability field will be of size N_A^2. The image is divided in single-phase units of $U \times U$ pixels (an example value U=3 is used in this section). Therefore, details on the scale less than U pixels are neglected.

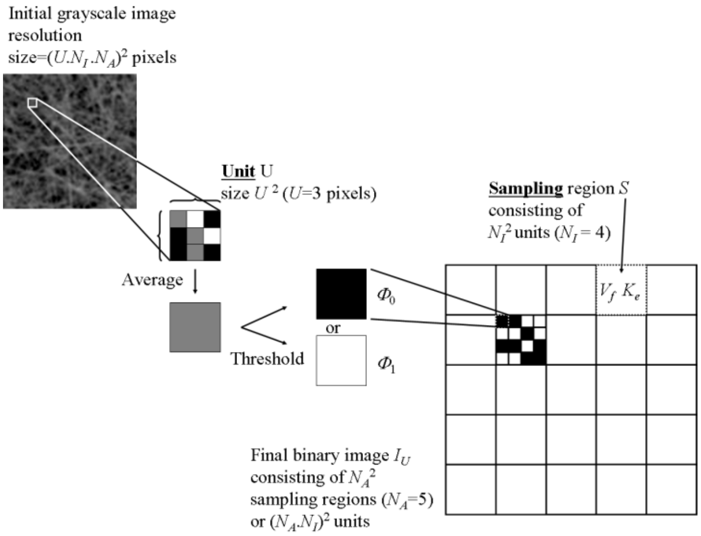

Fig. 2 Schematic of image sampling (U=3, N_I=4, N_A=5)

For statistical characterization and numerical efficiency, the large CSM images have to be represented as a random two-phase medium (Φ_0 and Φ_1). A threshold transformation is applied to the grayscale image to become a binary (two-phase) image (I_U) whose size is $(N_I N_A)^2$. The fiber volume fractions V_i of both phases are determined using the following criteria: (i) the overall V_f satisfies the measured areal weight, (ii) V_i and the average intensity of pixels covered by phase Φ_i satisfy the calibration formula of the lightbox apparatus[2], (iii) V_i should not be far from the average V_f of CSM, so as that both phases are porous media. A unique threshold level can be found to satisfy all of the above conditions.

One-point probability density function (PDF)

According to [3], for a given sampling region *S*, the 1-point PDF P_i is the ratio between the number of units of the phase Φ_i divided by the total number of units in *S*. P_i represents the probability of any point occurring in the phase Φ_i. Obviously, a constraint exists as $P_0 + P_1 = 1$. The effective fiber volume fraction V_f in a sampling region (*S*) is estimated:

$$V_f(S) = V_0 P_0 + V_1 P_1 \tag{2}$$

Two-point PDF

A heterogeneous microstructure can be completely characterized by a *n*-point PDF [3] defined as the probability of *n* points existing in a certain combination of phases. Obviously, the two-point PDF is most significant for capturing the clusters. For two points **x** and **x'** in I_U, the two-point PDF $P_{ij}\left(\mathbf{x},\mathbf{x}'\right)$ is defined as the probability of the vector $\mathbf{x}\text{-}\mathbf{x}'$ to be located with the head $x \in \Phi_i$ and the tail $x \in \Phi_j$ (i, j = 0, 1). From the two-phase image, $P_{ij}\left(x,x'\right)$ can be evaluated by accumulating the number of different states of (x,x') and finally normalized according to the definition of probability, i.e. $\sum_{i,j=0,1} P_{ij}\left(r\right) = 1$. For convenience, the discrete $P_{ij}\left(r\right)$ data can be fitted into appropriate analytical models [4]. So far, the tools characterizing the microstructure (1 and 2-point probability density functions) have been described. The following section will focus on the permeability evaluation.

EFFECTIVE DARCIAN PERMEABILITY EVALUATION

The main objective of this section is to calculate the permeability field of each sample from the images. First, the 1-point PDF is used along with Kozeny-Carman model to estimate the permeability from the microstructure. Second, keeping in mind the same objective, the 2-point PDF is used with continuum statistics. In parallel, permeability fields obtained from the two techniques are used as inputs in injection simulations and compared with experimental injections.

Kozeny-Carman model

The permeability field is calculated using the 1-point PDF descriptors. The fiber volume fraction is known to be the dominant factor for the overall flow resistance of fibrous media. The Kozeny-Carman (K-C) model of the isotropic permeability as a function of V_f is given as:

$$K = \frac{\left(1-V_f\right)^3}{5S_0^2V_f^2} \tag{3}$$

where S_0 a shape factor, which is assumed identical for close mixtures of the two phases. As a result, the ratio between the effective permeability of a sampling region (K_e) and the overall permeability of CSM (K_0) is expressed as:

$$\frac{K_e}{K_0} = \frac{\left(1-V_f\right)^3}{\left(1-V_{f0}\right)^3}\frac{\left(V_{f0}\right)^2}{\left(V_f\right)^2} \tag{4}$$

where V_f and V_{f0} denote the fiber volume fraction of the sampling region and the overall value, respectively. As the K-C model is derived by modeling the pore structure as a bundle of ducts through which the flow is described by a generalized Poiseuille equation, the sampling region must be large enough to be a porous medium. Also considering the calibration range of the lightbox, the smallest length of a sampling region is estimated as 14 pixels (i.e. 3.2mm) [2], resulting in a field containing 83×83 permeability values (Fig. 3(a)).

To assess the accuracy of the permeability field, the radial injection test is simulated using a MATLAB code combining the FEM and the Level Set technique for modeling the moving flow front [1]. The simulated flow pattern is compared with the corresponding experimental results, in terms of the flow front radii $R\left(\theta_i\right)$ as function of direction $\theta_i \in \left[0, 2\pi\right]$ at different time instants (when the flow front is recorded in experiments). In Figure 3(a), the permeability field (normalized by the overall equivalent value) and corresponding flow pattern are displayed for the smallest sampling size of 14 pixels (3.2mm). Although overall flow front trends can be captured, certain major fluctuations in the final flow front are missed by simulation. As expected, increasing the sampling region size (i.e., lowering spatial variability) increases the absolute error on the flow front positions (3.35% and 5.16% for 14 and 20 pixels respectively).

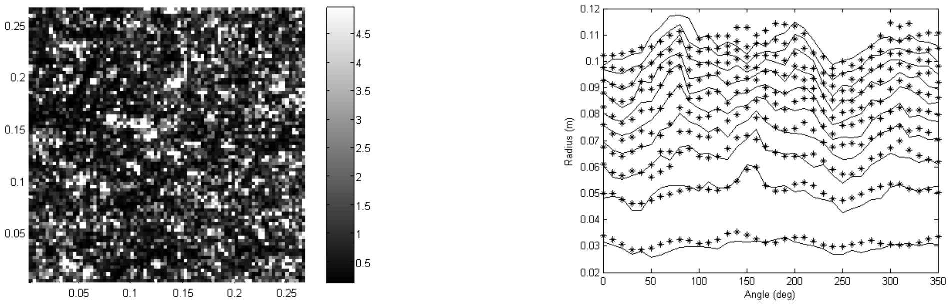

(a) Normalized permeability field

(b) Flow pattern (line: experiments; stars: simulations) at various times

Fig. 3 Results using the 1-point PDF with Kozeny-Carman (Sampling length 14 pixels, i.e. 3.2 mm)– Flow front position error=3.35%

Statistical continuum approach

The statistical continuum approach, developed based on works of Kroner [5], Adams [6], Garmestani [3] and Li [7], among others, has application in predicting macroscopic behavior of heterogeneous materials and microstructure sensitive design. The effective permeability in a region is commonly evaluated by imposing a macroscopic pressure gradient ∇p_0 on the region and solving for the resulted localized pressure gradient field $\nabla p(\mathbf{x})$. The permeability field of the same material sample as previously is evaluated and used to simulate the radial injection process. The sampling parameters are chosen to be U=3 pixels (0.7mm) and N_I=12, resulting in the sampling regions of size 9mm×9mm. The permeability field K_x normalized by the global equivalent value ($K_0 = \sqrt{K_x K_y}$) is displayed in Figure 4(a).

Comparing to the K-C results in Fig. 3(a), much stronger fluctuation in local permeability magnitude and significant local anisotropy can be noticed in Fig. 4(a). This effect is interesting because even though the sampling region size is even larger in Fig. 4(a) (compared to Fig. 3(a)), it does not smooth the flow fronts out. Quite inversely, the local fluctuations are increased (Fig. 4(b)) and accurately reproduced (error of 2.32%). Therefore the cluster-induced local anisotropy and strong fluctuation are well described by the 2-point PDF and continuum statistics.

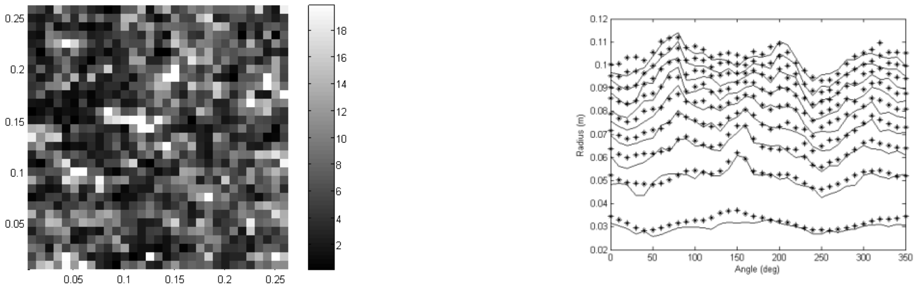

(a) K_x/K_0

(b) Flow pattern at various times – Flow front position error=2.32%

Fig. 4 Permeability field and simulated flow pattern

MARGINAL PDF

The reliable knowledge of the probabilistic distribution of material properties (V_f and K) is necessary for generating the random inputs for stochastic simulation. By comparison, the marginal PDF is similar at different locations in the field. The Maximum Entropy Principle (MEP) is a standard technique for evaluating the accurate marginal PDF from given moments of samples, without need for any assumption on the probabilistic model. Due to the small magnitude of K (10^{-10} m^2), the logarithmic value $Y(\omega) = \log(K(\omega))$ (K in m^2) is taken as the random variable to analyze. The MEP solution of the PDF can be validated by the empirical PDF, which can be directly estimated using common statistical software (e.g. Statistical Toolbox of MATLAB) based on the nonparametric models without any assumptions on the data-producing mechanism. Besides, a chosen parametric PDF model with the parameters calculated from the moments of the raw data can also be compared to estimate the validity of the model. Various PDF results are given for V_f and K_x in Fig. 5(a) and 5(b), respectively. It can be seen that both V_f and $\log(K_x)$ ($\log(K_y)$ in analogy) have a Gaussian PDF, which means that the log-normal PDF is an appropriate model for the permeability component.

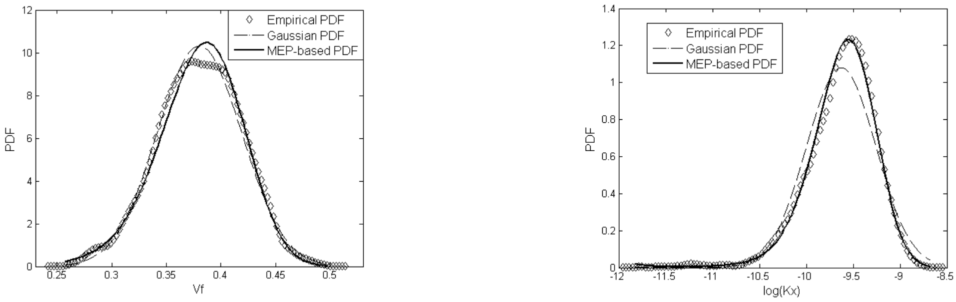

(a) V_f (b) $\log(K_x)$/m²

Fig. 5 Marginal PDF of fiber volume fraction and permeability

CONCLUSION

The highly disordered microstructure of the CSM leads to difficulty in the prediction of the permeability field and subsequently of the mold-filling pattern in the LCM processes. A methodology is developed, consisting in processing the gray-scale image of fabric samples to extract the statistical characteristics of the random microstructure, which is then incorporated in the formulation of the effective permeability based on the statistical continuum approach adapted for the Darcy's law. The effectiveness of the prediction method for the permeability field for the CSM has been validated by comparing the numerical simulation of mold-filling process with the radial injection experiments. When comparing to the traditional Kozeny-Carman model, the latter is found to be much less accurate in filling pattern prediction, due to the lack of two-point statistics containing clustering information. The effect of the sampling size on the prediction results has been analyzed. The accurate marginal PDF for V_f, K_x, K_y can be obtained in an exponential form using the MEP, which proves that V_f follows the Gaussian distribution, whereas K_x and K_y follow the log-normal PDF.

ACKNOWLEDGEMENTS: The authors wish to thank Assoc. Prof. S. Bickerton and the Center of Advanced Composite Materials (CACM) of University of Auckland (NZ) for the use of the experimental devices to acquire the raw data presented in the article. Also they are grateful to Conseil Général du Nord – Pas de Calais for funding part of the study.

REFERENCES

1. Zhang F, Cosson B, Comas-Cardona S, Binetruy C. Efficient stochastic simulation approach for RTM process with random fibrous permeability. Composites Science and Technology 71 (2011) 1478-1485.

2. Bickerton S, M. Battley and J.M. Gan, Automated Characterisation of Variability in Glass Fibre Reinforcement Architecture, 10th International Conference on Textile Composites, Lille, 26-28 Oct. 2010, Recent Advances in Textile Composites, Destech Publications, p. 148-156.
3. Garmestani H, Lin S, Adams B L. Statistical Continuum Theory for inelastic behavior of a two-phase medium. International Journal of Plasticity, 14 (1998) 719-731.
4. Corson, P. B. Correlation functions for predicting properties of heterogeneous materials. II. Empirical construction of spatial correlation functions for two phase solids. J. Applied Physics, 45 (1974b) 3165-3170.
5. Kroner, E. Statistical Modelling In Modelling Small Deformation of Polycrystals, ed. J. Gittus, and J. Zarka, Elsevier Applied Science, New York. (1987) 229p.
6. Adams, B L, Canova, G R, Molinari, A. A statistical formulation of viscoplastic behavior in heterogeneous polycrystals. Textures and Microstructures 11 (1989) 57-71.
7. Li D S, Saheli G, Khaleel M, Garmestani H. Quantitative prediction of effective conductivity in anisotropic heterogeneous media using two-point correlation functions. Computational Materials Science 38 (2006) 45-50.

NUMERICAL AND EXPERIMENTAL STUDY OF THE INFUSION PROCESS FOR LARGE SCALE INDUSTRIAL PARTS

Romain Agogué [1], Pierre Beauchêne [1], Jérémy Mazzolini [2] and Julien Valette [2]

[1] *ONERA, , DMSC, 29 av. de la Division Leclerc, 92322 Châtillon, France*
[2] *Tensyl, 1, place Moitessier - BP 3123 - 17000 La Rochelle - France*
Corresponding author's e-mail: romain.agogue@onera.fr

ABSTRACT: This work is dedicated to the modeling of the infusion process with a comparison between experimental data and simulation results, including material characterization. Two infusion cases are considered. First, a one dimensional flow experiment and, secondly a large scale industrial part with a stiffener and a spherical shape. We will first present the characterization of the compaction behavior of our materials (woven and interlock carbon fibre preforms). Dry and wetted compactions are considered. This characterization is an input of the proposed model, the output is the predicted thickness evolution of the fabrics depending on the infusion conditions. This prediction is then compared to experimental measurement of the thickness of the preform with respect to the time by measuring the local displacement of the vacuum bag. A digital image correlation is used for the 3D measurements of the displacement of the vacuum bag. This approach highlights the strong coupling between infusion and compaction and its effects on the part health.

KEYWORDS: *vacuum infusion, process simulation, experimental/numerical comparison, digital image correlation, small scale industrial demonstrator*

INTRODUCTION

Vacuum infusion is a very promising process due to its cost reduction in comparison with the RTM process. However, this process is more difficult to model because of the hydro-mechanical coupling between the resin flow and the preform behavior[**Error! Reference source not found.**], some models have been proposed to deal with this hydro-mechanical coupling [**Error! Reference source not found.**, **Error! Reference source not found.**, **Error! Reference source not found.**]. In particular, the thickness prediction at the end of the injection step is of prime importance for predicting whether the process would meet geometrical tolerance specified by industrials. In addition, part thickness has a strong influence on fibre volume fraction and thereby on performances of the composite parts.

Most of the time, the analysis of the vacuum infusion process is dealt on very simple flow experiment (such as 1D flow). However, the vacuum infusion process applied to complex parts is very interesting to highlight industrial problems and find solutions based on a deep understanding of underlying scientific topics. For that reason, the aim of this work is the modeling of the vacuum infusion process with a comparison between experimental data and simulation results on a small scale demonstrator.

First, a material characterization is shown to exhibit their compacting behavior. These characterizations are compared to in-situ measurements dealt in the second section, and are considered as an input for the proposed model in a third part of this paper.

MATERIAL CHARACTERIZATION

This first section is dedicated to the material characterization for modeling the vacuum infusion process. Thereby, two main properties are of prime importance for this model: the permeability and the compressibility of the preform. The permeability of carbon fibre was studied in a previous work [**Error! Reference source not found.**], consequently a focus on compaction is performed for the current study.

The power law is commonly used to describe the compaction curve [**Error! Reference source not found.**]. It is a simple law and describes well the compaction behavior at high compacting pressure (up to 0.1 MPa). Unfortunately, this law is less accurate for carbon fibre preforms for classical compacting pressure applied in vacuum infusion (lower than 0.1 MPa). For that reason, the Grimsley model [**Error! Reference source not found.**] (1) is preferred in this paper, whereas it is a 4 parameters model.

$$V_f(P) = \frac{V_{f0}}{1 - A_w + B_w\left(\frac{P}{C_w + P}\right)} \tag{1}$$

Where V_f is the fibre content of the preform, V_{f0} , A_w, B_w and C_w are parameters depending on the fabric.

A typical result of compaction experiment is shown on Fig. 1 for a dry stack of carbon fibre plies.

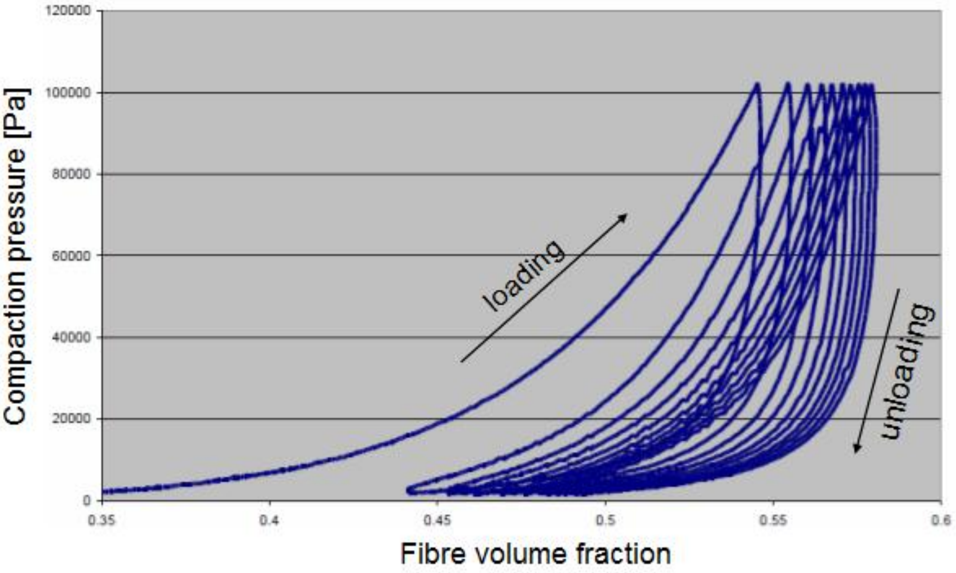

Fig. 1: Typical compaction experiment

EXPERIMENTAL DATA

A small scale demonstrator is used. This demonstrator (Fig. 2), with a length of 0.80 m and a width of 0.60 m, is composed of a planar area, a spherical shape (70 mm in height) and a stiffener (320 mm in length, 60 mm in width and 80 mm in height). Those shapes are typical in marine industry. A 15 mm fillet is manufactured on each sharp edge of this demonstrator, in particular on the base of the half-sphere and on the base of the stiffener.

Nine pressure sensors are used to register the pressure values at different location in time (denoted by P0 → P8 on Fig. 2). At last we use a Stereo Digital Image Correlation system (DIC) to measure the vacuum bag displacement which allows to measure the preform thickness in time as soon as a speckle is performed on the vacuum bag. Govignon *et al*. [**Error! Reference source not found.**] have already demonstrated the capability of a DIC system to monitor the displacement of the vacuum bag during the process. As it uses cameras, the DIC system is also used to register the flow front position.

At last, the weight of the pressure pot is registered so as to measure the resin flow rate.

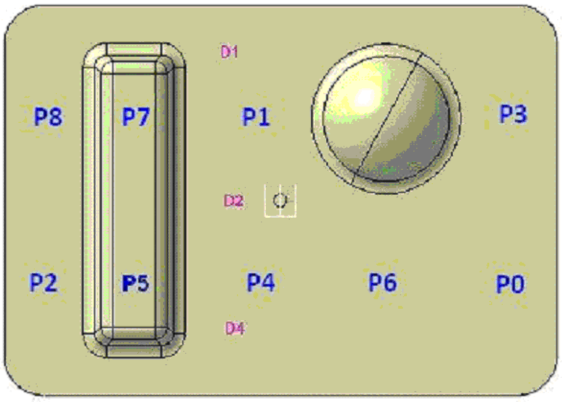

Fig. 2: Demonstrator used in this study

Injection gates are located all around the demonstrator (radial injection) and the vent gate is located in the centre of the demonstrator (*i.e*. the round in the centre of Fig. 2). The flow front position at several times is presented on Fig. 3. Injections are performed using silicon oil with a viscosity of 0.35 Pa.s.

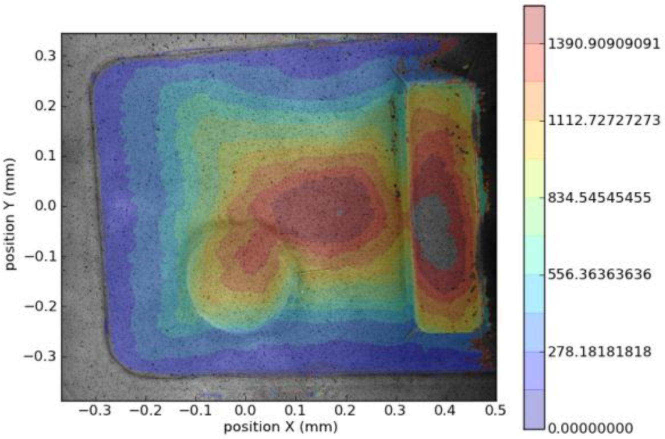

Fig. 3: experimental observation of the flow front position in time through 3 plies of G1100 (Hexcel)

Although a high radius fillet is manufactured at the connection of shapes and the planar area, difficulties in draping the preform often occur when applying the vacuum. Plies are not in contact with the mold in this curved area and it produces race tracing along the bases of the stiffener and the half-sphere (Fig. 3).

DIC is used to register a map of the thickness during the process. The vacuum bag displacement between the beginning and the end of the process is presented on Fig. 4.

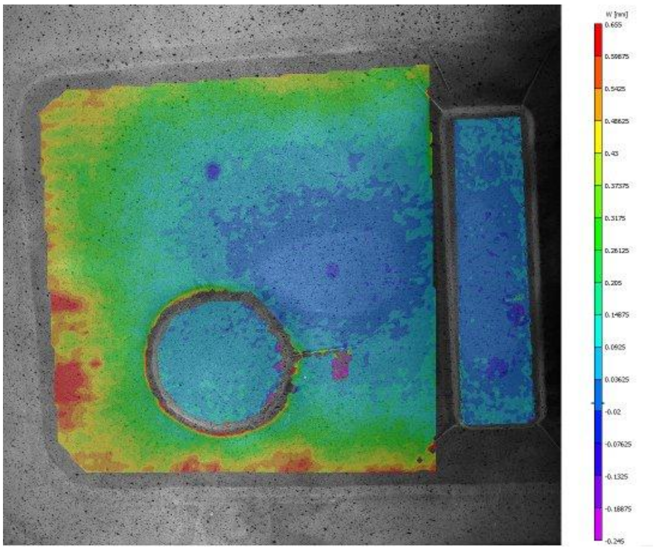

Fig. 4: experimental observation of the preform thickness at the end of the process. The preform is made of 3 plies of G1100 (Hexcel)

MACROSCALE SIMULATION

To build our model, several assumptions are done. The flow front propagation is supposed to be governed by the Darcy law (2), and the resin to be incompressible. This latest equation combined with the mass conservation of the fluid flow within a deformable porous medium leads to the equation (3). The system of equation to be solved is [**Error! Reference source not found.**]:

$$\vec{v} = \frac{\bar{\bar{k}}}{\mu} \nabla p \tag{2}$$

$$\frac{\partial h}{\partial t} + \nabla\left(h\vec{v}\right) = 0 \tag{3}$$

Where $\vec{v}$ is the velocity field [m.s^{-1}], $\bar{\bar{k}}$ is the permeability tensor [m²], μ is the dynamic viscosity [Pa.s] and p is the pressure field, h is the preform thickness [m].

In addition, we assume the permeability dependency with fibre volume fraction to be governed by the Kozeny-Carman law (4).

$$k = k_0 \frac{(1-v_f)^3}{v_f^{\ 2}} \qquad (4)$$

Where k is the permeability [m²], k_0 is a material-dependant constant to be defined with experimental data [m²] and v_f is the fibre volume fraction.

Moreover, the compacting behavior of reinforcements is assumed to be governed by the Grimsley model (1). The model is simplified by neglecting the post-filling effect of studies [**Error! Reference source not found.**] showing that this effect could have an effect on preform thickness before the gelation of the resin.

This set of four equations (1, 2, 3, 4) is introduced into a commercial finite elements software so as to solve the fully-coupled hydro-mechanical problem.

Because we want to predict the part thickness at the end of process, we assume that the resin has fully impregnated the preform and we only compute the steady state which is by far less time consuming than the transient calculation and is sufficient for the goal we want to reach.

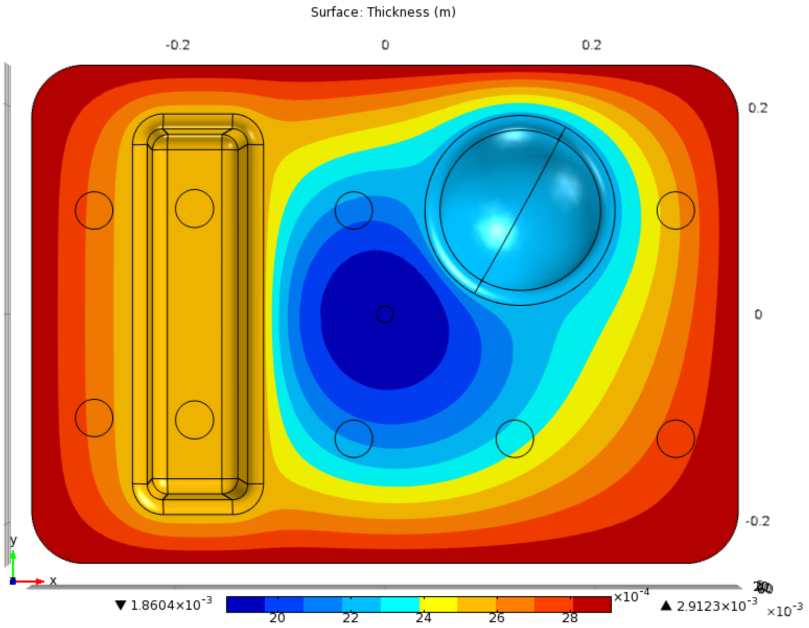

Fig. 5: Numerical prediction of the thickness of the preform at the end of the process (3 plies of G1100)

The effect of race tracking along the fillet on the preform thickness is investigated using the numerical models. A strong influence is observed. Edge effect strongly modifies the flow pattern and hence the pressure field of the fluid so modifies the compacting pressure.

CONCLUSIONS

Vacuum infusion process is applied to a small scale demonstrator. The preform thickness at the end of the process is evaluated to address the problem of geometrical tolerances due to the manufacturing process.

Digital image correlation is successfully used to monitor the full field displacement of the vacuum bag. Numerical predictions are compared to the experimental data produced during this study. A qualitative agreement is found between experimental data and numerical predictions. A more accurate simulation would use a more sophisticated compacting behavior, including relaxation.

ACKNOWLEDGMENTS: We acknowledge the readers that this work was conducted with the financial support of ANR, French National Research Agency, under the research program LCM3M.

REFERENCES

1. Tariq Ouahbi, Abdelghani Saouab, Joel Breard, Pierre Ouagne, and Sylvain Chatel. Modelling of hydro-mechanical coupling in infusion processes. *Composites Part A: Applied Science and Manufacturing*, 38(7):1646–1654, July 2007.

2. M.K. Kang, W.I. Lee, and H.T. Hahn. Analysis of vacuum bag resin transfer molding process. *Composites Part A: Applied Science and Manufacturing*, 32(11):1553 – 1560, 2001.

3. Q. Govignon, S. Bickerton, and P.A. Kelly. Simulation of the reinforcement compaction and resin flow during the complete resin infusion process. *Composites Part A: Applied Science and Manufacturing*, 41(1):45 – 57, 2010. <ce:title>Special Issue: Flow Processes in Composite Materials</ce:title>.

4. N.C. Correia, F. Robitaille, A.C. Long, C.D. Rudd, P. Simacek, and S.G. Advani. Analysis of the vacuum infusion moulding process: I. analytical formulation. *Composites Part A: Applied Science and Manufacturing*, 36(12):1645 – 1656, 2005.

5. Bertrand Laine. *Influence des déformations d'un renfort fibreux sur la perméabilité : modélisations et expériences*. PhD thesis, ParisTech Arts et Métiers, 2008.

6. Francois Robitaille and Raymond Gauvin. Compaction of textile reinforcements for composites manufacturing. i: Review of experimental results. *Polymer Composites*, 19(2):198–216, April 1998.

7. Brian W. Grimsley, Pascal Hubert, Xiaolan Song, Roberto J. Cano, Alfred C. Loos, and R. Byron Pipes. Flow and compaction during the vacuum assisted resin transfer molding process. In *International SAMPE Technical Conference*, 2001.

8. Q. Govignon, S. Bickerton, J. Morris, and P.A. Kelly. Full field monitoring of the resin flow and laminate properties during the resin infusion process. *Composites Part A: Applied Science and Manufacturing*, 39(9):1412 – 1426, 2008.

9. N. C. Correia, F. Robitaille, A. C. Long, C. D. Rudd, P. Simacek, and S. G. Advani. Use of resin transfer molding simulation to predict flow, saturation, and compaction in the vartm process. *Journal of Fluids Engineering*, 126(2):210–215, 2004.
10. Pavel Simacek, Dirk Heider, John W. Gillespie Jr., and Suresh Advani. Post-filling flow in vacuum assisted resin transfer molding processes: Theoretical analysis. *Composites Part A: Applied Science and Manufacturing*, 40(6-7):913 – 924, 2009.

MODELLING THE INTERNAL CORE PRESSURE DURING CURE OF OUT-OF-AUTOCLAVE HONEYCOMB PANELS

James Kratz and Pascal Hubert

McGill University, Department of Mechanical Engineering, 817 Sherbrooke St. West
Montreal, Quebec H3A 3C0, Canada
Corresponding author's e-mail: pascal.hubert@mcgill.ca

ABSTRACT: Honeycomb panels offer an extremely high stiffness-to-weight ratio, and their use in large structures can reduce labour and part count. Further cost savings can be achieved if good quality parts can be manufactured by vacuum bag only processing. Unfortunately, non-metallic cores readily absorb moisture from the atmosphere, which can be released as steam during elevated temperature processing. The internal core pressures become relevant when consolidating out-of-autoclave prepregs with vacuum bag pressure because of the reduced compaction pressure—a maximum of only 1 atmosphere is available—compared to 3 atmospheres usually used during autoclave processing of honeycomb panels. Therefore, during cure, the core pressure may increase to a level where gas flow through the skin is possible. To develop a better understanding of the possible internal core pressures encountered during cure, a model was developed to predict the pressure increase in honeycomb cells from absorbed moisture. A leak term was added to the model to account for gas flow through permeable plain weave skins during cure. The model was validated using an instrumented test fixture that measured the internal core pressure during cure with cores conditioned at increasing humidity levels.

KEYWORDS: *out-of-autoclave prepreg, honeycomb pressure, moisture, processing modelling.*

INTRODUCTION

Non-metallic honeycomb cores are usually dried ahead of lay-up to remove moisture that may have been absorbed from the atmosphere [1]. Drying non-metallic cores before cure may be suitable for small panels that can be vacuum bagged before re-absorbing moisture from the lay-up room environment, however, the increasing popularity of large integrated structures provides non-metallic cores a prolonged period to absorb moisture, given that lay-up times are on the order of days, opposed to hours for smaller parts. Large integrated structures offer the benefit of reduced part count and assembly time, but may be too large to fit into pre-existing autoclaves [2]. Given that installing a large autoclave is prohibitively expensive, and may offset the cost savings from manufacturing large integrated parts, vacuum bag only (VBO) processing of out-of-autoclave (OOA) prepregs in an atmospheric pressure oven has received further consideration in recent years.

In VBO processing, the maximum consolidation pressure at sea level is 100 kPa, whereas 100–300 kPa of positive pressure is common in autoclave processing of honeycomb panels [1]. The difference in consolidation pressure becomes important for suppressing voids and bonding the skin to the core when moisture is present within the honeycomb cells. The influence of temperature on the pressure of moist air in a void space, such as honeycomb cells, is shown in Fig. 1. Given that OOA prepregs are typically cured between 80–120 °C, the pressure within the honeycomb cells can exceed the applied consolidation pressure for high levels of relative humidity within the core. For a cure temperature of 120 °C, if the relative humidity level within the cells is above 60 %, the pressure within the honeycomb core will exceed the applied consolidation pressure in VBO processing, but would remain below the applied consolidation pressure used in autoclave processing.

As the pressure within the honeycomb core approaches the consolidation pressure, the possibility of gas flow through the skin becomes more likely. *Tavares et al.* [3] have demonstrated that prepregs are permeable during VBO curing. If prepregs allows gas to pass through the skin, the likelihood of disbonds decreases, but voids may remain entrapped in the cured skin. A higher pressure drop during cure would relate to more flow, and a greater chance of void formation in the composite skin.

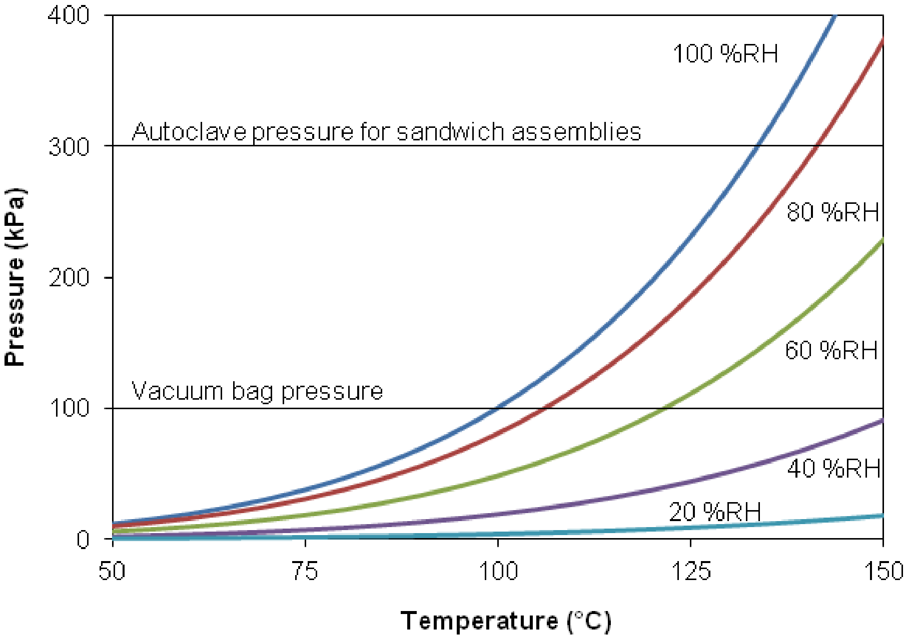

Fig. 1: Pressure evolution of moist air at given relative humidity for constant volumes.

In light of the possible pressure increase within the honeycomb cells during cure, the focus of this paper is to develop a model for the internal core pressure throughout the VBO manufacturing process. First, the pressure build-up within the core during elevated temperature processing is modeled based on residual air, and any off-gassing from the Nomex® core material. Second, the air permeability of the prepreg at elevated temperatures is used to model any air leakage from the core, through the skin, during cure. Finally, the model is compared to experiments performed using an instrumented test fixture that measures honeycomb core pressure.

MODEL DEVELOPMENT

The following sections describe the model development for honeycomb pressure during cure. The model was decoupled to predict the pressure increase in the cells from moisture, and the pressure loss due to the gas permeability of the skins. The total pressure in the honeycomb cells, P_{cell}, is described by

$$P_{cell} = P_{air} + P_{vapor} - P_{leak} \tag{1}$$

where P_{air} is the partial pressure contribution of dry air entrapped in the cells after a vacuum hold, P_{vapor} is the partial pressure of vapor entrapped after a vacuum hold and vapor that is devolved from the paper walls during elevated temperature processing, and P_{leak} is the pressure decrease caused by gas flow through the permeable skin. A schematic of the control volume used to calculate the honeycomb cell pressure is presented in Fig. 2.

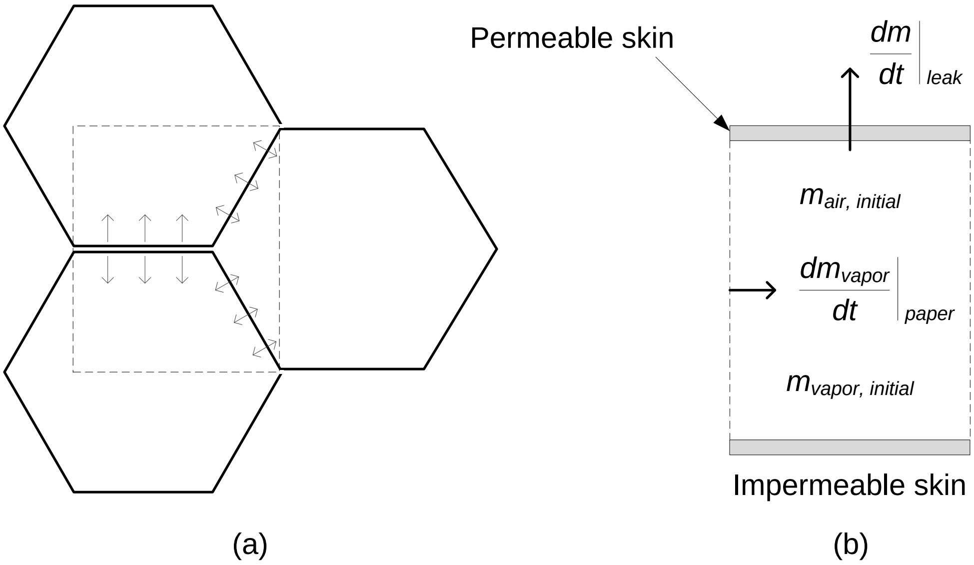

Fig. 2: Schematic of honeycomb cells. The repeating unit is shown in (a) with four paper walls exposed to release moisture. The control volume defined in this study is shown in (b) with the initial mass of air and water vapor remaining after the vacuum hold, the flux of water vapor from the paper walls, and the leak through the permeable bag-side skin. The tool-side skin is assumed to be impermeable. The total cell pressure is calculated based on the mass of air and vapor in the honeycomb cell.

Honeycomb pressure model

The increase in gas pressure during cure is governed by Fick's first law where the mass flux from one material is governed by the diffusion coefficient and the concentration gradient. The non-metallic honeycomb core used in this study is made from Nomex paper, and then dipped in a phenolic resin, resulting in a total paper thickness of less than 75 µm. Given that the paper walls are very thin and comprised of saturated and unsaturated regions of phenolic resin, an interface condition was used to describe the flow of water vapor from the paper into the cell, instead of a concentration gradient. *Zigrang and Bergmann* [4] showed that the moisture concentration at the interface of two materials is related by

$$\frac{M_I}{M_{u,I}} = \frac{M_{I+1}}{M_{u,I+1}} \tag{2}$$

where M is the percent moisture level by weight in adjacent materials I and $I + 1$, and M_u is the equilibrium percent moisture by weight at 100 % relative humidity. The mass flux, *dm/dt*, from the paper walls into the cell can be described by

$$\left.\frac{\mathrm{dm_{vapor}}}{\mathrm{dt}}\right|_{\mathrm{paper}} = -\rho D A_S \left(\frac{M_{paper}}{M_{paper,u}} - \frac{M_{cell}}{M_{cell,u}}\right) \tag{3}$$

where ρ is the density of water vapor, A_S is the exposed surface area of the honeycomb cells, and D is the diffusion coefficient described by the Arrhenius equation

$$D = D_0 \, exp^{-E_D/RT} \tag{4}$$

where D_0 is the pre-exponential factor, E_D is the activation energy, and R is the universal gas constant. If the initial core pressure, ambient humidity, and dry and initial moisture content of the core are known, the mass change of water vapor in the honeycomb cell, m_{vapor}, at time increment Δt can be calculated by

$$\left(m_{vapor}\right)_{t\,+\,\Delta t} = \left(m_{vapor}\right)_t + \left.\frac{\mathrm{dm_{vapor}}}{\mathrm{dt}}\right|_{\mathrm{paper}} \Delta t \tag{5}$$

assuming no leaks and that the diffusion coefficient is constant through Δt. The honeycomb cell pressure can now be calculated by the ideal gas law assuming the water vapour and air behave as ideal gasses:

$$\begin{gathered} P_{air} = \frac{m_{air} R_{air} T}{V_{cell}} \\ P_{vapor} = \frac{m_{vapor} R_{vapor} T}{V_{cell}} \end{gathered} \tag{6}$$

where m_{air} and m_{vapor} are the mass of air and water vapour, respectively, R is the gas constant for air and water vapour, T is the temperature, and V is volume of the cells. The pressure build-up within the cell, P_{air} and P_{vapor}, can be computed for each time step in Eqn. (1).

Gas leakage model

The flow of gas from the cell through the skin, *dm/dt*, can be modeled using Darcy's Law if the geometrical, skin material, and gas parameters are known

$$\left.\frac{dm}{dt}\right|_{leak} = \frac{\rho K A}{\mu} \frac{dP}{dl} \tag{7}$$

where K is the permeability of the bag-side skin, A is the cross-sectional area of the bag-side skin normal to flow (see Fig. 2b), μ is the viscosity of the gas, and *dP/dl* is the pressure gradient through the skin. The total mass lost through the skin can be computed for each time step, and the pressure lost in the cell can be computed by

$$P_{leak} = \left.\frac{dm}{dt}\right|_{leak} \Delta t \, (w_{air}R_{air} + w_{cell}R_{water})\frac{T}{V_{cell}} \tag{8}$$

where w is the mass fraction of air and water vapor in the cell. The total honeycomb core pressure during cure can be predicted using Eqn. (1) with inputs from Eqn. (6) and Eqn. (8).

EXPERIMENTS

Materials

The prepreg material used in this study was an OOA prepreg from Cytec Engineered Materials, Cycom 5320 T650-35 3K plain weave with a nominal areal weight of 196 g/m^2 and an initial resin content of 36 % by weight. The honeycomb core material was made from Nomex, and was 20 mm thick, with 3.125 mm cell diameter, and a density of 96 kg/m^3. A structural epoxy adhesive film from 3M, AF 163-2K with a 294 g/m^2 weight, was used to bond the skin to the core. The consumable materials were FEP release film (P3 with 0.38 mm perforations staggered by 6.35 mm), polyester breather, nylon vacuum bag, and sealant tape.

Pressure Measurement Fixture

To validate the model, a test fixture specifically designed to measure flow through the bag-side skin was used, and instrumented to measure the pressure differential across the skin. A schematic of the experimental setup is shown in Fig. 3. The main feature of the setup is a fixture with a square cavity (150 mm x 150 mm) that is 60 mm deep; this is where the internal core pressure was measured. Inside the cavity, three honeycomb cores were stacked such that

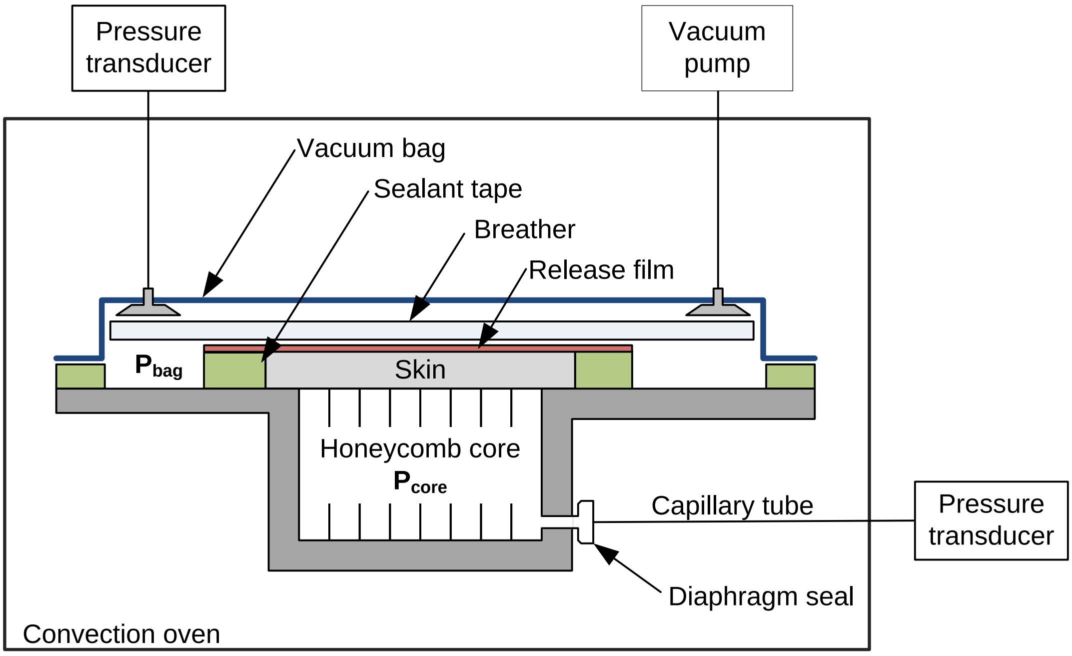

Fig. 3: Schematic of test fixture used to simulate the curing of honeycomb panels.

the core was flush with the top surface of the fixture. The ribbon direction of the centre core was perpendicular to the top and bottom cores to ensure gas flow between individual cells and an evenly distributed core pressure within the individual cells. The uncured skin (four layers of prepreg oriented at [0°] and one layer of adhesive film) was placed on top of the core, with a 25 mm overlap around the cavity. Sealant tape was placed around the perimeter of the skin to restrict air flow to the transverse direction. To complete the vacuum bag, one layer of breather was placed between the release film and vacuum bag, which was secured to the mould with sealant tape.

The fixture was instrumented with off-the-shelf sensors. The vacuum bag pressure, P_{bag}, was measured with a Wika A-10 pressure transmitter (range 0–1000 mbar) to evaluate the vacuum quality during the process. The pressure transmitter was placed outside the convection oven, and was connected to the vacuum bag by a vacuum valve and vacuum hose to prevent damage to the transmitter electronics. The honeycomb core pressure, P_{core}, was measured with a Wika S-10 pressure transmitter connected to a diaphragm seal by a capillary tube filled with paraffin oil (range 0–1000 mbar) to identify how the honeycomb core pressure evolves during cure.

Determination of Diffusion Constants

The diffusion coefficients for Eqn. (4) we obtained by curve fitting the pre-exponential factor and the activation energy to experiments performed with the fixture in Fig. 3. The Nomex core describe in the materials section was conditioning to three moisture levels, and a 6 mm aluminum plate was sealed over the cores to ensure no leaks occurred. The predicted honeycomb cell pressure build-ip using Eqn. (6) is plotted alongside experiments in Fig. 4. The model developed for Eqn. (6) fits the experimental data within 6 %. The model under-predicts the cell pressure by 6 % at the lowest moisture level tested, and over-predicts by 1 % at the highest moisture level.

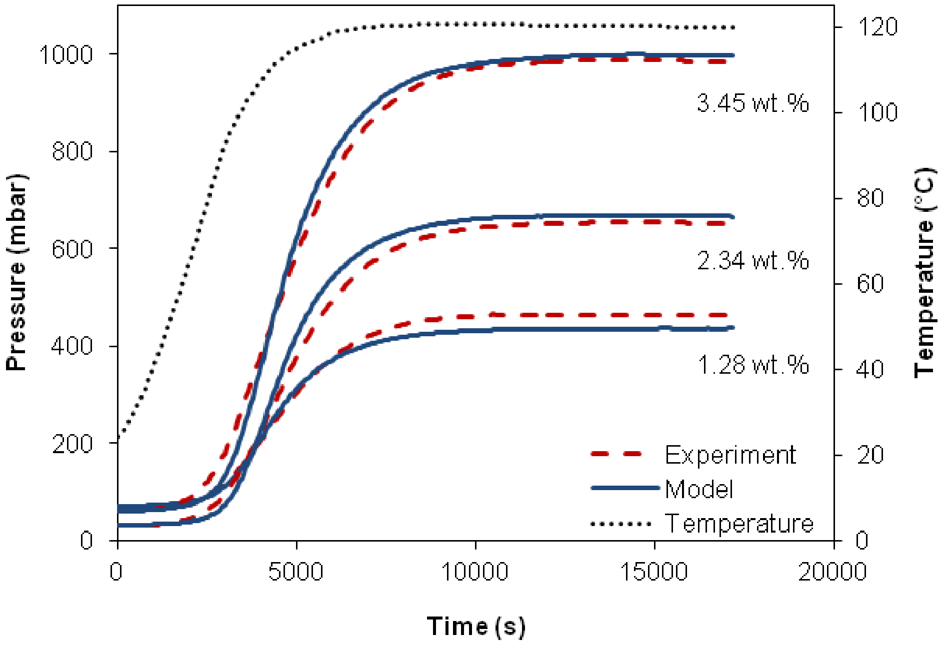

Fig. 4: Comparison of predicted and measured honeycomb core pressure in a sealed volume for the Nomex core describe in the Materials section.

Honeycomb Cell Pressure Measurements

Nomex cores were conditioned at ambient temperature (21 ± 2 °C) and four relative humidity levels: 12, 30, 70, and 99 %RH. The honeycomb samples were initially dried in a convection oven at 180 °C until the weight change was less than 0.01 wt.%. After drying, the samples were weighed daily until the change in moisture was less than 0.05 wt.%. The equilibrium moisture levels were 1.25, 2.05, 4.15 and 6.25 wt.%.

Experiments were performed with the conditioned honeycomb cores and the results are presented in Fig. 5, alongside the model predictions from Eqn. (1). A function describing the skin gas permeability for temperature was generated using experimental permeability data from previous experiments [5]. The model and experimental honeycomb cell pressure during cure follow the same trend as Fig. 4; the model under-predicts the cell pressure at lower moisture content and slightly over-predicts the experiments at higher content. The model fits very well for the 2.05 and 4.15 wt.% experiments. These moisture contents correspond to 30 and 70 % relative humidity (at 22 °C). The 1.25 and 6.25 wt.% experiments are extreme cases of 12 and 99 % relative humidity, respectively. In light of this, the model captures the core pressure behavior of honeycomb cores that would reach moisture equilibrium in normal lay-up room conditions.

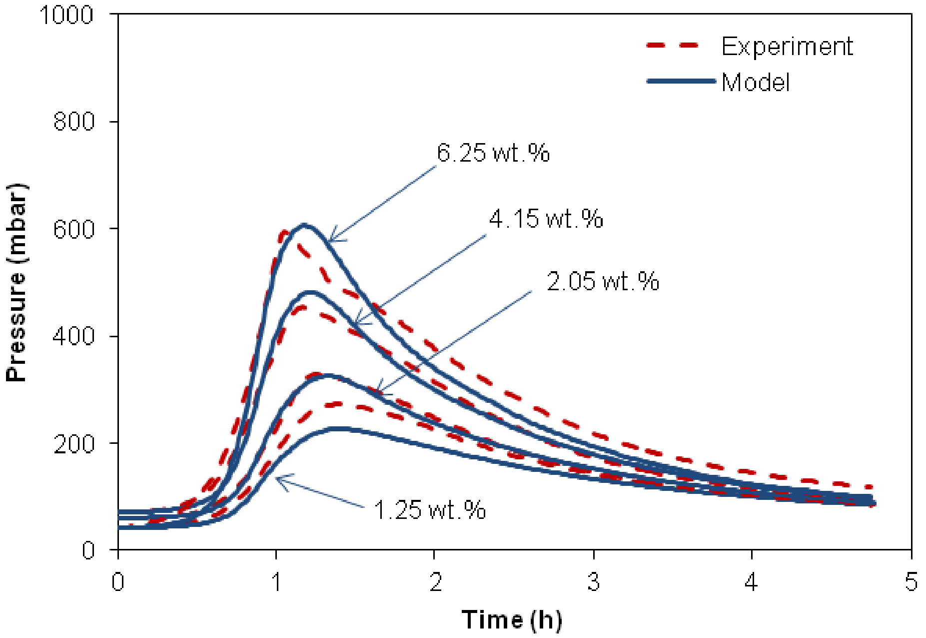

Fig. 5: Comparison of measured and predicted honeycomb core pressure during cure with a skin comprised of four prepreg plies and one layer of adhesive film.

CONCLUSIONS

A model was developed to predict the evolution of the honeycomb core pressure during cure of a sandwich panels manufactured by vacuum bag only processing with out-of-autoclave prepreg. A decoupled model consisting of two steps was used in this study. The first step used Fick’s law was to predict the mass transfer, and corresponding pressure build-up, during cure of honeycomb that had absorbed moisture from ambient conditions. The second step was to introduce a leak term using Darcy’s Law to relate the mass loss during cure, and corresponding pressure drop, to skin gas permeability. Experiments were performed with cores conditioned between 12–99 % relative humidity. The model captures the cell pressure behavior throughout the moisture range, although the fit is best for the cores conditioned to equilibrium at 30–70 % RH.

ACKNOWLEDGMENTS: We would like to acknowledge financial support from the Natural Sciences and Engineering Research Council of Canada (NSERC), the Consortium for Research and Innovation in Aerospace in Quebec (CRIAQ), Bell Helicopter Textron Canada Ltd., Bombardier Aerospace, and Delastek Inc.

REFERENCES

1. Campbell FC (2006), Manufacturing technology for aerospace structural materials, New York: Elsevier.

2. Russell JD, Shenk B, Holzwarth R, Swanson M, Paige D, Tresnak M, et al. (2009), ‘Advanced composite cargo aircraft’, *Proc. of the 41st SAMPE Fall Technical Conference*.

3. Tavares SS, Caillet-Bois N, Michaud V and Manson JAE (2010), ‘Non-autoclave processing of honeycomb sandwich structures: Skin through thickness air permeability during cure’, *Composites Part A: Applied Science and Manufacturing*, 41(5), 646-652.

4. Zigrang DJ and Bergmann HW (1980), ‘Response of graphite/epoxy sandwich panels to moisture and temperature transients’, *Journal of Spacecraft and Rockets*, 17, 219-225.

5. Kratz J, Centea T and Hubert P (2011) ‘Air permeability of out-of-autoclave honeycomb structures during processing,’ *Proc. of the 26th ASC Technical Conference (the Second Joint US-Canada Conference on Composites*.

OUT-OF-AUTOCLAVE PROCESSING OF RIBBED PARTS: TECHNICAL, ECONOMIC AND ENVIRONMENTAL ASSESSMENT

Rémy Teuscher, Robert. A. Witik, Amaël Cohades, Véronique Michaud

Laboratoire de Technologie des Composites et Polymères (LTC), Ecole Polytechnique Fédérale de Lausanne (EPFL), Station 12, CH 1015 Lausanne, Switzerland. Corresponding author's e-mail: veronique.michaud@epfl.ch

ABSTRACT: In this work, we compared autoclave and out-of-autoclave (OOA) processes in terms of cost, quality and environmental performance. The autoclave serves as the baseline process, and is compared with an OOA prepreg and infusion process to produce carbon fiber reinforced flat panels. The influence of pressure on part quality was assessed; cost and environmental performance were then compared for each production process. It was shown that although energy has a noteworthy contribution to environmental performance, its reduction plays a limited role in lowering part cost. The most significant contributor to both cost and environmental performance was carbon fiber production and conversion. A generic OOA prepreg ribbed part was then considered and an alternative method to improve rib quality in an OOA process was proposed.

KEYWORDS: *out-of-autoclave processing, prepreg, infusion, technical cost modeling, life cycle assessment.*

INTRODUCTION

The use of composite materials has increased within the aerospace sector in recent years as a means to achieve greater weight savings and reduce emissions during operation. The standard method for curing composites for primary aircraft structures has been the autoclave. Materials suppliers have recently begun to support the growth of OOA processing to reduce costs with the development of OOA specific prepregs [1]. These enable low void content laminates to be produced under atmospheric pressure with mechanical performance, which can fulfill the requirements of the aerospace industry, thus eliminating the need for an autoclave by enabling the use of conventional thermal ovens. Liquid resin processing techniques, such as resin infusion, are alternatives, which benefit from using lower cost dry fibers and low viscosity resin systems, which are combined at the location of component manufacture. Such techniques have already been proven in large structures within the marine industry and are now considered by the aerospace sector as possible lower cost alternatives to autoclave curing. Until now infusion processes have been used in applications such as the A400M upper cargo door [2], regional jet empennage [3] and some business jet applications [4].

Implementation of OOA processing is currently supported by technical studies in areas such as process simulation, and characterization of mechanical performance to ensure that composites produced meet the stringent requirements of the aerospace industry [5-7]. However, few publications quantify cost benefits or environmental performance. Hinrichsen [8] compared CFRP autoclave-manufacturing technologies with aluminum for the A380 aft pressure bulkhead, where autoclave processed composites achieved 15% and 11% reductions against aluminum in weight and cost respectively. Materials made up 50% of component cost, with half of this attributed to waste, thus concluding that cost and waste reduction of materials would have the largest effect upon reducing CFRP component costs. Kleineberg et al [9] investigated a low cost OOA resin infusion approach for stringer manufacture in the context of the European project ALCAS [10]. Materials contributed to the largest proportion of costs at 60%, with labor and tooling contributing to 25% and 14% respectively; Energy costs were found to be relatively insignificant, contributing to only 1% of total cost; however, no comparison was made with other processes and it is unclear what improvements were achieved over autoclave processing.

The aim of this work is to assess OOA technologies, (prepreg and vacuum infusion techniques) in terms of cost, environmental impact and part quality in order to identify the main drivers and routes of improvement of these techniques. A flat panel is first considered; an extension of this work towards ribbed parts is then introduced.

MATERIALS AND METHODS

Materials and processing conditions

The prepregs were carbon 2x2 twill fabrics (CF5904-A) with HTA 40 fibers and 40 wt% MTM®44-1 resin, produced by Umeco Structural Materials (formally Advanced Composite Group)[11]. For the cost and LCA analysis, a UD CF prepreg was considered, based on the same resin system. This MTM®44-1 material can be processed in or out of an autoclave, following the cure schedule given in Table 1.

Table 1: Processing conditions for MTM®44-1 prepreg

	Vacuum Bag Processing	Autoclave Processing
Ramp rate	1-2°C/min	1-2°C/min
Pressure	N/A	3-7 bar
Vacuum	<0.25 bar	<0.25 bar
Cure time	4 hours@130°C+post-cure or 2hours@130°C and 2hours@180°C	4 hours@130°C or 2hours @180°C

Cure was performed with the set-up recommended in the datasheet using a non-perforated peel-ply and, air-escape paths created with glass tows. 10 min debulking steps were carried out every 3rd layer, and at the end of lay-up for another 10 minutes. The cure time was 4 hours at 130°C for all cases. A post-cure was carried out for the OOA case, at 180°C for 2 hours, following the manufacturer’s datasheet.

Infusion tests were not performed in the frame of this study, but for the sake of cost and Life Cycle Assessment (LCA) comparison, RTM6 resin from Hexcel, used commonly in aeronautic applications was considered, with a cure at 120°C for 30 min, followed by a post-cure at 180°C for 2 hours. The VAP infusion process was assumed [12], using a Goretex membrane, as this has been shown to provide an aerospace accepted quality for the parts. The carbon fabric was assumed to be a non-crimp fabric, to provide part properties rather similar to the UD prepreg.

Technical cost analysis

Estimation of manufacturing costs for each process was carried out using a technical cost model developed at EPFL, and based upon an activity based costing (ABC) approach [13]. A production process is first defined containing all relevant operations, equipment, and labor to produce a specific component. The process is then segmented into discrete quantifiable activities and a cost estimate is prepared for each activity, from input parameters such as labor requirements and costs (direct and indirect), cycle times, materials costs, equipment costs, production volumes, energy use, scrap, reject rates, and overheads. Costs for each activity are then combined to give a total cost for the production process. Details are given in Ref. [13], and main cost values provided in Ref. [14].

Life Cycle Assessment

Life cycle assessment (LCA) is an internationally standardized methodological framework used for estimating and assessing environmental impacts of a product or service over its life cycle [15]. In this study a “cradle to gate” assessment was performed which included raw materials production and the manufacture of the part. Steps such as resin and fiber production, weaving, prepregging, transportation of materials, manufacturing energy consumption, consumables (and their incineration after use) are taken into account. The “use” and “end-of-life” phases after part production were not assessed since they were assumed to be identical and the weight variation between the different parts negligible. Commercially available LCA tools and databases have been employed for the modeling (Simapro software [16] and Ecoinvent database [17]). Impact 2002+ impact assessment method was chosen to fit the European location [18]. Main assumptions are similar to those provided in Ref.[14].

FLAT PANEL COMPARISON

Functional unit description

The functional unit (FU) is defined as a 400 x 400 x 4 mm CFRP panel, with a maximum deflection of 2mm when simply supported with a 190N point load applied at the center. The following manufacturing scenarios are considered in this study:

Scenario 1 (Autoclave): Autoclave curing with MTM®44-1 prepreg at 6 bars for the analysis, and 3 or 7 bars for the experimental part.

Scenario 2 (OOA prepreg): Thermal oven curing with MTM®44-1 prepreg, under vacuum only.

Scenario 3 (Infusion): Thermal oven curing with liquid resin infused (LRI) CF fabric.

Prepreg plate quality

Three panels were manufactured according to scenario 1, with 3 or 7 bars pressure (respectively test 1 and 2) and a cure schedule of 4 hours at 130°C, and according to scenario 2, with vacuum-bag curing only for 4 hours at 130°C, followed by post-cure at 180°C (denominated test 3). The lay-up was $[0/90; \pm45; 0/90; \pm45]_s$. Figure 1 shows micrographs of the three test samples, all showed good impregnation with void contents well below 1%. Volume fractions were close, ranging from 49% to 52% with increasing level of applied pressure. In the case of the autoclaved samples, a slight bleeding of the resin from the sides was observed, which would not be observed so extensively in larger parts, and led to the increase in V_f. Overall, it can be assumed that the OOA processes produced a similar level of part quality and compaction compared to the autoclave.

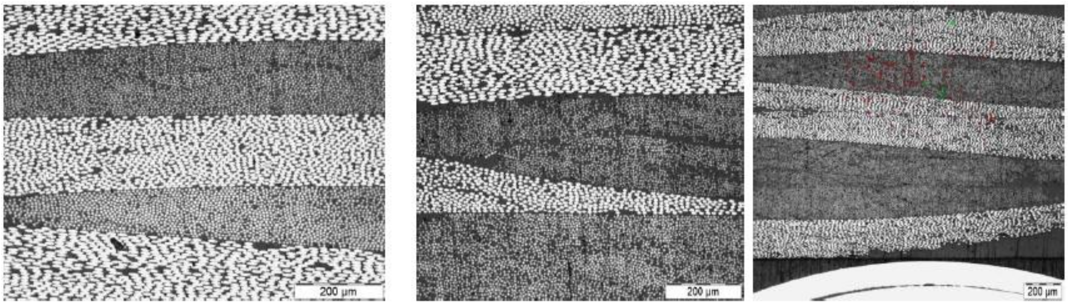

Fig. 1: Micrographs of test 1 (left), 2 (middle) and 3 (right)

Cost analysis

The system diagrams for the scenarios 1 to 3 are similar to those presented in Ref. [14], as well as the cost of the materials and consumables. Energy use and equipment are allocated on a utilization basis. Tooling was assumed to be a low-cost aluminum plate for each case. Cost and energy use for each process are detailed in Ref. [14].

Figure 2 shows the total estimated manufacturing cost per panel for each process with contributions from materials, labor, tooling, consumables and energy. The production cost with the baseline autoclave process was the highest at €229. The thermal oven infusion process resulted in the lowest cost panel at €195 representing a 15% reduction. Materials and labor accounted for a little above 50% and 35% respectively of the total costs for OOA prepreg processing and corresponded well with previous work [8,9]. Total prepreg purchase cost for the panel was €120 of which €24 was discarded due to the 20% cut factor assumed. The cut factor was relatively low compared to the 50% and 30% assumed in previous studies [8,9], but was influenced by the simplicity of the panel. Tooling cost accounted for less than 0.5% in this case due to the low cost of an aluminum plate; a higher proportion would be expected where more complex machined tooling is used, previous work from Kleineberg et al [9] suggested a 14% contribution to part cost. Energy cost had little influence on total part cost making up just 2% of total cost for the autoclave and as little as 0.7% for the remaining scenarios. Kleineberg et al [9] also noted the minimal contribution of energy cost to final part cost.

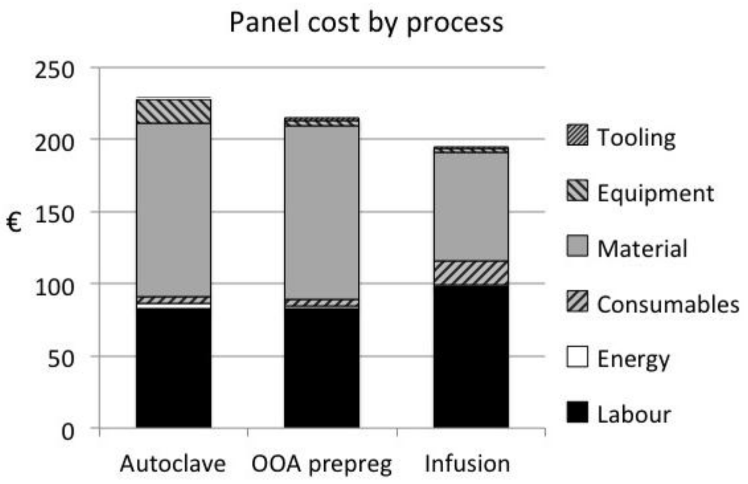

Fig. 2: Total production costs per panel in Euro for each scenario.

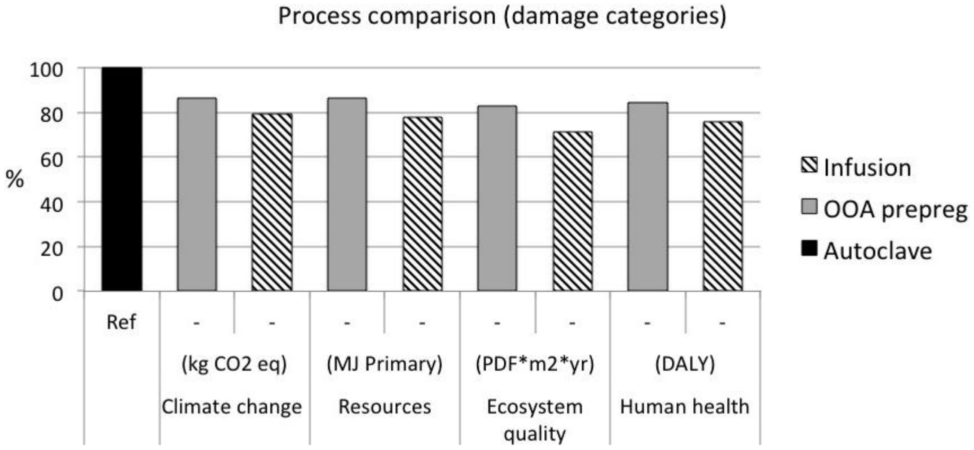

Fig. 3: Comparison of processes with damage end point categories, the far left bar represents the autoclave reference process to which alternative processes are compared.

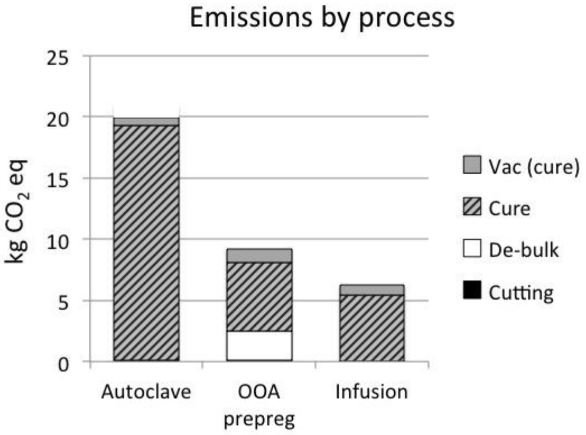

Fig. 4: Emissions related to energy use during processing for all scenarios

Life Cycle Assessment

The overall results of the LCA study are presented in Figure 3 at end point level, and show impacts related to the manufacture of a composite panel via each production scenario. Autoclave curing is the reference process shown on the far left of the figure. The remaining scenarios are compared to the reference with the four damage categories: climate change, resources, ecosystem quality and human health [18]. All OOA curing approaches in this study showed improved environmental performance over the autoclave process. Within the climate change category, CO_2 equivalent emissions were reduced by 14% for prepregs cured in a thermal oven. The infusion process performed better, reducing emissions by approximately 20%. The same trends in burden reductions and process ranking were achieved in each damage category. No impact shifts were observed between impact categories for all processes since all scenarios utilize the same materials with variations only in quantity and energy use. The remaining results from the study are, therefore, shown in CO_2 eq. emissions only.

Carbon fiber production was the most energy and emission intensive process, contributing to around 84% of environmental burdens from materials. Processing emissions result from the production of the energy used within the factory for equipment such as cutting machines, vacuum pumps, and ovens and accounted for 25% of the total for autoclave curing. A comparison of the processing related emissions for each scenario is shown in Figure 4. Cutting table operation contributed minimally to the overall impacts (0.6%) from panel manufacture due to the relatively short use times, resulting in 0.06 kg CO_2 eq. in the worst case. Curing resulted in largest proportion of process related emissions for all processes, although OOA approaches all required less energy and produced fewer emissions during this phase. The infusion processes had the shortest cycle times and lowest energy requirements, thus achieving reductions in emissions against the autoclave. Longer cycle times and the need for longer de-bulking for the OOA prepregs meant that they did not perform as well but still achieved reductions of 52%. Thermal oven operation was efficient and process time increase had little effect on energy use and resulting emissions.

Sensitivity analysis showed that the main driver, beyond the impact of carbon fibers, was process cycle time. We also found that energy consumption during cure did not depend much on the level of applied pressure, but was sensitive to the chosen cure cycle: from measurements in a lab-scale autoclave, a 12% reduction in energy consumption was achieved for the 2hour cure at 180°C and 6 bars, compared to the 4hour cure at 130°C and 6 bars. Out-of autoclave cure allows the use of an oven with a lower thermal inertia, hence further reductions in energy use can result. The cure cycle with 2 hours at 130°C and 2 hours at 180°C led to 13% reduction in energy use, compared to the 4 hours at 130°C followed by freestanding post-cure. It is worthy to note that adequate filling of the autoclave or oven with several parts would further reduce the energy consumption, cost and environmental burdens.

RIBBED PARTS

Since out of autoclave methods proved their advantage in terms of cost and environmental impact, and showed similar part quality for a simple flat panel, the next step is to extend the comparison to a more complex part shape. As ribbed parts are often produced in aeronautical parts, a generic T shaped stringer part was manufactured with OOA prepreg. The manufacturing process was based on literature [19-21] and recommendations from ALCAS project [10]. It is known that stringer webs are in general not sufficiently compacted in vacuum-bag processes, as the lateral pressure is not sufficient and not uniformly applied, so additional fixtures are required to improve pressure distribution and compaction of the vertical part. Figure 5 presents the dimensions of the part, as well as the manufacturing process, using two triangular aluminum blocks on each side, of dimensions 5x12x20 cm, with a radius of 5 mm at the location of the right angle.

A stringer was thus composed of two different parts: the lower part is composed of 8 layers of prepreg with the configuration: [0/90; ±45; 0/90; ±45]s; the upper part is composed of two L-Shaped parts that are each composed of 8 layers with the configuration: [0/90; ±45; 0/90; ±45]s. Debulking was performed as for the flat plates, and bagging as described in Ref. [11]. Figure 6 shows the resulting part thickness and volume fraction variations with location, as well as some micrographs taken in the flange and in the web. Overall, part quality was good, with a void content below 1% (except in the central joining part, red point on Figure 5, where no filler was used for the present experiment). Variations in part volume fractions were

Fig. 5: Schematic of the stringer configuration and manufacturing process steps.

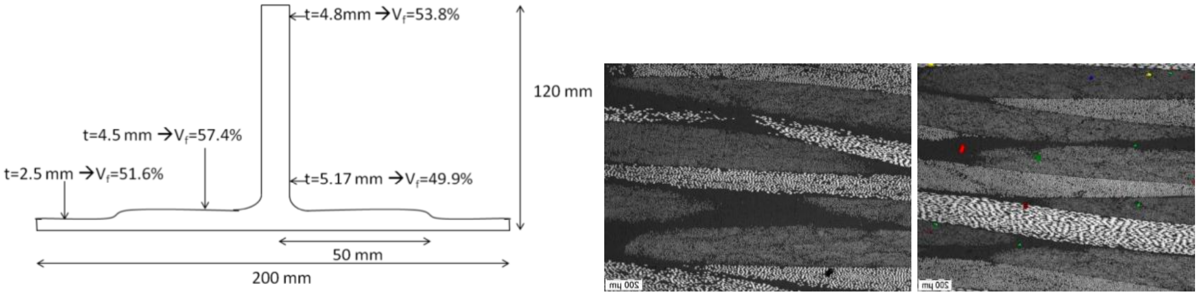

Fig. 6: Left: thickness and volume fraction variations in the stringers: center, micrograph of the flange part, right: micrograph of the web part.

however observed from 50 to 57%, with increased compaction under the aluminum blocks, and lower compaction at the bottom of the web.

Alternative manufacturing methods were thus proposed, where a Shape Memory Alloy (SMA) wire 0.5mm in diameter and pre-strained by about 2% was inserted in a cylindrical hole at the bottom part of the aluminum blocks, as shown in Figure 7. Additional pressure was thus created to force the aluminum blocks in closer contact during the cure at 120°C, above the transformation temperature of the NiTi Alloy. Preliminary results are encouraging; the thickness difference along the web was reduced from 0.37 mm to below 0.1 mm. An improved set-up to easily position and clamp the SMA wire during cure is under development.

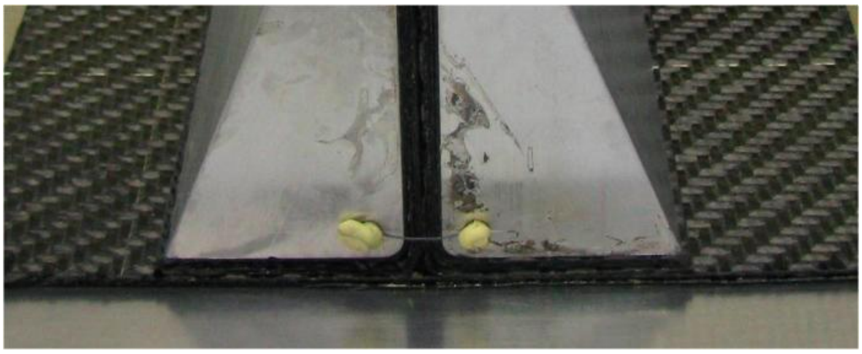

Fig. 7: Modified process with a SMA wire clamping the base of the aluminum blocks during cure.

CONCLUSIONS

Out-of-autoclave processes provide alternative methods to produce high quality parts, while decreasing the cost and environmental impact of the parts through a decrease in energy consumption with the use of low thermal inertia ovens, and potentially cycle time reduction. The gain is however limited, as material costs represents a large fraction of the total part cost, which is only slightly decreased with the use of dry fabrics versus prepregs. Finally, the production of complex shapes such as stringers is still more complex with OOA processes, and we proposed a simple method, relying on the use of local additional pressure on the web created during cure by SMA wires, to improve the compaction and uniformity of the cured parts.

ACKNOWLEDGMENTS: This work is supported by the EU-FP7 project Clean Sky, “Eco Design” ITD. We would like to thank Dr S. Cozien-Cazuc from Umeco for providing materials and technical data, and the partners of the RUAG Cluster for fruitful interactions.

REFERENCES

1. Gardiner, G., (2011) Out of Autoclave Prepregs: Hype or revolution? *High performance composites.*
2. Black, S., (Jan 2007). Inside Manufacturing: A400M Cargo Door Out of the Autoclave. *High Performance Composites*.
3. Yamashita, M., et al. (2008) ‘Development of advanced vacuum-assisted resin transfer moulding technology for use in an MRJ empennage Box Structure’. *Mitsubishi Heavy Industries Ltd technical review* 45, (4): p 1-4.
4. Steckelman, Y., et al. (2009) Development of Business Jet Components by Resin Infusion. *SAMPE Journal*; 45, (4): p 6-13.
5. Centea, T., Hubert, P., (2011) ‘Measuring the impregnation of an out-of-autoclave prepreg by micro-CT’. *Composites science and technology*; 77, (5): p 593-599.
6. Nightingale, C., Day. R.J.,(2002) ‘Flexural and interlaminar shear strength properties of carbon fibre/epoxy composites cured thermally and with microwave radiation’. *Composites Part A* 2002; 33, (7): p 1021-1030.
7. Li, W., Gillespie, J.W., Heider, D., (2004). ‘Process and Performance Evaluation of the Vacuum-Assisted Process’. *Journal of composite materials* 2004; 38, (20): p 1803-1814.
8. Hinrichsen, J.,(2001) ‘A380 – The Flagship for the new century’, *proceedings of JISSE-7,* Japan.

9. Kleineberg, M., et al. (2007) ALCAS Centre Wing Box-Lower Cover Low Cost Resin Infusion Stringer Manufacturing. *1st CEAS European Air and Space Conference*. p 727.
10. Advanced Low Cost Aircraft Structures (ALCAS) (http://alcas.twisoftware.com)
11. ACG, "MTM® 44-1 MATRIX RESIN Product Description," no. 924425, 2008
12. Filsinger, J., Lorenz, T., Stadler, F., Utecht,S (2001), 'Method and Device for Producing Fibre Reinforced Components Using an Injection Method', Geman Patent WO 01/68353 A1.
13. Wakeman, M. D., Månson, J-A. E., (2004) Cost Analysis. *In: Long AC, editor. Design and Manufacture of Textile Composites*. Cambridge: Woodhead Publishing.
14. R. A. Witik, F. Gaille, R. Teuscher, H. Ringwald, V. Michaud, J.A.E Månson (2012) 'The Economic and Environmental Assessment of Out-of-Autoclave Curing for Composite Materials', *Journal of Cleaner Production*, vol 29-30, pp.91-102, 2012.
15. International Organization for Standardization – ISO (2006): Environmental Management - Life Cycle Assessment - Requirements and Guidelines. International Standard ISO 14044, Geneva.
16. Simapro Software. *PRé Consultants website* (http://www.pre.nl/simapro/default.htm)
17. Ecoinvent Centre, Ecoinvent data v2.1, Ecoinvent reports No. 1–25, CD-ROM, Swiss Centre for Life, Cycle Inventories, Dübendorf, Switzerland (2009).
18. Jolliet, O., et al. (2003) 'IMPACT 2002+: A New Life Cycle Impact Assessment Methodology', *International Journal of Life cycle assessment*; 8, (6): 324-330.
19. X. Wang, F. Xie, M. Li, and Z. Zhang, (2010) "Influence of Core Fillers on Resin Flow and Fiber Compaction of Cocured Skin-to-Stiffener Structures," *Polymer*.
20. C. B. Xin, et al. (2011) "Experimental and numerical study on the effect of rubber mold configuration on the compaction of composite angle laminates during autoclave processing," *Composites Part A: Applied Science and Manufacturing*, vol. 42, no. 10, pp. 1353-1360.
21. X. Wang, F. Xie, M. Li, and Z. Zhang, (2010) "Influence of Tool Assembly Schemes and Integral Molding Technologies on Compaction of T-Stiffened Skins in Autoclave Process," *Journal of Reinforced Plastics and Composites*, vol. 29, pp. 1311-1322.

THE EFFECT OF OUT-TIME AND CURE CYCLE ON THE CONSOLIDATION OF OUT-OF-AUTOCLAVE PREPREGS

Timotei Centea [1], James Kratz [1] and Pascal Hubert [1]

[1] *Department of Mechanical Engineering, Faculty of Engineering, McGill University, MacDonald Engineering Building, 817 Sherbrooke St. West, Room 367, Montreal, Quebec, H3A 0C3, Canada. Corresponding author's e-mail: pascal.hubert@mcgill.ca*

ABSTRACT: Out-of-autoclave prepregs are initially only partially impregnated, with dry areas that allow initially gas transport and are subsequently infiltrated. The following experimental study focuses on the effect of prepreg out-time and cure cycle on consolidation phenomena for two OOA prepregs with different fabric architectures. First, both prepreg and neat resin are aged under controlled conditions to three different out-times, and the resin viscosity and prepreg microstructure are investigated by parallel plate rheometry and x-ray microtomography, respectively. Then, laminates are manufactured using four cure cycles in an instrumented tool capable of tracking part thickness in-situ; the cycles consisting of two different ramp rates (0.57 °C/min and 2.78 °C/min) and dwell temperatures (93 °C and 121 °C). Finally, the laminates are analyzed to determine their fibre volume fraction and porosity. The results show that the resin viscosity increases with out-time but that the prepreg microstructure remains the same; that the rate of consolidation during processing differs with out-time; that out-time can significantly reduce the quality of manufacturing laminates by inducing micro-porosity within the tows; and that higher ramp rates and dwell temperatures may mitigate or even eliminate this problem.

KEYWORDS: *out-of-autoclave, consolidation, flow, tow impregnation, infiltration, out-time, aging, cure cycle.*

INTRODUCTION

Out-of-autoclave (OOA) prepregs are vacuum bag processed in unpressurized ovens, with both the cure temperature (80 – 121 °C) and consolidation pressure (a maximum of atmospheric pressure, approximately 101.3 kPa or 1 atm) comparatively limited relative to traditional autoclave manufacturing. Due to these constraints, successful OOA processing requires the evacuation of any air entrapped between or within the prepreg plies. This evacuation occurs by means of a ply microstructure that is initially only partially impregnated. The dry areas, previously shown to be the fibre tow cores, form a relatively permeable network that allows gases to migrate towards the laminate perimeter and escape. Then, they are infiltrated by surrounding resin during heated consolidation [1, 2].

This infiltration flow, or tow impregnation, is likely to depend on the material properties of the tows and resin, and on process parameters such as pressure and temperature. In particular, the resin viscosity is likely to be of primary importance. The viscosity of OOA prepregs changes by several orders of magnitude during processing, depending on the cure cycle temperature profile and on the polymerization kinetics [3]. However, thermosetting resins may also undergo room-temperature polymerization if left at ambient conditions for extended periods [4]. The effects of room-temperature out-time prior to processing have already been shown to induce porosity and degrade mechanical performance of laminates manufactured using a standard cure cycle [5]. However, a previous study of OOA tow impregnation using an analytical model also suggested that changes in cure cycle ramp rate and dwell temperature may mitigate or even eliminate flow-induced micro-porosity in certain cases [6].

OBJECTIVES

The objectives of the present study were to experimentally investigate the effects of out-time and cure cycle on tow impregnation and understand the relationship between material properties, processing phenomena and final part quality. The study considered two prepregs made from different fabric architectures and was divided into four parts. First, prepreg and neat resin were exposed to three different levels of out-time. Second, changes to the resin viscosity and prepreg microstructure were investigated by parallel plate rheometry and x-ray microtomography. Third, laminates were manufactured using four different cure cycles in an instrumented fixture capable of tracking the laminate thickness in-situ. Finally, the microstructural quality of the laminates was determined using optical microscopy. Overall, by linking the changes in material properties to those in consolidation behavior and final part quality, a comprehensive understanding of the effects of cure cycle and out-time was gained.

MATERIALS

The two OOA prepregs chosen for this study were manufactured by Cytec Engineered Materials from Cycom 5320 epoxy resin and two different carbon fabrics: T650-35 PW, a plain weave (PW) and T650-35 8HS, an eight harness satin (8HS). The fabric areal weights were 195 g/m^2 and 370 g/m^2 for the PW and 8HS, respectively, and it was previously shown that the 8HS tows are thicker and have a higher fibre volume fraction than those of the PW [6]. Both prepregs had 3k tows and a 36 % resin content, an out-life of 21 days and a baseline out-time of 4 days. The recommended cure cycles for the 5320 resin consisted of ramp rates from 0.56 °C/min (1 °F/min) to 2.77 °C/min (5 °F/min) and of dwell temperatures from 93 °C (200 °F) to 121 °C (250 °F).

EXPERIMENTAL PROCEDURES

Resin and prepreg aging

Neat resin and prepreg were stored in sealed plastic bags at ambient conditions (22 ± 2 °C, 22.5 ± 1.5 % RH) and brought to three different levels of out-time: 4 days, the baseline; 21 days, the manufacturer-specified out-life; and 28 days, an extreme level intended to potentially induce defects. Once aged, the materials were kept frozen until processing.

Cure cycles

The four cure cycles of interest to this study combine the lowest and highest recommended ramp rates (0.57 °C/min and 2.78 °C/min) and dwell temperatures (93 °C and 121 °C), preceded by a four hour (± 30 minute) room temperature vacuum hold.

Resin and prepreg characterization

The evolution of the resin viscosity was determined using a TA Instruments AR2000 rheometer in 25 mm parallel plate mode for the three out-times and four cure cycles, with the temperature profiles imposed so as to simulate the thermal history measured during laminate manufacture (as described below). Furthermore, for each prepreg and out-time, samples were scanned using previously described procedures to measure potential changes in impregnation due to room-temperature flow [1].

Laminate manufacture

Laminates were manufactured in the instrumented fixture shown in Fig. 1, which consists of a tool plate and a sensor support. A standard vacuum bag assembly was installed on the tool, over a set of pressure ports used to draw vacuum and measure the bag pressure (using a WIKA A-10 sensor). It consisted of a layer of fluorinated ethylene propylene (FEP) release film, the laminate, edge breathing dams consisting of sealant tape wrapped in fibreglass cloth, a second layer of FEP film, a layer of breather and the vacuum bag. Laminate temperatures were measured at the top and bottom interfaces using type K thermocouples. The sensor support held a Micro-Epsilon eddyNCT3300 / U6 non-contact eddy current displacement sensor directly over the laminate. The sensor detected the displacement of a 75 mm by 75 mm by 2 mm steel target placed on top of the laminate, above the top release film and below the breather. Vacuum was drawn continuously using a Busch vacuum pump, while heat was applied by placing the entire fixture in a Thermal Product Solutions Blue M convection oven. All data was acquired using a digital acquisition system. Laminates were manufactured from both prepregs, for all three levels of out-time and using all four cure cycles, for a total of twenty-four plates. All laminates measured 100 mm by 152 mm (4” by 6”); the layups were $[0°/90°]_{8s}$ for the PW and $[0°/90°]_{4s}$ for the 8HS, respectively.

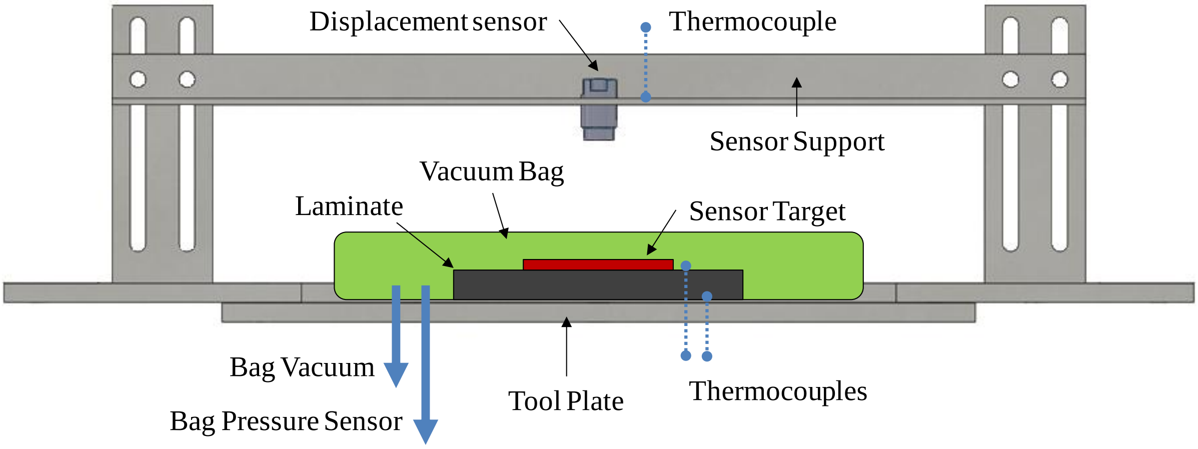

Figure 1: Laminate manufacture on instrumented tool.

Laminate microstructural analysis

After manufacture, laminate thicknesses were measured in six locations using a micrometer and averaged. Then, two samples approximately 50 mm long were sectioned from the area under the sensor's steel target, mounted, polished up to 1200 grit using a Buehler MetaServ2000 grinder/polisher and inspected using a Nikon Eclipse L150 microscope.

RESULTS AND DISCUSSION

Resin and prepreg characterization

The evolution of the resin viscosity was shown to change with out-time in two ways, as shown in Fig. 2 (a) for the 0.57 °C/min to 93 °C cycle. First, an increase in viscosity was seen at all points, shifting the curve upwards. Second, since high viscosities were reached more rapidly for higher out-times, the gel point was seen to shift to the left.

The microstructure of the unprocessed prepreg was analyzed by quantifying the average percent unsaturated area of 20 randomly chosen tows in the manner described in reference [1]. The results are shown in Fig. 2 (b). Within the measured variability of the material itself, these percent unsaturated areas showed no consistent trends. Hence, they suggest that there are no significant changes to the prepreg microstructure during extended out-time (such as tow impregnation due to capillary action). Interestingly, the results also show that the batch of PW material used for this study was more impregnated prior to processing than the 8HS (and than a different batch of the same PW prepreg previously investigated in [6]). This difference may be important as it reduced the flow length for full tow impregnation, regardless of out-time or cure cycle.

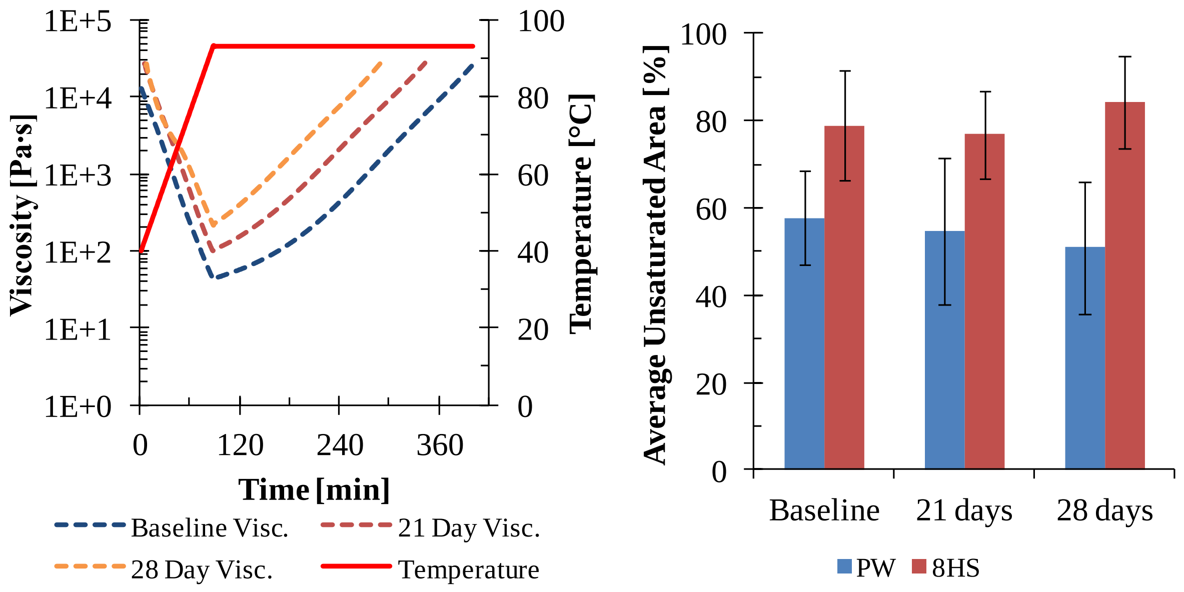

(a) (b)

Figure 2: (a) Resin viscosity versus out-time for the 0.57 °C/min to 93 °C cycle; (b) average percent unsaturated tow area versus out-time (with standard dev.).

Laminate manufacture

The prepreg plies were seen to become stiffer and warp with increasing out-time; the latter deformation was attributed to the polymerization of the outer resin layer and the unsymmetrical nature of PW and 8HS woven fabrics. Furthermore, both prepregs also lost the vast majority of their tack after 21 days, rendering laminate layup difficult.

The thermocouple and pressure sensor readings showed that all laminates were manufactured within the intended process parameter windows. No major thermal gradients occurred, with the largest instantaneous difference between top and bottom being approximately 3.3 °C. Similarly, the average recorded vacuum in the bag was below 40 mbar, for an average consolidation pressure of over 0.96 atm.

The data acquired from the in-situ displacement offered several insights into the consolidation phenomena that occurred during processing. Representative results are shown for the 0.57 °C/min to 93 °C cycle for the 8HS prepreg in Fig. 3. The laminate thickness curves were obtained by adding the displacement sensor data to the final thickness of each laminate, and were anchored on the time axis such that heating begins at the four hour mark.

The curves illustrate that the laminates changed thickness in two phases: first, once vacuum was drawn and the laminates underwent an initial compaction and second, once the temperature began to increase. Prior to vacuum application, the initial laminate thickness increased with out-time, a change attributed to the warp and lack of tack of the aged material. Furthermore, the thickness remained higher for aged samples during the room-temperature vacuum hold, likely due to the stiff consistency preventing ply adhesion and optimal nesting. During heated processing, a single decrease was observed in the thickness of the baseline laminates (beginning at time t = 4.75 h for the case shown in Fig. 3). This decrease, which is partly due to tow impregnation, occurred during the ramp, in agreement with results previously obtained by micro-CT, optical microscopy and modeling [1, 2, 6]. In contrast, for the aged laminates, a two-step change was observed. First, a comparatively rapid decrease occurred (at time t = 4.25 h in Fig. 3), bringing all three laminates to approximately the same thickness. It likely consisted of resin softening and further ply nesting, which did not fully occur at room temperature for higher out-times. Then, a second change began (at approximately t = 4.75 h in Fig. 3), likely denoting the onset of flow and tow impregnation. It may be noted that, with increasing out-time, this change occurred at a slower rate, over a longer period of time (more than an hour past the end of the ramp for the 28 day run in Fig. 3) and led to higher laminate thicknesses.

Similar curves were obtained for the remaining three cure cycles. The effect of out-time was clearly observed in all cases, with aged laminates showing the same changes relative to the baseline highlighted in Fig. 3. The thickness change curves also highlighted the effect of dwell temperature; laminates cured at 93 °C generally continued undergoing thickness changes during the dwell, past the minimum viscosity point, while those cured at 121 °C generally reached a stable thickness around the minimum viscosity point. The effect of ramp rate was more difficult to determine, with no clearly observable differences existing between 0.57 °C/min and 2.78 °C/min. Finally, the effect of material was noted in that, as expected due to the thicker, denser tows and the lower degree of initial impregnation, the flow time of the 8HS prepreg was between 15 and 35 minutes longer than that of the PW for the same cure cycle and out-time conditions.

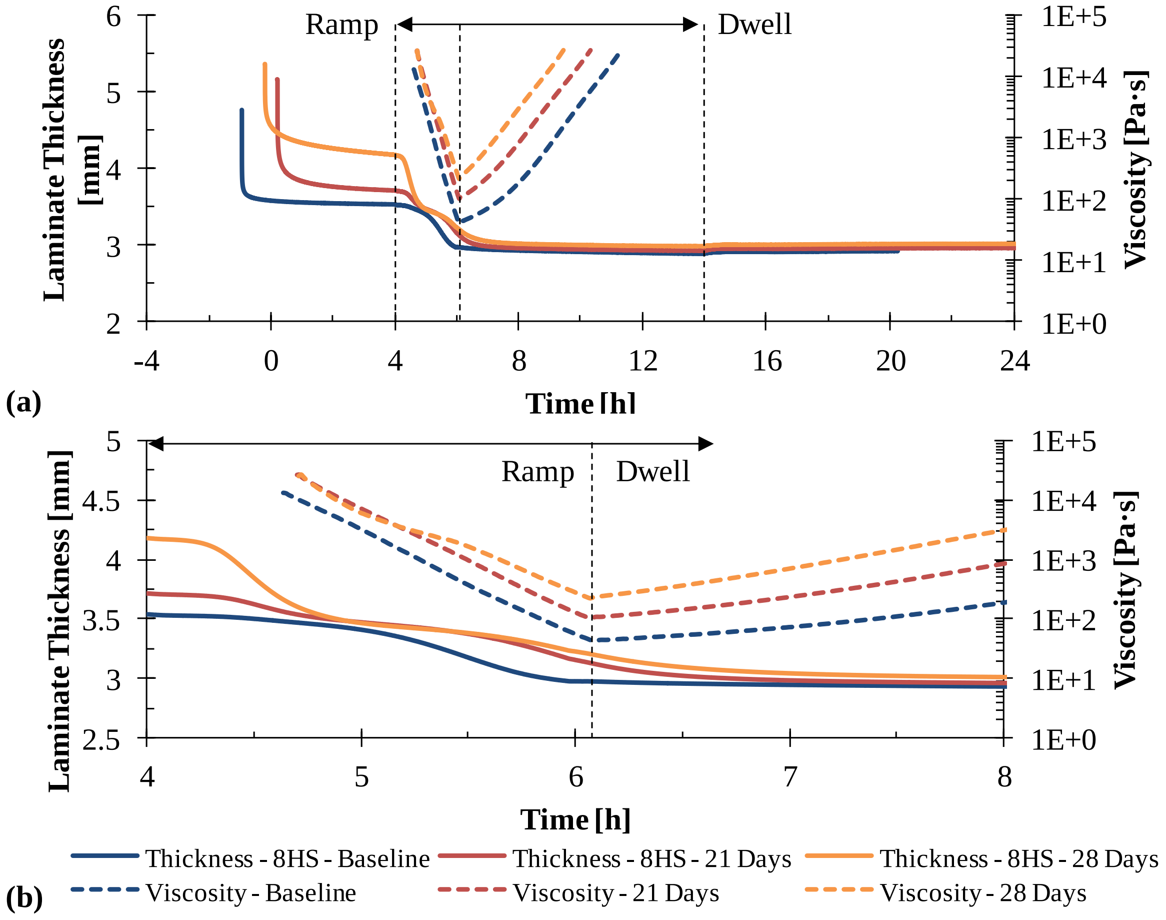

Figure 3: Laminate thickness evolution for different out-times, for the 8HS prepreg and the 0.57 °C/min to 93 °C cycle; (a) shows the entire cycle, (b) focuses on the flow period.

These results suggest that, as expected, the higher resin viscosities brought on by out-time led to a decrease in the rate of tow infiltration, and in some cases extended the flow past the minimum viscosity point and into the dwell. The dwell period was shown to involve an increase in resin viscosity due to polymerization (Fig. 2 (a)), which is likely to have further slowed down tow impregnation and, in extremis, even stopped it from completing.

Laminate microstructural analysis

The laminate thickness results are presented in Fig. 4. For all cases but one (2.78 °C/min to 121 °C), an increase in thickness, and hence a decrease in consolidation quality, was observed with increasing out-time; this may be due to reduced nesting, decreased fibre bed compaction and higher porosity. The effects of cure cycle were also visible. As shown in Fig. 4 (b) for the 8HS, higher ramp rates and dwells were shown to consistently lead to lower thickness values, and therefore better consolidation for a given out-time; this trend may be explained by the increased capacity for resin flow and fibre bed mobility offered by lower resin viscosities. These trends remained visible for the most part in the PW results shown in Fig. 4 (a), with the same exception of unexplained high thicknesses for the 2.78 °C/min to 121 °C cycle. Finally, Fig. 5 shows the effect of out-time and cure cycle on tow impregnation, expressed as a weighted average of unsaturated (dry) tow area in non-porous and 20 porous tows. Tow micro-porosity was found to be strongly associated to out-time, increasing from none at 4 days

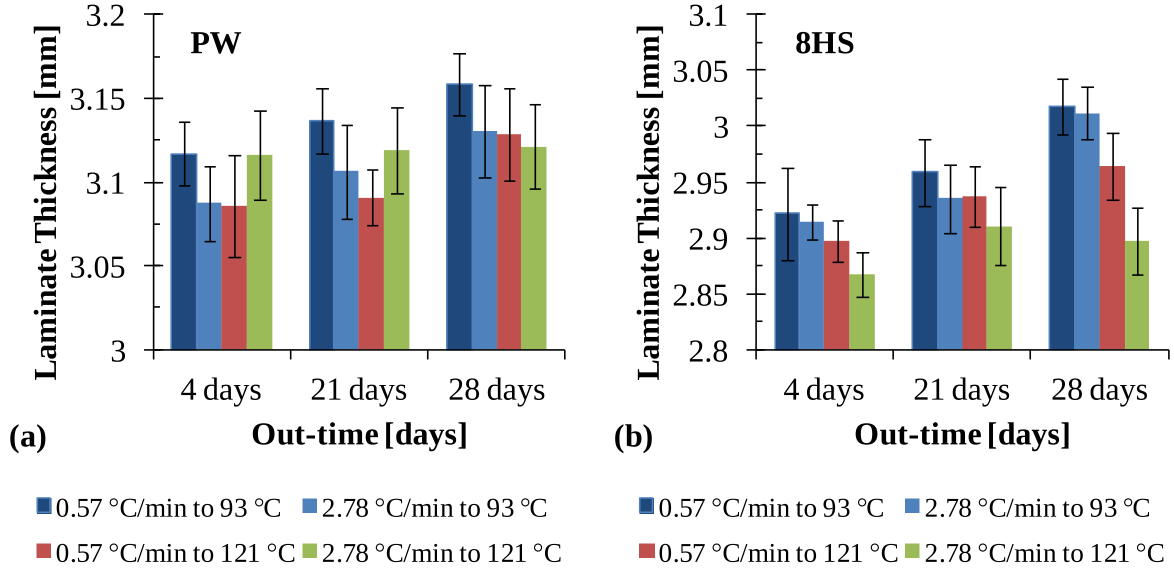

Figure 4: Laminate thickness versus out-time and cure cycle for (a) PW and (b) 8HS.

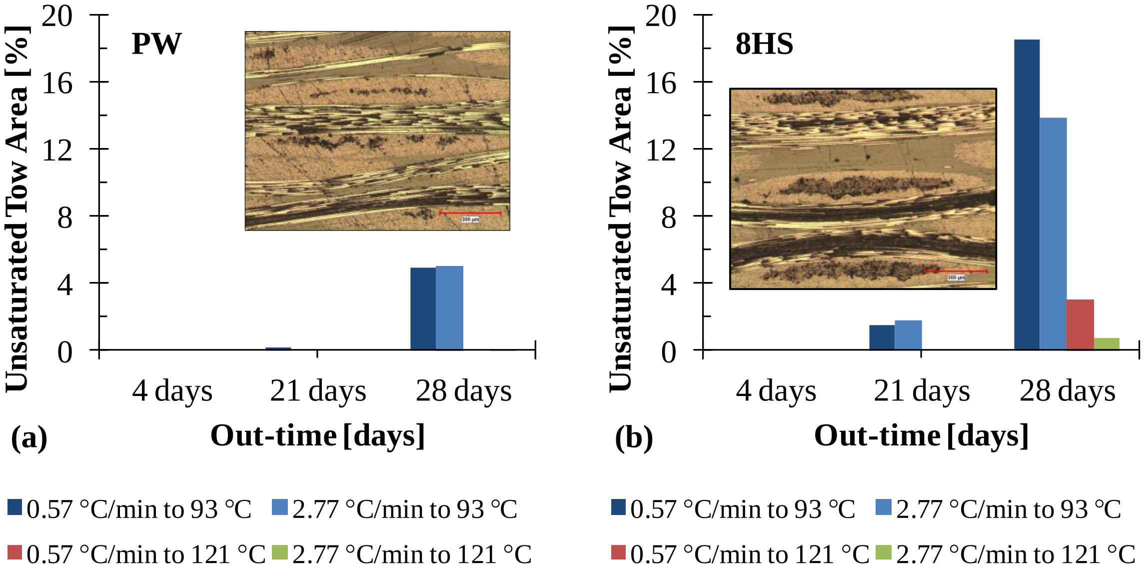

Figure 5: Average percent unsaturated tow areas for versus out-time and cure cycle for (a) PW and (b) 8HS. Insets: representative micrographs for the 28 day laminates cured using the 0.57 °C/min to 93 °C.

to close to 20 % (in some conditions) at 28 days. It also occurred predominantly in laminates cured at the lower (93 °C) dwell temperature; the higher (121 °C) dwell was conversely found to reduce or even eliminate porosity, even for the 28 day out-time, which exceeds the material's specified out-life. The effect of ramp rate was again found to be mixed, with higher ramp rates benefitting the 28 day 8HS laminates but not others. Finally, the influence of fabric architecture was found to be critical, with the 8HS and its less-impregnated, thicker and fibre-denser tows being much more prone to micro-porosity than the comparatively thinner, more permeable and initially more impregnated PW. These results highlight that the partially impregnated nature of OOA prepregs, coupled with high resin viscosities (and hence with low temperatures and extended out-times) may lead to significant and pervasive micro-porosity within cured parts, but that judicious cure cycle selection may control these defects.

CONCLUSIONS

The present study considered the effects of out-time and cure cycle on consolidation by examining changes to material properties, processing phenomena and final part quality. The results showed that out-time is associated with an increase in resin viscosity, a slower rate of laminate thickness change (and therefore of impregnation flow) and, under certain conditions, a significant decrease in laminate quality in terms of thickness and tow micro-porosity due to incomplete impregnation. They also show the significant effects of cure cycle: generally speaking, cycles with higher dwell temperatures and faster ramp rates were shown to lead to faster flow during processing, better consolidation (in terms of thickness) in most conditions and lower defect levels in the final parts at high out-times. Finally, the fibre bed properties were shown to have a critical impact on final part quality, with the lower fibre volume fraction and more impregnated PW prepreg shown to impregnate faster and be less prone to porosity than the comparatively fibre-denser and less impregnated 8HS.

ACKNOWLEDGEMENTS: The authors would like to acknowledge the support of the Natural Science and Engineering Research Council of Canada; the Consortium for Research and Innovation in Aerospace in Quebec; Bell Helicopter Textron; Bombardier Aerospace; Delastek; the National Research Council of Canada; the Center for Development of Composites in Quebec and McGill University, Concordia University and the University of British Columbia.

REFERENCES

1. Centea, T and Hubert, P (2011), ‘Measuring the impregnation of an out-of-autoclave prepreg by micro-CT’, *Composites Science and Technology*, 71(5), 593-599.
2. Fahrang, L and Fernlund, G (2011), ‘Void evolution and gas transport during cure in out-of-autoclave prepreg laminates’, *Proc. of SAMPE 2011*,CD-ROM.
3. Kratz, J, Hsiao, K, Fernlund, G and Hubert, P (2012), ‘Thermal models for MTM45-1 and Cycom 5320 out-of-autoclave prepreg resins’, *Journal of Composite Materials*, doi: 10.1177/0021998312440131.
4. Grunenfelder, LK and Nutt, SR (2012), ‘Prepreg age monitoring via differential scanning calorimetry’, *Journal of Reinforced Plastics and Composites*, 31(5), 295-302.
5. Grunenfelder, LK and Nutt, SR (2011), ‘Out Time Effects on VBO Prepreg and Laminate Properties’, *Proc. of SAMPE 2011*, CD-ROM.
6. Centea, T and Hubert, P (2011), ‘The Effect of Material and Process Parameters on Tow Impregnation and Micro-Void Formation in Out-of-Autoclave Prepregs’, *Proceedings of The 26th Annual Technical Conference of the American Society for Composites / The 2nd Joint US-Canada Conference on Composites*, CD-ROM.

INJECTION OF A COMPLEX PREFORM BY RTM. OPTIMISATION OF A MOULD DESIGN AND PROCESS PARAMETERS

R.AGOGUE[1,5], P.OUAGNE[1], D.SOULAT[4], C.H.PARK[2], J.BREARD[2], D. ZANELLI[3]

[1] *University of Orleans – Institut PRISME – France – pierre.ouagne@univ-orleans.fr- -*
[2] *University of Le Havre - Laboratoire Ondes et Milieux Complexes (LOMC) - France -– chung-hae.park@univ-lehavre.fr – joel.breard@univ-lehavre.fr*
[3]*Roxel Company – Direction Technique et Industrialisation– France – d.ZANELLI@roxelgroup.com*
[4] *ENSAIT – Gemtex -* damien.soulat@*ensait*.fr
[5] *ONERA - romain.agogue@onera.fr*

ABSTRACT: This work concerns the manufacturing of a composite tube using RTM process. During the preforming stage, a woven braid is laid down and stacked on a mandrel so that reinforcement plies form conical shapes with a defined angle. An innovative experimental preforming procedure has been developed to respect the specific angle. The resin injection step has been studied both experimentally and numerically. In this work a focus is applied on the optimization of the mould geometry and on the way the resin is injected within the preform to prevent the appearance of defects such as displacement of plies and porosity. Different optimization steps are described in this work and a mould geometry is proposed for this specific application and the quality of the part obtained is discussed and analysed.

KEYWORDS: Complex preform, RTM, Process parameters, Simulation, Braid permeability.

INTRODUCTION

This work concerns the manufacturing of a composite tube with 3D braided reinforcement by the RTM process. Specifically the influence of the preforming stage of the process on the resin injection is studied. Three-dimensional braided preforms were recognized as the most promising materials because of their low delamination tendency. Furthermore, the near-net-shape manufacturing, out-of-plane stiffness, strength, impact tolerance and ablation resistance recommend these materials [1]. Because braiding has the potential to produce complex shapes with fibre continuity at the edges and around holes and branches [2], braided structures are also used in several other applications, such as medical, automotive or sport equipment [3]. Classically, fibres are braided directly on a cylindrical mandrel with a conventional braiding machine. This process is an ancient technique, but as it could be automated, it is suitable for manufacturing reproducible preform for RTM process. The prediction of the fibre position along the mandrel as a function of the process parameters remains difficult. Consequently a lot of studies [4-6] concern the development of models which compute the characteristics of braided preforms. These characteristics could be the braid angle, the yarn volume fraction, the covering factor and finally the influence of these parameters on the permeability of the braid [7-8].

In this work application, each ply of fibre must have a specific orientation with the axis mandrel. As a consequence, a conventional braiding machine cannot be used. From specific 3D carbon braided reinforcement, an innovative experimental preforming procedure has been developed [9].

Three main properties have to be respected on the final composite part. First, the angle between plies of braid reinforcement and the tube axis must be equal to a specific value. Secondly, the preform has to present an important fibre volume ratio with a homogeneous distribution along and in the part. Thirdly, the level of macro porosity should not exceed the defined value to meet aerospace specifications (2% is a classical value).

From the 3D-braided reinforcement the experimental procedure consists in realizing one preform constituted by several plies [9]. Each ply must have a specific angle, (denoted α on figure 1.a) with the mandrel axis, and the preform must have a specific diameter given by the closed mould for the resin injection step. To realize this preform, a cylindrical mandrel with a conical base (figure1.a) is used. The braid length depending on the expected fibre volume fraction can be estimated and weighted. The braid is first slipped into the cylindrical mandrel and tied between two threads on a length which will define the ply. The first ply, with the expected orientation, is obtained by folding up the braid on the conical base of the mandrel. By using the same principle, the others plies can be superimposed on each other. A preform (figure1.b) contains approximately 120 plies, for 200g of carbon braided reinforcement.

In a second step the mould is closed and placed on the preform so that the resin can be injected (figure 1.c) under pressure or flow rate conditions, with a specific device developed at Orleans [10]. The outside flow front evolution can be measured as well as the time required to fill the mould.

This paper proposes to analyse the steps that led to the optimisation of the mould and particularly to the way the resin is injected in the preform in conjunction to the required quality of the part.

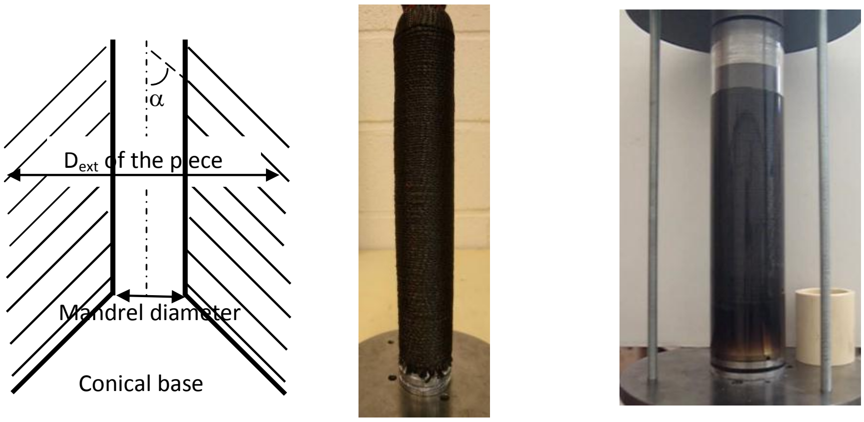

Fig. 1 (a) Scheme of the preform; (b) Final preform; (c) Resin evolution

Optimisation of the mould design and injection conditions

As mentioned in the previous section, the ply angles as well as a fibre volume fraction along the length of the tube should be homogeneous. The level of macro porosity should also be kept to a minimum value (below 2% for this application).

If the ply angle globally remains constant and will not be discussed here, figure 2 shows that the fibre volume fraction estimated from density measurements is not constant in a part injected with a pressure of 2 bars. In the first third of the part (from the bottom where the injection takes place), the fibre volume fraction is higher than what was expected. A difference of about 10 % is measured. In the second third of the part, (middle of the part), the fibre volume fraction decreases to reach values lower than what was expected. A difference of about 10% is also observed.

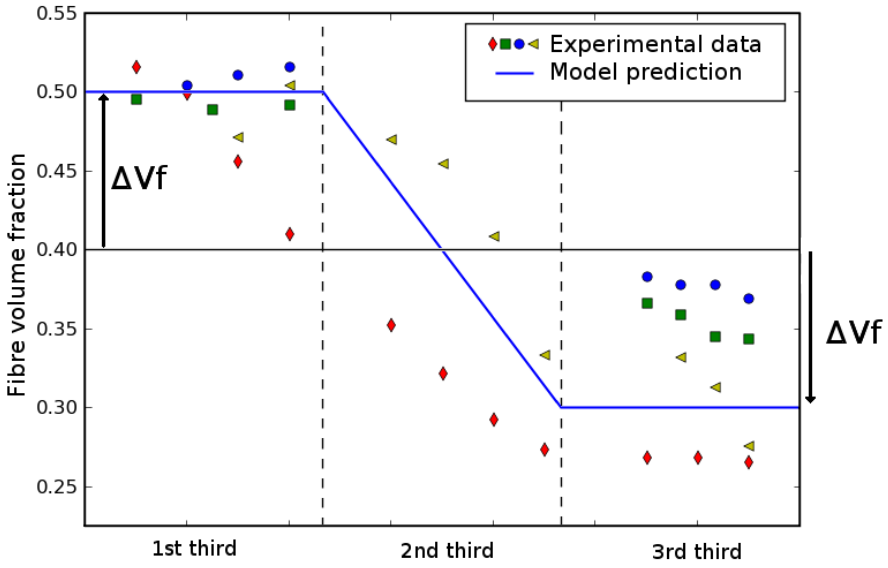

Figure 2: Fibre volume fraction as a function of the tube length

To explain this phenomenon, several hypothesis may be formulated. A first one consists in considering that the preforming was not homogeneous. A second one consists in considering that the injection phase changed the fibre volume fraction homogeneity. Some displacement and compaction of the plies in the first third of the part may have taken place.

As the preform is realized following a rigorous procedure, it is expected that compaction of the bottom plies of the preform took place. To confirm this hypothesis, some paint dots were applied at the extremity of chosen plies, and the movement of these ones was recorded using a video camera. Figure 3 shows that the bottom plies of the preforms do not remain in their initial position. It also shows that the distance between the dots becomes closer.

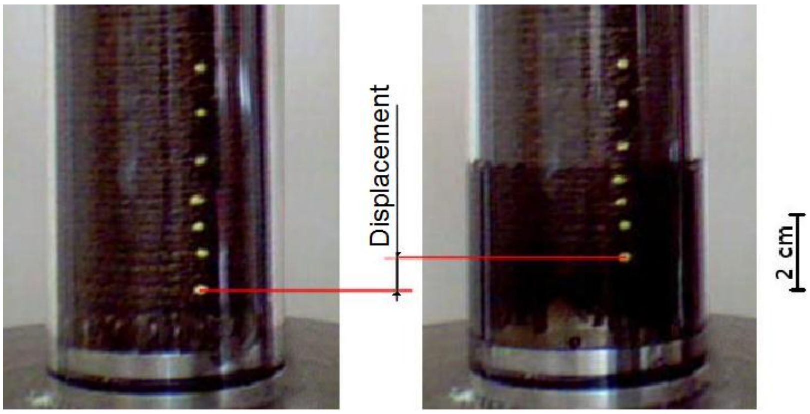

Figure 3: Influence of the fluid injection on the position of the bottom plies of the preform

The displacement of different marks, positioned along the tube axis, were recorded and reported in figure 4.

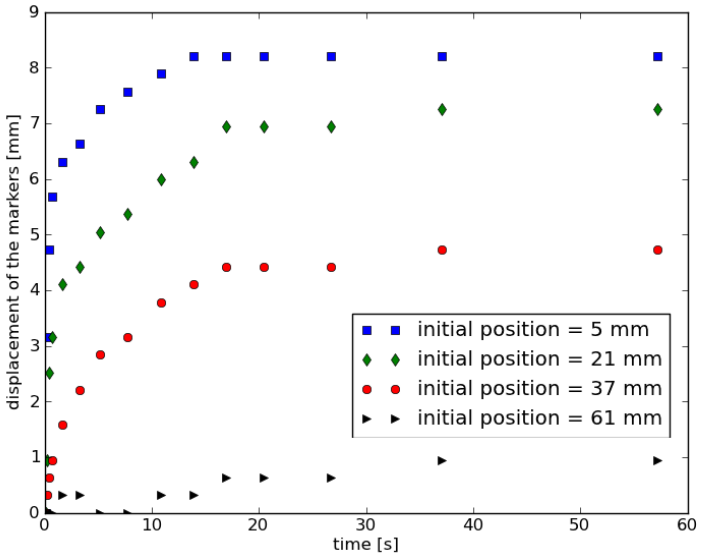

Figure 4: Displacement of the markers as a function of time during the injection

Figure 4 indicates that the displacement of the markers is more pronounced for the ones initially positioned closer to the injection gate. As an example the mark initially positioned 5 mm above the injection gate was submitted to a displacement of about 8 mm, whereas the mark positioned 61 mm above the gate was submitted to displacement lower than 1 mm.

The displacement of the ply and the non uniform fibre volume fraction cannot be accepted. For this reason, a porosity analysis of the part is not presented here as the part cannot be accepted in this state. However, the level of porosity is difficult to control on such a long part as the speed of resin is not constant and not necessarily within a processing window within which the porosity would be minimum. Indeed, different authors used the modified capillary number to define a processing window within which the macro and the micro porosity should not take place [11-14].

The capillary number is defined as follows:

$$Ca = \frac{\mu . v}{\gamma} \tag{1}$$

Where μ is the viscosity of the resin [Pa.s], v is a characteristic velocity of the resin flow [m/s], γ is the interfacial tension between the air and the resin [N.m^{-1}]. These studies [12-14] indicate that below a value of the capillary number of 0.0035 capillary flow dominates and macroporosities are expected to take place. Above a value of 0.0035, flow in macro pores dominates, and microporosity is expected to take place. A processing window between 0.0035 and 0.035 is generally defined.

Simulations carried out using a FEM code for RTM analysis [15] were used to define the capillary number processing window. Results are presented in figure 5. Figure 5 shows that the modified capillary number approach suggests that injection pressure should be raised above values of 30 bars. This cannot be considered as ply displacement (due to hydromechanical coupling [16]) already takes place for low injection pressure of 2 bars.

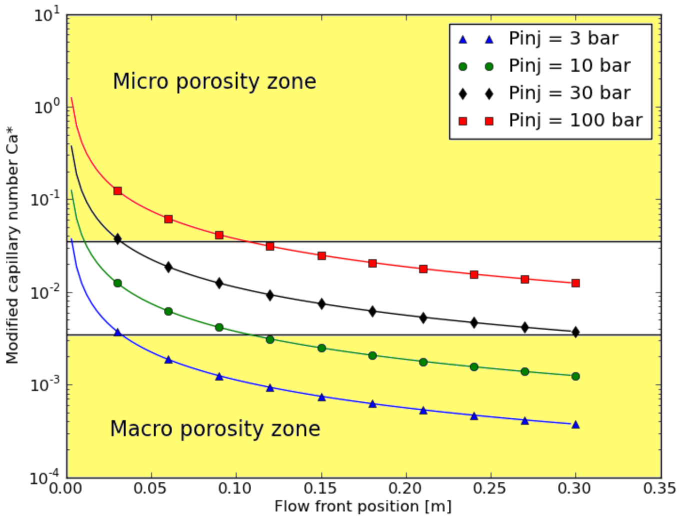

Figure 5: Simulation of the processing window based on the modified capillary number for the original injection mould

Solutions to prevent the displacement of the plies due to the injection of resin have been considered. The first one consists in allowing the resin to flow in a preferential channel along the preform as presented in Figure 6. In this case, the plies are held together by a gridded mesh.

This solution was tested and showed good results concerning the displacement of the plies. In this case, no displacement of the plies was observed. However, due to the space left between the preform and the mould, the preform thickness does not remain constant after the injection step as shown in Figure 7.

Figure 7 also indicates that macroscopic porosity takes place on the inside of the tube. This is not a problem as this part of the tube needs to be machined in any case to get rid of the yarns used to realize the preform. On the rest of the part, this global view does not indicate the presence of large macro pores, suggesting that the radial mode of injection with resin travelling shorter distances is promising.

An evolution of the concept is presented in Figure 8. It still consists in a radial injection. However, this time, the mould is fitted to the preform size and four small channels are machined in the inside part of the external shells in order to get radial injection.

Coupled to this mould design, an analysis based on the modified capillary number has been carried to optimise the injection pressure that should be applied.

Figure 9 shows that low pressure of about 1 bar or less should be applied to enter the processing window. This injection pressure was tested and a global view of the tube cross section does not show the presence of macroporosity in the useful zone (Figure 10). The large holes on the inside part of the tube are due to the yarn used to maintain the plies during the preforming. As this part is machined, this porosity is not considered as a problem for this application and the design of the mould can be considered as optimized for this particular application.

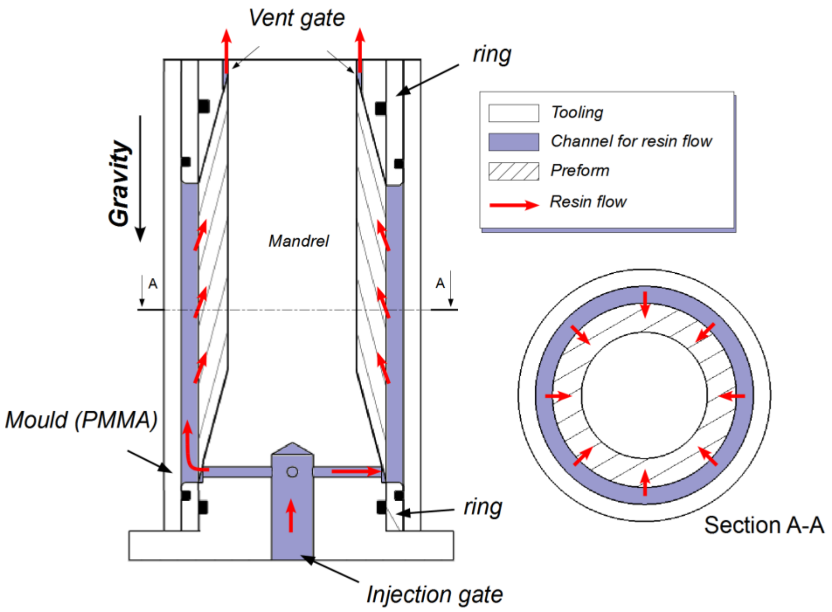

Figure 6: Radial injection mould

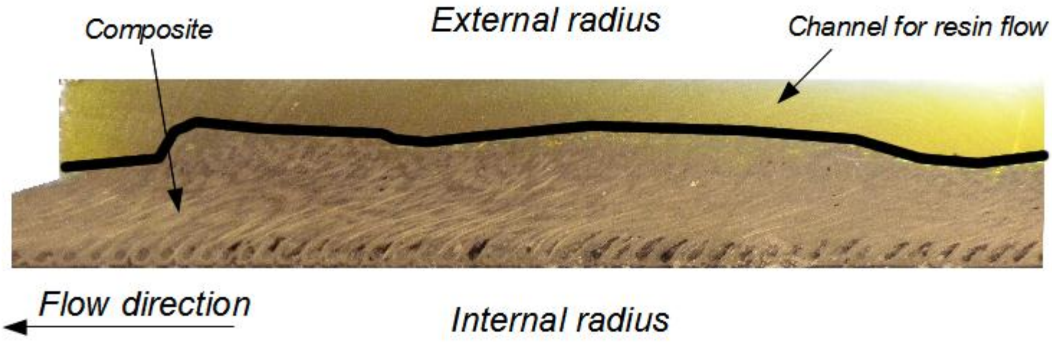

Figure 7: Longitudinal cross section of a tube manufactured by radial injection moulding

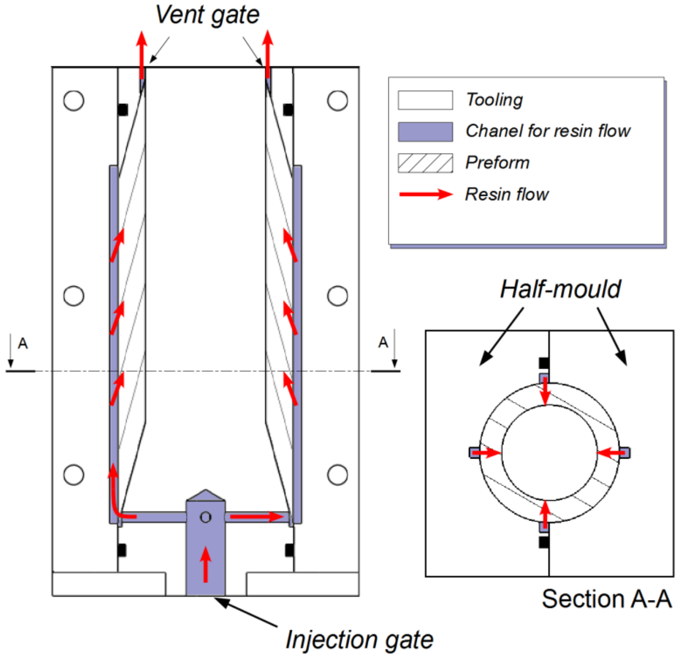

Figure 8: Radial injection mould with four preferential channels

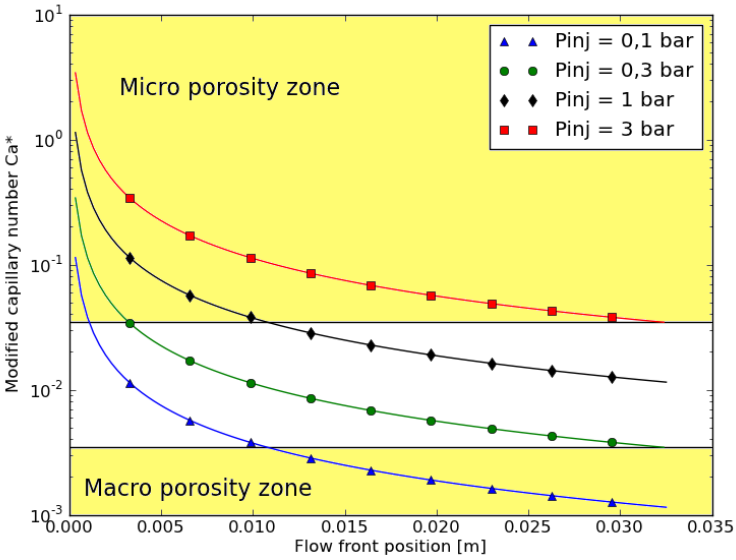

Figure 9: Simulation of the processing window based on the modified capillary number for the preferential four channel design mould

Figure 10: Cross section of a tube manufactured by radial injection moulding (4 preferential channel mould)

CONCLUSIONS

This work concerns the manufacturing of a composite tube from a 3D particular preform arrangement using RTM process. During the preforming step of the RTM process, a woven ribbon is laid down and stacked on a mandrel so that reinforcement plies form conical shapes with a defined angle. Preforming cannot be performed by using a classical braiding machine because of the specific and predefined orientation of the plies. Consequently, an innovative experimental preforming procedure has been developed. To avoid displacement of the plies, macro or micro void defects, the resin injection step requires to be optimized. Numerical and experimental approaches were used to optimise the design of a mould and the associated process parameters. The influence of the mould design, as well as the processing parameters such as the injection pressure or the imposed flow rate upon the number, the position and the size of possible defects have been evaluated.

ACKNOWLEDGMENTS

This work has been carried out in the scope the project LCM3M (ANR, French National Research Agency) and has been supported by ROXEL company.

REFERENCES

[1] D.S Li, J.L Li, L. Chen, Z.X Lu, D.N. Fang. Finite Element Analysis of Mechanical Properties of 3DFour-Directional Rectangular Braided Composites. Part 1: Microgeometry and 3D Finite Element Model Appl Compos Mater (2010) 17:373–387. DOI 10.1007/s10443-010-9126-2

[2] P. Potluri, A. Manan, M. Francke, R.J. Day. “Flexural and torsional behaviour of biaxial and triaxial braided composite structures”. *Composite Structures*, Vol. 75 pp. 377–386, 2006

[3] A.P. Mouritz, M.K. Bannister, P.J. Falzon, K.H. Leong. “Review of applications for advanced three-dimensional fibre textile Composites”. *Composites Part A*, Vol.30 pp. 1445–1461, 1999.

[4] L. Chen, X.M. Tao, C.L. Choy. “On the microstructure of three-dimensional braided preforms”. *Composites Science and Technology*, Vol. 59, pp.391-404, 1999.

[5] P. Potluri, A. Rawal, M. Rivaldi, I. Porat. “Geometrical modelling and control of a triaxial braiding machine for producing 3D preforms ». *Composites Part A*, Vol. 34 pp. 481-492, 2003.

[6] Y. Gao, J. Li. Effects of braiding angle on modal experimental analysis of three-dimensional and five-directional braided composites. Composites: Part B (2011), doi:10.1016/j.compositesb.2011.11.025

[7] A.C. Long. “Process modelling for liquid moulding of braided preforms”. *Composites Part A*, Vol. 32 pp. 941-953, 2001.

[8] X. Wu, J. Li, R.A. Shenoi.”Measurement of braided preform permeability”. *Composites Science and Technology*. Vol. 66, pp.3064–3069, 2006.

[9] D.SOULAT, G.HIVET, R.AGOGUE, A. TELMAR. “Fabrication of a Complex Preform by RTM Processes Parameters and Quality of the Part”. 14th International ESAFORM Conference on Material Forming. Queen’s University of Belfast. 27-29 April 2011. AIP Conference Proceedings Volume 1353, pp. 936-941.

[10] P.OUAGNE, D.SOULAT, R.AGOGUE, C.H. PARK, L. BIZET, J. BREARD, D.ZANELLI. ”Injection of a Complex Preform by RTM. Process Parameters and Quality of the Part.”. 10th International Conference on Flow Processes in Composite Material (FPCM 10), 11-15 Juillet 2010, Ascona (Suisse).

[11] Doh Hoon Lee, Woo Il Lee, and Moon Koo Kang. Analysis and minimization of void formation during resin transfer molding process. Composites Science and Technology, 66(16) :3281 – 3289, 2006.

[12] V. Rohatgi, N. Patel, and L. James Lee. Experimental investigation of flow induced microvoids during impregnation of unidirectional stitched fiberglass mat. Polymer omposites, 17(2) :161–170, 1996.

[13] Youssef K. Hamidi, Levent Aktas, and M. Cengiz Altan. Three-dimensional features of void morphology in resin transfer molded composites. Composites Science and Technology, 65(7-8) :1306 – 1320, 2005.

[14] Moon Koo Kang,Woo Il Lee, and H. Thomas Hahn. Formation of microvoids during resin-transfer molding process. Composites Science and Technology, 60(12- 13) :2427 – 2434, 2000.

[15] C.H. Park, A. Lebel, A. Saouab, J. Bréard, W.I. Lee, “Modeling and simulation of voids and saturation in liquid composite molding processes,” Composites Part A: Applied Science and Manufacturing, Vol. 42 (6), pp. 658-668, 2011.

[16] Ouagne P, Bréard J, Ouahbi T, Saouab A, and Park C-H. Hydro-Mechanical Loading and Compressibility of Fibrous Media for Resin Infusion Processes. *International Journal of Materials Forming* 3 (2010); 1287- 1294.

IN-MOULD GEL-COATING FOR RTM AND RIFT

John Summmerscales

Advanced Composites Manufacturing Centre, School of Marine Science and Engineering,
Reynolds Building, Plymouth University, Plymouth, PL4 8AA, England.
Corresponding author's e-mail: jsummerscales@plymouth.ac.uk

ABSTRACT: Styrene vapours from unsaturated polyester resin may affect worker health and comfort, can produce an odour nuisance for neighbours and may incur environmental burdens. In composite component manufacture, the adoption of closed mould processes (*e.g.* liquid composite moulding techniques including RTM and RIFT) significantly reduces styrene emissions. Gel-coats are applied to component surfaces for cosmetic reasons and/or to enhance durability or surface function. However, the coating is normally applied to the open mould and allowed to progress to the gel state over time while styrene vapours are released to the atmosphere. A novel concept for the in-mould gel-coating (IMGC) of fibre-reinforced polymer composites has been patented. Initial RTM studies were conducted with UK TSB "Meeting the Challenge of the Zero Emission Enterprise" funding and reported at FPCM-10. A postgraduate project demonstrated that the concept was viable in resin infusion under flexible tooling (RIFT, SCRIMP^{TM}, VARTM) processes. The on-going development of IMGC is continuing in the Framework Programme 7 funded InGeCt research project (FP7_R4SME_286520_InGeCt).

KEYWORDS: *Gel-coat, Resin Infusion under Flexible Tooling, Resin Transfer Moulding, RIFT, RTM, SCRIMP^{TM}, Styrene, Surface Quality, VARTM.*

INTRODUCTION

In many applications of fibre-reinforced polymer matrix composites, a separate surface finish (gel-coat) is required for cosmetic/aesthetic and/or durability/protection reasons. Traditionally the coating is painted or sprayed onto the open mould and partially cured before the structural laminate is moulded. The majority of structural laminates and gel-coats have an unsaturated polyester resin matrix. Exposed resin surfaces release styrene (a volatile organic compound which acts as a reactive diluent) vapour leading to an unpleasant working environment. In open moulding, up to ~25% of the styrene may be released during possessing.

Styrene has been the subject of extensive debate in respect of health and environmental issues. Styrene emissions can cause irritation and neurological effects. In the United States, the Department of Health and Human Services 12th Report on Carcinogens [1] listed styrene as "reasonably anticipated to be a human carcinogen". The European Commission Directive 1999/13/EC [2] aims "to prevent or reduce the direct and indirect effects of emissions of volatile organic compounds (VOC) on the environment and human health, by setting emission limits for such compounds and laying down operating conditions for installations using organic solvents". The Styrene Producers Association [3] "actively supports best standards for its workforce and also encourages all users of styrene to respect the national limits of their countries. Moreover, Styrene producers recommend the whole value chain to implement 20ppm (8hr TWA - time-weighted average) occupational exposure limit (OEL) in the European Union to ensure a safe environment for workers". This industry voluntary code is likely to be used as the basis for harmonisation of Occupational Exposure Levels (OELs) across the European Union (EU) at some time in the near future (Table 1).

Table 1: Styrene odour and time weighted average occupational exposure levels (OEL)

Condition	Level (ppm)	Reference
Odour threshold	0.08 - 0.32	9, 10
OEL for new build facilities in Sweden	10	11
Styrene Producers Association recommendation	20	3
Current UK voluntary code/legal OEL	50/100	12, 13
NIOSH (National Institute for Occupational Safety and Health) IDLH (Immediately Dangerous to Life or Health) level	700	14
Geometric mean for 15 minutes for workers with air purifying respirators inside a wind turbine blade during glue wipe task	970	15
Explosive limits in air	9000-68000	16

Styrene has potential environmental impacts with a photochemical oxidant creation potential (POCP) of 0.142 kg (relative to ethene at 1kg) [4]. The odour is perceived both by the workforce and beyond the factory boundary and the chemical may influence the behavior of wild animals [5-8].

The adoption of closed mould technologies for the production of composite parts has significantly reduced styrene emissions during manufacture. Current IMGC systems rely on controlled mould opening to create a gel-coat cavity after partial laminate resin cure. This increases the complexity of the tooling and limits the geometry of moulded parts to those having low moulding angles. In practice, gel-coating must still be undertaken under open-mould conditions as no viable in-mould gel-coating technology is commercially available.

This paper discusses a new development in in-mould gel-coating.

TSB ZEE IMGC PROJECT FOR IMGC FOR RTM [17-19]

The In-Mould Gel-Coating (IMGC) for polymer composites project was funded by the UK Technology Strategy Board under the Technology Programme for Collaborative R&D call Meeting the Challenge of the Zero Emission Enterprise (ZEE). Project management was by Pera International with Baltex, British Marine Federation, Magnum Venus Plastech (MVP), Performance Sailcraft Europe and Scott Bader Company Limited as partners. The project aimed to help the UK composites industry to remain competitive, to improved workplace conditions, to reduce environmental impact and hence to be prepared for future legislation regarding styrene emissions.

A novel method of applying the coating in a closed mould was developed [20] using a separation layer to keep apart the resin in the laminate and in the gel-coat (Fig. 1). This should eliminate virtually all styrene emissions to atmosphere. Successful development of this technology would be applicable to current resin transfer moulding operations with minimal capital outlay and would assist and encourage moulders currently using open mould manufacturing methods to move to closed mould resin transfer moulding methods. The studies indicated that this method would replace the current labour intensive process with one requiring minimal labour thereby providing significant economic incentives. The innovation should thus improve the ability of the industry to compete.

A flat panel mould was used at Plymouth to trial different spacer fabrics, gel-coats and other process variables using RTM and RTM-light processes. The panels were then subjected to surface finish analysis (Fig. 2) for coverage, thickness and quality and interface bond strength testing. A dome mould was used at MVP to assess this technology on curved components. The technology was successfully demonstrated, but there remains a need for cost-engineering of the separator fabric.

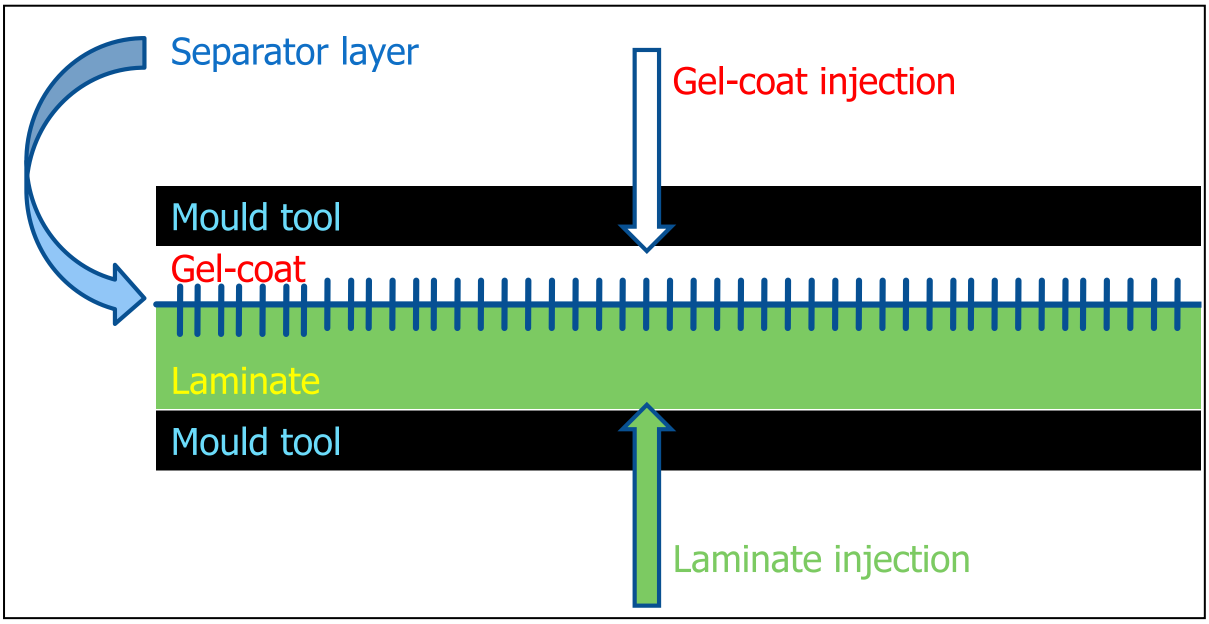

Fig. 1: Schematic of the IMGC InGeCt process

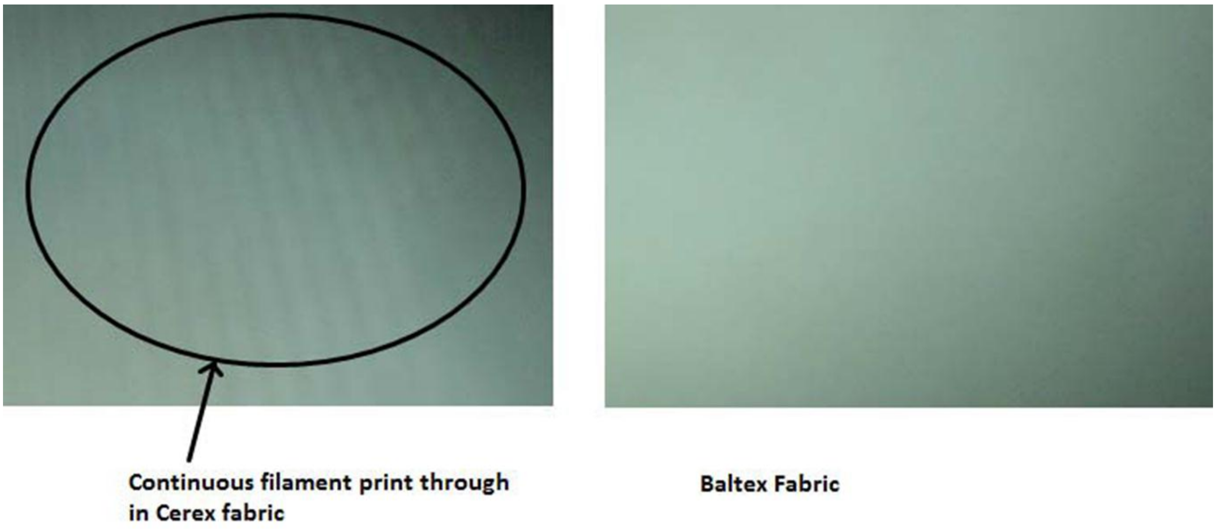

Fig. 2: comparison of surface finish for two different separator fabrics

POSTGRADUATE PROJECT ON IMGC FOR RIFT [21-22]

Muralidharan studied the IMGC process in the context of resin infusion under flexible tooling (RIFT [23, 24], a.k.a. SCRIMP or VARTM). The key variables were the spacer fabric, the number of layers in the laminate, the gel-coat and the resin injection strategy. While RIFT at a set vacuum level would be expected to perform more consistently than RTM, it was found that increasing the number of layers of reinforcement in the laminate reduced the gel-coat coverage and the gel-coat thickness. Injecting the gel-coat then the laminate resulted in better coverage than injecting the laminate before the gel-coat. Reduction of the gel-coat viscosity gave better surface coverage. The laminate resin and gel-coat feed pipes should not be located on the same edge of the laminate unless measures are taken to avoid constricting flow from the outer pipe due to compression of the flow medium/transport mesh by the inner pipe.

FRAMEWORK PROGRAMME 7 RESEARCH FOR SMEs InGeCt PROJECT

InGeCt (an **In**novative environmentally friendly **Ge**l **C**oa**t**ing technology for composites: www.ingect.eu) is a €1.4M project funded by the EU Framework Programme 7 (FP7) initiative to encourage Research for Small and Medium sized Enterprises (SME). The project partners are Advanced Composites Manufacturing Centre (England), Alan Harper Composites (England), Centro Tessile Cotoniero E Abbigliamento SpA (Italy), De IJssel Coatings BV (Netherlands), KMT Nord APS (Denmark), Lightweight Structures BV (Netherlands), Tessitura Valdolona SRL (Italy) and YKI Ytkemiska Institutet AB (Sweden). The main aim is to develop an innovative environmentally friendly gel-coating technology for composites for marine and wind-turbine applications to reduce VOC emissions, processing time and cost.

The project is further developing the in-mould gel-coating process to produce a low capital expenditure process requiring minimal equipment modification based on the innovative application of low-viscosity gel-coats and a separator/spacer fabric. The proof-of-concept work undertaken to date shows that this technology has the potential to achieve significant benefits beyond the current state-of-the-art to produce components that are fit for purpose whilst reducing styrene emissions to below 5ppm.

The overall aim of the InGeCt project is to develop technical textiles and gel-coat formulations in combination with process design and optimisation that will enable significant reductions in VOC emissions whilst reducing production times and manufacturing cost. The technology will therefore be very attractive to composites processors, giving significant economic and societal benefits to manufacturers and consumers. The technology will make a significant contribution to reducing VOC emissions and enable EU SMEs to meet their current and forthcoming legislative requirements.

QUANTIFICATION OF SURFACE FINISH [25]

A novel procedure has been developed for the assessment of the surface finish of in-mould gel-coated fibre-reinforced polymer matrix composites. The technique involves photographing the reflection from a coated surface on an opaque screen and analysing the image using fractal dimensions (FD – Fig. 3). The ranking of the quality of surface finish from this technique sensibly aligns with that obtained by human observation and by the commercial Wavescan DOI system [26]. The investment required for the new FD system is primarily that required for a high-resolution digital camera, and hence is less than 5% of the cost of the commercial instrument.

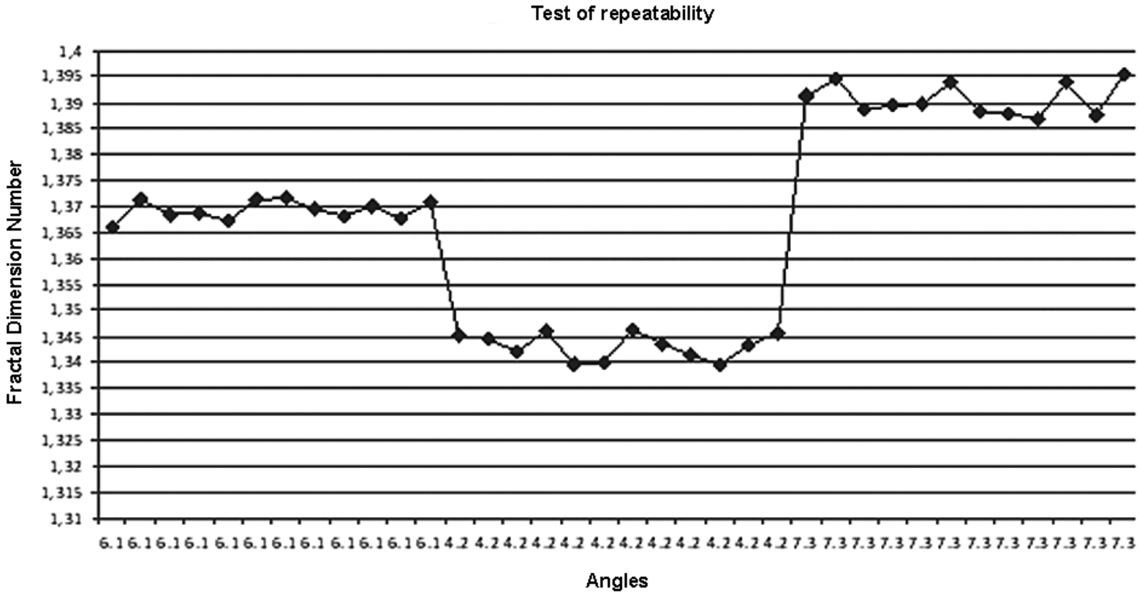

Fig. 3: Fractal dimensions for twelve tests on each of plate 6.1 (left), plate 4.2 (centre) and plate 7.3 (right)

CONCLUSIONS

Styrene vapours from unsaturated polyester resin may affect worker health and comfort, can produce an odour nuisance for neighbours and may incur environmental burdens. In composite component manufacture, the adoption of closed mould processes (*e.g.* liquid composite moulding techniques including RTM and RIFT) significantly reduces styrene emissions. Gel-coats are applied to component surfaces for cosmetic reasons and/or to enhance durability or surface function. However, the coating is normally applied to the open mould and allowed to progress to the gel state over time while styrene vapours are released to the atmosphere. A novel concept for the in-mould gel-coating (IMGC) of fibre-reinforced polymer composites has been patented. Initial RTM studies were conducted with UK TSB "Meeting the Challenge of the Zero Emission Enterprise" funding and reported at FPCM-10. A postgraduate project demonstrated that the concept was viable in resin infusion under flexible tooling (RIFT, SCRIMP^{TM}, VARTM) processes. The on-going development of IMGC is continuing in the Framework Programme 7 funded InGeCt research project (FP7_R4SME_286520_InGeCt).

ACKNOWLEDGEMENTS: The ZEE IMGC project was co-funded by the Technology Strategy Board Collaborative Research and Development programme (www.innovateuk.org). The InGeCt (www.ingect.eu) research is funded by the European Union's Seventh Framework Programme managed by REA-Research Executive Agency ([FP7/2007-2013] [FP7/2007-2011]) under grant agreement number FP7-SME-2011-1-286520. The author would like to thank William Rogers, Quentin Labrosse, Christopher Hoppins, Bharaneedharan Muralidharan and Nick Brooks for their respective contributions to the in-mould gel-coating research, the respective consortium members and David Warren (Anowo Limited) for the supply of additional trilaminate separator fabrics.

REFERENCES

1. 12th Report on Carcinogens (2011), US Department of Health and Human Services.

2. Council Directive 1999/13/EC on the limitation of emissions of volatile organic compounds due to the use of organic solvents in certain activities and installations (1999), Official Journal of the European Communities.

3. Faes E (undated circa 2011), Styrene Industry Recommends Occupational Exposure Limits, Styrene Producers Association letter.

4. Styrene: Part 1 – Environment, European Union Risk Assessment Report, European Chemicals Bureau Institute for Health and Consumer Protection Priority List 1 volume 27 (2002), European Commission Joint Research Centre report EUR 20541 EN, Luxembourg.

5. Kishi R., Katakura Y, Ikeda T, Chen BQ and Miyake H (1992), Neurochemical effects in rats following gestational exposure to styrene, Toxicol. Lett. 63(2), 141-146.

6. Mäkitie A, Pirvola U, Pyykkö I, Sakakibara H, Riihimäki V and Ylikoski J (2002), Functional and morphological effects of styrene on the auditory system of the rat, Archives of Toxicology, 76(1), 40-47.

7. Shen S, Zhang F, Gao L, Zeng S and Zheng J (2010), Detection of phenolic metabolites of styrene in mouse liver and lung microsomal incubations, Drug Metabolism and Disposition, 38(11), 1934-1943.

8. Carlson GP (2012), Modification of the metabolism and toxicity of styrene and styrene oxide in hepatic cytochrome P450 reductase deficient mice and CYP2F2 deficient mice, Toxicology, 294(2–3), 104–108.

9. May J (1966), Solvent odor thresholds for the evaluation of solvent odors in the atmosphere, *Staub-Reinhalt*, 26(9), 385-389.

10. Amoore JE and Hautala E (1983), Odor as an aid to chemical safety: odor thresholds compared with threshold limit values and volatilities for 214 industrial chemicals in air and water dilution, *Journal of Applied Toxicology*, 3(6), 272-290.

11. Åström BT (1997), Manufacturing of Polymer Composites, Chapman & Hall, London. ISBN 0-412-81960-0.

12. Norsodyne® 6417 Version Unsaturated Polyester Resin Technical Data Sheet (2005), Cray Valley, Stallingborough - Lincolnshire.

13. HSE information sheet: Assessing and controlling styrene levels during contact moulding of fibre-reinforced plastic (FRP) products (2003), Health and Safety Executive Plastics Processing Sheet 14, Sudbury - Suffolk.

14. Documentation for Immediately Dangerous To Life or Health Concentrations (IDLHs) - Styrene, (1994), Centers for Disease Control and Prevention, Atlanta - Georgia.

15. Hammond D, Garcia A and Feng HA (2011), Occupational exposure to styrene vapor in a fiber-reinforced wind blade manufacturing plant, *Annals of Occupational Hygiene*, 55(6), 591-600.

16. Styrene (2006), Chemical Safety Information from Intergovernmental Organizations, International Programme on Chemical Safety and the Commission of the European Communities.

17. Summerscales J, Hoppins C, Anstice P, Brooks N, Wiggers J, Yahathugoda D, Harper A, Wood C and Cooper M (2010), In-Mould Gel Coating for Resin Transfer Moulding, *Proc. 10th International Conference on Flow Processes in Composite Materials (FPCM-10)*, Ascona – Switzerland.

18. Summerscales J, Hoppins C, Anstice P, Brooks N, Wiggers J, Yahathugoda D, Harper A, Wood C and Cooper M (2010), In-Mould Gel Coating for Resin Transfer Moulding, *Proc. International Conference on Marine and Offshore Composites*, RINA, London.

19. Summerscales J, Hoppins C, Anstice P, Brooks N, Wiggers J, Yahathugoda D, Harper A, Wood C and Cooper M (2009), In-Mould Gel Coating for Resin Transfer Moulding, *Proc. International Conference on Manufacturing of Advanced Composites*, Belfast.

20. Harper AR, Summerscales J and Brooks N (2007), Production of composite mouldings, British Patent GB 2 432 336A.

21. Muralidharan B (2010), In-Mould Gel Coating by Resin Infusion under Flexible Tooling process, MSc Mechanical Engineering dissertation, University of Plymouth.

22. Muralidharan B and Summerscales J (2010), In-Mould Gel-Coating for Resin Infusion Processes using a Flow Medium, *Proc. 10th International Conference on Flow Processes in Composite Materials (FPCM-10)*, Ascona – Switzerland.

23. Summerscales J and Searle TJ (2005), Low-pressure (vacuum infusion) techniques for moulding large composite structures, *Proceedings of the Institution of Mechanical Engineers Part L: Journal of Materials Design and Applications*, 219(L1), 45-58.

24. Summerscales J (2012), Resin Infusion Under Flexible Tooling (RIFT), Encyclopedia of Composites – second edition, John Wiley & Sons, 2648 - 2658.

25. Labrosse Q, Hoppins CP and Summerscales J (2011), Objective assessment of the surface quality of coated surfaces, *Insight*, 53(1), 16-20.

26. Orange Peel and DOI measurement on high to semi gloss surfaces (2012), Altana BYK-Gardner USA, Columbia MD.

INVESTIGATION OF CO-LCM PROCESS AND THE CO-CURED LAMINAR INTERFACE OF CARBON FIBER COMPOSITES

Xuqiang Ma, Yizhuo Gu, Min Li*, Yanxia Li and Zuoguang Zhang

School of Materials Science and Engineering, Beihang University, Xueyuan Road, Haidian District, Beijing 100191, China. Corresponding author's e-mail: leemy@buaa.edu.cn

ABSTRACT: The carbon fiber/epoxy composite laminates were fabricated using co-LCM (co-cured liquid composite molding) process with prepreg stack. The compaction of the laminates and the diffusion of the epoxy resin in preperg and the epoxy resin for co-LCM were investigated. Mode-I delamination fracture toughness G_{1c} and short beam shear strength were measured to evaluate the co-cured laminar interface property of the composite laminates, and the data were compared with those manufactured solely by prepreg molding and LCM (liquid composite molding), respectively. Moreover, the effects of the fiber orientation at the co-cured laminar interface between prepreg part and LCM part on G_{1c} were studied. The results show that the laminates processed by co-LCM have high compaction degree in the intralaminar plies and no resin-rich area can be found between the plies. It demonstrates that interdiffusion of the two kinds of resins takes place at the co-cured laminar interface. The interlaminar fracture toughness of the co-cured laminates has the average of the data in comparison with the cases for the prepreg and the LCM laminates, and this result should be ascribed to the resin interdiffusion at the co-cured laminar interface. The fiber orientation between the prepreg and the LCM parts, at the co-cured laminar interface, has significant influences on the G_{1c} results, and [45/90] is better to resist the interlaminar fracture, as well to resist the propagation of the delamination.

KEYWORDS: *carbon fiber composites, co-LCM, prepreg, mode I interlaminar fracture toughness*

INTRODUCTION

Carbon fiber reinforced resin matrix composites have been widely used in aviation and aerospace for the remarkable performances of high strength-to-density and light weight. However, the cost of fabricating the composite part is relatively high, thus excellent product with low processing cost is one of hot research issues which have attracted many attention of researchers and engineers. Co-cured liquid composite molding [1,2] is a new manufacturing process of resin composites with the advantage of cost-saving. It combines the prepreg stacks with fiber perform, subsequently the fiber perform is infused by the resin for liquid composite molding. Finally integral composite product is co-cured with the prepreg part and LCM part in the oven. Generally, the complex structures such as stringer, joint part are processed by prepreg stacks and simple parts like skins in “T” or “I” stiffened structure are fabricated by LCM. Co-cured liquid composite molding could improve the designability on the basis of required performance for intricate structure by means of changes of fiber orientation and different perform, further achieve the purpose of time-saving and labor-saving with the advantages of reducing fasteners and assemble procedures and significantly simplifying tool design, resin infusion process for sole LCM. Co-cured liquid composite molding is established by an American company named Northrop Grumman for the first time and develops in the project of composite affordability initiative by United States department of defense. So it is a low-cost integral molding technology for carbon fiber reinforced resin matrix composites which presents bright prospect in future.

Obviously, two kinds of epoxy resins, resin in prepreg stacks and the resin for infusion, are utilized during this technology. The compatibility of two different epoxy resins has significant influences on the final performance of product. However, the investigation of fabricating process and matching ability of materials on co-cured liquid composite molding is seldom reported compared with co-injection resin transfer molding [3-6].

In our research, in order to evaluate the effect of fiber orientation and diffusion of two kinds of epoxy resins at the laminar interface, carbon fiber laminates were manufactured by co-cured liquid composite molding. Mode-I delamination fracture toughness and short beam shear strength were measured to investigated the co-cured laminar interface property of the composite laminates. These works can provide guides for the ply design and performance evaluation of composite products using this technology.

EXPERIMENTAL

Material

In this work, a unidirectional carbon fiber/epoxy resin prepreg tapes with the resin mass fraction of 38% and three-axial [0/45/90] carbon fiber fabric with the areal density of 417g/m^2 were cut into pieces with dimension of 270mm×200mm. The resin system for the preform infusion was self-made which contained the Biphenol A epoxy resin and modified multi-amine cure agent.

Fabricating of composite laminates

Three kinds of laminates were fabricated named A, B, and C respectively. The A samples were manufactured with prepreg by vacuum-bag technology; the B samples were made by vacuum infusion technique; and the C samples were molded with co-cured liquid composite molding.

A) Firstly, the 24-layer prepreg stacks were laid up with ply sequence of $[(45/90/-45/0)_3/(0/45/90/-45)_3]$ and pre-compacted under the condition of -0.1 MPa with temperature of 60 ^oC. Subsequently the prepreg stacks were cured with the temperature cycle which increased from room temperature to 130 ^oC at the rate of 2-3 ^oC/min and maintained 130 ^oC for 2 hours through vacuum-bag processing technique. The nominal cured thickness of the prepreg laminate is 3.33 mm. B) Eight pieces of three-axial carbon fiber fabric were stacked according to the sequence of [(45/90/-45)/(0/45/90)/(-45/0/45)/(90/-45/0)/(0/45/90)/(-45/0/45)/(90/-45/0)/(45/90/-45)]. The preform was sealed in the vacuum bag and then infused by the resin with the assistance of -0.1 MPa vacuum at 60 ^oC. After that, the vacuum bag was kept -0.1 MPa and placed in the oven with the temperature cycle of rising to 130 ^oC at 2-3 ^oC /min and holding for 2 hours. The final cured thickness of the laminate is 3.43 mm. C) The composite laminate fabricated by co-LCM process included twelve prepreg layers and four three-axial carbon fiber fabric which ensured to have preferably coherence with other two kinds of laminates on thickness. The schematic of co-cured liquid composite molding is presented in Fig.1. The temperature and vacuum cycle was same as that of the laminate B, and the nominal cured thickness was 3.36 mm.

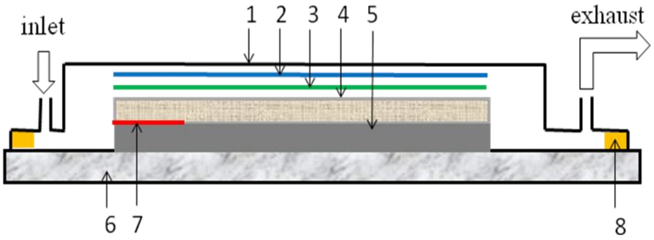

1-Vacuum bag; 2-Distribution media; 3-Peel ply; 4-Multiaxial fabric; 5-Prepreg; 6-Mold; 7-Teflon film; 8- Tacky tape.

Fig.1: Schematic of co-cured liquid composite molding

Mechanical property test

Mode-I delamination fracture toughness was measured to evaluate the co-cured laminar interface property of the composite laminates. As shown in Fig.1, the Teflon film was inserted at the co-cured laminar interface in-between the prepreg part and the LCM part, which served as a delamination initiator. Similarly, the Teflon film was also embedded on the mid-laminates which were fabricated solely by prepreg molding and LCM, respectively. After curing, the laminates using different process techniques were cut into species with dimension of 150 mm×25 mm, and the effective length of delamination initiator was 50 mm. Subsequently, the test for mode-I delamination fracture toughness was conducted based on ASTM D 5528 with a constant displacement rate 1.0 mm/min and the procedures were shown in Fig.2.

In the area without embedded Teflon film, the three kinds of laminates were cut into species with the dimension of 25 mm×6 mm for short beam shear test according to the standard of JC/T773-82(6).

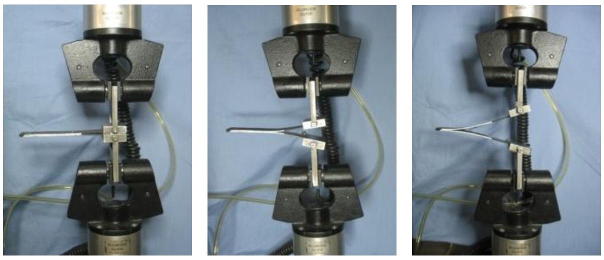

Fig.2: Process of mode-I interlaminar fracture test

Micrograph observation

Metallographic observation was used to investigate the micro-structure laminates. The cured laminates were cut into small pieces and the cross sections of samples were wet ground with successively finer silicon carbide paper and wet polished with chromium oxide. The polished sections were then observed by Olympus BX51M optical microscope. The crack surfaces of species after short beam test were also observed by the SEM and the interfacial adhesion between fiber and resin was analyzed.

RESULTS AND DISCUSSION

Analysis of co-LCM process

To clearly demonstrate the characters of co-LCM process, the fiber distribution and resin flow of laminates C were compared with laminates A and B. The micrographs of cross-sections of the laminates fabricated by the three types of processes are shown in Fig.3. Compared with Fig.3 (a), (b), the compaction of prepreg part and LCM part is very well which is presented in Fig.3(c). On one hand, no obvious resin rich region is found at the laminar interface between the two parts using co-LCM process, on the other hand, seldom defects are revealed by the micrograph. It exhibits favorable compatibility and fluidity between the two kinds of epoxies.

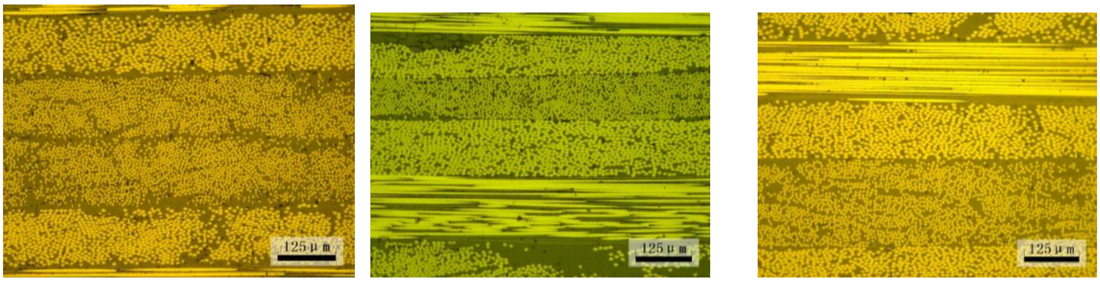

(a) prepreg laminate (b) fabric laminate by LCM (c) laminate processed by co-LCM

Fig.3: Micrographs of laminates

Fig.4 shows the viscosity evolution profile of the LCM process resin, in which the low viscosity platform reveals quite low, i.e. 0.15 Pa • s when the temperature is ranged from 50 to 140 ^{o}C. However, the viscosity of the resin of prepreg is 10 Pa • s at 60 ^{o}C. Thus, when the LCM preform was infusion by resin at 60 ^{o}C, the diffusion of two resins was believed to be merely occurred at the laminar interface due to significant discrepancy of the viscosities.

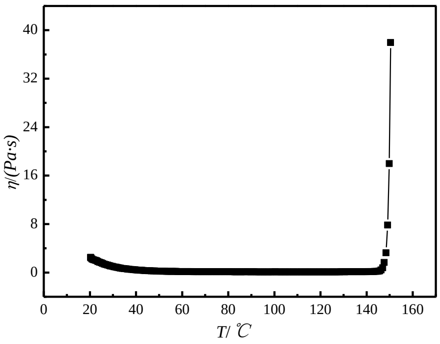

Fig. 4 The LCM resin viscosity as a function of temperature

Evaluation of co-LCM laminate

Generally, it is considered that the laminar interface which consists of the prepreg part and LCM part is the unique character for the co-LCM structure. In this paper, mode-I delamination fracture toughness is adopted to evaluate the ability of resisting damage among the laminates A, B and C mentioned above, respectively. The fiber orientation [0/0] at the laminar interface is chosen for the three kinds of laminates. The critical value of G for delamination growth for the laminates through different processes is measured. As presented in Fig.5, the results show that the LCM processed laminates give the maximum G_{1c} value. The co-LCM laminates reveal approximately equal G_{1c} value to the laminates manufactured solely by prepreg. Moreover, at the beginning 50 mm delamination length, the ability of resisting damage for laminates is decided by the weaker part. It is attributed to the Teflon film which prevents the diffusion between prepreg part and LCM part.

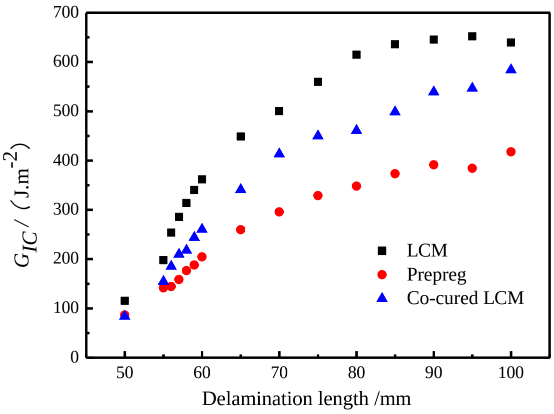

Fig.5: Delamination resistance curves of different laminates

As the delamination grows, the results of G_{1c} obtained are presented in Fig.5. It reveals that the maximum of critical value, i.e. G_{1c} comes from the LCM laminates; the smallest one is the prepreg laminates; while the co-LCM laminates display a middle value of G_{1c}. When the delamination length exceeds the original 50mm Teflon film, wherein the two different resins could diffuse to each other, G_{1c} is influenced by both the prepreg part and the LCM part in the co-LCM laminates.

Fig.6 and Fig.7 show the SEM fracture morphology at delamination area of the three kinds of laminates. From Fig.6 (a), little resin is adhered to the surface of fiber of prepreg laminates. In contrast, it is found that much resin remains on the fiber surface of the LCM laminates and the facture surface is rough, indicating that the LCM laminates are superior to prepreg laminates on delamination resistance. As shown in Fig.7 (a), the surface of fiber is smooth with rarely existing of resin in the prepreg part. However, from the morphology of LCM part, the fibers are embedded by the resin which exhibits river-like texture as the result of crack extension. It is proved that the diffusion of different resins does take place at the interface among prepreg layers, and only occurres at the laminar interface between prepreg part and LCM part.

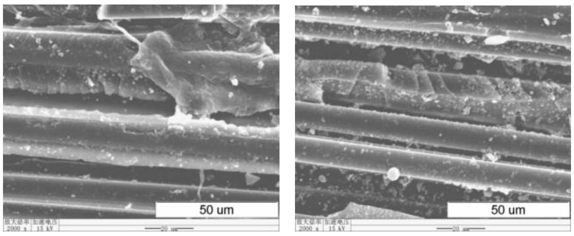

(a) prepreg laminate (b) LCM laminate

Fig.6: Fracture morphology at delaminate area of LCM and prepreg laminates, respectively.

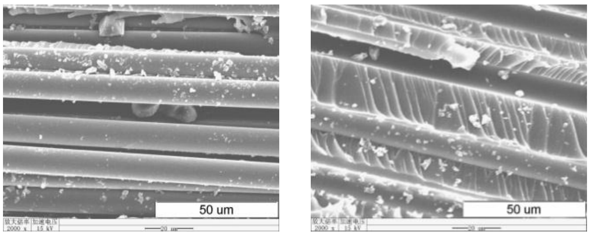

(a) Prepreg layer (b) LCM layer

Fig.7: Fracture morphology at delaminate area of co-LCM laminate

The interlaminar properties were evaluated by short beam shear test for the three kinds of laminates. The results are demonstrated in Fig.8. The shear strength of laminates fabricated by co-LCM process is equivalent to that of the laminate using LCM process which is approximately 45MPa. However, both of them are inferior to the laminates by prepreg process on the interlaminar shear strength which reaches about 60MPa as presented in Fig.8. The results indicate the interlaminar shear strength is depended on the weaker part for co-LCM process.

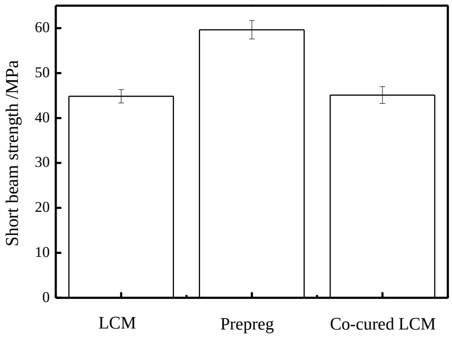

Fig.8: Short beam strength results for different composite laminates

Influence of interlaminar fiber orientation on G_{1c}

Delamination is the primary damage mode for resin composite laminates. Interlaminar fracture toughness of composite laminates was investigated by many researchers, especially the relationship between fiber orientation and interlaminar fracture toughness [7-10]. The fiber orientation of laminar interface of co-LCM process is an important parameter for stacking sequence design. Moreover, the laminar interface of co-LCM laminates is the unique feature which is different from laminates with other processes. So in our research, the effect of different interlaminar fiber orientation on G_{1c} was studied. The fiber orientation at the laminar interface between prepreg part and LCM part is detailed listed in Table 1.

Table 1: Fiber orientation at interface between prepreg part and liquid composite molding part

No.	Fiber orientation of two layers at interface	
	Prepreg layer	LCM layer
1	0	0
2	45	0
3	45	45
4	45	90

The G_{1c} of co-LCM laminates with different fiber orientation is presented in Fig.9. From Fig.9, the values of G_{1c} for fiber orientation of [45/0] and [45/90] are relatively high which reach 130 and 170 $J \bullet m^{-2}$,respectively. Compared with [45/0], the laminate with [0/0] exhibits low value on G_{1c} about 80 $J \bullet m^{-2}$. It is assumed that laminates with 45^o ply angle at the interlaminar interface by co-LCM process reveal excellent delamination resistance.

The delamination resistance curves also prove the results above as shown in Fig.10. As the delamination lengths develop from 55 to 65 mm, laminate with [0/0] at the laminar interface has the smallest value on G_{1c} among laminates with other fiber orientations. And the G_{1c} values of laminates with [45/45] and [45/90] approach to a constant after 65 mm. However, the value on G_{1c} for laminate with fiber sequence of [45/0] increases rapidly and finally reaches 1200 J • m^{-2} which is ascribed to off-axial delamination and unstable crack extension, and is not suitable for reflecting the ability of delamination resistance. Therefore, within the scope of this study, the [45/90] laminate has higher interlaminar fracture toughness than the other fiber orientation laminates.

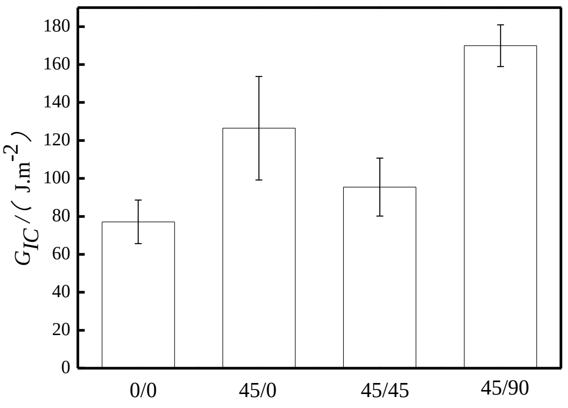

Fig.9: Critical G_{1c} values of laminates by co-LCM with different fiber orientation

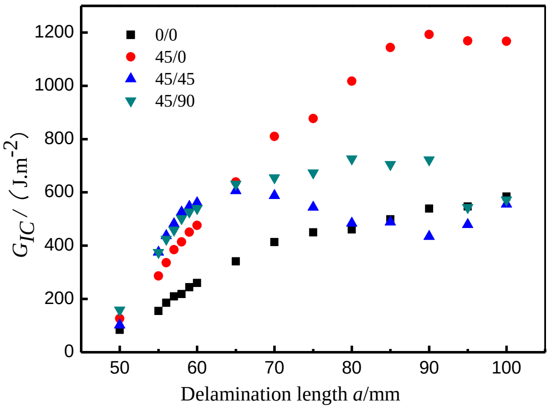

Fig.10: Delamination resistance curves of co-LCM laminates with different laminar interface fiber orientation

CONCLUSION

(1) Laminates processed by Co-LCM have high compaction degree in the interlaminar plies and no obvious resin-rich area can be found between the plies. Resin inter-diffusion only occurres at the laminar interface area as the result of viscosity difference between the prepreg resin and the LCM resin.

(2) The interlaminar fracture toughness of the co-cured laminates has the average value in comparison with the data of the prepreg laminates and the LCM laminates, which should be ascribed to the resin inter-diffusion at the co-cured laminar interface. However, the short beam shear tests of the co-cured laminates usually damage at the LCM part, which is relatively weaker than the prepreg part.

(3) The fiber orientation at the co-cured laminar interface in-between the prepreg and the LCM parts has significant influence on the resultant G_{Ic}, and the [45/90] laminate shows higher interlaminar fracture, as well to better resist the propagation of the delamination than the [0/0], [45/0], [0/45] laminates.

REFERENCES

1. Sheu CH, Shinazu DM, Kane DM (2004),'Co-cured vacuum-assisted resin transfer molding manufacturing method', *US Patent*, US 2004/0051214A1.

2. Husmann C H, Sheu CH and Shinazu DM (2008), 'Co-cured resin transfer molding manufacturing method', *US Patent*, US 7374715B2.

3. Gillio EF, Advani SG, Gillespie JW and Fink BK (1998), 'Investigation of the role of transverse flow in co-injection resin transfer molding', *Polymer composites*, 19(6), 738-746.

4. Fink BK, Gillespie J, Gillio E and Bernetich K (2000), 'One-step resin transfer molding of multifunctional composites consisting of multiple resins', *US Parent*, 6048488.

5. Harkare A, Gillespie JR (2004), 'In situ barrier layer formation for coinjection resin transfer molding', *Joumal of Thermoplastic Composite Materials,* 17(5), 387-409.

6. Yin CP (2009), 'Fabricating Load Bearing/Heat Insulation/Thermal Protection Integral Composite by Co-injection RTM Process', National University of defense technology, Changsha.

7. Yang Y, Chai YN, Chi J, Chen XM and Lin GW (2011), 'Experimental study on effect of fiber angel orientation and mixed-mode ratio on fracture toughness of fiber reinforced laminate', *Acta Materiae Compositae Sinica,* 28(1), 161-165.

8. Morais AB, Moura MF, Marques AT and Castro PT (2002), ‘Mode-I interlaminar fracture of carbon / epoxy cross-ply composites’, *Composites Science and Technology*, 62(5), 679-686.

9. Prombut P, Michel L, Lachaud F and Barrau JJ (2006), ‘Delamination of multidirectional composite laminates at 0°/*θ*° ply interfaces’, *Engineering Fracture Mechanics*, 73(16), 2427-2442.

10. Pereira AB and Morais AB (2004), ‘Mode-I interlaminar fracture of carbon/epoxy multidirectional laminates’, *Composites Science and Technology*, 64(13-14), 2261-2270.

Author List

The University of Auckland

The Faculty of Engineering

The Centre for Advanced Composite Materials

THE UNIVERSITY OF AUCKLAND
NEW ZEALAND
Te Whare Wānanga o Tāmaki Makaurau

Organised by:
The Centre for Advanced Composite Materials
Department of Mechanical Engineering
The University of Auckland
www.cacm.auckland.ac.nz